

---

# **FERROELECTRICS – PHYSICAL EFFECTS**

---

Edited by **Mickaël Lallart**

**INTECHWEB.ORG**

## **Ferroelectrics – Physical Effects**

Edited by Mickaël Lallart

### **Published by InTech**

Janeza Trdine 9, 51000 Rijeka, Croatia

### **Copyright © 2011 InTech**

All chapters are Open Access articles distributed under the Creative Commons Non Commercial Share Alike Attribution 3.0 license, which permits to copy, distribute, transmit, and adapt the work in any medium, so long as the original work is properly cited. After this work has been published by InTech, authors have the right to republish it, in whole or part, in any publication of which they are the author, and to make other personal use of the work. Any republication, referencing or personal use of the work must explicitly identify the original source.

Statements and opinions expressed in the chapters are these of the individual contributors and not necessarily those of the editors or publisher. No responsibility is accepted for the accuracy of information contained in the published articles. The publisher assumes no responsibility for any damage or injury to persons or property arising out of the use of any materials, instructions, methods or ideas contained in the book.

**Publishing Process Manager** Silvia Vlase

**Technical Editor** Teodora Smiljanic

**Cover Designer** Jan Hyrat

**Image Copyright** 2010. Used under license from Shutterstock.com

First published July, 2011

Printed in Croatia

A free online edition of this book is available at [www.intechopen.com](http://www.intechopen.com)  
Additional hard copies can be obtained from [orders@intechweb.org](mailto:orders@intechweb.org)

Ferroelectrics – Physical Effects, Edited by Mickaël Lallart

p. cm.

ISBN 978-953-307-453-5

**INTECH** OPEN ACCESS  
PUBLISHER

**INTECH** open

**free** online editions of InTech  
Books and Journals can be found at  
**[www.intechopen.com](http://www.intechopen.com)**



---

# Contents

---

## **Preface IX**

### **Part 1 General Ferroelectricity 1**

- Chapter 1 **Morphotropic Phase Boundary in Ferroelectric Materials 3**  
Abdel-Baset M. A. Ibrahim, Rajan Murgan,  
Mohd Kamil Abd Rahman and Junaidah Osman
- Chapter 2 **Relaxor-ferroelectric PMN-PT Thick Films 27**  
Hana Uršič and Marija Kosec
- Chapter 3 **Phase Diagramm, Crystallization Behavior and Ferroelectric Properties of Stoichiometric Glass Ceramics in the BaO-TiO<sub>2</sub>-B<sub>2</sub>O<sub>3</sub> System 49**  
Rafael Hovhannisyan, Hovakim Alexanyan,  
Martun Hovhannisyan, Berta Petrosyan  
and Vardan Harutyunyan
- Chapter 4 **Ferroelectric Properties and Polarization Switching Kinetic of Poly (vinylidene fluoride-trifluoroethylene) Copolymer 77**  
Duo Mao, Bruce E. Gnade and Manuel A. Quevedo-Lopez
- Chapter 5 **Charge Transport in Ferroelectric Thin Films 101**  
Lucian Pintilie
- Chapter 6 **Hydrogen in Ferroelectrics 135**  
Hai-You Huang, Yan-Jing Su and Li-Jie Qiao
- Chapter 7 **Thermal Conduction Across Ferroelectric Phase Transitions: Results on Selected Systems 155**  
Jacob Philip
- Chapter 8 **The Induced Antiferroelectric Phase - Structural Correlations 177**  
Marzena Tykarska

**Part 2 Piezoelectrics 193**

- Chapter 9 **Piezoelectric Effect in Rochelle Salt 195**  
Andriy Andrusyk

- Chapter 10 **Piezoelectricity in Lead-Zirconate-Titanate Ceramics –  
Extrinsic and Intrinsic Contributions 221**  
Johannes Frantti and Yukari Fujioka

- Chapter 11 **B-site Multi-element Doping Effect on Electrical  
Property of Bismuth Titanate Ceramics 243**  
Jungang Hou and R. V. Kumar

**Part 3 Magnetolectrics and Multiferroics 275**

- Chapter 12 **Magnetolectric Multiferroic Composites 277**  
M. I. Bichurin, V. M. Petrov and S. Priya

- Chapter 13 **Coupling Between Spins and Phonons Towards  
Ferroelectricity in Magnetolectric Systems 303**  
J. Agostinho Moreira and A. Almeida

- Chapter 14 **Ferroelectric Field Effect Control of Magnetism  
in Multiferroic Heterostructures 329**  
Carlos A. F. Vaz and Charles H. Ahn

- Chapter 15 **Effects of Doping and Oxygen Nonstoichiometry  
on the Thermodynamic Properties of Some  
Multiferroic Ceramics 347**  
Speranta Tanasescu, Alina Botea and Adelina Ianculescu

- Chapter 16 **Multifunctional Characteristics of B-site  
Substituted BiFeO<sub>3</sub> Films 373**  
Hiroshi Naganuma

**Part 4 Liquid Crystals and Optical Effects 405**

- Chapter 17 **Ferroelectric Liquid Crystals with  
High Spontaneous Polarization 407**  
Slavomír PirkI and Milada Glogarová

- Chapter 18 **Ferroelectric Liquid Crystals Composed  
of Banana-Shaped Thioesters 429**  
Stanisław Wróbel, Janusz Chruściel, Marta Wierzejska-Adamowicz,  
Monika Marzec, Danuta M. Ossowska-Chruściel,  
Christian Legrand and Redouane Douali

- Chapter 19 **Molecular Design of a Chiral Oligomer for Stabilizing a Ferrielectric Phase** 449  
Atsushi Yoshizawa and Anna Noji
- Chapter 20 **Memory Effects in Mixtures of Liquid Crystals and Anisotropic Nanoparticles** 471  
Marjan Krašna, Matej Cvetko, Milan Ambrožič and Samo Kralj
- Chapter 21 **Photorefractive Ferroelectric Liquid Crystals** 487  
Takeo Sasaki
- Chapter 22 **Linear and Nonlinear Optical Properties of Ferroelectric Thin Films** 507  
Bing Gu and Hui-Tian Wang
- Chapter 23 **Localized States in Narrow-Gap Ferroelectric-Semiconductor PbSnTe: Injection Currents, IR and THz Photosensitivity, Magnetic Field Effects** 527  
Alexander Klimov and Vladimir Shumsky
- Chapter 24 **Piezo-optic and Dielectric Behavior of the Ferroelectric Lithium Heptagermanate Crystals** 553  
A. K. Bain, Prem Chand and K. Veerabhadra Rao
- Chapter 25 **Compositional and Optical Gradient in Films of  $\text{PbZr}_x\text{Ti}_{1-x}\text{O}_3$  (PZT) Family** 579  
Ilze Aulika, Alexandr Dejneka, Silvana Mergan, Marco Crepaldi, Lubomir Jastrabik, Qi Zhang, Andreja Benčan, Maria Kosec and Vismants Zauls
- Chapter 26 **Photo-induced Effect in Quantum Paraelectric Materials Studied by Transient Birefringence Measurement** 603  
Toshiro Kohmoto and Yuka Koyama
- Chapter 27 **Photoluminescence in Doped PZT Ferroelectric Ceramic System** 619  
M. D. Durruthy-Rodríguez and J. M. Yáñez-Limón
- Chapter 28 **Photovoltaic Effect in Ferroelectric  $\text{LiNbO}_3$  Single Crystal** 641  
Zhiqing Lu, Kun Zhao and Xiaoming Li



---

# Preface

---

Ferroelectricity has been one of the most used and studied phenomena in both scientific and industrial communities. Properties of ferroelectric materials make them particularly suitable for a wide range of applications, ranging from sensors and actuators to optical or memory devices. Since the discovery of ferroelectricity in Rochelle Salt (which used to be used since 1665) in 1921 by J. Valasek, numerous applications using such an effect have been developed. First employed in large majority in sonars in the middle of the 20<sup>th</sup> century, ferroelectric materials have been able to be adapted to more and more systems in our daily life (ultrasound or thermal imaging, accelerometers, gyroscopes, filters...), and promising breakthrough applications are still under development (non-volatile memory, optical devices...), making ferroelectrics one of tomorrow's most important materials.

The purpose of this collection is to present an up-to-date view of ferroelectricity and its applications, and is divided into four books:

- *Material Aspects*, describing ways to select and process materials to make them ferroelectric.
- *Physical Effects*, aiming at explaining the underlying mechanisms in ferroelectric materials and effects that arise from their particular properties.
- *Characterization and Modeling*, giving an overview of how to quantify the mechanisms of ferroelectric materials (both in microscopic and macroscopic approaches) and to predict their performance.
- *Applications*, showing breakthrough use of ferroelectrics.

Authors of each chapter have been selected according to their scientific work and their contributions to the community, ensuring high-quality contents.

The present volume is interested in the explanation of the physical mechanisms that lie in ferroelectrics, and the associated effects that make ferroelectric materials so interesting in numerous applications.

After a general introduction on ferroelectric and ferroelectric materials (chapters 1 to 8), the book will focus on particular effects associated with ferroelectricity: piezoelec-

tricity (chapters 9 to 11), optical properties (chapters 12 to 16), and multiferroic and magnetoelectric devices (chapters 17 to 28), reporting up-to-date findings in the field.

I sincerely hope you will find this book as enjoyable to read as it was to edit, and that it will help your research and/or give new ideas in the wide field of ferroelectric materials.

Finally, I would like to take the opportunity of writing this preface to thank all the authors for their high quality contributions, as well as the InTech publishing team (and especially the publishing process manager, Ms. Silvia Vlase) for their outstanding support.

June 2011

**Dr. Mickaël Lallart**  
INSA Lyon, Villeurbanne  
France





# **Part 1**

## **General Ferroelectricity**



# Morphotropic Phase Boundary in Ferroelectric Materials

Abdel-Baset M. A. Ibrahim<sup>1</sup>, Rajan Murgan<sup>2</sup>,  
Mohd Kamil Abd Rahman<sup>1</sup> and Junaidah Osman<sup>3</sup>

<sup>1</sup>*School of Physics and Material Sciences, Faculty of Applied Sciences,  
Universiti Teknologi MARA, Selangor*

<sup>2</sup>*Gustavus Adolphus College, Saint Peter*

<sup>3</sup>*School of Physics, Universiti Sains Malaysia, Penang*

<sup>1,3</sup>*Malaysia*

<sup>2</sup>*USA*

## 1. Introduction

Certain solid solutions of perovskite-type ferroelectrics show excellent properties such as giant dielectric response and high electromechanical coupling constant in the vicinity of the morphotropic phase boundary (MPB). These materials are of importance to applications such as electrostrictive actuators and sensors, because of the large dielectric and piezoelectric constants (Jaffe et al., 1971; Sawaguchi, 1953; Kuwata et al., 1982; Newnham, 1997). The term “morphotropic” was originally used to refer to phase transitions due to changes in composition (Ahart et al., 2008). Nowadays, the term ‘morphotropic phase boundaries’ (MPB) is used to refer to the phase transition between the tetragonal and the rhombohedral ferroelectric phases as a result of varying the composition or as a result of mechanical pressure (Jaffe et al., 1954; Yamashita, 1994; Yamamoto & Ohashi, 1994; Cao & Cross, 1993; Amin et al., 1986; Ahart et al., 2008). In the vicinity of the MPB, the crystal structure changes abruptly and the dielectric properties in ferroelectric (FE) materials and the electromechanical properties in piezoelectric materials become maximum.

The common ferroelectric materials used for MPB applications is usually complex-structured solid solutions such as lead zirconate titanate -  $\text{PbZr}_{1-x}\text{Ti}_x\text{O}_3$  (PZT) and Lead Magnesium niobate-lead titanate  $(1-x)\text{PbMg}_{1/3}\text{Nb}_{2/3}\text{O}_3-x\text{PbTiO}_3$ , shortly known as PMN-PT. For example, PZT is a perovskite ferroelectrics which has a MPB between the tetragonal and rhombohedral FE phases in the temperature-composition phase diagram. However, these materials are complex-structured and require a complicated and costly process to prepare its solid solutions. Furthermore, the study of the microscopic origin of its properties is very complicated.

Recently, scientists started to pay attention to the MPB in simple-structured pure compound ferroelectric materials such as ferroelectric oxides. For example, a recent experimental study on lead titanate proved that  $\text{PbTiO}_3$  can display a large MPB under pressure (Ahart et al., 2008). These experimental results even showed richer phase diagrams than those predicted by first-principle calculations. Therefore, it is of particular importance to study the

fundamental theory of dielectric as well as piezoelectric properties of such materials in the vicinity of the MPB. Such knowledge helps engineering specific simple-structured nonlinear (NL) materials with highly nonlinear dielectric and piezoelectric properties.

Apart from first principle calculations, an alternative way to investigate the dielectric or the piezoelectric properties of these materials is to use the free energy formalism. In this chapter, we investigate the behavior of both the dynamic and the static dielectric susceptibilities in ferroelectrics in the vicinity of the MPB based on the free energy formalism. The origin of the large values of the linear and the nonlinear dielectric susceptibility tensor components is investigated using semi-analytic arguments derived from both Landau-Devonshire (LD) free energy and the Landau-Khalatnikov (LK) dynamical equation. We show that, not only the static linear dielectric constant is enhanced in the vicinity of the MPB but also the second and the third-order static nonlinear susceptibilities as well. Furthermore, the behavior of the dynamic nonlinear dielectric susceptibility as a function of the free energy parameters is also investigated for various operating frequencies. This formalism enables us to understand the enhancement of the dielectric susceptibility tensors within the concept of ferroelectric soft-modes. The input parameters used to generate the results is taken from an available experimental data of barium titanate  $\text{BaTiO}_3$  (A common simple-structured ferroelectric oxide). The effect of operating frequency, and temperature, on the dynamic dielectric susceptibility is also investigated. The enhancement of various elements of particular nonlinear optical NLO process such as second-harmonic generation (SHG) and third-harmonic generation (THG) is investigated. The enhancement of these linear and nonlinear optical processes is compared with typical values for dielectrics and ferroelectrics.

The importance of this calculation lies in the idea that the free energy material parameters  $\beta_1$  and  $\beta_2$  may be regarded as a function of the material composition. Therefore, this calculation can be used as one of the general guiding principles in the search for materials with large NL dielectric susceptibility coefficients. Such knowledge of MPB helps engineering specific NL materials with highly nonlinear dielectric properties. In addition, the work presented here may stimulate further interest in the fundamental theory of nonlinear response of single ferroelectric crystals with simple structure such as  $\text{BaTiO}_3$  or  $\text{PbTiO}_3$ . Such pure compounds with simple structure can be used for technological applications rather than material with complicated structure.

Ishibashi & Iwata (1998) were the first to propose a physical explanation of the MPB on the basis of a Landau-Devonshire-type of free energy with terms up to the fourth order in the polarization by adopting a “golden rule” and obtaining the Hessian matrix. They expressed the static dielectric susceptibility  $\chi(\omega=0)$  in terms of the model parameters. They found that  $\chi(\omega=0)$  diverges at the MPB. In the free-energy formalism, the MPB is represented by  $\beta_1 = \beta_2$  where  $\beta_1$  and  $\beta_2$  are material parameters represent the coefficients of the second and fourth-order invariants in the free energy  $F$ . They explained the large dielectric and piezoelectric constants in the MPB region as a result of transverse instability of the order parameter (Ishibashi & Iwata, 1999<sup>a,b,c</sup>; Ishibashi, 2001; Iwata et al., 2002<sup>a,b</sup>). Such transverse instability is perpendicular to the radial direction in the order-parameter space near the MPB (Iwata et al., 2005). However, the work by Ishibashi et al. was limited to the study of the MPB for the static linear dielectric constant only and never extended to include the nonlinear dielectric susceptibility. Perhaps, this is because the expressions of the nonlinear

dielectric susceptibility tensor components in terms of the free energy parameters were not yet formulated.

In earlier work by Osman et al. (1998<sup>a,b</sup>), the authors started to derive expressions for the nonlinear optical (NLO) susceptibilities of ferroelectric (FE) in the far infrared (FIR) spectral region based on the free energy formulation and Landau-Khalatnikov equation. The core part of this formulation is that the NLO susceptibilities are evaluated as a product of linear response functions. However, the work by Osman et al. was obtained under the approximation of a scalar polarization which only allows them to obtain specific nonlinear susceptibility elements. Soon after that, Murgan et al. (2002), presented a more general formalism for calculating all the second and third-order nonlinear susceptibility coefficients based on the Landau-Devonshire (LD) free energy expansion and the Landau-Khalatnikov (LK) dynamical equation. In their work they provided detailed results for all the nonvanishing tensor elements of the second and third -order nonlinear optical coefficients in the paraelectric, tetragonal and rhombohedral phase under single frequency approximation and second-order phase transitions.

Our aim here is then to utilize the expressions for the NLO susceptibility tensor components derived by Murgan et al (2002) to extend the study of the MPB to the second and third-order nonlinear susceptibility. Further, both the dynamic and static case is considered and an explanation based on the FE soft modes is provided. Because the expressions for the dielectric susceptibility given by Murgan et al. (2002) do not immediately relate to the MPB, we will first transform them into an alternative form that shows the explicit dependence on the transverse optical (TO) phonon mode and the longitudinal optical (LO) modes. The enhancement of the dynamic nonlinear susceptibility tensors is then investigated within the concept of the ferroelectric soft-mode with normal frequency  $\omega_r$ . Within the free energy formulation, the soft-mode  $\omega_r$  is found to include the parameter  $(\beta_1 - \beta_2)$  as well as the parameter  $(T - T_c)$ .

## 2. Background on morphotropic phase boundary (MPB)

Most studies on MPB is performed on a complex structured ferroelectric or piezoelectric materials such as PZT or PZN-PT and only recently studies on simple structure pure ferroelectric materials such as BaTiO<sub>3</sub> or PbTiO<sub>3</sub> took place. In this section we will shortly review both theoretical and experimental results on the most common MPB materials and its main findings. Early experimental work on MPB focused mainly on the behavior of piezoelectric constant. This is because most of the measurements were based on diffraction which measure distortion of a unit cell. For example, Shirane & Suzuki (1952) and Sawgushi (1953) found that PZT solid solutions have a very large piezoelectric response near the MPB region. Results of this kind are reviewed by Jaffe et al (1971) who first introduced the phrase "morphotropic phase diagram". A typical temperature-composition phase diagram for PZT is shown in Fig.1. The graph is after Noheda et al. (2000<sup>a</sup>). As shown in Fig. 1, the MPB is the boundary between the tetragonal and the rhombohedral phases and it occurs at the molar fraction compositions close to  $x = 0.47$ . In addition, the MPB boundary is nearly vertical in temperature scale. Above the transition temperature, PZT is cubic with the perovskite structure. At lower temperature the material becomes ferroelectric, with the symmetry of the ferroelectric phase being tetragonal ( $F_T$ ) for Ti-rich compositions and rhombohedral ( $F_R$ ) for Zr-rich compositions. Experimentally, the maximum values of the dielectric permittivity,

piezoelectric coefficients and the electromechanical coupling factors of PZT at room temperature occur at this MPB (Jaffe et al., 1971). However, the maximum value of the remanent polarization is shifted to smaller Ti contents.

For ferroelectrics with rhombohedral and tetragonal symmetries on the two sides of the MPB, the polar axes are (1,1,1) and (0,0,1) (Noheda et al., 1999). The space groups of the tetragonal and rhombohedral phases ( $P4mm$  and  $R3m$ , respectively) are not symmetry-related, so a first order phase transition is expected at the MPB. However, this has never been observed and, only composition dependence studies are available in the literature. Because of the steepness of the phase boundary, any small compositional inhomogeneity leads to a region of phase coexistence (Kakegawa et al., 1995; Mishra & Pandey, 1996; Zhang et al., 1997; Wilkinson et al., 1998) that conceals the tetragonal-to-rhombohedral phase transition. The width of the coexistence region has been also connected to the particle size (Cao & Cross, 1993) and depends on the processing conditions, so a meaningful comparison of available data in this region is often not possible.

Various studies (Noheda et al., 1999; Noheda et al., 2000a; Noheda et al., 2000b; Guo et al., 2000; Cox et al., 2001) have revealed further features of the MPB. High resolution x-ray powder diffraction measurements on homogeneous sample of PZT of excellent quality have shown that in a narrow composition range there is a monoclinic phase exists between the well known tetragonal and rhombohedral phases. They pointed out that the monoclinic structure can be pictured as providing a “bridge” between the tetragonal and rhombohedral structures. The discovery of this monoclinic phase led Vanderbilt & Cohen (2001) to carry out a topological study of the possible extrema in the Landau-type expansions continued up to the twelfth power of the polarization. They conclude that to account for a monoclinic phase it is necessary to carry out the expansion to at least eight orders. It should be noted that the free energy used to produce our results for the MPB means that our results apply only to the tetragonal and rhombohedral phases, however, since these occupy most of the  $(\beta_1, \beta_2)$  plane, the restriction is then not too severe.

As mentioned above, the common understanding of continuous-phase transitions through the MPB region from tetragonal to rhombohedral, are mediated by intermediate phases of monoclinic symmetry, and that the high electromechanical response in this region is related to this phase transition. High resolution x-ray powder diffraction measurements on poled  $PbZr_{1-x}Ti_xO_3$  (PZT) ceramic samples close to the MPB have shown that for both rhombohedral and tetragonal compositions the piezoelectric elongation of the unit cell does not occur along the polar directions but along those directions associated with the monoclinic distortion (Guo et al., 2000). A complete thermodynamic phenomenological theory was developed by Haun et al., (1989) to model the phase transitions and single-domain properties of the PZT system. The thermal, elastic, dielectric and piezoelectric parameters of ferroelectric single crystal states were calculated. A free energy analysis was used by Cao & Cross (1993) to model the width of the MPB region. The first principles calculations on PZT have succeeded in reproducing many of the physical properties of PZT (Saghi-Szabo et al., 1999; Bellaiche & Vanderbilt, 1999). However, these calculations have not yet accounted for the remarkable increment of the piezoelectric response observed when the material approaches its MPB. A complicating feature of the MPB is that its width is not well defined because of compositional homogeneity and sample processing conditions (Kakegawa et al., 1995).

Another system that has been extensively studied is the  $\text{Pb}(\text{Zn}_{1/3}\text{Nb}_{2/3})\text{O}_3$ - $\text{PbTiO}_3$  (PZN-PT) solid solution. It is a relaxor ferroelectric with a rhombohedral to tetragonal MPB similar to PZT. It shows excellent properties for applications such as sensors and electrostrictive actuators (Kuwata et al., 1981; Kuwata et al., 1982; Iwata et al., 2002<sup>b</sup>; Cross, 1987; Cross, 1994). The giant dielectric response in relaxors and related materials is the most important properties for applications. This is because the large dielectric response means a large dielectric constant and high electromechanical coupling constant.

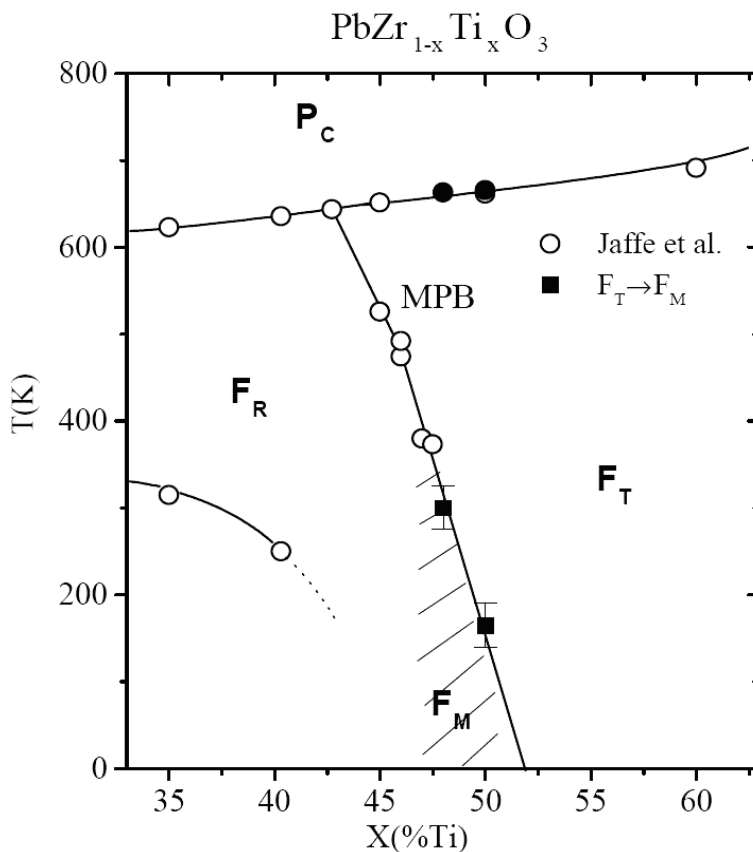


Fig. 1. The temperature-composition phase diagram for PZT where  $P_C$  is the paraelectric cubic phase,  $F_T$  is the ferroelectric tetragonal phase,  $F_R$  is the ferroelectric rhombohedral phase and  $F_M$  is the ferroelectric monoclinic phase. The nearly horizontal line represents the boundary between the paraelectric phase and the ferroelectric phase while the nearly vertical line represents the MPB between the tetragonal and the rhombohedral phase. The open circles represent the results obtained by Jaffe et al., (1971) while the black circles and squares represent the modifications introduced by Noheda et al., (2000<sup>a</sup>). The monoclinic phase existed at the MPB is represented by the dashed area. The graph is after Noheda et al. (2000<sup>a</sup>).

Iwata et al. (2002b; 2005) have theoretically discussed the phase diagram, dielectric constants, elastic constants, piezoelectricity and polarization reversal in the vicinity of the MPB in perovskite-type ferroelectrics and rare-earth-Fe<sub>2</sub> compounds based on a Landau-type free energy function. They clarified that the instability of the order parameter perpendicular to the radial direction in the order-parameter space near the MPB. Such instability is induced by the isotropy or small anisotropy of the free-energy function. In addition, the transverse instability is a common phenomenon, appearing not only in the perovskite-type ferroelectric oxides, but also in magnetostrictive alloys consisting of rare-earth-Fe<sub>2</sub> compound (Ishibashi & Iwata, 1999c), in the low-temperature phase of hexagonal BaTiO<sub>3</sub> (Ishibashi, 2001) and in shape memory alloys (Ishibashi & Iwata, 2003; Iwata & Ishibashi, 2003). They also noted that the origins of the enhancement of the responses near the MPB both in the perovskite-type ferroelectrics and the rare-earth-Fe<sub>2</sub> compounds are the same. Even more, Iwata & Ishibashi (2005) have also pointed out that the appearance of the monoclinic phase and the giant piezoelectric response can be explained as a consequence of the transverse instability as well.

A first principles study was done by Fu & Cohen (2000) on the ferroelectric perovskite, BaTiO<sub>3</sub>, which is similar to single-crystal PZN-PT but is a simpler system to analyze. They suggested that a large piezoelectric response could be driven by polarization rotation induced by an external electric field rotation (Fu & Cohen, 2000; Cohen, 2006). Recently, these theoretical predictions of MPB on a single BaTiO<sub>3</sub> crystal have been experimentally confirmed by Ahart et al. (2008) on a pure single crystal of PbTiO<sub>3</sub> under pressure. These results on BaTiO<sub>3</sub> and PbTiO<sub>3</sub> open the door for the use of pure single crystals with simple structure instead of complex materials like PZT or PMN-PT (PbMg<sub>1/3</sub>Nb<sub>2/3</sub>O<sub>3</sub>-PbTiO<sub>3</sub>) that complicates their manufacturing as well as introducing complexity in the study of the microscopic origins of their properties (Ahart et al., 2008). Moreover, Ahart et al. (2008) results on the MPB of PbTiO<sub>3</sub> shows a richer phase diagram than those predicted by first principle calculations. It displays electromechanical coupling at the transition that is larger than any known and proves that the complex microstructures or compositions are not necessary to obtain strong piezoelectricity. This opens the door to the possible discovery of high-performance, pure compound electromechanical materials, which could greatly decrease costs and expand the utility of piezoelectric materials. For the above mentioned reasons, we are motivated here to study the NL behavior of a pure single FE with simple crystal structure such as PbTiO<sub>3</sub> or BaTiO<sub>3</sub> at the MPB on the basis of the free-energy model.

### 3. The concept of morphotropic phase boundary (MPB) in the free energy

The first published paper on modeling the MPB using the Landau-Devonshire-type of free energy was made by Ishibashi and Iwata (1998). The authors basically used the free energy  $F$  as a function of the dielectric polarization in the following form;

$$F(P) = F_0 + \frac{\alpha}{2\epsilon_0} [P_x^2 + P_y^2 + P_z^2] + \frac{\beta_1}{4\epsilon_0^2} [P_x^4 + P_y^4 + P_z^4] + \frac{\beta_2}{2\epsilon_0^2} (P_x^2 P_y^2 + P_y^2 P_z^2 + P_z^2 P_x^2) \quad (1)$$

The former expression for the free energy may simply be written in the form  $F = F_0 + \Delta F$  where  $F_0$  is the free energy is for the paraelectric phase. In Eq. (1),  $\alpha$  is a temperature dependent coefficient with  $\alpha = a(T - T_c)$  where  $a$  is the inverse of the Curie

constant,  $T$  is the thermodynamic temperature, and  $T_c$  is the Curie temperature. The authors found that the static linear dielectric constant for both tetragonal and rhombohedral phases diverges at the MPB when  $\beta_1 = \beta_2$  in the free energy function. They proposed a phase diagram in the  $T - \beta_2/\beta_1$  plane to explain the MPB as a function of the material parameters  $\beta' = \beta_2/\beta_1$ . This diagram is reproduced in Fig. 2 for completeness. The vertical dotted line at  $\beta_1 = \beta_2$  represents the MPB between the rhombohedral and tetragonal phase for the static linear  $\chi(\omega=0)$ . The solid longitudinal line represents the boundary between the high temperature phase (Cubic) and the ferroelectric (FE) phases. It should be noted that the thermodynamic stability of the FE phases requires that  $F \rightarrow \infty$  as  $|P| \rightarrow \infty$  for any direction of the polarization  $P$ . In the region of the  $\beta$  plane defined by  $\beta_1 > \beta_2$  and  $\beta_1 + 2\beta_2 > 0$ , the cubic-rhombohedral transitions of the second-order occurs. And the region defined by  $\beta_2 > \beta_1 > 0$ , the cubic-tetragonal transition of the second-order occurs.

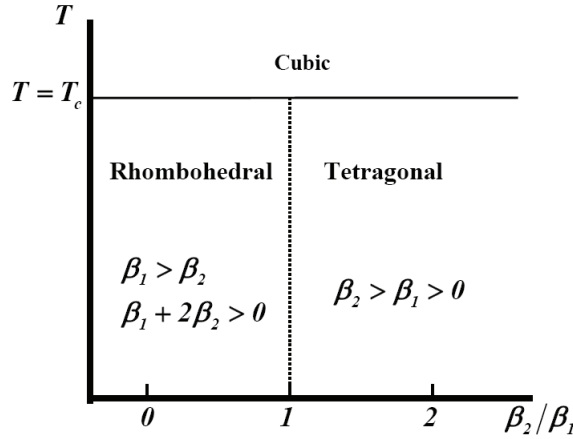


Fig. 2. The temperature-composition ( $T - \beta_2/\beta_1$ ) phase diagram with the vertical dotted line represents the MPB (after Ishibashi & Iwata 1998).

In Eq. (1), if  $\beta_1 = \beta_2$ , the free energy becomes isotropic and therefore, there is no difference between tetragonal and rhombohedral phases. To explain this, consider the polarization components  $P_x, P_y$  and  $P_z$  taken along a set of orthogonal geometrical axis and the free energy is represented by a surface where its shape depends on the value of  $\beta_1$  and  $\beta_2$ . The case of  $\beta_1 = \beta_2$ , the free energy is isotropic and represented by a sphere in the  $xyz$  frame of reference. In the tetragonal phase the free energy surface is elongated in the direction of the spontaneous polarization to assume the shape of an ellipse (Murgan et al., 2002a). For example, if the spontaneous polarization is taken along the  $z$ -direction, therefore, the ellipsoid is elongated along this axis as seen in Fig.3 which illustrates the uniaxial nature of the tetragonal symmetry. The intersection of the isotropic surface and the tetragonal surface occurs only at the  $P_x - P_y$  plane. In the rhombohedral phase, the spontaneous polarization is along the  $(1,1,1)$  direction and the free energy is not only elongated in the  $z$ -direction but also rotated as seen in Fig. 4. At the MPB the energy surface becomes isotropic but still rotated with reference to the original frame (Murgan et al., 2002a). In the previous theoretical

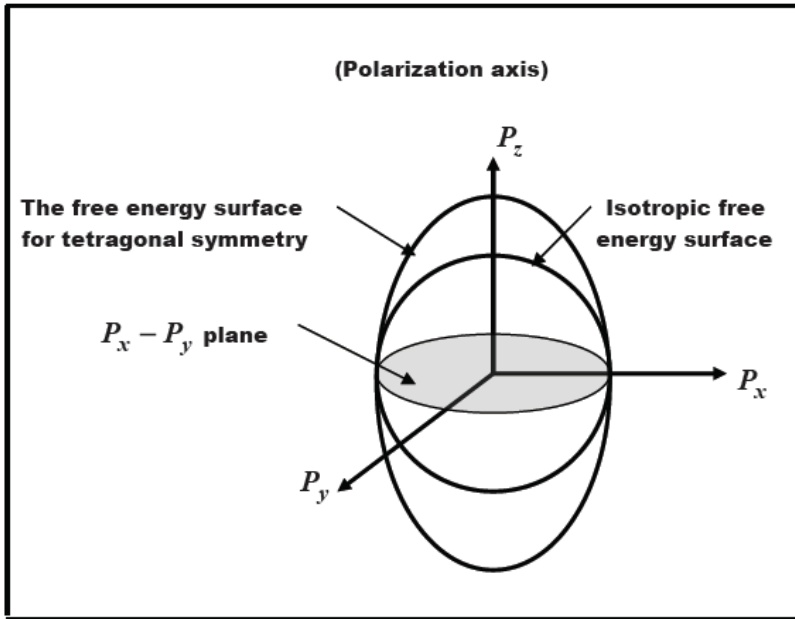


Fig. 3. The free energy surfaces for the isotropic and tetragonal systems (After Murgan et al., 2002<sup>a</sup>)

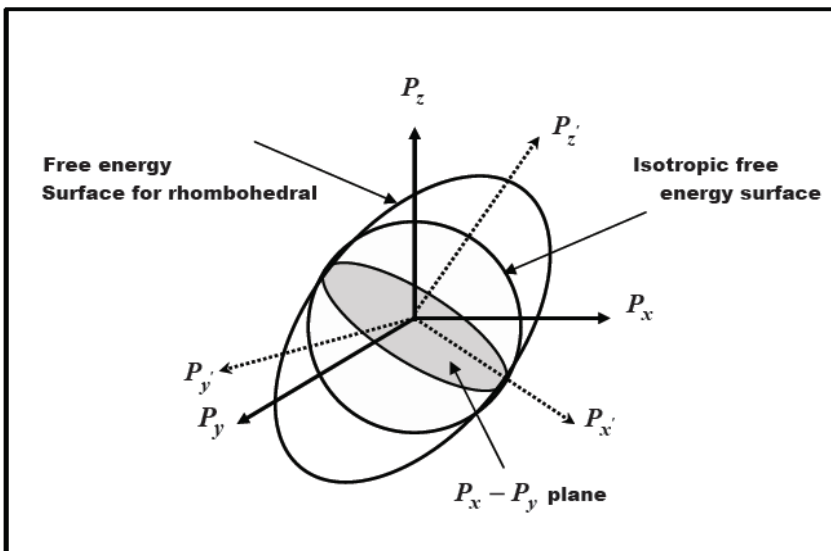


Fig. 4. The free energy surfaces for the isotropic and rhombohedral systems. ( After (Murgan et al., 2002<sup>a</sup>)

calculations using the free energy, Haun et al., (1989) had directly related the MPB to the composition in  $\text{PbZrO}_3\text{:PbTiO}_3$  solid solution family where the relation between the material parameters  $\beta_1$  and  $\beta_2$  were overlooked. In fact Ishibashi & Iwata (1998, 1999<sup>a</sup>, 1999<sup>b</sup>) proposed that the material parameter  $\beta^*$  may be considered a function of the mole fraction composition  $x$  passing through 1 at  $x=0.55$ . However, the relation between the material parameters  $\beta_1$  and  $\beta_2$  and the composition remains a topic of further investigations.

#### 4. Dielectric susceptibility from Landau-Devonshire free energy

Ishibashi & Orihara (1994) was the first to consider the Landau-Devonshire theory to give expressions for the nonlinear dynamic dielectric response by using the Landau-Khalatnikov (LK) equation. They evaluated the NLO coefficients and the third-order nonlinear (NL) susceptibility coefficients in the paraelectric (PE) phase above the Curie temperature  $T_c$ . Subsequently, Osman et al. (1998<sup>a,b</sup>) have extended the theory to evaluate the NLO coefficients in the FE phase. They have demonstrated that all second order  $\chi^{(2)}$  process vanishes naturally in the PE phase and that they are non zero in the FE phase due to the presence of the spontaneous polarization  $P_0$  that breaks the inversion symmetry. However, the former authors considered the free energy to be a function of a scalar polarization  $P$  Soon after that, Murgan et al. (2002), used a more general form of the free energy to calculate the dielectric susceptibility elements. In their expression, they considered the free energy expansion to be a function of a vector polarization  $Q$  and additional terms were added to Eq. (1). They considered a free energy of the following form;

$$\begin{aligned}
 F(P) = & F_0 + \frac{\alpha}{2\epsilon_0} [Q_x^2 + Q_y^2 + Q_z^2] \\
 & + \frac{\beta_1}{4\epsilon_0^2} [Q_x^4 + Q_y^4 + Q_z^4] + \frac{\beta_2}{2\epsilon_0^2} (Q_x^2 Q_y^2 + Q_y^2 Q_z^2 + Q_z^2 Q_x^2) + \frac{\alpha}{2\epsilon_0} [P_s^2 + 2Q_z P_s] \\
 & + \frac{\beta_1}{4\epsilon_0^2} [6Q_z^2 P_s^2 + 4Q_z^3 P_s + 4Q_z P_s^3 + P_s^4] + \frac{\beta_2}{2\epsilon_0^2} [(Q_z^2 + 2Q_z P_s + P_s^2)(Q_x^2 + Q_y^2)]
 \end{aligned} \quad (2)$$

In the above expression,  $P_i$  is the spontaneous polarization with its direction being along the tetragonal axes (considered in the z-direction). Eq. (2) for the free energy may simply be written in the form  $F = F_0 + \Delta F$  where  $F_0$  is the free energy is for the paraelectric phase and the polarization components in paraelectric phase is then related to the polarization in ferroelectric tetragonal phase by  $P_x = Q_x$ ,  $P_y = Q_y$  and  $P_z = Q_z + P_s$ . The magnitude of the spontaneous polarization  $P_s$  is given by the condition of minimum free energy  $\partial F_E(P)/\partial P_z = 0$  evaluated at  $P_z = P_s$ . The above expression for the free energy is more suitable for many real FE crystals that undergo successive phase transitions where additional terms are considered in comparison to Eq. (1). An important notice is that most FE, especially oxide ferroelectrics, exhibits a first-order phase transitions from the PE cubic phase to the FE phase. However, the phase transition from the cubic PE phase to the various symmetries of the lower-temperature phases can be treated as second-order provided certain conditions are fulfilled for lower symmetry groups (Haas, 1965). In the FE phase at temperatures much lower than the transition temperature, the type of transition is of no importance for the discussion of their physical properties (Ishibashi & Iwata 1998). Together with the free energy expression in Eq. (2), LK dynamical equation  $\dot{O}P_i = -\partial F/\partial P_i + E_i$  is

utilized to derive various dielectric susceptibility elements (Murgan et al. (2002)). The differential operator  $\hat{O} = \Gamma d/dt$  is used in case of relaxational dynamics while  $\hat{O} = M d^2/dt^2 + \Gamma d/dt$  is used for oscillatory dynamics with  $M$  and  $\Gamma$  being the effective mass and the damping constant respectively.

Expressions for the second-order nonlinear susceptibility tensor elements are shown in table 1 while expressions for third-order nonlinear susceptibility tensor components are shown in Table 2. In particular, table 1 shows the nonvanishing tensor elements for second-harmonic generation (SHG) and optical rectification (OR) while Table 2 shows the nonvanishing tensor elements for the third-harmonic generation (THG) and the intensity-dependent (IP) refractive index process. The expressions in both table 1 and Table 2 are all written in terms of the above linear response functions  $\sigma(\omega)$  and  $s(\omega)$  (Murgan et al., 2002). For SHG there are three independent elements and a total of seven nonvanishing elements while for OR there are four independent elements and a total of seven nonvanishing elements. For THG, there are five independent elements and a total of nine nonvanishing elements while for IP refractive index, there are eight independent elements and a total of a total of 15 nonvanishing elements. It should be noted that we were obliged to reproduce the results in able 1 and 2 to correct various mistakes found in the original work published by Murgan et al. (2002). The nonlinear dielectric susceptibility elements in Table 1 and 2 are given in terms of the following linear response functions in tetragonal symmetry;

Process, and $K$	Susceptibility $\chi^{(2)}$	Equation Number
SHG $K = 1/2$	$\chi_{zzz}^{(2)SHG} = -\frac{3}{\epsilon_0^3} \beta_1 P_s s(2\omega) s^2(\omega)$	(3)
$\chi_{ilm}^{(2)}(-2\omega; \omega, \omega)$ Symmetric on interchange of $(lm)$	$\chi_{zyy}^{(2)SHG} = \chi_{xxx}^{(2)SHG} = -\frac{\beta_2}{\epsilon_0^3} P_s s(2\omega) \sigma^2(\omega)$	(4)
	$\chi_{xzx}^{(2)SHG} = \chi_{yzy}^{(2)SHG} = \chi_{xxz}^{(2)SHG} = \chi_{yyz}^{(2)SHG} = -\frac{\beta_2}{\epsilon_0^3} P_s \sigma(2\omega) \sigma(\omega) s(\omega)$	(5)
Optical rectification (OR) $K = 1/2$ $\chi_{ilm}^{(2)}(0; -\omega, \omega)$	$\chi_{zzz}^{(2)OR} = -\frac{3}{\epsilon_0^3} \beta_1 P_s s(0)  s(\omega) ^2$	(6)
	$\chi_{zyy}^{(2)OR} = \chi_{zxx}^{(2)OR} = -\frac{\beta_2}{\epsilon_0^3} P_s s(0)  \sigma(\omega) ^2$	(7)
	$\chi_{xzx}^{(2)OR} = \chi_{yzy}^{(2)OR} = -\frac{\beta_2}{\epsilon_0^3} P_s \sigma(0) s(\omega) \sigma^*(\omega)$	(8)
	$\chi_{xxz}^{(2)OR} = \chi_{yyz}^{(2)OR} = -\frac{\beta_2}{\epsilon_0^3} P_s \sigma(0) \sigma(\omega) s^*(\omega)$	(9)

Table 1. The nonvanishing tensor elements for second-harmonic generation (SHG) and optical rectification (OR) in ferroelectric tetragonal symmetry (Murgan et al. 2002).

Process, and K	Susceptibility $\chi_{ilmn}^{(3)}$	Eq. number
Third-harmonic generation (THG) K = 1/4 Symmetric on interchange of (lmn)	$\chi_{x,xxx}^{(3)THG} = \chi_{y,yyy}^{(3)THG} = \frac{1}{\epsilon_0^3} \sigma(3\omega) \sigma^3(\omega) \left[ \frac{2\beta_2^2 P_s^2}{\epsilon_0^2} s(2\omega) - \beta_1 \right]$	(10)
	$\chi_{zzzz}^{(3)THG} = \frac{\beta_1}{\epsilon_0^3} s(3\omega) s^3(\omega) \left[ \frac{18P_s^2 \beta_1}{\epsilon_0^2} s(2\omega) - 1 \right]$	(11)
	$\chi_{y,xyy}^{(3)THG} = \chi_{x,xyx}^{(3)THG} = \frac{\beta_2}{3\epsilon_0^3} \sigma(3\omega) \sigma^3(\omega) \left[ \frac{2\beta_2 P_s^2}{\epsilon_0^2} s(2\omega) - 1 \right]$	(12)
	$\chi_{xzzz}^{(3)THG} = \chi_{yzzz}^{(3)THG} = \frac{1}{3} \frac{\beta_2}{\epsilon_0^3} \sigma(3\omega) \sigma(\omega) s^2(\omega) \left[ \frac{4\beta_2 P_s^2 \sigma(2\omega) + 6\beta_1 P_s^2 s(2\omega)}{\epsilon_0^2} - 1 \right]$	(13)
	$\chi_{zyyz}^{(3)THG} = \chi_{zxxx}^{(3)THG} = \frac{1}{3} \frac{\beta_2}{\epsilon_0^3} s(3\omega) \sigma^2(\omega) s(\omega) \left[ \frac{4\beta_2 P_s^2 \sigma(2\omega) + 6\beta_1 P_s^2 s(2\omega)}{\epsilon_0^2} - 1 \right]$	(14)
Intensity-dependent refractive index (IP) K = 3/4	$\chi_{xxxx}^{(3)IP} = \chi_{yyyy}^{(3)IP} = \frac{1}{\epsilon_0^3} \sigma^*(\omega) \sigma^3(\omega) \left[ \frac{2}{\epsilon_0^2} \beta_2^2 P_s^2 s(0) - \beta_1 \right]$	(15)
	$\chi_{zzzz}^{(3)IP} = \frac{\beta_1}{\epsilon_0^3} s^3(\omega) s^*(\omega) \left[ \frac{18\beta_1 P_s^2 s(0)}{\epsilon_0^2} - 1 \right]$	(16)
	$\chi_{y,xyy}^{(3)IP} = \chi_{x,xyx}^{(3)IP} = -\frac{\beta_2}{3\epsilon_0^3} \sigma^3(\omega) \sigma^*(\omega)$	(17)
	$\chi_{xxyy}^{(3)IP} = \chi_{yyxx}^{(3)IP} = \frac{\beta_2}{2\epsilon_0^3} \sigma^3(\omega) \sigma^*(\omega) \left[ \frac{2\beta_2 P_s^2 s(0)}{\epsilon_0^2} - \frac{2}{3} \right]$	(18)
Symmetric on interchange of (lm)	$\chi_{yzyy}^{(3)IP} = \chi_{xzzx}^{(3)IP} = \frac{\beta_2}{\epsilon_0^3} s^2(\omega) \sigma^*(\omega) \sigma(\omega) \left[ \frac{2\beta_2 P_s^2}{\epsilon_0^2} \sigma(0) - \frac{1}{3} \right]$	(19)
	$\chi_{yyzz}^{(3)IP} = \chi_{xzzz}^{(3)IP} = \frac{\beta_2}{\epsilon_0^3} \sigma^2(\omega) s(\omega) s^*(\omega) \left[ \frac{3P_s^2 \beta_1 \beta_2 s(0) + \beta_2 P_s^2 \sigma(0)}{\epsilon_0^2} \right]$	(20)
	$\chi_{zyyz}^{(3)IP} = \chi_{zxxx}^{(3)IP} = \frac{\beta_2}{\epsilon_0^3} \sigma^2(\omega) s(\omega) s^*(\omega) \left[ \frac{2P_s^2 \beta_2 \sigma(0)}{\epsilon_0^2} - \frac{1}{3} \right]$	(21)
	$\chi_{zzyy}^{(3)IP} = \chi_{zzxx}^{(3)IP} = \frac{\beta_2}{\epsilon_0^3} s^2(\omega) \sigma(\omega) \sigma^*(\omega) \left[ \frac{3\beta_1 P_s^2 s(0) + \beta_2 P_s^2 \sigma(0)}{\epsilon_0^2} - \frac{1}{3} \right]$	(22)

Table 2. The nonvanishing tensor elements for third-harmonic generation (THG) and intensity-dependent (IP) refractive index in ferroelectric tetragonal symmetry. (Murgan et al., 2002).

$$\sigma(\omega) = \left[ \Theta(\omega) + (\alpha/\varepsilon_0) + (\beta_2 P_s^2 / \varepsilon_0^2) \right]^{-1} \quad (23)$$

$$s(\omega) = \left[ \Theta(\omega) + (\alpha/\varepsilon_0) + (3\beta_1 P_s^2 / \varepsilon_0^2) \right]^{-1} \quad (24)$$

In the above, the frequency-dependent term is  $\Theta(n\omega) = -M(n\omega)^2 - i\Gamma(n\omega)$  for oscillatory dynamics while  $\Theta(n\omega) = -i\Gamma(n\omega)$  for relaxational dynamics and  $n$  is an integer number.  $P_s^2$  The linear dielectric susceptibility elements  $\chi_{ii}^{(1)}$  in tetragonal phase is written in terms of these uniaxial linear response functions as

$$\chi_{xx}^{(1)} = \chi_{yy}^{(1)} = \sigma(\omega)/\varepsilon_0 \quad , \quad \chi_{zz}^{(1)} = s(\omega)/\varepsilon_0 \quad (25)$$

where the linear dielectric susceptibility tensor  $\tilde{\chi}(\omega)$  is a  $3 \times 3$  diagonal matrix and the average linear susceptibility may be given by  $\chi_{av}(\omega) = (1/3)(\chi_{xx} + \chi_{yy} + \chi_{zz})$ .

## 5. The input parameters

To plot the dielectric susceptibility, various input parameter is required. Input parameters such as  $a, T_c$  and  $M$  are taken from the available experimental data of BaTiO<sub>3</sub> (Ibrahim et al 2007, 2008, 2010). For convenience, we may write the operating frequency  $\omega$  as some coefficient  $f$  multiplied by the resonance frequency  $\omega_0$  for FE material. Thus,  $f = \omega/\omega_0$  with  $\omega_0$  approximated from the simple equation  $\omega_0 \approx +\sqrt{-2a(T-T_c)}/\varepsilon_0 M$  for FE materials in tetragonal phase (Ibrahim et al., 2007, 2008, 2010). The parameter  $a = 1/C$  where  $C = 1.7 \times 10^5$  K is the Curie constant (Mitsui et al., 1976). This gives a value of  $\omega_0 \approx 1.4 \times 10^{14}$  Hz at room temperature. The thermodynamic temperature  $T$  is fixed at room temperature.

To estimate the value of  $\beta_1$  and  $\beta_2$ , we recall the following equation obtained by Ishibashi et al., (1998).

$$\varepsilon_{xx} = \left[ 2\beta_1 / (\beta_2 - \beta_1) \right] \varepsilon_{zz} \quad (26)$$

For ferroelectric material, the dielectric constant is approximated by  $\varepsilon_{xx} \approx \chi_{ii}$  since  $\chi_{ii} \gg 1$ . In tetragonal symmetry, expressions for both  $\varepsilon_{xx}$  and  $\varepsilon_{zz}$  may then be obtained by considering the static limit  $\omega \rightarrow 0$  of equation (5). This gives  $\varepsilon_{xx} = 1 / \left[ \alpha + \beta_2 P_s^2 / \varepsilon_0 \right]$  and  $\varepsilon_{zz} = 1 / \left[ \alpha + 3\beta_1 P_s^2 / \varepsilon_0 \right]$  (Murgan et al., 2002). Substituting  $\varepsilon_{xx}$  and  $\varepsilon_{zz}$  into Eq. (26) yields the simple relation  $\beta_2 = 3\beta_1$ . The value of  $\beta_1$  is then estimated from the spontaneous polarization equation  $P_s = -\varepsilon_0 \alpha / \beta_1$  in tetragonal phase. This yields  $\beta_1 = 7.58 \times 10^{-14} \text{ m}^3 \text{ J}^{-1}$  for  $P_s \approx 0.26 \text{ C.m}^{-2}$  at room temperature. Hence, a value of  $\beta_2 = 3\beta_1 = 2.27 \times 10^{-13} \text{ m}^3 \text{ J}^{-1}$  at room temperature. It should be noted that the value of  $\beta_1$  and  $\beta_2$  are very sensitive to the value of the spontaneous polarization. Estimation of the damping parameter  $\Gamma$  for BaTiO<sub>3</sub> may also be done by comparing the dielectric function in Eq. (4) and the equation  $\varepsilon_{zz}(\varepsilon) = \varepsilon_\infty + [s(\omega)/\varepsilon_0]$  obtained by Osman et al. (1989<sup>a</sup>). This yields the relation;

$$\Gamma = iM\omega - i \left[ \alpha(1 + 2\varepsilon_0) / \varepsilon_0 \omega (1 - \varepsilon_0) \right] \quad (27)$$

which express  $\Gamma$  as a function of  $M$ ,  $\alpha$  and  $\omega$ . For fixed values of  $P_s$  and  $\omega$ , we have numerically found that  $\Gamma$  changes by one order of magnitude (From  $10^{-6} - 10^{-7}$ ) over the

range of temperature from  $T = 0^\circ\text{C}$  to the  $T = T_c$ . On the other hand, the damping coefficient is relatively not a sensitive function of  $P_s$  or  $\omega$  in such a way that it maintains its order of magnitude over the relevant range of  $P_s$  or  $\omega$ . A similar procedure was done by Razak et al. (2002) to estimate the damping parameter of  $\text{PbTiO}_3$ . In fact, each oscillating mode in the crystal may assume different damping ratio in a real crystal and the stability of each mode depends on its damping ratio. The average damping parameter of all the relevant modes is usually obtained. However, for convenience, we have to fix the damping parameter at specific value within the range  $10^{-6} - 10^{-7}$  predicted by our Eq. (27). For example we may approximate the damping constant by  $\Gamma \approx 3.4 \times 10^{-7} \text{ Kg.m}^3.\text{A}^{-2}.\text{s}^{-3}$  which corresponds to  $P_s \approx 0.22 \text{ C.m}^{-2}$ ,  $\omega = 1.01\omega_0$ , and  $T \approx 387 \text{ K}$ .

## 6. Morphotropic phase boundary (MPB) in linear dielectric susceptibility

The divergence of the static dielectric susceptibility near the MPB for tetragonal and rhombohedral symmetry was first investigated by Ishibashi and Iwata (see for example Ishibashi & Iwata 1998). They have derived the static dielectric constant  $\chi(0)$  by adopting a "golden rule" and obtaining the Hessian matrix which is a  $3 \times 3$  matrix composed of the second derivatives of the free energy as a function of the polarization. They found that the static limit of  $\chi(\omega \rightarrow 0)$  diverges at  $\beta_1 = \beta_2$  in a  $\chi(0)$  versus beta  $\beta'$  diagram where  $\beta' = \beta_2/\beta_1$ . Especially for tetragonal symmetry, the  $\chi(0)$  diverges from the right side toward  $\beta' = 1$  (See Fig. 2).

In this section, we investigate the dynamic linear dielectric susceptibility  $\chi(\omega)$  and its MPB for FE material in tetragonal phase. We will study the effect of operating frequency  $\omega$  on the dynamic linear susceptibility as a function of the material parameters  $\beta_1$  and  $\beta_2$ . Therefore, the divergence of the static limit of the linear dielectric susceptibility  $\chi(0)$  at the MPB ( $\beta_1 = \beta_2$ ) is regarded as a special case. In the static limit, the results obtained here for the static  $\chi(0)$  shows similar divergence as those obtained by Ishibashi et al. (1998). To explain the behavior of  $\chi(\omega)$  in terms of FE soft modes, it is necessary to write  $\chi(\omega)$  in the following form;

$$\chi_{xx}^{(1)} = \chi_{yy}^{(1)} = \left\{ M\epsilon_0 \left[ -\omega^2 - i\omega(\Gamma/M) + \omega_{TO}^2 \right] \right\}^{-1} \quad (28)$$

$$\chi_{zz}^{(1)} = \left[ \epsilon_0 M \left( -\omega^2 - i\omega(\Gamma/M) + \omega_{LO}^2 \right) \right]^{-1} \quad (29)$$

We note that in deriving equations (27) and (28), we have used the spontaneous polarization for tetragonal phase defined by  $P_s^2 = -\epsilon_0 \alpha / \beta_1$ . In the above equations,  $\chi^{(1)}$  is written in terms of the lattice-vibrational modes, particularly,  $\chi_{xx}^{(1)}$  is written in terms of the transverse-optical (TO) mode characterized by its normal frequency  $\omega_{TO}^2 = a(T - T_c)(\beta_1 - \beta_2) / M\epsilon_0 \beta_1$  and  $\chi_{zz}^{(1)}$  is written in terms of its longitudinal-optical (LO) mode  $\omega_{LO}^2 = 2a(T - T_c) / \epsilon_0 M$ . The TO mode corresponds to the displacement of the free energy perpendicular to the polar axis while the LO mode corresponds to the displacement along the polar axis. Upon using  $\alpha = a(T - T_c)$  the pole position can be determined by the soft-mode frequency.

Since the stability region of the tetragonal phase lies at  $\beta_2 > \beta_1$ , the value of  $\omega_{TO}^2$  is positive. As anticipated, the soft-mode frequency shows that the term  $\beta_1 - \beta_2$  enters on the same

footing as the term  $(T - T_c)$  which make the dielectric susceptibility diverges either when  $T$  approaches  $T_c$  or when  $\beta_1$  approaches  $\beta_2$ . Therefore,  $\omega_{TO}$  has a double soft-mode character and the explicit limits are then  $\omega_{TO} \rightarrow 0$  as  $\beta_2 \rightarrow \beta_1$  or  $T \rightarrow T_c$  and  $\omega_{TO} \rightarrow \infty$  as  $\beta_1 \rightarrow 0$  (instability limit). The reason for the instability can be seen from the spontaneous polarization  $P_s^2 = -\varepsilon_0 \alpha / \beta_1$  where near the instability limit  $P_s$  becomes large and therefore  $\omega_{TO}$ . It is important to notice that the instability limit is a kind of an artifact; it results mainly due to the truncation of the free energy to the fourth order in the polarization. Thus, when  $\beta_1$  is very small, at least the sixth order terms in the polarization should be added to the free energy to avoid the instability.

Now the origin of the enhancement of the dielectric susceptibility is clear, when  $\beta_2 \rightarrow \beta_1$ , the value of the soft-mode frequency  $\omega_{TO}$  becomes smaller which leads to a direct enhancement of the values of  $\chi_{xx}^{(1)} = \chi_{yy}^{(1)}$  as seen in equation (27). The static dielectric constant can then be derived by setting  $\omega = 0$  in equations (27) and (28). This leads to a similar form to those equations obtained by Ishibashi et al. (1998). These are;

$$\chi_{xx}^{(1)} = \chi_{yy}^{(1)} = \beta_1 / [a(T - T_c)(\beta_1 - \beta_2)] = 1 / m\varepsilon_0 \omega_{TO}^2 \quad (30)$$

$$\chi_{zz}^{(1)} = -1 / [2a(T - T_c)] = -1 / \varepsilon_0 m \omega_{LO}^2 \quad (31)$$

In Eq. (29) and (30), the static linear dielectric constant shows that at the MPB,  $\chi_{xx}^{(1)}(\omega \rightarrow 0)$  and  $\chi_{yy}^{(1)}(\omega \rightarrow 0)$  diverge when  $\beta_1 = \beta_2$  at all temperatures while  $\chi_{zz}^{(1)}(\omega \rightarrow 0)$  diverges only at  $T \rightarrow T_c$ . In Fig. 5(a), we plot the complex dynamic dielectric susceptibility  $\chi_{xx}^{(1)}$  versus  $\beta^* = \beta_2 / \beta_1$  at single operating frequency  $f = \omega / \omega_0 = 0.1$ . A part from the element  $\chi_{zz}^{(1)}$  which remains constant over  $\beta^*$  because it is a function of the LO mode only, the other element  $\chi_{xx}^{(1)}$  shows a resonance-like behavior at certain value of  $\beta^*$ . At this peak, the dynamic response of the dielectric susceptibility is maximized. In a way, this resonance-like behavior is a function of the material composition through the parameter  $\beta^*$  and it is explainable within the concept of the ferroelectric soft-mode dynamics. We have numerically found that the value of  $|\chi_{xx}^{(1)}|$  at its maximum is  $2.4 \times 10^4$  which give a linear refractive index  $n = \sqrt{\text{Re}(\varepsilon_{xx}(\omega))} \approx 109$  at room temperature. Meanwhile, far from the pole, at  $\beta^* = 3$ , the dielectric constant is about 800 which results in a linear refractive index of 2.46. In fact, the value of the dielectric susceptibility decreases gradually from its maximum by increasing the value of  $\beta^*$ . The values of the dielectric constant obtained here for ferroelectric materials are huge in comparison to typical dielectrics or semiconductors. For amorphous dielectrics such as fused silica, the dielectric constant is in the range 2.5-3.5 while the linear refractive index is about 1.46. In typical semiconductors such as GaAs, the dielectric constant is about 13.2 and the linear refractive index is 3.6 (Glass, 1987).

To examine the effect of operating frequency, we plot the average value of the dynamic linear dielectric susceptibility versus  $\beta^*$  for different operating frequencies  $f$  (Fig. 5(b)). Other parameters kept unchanged. The general feature of these curves is that they all show a peak behavior where the dynamic linear susceptibility is maximum at certain value of  $\beta^*$ . This pole response is a strong function of the operating frequency. For example, curve (i) shows the linear susceptibility  $\chi_{av}^{(1)}(\omega)$  versus  $\beta^*$  for  $f = 2$ , this gives a maximum value of  $\chi_{av}^{(1)}(\omega) \approx 796$  at  $\beta^* = 9$ . Curve (ii) shows the linear susceptibility  $\chi_{av}^{(1)}(\omega)$  for  $f = 1.5$ , this gives

a maximum value of  $\chi_{av}^{(1)}(\omega) \approx 1060$  at  $\beta^* = 5.5$ . Upon decreasing the operating frequency further to  $f = 1.1$  (Curve (iii)), the linear susceptibility  $\chi_{av}^{(1)}(\omega)$  assumes a maximum value of 1447 at  $\beta^* = 3.42$ . Below the resonance, at  $f = 0.95$  (Curve (iv)),  $\chi_{av}^{(1)}(\omega)$  assumes a maximum value of 1676 at  $\beta^* = 2.81$ . Far below the resonance, at  $f = 0.5$  (Curve (v)),  $\chi_{av}^{(1)}(\omega)$  gives a maximum value of 3185 at  $\beta^* = 1.5$ . Finally, at  $f = 0.0$  (Curve (vi)), the static limit of the linear susceptibility  $\chi_{av}^{(1)}(0)$  in this case diverges at  $\beta^* = 1$ . This result for the static case coincide with the results obtained by Ishibashi (1998) using the Hessian matrix of the free energy. Therefore, we may generally conclude that, for the dynamic dielectric susceptibility, a systematic decrease of the operating frequency  $\omega = f\omega_0$  is accompanied by systematic enhancement of the linear dielectric susceptibility especially at its peak. However, decreasing the operating frequency is also accompanied a systematic decrease of  $\beta^*$  towards  $\beta^* = 1$ . At  $\omega = 0$ , the value of  $\chi_{av}^{(1)}(0)$  goes to infinity at  $\beta^* = 1$  since the soft-mode frequency  $\omega_{\gamma_0}$  becomes zero.

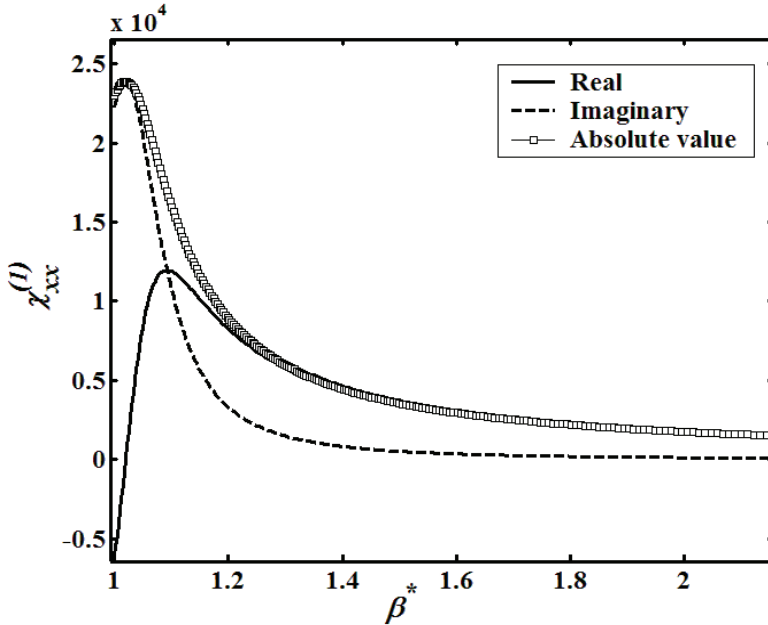


Fig. 5. (a) Linear dynamic dielectric susceptibility  $\chi_{xx}^{(1)}$  versus  $\beta^* = \beta_2/\beta_1$  in tetragonal phase at room temperature and operating frequencies  $f = \omega/\omega_0 = 0.1$ .

## 7. Morphotropic phase boundary in second-order nonlinear susceptibility

In the free energy formalism, there is only one underlying dynamic equation and the NLO coefficients take the form of products of linear response functions. This formalism does not explicitly show the dependence of the NL susceptibility on the MPB or the ferroelectric soft mode. As shown in Table 1 and table 2, the susceptibility elements takes the form of a product of linear response functions,  $s(n\omega)$  if the related suffix is  $z$ , and  $\sigma(n\omega)$  if it is  $x$  or  $y$

and the argument is the related frequency. In this case, it is convenient to transform the second-order NL susceptibility tensor elements to an alternative form that shows a direct dependence on the lattice-vibrational modes.

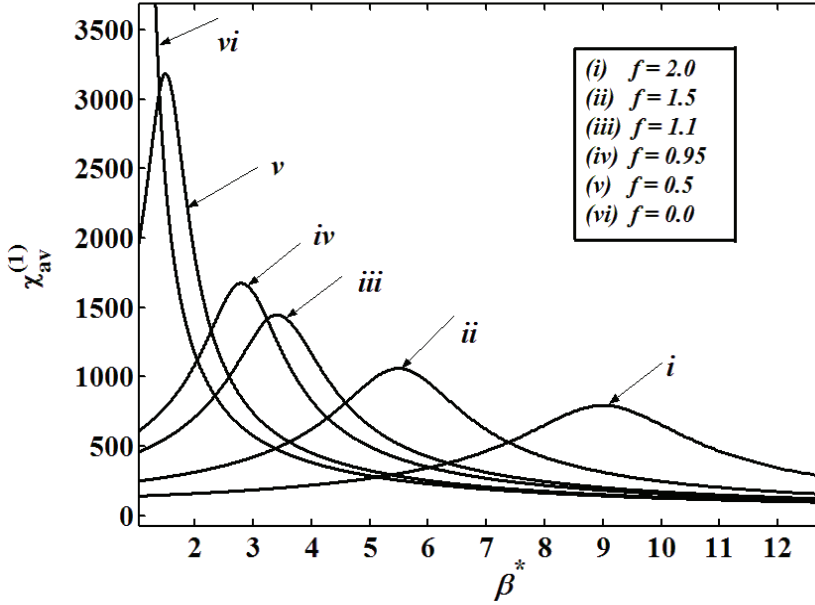


Fig. 5. (b) Linear dynamic dielectric susceptibility  $\chi_{av}^{(1)}$  versus  $\beta^* = \beta_2/\beta_1$  in tetragonal phase at room temperature for different operating frequencies  $f = \omega/\omega_0$  shows the improvement of the  $\chi_{av}^{(1)}(\omega)$  at the MPB.

These are the transverse-optical modes (TO) with normal frequency  $\omega_{TO}$  and the longitudinal-optical (LO) mode with frequency  $\omega_{LO}$ . In this case, the ferroelectric soft mode is one of these transverse-optical modes that soften when the thermodynamic temperature  $T$  approaches  $T_c$  or  $\beta^*$  approaches 1. For example, The SHG element  $\chi_{zyy}^{(2)SHG}$  may be expressed explicitly in terms of these modes in the following form;

$$\chi_{zyy}^{(2)SHG} = \chi_{zxx}^{(2)SHG} = -\beta_2 P_s \left/ \left\{ \epsilon_0^3 M^3 \left[ \frac{\Theta(2\omega)}{M} - \omega_{LO}^2 \right] \left[ \frac{\Theta(\omega)}{M} + \omega_{TO}^2 \right]^2 \right\} \right. \quad (32)$$

This is achieved by substituting the linear response functions  $\sigma(\omega)$  and  $s(\omega)$  in tetragonal symmetry from Eq. (3) and Eq. (4) into Eq. (7) and performing a series of algebraic manipulations. It should be noticed that the linear response functions for the second harmonics  $\sigma(2\omega)$   $s(2\omega)$  in Eq. (33) is responsible for the appearance of the function argument  $\Theta(2\omega)$  where  $\Theta(2\omega) = -M(2\omega)^2 - i\gamma(2\omega)$ . The static limits are then obtained by setting  $\omega = 0$  in Eq. (32) and performing further algebraic simplifications. The above second-order coefficient in Eq. (32) contains a tensor suffix corresponds to the output wave of frequency  $2\omega$ , and others correspond to the input of frequency  $\omega$ .

$$\chi_{zyy}^{(2)SHG}(\omega=0) = \chi_{zxx}^{(2)SHG} = \chi_{xzx}^{(2)SHG} = \beta_2 P_s / \epsilon_0^3 M^3 \omega_{TO}^4 \omega_{LO}^2 \quad (33)$$

The element  $\chi_{zyy}^{(2)SHG}$  in Eq. (32) contains one longitudinal optical mode  $\omega_{LO}^2 = 2\alpha/\epsilon_0 M$  corresponds to the output wave of frequency  $2\omega$  and one TO mode with frequency  $\omega_{TO}^2 = 2\alpha(\beta_1 - \beta_2)/\epsilon_0 M \beta_1$  corresponds to the input frequency  $\omega$ . Therefore, this element is expected to assume one peak at certain value of  $\beta^*$ . This expectation is assured upon plotting  $|\chi_{zyy}^{(2)SHG}|$  versus  $\beta^*$  for different operating frequencies as shown in Fig. 6(a). The main feature of those curves is that they all display a single pole at certain value of  $\beta^*$ . In the static case (curve *i*), the value of  $|\chi_{zyy}^{(2)SHG}(\omega \rightarrow 0)|$  increases systematically then diverges at the MPB between the tetragonal and rhombohedral phase where  $\beta^* = 1$ . As seen from Eq. (33), the static value of  $|\chi_{zyy}^{(2)SHG}(\omega \rightarrow 0)|$  only depends on  $\omega_{LO}$  and  $\omega_{TO}$ . Since  $\omega_{LO}$  is not a function of  $\beta^*$ , thus the enhancement in the values of  $|\chi_{zyy}^{(2)SHG}(\omega \rightarrow 0)|$  is mainly due to  $\omega_{TO}$ . The value of  $\omega_{TO}^2 = 2\alpha(\beta_1 - \beta_2)/\epsilon_0 M \beta_1$  decreases "softens" systematically when  $\beta_1$  approaches  $\beta_2$  which lead to a direct increment in the value of  $|\chi_{zyy}^{(2)SHG}(\omega \rightarrow 0)|$  till the divergence occur at  $\beta_1 \rightarrow \beta_2$  as  $\omega_{TO} \rightarrow 0$  at the MPB. It should be noted that, the association of a high static dielectric constant with a specific low frequency optical mode is experimentally observed on FE materials such as strontium titanate, SrTiO<sub>3</sub> (Kittel 1995; Sirenko et al., 2000; Katayama et al., 2007).

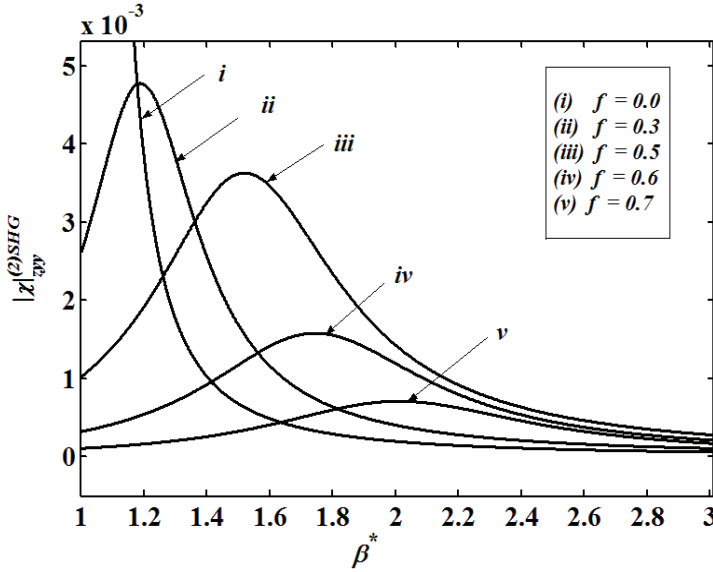


Fig. 6. (a) The nonlinear dielectric susceptibility  $\chi_{zyy}^{(2)SHG}(-2\omega; \omega, \omega)$  versus  $\beta^* = \beta_2/\beta_1$  in tetragonal phase at room temperature for different operating frequencies  $f = \omega/\omega_0$  shows the improvement of the MPB upon decreasing the operating frequency.

The other curves in Fig. 6(a) show that both the dynamic value of  $|\chi_{zyy}^{SHG}|$  around the MPB and the corresponding value of  $\beta^*$  are functions of the operating frequency. Particularly, at  $f = 0.3$  (curve *ii*), the maximum value of  $|\chi_{zyy}^{SHG}|$  is found to be around  $4.8 \times 10^{-3} \text{ mV}^{-1}$  at

$\beta^* \approx 1.2$ . At  $f = 0.5$  (curve *iii*), the maximum value of  $|\chi_{zyy}^{SHG}|$  was found to be around  $3.5 \times 10^{-3} \text{ mV}^{-1}$  at  $\beta^* \approx 1.5$ . At  $f = 0.6$  (curve *iv*), the maximum value of  $|\chi_{zyy}^{SHG}|$  was found to be around  $1.5 \times 10^{-3} \text{ mV}^{-1}$  at  $\beta^* \approx 1.7$ . At  $f = 0.7$  (curve *v*), the maximum value of  $|\chi_{zyy}^{SHG}|$  was found to be around  $0.4 \times 10^{-3} \text{ mV}^{-1}$  at  $\beta^* \approx 2$ . Therefore, a systematic increase of the operating frequency  $\omega = f\omega_0$  results in a systematic decrease of the maximum value of  $|\chi_{zyy}^{SHG}|$  and a systematic increase of the value  $\beta^*$  too. Thus the dynamic  $|\chi_{zyy}^{SHG}|$  assumes higher values at lower frequencies. The peaks exhibited by  $|\chi_{zyy}^{SHG}|$  can be viewed clearly upon plotting both the real and imaginary parts of the complex  $\chi_{zyy}^{SHG}$  at single operating frequency  $f = \omega/\omega_0 = 0.1$  as shown in Fig. 6(b). The graph shows that the single pole exhibited by  $|\chi_{zyy}^{SHG}|$  nearly at  $\beta^* \approx 1$  results from the resonance-like response exhibited by both real and imaginary parts of the complex  $\chi_{zyy}^{SHG}$ . The values obtained in Fig. 6(a) are typical for SHG in BaTiO<sub>3</sub> (Murgan et al., 2004). However, the maximum value of  $\chi_{zyy}^{SHG}$  obtained in Fig. 6(b) is dramatically increased ( $2.5 \times 10^{-2} \text{ mV}^{-1}$ ) at such low frequency. This value is higher than the typical values of BaTiO<sub>3</sub> by about two to three order of magnitude. Needless to say that the SHG value in ferroelectrics is initially very large (typically  $\chi^{(2)} \approx 10^{-11} \text{ mV}^{-1}$ ) compared with the order of magnitude for typical dielectric or semiconductors in the nonresonant region. This is not surprising for resonant effects in highly polarizable materials such as ferroelectrics. The TO mode softening may be explained as a result of the well-known phenomenon of LO-TO splitting, that is, the shift in frequency between longitudinal optical and transverse optical phonons at the Brillouin zone centre (Waser et al., 2006). In this case, the softening of the TO modes is caused by a partial compensation of the long-range electric fields on one hand and the short-range lattice elastic forces on the other hand.

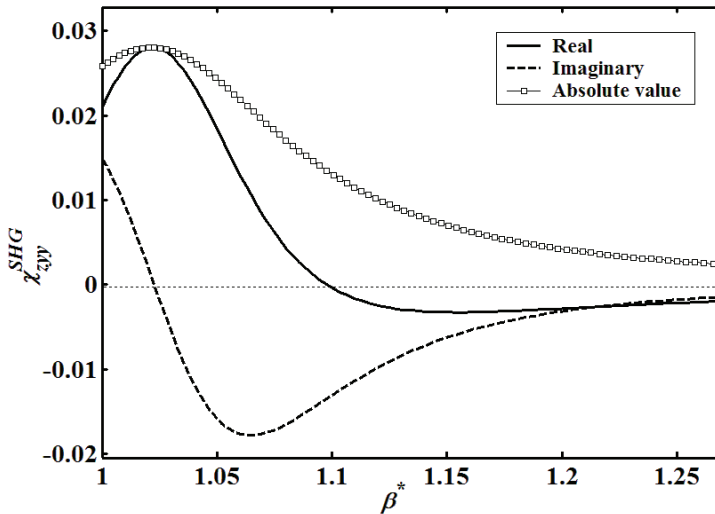


Fig. 6. (b) The real and imaginary part of the nonlinear dynamic dielectric susceptibility  $\chi_{zyy}^{(2)SHG}(-2\omega; \omega, \omega)$  versus  $\beta^* = \beta_2/\beta_1$  in tetragonal phase at room temperature and at operating frequency  $f = \omega/\omega_0 = 0.1$ .

## 8. Morphotropic phase boundary in third-order nonlinear susceptibility

The expressions for the third-order nonlinear susceptibility elements also consist of products of linear response functions. Table 2 shows the dynamic nonlinear susceptibility elements for the third-harmonic generation (THG) is also expressed in terms of the linear response functions  $\sigma(n\omega)$  and  $s(n\omega)$ . The integer number  $n$  may assume one, two or three. The elements in Table 2 may be written in terms of the TO and LO phonon frequencies following the same procedure describes in the previous chapter. For example, the third-harmonic element  $\chi_{zyyz}^{THG}$  in Eq. (17) may be written as;

$$\chi_{zyyz}^{-(3)THG} = \frac{-\beta_2}{3\epsilon_0^3 M^4 \left[ \frac{\Theta(3\omega)}{M} - \omega_{LO}^2 \right] \left[ \frac{\Theta(\omega)}{M} - \omega_{LO}^2 \right]} \times \left\{ 2 \frac{\beta_2 \omega_{LO}^2}{\beta_1 \left[ \frac{\Theta(2\omega)}{M} + \omega_{TO}^2 \right] \left[ \frac{\Theta(\omega)}{M} + \omega_{TO}^2 \right]^2} + 3 \frac{\omega_{LO}^2}{\left[ \frac{\Theta(2\omega)}{M} - \omega_{LO}^2 \right] \left[ \frac{\Theta(\omega)}{M} + \omega_{TO}^2 \right]^2} + \frac{1}{\left[ \frac{\Theta(\omega)}{M} + \omega_{TO}^2 \right]^2} \right\} \quad (34)$$

The linear response functions for the second-harmonics  $\sigma(2\omega)$   $s(2\omega)$  exists in Eq. (17) is responsible for the appearance of the function argument  $\Theta(2\omega)$  in Eq. (34) where  $\Theta(2\omega) = -4M\omega^2 - i2\Gamma\omega$ . The function argument  $\Theta(2\omega)$  is intrinsic part of the  $\chi^{(3)}$  response and they do not result from cascade processes in which two second-order process follow one another in time (Murgan et al., 2002). In nonlinear optics, a cascaded THG could arise from SHG followed by sum-frequency generation, or symbolically  $\omega + \omega \rightarrow 2\omega$ , then  $\omega + 2\omega \rightarrow 3\omega$ . The element  $\chi_{zyyz}^{THG}$  in Eq. (34) (apart from the prefactors and the LO modes) include two terms related to the TO modes. The first term include a TO mode propagating at the input frequency  $\omega$  while the second term include a TO mode propagating at  $2\omega$ . Therefore, the element  $\chi_{zyyz}^{THG}$  is expected to assume a double peak behavior which may lead to a complicated enhancement effects at two different values of  $\beta^*$ . In the static limit, Eq. (34) reduces to the following form;

$$\chi_{zyyz}^{-(3)THG} = \frac{-2\beta_2}{3\epsilon_0^3 M^4 \omega_{TO}^4 \omega_{LO}^4} \left[ \frac{\beta_2 \omega_{LO}^2}{\beta_1 \omega_{TO}^2} - 1 \right] \quad (35)$$

The former equation clearly indicates that the value of  $\chi_{zyyz}^{-(3)THG} \rightarrow \infty$  when the value of  $\omega_{TO} \rightarrow 0$  at the MPB.

A plot of  $\chi_{zyyz}^{THG}$  versus  $\beta^*$  is shown in Fig. 7(a). In the dynamic case, both the real (The  $\bullet\text{-}$  curve) and the imaginary parts (The  $\text{-o-}$  curve) of  $\chi_{zyyz}^{THG}$  assume a double peak behavior at two different values of  $\beta^*$  as predicted by Eq. (34). In Fig. 7(b), the value  $|\chi_{zyyz}^{THG}|$  is plotted versus  $\beta^*$  for different operating frequency. The main feature of these curves is that they all display a double peak response at certain value of  $\beta^*$  as predicted by Eq. (34). The value of  $\chi_{zyyz}^{THG}$  is generally increased upon decreasing the operating frequency  $f$ . As in the second-order case, this is due to the softening of the TO mode which results in a direct increment of  $\chi_{zyyz}^{THG}$ .

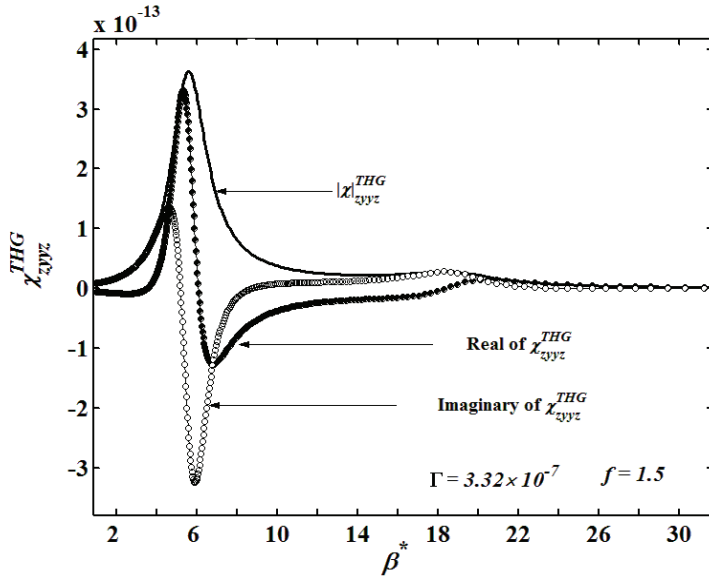


Fig. 7. (a) The third-order nonlinear susceptibility tensor element  $\chi_{zyyz}^{THG}$  versus  $\beta^* = \beta_2/\beta_1$  in tetragonal phase at room temperature for operating frequencies  $f = 1.5$  and for the static case at  $f = 0$ .

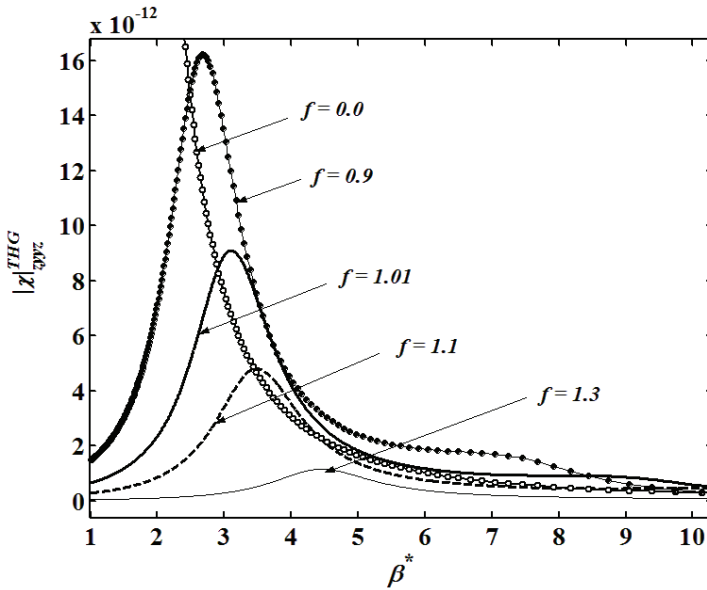


Fig. 7. (b) The absolute value nonlinear dielectric susceptibility  $|\chi_{zyyz}^{THG}|$  versus  $\beta^* = \beta_2/\beta_1$  in tetragonal phase at room temperature for different operating frequencies  $f = \omega/\omega_0$ .

For example, at  $f = 1.3$  (thin solid curve), the maximum value of  $|\chi_{zyyz}^{THG}|$  is found to be around  $1.15 \times 10^{-12} \text{ m}^2 \text{ v}^{-2}$  at  $\beta^* = 4.5$ . At  $f = 1.1$  (the dashed curve) the maximum value of  $|\chi_{zyyz}^{THG}|$  is  $4.8 \times 10^{-12} \text{ m}^2 \text{ v}^{-2}$  at  $\beta^* = 3.5$ . At  $f = 1.01$  (solid curve), the maximum value of  $|\chi_{zyyz}^{THG}|$  increases to  $9.1 \times 10^{-12} \text{ m}^2 \text{ v}^{-2}$  at  $\beta^* = 3$ . At  $f = 0.9$  (the -•- curve), the maximum value of  $|\chi_{zyyz}^{THG}|$  further increases to  $1.61 \times 10^{-11} \text{ m}^2 \text{ v}^{-2}$  at  $\beta^* = 2.7$ . In the static case with  $f = 0$  (the -o- curve), the value of  $|\chi_{zyyz}^{SHG}|$  diverges at  $\beta^* = 1$  as predicted by Eq. (35). From the numerically generated data, the typical value of the dynamic  $\chi^{(3)}$  in BaTiO<sub>3</sub> is found to lie within the range of  $10^{-13}$  to  $10^{-16}$  depending on the operating frequency. Similar values of  $\chi^{THG}$  for BaTiO<sub>3</sub> are found by Murgan et al., (2002). These values for THG in ferroelectrics are very large compared with typical semiconductors or dielectrics. For example, the  $\chi^{THG}$  for GaAs is about  $6.7 \times 10^{-19} \text{ m}^2 \text{ v}^{-2}$  while it is in the range of  $10^{-22} - 10^{-20}$  for Glass (Eaton, 1991). From our numerically generated data, the value of  $\chi^{(3)}$  in BaTiO<sub>3</sub> at its peak is increased by two or three orders of magnitude in comparison with the values far from its peak.

## 9. Conclusion

In this chapter we have examined the behavior of both linear and nonlinear dielectric susceptibility as a function the free energy parameters for different operating frequencies. Both dynamic and static dielectric susceptibility is examined. Within the free-energy formulation, the material-dependent nonlinear coefficients  $\beta_1$  and  $\beta_2$  may be assumed as function of the molar composition. Using both the free energy and Landau-Khalatnikov equation, the nonlinear dielectric susceptibility is written as a product of the linear response functions. This form of dielectric susceptibility is transformed into an alternative form that shows the explicit dependence on the transverse-optical (TO) and longitudinal-optical (LO) modes. The dielectric susceptibility is then investigated within the concept of the ferroelectric soft-mode with normal frequency  $\omega_{\tau_0}$  where the material parameters  $\beta_1$  and  $\beta_2$  enters on the same footing as temperature. The divergence of the static dielectric susceptibility at the MPB occurs when the ferroelectric soft-mode becomes zero as a result of  $\beta_1 \rightarrow \beta_2$  or  $T \rightarrow T_c$ . Most dielectric susceptibility elements are systematically enhanced upon decreasing the operating frequencies. In the vicinity of the MPB, the low-frequency limit linear dielectric susceptibility is increased by one to two orders of magnitude in comparison with the non-MPB value of the static dielectric susceptibility. For second-order NL elements, the dynamic NL susceptibility may assume single or double pole response. This actually depends on whether the dielectric susceptibility include a soft-mode corresponding to the input frequency  $\omega$  or two soft-modes corresponds to both  $\omega$  and  $2\omega$ . We found that the second-order NL process is enhanced by two orders of magnitude in the vicinity of the MPB in comparison with the non-MPB values. We have also demonstrated the systematic enhancement of the dynamic nonlinear susceptibility upon increasing the thermodynamic temperature of the material towards the Curie temperature. Within the third-order process, we have investigated both the THG and the intensity-dependant (IP) susceptibility. We have found that certain elements within the THG process assumes a triple-response at three different values of  $\beta^*$ . This phenomena occurs if the NL susceptibility element includes three different soft-modes frequencies

corresponds to  $\omega$ ,  $2\omega$  and  $3\omega$ . Other elements within the third-order NL process may assume single or double pole in their dynamic response. As in the second-order process, the third order process is enhanced at the MPB by two to three orders of magnitude. All nonlinear elements are found to diverge in the static limit upon approaching  $\beta' = 1$ . It should be noted that we have investigated the MPB within the tetragonal phase where  $\beta_2 > \beta_1 > 0$ , it will be very interesting to study the MPB for the rhombohedral phase within the free energy formalism. Finally we note that this calculation is important for designing a new material with higher nonlinearity for technological applications. This is achieved by investigating the MPB where the dielectric response is maximized.

## 10. Acknowledgement

The authors wish to express their sincere gratitude to Prof Y. Ishibashi and Prof D. R. Tilley for their fruitful discussion and support especially during their collaboration period with Universiti Sains Malaysia as visiting scientists.

## 11. References

- Ahart M., Somayazulu M., Cohen R. E., Ganesh P., Dera P., Mao H-k, Hemley R. J., Ren Y., Liermann P. and Wu Z. *Nature* 451, 545 (2008).
- Amin A., Newnhan R.E., and Cross L.E., *Phys. Rev. B* 34 1595 (1986).
- Bellaiche L. and Vanderbilt D., *Phys. Rev. Lett.* 83 1347 (1999).
- Cao W., and Cross L.E., *Phys. Rev. B* 47 4285 (1993).
- Cohen, R. E., *Nature* 441, 941 (2006).
- Cox D. E., Noheda B., Shirane G., Uesu Y., Fujishiro K., and Yamada Y., *Appl. Phys. Lett.* 79, 400 (2001)
- Cross L., *Ferroelectrics* 76, 241 (1987).
- Cross L., *Ferroelectrics* 151, 305 (1994).
- Eaton D. F., *Science, New Series*, Vol. 253, No. 5017, 281 (1991).
- Fu H., Cohen R., *Nature* 403, 281 (2000).
- Glass A. M., *Science, New Series*, 235(4792) 1003 (1987).
- Guo R., Cross L. E., Park S-E., Noheda B., Cox D. E., and Shirane G., *Phys. Rev. Lett.* 84, 5423 (2000).
- Haas C., *Phys. Rev.* 140, A863 (1965).
- Haun M. J., Furman E., Jang S.J., and Cross L.E., *Ferroelectrics* 99 13 (1989).
- Ibrahim A-B M. A., Tilley D. R., and Osman J., *Ferroelectrics*, 355 (1) 140 (2007).
- Ibrahim A-B M. A., Tilley D. R., and Osman J., *The Euro. Phys. J. B.*, 63(2) 1434 (2008). "Ferroelectric Optics: Optical bistability in Nonlinear Kerr ferroelectric materials"
- Ibrahim A-B M. A., Rahman M. K. A., and Osman J., a chapter in book, "*Ferroelectrics*", Coondoo I., (Ed), ISBN: 978-953-307-439-9, InTech, (2010), Available from: <http://www.intechopen.com/articles/show/title/ferroelectric-optics-optical-bistability-in-nonlinear-kerr-ferroelectric-materials>
- Ishibashi Y., and Orihara H., *Ferroelectrics* 156, 185 (1994).
- Ishibashi Y., and Iwata M., *Jpn. J. Appl. Phys.* 37, L985 (1998).
- Ishibashi Y., and Iwata M., *J. Phys. Soc. Jpn.* 68, 1353 (1999<sup>a</sup>).
- Ishibashi Y., and Iwata M., *Jpn. J. Appl. Phys.* 38, 800 (1999<sup>b</sup>).

- Ishibashi Y., Iwata M., J. Phys. Soc. Jpn. 68, 1353 (1999<sup>c</sup>)
- Ishibashi Y., and Iwata M., Jpn. J. Appl. Phys. 38, 1454 (1999<sup>d</sup>)
- Ishibashi Y., Ferroelectrics 264, 197 (2001).
- Ishibashi Y., Iwata M., J. Phys. Soc. Jpn. 72, 1675 (2003)
- Iwata M., Orihara H., and Ishibashi Y., Ferroelectrics 266, 57 (2002<sup>a</sup>)
- Iwata M., Araki T., Maeda M., Suzuki I., Ohwa H., Yasuda N., Orihara H., and Ishibashi Y., Jpn. J. Appl. Phys. 41, 7003 (2002<sup>b</sup>)
- Iwata M., Ishibashi Y., J. Phys. Soc. Jpn. 72, 2834 (2003)
- Iwata M., and Ishibashi Y., In "Ferroelectric thin films" by Okuyama M., and Ishibashi Y., Springer-Verlag Berlin Heidelberg, (2005).
- Jaffe B., Roth R. S. and Marzullo S., J. Appl. Phys. 25, 809 (1954)
- Jaffe B., Crook J. W. J., and Jaffe H.L., "Piezoelectric Ceramics", Academic Press, London (1971).
- Kakegawa K., <sup>1</sup>Department of Applied Chemistry, Faculty of Engineering, Chiba University, Katayama, I., Shimosato, H., Ashida, M., Kawayama, I., Tonouchi, M., Itoh, T., "Conference on Lasers and Electro-Optics CLEO", Pages 1-2 (2007).
- Kittel C., "Introduction to Solid State Physics", 7<sup>th</sup> ed. New York: Wiley, (1995).
- Kuwata J., Uchino K., and Nomura S., Ferroelectrics 37, 579 (1981)
- Kuwata J., Uchino K., and Nomura S., Jpn. J. Appl. Phys. 21 1298 (1982).
- Mishra S. K., and Pandey D., Appl. Phys. Lett. 69 1707 (1996)
- Mitsui T., Tatsuzaki I., and Nakamura E., "An Introduction to the Physics of Ferroelectrics", Gordon and Breach, London, (1976)
- Murgan R., Tilley D. R., Ishibashi Y., Webb J. F., and Osman J., J. Opt. Soc. Am. B 19 2007 (2002).
- Murgan R., Tilley D. R., Ishibashi Y., and Osman J., J. Fizik Malaysia. 23, 1 (2002<sup>a</sup>).
- Murgan R., Razak F., Tilley D. R., Tan T. Y., Osman J., and Halif M. N. A., Computational Material Science. 30 468 (2004).
- Newnham R., Mater. Res. Soc. Bull. 22 20 (1997).
- Noheda B., Cox D. E., Shirane G., Gonzalo J.A., Cross L.E., and Park S. E., Appl. Phys. Lett. 74, 2059 (1999).
- Noheda B., Gonzalo J., Cross L., Guo R., Park S.E., Cox D., Shirane G.: Phys. Rev. B 61, 8687 (2000<sup>a</sup>)
- Noheda B., Cox D., Shirane G., Guo R., Jones B., Cross L.: Phys. Rev. B 63, 014103, (2000<sup>b</sup>)
- Osman J., Ishibashi Y., and Tilley D. R., Jpn. J. of Appl. Phys. 37, 4887 (1998<sup>a</sup>).
- Osman J., Ishibashi Y., Lim S-C., and Tilley D. R., J. of Kor. Phys. Soc. 32, S446 (1998<sup>b</sup>).
- Razak F.1, Webb J. F., Murgan R., Ishibashi Y., Osman J., Ferroelectrics, 273 179, (2002).
- Saghi-Szabo G., Cohen R., and Krakauer H., Phys. Rev. B 59, 12771 (1999).
- Sawaguchi E., J. Phys. Soc. Jpn. 8, 615 (1953).
- Shirane G., Suzuki K., Jpn. J. Appl. Phys. 7 333 (1952).
- Sirenko A. A., Bernhard C., Golnik A., Clark A. M., Hao J., Si W, Nature, 404, 373 (2000).
- Vanderbilt D., and Cohen M.: Phys. Rev. B 63, 94108 (2001)
- Waser C. Böttger U., and Tiedke S., "Polar Oxides: Properties, Characterization, and Imaging", 4<sup>th</sup> edition, Weinheim, Wiley-VCH, (2005).
- Wilkinson A.P., Xu J., Pattanaik S., and Billinge J.L., Chem. Mat. 10 3611 (1998).
- Yamamoto T. and Ohashi S., Jpn. J. Appl. Phys., 34 5349 (1995).

Yamashita Y., Jpn. J. Appl. Phys., 33 5328 (1994).

Zhang S., Dong X., and Kojima S.. Jpn. J. Appl. Phys. 36 2994 (1997).

# Relaxor-ferroelectric PMN–PT Thick Films

Hana Uršič and Marija Kosec  
*Electronic Ceramics Department, Jožef Stefan Institute  
Slovenia*

## 1. Introduction

Electroceramic thick films are 2D (planar) structures that, in their simplest form, consist of a substrate, a bottom electrode, a ceramic film and a top electrode, with the thickness of an individual layer being typically between 1 and 100  $\mu\text{m}$ . The processing of thick films is similar to the processing of bulk ceramics, i.e., it involves powder synthesis, shaping and sintering. The major difference, however, is in the clamping of the film onto the substrate. The consequences of this are a constrained sintering, a possible reaction with the electrode or the substrate during firing, and the thermal stresses that are generated during the cooling. To minimize the chemical interaction of the film and the substrate the sintering temperature must be kept relatively low in comparison to that for the bulk. This requires a fine particle size for the powder and additives that form a liquid phase at the sintering temperature. This liquid phase must also be present to enable the densification under the constrained conditions, as was predicted and demonstrated in Kosec et al. (1999).

The effect of clamping the active film to the relatively stiff substrate results in smaller displacements in comparison to substrate-free structures. Due to the mismatch of the thermal expansion of the thick-film and substrate materials during the processing the properties of the thick films differ from those of the respective bulk ceramics. Furthermore, an additional drawback can be the deterioration of the thick film's properties due to its chemical interaction with the substrate. To ensure a sufficient displacement required for a certain application, different solutions have been proposed, such as a reduction in the thickness of the substrate, the processing of thick-film multilayer structures or the preparation of "substrate-free" structures.

In the world of technology there is a continuous, global increase of interest in the miniaturisation of devices, materials and system integration. Thick-film structures are a good example of the opportunities offered for the miniaturization of electromechanical systems by the successful implementation of new functional materials and technologies. Driven by the versatility of conventional thick-film technology, the processing of functional structures with thick films on different substrates is possible, along with many design possibilities.

In this chapter the progress in relaxor-ferroelectric  $\text{Pb}(\text{Mg}_{1/3}\text{Nb}_{2/3})\text{O}_3\text{-PbTiO}_3$  (PMN-PT) thick films is reported. The preparation procedures, the processing of PMN-PT thick films on different substrates, the structural and electrical characterization as well as PMN-PT thick-film devices are discussed. The phase composition and functional properties of PMN-PT thick films are discussed in terms of the thermal stresses generated in the films during

the thermal treatment. Due to these process-induced stresses the electrical and structural properties of the films can be changed dramatically in comparison to the unstressed films. Some representative examples of PMN-PT thick-film applications are described, including a novel approach to the manufacture of large-displacement “substrate-free” PMN-PT/Pt actuators using thick-film technology.

## 2. Relaxor-ferroelectric PMN-PT material

Ferroelectric and piezoelectric films are mostly based on lead oxide compounds, mainly  $\text{Pb}(\text{Zr,Ti})\text{O}_3$  (PZT) solid solutions. An alternative to PZT are the relaxor-based systems, where the term relaxor-ferroelectrics is used for solid solutions between relaxors such as  $\text{Pb}(\text{Mg}_{1/3}\text{Nb}_{2/3})\text{O}_3$  (PMN) and ferroelectrics such as  $\text{PbTiO}_3$  (PT) (Cross, 1987; Damjanovic, 2008). One of the most widely studied relaxor-ferroelectrics is  $\text{Pb}(\text{Mg}_{1/3}\text{Nb}_{2/3})\text{O}_3$ - $\text{PbTiO}_3$  (PMN-PT). These PMN-PT-based materials are characterized by a high dielectric permittivity, high piezoelectric properties, a high electrostriction, and are suitable for applications in multilayer capacitors, actuators, sensors and electro-optical devices (Park & Shrout, 1997a, 1997b).

The morphotropic phase boundary (MPB) in the  $(1-x)\text{Pb}(\text{Mg}_{1/3}\text{Nb}_{2/3})\text{O}_3$ - $x\text{PbTiO}_3$  system is located close to the  $x=0.35$  composition. The strong piezoelectric properties are related to the “polarization rotation” between the adjacent rhombohedral phase with the space group  $R\bar{3}m$  (subsequently referred to as the rhombohedral  $R\bar{3}m$  phase in the text) and tetragonal phase with the space group  $P4mm$  (subsequently referred to as the tetragonal  $P4mm$  phase) through one (or more) intermediate phase(s) of low symmetry, i.e., a monoclinic (orthorhombic or triclinic) phase (Davis et al., 2006; Noheda et al., 2001). As a consequence, the observation of a low-symmetry phase, e. g., a monoclinic phase, may suggest strong electromechanical responses.

It was shown (Singh & Pandey, 2003) that the MPB region of the PMN-PT ceramic material contains two monoclinic phases with the space groups  $Cm$  (subsequently referred to as the monoclinic  $Cm$  phase) and  $Pm$  (subsequently referred to as the monoclinic  $Pm$  phase) stable in the composition ranges  $0.27 < x < 0.30$  and  $0.31 < x < 0.34$ , respectively. For ceramics of the composition  $x = 0.35$ , the coexistence of the monoclinic  $Pm$  and the tetragonal  $P4mm$  phases was reported (Alguero et al., 2006, 2007; Carreaud et al., 2005; Singh & Pandey, 2003; Uršič et al., 2011a), stressing that the phase composition ratio between the monoclinic and the tetragonal phases depends on different parameters, such as the grain-size effect (Alguero et al., 2006, 2007; Carreaud et al., 2005) and the poling field (Uršič et al., 2011a) of the ceramics.

PMN-PT ceramics and a single crystal with its composition on the MPB can have the piezoelectric coefficients  $d_{33}$  as high as 700 pC/N (Kelly et al., 1997; Xia et al. 2007) and 1500–2800 pC/N (Park & Shrout, 1997a; Shrout et al., 1990; Zhang et al., 2001), respectively. The commonly used poling electric fields for the PMN-PT material vary from 2 to 3.5 kV/mm (Alguero et al., 2006, 2007; Leite et al. 2002; Kelly et al., 1997; Xia et al. 2007). On the other hand, the PMN-PT material with compositions  $x=0$ -0.1 shows relaxor behaviour (Cross et al., 1987; Swartz et al., 1982; Swartz et al., 1984) and are known as good electrostrictive materials (Kighelman et al., 2001; Uchino et al., 1890; Vikhnin et al., 2003; Zhao et al., 1995). Likewise, the electrostrictive effect of the MPB compositions was also reported to be relatively high (Bokov & Ye, 2002). Furthermore, due to its large responses to an applied electric field, the PMN-PT material was investigated as a promising material for actuator applications (Uršič et al., 2011).

### 3. PMN–PT thick films

#### 3.1 Processing of the PMN–PT thick films

The processing of relaxor or ferroelectric thick films has been discussed in the open literature by many authors. However, because of the lack of an assortment of commercially available thick-film materials and no conventional processing procedures the investigations made so far were carried out using different technological procedures and involved thick films with various compositions. The PMN–PT composition has recently been considered as an appropriate material for thick-film technology as it exhibits very good functional properties. The most commonly used method for the deposition of PMN–PT-based thick films is screen-printing (Akiyama et al., 1999; Gentil et al., 2004, 2005; Kosec et al., 2007, 2010; Uršič et al., 2008a, 2008b, 2010, 2011b). To form good-quality and high-performance PMN–PT thick films, a fine particle size of the PMN–PT powder is required. One way to prepare such powder is by mechanochemical synthesis (Kosec et al., 2007, 2010). In fig. 1 a (FE-SEM) micrograph and an X-ray diffraction (XRD) pattern of the 0.65PMN–0.35PT powder prepared by mechanochemical syntheses are shown. The families of planes for the 0.65PMN–0.35PT perovskite phase are given in brackets. It was shown by Rietveld refinement that the powder is not cubic; in fact the best fit was obtained for the monoclinic Pm phase. The particle size is sub-micrometre, i.e., the distribution is narrow with a median particle size  $d_{50}$  equal to 0.32  $\mu\text{m}$  (Kosec et al., 2010).

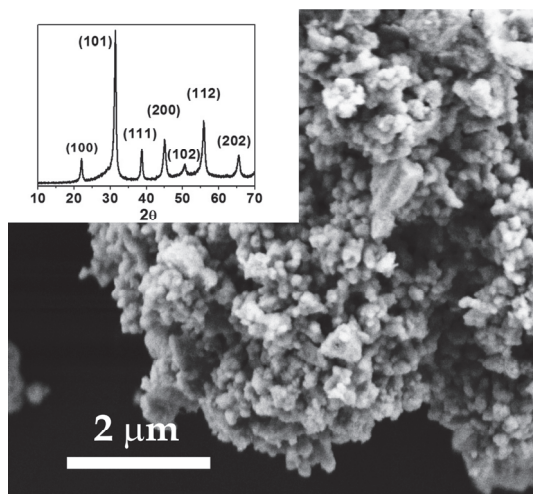


Fig. 1. The FE-SEM micrographs of 0.65PMN–0.35PT powder with 2 mol% excess of PbO prepared by mechanochemical synthesis. Inset: The XRD pattern of this powder. The families of the planes for the 0.65PMN–0.35PT perovskite phase are given in brackets.

For the screen-printing process the ceramic pastes are made by mixing the PMN–PT powder with different binders and organic carriers to obtain the suitable printability. The paste is then forced through the open areas of the screen onto the surface of the substrate. The scheme of the screen-printing procedure is shown in fig. 2 (top). After screen-printing the films are usually sintered for 2 h at temperatures between 800 and 1100°C (Gentil et al., 2004, 2005; Kosec et al., 2007, 2010; Uršič et al., 2008a, 2008b, 2010, 2011b). To minimize the

chemical interaction of the film and the substrate the sintering temperature is kept relatively low in comparison to that for the bulk ceramics, i.e., 1200°C. This requires additives that form a liquid phase at the sintering temperature.

To obtain a PMN-PT thick film with the desired functional response, the material has to be dense and without any secondary phase. In the literature the effect of different sintering aids on the densification of thick films was investigated and the best densification and a large increase in the grain size was obtained for the sintering aid  $\text{LiCO}_3$  (Gentile et al., 2005). The other way that the densification of the PMN-PT can be aided is by the presence of the PbO-rich liquid phase originating from the starting composition containing an excess of PbO. To keep the liquid phase in the film a lead-oxide-rich atmosphere can be created, e. g., using a packing powder rich in PbO. In the literature the atmosphere was achieved with  $\text{PbZrO}_3$  packing powder with an excess of PbO, short PZ/P (Gentil et al., 2004; Kuščer et al., 2008; Kosec et al., 2010; Uršič et al., 2008b, 2010) or with the packing powder PZ/P+PMN (Gentil et al., 2004). During heating the PbO sublimates from the high-surface-area packing powder, giving a PbO-saturated atmosphere around the thick film that keeps the PbO liquid in the film. Since the system is semi-closed, the PbO is lost slowly from the system, first from the powder and later from the film. Therefore, the time for which the liquid phase is present in the PMN-PT film depends on the amount of packing powder. The process is shown schematically in fig. 2 (bottom). The density of the films is proportional to the duration of the liquid-phase sintering and increases with the amount of packing powder, up to the limit where the amount of packing powder is too high, and after sintering of the film there is still enough PbO vapour to keep the PbO in the PMN-PT thick films (Kuščer et al., 2008; Kosec et al., 2010).

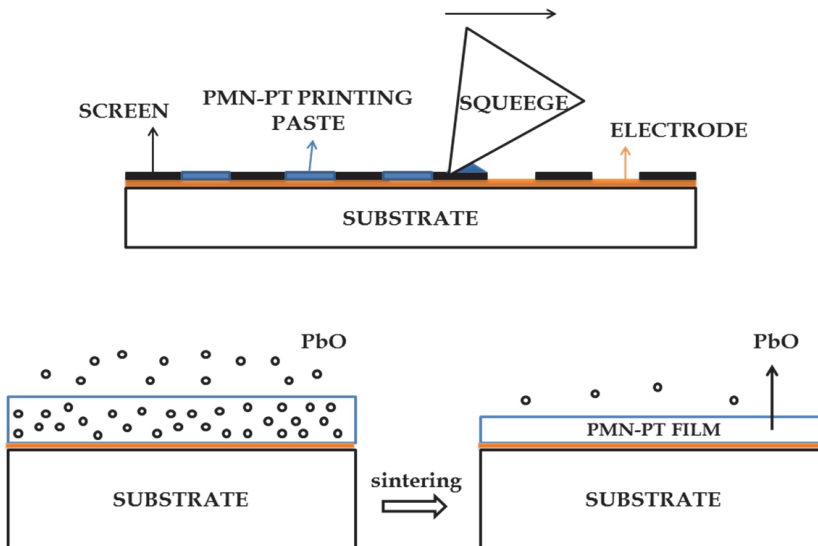


Fig. 2. The scheme of screen-printing (top) and sintering (bottom) of PMN-PT thick films.

In addition to the screen-printing, the successful experiments with electrophoretic deposition (Chen et al., 2009a, 2009b; Fan et al., 2009; Kuščer & Kosec, 2009), the hydrothermal process

(Chen et al., 2008) and sol-gel (Wu et al., 2007; Zhu et al., 2010) were reported. The PMN–PT thick-films were also prepared as single crystals by a modified Bridgman method and after the preparation they were bonded on Si substrates (Peng et al., 2010).

The proper selection of the materials, including the compatibility of the functional material with the electrodes and the substrates, is among the most important for the successful processing of thick-film structures. The most common substrate material used for PMN–PT thick films is polycrystalline  $\text{Al}_2\text{O}_3$  (alumina) (Gentil et al., 2004, 2005; Kosec et al., 2007, 2010; Uršič et al., 2008a, 2008b, 2010, 2011b, Fan et al., 2009; Kuščer & Kosec, 2009). However, PMN–PT- and PMN-based thick films were also processed on Si (Gentil et al., 2004; Wu et al., 2007; Zhu et al., 2010), Pt/Pt (Chen et al., 2009a, 2009b; Uršič et al., 2008, 2010), Ti (Chen et al., 2008), AlN (Uršič et al., 2010) and PMN–PT (Uršič et al., 2010, 2011b) substrates. In fig. 3 the photographs and the scanning-electron-microscope (SEM) micrographs of the 0.65PMN–0.35PT thick-film on the alumina substrate are shown. In order to prevent the chemical interactions between the PMN–PT film and the alumina substrate a  $\text{PbZr}_{0.53}\text{Ti}_{0.47}\text{O}_3$  (PZT) barrier layer was processed between the substrate and the bottom electrode (fig. 3(c)) (Kosec et al., 2010; Uršič et al., 2010). The use of a PZT-based barrier layer to prevent any film/substrate interactions has been proposed before for  $(\text{Pb},\text{La})(\text{Ti},\text{Zr})\text{O}_3$  (PLZT) thick films on alumina substrates (Holc et al., 1999; Kosec et al., 1999).

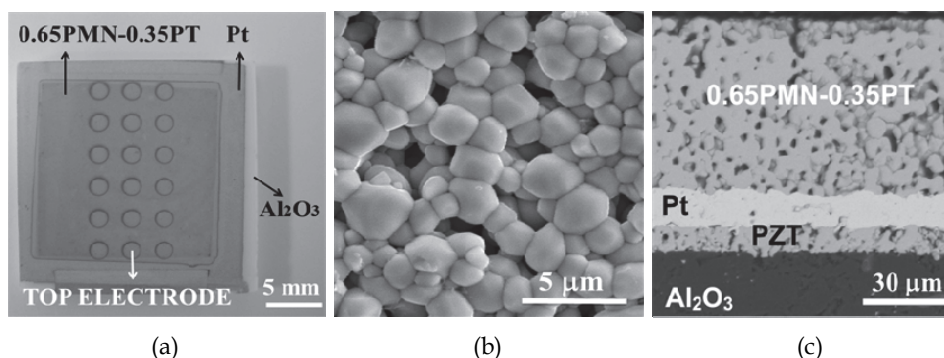


Fig. 3. (a) Photograph of the 0.65PMN–0.35PT thick film on  $\text{Al}_2\text{O}_3$  substrate. SEM micrographs of (b) the surface and (c) the cross-section of the 0.65PMN–0.35PT thick film on  $\text{Al}_2\text{O}_3$  substrate. The bottom electrode is Pt and the top electrode is sputtered Au. The PZT barrier layer is interposed between the  $\text{Al}_2\text{O}_3$  substrate and the Pt electrode.

### 3.2 Structural and electrical properties of PMN–PT thick films clamped on rigid substrates

In comparison with PMN (Gentil et al., 2004) and 0.80PMN–0.20PT (Chen et al., 2009b) thick films that exhibit relaxor behaviour, the 0.65PMN–0.35PT thick films on alumina substrate show ferroelectric behaviour (Gentil et al., 2004; Kosec et al., 2007; Uršič et al., 2008b). However, the properties of PMN–PT thick films depend not only on the material composition, but also on the compatibility of the functional materials with the electrodes, adhesion layers, substrate materials and technological parameters relating to their processing (Gentil et al., 2005; Uršič et al., 2010, 2011b). The films processed on substrates at elevated temperatures and cooled to room temperature are thermally stressed, due to the mismatch between the thermal expansion coefficient (TEC) of the film and the substrate.

Recent investigations (Uršič et al., 2010, 2011b) showed that due to the process-induced thermal stresses the structural and electrical properties of PMN-PT thick films with the MPB composition can be changed dramatically in comparison to the unstressed films.

For sake of clarity we now focus on 0.65PMN-0.35PT thick films on thick  $\text{Al}_2\text{O}_3$  and 0.65PMN-0.35PT substrates prepared under identical processing conditions, i.e., sintered at  $950^\circ\text{C}$  for 2 h and then cooled to room temperature. After cooling to room temperature the films on the  $\text{Al}_2\text{O}_3$  substrates are under compressive thermal stress, while the TEC of the substrate is higher than the TEC of the film. The basic equation for the thermal stress in a film clamped to a substrate, regardless of the film's thickness, is (Ohring, 1992):

$$\sigma_f(T) = (\alpha_s - \alpha_f)(T_2 - T_1)Y_f / (1 - \nu_f), \quad (1)$$

where  $\alpha_s$  is the TEC of the substrate ( $\text{K}^{-1}$ ),  $\alpha_f$  is the TEC of the film ( $\text{K}^{-1}$ ),  $Y_f$  is the Young's modulus of the film ( $\text{N}/\text{m}^2$ ) and  $\nu_f$  is the Poisson's ratio of the film. If the films are cooled down to room temperature then  $T_1$  is the processing temperature (K),  $T_2$  is room temperature (K) and  $\Delta T = T_2 - T_1$  is the temperature difference (K). Normally, thick films are considered in the same way as thin films; however, in the case of thick films, the thickness of the film plays an important role, and this fact cannot be neglected, as we have been able to demonstrate in Uršič et al., (2011b). The compressive residual stress in the 0.65PMN-0.35PT films on  $\text{Al}_2\text{O}_3$  substrates calculated from the basic eq. (1), regardless of the film thickness, is -168.5 MPa.

To evaluate the compressive thermal stress with respect to the film thickness, the  $x$  component of the thermal stress  $\sigma$  (the component parallel to the film surface  $\sigma_x$ ) of a 0.65PMN-0.35PT thick film on an  $\text{Al}_2\text{O}_3$  substrate was calculated using the finite-element (FE) method. The FE analysis of the stress was performed in two steps. First, the influence of the bottom Pt electrode and the PZT barrier layer were neglected. Fig. 4 (a) shows the distribution of the  $\sigma_x$  obtained for the 20- $\mu\text{m}$ -thick 0.65PMN-0.35PT film on a rigid 3-mm-thick  $\text{Al}_2\text{O}_3$  substrate. Due to the symmetry, the  $y$  component of the stress ( $\sigma_y$ ) is equal to the  $x$  component  $\sigma_x$ . In fig. 4 (b) the  $\sigma_x$  vs. the position on the top surface of the 20- $\mu\text{m}$ - and 100- $\mu\text{m}$ -thick films is shown. The red line in fig. 4 (a) shows the coordinates ( $x, y = 0, z = 20$  or 100) where the  $\sigma_x$  presented in fig. 4 (b) was calculated. The calculated stress  $\sigma_x$  in the film is compressive, with a value in the central position on the top surface ( $x = 0, y = 0, z = 20$  or 100) of -167.4 MPa and -162.7 MPa for the 20- $\mu\text{m}$ - and 100- $\mu\text{m}$ -thick films, respectively. The decrease of the  $\sigma_x$  on the boundaries of the films, see fig. 4 (b), is due to the free boundary condition.

In the second step the influences of the PZT barrier and the Pt bottom-electrode layers were studied. For this reason, the FE model was updated accordingly. The  $\sigma_x$  on the top surface of the 20- $\mu\text{m}$ - and 100- $\mu\text{m}$ -thick films for both models (with and without the Pt and PZT layers) is shown in fig. 4 (c). No major difference was observed between the solutions of these two models, which means that the thin PZT barrier layer and the Pt bottom electrode do not have much influence on the stress conditions in the 0.65PMN-0.35PT film on the rigid 3-mm-thick  $\text{Al}_2\text{O}_3$  substrate. The calculated values for  $\sigma_x$  in the central position on the top surface of the film ( $x = 0, y = 0, z = 20$  or 100) for the updated model are -168.1 MPa and -163.3 MPa for the 20- $\mu\text{m}$ - and 100- $\mu\text{m}$ -thick films, respectively (Uršič et al., 2011b).

In contrast, in the case of 0.65PMN-0.35PT films on 0.65PMN-0.35PT substrates, the film and substrate are made from the same material and therefore there is no mismatch between the TEC of the film and the substrate, hence the films on 0.65PMN-0.35PT substrates are not stressed. Fig. 5 shows SEM micrographs of the 0.65PMN-0.35PT thick-film surface and the cross-section of the film on the 0.65PMN-0.35PT substrate.

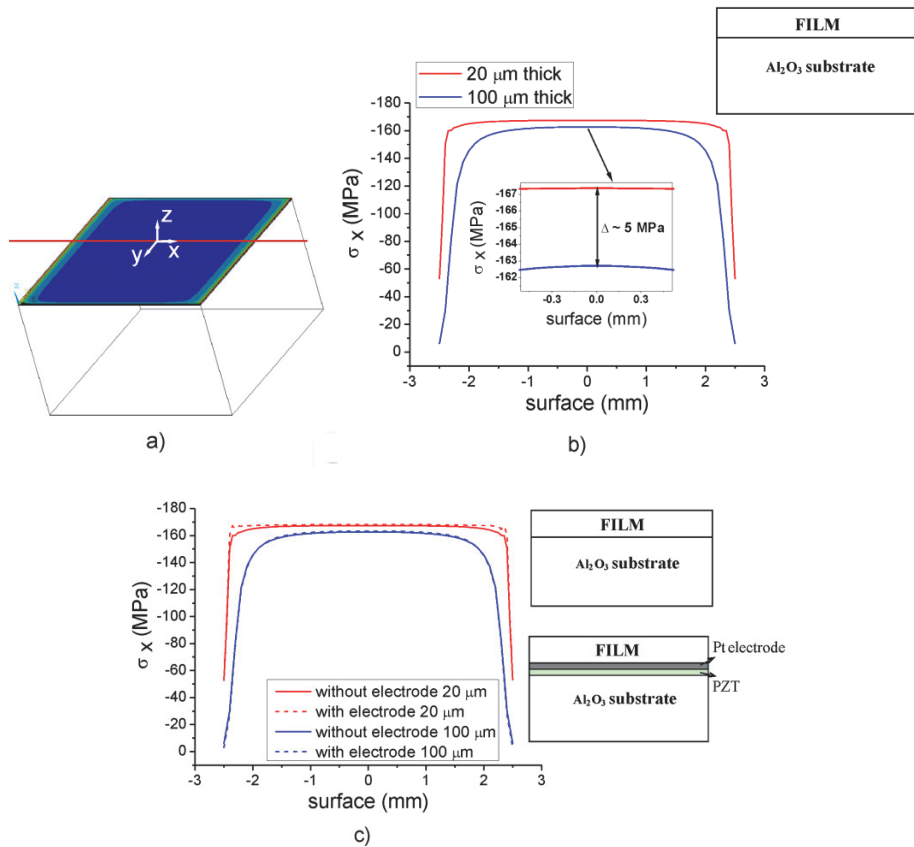


Fig. 4. (a) The model structure of the 0.65PMN-0.35PT film clamped on the thick alumina substrate and the  $\sigma_x$  distribution. The line shows the coordinates ( $x, y = 0, z = \text{top surface}$ ), where  $\sigma_x$  was calculated. (b) The  $\sigma_x$  vs. the position on the top surface of the 20- $\mu\text{m}$ - and 100- $\mu\text{m}$ -thick films. Inset: The enlarged central part of the graph. (c) The comparison of the  $\sigma_x$  shown in (b) with the updated calculation made for the structure including the Pt bottom electrode and the PZT barrier layer. Right: Schemes of the cross-section of the film-substrate structure (Reprinted with permission from [Uršič., H. et al., J. Appl. Phys. Vol. 109, No. 1.]. Copyright [2011], American Institute of Physics).

The 0.65PMN-0.35PT films on  $\text{Al}_2\text{O}_3$  substrates were sintered to a high density with a coarse microstructure, as can be seen in figs. 3 (b) and (c). The median grain size of these films is  $1.7 \mu\text{m} \pm 0.6 \mu\text{m}$ . In contrast, the films on the 0.65PMN-0.35PT substrates were sintered to a lower density and the microstructure consists of smaller grains, i.e.,  $0.5 \mu\text{m} \pm 0.2 \mu\text{m}$  (figs. 5 (a) and (b)). Hence, the substrates on which the films are clamped influence the microstructure of the films (Uršič et al., 2010).

Furthermore, in PMN-PT material the MPB shifts under the compressive stress (Uršič et al., 2011b). In figs. 6 (a) and (b) the measured XRD spectrum, the XRD spectrum calculated by a Rietveld refinement and the measured XRD spectra in the range from  $2\theta = 44.4^\circ$  to  $2\theta = 45.7^\circ$  are shown for 0.65PMN-0.35PT films on  $\text{Al}_2\text{O}_3$  and 0.65PMN-0.35PT substrates.

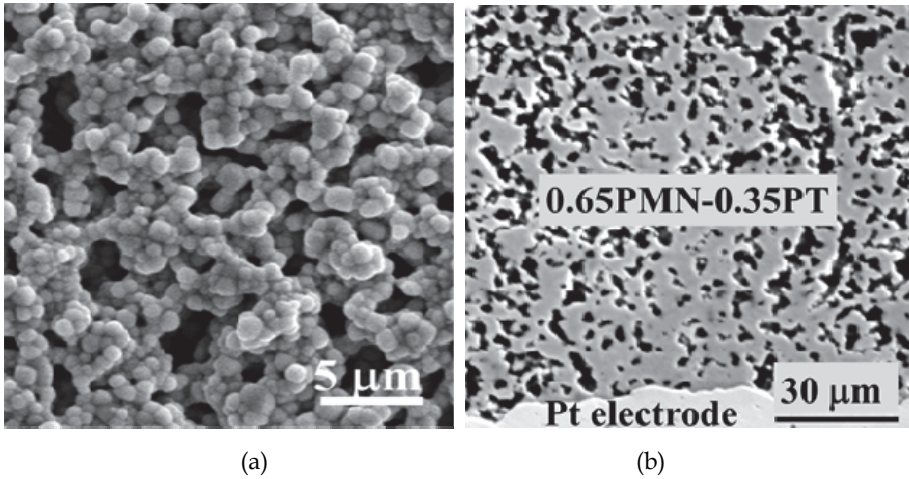


Fig. 5. SEM micrographs of (a) the surface and (b) the cross-section of the 0.65PMN-0.35PT thick film on the 0.65PMN-0.35PT substrate. The bottom electrode is Pt and the top electrode is sputtered Au.

The phase composition of the 0.65PMN-0.35PT films under compressive stress is a mixture of the monoclinic Pm and tetragonal P4mm phases, while the non-stressed films are monoclinic Pm (Uršič et al., 2010, 2011b). This is in agreement with previous results reported for bulk 0.65PMN-0.35PT ceramics, where it is shown that the ceramics with larger grains consist of the monoclinic Pm and tetragonal P4mm phases, while the ceramics with submicron grains are mainly monoclinic Pm (Alguero et al., 2007). In addition to the grain size effect, in thick films the residual compressive stresses also influence the phase composition of the films. This can be clearly seen from the fact that the higher percentage of tetragonal P4mm phase is obtained for films on Al<sub>2</sub>O<sub>3</sub> substrates rather than for “stress-free” bulk ceramics sintered at 1200°C with a similar grain size. The 20- $\mu$ m-thick film on the Al<sub>2</sub>O<sub>3</sub> substrate that is under a stress of -168.1 MPa contains 58% of the tetragonal phase and the rest is monoclinic phase, while the “stress-free” bulk ceramic with the same composition and similar grain size contains only 14% of the tetragonal phase. Furthermore, if the 0.65PMN-0.35PT film on the Al<sub>2</sub>O<sub>3</sub> substrate is thicker (for example, 100  $\mu$ m), it contains more monoclinic phase, which is more like the phase composition of the “stress-free” bulk ceramic (Uršič et al., 2011b).

The dielectric constant ( $\epsilon$ ) vs. temperature and the hysteresis loops of 0.65PMN-0.35PT thick films under compressive stress (films on Al<sub>2</sub>O<sub>3</sub> substrates) and unstressed films (films on 0.65PMN-0.35PT substrates) are shown in fig. 7. The films under compressive stress show ferroelectric behaviour; the phase-transition peak between the high-temperature (HT) cubic phase and the tetragonal P4mm phase is sharp, with the maximum value of the dielectric constant  $\epsilon_{\max} = 20,500$  at 1 kHz and no dependence of the peak temperature ( $T_{\max}$ ) at which  $\epsilon_{\max}$  is achieved can be observed (Uršič et al., 2008b). These films show saturated ferroelectric hysteresis loops with a remnant polarization  $P_r$  of 21  $\mu$ C/cm<sup>2</sup>. While the HT phase-transition peak of the unstressed films is broader, the  $\epsilon_{\max}$  is only 2100 at 1 kHz. For these films the  $P_r$  is 8  $\mu$ C/cm<sup>2</sup>.

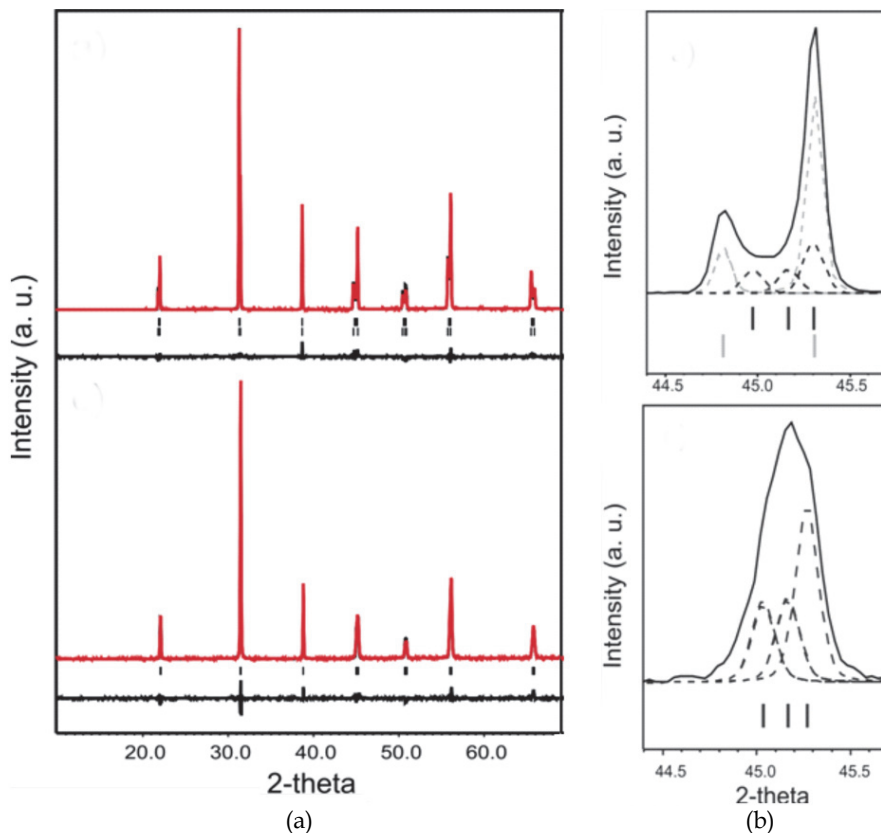


Fig. 6. (a) Measured (red), calculated (black) and difference (black curve at the bottom) curves of the XRD Rietveld refinement for 0.65PMN-0.35PT films deposited on  $\text{Al}_2\text{O}_3$  (top) and 0.65PMN-0.35PT (bottom) substrates. The top marks correspond to the tetragonal phase and the bottom ones to the monoclinic. (b) XRD diagrams of 0.65PMN-0.35PT thick films on  $\text{Al}_2\text{O}_3$  (top) and 0.65PMN-0.35PT (bottom) substrates in the range from  $2\theta = 44.4^\circ$  to  $2\theta = 45.7^\circ$ . The refined peak positions of the (002), (200) tetragonal (grey) and the (002), (200), (020) monoclinic (black) phases are marked. (Reprinted from J. Eur. Ceram. Soc., 30/10, Uršič, H. et al., Influence of the substrate on the phase composition and electrical properties of 0.65PMN-0.35PT thick films, pp. (2081–2092), Copyright (2010), with permission from Elsevier)

Similar behaviour was reported for the 0.65PMN-0.35PT bulk ceramic. The 0.65PMN-0.35PT ceramics show ferroelectric behaviour. However, when the average grain size of the 0.65PMN-0.35PT ceramics decreases to the submicron range and approaches the nanoscale, relaxor-type behaviour is observed down to room temperature, which causes a strong decrease in the electrical polarization (Alguero et al., 2007). From fig. 7 it can be clearly seen that the grain size effect also influences the properties of 0.65PMN-0.35PT thick films, in a similar way as in bulk ceramics, while the median grain size of films on the  $\text{Al}_2\text{O}_3$  and 0.65PMN-0.35PT substrates is  $1.7 \mu\text{m}$  and  $0.5 \mu\text{m}$ , respectively. However, the reason for

lower properties of the films on the 0.65PMN–0.35PT substrates is also the lower density of these films.

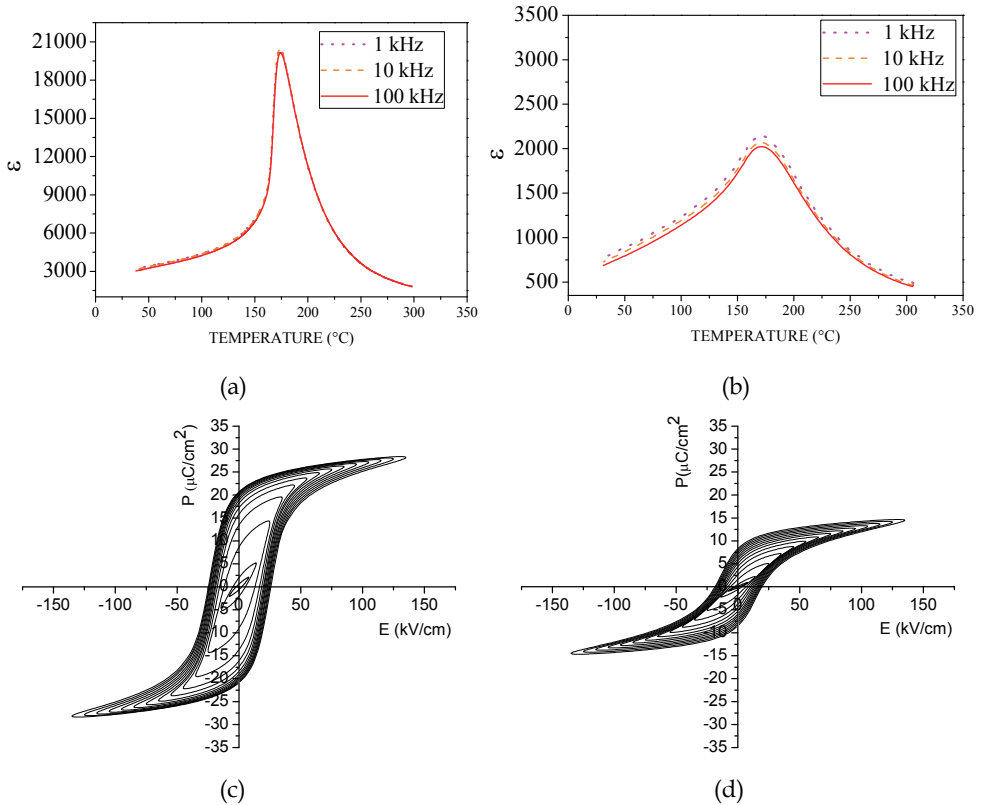


Fig. 7. The dielectric constant ( $\epsilon$ ) vs. temperature for 0.65PMN–0.35PT (a) thick films under compressive stress and (b) unstressed films. The hysteresis loops for 0.65PMN–0.35PT (c) thick films under compressive stress and (d) unstressed films.

### 3.3 Piezoelectric and electrostrictive properties of PMN–PT thick films

As already mentioned, the PMN (Gentil et al., 2004) and 0.80PMN–0.20PT (Chen et al., 2009b) thick films exhibit relaxor behaviour. These compositions are known to be good electrostrictive materials, while the 0.65PMN–0.35PT thick films on alumina substrates show ferroelectric and piezoelectric behaviour (Gentil et al., 2004; Kosec et al., 2007).

In piezoelectric and ferroelectric materials the mechanical stress  $T$  and the strain  $S$  are related to the dielectric displacement  $D$  and the electric field  $E$ , as indicated in the constitutive equations:

$$\{S\} = [s^E] \{T\} + [d] \{E\} \quad (2)$$

$$\{D\} = [d]^T \{T\} + [\varepsilon^T] \{E\} \quad (3)$$

where  $[s^E]$  is the compliance matrix evaluated at a constant electric field,  $[\varepsilon^T]$  is the permittivity matrix evaluated at a constant stress and  $[d]$  is the matrix of the piezoelectric coefficients.

The successful design of thick-film structures for various applications can take place only with a thorough knowledge of the electrical and electromechanical properties of the thick film. Since the effective material properties of the thick film depend not only on the material composition but also on the compatibility of the thick-film material with the substrate, the characterisation of the piezoelectric thick films is required before the design phase. Because of a lack of standard procedures for the characterization of thick films, special attention has to be paid to providing the actual material parameters. In order to obtain proper material parameters some unconventional characterisation approaches have been used, such as a nano-indentation test for the evaluation of the compliance parameters (Uršič et al., 2008a; Zarnik et al., 2008) or some standard-less methods for a determination of the piezoelectric coefficients of the thick films (Uršič et al., 2008a, 2008c).

The piezoelectric coefficients of the thick films differ from the coefficients of the bulk ceramics with the same composition. One of the main reasons for this is that the films are clamped by the substrates. For a clamped film the ratio  $D_3/T_3$  does not represent the piezoelectric coefficient  $d_{33}$  of the free sample, but an effective piezoelectric coefficient  $d_{33}^{eff}$  (Lefki & Dormans; 1994):

$$d_{33}^{eff} = d_{33} - 2d_{31} \frac{\frac{v_s}{Y_s} + s_{13}^E}{(s_{11}^E + s_{12}^E)}, \quad (4)$$

where  $d_{33}$  and  $d_{31}$  are the direct and the transverse piezoelectric coefficients, respectively, (C/N),  $s_{13}^E$ ,  $s_{11}^E$ ,  $s_{12}^E$  are the elastic compliance coefficients at a constant electric field ( $m^2/N$ ),  $v_s$  is the Poisson's ratio of the substrate, and  $Y_s$  is the Young's modulus of the substrate ( $N/m^2$ ).

Since for PMN–PT material  $d_{31} < 0$ ,  $s_{13} < 0$  and  $d_{31}$  is relatively large, the effective coefficient measured for the films is lower than that of the unclamped material ( $d_{33}^{eff} < d_{33}$ ). Generally, the characteristics of thick-film bending actuators mainly depend on the transverse piezoelectric coefficient  $d_{31}^{eff}$ . The material parameters reported in the open literature for PMN–PT thick films processed on  $Al_2O_3$  substrates are collected in Table 1. As is evident from these data, the elastic compliance of the 0.65PMN–0.35PT thick films was higher than those of the bulk ceramics, while the piezoelectric coefficients  $d_{31}$  and  $d_{33}$  were smaller in comparison with the bulk coefficients.

As the magnitude of the electric field strength increases in 0.65PMN–0.35PT thick films the contribution of the second-order electrostrictive effect also prevails (Uršič et al., 2008a, 2008b). The equation for the strain in the 0.65PMN–0.35PT material under an applied electric field is:

$$S_i = d_{ij}E_k + M_{ij}E_k^2, \quad (5)$$

where  $S$  is the strain,  $E$  (V/m) is the electric field,  $d$  (m/V) is the piezoelectric coefficient and  $M$  ( $m^2/V^2$ ) is the electrostrictive coefficient of the 0.65PMN–0.35PT material.

Coefficient (unit)	0.65PMN–0.35PT on Al <sub>2</sub> O <sub>3</sub> (Uršič et al., 2008a)	0.655PMN–0.345 PT bulk ceramics (Alguero et al., 2005)
$s_{11}^E$ (10 <sup>-12</sup> m <sup>2</sup> /N)	23.1	13.5
$s_{33}^E$ (10 <sup>-12</sup> m <sup>2</sup> /N)	24.8	14.5
$s_{12}^E$ (10 <sup>-12</sup> m <sup>2</sup> /N)	-8.20	-4.8
$s_{13}^E$ (10 <sup>-12</sup> m <sup>2</sup> /N)	-10.1	-5.9
$s_{44}^E$ (10 <sup>-12</sup> m <sup>2</sup> /N)	53	31.0
$s_{66}^E$ (10 <sup>-12</sup> m <sup>2</sup> /N)	62.5	36.6
$d_{31}$ (10 <sup>-12</sup> C /N)	-100	-223
$d_{33}$ (10 <sup>-12</sup> C /N)	140–190* (Gentil et al., 2004; Kuščer et al. 2009; Kosec et al., 2007, 2010; Uršič et al., 2011b)	480

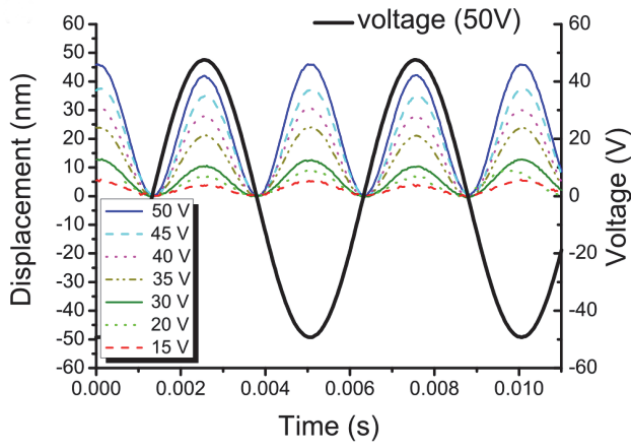
\*authors present the coefficient  $d_{33}$ , of the 0.65PMN–0.35PT thick film; however, following the reported experiments this coefficient is  $d_{33}^{eff}$

Table 1. The elastic and piezoelectric properties of the 0.65PMN–0.35PT thick films on Al<sub>2</sub>O<sub>3</sub> substrates. For comparison the properties of bulk 0.655PMN–0.345PT are added.

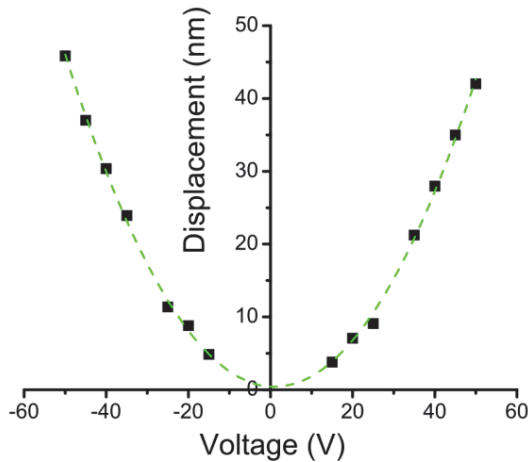
The second-order electrostrictive effect was measured for the 0.65PMN–0.35PT thick film on the alumina substrate. Measurements of displacement vs. time at different voltage amplitudes and displacement vs. voltage amplitude for the 0.65PMN–0.35PT thick film on the Al<sub>2</sub>O<sub>3</sub> substrate are shown in figs. 8 (a) and (b), respectively. The second-order electrostrictive coefficient  $M_{33}$  for the thick films is  $7.6 \cdot 10^{-16}$  m<sup>2</sup>/V<sup>2</sup> (Uršič et al., 2008b). In comparison with the  $M_{33}$  of 0.65PMN–0.35PT single crystals, i. e., from  $13$  to  $40 \cdot 10^{-16}$  m<sup>2</sup>/V<sup>2</sup> (Bookov & Ye, 2002), the measured electrostrictive coefficient for the 0.65PMN–0.35PT thick film is lower. There are several parameters that could reduce the electrostrictive coefficients of films, i.e., clamping of the film to the substrate and a lower dielectric constant in the films compared to single crystals. However, in comparison to the  $M_{33}$  value for PMN (x=0) thin films, which is  $8.9 \cdot 10^{-17}$  m<sup>2</sup>/V<sup>2</sup> (Kighelman et al., 2001), the value for thick films with the MBP composition is much higher.

### 3.4 PMN–PT thick-film functional structures for certain applications

The designers of 0.65PMN–0.35PT thick-film functional structures for certain applications should be aware of all the above-mentioned technological effects influencing the resulting properties of thick films. Since the effective material properties of the 0.65PMN–0.35PT thick film depend not only on the material composition, but also on its compatibility with the substrate and the electrodes, and the technological parameters relating to the film processing, the characterisation of these films is required before the design phase. Due to its large responses to an applied electric field the PMN–PT material has been investigated as a promising material for actuator applications (Uršič et al., 2008a, 2008b). The disadvantage of the PMN–PT material is that it can be depoled by the application of negative electric field, due to a switch of the domain walls.



(a)



(b)

Fig. 8. (a) Measurements of displacement vs. time at different voltage amplitudes for the 0.65PMN-0.35PT thick film on the  $\text{Al}_2\text{O}_3$  substrate. Measurement frequency 200 Hz. (b) The displacement vs. voltage amplitude for the 0.65PMN-0.35PT thick film on the  $\text{Al}_2\text{O}_3$  substrate. The dotted line (quadratic fit) between the measured values is just a guide to the eye. (Reprinted with permission from Uršič, H. et al., *J. Appl. Phys.* Vol. 103, No. 12.]. Copyright [2008], American Institute of Physics).

Recently, single-crystal thick films bonded to Si substrates were prepared for high-frequency ultrasonic transducers. The transducer exhibited a good energy-conversion performance with a very low insertion loss. This insertion loss is significantly better than what could be obtained using devices with conventional piezoelectric materials, such as PZT and polyvinylidene fluoride PVDF (Peng et al., 2010).

Driven by the versatility of conventional thick-film technology, various designs of thick-film piezoelectric actuators are possible. The simplest thick-film piezoelectric actuator design is a free-standing cantilever beam that can be realized as a bimorph or multimorph multilayer structure. In combination with the materials and technologies enabling 3D structuring, even arbitrarily shaped thick-film actuator structures can be feasible. According to the type of displacement, the most common thick-film piezoelectric actuators are categorised as cantilever- (or bending) and membrane-type actuators. The bending-type actuators are generally capable of larger displacements, but exert a weak generative force. Due to the clamping to the substrate they have smaller displacements in comparison to the substrate-free structures. Furthermore, the properties of the thick films differ from those of the respective bulk ceramics; in particular, the piezoelectric properties are weaker and can even be reduced by an interaction with the reactive substrates. All these effects should be considered in the design of the structure and the technological procedure (Uršič et al., 2011c).

A novel approach to manufacturing large-displacement PMN-PT/Pt actuators by using thick-film technology based on the screen printing of the functional layers was developed (Uršič et al., 2008a). The actuators were prepared by screen-printing the PMN-PT films over the Pt electrodes directly onto  $\text{Al}_2\text{O}_3$  substrates, which results in a poor adhesion between the electrodes and the substrates, enabling the PMN-PT/Pt thick-film composite structures to be simply separated from the substrates. In this way, “substrate-free” actuator structures were manufactured. The scheme of the cross-section and the photograph of the top view of the PMN-PT/Pt actuators are shown in fig. 9 (a) and (b). The PMN-PT/Pt actuator during a measurement of the displacement is shown in fig. 9 (c).

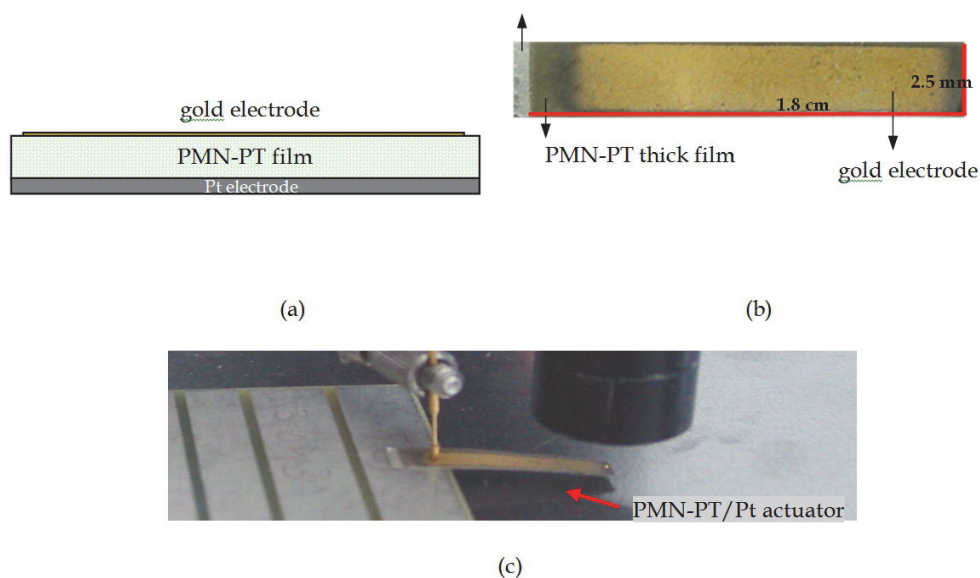


Fig. 9. (a) The scheme of the cross-section and (b) the photograph of the top view of the PMN-PT/Pt bimorph actuators. (c) The actuator during the measurement of displacement. The measurements were performed at the tip of the actuator's cantilever.

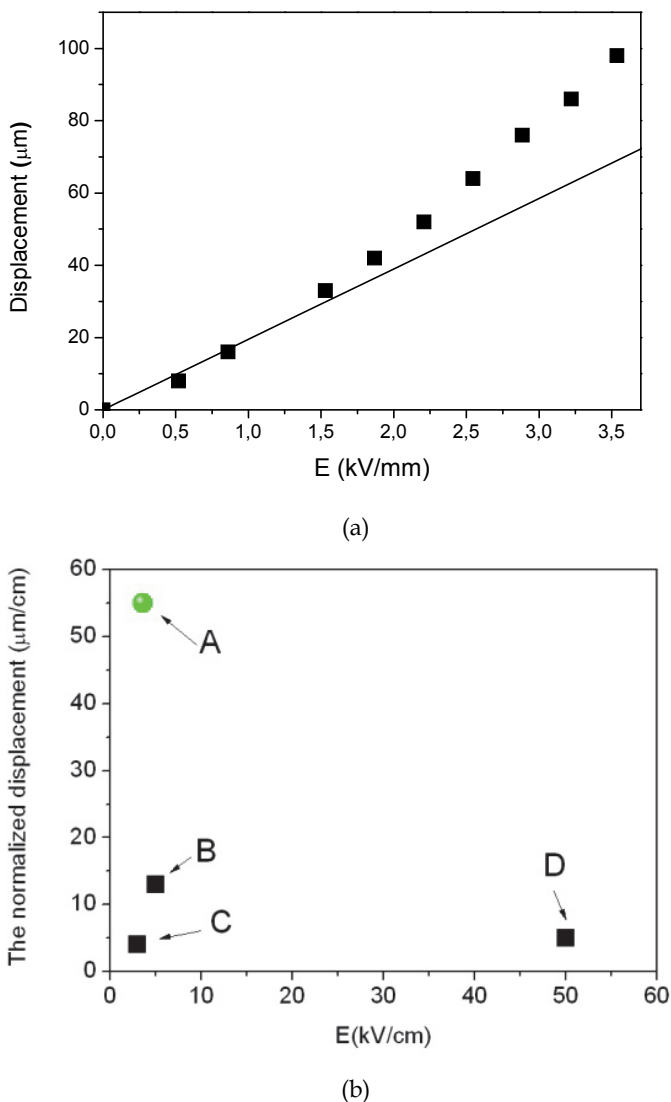


Fig. 10. (a) The bending displacement vs. applied electric field for the PMN-PT/Pt actuator and the linear finite-element model of the actuator bending (line). (b) The normalized displacement for the PMN-PT/Pt thick-film actuator in comparison with the data from the literature. Legend A: 0.65PMN-0.35PT/Pt thick-film actuator (Uršič 2008a), B: 0.65PMN-0.35PT+0.90PMN-0.10 actuator (Hall et al., 2006), C: 0.65PMN-0.35PT+0.90PMN-0.10PT actuator (Hall et al., 2005), D: PZT-thick film on alumina substrate, (Belavič et al. 2006; Zarnik et al., 2007). (Reprinted from Sens. Actuat. B Chem., 133 /2, Uršič, H. et al., A large-displacement  $65\text{Pb}(\text{Mg}_{1/3}\text{Nb}_{2/3})\text{O}_3\text{-}35\text{PbTiO}_3/\text{Pt}$  bimorph actuator prepared by screen printing, pp. (699-704), Copyright (2008), with permission from Elsevier).

The measurements of bending displacements were performed at the tip of the actuator's cantilever. The displacement vs. applied electric field for the PMN-PT/Pt actuator is shown in fig. 10 (a). In addition, the linear FE model of the actuator displacement is added. The measured normalized displacement (displacement per unit length) of these actuators is very high, i.e., 55  $\mu\text{m}/\text{cm}$  at 3.6 kV/cm (Uršič et al., 2008a). The comparison between the normalized displacements of PMN-PT/Pt thick-film actuators and PMN-PT actuators from the literature is shown in fig. 10 (b).

The characteristics of the actuators made by using PMN-PT differ from those of the linear piezoelectric actuators (e.g., PZT actuators), mainly because of the high electrostrictive effect in the PMN-PT material. This effect takes place particularly at larger electric fields (fig. 10(a)). However, under low applied electric fields, i.e., lower than 1.5 kV/cm for the MPB compositions (Feng et al., 2004; Uršič et al., 2008a), the major effect is the linear piezoelectric effect (fig. 10(a)). Hence, at low electric fields, not just PZT, but also PMN-PT actuators show a linear response to the applied electric field. For some applications, the 1.5 kV/cm is a large input value, for example, in mobile devices where a voltage of only 10 V is normally used (Ko et al., 2006). In any case, the PMN-PT material can be appropriate for bending actuators in applications operating at higher voltages, where the linearity of the response to the applied electric field is not required.

PMN-PT thick films have many potential applications. Depending on the application, different constructions and realisations of the PMN-PT thick-film structures are possible. The state of the art in the processing of PMN-PT structures is the development of new, effective functional structures with the desired output for specific applications. There are still a number of challenges to be faced in the production of PMN-PT structures and many possibilities for further improvements in their performance to meet the industrial demands for production.

#### 4. Conclusion

The progress in PMN-PT thick films is a consequence of the growing opportunities offered by micro-electromechanical systems. The relaxor-ferroelectric PMN-PT compositions are considered as appropriate materials for thick-film technologies, where they exhibit very good functional properties.

To form good-quality and high-performance PMN-PT thick films, a fine particle size of the PMN-PT powder is required. One way to prepare such a powder is mechanochemical synthesis. The most commonly used method for the deposition of PMN-PT-based thick films is screen-printing; however, a few experiments with electrophoretic deposition, the hydrothermal process and sol-gel were also reported. The proper selection of the materials, including the compatibility of the functional PMN-PT material with the electrodes and the substrates, is among the most important factors for the successful processing of PMN-PT thick-film structures.

The process-induced residual stresses in the thick-film structure and the possible reactions between the thick film and the reactive substrate may change considerably the functional properties of the films. The clamping of the PMN-PT film to the substrate influences the electro-active response of the film. In addition, the interactions between the PMN-PT film and the substrate may result in a deterioration of the material's functional properties.

New research has shown that the thermal residual stresses in the films have a great influence on the structural and electrical properties of the films. The difficulty is in separating the influence of the thermal stresses from the influence of the microstructure, while the thermal stresses and the microstructure have a great influence on the properties of the films. However, lately the phase composition of 0.65PMN-0.35PT thick films was compared to the phase composition of 0.65PMN-0.35PT bulk ceramics with a similar microstructure. In this way it was shown that the thermal residual stresses have a great influence on the phase composition of the thick films and, furthermore, that in PMN-PT thick films the morphotropic phase boundary shifts under the compressive stress.

PMN-PT thick films have many potential applications, although their production faces many challenges arising from the successful integration of different material systems. From all the latest discoveries we can conclude that a proper selection of a material compatible with the functional PMN-PT layer is of key importance for the successful processing of PMN-PT thick films and their integration into applicable structures. With the proper selection of the substrate material, the designer of PMN-PT thick-film structures can control the structural and electrical properties of the active thick film. Structures including piezo-active PMN-PT single-crystal layers and large displacement "substrate free" PMN-PT/Pt thick-film actuators were reported.

The state of the art is the development of new, effective methods for processing PMN-PT thick films with even better functional properties, new procedures for the characterization of thick films and the investigation of innovative design solutions for PMN-PT thick-film structures in different applications. There are still a number of challenges to be faced in the production of PMN-PT thick-film structures and the many possibilities for further improvements in their performance to meet the industrial demands for mass production. However, the basis for future investigations in this field would seem to be the development of new relaxor-ferroelectric thick films with the desired properties for specific applications.

## 5. Acknowledgment

The financial support of the Slovenian Research Agency in the frame of the program Electronic Ceramics, Nano-, 2D and 3D Structures (P2-0105) is gratefully acknowledged.

## 6. References

- Alguero, M.; Alemany, C.; Pardo, L.; Thi, M. P. (2005). Piezoelectric Resonances, Linear Coefficients and Losses of Morphotropic Phase Boundary  $\text{Pb}(\text{Mg}_{1/3}\text{Nb}_{2/3})\text{O}_3\text{-PbTiO}_3$  Ceramics, *J. Am. Ceram. Soc.*, Vol. 88, No. 10, (May 2005), pp. (2780-2787), doi: 10.1111/j.1551-2916.2005.00514.x
- Alguero, M.; Moure, A.; Pardo, L.; Holc, J. & Kosec M., (2006). Processing by mechanosynthesis and properties of piezoelectric  $\text{Pb}(\text{Mg}_{1/3}\text{Nb}_{2/3})\text{O}_3\text{-PbTiO}_3$  with different compositions, *Acta Materialia*, Vol. 54, No. 2, (September 2005), pp. (501-511), doi: 10.1016/j.actamat.2005.09.020

- Alguero, M.; Ricote, J. & Jimenez, R., (2007). Size effect in morphotropic phase boundary  $\text{Pb}(\text{Mg}_{1/3}\text{Nb}_{2/3})\text{O}_3$ -  $\text{PbTiO}_3$ , *Appl. Phys. Lett.*, Vol. 91, No. 12, (August 2007), pp. (112905 1–3), doi: 10.1063/1.2778471
- Akiyama, Y.; Yamanaka, K.; Fujisawa, E. & Kowata, Y. (1999). Development of lead zirconate titanate family thick films on various substrates, *Jpn. J. Appl. Phys.*, Vol. 38, No. 9B, (June 1999), pp. (5524–5527), doi: 10.1143/JJAP.38.5524
- Belavič, D.; Zarnik, M.S.; Holc, J.; Hrovat, M.; Kosec, M.; Drnovšek, S.; Cilenšek, J. & Maček S. (2006). Properties of lead zirconate titanate thick-film piezoelectric actuators on ceramic substrates, *Int. J. Appl. Ceram. Technol.*, Vol. 3, No. 6, (November 2006), pp. (448–454), doi: 10.1111/j.1744-7402.2006.02105.x
- Bokov, A. A. & Ye, Z. G. (2002). Giant electrostriction and stretched exponential electromechanical relaxation in  $0.65\text{Pb}(\text{Mg}_{1/3}\text{Nb}_{2/3})\text{O}_3$ - $0.35\text{PbTiO}_3$  crystals, *J. Appl. Phys.*, Vol. 91, No. 10, (February 2002), pp. (6656–6661), doi: 10.1063/1.1471371
- Carreaud, J.; Gemeiner, P.; Kiat, J. M.; Dkhil, B.; Bogicevic, C.; Rojac, T. & Malič, B. (2005). Size-driven relaxation and polar states in  $\text{PbMg}_{1/3}\text{Nb}_{2/3}\text{O}_3$ -based system, *Phys. Rev. B*, Vol. 72, No. 17, (November 2005), pp. (174115 1–6), doi: 10.1103/PhysRevB.72.174115
- Chen, X.; Fan, H.; Liu, L. & Ke, S. (2008). Low-temperature growth of lead magnesium niobate thick films by a hydrothermal process, *Ceramics International*, Vol. 34, No. 4, (October 2007) pp. (1063–1066), doi: 10.1016/j.ceramint.2007.09.080
- Chen, J.; Fan, H. Q.; Chen, X. L.; Fang, P.; Yang C. & Qiu, S. (2009a). Fabrication of pyrochlore-free PMN-PT thick films by electrophoretic deposition, *Journal of Alloys and Compounds*, Vol. 471, No. 1-2, (June 2008), pp. (L51-L53), doi: 10.1016/j.jallcom.2008.06.088
- Chen, J.; Fan, H.; Ke, S.; Chen, X.; Yang C. & Fang P. (2009b). Relaxor behavior and dielectric properties of lead magnesium niobate-lead titanate thick films prepared by electrophoresis deposition, *Journal of Alloys and Compounds*, Vol. 478, No. 1-2, (December 2008) pp. (853–857), doi: 10.1016/j.jallcom.2008.12.041
- Cross, L. E. (1987). Relaxor ferroelectrics, *Ferroelectrics*, Vol. 76, No. 3, (June 1987), pp. (241–67).
- Damjanovic, D. (2008). Lead-based piezoelectric materials, In: *Piezoelectric and Acoustic Materials for Transducer Applications*, Springer, Editors: A. Safari, E. K. Akgogan, Springer Science+Business Media, ISBN 978-0-387-76538-9, LLC 2008.
- Davis, M.; Damjanovic, D. & Setter, N. (2006). Electric-field-, temperature-, and stress-induced phase transitions in relaxor ferroelectric single crystals, *Phys. Rev. B* Vol. 73, No. 1, (October 2005), pp. (014115 1–16), doi: 10.1103/PhysRevB.73.014115
- Fan, H.; Chen, J. & Chen, X. (2008). Preparation and characterization of relaxor-based ferroelectric thick films with single perovskite phase, *Key Engineering Materials*, Vol. 368, (February 2008) pp. (24–26), doi: 10.4028/www.scientific.net/KEM.368-372.24
- Feng, Z.; He, Z.; Xu, H.; Luo, H. & Yin, Z. (2004). High electric-field-induced strain of  $\text{Pb}(\text{Mg}_{1/3}\text{Nb}_{2/3})\text{O}_3$ - $\text{PbTiO}_3$  crystals in multilayer actuators, *Solid State Communications*, Vol. 130, No. 8, (September 2003) pp. (557–562), doi: 10.1016/j.ssc.2004.03.006
- Gentil, S.; Damjanovic, D. & Setter, N. (2004).  $\text{Pb}(\text{Mg}_{1/3}\text{Nb}_{2/3})\text{O}_3$  and  $(1-x)\text{Pb}(\text{Mg}_{1/3}\text{Nb}_{2/3})\text{O}_3$ - $x\text{PbTiO}_3$  relaxor ferroelectric thick films: processing and electrical characterization,

- J. Electroceramics*, Vol. 12, No. 3, (July, 2003), pp. (151-161), doi: 10.1023/B:JEER.0000037720.39443.e3
- Gentil, S.; Damjanovic, D. & Setter N. (2005). Development of relaxor ferroelectric materials for screen-printing on alumina and silicon substrates, *J. Eur. Ceram. Soc.*, Vol. 25, No. 12, (April 2005), pp. (2125-2128), doi: 10.1016/j.jeurceramsoc.2005.03.210
- Hall, A.; Allahverdi, M.; Akdogan, E. K. & Safari, A. (2005). Piezoelectric/electrostrictive multimerial PMN-PT monomorph actuators, *J. Eur. Ceram. Soc.*, Vol. 25, No. 12, (April 2005), pp. (2991-2997), doi: 10.1016/j.jeurceramsoc.2005.03.196
- Hall, A.; Allahverdi, M.; Akdogan, E. K. & Safari, A. (2006). Fatigue properties of piezoelectric-electrostrictive  $\text{Pb}(\text{Mg}_{1/3}\text{Nb}_{2/3})\text{O}_3\text{-PbTiO}_3$  monolithic bilayer composites, *J. Appl. Phys.*, Vol. 100, No. 9, (July 2006), pp. (094105 1-7), doi: 10.1063/1.2358329
- Holc, J.; Hrovat, M & Kosec, M. (1999). Interactions between alumina and PLZT thick films, *Mat. Res. Bull.*, Vol. 34, No. 14-15, (March 1999), pp. (2271-2278), doi: 10.1016/S0025-5408(99)00227-5
- Lefki, K. & Dormans, G. J. M (1994). Measurement of piezoelectric coefficients in ferroelectric thin films, *J. Appl. Phys.* Vol. 76, No. 3, (April 1994), pp. (1764-1767), doi: 10.1063/1.357693
- Leite, E. R.; Scotch, A. M.; Khan, A.; Chan, H. & Harmer, M. P. (2002). Chemical heterogeneity in PMN-35PT ceramics and effects on dielectric and piezoelectric properties, *J. Am. Ceram. Soc.*, Vol. 85, No. 12, (December 2002), pp. (3018-24), doi: 10.1111/j.1151-2916.2002.tb00572.x
- Kelly, J.; Leonard, M.; Tantigate, C. & Safari, A. (1997). Effect of composition on the electromechanical properties of  $(1-x)\text{Pb}(\text{Mg}_{1/3}\text{Nb}_{2/3})\text{O}_3\text{-xPbTiO}_3$  ceramics, *J. Am. Ceram. Soc.*, Vol. 80, No. 4, (April 1997), pp. (957-964), doi: 10.1111/j.1151-2916.1997.tb02927.x
- Kighelman, Z.; Damjanovic, D. & Setter, N. (2001). Electromechanical properties and self-polarization in relaxor  $\text{Pb}(\text{Mg}_{1/3}\text{Nb}_{2/3})\text{O}_3$  thin films, *J. Appl. Phys.*, Vol. 89, No. 2, (October 2001), pp. (1393-1401), doi: 10.1063/1.1331339
- Ko, B.; Jung, J.S.; Lee & S. Y. (2006). Design of a slim-type optical pick-up actuator using PMN-PT bimerphs, *Smart Mater. Struct.*, Vol. 15, No. 6, (September 2006), pp. (1912-1918), doi: 10.1088/0964-1726/15/6/047
- Kosec, M.; Holc, J.; Malič, B. & Bobnar, V. (1999). Processing of high performance lead lanthanum zirconate titanate thick films, *J. Eur. Ceram. Soc.*, Vol. 19, No. 6/7, (June 1999), pp. (949-954), doi: 10.1016/S0955-2219(98)00351-3
- Kosec, M.; Holc, J.; Kuščer, D. & Drnovšek, S. (2007).  $\text{Pb}(\text{Mg}_{1/3}\text{Nb}_{2/3})\text{O}_3\text{-PbTiO}_3$  thick films from mechanochemically synthesized powder, *J. Eur. Ceram. Soc.*, Vol. 27, No. 13-15, (March 2007), pp. (3775-2778), doi: 10.1016/j.jeurceramsoc.2007.02.025
- Kosec, M.; Uršič, H.; Holc, J.; Kuščer, D. & Malič, B. (2010). High-performance PMN-PT thick films, *IEEE Trans. Ultrason. Ferroelectr. Freq. Control*, Vol. 57, No. 10, (October 2010), pp. (2205-2212), doi: 10.1109/TUFFC.2010.1679
- Kuščer, D. & Kosec, M. (2009)  $0.65\text{Pb}(\text{Mg}_{1/3}\text{Nb}_{2/3})\text{O}_3\text{-}0.35\text{PbTiO}_3$  thick films prepared by electrophoretic deposition from an ethanol-based suspension, *J. Eur. Ceram. Soc.*, Vol. 30, No. 6, (April 2010), pp. (1437-1444), doi: 10.1016/j.jeurceramsoc.2009.11.002

- Kuščer, D.; Skalar, M.; Holc, J.; Kosec, M. (2008). Processing and properties of 0.65Pb(Mg<sub>1/3</sub>Nb<sub>2/3</sub>)O<sub>3</sub>-0.35PbTiO<sub>3</sub> thick films, *J. Eur. Ceram. Soc.*, Vol. 29, No. 1, (June, 2008), pp. 105-113, doi: 10.1016/j.jeurceramsoc.2008.06.010
- Noheda, B.; Cox, D. E.; Shirane, G.; Park, S. E.; Cross, L. E. & Zhong, Z. (2001). Polarization rotation via a monoclinic phase in the piezoelectric 92% PbZn<sub>1/3</sub>Nb<sub>2/3</sub>O<sub>3</sub>-8% PbTiO<sub>3</sub>, *Phys. Rev. Lett.*, Vol. 86, No. 17, (April 2001), pp. (3891-3894), doi: 10.1103/PhysRevLett.86.3891
- Ohring, M. (1992). *The material science of thin films* (1992), Academic Press, ISBN 0-12-524990, New York.
- Park, S. E. & Shrout, T. R., (1997a). Ultrahigh strain and piezoelectric behavior in relaxor based ferroelectric single crystals, *J. Appl. Phys.*, Vol. 82, No. 4 (May 1997) pp. (1804–1811),doi: 10.1063/1.365983
- Park, S. E. & Shrout, T. R. (1997b). Relaxor based ferroelectric single crystals for electro-mechanical actuators, *Mat. Res. Innovat.*, Vol. 1, No. 1 (March 1997), pp. (20–25), doi: 10.1007/s100190050014
- Peng, J.; Lau, S. T.; Chao, C.; Dai, J. Y.; Chan, H. L. W.; Luo, H. S.; Zhu, B. P.; Zhou, Q. F. & Shung, K. K. (2010) PMN-PT single crystal thick films on silicon substrate for high-frequency micromachined ultrasonic transducers, *Appl. Phys. A*, Vol. 98, No. 1, (August 2010), pp. (233–237), doi: 10.1007/s00339-009-5381-1
- Singh, A. K. & Pandey, D. (2003). Evidence for M<sub>B</sub> and M<sub>C</sub> phases in the morphotropic phase boundary region of (1-x)[Pb.Mg<sub>1/3</sub>Nb<sub>2/3</sub>O<sub>3</sub>]-xPbTiO<sub>3</sub>: A Rietveld study, *Phys. Rev. B*, Vol. 67, No. 6, (November 2002), pp. (064102 1–12), doi: 10.1103/PhysRevB.67.064102
- Shrout, T. R.; Chang, Z. P.; Kim, N. & Markgraf, S. (1990) Dielectric behavior of single crystals near the (1-X) Pb(Mg<sub>1/3</sub>Nb<sub>2/3</sub>)O<sub>3</sub>-(x) PbTiO<sub>3</sub> morphotropic phase boundary, *Ferroelectrics Letters*, Vol. 12, No. 3, (September 1990), pp. (63-69), doi: 10.1080/07315179008201118
- Swartz, S. L. & Shrout, T. R. (1982). Fabrication of perovskite lead magnesium niobate. *Mat. Res. Bull.*, Vol. 17, No. 10, (October 1982), pp. (1245–1250), doi: 10.1016/0025-5408(82)90159-3
- Swartz, S. L.; Shrout, T. R.; Schulze, W. A. & Cross, L. E. (1984). Dielectric properties of lead-magnesium niobate ceramics. *J. Am. Ceram. Soc.*, Vol. 67, No. 5, (May 1984), pp. (311–315), doi: 10.1111/j.1151-2916.1984.tb19528.x
- Uchino, K; Nomura, S.; Cross, L. E.; Jang, S. E. & Newnham, R. E. (1890). Electrostrictive effect in lead magnesium niobate single crystals, *J. Appl. Phys.*, Vol. 51, No. 2, (February 1980), pp. 1142-1146, doi: 10.1063/1.327724
- Uršič, H.; Hrovat, M.; Holc, J.; Zarnik, M. S.; Drnovšek, S.; Maček, S. & Kosec, M. (2008a). A large-displacement 65Pb(Mg<sub>1/3</sub>Nb<sub>2/3</sub>)O<sub>3</sub>-35PbTiO<sub>3</sub>/Pt bimorph actuator prepared by screen printing, *Sens. Actuat. B Chem.*, Vol. 133, No. 2, (March 2008), pp. (699–704), doi: 10.1016/j.snb.2008.04.004
- Uršič, H.; Škarabot, M.; Hrovat, M.; Holc, J.; Skalar, M.; Bobnar, V.; Kosec, M. & Muševič, I. (2008b). The electrostrictive effect in ferroelectric 0.65Pb(Mg<sub>1/3</sub>Nb<sub>2/3</sub>-0.35PbTiO<sub>3</sub> thick films, *J. Appl. Phys.*, Vol. 103, No. 12, (April 2008), pp. (124101 1–4), doi: 10.1063/1.2938848

- Uršič, H.; Lowe, M.; Stewart, M.; Hrovat, M.; Belavič, D.; Holc, J.; Zarnik, M. S.; Kosec, M. & Cain, M. (2008c), PZT thick films on different ceramic substrates; piezoelectric measurements, *J. Electroceram.*, Vol. 20, No. 1, (September 2007), pp. (11-16), doi: 10.1007/s10832-007-9327-8
- Uršič, H.; Hrovat, M.; Holc, J.; Tellier, J.; Drnovšek, S.; Guiblin, N.; Dkhil, B. & Kosec, M. (2010). Influence of the substrate on the phase composition and electrical properties of 0.65PMN-0.35PT thick films, *J. Eur. Ceram. Soc.*, Vol. 30, No. 10, (April 2010), pp. (2081-2092), doi: 10.1016/j.jeurceramsoc.2010.04.010
- Uršič, H.; Tellier, J.; Hrovat, M.; Holc, J.; Drnovšek, S.; Bobnar, V.; Alguero, M.; & Kosec, M. (2011a). The effect of poling on the properties of 0.65Pb(Mg<sub>1/3</sub>Nb<sub>2/3</sub>)O<sub>3</sub>-0.35PbTiO<sub>3</sub> ceramics, *Jpn. J. Appl. Phys.*, Vol. 50, No. 3, (December 2010), pp. (035801 1-6), doi: 10.1143/JJAP.50.0358011
- Uršič, H.; Zarnik, M. S.; Tellier, J.; Hrovat, M.; Holc, J. & Kosec, M. (2011b). The influence of thermal stresses on the phase composition of 0.65Pb(Mg<sub>1/3</sub>Nb<sub>2/3</sub>)O<sub>3</sub>-0.35PbTiO<sub>3</sub> thick films, *J. Appl. Phys.* Vol. 109, No. 1, (November 2010), pp. (014101 1-5), doi: 10.1063/1.3526971
- Uršič, H.; Zarnik, M. S. & Kosec, M. (2011c). Pb(Mg<sub>1/3</sub>Nb<sub>2/3</sub>)O<sub>3</sub>-PbTiO<sub>3</sub> (PMN-PT) material for actuator applications, *Smart Materials Research*, in press, accepted January 2011, Article ID 452901, doi:10.1155/2011/452901
- Vikhnin, V. S.; Blinc, R. & Pirc, R. (2003). Mechanisms of electrostriction and giant piezoelectric effect in relaxor ferroelectrics, *J. Appl. Phys.*, Vol. 93, No. 12, (March 2003), pp. (9947-9952), doi: 10.1063/1.1575915
- Wu, A.; Vilarinho, P. M. & Kholkin, A. (2007) Low temperature preparation of ferroelectric relaxor composite thick films, *J. Am. Ceram. Soc.*, Vol. 90, No. 4, (March 2007), pp. (1029-1037), doi: 10.1111/j.1551-2916.2007.01587.x
- Xia, Z.; Wang, L.; Yan, W.; Li, Q. & Zhang, Y. (2007) Comparative investigation of structure and dielectric properties of Pb(Mg<sub>1/3</sub>Nb<sub>2/3</sub>)O<sub>3</sub>-PbTiO<sub>3</sub> (65/35) and 10% PbZrO<sub>3</sub>-doped Pb(Mg<sub>1/3</sub>Nb<sub>2/3</sub>)O<sub>3</sub>-PbTiO<sub>3</sub> (65/35) ceramics prepared by a modified precursor method, *Mat. Res. Bull.*, Vol. 42, No. 9, (September 2007), pp. (1715-1722), doi: 10.1016/j.materresbull.2006.11.024
- Zarnik M. S.; Belavič, D. & S. Maček. (2007). Evolution of the constitutive material parameters for the numerical modeling of structures with lead-zirconate-titanate thick films, *Sens. Actuat. A*, Vol. 136, No. 2, (January 2007), pp. (618-628), doi: 10.1016/j.sna.2007.01.010
- Zarnik, M. S.; Belavič, D.; Uršič, H. & Maček S. (2008). Numerical modelling of ceramic mems structures with piezoceramic thick films, *J. Electroceram.*, Vol. 20, No. 1, (September 2007), pp. (3-9), doi: 10.1007/s10832-007-9329-6
- Zhang, R.; Jiang, B. & Cao, W. (2001). Elastic, piezoelectric, and dielectric properties of multidomain 0.67Pb(Mg<sub>1/3</sub>Nb<sub>2/3</sub>)O<sub>3</sub>-PbTiO<sub>3</sub> single crystals, *J. Appl. Phys.*, Vol. 90, No.7, (June 2001), pp. (3471-3475), doi: 10.1063/1.1390494
- Zhao, J.; Zhang, Q. M.; Kim, N. & Shrout, T. (1995). Electromechanical properties of relaxor ferroelectric lead magnesium niobate-lead titanate ceramics, *Jpn. J. Appl. Phys.* Vol. 34, No. 10, (July 1995), pp. (5658-5663), doi: 10.1143/JJAP.34.5658

Zhu, B.; Han, J.; Shi, J.; Shung, K. K.; Wei, Q.; Huang, Y.; Kosec, M. & Zhou, Q. (2010) Lift-Off PMN-PT Thick Film for High-Frequency Ultrasonic Biomicroscopy, *J. Am. Ceram. Soc.*, Vol. 93, No. 10, (August 2010), pp. (2929-2931), doi: 10.1111/j.1551-2916.2010.03873.x

# Phase Diagramm, Crystallization Behavior and Ferroelectric Properties of Stoichiometric Glass Ceramics in the BaO-TiO<sub>2</sub>-B<sub>2</sub>O<sub>3</sub> System

Rafael Hovhannisyan, Hovakim Alexanyan, Martun Hovhannisyan,  
Berta Petrosyan and Vardan Harutyunyan  
*Institute of Electronic Materials  
Armenia*

## 1. Introduction

Binary borate and polytitanates compounds have currently been of considerable interest to the scientific community due to unique properties of barium titanate, barium polytitanates [Kong, 2010; Wakino, 1990], beta barium borate [Chen, C. & Liu, 1986] and recently revealed high negative thermal expansion of crystallized barium di-borate glass samples [Hovhannisyan, 2006]. It has also been revealed recently, that the single crystal of barium di-tanate is high-temperature ferroelectric with Curie temperature equal to 450-500°C [Waghmare et al., 2004; Akishige et al., 2006]. Park with co-authors reported a new barium titanium oxoborate crystal of Ba<sub>3</sub>Ti<sub>3</sub>O<sub>6</sub>(BO<sub>3</sub>)<sub>2</sub> and found out that the second harmonic generation (SHG) efficiency of this crystal is equal to 95% of the well known LiNbO<sub>3</sub> [Park et al., 2004]. These data have even strengthened the interest of studying the ternary BaO-TiO<sub>2</sub>-B<sub>2</sub>O<sub>3</sub> system even more.

Binary BaO-TiO<sub>2</sub> and BaO-B<sub>2</sub>O<sub>3</sub> systems are investigated rather in detail by various authors. The following eight binary barium titanates known in the BaO-TiO<sub>2</sub> system are: Ba<sub>2</sub>TiO<sub>4</sub> (2BaT), BaTiO<sub>3</sub> (BaT), BaTi<sub>2</sub>O<sub>5</sub> (Ba2T), Ba<sub>6</sub>Ti<sub>17</sub>O<sub>40</sub> (6Ba17T), Ba<sub>4</sub>Ti<sub>13</sub>O<sub>30</sub> (4Ba13T), BaTi<sub>4</sub>O<sub>9</sub>(Ba4T), Ba<sub>2</sub>Ti<sub>9</sub>O<sub>20</sub>(2Ba9T) and BaTi<sub>5</sub>O<sub>11</sub> (Ba5T) [Rase & Roy, 1955; O'Bryan & Thomson, 1974]. Levin with co-authors have studied the BaO-B<sub>2</sub>O<sub>3</sub> system and constructed its melting diagram. They discovered four Ba<sub>3</sub>B<sub>2</sub>O<sub>6</sub> (3BaB), BaB<sub>2</sub>O<sub>4</sub> (BaB), Ba<sub>4</sub>O<sub>7</sub>(Ba2B) and Ba<sub>8</sub>O<sub>13</sub> (Ba4B) compounds [Levin & McMurdie, 1949; Levin & Ugrinic, 1953]. Hubner synthesized three new Ba<sub>4</sub>B<sub>2</sub>O<sub>6</sub> (4BaB), Ba<sub>2</sub>B<sub>2</sub>O<sub>5</sub>(2BaB) and Ba<sub>2</sub>B<sub>10</sub>O<sub>17</sub> (2Ba5B) compounds [Hubner, 1969]. However, these compounds are not visible on the BaO-B<sub>2</sub>O<sub>3</sub> systems diagram constructed earlier by Levin with co-authors [Levin & McMurdie, 1949; Levin & Ugrinic, 1953].

Pavlikov with co-authors have studied the TiO<sub>2</sub>-B<sub>2</sub>O<sub>3</sub> system and didn't reveal binary compounds in it [Pavlikov et al., 1976]. Simple eutectic which is very close to B<sub>2</sub>O<sub>3</sub> (~2.9 mol% TiO<sub>2</sub>) was found and the presence of liquid immiscibility is supposed in the field of compositions containing 25-55 mol% of TiO<sub>2</sub> [Pavlikov et al., 1976]. One binary oxygen containing titanium boron compound- titanium borate, synthesized by Schmid is known now [Schmid, 1964]. Also the formation of TiBO<sub>3</sub> was revealed during interaction between borate glass melts and titanium alloy [Brow & Watkins, 1987].

Vicat & Aleonard for the first time have obtained  $\text{BaTi}(\text{BO}_3)_2$  (BaTB) ternary compound related to “Nordenskiöldine” group borates [Vicat & Aleonard, 1968]. Millet and co-authors studied  $\text{BaTiO}_3\text{-TiO}_2\text{-BaB}_2\text{O}_4$  subsystem in  $\text{BaO-TiO}_2\text{-B}_2\text{O}_3$  system and have found the second incongruent melting at  $950^\circ\text{C}$  ternary  $\text{Ba}_2\text{Ti}_2\text{B}_2\text{O}_9$  (2Ba2TB) compound. Between  $950\text{-}960^\circ\text{C}$  it decomposes with formation  $\text{BaTiO}_3$  and liquid [Millet et al., 1986]. Authors [Zhang et al., 2003] have studied subsolidus phase relations in the ternary  $\text{BaO-TiO}_2\text{-B}_2\text{O}_3$  system. They confirmed only the existence of two known BaTB and 2Ba2TB ternary compounds in this system. The pure 2Ba2TB phase has not been obtained under authors experiment conditions [Zhang et al., 2003]. It was in equilibrium with BB, BT, B2T and 4B13T.

However, Park with co-authors considered, that the  $\text{Ba}_2\text{Ti}_2\text{B}_2\text{O}_9$  composition was formulated incorrectly and should be re-formulated as  $\text{Ba}_3\text{Ti}_3\text{B}_2\text{O}_{12}$ , or more precisely  $\text{Ba}_3\text{Ti}_3\text{O}_6(\text{BO}_3)_2$  [Park et al, 2004]. Kosaka et al. have confirmed the data of Barbier's group and have shown necessity of reformulation of  $\text{Ba}_2\text{Ti}_2\text{B}_2\text{O}_9$  (2Ba2TB) compound as  $\text{Ba}_3\text{Ti}_3\text{O}_6(\text{BO}_3)_2$  (3Ba3TB) [Kosaka et al., 2005]. They have synthesized new glass ceramic composition with 3Ba3TB crystalline phase in the  $\text{BaO-TiO}_2\text{-B}_2\text{O}_3$  system and have found that its powder sample SHG intensities is 68 times as large as a-quartz powders .

Sholokhovitch & Varicheva have studied [50PbO+50B<sub>2</sub>O<sub>3</sub>, mol%]-PbTiO<sub>3</sub> -BaTiO<sub>3</sub>-Ba(BO<sub>2</sub>)<sub>2</sub> section of PbO-BaO-B<sub>2</sub>O<sub>3</sub>-TiO<sub>2</sub> fourfold system and observed eutectic at 32 mol% BaTiO<sub>3</sub> (m.p.906°C ) in the pseudo-binary Ba(BO<sub>2</sub>)<sub>2</sub>-BaTiO<sub>3</sub> system [Sholokhovitch & Varicheva, 1958]. Goto & Cross studied pseudo-binary BaTiO<sub>3</sub>-BaB<sub>2</sub>O<sub>4</sub> system for BaTiO<sub>3</sub> single crystals growth and also found simple eutectic with m.p.942°C at 32 mol% BaTiO<sub>3</sub> [Goto & Cross, 1969]. Simple eutectic with m.p.1010°C has also been found in BaB<sub>2</sub>O<sub>4</sub>-BaTi(BO<sub>3</sub>)<sub>2</sub> pseudo-binary system at 32 mol% BaTi(BO<sub>3</sub>)<sub>2</sub> [Hovhannisyan, 2004].

Interest to glass formation in ternary barium titanium borate system is mainly connected with developing the new composition of glass ceramics on the basis of barium titanates [Matveev et al, 1966; Bhargava et al., 1988a, 1988b, 1988c; Cerchez et al., 2000; Boroica et al., 2004], beta barium borate [Pernice et al., 1998; Feitosa et al., 2006] and 3Ba3TB [Kosaka et al., 2005]. We are fully confident, that experts and researchers will show interest to ceramics and glass ceramics on the basis of binary barium titanates and ternary barium boron titanates for a long time. However, it will be difficult to them to develop new practical compositions without presence of the first of all the phase diagram and glass forming diagram.

Hovhannisyan with co-workers have made the first attempt of the ternary  $\text{BaO-TiO}_2\text{-B}_2\text{O}_3$  system both glass forming and phase diagram construction [Hovhannisyan et al., 2008]. A large area of glass formation has been revealed in the  $\text{BaO-TiO}_2\text{-B}_2\text{O}_3$  system depending on melt's cooling ways. The new incongruent melted ternary  $\text{Ba}_2\text{TiB}_2\text{O}_7$  (2BaTB) compound has been revealed during the same composition glass crystallization. Clear correlation between glass forming ability and eutectic and peritectic areas has been observed in the investigated  $\text{BaO-TiO}_2\text{-B}_2\text{O}_3$  system [Hovhannisyan et al., 2008].

However, our further studies of glasses and glass ceramics in this system have shown necessity of both glass forming and phase diagram correction in the ternary  $\text{BaO-TiO}_2\text{-B}_2\text{O}_3$  system. Another aim of this work is both known and novel stoichiometric ternary barium titanium borates compounds investigations in glassy, glass ceramic and ceramic states. On the other hand we are seriously interested in giving additional information concerning the existence of two  $\text{Ba}_2\text{Ti}_2\text{B}_2\text{O}_9$  and  $\text{Ba}_3\text{Ti}_3\text{O}_6(\text{BO}_3)_2$  compounds.

## 2. Experimental

About two hundred samples of various binary and ternary compositions have been synthesized and tested in BaO-TiO<sub>2</sub>-B<sub>2</sub>O<sub>3</sub> system. Compositions were prepared from "chemically pure" grade BaCO<sub>3</sub>, H<sub>3</sub>BO<sub>3</sub> and TiO<sub>2</sub> at 2.5-5.0 mol % intervals. The most part of samples has been obtained as glasses by various cooling rates depending on melts glass forming abilities: as bulk glass plates with thickness 6,5 ± 7mm by casting on metallic plate (up to 10<sup>3</sup> K/s), as monolithic glass plates with thickness up to 3mm by casting between two steel plates (~10<sup>2</sup> K/s), and glass tapes through super cooling method (10<sup>3</sup>±10<sup>4</sup> K/s). The glass melting was performed at 1400-1500°C for 30-60 min with a 25-30 g batch in a 50 ml uncovered Pt crucible, using an air atmosphere and a "Superterm 17/08" electric furnace. Chemical composition of some glasses was controlled and corrected by results of the traditional chemical analysis. The final analysis results indicate a good compatibility of calculated and analytical values of B<sub>2</sub>O<sub>3</sub>, BaO and TiO<sub>2</sub>.

Samples of compositions laying outside of a glass formation field or having high melting temperature, have been obtained by solid-phase synthesis. Mixes (15-20 g) were carefully frayed in an agate mortar, pressed as tablets, located on platinum plates and passed the thermal treatment in "Naber" firm electric muffles. After regrinding powders were tested by DTA and X-ray methods. The synthesized samples of binary barium borate system compositions containing 60 mol% and more of BaO and also compositions containing over 90mol % B<sub>2</sub>O<sub>3</sub> had very low chemical resistance and were hydrolyzed on air at room temperature. In this connection the synthesized samples were kept in a dryer at 200°C.

DTA and X-ray diffraction data of glass and crystallized glass samples have been used for phase diagram construction in the ternary BaO-TiO<sub>2</sub>-B<sub>2</sub>O<sub>3</sub> system. The DTA analysis (platinum crucible, powder samples weight ~600 mg, heating rates 7.5 or 15K/min) on Q-1500 type derivatograph were carried out. Glass transition -T<sub>g</sub>, crystallization peaks -T<sub>cr</sub>, melting -T<sub>m</sub> and liquidus -T<sub>L</sub> temperatures have been determined from DTA curves. Reproducibility of temperatures effects on DTA curves from melting to melting was ±10K. The accuracy of temperature measurement is ±5 K.

Thermal expansion coefficient (TEC) and glass transition temperature (T<sub>g</sub>) measurements were made on a DKV-4A type vertical quartz dilatometer with a heating rate of 3K/min. Glass samples in the size of 4×4×50 millimeters have been prepared for TEC measurement. The dilatometer was graduated by the quartz glass and sapphire standards. The TEC measurement accuracy is ±(3±4)·10<sup>-7</sup>K<sup>-1</sup>, T<sub>g</sub> ±5 °C.

X-ray patterns were obtained on a DRON-3 type diffractometer (powder method, CuKα-radiation, Ni-filter). Samples for glass crystallization were prepared with glass powder pressed in the form of tablets. Crystallization process was done in the electrical muffles of "Naber" firm by a single-stage heat treatment. This was done within 1-60 hours around a temperature at which the maximum exothermal effects on glasses by DTA were observed.

Crystalline phases of binary and ternary compounds formed both at glasses crystallization and at solid-phase synthesis have been identified by using JCPDS-ICDD PDF-2 release 2008 database [ICDD, 2008].

Computerized methodic of ferroelectric hysteresis test and measurement of ferroelectric properties such as coercive field and remanent polarization at wide temperature (up to 250°C and frequency (10-5000Hz) ranges was used. Methodic based on the well known Sawyer - Tower's [Sawyer & Tower, 1930] modified scheme, which is allowing to

compensate phase shifts concerned with dielectric losses and conductivity. The desired frequency signal from waveform generator is amplifying by high voltage amplifier and applying to sample. The signals, from the measuring circuit output, proportional to applied field and spontaneous polarization are passing through high impedance conditioning amplifiers, converting by ADC and operating and analyzing in PC. The technique allows to perform tests of synthesized glass ceramics obtained by means of controlling crystallization of thin (above 30 micrometer thick) monolithic tape (film) specimens by applying up to 300kV/cm field to our thin samples (~50 micrometer thick) and obtain hysteresis loops for wide diversity of hard FE materials.

### 3. Results

#### 3.1 Glass forming and phase diagrams of the of the BaO-TiO<sub>2</sub>-B<sub>2</sub>O<sub>3</sub> system

The traditional method of phase diagram construction based on solid-phase sintered samples investigation takes long time and is not effective. The glass samples investigation technique is progressive, because the DTA curves have registered all processes taking place in glass samples, including the processes of glass crystallizations, quantity of crystal phases and temperature intervals of their formation and melting.

However, inadequate amount of glass samples restrict their use during phase diagram construction. The super-cooling method promotes the mentioned problem solving and open new possibilities for phase diagrams construction.

##### 3.1.1 Glass forming diagram of the BaO-TiO<sub>2</sub>-B<sub>2</sub>O<sub>3</sub> system

Figure 1 shows the experimental data on glass formation in the BaO-TiO<sub>2</sub>-B<sub>2</sub>O<sub>3</sub> system obtained by different authors from 1957 to 2008 [Imaoka & Yamazaki, 1957; Matveev et al., 1966; Bhargava et al., 1987; De Pablos & Duran, 1993; Kusumoto & Sekiya, 1994; Hovhannisyan et al., 2008]. For defining the glass forming ability of the pointed system, the authors of the mentioned works used different amounts of melt, glass melting crucibles, temperature–time melting regimes, and technological methods of melt cooling. The obtained data are hardly comparable and are “torn away” from the two main factors in glass formation: the liquidus temperature ( $T_l$ ) and melt cooling rate.

Figure 2 shows corrected glass formation diagram in the BaO-TiO<sub>2</sub>-B<sub>2</sub>O<sub>3</sub> system based on phase diagrams of the BaO-B<sub>2</sub>O<sub>3</sub>, BaO-TiO<sub>2</sub>, and B<sub>2</sub>O<sub>3</sub>-TiO<sub>2</sub> binary systems and controllable melt cooling rates. Using the term “diagram,” but not the glass formation region, we take into account the interrelation between the phase diagram and the glass forming ability of the system.

Super cooling technique constructed by our group allowed to expand the borders of glass formation in studied system. The largest glass forming area have been obtained under high melts cooling rates equal to  $(10^3\text{-}10^4)$  K/s (Fig.2-1). It includes: compositions content 2.5÷3.0 mol% TiO<sub>2</sub> around eutectic area  $e_9$  (~2.9 mol% TiO<sub>2</sub>) with m.p. ~450°C in the binary B<sub>2</sub>O<sub>3</sub>-TiO<sub>2</sub> system [Pavlikov et al., 1976]; compositions content 30÷35 mol% BaO around eutectic area  $e_7$  (~31.5 mol% BaO) with m.p. 1317°C in the binary BaO-TiO<sub>2</sub> system [Rase & Roy, 1955; O’ Bryan & Thomson, 1974], which include BaTi<sub>2</sub>O<sub>5</sub> composition. Area of glass formation from both these areas moves to eutectic areas  $e_1$  (16,5 mol% BaO) with m.p. 878°C [Levin & McMurdie, 1949; Levin & Ugrinic, 1953] and ~ 31.5 mol%B<sub>2</sub>O<sub>3</sub> content compositions in the binary BaO-B<sub>2</sub>O<sub>3</sub> system and includes Ba<sub>2</sub>B<sub>2</sub>O<sub>5</sub> and BaB<sub>2</sub>O<sub>4</sub> compositions (Fig.2-1). The transparent glass tapes have been obtained firstly for Ba<sub>3</sub>Ti<sub>3</sub>B<sub>2</sub>O<sub>12</sub> (3Ba3TB) composition by

its melt high cooling rate ( $10^3$ - $10^4$ ) K/s (Fig.2-1). The 3Ba3TB glass composition (Table 3) is located practically on the border of glass formation (Fig.2-1).

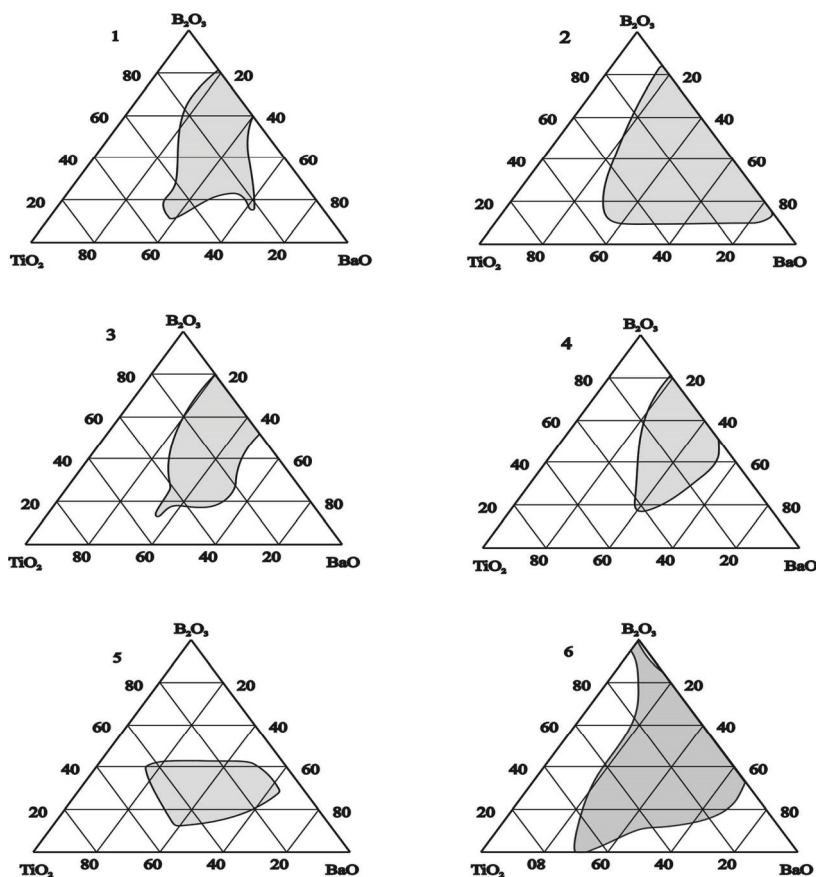


Fig. 1. Glass forming regions in the BaO-TiO<sub>2</sub>-B<sub>2</sub>O<sub>3</sub> system according to the data of the authors: 1- [Imaoka & Yamazaki, 1957]; 2- [Matveev et al., 1966]; 3- [Bhargava et al, 1987]; 4- [De Pablos & Duran, 1993]; 5- Kusumoto & Sekiya, 1994]; 6- [Hovhannisyan et al., 2008].

Loss of melts cooling speed to  $\sim 10^2$  K/s has naturally led to narrowing of glass formation area (Fig.2-2). However, this cooling rate is enough for monolithic glass plates with thickness up to 3mm fabrication by melts casting between two steel plates. The ternary BaTi(BO<sub>3</sub>)<sub>2</sub> (BaTB), Ba<sub>2</sub>Ti<sub>2</sub>B<sub>2</sub>O<sub>9</sub> (2Ba2TB) and Ba<sub>2</sub>TiB<sub>2</sub>O<sub>7</sub> (2BaTB) compounds have been obtained as bulk glass samples by this way. It was big surprise, that monolithic glass samples have been obtained for ternary glass compositions close to e<sub>5</sub> eutectic area(37.5 mol%B<sub>2</sub>O<sub>3</sub>) with m.p.915°C in the binary BaO-B<sub>2</sub>O<sub>3</sub> system and containing about 3÷4 mol% TiO<sub>2</sub> (Fig.2-2).

The further reduction of melts cooling rate to  $\sim 10$  K/s has allowed to reveal field of glass compositions with low crystallization ability and stable glass formation in the studied ternary BaO-TiO<sub>2</sub>-B<sub>2</sub>O<sub>3</sub> system (Fig.2-3).

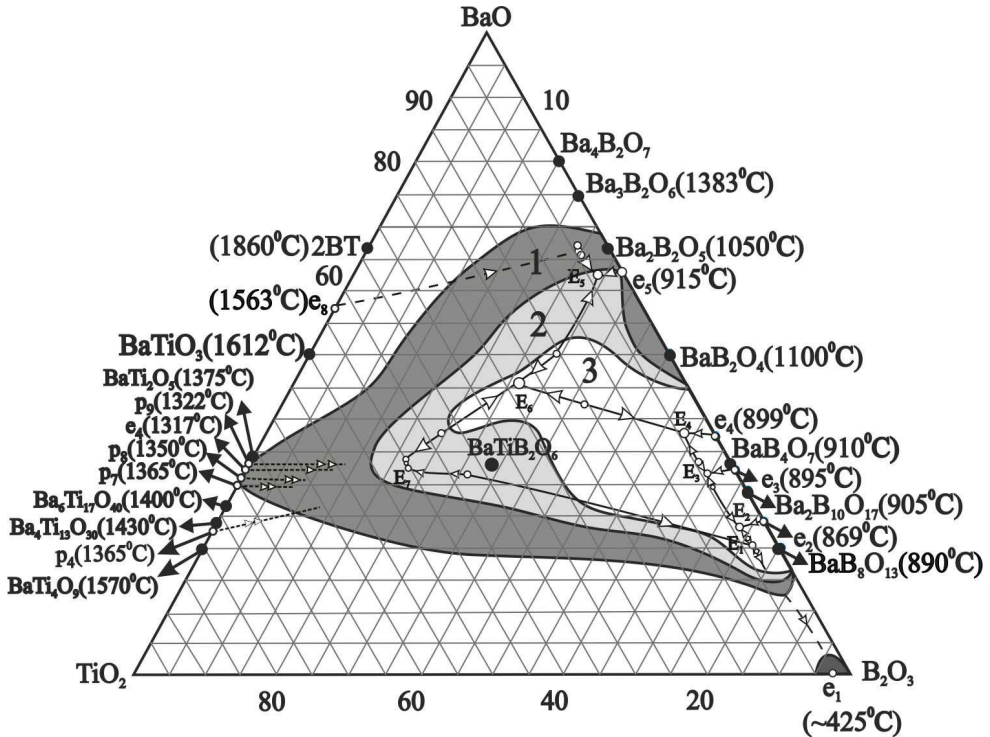


Fig. 2. Glass forming diagram in the BaO-B<sub>2</sub>O<sub>3</sub>-TiO<sub>2</sub> system depending of melts cooling rates: (10<sup>3</sup>-10<sup>4</sup>) K/s; 3~10<sup>2</sup> K/s; 2-up to 10 K/s;

Earlier we have reported about transparent glass sheets formation in the field of compositions being between eutectic e<sub>1</sub> in the binary B<sub>2</sub>O<sub>3</sub>-TiO<sub>2</sub> system and ternary eutectic E<sub>1</sub> [Hovhannisyanyan et al., 2008]. However, the present studies have not confirmed previous data. It was possible to obtain transparent glass sheets only in the narrow field of compositions close to eutectic e<sub>1</sub> area (Fig.2).

### 3.1.2 DTA study of the stoichiometric glass compositions in the BaO-TiO<sub>2</sub>-B<sub>2</sub>O<sub>3</sub> system

The glass nominal compositions in the BaO-TiO<sub>2</sub>-B<sub>2</sub>O<sub>3</sub> system examined in the present study and their DTA and dilatometric characteristics are given in Table 1. DTA curves for glasses corresponding to ternary and binary stoichiometric compositions are shown in Fig. 3, giving the peaks due to the glass transition, crystallization, melting, and liquidus temperatures.

On the DTA curve of the 33.33BaO · 33.33TiO<sub>2</sub> · 33.33B<sub>2</sub>O<sub>3</sub> (mol%) glass composition strong exothermic effect with maximum at 680°C and endothermic effect with minimum at 1080°C were observed, which show the crystallization and congruent melting of one well known crystalline BaTiB phase (Fig. 3, curve 1).

The similar picture is seen on the DTA curve of the 42.85BaO · 42.85TiO<sub>2</sub> · 14.28 B<sub>2</sub>O<sub>3</sub>(mol%) glass composition corresponding to stoichiometric 3Ba3TB crystalline compound: we have

strongly expressed exothermic effect at 625 °C and endothermic effects at 975°C, which show the crystallization and melting of one crystalline phase (Fig. 3, curve 3).

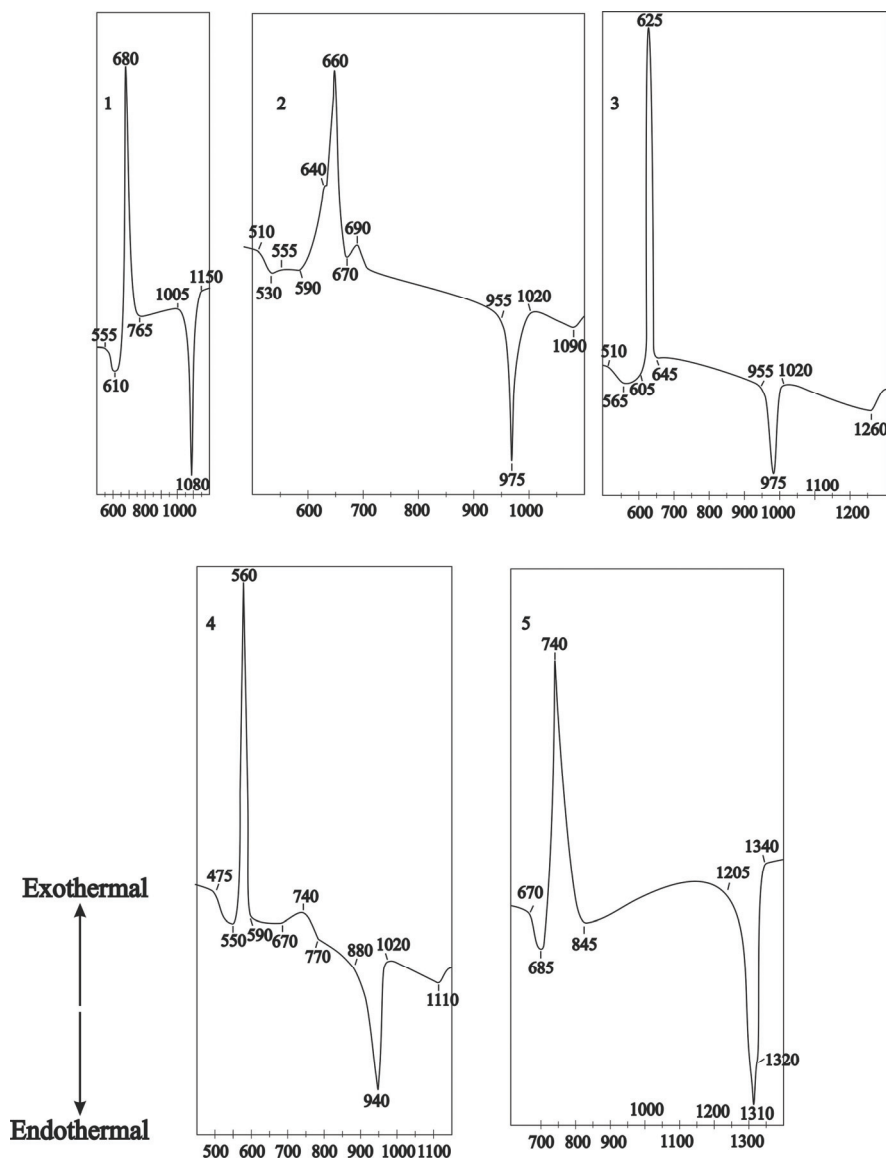


Fig. 3. DTA curves (heating rate 7.5K/min) of studied glass compositions (mol%) corresponding to stoichiometric compounds: 1-33.3BaO · 33.3TiO<sub>2</sub> · 33.3B<sub>2</sub>O<sub>3</sub> (BaTB), 2-40.0BaO · 40.0TiO<sub>2</sub> · 40.0B<sub>2</sub>O<sub>3</sub> (2Ba2TB), 3- 42.85BaO · 42.85TiO<sub>2</sub> · 14.28B<sub>2</sub>O<sub>3</sub> (3Ba3TB), 4-50.0BaO · 25.0TiO<sub>2</sub> · 25.0B<sub>2</sub>O<sub>3</sub> (2BaTB), and 5-33.3BaO · 66.7TiO<sub>2</sub> (Ba2T)

On the DTA curve of the 40BaO · 40TiO<sub>2</sub> · 20B<sub>2</sub>O<sub>3</sub> (mol%) glass composition three exothermic effects clear observed: two effects at 640°C (small) and at 660°C (high) are combined and third is weakly expressed at 690°C, which show processes of glass crystallization and probably of three phases formation (Fig.3, curve 2). Endothermic effect at temperature interval 955-1020 °C (minimum at 975 °C) is connected with the formed crystalline phases melting.

Glass compositions, mol%				Derivatographical characteristics				Dilatometric characteristics	
Sample	BaO	TiO <sub>2</sub>	B <sub>2</sub> O <sub>3</sub>	T <sub>g</sub> , °C	T <sub>cr</sub> , °C	T <sub>m</sub> , °C	T <sub>L</sub> , °C	T <sub>g</sub> , °C	TEC (α <sub>20-300</sub> ) · 10 <sup>-7</sup> K <sup>-1</sup>
BaTB	33.33	33.33	33.33	555	680	1080	1080	600	88
2Ba2TB	40.0	40.0	40.0	510	640, 660, 690	975	1090	570	107
3Ba3TB	42.85	42.85	14.30	510	625	975	1260	---	---
2BaTB	50.0	25.0	25.0	475	560, 740	940	1110	512	115
Ba2T	33.33	66.67	---	670	740	1310	1370	---	---

Table 1. Chemical compositions, derivatographical (glass transition -T<sub>g</sub>, crystallization peak -T<sub>cr</sub>, melting -T<sub>m</sub>, liquidus temperature -T<sub>L</sub>) and dilatometric characteristics (glass transition temperature -T<sub>g</sub>, thermal expansion coefficient -TEC) of BaO – TiO<sub>2</sub> – B<sub>2</sub>O<sub>3</sub> system glasses.

Two exothermic effects is seen on the DTA curve of the 50BaO · 25TiO<sub>2</sub> · 25B<sub>2</sub>O<sub>3</sub> (mol%) glass composition: strongly expressed effect at 585 °C and small diffused effect with maximum at 740°C (Fig. 3, curve 4). Both effects are connected with two crystalline phases formation. According to [Hovhannisyann et al., 2008] the first phase is new crystalline compound, formulated by us as Ba<sub>2</sub>TiB<sub>2</sub>O<sub>7</sub>. The 2BaTiB composition melted incongruently at 940 °C with melt and BaTiO<sub>3</sub> formation. The second weakly expressed endothermic effect on DTA curve at 1110°C is associated with BaTiO<sub>3</sub> dissolution in a melt (Fig. 3, curve 4).

On the DTA curve of the 33.3BaO · 66.67TiO<sub>2</sub> (mol%) glass composition strongly expressed exothermic effect with maximum at 740°C and endothermic effect with minimum at 1320°C were observed, which show the crystallization and melting of one crystalline phase (Fig.3 , curve 5). According to [Rase & Roy, 1955] the 33.3BaO · 66.67TiO<sub>2</sub> (mol%) composition is melted incongruently at 1310°C with melt and BaTiO<sub>3</sub> formation.

### 3.1.3 TEC study of the stoichiometric glass compositions in the BaO-TiO<sub>2</sub>-B<sub>2</sub>O<sub>3</sub> system

The isolines diagram of BaO-TiO<sub>2</sub>-B<sub>2</sub>O<sub>3</sub> system glasses TEC values is given on Fig.4. It is clear observed common regularity, that the increase of barium oxide amounts in glasses of binary BaO-B<sub>2</sub>O<sub>3</sub> system leads to increase of glasses TEC values. The same tendency is observed for glasses of ternary compositions: increasing of BaO amounts leads to increase glasses TEC values from 60 to 120 · 10<sup>-7</sup>K<sup>-1</sup>. The substitution of B<sub>2</sub>O<sub>3</sub> for TiO<sub>2</sub> in the area of low BaO content glass compositions (20-25 mol%) practically does not influence on the their TEC value. The same tendency is observed for the high BaO content glass compositions (55-60 mol%). It is seen in the central area of compositions that TEC values increase with the substitution of B<sub>2</sub>O<sub>3</sub> for TiO<sub>2</sub>. However, the major factor influencing on TEC value of studied glasses is the BaO amount in their compositions (Fig.4).

TEC values of glasses corresponding to the ternary barium titanium borates given in Table 3. The glass composition corresponds to BaTiB<sub>2</sub>O<sub>6</sub> (33.33BaO·33.33TiO<sub>2</sub>·33.33B<sub>2</sub>O<sub>3</sub>, mol%) has

TEC=88·10<sup>-7</sup>K<sup>-1</sup> and T<sub>g</sub>=555°C calculated from dilatometric curve. Reduction the B<sub>2</sub>O<sub>3</sub> and TiO<sub>2</sub> amount together with increasing of BaO amounts in glass compositions leads to increase TEC and reduction T<sub>g</sub> values: for glass composition 40BaO·40TiO<sub>2</sub>·20B<sub>2</sub>O<sub>3</sub>, mol % (Ba<sub>2</sub>Ti<sub>2</sub>B<sub>2</sub>O<sub>9</sub>) TEC=107·10<sup>-7</sup>K<sup>-1</sup> and T<sub>g</sub>= 570°C; for glass composition 50BaO·25TiO<sub>2</sub>·25B<sub>2</sub>O<sub>3</sub>, mol % (Ba<sub>2</sub>TiB<sub>2</sub>O<sub>7</sub>) TEC=115·10<sup>-7</sup>K<sup>-1</sup> and T<sub>g</sub>=512°C (Table 3).

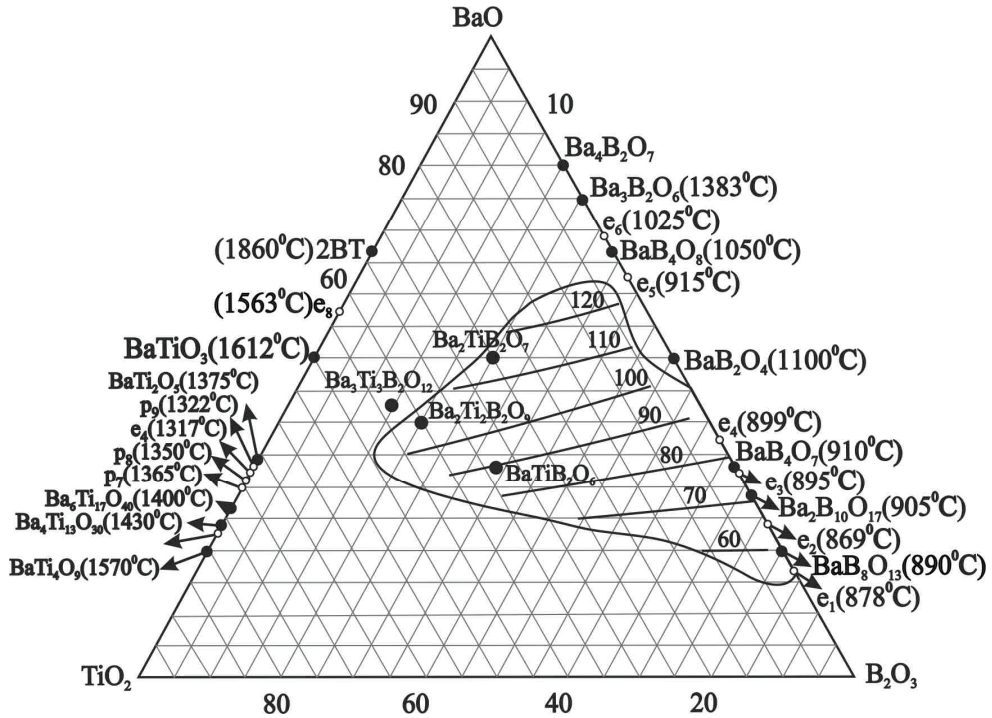


Fig. 4. BaO-TiO<sub>2</sub>-B<sub>2</sub>O<sub>3</sub> system's glasses TEC ( $\alpha_{20-300} \cdot 10^{-7}K^{-1}$ ) values isolines

### 3.1.4 Phase diagram of the BaO-TiO<sub>2</sub>-B<sub>2</sub>O<sub>3</sub> system

#### 3.1.4.1 Phase diagram of the pseudo-binary BaTiO<sub>3</sub> -BaTi(BO<sub>3</sub>)<sub>2</sub> system

The introduction of BaTB compound in pseudo-binary BaTiO<sub>3</sub> -BaTi(BO<sub>3</sub>)<sub>2</sub> system sharply reduced the melting point of initial barium titanate, reduced the crystallization abilities and resulted in the formation of simple eutectic area at 72 mol% BaTB content (38 BaO · 38 TiO<sub>2</sub> · 24 B<sub>2</sub>O<sub>3</sub>, mol%) with melting point 1020°C (Fig.5 A).

Available inconsistent data about existence of Ba<sub>2</sub>Ti<sub>2</sub>B<sub>2</sub>O<sub>9</sub> crystalline compound promoted more careful study of the BaTi(BO<sub>3</sub>)<sub>2</sub> -BaTiO<sub>3</sub> pseudo binary system. High sensitivity of our DTA equipment have allowed to reveal temperatures intervals of processes taking place in initial glass powder samples. Existence on DTA curve of 42.85BaO · 42.85TiO<sub>2</sub> · 14.28B<sub>2</sub>O<sub>3</sub> (mol%) glass composition corresponding to stoichiometric 3Ba<sub>3</sub>TB crystalline compound

only one strongly expressed exothermic (625 °C) and endothermic (975 °C) effects showed on existence of one crystalline phase. Really, X-ray analysis of products of 42.85BaO · 42.85TiO<sub>2</sub> · 14.28B<sub>2</sub>O<sub>3</sub> (mol%) glass powder samples crystallized in an interval 600-900 °C has revealed presence of only one 3Ba<sub>3</sub>TiB crystalline phase (Fig.6, curves 1-4). X-ray diffraction patterns of glass crystallization products identification have shown their full conformity with the known references data [Park et al., 2004; ICDD, 2008, File # 074-4273]. 3Ba<sub>3</sub>TiB compound is stable up to 950 °C. It decomposes on BaT and BaTB in temperature interval 950-1020 °C (Fig.5, A; Fig. 6, curve 5). The BaTiO<sub>3</sub> and melt formation is the result of 3Ba<sub>3</sub>TiB composition incongruent melting at temperature higher 1020 °C (Fig 6, curve 6). We have revealed that the 3Ba<sub>3</sub>TiB crystalline compound melted incongruently at 975 °C, with the formation of melt and barium titanate. The dissolution of these phases in a melt lead to the appearance on a DTA curve of the second, weakly expressed endothermic effect in an interval 1020-1260°C (Fig.3, curve 3).

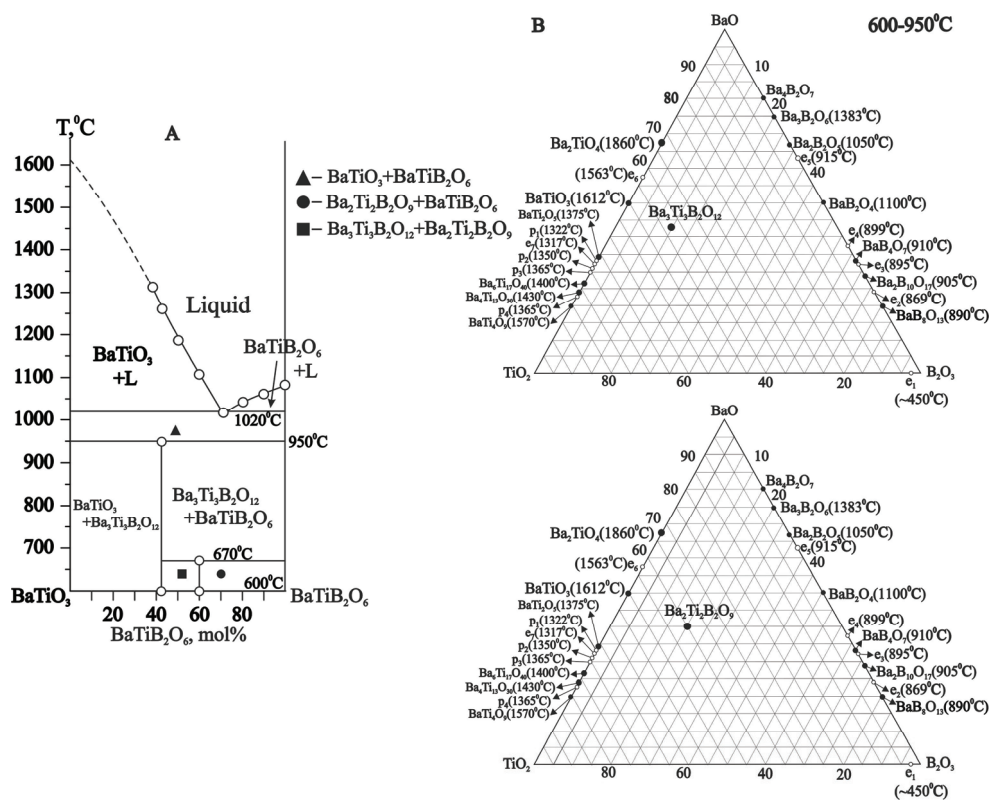


Fig. 5. Phase diagram of the pseudo-binary BaTiO<sub>3</sub> - BaTi(BO<sub>3</sub>)<sub>2</sub> system (A) and temperatures intervals of ternary Ba<sub>3</sub>Ti<sub>3</sub>B<sub>2</sub>O<sub>12</sub> (B) and Ba<sub>2</sub>Ti<sub>2</sub>B<sub>2</sub>O<sub>9</sub> (C) compounds existence on diagram.

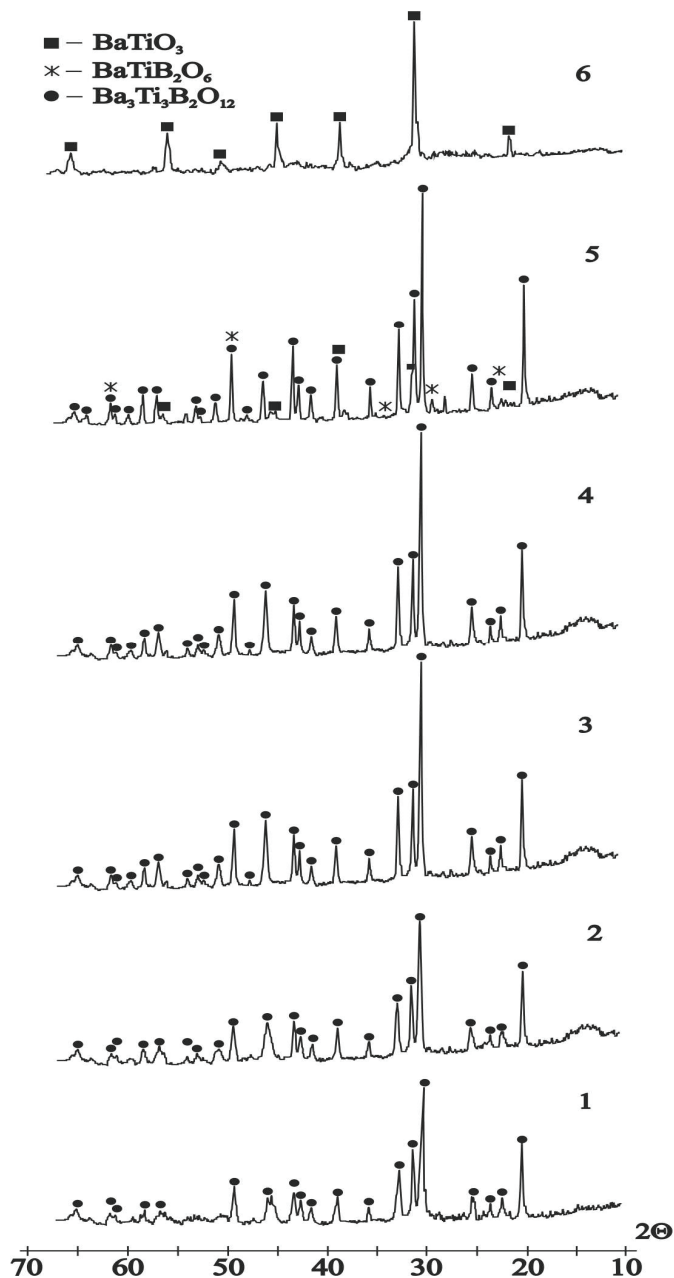


Fig. 6. XRD-patterns of the crystallized powder glass samples corresponding to Ba<sub>3</sub>Ti<sub>3</sub>B<sub>2</sub>O<sub>12</sub> composition: curve 1- 600°C 60h; curve 2- 660°C 24h, curve 3- 700°C 24h, curve 4- 900°C 24h, curve 5- 950°C 24h, curve 6- 1050°C 24h (samples 2-6 have been water quenched from heat treatment temperature).

The other picture was observed at the  $40\text{BaO} \cdot 40\text{TiO}_2 \cdot 20\text{B}_2\text{O}_3$  (mol%) glass composition crystallization. X-ray identification of products of  $40\text{BaO} \cdot 40\text{TiO}_2 \cdot 20\text{B}_2\text{O}_3$  (mol%) glass crystallization at temperature interval  $640\pm 660$  °C (first and second exothermic effects expressed on its DTA curve) within 24h has shown presence of new unknown crystalline phase in both samples. In our point of view it is new crystalline  $\text{Ba}_2\text{Ti}_2\text{B}_2\text{O}_9$  compound, which formed as single phase at the same composition glass crystallization. The x-ray powder diffraction patterns of new crystalline  $\text{Ba}_2\text{Ti}_2\text{B}_2\text{O}_9$  phase could be indexed on a orthorhombic crystal symmetry with lattice cell as follows :  $a=9.0404$  Å,  $b=15.1929$  Å,  $c=9.8145$  Å; unit cell volume  $V=1348.02\text{Å}^3$ ,  $Z=6$ , calculated density (D calc.)= $3.99\text{g}/\text{cm}^3$ ;  $D_{\text{exp.}}=3.25\text{g}/\text{cm}^3$ ;  $\alpha;\beta;\gamma=90,00^\circ$ (Table 2).

$2\theta$	dexp.	I/Io	h k l	$2\theta$	dexp.	I/Io	h k l
8.9821	9.83	9.08	0 0 1	41.1858	2.19	4.92	3 1 3
13.3220	6.65	6.00	1 0 1	41.5752	2,17	30.77	0 7 0
14.7387	6.01	6.46	0 2 1	43.2466	2.09	16.92	3 5 1
17.5044	5.06	6.77	0 3 0	43.4513	2.08	13.39	2 2 4
17.6637	5.02	17.38	1 2 1	43.9115	2.06	20.46	0 4 4
18.0535	4.91	16.77	0 0 2	44.1329	2.05	20.92	4 0 2
20.4821	4.33	5.69	2 1 0	44.8071	2.02	12.77	4 3 1
22.9091	3.88	7.69	2 2 0	45.5586	1.99	8.62	0 7 2
24.6422	3.61	38.46	2 2 1	46.0257	1.97	6.62	0 0 5
25.0566	3.55	41.84	0 4 1	46.2857	1.96	8.92	3 5 2
25.2844	3.52	62.92	0 3 2	46.7857	1.94	8.62	1 7 2
25.4128	3.50	44.77	1 4 0	47.3057	1.92	14.92	2 7 1
26.3303	3.38	17.69	2 3 0	48.6422	1.87	5.38	1 5 4
27.2477	3.27	53.69	0 0 3	48.9274	1.86	13.53	1 2 5
28.0342	3.18	100.00	2 3 1	49.2027	1.85	11.85	4 1 3
28.9573	3.08	38.61	1 0 3	49.4946	1.84	13.54	3 2 4
30.1623	2.96	11.23	3 1 0	49.7898	1.83	10.15	0 3 5
30.7928	2.90	6.52	0 5 1	50.6789	1.80	7.69	2 0 5
31.5856	2.83	9.69	3 1 1	50.9725	1.79	8.62	3 5 3
31.8159	2.81	8.87	3 2 0	51.2844	1.78	10.67	3 3 4
32.6545	2.74	9.85	0 3 3	51.5963	1.77	8.00	0 8 2
33.2727	2.69	10.31	3 2 1	51.9068	1.76	8.46	5 2 0
34.3245	2.61	42.76	2 1 3	52.2224	1.75	8.15	2 8 0
35.0265	2.56	20.31	3 0 2	52.5410	1.74	6.00	1 8 2
36.0357	2.49	5.23	1 5 2	52.8750	1.73	8.46	1 6 4
36.1786	2.48	4.92	0 4 3	53.2035	1.72	7.23	2 8 1
36.9643	2.43	17.23	3 2 2	54.9381	1.67	6.15	4 4 3
37.9464	2.37	12.92	1 0 4	56.7857	1.62	6.92	1 5 5
38.1034	2.36	16.77	3 4 0	57.9443	1.59	9.69	4 5 3
38.2586	2.35	12.15	2 3 3	58.3571	1.58	7.85	4 3 4
40.2124	2.24	21.28	2 5 2	59.1786	1.56	7.23	2 9 1
40.4148	2.23	25.08	0 5 3	59.5971	1.55	4.00	3 7 3
40.6018	2.22	23.38	3 0 3				

Table 2. X-ray characteristics of  $\text{Ba}_2\text{Ti}_2\text{B}_2\text{O}_9$  crystalline compound obtained at  $40.0\text{BaO} \cdot 40.0\text{TiO}_2 \cdot 20.0\text{B}_2\text{O}_3$ (mol%) glass composition crystallization at  $640^\circ\text{C}$ , 24 hours.

### 3.1.4.2 Phase diagram of the pseudo-binary BaB<sub>2</sub>O<sub>4</sub>-BaTiO<sub>3</sub> system

Study of pseudo-binary system BaB-BaT has revealed some interesting regularity. The liquidus curve constructed by us is the same as constructed by the Goto & Cross [Goto & Cross, 1969] (Fig.7). We have confirmed presence of pseudo-binary eutectic point with m.p.940°C containing 32 mol% BaTiO<sub>3</sub> (Fig.7). We have confirmed also information about existence of new crystalline Ba<sub>2</sub>TiB<sub>2</sub>O<sub>7</sub> (2BaBT) compound, which has been reported earlier at this system glasses crystallization [Hovhannisyanyan et al., 2008]. Strong exothermic effect at narrow temperature interval 560-590°C with maximum at 585°C is observe on DTA curve of 50.0BaO · 25.0TiO<sub>2</sub> · 25.0B<sub>2</sub>O<sub>3</sub> (mol%) glass composition (Fig.3, curve 4). The 2BaBT composition has incongruent melting at 940°C and decomposes on BaT and melt. Its liquidus temperature obtained from DTA curve and is equal to 1150°C(Fig.3, curve 4). The 2BaBT compound is not stable and is observed in narrow temperature interval (570-650°C) (Fig.7. A).

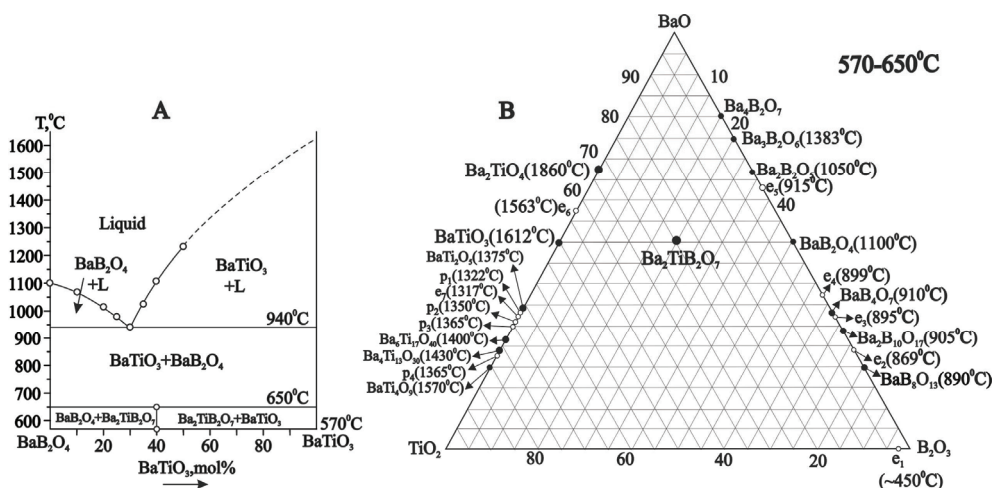


Fig. 7. Phase diagram of the pseudo-binary BaB<sub>2</sub>O<sub>4</sub>- BaTiO<sub>3</sub> system (A) and position of Ba<sub>2</sub>TiB<sub>2</sub>O<sub>7</sub> compound on it (B).

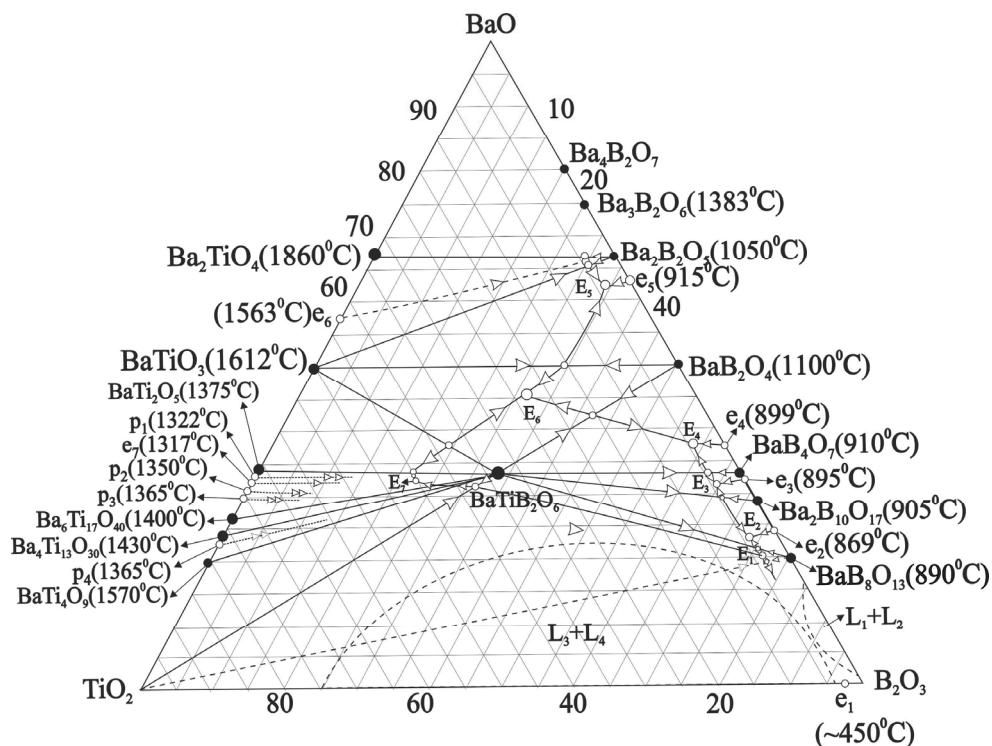
The pure 2BaBT phase crystallizes from the same glass composition crystallization at 585°C, 24 hours. The X-ray characteristics of Ba<sub>2</sub>TiB<sub>2</sub>O<sub>7</sub> were determined and are given in Table 3. The X-ray powder diffraction patterns of 2BaBT could be indexed on a rhombic crystal symmetry with lattice cell as follows : a=10.068 Å, b=13.911 Å, c=15.441 Å; unit cell volume V=2629.17Å<sup>3</sup>, Z =12, calculated density (D calc.)= 4.23g/cm<sup>3</sup>; D exp.=4.02g/cm<sup>3</sup>; α;β;γ =90,00°.

### 3.1.4.3 Phase diagram of the BaO-TiO<sub>2</sub>-B<sub>2</sub>O<sub>3</sub> ternary system

First of all we have deleted eutectic point e<sub>1</sub>, which has been for the first time wrongly put by Levin with co-workers on the binary BaO-B<sub>2</sub>O<sub>3</sub> diagram [Levin & McMurdie, 1949; Levin & Ugrinic, 1953], and then is repeated in our recent publications [Hovhannisyanyan, R. et al, 2008, Hovhannisyanyan, M. et al, 2009]. Such imperfect data very often committed many authors first of all at binary borate system diagram constructions [ACerS & NIST, 2004]. Because, this point indicate only sharp increase of liquidus temperature which is connected with stable phase separation, typical for many binary borate systems (Fig.8).

2 $\theta$	dexp.	I/I <sub>0</sub>	h k l	2 $\theta$	dexp.	I/I <sub>0</sub>	h k l	2 $\theta$	dexp.	I/I <sub>0</sub>	h k l
8.55	10.329	2.84	0 1 1	37.24	2.412	498	0 2 6	52.22	1.750	2.76	2 4 7
8.74	10.117	2.04	1 0 0	37.37	2.404	311	3 3 3	52.38	1.745	7.11	2 2 8
10.57	8.377	1.69	1 0 1	38.24	2.352	871	1 2 6	52.58	1.739	7.29	0 8 0
10.81	8.176	1.33	1 1 0	38.40	2.342	747	4 2 1	52.74	1.734	5.07	5 4 1
11.53	7.668	3.20	0 0 2	38.67	2.326	231	2 5 2	53.21	1.720	2.93	0 6 6
12.27	7.243	1.69	1 1 1	38.98	2.310	231	0 4 5	53.31	1.717	5.51	0 0 9
12.60	7.025	4.98	0 2 0	39.16	2.298	133	2 4 4	53.42	1.714	4.09	1 8 0
13.29	6.657	4.00	0 1 2	39.35	2.288	196	2 3 5	53.52	1.711	3.11	3 6 4
13.93	6.353	4.89	0 2 1	39.50	2.270	178	3 0 5	53.82	1.703	6.22	0 1 9
14.53	6.100	3.56	1 0 2	39.91	2.256	551	0 5 4	53.98	1.697	8.98	1 6 6
15.46	5.731	3.02	1 2 0	40.28	2.237	551	1 6 1	54.07	1.695	7.64	4 6 1
15.90	5.574	1.60	1 1 2	40.45	2.229	1031	4 1 3	54.14	1.693	6.40	1 0 9
16.49	5.374	3.47	1 2 1	40.57	2.222	960	3 3 4	54.74	1.675	3.20	5 1 5
16.92	5.236	1.78	0 2 2	40.86	2.207	293	0 0 7	54.91	1.671	2.76	0 7 5
17.19	5.151	1.87	0 0 3	41.00	2.199	338	2 5 3	55.56	1.653	3.11	5 4 3
17.51	5.058	1.96	2 0 0	41.16	2.191	249	4 3 1	55.68	1.649	3.91	1 7 5
18.36	4.828	2222	0 1 3	41.35	2.182	284	0 1 7	55.74	1.648	4.71	0 8 3
18.69	4.741	9.24	2 1 0	41.64	2.167	204	1 6 2	55.93	1.642	5.78	1 2 9
19.12	4.638	2.67	0 3 0	41.85	2.157	524	1 0 7	56.54	1.626	3.56	3 2 8
19.72	4.498	3.56	2 1 1	41.95	2.152	569	4 2 3	56.66	1.623	2.84	3 6 5
19.95	4.445	5.51	0 3 1	42.12	2.144	293	3 5 0	56.97	1.615	3.73	4 2 7
20.34	4.363	3.64	1 1 3	42.40	2.130	187	1 1 7	57.15	1.610	7.29	0 3 9
20.97	4.231	2.13	2 0 2	42.88	2.107	418	4 0 4	57.37	1.605	6.31	2 8 2
21.11	4.207	4.00	1 3 0	43.11	2.097	613	2 4 5	57.66	1.597	3.20	4 5 5
21.56	4.118	2.13	0 2 3	43.24	2.091	738	2 6 1	57.93	1.590	2.13	1 3 9
21.70	4.092	2.04	2 2 0	43.49	2.080	2378	4 1 4	58.14	1.585	3.20	5 3 5
22.05	4.026	3.91	2 1 2	43.59	2.075	1769	1 6 3	58.30	1.581	3.20	2 2 9
22.56	3.938	2.49	2 2 1	43.72	2.069	2347	0 4 6	58.47	1.577	2.67	6 3 0
22.97	3.870	4.18	0 0 4	43.97	2.058	1475	1 2 7	58.67	1.573	3.20	0 7 6
23.20	3.831	2.31	1 2 3	44.31	2.043	2556	3 0 6	58.84	1.568	8.80	1 5 8
23.78	3.739	3.82	0 1 4	44.41	2.038	2231	4 4 0	58.98	1.565	7.64	2 8 3
24.14	3.684	2.49	1 3 2	45.01	2.013	1511	5 0 0	59.28	1.558	4.27	4 7 0
24.46	3.636	2.31	2 2 2	45.35	1.998	187	5 0 1	59.51	1.552	7.73	4 7 1
24.75	3.596	4.00	2 0 3	45.78	1.980	187	3 5 3	59.79	1.546	6.84	0 9 0
25.19	3.490	100.00	1 1 4	45.97	1.973	284	4 4 2	60.09	1.539	2.84	0 4 9
26.08	3.414	1.96	2 3 0	46.19	1.964	347	3 2 6	60.28	1.534	2.67	0 1 10
26.24	3.393	1.42	0 4 1	46.64	1.946	1902	5 0 2	60.50	1.529	2.49	4 7 2
26.36	3.378	1.78	0 2 4	47.12	1.927	222	0 7 2	60.76	1.523	1.78	2 6 7
26.67	3.341	1.60	2 3 1	47.44	1.915	1627	2 4 6	60.93	1.519	2.22	3 1 9
27.15	3.280	2.48	3 0 1	47.56	1.910	1653	0 1 8	61.41	1.508	1.87	6 3 3
27.71	3.218	36.18	1 4 1	47.70	1.905	1529	3 6 0	61.79	1.500	3.73	5 3 6
28.87	3.089	93.60	0 0 5	47.85	1.900	1120	3 4 5	61.98	1.496	3.73	3 7 5
29.50	3.025	2.49	1 4 2	48.12	1.890	204	0 5 6	62.14	1.493	1.42	4 7 3
29.69	3.005	1.24	3 1 2	48.35	1.881	124	4 2 5	62.36	1.488	3.11	5 0 7
29.95	2.982	4.35	2 1 4	48.54	1.874	142	3 5 1	62.72	1.480	1.24	0 9 3
30.56	2.923	2.31	1 0 5	48.89	1.861	222	0 2 8	62.98	1.475	1.33	6 0 5
30.80	2.910	1.42	1 1 5	49.08	1.855	160	0 6 5	63.14	1.471	1.60	2 4 9
31.06	2.878	6.04	0 4 3	49.19	1.851	284	2 6 4	63.24	1.469	1.87	2 1 10
31.64	2.825	2.76	0 2 5	49.38	1.844	640	3 0 7	63.43	1.465	1.78	0 3 10
31.95	2.800	3.91	2 2 4	49.63	1.835	1191	2 7 1	63.66	1.461	1.33	6 3 4
32.71	2.736	9.33	0 5 1	49.70	1.833	1324	5 3 1	63.74	1.459	1.69	5 6 3
32.88	2.722	2.67	3 3 0	49.83	1.828	1511	3 1 7	63.93	1.455	2.67	4 3 8
33.45	2.677	36.18	3 3 1	49.97	1.824	1120	1 6 5	64.14	1.451	3.20	2 8 5
33.95	2.639	36.18	1 5 1	50.08	1.820	631	1 7 3	64.26	1.448	2.93	1 3 10
34.36	2.608	21.06	3 2 3	50.19	1.817	613	4 5 2	64.51	1.444	2.13	5 4 6
34.98	2.563	2.13	3 3 2	50.62	1.802	231	2 0 8	64.72	1.439	2.76	7 0 0
35.62	2.518	4.80	4 0 0	51.51	1.772	160	5 1 4	64.86	1.436	5.78	6 5 0
35.85	2.503	5.16	1 4 4	51.65	1.769	169	2 5 6	64.97	1.434	6.69	3 5 8
36.21	2.479	1.78	4 1 0	51.85	1.762	604	3 4 6	65.77	1.418	3.91	4 0 9
36.47	2.462	1.78	2 2 5	51.98	1.758	515	3 5 5				
36.84	2.438	2.40	2 5 0	52.12	1.753	222	1 3 8				

Table 3. X-ray characteristics of Ba<sub>2</sub>TiB<sub>2</sub>O<sub>7</sub> crystalline compound obtained at 50.0BaO · 25.0TiO<sub>2</sub> · 25.0B<sub>2</sub>O<sub>3</sub>(mol%) glass composition crystallization at 585°C, 24 hours



Point	$T_m$ , (°C)	Composition, mol% $B_2O_3:BaO:TiO_2$
E <sub>1</sub>	850	76.0:20.0:4.0
E <sub>2</sub>	835	75.0:21.0:4.0
E <sub>3</sub>	850	63.5:32.0:4.5
E <sub>4</sub>	860	58.0:38.0:4.0
E <sub>5</sub>	865	35.0:62.0:3.0
E <sub>6</sub>	930	31.5:45.0:23.5
E <sub>7</sub>	1000	22.6:32.1:45.3

Table 4. The melting temperature ( $T_m$ ) and compositions for ternary eutectic points in the BaO-B<sub>2</sub>O<sub>3</sub>-TiO<sub>2</sub> system

responsible for the strong anisotropy of the “Nordenskiöldine” group borates [Bayer, 1971]. It is very stable compound occupied dominating position in BaO-TiO<sub>2</sub>-B<sub>2</sub>O<sub>3</sub> system phase diagram (Fig.8). It has congruent character of melting at 1080°C (Fig.3, curve1). We have given a preference to study the process of directed crystallization of BaTiB composition based on above stated.

Thermal treatment at 670-690°C, 1 h is enough for full crystallization of the pressed powder glass samples. X-ray diffraction patterns of crystallization products (Fig.9, curve1) are identical to the references data [Vicat & Aleonard, 1968; ICDD, 2008, File # 35-0825].

The other pictures were observed for monolithic samples (Fig.9, curve 2). X-ray diffraction patterns determined from crystallized (630°C 4h+ 690°C 24h) tape samples surface indicated reorientation of crystalline structure, leading to increase of intensity of following reflexes : 5.47 Å (003) from 7% up to 70% (10 time), 2.51 Å (110) from 35 to 100%(3 time), 3.85 Å (102) from 75 to 100%.

At monolith glass sample crystallization at 630°C 4h+ 690°C 12h under direct current (DC) voltage 3.0 kV/cm X-ray diffraction patterns of samples surface again indicate reorientation of crystalline structure: reflexes 5.47 Å (003) decrease from 70% to 46%, 3.85 Å (102) decrease from 100 to 60%, 2.51 Å (110) from 100 to 42%, and reflex 2.97 Å (003) again began 100% (Fig.9, curve3).

X-ray diffraction patterns of BaTB glass tape sample surface crystallized at 630°C 12h+ 690°C 12h (Fig.8, curve4) indicate very strongly change of crystalline structure in relation to a sample received by a traditional powder method: reflex 5.47 Å (003) increase from 7% to 100 %, 3.85 Å (102) decrease from 100 to 10%, 2.51 Å (110) decrease from 100 to 42%, 2.97 Å (003) decrease from 100 to 35%, 2.73 Å increase from 3 to 51% , 1.82 Å increase from 3 to 43% again began 100% (Fig.9, curve4). Part of reflexes practically disappeared (are not visible) at the given regime of X-ray record: 2.73, 2.28, 2.15, 2.10, 2.06, 1.92, 1.61, 1.52 Å.

X-ray diffraction patterns of BaBT glass tape sample surface crystallized under DC 3kV/cm at 630°C 1h+ 690°C 4h again indicate reorientation of crystalline structure (Fig.9, curve5).

Processes of reorientation of the crystal structure, similar occurring with a monolithic sample are observed: reflexes 5.47 Å (003) sharply decrease from 100% to 38%, reflex 2.97 Å (003) again began 100%, 3.85 Å (102) increase from 10 to 58%, 2.51 Å (110) increase from 42 to 78% (Fig.9, curve5). Well observable reflexes 2.72, 2.62, 2.15, 2.10, 1.92, 1.61, 1.60, 1.52 Å have again appeared. Such impression is created, that under DC action the re-oriented structure tends to return to structure inherent in the initial sample received on powder technology.

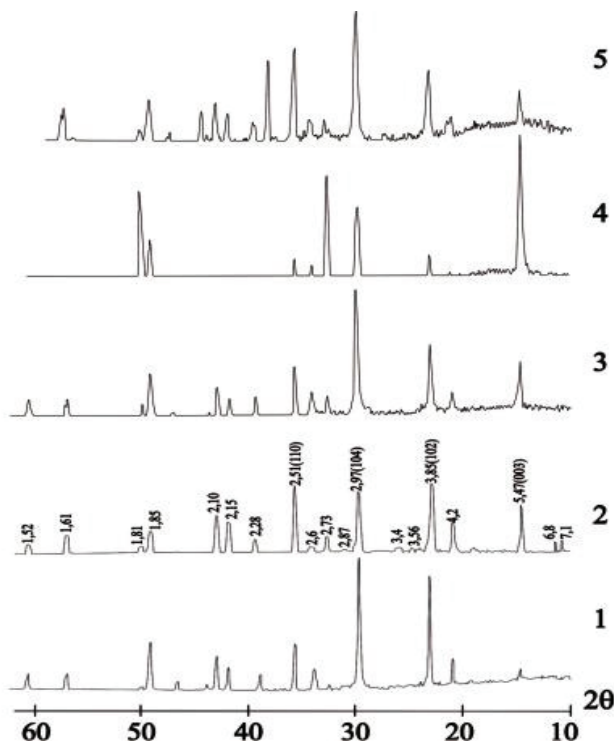


Fig. 9. XRD-patterns of the BaTB samples and  $[hkl]$ -indices attributed to the peaks of the BaTiB<sub>2</sub>O<sub>6</sub> crystallized glasses:

curve 1- pressed powder sample crystallized at 690°C 1h.

curve 2- monolithic glass sample crystallized at 630°C 4h+ 690°C 12h;

curve 3- monolithic glass sample crystallized at 630°C 4h+ 690°C 12h under DC 3kV/cm

curve 4- tape glass sample crystallized at 630°C 12h+ 690°C 12h

curve 5- tape glass sample crystallized at 630°C 1h+ 690°C 4h under DC 3kV/cm

### 3.2.2 Crystallization behavior of the stoichiometric glass Ba<sub>3</sub>Ti<sub>3</sub>O<sub>6</sub>(BO<sub>3</sub>)<sub>2</sub> composition

Having confirmed existence of 3Ba<sub>3</sub>TiB there was a necessity to study temperature intervals of its stability. We'll try to do it through glass powder samples crystallization using its DTA data (Fig.3, curve 3). Formation of pure 3Ba<sub>3</sub>TiB compound clear observed on X-ray diffraction patterns of the same composition glass powder samples crystallization at 600°C 60h - temperature of the crystallization beginning on the DTA curve (Fig.6, curve 1). The further increasing of thermal treatment temperatures (660, 700, 800 and 900°C) lead to indication only pure 3Ba<sub>3</sub>TiB crystalline compound in products of glass crystallization (Fig.6, curves 2-4). X-ray diffraction patterns of crystallization products (Fig.6, curves 1-4) are identical to the references data [Park et al., 2004; ICDD, 2008, File # 074-4273]. We have revealed that the 3Ba<sub>3</sub>TiB compound in an interval 950-1020°C decomposes with BaTiO<sub>3</sub> and BaTB formation (Fig.6, curve5). The 3Ba<sub>3</sub>TiB compound is melted incongruently at 975°C (Fig.3, curve 3), with formation of melt and BaTiO<sub>3</sub> at temperatures higher 1020 °C (Fig.6, curve 6).

### 3.2.3 Crystallization behavior of the stoichiometric glass $\text{Ba}_2\text{Ti}_2\text{B}_2\text{O}_9$ composition

Denying of existence of  $(2\text{Ba}_2\text{TiB})$  stoichiometric compounds from Barbier group [Park et al., 2004] after  $\text{Ba}_3\text{Ti}_3\text{B}_2\text{O}_{12}$  ( $3\text{Ba}_3\text{TiB}$ ) synthesis and characterization have increased an intrigue around  $2\text{Ba}_2\text{TiB}$  compound. According to references data both compounds had Hexagonal cell and very closed cell parameters:  $a = 8.7110 \text{ \AA}$ ,  $c = 3.9298 \text{ \AA}$  for  $3\text{Ba}_3\text{TiB}$  [ICDD, 2008, File#074-4273] and  $a = 8.7210 \text{ \AA}$ ,  $c = 3.933 \text{ \AA}$  for  $2\text{Ba}_2\text{TiB}$  [Millet et al., 1986]. It was impossible to pure synthesis of both compounds through solid phase reaction. We'll try to do it through glass tapes crystallization.

It was big surprising for us, when on the DTA curve of the  $40\text{BaO} \cdot 40\text{TiO}_2 \cdot 20\text{B}_2\text{O}_3$  (mol%) glass composition three exothermic effects have been observed: two effects at  $640^\circ\text{C}$  (small) and at  $660^\circ\text{C}$  (high) are combined and third is weakly expressed at  $690^\circ\text{C}$  (Fig.3, curve 2). X-ray identification of products of  $40\text{BaO} \cdot 40\text{TiO}_2 \cdot 20\text{B}_2\text{O}_3$  (mol%) glass composition crystallization at temperatures  $640$  and  $660^\circ\text{C}$  within 24h has shown presence of new unknown  $\text{Ba}_2\text{Ti}_2\text{B}_2\text{O}_9$  crystalline phase in both samples (Fig.10, curves 2, 3). Its X-ray characteristics have been determined and are given in Table 2. X-ray identification of crystallization products have shown of  $2\text{Ba}_2\text{TB}$  phase formation starting from  $600^\circ\text{C}$  (Fig.10, curve1).

The third exothermic effect on  $2\text{Ba}_2\text{TiB}$  glass DTA curve (Fig.3, curve 2) at  $690^\circ\text{C}$  is connected with its decomposition and  $3\text{Ba}_3\text{TiB}$ ,  $\text{BaTiB}$  compounds formation (Fig.10, curves 4, 5). Process of  $2\text{Ba}_2\text{TB}$  sample decomposition is continues up to  $950^\circ\text{C}$  24h. At this temperature the  $3\text{Ba}_3\text{TiB}$  phase is disappear and the  $\text{BaTiO}_3$  phase starts to appear together with  $\text{BaTiB}$  phase (Fig.10, curve 6). And finally we observed disappearance of both  $3\text{Ba}_3\text{TB}$  and  $\text{BaTB}$  phases at temperatures higher  $1020^\circ\text{C}$  (Fig.10, curve7).

The strong endothermic effect of melting with minimum at  $975$  is observed on DTA curve (Fig.3, curve 2). According to references data [Millet et al., 1986] the  $2\text{Ba}_2\text{TiB}$  composition between  $950\text{-}960^\circ\text{C}$  decomposes with  $\text{BaTiO}_3$  and liquid formation. In our cases together with  $\text{BaTiO}_3$  we have identified the  $\text{BaTB}$  in temperature interval  $950\text{-}1020^\circ\text{C}$  (Fig.10, curve 6), and  $\text{BaTiO}_3$  melt us results of incongruent melting at temperatures higher  $1020^\circ\text{C}$  (Fig.10, curves 7).

The same picture as for powder samples is observed for crystallized glass tapes of  $2\text{Ba}_2\text{TB}$  composition. We have X-ray amorphous transparent tape glass sample after thermal treatment at  $600^\circ\text{C}$  6h (Fig.11, curve1). Only new, pure  $2\text{Ba}_2\text{TB}$  phase is formed at next steps of thermal treatment:  $640^\circ\text{C}$  24h, and  $660^\circ\text{C}$  24h (Fig.11, curves 2,3). The  $2\text{Ba}_2\text{TB}$  compound decomposes with  $3\text{Ba}_3\text{TB}$  and  $\text{BaTB}$  phases formation at thermal treatment at  $700^\circ\text{C}$  24h (Fig.11, curve 4).

### 3.2.4 Crystallization behavior of the stoichiometric glass $\text{Ba}_2\text{TiB}_2\text{O}_7$ composition

X-ray identification of glass powder samples of  $50\text{BaO} \cdot 25\text{TiO}_2 \cdot 25\text{B}_2\text{O}_3$  (mol%) compositions thermal treated in an interval  $570\text{-}650$  24 h have shown pure  $2\text{BaTB}$  compound formation (Fig.12, curve1). The  $2\text{BaTB}$  compound decomposes on two phases:  $\text{BaTiO}_3$  and  $\text{BaB}_2\text{O}_4$  at temperature interval  $650\text{-}940^\circ\text{C}$  (Fig.12, curves 2, 3).

### 3.2.5 Crystallization behavior of the stoichiometric glass $\text{BaTi}_2\text{O}_5$ composition

Using our super cooling technique and special two step melting technology we have obtained  $\text{BaTi}_2\text{O}_5$  ( $\text{B}_2\text{T}$ ) compound in glass state (glass tapes with thickness  $0.03\text{ - }0.4\text{mm}$ ) and have studied processes of its crystallization. The initial glass tape sample thermal treated

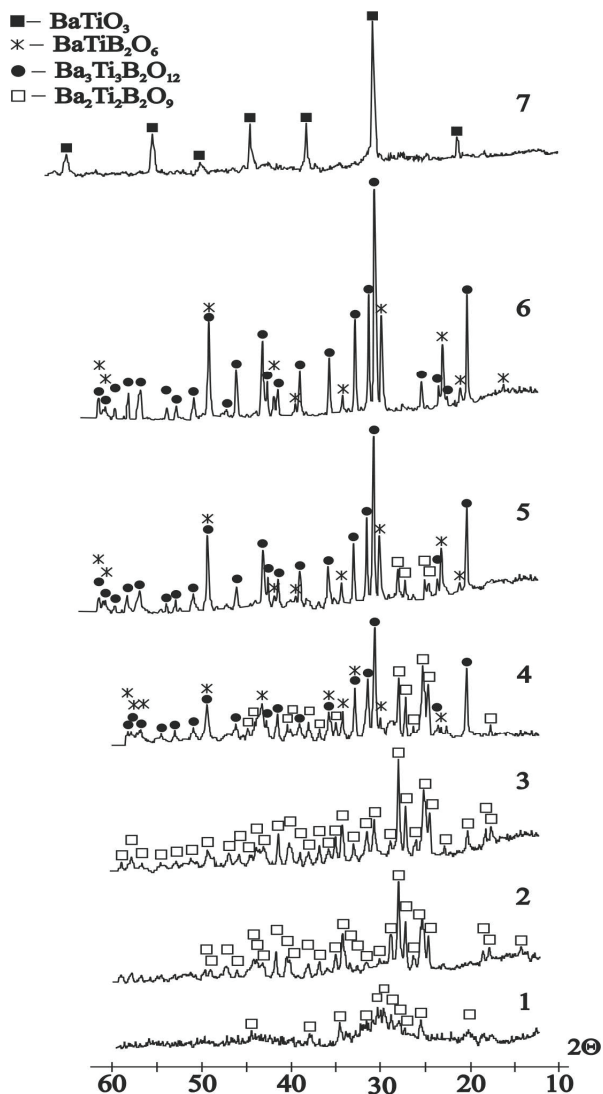


Fig. 10. XRD-patterns of the crystallized powder glass samples corresponding to Ba<sub>2</sub>Ti<sub>2</sub>B<sub>2</sub>O<sub>9</sub> composition:

curve 1- 600°C 60h;

curve 2- 640°C 24h;

curve 3- 660°C 24h;

curve 4- 700°C 24h;

curve 5- 740°C 24h;

curve 6- 950°C 24h;

curve 7- 1020°C 24h (samples 2-7 have been water quenched from heat treatment temperature).

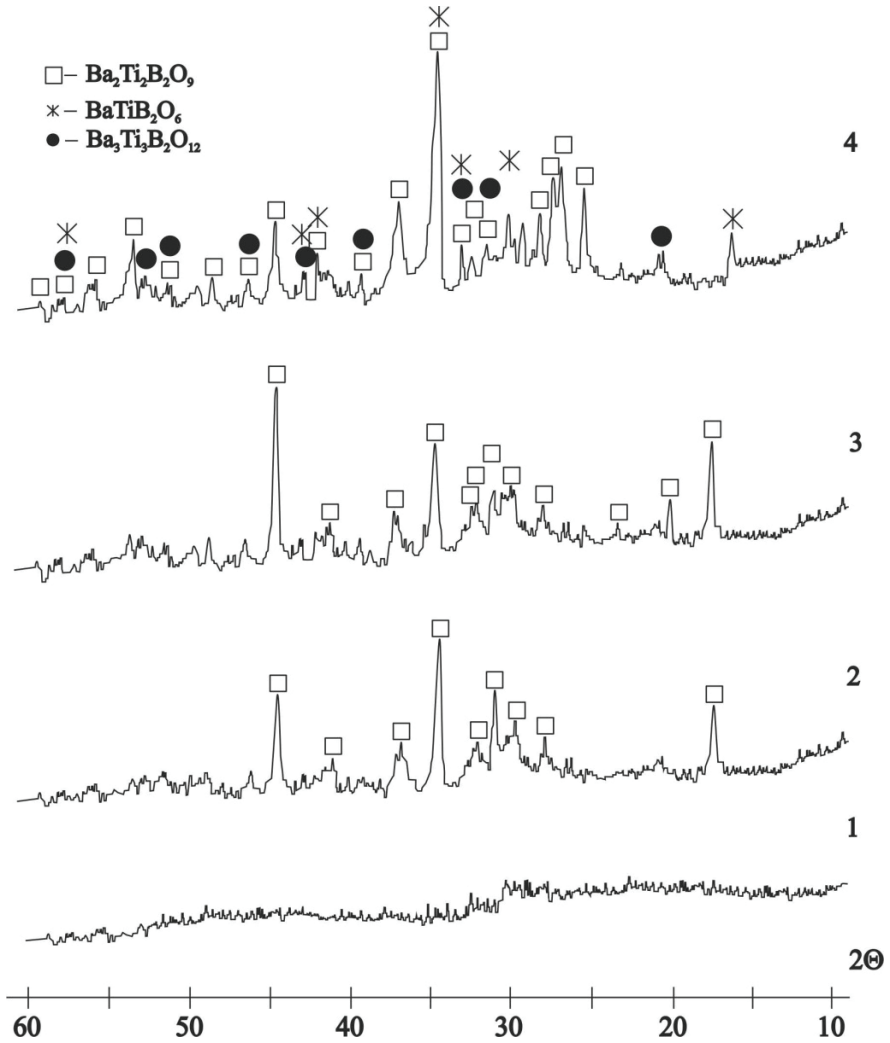


Fig. 11. XRD-patterns of the crystallized tape glass samples corresponding to  $\text{Ba}_2\text{Ti}_2\text{B}_2\text{O}_9$  (2Ba2TiB) composition:

curve 1- 600°C 6h;

curve 2- 640°C 24h;

curve 3- 660°C 24h;

curve 4- 700°C 24h

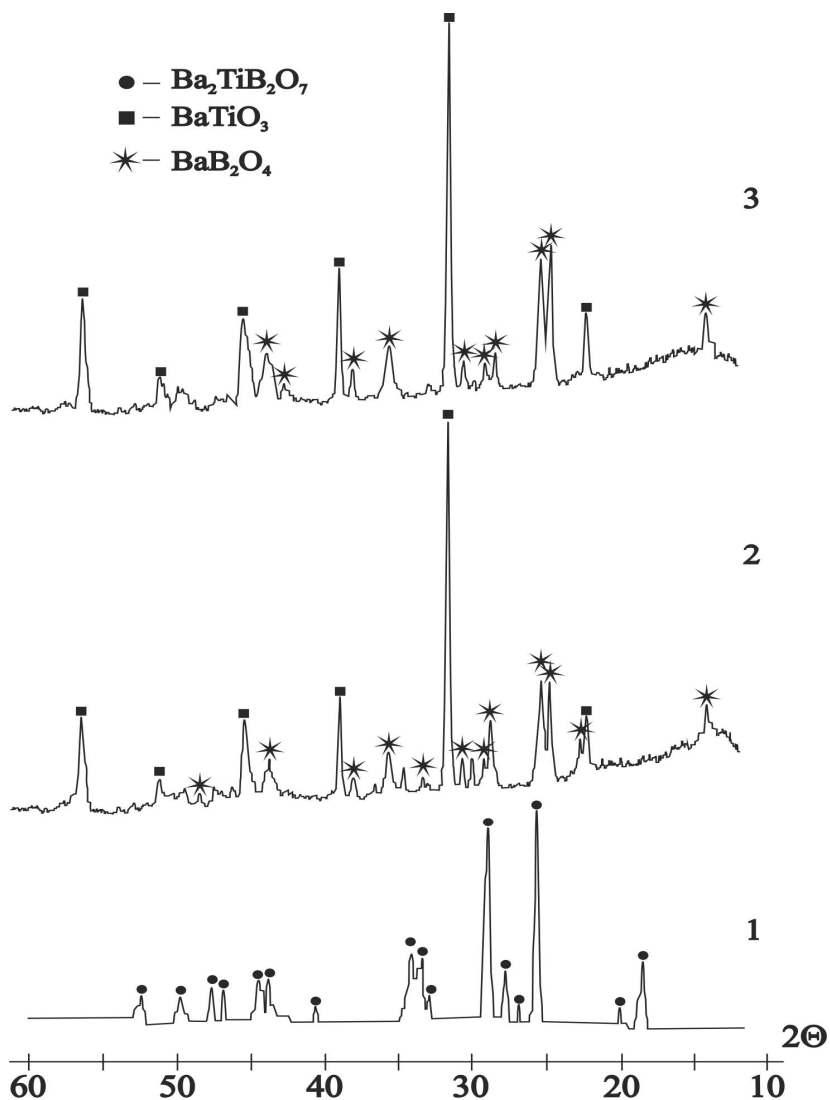


Fig. 12. XRD-patterns of the crystallized powder glass samples corresponding to Ba<sub>2</sub>TiB<sub>2</sub>O<sub>7</sub> composition:

curve 1- 585°C 24h;

curve 2- 730°C 24h;

curve 3- 800°C 24h;

at 680°C 12h is X-ray amorphous (Fig.13, curve1). The further increase of crystallization temperature (680°C 12h +740°C 12h) results in occurrence of BaTi<sub>2</sub>O<sub>5</sub> peaks [ICDD, 2008, File # 34-0133] with preservation of a transparency of a tape sample (Fig.13, curves 2,3). The BaTi<sub>2</sub>O<sub>5</sub> is dominating crystalline phase at studied crystallization regimes (Fig.13, curves 3-

4). However, we do not exclude presence of barium polytitanates in glass crystallization products in quantities not influencing on the end-product properties. We have observe on X-ray patterns strongly reorientation of formed barium di-titanate crystalline phase: reflex  $8.247 \text{ \AA}$  (hkl 002) increase from 9% and become 100% and  $3.47 \text{ \AA}$  (hkl 401) decrease from 100% to 0 (Fig.13, curves 2,3).

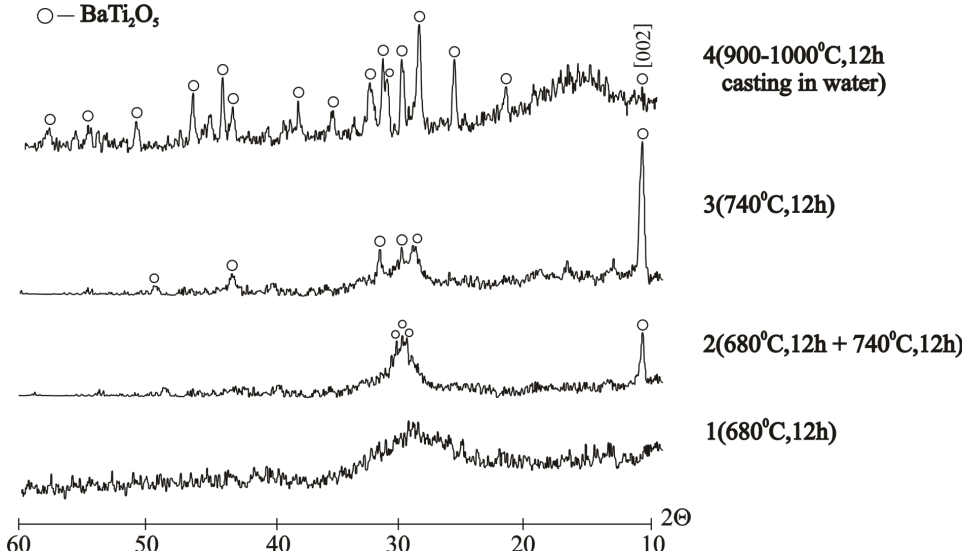


Fig. 13. XRD-patterns of the crystallized BaTi<sub>2</sub>O<sub>5</sub> glass tape samples obtained by super cooling technique:

curve 1- initial tape sample thermal treated at 680°C 12h -transparent;

curve 2- tape sample (680°C 12h +740 °C 12h)-transparent;

curve 3- tape sample 740 °C 12h- transparent;

curve 4- tape sample 900-1000 °C 12h, casting in water

#### 4. Ferroelectric properties of stoichiometric glasses in BaO-TiO<sub>2</sub>-B<sub>2</sub>O<sub>3</sub> system

The ferroelectric (polarization - electric field) hysteresis, is a defining property of ferroelectric materials. In the last twenty years it has become a subject of intensive studies due to potential applications of ferroelectric thin films in nonvolatile memories. In ferroelectric memories the information is stored as positive or negative remanent polarization state. Thus, the most widely studied characteristics of ferroelectric hysteresis were those of interest for this particular application: the value of the switchable polarization (the difference between the positive and negative remanent polarization,  $P_R - (-P_R)$ , dependence of the coercive field  $E_c$  on sample thickness, decrease of remanent or switchable polarization with number of switching cycles, polarization imprint, endurance, retention [Damyanovich, 2005]. Electric field induced polarization measurement was used for ferroelectric characterization of known and revealed first time new ternary BaTi(BO<sub>3</sub>)<sub>2</sub>, Ba<sub>2</sub>Ti<sub>2</sub>B<sub>2</sub>O<sub>9</sub>, Ba<sub>3</sub>Ti<sub>3</sub>B<sub>2</sub>O<sub>12</sub>, Ba<sub>2</sub>TiB<sub>2</sub>O<sub>7</sub> and binary BaTi<sub>2</sub>O<sub>5</sub> stoichiometric compositions glass ceramics.

#### 4.1 Polarization behavior of BaTi(BO<sub>3</sub>)<sub>2</sub>, Ba<sub>3</sub>Ti<sub>3</sub>B<sub>2</sub>O<sub>12</sub>, Ba<sub>2</sub>Ti<sub>2</sub>B<sub>2</sub>O<sub>9</sub>, Ba<sub>2</sub>TiB<sub>2</sub>O<sub>7</sub> glass ceramics

Electric field induced polarization (P) and remanent polarization (P<sub>r</sub>) were measured at room temperature for BaBT, 3Ba3TiB, 2Ba2TiB, 2BaTiB glass tape samples crystallized using various regimes (Fig.14).

Linear P-E curves are observed up to fields of 40-120 kV/cm for all measured samples with thickness 0.04-0.08mm. The polarization becomes nonlinear with increasing of applied electric field, and at 140-400 kV/cm the remanent polarization 2P<sub>r</sub> values were found 0.35, 3.89, 0.6 and 0.12 μC/cm<sup>2</sup> for the BaBT (Fig.14, A), 3Ba3TiB (Fig.14, B), 2Ba2TiB (Fig.14, C) and 2BaTiB (Fig.14, D) crystallized glass tape samples respectively. According to obtained results it is possible to conclude that samples are ferroelectrics. The highest remanent polarization value (2P<sub>r</sub>=3.89 μC/cm<sup>2</sup>) has 3Ba3TiB crystallized glass tape sample (Fig.14, B).

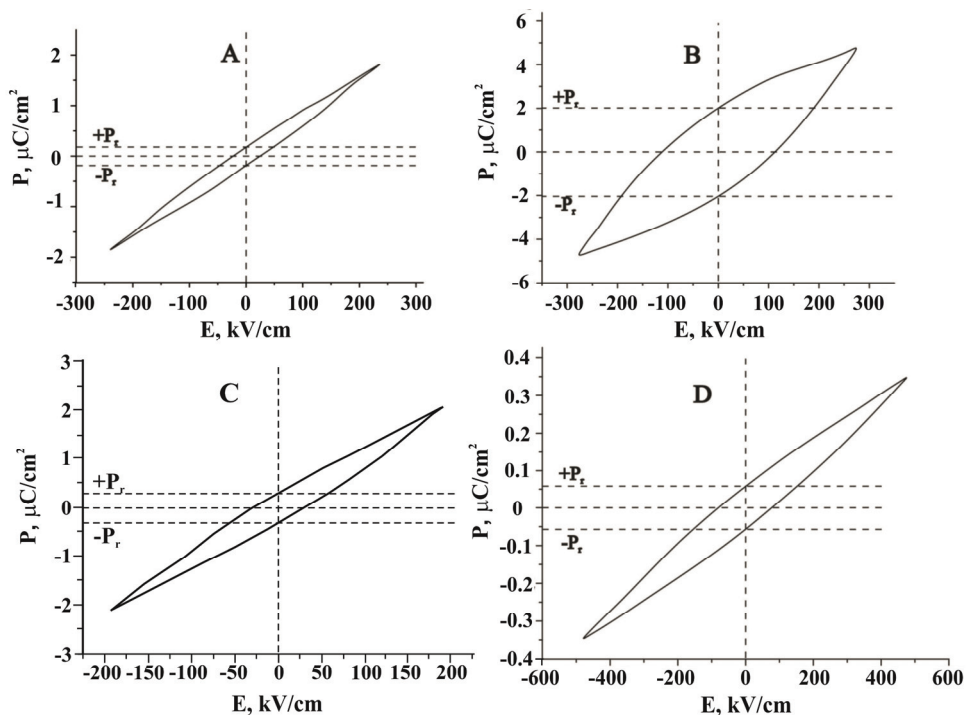


Fig. 14. Dependence of polarization (P) on electric field (E) for crystallized stoichiometric glass compositions:

- BaTiB<sub>2</sub>O<sub>6</sub> glass tape sample of 0.08 mm in thickness crystallized at 700°C 24h
- Ba<sub>3</sub>Ti<sub>3</sub>B<sub>2</sub>O<sub>12</sub> glass tape sample of 0.07 mm in thickness crystallized at 900°C 12h
- Ba<sub>2</sub>Ti<sub>2</sub>B<sub>2</sub>O<sub>9</sub> glass tape sample of 0.08 mm in thickness crystallized at 640°C 24h
- Ba<sub>2</sub>TiB<sub>2</sub>O<sub>7</sub> glass tape sample of 0.04 mm in thickness crystallized at 580°C 12h

#### 4.2 Polarization behavior of BaTi<sub>2</sub>O<sub>5</sub> glass ceramic

Electric field induced polarizations were measured at room temperature for BaTi<sub>2</sub>O<sub>5</sub> glass tape samples crystallized at various regimes. The high value of polarization (P~10μC/cm<sup>2</sup>)

and remanent polarization ( $2P_r = 6,2 \mu\text{Cu}/\text{cm}^2$ ) we observe for strongly oriented transparent glass ceramic at applied field  $220 \text{ kV}/\text{cm}$  (Fig.15).

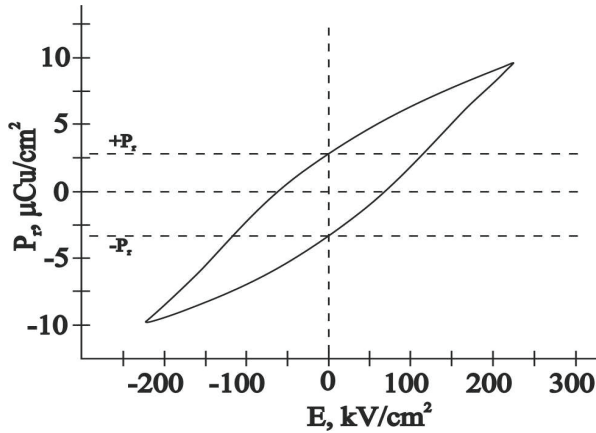


Fig. 15. Dependence of polarization ( $P$ ) on electric field ( $E$ ) for  $\text{BaTi}_2\text{O}_5$  crystallized glass tape ( $740^\circ\text{C}$  12h) of 0.08 mm in thickness

## 5. Discussion

Revision of phase diagrams of very complex ternary  $\text{BaO-TiO}_2\text{-B}_2\text{O}_3$  system has allowed us to study it more precisely. For this purpose glass samples have been used as initial testing substance for phase diagram construction. It is a very effective method, because it is possible to indicate temperature intervals of all processes taking place in glass samples: glass transition, crystallization, quantity of formed crystalline phases and their melting. Whereas, samples prepared by traditional solid phase synthesis are less informative and often lose a lot of information.

On the other hand super cooling technique created by our group allowed us to expand borders of glass formation from stable glass forming barium tetra borate up to binary di-barium borate and up to barium di-titanates which, together with compositions corresponding to ternary  $\text{BaTB}$ ,  $2\text{BaTB}$ ,  $2\text{Ba}_2\text{TB}$ ,  $3\text{Ba}_3\text{TB}$  compounds, have been obtained as glass tape with thickness of 30-400 microns (Fig.2). Large area of glass formation has allowed to have enough quantity of samples for DTA and X-ray investigations and  $\text{BaO-TiO}_2\text{-B}_2\text{O}_3$  system phase diagram construction.

There are very stable congruent melted binary barium titanate and barium borate and ternary barium boron titanate ( $\text{BaTB}$ ) compounds in the ternary system. They have dominating positions in ternary diagram and occupied the biggest part of it (Fig.8). However, mutual influence of these stable compounds and not-stable binary ( $\text{Ba}_2\text{T}$ ) and ternary compounds ( $2\text{Ba}_2\text{TB}$ ,  $3\text{Ba}_3\text{TB}$  and  $2\text{BaTB}$ ) lead to formation of seven ternary eutectic points (Table2), which have essential influence on liquidus temperature decrease and glass formation. Ternary eutectics  $E_5$ ,  $E_6$  and  $E_7$  together with binary eutectics  $e_7$  and  $e_6$  have allowed to outline the field of barium titanate crystallization on the  $\text{BaO-TiO}_2\text{-B}_2\text{O}_3$  system phase diagram. The  $\text{BaTiO}_3$  is very stable compound and occupies dominating position on the phase diagram (Fig.8). Ternary eutectics  $E_5$ ,  $E_6$  and  $E_4$  together with binary eutectics  $e_4$

and  $e_5$  have allowed to outline the field of barium borate crystallization. The BaB<sub>2</sub>O<sub>4</sub> is very stable compound also and occupied enough position on the studied ternary phase diagram (Fig.8). Ternary eutectics E<sub>1</sub>, E<sub>2</sub>, E<sub>3</sub>, E<sub>4</sub>, E<sub>6</sub> and E<sub>7</sub> have allowed to determine the field of crystallization of BaTB ternary compound. The BaTB is very stable compound also and occupies dominating position in the central part of the studied ternary BaO-TiO<sub>2</sub>-B<sub>2</sub>O<sub>3</sub> system phase diagram (Fig.8).

The clear correlation between glass forming and phase diagrams has been observed in studied system. The glass melting temperature and level of glass formation depending on the cooling rate of the studied melts are in good conformity with boundary curves and eutectic points (Fig.2 and 8). It is possible to ascertain confidently, that glass formation can serve as the rapid test method for phase diagram construction.

Common regularities of bulk glass samples TEC changes in studied BaO-TiO<sub>2</sub>-B<sub>2</sub>O<sub>3</sub> system have been determined: increase of BaO amounts leads to increase glasses TEC values from 60 to 120 · 10<sup>-7</sup>K<sup>-1</sup>. The substitution of B<sub>2</sub>O<sub>3</sub> for TiO<sub>2</sub> practically doesn't influence glasses TEC value (Fig.4).

We have tried also to answer in discussion among various scientific groups about the existence of 2Ba2TB and 3Ba3TB compounds [Millet et al., 1986; Zhang et al., 2003; Park et al, 2004; Kosaka et al., 2005]. We have revealed for the first time through glass samples of stoichiometric 3Ba3TB composition examination, that 3Ba3TB compound is very stable in an interval of 600-950°C. It decomposes in temperature interval 950-1020°C with BaTiO<sub>3</sub> and BaTB phase formation. Then, at temperature higher than 1020°C, it has incongruent melting with melt and BaTiO<sub>3</sub> formation (Fig.5A).

The next unexpected result was obtained at glass samples corresponding to 2Ba2TB composition crystallization. First of all we have revealed on its DTA curve the presence of three exothermic effects with maximums at 640, 660 and 690°C. We have confirmed the existents of 2Ba2TB compound in temperature interval 600-670°C. Its new X-ray powder diffraction patterns could be indexed on a orthorhombic crystal symmetry with lattice cell as follows : a=9.0404 Å, b=15.1929 Å, c=9.8145 Å; unit cell volume V=1348.02Å<sup>3</sup>, Z =6, calculated density (D calc.)= 3.99g/cm<sup>3</sup>; D exp.= 3.25 g/cm<sup>3</sup>; α;β;γ =90,00°(Table 2). However, its X-ray characteristics don't coincide with earlier reported data [Millet et al., 1986].

As a result of the pseudo-binary BaB<sub>2</sub>O<sub>4</sub>-BaTiO<sub>3</sub> system reinvestigation, a new ternary Ba<sub>2</sub>TiB<sub>2</sub>O<sub>7</sub> compound has been revealed and characterized at the same composition glass crystallization in the temperature interval of 570-650°C. The X-ray powder diffraction patterns of 2BaBT could be indexed on a rhombic crystal symmetry with lattice cell as follows : a=10.068 Å, b=13.911 Å, c=15.441 Å; unit cell volume V=2629.17Å<sup>3</sup>, Z =12, calculated density (D calc.)= 4.23g/cm<sup>3</sup>; D exp.=4.02 g/cm<sup>3</sup> ; α;β;γ =90,00°. X-ray characteristics of both 2Ba2TB and 2BaTB compounds were determined and are given in Tables 2 and 3.

Study of the directed crystallization processes have allowed to reveal, that at the given way of casting the oriented germs are induced in the glass tape, which at the further heat treatment results in oriented transparent and opaque GC formation (Fig.9). The impact of external electric field changes the direction of crystalline BaTiB<sub>2</sub>O<sub>6</sub> phase growth, i.e. reorients them (Fig.9).

Electric field induced polarization (P) and remanent polarization(P<sub>r</sub>) were measured at room temperature for BaBT, 3Ba3TiB, 2Ba2TiB, 2BaTiB glass tape samples crystallized at various regimes. All tested samples are ferroelectrics and shown loop of hysteresis.

Linear P-E curves are observed up to fields of 40-120 kV/cm for all measured samples with thickness 0.04-0.08mm. The polarization becomes nonlinear with an increase of applied electric

field, and at 140-400 kV/cm the remanent polarization  $2P_r$  values were found 0.35, 3.89, 0.08 and 0.12  $\mu\text{C}/\text{cm}^2$  for the BaBT (Fig.14, A),  $3\text{Ba}_3\text{TiB}$  (Fig.14, B),  $2\text{Ba}_2\text{TiB}$  (Fig.14, C) and  $2\text{BaTiB}$  (Fig.14, D) crystallized glass tape samples respectively. According to obtained results it is possible to conclude that samples are ferroelectrics. The  $3\text{Ba}_3\text{TiB}$  crystallized glass tape sample (Fig.14, B) has the highest remanent polarization value ( $2P_r=3.89 \mu\text{C}/\text{cm}^2$ ).

Studies of crystallization processes of barium di-titanate compositions glass tapes also have led to unexpected results. As far as it is difficult to receive this composition in glassy state as appeared so difficultly to crystallized it. All time we obtained transparent glass ceramics, which has residual polarization equal to  $6,2 \mu\text{Cu}/\text{cm}^2$  comes nearer to barium di-titanate single crystal ( $6,8 \mu\text{Cu}/\text{cm}^2$  [Akishige et al., 2006]). For comparison the value of residual polarization of known barium titanate is equal to  $25\mu\text{Cu}/\text{cm}^2$ . However, the barium di-titanate has  $T_c=470^\circ\text{C}$  [Akishige et al., 2006] as for BaT its value equal to  $124^\circ\text{C}$ .

## 6. Conclusion

The earlier published phase and glass forming diagrams of the ternary  $\text{BaO-TiO}_2\text{-B}_2\text{O}_3$  system have been revised and reconstructed. Seven ternary eutectics have been determined in it. Existence of three ternary  $\text{Ba}_2\text{TiB}_2\text{O}_7$ ,  $\text{Ba}_2\text{Ti}_2\text{B}_2\text{O}_9$  and  $\text{Ba}_3\text{Ti}_3\text{B}_2\text{O}_{12}$  incongruently melted compounds have been confirmed at the same glass compositions crystallization, temperatures borders of their existence and their X-ray characteristics have been determined.

The new  $\text{Ba}_2\text{TiB}_2\text{O}_7$  and  $\text{Ba}_2\text{Ti}_2\text{B}_2\text{O}_9$  compounds have been characterized. The X-ray powder diffraction patterns of  $\text{Ba}_2\text{TiB}_2\text{O}_7$  could be indexed on a rhombic crystal symmetry with lattice cell as follows:  $a=10.068 \text{ \AA}$ ,  $b=13.911 \text{ \AA}$ ,  $c=15.441 \text{ \AA}$ ; unit cell volume  $V=2629.17\text{\AA}^3$ ,  $Z=12$ , calculated density ( $D_{\text{calc.}}$ )=  $4.23\text{g}/\text{cm}^3$ ;  $D_{\text{exp.}}=4.02\text{g}/\text{cm}^3$ ;  $\alpha;\beta;\gamma=90,00^\circ$ . It is stable in temperature interval  $570\text{-}650^\circ\text{C}$ . The  $\text{Ba}_2\text{Ti}_2\text{B}_2\text{O}_9$  X-ray powder diffraction patterns could be indexed on a orthorhombic crystal symmetry with lattice cell as follows  $a=9.0404 \text{ \AA}$ ,  $b=15.1929 \text{ \AA}$ ,  $c=9.81455 \text{ \AA}$ ; unit cell volume  $V=1348.02\text{\AA}^3$ ,  $Z=6$ , calculated density ( $D_{\text{calc.}}$ )=  $3.99\text{g}/\text{cm}^3$ ;  $D_{\text{exp.}}=3.25\text{g}/\text{cm}^3$ ;  $\alpha;\beta;\gamma=90,00^\circ$ . It is stable in temperature interval  $600\text{-}670^\circ\text{C}$ . The  $\text{Ba}_3\text{Ti}_3\text{B}_2\text{O}_{12}$  is very stable compound in temperature interval  $600\text{-}900^\circ\text{C}$ .

The influence of various methods of melts casting on glass forming ability in the ternary  $\text{BaO-TiO}_2\text{-B}_2\text{O}_3$  system is investigated. The expanded glass formation area changes from stable glass forming barium tetra borate up to binary di-barium borate and up to barium di-titanate. Clear correlation between glass forming ability and eutectic areas have been revealed in investigated system.

Common regularities of bulk glass samples TEC changes in studied  $\text{BaO-TiO}_2\text{-B}_2\text{O}_3$  system have been determined: increasing of BaO amounts leads to increase glasses TEC values from 60 to  $120 \cdot 10^{-7}\text{K}^{-1}$ . The substitution of  $\text{B}_2\text{O}_3$  for  $\text{TiO}_2$  practically don't influence on glasses TEC value.

All synthesized tapes glass ceramics are ferroelectrics. The transparent barium di-titanate glass ceramics has high residual polarization value equal to  $6,2 \mu\text{Cu}/\text{cm}^2$ .

## 7. Acknowledgement

This work was supported by the International Science and Technology Center (Projects # A-952 & A-1486).

## 8. References

- Akishige, Y., Shigematsu, H., Tojo, T., Kawaji, H & Atake, T. (2006). Thermal properties on single crystals of ferroelectric barium dititanate. *Ferroelectrics*, Vol.336, pp. (47-56). The American Ceramic Society & National Institute of Standards and Technology [ACerS & NIST]. (2004). Phase Equilibria Diagrams. CD-ROM Database, Version 3.0, ISBN: 1-57498-215-X.
- Bayer, G. (1971). Thermal Expansion Anisotropy of Dolomite-type Borates  $Me^{2+}Me^{4+}B_2O_6$ . *Zeitschrift Fur Kristallographie*. Vol.133, pp. (85-90).
- Bhargava A., Snyder R.L., Condrate R.A. (1987). The Raman and infrared spectra of the glasses in the system BaO-TiO<sub>2</sub>-B<sub>2</sub>O<sub>3</sub>. *Mater.Res.Bull.*, vol. 22, No. 12, pp. (1603-1611).
- Bhargava, A., Snyder, R.L. & Condrate, R.A. (1988). Preparation of BaTiO<sub>3</sub> glass-ceramics in the system Ba-Ti-B-O. I. *Materials Letter*, Vol.7. No. 5-6, pp. (185-189).
- Bhargava A., Snyder, R.L. & Condrate, R.A. (1988). Preparation of BaTiO<sub>3</sub> glass-ceramics in the system Ba-Ti-B-O. II. *Materials Letter*, Vol.7. No. 5-6, pp. (190-196).
- Bhargava, A., Shelby, J.E. & Snyder, R.L. (1988). Crystallization of glasses in the system BaO-TiO<sub>2</sub>-B<sub>2</sub>O<sub>3</sub>. *J. Non-Cryst. Solids*, Vol.102, pp. (136-142).
- Boroica, L. et al. (2004). Study of titanates formed by crystallization in BaO-TiO<sub>2</sub>-B<sub>2</sub>O<sub>3</sub> system. Proceedings of the XX ICG in Kyoto, Sep. 27th-Oct 1st, 2004, PDF file No O-08-014, ISBN: 4-931298-43-5 C3858.
- Brow, R.K. & Watkins, R.D. (1987). In: *Technology of Glass, Ceramics or Glass Ceramics to Metal Sealing*, edited by Moddeman W.E. et al., Proceedings of the Winter Annual Meeting of Amer. Soc. Mech. Eng., Boston, MA, 1987, pp. (25-30).
- Cerchez, M., Boroica, L. & Huelsenberg, D. (2000). Glasses and crystallised glasses in the BaO-TiO<sub>2</sub>-B<sub>2</sub>O<sub>3</sub> system. *Phys. Chem. Glasses*, Vol.41, No. 5, pp. (233-235).
- Chen, C. & Liu, G. (1986). Recent Advances in Nonlinear Optical and Electro-Optical Materials. *Annual Review of Materials Science*, Vol.16, pp. (203-243).
- Damjanovic, D. (2005). Hysteresis in Piezoelectric and Ferroelectric Materials, In: *The Science of Hysteresis*, Mayergoyz, I & Bertotti, G., Vol. 3, pp.(337-465), Elsevier, ISBN: 0-1248-0874-3.
- De Pablos A. & Duran A. (1993). Glass forming and properties in the system B<sub>2</sub>O<sub>3</sub>-TiO<sub>2</sub>-MnOm (M= Li, Ba, Pb). Proceedings of the 2nd Intern. Conf. Fundamentals of Glass Science and Technology, Venice, 1993, pp. (363-368).
- Feitosa, C.A.C., Mastelaro, V.R., Zanatta, A.R., Hernandez A.C. & Zanotto, E.D. (2006). Crystallization, texture and second harmonic generation in TiO<sub>2</sub>-BaO-B<sub>2</sub>O<sub>3</sub> glasses. *Optical Mater.*, Vol.28, No. 8-9, pp.935-943.
- Goto, Y. & Cross, L.E. (1969). Phase Diagram of the BaTiO<sub>3</sub>-BaB<sub>2</sub>O<sub>4</sub> system and growth of BaTiO<sub>3</sub> crystals in the Melt. *Yogyo-Kyokai-shi*, Vol. 77, pp. ( 355-356).
- Hovhannisyanyan, R.M. (2004). BaB<sub>2</sub>O<sub>4</sub>, BaAl<sub>2</sub>B<sub>2</sub>O<sub>7</sub>, BaTi(BO<sub>3</sub>)<sub>2</sub>: glasses and glass ceramics on their basis. Proceedings of the XX ICG in Kyoto, Sep. 27th-Oct 1st, 2004, PDF file No O-07-056, ISBN: 4-931298-43-5 C3858.
- Hovhannisyanyan, R.M. (2006). Binary alkaline-earth borates: phase diagrams correction and low thermal expansion of crystallized stoichiometric glass compositions. *Phys.Chem.Glasses: Eur. J.Glass Sci. Technol. B*, Vol. 47, No. 4, pp. (460-465).
- Hovhannisyanyan, R.M. et al. (2008). Mutual influence of barium borates, titanates and borontitanates on phase diagram and glass formation in the BaO-TiO<sub>2</sub>-B<sub>2</sub>O<sub>3</sub> system. *Phys.Chem.Glasses: Eur. J.Glass Sci. Technol. B*, Vol. 49, No. 2, pp. (63-67).
- Hovhannisyanyan, M.R. et al. (2009). A study of the phase and glass forming diagrams of the BaO-Bi<sub>2</sub>O<sub>3</sub>-B<sub>2</sub>O<sub>3</sub> system. *Phys. Chem.Glasses: Eur. J.Glass Sci. Technol. B*, Vol.50, No. 6, pp. (323-328).

- Hubner, K.-H. (1969). Ueber die Borate  $2\text{BaO} \cdot 5\text{B}_2\text{O}_3$ , tief- $\text{BaO} \cdot \text{B}_2\text{O}_3$ ,  $2\text{BaO} \cdot \text{B}_2\text{O}_3$  und  $4\text{BaO} \cdot \text{B}_2\text{O}_3$ . *Neues Jahrb. Mineral., Monatsch.*, pp. (335-343).
- International Center for Diffraction Data [ICDD]. (2008). Powder Diffraction Fails, PDF-2 release database, Pennsylvania, USA, ISSN 1084-3116.
- Imaoka M. & Yamazaki T. (1957). Glass formation range borate systems between a-group elements. *Rep. Inst. Ind. Sci. Univ. Tokyo*, Vol. 6, No. 4, pp. (127-183).
- Kong, L.B., Li, S., Zhang, T.S., Zhai, J.W., Boey, F.Y.C. & Ma, J. (2010). Electrically tunable dielectric materials and strategies to improve their performances. *Progress in Materials Science*, Vol. 55, No. 8, pp. (840-893).
- Kosaka, S. et al. (2005). Synthesis and nonlinear optical properties of  $\text{BaTi}(\text{BO}_3)_2$  and  $\text{Ba}_3\text{Ti}_3\text{O}_6(\text{BO}_3)_2$  crystals in glasses with high  $\text{TiO}_2$  contents. *J. Solid State Chem.*, Vol.178, pp. (2067–2076).
- Kusumoto K. & Sekiya T. (1994). Preparation of barium titanate particles by glass crystallization method. *Rep. Governm. Ind. Res. Inst. Nagoya*, Vol. 43, No. 4-5, pp. (156-162).
- Levin, E.M. & McMurdie, H.F. (1949). The System  $\text{BaO}-\text{B}_2\text{O}_3$ . *J. Res. Nat. Bur. Standards*, Vol. 42, pp. (131-138).
- Levin, E.M. & Ugrinic, G.M. (1953). The System Barium Oxide-Boric Oxide- Silica. *J. Res. Nat. Bur. Standards*, Vol. 51, pp. (37-56).
- Matveev M.A., Khodskii L.G., Fisyuk G.K., Bolutenko A.I. & Strugach L.S. (1966). Some properties of glasses on the base of the systems  $\text{BaO}-\text{TiO}_2-\text{B}_2\text{O}_3$ ,  $\text{BaO}-\text{TiO}_2-\text{P}_2\text{O}_5$  and  $\text{BaO}-\text{TiO}_2-\text{SiO}_2$ . *Neorg.Mater.*, Vol. 2, No. 6, pp. (1119-1123).
- Millet, J.M., Roth, R.S. & Parker H.S. (1986). Phase relation between polytitanates of barium and the barium borates, vanadates, and molybdates. *J. Am.Ceram. Soc.*, Vol. 69, No.11, pp. (811-814).
- O'Bryan, H.M. & Thomson, J. (1974). Phase equilibria in the  $\text{TiO}_2$  – rich region of the system  $\text{BaO}-\text{TiO}_2$ . *J. Am.Ceram. Soc.*, Vol. 57, No. 12, pp. (522-526).
- Park, H., Bakhtiarov, A., Zhang, W., Vargas-Baca, I. & Barbier, J. (2004). Non-centrosymmetric  $\text{Ba}_3\text{Ti}_3\text{O}_6(\text{BO}_3)_2$ . *J. Solid State Chem.*, Vol. 177, pp. (159-164).
- Pavlikov, V.N., Yurchenko, V.F. & Tresvyatskiy, S.G. (1976). The  $\text{B}_2\text{O}_3-\text{TiO}_2$  system. *Zh. Neorg. Khim.*, Vol. 21, pp. (233-236).
- Pernice, P., Esposito, S. & Aronne, A. (1998). Structure and nonisothermal crystallization of glasses in the  $\text{BaO}-\text{TiO}_2-\text{B}_2\text{O}_3$  system. *Phys. Chem. Glasses*, Vol. 39, No. 4, pp. (222-227).
- Rase, D.E. & Roy, R. J. (1955). Phase equilibria in the system  $\text{BaO}-\text{TiO}_2$ . *J. Am.Ceram. Soc.*, Vol. 38, No. 3, pp. (102-113).
- Sawyer, C.B. & Tower, C. H. (1930). Rochelle Salt as a Dielectric. *Phys. Rev.*, Vol. 35, No.3, pp. (269 -273).
- Schmid H. (1964). X-ray evidence for  $\text{CrCO}_3$ ,  $\text{VBO}_3$  and  $\text{TiBO}_3$  with calcite structure. *Acta Cryst.*, Vol. 17, pp. (1080-1081).
- Sholokhovich, V.L. & Varicheva, V.I. (1958). The system  $\text{PbO}-\text{BaO}-\text{B}_2\text{O}_3-\text{TiO}_2$  study. *Izv. Akad. Nauk SSSR, Ser. Fiz.*, Vol. 22, pp. (1449-1452).
- Vicat, J. & Aleonard, S. (1968). Etude de borates  $\text{MeMe}^1(\text{BO}_3)_2$  de structure dolomite. *Materials Research Bulletin*, Vol.3, pp. (611-620).
- Waghmare, U., Sluiter, M. H.F., Kimura, T., Goto, T. & Kawazoe, Y. (2004). A lead-free high-TC ferroelectric  $\text{BaTi}_2\text{O}_5$ : a first-principles study, *Applied Physics Letter*, Vol. 84, No. 24, pp.(4917-4919).
- Wakino, K., Nishikawa, T., Ishikawa, Y. & Tamura, T. (1990). Dielectric resonator materials and their applications for mobile communication system. *Br. Ceram. Trans.*, Vol. 89, pp. (39-43).

# Ferroelectric Properties and Polarization Switching Kinetic of Poly (vinylidene fluoride-trifluoroethylene) Copolymer

Duo Mao, Bruce E. Gnade and Manuel A. Quevedo-Lopez  
*Department of Material Science and Engineering, The University of Texas at Dallas  
USA*

## 1. Introduction

The discovery of the piezoelectric properties of poly(vinylidene fluoride) (PVDF) by Kawai [Kawai, 1969], and the study of its pyroelectric and nonlinear optical properties [Bergman et al., 1971; Glass, 1971] led to the discovery of its ferroelectric properties in the early 1970s. Since that time, considerable development and progress have been made on both materials and devices based on PVDF. This work helped establish the field of ferroelectric polymer science and engineering [Nalwa, 1995a]. There are many novel ferroelectric polymers, such as poly(vinylidene fluoride) (PVDF) copolymers, poly(vinylidene cyanide) copolymers, odd-numbered nylons, polyureas, ferroelectric liquid crystal polymers and polymer composites of organic and inorganic piezoelectric ceramics [Nalwa, 1991 and Kepler & Anderson, 1992 as cited in Nalwa, 1995b; Nalwa, 1995a]. Among them, PVDF, and its copolymers are the most developed and promising ferroelectric polymers because of their high spontaneous polarization and chemical stability.

Ferroelectricity is caused by the dipoles in crystalline or polycrystalline materials that spontaneously polarize and align with an external electric field. The polarization of the dipoles can be switched to the opposite direction with the reversal of the electric field. Similar to inorganic ferroelectric materials such as  $\text{PbZr}_{0.5}\text{Ti}_{0.5}\text{O}_3$  (PZT) and  $\text{SrBi}_2\text{Ta}_2\text{O}_9$  (SBT), organic ferroelectric materials exhibit ferroelectric characteristics such as Curie temperature (the transition temperature from ferroelectrics to paraelectrics), coercive field (the minimum electric field to reverse the spontaneous polarization) and remanent polarization (the restored polarization after removing the electric field). However, the low temperature and low fabrication cost of organic ferroelectric materials enable them to be used in a large number of applications, such as flexible electronics.

In this chapter, the discussion is focused on poly(vinylidene fluoride-trifluoroethylene) [P(VDF-TrFE)], one of the most promising PVDF ferroelectric copolymers. The main objective of this chapter is to describe the ferroelectric properties of P(VDF-TrFE) copolymer and review the current research status of ferroelectric devices based on this material. The chapter is divided in six sections. The first section introduces the topic of organic ferroelectrics. The second section describes the material properties of the ferroelectric phase of P(VDF-TrFE) including phase structures, surface morphology, crystallinity and molecule chain orientation. Next, the electrical properties such as polarization, switching current, etc.

are discussed. In section four, the fundamental ferroelectric polarization switching mechanisms are introduced and the models for P(VDF-TrFE) thin films are reviewed. The nucleation-limited-switching (NLS) model, based on region-to-region switching kinetics for P(VDF-TrFE) thin film will be emphasized. The fifth section reviews the impact of annealing temperature, film thickness and contact dependence for P(VDF-TrFE) based ferroelectric capacitors. Finally, the most important results from this chapter will be summarized, and one of the P(VDF-TrFE) copolymer's potential applications as flexible non-volatile ferroelectric random access memory will be briefly discussed.

## 2. Material properties of P (VDF-TrFE) copolymer

P(VDF-TrFE) is a random copolymer synthesized using two homopolymers, PVDF and poly(trifluoroethylene) (PTrFE). The chemical formula is shown in Figure 1. PVDF is a crystalline polymer, has a monomer unit of  $-\text{CH}_2-\text{CF}_2-$ , in between polyethylene (PE) ( $-\text{CH}_2-\text{CH}_2-$ ) and polytetrafluoroethylene (PTFE) ( $-\text{CF}_2-\text{CF}_2-$ ) monomers. The similarity of PVDF to these two polymers gives rise to its physical strength, flexibility and chemical stability [Tashiro, 1995]. Its ferroelectric properties originate from the large difference in electronegativity between fluorine, carbon and hydrogen, which have Pauling's values of 4.0, 2.5 and 2.1, respectively [Pauling, 1960]. Most of the electrons are attracted to the fluorine side of the polymer chain and polarization is created [Salimi & Yousefi, 2004; Fujisaki et al., 2007]. The Curie temperature of PVDF is estimated to be above the melting temperature at 195-197 °C [Lovinger, 1986, as cited in Kepler, 1995]. The melting of the ferroelectric phase and recrystallization to the paraelectric phase may happen in the same temperature range. The addition of TrFE ( $-\text{CF}_2-\text{CFH}-$ ) into the PVDF system plays an important role in the phase transition behavior. TrFE modifies the PVDF crystal structure by increasing the unit cell size and inter-planar distance of the ferroelectric phase, as seen from X-ray diffraction measurements [Tashiro et al., 1984; Lovinger et al., 1983a, 1983b, as cited in Tashiro, 1995]. The interactions between each unit and between dipole-to-dipole are reduced, resulting in a lower Curie temperature. Therefore, it allows the copolymer to crystallize into the ferroelectric phase at temperatures below the melting point. The copolymer crystal structure, phase transition behavior and ferroelectric properties are affected by the ratio of VDF/TrFE content and the synthesizing conditions [Yamada & Kitayama, 1981]. The experimental data from UT Dallas shown in this chapter are for P(VDF-TrFE) copolymer with 70/30 (VDF/TrFE), synthesized using a suspension polymerization process. The ferroelectric properties are measured and tested at room temperature, except if stated otherwise.

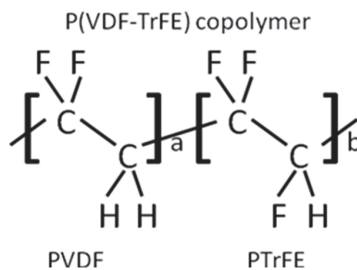


Fig. 1. The chemical formula of P(VDF-TrFE) random copolymer [Naber et al., 2005].

## 2.1 Phase structures

When the P(VDF-TrFE) copolymer chains are packed and form a solid material, there are four types of crystalline phases. The phase configurations are very similar to PVDF, including phase I ( $\beta$ ), phase II ( $\alpha$ ), phase III ( $\gamma$ ), and phase IV ( $\delta$ ) [Xu et al., 2000]. Among these four phases, only the  $\beta$  phase is the polar phase with a large spontaneous polarization along the b axis which is parallel to the C-F dipole moment, and perpendicular to the polymer chain direction (c axis) [Hu et al., 2009.]

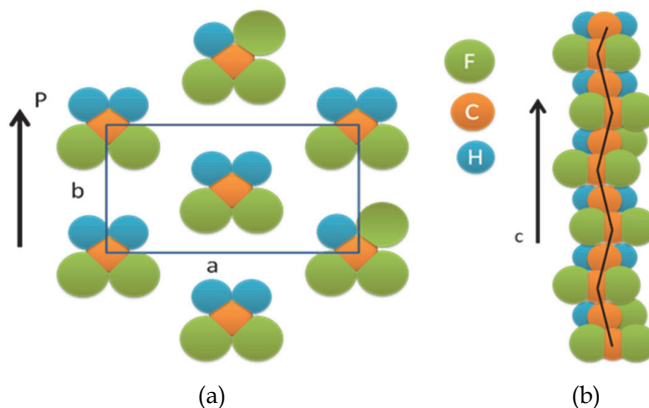


Fig. 2. (a) The schematic of the  $\beta$  phase crystal structure for P(VDF-TrFE) copolymer in the  $ab$  plane (the  $c$  axis is normal to the  $ab$  plane), and (b) along the  $c$  axis of the all-trans (TTTT) zigzag planar configuration from the top view.

The schematic of the  $\beta$  phase crystal structure is shown in Figure 2. The molecules are in a distorted, all-trans (TTTT) zigzag planar configuration. When the polymer is cooled from its melt state, it crystallizes into the  $\alpha$  phase. This crystal is nonpolar with the molecules in a distorted trans-gauche-trans-gauche' (TGIG') configuration, which is the state with the lowest energy. In the  $\gamma$  phase, the crystal has polar unit cells with molecules in the  $T_3GT_3G'$  configuration, and the dipole moment is smaller than phase I ( $\beta$ ). For the  $\delta$  phase, the crystal has the same configuration as the  $\alpha$  phase, but with a different orientation of the molecules' dipole moments in the unit cell [Kepler, 1995]. Different phases can be achieved by using different processing conditions. The material can transition between phases by using annealing, stretching and poling methods [Tashiro et al., 1981, as cited in Tashiro 1995]. In this chapter, the discussion is focused on the polar  $\beta$  phase.

## 2.2 Surface morphology of $\beta$ phase crystals

The mechanics and aggregation characteristics of the polymeric chains can be different when forming each crystalline phases, resulting in different surface morphologies. This can be studied using atomic force microscopy (AFM). Figure 3 shows a 3D  $1\mu\text{m}\times 1\mu\text{m}$  AFM image of a typical P(VDF-TrFE) film. The rod-like shape of the grains is attributed to the  $\beta$  phase crystallites. The size of the grains and the roughness of the surface are related to the annealing conditions and are sensitive to the maximum processing temperature [Park et al., 2006; Mao et al., 2010a]. The sample shown in Figure 3 corresponds to a 210 nm spin coated film annealed at 144 °C for 2 hours in vacuum. The length of the grains is approximately 180 nm with a surface RMS roughness of 14.6 nm [Mao et al., 2010a].

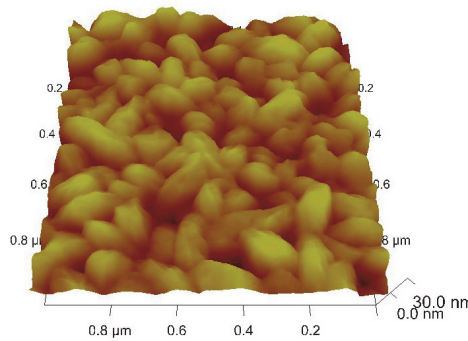


Fig. 3. AFM tapping mode height image of a 210 nm P(VDF-TrFE) film annealed at 144 °C for 2 hours in vacuum.

### 2.3 X-ray analysis for $\beta$ phase crystals

X-ray Diffraction (XRD) can be used to study the crystalline characteristics. The diffraction angle corresponds to the inter-planar spacing and orientation of the crystal planes, and the diffraction intensity indicates the quantity of the corresponding crystal planes, which relates to the degree of crystallinity. The crystal structure of P(VDF-TrFE) is normally related to the composition (mole ratio of VDF/TrFE) of the copolymer and the annealing process. In the  $\beta$  crystal phase of P(VDF-TrFE), the unit cell is orthorhombic, with each chain aligned and packed with the  $\text{CF}_2$  groups parallel to the  $b$  axis [Lando et al, 1966; Gal'perin & Kosmyrin, 1969; Hasegawa et al, 1972, as cited in Tashiro, 1995], as indicated in Figure 2 (a). Figure 4 shows the XRD results from a 210 nm P(VDF-TrFE) (VDF/TrFE of 70/30) film annealed at 144 °C and measured at room temperature. The diffraction peak at  $2\theta=19.9^\circ$  is attributed to the (110) and (200) orientation planes, which are associated with the polar  $\beta$  phase. From the position of this sharp peak, the inter-planar spacing  $b$  is determined to be 4.5 Å [Mao et al, 2010a]. The strong diffraction peak indicates a high degree of crystallinity in the  $\beta$  phase.

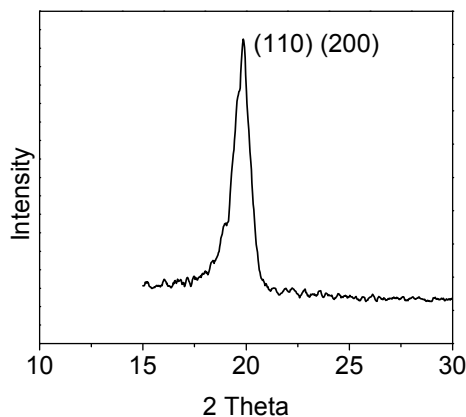


Fig. 4. XRD results for 210 nm  $\beta$  phase P(VDF-TrFE) (VDF/TrFE of 70/30) film annealed at 144 °C and measured at room temperature

## 2.4 Vibrational analysis for $\beta$ phase crystals

Molecular vibration analysis is a key to understanding the dynamics of a material. Fourier-transform infrared spectroscopy (FT-IR) can be used to detect the vibrational mechanics of a material system by monitoring the absorption of infrared energy. The incident electromagnetic field from the IR source interacts with the molecular bonding of the P(VDF-TrFE) film, resulting in a large absorption when the molecular vibration and the electric field component of the IR are perpendicular to each other. Each phase of the P(VDF-TrFE) polymer will provide a characteristic FT-IR spectrum. Details of the absorption band assignments can be found in the literature [Kobayashi et al, 1974; Reynolds et al, 1989; Kim et al, 1989]. Here we only discuss the three intense bands,  $1288\text{ cm}^{-1}$ ,  $850\text{ cm}^{-1}$ , and  $1400\text{ cm}^{-1}$  associated with the  $\beta$  phase of P(VDF-TrFE). The  $1288\text{ cm}^{-1}$  and  $850\text{ cm}^{-1}$  bands belong to the  $\text{CF}_2$  symmetric stretching with the dipole moments parallel to the polar  $b$  axis [Reynolds et al, 1989]. The  $1400\text{ cm}^{-1}$  band is assigned to the  $\text{CH}_2$  wagging vibration, with the dipole moment along the  $c$  axis. As illustrated in Figure 5 [Mao et al, 2010], a polarized IR source with the electrical component parallel to the substrate ( $p$ -polarized) is used to measure two P(VDF-TrFE) thin film samples. The strong absorption bands at  $1288\text{ cm}^{-1}$  and  $850\text{ cm}^{-1}$  in spectrum A (sample A) indicates that the polar  $b$  axis of the P(VDF-TrFE) copolymer chain is perpendicular to the substrate and the planar zigzag chains are aligned parallel to the substrate [Hu et al, 2009]. However, in spectrum B (sample B), weak absorption bands observed at  $1288\text{ cm}^{-1}$  and  $850\text{ cm}^{-1}$  indicate that the  $b$  axis is tilted away from the direction normal to the substrate. Additionally, the strong absorption band at  $1400\text{ cm}^{-1}$  band indicates the polymer chain ( $c$  axis) is tilted, and a significant number of the molecules are aligned normal to the substrate, which is undesirable for vertical polarization [Park et al, 2006; Mao et al, 2010a].

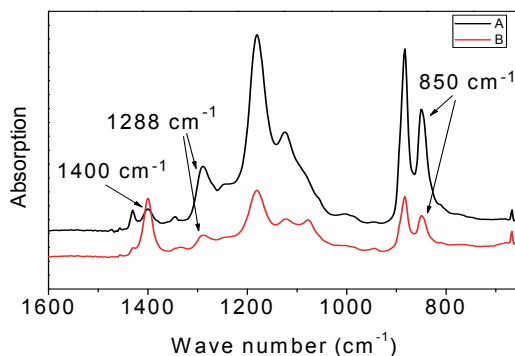


Fig. 5. FT-IR analysis of the  $\beta$  phase of P(VDF-TrFE) polymer films (A and B) with different polymer chain alignment characteristics. In sample A, the polymer chains are aligned parallel to the substrate, and in sample B, the polymer chains are tilted and some portions are aligned perpendicular to the substrate.

## 3. Electrical properties of P(VDF-TrFE) film

The fabrication of the polymer films into devices and the electrical characterization of the ferroelectric properties are introduced here. The discussion focuses on ferroelectric capacitors (FeCap), which is the fundamental device for studying this material.

### 3.1 Deposition of P(VDF-TrFE) films

There are two common methods to prepare P(VDF-TrFE) thin films. The first one is the melt and press method [Yamada & Kitayama, 1981]. The copolymer crystallizes into  $\alpha$  or  $\gamma$  phases when it is slowly cooled to room temperature from the melt. The film has a high degree of crystallinity. Stretching or poling process is required to achieve the  $\beta$  phase crystals. For the melt and press fabrication process, the film thickness is usually  $> 1 \mu\text{m}$ . Spin coating from solution is another common fabrication method. By changing the weight percentage of the polymer in solution, spin coating can be used to produce films with thickness  $\leq 100 \text{ nm}$ . Different crystal phases can be achieved from polymer dissolved in different solvents. Spin coat from 2-butanone or cyclohexanone solutions allow the film to be crystallized into the  $\beta$  phase directly. Another method of making ultra thin film reported by A.V. Bune et al. [Bune et al., 1998] is Langmuir-Blodgett deposition, which results in films which are a few monolayers thick and can be switched at 1 V. After making the films, thermal annealing is always used to increase the degree of crystallinity. The annealing will be discussed in section 5.

### 3.2 Electrical characterization methods for polarization

The application of an electric field across the FeCap with an amplitude higher than the coercive field will reverse the polarity of the dipoles, and induce a switching current flow through the external closed loop. The total number of dipoles determines the electric displacements or polarization of the film. By integrating the switching current in the time domain, the total number of the switched dipoles or charges can be calculated. Two types of waveforms are commonly used to measure the polarization, the triangular wave for hysteresis loop characterization and a sequence of pulses for the standard Positive Up Negative Down (PUND) method [Kin et al, 2008; Mao et al., 2010b], as shown in figures 6 (a) and (b), respectively.

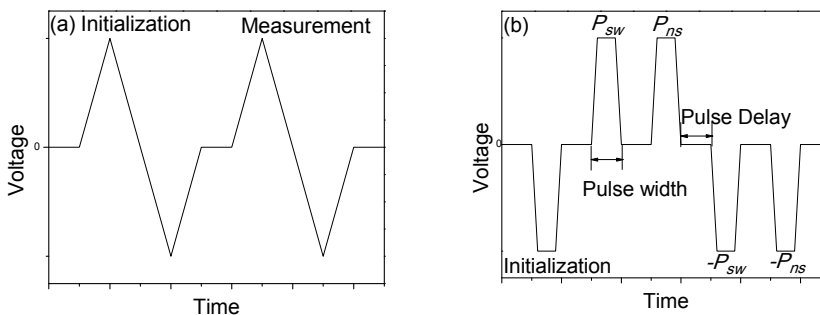


Fig. 6. The polarization measurement waveforms for (a) hysteresis loop and (b) PUND characterizations.

In the hysteresis loop measurement, the first triangular wave is used for initialization of the ferroelectric capacitor, followed by the second waveform for polarization measurement in both positive and negative directions. In the PUND measurement, switching polarization ( $P_{sw}$ ) and nonswitching polarization ( $P_{ns}$ ) are measured.  $P_{sw}$  corresponds to the current integration in the polarization switching transient, and  $P_{ns}$  corresponds to the current integration when the polarization has the same direction as the applied electric field. They are defined as [Mao et al., 2010b]

$$P_{sw} = P_s + P_r \quad (1)$$

$$P_{ns} = P_s - P_r \quad (2)$$

where  $P_s$  and  $P_r$  represent the spontaneous polarization and remanent polarization, respectively. The five sequential pulses represent initialization, measurement for  $P_{sw}$ ,  $P_{ns}$  in positive and negative directions, respectively.

### 3.3 Hysteresis loop measurement

The hysteresis loop is one of the most important tools to characterize ferroelectrics. A significant amount of information can be extracted from the hysteresis loop. Similar to other ferroelectrics, P(VDF-TrFE) copolymer exhibits remanent polarization. Figure 7 (a) shows the hysteresis loops measured at 1 Hz with different applied voltages for a FeCap with P(VDF-TrFE) film thickness of approximately 154 nm. As the voltage increases to 8 V, the FeCap starts to show hysteresis characteristics, and saturates at above 10 V.  $P_s$  and  $\pm P_r$  are plotted as a function of voltage in Figure 7 (b).  $P_s$  and  $P_r$  increase rapidly at voltage  $> 6$  V, and saturate at  $8.2 \mu\text{C}/\text{cm}^2$  and  $6.9 \mu\text{C}/\text{cm}^2$ , respectively. The coercive voltage ( $V_c$ ) is defined as the voltage when  $dP/dV$  reaches maximum, which is approximately 6.7 V, corresponding to a coercive field ( $E_c$ ) of 0.44 MV/cm.

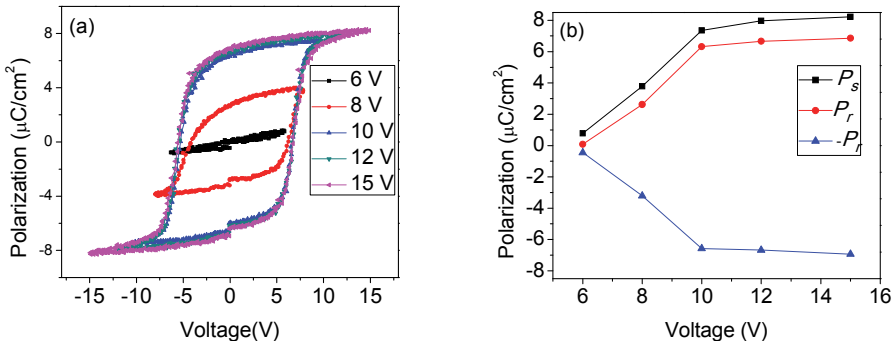


Fig. 7. (a) Hysteresis loops measured at different voltages for P(VDF-TrFE) FeCap, and (b)  $P_s$  and  $\pm P_r$  as a function of applied voltage.

### 3.4 PUND measurement

In the PUND method, a circuit is used to measure the currents in polarization switching and nonswitching transients, or measure the displacement and polarization of the FeCaps. In order to measure the polarization switching transient, we use a function generator to bias the FeCap, and measure the voltage across a linear resistor using an oscilloscope, as shown in Figure 8. The transient current can be calculated by dividing the voltage with the resistance.  $P_{sw}$  and  $P_{ns}$  can be calculated by integrating the current in the time domain.

Typical PUND measurement data from a P(VDF-TrFE) based FeCap (size of  $300\mu\text{m} \times 300\mu\text{m}$ ) are plotted in Figure 9. V1 and V2 represent the voltages measured from channel 1 and 2 of the oscilloscope, respectively. Rescaling V2 by  $1/R$  (1000 ohms in the measurement) gives the transient current. The 1<sup>st</sup>, 3<sup>rd</sup> and 5<sup>th</sup> pulses induce large responses, representing

the polarization switching of the dipoles, while the 2<sup>nd</sup>, 4<sup>th</sup>, and 6<sup>th</sup> pulses correspond to the nonswitching transient with small current responses, because the dipoles have already aligned in the same direction as the applied electric field. The sharp response for polarization switching indicates the fast rotation of the dipoles, and the large difference between the switching and nonswitching responses indicates a large remanent polarization.  $P_{sw}$  and  $P_{ns}$  are calculated from the transient switching current to be  $11.2 \mu\text{C}/\text{cm}^2$  and  $1.3 \mu\text{C}/\text{cm}^2$ , respectively. The switching current is a function of the applied electric field.

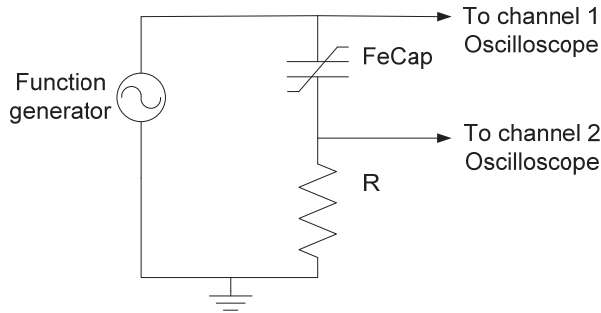


Fig. 8. The circuit schematic used to measure the currents in the switching and nonswitching transients using the PUND method.

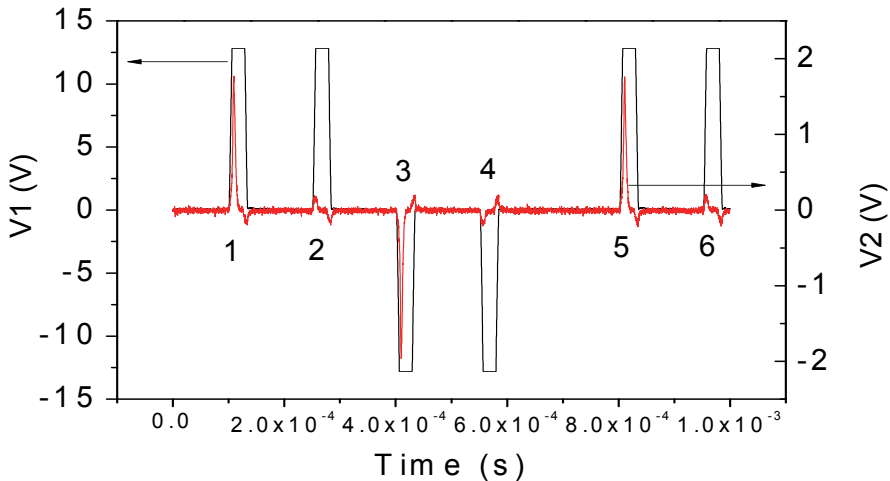


Fig. 9. The switching and nonswitching transient measurement of a P(VDF-TrFE) based FeCap using the PUND method.

### 3.5 Capacitance-voltage measurement

The nonlinearity of the dielectric response to electric field is also present in P(VDF-TrFE), as shown in Figure 10. An FeCap with P(VDF-TrFE) thickness of 154 nm is measured at 100

KHz. The dielectric permittivity is a function of  $dP/dV$ , which corresponds to the slope of the polarization-voltage plot. The dielectric constant is measured to be between 7.8 and 11, depending on the electric field [Mao et al., 2010a]. The peaks in the capacitance correspond to the polarization reversal of the dipoles, and the electric field for the peak capacitance corresponds to the coercive field [Lohse et al., 2001].

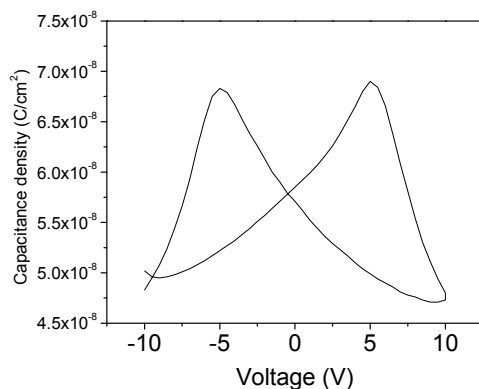


Fig. 10. The capacitance-voltage response of a 154 nm thick P(VDF-TrFE) based FeCap.

#### 4. Polarization switching kinetics of P(VDF-TrFE) thin films

Understanding the kinetics of polarization switching is important to the application of ferroelectric materials. The polarization dipole reversal mechanism of inorganic ferroelectric materials such as lead zirconate titanate (PZT) has been studied for many years. The switching kinetics in a single crystal ferroelectric is found to follow the classical model called the Kolmogorov-Avrami-Ishibashi (KAI) model [Lohse et al., 2001; Tagantsev et al, 2002]. The KAI model was developed by the group of Ishibashi, based on the statistical theory of Kolmogorov and Avrami (KA) [Kolmogorov, 1937; Avrami 1939; Avrami 1940; Avrami 1941, as cited in Lohse et al., 2001], which was originally developed for the modeling of the crystallization process in metals. However, for polycrystalline ferroelectric thin films, the switching kinetics were frequently found to disobey the KAI model [Lohse et al., 2001; Tagantsev et al, 2002]. In this section, the polarization switching mechanism and the KAI model will be briefly discussed, and correlated with a model based on region-by-region switching for P(VDF-TrFE) thin films [Tagantsev et al, 2002]. Some alternative models for P(VDF-TrFE) will also be briefly introduced.

##### 4.1 The polarization switching mechanism and KAI model

Ferroelectric polarization is defined as the electric dipole moment, or the displacement of charge density away from the center of the unit cell in the crystal lattice. The polarization direction can be switched by applying an electric field. The polarization switching process is commonly considered to be controlled by two mechanisms; domain nucleation and expansion [Merz, 1956; Kimura & Ohigashi, 1986]. The switching time is a function of the electric field, and for these two mechanisms, the switching time for each mechanism has a different dependence on the electric field. The domain nucleation process has an exponential relationship and can be expressed as [Merz, 1956]

$$\tau_0 = \tau_a e^{(E_0/E)^n} \quad (3)$$

where  $E_0$  is the activation field,  $\tau_a$  is the switching time at  $E = E_0$ , which corresponds to the fastest switching speed of the material, and  $n$  is a constant related to the dimension of the domain growth. For domain expansion, the reciprocal of  $1/\tau_0$  has a linear relationship as described in equation (4) [Merz, 1956];

$$\frac{1}{\tau_0} \sim \mu(E - E_1) \quad (4)$$

where  $\mu$  is the mobility of the domain expansion and  $E_1$  is a limiting electric field similar to a coercive field strength. The polarization switching of the ferroelectric is considered to be a combination of these two processes. Therefore, for a single crystal material, it exhibits a total switching time  $\tau_0$ , which is a function of applied electric field.

The KAI model describes the switching polarization phenomenon as initially being a uniform formation of the reversal nucleation centers, followed by the unrestricted expansion and overlapping of the domains throughout the sample. The volume of polarization can be mathematically expressed as [Lohse et al., 2001; Tagantsev et al, 2002];

$$p(t) = 1 - e^{-(t/\tau_0)^n} \quad (5)$$

where  $p(t)$  is the volume of the ferroelectric that has been switched in time  $t$ ,  $\tau_0$  is the switching time and  $n$  is a dimension constant. The electric displacement  $D$  can be expressed as [Tajitsu et al., 1987];

$$D = \epsilon E + P = \epsilon E + 2P_r(1 - e^{-(t/\tau_0)^n}) \quad (6)$$

where  $\epsilon$ ,  $E$ ,  $P$  and  $P_r$  are the linear dielectric permittivity, electric field, polarization and remanent polarization, respectively.

Due to the nature of polycrystalline ferroelectric thin films, the KAI assumptions are not always met. It was observed in many cases that the switching time increases and the distribution of the switching time broadens as the film thickness decreases [Lohse et al., 2001; Tagantsev et al, 2002]. In the P(VDF-TrFE) system, Tajitsu et al. proposed that the increase of switching time for thinner films correspond to the increase in the activation field, which is caused by the formation of a surface layer [Tajitsu, 1995]. Nakajima et al, found that the increase in the switching time happens for FeCaps with Al contacts, but for Au contact FeCaps, the switching time is independent with film thickness [Nakajima et al., 2005]. The film thickness and contact dependence of polarization switching will be discussed in section 5. To explain the broadening of the switching time distribution for P(VDF-TrFE) thin films, alternate methods have been proposed to model the polarization switching kinetics. They are introduced and discussed below.

#### 4.2 Region-by-region switching

The polarization switching process in a ferroelectric is affected by many factors, especially the nucleation rate of reversal domains, domain dimension, and the mobility of the domain wall [Tagantsev et al, 2002]. Different from single crystal materials, AFM and TEM studies

suggest that the switching process in thin films occur region-by-region [Colla et al., 1998; Ganpule et al. 2000; Kim et al., 2010]. The polarization switching process in one region does not necessarily expand through the neighboring regions and switch the whole film. Therefore, the switching of each region is independently determined by its own characteristics, such as nucleation rate and domain dimension. Based on this analysis, Tagantsev et al proposed a model called nucleation-limited-switching (NLS) for the polarization switching of a ferroelectric thin film [Tagantsev et al, 2002]. In this model, the assumption is that each region switches independently, and in each region, the switching process is dominated by the nucleation time of the first reversal domain. The switching of the whole system is controlled by the statistics of domain nucleation, instead of domain expansion in the KAI model.

For the P(VDF-TrFE) copolymer, polarization reversal originates from the rotation of the carbon-fluorine and carbon-hydrogen covalent bonding around the central chain of the polymer [Furukawa et al., 2006]. In thin film P(VDF-TrFE), the activation field for domain expansion is small (approximately 0.87 MV/cm) [Kim et al., 2010] compared to domain nucleation (approximately 7.8-12 MV/cm) [Tajitsu, 1995; Nakajima et al., 2005; Kusuma et al., 2010]. Therefore, the polarization switching dynamics are dominated by domain nucleation. Because of polycrystalline nature of thin films, they consist of many grains separated by grain boundaries. The NLS model better describes the switching process of this system. Therefore, it can be used to model the switching polarization as a function of time [Mao et al., 2010b].

In Figure 11,  $P_s$  is shown as a function of time for a FeCap with a P(VDF-TrFE) film thickness of 100 nm using the PUND method. The experimental data and the calculated response using the NLS model are plotted as symbols and solid lines, respectively. The polarization dispersion at a pulse width equal to 1 s (corresponding to  $\log(t) = 0$ ) is due to the high dc conductance of the devices caused by the increased dielectric leakage at high voltage and low frequencies [Nakajima et al., 2005]. These points are not included in the model calculation. The agreement between the experimental data and the model suggests the region-by-region polarization switching process in P(VDF-TrFE) system is a reasonable description.

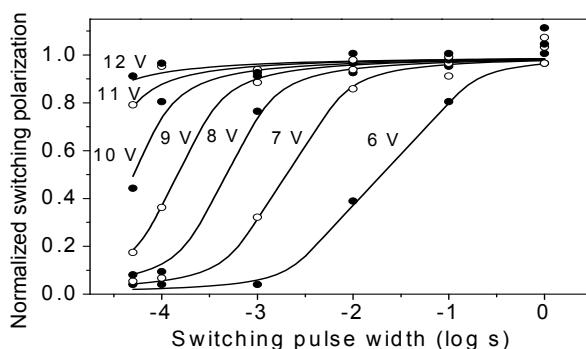


Fig. 11. The relationship of the normalized switching polarization and applied voltage pulse width in positive region. The symbols are experimental data and the lines are the calculated response using the NLS model. Reprinted from [Mao et al, 2010b] with permission.

Since the nucleation limited switching dynamic of P(VDF-TrFE) thin film dominate this switching polarization, the polarization switching time ( $\tau$ ) can be described as the delay time for domain nucleation, while the time for domain expansion can be neglected. The difference in domain dimensions, region sizes and especially the distribution of the nucleation centers and the nucleation rate of the reversal polarization among each region leads to a distribution of switching times throughout the film. For each region,  $\tau$  is a function of applied voltage, characterized by an individual activation voltage ( $V_0$ ). The dispersion of  $\tau$ , characterized by  $\tau_{\max}$  and  $\tau_{\min}$ , corresponding to the maximum and minimum  $V_0$  among all regions in the film can be extracted from the model and plotted as a function of applied voltage (symbols), as shown in Figure 12. The exponential relationship of  $\tau$  and applied voltage follows equation (3).  $\tau_{\max}$  is used to fit equation (3) (plotted as the solid line in Figure 12),  $\tau_0$  and  $E_0$  can be extracted as 5 ns and 9.6 MV/cm.

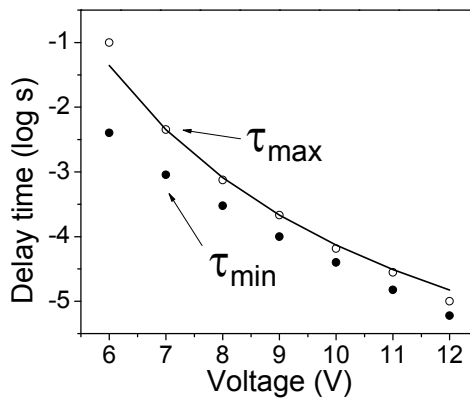


Fig. 12. Experimental  $\tau_{\max}$  and  $\tau_{\min}$  data from Figure 11 plotted as a function of applied voltage, and the fitting for  $\tau_{\max}$  in positive polarization region. Reprinted from [Mao et al, 2010b] with permission.

Figure 11 shows the switching dynamics ( $\pm P_{sw}$  versus time) for P(VDF-TrFE) with a distribution as long as three decades, compared to eight decades for the 135 nm Pb(Zr,Ti)O<sub>3</sub> system reported in the literature [Tagantsev et al, 2002]. The reduced range of switching dynamics in P(VDF-TrFE) films indicates a more uniform distribution of switching time, or activation field among the regions. One of the reasons could be the more uniform size of the regions and distribution of nucleation centers within the regions. Additionally, P(VDF-TrFE) has a much higher activation field of 9.6 MV/cm compared to Pb(Zr,Ti)O<sub>3</sub>, 0.77 MV/cm, therefore, the reversal polarization domain nucleation kinetics at room temperature for P(VDF-TrFE) are less dependent on thermal activation [Stolichnov et al., 2003; Mao et al., 2010b]

### 4.3 Surface roughness based model

As the film thickness decreases, the surface roughness becomes significant, resulting in a non-uniform electric field distribution. For the broadening of the switching time distribution, Nakajima et al proposed a model based on surface roughness [Nakajima et al., 2005]. The non-

uniform distribution of electric field on the ferroelectric thin film leads to different values of switching time on different regions, and causes the broadening of the switching time.

Using this method, the authors plotted the thickness distribution vs. average film thickness of four P(VDF-TrFE) samples (symbol) and fit the data with the Gaussian distribution function (line); as shown in Figure 13 (a). The electric field distribution across the film surface can be determined, which is correlated to the switching time using equation (3). The electric displacement  $D$  and polarization  $P$  can be calculated using equation (6). The calculated switching time distributions for different film thicknesses are plotted in Figure 13 (b) [Nakajima et al., 2005]. As seen for the 50 nm P(VDF-TrFE) films, the maximum amplitude of the surface roughness is approximately 20 nm, which causes a significant broadening of the switching time distribution, based on the model calculation shown in Figure 13 (b). Compared to the experimental results in Figure 19 (a) by the authors, the model predicts the correct trend, but the predicted distribution is slightly broader.

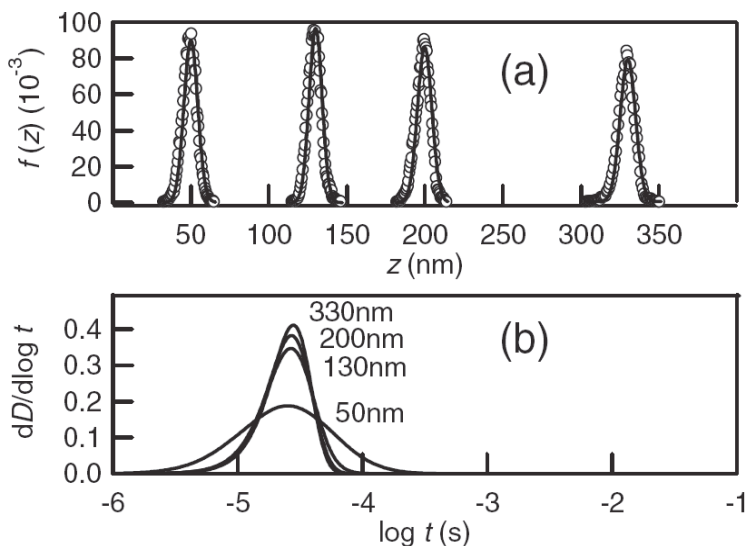


Fig. 13. The surface roughness for (a) The thickness distribution vs. the average film thickness of four P(VDF-TrFE) (75/25) copolymer thin films from 50-330 nm, and (b) the calculated differential switching time distribution at electric field of 120 MV/m. Reprinted from [Nakajima et al., 2005] with permission.

#### 4.4 Other model for P(VDF-TrFE) thin films

The switching kinetics of P(VDF-TrFE) thin films were also studied by Kimura et al [Kimura & Ohigashi, 1986], who proposed a model based on the defects in the crystalline phase. The defects can modulate the local electric field in the surrounding material and prevent domain growth. The effect of defects can be described as a dipole moment  $\Delta\mu$ , therefore, the C-F dipole moment can be affected by the defects and deviated from its intrinsic value. The  $\Delta\mu$  is non-uniformly distributed, which can broaden the distribution of switching time in the film [Kimura & Ohigashi, 1986].

## 5. Annealing, film thickness and contact dependence

The fabrication process and device structure are significant factors that need to be understood to optimize device performance. Thermal annealing, P(VDF-TrFE) film thickness and contacts are discussed in this section.

### 5.1 Thermal annealing

The main purpose for annealing P(VDF-TrFE) films is to increase the degree of crystallinity of the  $\beta$  phase and remove the residual solvent in the film [Mao et al., 2010a]. The microstructure and electrical performance of the polymer are related to the annealing temperature, time and temperature ramp up and cool down rate. The two phase transition temperatures, the Curie temperature ( $T_c$ ) and the melting temperature ( $T_m$ ) are critical in the annealing process [Mao et al., 2010a]. When heating above  $T_c$ , the ferroelectric materials loses spontaneous polarization and becomes paraelectrics. It is necessary to anneal the sample in the paraelectric phase, since the thermal energy allows the polymer chains to rearrange their orientation and position to form a more crystalline structure after cooling [Furukawa et al, 2006]. For P(VDF-TrFE) copolymer, if the films are annealed at temperatures above  $T_m$ , the  $\beta$  phase decreases and recrystallizes into the  $\alpha$  or  $\gamma$  phase when slowly cooled down. Therefore, to achieve high  $\beta$  phase crystallinity films of P(VDF-TrFE),  $T_c < T_{anneal} < T_m$  is required for annealing.

The annealing effects on the microstructure of the P(VDF-TrFE) film can be studied from the point of view of surface morphology, degree of crystallinity and molecular chain orientation. The characteristics of the  $\beta$  phase P(VDF-TrFE) have been discussed in section 2. For 70/30 P(VDF-TrFE) films ( $T_c=118$  °C,  $T_m =144$  °C) annealed at temperatures below  $T_m$ , increasing the annealing temperature causes a dramatic increase in grain size, as shown in the AFM height images in Figure 14 (a)-(d). The increase in the crystallinity of  $\beta$  phase is reflected in the XRD results, as the diffraction intensity increased for the (110), (200) diffraction peaks at  $2\theta=19.9^\circ$ , which is shown in Figure 15. When annealed above  $T_m$ , the  $\beta$  phase grains disappeared and the characteristics of the surface morphology change significantly (Figure 14 (e)). The melting and recrystallization process are also recognized as a decrease of the crystallinity of  $\beta$  phase in XRD data (Figure 15). The surface roughness increases dramatically as the annealing temperature increase above  $T_c$  [Mao et al., 2010a].

The effects of annealing on molecular bond and polymer chain orientation can be clearly detected using polarized FT-IR, as discussed in section 2. Figure 16 [Mao et al. 2010a] shows the p-polarized FT-IR results for the P(VDF-TrFE) film annealed at different temperatures. When annealed below  $T_c$  (at 65 °C), the molecular and polymer chains do not have sufficient energy to align, therefore, they have a random orientation, as shown by the low IR absorption at 850 and 1288  $\text{cm}^{-1}$ . When annealed above  $T_c$  but below  $T_m$ , the higher thermal energy allows the polymer chains to start to reorient and align parallel to the substrate, as indicated by the increase of the IR absorption at 850 and 1288  $\text{cm}^{-1}$  (118-144 °C). Annealing above  $T_m$ , the polymer chains start to rotate and partially align normal to the substrate, and the  $\beta$  phase decreases, observed by the increase of the IR absorption at 1400  $\text{cm}^{-1}$  and the decrease of the 850 and 1288  $\text{cm}^{-1}$  bands.

For the electrical properties of P(VDF-TrFE) FeCaps,  $P_s$ ,  $P_r$  and  $E_c$  of the FeCap depend mainly on the molecular and polymer chain orientation of the  $\beta$  phase crystals, as shown in Figure 17. The FeCaps were annealed at different temperature before the deposition of the top contacts. In Figure 17, FeCaps annealed below  $T_c$  or above  $T_m$  show low  $P_s$ ,  $P_r$  and large

$E_c$ . When annealed between  $T_c$  and  $T_m$ , high  $P_s$ ,  $P_r$  and low  $E_c$  are achieved, with negligible difference as a function of temperature.

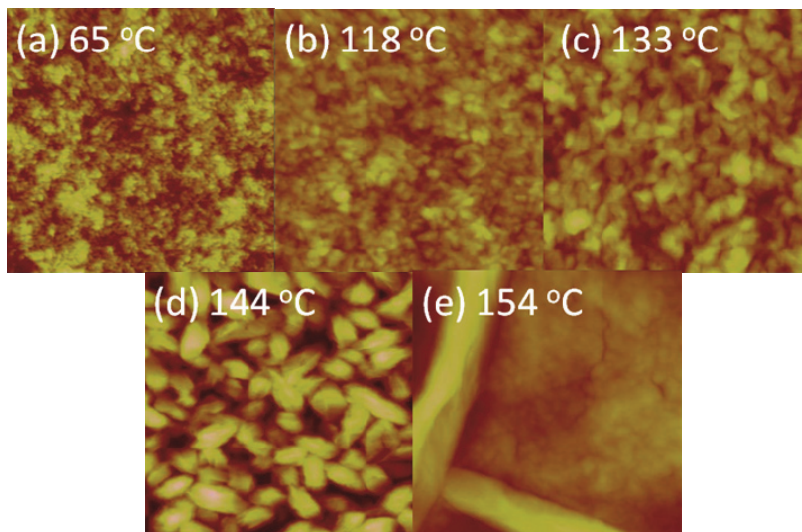


Fig. 14. AFM  $1\mu\text{m}\times 1\mu\text{m}$  height images of P(VDF-TrFE) film annealed at different temperatures. (a)  $65\text{ }^\circ\text{C}$ , (b)  $118\text{ }^\circ\text{C}$ , (c)  $133\text{ }^\circ\text{C}$ , (d)  $144\text{ }^\circ\text{C}$ , and (e)  $154\text{ }^\circ\text{C}$ . The height scales are  $30\text{ nm}$  for (b), (c), (d),  $10\text{ nm}$  for (a), and  $100\text{ nm}$  for (e). All of the images were collected at room temperature.

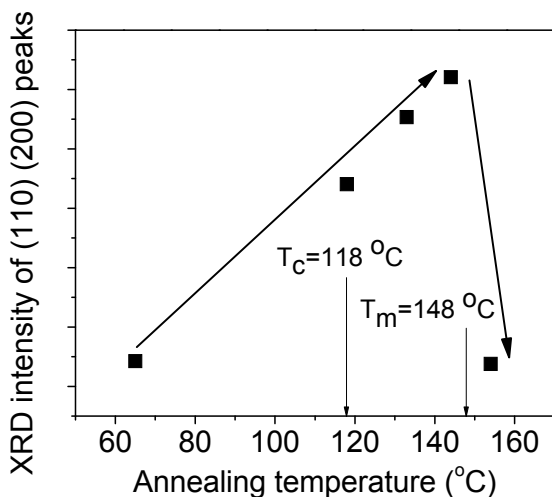


Fig. 15. XRD intensity of (110), (200) orientations after different annealing temperatures. The (110), (200) diffraction peaks at  $2\theta=19.9^\circ$  are attributed to the  $\beta$  phase of P(VDF-TrFE).

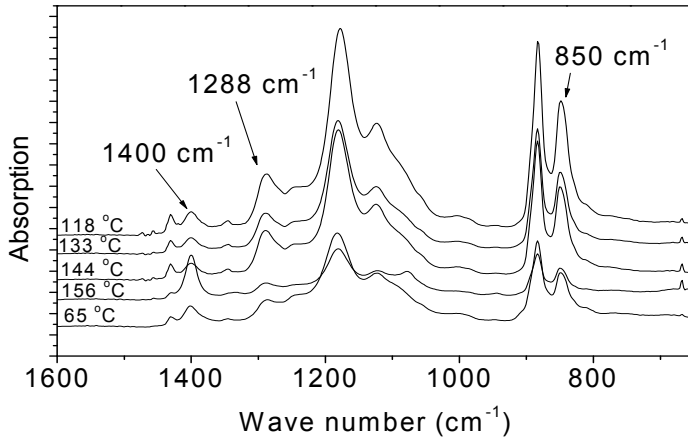


Fig. 16. Polarized FT-IR results for P(VDF-TrFE) films annealed at different temperatures. The different absorption at 850, 1288 and 1400  $\text{cm}^{-1}$  bands represent the annealing temperature affects on polymer chain alignment. Reprinted from [Mao et al., 2010a] with permission.

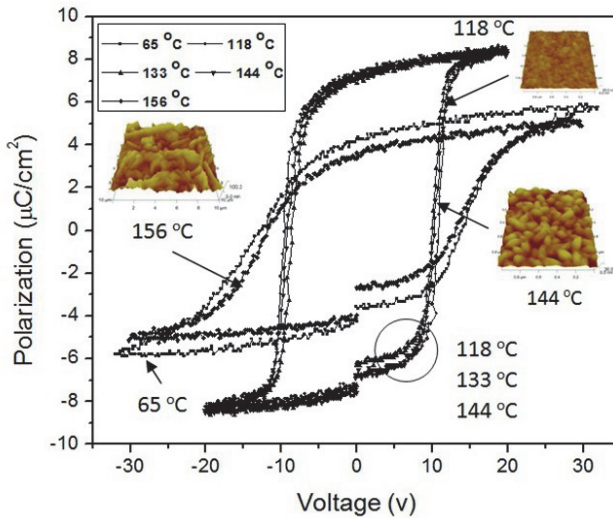


Fig. 17. The hysteresis loops of P(VDF-TrFE) FeCaps annealed at different temperatures. Reprinted from [Mao et al., 2010a] with permission.

## 5.2 P(VDF-TrFE) film thickness dependence

For P(VDF-TrFE) copolymers,  $E_c$  is large, approximately 0.5 MV/cm, and depends on the VDF/TrFE ratio. For low voltage applications, it is necessary to reduce the film thickness,

while maintaining good ferroelectric properties. It has been shown that as the film thickness decreases, the grain size decreases, along with a decrease in the degree of crystallinity [Mao et al., 2010a]. The x-ray diffraction angle ( $2\theta$ ) for the (110) (200) orientation of the  $\beta$  phase remains constant, indicating that the inter-planar spacing,  $b$ , in the crystal lattice does not change for thinner films [Mao et al., 2010a].

Merz studied the film thickness dependence of switching kinetics for  $\text{BaTiO}_3$  crystals and found the activation field increases as the film thickness decreases, which is attributed to the formation of an interfacial layer between the ferroelectric crystal and the contacts [Merz, 1956]. Based on Merz's approach, Tajitsu [Tajitsu, 1995] and Xia et al [Xia et al., 2001] studied the switching kinetics of P(VDF-TrFE) FeCaps with Al contacts for different ferroelectric film thicknesses. Their experimental data suggest that the increase in polarization switching time as the P(VDF-TrFE) film thickness decreases can possibly be explained by the formation of an interfacial layer.

In Merz's approach, the thickness dependence of  $E_0$  for thin films can be expressed as [Merz, 1956]

$$E_0 = E_{01} + \left(\frac{\beta}{d}\right) \quad (7)$$

where  $E_{01}$  is the activation field for thick films,  $\beta$  is an experimental fitting parameter and  $d$  is the film thickness.

The interfacial layer can be treated as a dielectric layer electrically connected in series with the ferroelectric film; therefore, from [Merz, 1956]

$$V_{\text{total}} = V_f + V_{it} \quad (8)$$

where  $V_{\text{total}}$ ,  $V_f$  and  $V_{it}$  are the total applied voltage, voltage drop across the ferroelectric film and the interfacial dielectric layer, respectively. The charge continuity at the boundary of the two interfaces can be expressed as [Merz, 1956]

$$\frac{V_{\text{total}}}{V_f} = \frac{\epsilon_f \cdot d_{it}}{\epsilon_{it} \cdot d_f} + 1 \quad (9)$$

where  $\epsilon_f$  and  $\epsilon_{it}$  are the dielectric permittivity of the ferroelectric and interfacial layers,  $d_f$  and  $d_{it}$  are the thickness of the ferroelectric and interfacial layers, respectively. Due to  $d_f \gg d_{it}$  and  $\epsilon_f/d_f \ll \epsilon_{it}/d_{it}$  [Xia et al., 2001], (9) can be rewritten as [Xia et al., 2001]

$$E_f = E_{\text{total}} \left(1 - \frac{\epsilon_f \cdot d_{it}}{\epsilon_{it} \cdot (d_f + d_{it})}\right) \quad (10)$$

where  $E_f$  and  $E_{\text{total}}$  are the electric field across the ferroelectric material and the applied electric field.

Xia et al characterized P(VDF-TrFE) FeCaps with the film thickness ranged from 600 to 120 nm, and used this approach to analyze the switching time dependence. If the interfacial model is not incorporated, a clear thickness dependence of switching time can be found (Figure 18 (a)), as the switching time increases for thinner films. When the interfacial layers are taken into account, switching time is much less dependent on film thickness, as shown in Figure 18 (b).

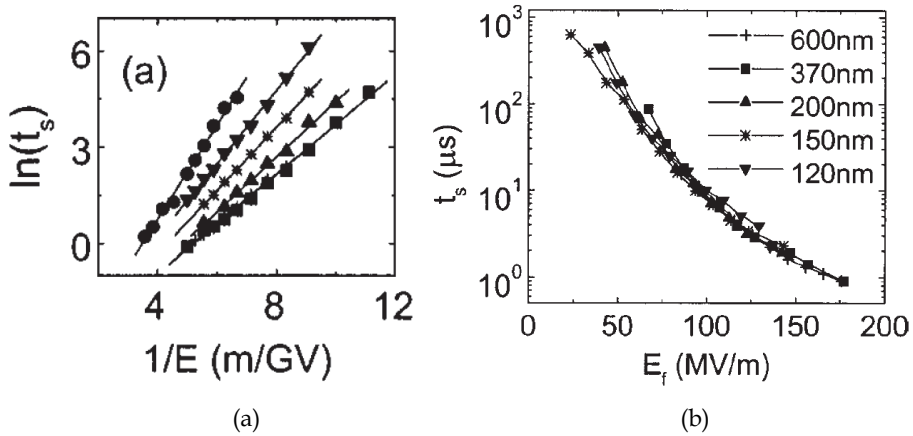


Fig. 18. (a) Switching time as a function of  $1/E$  with different film thicknesses for (from right to left) 600, 370, 200, 150, 120 nm films and (b) switching time as a function of  $E_f$  using the interfacial layer model. Reprinted from [Xia et al., 2001] with permission.

### 5.3 Contact dependence

Metal is the most commonly used material for FeCap contacts. For organic electronic systems, the physical and chemical processes on the interface need to be considered when metal is deposited on the organic materials. Reactive metals such as Ti, Ni and Al can react with the organic materials and form an interfacial layer, which can degrade the electrical properties [Xu et al., 2009]. For P(VDF-TrFE) copolymer, Ti and Ni can react with the fluorine atom in the  $-\text{CF}_2-$  components and create  $\text{TiF}_x$  and  $\text{NiF}_x$  at the interface, respectively [Xu et al., 2009; Chen & Mukhopadhyay, M., 1995]. For chemically inert metals, such as Au, less chemical reaction occurs between the metal atom and P(VDF-TrFE). However, it is easy for the metal to diffuse into the low density polymer film, creating a large leakage current for thinner films.

Nakajima et al studied the P(VDF-TrFE) FeCaps using different contact metals as Al and Au. The switching time distribution broadens as the film thickness decreases for FeCap with both contacts. However, the authors found that the switching time increase with decreasing film thickness only for the FeCaps with Al contact, not for Au contact FeCaps. The authors suggest that the increase of the switching time is attributed to an interfacial dielectric layer formed when Al is deposited on P(VDF-TrFE), which is in agreement with the above discussion. This interfacial layer helps reduce the leakage current, while degrading the polarization switching speed. No interfacial layer is formed between P(VDF-TrFE) and Au. Therefore, the switching time does not increase with decreasing film thickness.

It has also been demonstrated that by using polymeric electrodes, device performance and reliability can be improved. The improvement can be attributed to better adhesion, wetting and similar chemical properties of the surface, compared to metal contacts. Naber et al found that adding a conducting polymer poly(3,4-ethylenedioxythiophene):poly(styrenesulfonicacid) (PEDOT: PSS) on top of Al or indium-tin-oxide (ITO) for bottom contact improves both the  $P_r$  and switching time for films as thin as 65 nm of P(VDF-TrFE) [Naber et al., 2004]. Xu et al demonstrated that both polypyrrole-poly(styrene sulfonate) and

PEDOT-PSSH can be used as buffer conducting polymer layers for P(VDF-TrFE) top and bottom contacts. Improved device performance with higher  $P_r$  and faster switching speeds were achieved. A  $P_r$  of more than 70% of its initial value can be achieved after  $1 \times 10^7$  cycles of switching for 50 nm thick P(VDF-TrFE) film devices, as shown in Figure 20 [Xu et al., 2007, 2009]. Xu et al also found that the conducting polymer buffer layers improve the degree of crystallinity of the thin films [Xu et al., 2009].

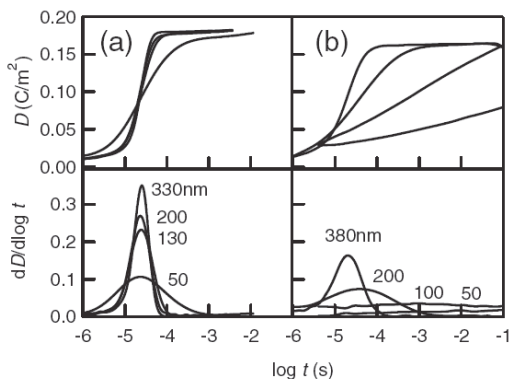


Fig. 19. The polarization switching behaviors for (a) Au contact FeCap, and (b) Al contact FeCaps. Reprinted from [Nakajima et al., 2005] with permission.

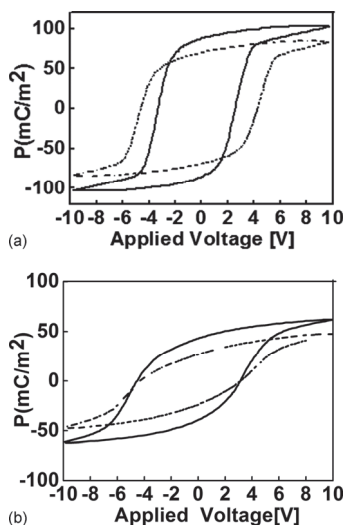


Fig. 20. Hysteresis loops for 50 nm of P(VDF-TrFE) film with Ti as the top and bottom contacts; (a) with two PEDOT-PSSH buffer layers between P(VDF-TrFE) and Ti for top and bottom contacts, (b) without buffer layers. Solid lines and dashed lines are the measurement before and after  $1 \times 10^7$  cycles of switching, respectively. Reprinted from [Xu et al., 2009] with permission.

## 6. Conclusions

In this chapter, the material and electrical properties, and the ferroelectric polarization switching kinetics of P(VDF-TrFE) copolymer have been reviewed. The ferroelectric properties originate from the large difference in the electronegativity between the fluorine, carbon and hydrogen atoms. The polymer phase structure, surface morphology, crystallinity, and molecular chain orientation associated with the ferroelectric  $\beta$  phase have been discussed. The P(VDF-TrFE) copolymer exhibits a high spontaneous polarization  $> 8 \mu\text{C}/\text{cm}^2$  (depending on fabrication process and mole ratio of VDF/TrFE) and a square like hysteresis loop. The sharp peak in the switching current indicates the fast rotation of the dipole around the polymer chain.

To illustrate the switching kinetics of P(VDF-TrFE) thin films, two basic polarization switching mechanisms, reversal polarization nucleation and domain wall expansion were reviewed. A commonly accepted statistical model (KAI) for single crystal polarization switching was discussed and extended to models to explain the switching time broadening for P(VDF-TrFE) thin films, including the nucleation-limited-switching (NLS) model based on region-to-region switching kinetics, surface roughness based model, etc. The NLS model can be successfully used to fit P(VDF-TrFE) switching data and  $\tau_0$  and  $E_0$  can be extracted as 5 ns and 9.6 MV/cm.

The annealing temperature, film thickness and contacts were then discussed. For annealing above  $T_c$  but below  $T_m$ , the grain size and the crystallinity of the (110) (200) orientation of the  $\beta$  phase increases, the polymer chains align parallel to the substrate with the polarization dipole moment perpendicular to the substrate. At annealing above  $T_m$ , the surface morphology changes significantly, the degree of crystallinity in the  $\beta$  phase decreases dramatically, and the polymer chains tend to align normal to the substrate. As the film thickness decreases, the grain size and degree of crystallinity decrease. The increase switching time as film thickness decreases can possibly be explained by the formation of an interfacial layer. For the contact, reactive metals induce an interfacial layer, which causes an increase in the switching time. P(VDF-TrFE) FeCaps with Au contacts do not have this film thickness effect, but as the film becomes thinner than 100 nm, the diffusion of Au atoms increases the leakage current. Therefore, thin films with high quality are required. Using conducting polymers, such as PEDOT: PSS and polypyrrole-poly(styrene sulfonate) as a buffer layer for the contacts show improved electrical performance in remanent polarization, switching time and reliability for thin film P(VDF-TrFE) based FeCaps.

One of the most important applications of P(VDF-TrFE) copolymer is ferroelectric nonvolatile memory (FeRAM). The two stable states of the ferroelectric material in positive and negative directions can be used as digital data "1" and "0", and the remanent polarization leads to data storage with the power off (nonvolatile). Due to the low temperature, solution process of P(VDF-TrFE) films, it is compatible with large area and flexible electronic applications. Even though the polarization switching speed of P(VDF-TrFE) is slow ( $\sim 1 \mu\text{s}$ ) compared to PZT ( $\sim 10 \text{ ns}$ ), it is much faster than the conventional flash memory ( $100 \mu\text{s}$ ) in writing and programming. Moreover, it is reliable with more than  $1 \times 10^7$  cycles of switch [Mao et al., 2011a], and can be used in low voltage applications [Fujisaki et al., 2007]. The memory cell can be constructed by combining access transistors with the ferroelectric capacitors. The circuit structure depends on the number of access transistors and ferroelectric capacitors [Arimoto & Ishiwara, 2004]. One transistor-one capacitor (1T1C) FeRAM elements based on P(VDF-TrFE) were recently demonstrated by the authors [Mao,

et al., 2011b]. Ferroelectric transistors can also be fabricated using P(VDF-TrFE) for each bit in FeRAM [Naber et al., 2005; Lee et al., 2009], however, the reliability still needs to be improved for future applications.

## 7. Acknowledgements

The work at UT Dallas was partially financial supported by the Army Research Laboratory (ARL). The authors would also like to thank Dr. Scott R. Summerfelt of Texas Instruments and Dr. Eric Forsythe from ARL for many helpful discussions.

## 8. References

- Arimoto, Y. & Ishiwara, H., (2004). Current status of ferroelectric random-access memory, *MRS Bulletin*, Vol. 29, No. 11, pp. 823-828, doi: 10.1557/mrs2004.235
- Bergman, J. G.; Jr. McFee, J. H. & Crane, G. R., (March 1971) Pyroelectricity and Optical Second Harmonic Generation in Polyvinylidene Fluoride Films, *Appl. Phys. Lett.*, Vol 18, No. 5, pp. 203-205
- Bune, A. V.; Fridkin, V. M.; Ducharme, S.; Blinov, L. M.; Palto, S. P.; Sorokin, A. V.; Yudin, S. G. & Zlatkin, A., (1998) Two-dimensional ferroelectric films, *Nature*, Vol. 391, No. 6670, pp. 874-877
- Chen, T. C. S. & Mukhopadhyay, S. M., Metallization of electronic polymers: A comparative study of Polyvinylidene fluoride, polytetrafluoroethylene, and polyethylene, *J. Appl. Phys.*, Vol. 78, No. 9, pp. 5422-5426
- Colla, E. L.; Hong, S.; Tagantsev, A. K.; Setter, N. & No, K., (1998). Direct observation of region by region suppression of the switchable polarization (fatigue) in Pb(Zr, Ti)O<sub>3</sub> thin film capacitors with Pt electrodes, *Appl. Phys. Lett.*, Vol. 72, No. 21, pp. 2763-2765
- Fujisaki, S.; Ishiwara, H. & Fujisaki, Y. (2007). Low-voltage operation of ferroelectric poly(vinylidene fluoride-trifluoroethylene) copolymer capacitors and metal-ferroelectric-insulator-semiconductor diodes, *Appl. Phys. Lett.*, Vol. 90, p. 162902
- Furukawa, T.; Nakajima, T. & Takahashi, Y., (2006). Factors governing ferroelectric switching characteristics of thin VDF/TrFE copolymer films, *IEEE Trans. Dielectr. Electric. Insul.*, Vol. 13 No. 5, pp. 1120-1131, ISSN: 1070-9878
- Ganpule, C. S.; Nagarajan, V.; Li, H.; Ogale, A. S.; Steinhauer, D. E.; Aggarwal, S.; Williams, E.; Ramesh, R & Wolf P. De, (2000). Role of 90 domains in lead zirconate titanate thin films, *Appl. Phys. Lett.*, Vol. 77, No. 2, pp. 292-294
- Glass, A. M., (December 1971). Pyroelectric Properties of Polyvinylidene Fluoride and Its Use for Infrared Detection, *J. Appl. Phys.*, Vol. 42, No. 13, pp. 5219-5222
- Hu, Z. J.; Tian, M. W; Nysten, B. & Jonas, A. M., (2009). Regular arrays of highly ordered ferroelectric polymer nanostructures for non-volatile low-voltage memories, *Nat. Mater.* Vol. 8, No. 1, pp. 62-67
- Kawai, H. (1969). The Piezoelectricity of Poly(vinylidene Fluoride), *Jpn. J. Appl. Phys.*, Vol. 8, pp. 975-976
- Kepler, R. G, Ferroelectric, pyroelectric, and piezoelectric properties of poly(vinylidene fluoride), In: *Ferroelectric polymers chemistry, physics, and applications*, Hari Singh Nalwa, pp. 183-232, Marcel Dekker, Inc., New York

- Kimura, K. & Ohigashi, H., (1986). Polarization behavior in vinylidene fluoride-trifluoroethylene copolymer thin films, *Jpn. J. Appl. Phys.*, Vol. 25, No. 3, pp. 383-387
- Kim, K. J.; Reynolds, N. M. & Hsu, S. L. (1989). Spectroscopic analysis of the crystalline and amorphous phases in a vinylidene fluoride/trifluoroethylene copolymer, *Macromolecules*, Vol. 22, No. 12, pp. 4395-4401
- Kim, Y.; Kim, W.; Choi, H.; Hong, S.; Ko, H.; Lee, H. & No, K., (2010). Nanoscale domain growth dynamics of ferroelectric poly(vinylidene fluoride-co-trifluoroethylene) thin films, *Appl. Phys. Lett.*, Vol. 96, No. 1, p. 012908
- Kin, N.; Takai, K. & Honda, K., (2008). High speed pulse measurement of micro ferroelectric capacitors using a multi-probe atomic force microscope, *Jpn. J. Appl. Phys.*, Vol. 47, No. 6, pp. 4638-4642
- Kobayashi, M.; Tashiro, K. & Tadokoro, H., (1975). Molecular vibrations of three crystal forms of poly(vinylidene fluoride), *Macromolecules*, Vol. 8, No. 2, pp. 158-171
- Kusuma, D. Y.; Nguyen, C. A. & Lee, P. S., (2010). Enhanced ferroelectric switching characteristics of P(VDF-TrFE) for organic memory devices, *J. Phys. Chem B*, Vol. 114, No. 42, pp. 13289-13293
- Lee, K. H.; Lee, G.; Lee, K.; Oh, M. S. & Im, S., (2009). Flexible low voltage nonvolatile memory transistors with pentacene channel and ferroelectric polymer, *Appl. Phys. Lett.*, Vol. 94, No. 9, p. 093304
- Lohse, O.; Grossmann, M.; Boettger, U.; Bolten, D. & Waser, R., (2001). Relaxation mechanism of ferroelectric switching in Pb(Zr,Ti)O<sub>3</sub> thin films, *J. Appl. Phys.*, Vol. 89, No. 4, pp. 2332-2336
- Mao, D.; Quevedo-Lopez, M. A.; Stiegler, H.; Alshareef, H. N. & Gnade, B. E., (2010). Optimization of poly(vinylidene fluoride-trifluoroethylene) film as non-volatile memory for flexible electronics, *Org. Electron.* Vol. 11, No. 5, pp. 925-932
- Mao, D.; Mejia, I.; Stiegler, H.; Gnade, B. E. & Quevedo-Lopez, M. A., (2010) Polarization behavior of poly(vinylidene fluoride-trifluoroethylene) copolymer ferroelectric thin film capacitors for nonvolatile memory application in flexible electronics, *Org. Electron.*, Vol. 108, No. 9, p. 094102, doi:10.1063/1.3500428
- Mao, D.; Mejia, I.; Stiegler, H.; Gnade, B. E.; Quevedo-Lopez, M. A., (2011). Fatigue characteristics of Poly(vinylidene fluoride-trifluoroethylene) copolymer ferroelectric thin film capacitors for flexible electronics memory applications, submitted to *Org. Electron.*
- Mao, D.; Mejia, I.; Singh, M.; Stiegler, H.; Gnade, B. E. & Quevedo-Lopez, M. A., (2011). Ferroelectric random access memory based on one transistor one capacitor device structure for flexible electronics, in preparation.
- Merz, W. J., (1956). Switching time in ferroelectric BaTiO<sub>3</sub> and its dependence on crystal thickness, *J. Appl. Phys.*, Vol. 27, No. 8, pp. 938-943
- Naber, R. C. G.; Blom, P. W. M.; Marsman, A. W. & Leeuw, D. M., (2004). Low voltage switching of a spin cast ferroelectric polymer, *Appl. Phys. Lett.*, Vol. 85, No. 11, pp. 2032-2034
- Naber, R. C. G.; Tanase, C.; Blom, P. W. M.; Gelinck, G. H.; Marsman, A. W.; Touwslager, F. J.; Setayesh, S. & De leeuw, D. M., (2005). High-performance solution-processed polymer ferroelectric field-effect transistors, *Nat. Mater.*, Vol. 4, pp. 243-248

- Nakajima, T.; Abe, R.; Takahashi, Y. & Furukawa, (2005). Intrinsic switching characteristics of ferroelectric ultrathin vinylidene fluoride/trifluoroethylene copolymer films revealed using Au electrode, *Jpn. J. Appl. Phys.*, Vol. 44, No. 45, pp. L 1358-L 1388
- Nalwa, H. S., (1995a) *Ferroelectric polymers chemistry, physics, and applications*, Marcel Dekker, Inc, New York
- Nalwa, H. S., (1995b). Ferroelectric nylons, In: *Ferroelectric polymers chemistry, physics, and applications*, Hari Singh Nalwa, pp. 63-181, Marcel Dekker, Inc., New York
- Park, Y. J.; Kang, S. J; Park, C.; Kim, K. J.; Lee, H. S; Lee, M. S; Chung, U. I & Park, I. J., (2006). Irreversible extinction of ferroelectric polarization in P(VDF-TrFE) thin films upon melting and recrystallization, *Appl. Phys. Lett.*, Vol 88, p. 242908
- Pauling, L. (1960). The Nature of the Chemical Bonding, (3<sup>rd</sup> edition), *Cornell University Press*, Ithaca, NY, p. 644
- Reynolds, N. M.; Kim, K. J.; Chang, C. & Hsu, S. L., (1989). Spectroscopic analysis of the electric field induced structural changes in vinylidene fluoride/trifluoroethylene copolymers, *Macromolecules*, Vol. 22, No. 3, pp. 1092-1100
- Salimi, A & Yousefi, A. A. (2004). Conformational changes and phase transformation mechanisms in PVDF solution-cast films, *Journal of Polymer Science Part B: Polymer Physics*, Vol. 42, No. 18, pp. 3487-3495
- Stolichnov, I.; Tagantsev, A.; Setter, N.; Cross, J. S. & Tsukada, M., (2003). Crossover between nucleation-controlled kinetics and domain wall motion kinetics of polarization reversal in ferroelectric films, *Appl. Phys. Lett.*, Vol. 83, No. 16, pp. 3362-3364
- Tagantsev, A. K.; Stolichnov, I.; Setter, N.; Cross, J. S. & Tsukada, M., (2002). Non-Kolmogorov-Avrami switching kinetics in ferroelectric thin films, *Phys. Rev. B*, Vol. 66, No. 21, p. 214109
- Tajitsu, Y.; Ogura, H.; Chiba, A. & Furukawa, T. (1987). Investigation of switching characteristics of vinylidene fluoride/trifluoroethylene copolymers in relation to their structures, *Jpn. J. Appl. Phys.*, Vol. 26, No. 4, pp. 554-560
- Tajitsu, Y., (1995). Effects of thickness on ferroelectricity in vinylidene fluoride and trifluoroethylene copolymers, *Jpn. J. Appl. Phys.*, Vol. 34, Part 1, No. 9B, pp. 5418-5423, doi: 10.1143/JJAP.34.5418
- Tashiro, K., (1995). Crystal structure and phase transition of PVDF and related copolymers, In: *Ferroelectric polymers chemistry, physics, and applications*, Hari Singh Nalwa, pp. 63-181, Marcel Dekker, Inc., New York
- Xia, F.; Xu, H. S.; Fang, F.; Razavi, B.; Cheng, Z.-Y.; Lu, Y.; Xu, B. M. & Zhang, Q. M., (2001). Thickness dependence of ferroelectric polarization switching in poly(vinylidene fluoride-trifluoroethylene) spin cast films, *Appl. Phys. Lett.*, Vol. 78, No. 8, pp. 1122-1124
- Xu, H. S.; Shanthi, G.; Bharti, V & Zhang, Q. M, (2000). Structure, Conformational, and Polarization Changes of Poly(vinylidene fluoride-trifluoroethylene) Copolymer induced by high-energy electron irradiation, *Macromolecules*, Vol. 33, No. 11, pp. 4125-4131, doi: 10.1021/ma9919561
- Xu, H. S.; Zhong, J. H.; Liu, X. B.; Chen, J. H. & Shen, D., (2007). Ferroelectric and switching behavior of poly(vinylidene fluoride-trifluoroethylene) copolymer ultrathin films with polypyrrole interface, *Appl. Phys. Lett.*, Vol. 90, No. 9, p. 092903, doi: 10.1063/1.2710477.

- Xu, H. S.; Liu, X. B.; Fang, X. R.; Xie, H. F.; Li, G. B.; Meng, X. J.; Sun, J. L. & Chu, J. H., (2009). Domain stabilization effect of interlayer on ferroelectric poly(vinylidene fluoride- trifluoroethylene) copolymer ultrathin film, *J. Appl. Phys.*, Vol. 105, No. 3, p. 034107,
- Yamada, T.; Kitayama, T., (1981). Ferroelectric properties of vinylidene fluoride-trifluoroethylene copolymers, *J. Appl. Phys.*, Vol. 52, No. 11, pp. 6859-6863

# Charge Transport in Ferroelectric Thin Films

Lucian Pintilie

*National Institute of Materials Physics, Bucharest-Magurele  
Romania*

## 1. Introduction

Ferroelectrics are multifunctional materials exhibiting a host of appealing properties resulting from the presence of the spontaneous polarization, which is a polarization occurring in the absence of an applied electric field, due to a structural transformation taking place at a certain temperature (Uchino, 2000; Lines & Glass, 1977). Among the most important properties are: ferroelectricity-the ability to switch the spontaneous polarization by the application of a suitable electric field; piezoelectricity-the ability to produce a voltage by the application of a mechanical stress, or the ability to change the strain by applying a voltage; pyroelectricity-the ability to generate current when heated/cooled; birefringence-different refraction indices along the polar axis and on other crystalline directions, etc. It is thus of no wonder that ferroelectric materials, especially those with perovskite structure (e.g.  $\text{Pb}(\text{Zr,Ti})\text{O}_3$ , known as PZT, or  $\text{BaTiO}_3$ ), quickly found a lot of applications in the electronic industry, security, medicine, different type of automations, etc. In most of the applications the ferroelectrics are used as capacitors, either as bulk ceramics or single crystals or as thin films of polycrystalline or epitaxial quality (Izyumskaya et al., 2008; Dawber et al. 2). Also, most of the applications are based on the application of an external voltage on the ferroelectric capacitor, leading unavoidable to the occurrence of a leakage current. If in the case of bulk ferroelectrics, especially in the form of ceramics, the leakage is usually negligible, only the currents due to polarization variations being of significant value (e.g. pyroelectric or reversal currents), in the case of the thin films the leakage currents can be so large that they hidden any contribution from polarization variation. This fact is not acceptable in applications which are based on reading currents due to polarization changes under the influence of an external voltage, as is the case for the read/write process in non-volatile ferroelectric memories (Scott J. F., 2000). Solutions to reduce the leakage can be found only if the conduction mechanism is correctly understood, as well as the impact of leakage on other macroscopic properties. For example, the leakage can have a significant impact on the hysteresis loop, considering that the loop is obtained by the integration of the charge released during the polarization switching. A large leakage current, over-imposed on the switching current will alter the hysteresis, masking the presence of ferroelectricity in the analyzed sample. Therefore, the study of the charge transport in ferroelectric thin films is of high importance for all the applications using ferroelectric capacitors subjected to an applied external voltage, in order to identify the conduction mechanisms responsible for the leakage current (Chentir et al. 2009; Pabst et al. 2007; Meyer et al., 2005; Horii et al., 1999). Traditionally, the possible conduction mechanisms in ferroelectric thin films are divided in two major classes (Pintilie L. & Alexe M., 2005; Pintilie L. et al., 2005):

1. Bulk limited: ohmic-type conduction; space charge limited currents (SCLC); Pool-Frenkel emission from the deep traps (PFE); hopping.
2. Interface limited: thermionic emission over the potential barrier at the electrode interface, known also as Schottky emission (SE); electric field assisted tunneling or Fowler-Nordheim tunneling (FNT).

For very thin films, direct tunneling is also possible. The classic way to investigate the charge transport through ferroelectric films is to record the current-voltage (I-V) characteristic, eventually at different temperatures, and then to see if the experimental curve fits one of the above mentioned conduction mechanisms. Problems occur when more than one conduction mechanisms fit the experimental data. For example, when representing the I-V characteristic in log-log scale we may find that on some voltage range the slope is near unity and that on a higher voltage range the slope is near 2. In between could be a very narrow voltage range where the slope is much higher, usually around 10. From these data we may conclude that at low voltage the conduction is ohmic and that at high voltage the conduction is dominated by trap controlled space charge limited currents. However, the same set of experimental data may fit the Schottky emission or the Pool-Frenkel emission if we draw the  $\ln(I) \sim V^{1/2}$  representation. Some more insight can bring the temperature measurements, considering that the temperature dependence is not exactly the same for the above mentioned conduction mechanisms. Even more information can be obtained by recording the I-V characteristic on films with different thicknesses, because different conduction mechanisms may have different thickness dependencies (e.g. SCLC varies as  $d^{-3}$ , with  $d$  the thickness of the film, while the hopping is proportional with  $d$ ) (Kao & Hwang, 1981).

The classic recipe was applied on a large amount of samples, of different ferroelectric materials. The idea was to find the dominant conduction mechanism in each material and, consequently, to find ways to reduce the leakage current. However, there are some problems if considering the existing literature regarding the origin of the leakage current in ferroelectric thin films:

- Several conduction mechanisms were found for the same material. This is because the effect of the structural quality on the charge transport is not considered. Whatever is pure polycrystalline, textured or epitaxial the ferroelectric thin film capacitor is regarded as a black box on which a voltage is applied in order to read a current. It is neglected the fact that any structural defect can impact the density of the free carriers or their mobility.
- Different metals are used for electrodes, neglecting the fact that the metal-ferroelectric interface is part of the ferroelectric capacitor on which the I-V measurement is performed. The fit of the experimental data with one or another of the conduction mechanisms is performed without investigating the interface properties and behavior, whatever the metal contact is ohmic or rectifying (Tang et al., 2003; Nunez & Nardelli, 2008).
- The tendency to generalize a model to different ferroelectric materials, neglecting the subtle structural details. For example, the origin of the ferroelectricity in  $\text{PbTiO}_3$  and  $\text{BaTiO}_3$  is thought to be the same. However, the ferroelectric phase in  $\text{PbTiO}_3$  is stable up to a higher temperature than in  $\text{BaTiO}_3$ . This is because of the different natures of the Pb-O and Ba-O bonds. The Ba-O bond is nearly an ideal ionic bond, while the Pb-O bond has a high degree of covalency. Thus, sharing the electrons helps to stabilize the spontaneous polarization (Cohen, 1992). Consequently, we should expect different electronic properties for  $\text{PbTiO}_3$  and  $\text{BaTiO}_3$  including different mechanisms for the charge transport.

- The effect of the ferroelectric polarization on the charge transport is not considered. In an ideal, monodomain, ferroelectric the elemental dipoles are oriented head-to-tail to give the macroscopic polarization. It means that the bulk has a zero net charge. All the polarization charges are located near the electrode interfaces, positive on one side and negative on the other. These sheets of bound charges must have a certain effect on the interface properties, as for example the barrier height or the width of the depleted region.

In the following pages some of the above mentioned problems will be analyzed in more details. First, several considerations regarding the metal-ferroelectric interface and the effect of the local microstructure on the charge transport will be presented. Then the conduction mechanisms in some prototype perovskite ferroelectric thin films will be analyzed, discussing the differences and the similarities. The last part will be dedicated to phenomena related to charge transport, as for example the integration method applied to obtain the hysteresis loop or the photovoltaic/photoconductive properties of perovskite ferroelectrics.

## 2. The ferroelectric capacitor and its electrical properties

The prototype sample for current-voltage (I-V) measurements is the ferroelectric capacitor. The sample consists of two inter-connected systems: the electrode interfaces, including the possible presence of a depletion region, and the bulk. In the following part the influence of the polarization charges on the specific properties of the interface (built-in potential, maximum electric field, capacitance) will be analyzed. Further on, the effect of the microstructure on the electric properties of ferroelectrics, with special emphasis on charge transport, will be discussed by comparing polycrystalline and epitaxial films.

### 2.1 Metal-ferroelectric interface

The ferroelectric capacitor consists of a slab of ferroelectric material with two metal layers deposited on opposite faces of the slab in such a way that the ferroelectric polarization is perpendicular on the metal electrodes. In the ideal case the electric dipoles inside the ferroelectric are head-to-tail oriented, so that they end with a sheet of positive charge near one electrode interface and one sheet of negative charge near the other interface. The bulk of the film is free of any net polarization charges because these cancel each other except the interfaces with the electrodes.

Considering this, it is expected that the charges associated to ferroelectric polarization which are present near the electrode interfaces will affect the quantities specific to classic metal-semiconductor Schottky contacts. Therefore, a model was developed to take into consideration the effect of polarization charges on the interface properties. Here, the main results of the model will be summarized (Pintilie L. & Alexe M., 2005).

The equations giving the specific quantities of a Schottky contact are the following:

- The built-in potential

$$V_{bi}' = V_{bi} \pm \frac{P}{\epsilon_0 \epsilon_{st}} \delta \quad (1)$$

- The maximum field at the interface

$$E_m = \sqrt{\frac{2qN_{eff}(V + V_{bi}')}{\epsilon_0 \epsilon_{st}}} \pm \frac{P}{\epsilon_0 \epsilon_{st}} \quad (2)$$

- The width of the depleted region

$$w = \sqrt{\frac{2\epsilon_0\epsilon_{st}(V + V_{bi}')}{qN_{eff}}} \quad (3)$$

The notations are:  $V_{bi}$  – the built-in potential in the absence of the ferroelectric polarization;  $P$  – ferroelectric polarization;  $\delta$  – the distance between the polarization sheet of charge and the physical metal-ferroelectric interface;  $\epsilon_0$  – the permittivity of the vacuum;  $\epsilon_{st}$  – the static dielectric constant;  $q$  – the electron charge;  $N_{eff}$  – the effective density of space charge in the depleted region (takes into consideration the ionized donors and acceptors, but also the trapping centers carrying a net charge after capturing a charge carrier). It can be seen that all the specific quantities are affected by the presence of the polarization charges. More of that, the effect is not symmetric, because the polarization charges have opposite signs at the two interfaces. It results that the presence of the polarization can make a symmetric structure, with same metals as electrodes, asymmetric. The band diagram of such a structure is presented in fig. 1.

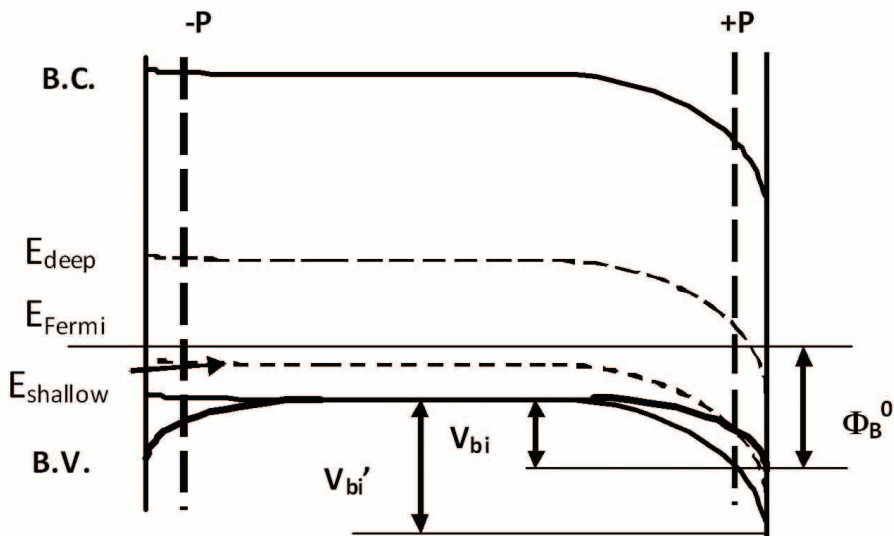


Fig. 1. The band diagram for a metal-ferroelectric-metal structure. The notations are: B.C.- conduction band; B.V.-valance band,  $V_{bi}$ -the built-in voltage in the absence of the ferroelectric polarization;  $V_{bi}'$ -the built-in voltage with polarization;  $\Phi_B^0$ -the potential barrier in the absence of the ferroelectric polarization.

The figure was made for the case of a p-type ferroelectric, but the discussion is valid also in case of a n-type material. It can be seen that the band bending increases near the interface with positive polarization charge because this charge will reject the holes (positive charges) from the interface region. This will lead to a larger built-in potential compared to the case when the polarization is missing. The opposite takes place to the other interface, were the negative polarization charge will attract holes, leading to a smaller band bending. The

conclusion is that the presence of the ferroelectric polarization makes the metal-ferroelectric-metal (MFM) structure asymmetric from the point of view of interfaces behavior. This will have consequences on all the electric properties, including the charge transport.

It worth to notice that the above results are valid no matter the ferroelectric film is polycrystalline or epitaxial. Differences may come from the density of the grain barriers. If the films are columnar, then it may have the same behavior from the point of view of interfaces as in the case of an epitaxial film. The overall film properties will be dominated by the interfaces. If there are several grains in between the electrodes, then the behavior may change, leading to a less and less visible effects from the part of electrode interfaces as the number of the grain barriers between the electrodes increases. The truly polycrystalline films are expected to behave as bulk ceramics, with properties dominated by the bulk and much reduced influence from the metal-ferroelectric interface. This aspect will be discussed in more detail in the following paragraph.

## 2.2 Microstructure and the electric properties of ferroelectrics

The fig. 2 shows the capacitance-voltage (C-V) characteristics obtained in the case of two ferroelectric films, with nominally the same composition (PZT 40/60, were 40/60 is the Zr/Ti ratio), but with different microstructure: one polycrystalline, with top and bottom Pt electrodes, and one epitaxial, with top and bottom SrRuO<sub>3</sub>-SRO electrodes. Therefore, both MFM structures are, nominally, symmetrical.

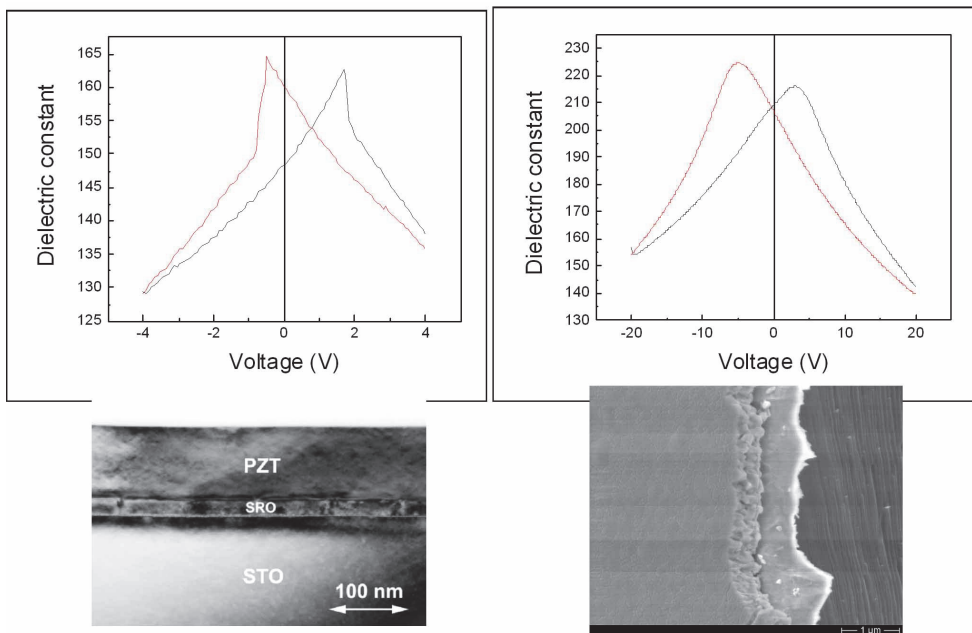


Fig. 2. The C-V characteristics in the case of an epitaxial PZT film (left) and in the case of a polycrystalline PZT film. The films have the same composition and about the same thickness.

Figure 2 reveals how deep can be the effect of the microstructure on the shape of the C-V characteristic, but also on the value of the dielectric constant. For example, in the case of the epitaxial films the switching is marked by sharp peaks in the capacitance, accompanied by abrupt changes in the capacitance values once the polarization was reversed. In the case of polycrystalline films the switching produces rounded, broad peaks, with no abrupt changes in the capacitance value. The value of the dielectric constant, calculated as for a plan-parallel capacitor, is higher for the polycrystalline films. This fact can be explained by the presence of grain boundaries, which can bring an additive contribution to the polarization charges. Although hard to be comprehended, any interfacial charge brings an additive contribution to the overall capacitance of the film, which can be simulated as a parallel-connected capacitor to the ideal ferroelectric capacitor (no other charges in the film except the polarization ones).

The results of the C-V measurements correlate well with those of the hysteresis ones, shown in figure 3. The measurements were made in the same conditions: at 1 kHz and using a triangular shape voltage for the dynamic mode; at 100 Hz and using a delay time of 1 second, with triangular shape voltage pulses, for the static mode. Figure 3 shows an almost rectangular loop in the case of the epitaxial film, while in the case of the polycrystalline film the loop is elongated along the voltage axis. Several observations can be made when analyzing the two loops:

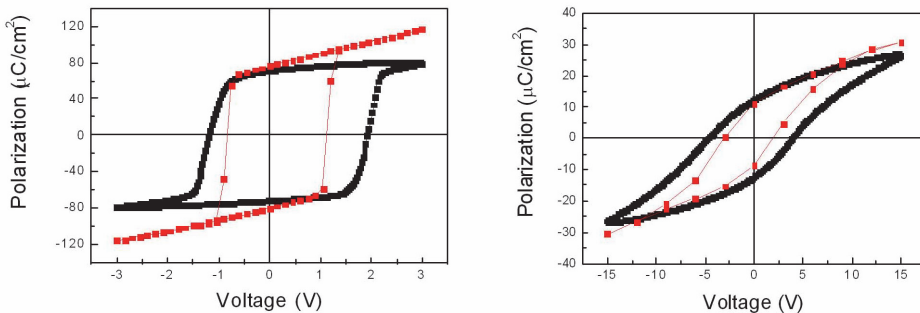


Fig. 3. The hysteresis loops in the case of an epitaxial PZT film (left) and in the case of a polycrystalline PZT film. The films have the same composition and about the same thickness. With black is the hysteresis loop recorded in the dynamic mode; with red is the hysteresis loop recorded in the static mode.

- The switching is much faster in the epitaxial film. The switching comprises three distinct steps: the nucleation of ferroelectric domains with opposite direction of polarization; the growth of the ferroelectric domains with polarization parallel to the applied electric field (Tagantsev et al., 2002; Shur et al., 2001; Lohse et al., 2001); the compensation of the depolarization field occurring just after the switching is taking place (Jiang et al., 2007). The models proposed for switching considers only the first two steps, which can be very fast (switching times of the order of nanoseconds). However, the third step is the one who define the switching speed in the hysteresis measurements, because the compensation of the depolarization field is the slowest process. The compensation is made with free charges coming from the bulk of the ferroelectric or from the external circuitry including the metal electrodes. It comes that

the electrical time constant, defining the ability of the MFM system to respond to a rapid change in the polarization charge near the metal-ferroelectric interfaces, is the most important time factor in setting up the shape of the hysteresis loop. If the compensation is fast, then the hysteresis loop is rectangular, which is possible for epitaxial films having larger concentration of free carriers (lower resistivity  $\rho$ ) and lower static dielectric constant  $\epsilon_{st}$ . We remind here that the hysteresis measurement was performed with a triangular voltage wave, thus the voltage can be converted into time. A small voltage domain for switching means, in fact, a short time for compensating the depolarization field. A large voltage domain for switching, as is the case for the polycrystalline film, means a long time for compensation of the depolarization field. This fact can be explained by the much larger amount of structural defects, especially grain boundaries, acting as trapping-scattering center for the free carriers, thus reducing their concentration and mobility. The consequence is a much higher resistivity for polycrystalline films compared to very high quality epitaxial ones, where only point defect can exist. The point defects may contribute to the decrease of resistivity if they act as donors or acceptors in the ferroelectric material. Another effect of the grain boundaries in polycrystalline films is the increase of the static dielectric constant due to the extrinsic effects. Therefore, both the increase of resistivity and dielectric constant leads to a slower response time of the polycrystalline film to any change in polarization state. It was assumed that the resistance of the external circuitry is much smaller than that of the MFM structure, and that the capacitance of the external circuitry is parallel connected to the capacitance of the MFM structure, and is of negligible value.

- The coercive voltage is smaller in the case of epitaxial film, considering that the thicknesses are about the same. This fact suggests that the absence of grain boundaries is beneficial for polarization switching in the sense that these are no longer obstructing the movement of the ferroelectric domains.
- The remnant polarization is much higher in the case of the epitaxial film. This is, again, an effect of the microstructure. The slow compensation of the depolarization field in polycrystalline film leads to the so-called back-switching phenomena, reflected in a wide voltage domain for switching (Picinin et al., 2004; Wu et al. 2008). The final consequence is an elongation of the hysteresis loop along the voltage axis and a large difference between the remnant polarization and the saturation polarization. Once the applied external field is removed, a large part of the polarization becomes randomly oriented due to local fields generated by the charged defects, and because of the incomplete compensation of the depolarization field. These phenomena are not present in the epitaxial film, where the saturation polarization is practically equal with the remnant polarization, fact which leads to a rectangular shape of the hysteresis.

The way to interpret the linear part of the hysteresis loop will be discussed later on in the chapter. The microstructure will have a strong effect on the current-voltage characteristics (I-V) as well (see figure 4).

Regarding the I-V characteristics from figure 4, it can be seen that the current density increases as the quality of the film is enhanced. This fact is consistent with the discussion regarding the hysteresis loop. A very good epitaxial film is associated to a low resistivity, suggested by the rectangular shape of the hysteresis, thus the current density is high. In polycrystalline films, all the structural defects, especially the grain boundaries, are affecting the charge transport either by trapping carriers (lower concentration) or by scattering the

carriers (lower mobility). The effect is a significant increase in the resistivity, reflected in a lower current density compared to the epitaxial layers.

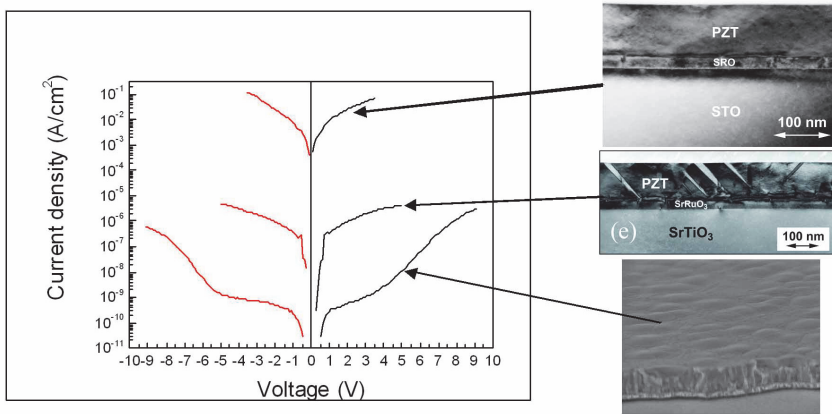


Fig. 4. The I-V characteristics in the case of PZT films with different structural qualities. In all cases the electrodes were from the same metal.

An interesting phenomenon was observed in the epitaxial films, while analyzing the recorded charge and current hysteresis loops. We remind here that the actual equipments used for investigating the ferroelectric properties of thin films allows the simultaneous recording of the current and of the integrated charge which gives the hysteresis loop. It was observed that in the films containing defects spreading from one electrode to the other the hysteresis loop opens in a strange way (see figure 5). At low voltages the film shows a very large leakage current and no ferroelectric hysteresis. By the gradual increase of the applied voltage, at some voltage value, the leakage current drops abruptly and the well-known shape of the ferroelectric hysteresis is obtained. This phenomenon can be explained by admitting that the defects spreading between the electrodes can act as conduction paths, of very low resistance, leading to large currents at relatively low voltages. At some voltage, these paths breakdown similar to a normal fuse in an electric circuit, thus the high conduction paths disappear and the behavior of the ferroelectric film returns to normal. This assumption is supported by the finding that stacking faults occur in ferroelectric thin films, where an oxygen atom is missing, leading to a row of Pb atoms between electrodes acting as metal wires in a fuse (Vrejoiu & al., 2006). Threading dislocations may also play the role of low conduction paths. The “fuse like” behavior is not present in high quality films, free of stacking faults or dislocations.

Considering the effect of microstructure on the current density and on the shape of the I-V characteristics, it is natural to assume that the conduction mechanisms are different in epitaxial and polycrystalline films. Further on in the chapter only the epitaxial films will be considered. This is because the interest is to obtain information about the intrinsic properties of the material. Such information can be obtained by using single crystal-like quality films, not polycrystalline samples. In the last case the intrinsic properties of the material are masked by the dominance of the extrinsic contributions coming from the structural defects. Therefore, it is not recommended to take the values obtained for dielectric constant, polarization, resistivity, etc. in the case of polycrystalline films as materials constant for a

certain ferroelectric material. These quantities are too much dependent on microstructure, which explains very well the large spread of values in the literature, covering orders of magnitude. In order to obtain the intrinsic properties it is necessary to use high quality epitaxial films, and even in this case the results may be altered by the presence of point defects and of the strain imposed by the substrate. In any case the results are much closer to the intrinsic values than in the case of polycrystalline films.

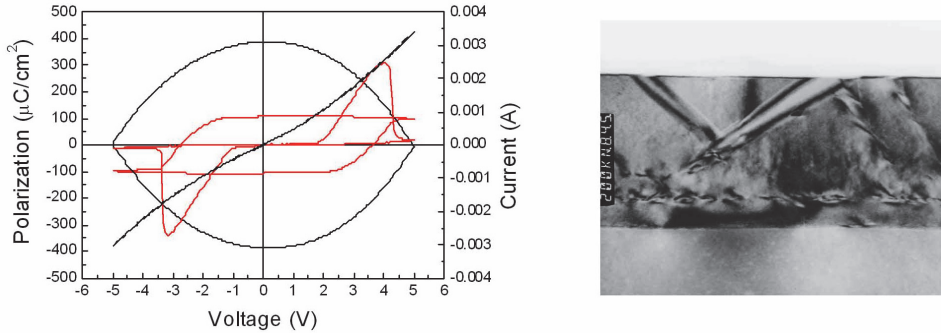


Fig. 5. Left-the hysteresis loops obtained on a fresh contact (black line) and on the same contact after a few cycles up to high voltages to breakdown the high conduction paths existing in the defective epitaxial film. The microstructure is shown in the right TEM photograph.

### 3. Conduction mechanisms in some representative ferroelectric materials

In the following pages the conduction mechanisms in epitaxial films of PZT20/80, BaTiO<sub>3</sub> and BiFeO<sub>3</sub> will be analyzed. All the films were grown by pulsed laser deposition on SrRuO<sub>3</sub>/SrTiO<sub>3</sub> (SRO/STO) substrates. We mention here that the identification of the dominant conduction mechanism had required extensive current measurement at different temperatures and thicknesses of the films.

#### 3.1 Conduction mechanism in epitaxial PZT20/80

A series of high quality epitaxial PZT20/80 films, with different thicknesses, were grown by PLD in order to investigate the charge transport mechanism (Vrejoiu & al., 2006). The thickness dependence of the I-V characteristics measured at room temperature is presented in figure 6. It can be observed that:

- The characteristics are relatively symmetric with voltage polarity, and they have the same shape. However, the small asymmetry for positive and negative voltages suggests that the Pool-Frenkel emission from the traps is not the dominant conduction mechanism, as the I-V characteristic should be symmetric in this case.
- The spread in current density values is not so large, being below one order of magnitude for thicknesses between 50 nm and 270 nm. This finding suggests that SCLC is not the dominant conduction mechanism in epitaxial PZT. In the case of SCLC mechanism the current density varies as  $d^{-3}$ , where  $d$  is the thickness. For a 5 times thickness variation the current density should differ with more than two orders of magnitude, which is not the case.

It can be concluded that the dominant conduction mechanism at room temperature is not bulk limited, but is interface limited (Pintilie L. & al., 2007). Current measurements at different temperatures were performed in order to distinguish between Schottky emission over the barrier and Fowler-Nordheim tunneling through the potential barrier at the metal-PZT interface. The results of the temperature measurements are presented in figure 7.

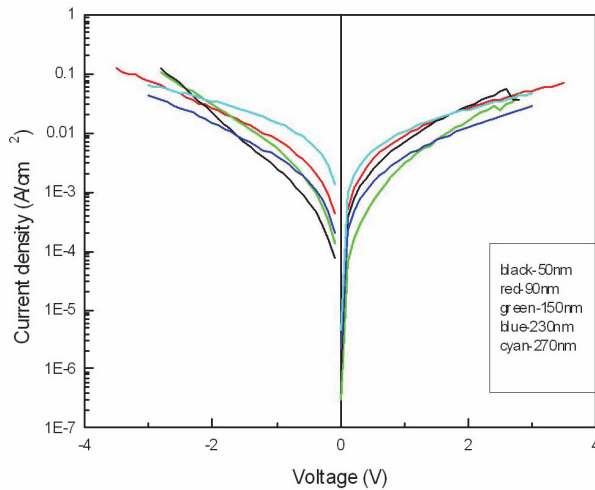


Fig. 6. The thickness dependence of the I-V characteristics in the case of epitaxial PZT20/80 films. Measurements performed at room temperature. The delay time for current measurements, meaning the time between changing the voltage and reading the current, was 1 second.

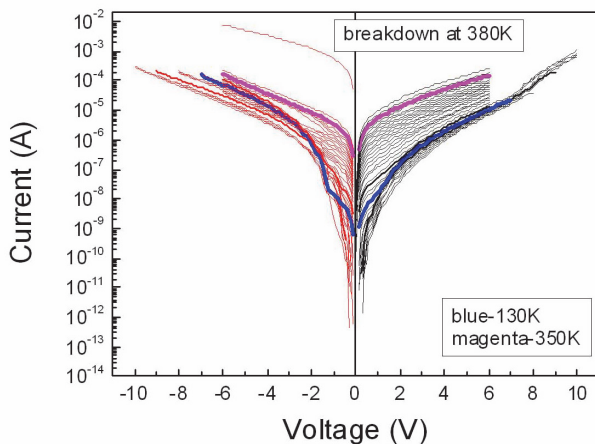


Fig. 7. The temperature dependence of the I-V characteristics in the case of epitaxial PZT20/80 films. Measurements performed on a sample with thickness of 230 nm.

The temperature measurements had revealed two temperature domains:

- Below 130 K the FN tunneling is the dominant conduction mechanism, the current density being practically independent of temperature.
- Between 130 K and 350 K the dominant conduction mechanism is the Schottky emission. Over 350 K the film suffer breakdown.

It is interesting to note also that the asymmetry is more pronounced at low temperatures. This is due to the fact that the two SRO/PZT interfaces were processed slightly different. The bottom one had suffered a temperature annealing during the deposition of the PZT film and is influenced by the strain imposed by the thick STO substrate. The top SRO/PZT interface had suffered a shorter temperature annealing and is less exposed to strain. Therefore, the density of the interface defects affecting the interface properties can be different. This fact can induce asymmetry at different temperatures if one considers that the occupancy of the interface states is temperature dependent. Further on calculations will be made only for the positive part of the I-V characteristic, which is assumed to be related to the bottom SRO/PZT interface (less defective interface). The analysis was done by using the following equation for the current density (Cowley & Sze, 1965; Levine, 1971):

$$J = A^* T^2 \exp\left(-\frac{q}{kT}\left(\Phi_B^0 - \sqrt{\frac{qE_m}{4\pi\epsilon_0\epsilon_{op}}}\right)\right) \quad (4)$$

where  $A^*$  is Richardson's constant,  $\Phi_B^0$  is the potential barrier height at zero applied field,  $E_m$  is the electric field,  $T$  is the temperature, and  $\epsilon_{op}$  is the dynamic (high frequency) dielectric constant. The electric field  $E_m$  should be the maximum field at the Schottky interface. Two representations can be used:

- One at constant temperature

$$\ln\left(\frac{J}{T^2}\right) \sim \ln(A^*) - \frac{q\Phi_B^0}{kT} - f(V^{1/2}) \quad (5)$$

- One at constant voltage

$$\ln\left(\frac{J}{T^2}\right) \sim \ln(A^*) - \frac{q}{kT}\Phi_{app} \quad (6)$$

The apparent potential barrier at a give voltage  $V$  is given by:

$$\Phi_{app} = \Phi_B^0 - \sqrt{\frac{qE_m}{4\pi\epsilon_0\epsilon_{op}}} \quad (7)$$

Details regarding calculations and discussion can be found elsewhere (Pintilie L. & al., 2007). Important fact is that the potential barrier rendered by using the classical equation for thermionic (Schottky) emission over the potential barrier is of only 0.12-0.13 eV, which is very low compared to other reports on polycrystalline PZT films. Another problem is that the value of the effective Richardson's constant is too low, of about  $10^{-7}$  A/cm<sup>2</sup>K<sup>2</sup>. The conclusin is that the classical Schottky emission is not working properly in this case. This theory can be used only if the mean free path of the injected carriers is larger than the film

thickness. In the case of ferroelectrics, even they are of epitaxial quality, the mean free path is of about 10-20 nm. This value is considerably lower compared to the film thickness, which is usually above 100 nm. For the case when the mean free path is smaller than the film thickness then the Schottky-Simmons equation has to be used (Simmons, 1965):

$$J = 2q \left( \frac{2\pi m_{eff} kT}{h^2} \right)^{3/2} \mu E \exp \left( -\frac{q}{kT} \left( \Phi_B^0 - \sqrt{\frac{qE_m}{4\pi\epsilon_0\epsilon_{op}}} \right) \right) \quad (8)$$

$m_{eff}$  stands for the effective mass, and  $\mu$  is the carrier mobility in PZT. The following representation was used to obtain the potential barrier:

$$\ln \left( \frac{J}{T^{3/2}} \right) = \ln \left( 2q \left( \frac{2\pi m_{eff} k}{h^2} \right)^{3/2} \mu E \right) - \frac{q}{kT} \left( \Phi_B^0 - \sqrt{\frac{qE_m}{4\pi\epsilon_0\epsilon_{op}}} \right) \quad (9)$$

The obtained value is of only 0.12 eV, like in the case of classical Schottky emission. The solution to explain such a low value for the potential barrier is to take into consideration the fact that the ferroelectric polarization is affecting the maximum electric field at the interface, like in equation (2). Considering equation (2) in equation (8), there can be two possibilities:

1.  $\sqrt{\frac{2qN_{eff}V}{\epsilon_0\epsilon_{st}}} \ll \frac{P}{\epsilon_0\epsilon_{st}}$  then the current density can be written as:

$$J = 2q \left( \frac{2\pi m_{eff} kT}{h^2} \right)^{3/2} \mu E \exp \left( -\frac{q}{kT} \left[ \left( \Phi_B^0 - \sqrt{\frac{qP}{4\pi\epsilon_0^2\epsilon_{op}\epsilon_{st}}} \right) - \sqrt{\frac{2q^2N_{eff}V}{8\pi\epsilon_0\epsilon_{op}P}} \right] \right) \quad (10)$$

From equation (10) it can be seen that the potential barrier is reduced with a term depending on ferroelectric polarization. The „apparent” potential barrier, the one which is estimated from the graphical representation (9), is:

$$\Phi_{app}^0 = \Phi_B^0 - \sqrt{\frac{qP}{4\pi\epsilon_0^2\epsilon_{op}\epsilon_{st}}} \quad (11)$$

The real potential barrier can be obtained after adding the polarization term. For the epitaxial PZT the polarization is around 100  $\mu\text{C}/\text{cm}^2$ , while the static and optic dielectric constants are 80 and 6.5 respectively. With this numbers, the contribution of the polarization term in equation (11) is about 0.6 eV. This value must be added to the one of 0.13 eV obtained from the graphical representation, leading to a potential barrier at zero volts of about 0.73 eV.

2.  $\sqrt{\frac{2qN_{eff}V}{\epsilon_0\epsilon_{st}}} \gg \frac{P}{\epsilon_0\epsilon_{st}}$  then the current density can be written as:

$$J = 2q \left( \frac{2\pi m_{eff} kT}{h^2} \right)^{3/2} \mu E \exp \left( -\frac{q}{kT} \left( \Phi_B^0 - \sqrt{\frac{q}{4\pi\epsilon_0\epsilon_{op}}} \sqrt{\frac{2qN_{eff}(V + V_{bi}')}{\epsilon_0\epsilon_{st}}} \right) \right) \quad (12)$$

Returning to the equation (8) and to the representation (9), the pre-exponential term is dependent on the applied electric field. It was found that the pre-exponential term has a linear dependence on the applied voltage. This fact suggests a non-zero electric field in between the depleted regions located near the electrode interfaces (see figure 8).

The mobility of the carriers was estimated from the pre-exponential term in equation (8) and a value of about  $10^{-6}$  cm<sup>2</sup>/Vs was obtained. This low value is a consequence of the polar order, similar to the phenomenon observed in AlGaIn. It was shown in this case that the mobility can be reduced from about 3000 cm<sup>2</sup>/Vs to less than 10 cm<sup>2</sup>/Vs just because the high polarity of the material (Zhao & Jena, 2004). The effective mass used to estimate the mobility was about  $0.8m_0$  ( $m_0$  is the mass of the free electron), and was deduced from the current-voltage characteristics at low temperature, where the Fowler-Nordheim tunneling is dominant. It can be concluded that in epitaxial PZT films of very good quality the dominant conduction mechanism is a combination between interface limited injection and bulk limited drift-diffusion, and that the electric field is non-zero throughout the film thickness.

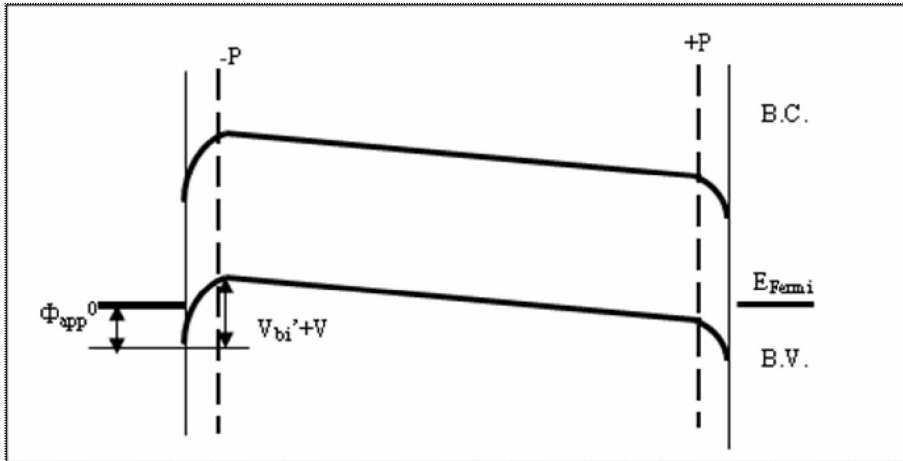


Fig. 8. The electric field distribution inside a ferroelectric PZT thin film. Near the electrodes the electric field is given by equation (2), while in the volume is an uniform field given by  $V/d$ , where  $d$  is the film thickness. The other notations are: B.C.-conduction band; B.V.-valence band;  $E_{Fermi}$ -the Fermi level; P-ferroelectric polarization;  $\Phi_{app}^0$ -the apparent potential barrier at zero volts given by equation (11);  $V_{bi}'$ -the built-in voltage given by equation (1).

### 3.2 Conduction mechanism in epitaxial BaTiO<sub>3</sub>

The conduction mechanism in epitaxial BaTiO<sub>3</sub> was investigated on a set of samples with different thicknesses (Pintilie L., 2009; Petraru et al., 2007). The corresponding I-V characteristics are shown in figure 9, for room temperature.

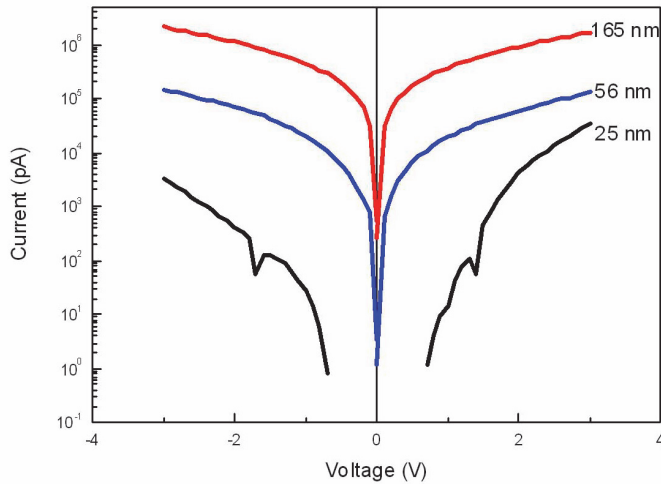


Fig. 9. I-V characteristics at room temperature for epitaxial films with different thicknesses. The electrodes were of SRO/PT with an area of 40x40 microns.

It is interesting to note that, contrary to the PZT films where no significant thickness dependence was observed (see figure 6), in the case of the BaTiO<sub>3</sub> films there is an increase of the current with the thickness of the film. This fact is unusual for ferroelectrics, where the current is expected to increase with decreasing the thickness. The only mechanism which allows an increase of the current with thickness is the hopping conduction (Rybicki et al., 1996; Angadi & Shivaprasad, 1986). The hopping can be thermally activated or of variable range. These two have different temperature dependencies. The thermally activated hopping of small polaron has the following temperature dependence (Boettger & Bryskin, 1985):

$$\sigma \sim T^{-3/2} \exp\left(-\frac{W_a}{kT}\right) \quad (13)$$

Here  $T$  is the temperature and  $W_a$  is the activation energy for the hopping mechanism. In the case of the variable range hopping the temperature dependence is (Demishev et al., 2000):

$$\sigma \sim \exp\left[-\left(\frac{T_0}{T}\right)^n\right] \quad (14)$$

Here  $T_0$  is a characteristic temperature for the hopping conduction. The exponent  $n$  is  $1/4$  for 3D systems (bulk), while for 2D systems (thin films) is  $1/3$  and for 1D systems (wires) is  $1/2$ . The graphical representations of equations (13) and (14) are presented in figure 10. Although at very low temperatures is hard to decide between the two hopping mechanisms, it seems that at higher temperature the thermally activated hopping of small polaron is most probable mechanism in BaTiO<sub>3</sub> epitaxial films. The activation energy for the high temperature range was estimated to about 0.2 eV.

Another problem is the non-linearity of the I-V characteristic. The following equation for the current density could explain the non-linearity:

$$j \sim \sinh\left(\frac{qEa}{2kT}\right) \exp\left(-\frac{W_a}{kT}\right) \tag{15}$$

Here  $a$  is the distance between the nearest neighbors.

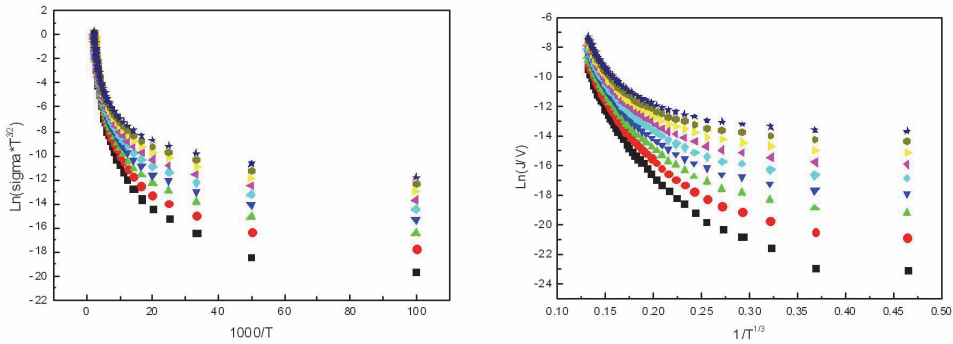


Fig. 10. The representation of equation (13) on the left and of the equation (14) on the right. The representations were made for different voltages applied on the film of 165 nm thickness.

The current is represented as a function of  $\sinh(\alpha V)$  at constant temperature, where  $\alpha$  is given by  $(qa)/(2kTw)$ , with  $w$  being the thickness of the layer over which the voltage drop is equal with the applied voltage  $V$ . These representations, shown in figure 11 for two temperatures, have to be linear if the equation (15) is valid.

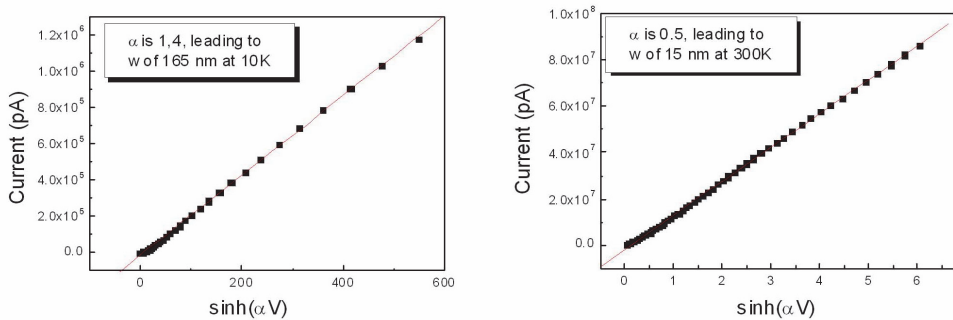


Fig. 11. The representation of the current as a function of  $\sinh(\alpha V)$  at two different temperatures, in accordance with the equation (15). The data are for the BaTiO<sub>3</sub> film of 165 nm thickness.

The linearity is obtained by adjusting the parameter  $\alpha$ , which means the change in the thickness  $w$ . At very low temperatures the value obtained for  $w$  is of 165 nm, which is the same with the film thickness. At room temperature the value for  $w$  is of about 15 nm, much lower than the film thickness. All the estimations were made considering a value of about 4 angstroms between nearest neighbors. The results suggest that the BaTiO<sub>3</sub> film is fully

depleted at low temperatures, and is only partly depleted at room temperature. It maybe that the thickness of 15 nm is the thickness of the depletion region at room temperature. This is the high resistivity part of the film, and most of the applied voltage drops on it (Zubko et al., 2006).

The above presented data convey to the conclusion that the most probable conduction mechanism in epitaxial BaTiO<sub>3</sub> film is the thermally activated hopping of small polarons. Going further, it can be that the injection in the film is still interface controlled like in PZT, with the difference that the movement of the injected carriers inside the film is no longer through a band conduction mechanism like in PZT but is through a hopping mechanism in a narrow band located in the gap and associated to some kind of structural defects. An example can be the oxygen vacancies, which can arrange along the polarization axis allowing the hopping of injected electrons from one vacancy to the other.

It is interesting to remark that two ferroelectric materials, with very similar crystalline structures (both are tetragonal perovskites in the ferroelectric phase) and with similar origin of ferroelectricity, show different electric properties especially regarding the charge transport. A possible explanation for this difference can be that the Ba-O bond is an almost ideal ionic bond while the Pb-O one has a significant degree of covalency. Therefore, BaTiO<sub>3</sub> behaves like a ferroelectric dielectric and PZT20/80 behaves like a ferroelectric semiconductor. There are some theoretical studies showing that the higher is the covalency of the A-O bond (the general formula of perovskites is ABCO<sub>3</sub>), the higher is the Curie temperature because the electrons shared between the A and O atoms help to stabilize the ferroelectric polarization at higher temperatures than a pure ionic bond (Kuroiawa et al., 2001).

### 3.3 Conduction mechanism in epitaxial BiFeO<sub>3</sub>

A very interesting ferroelectric material is BiFeO<sub>3</sub>. The difference compared to BaTiO<sub>3</sub> and PZT is that BiFeO<sub>3</sub> is also antiferromagnetic, thus is a multiferroic, and that the origin of the ferroelectricity is electronic (lone pair) and is not related to ionic displacements. Its band gap is also smaller, around 2.8 eV compared to around 4 eV in the case of PZT or BaTiO<sub>3</sub> (Wang et al., 2003). It is thus expected to have a larger leakage current in BiFeO<sub>3</sub> films than in other perovskite ferroelectric layers (Nakamura et al., 2009; Shelke et al., 2009). This fact would be detrimental for recording the hysteresis loop. However, good Schottky contact can limit the leakage allowing hysteresis measurements in good conditions.

The charge transport was extensively studied in BiFeO<sub>3</sub> films of about the same thickness (100 nm) but grown with different orientations ((100), (110) and (111)). The orientation was imposed by the substrate, which was in all cases SrTiO<sub>3</sub> single crystal. The bottom contact was SrRuO<sub>3</sub>, while the top contact was Pt. The I-V measurements were performed at different temperatures. The results are shown in figure 12 (Pintilie L. et al., 2009)

In all cases a significant increase of the current density with temperature can be observed. This fact strongly suggests a conduction mechanism like Pool-Frenkel emission from the traps or Schottky emission over potential barrier at the metal-ferroelectric interface. The relative symmetry of the I-V characteristic supports the Pool-Frenkel emission from the traps. Complementary C-V measurements have revealed an asymmetric behavior, which is not possible if the capacitance is dominated by the bulk but is possible if the interface related capacitances dominate the overall capacitance of the MFM structure.

Considering all these results, the I-V characteristics were analyzed similar to the PZT20/80 films (see sub-chapter 3.1). Equation (10) was used to extract the  $V^{1/2}$  dependency (see figure 13) of the apparent potential barrier and then the apparent potential barrier at zero volts, given by the equation (11), was extracted from the intercept at origin.

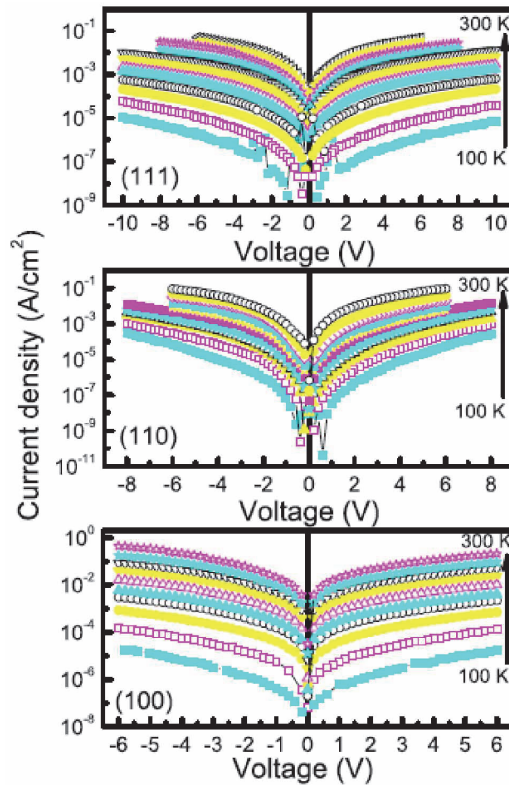


Fig. 12. The I-V characteristics at different temperatures for  $BiFeO_3$  films with different orientations (these are mentioned in the down-left corner of the graphic).

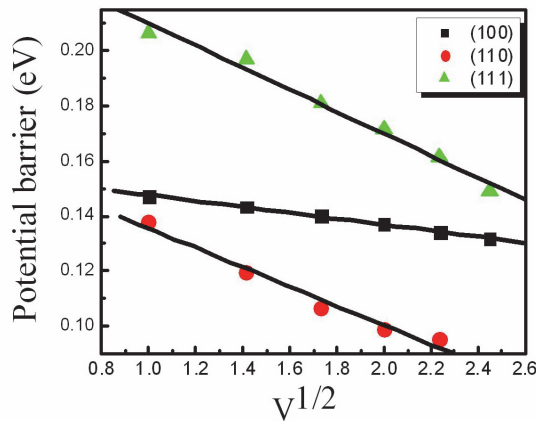


Fig. 13.  $V^{1/2}$  dependence of the apparent potential barrier for  $BFO$  films deposited on  $STO$  substrates with different orientations.

In order to estimate the true potential barrier at zero volts it is necessary to know the value of the ferroelectric polarization and of the dielectric constant. Figure 14 shows the hysteresis loops recorded for the three orientations of the BiFeO<sub>3</sub> films.

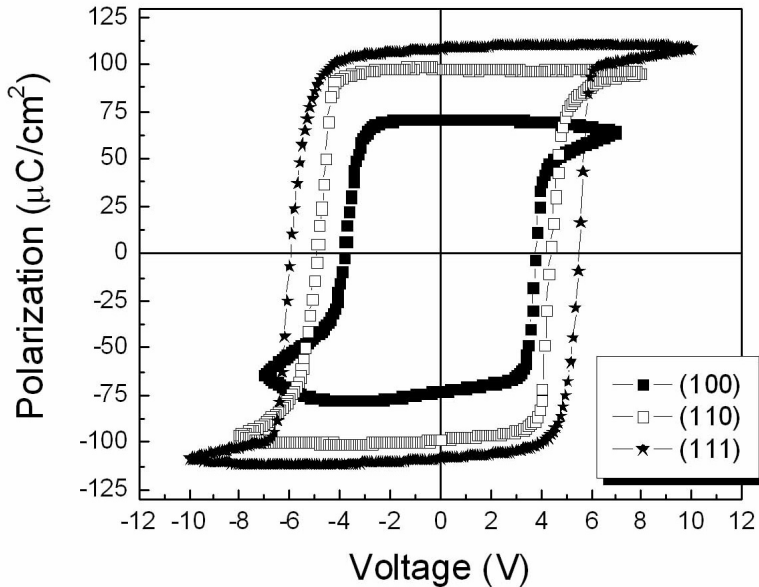


Fig. 14. The hysteresis loops for BiFeO<sub>3</sub> films with different orientations.

The values for the static dielectric constant were determined from capacitance measurements at 1000 Hz. The value of the optical dielectric constant was taken as 5.6. The estimated values for the potential barriers are given in Table I.

Orientation	Polarization ( $\mu\text{C}/\text{cm}^2$ )	Static dielectric constant	True potential barrier estimated using the equation (11) (eV)
(100)	73	102	0.62
(110)	102	83	0.77
(111)	115	73	0.92

Table 1. The orientation dependence of spontaneous polarization  $P_S$ , static dielectric constant  $\epsilon_{st}$ , and true potential barrier at zero field  $\Phi_B^0$ .

The highest potential barrier is obtained for the (111) orientation, which is consistent with the current measurements (showing the lowest current density for this orientation) and with the results of hysteresis measurements (showing that for (111) orientation the hysteresis loop is the less affected by the leakage current).

It can be concluded that the leakage current in BiFeO<sub>3</sub> films can be reduced by engineering the potential barrier at the metal-ferroelectric interface. This leads us to the next chapter,

which is discussing the effect of the metal electrode on the electric properties of ferroelectric thin films.

#### 4. The influence of the metal electrodes on the electric properties of ferroelectric thin films

##### 4.1 The case of epitaxial PZT thin films

Several metals were tested as electrodes on the same epitaxial PZT20/80 thin film deposited on SRO/STO substrate (see figure 15, showing that all the electrodes were deposited, by using shadow masks, on the same film). This allowed ones to compare the electrical properties of the same PZT film, with the same bottom SRO contact, but with different top metals as electrodes (Pintilie L. et al., 2008). Practically the bottom interface is the same in all cases, just the top metal-ferroelectric interface is changed by changing the metal.

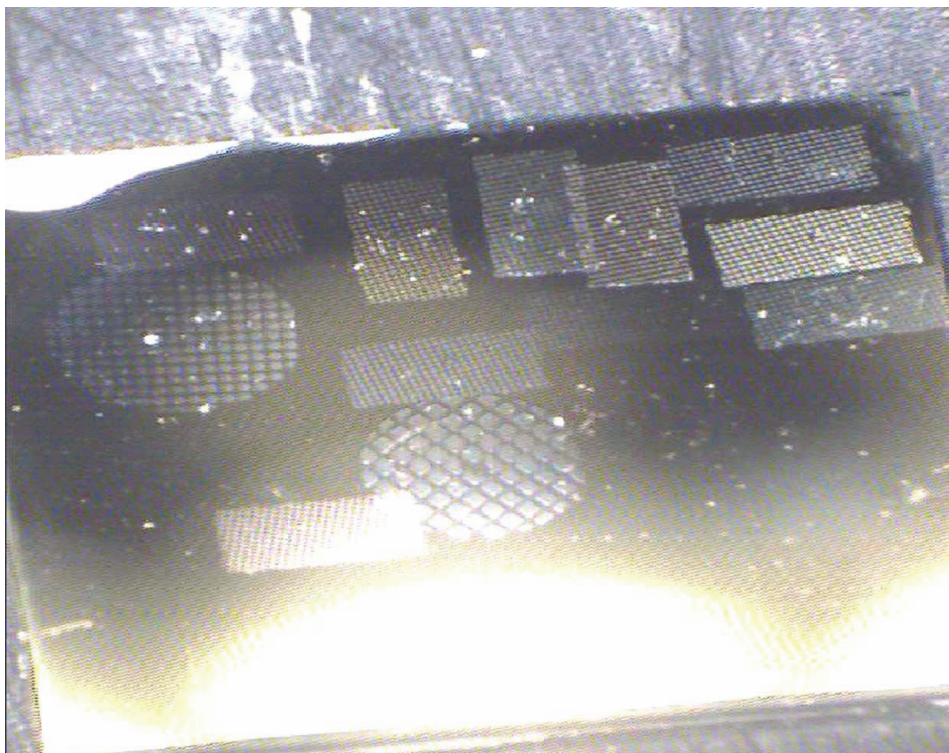


Fig. 15. Photograph showing different metal electrodes deposited on the same epitaxial PZT20/80 film.

The main properties of metals used as electrodes are presented in the Table II. The metals can be divided in three main categories: with complete d-shell (Pd, Au, Cu and Ag); with incomplete d-shell (Pt, Ni, Cr and Ta); without d-electrons (Al).

Standard electrical measurements were performed: hysteresis; I-V and C-V characteristics. The main results are presented in figures 16-18.

Metal	Work Function	Electronegativity
Pd	5.12	2.20
Au	5.1	2.40
Cu	4.65	1.90
Ag	4.26	1.93
Pt	5.65	2.20
Ni	5.15	1.91
Cr	4.5	1.66
Ta	4.25	1.50
Al	4.28	1.61

Table 2. Work function and electronegativity for the metals used as top contacts.

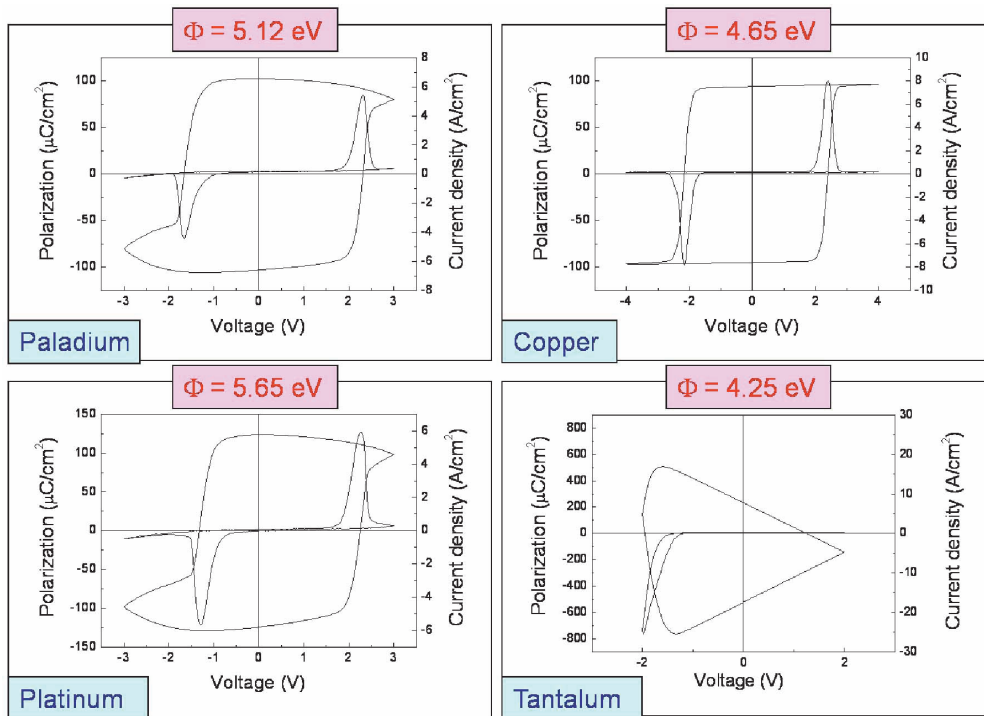


Fig. 16. Hysteresis loops obtained in the case of four representative metals from Table II, used as top electrodes on the same epitaxial PZT20/80 film.

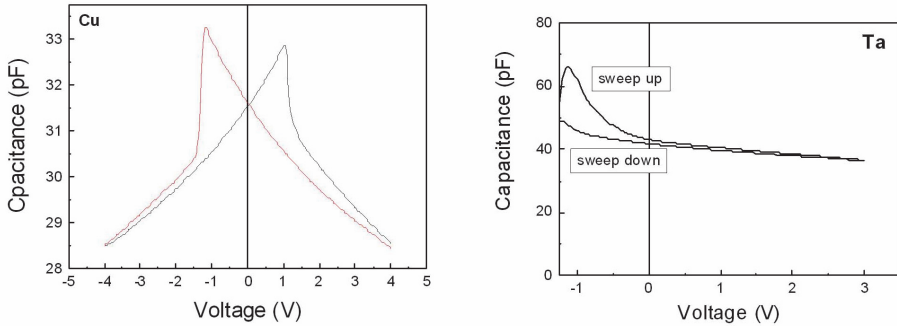


Fig. 17. C-V characteristics in the case of the two metals giving the extreme results in the electric measurements. The Cu electrode gives the best results compared to the other metals, including Ta. The electrode area was the same for the two metals.

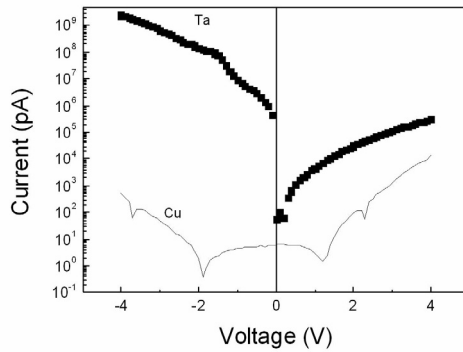


Fig. 18. The I-V characteristics, measured in the same conditions at room temperature, for the two metals with extreme results in the electric measurements. The electrode area was the same for the two metals.

Analyzing the results of the electrical measurements, several interesting conclusions could be drawn:

- The value of the static dielectric constant is dependent on the metal used as the top electrode. This fact can be seen from figure 19. We remind here that the capacitance measurements were performed in the same conditions for all the metals used as top electrodes. This is a very interesting result supporting the idea that, at least in the case of epitaxial PZT films, the capacitance of the MFM structure is dominated by the interfaces and has nothing in common with the intrinsic value of the ferroelectric material itself. The finding is in line with other studies showing that the static dielectric constant in the case of PZT films, even they are of epitaxial quality, is dominated by extrinsic contributions, and that the intrinsic dielectric constant of the PZT without defects and metal interfaces is of low value (Sai et al., 2002; Ang & Yu, 2004).
- There is no correlation between the current density and the work function of the metals used as top electrodes. As can be seen from the above presented data, the best results in term of leakage current are given by Cu top electrodes, although the work function of

Cu is lower than for Pt or Au. There is some correlation between the magnitude of the leakage current and electronegativity or the number of electrons on the d-shell. It was observed that the leakage current increases as the electronegativity and the number of the electrons on the d-shell decreases. In any case, further studies are needed in order to fully understand the way in which the metal-ferroelectric interface is forming while the metal contact is deposited. Recent studies have shown that both the potential barrier and the polarization can be tuned by using different metals as electrodes, partly confirming the experimental results presented in this study (Prabhumirashi & Dravid, 2005; Dong et al. 2006; Nunez & Nardelli, 2008).

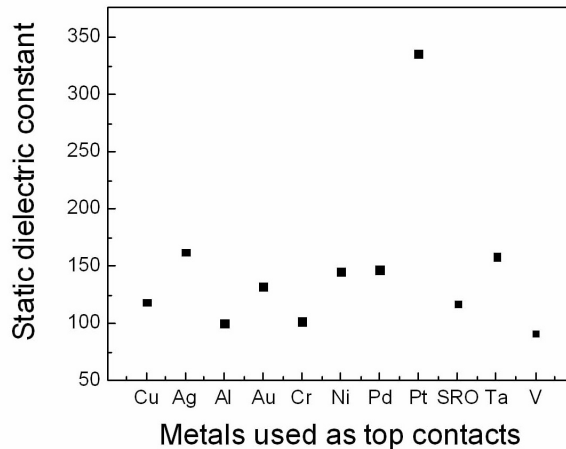


Fig. 19. The dielectric constant calculated from the capacitance of the MFM structures realized by depositing different top metals on the same PZT20/80 film, with the same bottom SRO electrode.

It was studied the influence of different metals used as top electrodes on a PZT polycrystalline film deposited by sol-gel on a Pt/Si substrate. In this case the bottom electrode is in all cases Pt. Only the hysteresis loops will be presented in figure 20.

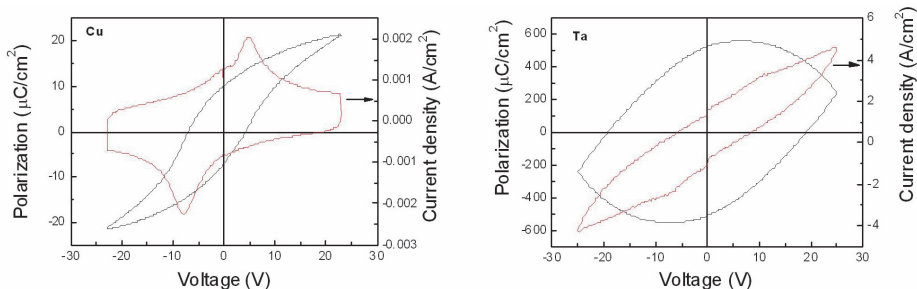


Fig. 20. The hysteresis loops, polarization and corresponding current, obtained in the case of top Cu and Ta contacts used on a polycrystalline PZT film deposited by sol-gel on Pt/Si substrate.

The results are only partly similar with those obtained in the case of epitaxial films with the same metals as top contacts. It can be seen that the leakage current has significantly increased when Ta is used as top contact. This fact affects the hysteresis loop, which is inflated and is losing its specific shape for ferroelectrics. However, the loops are symmetric in both cases. By contrast, the hysteresis loop is completely asymmetric when Ta is used on epitaxial films (see figure 16). It appears that the bulk contribution is dominant in the case of polycrystalline films, although the injection of the charge carriers is still controlled by the potential barrier at the electrodes, which are different from one metal to another. It is not clear yet why the Cu gives almost symmetric loops both for epitaxial and polycrystalline films, especially considering that the bottom electrode is different: SRO for epitaxial and Pt for polycrystalline. A possible explanation can be that the ferroelectric polarization is controlling the band alignment at the metal interfaces and, by consequence, the potential barriers. This effect is pregnant in the case of epitaxial films, while in the case of polycrystalline ones is somehow smeared by the grain boundaries interposed between the two metal-PZT interfaces.

#### 4.2 The ferroelectric Schottky diode

From the results presented in the previous paragraph it was concluded that Ta forms an ohmic contact on epitaxial PZT. This fact allowed the construction and characterization of the first single ferroelectric Schottky diode presenting the specific features in both I-V and C-V characteristics (see figure 17 for the C-V characteristic and figure 21 for the I-V characteristic).

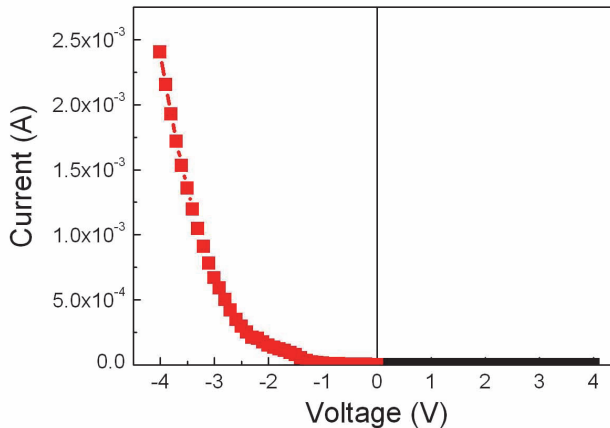


Fig. 21. The I-V characteristics in the case of a Ta-PZT-SRO single ferroelectric Schottky diode. The rectifying ratio at 3 V is larger than  $10^4$ .

Very similar results were obtained using Al top contacts on epitaxial PZT-SRO structures. The corresponding C-V and I-V characteristics are presented in figure 22.

Without going into further details, it appears that ferroelectric Schottky diodes can be obtained by using metals with few electrons on the d-shell or with no d-shell at all as top contacts on epitaxial PZT-SRO structures.

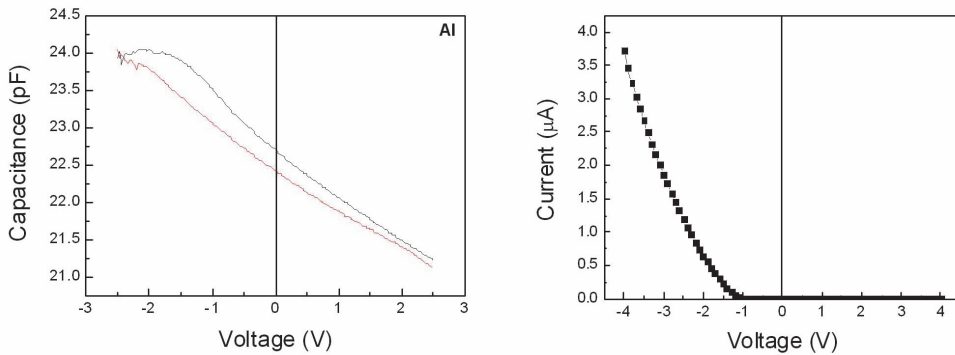


Fig. 22. The C-V characteristic (left) and the I-V characteristics (right) in the case of an Al-PZT-SRO ferroelectric Schottky diode.

## 5. Other properties related to the charge transport in ferroelectric thin films

### 5.1 The hysteresis loop

The hysteresis loop is obtained by integrating the current flowing through the MFM structure and the external circuit during the polarization reversal. The true current and the corresponding integrated charge are given by:

$$j(V) = j_l(V) + j_{tr}(V) + \frac{\partial D(V)}{\partial t} \quad (16)$$

$$Q(V) = \int j_l(V)dt + \int j_{tr}(V)dt + D(V)$$

Here the notations are:  $j_l$ -the leakage current;  $j_{tr}$ -the emission current from the traps;  $D$ -electric displacement;  $V$ -applied voltage;  $Q$ -integrated charge. In the ideal case, of an insulating ferroelectric with perfect structure, the leakage current and the emission current from the traps at constant voltage are null and the result is the well known theory of the Sawyer-Tower circuit. However, in ferroelectric thin films both  $j_l$  and  $j_{tr}$  components can be different from zero. It is clear that the main contribution can come from the leakage current, which is present in any ferroelectric thin film no matter the crystalline quality. The larger is the leakage current the larger will be its contribution to the integrated charge  $Q$ . The consequence can be a significant alteration of the hysteresis loop, which become inflated up to the limit when the shape does no longer resemble the specific shape of the ferroelectric hysteresis, making difficult the identification of the ferroelectricity in the studied material. Sometimes this drawback can be overcome by analyzing the current hysteresis. If the current peaks associated to the polarization switching are still visible, then it can be concluded that the material is still ferroelectric. The problem is when the leakage current is so large that it hidden the switching peaks making almost impossible the identification of the ferroelectric phase only from the hysteresis measurements. We remind here that electrical hysteresis can be used to confirm the presence of the ferroelectric phase in a certain material only if:

- The saturation of the ferroelectric polarization is clearly obtained and the linear regime is clearly visible in the loop. It has to be mentioned here that the quantity which is

determined from the hysteresis loops is not exactly the spontaneous polarization of the ferroelectric  $P_s$ , but the electric displacement  $D$ . The two are related through the following equation:

$$D = \epsilon_0 \epsilon E + P_s \quad (17)$$

- Here  $\epsilon$  is the static dielectric constant of the ferroelectric, including the linear response of the material to an applied electric field. When the ferroelectric polarization is saturated, then  $P_s$  is constant and a further increase in  $D$  is possible only through the linear term in  $E$ . An example of an almost ideal hysteresis is presented in figure 23.

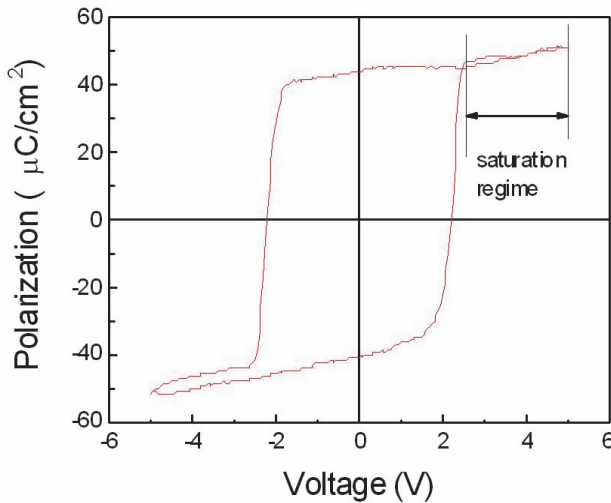


Fig. 23. The hysteresis loop showing the saturation regime of the ferroelectric polarization.

- The remnant polarization should not depend on the measuring frequency of the hysteresis. Usually the hysteresis measurements are performed at frequencies between 100 Hz and 10 kHz. Therefore, a single hysteresis loop at a specific frequency is not an irrefutable fingerprint for the presence of ferroelectricity in the studied material.
- The presence of the ferroelectricity, suggested by the presence of a hysteresis loop, must be confirmed by another quantity showing hysteretic behavior. The easiest way is to look to the current hysteresis recorded during the hysteresis measurements. If the current peaks associated to switching are present, then the materials is almost sure ferroelectric. An independent C-V measurement can bring further confirmation if the characteristic has the specific butterfly shape shown in figure 2.

In conclusion, the hysteresis measurement only is not enough to decide if a material is ferroelectric or not.

Returning to equation (17), it can be seen that the dielectric constant can be estimated from the slope of the hysteresis loop in the saturation (linear) regime. Sometimes it is possible to obtain large values for the dielectric constant, larger than the values obtained from capacitive measurements. This fact can be explained by taking into consideration the contribution of  $j_{tr}$ . This is valid especially if the hysteresis measurement is performed at low

frequencies (1-100 Hz). In this frequency range can be traps responding to the external voltage variations. The capacitance measurements are performed at frequencies higher than 1 kHz, where the traps may be no longer responsive. It is worth to remind that the traps are energetic levels located in the forbidden band and associated to some structural defects such as vacancies, interstitials, or complex defects. During an electrical measurements based on a voltage variation, non-equilibrium carriers are injected into the film. Some of these carriers can be trapped on trapping centers located in the depleted regions associated to the presence of the Schottky contacts at the metal-ferroelectric interfaces. The occupation state of a trapping center is time and temperature dependent, meaning that the trapped carriers can be released in time or by heating to a certain temperature. In the case of the hysteresis measurements the temperature is constant, but the trapped carrier can be released in time if, for example, the period of the hysteresis measurement is longer than the emission time constant of the trapping center. The current obtained in this case is given by (Sze, 1981; Schroder, 1998):

$$I_{tr}(t) = \frac{qAw_tN_{T0}}{\tau} \exp\left(-\frac{t}{\tau}\right) \quad (18)$$

Here the notations are: A-electrode area;  $w_t$ -the width of the depleted region;  $N_{T0}$ -the density of the traps;  $\tau$ -the emission time constant from the traps; t-measuring time. Considering a triangular shape for the applied voltage in a hysteresis measurement, with frequency  $f$  and amplitude  $V_a$ , it can be shown that the integrated charge due to the emission from the traps adds to the total charge  $Q$  in the following form:

$$Q(V) = \left( \frac{\epsilon_0 \epsilon A}{d} - \frac{qAw_tN_{T0}}{4\tau V_a f} \right) V + AP_S(V) \quad (19)$$

Here  $d$  is the thickness of the ferroelectric film. It can be seen that the traps bring a significant contribution to the static dielectric constant:

$$\epsilon_{app} = \epsilon + \frac{qdw_tN_{T0}}{4\epsilon_0\tau V_a f} \quad (20)$$

If the trap density  $N_{T0}$  is null, then the second term in (20) disappear and the dielectric constant is not altered. If the trap density is not null and the frequency is low, then the second term in equation (20) can bring a significant contribution to the static dielectric constant. This contribution decreases with increasing the frequency because the traps are no longer responsive to the applied electric field. The frequency dependence of the dielectric constant evaluated from the saturation part of the hysteresis loop is shown in figure 24. It can be seen that, indeed, the dielectric constant varies as  $1/f$ .

The presence of the traps can affect significantly the electric properties of the ferroelectric thin films. The charged traps generate local electric fields, pinning the polarization and leading to back-switching phenomena (Warren et al., 1994). The consequence is the elongated shape of the hysteresis. They can bring also additive contribution to the dielectric constant and a significant frequency dependence of this quantity. Finally, the traps can alter the density of the free carriers, leading to an apparent increase in the resistivity, and to a lower leakage current when non-equilibrium carriers are injected into the ferroelectric film. In principle, the traps are

unavoidable, but their density and types can be reduced by increasing the crystal quality. In the high quality epitaxial films only point defects are expected, thus the extrinsic effects associated to the presence of traps are very much reduced.

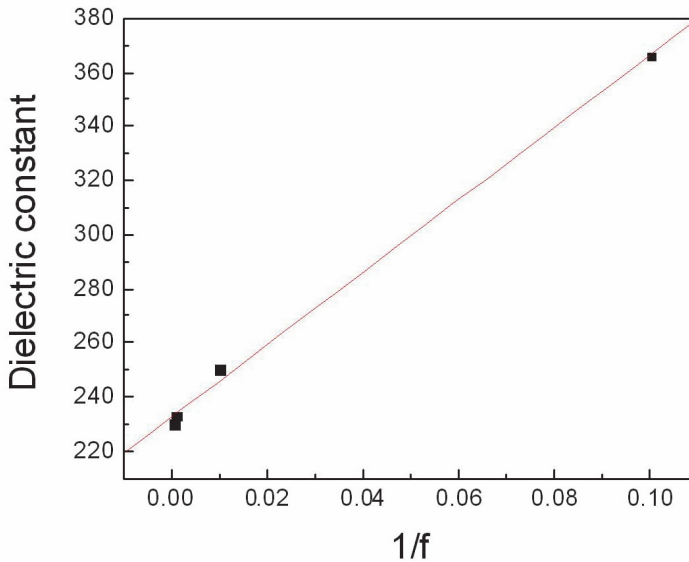


Fig. 24. The frequency dependence of the dielectric constant estimated from the linear part of the hysteresis loop (the saturation regime of spontaneous ferroelectric polarization).

## 5.2 The photoelectric properties of ferroelectrics

The ferroelectric materials with perovskite structure can be regarded as wide gap semiconductors if they are in the form of epitaxial thin films. This assumption is valid mainly for PZT and BiFeO<sub>3</sub> but can work also in the case of BaTiO<sub>3</sub>. The presence of the Schottky contacts, with space charge regions near the electrodes, suggests the presence of the photovoltaic effect similar to the one encountered in semiconductor diode devices (Qin et al., 2009; Yang et al., 2009). This effect is different from the bulk photovoltaic effect which is present in the thick films or in massive ferroelectric ceramics and single crystals. Therefore, the short-circuit current was measured and its relation with the ferroelectric polarization was studied (Pintilie L. et al., 2007). A summary of the main results obtained on epitaxial PZT thin films is presented below:

- The sign of the short-circuit photocurrent is dependent on the orientation of the ferroelectric polarization. In the ideal case the sign should change when the polarization orientation is changed. When an important imprint is present in the film, favoring one of the two orientation of ferroelectric polarization then the photocurrent does not change the sign. The fact that the photocurrent changes the sign when the polarization changes the orientation can be speculated in non-volatile memories as a non-destructive readout procedure of the written information (Kholkin et al., 1997).
- The magnitude of the short-circuit photocurrent depends on the magnitude of the ferroelectric polarization. This is supported by the fact that, for contacts with negligible

imprint, the short-circuit photocurrent describes a hysteresis loop similar to the one described by the ferroelectric polarization when the applied voltage is varied (Yang et al., 2000). Because the magnitude of the polarization is dependent also on the existing imprint in the film, the short-circuit photocurrent is also dependent on the imprint. This fact can be speculated to map the imprint in a ferroelectric film by using a non-destructive method (Pintilie L. et al., 2010).

- The spectral range is in the blue-UV domain. For high quality epitaxial films the maximum sensibility is obtained at wavelengths between 270-290 nm, and can reach values of about 0.1 A/W. This can make the ferroelectric thin films attractive for solid state UV detectors, at least for applications where the magnitude of the generated photo-signal is not so important.
- The ferroelectric Schottky diode shows a significant photovoltaic effect. It was observed that the short-circuit photocurrent is not changing the sign when the polarization orientation was changed by external poling. This is confirming the fact that only one direction of polarization is stable in the ferroelectric Schottky diode.

Short-circuit photocurrent was measured also in polycrystalline films. A typical spectral distribution is shown in figure 25. Short-circuit current was measured also on BaTiO<sub>3</sub> films (see figure 26), as well as in BiFeO<sub>3</sub> films. However, in the last case the magnitude of the short-circuit photocurrent is very much reduced by the presence of high density of free carriers, leading to a high recombination rate.

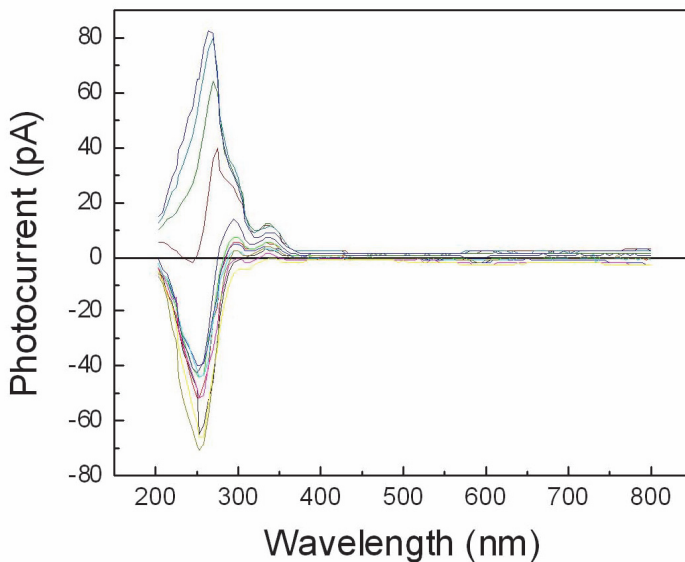


Fig. 25. The spectral distribution of the short-circuit photocurrent measured after poling the polycrystalline PZT film with different applied voltages. It was also observed that the short-circuit photocurrent is present on a large temperature domain (see results presented in figure 27 for PZT films). This fact offers the possibility to study the possible temperature dependence of the energy gap in ferroelectric materials with perovskite structures.

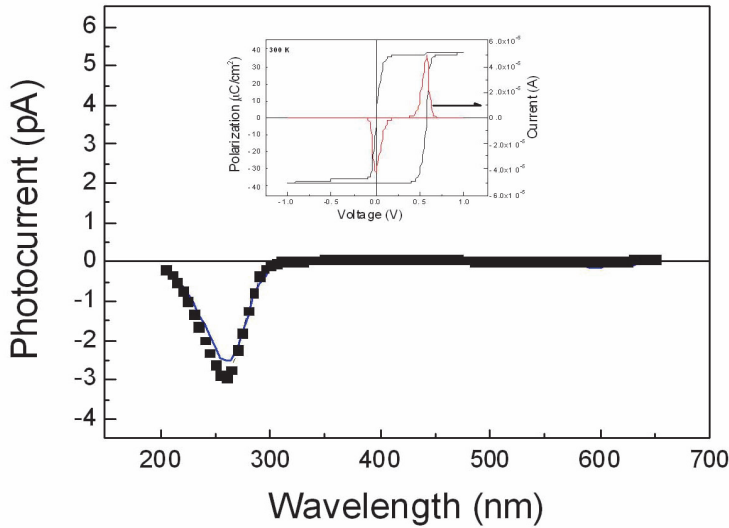


Fig. 26. The spectral distribution of the short-circuit photocurrent in the case of an epitaxial BaTiO<sub>3</sub> film. The inset shows the hysteresis loop for the same film. A large imprint is observed, which is consistent with the fact that the short-circuit photocurrent is not changing the sign when the BaTiO<sub>3</sub> film is poled with opposite applied electric fields which should impose opposite directions for the ferroelectric polarization.

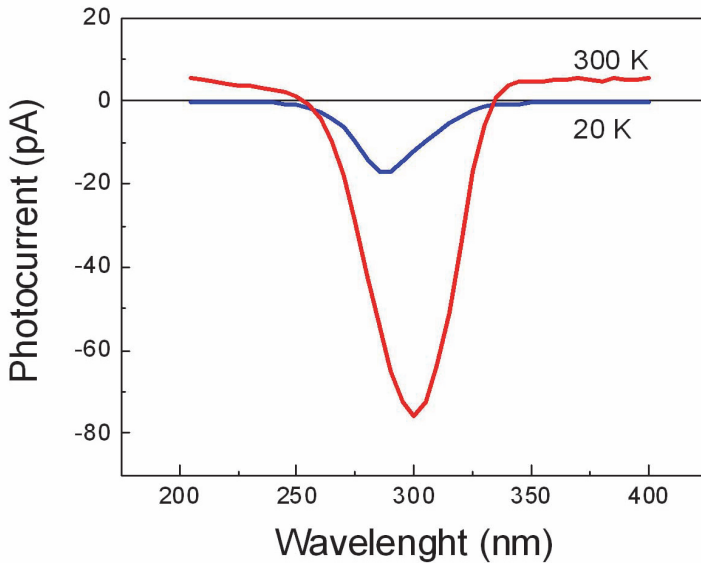


Fig. 27. The spectral distribution of the short-circuit photocurrent in the case of an epitaxial PZT film, at different temperatures. A shift towards shorter wavelengths of the peak sensitivity can be observed at low temperatures compared to room temperature, which can be related to an increase of the energy gap of the PZT

## 6. Conclusions

The results presented above shed some light regarding the charge transport in ferroelectric thin films and its intimate relation with the presence of the ferroelectric polarization. The charge transport can impact all the electric/ferroelectric properties of the ferroelectric thin film. Therefore is not advisable to treat or model separately the experimental results obtained by measuring capacitance, current or hysteresis. The proposed model should be able to simulate all the features observed in the experimental characteristics, including voltage, frequency and temperature dependencies.

In any case, the technological advance in the deposition methods will allow in the near future a more precise control of the structural defects, especially impurities and vacancies. This will be an important step-forward because will allow a more precise control of the free carrier concentration, type and mobility. On the other hand, the in depth understanding of the metal-ferroelectric interface will allow the leakage current control through the precise engineering of the potential barrier at the interface. All these advances will open new perspectives in manufacturing new ferroelectric electronic devices and sensors.

## 7. Acknowledgment

The author acknowledges the financial support from the following agencies and projects: Volkswagen Stiftung under Contract No. I/77738; DINAFER-2-CEEX-06-11-44 project funded by Ministry of Education and Research, Romania; German Science Foundation (DFG) through Contract No. SFB 762; Romanian Ministry of Education and Research through the Contract No. PNII-72-149-HETOX; FP7 project IFOX, grant agreement number 246102.

## 8. References

- Angadi, M. A. & Shivaprasad, S. M. (1986). Temperature-dependent resistivity of discontinuous manganese films, *Journal of Materials Science Letters*, Vol. 5, pp. 405-407, ISSN 0022-2461
- Ang, C. & Yu, Z. (2004). Dielectric behavior of  $\text{PbZr}_{0.52}\text{Ti}_{0.48}\text{O}_3$  thin films: Intrinsic and extrinsic dielectric responses, *Applied Physics Letters*, Vol. 85, No.17, pp. 3821-3823, ISSN: 0003-6951
- Boettger, U. & Bryskin, V. (1985). *Hopping Conduction in Solids*, Akademie Verlag, Berlin, Germany
- Chentir, M; Bouyssou, E; Ventura, L. & Anceau, C. (2009). Leakage current evolution versus dielectric thickness in lead zirconate, titanate thin film capacitors, *Journal of Applied Physics*, Vol.105, No. 6, Article Number 061605, ISSN: 0021-8979
- Cohen, R. E. (1992). Origin of Ferroelectricity in perovskite oxides, *Nature*, Vol. 358, pp. 136-138, ISSN 0028-0836
- Cowley, A. M. & Sze, S. M. (1965). Surface states and barrier height of metal-semiconductor systems, *Journal of Applied Physics*, Vol. 36, No. 10. pp. 3212-3220, ISSN: 0021-8979
- Dawber, M.; Rabbe, K. M. & Scott, J. F. (October 2005). Physics of thin-film ferroelectric oxides, *Review of Modern Physics*, Vol. 77, No. 4, pp. 1083-1130, ISSN 0034-6861

- Demishev, S. V.; Pronin, A. A.; Sluchanko, N. E.; Samarin, N. A.; Lyapin, A. G.; Brazhkin, V. V.; Varfolomeeva, T. D. & Popova, S. V. (2000). 1D–3D Crossover in Hopping Conduction of Carbynes, *JETP Letters*, Vol. 72, No. 7, pp. 381–384, ISSN 0021-3640
- Dong, Y. F.; Wang, S. J.; Feng, Y. P. & Huan, A. C. H. (2006). Chemical tuning of band alignments for metal gate/high-k oxide interfaces, *Physical Review B*, Vol. 73, No. 4, Article Number 045302, ISSN 1098-0121
- Horii, S.; Yokoyama S.; Nakajima, H. & Horita, S. (1999). Thickness dependence of materials properties in epitaxial  $\text{Pb}(\text{Zr}_x\text{Ti}_{1-x})\text{O}_3$  films on  $\text{Ir}/(100) (\text{ZrO}_2)_{1-x}(\text{Y}_2\text{O}_3)_x/(100)$  Si structures, *Japanese Journal of Applied Physics*, Vol. 38, pp. 5378-5382, ISSN 0021-4922
- Izyumskaya, N.; Alivov, Y.I.; Cho, S. J.; H. Morkoç, H; Lee, H. & Kang, Y. S. (July 2007). Processing, Structure, Properties, and Applications of PZT Thin Films, *Critical Reviews in Solid State and Materials Sciences*, Vol. 32, pp.111–202, ISSN: 1040-8436
- Jiang, A. Q.; Lin, Y. Y. & Tang, T. A. (2007). Interfacial-layer modulation of domain switching current in ferroelectric thin films, *Journal of Applied Physics*, Vol.101, No. 10, Article Number 104105, ISSN: 0021-8979
- Kao, K. C. & Hwang, W. (1981). *Electronic Transport in Solids*, International series in the Science of the Solid State, vol. 14. General editor B.R. Pamplin, Pergamon Press, Oxford, U. K.
- Kholkin, A.; Boiarkine, O. & Setter, N. (1997). Transient photocurrents in lead zirconate titanate thin films, *Applied Physics Letters*, Vol. 72, No.1, pp. 130-132, ISSN: 0003-6951
- Kuroiwa, Y.; Aoyagi, S. & Sawada, A. (2001). Evidence for Pb-O Covalency in Tetragonal  $\text{PbTiO}_3$ , *Physical Review Letters*, Vol. 87, No. 21, Article Number 217601, ISSN 0031-9007
- Levine, J. D. (1971). Schottky barriers anomaly and interface states, *Journal of Applied Physics*, Vol. 42, No. 10. Pp. 3991-3999, ISSN: 0021-8979
- Lines, M. E. & Glass, A. M. (1977). *Principles and Applications of Ferroelectrics and Related Materials*, Clarendon Press, Oxford, UK
- Lohse, O.; Grossmann, M.; Boettger, U.; Bolten, D. & Waser, R. (2001). Relaxation mechanism of ferroelectric switching in  $\text{Pb.Zr.Ti.O}_3$  thin films, *Journal of Applied Physics*, Vol.89, No. 4, pp. 2332-2336, ISSN: 0021-8979
- Meyer, R; Waser, R.; Prume, K.; Schmitz, T. & Tiedke, S. (2005). Dynamic leakage current compensation in ferroelectric thin-film capacitor structures, *Applied Physics Letters*, Vol. 86, No.14, Article Number. 142907, ISSN: 0003-6951
- Nakamura, Y.; Nakashima, S. & Okuyama, M. (2009). Improvement of ferroelectric properties of  $\text{BiFeO}_3$  thin films by postmetallization annealing and electric field application, *Journal of Applied Physics*, Vol.105, No. 6, Article Number 061616, ISSN: 0021-8979
- Núñez, M. & Nardelli, M. B (2008). Interface phase and tuning of polarization in metal-ferroelectric junctions: A theoretical study, *Applied Physics Letters*, Vol. 92, No.25, Article Number. 252903, ISSN: 0003-6951
- Pabst, G. W.; Martin, L. W.; Chu, Y. & Ramesh, R. (2007). Leakage mechanisms in  $\text{BiFeO}_3$  thin films, *Applied Physics Letters*, Vol. 90, No.7, Article Number. 072902, ISSN: 0003-6951

- Petraru, A.; Pertsev, N. A.; Kohlstedt, H.; Poppe, U.; Waser, R.; Solbach, A. & Klemradt, U. (2007). Polarization and lattice strains in epitaxial BaTiO<sub>3</sub> films grown by high-pressure sputtering, *Journal of Applied Physics*, Vol.101, No. 11, Article Number 114106, ISSN: 0021-8979
- Picinin, A.; Lente, M. H.; Eiras, J. A. & Rino, J. P. (2004). Theoretical and experimental investigations of polarization switching in ferroelectric materials, *Physical Review B*, Vol. 69, No. 6, Article Number 064117, ISSN 1098-0121
- Pintilie, L. & Alexe, M. (December 2005). Metal-Ferroelectric-Metal heterostructures with Schottky contacts I. Influence of the ferroelectric properties, *Journal of Applied Physics*, Vol. 98, No. 12, Article Number 123103, ISSN: 0021-8979
- Pintilie, L.; Boerasu, I.; Gomes, M.J.M.; Zhao, T.; Ramesh, R. & Alexe, M. (December 2005), Metal-ferroelectric-metal structures with Schottky contacts. II. Analysis of the experimental current-voltage and capacitance-voltage characteristics of Pb(Zr,Ti)O<sub>3</sub> thin films, *Journal of Applied Physics*, Vol. 98, No. 12, Article Number 123104, ISSN: 0021-8979
- Pintilie, L.; Vrejoiu, I.; Hesse, D.; LeRhun, G. & Alexe, M. (March 2007), Ferroelectric polarization-leakage current relation in high quality epitaxial Pb(Zr, Ti)O<sub>3</sub> films, *Physical Review B*, Vol. 75, No. 10, Article Number 104103, ISSN: 1098-0121
- Pintilie, L.; Vrejoiu, I.; Rhun, G. Le & Alexe, M. (March 2007). Short-circuit photocurrent in epitaxial lead zirconate-titanate thin films, *Journal of Applied Physics*, Vol.101, No. 6, Article Number 064109, ISSN: 0021-8979
- Pintilie L. (March 2009). Advanced electrical characterization of ferroelectric thin films: facts and artifacts, *Journal of Optoelectronics and Advanced Materials*, Vol. 11, No.3, pp.215-228 , ISSN: 1454-4164
- Pintilie, L.; Dragoi, C.; Chu, Y. H.; Martin, L. W.; Ramesh, R. & Alexe, M. (June 2009), Orientation-dependent potential barriers in case of epitaxial Pt-BiFeO<sub>3</sub>-SrRuO<sub>3</sub> capacitors, *Applied Physics Letters*, Vol. 94, No.23, Article Number. 232902, ISSN: 0003-6951
- Pintilie, L.; Vrejoiu, I.; Hesse, D. & Alexe, M. (2008). The influence of the top-contact metal on the ferroelectric properties of epitaxial ferroelectric Pb(Zr<sub>0.2</sub>Ti<sub>0.8</sub>)O<sub>3</sub> thin films, *Journal of Applied Physics*, Vol.104, No. 11, Article Number 114101, ISSN: 0021-8979
- Pintilie, L.; Stancu, V.; Vasile, E. & Pintilie, I. (2010). About the complex relation between short-circuit photocurrent, imprint and polarization in ferroelectric thin films, *Journal of Applied Physics*, Vol.107, No. 11 Article Number 114111, ISSN: 0021-8979
- Prabhumirashi, P. & Dravid, V. P. (2005). Atomic-scale manipulation of potential barriers at SrTiO<sub>3</sub> grain boundaries, *Applied Physics Letters*, Vol. 87, No.12, Article Number 121917, ISSN: 0003-6951
- Qin, M.; Yao, K. & Liang, Y. C. (2009). Photovoltaic characteristics in polycrystalline and epitaxial (Pb<sub>0.97</sub>La<sub>0.03</sub>)(Zr<sub>0.52</sub>Ti<sub>0.48</sub>)O<sub>3</sub> ferroelectric thin films sandwiched between different top and bottom electrodes, *Journal of Applied Physics*, Vol.105, No. 6, Article Number 061624, ISSN: 0021-8979
- Rybickiy, J.; Rybickay, A.; Feliziani, S. & Chybicki, M. (1996). The thickness dependence of the hopping time-of-flight current profiles in spatially non-uniform thin dielectric layers, *J. Phys.: Condens. Matter*, Vol. 8, pp. 2089–2093, ISSN 0953-8984

- Sai, N.; Rabe, K. M. & Vanderbilt, D. (2002). Theory of structural response to macroscopic electric fields in ferroelectric systems, *Physical Review B*, Vol. 66, No. 10, Article Number 104108, ISSN 1098-0121
- Schroeder, D. K. (1998). *Semiconductor material and device characterization*, Wiley-Interscience, New York, USA, ISBN 0-471-24139-3
- Scott, J. F. (2000). *Ferroelectric Memories*, in Advanced Microelectronics Series, edited by K. Itoh and T. Sakurai, Springer-Verlag, Berlin, Heidelberg, Germany
- Shelke, V.; Harshan, V. N.; Kotru, S. & Gupta, A. (2009). Effect of kinetic growth parameters on leakage current and ferroelectric behavior of BiFeO<sub>3</sub> thin films, *Journal of Applied Physics*, Vol.106, No. 10, Article Number 104114, ISSN: 0021-8979
- Shur, V. Ya.; Nikolaeva, E. V.; Shishkin, E. I.; Kozhevnikov, V. L.; Chernykh, A. P.; Terabe, K. & Kitamura, K. (2001). Polarization reversal in congruent and stoichiometric lithium tantalite, *Applied Physics Letters*, Vol. 79, No.19, pp. 3146-3148, ISSN: 0003-6951
- Simmons, J. G. (1965). Richardson-Schottky in solids, *Physical Review Letters*, Vol. 15, No. 25, pp. 967-968, ISSN 0031-9007
- Sze, S. M. (1981). *Physics of Semiconductor Devices*, 2<sup>nd</sup> ed. John Wiley & Sons, USA, ISBN 0-471-05661-8
- Tagantsev, A. K.; Stolichnov, I.; Setter, N.; Cross J. C. & Tsukada, M. (2002). Non-Kolmogorov-Avrami switching kinetics in ferroelectric thin films, *Physical Review B*, Vol. 66, Article Number 214109, ISSN 1098-0121
- Tang, X. G.; Wang, J.; Zhang, Y. W. & Chan H. L. W. (2003), Leakage current and relaxation characteristics of highly .111.-oriented lead calcium titanate thin films, *Journal of Applied Physics*, Vol.94, No. 8, pp. 5163-5166, ISSN: 0021-8979
- Uchino, K. (200). *Ferroelectric Devices*, Marcel Dekker, New York, SUA
- Vrejoiu, I.; Le Rhun, G.; Zakharov, N. D.; Hesse, D.; Pintilie, L. & Alexe, M. (October 2006), Threading dislocations in epitaxial ferroelectric PbZr<sub>0.2</sub>Ti<sub>0.8</sub>O<sub>3</sub> films and their effect on polarization backswitching, *Philosophical Magazine*, Vol.86, No.28, pp. 4477-4486, ISSN: 1478-6435
- Vrejoiu, I.; Le Rhun, G.; Pintilie, L.; Hesse, D.; Alexe, M. & Goesele, U. (July 2006), Intrinsic ferroelectric properties of strained tetragonal PbZr<sub>0.2</sub>Ti<sub>0.8</sub>O<sub>3</sub> obtained on layer-by-layer grown, defect-free single-crystalline films, *Advanced Materials*, Vol.18, No.13, pp.1657-+, ISSN: 0935-9648
- Wang, J.; Neaton, J. B.; Zheng, H.; Nagarajan, V.; Ogale, S. B.; Liu, B.; Viehland, D.; Vaithyanathan, V.; Schlom, D. G.; Waghmare, U. V.; Spaldin, N. A.; Rabe, K. M.; Wuttig, M. & Ramesh, R. (2003). Epitaxial BiFeO<sub>3</sub> Multiferroic Thin Film Heterostructures, *Science*, Vol. 299, pp. 1719-1722, ISSN 0036-8075
- Warren, W. L.; Dimos, D.; Tuttle, B. A.; Nasby, R. D. & Pike, G. E. (1994). Electronic domain pinning in Pb(Zr,Ti)O<sub>3</sub> thin films and its role in fatigue, *Applied Physics Letters*, Vol. 65, No.8, pp. 1018-1020, ISSN: 0003-6951
- Wu, A; Vilarinho, P. M.; Wu, D. & Gruverman, A. (2008). Abnormal domain switching in Pb(Zr,Ti)O<sub>3</sub> thin film capacitors, *Applied Physics Letters*, Vol. 93, No.26, Article Number 262906, ISSN: 0003-6951
- Yang, Y. S.; Lee, S. J.; Yi, S.; Chae, B. G.; Lee, S. H.; Joo, H. J. & Jang, M. S. (2000). Schottky barrier effects in the photocurrent of sol-gel derived lead zirconate titanate thin film capacitors, *Applied Physics Letters*, Vol. 76, No.6, pp. 774-776, ISSN: 0003-6951

- Yang, S. Y.; Martin, L. W.; Byrnes, S. J.; Conry, T. E.; Basu, S. R.; Paran, D.; Reichertz, L.; Ihlefeld, J.; Adamo, C.; Melville, A.; Chu, Y.-H.; Yang, C.-H.; Musfeldt, J. L.; Schlom, D. G.; Ager III, J. W. & Ramesh, R. (2009). Photovoltaic effects in BiFeO<sub>3</sub>, *Applied Physics Letters*, Vol. 95, No.6, Article Number 062909, ISSN: 0003-6951
- Zhao, W. & Jena, D. (2004). Dipole scattering in highly polar semiconductor alloys, *Journal of Applied Physics*, Vol. 96, No. 4. pp. 2095-2101, ISSN: 0021-8979
- Zubko, P.; Jung, D. J.; & Scott, J. F. (2006). Space charge effects in ferroelectric thin films, *Journal of Applied Physics*, Vol.100, No. 11, Article Number 114112, ISSN: 0021-8979

# Hydrogen in Ferroelectrics

Hai-You Huang, Yan-Jing Su and Li-Jie Qiao  
*University of Science and Technology Beijing  
China*

## 1. Introduction

It is well known that the ferroelectric random access memories (FRAM) as one of the most important applications of ferroelectric thin film have attracted much attention. However, the introduction of hydrogen into ferroelectric materials may cause severe degradations in dielectric properties, ferroelectric properties, optical properties and mechanical properties. Ferroelectricity is the most important property of ferroelectrics and the researches on hydrogen in ferroelectrics begin just from the effects on ferroelectric properties. Ferroelectric thin film is often integrated with existing Si technology to fabricate reliable nonvolatile memories. In Si technology, a forming gas (hydrogen containing gas) anneal at about 400 °C needs to carry on tying up dangling bonds at the Si/SiO<sub>2</sub> interface and reducing interface-trapped charges (Katz, 1988). Unfortunately, hydrogen could enter into ferroelectric thin film during annealing in forming gas and generates severe issue. For example, both Pb(Zr,Ti)O<sub>3</sub> (PZT) and SrBi<sub>2</sub>Ta<sub>2</sub>O<sub>9</sub> ferroelectric thin-film capacitors lose their polarization hysteresis characteristics as a result of such an anneal (Aggarwal et al., 1998; Shimanoto et al., 1997; Kushida-Abdelghafar et al., 1996; Han & Ma 1997).

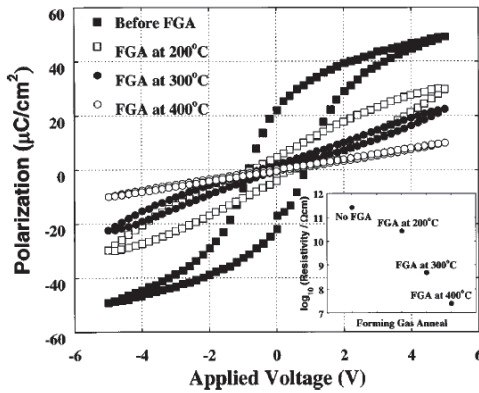
Besides the ferroelectricity, ferroelectric materials also have been wildly applied due to other important properties. Because that many ferroelectric ceramics, such as PZT and BaTiO<sub>3</sub>, are excellent insulator against current, they are used to electric industry as capacitor. Hydrogen can increase leakage current and induce the insulator to a semiconductor (Huang et al., 2007 & Chen et al., 2011). Ferroelectric materials, especially its single crystals, have been widely used in optical devices because of its special optical properties such as photorefractive effect and nonlinear optical effect. Hydrogen can change the optical properties of ferroelectric materials (Wu et al., 2009). The mechanical property is another important property to sure ferroelectric devices could be used reliably. Hydrogen fissure (Peng et al., 2004) and hydrogen-induced delayed fracture (Huang et al., 2005; Zhang et al., 2008; Wang et al., 2003a, 2003b) could occur in some conditions.

This chapter reviews the effects of hydrogen on the properties of ferroelectric materials. This chapter is organized as follows: first of all, some background leading to the research interest of hydrogen in ferroelectric materials are introduced in section 1. In section 2 to 5, the effects of hydrogen on the ferroelectric properties (section 2), on the dielectric properties (section 3), on the optical properties (section 4) and on the mechanical properties (section 5) of ferroelectric materials are discussed in detail, respectively. In the end of this chapter, we conclude in section 6 where the important results of this research area are briefly summarized and outstanding problems and future directions are discussed.

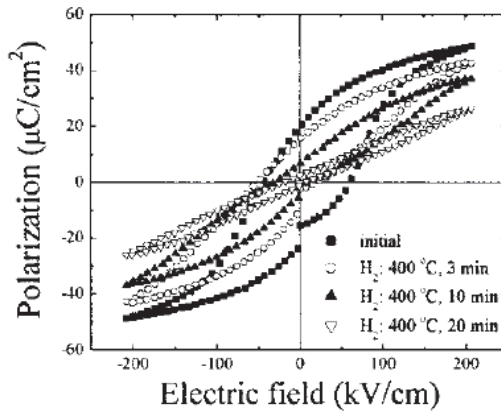
## 2. Effects of hydrogen on ferroelectricity

### 2.1 Hydrogen reduces remanent polarization

In a ferroelectric material, there are lots of ferroelectric domains. The electric dipoles create by positive and negative bound charges in each domain are called spontaneous polarization vectors, which point to the positive poles of domains. Ferroelectric domain (polarization vector) can rotate  $90^\circ$  or  $180^\circ$  induced by applied force  $F$  or electric field  $E$ , known as domain switching. When the applied electric field is large enough all polarization vectors of domains have the same direction with the field, resulting in saturation polarization  $P_s$ . When the field is removed, i.e.,  $E=0$ , the polarization does not back to zero, but equals to remanent polarization  $P_r$ , that means a hysteresis effect of polarization. The hysteresis loop can be measured by change the field, as shown in Figure 1(Aggarwal et al., 1998 & Joo et al., 2002).



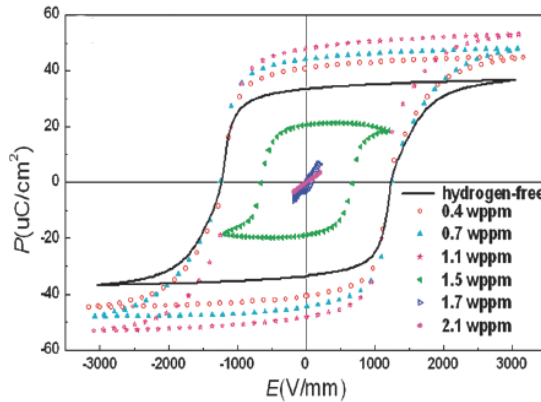
(a)



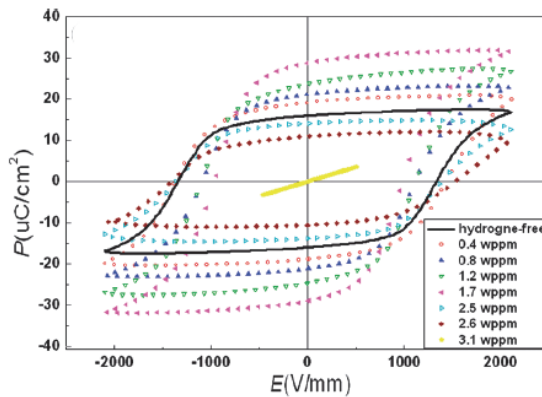
(b)

Fig. 1. Hydrogen charging causes hysteresis loop narrow and reduce the remanent polarization ((a)Aggarwal et al., 1998 & (b) Joo et al., 2002)

Ferroelectric materials have piezoelectricity, which is the generation of polarization charges as a result of applied stress or strain. The electric displacement vector  $D$  is proportional to the stress tensor  $T$  with a coefficient  $d$ , piezoelectric constant tensor. For perovskite structure ferroelectric materials, such as  $BaTiO_3$  or PZT, piezoelectric constant tensor has only three independent components,  $d_{15}=d_{24}$ ,  $d_{31} = d_{32}$ ,  $d_{33}$ . Generally,  $d_{33}$  is used as the piezoelectric constant. Many experimental results have indicated that hydrogen caused a serious degradation of ferroelectric and dielectric properties of ferroelectric materials (Joo et al., 2002; Ikarashi, 1998 & Tamura et al., 1999). Charging of hydrogen could make the hysteresis loop narrow or disappear, i.e., make  $P_r$  decrease, as shown in Figure 1 (Aggarwal et al., 1998 & Joo et al., 2002). The hysteresis loops of PZT thin film capacitor with Pt electrode continuously narrowed after a annealing at 400 °C in a forming gas with 5%  $H_2$  for 3 to 20 min, as shown in Figure 1b (Joo et al., 2002). With the annealing temperature increasing, the hysteresis loops also gradually narrowed and became a straight line at 400 °C (Aggarwal et al., 1998).



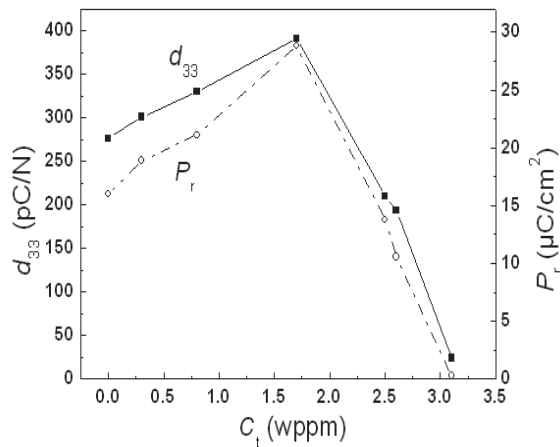
(a)



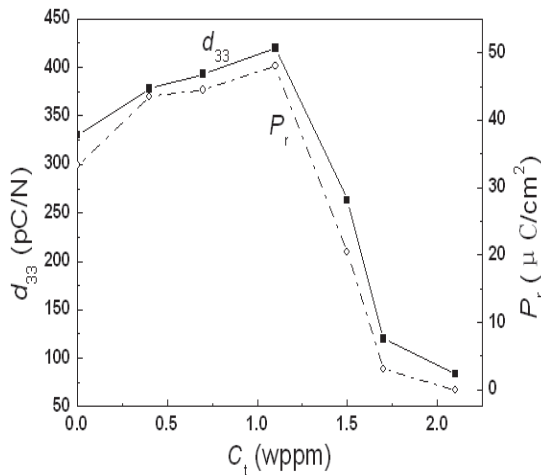
(b)

Fig. 2. The effects of hydrogen on hysteresis loops (a) PZT & (b) PZNT (Wu et al., 2010)

Our work shows that both for PZT and PZNT (91%PZN+9%PT), when hydrogen concentration in ferroelectric material,  $C_t$ , introduced by electrolysis or annealing in hydrogen gas is less than a critical concentration,  $C^*$  (for PZT,  $C^*=10$  ppm and for PZNT,  $C^*=14$  ppm), with the increase in hydrogen concentration, the hysteresis loop widens and  $P_r$  increases. However, when the hydrogen concentration is more than the critical value of  $C^*$ , hysteresis loop narrows and  $P_r$  falls with the increase in hydrogen concentration, as shown in Figure 2 (Wu et al., 2010). The effects of hydrogen concentration on  $P_r$  and  $d_{33}$  are shown in Figure 3 (Wu et al., 2010). When  $C_t < C^*$ , hydrogen can elevate both  $P_r$  and  $d_{33}$ . If  $C_t > C^*$ ,  $P_r$  and  $d_{33}$  decrease sharply with the raise of  $C_t$ .



(a)



(b)

Fig. 3. The effects of hydrogen on  $P_r$  and  $d_{33}$  (a) PZT & (b) PZNT (Wu et al., 2010)

## 2.2 Hydrogen-hindered ferroelectric phase transition

The polarization-voltage hysteresis loop of PZT film disappeared gradually after forming gas annealing above its Curie temperature, as shown in Fig.1. No hysteresis implies that it is a cubic paraelectricity. Therefore, it seems that hydrogen entered above its Curie temperature can hinder the phase transition of the PZT film from cubic paraelectricity to tetragonal ferroelectricity.

X-ray diffraction (XRD) and heating differential scanning calorimetry (DSC) patterns of PZT ceramics in different charging conditions are shown in Figures 4a and 4b, respectively (Huang, et al., 2006). The appearance of double peaks in curves A, B, C, and E in Figure 4a corresponds to tetragonal phase and no double peaks in curve D corresponds to cubic phase. The ratios of  $c$  to  $a$  axis calculated based on curves A-E in Figure 4a were 1.0114, 1.0128, 1.0113, 1.0000, and 1.0077, respectively. The calculation of  $c/a$  also proves that curve D corresponds to cubic phase and the others correspond to tetragonal phase. Figure 4b indicates that there is an endothermic transition from tetragonal ferroelectricity to cubic paraelectricity at its Curie temperature of 300 °C for the samples uncharged and charged below the Curie temperature, as shown by curves A, B, and C in Figure 4b. For the sample charged in H<sub>2</sub> at 450 °C, however, there is no endothermic peak from 25 to 450 °C, as shown by curve D in Figure 4b. After outgassing at 800 °C, however, the endothermic peak appears again at the Curie temperature of 300 °C, as shown by curve E in Figure 4b. These results indicate that the lattice parameters and the tetragonal structure of the PZT do not change after charging at the temperature below the Curie temperature. However, if the charging temperature is higher than the Curie temperature, the PZT will be a cubic paraelectricity instead of tetragonal ferroelectricity after cooling to room temperature. After outgassing at 800 °C, the tetragonal ferroelectricity is restored. Therefore, hydrogen charged above its Curie temperature can hinder the phase transition from cubic to tetragonal during cooling to room temperature.

First principles plane-wave pseudopotential density functional theory was applied to calculate the effect of hydrogen on the ferroelectric phase transition in perovskite structure ferroelectricity based on energy calculation method. A hydrogen atom was put into the perovskite-type unit of cubic and tetragonal PbTiO<sub>3</sub> and then its possible locations were looked for. Figure 5a is a tetragonal PbTiO<sub>3</sub> with one H in the unit cell and A, B, and C are three possible sites H occupied. Calculation showed that the minimum values of total energies corresponding to site A at (0.5, 0.25, 0.05), tetrahedral interstitial site B at (0.25, 0.25, 0.25), and site C between Ti and apical O(1) ion at (0.5, 0.5, 0.25) were -4601.73, -4601.04, and -4600.15 eV, respectively. When hydrogen occupied site A, B, or C, the distances between H and O(1) were 0.1016 nm, 0.1485 nm, and 0.1529 nm, respectively. Hydrogen should occupy site A, the total energy is the lowest and the distance between H and O(1) has a smallest value, compared to sites B and C, which are the possible sites proposed by Aggarwal et al. (Aggarwal et al., 1998) The distance 0.1016 nm means that a strong interaction between H and O(1) exists, which can result in the overlap of the electronic clouds between H and O(1), as shown in Figure 5b. The calculation is consistent with the experimental results (Aggarwal et al., 1998 & Joo et al., 2002), i.e., existing O-H bonds in PZT ceramics. Calculation showed that the electron overlap populations between O-Ti were 0.98 for hydrogen-free PbTiO<sub>3</sub> and 0.70 for hydrogenated PbTiO<sub>3</sub>, respectively. Hydrogen decreases the electron overlap population between O-Ti means that hydrogen weakens the interaction between O-Ti. It has been pointed out that the stronger the hybridization between the two atoms, the larger tendency to form bond or interaction between two atoms. Therefore, hydrogen decreases the overlap population between O-Ti and weakens the hybridization between O-Ti, resulting in the decrease of stability of tetragonal ferroelectric phase.

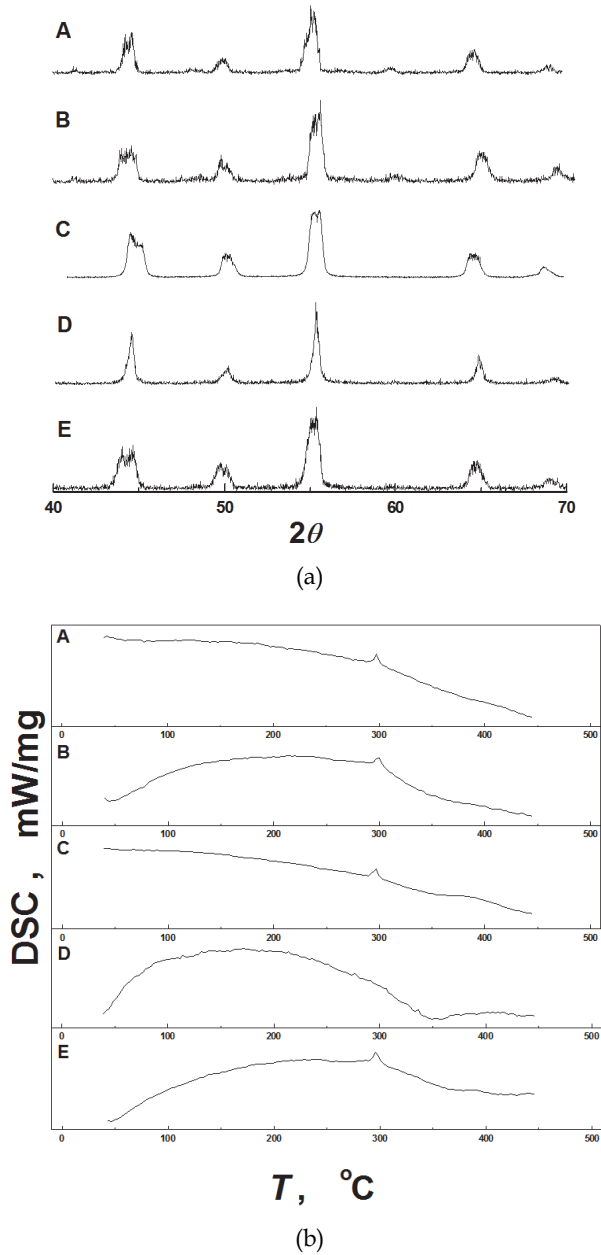
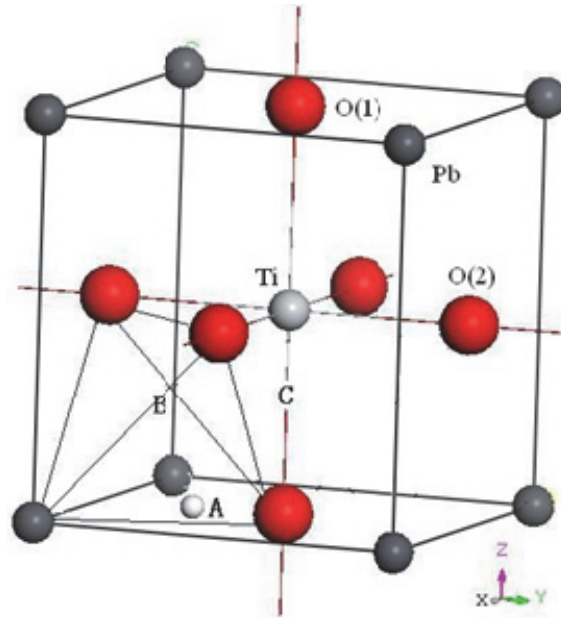
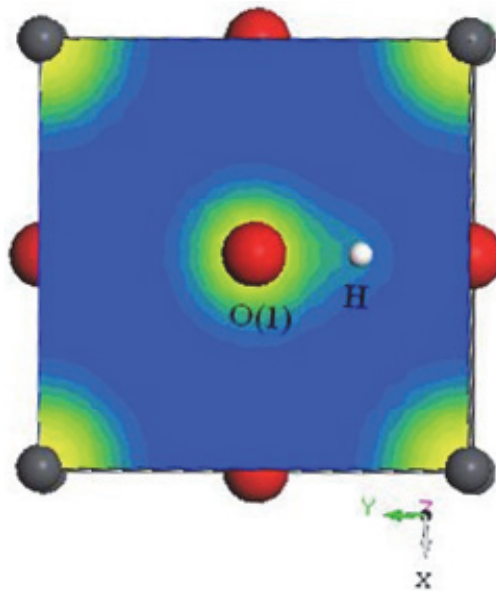


Fig. 4. XRD (a) and DSC (b) patterns of PZT-5H in different charging conditions A, hydrogen-free; B, charging at 400 mA/cm<sup>2</sup> in solution at 20°C ; C, charging in H<sub>2</sub> at 250°C; D, charging in H<sub>2</sub> with  $P_{H_2}$  = 0.4 MPb at 450 °C; E, outgassing at 800°C after charging in H<sub>2</sub> at 450°C (Huang, et al., 2006)



(a)



(b)

Fig. 5. Unit cell of tetragonal  $\text{PbTiO}_3$  containing one hydrogen atom (a), and electronic clouds of XOY plane (b) (Huang, et al., 2006)

The variation of the total energy with the displacement of Ti along the *c* axis for hydrogen-free and hydrogenated PbTiO<sub>3</sub> is shown in Figure 6. Figure 6a indicates that for hydrogen-free PbTiO<sub>3</sub> with the tetragonal structure, there are two lowest energy sites for Ti in the *c* axis which are  $\pm 0.016$  nm from the center of the unit cell. The calculation result is consistent with the experimental value of  $\pm 0.017$  nm. Figure 6b, however, shows that for the hydrogenated tetragonal structure, the double-lowest-energy sites of Ti along the *c* axis disappear and the lowest energy site located at the center of the cell. Therefore, when hydrogen enters into the cubic PbTiO<sub>3</sub> above its Curie temperature, the cubic structure continues to be a stable structure during cooling because for Ti there is no lower energy site than the center of the cell. As a result, ferroelectric tetragonal structure in PbTiO<sub>3</sub> charged above the Curie temperature will not appear during cooling to room temperature because of no displacement of Ti along the *c* axis. The calculation can explain the experiment that hydrogen charged above its Curie temperature will hinder phase transition of PZT from cubic paraelectricity to tetragonal ferroelectricity.

Figure 4, however, also indicates that PZT keeps a tetragonal structure after charging at the temperature below the Curie temperature. The reason is the existence of energy barrier from tetragonal to cubic which composed of elastic energy, depoling energy, and static electric energy. Besides the insufficient thermal energy, hydrogen entered into tetragonal PZT during charging below the Curie temperature cannot provide an additive energy to overcome the energy barrier, and then the tetragonal structure cannot transform to cubic structure during charging below the Curie temperature.

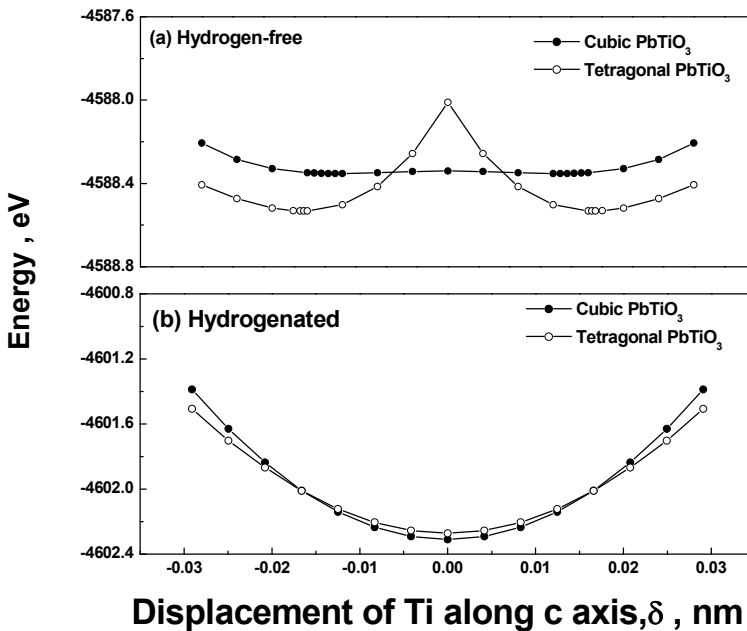


Fig. 6. Total energy vs. displacement of Ti along *c* axis, the original is the centre of the cell (a) hydrogen-free PbTiO<sub>3</sub>, (b) hydrogenated PbTiO<sub>3</sub> (Huang, et al., 2006)

### 3. Hydrogen induced semiconductor transformation of ferroelectrics

Ferroelectric or piezoelectric ceramics, such as PZT, is an insulator. However, after annealing in a forming gas containing H<sub>2</sub> or electrode plating process, hydrogen can enter into the ceramics and makes its resistivity from 10<sup>12</sup>-10<sup>13</sup> Ω cm down to 10<sup>6</sup>-10<sup>7</sup> Ω cm sharply, resulting in becoming a semiconductor (Han & Ma, 1997). The resistivity and capacitance of multilayer ferroelectric ceramic capacitors degrade to a semiconductor and the dielectric loss increases after hydrogen charging in NaOH (Chen et al., 1998). Figure 7a illustrates the leakage current in PZT ceramics increased sharply after electrolysis or hydrogen gas charging. The semiconductorization of ferroelectric ceramics by hydrogen can be restored by outgassing. For example, after outgassing of hydrogen at a temperature higher than 400 °C, the hydrogenated PZT restores an insulator, as shown in Figure 7b (Huang et al., 2007). A very few hydrogen can lower the resistivity of PZT from 10<sup>13</sup> Ω cm to 10<sup>8</sup> Ω cm. carrier concentration increases rapidly with the raise of hydrogen concentration (Huang et al., 2007). Hall effect measurements show that PZT ceramics change into n-type semiconductor after hydrogen charging (Huang et al., 2007).

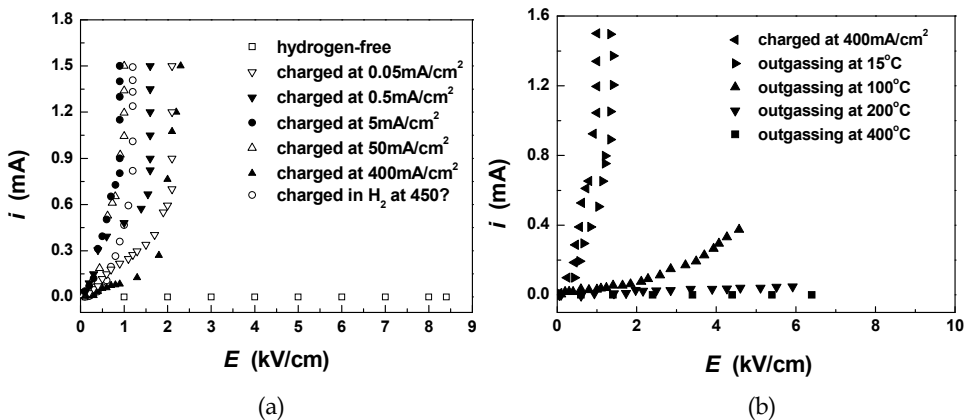


Fig. 7. The effects of hydrogen charging (a) and outgassing (b) on the leakage current in PZT (Huang et al., 2007)

The first principles calculation was applied to investigate the effect of hydrogen on the conductivity of ferroelectric materials. The variations of density of states of every atom in PZT with energy difference  $E-E_F$  ( $E_F$  is Fermi energy) were calculated (Wu, 2009). If not hydrogen, the total density of states of all atoms in PZT vs  $E-E_F$ , as shown in Figure 8a, where AB is the valence band, BC is the forbidden band and CD is the empty band. If the hydrogen concentration  $C_H=1536$  wppm, the whole curve move to low energy (left) after hydrogen charging, so that the energy of parts of the empty band is less than the Fermi energy and becomes the bottom of conduction band, which was filled by electrons mainly from H 1S (Ti, Pb, Zr also contribute them free electrons). As a result, the forbidden band does no longer exist and the material becomes a conductor, as shown in Figure 8b. When  $C_H$  reduces to 770 wppm, the energy of parts of the empty band is still below the Fermi energy and it is still a conductor, as shown in Figure 8c. When  $C_H=96$  wppm, all empty band higher than the  $E_F$ , so there is a narrow band gap that means the material becomes a

semiconductor, as shown in Figure 8d. For PZT, no matter what method of hydrogen charging was applied, saturation hydrogen concentration is less than 96 wppm. Thus, it is impossible to make PZT to a conductor by hydrogen charging, but hydrogen can make PZT into a semiconductor.

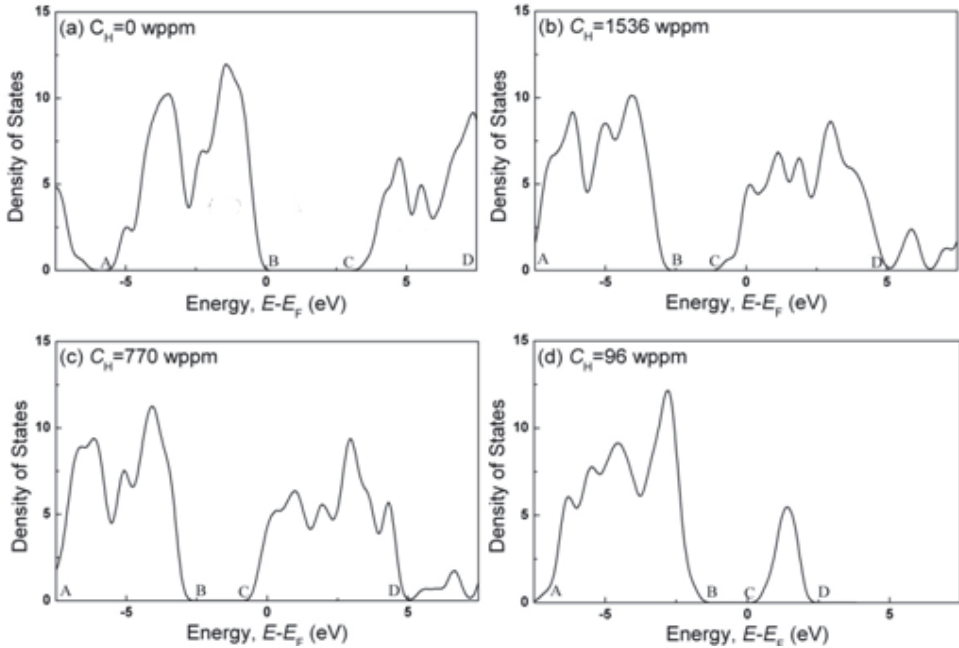


Fig. 8. Density of states for PZT with different  $C_H$  (Wu, 2009)

Why hydrogen charging make the PZT into a semiconductor from an insulator. One view is that H can react with  $O^{2-}$  to form  $H_2O$  and oxygen vacancy with two electrons  $V(2e)$  (Chen et al., 1998), i.e.,



The two electrons of oxygen vacancy can ionize and induce insulating ferroelectric ceramic to be semiconductor. However, because  $H_2O$  molecule is too large to locate in the lattice, the reaction (1) can only occur on the surface of ferroelectric ceramic and make the reaction to continue through migration of  $O^{2-}$  to the surface. Nevertheless, the diffusion coefficient of O is very small in the ceramics at room temperature (in  $BaTiO_3$  at room temperature  $D_O=1.1 \times 10^{-15} \text{ cm}^2/\text{s}$ ) (Huang et al., 2007). Considering hydrogen charging for 45h at room temperature, the maximum diffusion distance is only  $0.53 \mu\text{m}$ . However, the experimental value of transition distance is up to  $0.9 \text{ mm}$  (see Figure 9), which is  $10^3$  times as large as the calculative maximum diffusion distance of O (Huang et al., 2007). Another view is that a part of  $PbO$  reduced to  $Pb$  by H, i.e., (Han & Ma, 1997)



A small amount of Pb can become the ceramics into the semiconductor. For the same reason, the reaction can't be achieved kinetically. Figure 8 shows that 1S electron of H can across the band gap and into conduction band, such as if  $C_H > 96$  ppm, the electrons in the bottom of conduction band (mainly from H 1S) to become a conductor. In fact, the  $C_H < 96$  ppm, so the hydrogen charging is impossible to make PZT be a conductor. However, the density of states of hydrogenated ferroelectric ceramics moves to left and narrows the band gap to a lever of semiconductor. 1S electron of H can be as free electron and degrade the electrical resistivity drastically.

#### 4. Effects of hydrogen on optical properties

After hydrogen charging, the color of PZT became black (Chen et al., 1998 & Joo et al. 2002). Beside PZT, for BaTiO<sub>3</sub> single crystals, the color became darker and is absent transparent after hydrogen charging, as shown in Figure 9 (Huang et al. 2007 & Wu et al. 2009). The darker color means more visible light are absorbed. The experiments show that the absorption coefficient of PZT and BaTiO<sub>3</sub> within visible region significantly heighten after hydrogen charging, as shown in Figure 10 (Wu et al. 2009).

The phenomena of hydrogen changing the color of PZT can be used to measure the diffusion coefficient of hydrogen in PZT. 0.9 mm-thick PZT sample was charged of hydrogen from single side for 2.5h, 10h, 20h and 45h. The cross section of hydrogenated sample was shown in Figure 11a, and the average diffusion distance of hydrogen  $x$  for different charging time  $t$  can be measured, as shown in Figure 11b. Based on the linear relationship between  $x$  and  $t^{1/2}$ , i.e.,  $x = 4\sqrt{Dt}$ , the diffusion coefficient of hydrogen in PZT  $D = 4.9 \times 10^{-8}$  cm<sup>2</sup>/s at room temperature can be obtained (Huang et al. 2007).

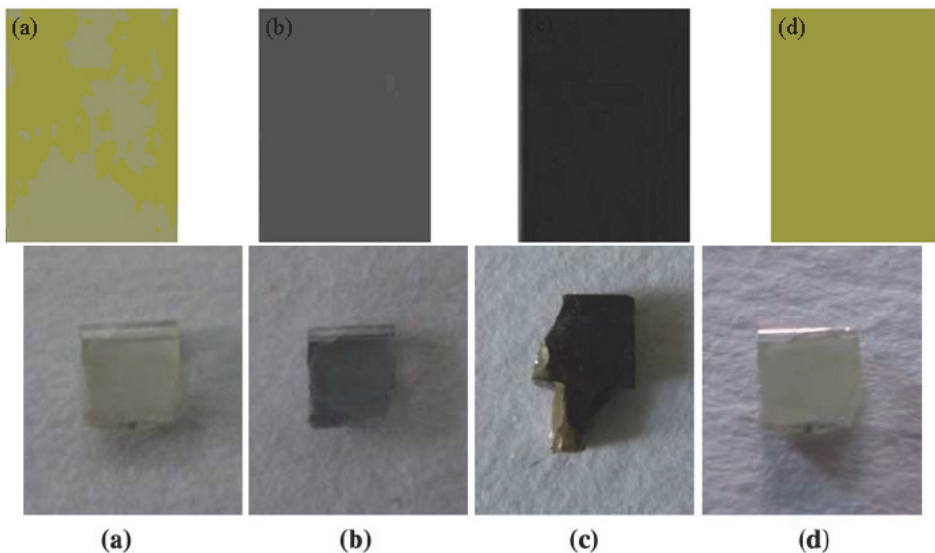
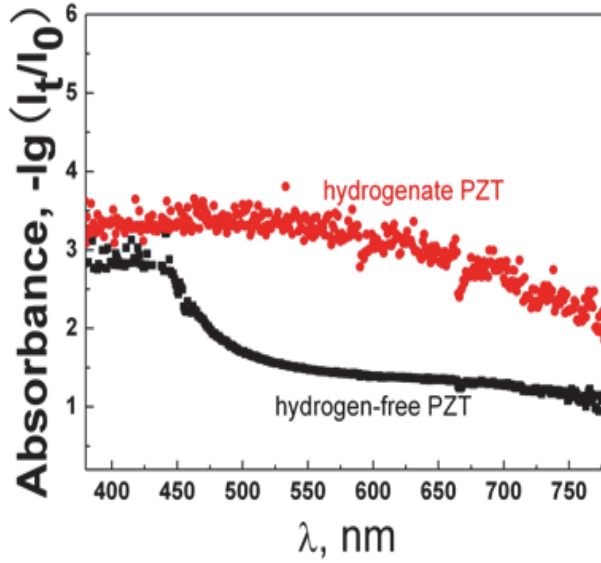
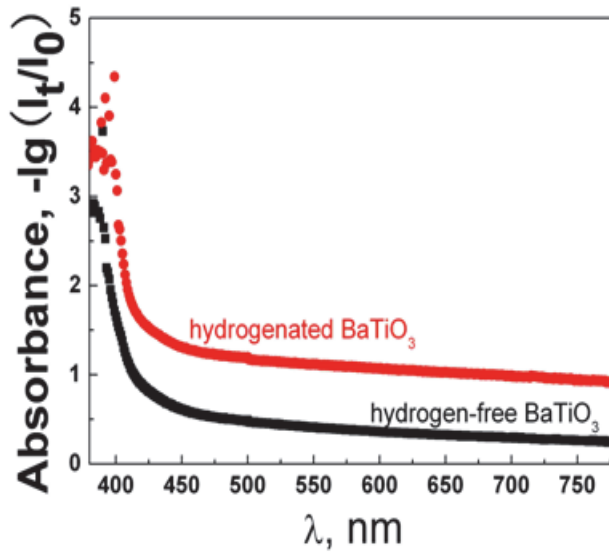


Fig. 9. The color changes of PZT (upper) and BaTiO<sub>3</sub> (lower) before and after hydrogen charging (a) before hydrogen charging, (b) electrolytically charged, (c) charged in H<sub>2</sub> gas, (d) outgassing after charging (Huang et al. 2007 & Wu et al. 2009)



(a)



(b)

Fig. 10. Hydrogen increases the absorption coefficient within visible region (a)PZT & (b)BaTiO<sub>3</sub> (Wu et al. 2009)

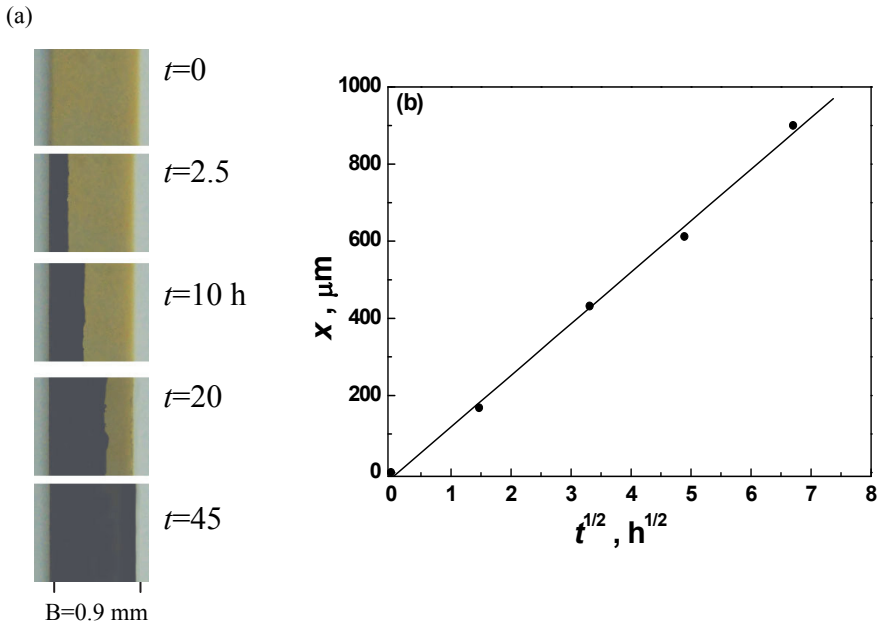


Fig. 11. Diffusion of hydrogen in PZT ceramics (a) color change and (b) diffusion distance at different time (Huang et al. 2007)

## 5. Hydrogen induced cracking

### 5.1 Hydrogen fissure in PZT ferroelectric ceramics without loading

Three groups of PZT ferroelectric ceramics were used to investigate hydrogen fissure without any loading. The group I samples were polarized by a high electric field (30kV/cm) at room temperature and a large internal stress was induced. The group II samples were polarized at high temperature (400 °C, higher than the Curie point) by a small electric field (2kV/cm), and then furnace cooled to room temperature, in which there was little internal stress. The third group of samples was not polarized. We called the three groups of samples as HP, SP and UP samples, respectively. Hydrogen charging was carried out for all samples in a 0.2mol/l NaOH +0.25 g/l  $\text{As}_2\text{O}_3$  solution with various current densities  $i$ . For the HP samples, appeared four discontinuous microcracks like a, b, c and d appeared on the surface after hydrogen charging with  $i=5$  mA/cm<sup>2</sup> for 4h, as shown in Figure 12 (Peng et al., 2004). These microcracks initiated and grew along the grain boundaries. Experiment showed that no hydrogen fissure was found after charging for 48h when  $i=0.05$  mA/cm<sup>2</sup>, but when  $i \geq 0.5$  mA/cm<sup>2</sup>, after a certain incubation period, hydrogen fissure can form. However, for SP samples and UP samples, when  $i \leq 300$  mA/cm<sup>2</sup>, on hydrogen fissure formed for 48 h. hydrogen fissure appeared until  $i=400$  mA/cm<sup>2</sup>, as shown in Table 1 (Peng et al., 2004). In order to measure hydrogen concentration  $C_H$ , some samples were charged for 100 h with various current densities, and then put into a glass tube filled with silicon oil. The  $C_H$  can be calculated by Eq.3 based on the saturation volume of hydrogen  $V(\text{cm}^3)$ .

$$C_H(\text{wppm})=10^6 \times 2n(\text{g})/m(\text{g})=2 \times 10^{-6} V(\text{cm}^3)/82.06m(\text{g})T(\text{k}) \quad (3)$$

where  $n(\text{g})=PV/RT=V(\text{cm}^3)/82.06T(\text{K})$  is the molar number of hydrogen under 1 atm,  $m(\text{g})$  is the weight of the sample and  $T(\text{K})$  is temperature. The values of  $C_H$  corresponding to various  $i$  were also listed in Table 1

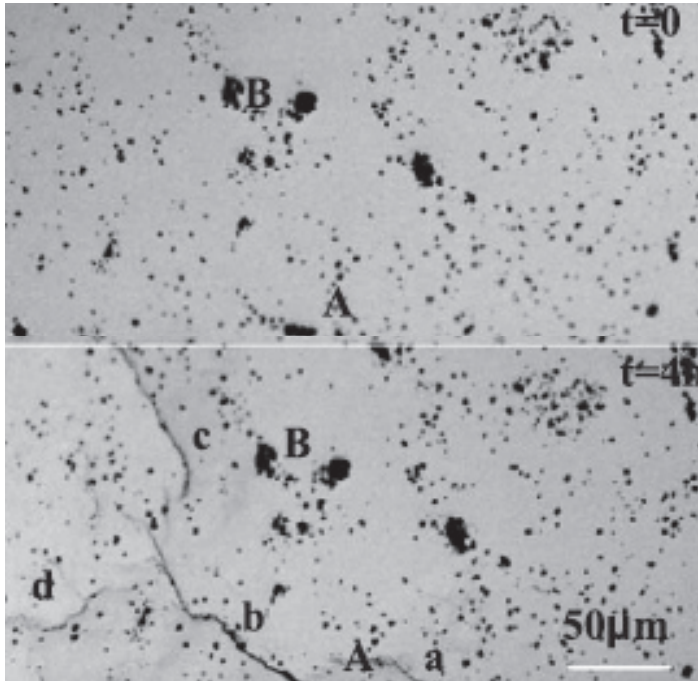


Fig. 12. Hydrogen fissure after charging at 5 mA/cm<sup>2</sup> for 4 h; a to d are fissures, and A and B are marks for location (Peng et al., 2004)

$i$ , mA/cm <sup>2</sup>	0.05	0.5	5	50	300	400
$C_H$ , wppm	0.92	2.61	4.8	7.16	9.84	10.3
HP samples	no	yes	yes	yes	yes	--
SP samples	no	no	no	no	no	yes
UP samples	no	no	no	no	no	yes

Table 1. Hydrogen concentration and fissure appearance corresponding to various charging current densities (Peng et al., 2004)

There are many cavities and microholes in the grain boundary of sintered PZT ceramics. During hydrogen charging H atoms enter into the holes and generate H<sub>2</sub>, which can induce an internal pressure  $P$ . When the hydrogen pressure is large enough, the normal stress on the holes wall  $P/2$  equals to the cohesive strength  $\sigma_{th}(H)$  at grain boundary,

which has been reduced by atomic hydrogen, hydrogen fissure or microcrack will form. If there is a extra internal stress  $\sigma_i$ , the critical hydrogen pressure for cracking can be decreased from  $P=2\sigma_{th}(H)$  to  $P^*=2\sigma_{th}(H)-\sigma_i$ . Because there is a large internal stress in HP sample, which can promote crack nucleation, so hydrogen fissure appear when  $i=0.5\text{mA}/\text{cm}^2$ . The microcracks are found in SP and UP samples only when  $i=400\text{ mA}/\text{cm}^2$  for absence of internal stress.

**5.2 Hydrogen reduce fracture toughness of ferroelectric material**

Vickers indentation was carried out on the surfaces of three ferroelectric ceramic samples to obtain indentation fracture toughness  $K_{IC}$  according to Eq.4.

$$K_I = 0.0638P / d\sqrt{l} \tag{4}$$

where  $P$  is the load,  $d$  is diagonal length of the indentation and  $l$  is the crack length. Then, the samples with indentation cracks were charged into 4.1 ppm, 8.1 ppm and 12.1 ppm hydrogen, respectively. Unloaded indentation cracks can grow induced by the indentation residual stress during charging. The indentation crack length after hydrogen charging was measured to calculate the threshold stress intensity factor of hydrogen-induced delayed cracking (HIDC),  $K_{IH}$ , by Eq.4. New indentations were carried out on the surface of hydrogenated samples. The fracture toughness for hydrogenated sample  $K_{IC}(H)$  can also be obtained. The experiments indicated that both  $K_{IH}/K_{IC}$  and  $K_{IC}(H)/K_{IC}$  decreased linearly with the increasing  $C_H$ , as shown in Figure 13 (Zhang et al., 2008).

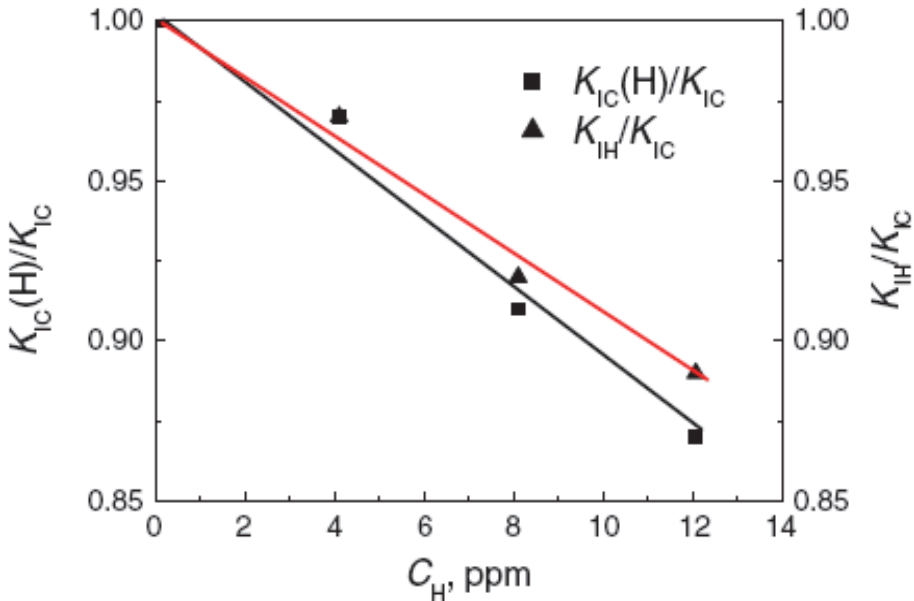


Fig. 13. Hydrogen concentration dependence of the relative fracture toughness of charged samples,  $K_{IH}/K_{IC}$ , and of the normalized threshold stress intensity factor of hydrogen-induced cracking induced by residual stress,  $K_{IC}(H)/K_{IC}$  (Zhang et al., 2008)

The crack length increased with increasing hydrogen concentration in the samples. Therefore, the cracks can also grow with the prolongation of dwell time during indentation test in a pre-charged sample since the hydrogen concentration will increase at the indentation crack tips by stress-induced diffusion. The experimental results indicate that the longer the indentation load hold, the larger the indentation crack length is, and the smaller fracture toughness,  $K_{IC}(H,t)$  measures, as shown in Figure 14 (Zhang et al., 2008). Under a constant load, the H IDC can occur by the stress-induced hydrogen diffusion and enrichment.

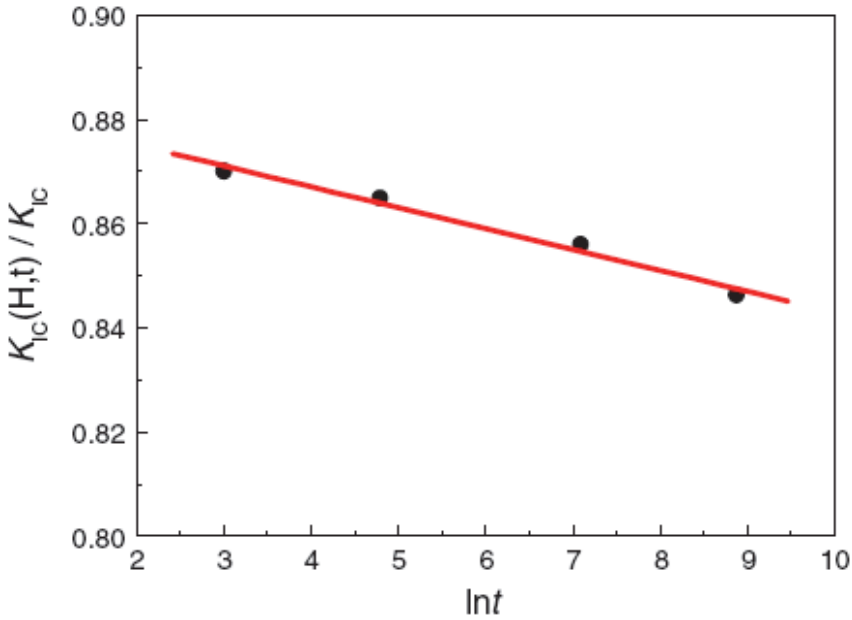


Fig. 14. The normalized fracture toughness  $K_{IC}(H,t)/K_{IC}$  versus the logarithm of the dwell time during the indentation test for the charged sample (Zhang et al., 2008)

### 5.3 Hydrogen-induced delayed cracking in ferroelectric ceramics

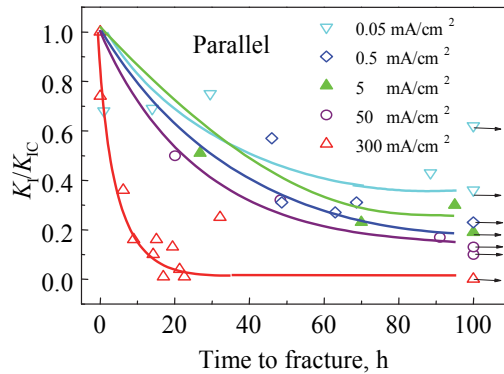
During single-edge-notched-tensile sample of PZT ferroelectric ceramics hydrogen charging dynamically in 0.2mol/l NaOH+0.25 g/l  $As_2O_3$  solution, hydrogen-induced delayed cracking (H IDC) can occur (Wang et al., 2003a) and depends on the relative orientation between notch plane and the polarization vector, i.e., the H IDC also shows anisotropy in ferroelectric ceramics, as shown in Figure 15 (Wang et al., 2003b). Hydrogen concentration  $C_H$  under different charging current densities is given in Table 2. The curve of  $K_{IH}/K_{IC}$  vs  $i$  or  $C_H$  can plot based on Table 2 and one can find a linear relationship between  $K_{IH}/K_{IC}$  and the  $\ln C_H$  (Wang et al., 2003b)

$$K_{IH}^a / K_{IC}^a = K_{IH}^b / K_{IC}^b = 0.4 - 0.15 \ln C_H \quad (5)$$

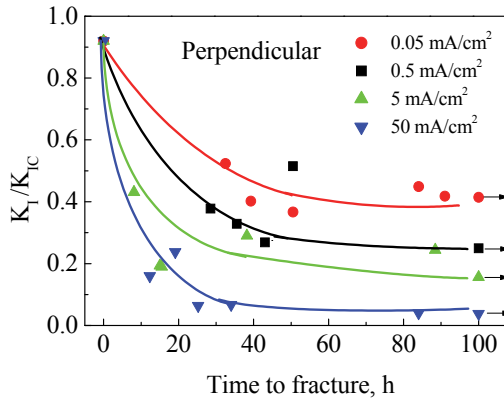
where superscript a and b denote polarization vector parallel and perpendicular to the crack plane, respectively.  $K_{IC}^a = 1.53 \text{ MPam}^{1/2}$  and  $K_{IC}^b = 1.12 \text{ MPam}^{1/2}$  for PZT ferroelectric

$i$ (mA/cm <sup>2</sup> )	0.05	0.5	5	50	300
$C_H$ (ppm)	0.92	2.61	4.8	7.16	9.84
$K_{IH}^a$ (MPam <sup>1/2</sup> )	0.54	0.34	0.28	0.13	0.01
$K_{IH}^b$ (MPam <sup>1/2</sup> )	0.36	0.26	0.17	0.08	-
$K_{IH}^a / K_{IC}^a$	0.40	0.25	0.21	0.10	0.01
$K_{IH}^b / K_{IC}^b$	0.40	0.28	0.19	0.09	-

Table 2. The threshold stress intensity factors of HIDC corresponding to various hydrogen concentrations (Wang et al., 2003b)



(a)



(b)

Fig. 15. The normalized stress intensity factor vs time to fracture during dynamically charging with various  $i$  (the arrows mean no fracture within 100 h). (a) Polarization direction parallel to the crack plane; (b) Polarization direction perpendicular to the crack plane (Wang et al., 2003b)

ceramics. Eq.5 suggests that the  $t$  anisotropy of  $K_{IH}$  is entirely caused by the anisotropy of fracture toughness.

## 6. Conclusion

In this chapter, the effects of hydrogen on main properties of ferroelectric materials are reviewed. Even if a little amount of hydrogen enters a ferroelectric material, the ferroelectricity and dielectric properties would be degraded, such as hydrogen causes hysteresis loop narrower, reduces remnant polarization, increases leakage current, etc. If great amount hydrogen is charged into ferroelectrics, hydrogen fissure and hydrogen-induced delayed cracking can occur. Fortunately, hydrogen can escape from the hydrogenated ferroelectric materials and properties can restore after a heat treatment. Therefore, outgassing treatment is an effectual method to prevent hydrogen damage. Although most of reports about hydrogen in ferroelectrics proved that hydrogen has negative influence, hydrogen can't be consider completely harmful to the ferroelectric materials. For example, a very small amount of hydrogen can enhance the ferroelectricity. Now, the mechanism of enhancement effect is not clear yet, but this phenomenon enough to absorb more interests to develop the potential role of hydrogen in ferroelectric materials.

## 7. Acknowledgment

Authors acknowledge support from the National Nature Science Foundation of China under grants 51072021 and 50632010 and from Beijing Municipal Commission of Education under YB20091000801 grant.

## 8. References

- Aggarwal, S.; Perusse, S. R.; Tipton, C. W.; Ramesh, R.; Drew, H. D.; Venkatesan, T.; Romero, D. B.; Podobedov, V. B. & Weber, A. (1998). Effect of hydrogen on  $Pb(Zr,Ti)O_3$ -based ferroelectric capacitors. *Applied Physics Letters*, Vol.73, No.14, pp. 1973-1975, ISSN 0003-6951
- Chen, F.; Chen, W. P.; Wang, Y.; Hu, Y. M.; Shen, Z. J. & Chan, H. L. W. (2011). Effects of forming gas annealing on  $LiNbO_3$  single crystals. *Physica B: Condensed Matter*, Vol. 406, No.3, pp. 683-686, ISSN 0921-4526
- Chen, W. P.; Li, L. T.; Qi, J Q. & Gui Z. L. (1998). Effect of electrochemical hydrogen charging on  $Ba_{1-x}Pb_xTiO_3$ -Based semiconducting ceramics. *Journal of Materials Science Letters*, Vol.17, No.11, pp.899-900, ISSN 0261-8028
- Joo, H. J.; Lee, S. H.; Kim, J. P.; Ryu, M. K. & Jang, M. S. (2002). Effect of hydrogen on the electrical and optical properties in ferroelectric  $Pb(Zr,Ti)O_3$  thin films. *Ferroelectrics*, Vol.272, No.1, pp.149-154, ISSN 1563-5112
- Han, J. P. & Ma, T. P. (1997). Electrode dependence of hydrogen-induced degradation in ferroelectric  $Pb(Zr,Ti)O_3$  and  $SrBi_2Ta_2O_9$  thin films. *Applied Physics Letters*, Vol.71, No.9, pp. 1267-1269, ISSN 0003-6951
- Huang, H. Y.; Chu, W. Y.; Su, Y. J.; Qiao, L. J. & Gao, K. W. (2005). Combined effect of electric field and residual stress on propagation of indentation cracks in a PZT-5H

- ferroelectric ceramic. *Materials Science and Engineering B*, Vol. 122, No.1, pp. 1-6, ISSN 0921-5107
- Huang, H. Y.; Chu, W. Y.; Su, Y. J.; Li, J. X.; Qiao, L. J. & Shi, S. Q. (2006). Experiment and first principles investigation on the hydrogen-hindered phase transition of ferroelectric ceramics. *Applied Physics Letters*, Vol.89, No.142904, ISSN 0003-6951
- Huang, H. Y.; Chu, W. Y.; Su, Y. J.; Gao, K. W.; Li, J. X. & Qiao, L. J. (2007). Hydrogen-induced semiconductor transformation of PZT ferroelectric ceramics. *Journal of the American Ceramics Society*, Vol. 90, No.7, pp. 2062 – 2066, ISSN 0002-7820
- Ikarashi, N. (1998) Analytical transmission electron microscopy of hydrogen-induced degradation in ferroelectric  $\text{Pb}(\text{Zr,Ti})\text{O}_3$  on a Pt Electrode. *Applied Physics Letters*, Vol.73, No.14, pp.1955-1957, ISSN 0003-6951
- Katz, L. E. (1988). In: VLSI Technology (2nd ed), S. M. Sze (Ed), pp. 127, McGraw-Hill, ISBN 978-007-0627-35-2, New York
- Kushida-Abdelghafar, K.; Miki, H.; Torii, K. & Fujisaki, Y. (1996). Electrode-induced degradation of  $\text{Pb}(\text{Zr}_x\text{Ti}_{1-x})\text{O}_3$  (PZT) polarization hysteresis characteristics in Pt/PZT/Pt ferroelectric thin-film capacitors. *Applied Physics Letters*, Vol.69, No.21, pp. 3188-3190, ISSN 0003-6951
- Pen, X.; Su, Y. J.; Gao, K. W.; Qiao, L. J. & Chu, W. Y. (2004). Hydrogen fissure in PZT ferroelectric ceramic, *Materials Letters*, Vol.58, No.15, pp. 2073-2075, ISSN 0167-577x
- Shimamoto, Y.; Kushida-Abdelghafar, K.; Miki, H. & Fujisaki, Y. (1997).  $\text{H}_2$  damage of ferroelectric  $\text{Pb}(\text{Zr,Ti})\text{O}_3$  thin-film capacitors-The role of catalytic and adsorptive activity of the top electrode. *Applied Physics Letters*, Vol.70, No.23, pp. 3096-3097, ISSN 0003-6951
- Tamura, T.; Matsuura, K.; Ashida, H.; Kondo, K. & Otani, S. (1999). Hysteresis variations of  $(\text{Pb,L a})(\text{Zr,Ti})\text{O}_3$  capacitors baked in a hydrogen atmosphere. *Applied Physics Letters*, Vol.74, No. 22, pp.3395-3397, ISSN 0003-6951
- Wang, Y.; Chu, W. Y.; Qiao, L. J. & Su, Y. J. (2003a). Hydrogen-induced delayed fracture of PZT ceramics during dynamic charging under constant load · *Materials Science and Engineering B*, Vol. 98, No.1, pp. 1-5, ISSN 0921-5107
- Wang, Y.; Chu, W. Y.; Su, Y. J.; Qiao, L. J. & Gao, K. W. (2003b) · Hydrogen-induced cracking and its anisotropy of a PZT ferroelectric ceramics · *Science in China E*, Vol.46, No.3, pp.318-325, ISSN 1674-7321
- Wu, M.; Huang, H. Y.; Jiang, B.; Chu, W. Y.; Su, Y. J.; Li, J. X & Qiao, L. J. (2009). Experiments and first principles calculations on the effects of hydrogen on the optical properties of ferroelectric materials. *Journal of Materials Science*, Vol. 44, No.21, pp. 5768-5772, ISSN 0022-2461
- Wu, M. (2009). Study of effect of hydrogen on the properties of ferroelectric ceramics. Doctoral dissertation, University of Science and Technology Beijing.
- Wu, M.; Huang, H. Y.; Chu, W. Y.; Guo, L. Q.; Qiao, L. J.; Xu, J. Y. & Zhang, T. Y. (2010). Tuning the ferroelectric and piezoelectric properties of  $0.91\text{Pb}(\text{Zn}_{1/3}\text{Nb}_{2/3})\text{O}_3$ - $0.09\text{PbTiO}_3$  single crystals and lead zirconate titanate ceramics by doping hydrogen. *Journal of Physical Chemistry C*, Vol.114, No.21, pp. 9955-9960, ISSN 1932-7447

---

Zhang, H.; Su, Y. J.; Qiao, L. J. & Chu, W. Y. (2008). The Effect of Hydrogen on the Fracture Properties of  $0.8(\text{Na}_{1/2}\text{Bi}_{1/2})\text{TiO}_3$ - $0.2(\text{K}_{1/2}\text{Bi}_{1/2})\text{TiO}_3$  Ferroelectric Ceramics. *Journal of Electronic Materials*, Vol.37, No. 3, pp.368-372, ISSN 0361-5235

# Thermal Conduction Across Ferroelectric Phase Transitions: Results on Selected Systems

Jacob Philip

*Department of Instrumentation and STIC, Cochin University of Science and Technology  
India*

## 1. Introduction

A *ferroelectric* phase transition represents a special class of structural phase transition characterized by the appearance of a spontaneous polarization in the material. Above the Curie temperature the transition often follows a diverging differential dielectric response or permittivity  $\epsilon$ , which varies with temperature in an approximate Curie-Weiss manner  $\epsilon = C/(T-T_0)$ , where  $T_0$  is the Curie-Weiss temperature, which is equal to the Curie temperature  $T_c$  for a continuous transition. The crystalline phase which undergoes transformation to the ferroelectric form at  $T_c$  is the *paraelectric* one. Below  $T_c$  in the absence of an applied field, there are at least two directions along which a spontaneous polarization can develop. To minimize the depolarizing fields different regions of the crystal polarize in each of these directions, each volume of uniform polarization being called a *domain*. The resulting *domain structure* usually results in a near complete compensation of polarization and the crystals consequently exhibit very small pyroelectric effects until they are poled by the application of a field.

A ferroelectric transition is usually associated with the condensation of a *soft* (or low-frequency) mode of lattice motion at the Brillouin-zone centre. Structural transitions triggered by zone-centre soft modes are generally termed *ferrodistortive*, and in this sense ferroelectrics constitute a subgroup of the class of *ferrodistortive* transitions. This subgroup involves the condensation of a polar or optically active mode whose condensation causes the appearance of a long range polar order. If the transition is strongly first order then mode softening may not occur to a significant degree, and in this situation, there is also a possibility that the large polarization which sets in discontinuously at  $T_c$  may not be reversible, or the low temperature phase may be pyroelectric only. Ferroelectric transitions are categorized as being either *displacive* or *order-disorder* in character. This distinction is generally made in terms of whether the paraelectric phase is microscopically nonpolar (displacive) or only nonpolar in a macroscopic or thermally averaged sense (order-disorder). The displacive or order-disorder character is often defined in terms of the dynamics of the phase transition, as to whether the soft mode is a propagating or diffusive type respectively. The displacive or propagating soft mode is a damped optic phonon, representing small quasi-harmonic motion about the mean position, while the diffusive soft mode represents large amplitude thermal hopping motion between the domain wells.

Although most ferroelectrics are ferrodistortive (common examples being barium titanate, sodium nitrite, and triglycine sulphate) some are not. To understand this it is necessary to recognize that, because of the existence of coupling between modes, it is not a necessary

condition for ferroelectricity that a zone centre polar mode should be driving the instability. Sometimes a driving antidistortive mode can couple directly or indirectly to a zone centre polar mode and upon condensation induce a small spontaneous polarization in an indirect fashion. In this case the primary order parameter is antidistortive in character while the spontaneous polarization is said to be a secondary order parameter of the transition. There can of course be only one primary order parameter (at least for a continuous or near continuous transition), but there may be many induced or secondary order parameters resulting from couplings to the primary order parameter. All the known antiferroelectrics (examples: lead zirconate, ammonium dihydrogen phosphate etc.) are intrinsically antidistortive, although one can conceive of a ferrodistoritive antiferroelectric as one having an antiparallel arrangement of electric dipoles occurring within a primitive cell of the higher-symmetry phase. Such a phase is characterized by the condensation of an antipolar zone-centre soft mode.

Once the importance of coupling between polar modes and other modes has been recognized it is clear that, via the piezoelectric interaction (or coupling to acoustic modes), a spontaneous strain will be virtually a universal characteristic of ferroelectrics since all ferroelectrics are piezoelectric. If this strain can be switched by application of stress then an obvious parallel in elastic terms exists with ferroelectricity. This property is termed ferroelasticity, and a crystal is said to be ferroelastic when it has two or more orientation states in the absence of mechanical stress (and electric field) and can be shifted from one to another of these states by mechanical stress. Intrinsic ferroelastic transitions are associated with the condensation of long-wavelength acoustic phonons and many are known.

The optical and acoustic phonon modes involved in ferroelectric and ferroelastic phase transitions can be probed with Brillouin light scattering and ultrasonic techniques. When phonon modes soften, the involved elastic constants undergo anomalous variations which get reflected in ultrasound velocity and attenuation. Elaborate reviews on these subjects have appeared in literature (Luthi & Rehwald, 1980; Cummins, 1990). Other popular techniques used to probe modes in ferroelectrics are dielectric spectroscopy (Grigas, 1996) and neutron scattering (Dorner, 1981). A number of books and reviews on these subjects have appeared in literature (Lines & Glass, 1977). Though technique like measurement of thermal conductivity across phase transition can reveal information about the coupling between ferroelectric soft modes and thermal phonons, not many measurements have appeared in literature on this. The few measurements that have appeared in literature have used the well established steady-state methods of measuring thermal conductivity (Dettmer et al., 1989).

There are several ferroelectrics that undergo successive phase transitions with *incommensurate phases* (I-phase) from a symmetrical paraelectric to an incommensurate phase at  $T_i$  and then from the incommensurate phase to a commensurate polar phase at  $T_c$  (Cummins, 1990, Blinc & Levanyuk, 1986). This phase transition sequence can be qualitatively described in terms of the phenomenological Landau theory of phase transitions (Toledano & Toledano, 1987). The appearance of an I-modulated structure can be observed experimentally as satellite peaks in X-ray or neutron diffraction patterns. In the I-phase, at temperatures close to  $T_i$ , the I-modulation wave is harmonic, but as the temperature approaches  $T_c$ , the ideal crystal can be considered as a system of equally spaced commensurate constant-phase domains separated by narrow phase varying regions, i.e., phase solitons. The presence of these modulation waves can influence heat conduction in ferroelectric crystals in two distinctive ways. As has been shown earlier, an interaction

manifested in sound attenuation exists between the acoustical waves and the I-modulation waves in the I-phase (Levanyuk et al., 1992; Lebedev et al., 1992). The usual expression for the thermal conductivity in an insulating crystal is given by

$$\lambda = \frac{1}{3} C \cdot \bar{v} \cdot l \quad (1)$$

where  $C$ ,  $\bar{v}$  and  $l$  denote the specific heat, group velocity, and mean free path for phonons, respectively (Ashcroft & Mermin, 1976). The incommensurate modulation waves can affect the mean free path and, consequently, can cause an anomalous variation of thermal conductivity in the I-phase. Another possibility is that the modulation waves may participate directly in heat conduction as carriers. In this case, one would expect the modulation waves to enhance the thermal conductivity by the sliding motion in addition to causing the usual phonon scattering effect. The effect of sliding modulation waves on thermal conductivity has been investigated earlier within a phenomenological approach (Levanyuk et al., 1992). In spite of the fact that measurement of thermal properties across transition points is highly relevant to understand the coupling between modes, only limited experimental work has appeared on this in literature.

## 2. Overview of thermal properties across ferroelectric phase transitions

In the few measurements of the variations of thermal conductivity near ferroelectric phase transitions reported in literature, steady state methods have been employed. One of the first measurements was on BaTiO<sub>3</sub> by Mante & Volger (1967). Their results show dips in thermal conductivity at temperatures corresponding to phase transition points. The results are explained in terms of mode conversion near the transition points. The low lying temperature dependant optical phonon branches can get zero energy at zero wave-vector, which causes permanent polarization of the crystal. Near the transition temperature the optical branches have energies comparable to those of the acoustic branches which usually transport the heat. This influences the number of scattering processes in which optical phonons participate, resulting in a reduction of the conductivity due to acoustic branches. In case transverse optical phonon branch shows enough dispersion and is not scattered too much, one can expect additional conductivity which might compensate for the effect of decreased conduction by the acoustic phonons.

Thermal conductivities and specific heat capacities of a wide spectrum of ferroelectrics, BaTiO<sub>3</sub>, PbTiO<sub>3</sub>, KNbO<sub>3</sub>, KTaO<sub>3</sub>, NaNbO<sub>3</sub> and Pb(Mg<sub>1/3</sub>Nb<sub>2/3</sub>)O<sub>3</sub> (PMN) single crystals have been measured from 2 to 390 K (Tachibana et al., 2008). Pronounced jumps are found at structural transitions in BaTiO<sub>3</sub> and KNbO<sub>3</sub>. A low-temperature anomaly from soft optical phonons is observed in KTaO<sub>3</sub>. For PMN and NaNbO<sub>3</sub>, glass-like behaviour is observed in both thermal conductivity and heat capacity measurements. The glass-like behaviour in NaNbO<sub>3</sub> is associated with the phase separation phenomena which have been reported in earlier studies. Thermal analysis techniques such as differential scanning calorimetry (DSC) have been employed by several researchers to probe ferroelectric phase transitions (Setter & Cross, 1980, Podlojenov et al., 2006).

Belov & Jeong (1998) have reported thermal conductivity measurements for two ferroelectric crystals, (NH<sub>4</sub>)<sub>2</sub>BeF<sub>4</sub> and Rb<sub>2</sub>ZnCl<sub>4</sub>, with incommensurate phases. It is found that anomalies exist in the thermal conductivities of these crystals in the I-phases. I-modulation waves cause anomalies in the heat transport processes by scattering of heat carrying phonons

rather than by their direct participation as heat carriers. They have employed the steady-state technique for their measurements. Comparatively large samples, of size typically greater than 5 mm<sup>3</sup>, are needed for these techniques in order to avoid boundary effects. Moreover, comparatively large rises in temperature are often necessary to obtain a reasonably high signal to-noise ratio, which lead to considerable temperature gradients being set up in the sample. These drawbacks make these techniques unsuitable for studying critical thermal conductivity behaviour near phase transitions.

Thermal wave measurements based on a photothermal effect, such as the photothermal deflection technique, photoacoustic method and photopyroelectric measurement do not disturb the thermal equilibrium of the sample during transitions. In these techniques one measures the thermal diffusivity, rather than thermal conductivity. Thermal diffusivity measurements do not suffer from heat losses from the sample during measurements and hence are more accurate than a direct measurement of thermal conductivity by the steady state method. With a proper choice of boundary conditions, photothermal techniques make a simultaneous measurement of thermal diffusivity and thermal effusivity possible, from which the thermal conductivity and specific heat capacity can be extracted. The photopyroelectric technique has been used earlier to measure the variations of thermal conductivity and heat capacity of a few crystalline solids as they undergo phase transitions with temperature (Marinelli et al., 1990; Zammit et al., 1988; Mandelis et al., 1985).

### 3. The photopyroelectric technique

Complete characterization of the thermal properties of a material requires the determination of the thermal transport properties such as the thermal conductivity as well as the specific heat capacity. Techniques for high resolution measurement of specific heat capacity are well established (Kasting et al., 1980; Thoen et al., 1982). It has been shown that photothermal techniques allow simultaneous measurement of specific heat capacity  $c_p$  and thermal conductivity  $\lambda_s$  (Marinelli et al., 1990). The photoacoustic technique has been used for the simultaneous determination of the thermal diffusivity, thermal conductivity and heat capacity of liquid-crystalline compounds (Zammit et al., 1988). A somewhat similar technique has been used for measuring the thermal diffusivity and heat capacity of solids at room temperature using a photopyroelectric (PPE) detector (Mandelis et al., 1985; John et al., 1986). This technique enables simultaneous determination of thermal diffusivity, thermal effusivity, thermal conductivity and heat capacity as a function of temperature. Moreover, this technique allows studies of critical behaviours of thermal parameters when the material undergoes a transition. Marinelli et al. (1990) developed a technique to determine thermal diffusivity, thermal conductivity and heat capacity simultaneously at low temperatures with a pyroelectric detector kept in vacuum. At temperatures above room temperature, the boundary conditions involved in the theory of this method are not easy to satisfy, so that application of the method can lead to errors in measurement.

A photothermal technique for the simultaneous determination of the thermal conductivity and specific heat capacity near solid state phase transitions using a pyroelectric detector kept in contact with a thermally thick backing medium has been developed by Menon & Philip (2000). The PPE technique has some distinct advantages, such as its simplicity, good sensitivity and ability to perform nondestructive probing, over other photothermal methods. In this measurement the sample is heated by a modulated light source on one side and the temperature oscillations on the opposite side of the sample are detected with a

pyroelectric detector, supported on a thermally thick conductive backing. Since the PPE signal depends on properties of the detector which are also temperature dependent, an accurate temperature calibration of the system must be carried out. The advantage of a thermally thick backing is that there will be sufficient heat exchange between the heated pyroelectric detector and the backing, so that signal fluctuations are reduced to a minimum. This method can, in principle, be adapted to all temperature ranges for all samples and is not limited by the thermal properties of the sample.

The PPE effect is based on the use of a pyroelectric transducer to detect the temperature rise due to periodic heating of a sample by induced light. The temperature variations in the detector give rise to an electrical current, which is proportional to the rate of change of the average heat content, given by (Mandelis & Zver, 1985)

$$i_d = P A \left( \frac{\partial \theta(t)}{\partial t} \right) \quad (2)$$

where  $P$  is the pyroelectric coefficient of the detector,  $A$  is the area of the detector and

$$\theta(t) = \left( \frac{1}{L_d} \right) \int_0^{L_d} \theta(x, t) dx \quad (3)$$

is the spatially averaged temperature variation over the thickness of the detector,  $L_d$ .

For a thermally thick sample with  $\mu_s < L_s$ , and a thermally thick pyroelectric detector with  $\mu_d < L_d$ , where  $\mu_s$  and  $\mu_d$  are the thermal diffusion lengths of the sample and detector respectively, the expressions for the PPE amplitude and phase expressions for the values of the thermal diffusivity  $\alpha_s$  and effusivity  $e_s$  which allow a simultaneous determination of the thermal conductivity and heat capacity if the density  $\rho_s$  of the sample is known. The expressions for the temperature dependent PPE amplitude and phase under the above conditions are given by (Menon & Philip, 2000)

$$V(f, T) = \left( \frac{I_0 \eta_s A R d}{L_d \sqrt{1 + (f/f_c)^2}} \right) \left( \frac{P(T)}{\rho_d(T) c_{pd}(T)} \right) \frac{\exp \left( - \left\{ \sqrt{\frac{\pi f}{\alpha_s}} \right\} L_s \right)}{\left( \frac{e_s(T)}{e_d(T)} + 1 \right)} \quad (4a)$$

$$\phi(f, T) = -\tan^{-1} \left( \frac{f}{f_c} \right) - \left( \sqrt{\frac{\pi f}{\alpha_s(T)}} \right) L_s \quad (4b)$$

where  $T$  is the temperature and  $c_{pd}$  and  $\rho_d$  are the heat capacity (at constant pressure) and density of the detector respectively.  $f_c$  is the characteristic frequency at which the sample goes from a thermally thin to thermally thick regime. From these two expressions it is clear that the thermal diffusivity  $\alpha_s$  of the sample can be calculated from the phase of the PPE signal, which when substituted into the expression for the PPE amplitude, gives the thermal effusivity of the sample. From these the thermal conductivity and heat capacity of the sample can be calculated from the following relations:

$$\lambda_s(T) = e_s(T) \sqrt{\alpha_s(T)} \quad (5a)$$

$$c_{ps}(T) = \frac{e_s(T)}{\rho_s(T)\sqrt{\alpha_s(T)}} \quad (5b)$$

A temperature calibration of the PPE detector is necessary here as all the parameters in equations (4a) and (4b) are temperature dependent. All the thermal parameters can be calculated as functions of the sample temperature, provided that the temperature dependences of the parameters of the pyroelectric detector are known.

#### 4. Experimental methods in PPE measurements

A sample set-up of the type shown in Fig. 1 is generally used for these measurements (Menon & Philip, 2000). A 120 mW He - Cd laser of  $\lambda = 442$  nm, modulated by a mechanical chopper, has been used as the optical heating source. A 28  $\mu\text{m}$  thick film of PVDF with pyroelectric coefficient  $P = 0.25 \times 10^{-8}$  V cm $^{-1}$  K $^{-1}$  at room temperature has been used as the pyroelectric detector. The sample is attached to the pyroelectric detector with a thermally very thin layer of a heat sink compound whose contribution to the signal is negligible. The pyroelectric detector attached to the sample is placed on a thermally thick backing medium (copper) which satisfies the boundary condition specified above. The frequency of modulation of the light is kept high enough to ensure that the PVDF film, the sample and the backing medium are all thermally thick. The signal output is measured with a lock-in amplifier. The sample-detector-backing assembly is enclosed in a chamber whose temperature can be varied and controlled as desired. Measurements as a function of temperature have been made at a low heating rate with special care near transition points. A block diagram of the experimental set up is shown in Fig. 2 for illustration.

The experimental set up and procedure should be calibrated and tested to ensure that even minor variations in heat capacity and thermal conductivity do get reflected in the measurements. Practically one measures the PPE amplitude and phase as function of modulation frequency, limiting the frequency to low values so that the sample, detector and backing are all thermally thick. From the amplitude and phase variations one can determine the thermal effusivity and thermal diffusivity following equations (4a) and (4b) respectively. From the values of thermal diffusivity and thermal effusivity, the values of thermal conductivity and specific heat capacity can be determined following equations (5a) and (5b).

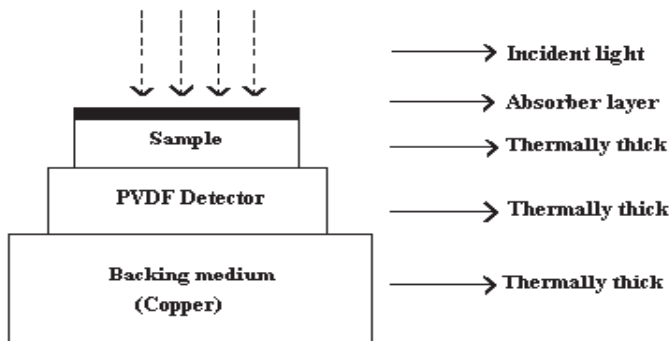


Fig. 1. The sample configuration for the photopyroelectric set-up

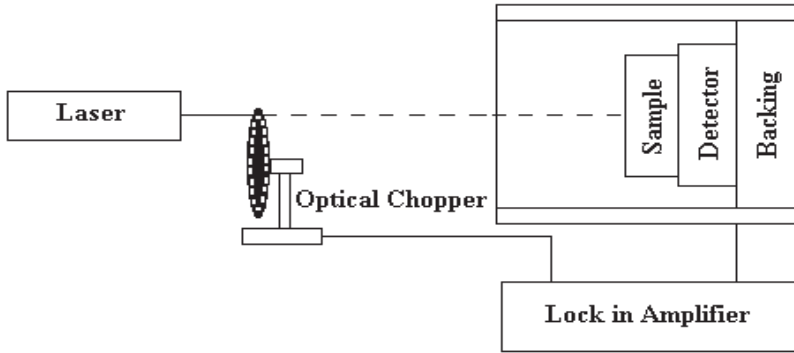


Fig. 2. Block diagram of the experimental set-up used for PPE measurements

Practically one measures the photopyroelectric signal amplitude and phase as function of modulation frequency. One will have inverse frequency dependence for the amplitude and phase beyond the critical frequency when the boundary conditions assumed are satisfied. A fitting of the variations of PPE amplitude and phase with the relations connecting thermal diffusivity and effusivity with phase and amplitude respectively enables one to determine the thermal diffusivity and effusivity. Typical variations of PPE amplitude and phase with modulation frequency obtained during PPE measurements in  $\text{K}_2\text{SeO}_4$  are shown in figures 3a and 3b respectively. The peaks in the curves correspond to characteristic modulation frequency for the sample.

## 5. Results on specific systems and discussion

The variations in the thermal properties of the ferroelectric crystal Triglycine sulphate (TGS) were reported by Menon & Philip (2000). TGS crystals undergo a para-ferroelectric phase transition at  $49.4^\circ\text{C}$ . This crystal has a monoclinic structure at room temperature. Platelets of the crystal of sub-millimeter thickness were cut with faces normal to  $a$ ,  $b$  and  $c$  axes so that the direction of propagation of thermal waves was along one of the axes. A very thin layer of carbon black was coated onto the illuminated surface of the sample to enhance its optical absorption. Measurements were carried out as a function of temperature from room temperature ( $26^\circ\text{C}$ ) to  $55^\circ\text{C}$ . The thermal thickness of the sample in these experiments was verified by plotting the PPE amplitude and phase against modulation frequency at a number of temperatures between room temperature and  $55^\circ\text{C}$ . The variations of the PPE amplitude and phase as functions of temperature were measured keeping the modulation frequency fixed at 40 Hz. From these, the thermal diffusivity ( $a_s$ ) and effusivity ( $e_s$ ) along the  $b$  axis of TGS were determined as functions of temperature. These are shown in Fig. 4a. The temperature variations of  $\lambda_s$  along the  $b$  axis and  $c_{ps}$  were also determined (shown in Fig. 4b). The heat capacity results presented in Fig. 4b agree with those already reported in the literature (Strukov & Levanyuk 1998). Their results showed that thermal conductivity along the  $b$  axis has a minimum value at the transition point. Measurements of the thermal diffusivity or conductivity along  $a$ - and  $c$ - axes did not reveal any anomaly at the phase transition temperature. This was in agreement with thermal diffusivity measurements along these axes reported earlier (Gaffar et al., 1987).

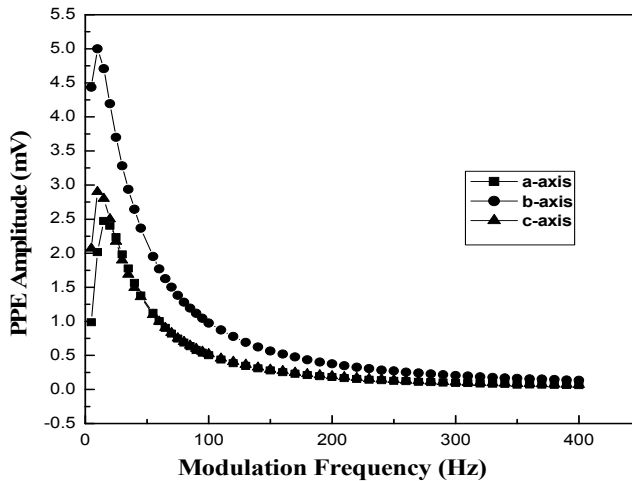


Fig. 3. (a) Frequency dependence of the photo-pyroelectric amplitudes along the three principal axes of  $K_2SeO_4$  at room temperature (Philip & Manjusha, 2009)

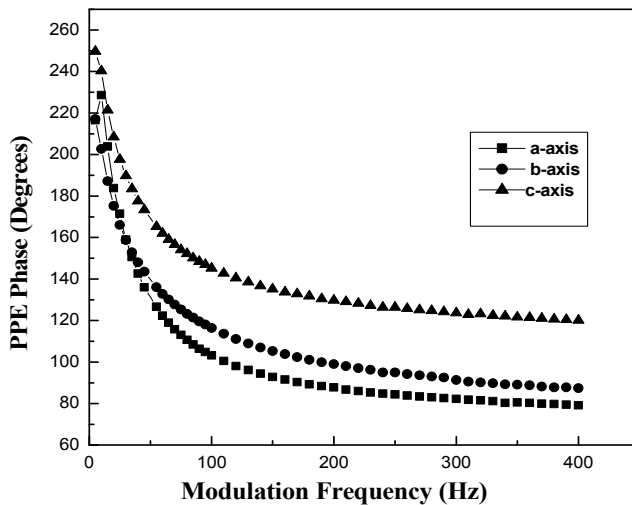


Fig. 3. (b) Frequency dependence of the photopyroelectric phases along the three principal axes of  $K_2SeO_4$  at room temperature (Philip & Manjusha, 2009)

Ferroelectric crystals, which exhibit incommensurate phase transitions include ammonium fluroberrylate (Iizumi & Gesi, 1977), potassium selenate (Iizumi et al., 1977), sodium nitrite (Yamada et al., 1963), thiourea (Goldsmith & White, 1959) etc. Thiourea, with the chemical formula  $SC(NH_2)_2$ , undergoes successive phase transitions at 169 K ( $T_1$ ), 176 K ( $T_2$ ), 180 K ( $T_3$ ) and 202 K ( $T_4$ ). Among the five phases (called I, II, III, IV and V) in the order of increasing temperature, two of them (I and III) are ferroelectric and a superlattice structure appears in the II, III and IV phases (Elcombe & Tayler, 1968). The crystal structure in the

room temperature phase V above  $T_4$  is orthorhombic and belongs to the space group  $D^{16}_{2h}-Pbnm$  with four molecules per unit cell ( $Z = 4$ ). The phase I below  $T_1$  is a ferroelectric one having spontaneous polarization along the  $b$ -axis, whose crystal structure is also orthorhombic with four molecules per unit cell ( $Z = 4$ ).

In the three intermediate phases, II, III and IV between  $T_1$  and  $T_4$ , Shiozaki (1971) analyzed X-ray reflection spectra and concluded that the crystal has an in-commensurate structure. According to his analysis, just above  $T_4$  the crystal has a superstructure along the  $c$ -axis with a period about eight times as large as that of phase IV. The period of the super structure increases as temperature decreases. So in the vicinity of  $T_1$ , the period is about ten times as large and at  $T_1$  the crystal transforms to the ferroelectric phase I, where the period of the unit cell of the prototype is restored. More elaborate descriptions of the properties of thiourea are available in literature (Wada et al., 1978, Mouden et al., 1978, Mc Kenzie, 1975a, Mc Kenzie, 1975b, Delahigue et al., 1975, Chapelle & Benoit, 1977).

The thermal properties described above during the incommensurate-commensurate phase transition in thiourea were measured employing PPE technique (Menon & Philip, 2003). Measurements have been done along the three principal directions of thiourea and the observed anisotropy in thermal transport is discussed. The crystals were cut with their faces normal to the [100], [010] and [001] directions of the crystallographic  $a$ -,  $b$ - and  $c$ -axes respectively. Measurements were carried out illuminating the three cut sample faces so that the propagation of the thermal wave is along one of the symmetry directions. The variations of thermal conductivity and heat capacity as functions of temperature across the transition temperatures were measured as outlined above.

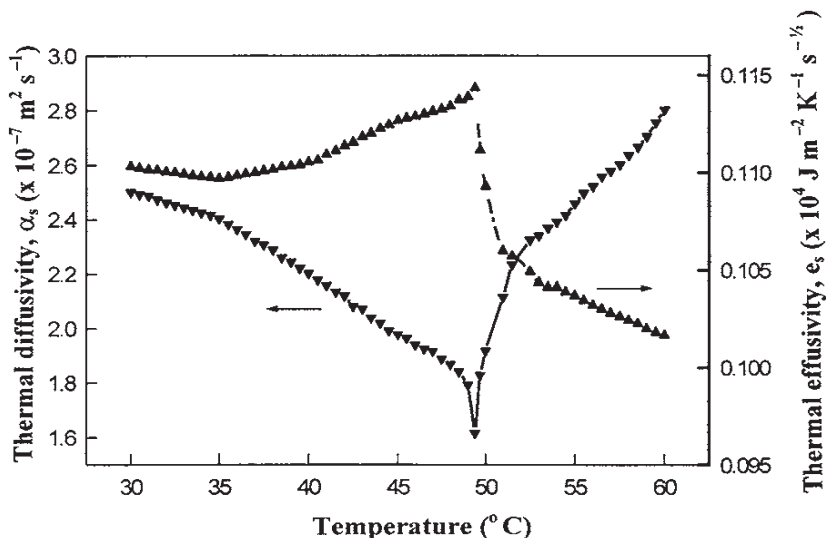


Fig. 4. (a) Variations of the thermal diffusivity (inverted triangles) and thermal effusivity (triangles) with temperature for TGS along the  $b$  axis (Menon & Philip, 2000)

It was seen that both PPE amplitude and phase clearly reflect the three successive phase transitions in thiourea. The maximum anomaly was at  $T_1$ , the temperature at which transition to an in-commensurate phase took place. Anomalies were measured along  $a$ ,  $b$

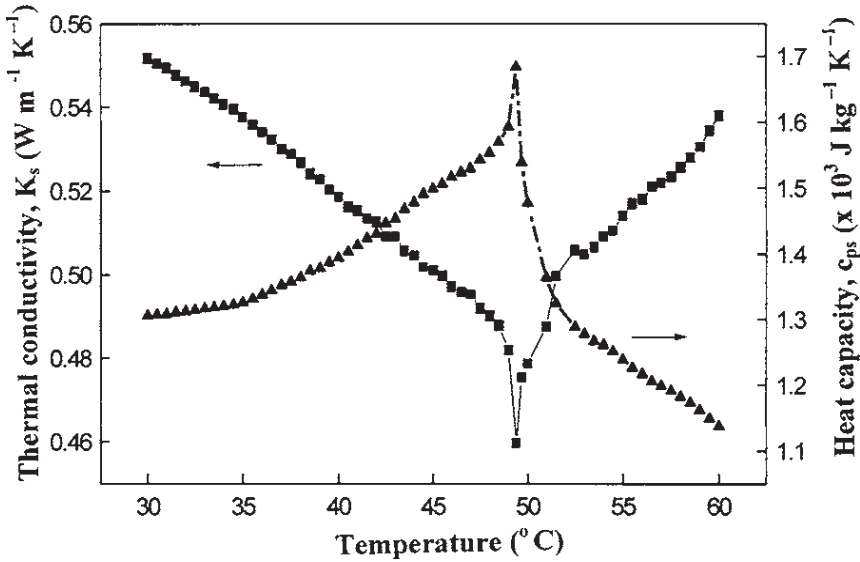


Fig. 4. (b) Variations of the thermal conductivity (inverted triangles) and heat capacity (triangles) with temperature along the  $b$ -axis (Menon & Philip, 2000)

and  $c$  directions at the same temperatures. The maximum variation was seen along the  $b$ -direction, the direction in which the crystal possesses spontaneous polarization in the ferroelectric phase. Fig. 5a shows the variations of thermal diffusivity and thermal effusivity with temperature along the  $b$ -axis of thiourea single crystal. As can be seen in this figure, thermal diffusivity shows a decrease with temperature, with distinct minima at the three phase transition points at  $T_1 \approx 169$  K,  $T_3 \approx 176$  K and  $T_4 \approx 202$  K, in agreement with the already reported values of transition temperatures. Thermal effusivity exhibits an inverse behaviour. It increases with temperature, with sharp peaks occurring at the transition temperatures. Taking into account the various uncertainties of the measurement, the overall uncertainty in the values of  $\alpha$  and  $e$  are estimated to be less than 5%. Similar anomalies with smaller magnitudes have been obtained for the  $a$ - and  $c$ -directions as well.

Figure 5b shows the variation of heat capacity of thiourea with temperature. As can be seen in this figure, the three transitions get clearly reflected in the temperature variation of heat capacity as clear anomalies at the transition points. These heat capacity values agree with the values reported by earlier workers (Hellwege & Hellwege, 1969). As can be seen, there is no direction dependence for heat capacity. Figure 5c shows the temperature variation of thermal conductivity along the three symmetry directions ( $a$ ,  $b$  and  $c$ ) of thiourea. The thermal conductivity exhibits significant anisotropy, as is evident from Fig. 5c. The three transitions get clearly reflected in the thermal conductivity variations as well. The maximum anomaly at the transition temperatures is seen along the  $b$ -axis. The maximum thermal conduction occurs in the direction of predominant covalent bonding, which is along the  $b$ -axis in thiourea. This is the direction of spontaneous polarization in this crystal.

Dicalcium Lead Propionate (DLP, with chemical formula  $\text{Ca}_2\text{Pb}(\text{C}_2\text{H}_5\text{COO})_6$ , belonging to the family of double propionates, is ferroelectric below 333K along the  $c$ -axis (Nakamura et al 1965). It undergoes a para to ferro electric phase transition at 333K ( $T_{c1}$ ), which is a second

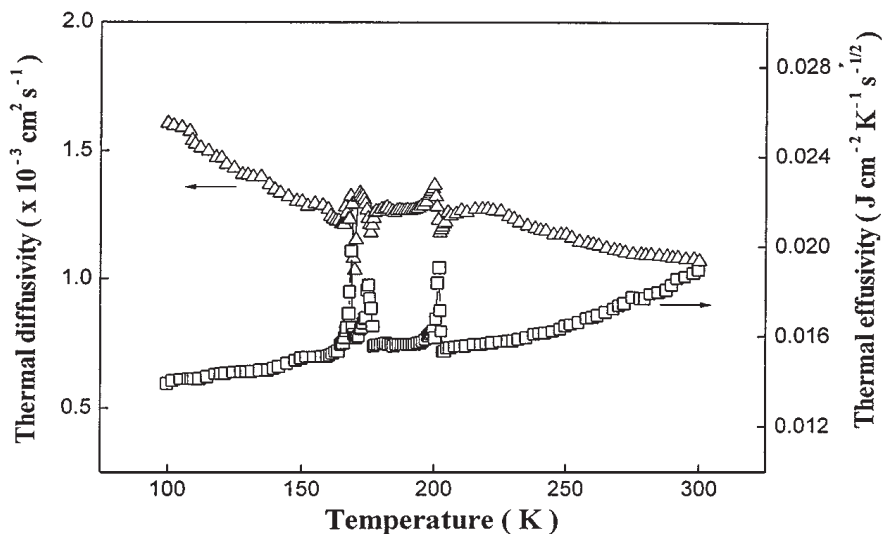


Fig. 5. (a) Temperature variations of thermal diffusivity and thermal effusivity along the *b*-axis of thiourea single crystal. Similar variations to a lesser extent were exhibited by *a*- and *c*-directions (Menon & Philip, 2003)

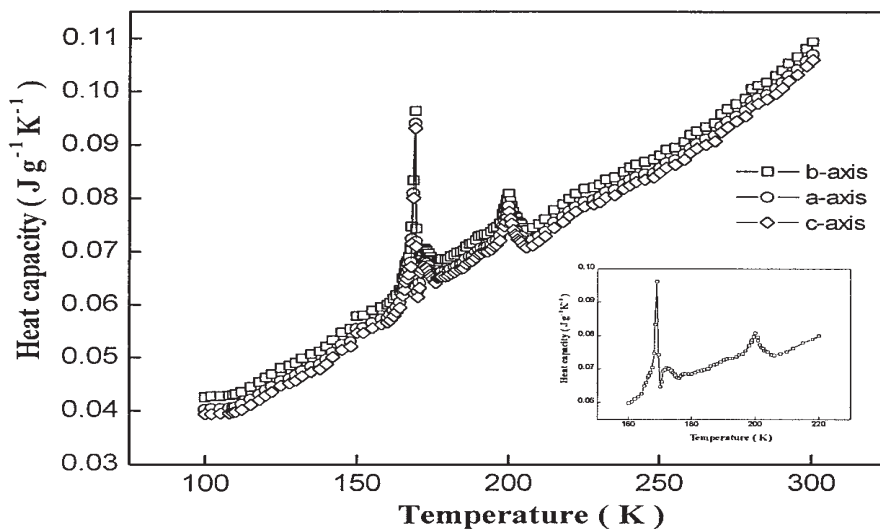


Fig. 5. (b) Temperature variation of heat capacity along three principal directions of thiourea single crystal. The inset shows the variation of heat capacity between 160 K and 220 K along the *b*-axis (Menon & Philip, 2003)

order one. Upon decreasing the temperature further, it undergoes another phase transition at 191K ( $T_{c2}$ ), which is first order. The transition at  $T_{c1}$  is associated with the movement of the ethyl group ( $C_2H_5$ ) (Nakamura et al., 1978), but the one at  $T_{c2}$  is still not understood

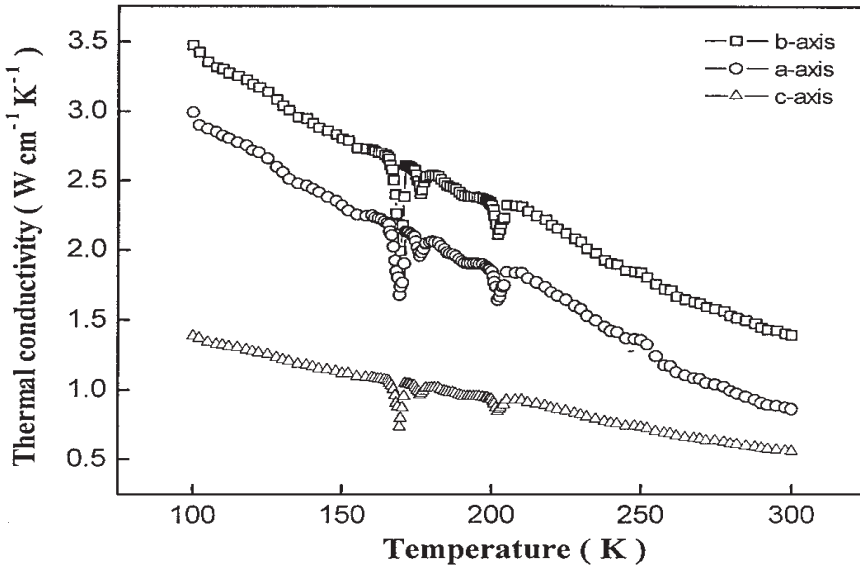


Fig. 5. (c) Temperature variations of thermal conductivity along three principal directions of thiourea single crystal. (Menon & Philip, 2003)

well. Even below this transition temperature the material continues to remain ferroelectric. Based on the measurement of the hydrostatic pressure dependence of the crystal structure of DLP above and below the respective phase transitions, Gesi & Ozawa (1975) have proposed that the phases above and below  $T_{C2}$  are isomorphous to each other. However, on the basis of polarizing microscopic observations and dielectric constant measurements, Gesi (1984) has concluded that the two phases above and below  $T_{C2}$  are not isostructural.

The crystal structure of DLP is tetragonal at room temperature (Ferroni & Orioli, 1959). The lead atoms are located at  $4a$  positions and calcium atoms at  $8b$  positions. Studies on the pyroelectric properties of DLP associated with its phase transitions have led to the conclusion that DLP crystal between  $T_{C1}$  and  $T_{C2}$  is tetragonal and polar, the point group in this phase being  $C_4$  or  $C_{4v}$  (Osaka et al., 1975). Raman, infrared and dielectric properties of this crystal has been studied by earlier workers (Nagae et al., 1976, Takashige et al., 1978). The phase diagrams of mixed crystal system DSP-DLP, where DSP stands for Dicalcium Strontium propionate, has been determined by Nagae et al. (1976) from dielectric and dilatometric measurements. Nage et al., (1976) have reported Raman scattering spectra of DSP and DLP between 73 and 423K. They concluded that both phase transitions of these two materials are of the order – disorder type since no soft modes are observed, implying that these transitions are most probably isomorphous. Takashige et al. (1978) have reported the piezoelectric and elastic properties of ferroelectric DLP over a wide temperature region, including the ferroelectric-paraelectric phase transition point ( $T_{C1}$ ).

Even though the specific heat of DLP was reported way back in 1965 (Nakamura et al., 1965), other thermal properties such as thermal conductivity were not. Moreover, systematic thermal analysis following thermogravimetry or scanning calorimetry through  $T_{C1}$  and  $T_{C2}$  have not been reported. These measurements in DLP through the transition temperatures have been reported by Manjusha & Philip (2008). These authors have reported thermal

transport properties of the sample, thermal diffusivity, effusivity, conductivity and specific heat capacity as a function of temperature following PPE technique. The anisotropy in thermal diffusivity/conductivity along the principal axes as well as their variation through these transition temperatures was measured.

The variations of thermal properties, shown in figures 6a and 6b, clearly indicate that the thermal properties undergo anomalous variations during phase transitions at 191 K and 333 K. In general, the thermal diffusivity and thermal conductivity show an anomalous decrease during transitions, whereas the heat capacity shows a corresponding anomalous increase. Being an electrical insulator crystal, the major contribution to the heat capacity of DLP is from lattice phonons and the electronic contribution to heat capacity is very small. As the phonon modes undergo variations due to mode instability at the transition points, they absorb excess energy giving rise to enhancement in heat capacity. This is found to get reflected in the DSC curve as well. Again, during the transitions, the phonon mean-free path increases, resulting in a decrease in thermal resistance or a corresponding increase in thermal diffusivity and thermal conductivity. The anisotropy in thermal conductivity is not very high for this crystal. The maximum thermal conduction occurs along the *c*-axis, which is the direction of spontaneous polarization.

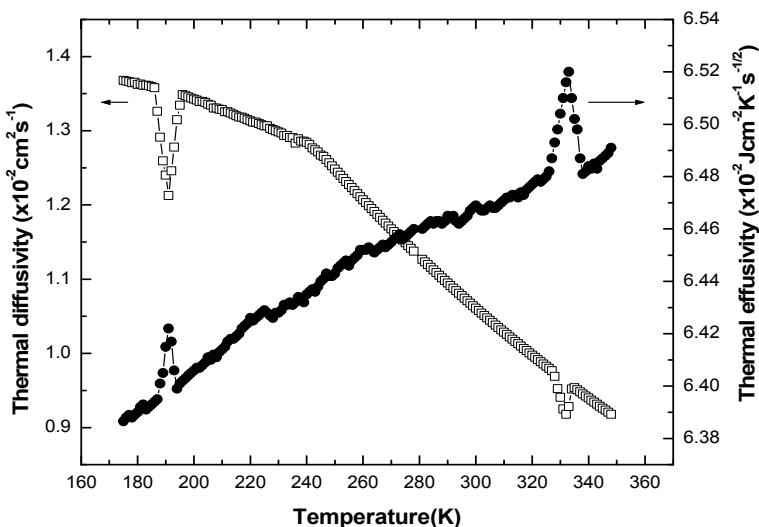


Fig. 6. (a) Variation of thermal diffusivity and thermal effusivity for DLP crystal, cut with faces normal to the *c*-axis (Manjusha & Philip, 2008)

Many experimental and theoretical studies have been carried out by different workers to understand the mechanisms of phase transitions in potassium selenate ( $K_2SeO_4$ ) single crystals, ever since the discovery of ferroelectricity and successive phase transitions in this crystal (Aiki *et al.*, 1969). With the occurrence of ferroelectric phase, this material undergoes an incommensurate phase (IC phase) transition. Potassium selenate undergoes three successive phase transitions at temperatures  $T_1 = 745$  K,  $T_2 = 129.5$  K and  $T_3 = 93$  K (Aiki *et al* 1969). The crystal exhibits hexagonal structure in phase I, with space group  $D_{46h}$  ( $P63/mmc$ ) (Shiozaki *et al* 1977), which changes to an orthorhombic structure (phase II) with space

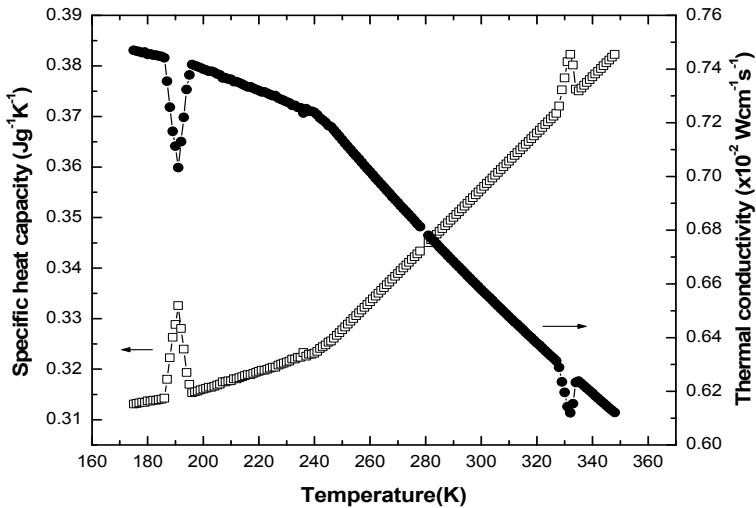


Fig. 6. (b) Variation of thermal conductivity and specific heat capacity for DLP crystal, cut with faces normal to the  $c$ -axis (Manjusha & Philip, 2008)

group  $D_{16h}$  ( $Pnam$ ) at  $T_1$  (Kalman *et al* 1970). Then, phase II changes into an incommensurate one (phase III) at  $T_2$  (Iizumi *et al.*, 1977); this is a second order phase transition. It undergoes an IC phase transition at  $T_3$ , below which the crystal is commensurate and ferroelectric with a small spontaneous polarization along the  $c$  direction.

Many experimental studies such as dielectric measurements (Aiki *et al.*, 1969, Aiki *et al.*, 1970), X-ray and neutron diffraction (Iizumi *et al.*, 1977; Ohama, 1974; Terauchi *et al.*, 1975), ESR (Aiki, 1970), Raman and Brillouin scattering (Wada *et al.*, 1977a; Wada *et al.*, 1977b; Yagi *et al.*, 1979), ultrasound velocity, attenuation and dispersion studies (Hoshizaki *et al.*, 1980; Shiozaki, 1977) etc have been reported near  $T_2$  and  $T_3$ . The variations in specific heat capacity and thermal expansion of  $K_2SeO_4$  in the low temperature phase have also been reported before (Aiki *et al.*, 1970; Gupta *et al.*, 1979). Thermal expansion along the  $c$ -axis exhibits a discontinuity at the incommensurate to commensurate transition. Specific heat measurements show anomalies at  $T_2$  and  $T_3$ , indicating that the transition at  $T_2$  is second order and that the one at  $T_3$  is first order (Aiki *et al.*, 1970). In spite of all these measurements reported at temperatures  $T_3$  and  $T_2$ , only very few experimental results have been reported near  $T_1$  (Unruh *et al.*, 1979; Inoue *et al.*, 1979; Cho & Yagi, 1980; Gupta *et al.*, 1979) because of the inherent difficulties involved in carrying out precision experiments at high temperatures. The variation of the specific heat capacity across the structural transition at  $T_1$  has not been reported so far for this material. More experimental data are still required for a better understanding of the high temperature phase of this material.

The thermal diffusivity, thermal conductivity and heat capacity of  $K_2SeO_4$  as it goes through the IC phase between 129.5 and 93 K have been measured by Philip & Manjusha (2009). The anisotropy in thermal conductivity along the three principal directions of this crystal and its variation with temperature are brought out and discussed by these authors. Differential scanning calorimetric (DSC) measurements across the high temperature phases have been carried out to determine anomalies in enthalpy during transition from phase I to phase II, and

the calorimetric ratio method adopted to determine the variation of specific heat capacity with temperature across the high temperature transition point  $T_1$ . The results from PPE and calorimetric measurements have been combined to plot the variation of specific heat with temperature through all the four phases of  $K_2SeO_4$ , and the results discussed below.

PPE measurements were done at temperatures between 85 and 300 K. Thermal diffusivity and effusivity along the  $c$  axis, plotted against temperature are shown in Fig. 7a. From the diffusivity and effusivity values, the values of the thermal conductivity and specific heat capacity have been computed, and these are plotted in Fig 7b. Since the values of these thermal parameters for  $a$  and  $b$  axes are not very different from the corresponding values obtained for the  $c$ -axis, they are not reproduced. It can be noticed that the thermal conductivity along the  $c$  axis, which is the direction of spontaneous polarization for this crystal, is slightly more than that along  $a$ - or  $b$ -axis at all temperatures. The anisotropy in thermal conductivity is small and decreases as the temperature is lowered. The variations along the  $c$  axis clearly indicate that the thermal properties undergo anomalous variation during phase transitions at 93 and 129.5 K. Thermal conductivity and heat capacity exhibit maxima at the phase transition temperatures 93 and 129.5 K. Moreover, there is an overall enhancement in thermal conductivity in the IC phase of  $K_2SeO_4$  between 93 and 129.5 K. The maxima in thermal conductivity at the phase transition temperatures can be explained in terms of the increase in phonon mean free path or decrease in phonon-phonon and phonon-defect collision rates. Again, the anomalous variation in specific heat capacity is due to softening of phonon modes and the corresponding enhanced contribution of phonon modes to the specific heat capacity.

The IC phase in  $K_2SeO_4$  has been observed experimentally as satellite peaks in the x-ray and neutron diffraction patterns (Iizumi et al., 1977). In the IC phase of  $K_2SeO_4$  at temperatures close to  $T_2$ , the incommensurate modulation wave is pure harmonic. But as the temperature approaches  $T_3$ , nonlinear phase modes, which are equally spaced commensurate constant phase domains separated by narrow phase varying regions called phase solitons, emerge. The presence of these modulation waves or phase solitons can influence heat conduction in ferroelectric crystals in two different ways, as outlined below.

The phase solitons can affect the mean free path of thermal phonons via scattering and hence can cause anomalous variation of thermal conductivity in the IC phase. Another possibility is that the modulation waves themselves can act as heat carriers, resulting in an enhancement in thermal conductivity. Whether the thermal conductivity increases or decreases during an IC phase transition depends on which factor dominates in the process. One can isolate thermal conductivity enhancement in the IC phase by computing the value of  $(\lambda - \lambda_{bg})$  where  $\lambda$  is the total thermal conductivity and  $\lambda_{bg}$  is the background thermal conductivity in the absence of occurrence of IC modulation. In general, for an insulating crystal,  $\lambda_{bg}$  follows an inverse temperature ( $T$ ) variation.

The theory of heat conduction in a ferroelectric crystal with a two-component order parameter has been developed by Levanyuk and co-workers (Levanyuk et al., 1992). The theory considers heat conduction along the modulation axis of a system that undergoes IC phase transition. According to this, the thermal conductivity due to phase solitons is given by

$$\lambda = \lambda_{bg} + \left( c_0^2 T \rho^2 / \gamma \right) \quad (6)$$

where  $c_0$  and  $\gamma$  are constants and  $\rho$  is the magnitude of the order parameter. One can see that the phase solitons enhance the thermal conductivity of  $K_2SeO_4$  in the IC phase. It has also

been shown that the enhancement in thermal conductivity is related to the excess specific heat  $c_e$  due to order parameter fluctuation as

$$\frac{\partial(\lambda - \lambda_{bg})}{\partial T} \approx c_e \quad (7)$$

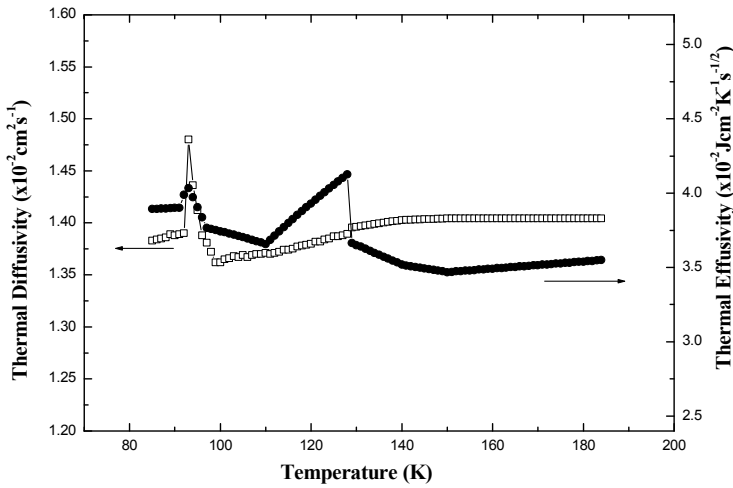


Fig. 7. (a) Variation of the thermal diffusivity and thermal effusivity along the  $c$ -axis of  $K_2SeO_4$  (Philip & Manjusha, 2009)

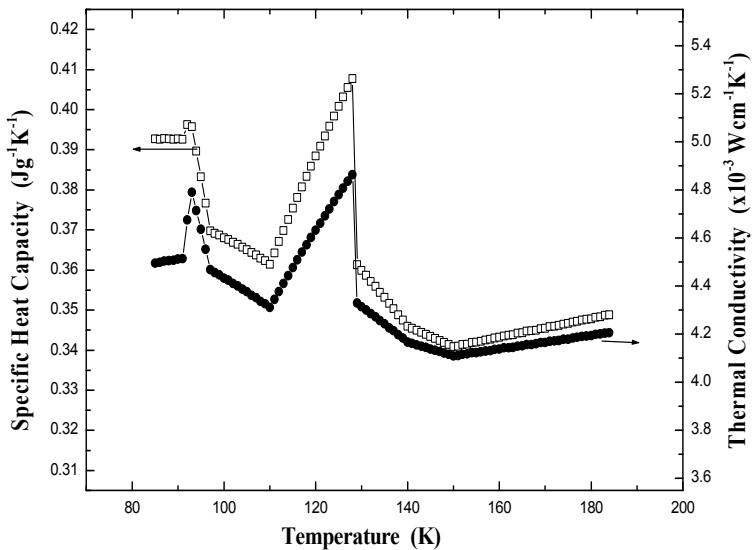


Fig. 7. (b) Variations of the thermal conductivity along the  $c$  axis and specific heat capacity of  $K_2SeO_4$  (Philip & Manjusha, 2009)

This explains the enhancement in specific heat in the modulation phase of the crystal. Even without the effects expressed in equations (6) and (7), the modulation waves can cause anomalies in  $(\lambda - \lambda_{bg})$  by strongly scattering the heat carrying phonons. In the IC phase between 93 and 129.5 K, one can note that the background thermal conductivity and the specific heat decrease gradually as the temperature increases. This variation of thermal conductivity is normal for a solid, but the variation of the specific heat is just opposite to the normal behaviour for solids. This can be attributed to the increase in the heat capacity of the modulation waves with decrease in temperature. As the system approaches the low temperature commensurate phase, it becomes more and more ordered, resulting in a decrease in entropy or increase in heat capacity. The modulation waves are so strong in the IC phase that the contribution of modulation waves to the overall heat capacity of the system is much more than the contribution of normal phonon modes to heat capacity. This results in an overall increase in heat capacity as the temperature decreases in the IC phase. The DSC curve during the heating cycle shows a clear peak occurring at 745 K, indicating that the phase transition at this temperature is endothermic. The variation of specific heat capacity with temperature up to a temperature well above 745 K has been determined by the DSC ratio method. These results have been combined with the results shown in figure 7b to plot the variation of heat capacity with temperature encompassing all the four phases of  $K_2SeO_4$ . This is shown in Fig. 8. So figure 8 contain the variation of specific heat of  $K_2SeO_4$  through all the three transition temperatures  $T_1$ ,  $T_2$  and  $T_3$  (and through all the four phases). The anomalous variation of heat capacity during transitions can be understood as due to softening of the phonon modes and the corresponding enhanced contribution of phonon modes to the specific heat capacity of the system.

In order to estimate the quantity of excess heat capacity due to the structural phase transition at 745 K, the contribution of the normal heat capacity shall be subtracted from the measured molar heat capacity. The background lattice heat capacity was approximated by a third-order polynomial. The excess of the molar heat capacity  $\Delta C_p$  was plotted against  $(T - T_c)$  and it is found to have a shape typical for a continuous phase transition. At  $T = T_c$ ,  $\Delta C_p$  is found to be  $0.112 \pm 0.003 \text{ J K}^{-1} \text{ mol}^{-1}$ . The specific heat critical exponent  $\alpha$  was obtained from the slope of  $\log(\Delta C_p)$  versus  $\log(T - T_c)$ . The value of  $\alpha$  is found to be  $-0.0853 \pm 0.0002$ , which is close to zero. This value for  $\alpha$  is typical for a mean field model of a phase transition (Strukov & Levanyuk, 1998). The Landau theory gives a simple relation between the excess entropy and the order parameter  $P_s$  (spontaneous polarization), given by

$$\Delta S(T) = -(1/2)[A_0 P_s^2] \quad (8)$$

One can acquire more information about the nature of the phase transition from the excess entropy  $\Delta S$ . The most direct way to determine  $\Delta S$  is from a measurement of the excess heat capacity as a function of temperature:

$$\Delta S(T) = \int_{T_0}^T \frac{\Delta C_p}{T} dT \quad (9)$$

The transition entropy has been calculated from the above equation, and is obtained as  $\Delta S = 0.49 \pm 0.03 \text{ J K}^{-1} \text{ mol}^{-1}$ . This is typical of a structural phase transition. However, this is much smaller than the transition entropy predicted by the order-disorder model in the mean field theory. Other mechanisms such as tunnelling may have to be taken into account to reduce this discrepancy with experiment.

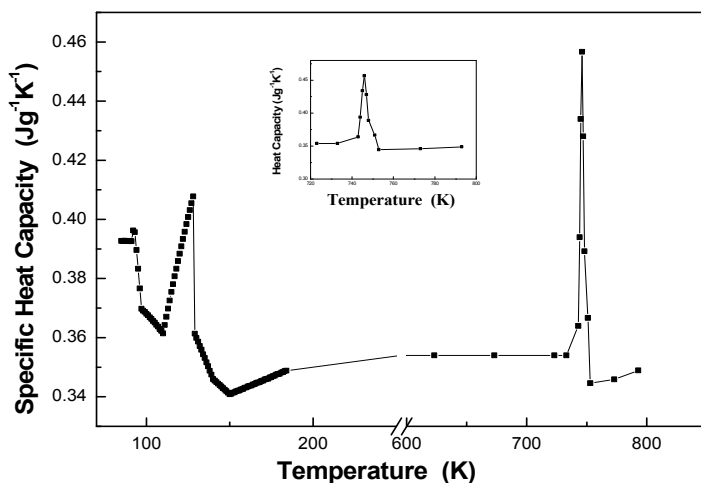


Fig. 8. Variation of the specific heat capacity with temperature through all the four phases of  $K_2SeO_4$ . The inset shows the variation close to the high temperature transition point (Philip & Manjusha, 2009)

## 6. Conclusions

The results presented in the above section show that a photothermal technique such as the photopyroelectric technique is a convenient and sensitive one to measure thermal conductivity and specific heat capacity of ferroelectric crystals as they undergo phase transitions. Photothermal techniques do not suffer from the disadvantages of steady state techniques. In a photothermal technique one actually measures the thermal diffusivity which is independent of heat losses from the sample. With a careful control of the sample boundary conditions the PPE technique has proven to be a sensitive and convenient one to measure thermal transport properties of solids that undergo ferroelectric phase transitions.

Even though not much attention has been paid to the measurement of thermal properties for probing phase transitions in solids, it is now more and more obvious that thermal transport measurements yield critical information to throw more light on fine features of ferroelectric transitions, particularly those involving incommensurate modulation of the lattice. Measurement of fine features of the variations of thermal conductivity and specific heat capacity with temperature, without disturbing the system, provides valuable information about the interactions involved in the processes.

## 7. Acknowledgements

The author thanks University Grants Commission (New Delhi) and Cochin University of Science and Technology for financial support provided for the publication of this article.

## 8. References

Aiki, H. (1970). ESR Study of  $\gamma$ -Irradiated  $K_2SeO_4$ , *J. Phys. Soc. Japan* 29, 379-88

- Aiki, K.; Hukuda, K.; Koga, H. & Kobayashi, T. (1970). Dielectric and thermal study of  $K_2SeO_4$  transitions, *J. Phys. Soc. Japan* 28, 389-94
- Aiki, K.; Hukuda, K. & Matumura, O. (1969). Ferroelectricity in  $K_2SeO_4$ , *J. Phys. Soc. Japan* 26, 1064
- Ashcroft, N. W. & Mermin, N. D. (1976). *Solid State Physics* (Holt, Rinehart and Winston, New York) Chap. 25
- Badarinath, K. V. S. & Radhakrishna, S. (1984). Studies on the ferroelectric-paraelectric transition of dicalcium lead propionate, *J. Mat. Sci. Lett.* 3, 575-577
- Belov, A. & Jeong, Y. H. (1998). Anomalous heat conduction in ferroelectric crystals with incommensurate phases, *J. Korean Phys. Society* 32, 452 - 455
- Bhat, S. V.; Dhar, V. & Srinivasan, R. (1981). ESR studies on phase transitions in double propionates, *Ferroelectrics* 39, 1167
- Blinic, R. & Levanyuk, A. P. (1986). *Incommensurate Phases in Dielectrics 1 & 2*, (North-Holland, Amsterdam)
- Chapelle, J. P. & Benoit, J. P. (1977). Raman study of external frequencies of thiourea with temperature, *J. Phys. C: Solid State Phys.* 10, 145-51
- Cho, M. & Yagi, T. (1980). Brillouin scattering study of the Hexagonal-Orthorhombic phase transition in  $K_2SeO_4$ , *J. Phys. Soc. Japan* 49, 429-430
- Cummins, H. Z. (1990). Experimental studies of structurally incommensurate crystal phases, *Phys. Reports* 5 & 6, 211
- Delahaigue, A.; Khelifa, B. & Jouve, P. (1975). Soft mode in thiourea by Raman measurements, *Phys. Stat. Solidi (b)* 72, 585-89
- Dettmer, E. S.; Romenesko, B. M.; Charles Jr., H. K.; Carkhuff, B. G. & Mewll, D. J. (1989). Steady-state thermal conductivity measurements of AlN and SiC substrate materials, *IEEE Transactions on Components, Hybrids, and Manufacturing Technology*, 12, 543-548
- Dorner, B. (1981). Investigation of structural phase transformations by inelastic neutron scattering in Structural Phase Transitions I (editors: K A Muller & H. Thomas, in *Topics in Current Physics* Vol. 23, Springer-Verlag, Berlin)
- Elcombe, M. & Tayler, J. C. (1968). A neutron diffraction determination of the crystal structures of thiourea and deuterated thiourea above and below the ferroelectric transition, *Acta Cryst. A* 24, 410 -20
- Ferroni, E. & Orioli, P. (1959). Zur kristallstruktur von  $PbCa_2(CH_3CH_2COO)_6$ , *Z. Krist.* 111, 362
- Gaffar, M. A.; Mebed, M. M. & El-Fadl, A. (1987). Thermal Diffusivity of Pure and Doped TGS Crystals, *Phys. Status Solidi a* 104, 879- 884
- Gesi, K. (1984). Reinvestigation of pressure-Induced II-III transitions in Ferroelectric  $Ca_2Sr(C_2H_5COO)_6$  and  $Ca_2Pb(C_2H_5COO)_6$ , *J. Phys. Soc. Japan* 53, 1602-1605
- Gesi, K. & Ozawa, K. (1975). Effect of Hydrostatic pressure on the phase transitions in Ferroelectric  $Ca_2Sr(C_2H_5COO)_6$  and  $Ca_2Pb(C_2H_5COO)_6$ , *J. Phys. Soc. Jpn.* 39, 1026-1031
- Goldsmith, G. J. & White, J. G. (1959). Ferroelectric behavior of Thiourea, *J. Chem. Phys.* 31, 1175-1187
- Grigas, J. (1996). *Microwave dielectric spectroscopy of ferroelectrics and related materials* (Gordon and Breach Publishers)

- Gupta, S. S.; Karan, S. & Gupta, S. P. S. (2000). Growth and defect characterization in single crystals of Ferroelectric Ammonium Sulphate, *Japan J. Appl. Phys.* 39, 2736-40
- Hellwege, K. H. & Hellwege, A. M. (editors) *Landolt - Bornstein New Series* (1969) Vol 3 ed: (Springer - Verlag, New York) p. 477
- Hoshizaki, H.; Sawada, A.; Ishibashi, Y.; Matsuda, T. & Hatta, I. (1980). Ultrasonic study of  $K_2SeO_4$  in the temperature range of the incommensurate phase transition, *Japan. J. Appl. Phys.* 19, L324-26
- Inoue, K.; Suzuki, K.; Sawada, A.; Ishibashi, Y. & Takagi, Y. (1979). A test of centrosymmetry of the hexagonal phase in  $K_2SeO_4$ , *J. Phys. Soc. Japan* 46, 608-10
- Iizumi, M.; Axe, J. D.; Shirane, G. & Shimaoka, K. (1977). Structural phase transformation in  $K_2SeO_4$ , *Phys. Rev. B* 15, 4392
- Iizumi, M. & Gesi, K. (1977). Incommensurate phase in  $(ND_4)_2BeF_4$ , *Solid State Commun* 22, 37-39
- John, P. K.; Miranda, L. C. M. & Rastogi, A. C. (1986). Thermal diffusivity measurement using the photopyroelectric effect, *Phys. Rev. B* 34, 4342-4345
- K'alm'an, A.; Stephens, J. S. & Cruickshank, D. W. J. (1970). The crystal structure of  $K_2SeO_4$ , *Acta Crystallogr. B* 26, 1451-54
- Kasting, G. B.; Garland, C. W. & Lushington, K. J. (1980). Critical heat capacity of octylcyanobiphenyl (8CB) near the nematic-smectic A transition, *J. de Physique* 41, 879
- Lebedev, N. I.; Levanyuk, A. P.; Minyukov, S. A. & Vallade, M. (1992). Elastic anomalies at structural phase transitions: a consistent perturbation theory. II. Two-component order parameter including the case of incommensurate phase, *J. Phys. I (France)* 2, 2293-97
- Levanyuk, A. P.; Minyukov, S. A. & Vallade, M. (1992). Elastic anomalies at structural phase transitions: a consistent perturbation theory. I. One component order parameter, *J. Physique I (France)* 2, 1949-63
- Lines, M. E. & Glass, A. M. (1977). *Principles and Applications of Ferroelectrics and related Materials* (Clarendon Press, Oxford, 1977)
- Luthi, B. & Rehwald, W. (1981). Ultrasonic studies near structural phase transitions, in *Structural Phase Transitions I* (ed: K A Muller & H Thomas, in *Topics in Current Physics* Vol. 23, Springer-Verlag, Berlin)
- Mandelis, A.; Care, F.; Chan, K. K. & Miranda, L. C. M. (1985). Photopyroelectric detection of phase transitions in solids, *Appl. Phys. A* 38, 117
- Mandelis, A. & Zver, M. M. (1985). Theory of photopyroelectric spectroscopy of solids, *J. Appl. Phys.* 57, 4421- 4430
- Manjusha, M. V. & Philip, J. (2008). Thermal properties of Dicalcium Lead Propionate across the prominent transition temperatures, *Ferroelectrics Letters* 35, 107 - 118
- Mante, A. J. H. & Volger, J. (1967). The thermal conductivity of  $BaTiO_3$  in the neighborhood of its ferroelectric transition temperatures, *Phys. Letters* 24A, 139
- Marinelli, M. ; Murtas, F.; Mecozzi, M. G.; Zammit, U.; Pizzoferrato, R.; Scudieri, F.; Martellucci, S. & Marinelli, M. (1990). Simultaneous determination of specific heat, thermal conductivity and thermal diffusivity at low temperature via the photopyroelectric technique, *Appl. Phys. A* 51, 387-393

- Mc Kenzie, D. R. (1975a). Neutron and Raman study of the lattice dynamics of deuterated thiourea, *J. Phys. C: Solid State Phys.* 8, 2003
- Mc Kenzie, D. R. (1975b). The antiferroelectric transition in thiourea studied by thermal neutron scattering, *J. Phys. C: Solid State Phys.* 8, 1607
- Menon, C. P. & Philip, J. (2000). Simultaneous determination of thermal conductivity and heat capacity near solid state phase transitions by a photopyroelectric technique, *Meas. Sci. Technol.* 11, 1744-1749
- Menon, C. P. & Philip, J. (2003). Thermal properties of Thiourea studied using Photopyroelectric technique, *Ferroelectrics* 287, 63-70
- Moudden, A. H. ; Denoyer, F. ; Benoit, J. P. & Fitzgerald, W. (1978). Inelastic neutron scattering study of commensurate-incommensurate phase transition in thiourea, *Solid State Commun.* 28, 75
- Nagae, Y. ; Wada, M. ; Ishibashi, Y & Takagi, Y. (1976). Raman Scattering Spectra of  $\text{Ca}_2\text{Sr}(\text{C}_2\text{H}_5\text{CO}_2)_6$  and  $\text{Ca}_2\text{Pb}(\text{C}_2\text{H}_5\text{CO}_2)_6$ , *J. Phys. Soc. Jpn.* 41, 1659-1662
- Nakamura, N.; Akamura, H.; Suga, H.; Chihara, H. & Seki, S. (1965). Phase transitions in crystalline divalent metal dicalcium propionates I. Calorimetric and dielectric investigations of strontium and lead dicalcium propionates, *Bull. Chem. Soc. Jpn.* 8, 1779-1787
- Nakamura, N.; Suga, H. ; Chihara, H & Seki, S. (1978). Phase transitions in crystalline divalent metal dicalcium propionates. II. Proton magnetic resonance investigation, *Bull. Chem. Soc. Jpn.* 41, 291-296
- Ohama, N. (1974). Superstructure of potassium selenate  $\text{K}_2\text{SeO}_4$ , *Mater. Res. Bull.* 9, 283-88
- Osaka, T; Makita, Y & Gesi, K. (1975). Pyroelectricity of dicalcium lead propionate associated with its phase transitions, *J. Phys. Soc. Jpn.* 38, 292
- Philip, J. & Manjusha, M. V. (2009). Thermal transport across incommensurate phases in potassium selenate: Photo-pyroelectric and calorimetric measurements, *J. Phys.: Condens. Matter* 21, 045901
- Podlojenov, S; Stade, J; Burianek, M & Mühlberg, M. (2006). Study on the ferroelectric phase transition in potassium lithium niobate (KLN), *Cryst. Res. Technol.* 41,344 - 348
- Setter, N. & Cross, L. E. (1980). The contribution of structural disorder to diffuse phase transitions in ferroelectrics, *J. Materials Science* 15, 2478-2482
- Shiozaki, Y. (1971). Satellite X-ray scattering and structural modulation of thiourea, *Ferroelectrics* 2, 245-60
- Shiozaki S; Sawada A; Ishibashi, Y & Takagi, Y. (1977). Hexagonal-orthorhombic phase transition and ferroelasticity in  $\text{K}_2\text{SO}_4$  and  $\text{K}_2\text{SeO}_4$ , *J. Phys. Soc. Japan* 43, 1314-19
- Standnicka, K.; Glazer, A. M. & Bismayer, U. (1990). The phase diagram of dicalcium strontium/lead propionate, *Phase transitions* 27, 73-80
- Strukov, B. A. & Levanyuk, A. P. (1998). *Ferroelectric Phenomena in Crystals* (Springer, Berlin)
- Sunil Misra, K. & Jerzak, S. (1989).  $\text{Mn}^{2+}$  EPR study of phase transitions in dicalcium lead propionate  $\text{Ca}_2\text{Pb}(\text{C}_2\text{H}_5\text{COO})_6$ : Determination of critical exponent below the ferroelectric phase transition and comparison with EPR studies on  $\text{Ca}_2\text{Ba}(\text{C}_2\text{H}_5\text{COO})_6$  and  $\text{Ca}_2\text{Sr}(\text{C}_2\text{H}_5\text{COO})_6$ , *Phy. Rev. B* 39, 2041-2050
- Tachibana, M.; Kolodiazhyi, T. & Takayama-Muromachi, E. (2008). Thermal conductivity of perovskite ferroelectrics, *Appl. Phys. Letters* 93, 092902

- Takashige, M.; Hirotsu, S.; Sawada, S. & Humano, K. (1978). Piezoelectric and elastic properties of Dicalcium lead propionate, *J. Phys. Soc. Jpn.* 45, 558-564
- Terauchi, H; Takenaka, H & Shimaoka, K. (1975). Structural Phase Transition in  $K_2SeO_4$ , *J. Phys. Soc. Japan* 39, 435-39
- Thoen, T; Marynissen, H & Van Dael, W.(1982). Temperature dependence of the enthalpy and the heat capacity of the liquid-crystal octylcyanobiphenyl (8CB) *Phys. Rev. A* 26, 2886-2905
- Toledano, J. & Toledano, P. (1987). *The Landau theory of phase transitions* (World Scientific, Singapore), Chapter 5
- Unruh, H. G.; Eller, W. & Kirf, G. (1979). Spectroscopic and dielectric investigations of  $K_2SeO_4$ , *Phys. Status Solidi a* 55, 173-80
- Wada, M.; Sawada, A.; Ishibashi, Y. & Takagi, Y. (1977). Raman scattering spectra of  $K_2SeO_4$ , *J. Phys. Soc. Japan* 42, 1229-34
- Wada, M.; Sawada, A.; Ishibashi, Y. & Takagi, Y. (1978). Raman scattering spectra of  $SC(NH_2)_2$ , *J. Phys. Soc. Jpn.* 45, 1905-10
- Wada, M.; Uwe, H.; Sawada, A.; Ishibashi, Y.; Takagi, Y & Sakudo, T (1977). The lower frequency soft-mode in the ferroelectric phase of  $K_2SeO_4$ , *J. Phys. Soc. Japan* 43, 544
- Yamada, Y.; Shibuya, I. & Hoshino, S. (1963). Phase transition in  $NaNO_2$ , *J. Phys. Soc. Japan* 18, 1594-1603
- Yagi, T.; Cho, M. & Hidaka, Y. (1979). Brillouin scattering study of the paraelectric-incommensurate phase transition in  $K_2SeO_4$ , *J. Phys. Soc. Japan* 46, 1957-58
- Zammit, U.; Marinelli, M.; Pizzoferrato, R.; Scudieri, F. & Martellucci, S. (1988). Photoacoustics as a technique for simultaneous measurement of thermal conductivity and heat capacity, *J. Phys. E: Sci. Instrum.* 21, 935-937

# The Induced Antiferroelectric Phase - Structural Correlations

Marzena Tykarska

*Institute of Chemistry, Military University of Technology, Warsaw  
Poland*

## 1. Introduction

Chiral synclinic ( $\text{SmC}^*$ ) as well as anticlinic ( $\text{SmC}^*_A$ ) phases are promising in the display application. The displays using these phases are characterized by shorter response time and larger viewing angle in comparison to nematic displays. In displays based on surface stabilized ferroelectric liquid crystals (SSFLC) the permanent polarisation of layers as well as pretransitional effect appear. In displays based on surface stabilized antiferroelectric liquid crystals (SSAFLC) the permanent polarisation of layers does not appear but the pretransitional effect still exists thus leading to small contrast; the advantage is that the gray scale is big. In displays based on surface stabilized orthoconic antiferroelectric liquid crystals (SSOAFLC) the advantages of antiferroelectric phase remain and disadvantages vanishes because the lack of pretransitional effect leads to the excellent contrast ratio. Thus antiferroelectric phase is even better than ferroelectric phase for display application. Unfortunately the number of compounds with antiferroelectric phase is limited [Fukuda et al. 1994, Matsumoto et al. 1999, Drzewiński et al. 2002]. Only mixtures have application meaning in display technology, because they enable to adjust the properties in a broader range. The induction of antiferroelectric phase is a way to increase the potential number of compounds useful for mixtures preparation, because the compounds not having this phase may be used for this purpose. In mixtures of compounds different non-additive behaviors can be found such as destabilization, enhancement or induction. For example when two compounds having antiferroelectric phase are mixed together the thermal stability of this phase can be increased because additional intermolecular interaction appears between molecules, see Fig. 1a. When one of compounds has similar structure to compounds forming  $\text{SmC}^*_A$  phase but does not form this phase by itself (compound C in Fig. 1b) it can still give the enhancement of this phase in a mixture. This compound has so called virtual antiferroelectric phase. The compound with virtual antiferroelectric phase can be mixed with the compound of similar structure to compound B but not forming antiferroelectric phase then induction of antiferroelectric phase appears, Fig. 1c.

The induction and enhancement of antiferroelectric phase was observed for the first time in 2000 by Dąbrowski and Gauza [Gauza et al. 2000, Dąbrowski 2000, Gauza et al. 2002].

The first system in which the induction was observed was the bicomponent mixture of compounds 1 and 2 [Dąbrowski 2000].

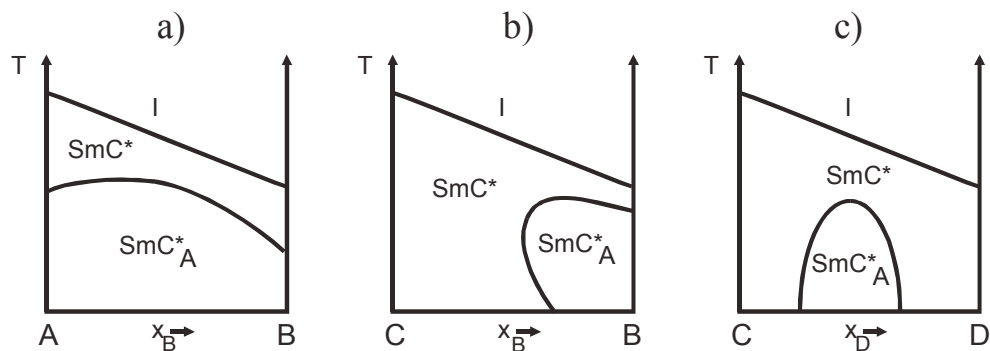
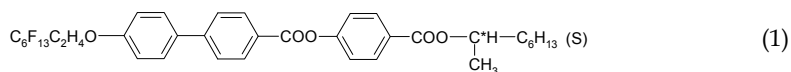
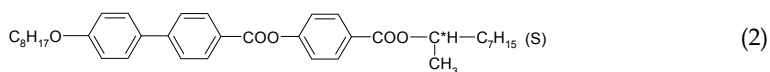


Fig. 1. Schematic phase diagrams with enhanced (a, b) and induced (c) antiferroelectric phase



Cr<sub>1</sub> 80.07 Cr<sub>2</sub> 98.9 SmC\* 141.4 SmC\* $\alpha$  149.0 SmA 184.0 I [Drzewiński et al. 1999, Mandal et al. 2006]



Cr 79.0 (SmI\* 65.8) SmC\* 118.6 SmC\* $\alpha$  119.6 SmA 144.1 I [Gauza et al. 2000, Kobayashi et al. 1999]

Their phase diagram is presented in Fig. 2. Compounds 1 and 2 do not form antiferroelectric phase, but this phase appears in their mixture for the middle concentrations. The highest thermal stability corresponds to composition 1:1.

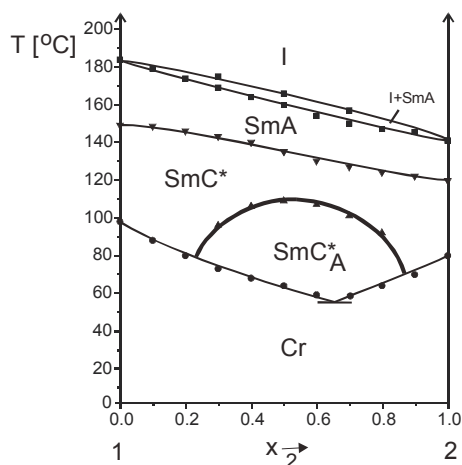


Fig. 2. Phase diagram of the system 1-2 [Dąbrowski 2000].

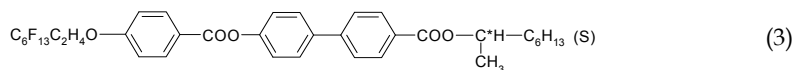
Next many new systems were found in which the induction of antiferroelectric phase was observed [Tykarska et al. 2006, Skrzypek and Tykarska 2006, Tykarska and Skrzypek 2006, Czupryński et al. 2007]. The compounds giving the induction of  $\text{SmC}^*_A$  phase have to differ in polarity. Usually one of compounds is of lower polarity (terminating with an alkyl terminal chain) and another one with fluoroalkyl terminal chain or with terminal chain terminated with cyano group. The comparison of the ability of fluoro- and cyanoterminated compounds for the induction of  $\text{SmC}^*_A$  phase is given. The influence of the rigid core and nonchiral chain length is tested. The analysis is made based on phase diagrams constructed with the use of polarized optical microscopy of the mixtures of polar compounds with compounds of few homologous series with alkylated terminal chain.

The special attention is put to antiferroelectric phase this is why the subphases of ferroelectric phase as well as smectic I\* phase are not marked on phase diagrams.

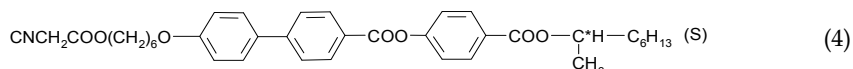
## 2. Systems with different polarity

### 2.1 The structure of compounds giving the induction or enhancement

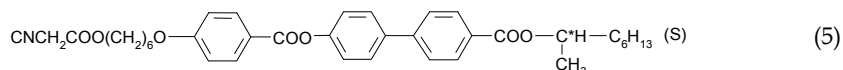
The structure of compounds used for testing the ability of more polar compounds for the induction of  $\text{SmC}^*_A$  phase are given by formulas 1, 3-5:



$\text{Cr}_1$  94.3  $\text{Cr}_2$  97.9  $\text{SmC}^*$  155.6  $\text{SmA}$  184.6 I [Drzewiński et al. 1999]

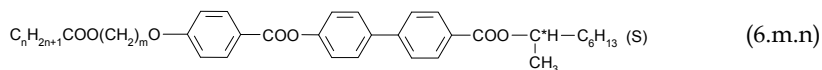


$\text{Cr}$  62.2  $\text{SmC}^*$  90.5  $\text{SmA}$  97.6 I [Dziaduszek et al. 2006]



$\text{Cr}$  69.6 ( $\text{SmC}^*$  61.6)  $\text{SmA}$  80.2 I [Dziaduszek et al. 2006]

Compounds of smaller polarity used as a second component of mixtures have alkyl terminal chain. The used compounds belong to the homologous series 6.m.n and 7.m.n [Drzewiński et al. 1999, Gąsowska et al. 2004]:



$$m=3$$

$n=1$   $\text{Cr}$  72.3  $\text{SmA}$  104.3 I

$n=2$   $\text{Cr}$  80.6  $\text{SmA}$  106.7 I

$n=3$   $\text{Cr}$  109.9 ( $\text{SmA}$  107.1) I

$n=4$   $\text{Cr}$  111.9 ( $\text{SmA}$  104.8) I

$n=5$   $\text{Cr}$  71.3  $\text{SmC}^*$  75.2  $\text{SmA}$  101.1 I

$n=6$   $\text{Cr}$  71.4  $\text{SmC}^*$  75.1  $\text{SmA}$  97.1 I

n=7 Cr 67.2 SmC\* 78.2 SmA 95.7 I

m=6

n=1 Cr 70.6 (SmC\* 69.8) SmA 98.8 I

n=2 Cr 54.6 (SmC\*<sub>A</sub> 43.0) SmC\* 74.4 SmA 96.1 I

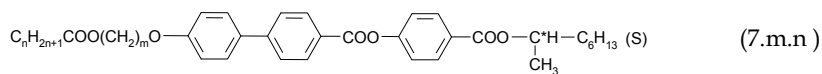
n=3 Cr 76.0 (SmC\*<sub>A</sub> 58.0 SmC\* 75.1) SmA 89.0 I

n=4 Cr 76.2 (SmC\*<sub>A</sub> 68.0 SmC\* 74.9) SmA 87.2 I

n=5 Cr 64.9 (SmC\*<sub>A</sub> 57.0) SmC\* 73.0 SmA 84.6 I

n=6 Cr 54.9 SmC\*<sub>A</sub> 64.4 SmC\* 72.6 SmA 83.1 I

n=7 Cr 50.5 SmC\*<sub>A</sub> 60.3 SmC\* 71.7 SmA 82 I



m=3

n=1 Cr 62.6 (SmI\* 52.7) SmA 129.7 I

n=2 Cr 77.3 (SmI\* 49.2) SmC\*<sub>A</sub> 88.2 SmA 123.6 I

n=3 Cr 66.6 (SmI\* 43.0) SmC\*<sub>A</sub> 92.4 SmA 117.3 I

n=4 Cr 62.2 (SmI\* 31.9) SmC\*<sub>A</sub> 92.8 SmA 111.7 I

n=5 Cr 73.6 (SmI\* 26.3) SmC\*<sub>A</sub> 92.5 SmA 109.1 I

n=6 Cr 69.2 (SmI\* 22.0) SmC\*<sub>A</sub> 91.0 SmC\* 92.2 SmA 106.6 I

n=7 Cr 49.5 (SmI\* 25.0) SmC\*<sub>A</sub> 89.9 SmC\* 91.9 SmA 105.4 I

m=6

n=1 Cr 66.7 (SmC\*<sub>A</sub> 48.0) SmC\* 104.9 SmA 117.3 I

n=2 Cr 58.1 SmC\*<sub>A</sub> 95.2 SmC\* 103.5 SmA 112.2 I

n=3 Cr 61.0 SmC\*<sub>A</sub> 87.5 SmC\* 98.1 SmA 104.5 I

n=4 Cr 64.8 SmC\*<sub>A</sub> 93.3 SmC\* 96.2 SmA 101.7 I

n=5 Cr 68.4 SmC\*<sub>A</sub> 87.6 SmC\* 93.9 SmA 99.5 I

n=6 Cr 68.5 SmC\*<sub>A</sub> 89.8 SmC\* 91.7 SmA 97.5 I

n=7 Cr 70.4 SmC\*<sub>A</sub> 85.9 SmC\* 89.9 SmA 96.9 I

Phase diagrams for all compounds 6.m.n and 7.m.n have been constructed, but here only chosen phase diagrams are presented.

## 2.2 Systems with fluoroterminated compounds

Mixtures of compound 1 with compounds 6.m.n and 7.m.n show different behaviour depending on the existence or not of SmC\*<sub>A</sub> phase in alkylated compounds. In case of compounds 6.3.n, none of them have SmC\*<sub>A</sub> phase thus the induction of this phase appears in all mixtures with compound 1, Fig. 3 [Tykarska et al. 2006, Tykarska and Skrzypek 2006]. In case of compounds 6.6.n and 7.3.n the shortest compounds does not form SmC\*<sub>A</sub> phase thus the induction of SmC\*<sub>A</sub> phase is observed for their mixtures with compound 1 but for longer homologues forming SmC\*<sub>A</sub> phase by themselves the enhancement of this phase appears in the mixtures, Figs. 4 [Tykarska and Skrzypek 2006] and 5. In case of compounds 7.6.n all members form SmC\*<sub>A</sub> phase thus the enhancement of this phase in the mixtures with compound 1 in all cases is observed, Fig. 6.

The maximum temperature of existence of antiferroelectric phase in pure compounds with alkylated terminal chain are presented in Fig. 7a. Taking into account ability of pure

compounds for formation of  $\text{SmC}^*_A$  phase it can be found that compounds with biphenylate core ( $\text{PhPhCOOPh}$ , 7.m.n) have bigger tendency for creation of anticlinic ordering in comparison to compounds with benzoate core ( $\text{PhCOOPh}$ , 6.m.n). There is no big difference in thermal stability of  $\text{SmC}^*_A$  phase between compounds with biphenylate structure and different polymethylene length  $m=3$  and 6 (7.3.n and 7.6.n series), but for compounds with benzoate core (6.m.n) only longer polymethylene spacer ( $m=6$ ) let the  $\text{SmC}^*_A$  phase to be formed and shorter one ( $m=3$ ) does not.

The maximum temperature of existence of antiferroelectric phase in the mixtures of compounds 6.m.n and 7.m.n with compound 1 are presented in Fig. 7b. Increasing the number of carbon atoms in a nonchiral terminal alkyl chain ( $n$ ) causes that the maximum temperature of induced antiferroelectric phase existence in the mixture decreases. There is an exception, because for compounds with hexamethylene spacer  $m=6$  and one carbon atom in alkyl group  $n=1$  (6.6.1 and 7.6.1) the maximum temperatures are lower than for corresponding homologues  $n=2$  (6.6.2 and 7.6.2), Fig. 7b. Although the maximum temperature of induced  $\text{SmC}^*_A$  phase decreases, the temperature-concentration area of existence of this phase in phase diagrams increases, thus one can say that the tendency for creation of  $\text{SmC}^*_A$  phase increases with the increase of alkyl chain length. Also shorter compounds in pure state do not form  $\text{SmC}^*_A$  phase.

The comparison of the influence of polymethylene spacer length on the ability for induction of  $\text{SmC}^*_A$  phase in mixtures shows that more convenient for this purpose is trimethylene spacer ( $m=3$ ), because the maximum temperature of this phase existence is higher than for corresponding hexamethylene compounds ( $m=6$ ), Fig. 7b. It is opposite to the situation in pure compounds, for which compounds with hexamethylene spacer ( $m=6$ ) form anticlinic arrangement easier, also the number of compounds with  $\text{SmC}^*_A$  phase is bigger than in series with trimethylene spacer ( $m=3$ ).

The comparison of the influence of the core structure on the ability for induction of  $\text{SmC}^*_A$  phase shows that biphenylate core is more convenient than benzoate core for the stability of antiferroelectric ordering because in the former case the maximum temperature as well as temperature-concentration area of existence of  $\text{SmC}^*_A$  phase in mixtures with compound 1 observed on phase diagrams are higher. This may be conclude also from the fact that bigger number of compounds with biphenylate core form  $\text{SmC}^*_A$  phase in pure state.

Mixing the compounds of the series 6.m.n and 7.m.n with compound 3, which has benzoate core instead of biphenylate as it is for compound 1, it can be noticed that the rules observed for alkylated compounds, namely that biphenylate core favours antiferroelectric ordering more than benzoate core and for the same core the trimethylene spacer gives bigger induction of  $\text{SmC}^*_A$  phase, is true also in these mixtures. For example, in mixtures of compound 3 with compounds 6.3.1, 6.6.1 and 7.3.1 ( $n=1$  in each case) maximum temperature of induced  $\text{SmC}^*_A$  phase is higher in mixture with biphenylate compound 7.3.1 (Fig. 8c) than with benzoate compound 6.3.1 (Fig. 8a). In both compounds there is trimethylene spacer, but the smallest induction is observed for benzoate compound with hexamethylene spacer 6.6.1, Fig. 8b.

It can be noticed that the ability for induction of  $\text{SmC}^*_A$  phase of compound 3 is smaller than for compound 1. The rule observed for alkylated compounds (that biphenylate core favours antiferroelectric ordering more than benzoate core) is valid also for fluorinated compounds. It is well visible after comparing the phase diagrams presented in Fig. 8a with Fig. 3a, and Fig. 8b with Fig. 4a, as well as Fig. 8c with Fig. 5a; the temperature-concentration area of existence of  $\text{SmC}^*_A$  phase is smaller for mixtures with compound 3.

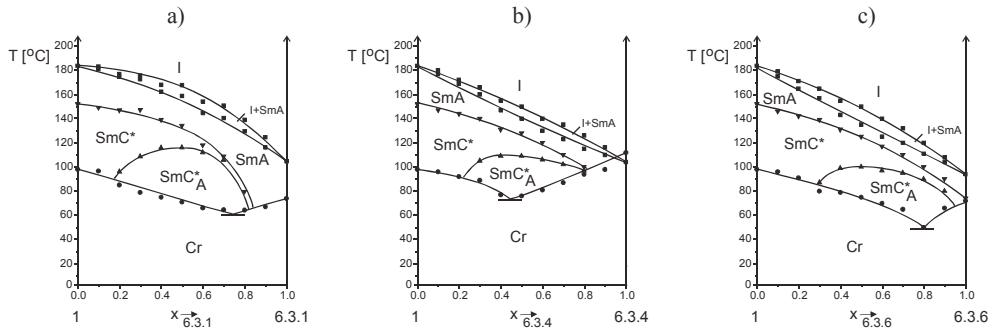


Fig. 3. Phase diagrams of bicomponent mixtures of compound 1 with compounds 6.3.1 (a), 6.3.4 (b) and 6.3.6 (c); [Tykarska et al. 2006, Tykarska and Skrzypek 2006]

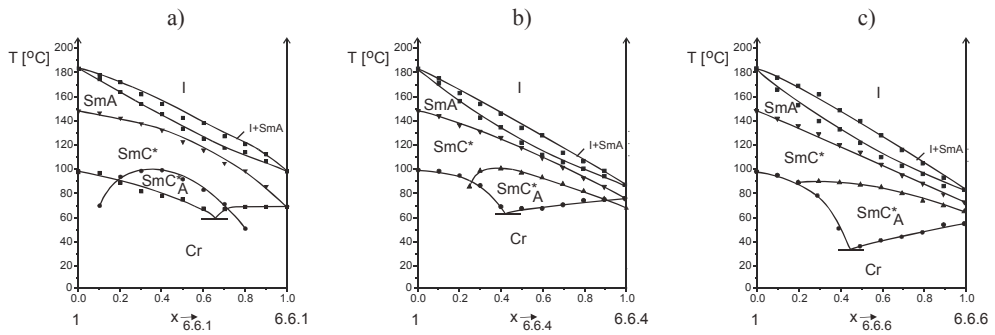


Fig. 4. Phase diagrams of bicomponent mixtures of compound 1 with compounds 6.6.1 (a), 6.6.4 (b) and 6.6.6 (c); [Tykarska and Skrzypek 2006]

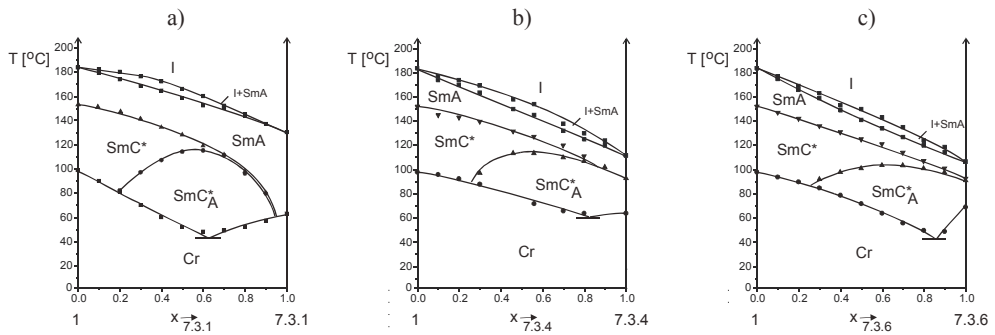


Fig. 5. Phase diagrams of bicomponent mixtures of compound 1 with compounds 7.3.1 [Czupryński 2007] (a), 7.3.4 (b) and 7.3.6 (c)

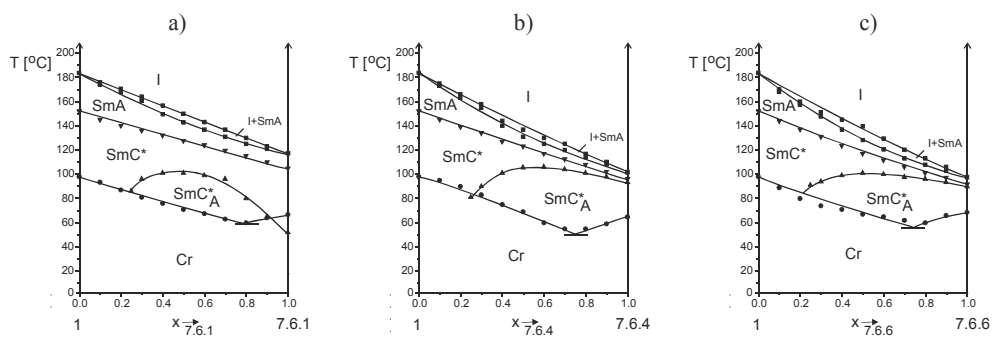


Fig. 6. Phase diagrams of bicomponent mixtures of compound 1 with compounds 7.6.1 (a), 7.6.4 (b) and 7.6.6 (c)

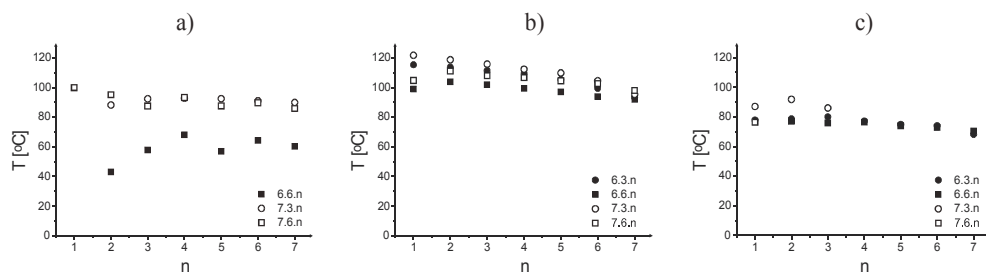


Fig. 7. Comparison of maximum temperature of existence of  $SmC^*_A$  phase in pure compounds of series 6.m.n and 7.m.n (a), and in their mixtures with compound 1 (b) and compound 4 (c)

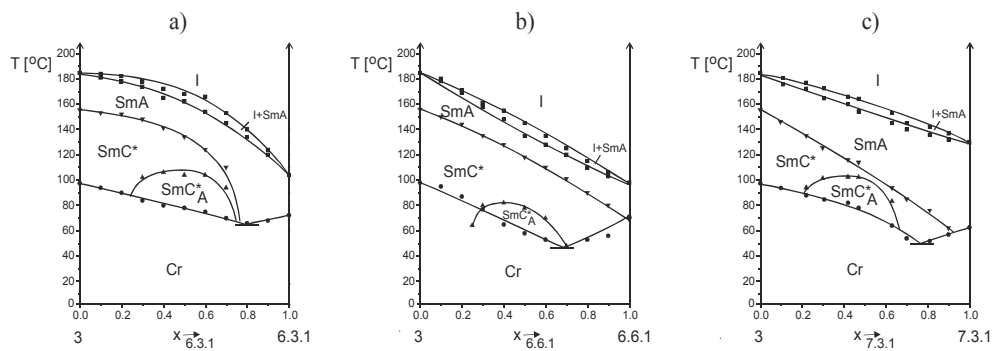


Fig. 8. Phase diagrams of bicomponent mixtures of compound 3 with compounds 6.3.1 (a) [Czupryński 2007], 6.6.1 (b) and 7.3.1 (c)

### 2.3 Systems with cyanoterminated compounds

Mixing the compounds of the series 6.m.n and 7.m.n with compound 4, which has the same biphenylate core as compound 1 but different nonchiral chain, namely terminated with cyano group, the induction of  $\text{SmC}^*_A$  phase is also observed. The rules for structure correlations with the induction of  $\text{SmC}^*_A$  phase of alkylated compounds in these systems are the same as were observed for fluorinated compounds. For example, the compound 4 mixed with members of homologous series of benzoate compounds with hexamethylene spacer 6.3.n gives the induction for all members and the temperature-concentration area of existence of this phase increases with the increase of alkyl chain length, Fig. 9. Maximum temperature of existence of  $\text{SmC}^*_A$  phase in mixtures is presented in Fig. 7c. The compositions corresponding to maximum temperature of existence of  $\text{SmC}^*_A$  phase are shifted in the direction of the excess of cyanoterminated compound in phase diagrams for most of the systems.

Compound 4 in mixtures with compounds 6.6.n does not give the induction of  $\text{SmC}^*_A$  phase in the case of compound 6.6.1 (Fig. 10a) because the tendency of cyanoterminated compounds for induction is smaller than in the case of fluoroterminated compounds. For compounds with longer alkyl chains 6.6.n the enhancement of  $\text{SmC}^*_A$  phase is observed (Fig. 10b and c), the same as for fluoroterminated compounds, but the maximum temperature of existence of the induced  $\text{SmC}^*_A$  phase in this case is smaller.

Compound 4 in mixtures with compounds 7.3.n gives the induction of  $\text{SmC}^*_A$  phase in the case of compound 7.3.1 (Fig. 11a), but for compounds with longer alkyl chains the enhancement of  $\text{SmC}^*_A$  phase is observed, Fig. 11b and c. It is interesting that the highest temperature of  $\text{SmC}^*_A$  phase existence is for pure compounds in case of mixtures with alkylated compounds having more than 3 carbon atoms in alkyl group. This is why these mixtures are not presented in Fig. 7c. In case of mixtures of compound 4 with compounds 7.6.n, homolog 7.6.1 is the only one which gives the induction. In case of longer homologs the enhancement of  $\text{SmC}^*_A$  phase is observed, but the temperature range of existence of this phase in mixtures is smaller than for pure alkylated compounds this is why they are not marked in Fig. 7c.

Compound 5 being the analog of compound 4, but having benzoate rigid core, has much smaller ability for induction of  $\text{SmC}^*_A$  phase because the number of compounds which give the induction in mixtures with compound 5 is smaller than in case of compound 4.

In mixtures of compound 5 with members of series 6.3.n it has been found that the induction appears for longer homologues ( $n=6$  and  $7$ ), but for shorter homologues ( $n=1-5$ ) the induction does not appear, Figs. 12a ( $n=2$ ) and 12b ( $n=6$ ).

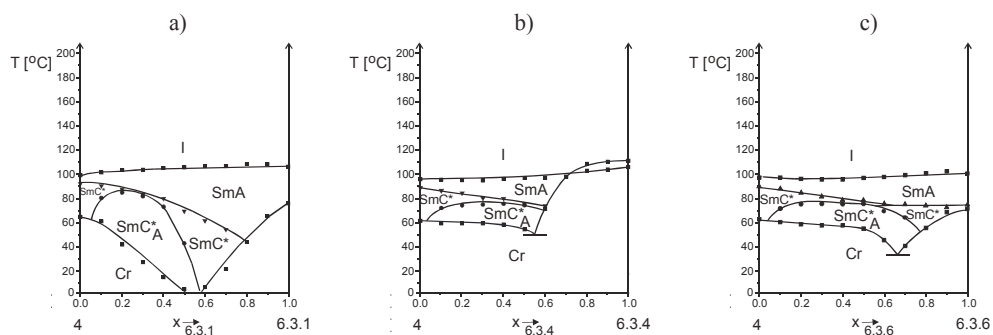


Fig. 9. Phase diagrams of bicomponent mixtures of compound 4 with compounds 6.3.1 (a), 6.3.4 (b) and 6.3.6 (c); [Skrzypek and Tykarska 2006, Czupryński 2007]

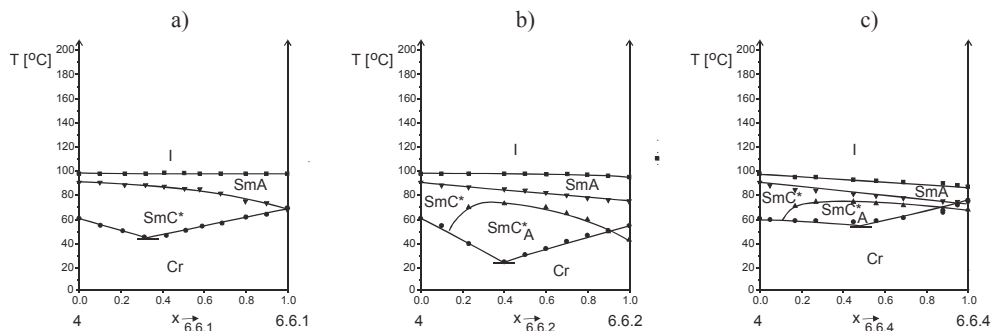


Fig. 10. Phase diagrams of bicomponent mixtures of compound 4 with compounds 6.6.1 (a), 6.6.2 (b) and 6.6.4 (c)

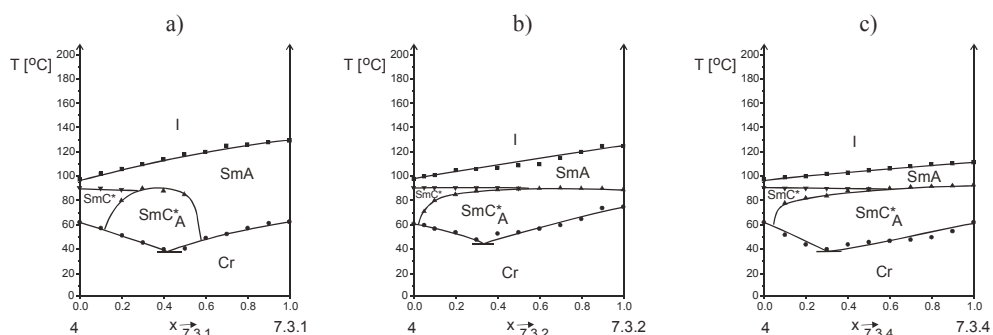


Fig. 11. Phase diagrams of bicomponent mixtures of compound 4 with compounds 7.3.1 (a), 7.3.2 (b) and 7.3.4 (c)

The comparison of induction ability of compounds 4 and 5 lead to the conclusion that compounds with biphenylate core more favourise antiferroelectric ordering than with benzoate core, similarly as it was observed for fluorinated compounds and alkylated compounds.

## 2.4 Comparison of systems with fluoroterminated and cyanoterminated compounds

When compounds: one with fluoroterminated group (1) and the other with cyanoterminated group (4), are mixed together they do not give the induction of SmC\*\_A phase [Tykarska et al. 2011]. The ability for induction of SmC\*\_A phase of both compounds (1 and 4) in ratio 2:1, 1:1 and 1:2 has been checked. Such bicomponent mixtures were doped with 6.3.2 compound. The results are presented in collective phase diagram presented in Fig. 13a, in which the curves separated SmC\*\_A phase from other phases for all tested systems have been marked [Tykarska et al. 2011]. The dependence is not linear with the concentration of compound 4, Fig. 13b. Compound with fluoroalkyl group 1 has stronger ability for induction of SmC\*\_A phase and it forces the arrangement of molecules in mixtures. In the phase diagram (Fig. 13a) the boundary of the temperature-concentration region of existence of SmC\*\_A phase in phase diagram for all mixtures containing compound 1 are close to each other but further from the curve corresponding to the mixture with cyanoterminated compound 4.

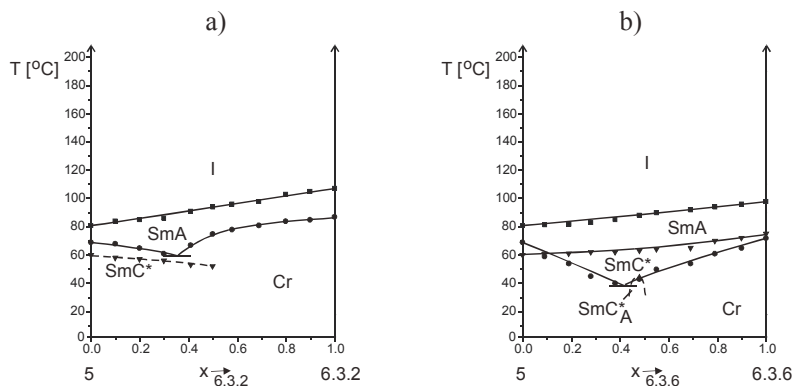


Fig. 12. Phase diagrams of bicomponent mixtures of compound 5 with compounds 6.3.2 (a) and 6.3.6 (b)

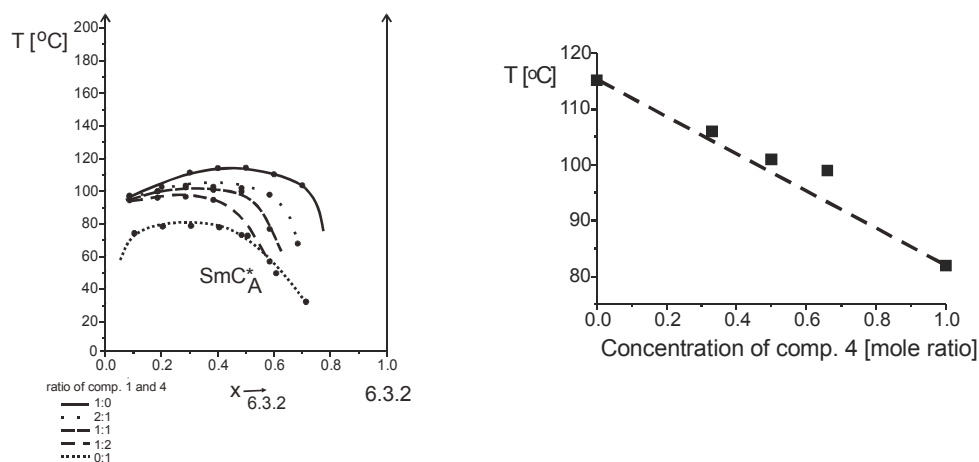


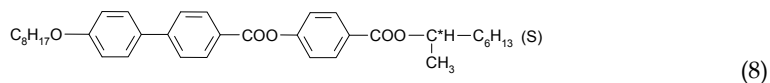
Fig. 13. The collective phase diagram showing curves corresponding to phase transition temperature from SmC\*<sub>A</sub> phase in mixtures of different concentration of compounds 1 and 4 (1:0, 2:1, 1:1, 1:2 and 0:1) with compound 6.3.2 (a), maximum temperature of SmC\*<sub>A</sub> existence versus concentration of compound 4 (b) [Tykarska et al. 2011]

The results of dielectric measurements, described in Ref. [Skrzypek et al. 2009], prove that the induced phase is really antiferroelectric phase. Properties of SmC\*<sub>A</sub> phase obtained by the induction are the same as properties of SmC\*<sub>A</sub> phase in pure compounds and their mixtures [Czupryński et al. 2007, Tykarska et al. 2008, Dąbrowski et al. 2004].

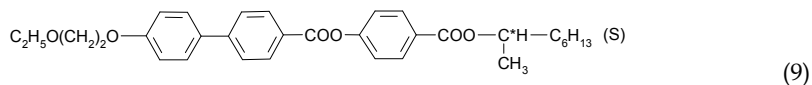
### 3. Systems with similar polarity

#### 3.1 The structure of compounds

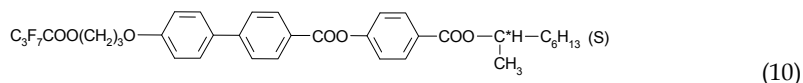
The compounds of the structure given by formulas 8-13 were used for showing the dependence of miscibility in systems of similar polarity with and without SmC\*<sub>A</sub> phase.



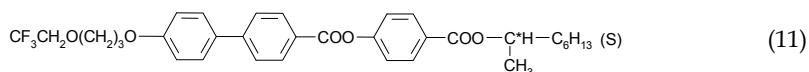
Cr 82.7 (SmI\* 65.3) SmC\*<sub>A</sub> 118.2 SmC\*<sub>γ</sub> 119.1 SmC\*<sub>β</sub> 120.0 SmC\*<sub>α</sub> 121.9 SmA 147.6 I [Chandani et al. 1989, Mandal et al. 2006]



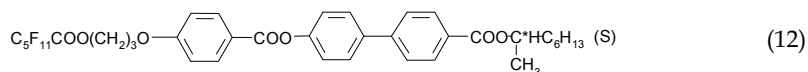
Cr 102.8 (SmI\* 90.2) SmA 148.5 I [Drzewiński et al. 1999]



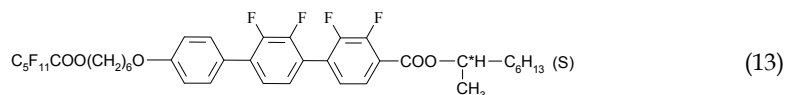
Cr 82.1 (SmI\* 54.0) SmC\*<sub>A</sub> 122.0 SmC\* 124.5 SmA 129.9 I [Drzewiński et al. 1999]



Cr 107.8 SmC\*<sub>A</sub> 124.4 SmA 134.1 I [Drzewiński et al. 1999]



Cr 61.2 SmC\*<sub>A</sub> 118.5 SmC\* 128.3 SmA 137.8 I [Gąsowska 2004]



Cr 49.0 (SmC\* 47.4) SmA 58.6 I [Kula 2008]

### 3.2 Both compounds are alkyloterminated

Usually when compounds of the same polarity are mixed together no one expect the non-additive behaviour. Characteristic examples of mixtures of compounds with alkyl chain are presented in Fig. 14. When both compounds do not form SmC\*<sub>A</sub> phase by themselves, this phase does not induces in their mixture (system 2-6.3.7), Fig. 14a. When both compounds form SmC\*<sub>A</sub> phase thus it mixes additively (system 8-7.3.2), Fig. 14b. In mixtures, in which one compound forms SmC\*<sub>A</sub> phase, but the other does not, this phase destabilizes less (system 8-9) or more (system 7.3.2-9) with the increase of the concentration of the compound without this phase, Fig. 15a and b.

### 3.3 Both compounds are fluoroterminated

Similar situation is observed when both compounds are of the same polarity but they are terminated with fluoroalkyl group. When both compounds do not form SmC\*<sub>A</sub> phase by themselves, this phase does not induces in their mixture (system 1-3), Fig. 16a. When both compounds form SmC\*<sub>A</sub> phase thus it mixes additively (system 10-11), Fig. 16b. In mixtures,

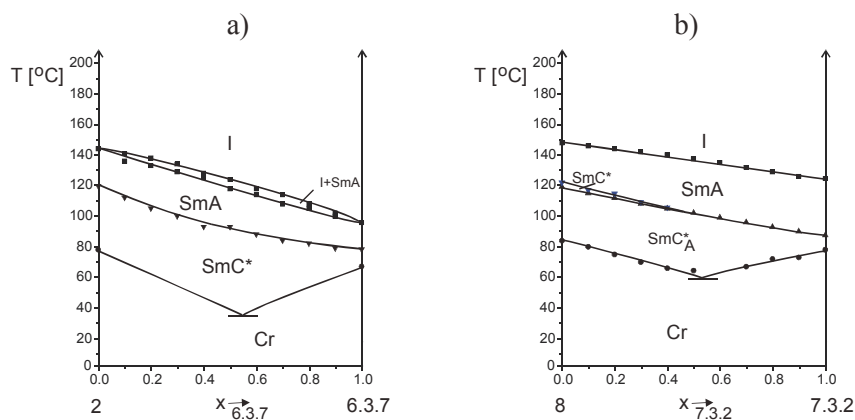


Fig. 14. Phase diagrams of bicomponent mixtures of compounds with alkyl group with additive miscibility of  $\text{SmC}^*$  phase - system 2-6.3.7 (a), and with additive miscibility of  $\text{SmC}^*_A$  phase - system 8-7.3.2 (b)

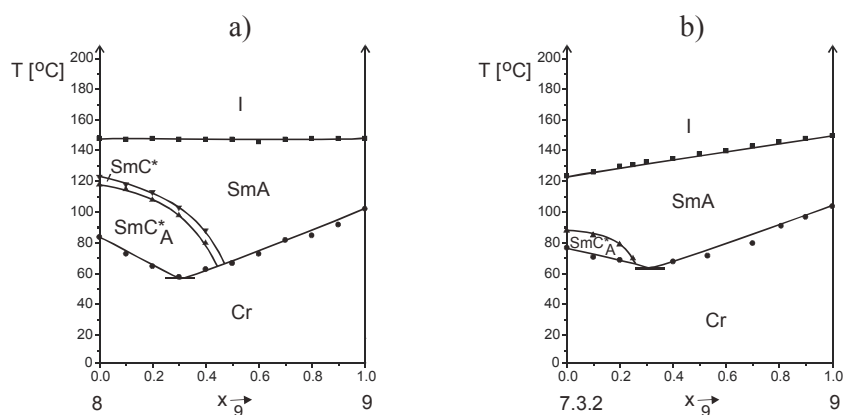


Fig. 15. Phase diagrams of bicomponent mixtures of compounds with alkyl group with destabilization of  $\text{SmC}^*_A$  phase - weaker in system 8-9 (a), and stronger in system 7.3.2-9 (b)

in which only one compound forms  $\text{SmC}^*_A$  phase, this phase usually destabilizes, but few systems were found in which the small enhancement of  $\text{SmC}^*_A$  phase was observed instead of destabilization, Fig. 17. The biggest enhancement was observed in case of compound 11 (Fig. 17a), having only one perfluorinated carbon atom in alkyl chain, thus the system is similar to the typical systems observed for compounds with different polarity. Increasing the number of perfluorinated carbon atoms to three (compound 10) or to five (compound 12) causes that the enhancement becomes smaller, Figs. 17b and c.

The presented results show that the compounds which are terminated with fluoroalkyl group and do not form  $\text{SmC}^*_A$  phase (e.g. compound 1) have big tendency to form anticlinic order when they are placed in the suitable matrix. The most appropriate for this purpose is the neighbourhood of compounds of smaller polarity, favourably terminated with alkyl chain, because then the additional molecular interaction appears. A system was found,

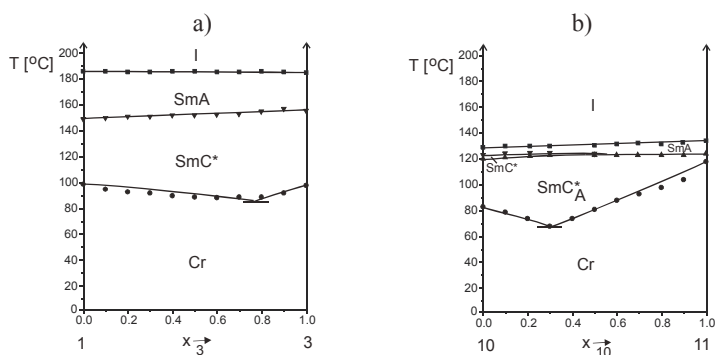


Fig. 16. Phase diagrams of bicomponent mixtures of compounds with fluoroalkyl group with additive miscibility of SmC\* phase - system 1-3 (a), and with additive miscibility of SmC\*\_A phase - system 10-11 (b)

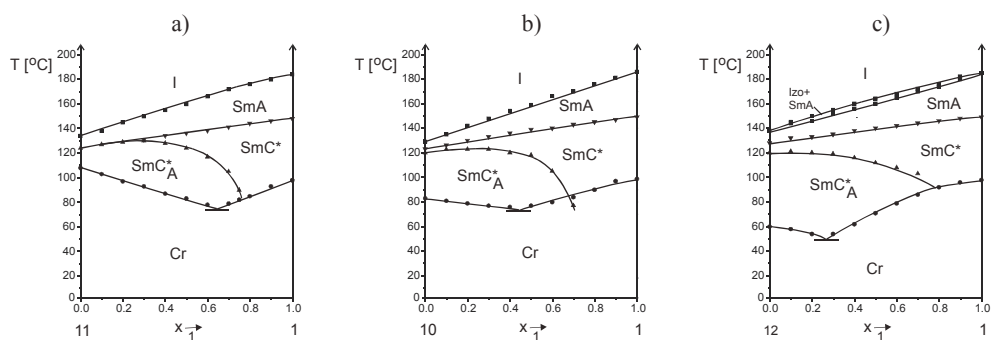


Fig. 17. Phase diagrams of bicomponent mixtures of compound 1 with compounds 11 (a), 10 (b) and 12 (c) giving the small enhancement of SmC\*\_A phase

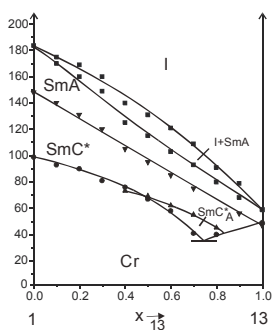


Fig. 18. Phase diagrams of bicomponent mixtures of compounds 1-13 with fluoroalkyl group giving the induction of SmC\*\_A phase

composed only of compounds with fluoroalkyl group, giving the induction of  $\text{SmC}^*_A$  phase. Compound 1 was doped with compound 13, having terphenyl rigid core laterally substituted by four fluorine atoms, Fig. 18. This example is an exception from the rule that induction of  $\text{SmC}^*_A$  phase can appear in mixtures of compounds differing in the polarity. The steric factors play also crucial role in this behaviour, because the induction of  $\text{SmC}^*_A$  phase was not found in mixtures of both nonchiral compounds. For the last system, it cannot be also excluded that the appearance of  $\text{SmC}^*_A$  phase could be a result of interactions between nonfluorinated and fluorinated rigid core.

#### 4. Conclusion

There are many systems in which the induced antiferroelectric phase can be observed. Compounds with polar group (1, 3-5) have virtual  $\text{SmC}^*_A$  phase. They have similar structure to compounds forming  $\text{SmC}^*_A$  phase by themselves; e.g. the structure of compound 1 and 4 is similar to the structure of the first antiferroelectric compound MHPOBC; they have the same rigid core and chiral terminal chain. The placement of molecules of compounds with virtual  $\text{SmC}^*_A$  phase, which have a tendency to form the antiferroelectric phase but cannot fulfil all conditions, in a suitable matrix of less polar compounds causes the appearance of an antiferroelectric phase.

The ability of more polar compounds with virtual  $\text{SmC}^*_A$  phase for induction of this phase decreases in the following order: compounds 1, 3, 4 and 5. Compounds with cyano group in terminal chain have smaller ability than compounds with fluoroalkyl group. Compounds with biphenylate core have bigger ability than compounds with benzoate core. The same is observed in group of less polar compounds with alkyl group in the terminal chain, i.e. the biphenylate core is more preferable, as well as the increase of the terminal chain causes the increase of tendency to induce  $\text{SmC}^*_A$  phase.

In systems of similar polarity nonadditive behaviour can be observed when fluorinated part of the non-branched chain is short.

The appearance of liquid crystalline phases is possible due to intermolecular interactions. Interactions between permanent dipoles play a crucial role but interactions between induced dipoles cannot be neglectable. The steric interactions are also important.

The possibility of obtaining antiferroelectric phase from compounds forming  $\text{SmC}^*$  phase or only  $\text{SmA}$  phase broadens the range of compounds useful for preparation of antiferroelectric mixtures for display application.

#### 5. References

- Chandani, A.D.L., Górecka, E., Ouchi, Y., Takezoe, H. & Fukuda, A. (1989). Antiferroelectric Chiral Smectic Phases Responsible for the Tristable Switching in MHPOBC, *Jpn.J.Appl.Phys.*, Vol.28, No.7, (July 1989), pp. L1265-L1268, ISSN 0021-4922
- Czupryński, K., Skrzypek, K., Tykarska, M. & Piecek, W. (2007). Properties of induced antiferroelectric phase, *Phase Transitions*, Vol.80, No.6-7, (June 2007), pp. 735-744, ISSN 0141-1594
- Dąbrowski, R. (2000). Liquid crystals with fluorinated terminal chains and antiferroelectric properties, *Ferroelectrics*, Vol.243, No.1, (May 2000), pp. 1-18, ISSN 0015-0193

- Dąbrowski, R., Czupryński, K., Gąsowska, J., Otón, J., Quintana, X., Castillo, P. & Bennis, N. (2004). Broad temperature range antiferroelectric regular mixtures, *Proceedings of SPIE*, Vol.5565, (2004), pp. 66-71, ISSN 0277-786X
- Drzewiński, W., Czupryński, K., Dąbrowski, R. & Neubert, M. (1999). New antiferroelectric compounds containing partially fluorinated terminal chains. Synthesis and mesomorphic properties, *Mol.Cryst.Liq.Cryst.*, Vol.328, (August 1999), pp. 401-410, ISSN 1058-725X
- Drzewiński, W., Dąbrowski, R. & Czupryński, K. (2002). Synthesis and mesomorphic properties of optically active (S)-(+)-4-(1-methylheptyloxycarbonyl)phenyl 4'-(fluoroalkanoyloxyalkoxy)biphenyl-4-carboxylates and 4'-(alkanoyloxyalkoxy)biphenyl-4-carboxylates, *Polish J.Chem.*, Vol.76, No.2-3, (February 2002), 273-284, ISSN 0137-5083
- Dziaduszek, J., Dąbrowski, R., Czupryński, K. & Bennis, N. (2006). , *Ferroelectrics*, Vol.343, No.1, (November 2006), pp. 3-9, ISSN 0015-0193
- Fukuda, A., Takanishi, Y., Isozaki, T., Ishikawa, K. & Takezoe, H. (1994). Antiferroelectric chiral smectic liquid crystals, *J.Mater.Chem.*, Vol.4, No.7, (January 1994), pp. 997-1016, ISSN 0959-9428
- Gauza, S., Czupryński, K., Dąbrowski, R., Kenig, K., Kuczyński, W. & Goc, F. (2000). Bicomponent systems with induced or enhanced antiferroelectric SmC<sub>A</sub>\* phase, *Mol.Cryst.Liq.Cryst.*, Vol.351, (November 2000), 287-296, ISSN 1058-725X
- Gauza, S., Dąbrowski, R., Czupryński, K., Drzewiński, W. & Kenig, K. (2002). Induced antiferroelectric smectic C<sub>A</sub>\* phase. Structural correlations, *Ferroelectrics*, Vol.276, (January 2002), pp. 207-217, ISSN 0015-0193
- Gąsowska, J. (2004). PhD thesis, WAT, Warsaw.
- Gąsowska, J., Dąbrowski, R., Drzewiński, W., Filipowicz, M., Przedmojski, J. & Kenig, K. (2004). Comparison of mesomorphic properties in chiral and achiral homologous series of high tilted ferroelectrics and antiferroelectrics, *Ferroelectrics*, Vol.309, No.1, (2004), pp. 83-93, ISSN 0015-0193
- Kobayashi, I., Hashimoto, S., Suzuki, Y., Yajima, T., Kawachi, S., Imase, T., Terada, M. & Mikami, K. (1999). Effects of Conformation of Diastereomer Liquid Crystals on the Preference of Antiferroelectricity, *Mol.Cryst.Liq.Cryst.A*, Vol.328, (August 1999), pp. 131-137, ISSN 1058-725X
- Kula, P. (2008). PhD thesis, WAT, Warsaw.
- Mandal, P.K., Jaishi, B.R., Haase, W., Dąbrowski, R., Tykarska, M. & Kula, P. (2006). Optical and dielectric studies on ferroelectric liquid crystal MHPO(13F)BC: Evidence of SmC\*<sub>α</sub> phase presence, *Phase Transitions*, Vol.79, No.3, (March 2006), pp. 223-235, ISSN 0141-1594
- Matsumoto, T., Fukuda, A., Johno, M., Motoyama, Y., Yuki, T., Seomun, S.S. & Yamashita M. (1999). A novel property caused by frustration between ferroelectricity and antiferroelectricity and its application to liquid crystal displays-frustoelectricity and V-shaped swiching, *J.Mater.Chem.*, Vol.9, No.9, (1999), pp. 2051-2080 ISSN 0959-9428
- Skrzypek, K. & Tykarska, M. (2006). The induction of antiferroelectric phase in the bicomponent system comprising cyano compound, *Ferroelectrics*, Vol.343, No.1, (November 2006), pp. 177-180, ISSN 0015-0193

- Skrzypek, K., Czupryński, K., Perkowski, P. & Tykarska, M. (2009). Dielectric and DSC Studies of the Bicomponent Systems with Induced Antiferroelectric Phase Comprising Cyano Terminated Compounds, *Mol.Cryst.Liq.Cryst.*, Vol.502, (2009), 154-163, ISSN 1542-1406
- Tykarska, M. & Skrzypek, K. (2006). The enhancement and induction of antiferroelectric phase, *Ferroelectrics*, Vol.343, No.1, (November 2006), pp. 193-200, ISSN 0015-0193
- Tykarska, M., Dąbrowski, R., Przedmojski, J., Piecek, W., Skrzypek, K., Donnio, B. & Guillon, D. (2008). Physical properties of two systems with induced antiferroelectric phase, *Liq.Cryst.*, Vol.35, No.9, (September 2008), pp. 1053-1059, ISSN 0267-8292
- Tykarska, M., Skrzypek, K., Ścibior, E. & Samsel, A. (2006). Helical pitch in bicomponent mixtures with induced antiferroelectric phase, *Mol.Cryst.Liq.Cryst.*, Vol.449, No.1, (July 2006), pp. 71-77, ISSN 1542-1406
- Tykarska, M., Garbat, K. & Rejmer, W. (2011). The influence of the concentration of fluoro- and cyanoterminated compounds on the induction of antiferroelectric phase and on helical pitch, *Mol.Cryst.Liq.Cryst.*, accepted for publication 2011.

## **Part 2**

### **Piezoelectrics**



# Piezoelectric Effect in Rochelle Salt

Andriy Andrusyk  
*Institute for Condensed Matter Physics  
Ukraine*

## 1. Introduction

For the last several years there has been significant progress in the development of new piezoelectric materials (relaxor ferroelectric single crystals (Park & Shrout, 1997), solid solutions with high transition temperature (Zhang et al., 2003), lead-free materials (Saito et al., 2004)) and in understanding of mechanisms of the piezoelectric coupling in ferroelectric piezoelectrics (Fu & Cohen, 2000; Guo et al., 2000). This progress was triggered in particular by the wide use of piezoelectric effect in a variety of devices (resonators, tactile sensors, bandpass filters, ceramic discriminators, SAW filters, piezoresponse force microscopes and others).

What concerns theoretical study of the piezoelectric effect, significant efforts were made in first-principles calculations. Such calculations are possible for the ferroelectrics with a relatively simple structure, in particular for simple and complex perovskites (Bellaiche et al., 2000; Garcia & Vanderbilt, 1998). For compounds with a complex structure often only the research within the Landau theory is possible. The structure complexity justifies the application of semimicroscopic models considering only that characteristic feature of the microscopic structure which is crucial in explaining the ferroelectric transition or the piezoelectric effect. Such models are adequate for the crystal under study if they are able to explain the wide range of physical properties.

In this chapter sodium potassium tartrate tetrahydrate  $\text{NaKC}_4\text{H}_4\text{O}_6 \cdot 4\text{H}_2\text{O}$  (Rochelle salt or RS) is studied on the base of the semimicroscopic Mitsui model.

The microscopic mechanism of ferroelectric phase transitions in RS was the subject of numerous investigations. Studies based on x-ray diffraction data (Shiozaki et al., 1998) argued that these were the order-disorder motions of O9 and O10 groups, coupled with the displacive vibrations of O8 groups, which were responsible for the phase transitions in Rochelle salt as well as for the spontaneous polarization. Later it was confirmed by the inelastic neutron scattering data (Hlinka et al., 2001). Respective static displacements initiate the emergence of dipole moments in local structure units in ferroelectric phase. Such displacements can be interpreted also as changes in the population ratio of two equilibrium positions of sites in the paraelectric structure (revealed in the structure studies (Noda et al., 2000; Shiozaki et al., 2001)). The order-disorder pattern of phase transitions in RS forms the basis of the semimicroscopic Mitsui model (Mitsui, 1958). In this model the asymmetry of occupancy of double local atomic positions and compensation of electric dipole moments occurring in paraelectric phases were taken into account.

Recently (Levitskii et al., 2003) Mitsui model as applied to RS was extended by accounting of the piezoelectric coupling between the order parameter and strain  $\varepsilon_4$ . Later this model was extended to the four sublattice type (Levitskii et al., 2009; Stasyuk & Velychko, 2005) that gives more thorough consideration of real RS structure. We performed our research of piezoelectric effect in Rochelle salt on the basis of the Mitsui-type model containing additional term of transverse field type responsible for dynamic flipping of structural elements (Levitskii, Andrusyk & Zachek, 2010; Levitskii, Zachek & Andrusyk, 2010). Originally, this term was added with the aim to describe resonant dielectric response which takes place in RS in submillimeter region. First, we provide characteristics of ferroelectric phase transitions in RS and experimental data for constants of physical properties of RS. Then, we present our study results (thermodynamic and dynamic characteristics) obtained within Mitsui model for RS. Specifically, we calculate permittivity of free and clamped crystals, calculate piezoelectric stress coefficient  $e_{14}$ , elastic constant  $c_{44}^E$ . The key attention is given to investigation of the phenomenon of piezoelectric resonance.

## 2. Physical properties of Rochelle salt

Rochelle salt (RS),  $\text{NaKC}_4\text{H}_4\text{O}_6 \cdot 4\text{H}_2\text{O}$  is the oldest and has been for a long time the only known ferroelectrics. RS has been the subject of numerous studies over the past 60 years. It is known for its remarkable ferroelectric state between two Curie points  $T_{c1} = 255\text{ K}$  and  $T_{c2} = 297\text{ K}$  (Jona & Shirane, 1965). Second order phase transitions occur at both Curie points. The crystalline structure of RS proved to be complex. It is orthorhombic (space group  $D_2^3-P2_12_12$ ) in the paraelectric phases and monoclinic (space group  $C_2^2-P2_1$ ) in the ferroelectric phase (Solans et al., 1997). Spontaneous polarization is directed along the  $a$  crystal axis; it is accompanied by a spontaneous shear strain  $\varepsilon_4$ . There are four formula units ( $Z = 4$ ; 112 atoms) in the unit cell of Rochelle salt in both ferroelectric and paraelectric phase. In recent study (Görbitz & Sagstuen, 2008) the complete Rochelle salt structure in paraelectric phase was described.

Due to the symmetry of RS crystal structure some elements of material tensors are zeroes. In RS case material tensors in Voigt index notations are of the form presented below (Shuvalov, 1988).

Elastic stiffnesses or elastic constants ( $c_{ij}^E = (\partial\sigma_i/\partial\varepsilon_j)_E$ ):

$$(c^E) = \begin{pmatrix} c_{11} & c_{12} & c_{13} & c_{14} & 0 & 0 \\ c_{12} & c_{22} & c_{23} & c_{24} & 0 & 0 \\ c_{13} & c_{23} & c_{33} & c_{34} & 0 & 0 \\ c_{14} & c_{24} & c_{34} & c_{44} & 0 & 0 \\ 0 & 0 & 0 & 0 & c_{55} & c_{56} \\ 0 & 0 & 0 & 0 & c_{56} & c_{66} \end{pmatrix} \quad (1)$$

Coefficients of piezoelectric stress ( $e_{ij} = (\partial P_i/\partial\varepsilon_j)_E = -(\partial\sigma_j/\partial E_i)_\varepsilon$ ):

$$(e) = \begin{pmatrix} e_{11} & e_{12} & e_{13} & e_{14} & 0 & 0 \\ 0 & 0 & 0 & 0 & e_{25} & e_{26} \\ 0 & 0 & 0 & 0 & e_{35} & e_{36} \end{pmatrix} \quad (2)$$

Dielectric permittivity ( $\chi_{ij}^\alpha = (\partial P_i / \partial E_j)_\alpha$ , where  $\alpha$  is  $\sigma$  or  $\varepsilon$ ):

$$(\chi^{\sigma,\varepsilon}) = \begin{pmatrix} \chi_{11} & 0 & 0 \\ 0 & \chi_{22} & \chi_{23} \\ 0 & \chi_{23} & \chi_{33} \end{pmatrix} \quad (3)$$

It is necessary to make some comments about the notations. Superscripts to the matrices of physical properties indicate that a physical characteristic denoted by a superscript is constant or zero (for instance  $c$ ) with superscript  $E$  denotes matrix of elastic constants at constant electric field: ( $c^E$ ). We omitted superscripts  $E$  and  $\sigma, \varepsilon$  for components of tensors ( $c^E$ ) and ( $\chi^{\sigma,\varepsilon}$ ) respectively but keep them in mind. Notation ( $\chi^{\sigma,\varepsilon}$ ) denotes two different tensors: ( $\chi^\sigma$ ) and ( $\chi^\varepsilon$ ) which we will call tensors of dielectric permittivity at constant stress and strain respectively. We will also call them tensor of free crystal dielectric permittivity (zero stress is assumed) and of clamped crystal dielectric permittivity. Hereinafter coefficients equal to zero in paraelectric phases are presented in bold.

Experimental data for physical constants are presented in Figs. 1, 2, and 3.

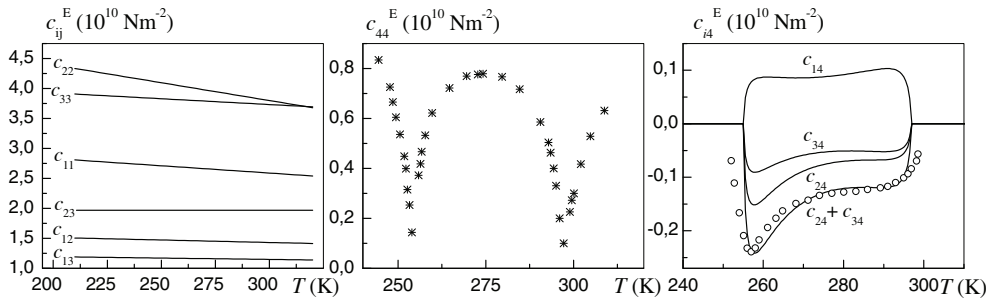


Fig. 1. Rochelle salt elastic constants. Solid lines for  $c_{ij}$  ( $i, j = 1, 2, 3$ ) are experimental data (Mason, 1950), \* correspond to  $c_{44}$  (Yu. Serdobolskaya, 1996),  $\circ$  correspond to  $c_{24}^E + c_{34}^E$  (Shiozaki et al., 2006). Lines for  $c_{14}^E, c_{24}^E, c_{34}^E$  are the results of theoretical calculations (Levitskii et al., 2005).

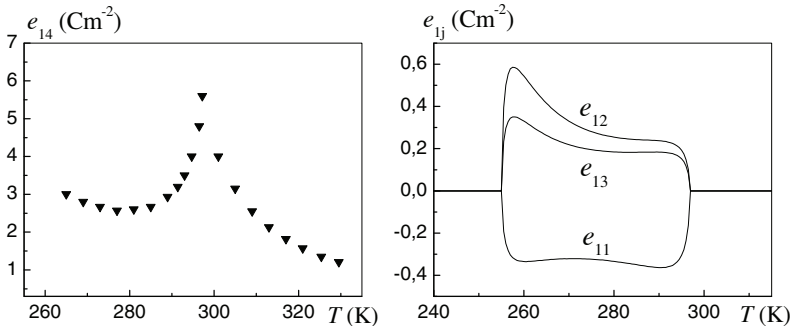


Fig. 2. Rochelle salt coefficients of piezoelectric stress. Points  $\blacktriangledown$  are experimental data (Beige & Kühnel, 1984) for  $e_{14}$ . Solid lines correspond to the results of theoretical calculations  $e_{1j}$  ( $j = 1, 2, 3$ ) (Levitskii et al., 2005).

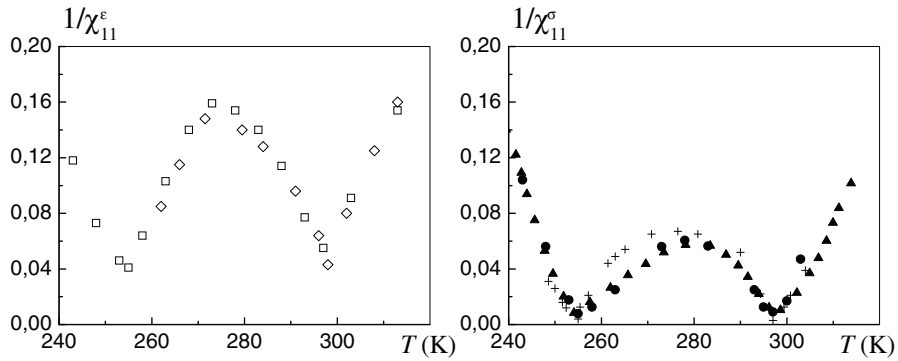


Fig. 3. Experimental data for clamped and free crystal inverse dielectric permittivity of Rochelle salt.  $1/\chi_{11}^e$ :  $\square$  (Sandy & Jones, 1968),  $\diamond$  (Mueller, 1935).  $1/\chi_{11}^o$ :  $+$  (Yurin, 1965),  $\bullet$  (Mason, 1939),  $\blacktriangle$  (Taylor et al., 1984).

As Fig. 1 shows elastic constants  $c_{ij}^E$  ( $i, j = 1, 2, 3$ ) do not change their behaviour in phase transition points, whereas constant  $c_{44}^E$  becomes zero at the transition point. Besides,  $c_{44}$  is strongly dependent on  $T$  as  $c_{ij}^E$  ( $i, j = 1, 2, 3$ ) are almost independent of  $T$ . Constants  $c_{14}^E$ ,  $c_{24}^E$ ,  $c_{34}^E$ , as it is expected on symmetry grounds, are equal to zero in paraelectric phases. There are no experiments for  $c_{14}^E$  and there are no experiments for  $c_{24}^E$ ,  $c_{34}^E$  measured separately. There is only the experiment for  $c_{24}^E + c_{34}^E$  (Shiozaki et al., 2006). However,  $c_{14}^E$ ,  $c_{24}^E$ , and  $c_{34}^E$  were estimated theoretically (Levitskii et al., 2005) and the result of estimation is presented in Fig. 1. Correspondent result for  $c_{24}^E + c_{34}^E$  is compared to experimental data where good agreement was derived.

Fig. 2 presents temperature dependencies of piezoelectric stress coefficients. As one can see coefficients  $e_{11}$ ,  $e_{12}$ ,  $e_{13}$  differ from zero only inside ferroelectric phase. Coefficient  $e_{14}$  has sharp (but finite) peak in the transition point, whereas coefficients  $e_{11}$ ,  $e_{12}$ ,  $e_{13}$  do not have it. Free and clamped crystal longitudinal susceptibilities are presented in Fig. 3. Free crystal susceptibility has singularities in transition point, whereas clamped susceptibility remains finite.

### 3. Thermodynamic characteristics of Rochelle salt

#### 3.1 Theoretical study of the Mitsui model

We give consideration to a two-sublattice order-disorder type system with an asymmetric double-well potential. Hamiltonian of such system is referred to as the Mitsui Hamiltonian. We assume this system has essential piezoelectric coupling of the order parameter with component of strain tensor  $\epsilon_4$  which should be accounted. We suppose the polarization is directed along  $x$ -axes and arises due to the structural units ordering in the one of two possible equilibrium positions. Precisely this case occurs in RS and such modified Mitsui model was considered earlier (Levitskii et al., 2003). We complement this model with transverse field to take into account the possibility of dynamic ordering units flipping between two equilibrium

positions. The resulting Hamiltonian is of the following form:

$$H = U_0 - \sum_{q,q'} \left[ \frac{J_{qq'}}{2} (S_{q1}^z S_{q'1}^z + S_{q2}^z S_{q'2}^z) + K_{qq'} S_{q1}^z S_{q'2}^z \right] - \sum_{qf} \left[ \Omega S_{qf}^x + (\Delta_f - 2\psi_{14}\varepsilon_4 + \mu E_1) S_{qf}^z \right]. \quad (4)$$

where

$$U_0 = N \left[ \frac{1}{2} v c_{44}^{E0} \varepsilon_4^2 - v e_{14}^0 E_1 \varepsilon_4 - \frac{1}{2} v \chi_{11}^{\varepsilon 0} E_1^2 \right]. \quad (5)$$

represent the elastic, piezoelectric, and electric energies attributed to a host lattice, in which potential the pseudospin moves (with the 'seed' elastic constant  $c_{44}^{E0}$ , the coefficient of piezoelectric stress  $e_{14}^0$ , and dielectric susceptibility  $\chi_{11}^{\varepsilon 0}$ );  $v$  is a volume of cell, containing a pair of pseudospins (ordering units or dipoles) of one lattice site  $\mathbf{q}$  and different sublattices  $f = 1, 2$  (further we will call it a unit cell<sup>1</sup>), and  $N$  is a number of unit cells. The first sum describes direct interaction of the ordering units:  $J_{qq'} = J_{q'q}$  and  $K_{qq'} = K_{q'q}$  are interaction potentials between pseudospins belonging to the same and to different sublattices, respectively. The first term in the second sum is the transverse field; the second term describes a) energy, associated with asymmetry of the potential, where  $\Delta_f$  is asymmetry parameter:  $\Delta_1 = -\Delta_2 = \Delta$ , b) interaction energy of pseudospin with the field, arising due to the piezoelectric deformation  $\varepsilon_4$  and  $\psi_{14}$  is parameter of piezoelectric coupling, c) interaction energy of pseudospin with external electric field  $E_1$ , where  $\mu$  is effective dipole moment of the model unit cell.

We conduct the study within the mean field approximation (MFA). Performing identical transformation

$$S_{qf}^z = \langle S_{qf}^z \rangle + \Delta S_{qf}^z \quad (6)$$

and neglecting the quadratic fluctuations, we rewrite the initial Hamiltonian (4) as

$$H_{\text{MFA}} = U_0 + \sum_{q,q'} \left[ \frac{J_{qq'}}{2} \left( \langle S_{q1}^z \rangle \langle S_{q'1}^z \rangle + \langle S_{q2}^z \rangle \langle S_{q'2}^z \rangle \right) + K_{qq'} \langle S_{q1}^z \rangle \langle S_{q'2}^z \rangle \right] - \sum_{qf} \mathcal{H}_{qf} S_{qf}, \quad (7)$$

where  $\mathcal{H}_{qf}$  are the mean local fields having effect on the pseudospins  $S_{qf}$ :

$$\begin{aligned} \mathcal{H}_{qf}^x &= \Omega, \quad \mathcal{H}_{qf}^y = 0, \quad \mathcal{H}_{qf}^z = h_{qf}, \\ h_{q1} &= \sum_{q'} \left[ J_{qq'} \langle S_{q'1}^z \rangle + K_{qq'} \langle S_{q'2}^z \rangle \right] + \Delta - 2\psi_{14}\varepsilon_4 + \mu E_1 \end{aligned} \quad (8a)$$

$$h_{q2} = \sum_{q'} \left[ J_{qq'} \langle S_{q'2}^z \rangle + K_{qq'} \langle S_{q'1}^z \rangle \right] - \Delta - 2\psi_{14}\varepsilon_4 + \mu E_1. \quad (8b)$$

Within MFA we can calculate mean equilibrium values of the pseudospin operators:

$$\langle S_{qf} \rangle = \text{Sp}(S_{qf} \rho_{\text{MFA}}), \quad (9)$$

<sup>1</sup> Actual unit cell of the Rochelle salt crystal contains two pairs of pseudospins of two lattice sites and different sublattices; therefore, we should set the value of the model unit cell volume to be half of the crystal unit cell volume.

where

$$\rho_{\text{MFA}} = \frac{\exp\left(-\frac{H_{\text{MFA}}}{k_B T}\right)}{\text{Sp} \exp\left(-\frac{H_{\text{MFA}}}{k_B T}\right)}, \quad (10)$$

and  $k_B$  is the Boltzmann constant. After calculations we derive

$$\langle S_{qf} \rangle = \frac{1}{2} \frac{\mathcal{H}_{qf}}{\mathcal{H}_{qf}} \tanh \frac{\mathcal{H}_{qf}}{2k_B T}, \quad (11)$$

where  $\mathcal{H}_{qf} \equiv \left| \mathcal{H}_{qf} \right| = \lambda_{qf} = \sqrt{\Omega^2 + h_{qf}^2}$ .

Free energy of a crystal within MFA

$$F(4) = -k_B T \ln \text{Sp} \exp\left(-\frac{H_{\text{MFA}}}{k_B T}\right)$$

is following:

$$F(4) = U_0 + \sum_{qq'} \left[ \frac{J_{qq'}}{2} \left( \langle S_{q1}^z \rangle \langle S_{q'1}^z \rangle + \langle S_{q2}^z \rangle \langle S_{q'2}^z \rangle \right) + K_{qq'} \langle S_{q1}^z \rangle \langle S_{q'2}^z \rangle \right] - k_B T \sum_{qf} \ln \left( 2 \cosh \frac{\lambda_{qf}}{2k_B T} \right). \quad (12)$$

In homogeneous external field the system of  $6N$  equations (11) has a lot of solutions, with a homogeneous one among others:  $\langle S_{qf} \rangle \equiv \langle S_{qf} \rangle_0 \neq f(q)$ . In case of a Rochelle salt crystal we have  $J_{qq'} > 0$ ,  $K_{qq'} > 0$  and it is homogeneous solution which provides free energy minimum. In this case, system of equations reduces into system

$$\langle S_{qf} \rangle_0 = \frac{1}{2} \frac{\mathcal{H}_f^{(0)}}{\mathcal{H}_f^{(0)}} \tanh \frac{\mathcal{H}_f^{(0)}}{2k_B T}, \quad (13)$$

where the local field  $\mathcal{H}_f^{(0)}$  is following:

$$\mathcal{H}_f^{(0)x} = \Omega, \quad \mathcal{H}_f^{(0)y} = 0, \quad \mathcal{H}_f^{(0)z} = h_f,$$

$$h_1 = J_0 \langle S_{q1}^z \rangle_0 + K_0 \langle S_{q2}^z \rangle_0 + \Delta - 2\psi_{14}\varepsilon_4 + \mu E_1, \quad (14a)$$

$$h_2 = J_0 \langle S_{q2}^z \rangle_0 + K_0 \langle S_{q1}^z \rangle_0 - \Delta - 2\psi_{14}\varepsilon_4 + \mu E_1, \quad (14b)$$

where

$$J_0 = \sum_{q'} J_{qq'}, \quad K_0 = \sum_{q'} K_{qq'}; \quad \mathcal{H}_f^{(0)} \equiv \left| \mathcal{H}_f^{(0)} \right| = \lambda_f, \quad \lambda_f = \sqrt{\Omega^2 + h_f^2}.$$

z-component of this equation system forms two-equation system ( $f = 1, 2$ ) to determine  $\langle S_{qf}^z \rangle_0$ :

$$\langle S_{qf}^z \rangle_0 = \frac{h_f}{2\lambda_f} \tanh \frac{\lambda_f}{2k_B T}. \quad (15)$$

Having introduced new variables

$$\xi = \langle S_{q1} \rangle_0 + \langle S_{q2} \rangle_0, \quad \sigma = \langle S_{q1} \rangle_0 - \langle S_{q2} \rangle_0 \quad (16)$$

( $\xi^z$  and  $\sigma^z$  are ferroelectric and antiferroelectric ordering parameters), we obtain system of equations (15) in a form:

$$\begin{cases} \xi^z = \frac{1}{2} \left[ \frac{\tilde{h}_1}{\tilde{\lambda}_1} \tanh \frac{\tilde{\lambda}_1}{2T} + \frac{\tilde{h}_2}{\tilde{\lambda}_2} \tanh \frac{\tilde{\lambda}_2}{2T} \right], \\ \sigma^z = \frac{1}{2} \left[ \frac{\tilde{h}_1}{\tilde{\lambda}_1} \tanh \frac{\tilde{\lambda}_1}{2T} - \frac{\tilde{h}_2}{\tilde{\lambda}_2} \tanh \frac{\tilde{\lambda}_2}{2T} \right], \end{cases} \quad (17)$$

where unknowns  $\xi^z$  and  $\sigma^z$  are defined at given  $T$ ,  $E_1$ ,  $\varepsilon_4$ . In system (17) the following notations are used:

$$\begin{aligned} \tilde{h}_f &= h_f/k_B, \quad \tilde{\lambda}_f = \sqrt{\tilde{\Omega}^2 + \tilde{h}_f^2}, \\ \tilde{h}_1 &= \tilde{R}_0^+ \xi^z + \tilde{R}_0^- \sigma^z + \tilde{\Delta} - 2\tilde{\psi}_{14}\varepsilon_4 + \tilde{\mu}E_1, \\ \tilde{h}_2 &= \tilde{R}_0^+ \xi^z - \tilde{R}_0^- \sigma^z - \tilde{\Delta} - 2\tilde{\psi}_{14}\varepsilon_4 + \tilde{\mu}E_1. \end{aligned} \quad (18)$$

Here

$$\tilde{\Omega} = \frac{\Omega}{k_B}, \quad \tilde{\Delta} = \frac{\Delta}{k_B}, \quad \tilde{\psi}_{14} = \frac{\psi_{14}}{k_B}, \quad \tilde{\mu} = \frac{\mu}{k_B}, \quad \tilde{R}_0^\pm = \frac{\tilde{J}_0 \pm \tilde{K}_0}{2}, \quad \tilde{J}_0 = \frac{J_0}{k_B}, \quad \tilde{K}_0 = \frac{K_0}{k_B}. \quad (19)$$

The system (17) is system of two equations with unknowns  $\xi^z$  and  $\sigma^z$ .

When values  $\xi^z$  and  $\sigma^z$  are defined, we can calculate values  $\xi^x$  and  $\sigma^x$  using (13) and (16):

$$\xi^x = \frac{1}{2} \left[ \frac{\tilde{\Omega}}{\tilde{\lambda}_1} \tanh \frac{\tilde{\lambda}_1}{2T} + \frac{\tilde{\Omega}}{\tilde{\lambda}_2} \tanh \frac{\tilde{\lambda}_2}{2T} \right], \quad \sigma^x = \frac{1}{2} \left[ \frac{\tilde{\Omega}}{\tilde{\lambda}_1} \tanh \frac{\tilde{\lambda}_1}{2T} - \frac{\tilde{\Omega}}{\tilde{\lambda}_2} \tanh \frac{\tilde{\lambda}_2}{2T} \right];$$

values  $\xi^y$ ,  $\sigma^y$  are equal to zero.

Free energy per model unit cell  $f(4) = F(4)/(k_B N)$  in variables  $\xi^z$  and  $\sigma^z$  is following:

$$f(4) = \frac{\tilde{v}}{2} c_{44}^{E0} \varepsilon_4^2 - \tilde{v} e_{14}^0 \varepsilon_4 E_1 - \frac{\tilde{v}}{2} \chi_{11}^{\varepsilon 0} E_1^2 + \frac{\tilde{R}_0^+}{2} (\xi^z)^2 + \frac{\tilde{R}_0^-}{2} (\sigma^z)^2 - T \sum_f \ln \left( 2 \cosh \frac{\tilde{\lambda}_f}{2T} \right), \quad (20)$$

where  $\tilde{v} = \frac{v}{k_B}$ . By differentiating free energy we can find dielectric, elastic, and piezoelectric properties of the Rochelle salt.

The conditions

$$\frac{1}{\tilde{v}} \left( \frac{\partial f(4)}{\partial \varepsilon_4} \right)_{E_1, T} = \sigma_4, \quad \frac{1}{\tilde{v}} \left( \frac{\partial f(4)}{\partial E_1} \right)_{\varepsilon_4, T} = -P_1$$

yield the following expression for stress  $\sigma_4$  and polarization  $P_1$ :

$$\sigma_4 = c_{44}^{E0} \varepsilon_4 - e_{14}^0 E_1 + \frac{2\tilde{\psi}_{14}}{\tilde{v}} \xi^z, \quad (21a)$$

$$P_1 = e_{14}^0 \varepsilon_4 + \chi_{11}^{\varepsilon 0} E_1 + \frac{\tilde{\mu}}{\tilde{v}} \xi^z. \quad (21b)$$

Independent variable is stress rather than deformation, so we need express local fields in terms of  $\sigma_4$  when solving system (17). Having used (21a) we derive

$$\varepsilon_4 = \frac{\sigma_4}{c_{44}^{E0}} + \frac{e_{14}^0}{c_{44}^{E0}} E_1 - \frac{2\tilde{\psi}_{14}}{\tilde{\nu}c_{44}^{E0}} \zeta^z. \quad (22)$$

On the basis of Eq. (22) we can rewrite local fields in the following way:

$$\tilde{h}_1 = \tilde{R}_0^{'+} \zeta^z + \tilde{R}_0^- \sigma^z + \tilde{\Delta} - \frac{2\tilde{\psi}_{14}}{c_{44}^{E0}} \sigma_4 + \tilde{\mu}' E_1, \quad (23a)$$

$$\tilde{h}_2 = \tilde{R}_0^{'+} \zeta^z - \tilde{R}_0^- \sigma^z - \tilde{\Delta} - \frac{2\tilde{\psi}_{14}}{c_{44}^{E0}} \sigma_4 + \tilde{\mu}' E_1, \quad (23b)$$

where  $\tilde{R}^{'+}$  and  $\tilde{\mu}'$  are following:

$$\tilde{R}_0^{'+} = \tilde{R}_0^+ + \frac{4\tilde{\psi}_{14}^2}{\tilde{\nu}c_{44}^{E0}}, \quad \tilde{\mu}' = \tilde{\mu} - \frac{2\tilde{\psi}_{14}e_{14}^0}{c_{44}^{E0}}. \quad (24)$$

System (17) with local fields (23), considered at  $\sigma_4 = 0$ ,  $E_1 = 0$ , has solutions of two types:  $\zeta^z = 0$  and  $\zeta^z \neq 0$ . The minimum Helmholtz free energy ( $g(4) = f(4) - \tilde{\nu}\sigma_4\varepsilon_4$ ) condition defines which of the solutions is actually realized at each particular  $T$ . The solution of first type describes paraelectric phase and the solution of second type describes ferroelectric phase. In paraelectric phase we have also  $\sigma^x = 0$ .

We will calculate elastic, piezoelectric, and dielectric constants by differentiation  $P_1$  (21b) and  $\sigma_4$  (21a) at constant  $T$ :

$$dP_1 = e_{14}d\varepsilon_4 + \chi_{11}^\varepsilon dE_1, \quad (25a)$$

$$d\sigma_4 = c_{44}^E d\varepsilon_4 - e_{14}dE_1. \quad (25b)$$

Here  $\chi_{11}^\varepsilon$  is longitudinal dielectric susceptibility at constant strain,  $c_{44}^E$  is elastic constant at constant field,  $e_{14}$  is coefficient of the piezoelectric stress.

The result is following:<sup>2</sup>

$$\chi_{11}^\varepsilon = \left( \frac{\partial P_1}{\partial E_1} \right)_{\varepsilon_4} = \chi_{11}^{\varepsilon 0} + \frac{\tilde{\mu}}{\tilde{\nu}} \left( \frac{\partial \zeta^z}{\partial E_1} \right)_{\varepsilon_4} = \chi_{11}^{\varepsilon 0} + \frac{\tilde{\mu}^2}{\tilde{\nu}} f_1(T, \sigma_4, E_1), \quad (26)$$

where

$$f_1(T, \sigma_4, E_1) = \frac{e_1 - \tilde{R}_0^-(e_1^2 - e_2^2)}{1 - e_1(\tilde{R}_0^+ + \tilde{R}_0^-) + \tilde{R}_0^+\tilde{R}_0^-(e_1^2 - e_2^2)} \quad (27)$$

and following notations are used:

$$e_1 = \frac{a_1 + a_2}{4T} + \frac{\tilde{\Omega}^2(b_1 + b_2)}{2}, \quad e_2 = \frac{a_1 - a_2}{4T} + \frac{\tilde{\Omega}^2(b_1 - b_2)}{2}, \quad (28)$$

$$a_i = \frac{\tilde{h}_i^2}{\tilde{\lambda}_i^2} - \eta_i^2, \quad b_i = \frac{\eta_i}{\tilde{h}_i \tilde{\lambda}_i^2}, \quad (i = 1, 2); \quad \eta_1 = \zeta^z + \sigma^z, \quad \eta_2 = \zeta^z - \sigma^z.$$

<sup>2</sup> All partial derivatives of  $\zeta^z$  were derived by differentiating Eq. (17).

Coefficient of the piezoelectric stress:

$$e_{14} = \left( \frac{\partial P_1}{\partial \varepsilon_4} \right)_{E_1} = e_{14}^0 - \frac{2\tilde{\mu}\tilde{\psi}_{14}}{\tilde{v}} f_1(T, \sigma_4, E_1). \quad (29)$$

Elastic constant at constant field:

$$c_{44}^E = \left( \frac{\partial \sigma_4}{\partial \varepsilon_4} \right)_{E_1} = c_{44}^{E0} - \frac{4\tilde{\psi}_{14}^2}{\tilde{v}} f_1(T, \sigma_4, E_1). \quad (30)$$

Coefficient of the piezoelectric strain  $d_{14} = (\partial P_1 / \partial \sigma_4)_{E_1}$  and dielectric susceptibility of free crystal  $\chi_{11}^\sigma = (\partial P_1 / \partial E_1)_{\sigma_4}$  could be derived through  $e_{14}$ ,  $c_{44}^E$  and  $\chi_{11}^\varepsilon$ :

$$d_{14} = \frac{e_{14}}{c_{44}^E}, \quad \chi_{11}^\sigma = \chi_{11}^\varepsilon + e_{14}d_{14}.$$

We may notice that at  $\tilde{\Omega} = 0$  all results presented here coincide with the results of previous calculations (Levitskii et al., 2003), where transverse field was not taken into account.

### 3.2 Results of calculations for Rochelle salt

The proposed model was used for analysis of physical properties of Rochelle salt crystal that is not externally affected ( $E_1 = 0, \sigma_4 = 0$ ). To obtain specific numerical results it is necessary first of all to derive theory model parameters for calculations. Deriving procedure was described in (Levitskii, Zachek & Andrusyk, 2010) and here we will restrict ourselves to parameters presenting:

$$\begin{aligned} \tilde{\Omega} &= 113.467 \text{ K}, \quad \tilde{J}_0 = 813.216 \text{ K}, \quad \tilde{K}_0 = 1447.17 \text{ K}, \quad \tilde{\Delta} = 719.937 \text{ K}, \quad \tilde{\psi}_4 = -720.0 \text{ K}, \\ c_{44}^{E0} &= 1.224 \times 10^{10} \text{ Nm}^{-2}, \quad e_{14}^0 = 31.64 \times 10^{-2} \text{ Cm}^{-2}, \quad \chi_{11}^{\varepsilon 0} = 0.0, \\ \mu(T) &= a + k(T - 297), \quad a = 8.157 \times 10^{-30} \text{ Cm}, \quad k = -0.0185 \times 10^{-30} \text{ CmK}^{-1}. \end{aligned} \quad (31)$$

Unit cell volume (volume per two pseudospins from the same site and different sublattices) is  $v = 5.219 \times 10^{-22} \text{ cm}^3$  (Bronowska, 1981).

The results of calculations made for static dielectric characteristics are shown together with experimental data in Fig. 4. The derived agreement is very good considering that Mitsui model is rather inaccurate model of RS and the used MFA is a weak approximation.

Besides, we derived that dielectric permittivity of the free crystal has singularity in the transition points while dielectric permittivity of the clamped crystal doesn't. Elastic constant  $c_{44}$  becomes equal to zero at the transition points, coefficient of the piezoelectric stress  $e_{14}$  doesn't have singularity in the transition point. All these results agree with the prediction of the Landau theory for the behaviour of physical characteristics in the vicinity of the transition points. However, presented semimicroscopic approach has an advantage over the Landau theory: it allowed to explain physical properties of Rochelle salt in wide temperature range containing both transition points in natural way. Besides that Mitsui model gives some insight into microscopical mechanism of the phase transition of Rochelle salt.

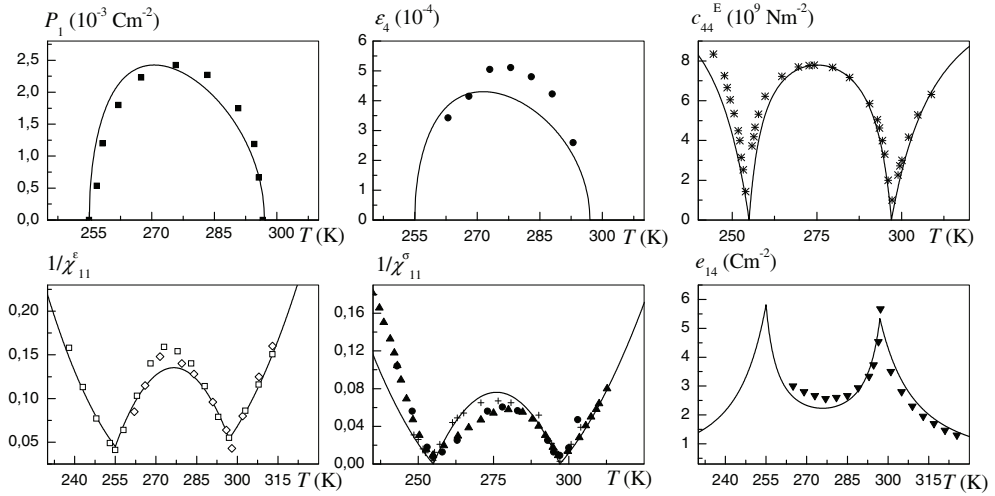


Fig. 4. Theoretical and experimental physical characteristics of Rochelle salt. Solid line corresponds to calculations, Points are the experimental data.  $P_1(T)$ : ■ (Cady, 1964),  $\epsilon_4(T)$ : ● (Ubbelohde & Woodward, 1946),  $c_{44}^E$ : \* (Yu. Serdobolskaya, 1996),  $1/\chi_{11}^\epsilon(T)$ : □ (Sandy & Jones, 1968), ◇ (Mueller, 1935),  $1/\chi_{11}^\sigma(T)$ : ▲ (Taylor et al., 1984),  $e_{14}(T)$ : ▼ (Beige & Kühnel, 1984).

## 4. Dynamic properties of Rochelle salt

### 4.1 Order parameter dynamics. Dielectric susceptibility of a clamped crystal

We consider dynamic properties of the system with Hamiltonian (4) within the Bloch equations method

$$\hbar \frac{d\langle \mathbf{S}_{qf} \rangle_t}{dt} = \langle \mathbf{S}_{qf} \rangle_t \times \mathcal{H}_{qf}(t) - \frac{\hbar}{T_1} \left[ \langle \mathbf{S}_{qf} \rangle_{t\parallel} - \overline{\langle \mathbf{S}_{qf} \rangle_t} \right]. \quad (32)$$

Right part of this equation consists of two terms.

The first term is Heisenberg part of the motion equation, calculated within random phase approximation (RPA), where ‘ $\times$ ’ denotes the vector product and  $\mathcal{H}_{qf}(t)$  are the instantaneous values of the local fields:<sup>3</sup>

$$\mathcal{H}_{qf}^x(t) = \Omega, \quad \mathcal{H}_{qf}^y = 0, \quad \mathcal{H}_{qf}^z(t) = h_{qf}(t), \quad (33)$$

<sup>3</sup> Original Heisenberg part of the motion equation is  $-i\langle [\mathbf{S}_{qf}, H] \rangle_t$ . Within RPA mean value of commutator with time dependent statistical operator in form of (10) is to be calculated. Doing necessary calculations one can derive that

$$-i\langle [\mathbf{S}_{qf}, H] \rangle_t = \langle \mathbf{S}_{qf} \rangle_t \times \mathcal{H}_{qf}(t).$$

$$h_{q1}(t) = \sum_{q'} \left[ J_{qq'} \langle S_{q'1}^z \rangle_t + K_{qq'} \langle S_{q'2}^z \rangle_t \right] + \Delta - 2\psi_{14}\varepsilon_{4q}(t) + \mu E_{1q}(t), \quad (34a)$$

$$h_{q2}(t) = \sum_{q'} \left[ J_{qq'} \langle S_{q'2}^z \rangle_t + K_{qq'} \langle S_{q'1}^z \rangle_t \right] - \Delta - 2\psi_{14}\varepsilon_{4q}(t) + \mu E_{1q}(t). \quad (34b)$$

The second term describes relaxation of the pseudospin component  $\langle \mathbf{S}_{qf} \rangle_{t\parallel}$  (longitudinal to the instantaneous value of the local field) towards its quasiequilibrium value with a characteristic time  $T_1$ .<sup>4</sup> Quasiequilibrium mean values  $\overline{\langle \mathbf{S}_{qf} \rangle}_t$  are defined as (see Eq. (11)):

$$\overline{\langle \mathbf{S}_{qf} \rangle}_t = \frac{1}{2} \frac{\mathcal{H}_{qf}(t)}{\mathcal{H}_{qf}(t)} \tanh \left[ \frac{1}{2k_B T} \mathcal{H}_{qf}(t) \right]. \quad (35)$$

Relaxation term describes non-equilibrium processes in a pseudospin system. In real situation, a pseudospin system is not an isolated system, whereas it is a part of a larger system. That part of extended system which is not a pseudospin subsystem appears as thermostat that behaves without criticality. Respectively, pseudospin excitations relax due to the interaction with thermostat to their quasiequilibrium values for a characteristic relaxation time  $T_1$ . As far as a phase transition is a collective effect and the relaxation term in Eq. (32) describes individual relaxation of each pseudospin, it becomes clear that relaxation time  $T_1$  should have no singularity at the Curie point. Relaxation time can be derived *ab initio* but we consider it to be a model parameter and take it to be independent from temperature.

In the same way it can be explained why relaxation in Eq. (32) occurs towards quasiequilibrium state and not to thermodynamic equilibrium state. Relaxation term describes individual relaxation of pseudospin, which 'is not aware' of the state of thermodynamic equilibrium but 'is aware' of the state of its environment at a particular moment. At every moment this environment creates instantaneous molecular fields which define quasiequilibrium state. Instantaneous quasiequilibrium average of pseudospin operators are defined from Eq. (9), (10) but with molecular fields Eq. (33), (34). Making necessary calculations we obtain quasiequilibrium average  $\overline{\langle \mathbf{S}_{qf} \rangle}_t$  in form of Eq. (35). Eventually, of course, quasiequilibrium values follow to equilibrium ones and relaxation leads excited system to thermodynamic equilibrium state.

As we are interested in linear response of the system to a small external variable electric field

$$\delta E_{1q}(t) \quad (E_{1q}(t) = E_1 + \delta E_{1q}(t)),$$

it is sufficiently to present  $\langle \mathbf{S}_{qf} \rangle_t$  as a sum of constant term  $\langle \mathbf{S}_{qf} \rangle_0$  (mean equilibrium value, calculated in MFA) and time dependent small deviation  $\delta \langle \mathbf{S}_{qf} \rangle_t$ :

$$\langle \mathbf{S}_{qf} \rangle_t = \langle \mathbf{S}_{qf} \rangle_0 + \delta \langle \mathbf{S}_{qf} \rangle_t. \quad (36)$$

<sup>4</sup> Sometimes one writes third term  $-\frac{\hbar}{2} \langle \mathbf{S}_{qf} \rangle_{t\perp}$ , describing decay process of the transverse component of pseudospin  $\langle \mathbf{S}_{qf} \rangle_{t\perp}$ , though it can be shown (Levitskii, Andrusyk & Zachek, 2010) that its impact on Rochelle salt dynamics is negligible.

Similarly:

$$\mathcal{H}_{qf}(t) = \mathcal{H}_f^{(0)} + \delta\mathcal{H}_{qf}(t), \quad \overline{\langle \mathbf{S}_{qf} \rangle}_t = \langle \mathbf{S}_{qf} \rangle_0 + \delta\overline{\langle \mathbf{S}_{qf} \rangle}_t. \quad (37)$$

Now, we can linearize motion equation (32) by retaining terms, which are linear in deviations  $\delta\langle \mathbf{S}_{qf} \rangle_t, \delta\mathcal{H}_{qf}(t), \delta\overline{\langle \mathbf{S}_{qf} \rangle}_t$ :

$$\hbar \frac{d\delta\langle \mathbf{S}_{qf} \rangle_t}{dt} = \delta\langle \mathbf{S}_{qf} \rangle_t \times \mathcal{H}_f^{(0)} + \langle \mathbf{S}_{qf} \rangle_0 \times \delta\mathcal{H}_{qf}(t) - \frac{\hbar}{T_1} \left[ \delta\langle \mathbf{S}_{qf} \rangle_{t\parallel} - \delta\overline{\langle \mathbf{S}_{qf} \rangle}_{t\parallel} \right], \quad (38)$$

where

$$\begin{aligned} \delta\mathcal{H}_{qf}^x(t) &= 0, \quad \delta\mathcal{H}_{qf}^y(t) = 0, \\ \delta\mathcal{H}_{q1}^z(t) &= \sum_{q'} J_{qq'} \delta\langle S_{q'1}^z \rangle_t + \sum_{q'} K_{qq'} \delta\langle S_{q'2}^z \rangle_t - 2\psi_{14} \delta\varepsilon_{4q}(t) + \mu \delta E_{1q}(t), \\ \delta\mathcal{H}_{q2}^z(t) &= \sum_{q'} K_{qq'} \delta\langle S_{q'1}^z \rangle_t + \sum_{q'} J_{qq'} \delta\langle S_{q'2}^z \rangle_t - 2\psi_{14} \delta\varepsilon_{4q}(t) + \mu \delta E_{1q}(t). \end{aligned}$$

Now, we transform equation (38) into a form involving single variable  $\delta\langle \mathbf{S}_{qf} \rangle_t$ , then Fourier transform into the frequency domain and Fourier transform to k-space,<sup>5</sup> introduce new theory parameters

$$\tilde{R}_k^+ = \frac{\tilde{J}_k + \tilde{K}_k}{2}, \quad \tilde{R}_k^- = \frac{\tilde{J}_k - \tilde{K}_k}{2} \quad (\tilde{J}_k = J_k/k_B, \quad \tilde{K}_k = K_k/k_B), \quad (39)$$

and introduce new variables  $\delta\xi_k(t), \delta\sigma_k(t)$

$$\delta\langle \mathbf{S}_{k1} \rangle_t = \frac{\delta\xi_k(t) + \delta\sigma_k(t)}{2}, \quad \delta\langle \mathbf{S}_{k2} \rangle_t = \frac{\delta\xi_k(t) - \delta\sigma_k(t)}{2}. \quad (40)$$

Upon application of these transformations, the Bloch equation (38) reduces to system of linear differential equations of the following matrix form:

$$\left( A_k - i \frac{\hbar}{k_B} \omega \cdot I \right) \delta x_k(\omega) = (\tilde{\mu} \delta E_{1k}(\omega) - 2\tilde{\psi}_{14} \delta\varepsilon_{4k}(\omega)) b. \quad (41)$$

<sup>5</sup> Fourier transform to k-space is

$$A_q = \sum_k a_k \exp(ikq), \quad a_k = \frac{1}{N} \sum_q A_q \exp(-ikq)$$

for values dependent on  $q$  (like  $\delta\langle S_{q1}^z \rangle_t$  and others) and

$$M_{q_1 q_2} = \frac{1}{N} \sum_k m_k \exp(ik(q_1 - q_2)), \quad m_k = \sum_{q_2} M_{q_1 q_2} \exp(-ik(q_1 - q_2)).$$

for interaction constants dependent on  $q_1$  and  $q_2$  (like  $J_{qq'}$  and others). Here the dependency of  $M_{q_1 q_2}$  on difference  $q_1 - q_2$  was used.

The following notations are used in this equation:  $I$  is identity matrix,  $i$  is the imaginary unit,

$$A_k = \begin{pmatrix} a_{11} & a_{12} & -\tilde{\Omega} & 0 & a_{15} & a_{16} \\ a_{21} & a_{22} & 0 & -\tilde{\Omega} & a_{16} & a_{15} \\ a_{31} & a_{32} & 0 & 0 & a_{35} & a_{36} \\ a_{41} & a_{42} & 0 & 0 & a_{36} & a_{35} \\ a_{51} & a_{52} & -a_{35} & -a_{36} & a_{55} & a_{56} \\ a_{61} & a_{62} & -a_{36} & -a_{35} & a_{56} & a_{55} \end{pmatrix}, \quad \delta x_k(\omega) = \begin{pmatrix} \delta \zeta_k^z(\omega) \\ \delta \sigma_k^z(\omega) \\ \delta \zeta_k^y(\omega) \\ \delta \sigma_k^y(\omega) \\ \delta \zeta_k^x(\omega) \\ \delta \sigma_k^x(\omega) \end{pmatrix}, \quad b = \begin{pmatrix} b_1 \\ b_2 \\ \zeta^x \\ \sigma^x \\ b_5 \\ b_6 \end{pmatrix}. \quad (42)$$

Matrix  $A_k$  components:

$$\begin{aligned} a_{11} &= U_1 + \tilde{R}_k^+ G_1, & a_{12} &= U_2 + \tilde{R}_k^- G_2, & a_{15} &= V_1, & a_{16} &= V_2, \\ a_{21} &= U_2 + \tilde{R}_k^+ G_2, & a_{22} &= U_1 + \tilde{R}_k^- G_1, \\ a_{31} &= \tilde{\Omega} - \tilde{R}_k^+ \zeta^x, & a_{32} &= -\tilde{R}_k^- \sigma^x, & a_{35} &= -[\tilde{R}_0^+ \zeta^z - 2\tilde{\psi}_{14} \varepsilon_4], & a_{36} &= -[\tilde{R}_0^- \sigma^z + \tilde{\Delta}], \\ a_{41} &= -\tilde{R}_k^+ \sigma^x, & a_{42} &= \tilde{\Omega} - \tilde{R}_k^- \zeta^x, \\ a_{51} &= V_1 + \tilde{R}_k^+ H_1, & a_{52} &= V_2 + \tilde{R}_k^- H_2, & a_{55} &= W_1, & a_{56} &= W_2, \\ a_{61} &= V_2 + \tilde{R}_k^+ H_2, & a_{62} &= V_1 + \tilde{R}_k^- H_1; \end{aligned} \quad (43)$$

components of vector  $b$ :

$$b_1 = -G_1, \quad b_2 = -G_2, \quad b_5 = -H_1, \quad b_6 = -H_2, \quad (44)$$

where following notations were used

$$\begin{aligned} U_{1,2} &= -\frac{1}{2T'_1} \left( \frac{\tilde{\varepsilon}_1^2}{\tilde{\lambda}_1^2} \pm \frac{\tilde{\varepsilon}_2^2}{\tilde{\lambda}_2^2} \right), & V_{1,2} &= -\frac{1}{2T'_1} \left( \frac{\tilde{\Omega} \tilde{\varepsilon}_1}{\tilde{\lambda}_1^2} \pm \frac{\tilde{\Omega} \tilde{\varepsilon}_2}{\tilde{\lambda}_2^2} \right), & G_{1,2} &= K_1 \frac{\tilde{\varepsilon}_1^2}{\tilde{\lambda}_1^2} \pm K_2 \frac{\tilde{\varepsilon}_2^2}{\tilde{\lambda}_2^2}, \\ W_{1,2} &= -\frac{1}{2T'_1} \left( \frac{\tilde{\Omega}^2}{\tilde{\lambda}_1^2} \pm \frac{\tilde{\Omega}^2}{\tilde{\lambda}_2^2} \right), & H_{1,2} &= K_1 \frac{\tilde{\Omega} \tilde{\varepsilon}_1}{\tilde{\lambda}_1^2} \pm K_2 \frac{\tilde{\Omega} \tilde{\varepsilon}_2}{\tilde{\lambda}_2^2}, & K_{1,2} &= \frac{1}{T'_1} \frac{1}{4T \cosh^2 \frac{\tilde{\lambda}_{1,2}}{2T}}, \end{aligned}$$

and relaxation time  $T'_1$  is

$$T'_1 = \frac{k_B}{\hbar} T_1. \quad (45)$$

It is convenient to present the solution of Eq. (41) in a form

$$\delta x_k(\omega) = (\tilde{\mu} \delta E_{1k}(\omega) - 2\tilde{\psi}_{14} \delta \varepsilon_{4k}(\omega)) \left[ \left( A_k - i \frac{\hbar}{k_B} \omega \cdot I \right)^{-1} b \right], \quad (46)$$

where we denote the inverse of matrix  $\left( A_k - i \frac{\hbar}{k_B} \omega \cdot I \right)$  by  $\left( A_k - i \frac{\hbar}{k_B} \omega \cdot I \right)^{-1}$ .

Now it is useful to present all variables in Eq. (21b) as a sum of constant (equilibrium) term and small variation term. The result for  $\delta P_{1k}(\omega)$  is

$$\delta P_{1k}(\omega) = e_{14}^0 \delta \varepsilon_{4k}(\omega) + \chi_{11}^{\varepsilon 0} \cdot \delta E_{1k}(\omega) + \frac{\tilde{\mu}}{\vartheta} \cdot \delta \zeta_k^z(\omega). \quad (47)$$

If to note that  $\delta\zeta_k^z(\omega)$  is the first component of vector  $\delta x_k(\omega)$ , variation of polarization can be presented as

$$\delta P_{1k}(\omega) = e_{14}(\mathbf{k}, \omega)\delta\varepsilon_{4k}(\omega) + \chi_{11}^\varepsilon(\mathbf{k}, \omega)\delta E_{1k}(\omega). \quad (48)$$

Here  $\chi_{11}^\varepsilon(\mathbf{k}, \omega)$  is dynamic susceptibility of a clamped crystal ( $\delta\varepsilon_{4k}(\omega) = 0$ ), and  $e_{14}(\mathbf{k}, \omega)$  is dynamic coefficient of the piezoelectric stress:

$$\chi_{11}^\varepsilon(\mathbf{k}, \omega) = \chi_{11}^{\varepsilon 0} + \frac{\tilde{\mu}^2}{\tilde{\nu}}F_1(\mathbf{k}, i\omega), \quad e_{14}(\mathbf{k}, \omega) = e_{14}^0 - \frac{2\tilde{\psi}_{14}\tilde{\mu}}{\tilde{\nu}}F_1(\mathbf{k}, i\omega). \quad (49)$$

The following notation was used:

$$F_1(\mathbf{k}, i\omega) = \left[ \left( A_k - i\frac{\hbar}{k_B}\omega \cdot I \right)^{-1} b \right]_1, \quad (50)$$

where subscript '1' denotes the first component of the vector derived by multiplication of matrix  $\left( A_k - i\frac{\hbar}{k_B}\omega \cdot I \right)^{-1}$  and vector  $b$ .

Analysis shows that  $F_1(\mathbf{0}, 0) = f_1(T, \sigma_4, E_1)$  at any relaxation times  $T_1$ . Therefore, all dynamic physical characteristics are equal to correspondent static characteristics at  $\omega = 0$ .

The best agreement between theory and experiment for RS is reached at (Levitskii, Andrusyk & Zachek, 2010)

$$T_1 = 1.767 \times 10^{-13} \text{ s} \quad (T_1' = 2.313 \times 10^{-2} \text{ K}). \quad (51)$$

It is easily seen that the function  $F_1(\mathbf{k}, i\omega)$  is a rational function of  $i\omega$ , where numerator is polynomial function of degree not higher than 5 and denominator is polynomial function of degree 6. Therefore, we can decompose function  $F_1(\mathbf{k}, i\omega)$  into partial fractions:

$$F_1(\mathbf{k}, i\omega) = \sum_{i=1}^n \frac{k_i \tau_i}{1 + i\omega \tau_i} + \sum_{j=1}^m \frac{M_j(i\omega) + N_j}{(i\omega)^2 + p_j(i\omega) + q_j}. \quad (52)$$

Here coefficients  $k_i$ ,  $\tau_i$ ,  $M_j$ ,  $N_j$ ,  $p_j$ ,  $q_j$  are real numbers,  $n$  is number of real (equal to  $-1/\tau_i$ ) eigen values and  $2m$  is number of complex eigen values of matrix  $A_k$ . Values  $n$  and  $2m$  are defined by theory parameters and temperature. However, matrix  $A_k$  has 6 eigen values in total. The first sum in Eq. (52) is a contribution of Debye (relaxation) modes into order parameter dynamics, and the second sum is a contribution of resonance modes. In RS case we have  $n = 2$ ,  $m = 2$  at all temperatures.

The results of calculations performed in the center of the Brillouin zone ( $\mathbf{k} = 0$ ) are presented below. Fig. 5 presents frequency dependencies of dielectric permittivity of clamped crystal in dispersion region ( $10^9 \text{ Hz} - 10^{11} \text{ Hz}$ ) calculated theoretically along with experimental data. As figure shows, Mitsui model is able to describe dielectric permittivity in dispersion region.

The correspondence between theory and experimental data for dynamic dielectric permittivity deserves special attention. Methods for experimental measurements of dynamic dielectric permittivity does not allow to assert that namely clamped crystal permittivity was

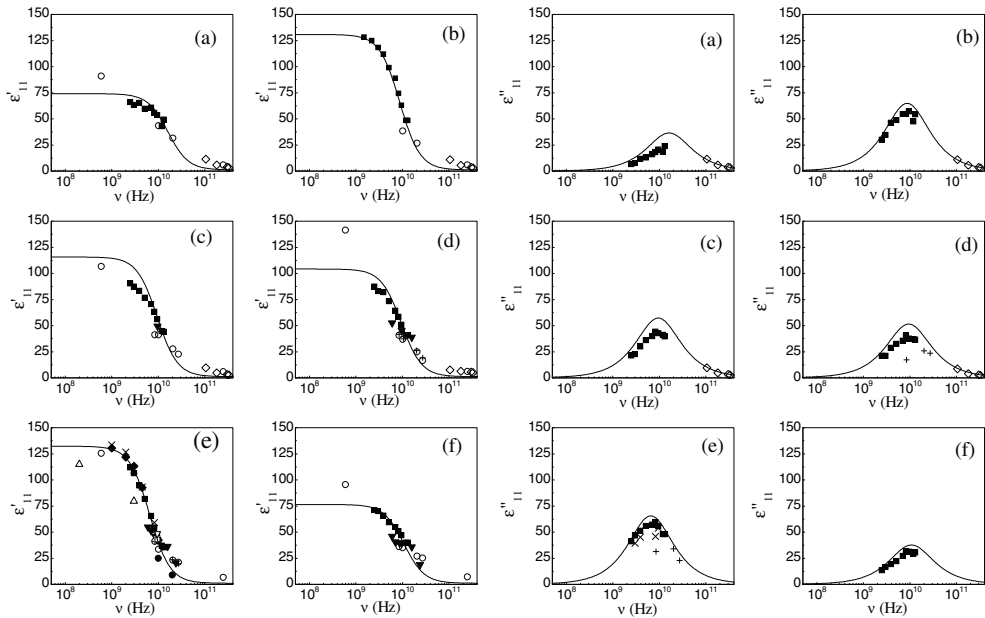


Fig. 5. The frequency dependence of the real and imaginary part of dielectric permittivity, calculated theoretically (lines) at different temperatures  $T$  (K): (a) 235, (b) 245, (c) 265, (d) 285, (e) 305, (f) 315. Points represent experimental data: ■ (Sandy & Jones, 1968), ○ (Poplavko et al., 1974), + (Pereverzeva, 1974), ▼ (Deyda, 1967), ● (Akao & Sasaki, 1955), ◆ (Müser & Potthaest, 1967), × (Kołodziej, 1975), ◇ (Volkov et al., 1980), △ (Sandy & Jones, 1968), ▽ (Jäckle, 1960).

measured. However, in the next subsection it will be demonstrated that frequency clamping of a crystal occurs in microwave region and the experimental data for dielectric permittivity in this region correspond specifically to theoretically calculated dielectric permittivity of a clamped crystal

Analysis testifies that the contribution of one relaxation mode constitutes more than 99% of the total permittivity along the whole temperature range at frequencies  $10^8$  Hz –  $10^{12}$  Hz. This mode is responsible for ferroelectric instability. Thus, dynamics of RS within microwave region is of Debye relaxation type. The same conclusion was derived within the model without transverse field (Levitskii et al., 2003).

Temperature dependencies of relaxation time of the mode responsible for ferroelectric instability obtained here and correspondent experimental data are presented in Fig. 6. As this figure shows the model with the piezoelectric coupling successfully solves the problem encountered by the conventional theories – incorrect temperature dependence of relaxation times near the Curie points. Theoretical temperature curve of  $\tau^{-1}(T)$  obtained here has two finite minima at the transition points, as opposed to vanishing of the inverse relaxation time obtained within the Mitsui model without piezoelectric coupling (Žekš et al., 1971).

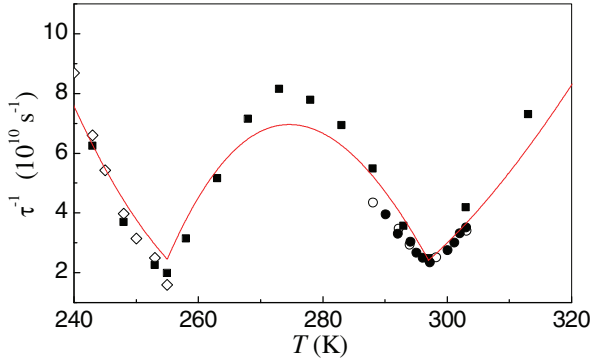


Fig. 6. Dependency of inverse relaxation times on temperature. Solid line presents the result of calculation. Points present experimental data: ● (Müser & Potthast, 1967), ■ (Sandy & Jones, 1968), ○ (Kołodziej, 1975), ◇ (Volkov et al., 1980).

#### 4.2 Dynamics of deformation. Dielectric susceptibility of a free crystal

We shall now give detailed consideration to dynamic dielectric response of a free crystal. Expression for the stress variation is obtained in a similar way to Eq. (48)

$$\delta\sigma_{4k}(\omega) = c_{44}(\mathbf{k}, \omega)\delta\varepsilon_{4k}(\omega) - e_{14}(\mathbf{k}, \omega)\delta E_{1k}(\omega), \quad (53)$$

where

$$c_{44}(\mathbf{k}, \omega) = c_{44}^{E0} - \frac{4\psi_{14}^2}{\delta} F_1(\mathbf{k}, i\omega) \quad (54)$$

and  $e_{14}(\mathbf{k}, \omega)$  is presented in Eq. (49).

Expressing Eq. (53)  $\delta\varepsilon_{4k}(\omega)$  through  $\delta\sigma_{4k}(\omega)$  and taking account of Eq. (48) we can write:

$$\delta P_{1k}(\omega) = d_{14}(\mathbf{k}, \omega)\delta\sigma_{4k}(\omega) + \chi_{11}^\sigma(\mathbf{k}, \omega)\delta E_{1k}(\omega), \quad (55)$$

where

$$d_{14}(\mathbf{k}, \omega) = \frac{e_{14}(\mathbf{k}, \omega)}{c_{44}(\mathbf{k}, \omega)}, \quad \chi_{11}^\sigma(\mathbf{k}, \omega) = \chi_{11}^\varepsilon(\mathbf{k}, \omega) + e_{14}(\mathbf{k}, \omega)d_{14}(\mathbf{k}, \omega). \quad (56)$$

It is well to bear in mind that value  $\chi_{11}^\sigma(\mathbf{k}, \omega)$  is not free crystal permittivity. For the crystal not affected by external mechanical stress the condition  $\delta\sigma_{4q} = 0$  is true for all sites on the crystal surface, while all the internal stresses and strains are determined by Newtonian equations. Thus, to study dynamic dielectric response of a free crystal, in addition to the study of pseudospin system response it is needed to consider the dynamic deformation response of a crystal lattice caused by piezoelectric coupling. We will describe internal stresses and strains dynamics by Newtonian equations of motion for continuum (Authier, 2003, chap. 1.3). This approach is justified by virtue of the fact that, as we will see, in the frequency range under the study ( $10^4$  Hz –  $10^7$  Hz), characteristic length of stress and strain change in the crystal is much larger than unit cell size.

We will have to join Eq. (55) obtained for discrete medium with the equations describing the dynamics of deformations, which are the continuum equations. This could be done by considering that physical characteristics  $A_k(\omega)$  (polarization, stress and electric field) change

little within the unit cell. In our case this condition is satisfied very well. So, we can write:

$$A_k(\omega) = \frac{1}{N} \sum_q a_q \exp(-i \mathbf{k} \mathbf{q}) \simeq \frac{1}{V} \int a(\mathbf{r}) \exp(-i \mathbf{k} \mathbf{r}) d\mathbf{r}. \quad (57)$$

For simplicity we will assume that physical coefficients are not dependent on wavevector:

$$c_{44}(\mathbf{k}, \omega) = c_{44}(\omega), \quad e_{14}(\mathbf{k}, \omega) = e_{14}(\omega), \quad \chi_{11}^{\varepsilon, \sigma}(\mathbf{k}, \omega) = \chi_{11}^{\varepsilon, \sigma}(\omega). \quad (58)$$

Let us consider the equation describing the dynamics of deformations of a thin rectangular plate  $a \times b$  of Rochelle salt crystal cut in the (100) plane ( $X$  cut) (specific numerical calculations will be made for the crystal plate of  $1 \times 1 \text{ cm}^2$ ):

$$\rho \frac{\partial^2 u_i}{\partial t^2} = \sum_j \frac{\partial \sigma_{ij}}{\partial x_j} \quad (59)$$

Here  $\rho = 1.767 \text{ g/cm}^3$  is crystal density (we suppose it is not temperature dependent),  $u_i$  are components of the displacement vector, and  $\sigma_{ij}$  are components of the stress tensor. Similarly to above, we decompose all physical characteristics in Eq. (59) into the sum of equilibrium static part and small deviation. We also assume that oscillating process occurs in  $yz$ -plane. It means that all values are uniformed along  $x$ -axes and  $u_x = 0$ . Then system of equations (59) is reduced to

$$\left. \begin{aligned} -\rho\omega^2 \delta u_y &= \frac{\partial \delta \sigma_{yy}}{\partial y} + \frac{\partial \delta \sigma_{yz}}{\partial z} \\ -\rho\omega^2 \delta u_z &= \frac{\partial \delta \sigma_{yz}}{\partial y} + \frac{\partial \delta \sigma_{zz}}{\partial z} \end{aligned} \right\} \quad (60)$$

where equations are already Fourier transformed into the frequency domain. Strain tensor variations can be expressed in terms of displacements:

$$\delta \varepsilon_{ij} = \frac{1}{2} \left( \frac{\partial \delta u_i}{\partial x_j} + \frac{\partial \delta u_j}{\partial x_i} \right). \quad (61)$$

By differentiating system (60) we can transform it to the form with unknowns  $\delta \varepsilon_\alpha$ :

$$\begin{aligned} -\rho\omega^2 \delta \varepsilon_2 &= \frac{\partial^2 \delta \sigma_2}{\partial y^2} + \frac{\partial^2 \delta \sigma_4}{\partial y \partial z} \\ -\rho\omega^2 \delta \varepsilon_3 &= \frac{\partial^2 \delta \sigma_4}{\partial y \partial z} + \frac{\partial^2 \delta \sigma_3}{\partial z^2} \\ -\rho\omega^2 \delta \varepsilon_4 &= \frac{\partial^2 \delta \sigma_2}{\partial y \partial z} + \frac{\partial^2 \delta \sigma_3}{\partial y \partial z} + \left( \frac{\partial^2}{\partial y^2} + \frac{\partial^2}{\partial z^2} \right) \delta \sigma_4 \end{aligned} \quad (62)$$

where Voigt's one-index notations and correspondence between strains in tensor and Voigt's notations  $\delta \varepsilon_2 = \delta \varepsilon_{yy}$ ,  $\delta \varepsilon_3 = \delta \varepsilon_{zz}$ ,  $\delta \varepsilon_4 = 2\delta \varepsilon_{yz}$  were used.

Considering the form of elastic tensor Eq. (1) and tensor of piezoelectric stress Eq. (2) we can write:

$$\begin{aligned}
 \delta\sigma_2 &= c_{22}\delta\varepsilon_2 + c_{23}\delta\varepsilon_3 + c_{24}\delta\varepsilon_4 - e_{12}\delta E_1 \\
 \delta\sigma_3 &= c_{23}\delta\varepsilon_2 + c_{33}\delta\varepsilon_3 + c_{34}\delta\varepsilon_4 - e_{13}\delta E_1 \\
 \delta\sigma_4 &= c_{24}\delta\varepsilon_2 + c_{34}\delta\varepsilon_3 + c_{44}\delta\varepsilon_4 - e_{14}\delta E_1.
 \end{aligned} \tag{63}$$

All stresses and strains are functions of both frequency and coordinates. Elastic constants depend on frequency and are coordinates-independent (resulting from Eq. (58)).

We are interested in effects occurring at frequencies  $10^4$  Hz –  $10^8$  Hz, that is why for the crystal plate  $1 \times 1$  cm<sup>2</sup> the field  $\delta E_1$  can be considered as homogeneous. Under these conditions, the system Eq. (62) can be rewritten as:

$$\begin{aligned}
 -\rho\omega^2\delta\varepsilon_2 &= c_{22}\frac{\partial^2\delta\varepsilon_2}{\partial y^2} + c_{23}\frac{\partial^2\delta\varepsilon_3}{\partial y^2} + c_{24}\frac{\partial^2\delta\varepsilon_4}{\partial y^2} + c_{24}\frac{\partial^2\delta\varepsilon_2}{\partial y\partial z} + c_{34}\frac{\partial^2\delta\varepsilon_3}{\partial y\partial z} + c_{44}\frac{\partial^2\delta\varepsilon_4}{\partial y\partial z} \\
 -\rho\omega^2\delta\varepsilon_3 &= c_{23}\frac{\partial^2\delta\varepsilon_2}{\partial z^2} + c_{33}\frac{\partial^2\delta\varepsilon_3}{\partial z^2} + c_{34}\frac{\partial^2\delta\varepsilon_4}{\partial z^2} + c_{24}\frac{\partial^2\delta\varepsilon_2}{\partial y\partial z} + c_{34}\frac{\partial^2\delta\varepsilon_3}{\partial y\partial z} + c_{44}\frac{\partial^2\delta\varepsilon_4}{\partial y\partial z} \\
 -\rho\omega^2\delta\varepsilon_4 &= (c_{22} + c_{23})\frac{\partial^2\delta\varepsilon_2}{\partial y\partial z} + (c_{23} + c_{33})\frac{\partial^2\delta\varepsilon_3}{\partial y\partial z} + (c_{24} + c_{34})\frac{\partial^2\delta\varepsilon_4}{\partial y\partial z} + c_{24}\Delta\delta\varepsilon_2 \\
 &\quad + c_{34}\Delta\delta\varepsilon_3 + c_{44}\Delta\delta\varepsilon_4
 \end{aligned} \tag{64}$$

where  $\Delta \equiv \left(\frac{\partial^2}{\partial y^2} + \frac{\partial^2}{\partial z^2}\right)$ .

This system of equations should be supplemented by boundary conditions, which imply that stress is equal to zero on the crystal boundaries:

$$\begin{aligned}
 (c_{22}\delta\varepsilon_2 + c_{23}\delta\varepsilon_3 + c_{24}\delta\varepsilon_4 - e_{12}\delta E_1)|_{\Sigma} &= 0 \\
 (c_{23}\delta\varepsilon_2 + c_{33}\delta\varepsilon_3 + c_{34}\delta\varepsilon_4 - e_{13}\delta E_1)|_{\Sigma} &= 0 \\
 (c_{24}\delta\varepsilon_2 + c_{34}\delta\varepsilon_3 + c_{44}\delta\varepsilon_4 - e_{14}\delta E_1)|_{\Sigma} &= 0,
 \end{aligned} \tag{65}$$

where  $\Sigma$  is a rectangle with sides  $a \times b$  in  $yz$ -plane. This system is a closed equation system and allows one to describe the dynamics of deformation of a Rochelle salt crystal. This system of equations and its boundary conditions are of a simpler form in paraelectric phases:

$$\begin{aligned}
 -\rho\omega^2\delta\varepsilon_2 &= c_{22}\frac{\partial^2\delta\varepsilon_2}{\partial y^2} + c_{23}\frac{\partial^2\delta\varepsilon_3}{\partial y^2} + c_{44}\frac{\partial^2\delta\varepsilon_4}{\partial y\partial z} \\
 -\rho\omega^2\delta\varepsilon_3 &= c_{23}\frac{\partial^2\delta\varepsilon_2}{\partial z^2} + c_{33}\frac{\partial^2\delta\varepsilon_3}{\partial z^2} + c_{44}\frac{\partial^2\delta\varepsilon_4}{\partial y\partial z} \\
 -\rho\omega^2\delta\varepsilon_4 &= (c_{22} + c_{23})\frac{\partial^2\delta\varepsilon_2}{\partial y\partial z} + (c_{23} + c_{33})\frac{\partial^2\delta\varepsilon_3}{\partial y\partial z} + c_{44}\Delta\delta\varepsilon_4,
 \end{aligned} \tag{66}$$

$$\begin{aligned}
(c_{22}\delta\varepsilon_2 + c_{23}\delta\varepsilon_3)|_{\Sigma} &= 0 \\
(c_{23}\delta\varepsilon_2 + c_{33}\delta\varepsilon_3)|_{\Sigma} &= 0 \\
(c_{44}\delta\varepsilon_4 - e_{14}\delta E_1)|_{\Sigma} &= 0.
\end{aligned} \tag{67}$$

One can proceed with further simplifications. Consider that elastic constants  $c_{22}, c_{23}, c_{33}$  are of the same order and are much larger than  $c_{44}$  (see Fig. 1), especially in the vicinity of a critical point. Then  $\delta\varepsilon_2$  and  $\delta\varepsilon_3$  become small compared to  $\delta\varepsilon_4$  and can be treated as zero. Therefore, system Eq. (66) and boundary conditions Eq. (67) reduce to

$$\Delta\delta\varepsilon_4 + \frac{\rho\omega^2}{c_{44}}\delta\varepsilon_4 = 0 \tag{68a}$$

$$\delta\varepsilon_4|_{\Sigma} = \frac{e_{14}}{c_{44}}\delta E_1. \tag{68b}$$

Similarly, equation (68) can be obtained for ferroelectric phase.

It is noteworthy that in paraelectric phase in case of small  $c_{22}, c_{23}, c_{33}$  we would receive equation (68) again. However, in this case strains  $\delta\varepsilon_2$  and  $\delta\varepsilon_3$  are not equal to zero:

$$\delta\varepsilon_2 = \delta\varepsilon_3 = -\frac{c_{44}}{\rho\omega^2} \frac{\partial^2 \delta\varepsilon_4}{\partial y \partial z}.$$

It is more convenient to solve equation 68 by rewriting it in terms of the variation of stress. Taking into account Eq. (53), from which

$$\delta\varepsilon_4(\omega) = \frac{1}{c_{44}(\omega)}\delta\sigma_4(\omega) + \frac{e_{14}(\omega)}{c_{44}(\omega)}\delta E_1(\omega) \tag{69}$$

and taking into account field homogeneity we can write:

$$\Delta\delta\sigma_4 + \frac{\rho\omega^2}{c_{44}}\delta\sigma_4 = -\frac{\rho\omega^2}{c_{44}}e_{14}\delta E_1 \tag{70a}$$

$$\delta\sigma_4|_{\Sigma} = 0. \tag{70b}$$

By introducing a new variable  $u(\omega, y, z)$ , where

$$\delta\sigma_4 = -u(\omega, y, z) \cdot e_{14}(\omega)\delta E_1(\omega) \tag{71}$$

and considering Eq. (55) we obtain the expression for free crystal permittivity in the center of the Brillouin zone:

$$\tilde{\chi}_{11}^{\sigma}(\omega) = \chi_{11}^{\sigma}(\omega) + N(\omega)(\chi_{11}^{\varepsilon}(\omega) - \chi_{11}^{\sigma}(\omega)), \tag{72}$$

where

$$N(\omega) = \frac{1}{ab} \int_0^a \int_0^b dy dz u(\omega, y, z), \tag{73}$$

and  $u(\omega, y, z)$  is a solution for

$$\Delta u + \frac{\rho\omega^2}{c_{44}(\omega)}u = \frac{\rho\omega^2}{c_{44}(\omega)} \quad (74a)$$

$$u|_{\Sigma} = 0. \quad (74b)$$

It is easy to see that in the limit of low and high frequencies one has:

$$\begin{aligned} \omega \rightarrow 0: \quad u(y, z) \rightarrow 0 &\implies N(\omega) \rightarrow 0 \implies \tilde{\chi}_{11}^{\sigma}(\omega) \rightarrow \chi_{11}^{\sigma}(\omega) \\ \omega \rightarrow \infty: \quad u(y, z) \rightarrow 1 &\implies N(\omega) \rightarrow 1 \implies \tilde{\chi}_{11}^{\sigma}(\omega) \rightarrow \chi_{11}^{\varepsilon}(\omega). \end{aligned} \quad (75)$$

From Eq. (74) and Eq. (75) it is clear that  $\chi_{11}^{\sigma}(\omega)$  would be the permittivity of free crystal in case of completely rigid material of crystal ( $c_{44}(\omega) = \infty$ ) or at its zero inertia ( $\rho = 0$ ). Eq. (74) is inhomogeneous Helmholtz equation with zero Dirichlet boundary conditions. It has the following solution:<sup>6</sup>

$$\begin{aligned} u(\omega, y, z) = \sum_{i,j=0}^{\infty} \frac{16}{1 - \frac{c_{44}(\omega)}{\rho\omega^2} \pi^2 \left( \frac{(2i+1)^2}{a^2} + \frac{(2j+1)^2}{b^2} \right)} \cdot \frac{1}{\pi^2(2i+1)(2j+1)} \\ \times \sin \frac{\pi(2i+1)y}{a} \sin \frac{\pi(2j+1)z}{b}. \end{aligned} \quad (78)$$

<sup>6</sup> The solution of Eq. (74) can be obtained in the following way. It can be written as

$$u(y, z) = \sum_{k,n=1}^{\infty} \frac{(v, \psi_{kn})}{\lambda_{kn}} \cdot \psi_{kn}(y, z), \quad (76)$$

where  $v \equiv \frac{\rho\omega^2}{c_{44}(\omega)}$ ,  $(f, g)$  denotes scalar product of functions  $f(y, z)$  and  $g(y, z)$ :

$$(f, g) = \int_{\Sigma} fg \, d\Sigma,$$

$\psi_{kn}(y, z)$  and  $\lambda_{kn}$  are eigenfunctions and eigenvalues of the Helmholtz operator  $\Delta + v$  on a domain  $\Sigma$  (rectangle  $a \times b$ ):

$$\begin{aligned} \psi_{kn}(y, z) &= \frac{2}{\sqrt{ab}} \sin \frac{\pi ky}{a} \sin \frac{\pi nz}{b}, \\ \lambda_{kn} &= -\pi^2 \left( \frac{k^2}{a^2} + \frac{n^2}{b^2} \right) + v, \end{aligned}$$

which is easily checked directly. Let us use the known fact that the system of eigenfunctions of a Hermitian operator (which is the Helmholtz operator) is a complete set of orthogonal functions. Therefore, any analytic function can be decomposed into a series of functions  $\psi_{km}$ . For  $v$  treated as a function the decomposition can be written

$$v = \sum_{k,n} a_{kn} \psi_{kn}, \quad (77)$$

where

$$a_{pq} = (v, \psi_{pq}),$$

which is easy to obtain by calculating the scalar product of left and right parts of Eq. (77) and  $\psi_{pq}$ . Now, by substitution of Eq. (76) into Eq. (74) we see that Eq. (76) is the needed solution.

After performing the integration we get  $N(\omega)$ :

$$N(\omega) = \sum_{i,j=0}^{\infty} \frac{64}{1 - \frac{c_{44}(\omega)}{\rho\omega^2} \pi^2 \left( \frac{(2i+1)^2}{a^2} + \frac{(2j+1)^2}{b^2} \right)} \cdot \frac{1}{[\pi^2(2i+1)(2j+1)]^2}, \quad (79)$$

where at small  $\text{Im}[c_{44}(\omega)]$  resonance frequencies are equal

$$\omega_{i,j} = \sqrt{\frac{c_{44}(\omega)}{\rho}} \pi \sqrt{\frac{(2i+1)^2}{a^2} + \frac{(2j+1)^2}{b^2}}. \quad (80)$$

Previously, for a square lattice the following resonance frequencies were obtained (Moina et al., 2005):

$$\omega_i = \sqrt{\frac{c_{44}(\omega)}{\rho}} \pi \frac{(2i+1)}{a}, \quad (81)$$

while our study has shown that resonance occurs at frequencies

$$\omega_{i,j} = \sqrt{\frac{c_{44}(\omega)}{\rho}} \pi \sqrt{\frac{(2i+1)^2 + (2j+1)^2}{a^2}}. \quad (82)$$

In particular, for the first resonance frequency we obtained a value

$$\omega_{0,0} = \frac{\pi}{a} \sqrt{\frac{2c_{44}(\omega)}{\rho}} \quad (83)$$

while the previous result claims

$$\omega_0 = \frac{\pi}{a} \sqrt{\frac{c_{44}(\omega)}{\rho}}. \quad (84)$$

Besides, one can see that resonance frequencies derived here are more compact compared to the previous result. Unfortunately, we have not found appropriate experimental data that could verify which of the two is correct.

It should be noted that due to the presence of imaginary part in  $c_{44}(\omega)$ , resonance peaks of dielectric permittivity of free crystal do not have singularity. According to Eq. (80) when approaching a phase transition point, the frequency of the first resonance peak tends to zero. Analysis of Eq. (82) shows that in case of square plate resonance frequencies degeneracy  $\omega_{i,j} = \omega_{j,i}$  occurs. And in case of rectangular plate with  $a$  and  $b$ , which are little different from each other, resonance spectrum consists of couples of close resonance frequencies  $\omega_{i,j}$  and  $\omega_{j,i}$ .

Let us show the results of the calculation of dynamic permittivity of free crystal for a thin plate of X-cut Rochelle salt crystal of size  $1 \times 1 \text{ cm}^2$ . Fig. 7 illustrates frequency dependence of dynamic permittivity in the paraelectric phase at  $T = 305 \text{ K}$ .

As it is illustrated in this figure, at  $\omega \rightarrow 0$  we obtain static permittivity of free crystal. Below the first resonance peak, the dielectric permittivity almost coincides with the static permittivity of free crystal. In the range  $10^4 \text{ Hz} - 10^8 \text{ Hz}$  one gets numerous resonance peaks. Above the resonance range, crystal is 'clamped' by the frequency and at  $10^9 \text{ Hz} - 10^{11} \text{ Hz}$  for dynamic permittivity one gets susceptibility of clamped crystal, considered in

previous subsection. Similar behaviour of dynamic permittivity of free crystal is observed in low-temperature paraelectric and ferroelectric phases.

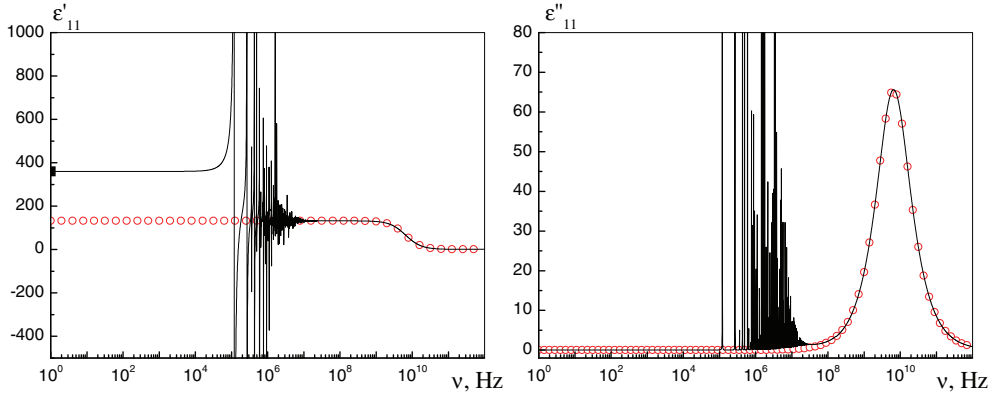


Fig. 7. Dynamic free crystal dielectric permittivity (solid line) at  $T = 305$  K. Points  $\circ$  present clamped crystal dielectric permittivity at  $T = 305$  K. Point  $\blacksquare$  presents static free crystal permittivity.

Figs. 8, 9, 10, 11 present distributions of absolute value, real part and imaginary part of function  $u(y, z)$ . White colour denotes small value, black colour denotes large value. Calculations were performed for square plate  $1 \times 1$  cm<sup>2</sup> at  $T = 305$  K and different frequencies. Internal stress is proportional to the function  $u$  (see Eq. (71)), while according to Eq. (69) strain is

$$\delta\varepsilon_4 = (1 - u(\omega, y, z)) \frac{e_{14}(\omega)}{c_{44}(\omega)} \delta E_1(\omega). \quad (85)$$

As might be expected, at low frequency ( $\nu = 10^5$  Hz, Fig. 8) the amplitude of stress in the center of the plate is maximum and it gradually reduces to zero when approaching the plate edge. When increasing the frequency ( $\nu = 2.5 \times 10^5$  Hz and  $\nu = 5.95 \times 10^5$  Hz) the regions with large and small stress amplitude start alternating (Figs. 9 and 10). However, one can see that characteristic length of stress (strain) altering is much greater than lattice sizes and, hence, approach of continuum medium to considering of the deformation dynamics is justified. Upon further increase of frequency, the stress becomes uniformed throughout the crystal volume, but close to the crystal edge it slightly increases, and then is reduced to zero at the crystal boundary. At frequencies higher than the piezoelectric resonance frequencies the crystal is clamped by frequency and internal stress is defined as  $\delta\sigma_4(\omega) = -e_{14}(\omega)\delta E_1(\omega)$ . Crystal plate of  $1 \times 1$  cm<sup>2</sup> can be considered as clamped at  $T = 305$  K  $\nu = 5 \times 10^7$  Hz according to Fig. 7. Distribution diagram of  $u$  in Fig. 11 visualize phenomenon of crystal clamping.

## 5. Concluding remarks

In this chapter we considered piezoelectric effect in Rochelle salt. We based our study on the Mitsui model which explains the ferroelectric phase transition in Rochelle salt at microscopic level and is able to describe its thermodynamic and dynamic (dielectric relaxation) properties. Results obtained for the physical coefficients were used for study of piezoelectric resonance. It should be noted that the ratio between the elastic constants of Rochelle salt allowed to reduce

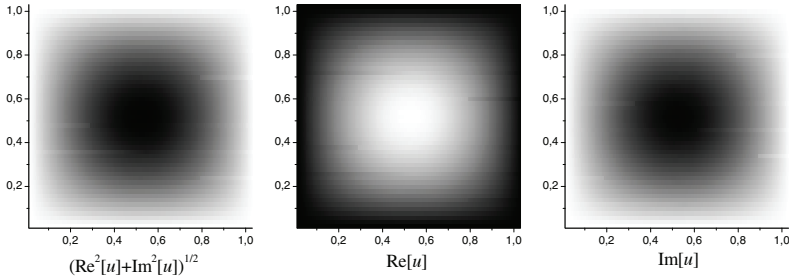


Fig. 8. Distributions of absolute value, real part and imaginary part of  $u(y, z)$  at  $\nu = 10^5$  Hz.

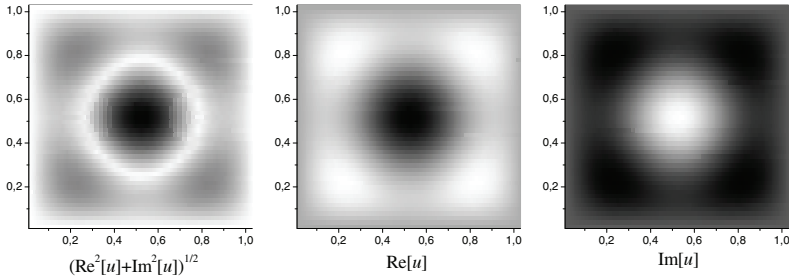


Fig. 9. Distributions of absolute value, real part and imaginary part of  $u(y, z)$  at  $\nu = 2.6 \times 10^5$  Hz.

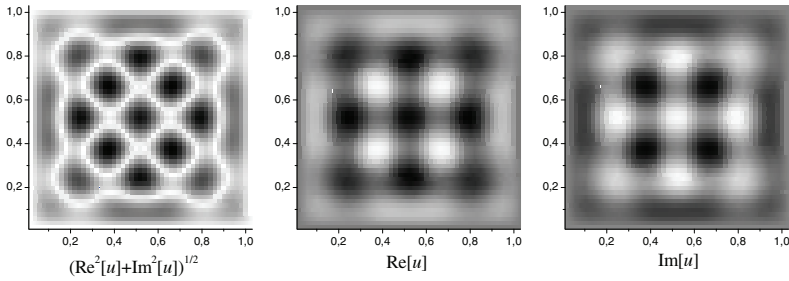


Fig. 10. Distributions of absolute value, real part and imaginary part of  $u(y, z)$  at  $\nu = 5.95 \times 10^5$  Hz.

the original system of equations for the dynamics of deformations to Helmholtz equation with known boundary condition. This simplification allowed to obtain the solution analytically. Analytical solution, in turn, allowed to obtain resonant frequencies and explicitly showed the phenomenon of frequency crystal clamping.

Nevertheless, the proposed approach has some drawbacks. Specifically, the dynamic strain change along  $x$  axis was neglected. We assume that for a thin plate such neglect is justified, but this assumption should be confirmed by numerical calculations. Consideration of strain change along  $x$  axis will make it possible not to be restricted by a thin plate.

Also, some important issues remain unexplored. In particular, the influence of ferroelectric phase transition on piezoelectric resonance remains open. The study of this issue requires to consider the system Eq. (64), which can be performed only numerically.

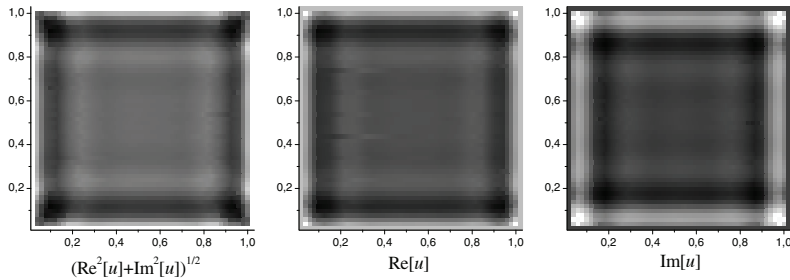


Fig. 11. Distributions of absolute value, real part and imaginary part of  $u(y, z)$  at  $\nu = 5 \times 10^7$  Hz.

The model approach applied in this paper provides certain advantages over the phenomenological approaches. In particular, the Mitsui model allowed us to get  $c_{44}^E(\omega)$  elastic constant, for which no experimental data are available, but which is needed for the study of piezoelectric resonance. The Mitsui model describes physical properties of other ferroelectric compounds, including  $\text{RbHSO}_4$ ,  $\text{NH}_4\text{HSO}_4$  (which are piezoelectric in the ferroelectric phase) and others. The results obtained here can be applied to these and other ferroelectric compounds with piezoelectric effect.

## 6. References

- Akao, H. & Sasaki, T. (1955). Dielectric dispersion of Rochelle salt in the microwave region, *J. Chem. Phys.* 23(12): 2210–2214.
- Authier, A. (ed.) (2003). *Physical Properties of Crystals*, Vol. D of *International Tables for Crystallography*, Kluwer Academic Publishers, Dordrecht.
- Beige, H. & Kühnel, A. (1984). Electromechanical coefficients at ferroelectric phase transitions, Rochelle salt and  $\text{RbHSO}_4$ , *Phys. Status Solidi A* 84: 433–437.
- Bellaiche, L., García, A. & Vanderbilt, D. (2000). Finite-temperature properties of  $\text{Pb}(\text{Zr}_{1-x}\text{Ti}_x)\text{O}_3$  alloys from first principles, *Phys. Rev. Lett.* 84(23): 5427–5430.
- Bronowska, W. J. (1981). Thermal expansion and phase transitions of sodium potassium tartrate tetrahydrate (RS), *J. Appl. Crystallogr.* 14: 203–207.
- Cady, W. (1964). *Piezoelectricity: An introduction to the theory and applications of electromechanical phenomena in crystals*, Dover, New York.
- Deyda, H. (1967). Das temperaturerhalten der dielektrizitätskonstante von seignettesalt im mikrowellengebiet, *Z. Naturforsch* 22a: 1139–1140.
- Fu, H. & Cohen, R. E. (2000). Polarization rotation mechanism for ultrahigh electromechanical response in single-crystal piezoelectrics, *Nature* 403: 281–284.
- Garcia, A. & Vanderbilt, D. (1998). Electromechanical behavior of  $\text{BaTiO}_3$  from first principles, *Appl. Phys. Lett.* 72(23): 2981–2984.
- Görbitz, C. H. & Sagstuen, E. (2008). Potassium sodium (2*r*,3*r*)-tartrate tetrahydrate: the paraelectric phase of Rochelle salt at 105 K, *Acta Cryst. E* 64(4): m507–m508.
- Guo, R., Cross, L. E., Park, S.-E., Noheda, B., Cox, D. E. & Shirane, G. (2000). Origin of the high piezoelectric response in  $\text{PbZr}_{1-x}\text{Ti}_x\text{O}_3$ , *Phys. Rev. Lett.* 84(23): 5423–5425.
- Hlinka, J., Kulda, J., Kamba, S. & Petzelt, J. (2001). Resonant soft mode in Rochelle salt by inelastic neutron scattering, *Phys. Rev. B* 63: 052102–4.

- Jäckle, W. (1960). Dielectric properties of the Rochelle salt, *Z. Angew. Math. Phys.* 12: 148–150.
- Jona, F. & Shirane, G. (1965). *Ferroelectric Crystals*, Dover Publications, New York.
- Kołodziej, H. A. (1975). *Dielectric relaxation in ferroelectrics of order-disorder type*, Vol. 2, The Chemical Society, Burlington House, London, pp. 249–287.
- Levitskii, R. R., Andrusyk, A. & Zachek, I. R. (2010). Dynamics of the rochelle salt  $\text{NaKC}_4\text{H}_4\text{O}_6 \cdot 4\text{H}_2\text{O}$  crystal studied within the Mitsui model extended by piezoelectric interaction and transverse field, *Condens. Matter Phys.* 13(1): 13705.
- Levitskii, R. R., Zachek, I. R. & Andrusyk, A. (2010). The thermodynamics of the Rochelle salt  $\text{NaKC}_4\text{H}_4\text{O}_6 \cdot 4\text{H}_2\text{O}$  crystal studied within the Mitsui model extended by piezoelectric interaction and transverse field, *J. Phys. Stud.* 14(3): 3701.
- Levitskii, R. R., Zachek, I. R. & Moina, A. P. (2005). Monoclinic elastic and piezoelectric properties of Rochelle salt. Description within the modified Mitsui model, *Condens. Matter Phys.* 8(4(44)): 881–890.
- Levitskii, R. R., Zachek, I. R., Vdovych, A. S. & Stasyuk, I. V. (2009). The effect of transverse electric fields on dielectric, piezoelectric, elastic and thermal properties of the Rochelle salt  $\text{Rb}(\text{H}_x\text{D}_{1-x})_2\text{PO}_4$ , *Condens. Matter Phys.* 12(2): 295–317.
- Levitskii, R. R., Zachek, I. R., Verkholyak, T. M. & Moina, A. P. (2003). Dielectric, piezoelectric, and elastic properties of the Rochelle salt  $\text{NaKC}_4\text{H}_4\text{O}_6 \cdot 4\text{H}_2\text{O}$ : A theory, *Phys. Rev. B* 67(17): 174112.
- Mason, W. P. (1939). A dynamic measurement of the elastic, electric and piezoelectric constants of rochelle salt, *Phys. Rev.* 55(8): 775–789.
- Mason, W. P. (1950). *Piezoelectric Crystals and Their Application to Ultrasonics*, Van Nostrand, New York.
- Yu. Serdobolskaya, O. (1996). Elastic properties of the Rochelle salt, the system with double critical point, *Sol. Stat. Phys.* 38(5): 1529–1535.
- Mitsui, T. (1958). Theory of the ferroelectric effect in Rochelle salt, *Phys. Rev.* 111(5): 1529–1567.
- Moina, A. P., Levitskii, R. R. & Zachek, I. R. (2005). Piezoelectric resonance and sound attenuation in the Rochelle salt  $\text{NaKC}_4\text{H}_4\text{O}_6 \cdot 4\text{H}_2\text{O}$ , *Phys. Rev. B* 71(13): 134108.
- Mueller, H. (1935). Properties of Rochelle salt, *Phys. Rev.* 47(2): 175–191.
- Müser, H. E. & Potthaest, J. (1967). Zum dielektrischen Verhalten von Seignettesalz im Bereich der decimeter- und zentimeterwellen, *Phys. Status Solidi* 24(1): 109–113.
- Noda, N., Nozaki, R. & Shiozaki, Y. (2000). Calorimetric measurements of the phase transition in Rochelle salt-ammonium Rochelle salt mixed crystals, *Phys Rev B* 62: 12040–12044.
- Park, S. E. & Shrout, T. R. (1997). Ultrahigh strain and piezoelectric behavior in relaxor based ferroelectric single crystals, *J. Appl. Phys.* 82(4): 1804–1811.
- Pereverzeva, L. P. (1974). *Dynamic properties and dispersion of the dielectric permittivity in the ferroelectrics with hydrogen bonds*, Kaunas, pp. 223–227.
- Poplavko, Y. M., Meriakri, V. V., Pereverzeva, L. P., Alesheckin, V. V. & Molchanov, V. I. (1974). Investigation of the dielectric properties of Rochelle salt at frequency 1–300 GHz, *Sov. Phys. Solid State* 15(8): 1672–1673.
- Saito, Y., Takao, H., Tani, T., Nonoyama, T., Takatori, K., Homma, T., Nagaya, T. & Nakamura, M. (2004). Lead-free piezoceramics, *Nature* 432: 84–87.
- Sandy, F. & Jones, R. V. (1968). Dielectric relaxation of Rochelle salt, *Phys. Rev.* 168(2): 481–493.
- Shiozaki, Y., Nakamura, E. & Mitsui, T. (eds) (2006). *67A-1 NaKC<sub>4</sub>H<sub>4</sub>O<sub>6</sub>·4H<sub>2</sub>O [F]*, Vol. 36C of *Landolt-Börnstein — Group III Condensed Matter Numerical Data and Functional Relationships in Science and Technology*, Springer-Verlag, Berlin.

- Shiozaki, Y., Shimizu, K. & Nozaki, R. (2001). Disordered feature in Rochelle salt, *Ferroelectrics* 261: 239–244.
- Shiozaki, Y., Shimizu, K., Suzuki, E. & Nozaki, R. (1998). Structural change in the paraelectric phase of Rochelle salt, *J. Korean Phys. Soc* 32: S192–S194.
- Shuvalov, L. A. (ed.) (1988). *Modern Crystallography IV: Physical Properties of Crystals*, Springer-Verlag, Berlin.
- Solans, X., Gonzalez-Silgo, C. & Ruiz-Perez, C. (1997). A structural study on the Rochelle salt, *J. Solid State Chem.* 131(2): 350–357.
- Stasyuk, I. V. & Velychko, O. V. (2005). Theory of Rochelle salt: Beyond the Mitsui model, *Ferroelectrics* 316(1): 51–58.
- Taylor, W., Lockwood, D. J. & Labbe, H. J. (1984). Raman spectroscopy and dielectric constants of ferroelectric Rochelle salt and calcium tartrate, *J. Phys. C.: Solid State Phys.* 17: 3685–3699.
- Ubbelohde, A. R. & Woodward, I. (1946). Crystals structural and thermal characteristics. The role of hydrogen bonds in Rochelle salt, *Proc. Roy. Soc.* 185: 448–452.
- Volkov, A. A., Kozlov, G. V. & Lebedev, S. P. (1980). Submillimeter dielectric spectra of Rochelle salt, *Sov. Phys. JETP* 52(4): 722–726.
- Žekš, B., Shukla, G. G. & Blinc, R. (1971). Dynamics of ferroelectric Rochelle salt, *Phys. Rev. B* 3(7): 2306–2309.
- Yurin, A. (1965). *Bull. Acad. Sci. USSR, Phys. Ser. (Engl. Transl.)* 29: 2001.
- Zhang, S., Randall, C. A. & Shrout, T. R. (2003). High Curie temperature piezocrystals in the BiScO<sub>3</sub>-PbTiO<sub>3</sub> perovskite system, *Appl. Phys. Lett.* 83: 3150–3152.

# Piezoelectricity in Lead-Zirconate-Titanate Ceramics – Extrinsic and Intrinsic Contributions

Johannes Frantti and Yukari Fujioka  
*Aalto University School of Science and Technology*  
*Department of Applied Physics*  
*Finland*

## 1. Introduction

Changes in charge density as a response to an external stimuli form basis for numerous applications. Knowing where the atoms are allows numerous deductions to be drawn solely on symmetry arguments. Symmetry essentially dictates what is possible, though typically it does not give absolute values for physical properties. An example is provided by ferroelectrics (Lines & Glass, 1998). Ferroelectrics are a special case of pyroelectric materials, whose properties depend on the spatial scale considered. Single crystals are rather trivial case in which straightforward tensor formulation gives precise description of the physical properties. Obviously, knowledge of single crystal properties is not sufficient, as most materials utilized in applications are polycrystalline. Thus, one must understand how individual crystals are connected and how such a system responds to an external stimulus. This serves as a basis for dividing materials response to an intrinsic and extrinsic contributions. The former is essentially a single crystal response, whereas the latter takes into account the coupling between individual crystals and changes due to the phase transition induced by a stimuli. In practice, the stimuli are stress, heat or electric field. The importance of understanding the intrinsic and extrinsic contributions is not only related to the magnitude but also to the reversibility of the process. Piezoelectric actuators are based on the change in the charge density due to an external stress or change in dimensions by an applied electric field. Very challenging task is to produce a material yielding a reversible response, as the piezoelectric actuators used in atomic force microscopes demonstrate. Activities are ongoing to develop better materials for high precision devices (Hinterstein et al., 2011; Hoffmann & Kungl, 2004). Another topical application is related to the piezoelectric energy harvesting in which a practical way of extracting energy is achievable through the Ericsson energy conversion cycle (Pruvost et al., 2010). Similarly, pyroelectric materials are utilized in infrared radiation detection matrices or pyroelectric energy harvesting components (Olsen & Evans, 1983). In each case it is essential to understand the contribution of grain boundaries, ferroelectric domains within the grains, changes in fractions of different crystal species and the intrinsic contribution within an individual domain. As a further issue one must consider time-dependent phenomena, which reflect the fact that different contributions to polarization

reversal dominate in different time-domains. An example where time-dependent phenomena are crucial is ferroelectric memory (Dawber et al., 2005).

Classical yet actively studied piezoelectric system is lead-zirconate titanate (PZT) (Jaffe et al., 1970). Though nearly all methods one can imagine have been applied to study the structural properties of PZT, the most widely used techniques are spectroscopic, x-ray and neutron powder diffraction, and transmission electron microscopy and electron diffraction (Glazer et al., 2004; Ricote et al., 1998). Since the early study of the lattice dynamics of lead titanate (Burns & Scott, 1970), Raman scattering has been successfully applied to study the lattice dynamics of PZT based ceramics as a function of composition and temperature (Frantti et al., 1999a;b; Souza-Filho et al., 2002), stress (Ohno et al., 2006) or to address the domain configuration in thin films (Nishida et al., 2005). Understanding the domain formation is crucial when thin films are deposited. By a correct choice of single crystal substrate material and crystal cut one can deposit highly oriented thin films, though perfectly epitaxial films may not easily be achieved. Frequently deposition is carried out with *in-situ* substrate heating, which means that different domains are formed to relieve the stress due to the differences in the thermal expansion coefficient of the film and substrate, besides the usual straining or misfit dislocation formation (Kolasinski, 2008; Lüth, 2001). Raman spectroscopy has been notably useful for studying structural properties small particle size powders (Camargo et al., 2009) or fibres (Kozielski et al., 2010) as x-ray diffraction techniques often have limited ability to distinguish crystal symmetries of nanoscale structures. Even dielectric properties of nanosized powders can be accessed via the Lyddane-Sachs-Teller relation (Kano et al, 2007). In contrast to the powder diffraction techniques electron microscopy techniques have the advantage to pinpoint the area under study. The disadvantage (or at least an aspect to be kept in mind) is that sample thinning modifies the domain configuration of the sample, as is discussed below. Constructing a picture of PZT thus relies on data collected on very different type samples and techniques. Both phenomenological and first-principles modelling techniques are required to fulfill the missing data (experimentally not accessible) or to interpret the experimental results.

The present text aims to review symmetry based methods for initial stage structural studies. Combined crystallographical and thermodynamical methods prove to be very useful for understanding possible domain configurations in ferroelectric oxides. In this chapter basic piezo-, pyro-, and ferroelectric concepts are summarized, after which crystallographical aspects of domain formation in ferroelectrics are briefly summarized. The rest of the chapter focuses on the intrinsic and extrinsic contributions in PZT.

## 2. Definitions

### 2.1 Crystal symmetry constraints for piezo-, pyro-, and ferroelectricity

Piezoelectricity is exhibited in all but one (exception is the crystal class 432) noncentrosymmetric crystal class and is described by a third-rank tensor. Piezoelectric phenomena cover two cases, direct and converse effects, which, when matrix notation is used, are summarized by equations (see, e.g., (Newnham, 2005; Nye, 1995))

$$P_i = d_{ij}X_j \text{ direct effect} \quad (1)$$

$$x_i = d_{ij}E_j \text{ converse effect} \quad (2)$$

in which  $P_i$  is the polarization (in units  $\text{Cm}^{-2}$ ),  $X_j$  is the applied stress using the Voigt notation (in units  $\text{Nm}^{-2}$ ),  $x_i$  is the strain,  $E_j$  is the applied electric field (in units  $\text{Vm}^{-1}$ ) and  $d_{ij}$  are the piezoelectric constants (either in units of  $\text{CN}^{-1}$  or  $\text{mV}^{-1}$ ). Thermodynamic consideration shows that the piezoelectric constants for direct and converse effects are the same (see, e.g., (Dove, 2003; Nye, 1995)). Fig. 1 illustrates the direct piezoelectric effect in the case of a tetragonal (space group  $P4mm$ )  $\text{ABO}_3$  perovskite (Dove, 2003). Though crystals point groups symmetry (or crystal class) alone suffices to determine the number of piezoelectric constants, the practical situation is more involved as it is the whole sample, typically ceramic pellet or thin film, which gives the response to an applied stimulus. Further, the piezoelectric constants are not quite constants but do depend on temperature or the applied stimulus, such as applied electric field or stress. These issues are addressed in section 6.

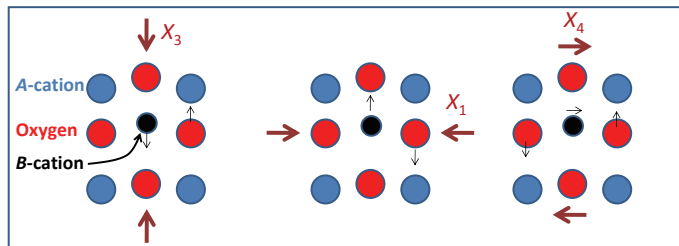


Fig. 1. Understanding the relationship between the crystal structure and property is crucial. Given example is for tetragonal (space group  $P4mm$ ) perovskite single crystal. Classical examples are  $\text{BaTiO}_3$  and  $\text{PbTiO}_3$ . In the absence of external stimuli polarization appears along the  $c$ -axis. Application of stress  $X_1$ ,  $X_3$  and  $X_4$  in turn results in the illustrated changes in polarization. Figure after M. Dove (Dove, 2003).

Figure 2 depicts pyroelectric and ferroelectric phenomena (Lines & Glass, 1998). Pyroelectricity is a phenomenon found in crystals with a permanent electric dipole moment. The magnitude of this moment depends on temperature, which is the basis for experimental observation of the phenomenon. Symmetry consideration dictates that pyroelectricity can only occur in the ten crystal classes (Klapper & Hahn, 2005):  $6mm$ ,  $4mm$ , and their subgroups  $6$ ,  $4$ ,  $3m$ ,  $3$ ,  $mm2$ ,  $2$ ,  $m$ ,  $1$ . All classes are piezoelectric, so the pyroelectric materials are a special case of piezoelectric materials. This also brings an experimental difficulty concerning the practical determination of the possible pyroelectricity of the crystal: within the crystal temperature changes inhomogeneously, which causes strains. Strains in turn add piezoelectric contribution to the measured electric charges. This means that often one can only conclude that the studied crystal lacks a centre of symmetry. Ferroelectric crystals are those pyroelectric materials in which the direction of the permanent electric dipole moment can be changed by an electric field.

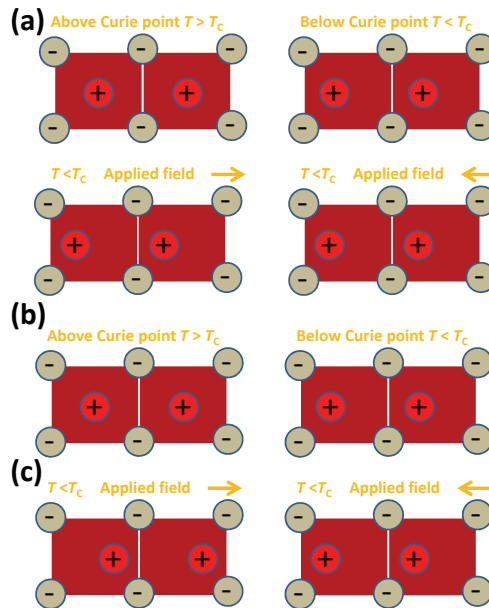


Fig. 2. Schematic illustration of the (a) pyroelectricity and (b) ferroelectricity. Figure after Lines and Glass(Lines & Glass, 1998).

### 3. Twins and ferroelectric domains

Theory of twinning is rich and consequently the terminology used in literature is sometimes ambiguous. In the following brief summary of twinning we adopt the definitions given in refs. (Hahn & Klapper, 2003; Koch, 2004) according to which an intergrowth of two or more macroscopic, congruent or enantiomorphic, individuals of the same crystal species is called a twin, if the orientation relations between the individuals occur frequently and are crystallographic. The individuals are called twin components or (twin) domains.

#### 3.0.0.1 Twin law and twin elements.

Twin domains are brought into parallel orientation with each other by a symmetry operation, the twin operation. Twin operation may occur only once in a macroscopic scale, and cannot be a symmetry operation of either of the twin domains.

Twins can be classified by their origin (for example, growth twins and transformation twins) or from crystallographical viewpoint. For ferroelectric domain formation, transformation twins are central. Crystallographically important transformation twins can be classified as merohedral and pseudo-merohedral twins.

#### 3.1 Transformation twins

Transformation twins are formed when a phase transition between the prototype phase, virtual or real (space group  $G$ ) and a lower symmetry phase (space group  $H$ ) takes place.

By further assuming that the two phases possess a group-subgroup relationship crucial information about twin domain formation can be extracted from the International Tables for Crystallography, Volume A (ITCA) (Hahn, 2005), which tabulates maximal non-isomorphic subgroups  $H$ , Type I: *translationengleiche* ( $t$ ) subgroups in which all translations are retained, Types IIa and IIb: *klassengleiche* ( $k$ ) subgroups, which are obtained by 'decentering' the conventional cell and enlarging the conventional cell, respectively. Thus, not all translations are retained. Three cases can now be distinguished (Hahn & Klapper, 2003): (1)  $H$  is a  $t$  subgroup of  $G$ , (2)  $H$  is a  $k$  subgroup of  $G$ , (3) Cases 1 and 2 occur together ( $H$  is a general subgroup of  $G$ ). Transformation twins provide a close link to the Landau's phase transition theory. The equivalent solutions for the order parameter are represented by different twin domains.

### 3.2 Merohedral twins

Merohedral (non-ferroelastic) twinning corresponds to the case where the twin-element is an element of the crystal system (the crystal class of the lattice) but not an element of the point group of the crystal (crystal class). Characteristic feature of the merohedral twinning is that the lattices of all twin domains coincide exactly. The merohedral twinning corresponds to non-ferroelastic phase transition and ferroelectric domains can be formed, as the example of lithium niobate ( $\text{LiNbO}_3$ ) demonstrates.

#### 3.2.0.2 Example: domains in lithium niobate.

At elevated temperatures (transition is reported to occur between 1323 and 1473 K, depending on the sample stoichiometry)  $\text{LiNbO}_3$  has the high-symmetry phase  $R\bar{3}c$ , which transforms via nearly second order transition to ferroelectric  $R3c$  phase, so that an inversion is lost in the transition. The transition is classified as an order-disorder type with a displacive component (Boysen & Altorfer, 1994; Hsu et al., 1997). No change in crystal system occurs, the twin element being an inversion element. The transition is non-ferroelastic ferroelectric in which  $180^\circ$  domains are formed. Thus, the possible domains are limited by crystallographical considerations, though domain boundaries are characteristically rounded.

### 3.3 Pseudo-merohedral twins

An important special case of pseudo-merohedral twins are twins formed in ferroelastic phase transition. In the following we consider a phase transition from the prototype phase to a ferroelastic and ferroelectric phase possessing a group-subgroup relationship though the transition is not necessarily continuous. However, it is necessary that the crystal system is changed in the transition. From the metrical viewpoint the differences in lattice parameters between the high- and low-symmetry phases are small. The structural symmetries lost in the phase transition are preserved as pseudosymmetries (Hahn & Klapper, 2003; Strukov & Levanyuk, 1998). We further assume that the transition is displacive so that the atoms in the lower symmetry phase are slightly shifted from their high-symmetry positions. This covers technologically important ferroelastic-ferroelectrics, such as Rochelle salt and  $\text{BaTiO}_3$ .

#### 3.3.0.3 Example: domain formation in tetragonal and rhombohedral lead zirconate titanate.

Lead zirconate titanate [ $\text{Pb}(\text{Zr}_x\text{Ti}_{1-x})\text{O}_3$ , PZT] possess a cubic perovskite crystal structure (space group  $Pm\bar{3}m$ ) above the Curie temperature (increasing from about 520 K to 765 K

with increasing Ti content). Titanium rich PZT (up to roughly  $x = 0.50$ ) transforms via first order transition to the tetragonal, space group  $P4mm$ , phase. When  $1 < x < 0.55$  the cubic phase transforms to rhombohedral  $R3m$  phase via (nearly) second-order transition. Following (Hahn & Klapper, 2003) the transitions are theoretically divided into two steps, both involving a transition to a maximal non-isomorphic subgroup. First is a ferroelastic, non-ferroelectric transition:

Ti-rich PZT  $Pm\bar{3}m \rightarrow P4/mmm$  ( $t$  transition)

Zr-rich PZT  $Pm\bar{3}m \rightarrow R\bar{3}m$  ( $t$  transition)

Transition to the  $P4/mmm$  phase corresponds to the loss of threefold rotation axes (the list of elements preserved in the transition are listed in the ITCA), which results in three spontaneously strained (nearly  $90^\circ$ ) twin domains in each which the tetragonal  $c$ -axis points towards one of the three former cubic  $a$ ,  $b$  and  $c$  axes. The lattice distortion is small, so the aforementioned condition for pseudo-merohedral twinning is fulfilled. Transition to the  $R\bar{3}m$  phase means a loss of fourfold axes, fourfold axes with centre of symmetry,  $\{100\}$  mirror planes, leaves inversion centre, one pair of threefold rotation axis, one pair of threefold rotation with centre of symmetry and three twofold rotation axes. This leads to four ferroelastic  $70.5^\circ$  twin domains related by the lost (cubic)  $\{100\}$  mirror planes. All domains ( $P4/mmm$  and  $R\bar{3}m$ ) are centrosymmetric.

The second transition is between the ferroelastic and ferroelectric phases and involves ionic displacements resulting in the loss of inversion:

Zr-rich PZT  $P4/mmm \rightarrow P4mm$  ( $t$  transition)

Ti-rich PZT  $R\bar{3}m \rightarrow R3m$  ( $t$  transition)

Each twin domain splits into two antiparallel polar ferroelectric  $180^\circ$  domains.

#### 3.3.0.4 Two-phase systems.

Numerous studies have been conducted to understand the behaviour of morphotropic phase boundary (MPB) lead zirconate titanate. After a monoclinic  $Cm$  phase was reported to exist in PZT within the MPB region (Noheda et al., 1999; 2000) many studies were dedicated to understand the electromechanical properties through the crystallographical properties of the single  $Cm$  phase. However, it turned out that the  $Cm$  phase co-exists with the rhombohedral  $R3c$  phase (Frantti et al., 2002; Yokota, 2009). There are many reports which use the  $Cc$  symmetry, instead of the  $R3c$  symmetry. It has been very difficult to prepare single crystal PZT and most of the studies focused on either ceramic pellet or on powder samples. The symmetry choice has been very controversial topic (see, e.g., review (Frantti, 2008b) and references therein) and it was not until very recently that a detailed neutron diffraction study on PZT single crystals could solve the issue by providing data which ruled out the  $Cc$  symmetry (Phelan et al., 2010). The study found that the  $R3m/R3c$  and  $Cm$  domains coexist. This is important finding as it provides an explanation to the exceptionally good piezoelectric properties of PZT ceramics, which is discussed in section 7.2. As the results given in ref. (Yokota, 2009) reveal, the two-phase co-existence is extended towards large Zr-contents so that there is no clear phase boundary. In the first-order phase transition both phases co-exists, though it is not obvious why the  $Cm$  phase (slightly distorted version of the tetragonal  $P4mm$  phase) is found in large composition range, extending from  $x = 0.52$  up to 0.92 (Frantti et al., 2002; Noheda et al., 1999; 2000; Yokota, 2009). The reason for the distortion is not clear, though it seems important to consider the contact relationships between the two phases (intergrowth of the rhombohedral and monoclinic crystals).

## 4. Mechanical and electrical compatibility conditions

In practice, ferroelectrics show small number of domain boundary types, which can be understood by considering mechanical and electrical compatibility conditions. In the case of mechanical boundary condition a simple method is to consider the strain on the crystals separated by the twin domain boundary (given, e.g., in ref. (Hahn & Klapper, 2003)) and to look for stress-free contact planes. Mechanical compatibility condition means that the boundaries minimizing the strain energy are favored.

Figure 3 shows charged and non-charged  $180^\circ$  merohedral and  $90^\circ$  zigzag domain boundary possessing large domain wall energy (Hahn & Klapper, 2003), and a method to introduce  $180^\circ$  tail-to-tail (TT) and head-to-head (HH) domains by providing charge compensation through acceptor and donor layers (Wu & Vanderbilt, 2006). In ferroelectrics one must also consider the contribution of electrical charges at the boundaries. Basically charge neutral boundaries are energetically favored, expressed by the condition  $P_n(2) - P_n(1) = \rho = 0$ , where  $P_n(1)$  and  $P_n(2)$  are the components of the spontaneous polarization normal to the boundary of the two domains and  $\rho$  is the charge density. The situation can be different in conducting (either in prototype phase or ferroelectric phase) samples due to the ferroelectric polarization compensated by free charge carriers. In practice in insulating materials HH and TT domains are ruled out as the electrostatic energy makes them unfavorable. Thus, the merohedral twins are characteristically  $180^\circ$  domains with interfaces parallel to the polarization axes. It was proposed, based on the first-principles calculations, that HH and TT domains could be stabilized by inserting donor and acceptor layers to compensate the charge otherwise formed in the domain wall (Wu & Vanderbilt, 2006). As a case study  $\text{PbTiO}_3$  based ferroelectric 8-cell superlattice with  $\text{Sc}^{3+}\text{O}_2$  (acceptor layer) and  $\text{Nb}^{5+}\text{O}_2$  (donor layer) was studied, with the prediction that such a structure would be stable with a ground state symmetry  $Pmm2$ . Analysis of local polarization revealed that the superlattice is antiferroelectric in the  $[001]$  direction, and ferroelectric in the  $[100]$  direction.

### 4.1 Why to worry about domains

#### 4.1.1 Ferroelectric hysteresis

Measuring the polarization as a function of electric field, *i.e.*, hysteresis loop, measures the energy required to twice reverse the polarization direction. In ceramics a large fraction of the energy necessary for polarization reversal is consumed to domain wall motion. Depending on the applications one deliberately modifies the composition so that the coercive field is either large (hard ferroelectric) or small (soft ferroelectric) material. In PZT this is achieved by controlling the domain wall motion by doping with higher- or lower-valent ions (Jaffe et al., 1970). Controlling the amount and position in the ceramics is thus crucial: it makes a difference if the dopants are segregated in the grain boundaries or if they are homogeneously distributed. Useful models and practical examples of spatial distribution of dopant atoms in polycrystalline materials are provided in ref. (Phillips, 2001). Fig. 4 shows a hysteresis loop, plotting polarization versus applied field  $E$ , characteristic to a soft ferroelectric material as seen from the low value of the coercive field  $E_C$ . In the case of hard ferroelectric material the coercive field is larger and the shape of the loop is more rectangular. Characteristically hysteresis is measured at quasi-static conditions, which implies that the  $E_C$  value is determined by the polarization reversal mechanisms dominant in the static limit. The mechanism *do* depend on the timescale in concern and also on the sample geometry.

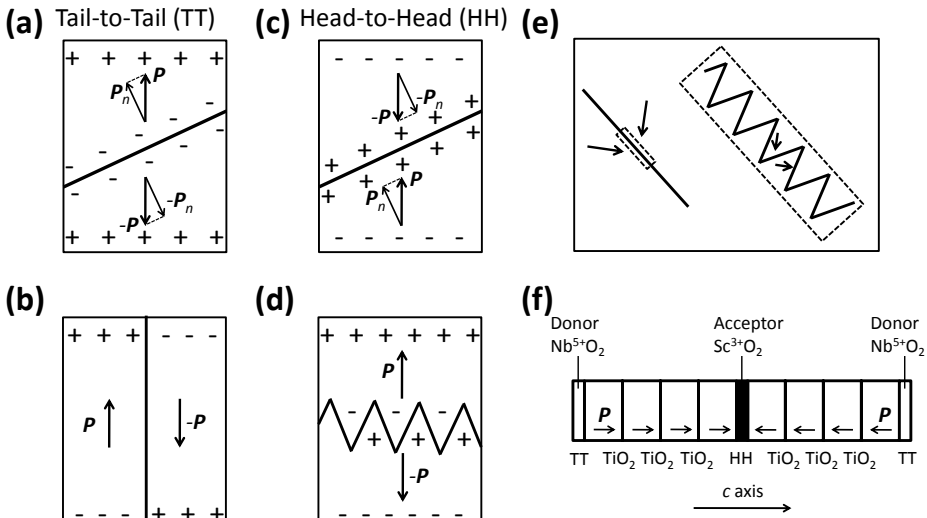


Fig. 3. (a) Tail-to-tail, (b) uncharged, (c) head-to-head and (d) charged zigzag  $180^\circ$  merohedral domain boundaries. The boundary (b) is also common among pseudo-merohedral domain boundaries. Figures (a) to (d) after ref. (Hahn & Klapper, 2003). Panel (e) shows the  $90^\circ$  pseudo-merohedral domain boundary which at first glance appears as a head-to-head domain boundary, but in a detailed study turned out to be a zigzag boundary where all boundaries are head-to-tail, shown in the right-hand corner. Figure after ref. (Lines & Glass, 1998; Yakunin et al, 1972). Panel (f) shows a ferroelectric superlattices used in a first-principles computational study in which head-to-head and tail-to-tail domain boundaries are stabilized by placing donor and acceptor layers to serve as charge compensation layers (Wu & Vanderbilt, 2006).

The first aspect is discussed in section 4.1.3 by reviewing very recent studies, whereas the latter obviously involves depolarization field and phenomena related to the substrate and thin-film interactions. Technologically important case is a thin film capacitor, in which case the depolarization field significantly affects the  $E_C$  value. A finite-element study of the topic is given in ref. (Pane et al., 2008).

#### 4.1.1.1 Irreversibility of domain switching in PZT.

The equations describing the piezoelectric responses (section 2) are linear, which is usually a valid approximation. There are, however, cases in which the linearity assumption ceases to be accurate. The most obvious is the vicinity of the phase transition which may result in large changes in piezoelectric constants (Frantti et al., 2007), which is an intrinsic contribution. This means that when a phase is about to change to another phase or orientation state (domain switching) external stimulus (temperature, stress, electric field) can cause large changes in the materials response (strain or induced charge). Many applications, such as actuators required to operate in a precise and repeatable manner, require that the change is reversible, which is not obvious. One may recall that many piezoelectric solid-solutions, PZT being a textbook example, have a composition adjusted so that two competing phases, tetragonal

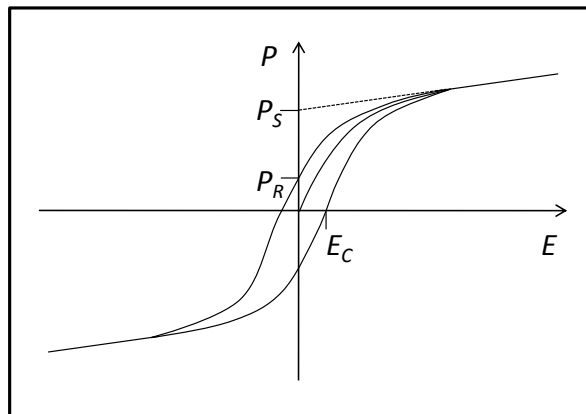


Fig. 4. Schematic illustration of the hysteresis loop with characteristic values indicated: coercive field  $E_C$ , remanent polarization  $P_R$  and  $P_S$ , taken as the saturation value of the polarization extrapolated to zero field.

(or the  $Cm$  phase, which can be considered as pseudotetragonal for most of the purposes) and rhombohedral, are energetically almost as favorable. By symmetry, the transition from tetragonal to rhombohedral phase must be of first order, which implies that there is a hysteresis related to the transition. This hysteresis means that the response of the system depends on the history, so that the response to heating and cooling are frequently different. Also extrinsic contribution results in non-linearities.

The quasi-static (a cyclic driving electric field was applied during the diffraction experiment using unipolar and bipolar square waves at 1 Hz and amplitudes equal to or below the coercive field) time-dependent studies carried out by stroboscopic neutron and x-ray powder diffraction data collection technique on pure and La- or Fe-doped PZT samples with composition in the vicinity of the morphotropic phase boundary, show that already below coercive field non-linear terms become significant, which was related to the non- $180^\circ$  domain switching (Jones et al., 2006; Pramanick et al., 2009a;b).

#### 4.1.2 Kittel's law and domains in thin films

An example where the size, shape and sample preparation method affect ferroelectric domain formation are thin films (either free-standing or deposited on a substrate) or samples prepared for transmission electron microscopy (TEM) studies. An insulating ferroelectric materials splits into several domains to minimize the energy of the crystal geometry dependent depolarization electric fields due to the uncompensated dipoles on the surface (assuming that there are no free charges available or at least that the domain formation occurs before the compensation takes place). In the simplest model the splitting of materials into domains oriented so that their net polarization is zero is limited by the cost due to domain wall creation. Thus, in the simplest terms one has, in addition to the usual polynomial order parameter expansion two other contributions to the ferroelectric free energy: depolarization field and domain wall energy. An illustrative example is provided by the model for  $180^\circ$  domains in which case one can derive so called Kittel's law according to which the width of the domains

is proportional to the square root of the thickness. In his original work Kittel considered ferromagnetic materials (Kittel, 1946). Analogous treatment was applied to ferroelectric materials by Mitsui and Furuichi (Mitsui & Furuichi, 1953) and to ferroelastic materials by Roytburd (Roytburd, 1976) and were summarized in ref. (Schilling et al., 2006). Following ref. (Lines & Glass, 1998) the essential result is summarized by the equation  $d = \left(\frac{\sigma t}{\epsilon^* P_0^2}\right)^{1/2}$ , where  $d$  is the domain width,  $t$  the domain thickness,  $P_0$  is the polarization at the center of a domain,  $\sigma$  is the domain wall energy per unit area and  $\epsilon^*$  is a constant depending on the dielectric constants of the ferroelectric. Other expressions for the Kittel's law consider the influence of substrate, which can be significant and change the proportionality constant, are discussed in ref. (Streiffner et al., 2002). The proportionality  $d \propto t^{1/2}$ , however, remains. Similar relationship between domain width and thickness, but with different proportionality constants, is found for 90° domains in epitaxial ferroelectric and ferroelastic films (Pertsev & Zembilgotov, 1995). A TEM study conducted on free-standing lamellae showed that when the thickness gradient is *perpendicular* to the domain walls the domain width continuously decreases with decreasing thickness, following the Kittel's law (Schilling et al., 2006). The study found two other mechanisms occurring in thin lamellae: bifurcation in domains *parallel* to the thickness gradient and discrete period changes at the interface between clusters of stripes perpendicular to each other. As the domain wall motion and nucleation of new domains are important for polarization reversal, the thickness and geometry dependent factors are central for designing thin film components, such as ferroelectric memory cells. For fundamental research it is evidently crucial to understand the domain formation in bulk materials (say, used in many neutron powder diffraction studies) and in thin films prepared for TEM studies in order to avoid wrong conclusions.

#### 4.1.3 Time-dependent studies of polarization reversal in PZT

Polarization reversal may involve the growth of existing domains, domain-wall motion or the nucleation and growth (either along the polar direction or by sideways motion of 180°) of new antiparallel domains (Dawber et al., 2005; Lines & Glass, 1998). The mechanism dominating depends on the material, applied field and electrode type, sample geometry and *time domain*. In ferroelectrics polarization reversal is typically modelled to be inhomogeneous, where nuclei of domains with polarization parallel to the applied field initially form at the electrodes, grow forward direction (typically considered to be fast process, addressed below) and then grow by sideways motion (slow in perovskite oxides) (Dawber et al., 2005).

In low-frequency experiments the breakdown field is at around 100 and 200 MV/m. Breakdown, however, is not an instantaneous phenomenon, and thus for a short times one can apply much larger fields than breakdown field. Recently, experimental studies of short-time structural changes in ferroelectric thin films became accessible through x-ray synchrotron instruments. Time-dependent phenomena, notably the nonlinear effects in the coupling of polarization with elastic strain and the initial stage of polarization switching were addressed in refs. (Grigoriev et al., 2008; 2009). In these studies capacitors containing 35 nm thick epitaxial  $\text{Pb}(\text{Zr}_{0.20}\text{Ti}_{0.80})\text{O}_3$  ferroelectric thin films were studied by time-resolved x-ray microdiffraction technique in which high-electric field (up to several hundred MV/m) pulses were synchronized to the synchrotron x-ray pulses. Demonstration of the capability of the technique is an experiment where 8 ns long electrical pulses of 24.4 V were applied to the PZT capacitor, yielding 2.7 % strain, record among piezoelectric strains (year 2008)

(Grigoriev et al., 2008). The same study revealed that the piezoelectric  $d_{33}$  coefficient only slightly increases when the applied field increases to 160 MV/m, whereas more strong increase occurs above 180 MV/m so that the  $d_{33}$  coefficient has the low-field value at 395 MV/m. The increased  $d_{33}$  coefficient value between 180 and 395 MV/m was assigned to the Ti-O bond elongation (Grigoriev et al., 2008). Another technologically relevant finding was related to the initial stage of polarization switching: a series of 50 ns duration pulses did not switch the polarization if the field was below 150 MV/m, even when the total pulse duration was several milliseconds (Grigoriev et al., 2009). It is also worth to note that 150 MV/m was estimated to be three times the *low-frequency*  $E_C$  and in low-frequency hysteresis measurements 1 ms above the  $E_C$  is sufficient for polarization reversal. To address the stability of unswitched polarization states three possible explanations were considered: (i) slow initial domain propagation, limited by the time required for the establishment of charge distribution necessary for the movement of curved (charged) domain walls (Landauer, 1957), (ii) disappearance of small domains between pulses and (iii) nucleation times are longer than 50 ns applied in the study (Grigoriev et al., 2009). The first and third explanation were found plausible, whereas the second explanation was ruled out as it was estimated that 50 ns is sufficient for a nucleated domain to reach stable size (which can be estimated through thermodynamical considerations, see ref. (Strukov & Levanyuk, 1998)).

## 5. Intrinsic and extrinsic contributions

Terms intrinsic and extrinsic contribution are commonly used in literature. Though both contributions frequently occur simultaneously, it is helpful to trace the origin of the piezoelectric response down to atomic scale. Piezoelectric materials response involves changes in the primitive cell level and also in the larger scale, in which case the motion of domain boundaries and grain boundaries must be taken into account. Fig. 5 illustrates a polycrystalline material consisted of grains, which in turn contain domains. The applied stimulus is transmitted via grains, and results in changes in grain boundaries and domain wall motion. Both are examples of an extrinsic contribution. The stimulus also causes changes within a primitive cell, an example is the shift of an oxygen octahedra with respect to A-cations in perovskites, Fig. 1. The structure of the sample structure significantly influences its response to an external stimulus, examples being poled polycrystalline ceramics and non-twinned single crystals. Correct treatment of piezoelectric response requires the determination of the texture present in the sample as it is the whole system, consisted of variously oriented domains (or crystallographical twins), which responds to an external stimulus. After the texture, or preferred orientation, is known appropriate angular averages of piezoelectric constant can be determined. For instance, electrically poled ceramics belong to symmetry group  $\infty m$  (Newnham, 2005). Texture, and individual piezoelectric constants, change as sufficiently large stimuli are applied. This section summarizes the changes occurring in the atomic scale in piezoelectric materials by dividing the response to changes occurring in the individual primitive cells and changes occurring in the domain distribution.

## 6. Intrinsic contribution

By intrinsic term one refers to the changes in electric polarization within a domain as a response to an external stimulus. This implies that no domain wall motion or changes in

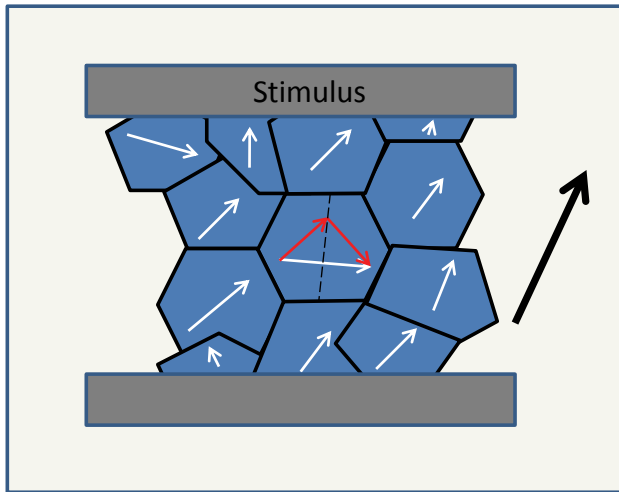


Fig. 5. Schematic illustration of different contributions resulting in the net polarization (black arrow). When stress is applied to a polycrystalline material, the effect is transmitted via grains (polygons). Each grain in turn is divided into domains, exemplified by a  $90^\circ$  domain wall (dashed line). Red arrows indicate the polarization directions within the domains, and the white arrow is the resultant polarization.

phase fraction is taken into account. An example is given in Fig. 1 in which the piezoelectric response of a  $ABO_3$  perovskite is shown for different applied stress. As a special case of an intrinsic response is the  $180^\circ$  domain reversal. It is also worth noting that applied stimuli frequently breaks the equilibrium symmetry, though the symmetry changes may not always be experimentally resolved. Computationally the piezoelectric and elastic constants can be determined by first-principles techniques, which is a very useful method for estimating the pure intrinsic contribution. Notable care should be paid on the phase stability, as computation of the crystal properties of unstable phases results in meaningless results. In the context of pressure induced transitions in  $PbTiO_3$  the phase stability issues were addressed in refs. (Frantti et al., 2007; 2008a). Recent inelastic neutron scattering study suggests that a phase instability induced by a polar nanoregion-phonon interaction contributes to the ultrahigh piezoelectric response of  $Pb(Zn_{1/3}Nb_{2/3})O_3$ -4.5% $PbTiO_3$  and related relaxor ferroelectric materials (Xu et al., 2008). Presently an *ab-initio* computational modelling of a PZT solid-solution is a formidable task as it would require enormous supercells. One way to bypass this problems is to mimic the 'chemical pressure' (partial substitution of Ti by Zr) by hydrostatic pressure. Density-functional theory (DFT) computations predict that at 0 K (ground state) a phase transition between tetragonal  $P4mm$  and rhombohedral  $R3c$  phase take place at 9.5 GPa pressure (Frantti et al., 2007), which suggests that some insight about the PZT system can be drawn. Significant increase of certain piezoelectric constants, notably the  $d_{15}$ , was observed once the phase transition was approached. Thus, the vicinity of the phase transition causes that also intrinsic contribution is significantly increased. Experimental and computational studies suggest that the curvature of the phase boundary is determined by two factors, the entropy term favouring the tetragonal phase, and the oxygen octahedral tilting

giving an advantage for the rhombohedral  $R3c$  phase (Frantti et al., 2009). Octahedral tilting, characteristic to the  $R3c$  phase, allows efficient volume compression (Thomas & Beitollahi, 1994).

In thin films biaxial stress can be used to tune the piezoelectric properties by deliberately straining the material, in which case strain engineering is a term used for a thin film technology method applied to improve the piezoelectric properties (Janolin, 2009). The phase diagram in thin films is often quite different from the one found for bulk ceramics, which in turn may result in significant differences in electromechanical response (Janolin, 2009; Liu et al., 2010). The interplay between film thickness and different stress has a large impact on stress relaxation mechanism (Janolin, 2009; Liu et al., 2010).

### 6.1 Notes on polarization rotation model

There have been attempts to explain the piezoelectric response of many perovskite solid solution systems in the vicinity of the morphotropic phase boundary through (more or less) continuous polarization rotation. Characteristically, the morphotropic phase boundary separates tetragonal and rhombohedral phases. The common feature of these models is that focus is put on the intrinsic part of the piezoelectric response, specifically on the rotation of polarization vector between the tetragonal polarization direction,  $\langle 001 \rangle$ , and rhombohedral polarization direction,  $\langle 111 \rangle$ , and the extrinsic contributions are simply discarded. This type of transition route was essentially based on the computational study on monodomain  $\text{BaTiO}_3$  according to which it takes less energy to rotate the polarization along the 110 plane than through path which is consisted of segments parallel to the unit cell edges (Fu & Cohen, 2000), which was commonly believed to explain the high electromechanical response observed in many perovskite oxide solid-solutions. However, the transition between the tetragonal and rhombohedral phases is necessarily of first order, implying hysteretic transition in which the phase proportions between the two phases varies as a function of composition.

The small but unambiguous monoclinic distortion (space group  $Cm$ , monoclinic  $c$ -axis is deviated by a less than half degree from the tetragonal  $c$ -axis, in contrast to the  $55^\circ$  required to have a continuous rotation) observed in lead-zirconate-titanate ceramics within the MPB (Frantti et al., 2000; Noheda et al., 1999) and Zr-rich area (Yokota, 2009) suggests that one should consider the role of the  $Cm$  phase for the electromechanical properties. Though some reports in rather straightforward manner linked the exceptional electromechanical properties of lead-based piezoelectrics, such as PZT, to be due to the monoclinic distortion(s) serving as a bridging phase(s) between the rhombohedral and tetragonal phases (see also discussion ref. (Frantti et al., 2008a)), the following points should be noted:

- even though the polarization direction of the  $Cm$  phase can point in any direction in the mirror plane (as far as crystal symmetry is considered), experiments reveal that the monoclinic  $\beta$  angle remains roughly constant through the whole composition area, being about  $90.5^\circ$ : if there would be a continuous rotation from tetragonal to rhombohedral direction, it would be easily seen by standard diffraction techniques. However, no evidence for that is reported.
- the treatment given in ref. (Sergienko et al., 2002) shows that the phase transition between monoclinic and tetragonal phases can be of second order, the transition between rhombohedral and monoclinic phases must be of first order. This is consistent with the

observed two-phase co-existence of  $R3c$  and  $Cm$  phases (Frantti et al., 2002; Yokota, 2009): *i.e.*, the  $Cm$  phase is not observed alone.

Our interpretation is that the monoclinic phase is not stable alone, but is probably due to the interaction between rhombohedral and tetragonal phases. In this spirit, it is worth to experimentally look the crystal boundary between rhombohedral and monoclinic phase. Certain external stimuli (e.g.,  $X_1$  and  $X_4$ ) break the tetragonal symmetry, the magnitude of which can be estimated from the elastic constants. Thus, even internal stresses are able to lower the symmetry and the significance of the monoclinic distortion might be a stress relief, as was suggested in ref. (Topolov & Turik, 2001)

We note that there are computational and experimental reports on  $PbTiO_3$  according to which hydrostatic pressure would induce monoclinic phase(s) intermediating the  $P4mm$  and  $R3m$  phases. However, it turned out that the computational study was carried out for an unstable phase (as could be revealed by enthalpy values and phonon instabilities) and the experimental data was interpreted in terms of a wrong structural model (the model Bragg reflection positions and peak intensities did not match with the experimental data). For more details, see refs. (Frantti et al., 2007) and (Frantti et al., 2008a). It is the opinion of the authors that after the intrinsic and extrinsic contributions are properly taken into account, an accurate and sufficient description for piezoelectricity is achieved.

## 7. Extrinsic contribution

Modeling extrinsic contribution is challenging, as it requires a description for domain boundary motion, which itself is rather complex process, and also a model for changes in phase fractions. Below a crystal boundary motion in an intergrowth and domain switching are discussed.

### 7.1 Changes in phase fractions

Studies of materials operating in the vicinity of the first-order phase transition require notable care as even small quantities of energy (e.g., in the form of heat or due to an applied field) can cause significant changes in the phase fractions. This is evidenced in PZT powders with composition at the MPB region by phase fraction changes in (pseudo-)tetragonal and rhombohedral phases as a function of temperature (Frantti et al., 2003). The two-phase co-existence is found in the Zr-rich side of MPB (Yokota, 2009), consistently with ref. (Sergienko et al., 2002) according to which the phase transition between monoclinic and rhombohedral phase is of first-order. The mechanism behind transformation is not yet clear, but it is probable that there are regions in which rhombohedral and monoclinic crystals are grown together. The phase transformation mechanism is crucial for the understanding of the piezoelectric response of PZT. Detailed studies to understand the atomic scale structure of the contact plane separating the two phases within the intergrowth and the movement of the plane under external stimuli are yet missing.

Fig. 6 shows an intergrowth of rhombohedral and monoclinic crystals. Though the reality is more complex, this type of intergrowth, and the contact plane motion, are suggested to have a crucial role for electromechanical response. Analogously to the domain boundary motion, phase transition (and changes in phase fractions) result in once the boundary moves. Needless to say, Fig. 6 does not imply continuous rotation, in contrast experiments indicate

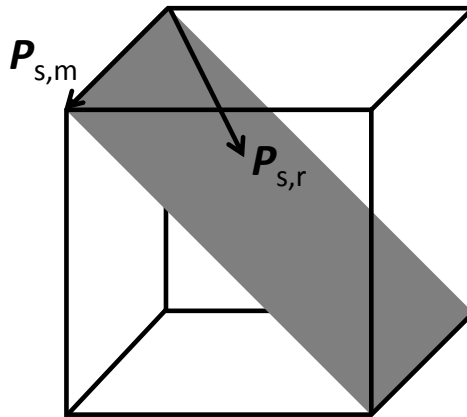


Fig. 6. Schematic illustration of an intergrowth of rhombohedral crystal (below the gray plane) and monoclinic crystal (above the gray plane). The directions of the spontaneous polarization in the monoclinic and rhombohedral phases are labelled as  $P_{s,m}$  and  $P_{s,r}$ . Motion of the gray plane by external stimuli corresponds to a change in the phase fractions and would lead to large electromechanical response. No continuous polarization is involved.

discontinuous change. The electric and mechanical boundary conditions should serve as reasonable limiting factors when possible intergrowths are considered. Experimental studies are challenged by the fact that sample thinning influences the samples domain and grain boundary structure, implying that it is not straightforward to compare the results obtained from transmission electron microscopy technique and neutron powder diffraction studies (see section 4.1.2).

## 7.2 Domain switching

Figure 7 shows schematically the importance of a domain boundary. The lattice points of both domains are common at the boundary (implying no strain, so that the mechanical boundary condition is fulfilled), and since the polarization component perpendicular to the boundary does not change, also electrical compatibility requirement is fulfilled. However, the atom positions corresponding to the different domains at the boundary do not overlap: the atoms at the boundary region are disordered. One expects that also the polarization changes gradually in the domain wall, as is discussed in section 7.2.0.1. By applying external stimulus (e.g., stress) one domain state is preferred. In the simplest (perhaps excessively simple) picture the domain boundary sweeps through the energetically unfavorable domain. Now, there is an energy barrier for moving the atoms in the boundary zone. Obviously, if the difference between the atomic positions (shown in the upper part in Fig. 7(a)) is not large, switching is easy. Fig. 7(b) shows one way to diminish the stress in domain boundary by introducing a centrosymmetric cubic layer. The strain changes once one moves from the interior of the domain through the domain boundary, implying elastic energy which one must overcome in order to move the domain boundary

A study about the domain switching showed that the  $90^\circ$  domains in single phase tetragonal phase (titanium rich PZT) hardly switch, whereas the domains in the two-phase region switch (Li et al., 2005). Texture and strain analysis of the ferroelastic behavior of  $\text{Pb}(\text{Zr}_{0.49}\text{Ti}_{0.51})\text{O}_3$  by in situ neutron diffraction technique showed that the rhombohedral phase plays a significant role in the macroscopic electromechanical behavior of this material (Rogan et al., 2003). Figure

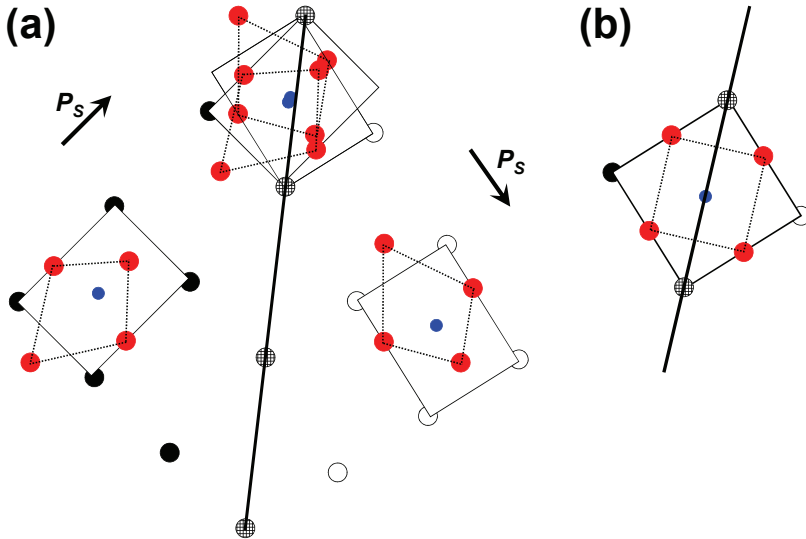


Fig. 7. (a) Schematic illustration of the (nearly)  $90^\circ$  domains in tetragonal  $\text{ABO}_3$  perovskite. Continuous bold line shows the domain boundary. Black and unfilled spheres illustrate the lattice points of the different domains. The domain boundary lattice points are indicated by crosshatched spheres. Oxygen octahedra are shown by dotted lines. Red spheres indicate oxygen and the blue spheres indicate the B cations. Note that in this case, both electrical and mechanical boundary conditions are fulfilled. However, the atoms at the boundary are about to decide which domain they prefer, which causes disorder in atomic positions. This is crucial for domain switching and the magnitude of disorder depends on structural parameters. (b) One possibility to introduce long range order along the boundary is to allow finite width for the domain boundary by introducing a cubic layer. This also means that the electric polarization is zero at the boundary. Presumably this type of layer is formed in structures which do not significantly deviate from the cubic structure.

8 shows the experimental lattice parameters of PZT as a function of temperature. In the vicinity of the phase boundary the  $c$  axis significantly shortens and the  $a$  axis lengthens so that the  $c/a$  axis ratio drops to one in the phase boundary area. Geometrical consideration shows that this makes it easier to match the pseudo-tetragonal (precisely, monoclinic  $Cm$ ) and rhombohedral crystals. This in turn suggests easier crystal boundary motion.

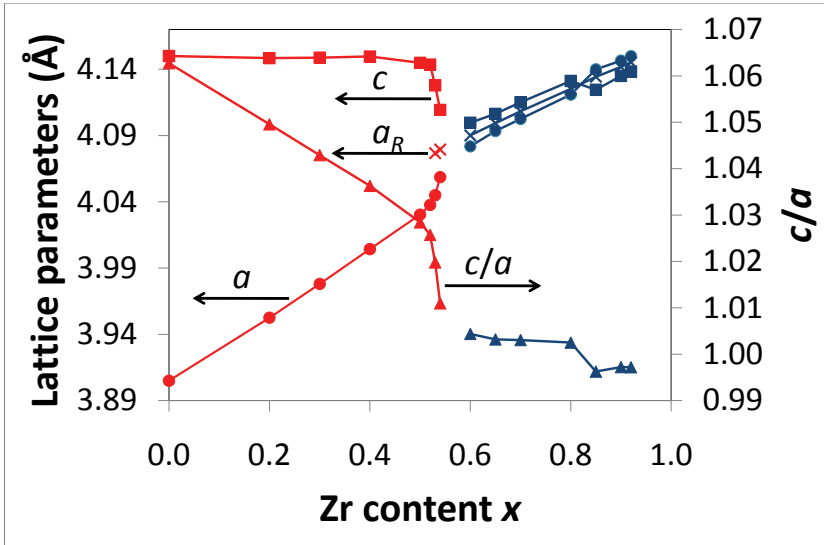


Fig. 8. Room-temperature tetragonal (space group  $P4mm$ ) and pseudo-tetragonal (space group  $Cm$ )  $a$  (filled spheres) and  $c$  axis (filled squares) parameters and the  $c/a$  axis ratio (filled triangles). Lattice parameter,  $a_R$ , for rhombohedral phase (space group  $R3c$ ) is indicated by crosses. In the case of the monoclinic  $Cm$  phase (structure slightly deviates from the tetragonal structure) the average of the  $a$  and  $b$  axes were divided by  $\sqrt{2}$ , whereas  $a_R = \frac{1}{3}\sqrt{3a_H^2 + (c_H/2)^2}$ , where  $a_H$  and  $c_H$  are the hexagonal lattice parameters. The data indicated by black colour are from. refs. (Frantti et al., 2000; 2002; 2003) and the data indicated by blue colour are from. ref. (Yokota, 2009).

### 7.2.0.1 Domain wall width.

We summarize the description given in ref. (Strukov & Levanyuk, 1998) for a domain boundary (parallel to  $yz$  plane) width estimation in a case that an infinitely large crystal is divided in two domains, one with  $x < 0$  and the other with  $x > 0$ . To find out how the order parameter  $\eta$  (in this case proportional to the spontaneous polarization) changes cross the boundary one includes a gradient term, proportional to  $(\frac{\partial\eta}{\partial x})^2$ , to the density of the thermodynamic potential  $\varphi(\eta)$ . By expanding the thermodynamic potential up to fourth order in order parameter and integrating over the entire crystal volume one gets the thermodynamic potential  $\int_v \varphi(\eta) dv = \int_v [\varphi_0 + \frac{1}{2}A\eta^2 + \frac{1}{4}B\eta^4 + \frac{1}{2}C(\frac{\partial\eta}{\partial x})^2] dv$ . A solution  $\eta(x)$ , which minimizes the thermodynamic potential, is obtained through variational computation with boundary conditions  $\eta \rightarrow \eta_0$  when  $x \rightarrow \infty$  and  $\eta \rightarrow -\eta_0$  when  $x \rightarrow -\infty$ , where  $\eta_0$  is a solution obtained for a homogeneous crystal. The solution is  $\eta(x) = \pm\sqrt{-A/B} \tanh(\frac{x}{2\sqrt{C/(-2A)}})$  (Strukov & Levanyuk, 1998).

## 8. Conclusions

Piezoelectric contribution in lead-zirconate-titanate (PZT) ceramics was reviewed and classified to intrinsic and extrinsic contributions. Models of intrinsic contribution were

addressed in light of recent experimental and theoretical studies. The very controversial polarization rotation model was addressed. Extrinsic contribution, consisted of grain boundary movement, domain wall movement, movement of the boundaries between crystal intergrowths and changes in phase fractions significantly contribute to the piezoelectric response of ceramics. Crystal symmetry analysis is not only useful for reducing the number of piezoelectric constants in single crystals, but finds applications in ferroelectric domain formation both in bulk ceramics and in thin films. Domain distribution depends on the sample size and shape, and the type of domain boundaries is affected by the sample preparation route. An example of the first case is Kittel's law, whereas changes in electrical conductivity between differently synthesized samples often result in different types of domain boundaries. Different contributions have characteristically different time-dependencies. Contemporary synchrotron facilities allow time-dependent studies down to 10 ns, making time-dependent studies feasible.

## 9. Acknowledgments

This work was supported by the Academy of Finland (COMP Centre of Excellence Program 2006-2011) and Con-Boys Ltd. We are grateful to both of them.

## 10. References

- Boysen, H. & Altorfer, F. (1994). A Neutron Powder Investigation of the High-Temperature Structure and Phase Transition in  $\text{LiNbO}_3$ . *Acta Cryst. B*, Vol. 50, 405-414.
- Burns, G. & Scott, B. A. (1970). Raman Studies of Underdamped Soft Modes in  $\text{PbTiO}_3$ . *Phys. Rev. Lett.*, Vol. 25, 167-170.
- Camargo, E. R.; Leite, E. R. & Longo, E. (2009). Synthesis and characterization of lead zirconate titanate powders obtained by the oxidant peroxo method. *Journal of Alloys and Compounds*, Vol. 469, 523-528.
- Dawber, M; Rabe, K. M. & Scott, J. F. (2005). Physics of thin-film ferroelectric oxides. *Rev. Mod. Phys.*, Vol. 77, 1083-1130.
- Dove, M. T. (2003). *Structure and Dynamics: an Atomic View of Materials*, Oxford University Press, ISBN 0-19-850678-3, New York.
- Frantti, J.; Lantto, V.; Nishio, S. & Kakihana, M. (1999). Effect of A- and B-cation substitutions on the phase stability of  $\text{PbTiO}_3$  ceramics. *Phys. Rev. B*, Vol. 59, 12-15.
- Frantti, J.; Lappalainen, J.; Lantto, V.; Nishio, S. & Kakihana, M. (1999). Low-temperature Raman studies of  $\text{Pb}(\text{Zr}_x\text{Ti}_{1-x})\text{O}_3$  and  $\text{Pb}_{1-3y/2}\text{Nd}_y\text{TiO}_3$  ceramics. *Jpn. J. Appl. Phys.*, Vol. 38, 5679-5682.
- Frantti, J.; Lappalainen, J.; Eriksson, S.; Lantto, V.; Nishio, S.; Kakihana, M.; Ivanov, S. & H. Rundlöf. (2000). Neutron diffraction studies of  $\text{Pb}(\text{Zr}_x\text{Ti}_{1-x})\text{O}_3$  ceramics. *Jpn. J. Appl. Phys.*, Vol. 39, 5697-5703.
- Frantti, J.; Ivanov, S.; Eriksson, S.; Rundlöf, H.; Lantto, V.; Lappalainen, J. & Kakihana, M. (2002). Phase transitions of  $\text{Pb}(\text{Zr}_x\text{Ti}_{1-x})\text{O}_3$ . *Phys. Rev. B*, Vol. 64, 064108.
- Frantti, J.; Eriksson, S.; Hull, S.; Lantto, V.; Rundlöf, H. & Kakihana, M. (2003). Composition variation and the monoclinic phase within  $\text{Pb}(\text{Zr}_x\text{Ti}_{1-x})\text{O}_3$  ceramics. *J. Phys.: Condens. Matter*, Vol. 15, No. 35, 6031-6041.

- Frantti, J.; Fujioka, Y. & Nieminen, R. M. (2007). Pressure-Induced Phase Transitions in  $\text{PbTiO}_3$ : A Query for the Polarization Rotation Theory. *J. Phys. Chem. B*, Vol. 111, No. 17, 4287-4290.
- Frantti, J.; Fujioka, Y. & Nieminen, R. M. (2008). Evidence against the polarization rotation model of piezoelectric perovskites at the morphotropic phase boundary. *J. Phys.: Condens. Matter*, Vol. 20, No. 47, 472203-472207.
- Frantti, J. (2008). Notes of the Recent Structural Studies on Lead Zirconate Titanate. *J. Phys. Chem. B*, Vol. 112, No. 21, 6521-6535.
- Frantti, J.; Fujioka, Y.; Zhang, J.; Vogel, S. C.; Wang, Y.; Zhao, Y. & Nieminen, R. M. (2009). The Factors Behind the Morphotropic Phase Boundary in Piezoelectric Perovskites. *J. Phys. Chem. B*, Vol. 113, No. 23, 7967-7972.
- Fu, H. & Cohen, R. E. (2000). Polarization rotation mechanism for ultrahigh electromechanical response in single-crystal piezoelectrics. *Nature Letters*, Vol. 403, 281-283.
- Glazer, A. M.; Thomas, P. A.; Baba-Kiski, K. Z.; Pang, G. K. H. & Tai, C. W. (2004). Influence of short-range and long-range order on the evolution of the morphotropic phase boundary in  $\text{Pb}(\text{Zr}_{1-x}\text{Ti}_x)\text{O}_3$ . (2004). *Phys. Rev. B*, Vol. 70, 184123.
- Grigoriev, A.; Sichel, R.; Lee, H. N., Landahl, E. C.; Adams, B.; Dufresne, E. M. & Evans, P. G. (2008). Nonlinear Piezoelectricity in Epitaxial Ferroelectrics at High Electric Fields. *Phys. Rev. Lett.*, Vol. 100, 027604.
- Grigoriev, A.; Sichel, R. J.; Jo, J. Y.; Choudhury, S.; Chen, L-Q.; Lee, H. N.; Landahl, E. C.; Adams, B. W.; Dufresne, E. M. & Evans, P. G. (2009). Stability of the unswitched polarization state of ultrathin epitaxial  $\text{Pb}(\text{Zr}, \text{Ti})\text{O}_3$  in large fields. *Phys. Rev. B*, Vol. 80, 014110.
- Hahn, Th. & Klapper, H. (2003). Twinning of Crystals, In: *International Tables for Crystallography D: Physical Properties of Crystals*, A. Authier, (Ed.), 393-448, Kluwer Academic Publishers, ISBN 1-4020-0714-0, Dordrecht.
- Hahn, Th. & Klapper, H. (2005). *International Tables for Crystallography A: Space-group Symmetry*, Th. Hahn, (Ed.), Kluwer Academic Publishers, ISBN 0-7923-6590-9, Dordrecht.
- Hinterstein, M.; Hoelzel, M.; Kungl, H.; Hoffmann, M. J.; Ehrenberg, H. & Fuess, H. (2011). In situ neutron diffraction study of electric field induced structural transitions in lanthanum doped lead zirconate titanate. *Zeitschrift Fur Kristallographie*, Vol. 226, 155-162.
- Hoffmann, M. J. & Kungl, H. (2004). High strain lead-based perovskite ferroelectrics. *Current Opinion in Solid State and Materials Science*, Vol. 8, 51-57.
- Hsu, R.; Maslen, E. N.; Du Boulay, D. & Ishizawa, N. (1997). Synchrotron X-ray Studies of  $\text{LiNbO}_3$  and  $\text{LiTaO}_3$ . *Acta Cryst. B*, Vol. 53, 420-428.
- Jaffe, B.; Cook, W. R. & Jaffe, H. (1971). *Piezoelectric Ceramics*, Academic Press, ISBN 0123795508, New York.
- Janolin, P.-E. (2009). Strain on ferroelectric thin films. *J. Mater. Sci.*, Vol., 44, 5025-5048.
- Kano, J.; Tsukada, S.; Zhang, F.; Karaki, T.; Adachi, M. & Kojima, S. (2007). Characterization of Dielectric Property of Nanosized  $(\text{Pb}_{0.7}\text{Sr}_{0.3})\text{TiO}_3$  Powders Studied by Raman Scattering. *Jpn. J. Appl. Phys.*, Vol. 46, No. 10B, 7148-7150.
- Kittel, C. (1946). Theory of the Structure of Ferromagnetic Domains in Films and Small Particles. *Phys. Rev.*, Vol. 70, 965-971.

- Klapper, H & Hahn, Th. (2005). Point-group Symmetry and Physical Properties of Crystals, In: *International Tables for Crystallography A: Space-group Symmetry*, Th. Hahn, (Ed.), 804-808, Kluwer Academic Publishers, ISBN 0-7923-6590-9, Dordrecht.
- Koch, E. (2004). Twinning, In: *International Tables for Crystallography C: Mathematical, Physical and Chemical Tables*, E. Prince, (Ed.), 10-14, Kluwer Academic Publishers, ISBN 1-4020-1900-9, Dordrecht.
- Kolasinski, K. W. (2008). *Surface Science: Foundations of Catalysis and Nanoscience*, John Wiley & Sons Ltd, ISBN 978-0-470-03308-1, West Sussex, England.
- Kozielski, L; Buixaderas, E.; Clemens, F. & Bujakiewicz-Korónska. (2010). PZT Microfibre defect structure studied by Raman spectroscopy. *J. Phys. D: Appl. Phys.*, Vol. 43, 415401.
- Jones, J. L.; Hoffman, M.; Daniels, J. E. & Studer, A. J. (2006). Direct measurement of the domain switching contribution to the dynamic piezoelectric response in ferroelectric ceramics. *Appl. Phys. Lett.*, Vol. 89, No. 9, 092901.
- Landauer, R. (1957). Electrostatic Considerations in BaTiO<sub>3</sub> Domain Formation During Polarization Reversal. *J. Appl. Phys.*, Vol. 28, 227-234.
- Li, J. Y.; Rogan, R. C.; Üstündag, E. & Bhattacharya, K. (2005). Domain switching in polycrystalline ferroelectric ceramics. *Nature Materials*, Vol. 4, 776-781.
- Lines, M. E. & Glass, A. M. (2001). *Principles and Applications of Ferroelectrics and Related Materials*, Oxford University Press in Oxford Classic Series, ISBN 0-19-850778-X, Oxford.
- Liu, Y. Y.; Zhu, Z. X.; Li, J.-F. & Li, J. Y. (2010). Misfit strain modulated phase structures of epitaxial Pb(Zr<sub>1-x</sub>Ti<sub>x</sub>)O<sub>3</sub> thin films: The effect of substrate and film thickness. *Mechanics of Materials*, Vol. 42, 816-826.
- Lüth, H. (2001). *Solid Surfaces, Interfaces and Thin Films*, Springer-Verlag, ISBN 3-540-58576-1, Berlin, Heidelberg.
- Mitsui, T. & Furuichi, J. (1953). Domain Structure of Rochelle Salt and KH<sub>2</sub>PO<sub>4</sub>. *Phys. Rev.*, Vol. 90, 193-202.
- Newnham, R. E. (2005). *Properties of Materials: Anisotropy, Symmetry, Structure*, Oxford University Press, ISBN 0-19-852076-X, New York.
- Nishida, K.; Osada, M.; Wada, S.; Okamoto, S.; Ueno, R.; Funakubo, H. & Katoda, T. (2005). Raman Spectroscopic Characterization of Tetragonal PbZr<sub>x</sub>Ti<sub>1-x</sub>O<sub>3</sub> Thin Films: A Rapid Evaluation Method for *c*-Domain Volume. *Jpn. J. Appl. Phys.*, Vol. 25, No. 25, L827-L829.
- Noheda, B.; Cox, D. E.; Shirane, G.; Gonzalo, J. A.; Cross, L. E. & Park, S.-E. (1999). A monoclinic ferroelectric phase in the Pb(Zr<sub>1-x</sub>Ti<sub>x</sub>)O<sub>3</sub> solid solution. *Appl. Phys. Lett.*, Vol. 74, 2059-2061.
- Noheda, B.; Gonzalo, J. A.; Cross, L. E.; Guo, R.; Park, S.-E.; Cox, D. E. & Shirane, G. (2000). Tetragonal-to-monoclinic phase transition in a ferroelectric perovskite: The structure of PbZr<sub>0.52</sub>Ti<sub>0.48</sub>O<sub>3</sub>. *Phys. Rev. B*, Vol. 61, 8687-8695.
- Nye, J. F. (1995). *Physical Properties of Crystals*, Oxford University Press, ISBN 0-19-851165-5, New York.
- Ohno, T.; Matsuda, T.; Ishikawa, K. & Suzuki, H. (2006). Thickness Dependence of Residual Stress in Alkoxide-Derived Pb(Zr<sub>0.3</sub>Ti<sub>0.7</sub>)O<sub>3</sub> Thin Film by Chemical Solution Deposition. *Jpn. J. Appl. Phys.*, Vol. 45, No. 9B, 7265-7269.

- Olsen, R. B. & Evans, D. (1983). Pyroelectric energy conversion: Hysteresis loss and temperature sensitivity of a ferroelectric materials. *J. Appl. Phys.*, Vol. 54, 5941-5944.
- Pane, I.; Fleck, N. A.; Huber, J. E. & Chu, D. P. (2008). Effect of geometry upon the performance of a thin film ferroelectric capacitor. *International Journal of Solids and Structures*, Vol 45, 2024-2041.
- Pertsev, N. A. & Zembilgotov, A. G. (1995). Energetics and geometry of 90° domain structures in epitaxial ferroelectric and ferroelastic films. *J. Appl. Phys.*, Vol. 78, 6170-6180.
- Phelan, D.; Long, X.; Xie, Y.; Ye, Z.-G.; Glazer, A. M.; Yokota, H.; Thomas, P. A. & Gehring, P. M. (2010). Single Crystal Study of Competing Rhombohedral and Monoclinic Order in Lead Zirconate Titanate. *Phys. Rev. Lett.*, Vol. 105, 207601.
- Phillips, R. B. (2001). *Crystals, Defects and Microstructures: Modeling Across Scales*, Cambridge University Press, ISBN 0-521-79357-2, Cambridge.
- Pramanick, A.; Damjanovic, D.; Nino, J. C. & Jones, J. (2009). Subcoercive Cyclic Electrical Loading of Lead Zirconate Titanate Ceramics I: Nonlinearities and Losses in the Converse Piezoelectric Effect. *J. Am. Ceram. Soc.*, Vol. 92, No. 10, 2291-2299.
- Pramanick, A.; Daniels, J. E. & Jones, J. (2009). Subcoercive Cyclic Electrical Loading of Lead Zirconate Titanate Ceramics II: Time-resolved X-ray Diffraction. *J. Am. Ceram. Soc.*, Vol. 92, No. 10, 2300-2310.
- Pruvost, S.; Hajjaji, A.; Lebrun, L.; Guyomar, D. & Boughaleb, Y. (2010). Domain switching and Energy Harvesting Capabilities in Ferroelectric Materials. *J. Phys. Chem. C*, Vol. 114, 20629-20635.
- Ricote, J.; Corker, D. L.; Whatmore, R. W.; Impey, S. A.; Glazer, A. M.; Dec, J. & Roleder, K. (1998). A TEM and neutron diffraction study of the local structure in the rhombohedral phase of lead zirconate titanate. *J. Phys.: Condens. Matter*, Vol. 10, 1767-1786.
- Rogan, R. C.; Üstündağ, E.; Clausen, B. & Daymond M. R. (2003). Texture and strain analysis of the ferroelastic behavior of  $\text{Pb}(\text{Zr,Ti})\text{O}_3$  by in situ neutron diffraction. *J. Appl. Phys.*, Vol. 93, No. 7, 4104-4111.
- Roitburd, A. L. (1976). Equilibrium Structure of Epitaxial Layers. *Phys. Status Solidi A*, Vol. 37, 329-339.
- Schilling, A.; Adams, T. B.; Bowman, R. M.; Gregg, J. M.; Catalan, G. & Scott, J. F. (2006). Scaling of domain periodicity with thickness measured in  $\text{BaTiO}_3$  single crystal lamellae and comparison with other ferroics. *Phys. Rev. B*, Vol. 74, 024115.
- Sergienko, I. A.; Gufan, Y. M. & Urazhdin, S. (2002). *Phys. Rev. B*, Vol. 65, 144104.
- Souza Filho, A. G.; Lima, K. C. V.; Ayala, A. P.; Guedes, I.; Freire, P. T. C.; Melo, F. E. A., Mendes Filho, J.; Araújo, E. B. & Eiras, J. A. (2002). Raman scattering study of the  $\text{PbZr}_{1-x}\text{Ti}_x\text{O}_3$  system: Rhombohedral-monoclinic-tetragonal phase transitions. *Phys. Rev. B*, Vol. 66, 132107.
- Streiffer, S. K.; Eastman, J. A.; Fong, D. D.; Thompson, C.; Munkholm, A.; Ramana Murty, M. V.; Auciello, O.; Bai, G. R. and Stephenson, G. B. (2002). Observation of Nanoscale 180° Stripe Domains in Ferroelectric  $\text{PbTiO}_3$  Thin Films. *Phys. Rev. Lett.*, Vol. 89, 067601.
- Strukov, B. A. & Levanyuk, A. P. (1998). *Ferroelectric Phenomena in Crystals: Physical Foundations*, Springer-Verlag, ISBN 3-540-63132-1, Berlin.

- Thomas, N. W. & Beitollahi, A. (1994). Inter-Relationship of Octahedral Geometry, Polyhedral Volume Ratio and Ferroelectric Properties in Rhombohedral Perovskites. *Acta Cryst. B*, Vol. 50, 549-560.
- Topolov, V. Y. & Turik, A. V. (2001). A new monoclinic phase and features of stress relief in  $\text{PbZr}_{1-x}\text{Ti}_x\text{O}_3$  solid solutions. *J. Phys. Condens. Matter*, Vol. 13, L771-L775.
- Yakunin, S. I.; Shakmanov, V. V.; Spivak, G. V. & Vasiléva, N. V. (1972). Microstructure of domains and domain boundaries of  $\text{BaTiO}_3$  single crystalline films. *Fiz. Tverd. Tela*, Vol. 14, 373-377, *Sov. Phys. Solid State* (English Transl.), Vol. 14, 310.
- H. Yokota, N. Zhang, A. E. Taylor, P. Thomas, and A. M. Glazer (2009). Crystal structure of the rhombohedral phase of  $\text{PbZr}_{1-x}\text{Ti}_x\text{O}_3$  ceramics at room temperature *Phys. Rev. B*, Vol. 80, 104109.
- Wu, X. & Vanderbilt, D. (2006). Theory of hypothetical ferroelectric superlattices incorporating head-to-head and tail-to-tail  $180^\circ$  domain walls. *Phys. Rev. B*, Vol. 73, 020103.
- Xu, G.; Wen, J.; Stock, C. & Gehring, P. M. (2008). Phase instability induced by polar nanoregions in a relaxor ferroelectric system. *Nature Materials*, Vol. 7, 562-566.

# B-site Multi-element Doping Effect on Electrical Property of Bismuth Titanate Ceramics

Jungang Hou<sup>1</sup> and R. V. Kumar<sup>2</sup>

<sup>1</sup>*School of Metallurgical and Ecological Engineering, University of Science and Technology*

<sup>2</sup>*Department of Materials Science and Metallurgy, University of Cambridge*

<sup>1</sup>*China*

<sup>2</sup>*United Kingdom*

## 1. Introduction

This article represents a systematic review of the behaviour of B-site multi-element doping effect on electrical property of bismuth titanate ceramics. Bismuth titanate,  $\text{Bi}_4\text{Ti}_3\text{O}_{12}$  (BIT) is a potential candidate for high-temperature device applications due to their high dielectric constant, Curie temperature ( $T_c$ ), breakdown strength, anisotropy and, low dielectric dissipation factor, therefore attracting considerable commercial interest in applications such as high temperature piezoelectric devices, memory storage and optical displays. These features make bismuth layer-structured ferroelectrics (BLSFs) attractive in the field of developing lead-free piezoelectric materials. BIT is a well-known member of the BLSFs, which can be represented by a general formula  $(\text{Bi}_2\text{O}_2)^{2+}(\text{A}_{m-1}\text{B}_m\text{O}_{3m+1})^{2-}$ , where A represents a mono-, di, or trivalent ion, such as  $\text{La}^{3+}$ ,  $\text{Nd}^{3+}$ ,  $\text{Pr}^{3+}$ ,  $\text{Sm}^{3+}$ , etc., B stands for transition-metal cations like  $\text{Ti}^{4+}$ ,  $\text{Nb}^{5+}$ ,  $\text{Ta}^{5+}$ ,  $\text{W}^{6+}$ , etc., and  $m$  is the number of  $\text{BO}_6$  octahedra in the perovskite-like layer ( $m=1-5$ ) (Aurivillius, 1949; Kumar, 2001; Markovec, 2001; Nagata, 1999; Noguchi, 2000; Sugibuchi, 1975; Shimakawa, 2000; Subbarao, 1961; Shulman, 2000; Shimazu, 1980; Takenaka, 1981). The layer structure of  $\text{Bi}_4\text{Ti}_3\text{O}_{12}$  ( $m=3$ ) consists of three perovskite-like  $(\text{Bi}_2\text{Ti}_2\text{O}_{10})^{2-}$  units with a pseudo-perovskite layer structure, sandwiched between  $(\text{Bi}_2\text{O}_2)^{2+}$  layers along its crystallographic  $c$  axis. In the  $(\text{Bi}_2\text{Ti}_2\text{O}_{10})^{2-}$  units, Ti ions are enclosed by oxygen octahedra, and Bi ions occupy the spaces in the framework of octahedral (Subbarao, 1950).

BIT is of interest in high-temperature piezoelectric sensors, because it remains ferroelectric up to 675 °C and offers relatively high piezoelectric property (Subbarao, 1961). However, the high leakage current and domain pinning due to defects in BIT have appeared as obstacles for further applications. The reasons for such problems are suggested due to the instability in the oxidation state of Ti ions and the volatile property of Bi during the sintering process (Nagata, 1999). Great efforts have been made to solve the high-leakage current, by incorporation of W, Nb or Ta dopants, as these can significantly decrease the conductivity in BIT (Hong, 2000; Markovec, 2001; Shulman, 1999; Takenaka, 1981; Villegas, 1999; Zhang, 2004). Unfortunately, the piezoelectric effect in the high Curie temperature BIT is relatively low, with coefficient values typically less than 20 pC N<sup>-1</sup> found for both pure and modified  $\text{Bi}_4\text{Ti}_3\text{O}_{12}$ . Thus, it is a challenge to seek a rational pathway to improve the electrical property of BIT ceramics.

We have reported in our publications, the effects of composition and crystal lattice structure upon microstructure, dielectric, piezoelectric and electrical properties of BIT,  $\text{Bi}_4\text{Ti}_3\text{-}_x\text{W}_x\text{O}_{12+x}+0.2\text{wt}\%\text{Cr}_2\text{O}_3$  (BTWC),  $\text{Bi}_4\text{Ti}_{3-2x}\text{Nb}_x\text{Ta}_x\text{O}_{12}$  (BTNT) and  $\text{Bi}_4\text{Ti}_{3-2x}\text{Nb}_x\text{Ta}_{x-y}\text{Sb}_y\text{O}_{12}$  (BTNTS) ceramics have been widely investigated (Hou et al, 2009, 2010 and 2011). The processing of as-synthesized BIT were optimized and the main parameters were determined, and confirmed that the piezoelectric coefficient ( $d_{33}$ ) of undoped BIT is  $8 \text{ pC N}^{-1}$ . As for BTWC, the results have shown the systematic changes in the lattice parameters; the formation of secondary phase(s) at higher levels of W/Cr doping; and the increase in dielectric constant and loss at room temperature with increase of doping content. A higher value of  $d_{33}$ , at  $22 \text{ pC N}^{-1}$ , was obtained for the sample with  $x=0.025$ , which may result directly from lowering conductivity. With regard to BTNT and BTNTS, the results have shown the formation of orthorhombic structure for all the samples within these family of dopants; the addition of Nb/Ta caused a remarkably suppressed grain growth while there is not much difference in grain size for BTNTS; as the doping content was increased, the Curie temperatures of BTNT decreased significantly, to as low as  $630^\circ\text{C}$  while the difference is not very significant for BTNTS. The co-doping at B-site could induce the distortion of oxygen octahedral and reduce the oxygen vacancy concentration, resulting in the enhancement of  $d_{33}$ . Especially, the highest values of 26 and  $35 \text{ pC N}^{-1}$ , were obtained for  $\text{Bi}_4\text{Ti}_{2.98}\text{Nb}_{0.01}\text{Ta}_{0.01}\text{O}_{12}$  and  $\text{Bi}_4\text{Ti}_{2.98}\text{Nb}_{0.01}\text{Ta}_{0.002}\text{Sb}_{0.008}\text{O}_{12}$ , respectively. The activation energy associated with the electrical relaxation and DC conductivity were determined from the electric modulus spectra, suggesting the movements of oxygen ions are possible for both ionic conductivity as well as the relaxation process. To ascertain the electrical conduction mechanism in the ceramics, various physical models have been proposed, suggesting the conductivity behavior of the ceramics can be explained using correlated barrier hopping model. All measurements demonstrated that BTNT ceramics are promising candidates for high temperature applications.

## 2. W/Cr modified $\text{Bi}_4\text{Ti}_3\text{O}_{12}$ ceramics

Bismuth titanate,  $\text{Bi}_4\text{Ti}_3\text{O}_{12}$  (BIT) is a potential candidate for high-temperature device applications due to their high Curie temperature ( $T_c$ ) and an excellent fatigue endurance property. However, the piezoelectricity of pure BIT ceramics is relatively very low ( $d_{33} < 8 \text{ pC N}^{-1}$ ). The piezoelectric properties can be enhanced by grain orientation techniques. However these methods are not cost effective. So, it is favourable to optimize piezoelectric properties via structural modification using appropriate doping. In this connection, to improve the piezoelectric properties of BIT, ions substitution with other cations have been considered and explored. It has been shown that doping with donor cations such as  $\text{Nb}^{5+}$ ,  $\text{V}^{5+}$  or  $\text{Ta}^{5+}$  in the  $\text{Ti}^{4+}$  positions decreases electrical conductivity and improves piezoelectric properties of BIT ceramics (Du, 2009; Shulman, 1999; Tang, 2007). Cr doping is another one of the most adopted strategies to tailor the dielectric and piezoelectric properties of ferroelectrics to practical specifications. It is well known that Cr is effective in decreasing the aging effect and decreasing dielectric loss thus the effect of doping of  $\text{Cr}^{3+}$  is that of stabilizer of piezoelectric and dielectric properties (Li, 2008; Yang, 2007). The density of ceramics can be increased using small amount of  $\text{Cr}_2\text{O}_3$ . However, large content of  $\text{Cr}_2\text{O}_3$  will inhibit grain growth because of accumulation of  $\text{Cr}^{3+}$  at the grain boundary, which results in decrease in the grain size (Hou et al, 2005; Takahashi, 1970).

It is noted that the studies concerning the effect of  $W^{6+}$  doping on electrical and sintering behavior have been reported earlier (Jardiel, 2006, 2008; Villegas, 2004). However reports on W/Cr doped BIT ceramics are scarce. We have made an attempt to optimize the W/Cr doping to yield enhanced piezoelectric and dielectric properties of BIT ceramics. The influence of W/Cr doping on the structural, sintering behavior, dielectric, electrical conductivity and piezoelectric properties of BIT ceramics is reported in this section.

Fig. 1 (A) shows the X-ray diffraction patterns of BITWC ceramics at room temperature. Diffraction data does not show any evidence of the formation of tungsten and chromium oxide or associated compounds that contain bismuth or titanium. Therefore, the BITWC ceramics maintains a layer structure similar to the perovskite BIT even under extensive modifications by  $W^{6+}/Cr^{3+}$ .

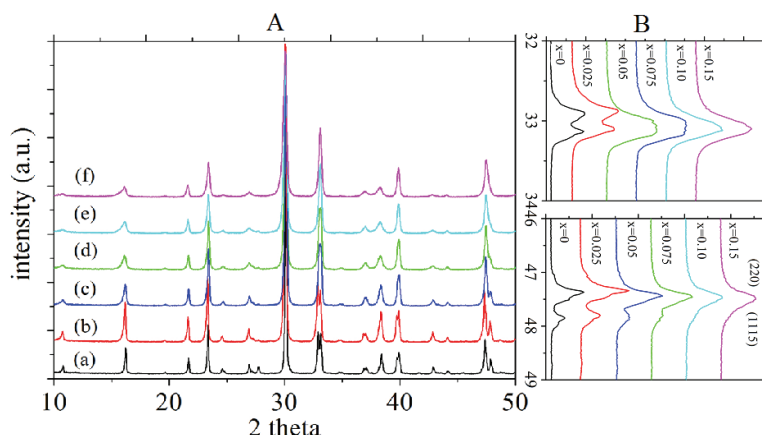


Fig. 1. (A) XRD patterns of BITWC with different W/Cr content: (a) 0.0, (b) 0.025, (c) 0.05, (d) 0.075, (e) 0.10 and (f) 0.15. (B) Evolution of XRD patterns associated with the peaks of (020)/(200) and (220)/(1115) of BITWC powders with different W/Cr content.

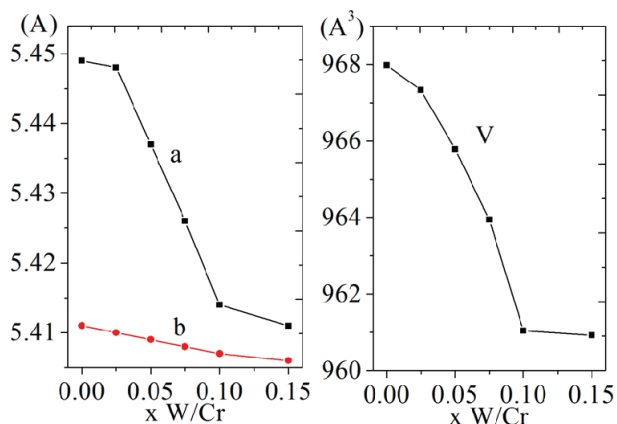


Fig. 2. Variation in lattice parameters of BITWC powders calcined at 800 °C for 4 h vs. different amount of W/Cr doping.

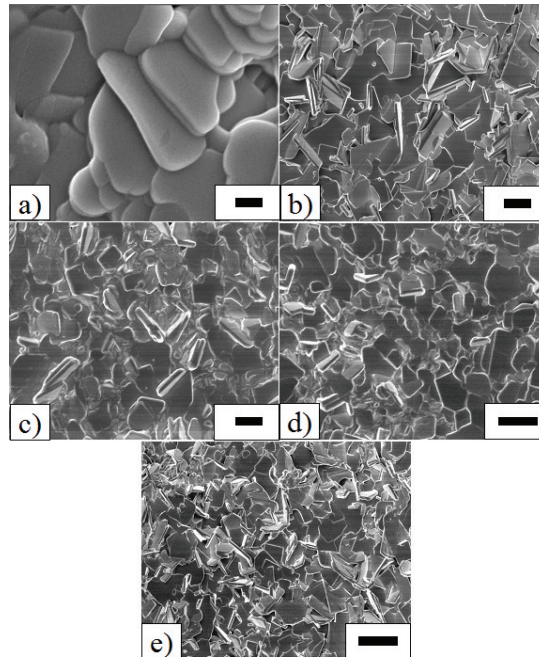


Fig. 3. SEM images of polished and thermal etched surfaces of various samples: (a) 0.025, (b) 0.05, (c) 0.075, (d) 0.10 and (e) 0.15. Scale represented in the figures is 3  $\mu\text{m}$ .

Evolution of XRD patterns associated with the peaks of (020)/(200) and (220)/(1115) of BITWC with different W/Cr content are shown in Fig. 1 (B). For sample with 0.025W/Cr, the (020) diffraction pattern at  $2\theta=33^\circ$  is clearly split into two (020) and (200) peaks in the orthorhombic phase thus the lattice constants  $a \neq b$ . With increasing W/Cr content, the splitting between the (020) and (200) peaks is decreased, indicating the reduction of the orthorhombicity  $a/b$ . When  $x=0.05$ , only the reflection (020) can be observed and the (020) reflections have shifted to higher  $2\theta$  values, indicating a decrease in the lattice parameters  $a$  and  $b$  in the crystal structure. From Fig. 1 (B) the (220) reflections are observed to shift upwards in the orthorhombic form and the reflection (1115) is absent at  $x=0.10$ . That means the modification of tungsten and chromium for titanium ions distorts the positions of ions in the lattice, which may result from the different lattice strain relating to different ionic radius and outer electronic configuration between  $\text{W}^{6+}$  and  $\text{Cr}^{3+}$ . As typically shown in Fig. 2, the decrease of the orthorhombic lattice parameters  $a$  and  $b$ , and lattice volume  $V$  of the BIT phase with an increasing amount of W/Cr doping are obvious, especially for the composition with W/Cr being less than 0.10. Further an increase in the amount of W/Cr to 0.15 does not cause a change of cell dimensions based on XRD results. However, no significant drop in lattice parameter,  $c$ , is found in BITWC powders calcined at 800  $^\circ\text{C}$  for 4 h. It is observed that the almost no volume change could be found for powders with W/Cr doping more than 0.10, allows us to further study the possibility of the formation of a second phase like  $\text{Bi}_6\text{Ti}_3\text{WO}_{18}$  and  $\text{Bi}_6\text{Ti}_5\text{WO}_{22}$  in the samples (Jardiel, 2008), although any secondary phases were not found by XRD techniques because of the limitation of XRD intensity below a certain concentration. A careful examination of the XRD patterns in Figs. 1

(B) reveal that apart from the decrease of the lattice parameters and the difference between the a and b parameters, the peaks have broadened. The (1115) peaks in the patterns of  $x=0.10$  and  $0.15$  appear as a weak shoulder on the right of the corresponding (220) peaks. Although the line-broadening of XRD peaks can have various origins, including grain size and dislocation structure (Snyder, 1999), it is expected that the observed line-broadening can be attributed to micro-strain in the material.

Fig. 3 shows the SEM images of the polished and thermally etched surfaces of BITWC ceramics. It is observed that the average grain size decreased with W/Cr doping ranging from approximately  $10\ \mu\text{m}$  to  $1\ \mu\text{m}$ , which suggest that W/Cr control the growth of the plate-like grains. It is reported that  $\text{WO}_3$  influences the grain growth kinetics due to the slowing of grain boundary diffusion processes (Jardiel, 2008). The aspect ratio of the grains decreases with increase of W/Cr doping as shown in Fig. 3. This will lead to a better arrangement of the particles during the sintering processes and consequently to an enhanced densification of the ceramics. Table I shows the EDS analysis data of BITWC ceramics. When  $x \leq 0.05$ , the experimentally observed atomic ratios agreed with the initial compositions signifies that the BITWC ceramics are single phase. This shows that the  $\text{W}^{6+}/\text{Cr}^{3+}$  cations were incorporated into the layered perovskite structure and presumably occupied  $\text{Ti}^{4+}$  sites. While for  $x \geq 0.075$  compositions, EDS results were not in agreement with the initial theoretical atomic ratios. This indicates the presence of the secondary phases in the samples.

Element	BIT	$x=0.025$	$x=0.05$	$x=0.075$	$x=0.1$	$x=0.15$
Bi	4.00	3.98	3.97	3.96	3.93	3.87
Ti	2.99	2.98	2.94	2.91	2.86	2.81
W	0	0.025	0.05	0.076	0.11	0.16
Cr	0	0.4	0.4	0.39	0.4	0.37
O	12.00	12.00	12.00	12.08	12.09	12.16

Table 1. Energy-Dispersive Spectra (EDS) Analysis Data for BITWC ceramics

Fig. 4 (a) shows the variation of the real part of impedance ( $Z'$ ) with frequency at various temperatures for  $x = 0.025$  composition. It is observed that the magnitude of  $Z'$  decreases with increase in both frequency as well as temperature, indicating an increase in ac conductivity with rise in temperature and frequency. The  $Z'$  values for all temperatures merge at high frequencies. Similar trends were observed for the other compositions which are not depicted in the Fig. 4. Fig. 4 (b) shows the normalized imaginary parts of impedance ( $Z''/Z''_{\text{max}}$ ) as a function of frequency at the selected temperatures. The values of ( $Z''/Z''_{\text{max}}$ ) are observed to shift to higher frequencies with increasing temperature consistent with temperature dependent electrical relaxation behavior. These observed relaxation processes for the studied samples could be attributed to the presence of defect/vacancies.

Relaxation processes in many electric, magnetic, mechanical and other systems are governed by the Kohlrausch-Williams-Watts (KWW) law (Williams, 1970),

$$\phi(t) = \exp\left[-\left(\frac{t}{\tau}\right)^\beta\right] \quad (1)$$

where  $\tau$  is the relaxation time and  $0 < \beta \leq 1$  is the parameter which indicates the deviation from Debye-type relaxation. The dielectric behaviour of the present ceramics is rationalized by invoking modified KWW function suggested by Bergman (Bergman, 2000). The imaginary part of the electric modulus ( $Z''$ ) can be defined as:

$$\frac{Z''}{Z''_{\max}} = \frac{1}{(1-\beta) + \frac{\beta}{1+\beta} \left[ \beta(f_{\max}/f) + (f/f_{\max})^{\beta} \right]} \quad (2)$$

where  $Z''_{\max}$  is the peak value of the  $Z''$  and  $f_{\max}$  is the corresponding frequency. Theoretical fit of Eq. 2 to the experimental data is shown in Fig. 4 (b) as the solid lines. It is seen that the experimental data are well fitted to this model except in the low frequency regime which may be due to electrode effect associated with the samples. From the fitting of  $Z''$  versus frequency plots, the value of  $\beta$  was determined and found to be temperature independent. The value of  $\beta$  is found to be  $0.82 \pm 0.02$  in the 400-600 °C temperature range. Eq. 2 can be fitted for other compositions under study which are not shown in Fig. 4.

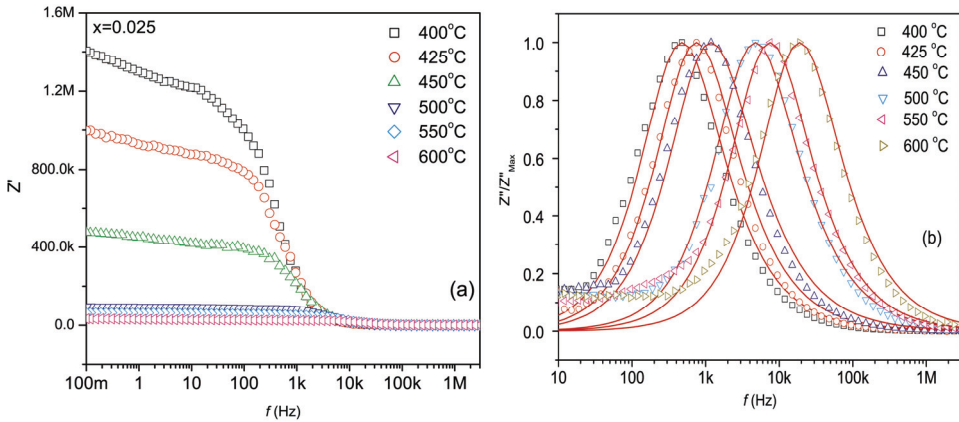


Fig. 4. (a) Real and (b) imaginary parts of impedance versus frequency plots at various temperatures and the solid lines are the theoretical fit.

Fig. 5 depicts the variation of relaxation frequency with an inverse of absolute temperature for the composition of  $x=0.025$ . The activation energy for electrical relaxation can be calculated using Arrhenius relation as:

$$f_m = f_o \exp\left(-\frac{E}{kT}\right) \quad (3)$$

where  $f_o$  is the pre exponential factor,  $k$  is the Boltzmann constant, and  $T$  is the absolute temperature. Activation energy was calculated from the linear fit of the experimental data as shown in Fig. 5 for  $x=0.025$  samples. Activation energy was estimated for the other compositions under study and the plot for activation energy versus composition is shown in the inset of Fig. 5. The activation energy increases with the W/Cr content, which suggests a decrease of oxygen vacancy concentration (Coondoo, 2007).

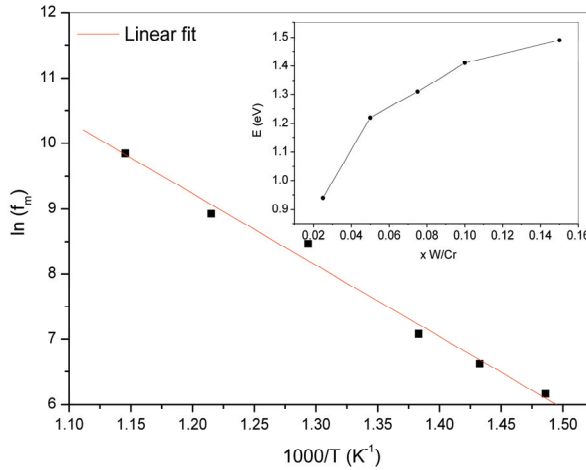


Fig. 5. Arrhenius plot for relaxation frequency versus temperature and inset shows variation of activation energy with  $x$ .

T (°C)	$R_1$ (ohm)	CPE (1) [nF]	$n_1$	$R_2$ (ohm)	CPE (2) [F]	$n_2$	$R_3$ (ohm)
450	$1.98 \times 10^5$	1.26	0.88	$1.14 \times 10^5$	$3 \times 10^{-6}$	0.60	6333
500	$5.7 \times 10^4$	1.8	0.89	$3.3 \times 10^4$	$2 \times 10^{-5}$	0.5	1300
550	$2.2 \times 10^4$	1.66	0.89	$1.5 \times 10^4$	$1 \times 10^{-5}$	0.41	268
600	$1.1 \times 10^4$	1.2	0.9	7871	0.037	0.35	0.01

Table 2. Cole-Cole fitted parameters for the  $x=0.025$  samples

If we scale each  $Z''$  with  $Z''_{max}$  and each  $f$  with  $f_{max}$ , the entire curves collapse into a single master curve as shown in the Fig. 6 for  $x=0.025$  samples. The scaling nature of  $Z''$  implies that the relaxation shows the same mechanism in the entire temperature range. Similar behaviors were also observed for the other compositions ( $x = 0.05, 0.075, 0.1$  and  $0.15$ ) under study which are not shown here in the figure.

Figs. 7 depict complex impedance plots at 600 °C temperatures for  $x=0.025$  samples. The complex impedance plots were resolved with two depressed semicircles corresponding to grain and grain boundaries. The impedance data for  $x=0.025$  samples were fitted using superimposition of two Cole-Cole expressions as:

$$Z^* = \frac{R_1}{[1 + (i\omega\tau_1)^{n1}]} + \frac{R_2}{[1 + (i\omega\tau_2)^{n2}]} \tag{4}$$

where  $R_1, R_2, \tau_1$  and  $\tau_2$  are resistance and relaxation times from grain and grain boundaries, respectively. The factors  $n_1$  and  $n_2$  indicate poly-dispersive multi Debye type relaxation. If the values are unity then the relaxation is explained by Debye type response. Experimental data were fitted using the software “ZsimpWin” as shown in Fig 7(a-d). The electrical contribution of the grains and grain boundaries was introduced by using an equivalent circuit as shown in inset of Fig 7(a). The results show the well-fitted impedance plots to the

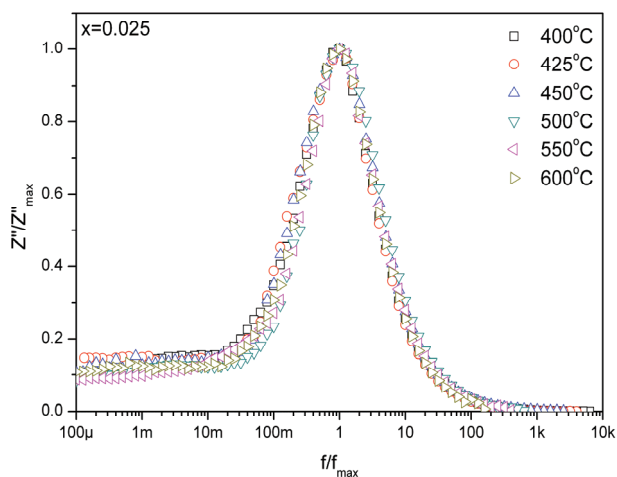


Fig. 6. Scaling behaviour of  $Z''$  at various temperatures.

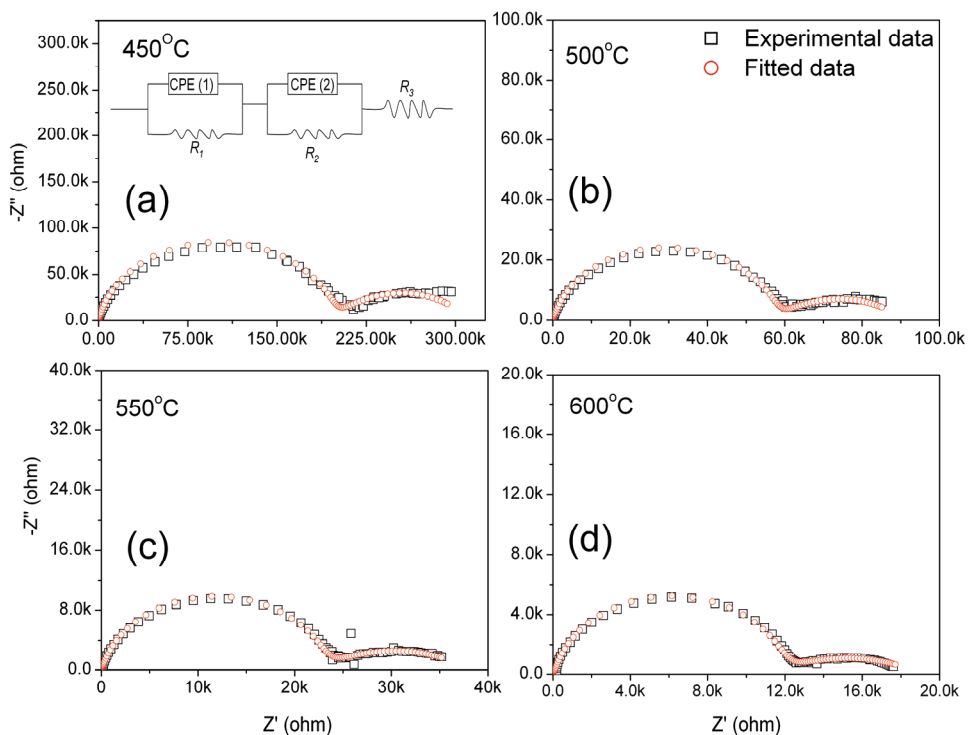


Fig. 7. Cole-Cole plots for  $x=0.025$  BITWC samples at various temperatures.

experimental data. The capacitors in the equivalent circuit are universal capacitors ( $C^* = A(i\omega)^{n-1}$ ), as introduced by Jonscher (Jonscher, 1977). Fitted parameters are reported in the Table II.

In order to study the relaxation mechanism for various compositions, the plots of ( $Z''/Z''_{\max}$ ) versus  $f/f_{\max}$  are shown in Fig. 8 for the compositions under study at 600 °C. It is to be noted that relaxation peaks are completely overlapped. This indicates that the relaxation mechanism is invariant with W/Cr content. However, the plots have not merged in the lower frequency regime. It is due to the extrinsic phenomenon associated with the samples.

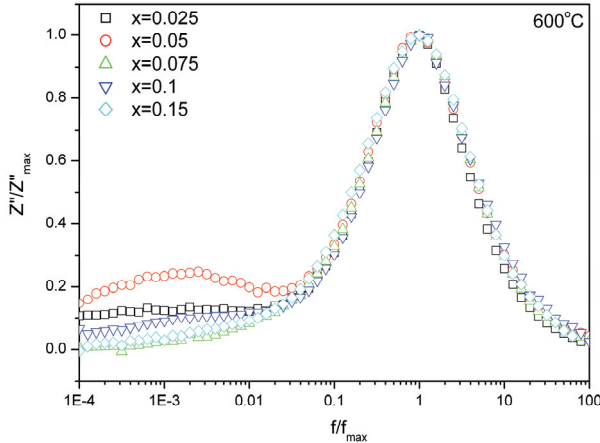


Fig. 8. Scaling plots for various values of  $x$  at a temperature of 600°C.

Dielectric constant and dielectric loss were calculated at various frequencies and temperatures (for the compositions under study) from the impedance data using the following relations:

$$\varepsilon' = \frac{-Z''}{\omega C_0 (Z'^2 + Z''^2)} \quad (5)$$

$$\tan \delta = \frac{Z'}{-Z''} \quad (6)$$

where  $C_0$  is the equivalent vacuum capacitance ( $= \varepsilon_0 A / t$ ) of the sample.  $A$  and  $t$  are area and thickness of the sample. Fig. 9 shows the dielectric permittivity and dielectric loss ( $\tan \delta$ ) of W/Cr-doped BIT as a function of temperature measured at a frequency of 100 kHz. The dielectric peaks occur when the temperature is higher than 640 °C, which corresponds to the Curie temperatures. The Curie temperatures of BITWC are found to be slightly lower than that of BIT ceramic, and gradually decreased from 675 to 640 °C with increasing W/Cr content, which may partially arise from the difference of ionic radii ( $W^{6+}$ : 0.62 Å,  $Cr^{3+}$ : 0.52 Å, and  $Ti^{4+}$ : 0.605 Å) and partially result from an decrease in the lattice distortion (Kan, 2004; Lopatin, 1989; Nagata, 2004; Villegas, 2004). A small hump is observed in temperature dependence dielectric constant plots for higher compositions of BITWC ceramics ( $x > 0.075$ )

(as shown in inset of Fig. 9). This may be due to the presence of secondary phase in the ceramics (Hyatt, 2005; Luo, 2001). There is a sudden increase of loss ( $\tan \delta$ ) in the curve, with a peak position slightly below the  $T_c$ . After the  $T_c$ , the loss ( $\tan \delta$ ) reaches a minimum value and then begins to increase once again. This dielectric loss valley is corresponding to the dielectric peak, i.e., the Curie temperature. The selected room temperature properties of BITWC ceramics are characterized and listed in Table III. With increasing of W/Cr contents, the Curie temperature and the dielectric loss decreased whilst the dielectric permittivity and loss vary sluggishly.

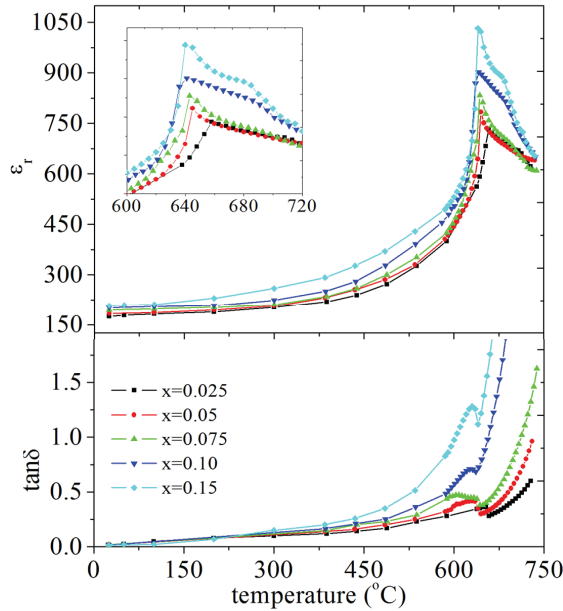


Fig. 9. Temperature dependence of dielectric constant and loss for the BITWC ceramics on W/Cr content.

In order to further elucidate the transport mechanism in the present ceramics, the electrical conductivity at different temperatures is studied. Electrical conductivity can be calculated from the dielectric data as:

$$\sigma(\omega) = \omega \cdot \epsilon_0 \cdot \epsilon' \cdot \tan \delta \quad (7)$$

where  $\omega$  is the angular frequency and  $\epsilon_0$  is the vacuum permittivity. Fig. 10 shows the frequency dependent (0.1 Hz-3 MHz) electrical conductivity at various temperatures for 0.025BITWC. Similar trends were found for other samples which are not mentioned in here Fig. 10. The electrical conductivity depends on frequency according to the “universal dynamic response” and can be related as  $\sigma(\omega) = \sigma_{DC} + A \cdot \omega^n$ , where  $A$  is the temperature dependent parameter and the exponent  $n$  is a characteristic parameter representing the many body interactions of the electrons, charges and impurities. It varies from 0 to 1 and for ideal Debye type behaviour it is equal to 1 (Jonscher, 1977). In Fig. 10, at all the

temperatures, the conductivity is independent of frequency at low frequency regime. Above a characteristic frequency, the conductivity increases with increase in frequency with characteristics  $\omega^n$  dependence. The conductivity increases with increasing temperature due to thermal activation of conducting species in the samples. The frequency response of the other compositions also behaved similarly. Electrical conduction in BITWC ceramics is expected to result mainly from the defects presented in the lattice. These defects could come from the volatilisation of  $\text{Bi}_2\text{O}_3$  during sintering, which could result in oxygen and bismuth vacancies. The variation of dc conductivity ( $\sigma_{DC}$ ) with temperature can be described by Arrhenius equation as;

$$\sigma_{DC} = \sigma_0 \exp\left(-\frac{E_{DC}}{kT}\right) \quad (8)$$

Where  $\sigma_0$  is pre-exponential factor and  $E_{DC}$  is activation energy associated with dc conductivity. Fig. 11 shows dc conductivity as a function of inverse of absolute temperature. From the slope of the linear fit, we can estimate activation energy associated with dc conduction. The variation of the activation energy with the W/Cr ( $x$ ) content is depicted in the inset of Fig. 11. The activation energy (0.9 eV) for the conductivity of  $x=0.025$  samples suggested an extrinsic conduction mechanism. With increasing W/Cr doping, the activation energy increased from  $\sim 0.9$  to  $\sim 1.5$  eV. This is associated with a change from extrinsic to intrinsic conductivity (Takahashi, 2003; Zhou, 2006; Zhang, 2009). It is well known that the intrinsic electronic conductivity activation energy is equal to half of the energy of the band gap ( $E_g$ ). The reported value for the band gap is 3.3 eV for  $\text{Bi}_4\text{Ti}_3\text{O}_{12}$  ceramics (Ehara, 1981) which is in close agreement with that of the present results (1.5 eV). It is interesting to note that the values for activation energy of dc conduction and electrical relaxation (Fig. 5) are in close agreement which indicates that the same ions are responsible for the both the processes (dc conduction and relaxation).

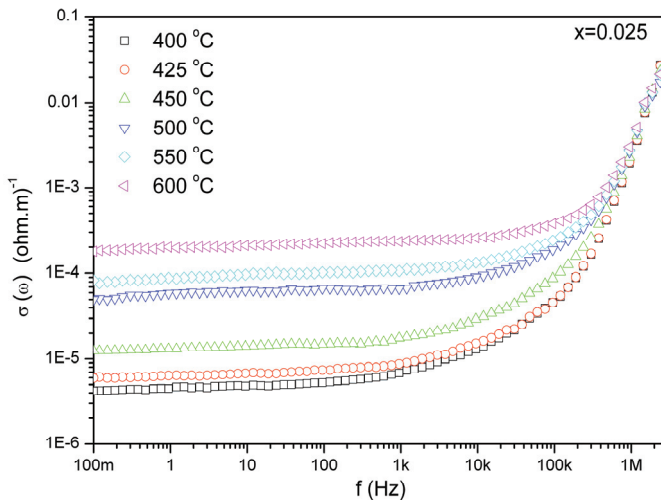


Fig. 10. Frequency dependent electrical conductivity at various temperatures.

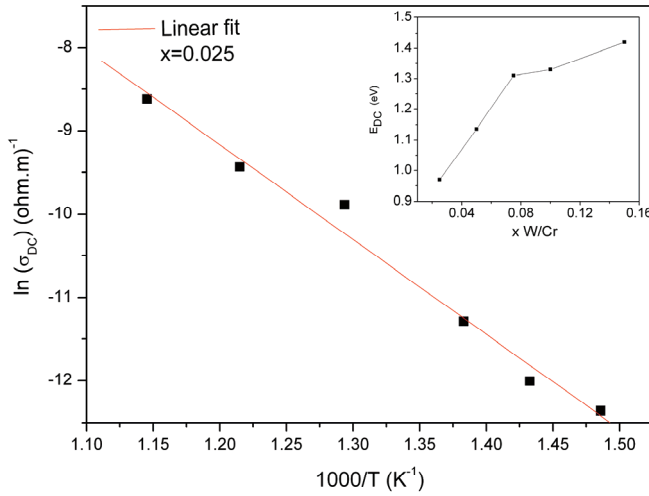


Fig. 11. Arrhenius plot for dc conductivity for  $x=0.025$  sample and inset shows variation of activation energy with W/Cr content.

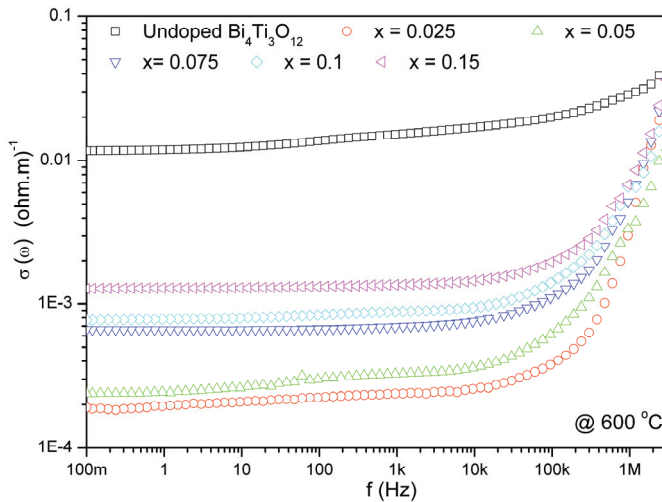


Fig. 12. Frequency dependent electrical conductivity for various W/Cr content

To further investigate the conductivity for all the compositions, we have plotted frequency dependent (0.1Hz-3MHz) electrical conductivity for all the compositions under study at 600 °C temperature as shown in Fig. 12. It is interesting to note that electrical conductivity of  $x=0.025$  sample decreases significantly as compared with that of undoped BIT ceramics. Consequently conductivity increases with further increase in W/Cr content. In BIT ceramics, hole compensation of bismuth vacancies promotes  $p$ -type electronic conductivity. Under charge neutrality restriction, when  $W^{6+}$  substitutes  $Ti^{4+}$ , two positive charge centers at W site

and two electrons will be created. These electrons neutralize the influence of the holes. The conductivity decreases with donor doping to a minimum value where the concentration of electron holes matches the electron concentration ( $p=n$ ). With a further increase in the donor ( $W^{+6}$ ) concentration the conductivity becomes  $n$ -type and starts to increase again. The minimum conductivity appears at a lower W/Cr content doped BIT ceramics ( $x=0.025$ ). Presence of secondary phase in higher concentration doped ( $x>0.075$ ) ceramics can also play crucial role in the conductivity behaviour (Hyatt et al. 2005; Jardiel et al. 2006). It is reported that the  $\text{Bi}_6\text{Ti}_3\text{WO}_{18}$  ceramics have higher conductivity than  $\text{Bi}_4\text{Ti}_3\text{O}_{12}$  ceramics which results higher conductivity associated with the ceramics of higher concentration ( $x > 0.075$ ). However, it is reported in the literature that the conductivity decreases up to concentration of  $x = 0.08$  and consequently increases in sluggish manner with increase in the W doping (Jardiel, 2008). The reported value of dc conductivity at 600 °C is  $3.2 \times 10^{-5} (\text{ohm cm})^{-1}$  for the W doping concentration of 0.05 (Jardiel, 2008). While in the present investigations, the value of dc conductivity is found to be  $2.38 \times 10^{-6} (\text{ohm cm})^{-1}$  for the  $x=0.05$  W/Cr doping at 600 °C. This difference in the value of electrical conductivity can be attributed to microscopic heterogeneity and random arrangement of cations in the structure due to the presence of Cr ions along with W and Ti ions at B-site. The interaction between the cations controls the conduction and dielectric mechanisms of the present ceramics. A defect chemistry expression for W doping can be written as



It shows that the oxygen vacancies are reduced upon the substitution of donor  $W^{6+}$  ion for  $\text{Ti}^{4+}$ . Hence, it is reasonable to believe that the conductivity in BIT ceramics is suppressed by donor doping.

The piezoelectric constant ( $d_{33}$ ) was measured at room temperature for all the compositions. All the samples were electrically poled prior to piezoelectric measurements. It is interesting to observe that the sample for  $x=0.025$  has higher  $d_{33}$  coefficient than that of the other compositions (Table III). It is related to the fact that composition corresponding to  $x=0.025$  has lowest conductivity among the samples studied in this work and thus allowing for better poling. The gained increment in  $d_{33}$  by W/Cr co-doping is very desirable, indicating a significant improved piezoelectric property due to W/Cr modification.

$\text{Bi}_4\text{Ti}_{3-x}\text{W}_x\text{O}_{12+x}$ +0.2wt% $\text{Cr}_2\text{O}_3$	$T_c$ (°C)	$\epsilon'$ at 100 kHz,	$\tan \delta$ at 100 kHz,	$d_{33}(\text{pC N}^{-1})$
$x=0.025$	658	178	0.02	22
$x=0.050$	650	186	0.021	17
$x=0.075$	648	197	0.023	16
$x=0.100$	645	205	0.028	14
$x=0.150$	640	211	0.028	12

Table 3. Physical characteristics for W/Cr modified BIT ceramics at room temperature.

The crystallographic evolution and phase analysis of  $\text{Bi}_4\text{Ti}_3\text{O}_{12}$ :W/Cr ceramics were determined by the XRD and the microstructural morphology was studied by SEM analysis.

The modification of W/Cr significantly improved the piezoelectric activity of the  $\text{Bi}_4\text{Ti}_3\text{O}_{12}$ :W/Cr ceramics. The Curie temperature decreased slightly with W/Cr modification increasing. Electrical relaxation mechanism was found to be similar for all the compositions. The excellent piezoelectric and dielectric properties coupled with high Curie temperature, demonstrated that the  $\text{Bi}_4\text{Ti}_{2.975}\text{W}_{0.025}\text{O}_{12.025}+0.2\text{wt}\%\text{Cr}_2\text{O}_3$  ( $x=0.025$ ) ceramics are promising candidates for high temperature applications.

### 3. Nb/Ta modified $\text{Bi}_4\text{Ti}_3\text{O}_{12}$ ceramics

Doped BIT is of interest in high-temperature piezoelectric sensors, because it remains ferroelectric at  $T > 600^\circ\text{C}$  and offers relatively high piezoelectric property (Kumar, 2001; Nagata, 1999; Noguchi, Sugibuchi, 1975; Shimakawa, 2000; Subbarao, 1961; 2000; Shulman, 2000; Shimazu, 1980). High leakage current and domain pinning due to defects in undoped BIT have appeared as obstacles for further applications. Unfortunately, the piezoelectric effect in high Curie temperature BIT is relatively low, with coefficient values less than  $10\text{ pC N}^{-1}$  for pure BIT and less than  $20\text{ pC N}^{-1}$  for modified  $\text{Bi}_4\text{Ti}_3\text{O}_{12}$ . To improve the piezoelectric property, Nb/Ta co-modified BIT ceramics were fabricated by a conventional solid-state reaction process and the influence of the  $\text{Nb}_2\text{O}_5/\text{Ta}_2\text{O}_5$  additive on the structure and electrical properties of the ceramics was investigated. The composition  $\text{Bi}_4\text{Ti}_{3-2x}\text{Nb}_x\text{Ta}_x\text{O}_{12}$  (BTNT,  $x=0, 0.01, 0.02, 0.04, 0.06$ ) polycrystals were prepared by the conventional solid-state reaction technique.

To investigate the effect of Nb/Ta modified BIT ceramics on the phase stability,  $\text{Bi}_4\text{Ti}_{3-2x}\text{Nb}_x\text{Ta}_x\text{O}_{12}$  powders calcined at  $800^\circ\text{C}$  for 4 h were prepared and their crystal structures were analyzed using XRD. Fig. 13 shows the XRD patterns of all samples. Diffraction data does not show any evidence of the formation of niobium and tantalum oxides or associated compounds that contain bismuth or titanium. This observation indicates that Nb/Ta ions in the BTNT ceramics do not form minority phase or segregate from the interior grain but dissolve into the perovskite lattice. Therefore, the BTNT ceramics maintains a layer structure similar to the perovskite BIT.

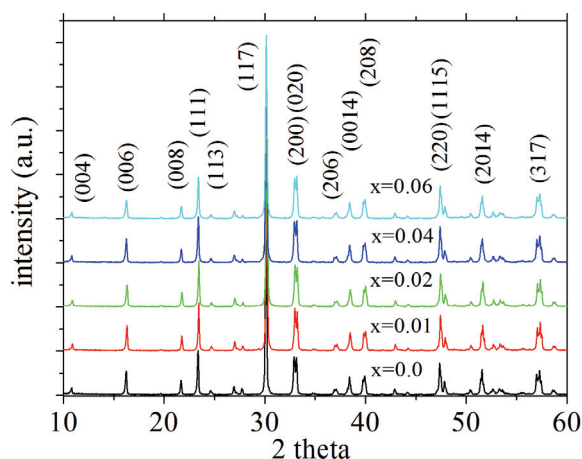


Fig. 13. XRD patterns of  $\text{Bi}_4\text{Ti}_{3-2x}\text{Nb}_x\text{Ta}_x\text{O}_{12}$  powders calcined at  $800^\circ\text{C}$  for 4 h on different Nb/Ta amounts.

The microstructures of BTNT ceramics are shown in Fig. 14. As figure 14 show average grain size ranging from approximately 40  $\mu\text{m}$  to 1 $\mu\text{m}$  in length decreased with increase of Nb/Ta amount, which suggested that the additive controlled the growth of the plate-like grains. The porosity was mainly located on grain boundaries. As is well known, both sintering and grain growth are closely associated with ion migration. Thus if the incorporation of  $\text{Nb}^{5+}/\text{Ta}^{5+}$  into BIT led to an increase in the activating energy for ion migration, a reduction in the rate of grain growth would be expected with increasing amounts of Nb/Ta. Furthermore, according to the sintering theory, the particle surface energy and grain boundary energy are the major driving forces for sintering and grain growth.

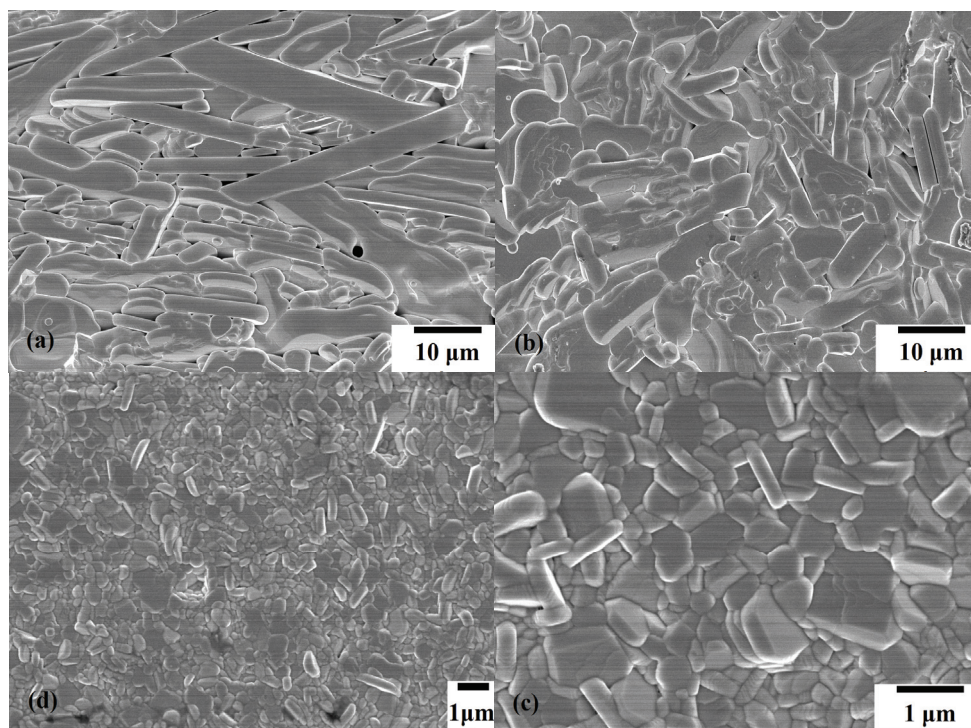


Fig. 14. SEM images of  $\text{Bi}_4\text{Ti}_{3-2x}\text{Nb}_x\text{Ta}_x\text{O}_{12}$  ceramics on different Nb/Ta amount: (a)  $x=0.01$ , (b)  $x=0.02$ , (c)  $x=0.04$ , (d)  $x=0.06$ .

BTNT ceramics sintered at the temperatures giving maximum density values were used for the measurement of dielectric property. Fig. 15 shows the permittivity,  $\epsilon_r$ , and dielectric loss,  $\tan\delta$ , of Nb/Ta-doped BIT ceramics as a function of temperature measured at a frequency of 100 KHz. The Curie temperatures of BTNT ceramics are found to be slightly lower than that of BIT ceramic, and gradually decreased from 675 to 630  $^\circ\text{C}$  with increasing Nb/Ta amounts due to the contribution of space charge and ionic motion (Fouskova, 1970). Moreover, the phase transition peaks become broad and diffusive, which may result from the cation-exchange between  $\text{Ti}^{4+}$  in  $\text{TiO}_6$  octahedra and  $\text{Nb}^{5+}/\text{Ta}^{5+}$  at the B sites to release the misfit strain due to the similar ionic radii (Nb: 0.69  $\text{\AA}$ , Ta: 0.64  $\text{\AA}$ , Ti: 0.605  $\text{\AA}$ ). For the dielectric

loss, there is a sudden increase in the curve, with a peak position slightly below the Curie temperature,  $T_c$ . After the  $T_c$ , the dielectric loss reaches a minimum value and then begins to increase once again. With increasing Nb/Ta amounts the peaks of the dielectric loss shifted to the lower temperature and even became flatter. So the activation energy of oxygen vacancy correspondingly increased with the distortion of lattice after doping enhances its hopping barrier. It is clear that the introduction of the  $Nb^{5+}/Ta^{5+}$  at B-site in BIT as donor impurities can effectively reduce the oxygen vacancies, which may be elucidated by the defect reaction:

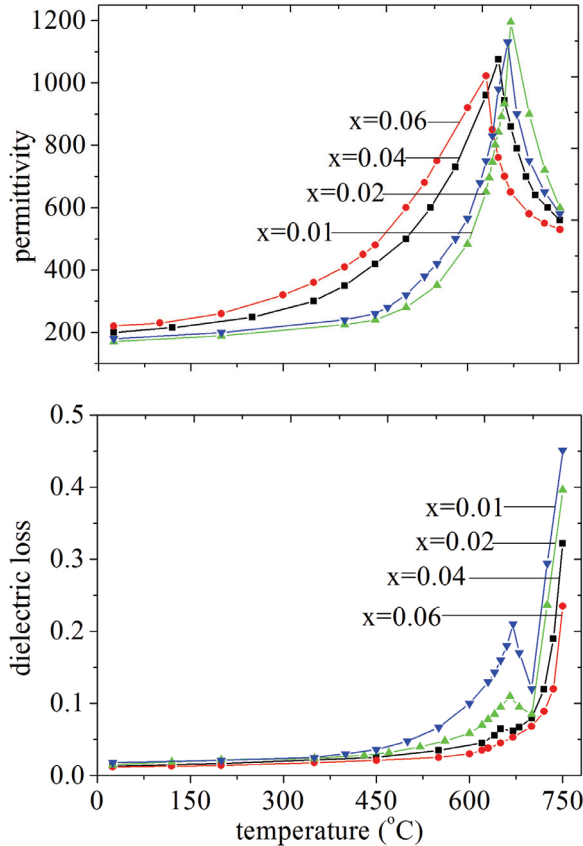
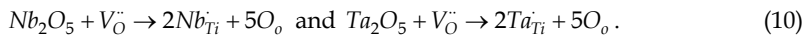


Fig. 15. Temperature dependence of permittivity and dielectric loss for BTNT ceramics on Nb/Ta amounts.



A decrease of the oxygen vacancy after the  $Nb^{5+}/Ta^{5+}$  doping results in the depression of the dielectric loss peak, which was consistent with previous reports (Shulman, 2000, 1996; Villegas, 1999). Thus B-site doping of equal valence can screen the effect of oxygen vacancy, which is contributing to an enhancement of the dielectric property of BTNT ceramics.

The selected room temperature properties of BTNT ceramics as a function of Nb/Ta amounts are characterized. Fig. 16c shows the permittivity and dielectric loss of the BTNT ceramics as a function of Nb/Ta amount. It was found that the room temperature permittivity of BTNT ceramics increased drastically whilst the dielectric loss decreased due to the depression of the oxygen vacancies with increasing Nb/Ta amounts. Figure 16a and 16b show the piezoelectric coefficient  $d_{33}$  and Curie temperature  $T_c$  of the BTNT ceramics for varying amounts of Nb/Ta. The  $d_{33}$  values first increased and reached a maximum value of 26 pC N<sup>-1</sup> for samples with  $x=0.01$ . However, previous research has shown that doping a small amount of Nb<sub>2</sub>O<sub>5</sub> or Ta<sub>2</sub>O<sub>5</sub> resulted in an increase in the  $d_{33}$ , from 8 to 20 pC N<sup>-1</sup> (Shulman, 1996, Shulman, 2000). The gained increment in  $d_{33}$  by Nb/Ta co-doping is very desirable, indicating a significant improvement in the piezoelectric property. The change in piezoelectric properties was explained with a grain size effect, namely, a sound grain growth with the addition of Nb<sub>2</sub>O<sub>5</sub>/Ta<sub>2</sub>O<sub>5</sub>, enables a consummate development of ferroelectric domains and thus improves the piezoelectric properties. As a result, there may be more crystallographic directions suitable for polarization, facilitating piezoelectricity. Based on decreasing dielectric loss, it's proposed that the grain size effects play a dominant role in the piezoelectric response. On the other hand, with decrease in oxygen vacancies diffusing to the domain wall in bulk, the pinning of the domain wall can decrease and the number of available switching domain walls can increase, resulting in enhancement of the  $d_{33}$ . But a further increase of concentration of Nb/Ta in BIT could act as pinning centres for domain walls and reduce their contribution to the piezoelectric effect, which is consistent with the previous reports that the addition of Nb and other cations in perovskite layer with dimensional mismatch between perovskite and bismuth oxide layers (Armstrong, 1972). It also can be seen the Nb/Ta doping causes more drastic decrease in the values of  $T_c$ . Thermal annealing behavior for the control and Nb/Ta modified BIT ceramics are shown in Figure 16d, where the piezoelectric coefficient,  $d_{33}$  are plotted against the annealing temperature. The values of  $d_{33}$  of the BTNT ceramics show no obvious drop, when the annealing temperature is lower than 500 °C. This reveals that BTNT orthorhombic structured materials are very stable to thermal annealing. When annealing temperature is higher than 500 °C, about 74 % of  $T_c$ , the piezoelectric coefficient of all BTNT ceramics decreases sharply, and tends to zero when the annealing temperature is above  $T_c$ .

The B-site vacancies Bi<sub>4</sub>Ti<sub>3-2x</sub>Nb<sub>x</sub>Ta<sub>x</sub>O<sub>12</sub> ceramics were synthesized by the solid-state reaction process. The analysis of the structure and the morphology were performed by XRD and FESEM. All the specimens maintained the orthorhombic structure and the addition of Nb<sub>2</sub>O<sub>5</sub>/Ta<sub>2</sub>O<sub>5</sub> caused a remarkably suppressed grain growth, which plays the dominant role in the piezoelectric response. This work also presented the considerable influence of Nb<sub>2</sub>O<sub>5</sub>/Ta<sub>2</sub>O<sub>5</sub> additive on the dielectric and piezoelectric properties. The Curie temperature,  $T_c$ , decreased from 675 to 630 °C while the permittivity increased drastically. The Nb/Ta doping at B-site could induce the distortion of oxygen octahedral and reduce the oxygen vacancy concentration by the compensating effect which is contributed to the enhancement of piezoelectric activity. The high piezoelectric coefficient  $d_{33}$  of Bi<sub>4</sub>Ti<sub>2.98</sub>Nb<sub>0.01</sub>Ta<sub>0.01</sub>O<sub>12</sub> ceramics controlled by precisely optimizing Nb/Ta amounts is found to be 26 pC N<sup>-1</sup>. All measurements demonstrated that BTNT ceramics are the promising candidates for high temperature applications.

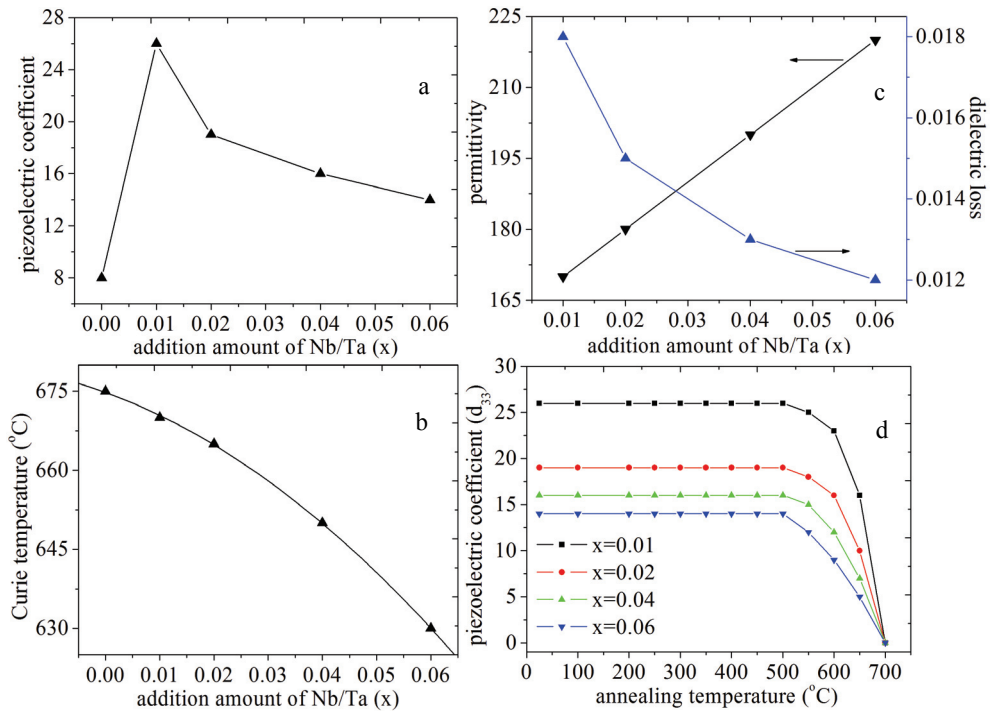


Fig. 16. Properties of  $\text{Bi}_4\text{Ti}_{3-2x}\text{Nb}_x\text{Ta}_x\text{O}_{12}$  ceramics for different Nb/Ta amounts at room temperature (a,b,c), effect of annealing temperature for 2 h on  $d_{33}$  of  $\text{Bi}_4\text{Ti}_{3-2x}\text{Nb}_x\text{Ta}_x\text{O}_{12}$  ceramics (d).

#### 4. Nb/Ta/Sb modified $\text{Bi}_4\text{Ti}_3\text{O}_{12}$ ceramics

Lead-based piezoelectric ceramics such as  $\text{Pb}(\text{Zr},\text{Ti})\text{O}_3$  (PZT), are widely used in piezoelectric actuators, sensors, and transducers due to their high relative permittivity, large remnant polarization, and excellent piezoelectric coefficients (Jaffe, 1971; Uchino, 2000). However, evaporation of toxic lead oxides during high temperature sintering produces environmental toxic burden and also generates instability of the composition and electrical properties of the ceramics. Thus, investigation of the possible use of ecologically clean lead-free ceramics in the field of science and technology is of great interest.

Bismuth titanate,  $\text{Bi}_4\text{Ti}_3\text{O}_{12}$  (BIT) is considered to be an excellent candidate as a key lead-free piezoelectric material owing to promising piezoelectric and ferroelectric properties. It is also a promising material for high temperature piezoelectric applications because of the high Curie temperature. However, as the spontaneous polarization movements are restricted to the  $a(b)$  plane of the unit cell (the  $c$ -axis component can be neglected), the ferroelectric and piezoelectric properties are much lower than those of PZT materials. It is likely, the piezoelectricity of pure BIT ceramics is low ( $d_{33} < 8 \text{ pC N}^{-1}$ ), due to the fact that it has high electrical conductivity and high coercive field which impedes the poling process (Ahn, 2009; Hou, 2010; Shulman, 2000, 1996; Villegas, 2004). The piezoelectric properties can be enhanced by grain orientation techniques (Jones, 2005; Zhang, 2005). However, these

processing methods such as hot forging or tape casting methods are not as cost effective as the production of ceramics via traditional powder pressing technologies. So, it is favourable to optimize piezoelectric properties via structural modification using appropriate doping. In this context, cations substitution to improve the piezoelectric properties of BIT have been considered and explored. It has been shown that the doping with donor cations such as  $\text{Nb}^{5+}$ ,  $\text{W}^{6+}$  or  $\text{Ta}^{5+}$  in the  $\text{Ti}^{4+}$  positions decreases electrical conductivity and improves piezoelectric properties of BIT ceramics (Azurmendi, 2006; Hou et al, 2010; Hong, 2000). We have reported that the value of  $d_{33}$  was 26  $\text{pC N}^{-1}$  for Nb/Ta doped BIT ceramics, fabricated via the conventional solid state reaction route (Hou, 2009).

It is noted that the studies concerning the effect of Sb doped lead-free piezoelectric ceramics have been reported earlier, exhibiting high-performance piezoelectric and dielectric properties (Saito, 2004; Zhao, 2008; Zhang, 2010). However, reports on Sb-doped BIT ceramics are scarce. To further study the piezoelectric property,  $\text{Sb}_2\text{O}_3$  has been considered for modifying  $\text{Bi}_4\text{Ti}_{3-2x}\text{Nb}_x\text{Ta}_x\text{O}_{12}$  (BTNT) ceramics via the conventional solid-state reaction route. The influence of the  $\text{Sb}_2\text{O}_3$  additive on the structural, morphological, dielectric, electrical conductivity and piezoelectric properties of the ceramics is investigated in this work.

Fig. 17 shows XRD patterns of BTNTS powders calcined at 800 °C for 4 h. The XRD analysis of BTNTS ceramic powders revealed the presence of BTNTS phase. Therefore, the BTNTS ceramics in the Sb substituted structure can maintain a layer perovskite structure similar to the parent BIT perovskite.

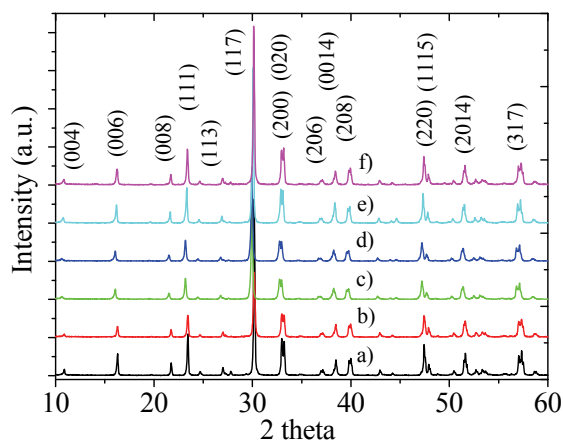


Fig. 17. XRD patterns of BTNTS powders calcined at 800 °C for 4 h with varying concentration of  $\text{Sb}_2\text{O}_3$ : a) 0BTNTS, b) 2BTNTS, c) 4BTNTS, d) 6BTNTS, e) 8BTNTS, f) 10BTNTS

The microstructures of BTNTS ceramics are shown in Fig. 18. The average grain size can be observed to be varying with the content of  $\text{Sb}_2\text{O}_3$ , suggesting that the additive controlled the growth of the plate-like grains of BTNTS. 8BTNTS ceramic has slight larger grains while there is a small variation in grain size for the other samples. Change in the microstructure with doping content is due to the reported formation of liquid phase (sillenite phase) which is generally observed during the synthesis of BIT (Rojero et al. 2010) (Although, this secondary phase was not detected in XRD due to small amounts (Fig. 17)). This liquid phase is increasing

with the increase in  $\text{Sb}_2\text{O}_3$  content and avail grain growth. 8BTNTS ceramic has larger grain size due to the presence of larger quantity of sillenite phase. However 10BTNTS ceramic samples were observed with smaller grains (Fig. 18(f)). It may be due to excess amount of antimony (after formation of solid solution) which reacted with sillenite phase and reduced it.

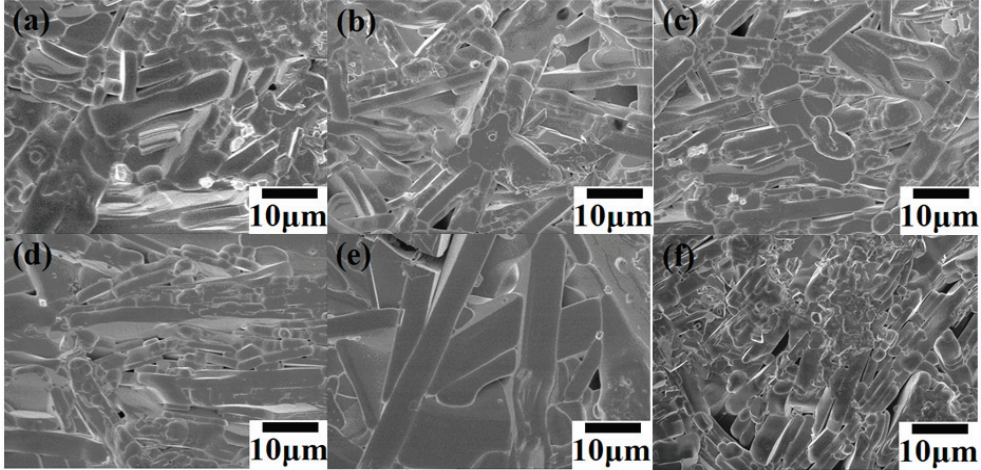


Fig. 18. SEM images of BTNTS ceramics with different  $\text{Sb}_2\text{O}_3$  content: a) 0BTNTS, b) 2BTNTS, c) 4BTNTS, d) 6BTNTS, e) 8BTNTS, f) 10BTNTS

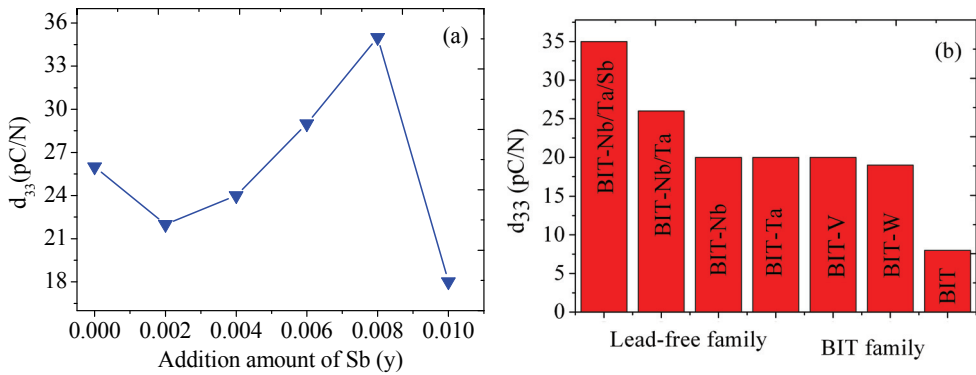


Fig. 19. Piezoelectric coefficients ( $d_{33}$ ) of BTNTS ceramics with different  $\text{Sb}_2\text{O}_3$  content at room temperature (a), comparison of  $d_{33}$  among 8BTNTS and BIT family (b) (BIT, BIT-W, BIT-Ta BIT-Nb, BIT-V, BIT-Nb/Ta)

Fig. 19 shows the variation of the piezoelectric coefficient ( $d_{33}$ ) with respect to the content of  $\text{Sb}_2\text{O}_3$  for the BTNTS ceramics. The value of  $d_{33}$  was found to be highest (35 pC N<sup>-1</sup>) for 8BTNTS ceramics. The  $d_{33}$  value is lower with deviation from 8BTNTS composition in both directions of increasing or decreasing the content of  $\text{Sb}_2\text{O}_3$ , but in all other compositions from 0 to 8, exceeds the hitherto maximum value of  $\sim 20$  pC N<sup>-1</sup>. The  $d_{33}$  (35 pC N<sup>-1</sup>) of

8BTNTS is 337.5%, 84.2%, 75% and 34.6% higher than that of BIT (Shulman, 1996), W-doped BIT (Zhang, 2004), V-doped BIT (Tang, 2006), Nb-doped BIT (Shulman, 2000), Ta-doped BIT (Hong, 2000), and Nb/Ta-doped BIT (Hou et al, 2009). The thermal annealing behaviors for the 0BTNTS, 8BTNTS and 10BTNTS ceramics are shown in Fig. 20, where the piezoelectric coefficient,  $d_{33}$  are dependent on the annealing temperature. The  $d_{33}$  values of the BTNTS ceramics show no obvious drop, when the annealing temperature is lower than 500 °C. This indicates that BTNTS monoclinic structured materials are very stable to thermal annealing. When annealing temperature is higher than 500 °C, the piezoelectric coefficients of the 0BTNTS, 8BTNTS and 10BTNTS ceramics decrease sharply, and tend to zero when the annealing temperature is above Curie temperature (675 °C). No obvious degradation of the 0BTNTS, 8BTNTS and 10BTNTS ceramics is observed below 500 °C.

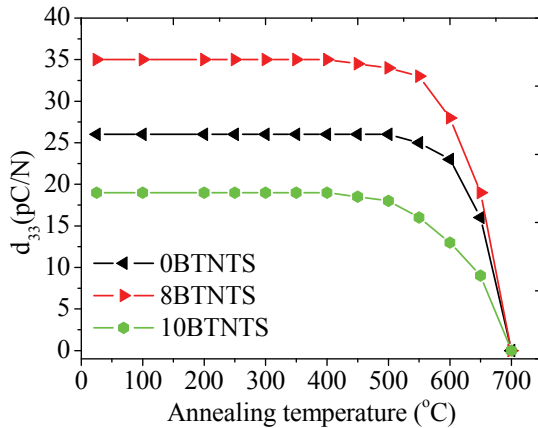


Fig. 20. Effect of annealing temperature for 2 h on  $d_{33}$  for 0BTNTS, 8BTNTS and 10BTNTS ceramics

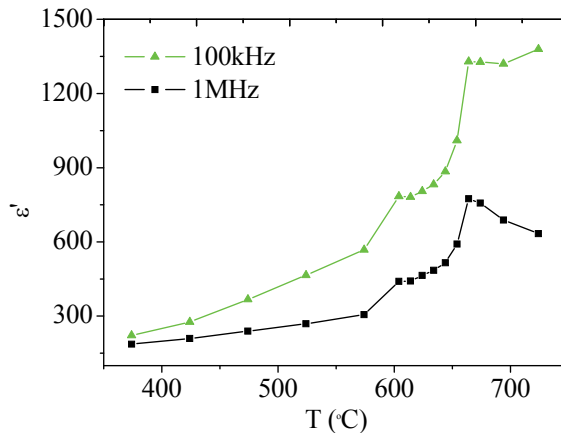


Fig. 21. Temperature dependence of permittivity for  $\text{Bi}_4\text{Ti}_{2.98}\text{Nb}_{0.01}\text{Ta}_{0.002}\text{Sb}_{0.008}\text{O}_{12}$  ceramics at 100 kHz and 1 MHz

It is well known that the electrical properties are of fundamental importance for the piezoelectric applications. It is therefore worthwhile to investigate these properties over a moderately wide frequency and temperature range for 8BTNTS samples (highest  $d_{33}$  value among the  $\text{Bi}_4\text{Ti}_3\text{O}_{12}$ -based ceramics). Fig. 21 shows the permittivity,  $\epsilon_r$ , of  $\text{Bi}_4\text{Ti}_{2.98}\text{Nb}_{0.01}\text{Ta}_{0.002}\text{Sb}_{0.008}\text{O}_{12}$  ceramics as a function of the temperature measured at 100 KHz and 1 MHz. Two peaks are observed at around 600 °C and 660 °C (at both frequencies (100 KHz and 1 MHz)) corresponding to the phase transformation of secondary and 8BTNTS phases, respectively. To confirm our results, the differential scanning calorimetric trace for 8BTNTS ceramics is depicted in Fig. 22. The sharp peak at 664 °C is associated with the phase transformation and ascribed as a Curie temperature which is in close agreement with that of the permittivity versus the temperature plots (Fig. 21). Though, another peak (600°C) was not detected in DSC trace.

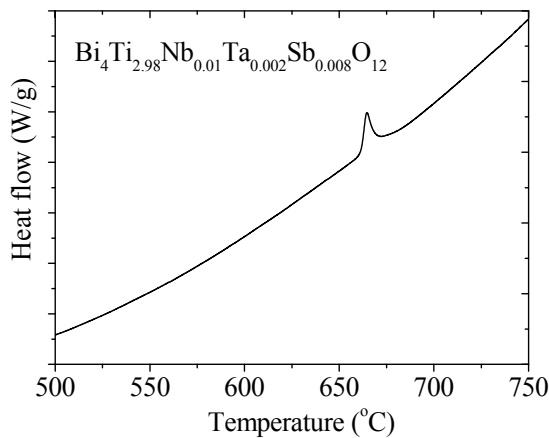


Fig. 22. DSC curve of  $\text{Bi}_4\text{Ti}_{2.98}\text{Nb}_{0.01}\text{Ta}_{0.002}\text{Sb}_{0.008}\text{O}_{12}$  ceramic

Fig. 23 depicts the frequency dependent (0.1 Hz~3 MHz) electrical conductivity for all the compositions at 600 °C. It is interesting to note that the electrical conductivity of 8BTNTS decreases significantly as compared with that of other ceramics. This difference in the value of electrical conductivity may be attributed to microscopic heterogeneity and random arrangement of cations in the structure due to Sb/Nb/Ta/Ti ions at B-site. We have reported that addition of Nb and Ta can directly introduce additional electrons for neutralizing the effect of  $p$ -type conductivity commonly observed in pure BIT (Shulman, 1996). These dopants also decrease the concentration of oxygen vacancy in the BIT doped by Nb/Ta. Sb has 3+ oxidation state in  $\text{Sb}_2\text{O}_3$  (0.76 Å ionic radii) and can not be fitted on  $\text{Ti}^{4+}$  site (0.605 Å). However it is reported (Peiteado, 2006) that  $\text{Sb}^{3+}$  is unstable above 500 °C and completely transform into  $\text{Sb}^{5+}$  (0.60 Å ionic radii) in the presence of  $\text{Bi}_2\text{O}_3$  oxide. It indicates that in the present study,  $\text{Sb}^{5+}$  ions are accommodated at  $\text{Ti}^{4+}$  sites since samples were sintered at 1100 °C. The amount of Sb added to the Nb/Ta doped BIT is in relatively small concentrations at the B-sites in the perovskite structure. In addition to the effect of reducing  $p$ -type conductivity, and decreasing oxygen vacancy concentration we can expect greater domain wall movement. Thus, Sb has the effect of controlling this switch to  $n$ -type conductivity while not impairing the decrease in  $p$ -type conductivity. In addition to donor

effect of antimony, it is noticed that the microstructures of these samples are also doping dependent (Fig. 18). Scanning electron micrographs (Fig. 18) show that 8BTNTS ceramics have larger grain size than that of the other investigated samples. It is reported that microstructure plays for electrical properties of BIT ceramics (Jardiel, 2006). Due to the decrease in electrical conductivity, the polarization is aided, facilitating the improved piezoelectricity. The possible explanation may be ascribed to decrease in the concentration of oxygen vacancies that can diffuse to domain walls in the piezoelectric ceramic, resulting in lowering the pinning of the domain walls, thus increasing the number of available switching domain walls and resulting in the enhancement of  $d_{33}$  (Zhang, 2006).

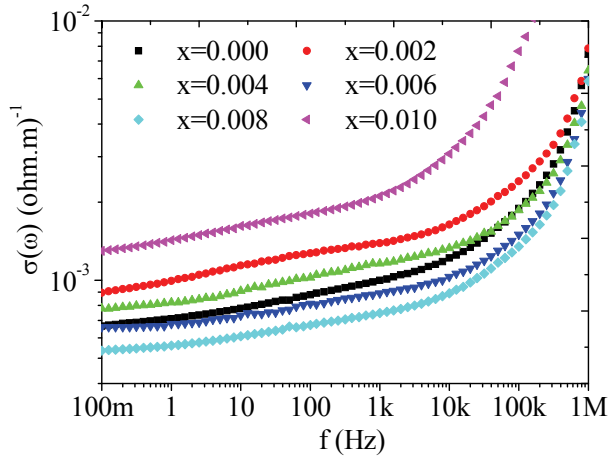


Fig. 23. Electrical conductivity of BTNTS ceramics with different  $\text{Sb}_2\text{O}_3$  content at  $600^\circ\text{C}$

In order to understand the conductivity mechanism in BTNTS ceramics, the ac conductivity plots that were obtained in the  $300\sim 600^\circ\text{C}$  temperature range for the 8BTNTS ceramics are shown in Fig. 24. The conductivity increases with increasing temperature due to thermal activation of conducting species in the samples. It exhibits two relaxations at different frequency region. The low frequency relaxation can be attributed to the grain boundary. As the frequency increases, the grain boundary resistance might become less than that of grain and grains dominate conductivity. The resistance and capacitance associated with grain and grain boundary interplay between their capacitive and dielectric contributions depending upon the frequency range. The high frequency conductivity is entirely due to the hopping of localized charge carriers. The bulk DC conductivity is difficult to ascertain from the above data (Fig. 24) because of significant contributions of grain boundary to the conductivity in low frequency regime.

The electric modulus approach was invoked to elucidate the electrical transport mechanism in 8BTNTS ceramics. The physical nature of the electric modulus (Macedo, 1972) is used to make a correlation between the conductivity and the relaxation of ions in these materials. This approach can effectively be employed to study bulk electrical behaviour of the moderately conducting samples. The complex electric modulus ( $M^*$ ) is defined in terms of the complex dielectric constant ( $\epsilon^*$ ) and is represented as:

$$M^* = (\epsilon^*)^{-1} \quad (11)$$

$$M' + iM'' = \frac{\epsilon_r'}{(\epsilon_r')^2 + (\epsilon_r'')^2} + i \frac{\epsilon_r''}{(\epsilon_r')^2 + (\epsilon_r'')^2} \quad (12)$$

where  $M'$ ,  $M''$  and  $\epsilon_r'$ ,  $\epsilon_r''$  are the real and imaginary parts of the electric modulus and dielectric constant, respectively. Effects of electrode polarization and the electrical conductivity can be suppressed using the electric modulus formalism. The real and imaginary parts of the modulus at different temperatures are calculated using Eq. 12 for the 8BTNTS ceramics and depicted in Figs. 25 (a) and 25 (b), respectively.

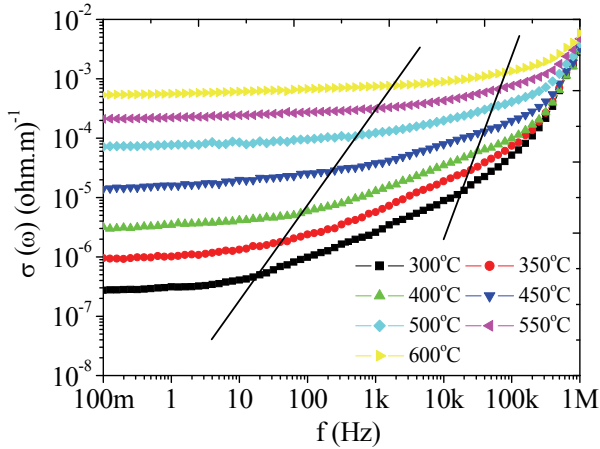


Fig. 24. Frequency dependence of ac conductivity at different temperatures for 8BTNTS ceramics

It is seen from Fig. 25 (a) that at low frequencies,  $M'$  approaches zero at all the temperatures under study suggesting the suppression of electrode polarization effects.  $M'$  reaches a maximum value corresponding to  $M_\infty = (\epsilon_\infty)^{-1}$  due to the relaxation process. It is also observed that the value of  $M_\infty$  decreases with the increase in temperature. The imaginary part of the electric modulus (Fig. 25 (b)) is indicative of the energy loss under electric field. The  $M''$  peak shifts to higher frequencies with increasing temperature. This suggests the involvement of temperature-dependent relaxation processes in the present ceramics. The frequency region below the  $M''$  peak indicates the range in which ions drift to long distances. In the frequency range which is above the peak, the ions are spatially confined to potential wells and free to move only within the wells. The frequency range where the peak occurs is suggestive of the transition from long-range to short-range mobility of ions.

The relaxation time associated with the process was determined from the plot of  $M''$  versus frequency. The activation energy involved in the relaxation process of ions can be obtained from the temperature dependent relaxation frequency ( $f_{max}$ ) as:

$$f_{max} = f_0 \exp\left(-\frac{E_R}{kT}\right) \quad (13)$$

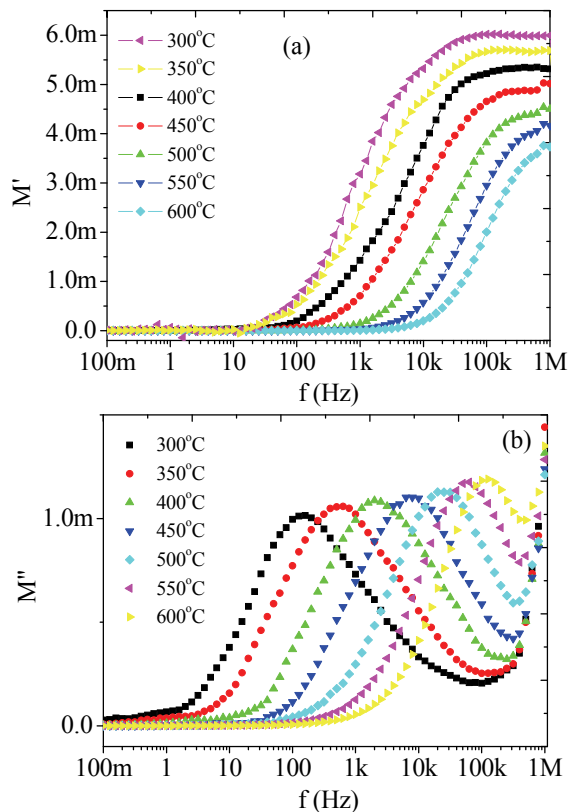


Fig. 25. (a) Real and (b) imaginary parts of the electric modulus as a function of frequency at different temperatures for 8BTNTS ceramics

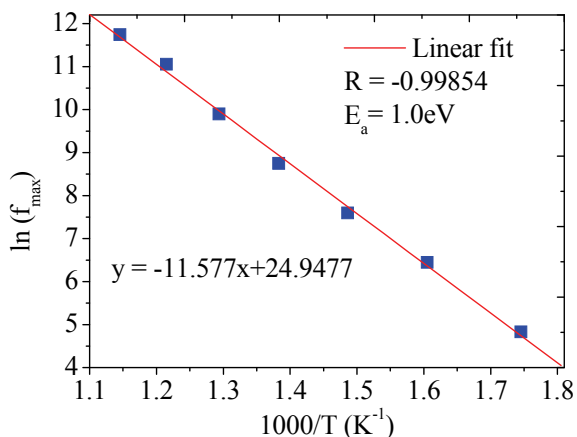


Fig. 26.  $\ln(f_{max})$  versus  $1000/T$  for 8BTNTS ceramics

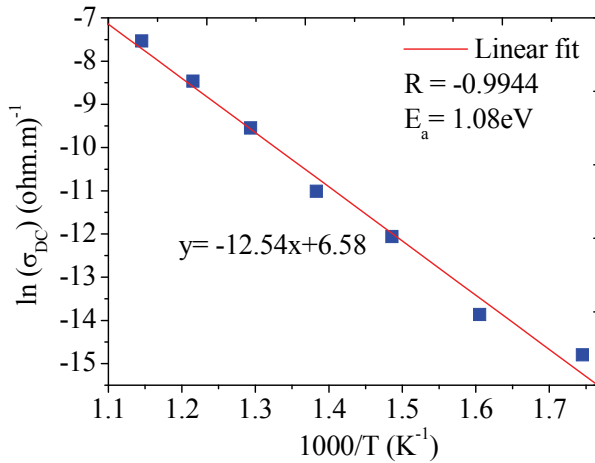


Fig. 27.  $\ln(\sigma_{DC})$  versus  $1000/T$  for 8BTNTS ceramics

where  $E_R$  is the activation energy associated with the relaxation process,  $f_0$  is the pre-exponential factor,  $k$  is the Boltzmann constant and  $T$  is the absolute temperature. Fig. 26 shows a plot between  $\ln(f_{max})$  and  $1000/T$  along with the theoretical fit (solid line) to the above equation (Eq. 13). The value that is obtained for  $E_R$  is  $1.00 \pm 0.03$  eV, which is ascribed to the motion of oxygen ions and is consistent with more reported in the literature. The value of activation energy for 8BTNTS ceramics is higher than that of activation energy reported for pure BIT (Uchino, 2000). An increase in the activation energy as compared to BIT is an indication of the reduction of oxygen vacancies in 8BTNTS ceramics. This is due to the fact that the hole compensation of bismuth vacancies promotes  $p$ -type electronic conductivity. When  $Sb^{5+}$  &  $Nb^{5+}$  &  $Ta^{5+}$  ions substitute  $Ti^{4+}$  and electrons will be created under charge neutrality restriction. These electrons neutralize the influence of the holes. The conductivity decreases with donor doping to a minimum value where the concentration of electron holes matches the electron concentration ( $p = n$ ). With a further increase in the donor ( $Sb^{5+}$  &  $Nb^{5+}$  &  $Ta^{5+}$ ) concentration the conductivity becomes  $n$ -type and starts to increase again.

The electric modulus can be expressed as the Fourier transform of a relaxation function  $\phi(t)$ :

$$M^* = M_\infty \left[ 1 - \int_0^\infty \exp(-\omega t) \left( -\frac{d\phi}{dt} \right) dt \right] \quad (14)$$

where the function  $\phi(t)$  is the time evolution of the electric field within the materials and is usually taken as the Kohlrausch-Williams-Watts (KWW) function (Kohlrausch, 1954; Williams, 1970):

$$\phi(t) = \exp \left[ - \left( \frac{t}{\tau_m} \right)^\beta \right] \quad (15)$$

where  $\tau_m$  is the conductivity relaxation time and the exponent  $\beta$  ( $0 < \beta < 1$ ) indicates the deviation from Debye type relaxation. The smaller the value of  $\beta$ , the larger is the deviation

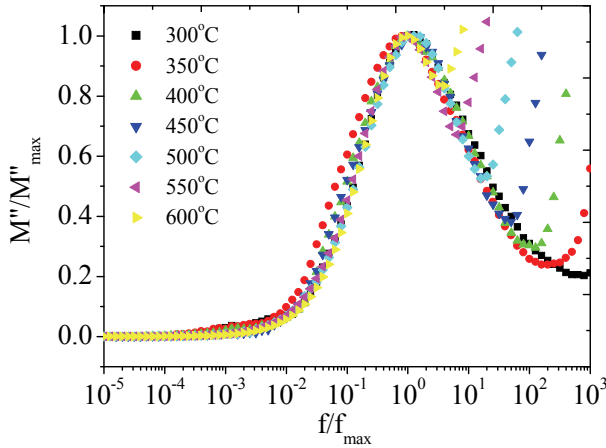


Fig. 28. Normalized plots of electric modulus against normalized frequency at various temperatures for 8BTNTS ceramics

from Debye-type relaxation. When  $\beta$  is close to zero, there exists a strong correlation between the hopping ions and its neighbouring ions. The  $\beta$  was calculated at different temperatures using the electric modulus formalism. For the ideal Debye type relaxation, the full-width half maximum (FWHM) of imaginary part of electric modulus is 1.14 decades. Therefore,  $\beta$  can be defined as  $1.14/\text{FWHM}$ . One can estimate DC conductivity at different temperatures using the electrical relaxation data. The DC conductivity can be expressed as (Ngai, 1984):

$$\sigma_{DC}(T) = \frac{\epsilon_o}{M_\infty(T) * \tau_m(T)} \left[ \frac{\beta}{\Gamma\left(\frac{1}{\beta}\right)} \right] \quad (16)$$

where  $\epsilon_o$  is the free space dielectric constant,  $M_\infty(T)$  is the reciprocal of high frequency dielectric constant and  $\tau_m(T)(1/2\pi f_{max})$  is the temperature dependent relaxation time. This equation is applicable to a variety of materials with low concentrations of charge carriers (Takahashi, 2004; Vaish, 2009). Calculation for DC conductivity from AC conductivity formalism causes a large error (due to electrode effect) that can be circumvented from the electrical relaxation formalism. Fig. 27 shows the DC conductivity data obtained from the above expression (Eq. 16) at various temperatures. The activation energy for the DC conductivity was calculated from the plot of  $\ln(\sigma_{DC})$  versus  $1000/T$  for BTNTS ceramics, which is shown in Fig. 27. The plot is found to be linear and fitted using following the Arrhenius equation,

$$\sigma_{DC}(T) = B \exp\left(-\frac{E_{DC}}{kT}\right) \quad (17)$$

where  $B$  is the pre-exponential factor and  $E_{DC}$  is the activation energy for the DC conduction. The activation energy is calculated from the slope of the fitted line and found to be  $1.08 \pm 0.02$  eV. This value for activation energy is in close agreement with the activation energy for

electrical relaxation. Fig. 28 represents the normalized plots of electric modulus  $M''$  as a function of frequency wherein the frequency is scaled by the peak frequency. A perfect overlapping of all the curves on a single master curve is not found. This shows that the conduction mechanism changed with temperature which is in good agreement with that of reported in literature (Takahashi et al 2004). Takahashi et al. reported that BIT exhibits mixed (ionic-p-type) conduction at high temperature and ionic conductivity was larger than hole conductivity in Curie temperature range.

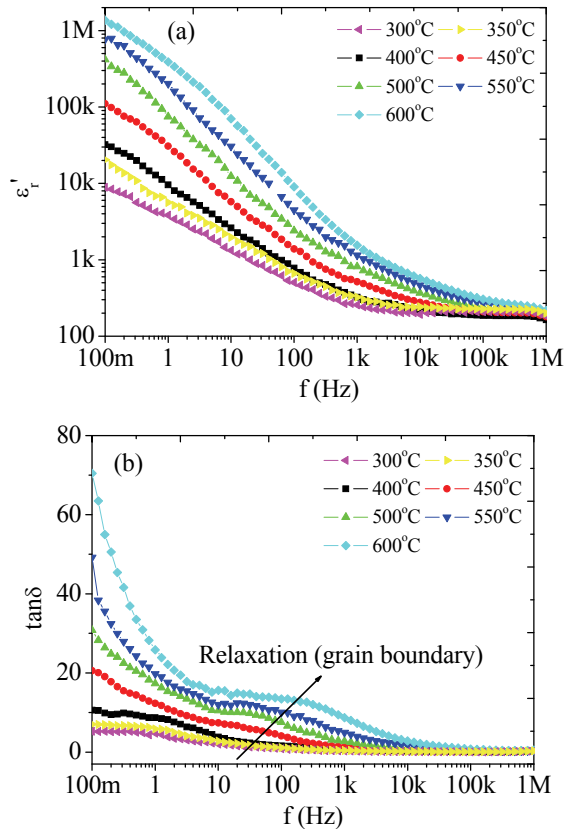


Fig. 29. The frequency dependence of (a) the dielectric constant and (b) loss at various temperatures for 8BTNTS ceramics

Fig. 29 shows the frequency dependence plots of permittivity ( $\epsilon'$ ) and dielectric loss ( $\tan\delta$ ) at various temperatures for 8BTNTS ceramics. It is evident that at all the temperatures (Fig. 29 (a)), the value of  $\epsilon'$  decreases with increasing frequency and attains a constant value. The high value of the dielectric constant in low-frequency regions is an extrinsic phenomenon arising due to the presence of metallic or blocking electrodes which do not permit the mobile ions to transfer into the external circuit, and as a result, mobile ions pile up near the

electrodes and give a large bulk polarization in the materials as well as oxygen ion polarization at grain boundaries. When the temperature rises, the dispersion region shifts towards higher frequencies and the nature of the dispersion changes at low frequencies due to the electrode polarization along with grain boundary effects. A plateau region at 500 °C was observed at moderately low frequencies that shifted to higher frequencies with increase in temperature (600 °C). This plateau region distinguished electrode polarizations to the grain boundary polarizations. The variation in the  $\tan\delta$  with the temperature at various frequencies (Fig. 29(b)) is consistent with that of the dielectric behaviour. The loss decreases with increase in frequency at different temperatures (300-600 °C). It is also observed that the dielectric loss increases with increase in temperature which is attributed to the increase in conductivity of the ceramics due to thermal activation of conducting species. The clear relaxation peak was not encountered at any temperature under study because of dominant DC conduction losses due to high oxygen ion mobility in the temperature range under study.

## 5. Conclusions

We have reported the effects of composition and crystal lattice structure upon microstructure, dielectric, piezoelectric and electrical properties of BIT,  $\text{Bi}_4\text{Ti}_3\text{-}_x\text{W}_x\text{O}_{12+x}+0.2\text{wt}\%\text{Cr}_2\text{O}_3$  (BTWC),  $\text{Bi}_4\text{Ti}_{3-2x}\text{Nb}_x\text{Ta}_x\text{O}_{12}$  (BTNT) and  $\text{Bi}_4\text{Ti}_{3-2x}\text{Nb}_x\text{Ta}_{x-y}\text{Sb}_y\text{O}_{12}$  (BTNTS) ceramics. WE have shown how doping can increase the piezoelectric coefficient of BIT. For the W/Cr samples, a  $d_{33}$  coefficient of 22 pC N<sup>-1</sup> was measured for  $x=0.025$ . The piezoelectric coefficient  $d_{33}$  of  $\text{Bi}_4\text{Ti}_{2.98}\text{Nb}_{0.01}\text{Ta}_{0.01}\text{O}_{12}$  ceramics controlled by precisely optimizing Nb/Ta amounts is found to be 26 pC N<sup>-1</sup>. The highest room temperature value of the piezoelectric coefficient is found to be 35 pC N<sup>-1</sup> for 8BTNTS ceramics. The antimony incorporation into the BTNT ceramics controlled electrical conductivity through reduction in the ionic and electronic conductivities as well as altered microstructure. The activation energy associated with the electrical relaxation determined from the electric modulus spectra was found to be  $1.0 \pm 0.03$  eV, close to that of the activation energy for DC conductivity ( $1.08 \pm 0.02$  eV). It suggests that the movements of oxygen ions are responsible for both ionic conduction as well as the relaxation process. These results demonstrated that 8BTNTS ceramic is a promising candidate for high temperature piezoelectric applications.

## 6. References

- Aurivillius, B. (1949) Mixed Bismuth Oxides with Layer Lattices: I. Structure Type of  $\text{CaBi}_2\text{B}_2\text{O}_9$ . *Ark. Kemi.* vol. 1, no. 54, pp. 463–480.
- Ahn, C.; Jeong, E.; Kim, Y.; et al. (2009) Piezoelectric Properties of Textured  $\text{Bi}_{3.25}\text{La}_{0.75}\text{Ti}_2.97\text{V}_{0.03}\text{O}_{12}$  Ceramics Fabricated by Reactive Templated Grain Growth Method. *J. Electroceramics*, 23, 392.
- Azurmendi, N.; Caro, I.; Caballero, A.; et al. (2006) Microwave-Assisted Reaction Sintering of Bismuth Titanate-Based Ceramics. *J. Am. Ceram. Soc.*, 89, 1232.
- Armstrong, R.; Newnham, E. (1972) Bismuth titanate solid solutions. *Mater. Res. Bull.* 7, 1025.
- Bergman, R. (2000) General Susceptibility Functions for Relaxations in Disordered Systems. *J. Appl. Phys.* 88, 1356. 179.
- Coondoo, I.; Jha A. and Agarwal S. (2007) Enhancement of dielectric characteristics in donor doped Aurivillius  $\text{SrBi}_2\text{Ta}_2\text{O}_9$  ferroelectric ceramics. *J. Eur. Ceram. Soc.*, 27, 253.

- Du, H.; Tang, L. & Kaskel, S. (2009) Preparation, Microstructure, and Ferroelectric Properties of  $\text{Bi}_{3.25}\text{La}_{0.75}\text{Ti}_{3-1}\text{M}_x\text{O}_{12}$  (M = Mo, W, Nb, V) Ceramics. *J. Phys. Chem. C*, 113, 1329.
- Ehara, S.; Muramatsu, K.; Shimazu, M.; et al. (1981) Dielectric Properties of  $\text{Bi}_4\text{Ti}_3\text{O}_{12}$  Below the Curie Temperature. *Jpn. J. Appl. Phys.*, 20, 877.
- Fouskova, A.; Cross, L. (1970) Dielectric Properties of Bismuth Titanate. *J. Appl. Phys.* 41, 2834.
- Hong, S.; Horn, J.; McKinstry, S.; et al. (2000) Dielectric and Ferroelectric Properties of Ta-doped Bismuth Titanate. *J. Mater. Sci. Lett.*, 19, 1661.
- Hong, S.; Horn, J.; McKinstry, S.; et al. (2000) Dielectric and Ferroelectric Properties of Ta-doped Bismuth Titanate. *J. Mater. Sci. Lett.*, 19, 1661.
- Hou, J.; Qu, Y.; Rahul, V.; Krsmanovic, D.; Kumar, R.V. (2010) Crystallographic Evolution, Dielectric and Piezoelectric Properties of  $\text{Bi}_4\text{Ti}_3\text{O}_{12}$ :W/Cr Ceramics. *J. Am. Ceram. Soc.* 93, 1414.
- Hou, J.; Kumar, R.V.; Qu, Y.; Krsmanovic, D. (2009) B-site Doping Effect on Piezoelectric Property of  $\text{Bi}_4\text{Ti}_{3-2x}\text{Nb}_x\text{Ta}_x\text{O}_{12}$  Ceramics. *Scripta Materialia*, 61, 664.
- Hou, J.; Rahul, V.; Qu, Kumar, R.V.; (2010) Dielectric and Pyroelectric Properties of  $\text{Bi}_4\text{Ti}_{2.98}\text{Nb}_{0.01}\text{Ta}_{0.01}\text{O}_{12}$  Ceramics. *Mater. Chem. Phys.* 121, 32.
- Hou, J.; Kumar, R.V.; Qu, Y.; Krsmanovic, D. Controlled synthesis of photoluminescent  $\text{Bi}_4\text{Ti}_3\text{O}_{12}$  nanoparticles from metal-organic polymeric precursor. *J. Nanopart. Res.*, 2010, 12, 563.
- Hou, J.; Kumar, R.V.; Qu Y.; Krsmanovic, D. Controlled synthesis of photoluminescent  $\text{Bi}_4\text{Ti}_3\text{O}_{12}$  nanoparticles from metal-organic polymeric precursor. *J. Nanopart. Res.*, 2010, 12, 563.
- Hong, S.; McKinstry, S.; Messing, G. (2000) Dielectric and Electromechanical Properties of Textured Niobium Doped Bismuth Titanate Ceramics. *J. Am. Ceram. Soc.* 83, 113.
- Hou, Y.; Lu, P.; Zhu, M.; et al. (2005) Effect of  $\text{Cr}_2\text{O}_3$  Addition on the Structure and Electrical Properties of  $\text{Pb}((\text{Zn}_{1/3}\text{Nb}_{2/3})_{0.20}(\text{Zr}_{0.50}\text{Ti}_{0.50})_{0.80})\text{O}_3$  Ceramics. *Mater. Sci. Eng. B*, 116, 104.
- Hyatt, N.; Reaney I. & Knight K. (2005) Ferroelectric-Paraelectric Phase Transition in the  $n = 2$  Aurivillius Phase  $\text{Bi}_3\text{Ti}_{1.5}\text{W}_{0.5}\text{O}_9$ : A Neutron Powder Diffraction Study. *Phys. Rev. B*, 71, 241191.
- Jardiel, T.; Caballero, A.; Villegas, M. (2006) Sintering Kinetic of  $\text{Bi}_4\text{Ti}_3\text{O}_{12}$  based Ceramics. *Bol. Soc. Esp. Ceram. V.*, 45, 202.
- Jardiel, T.; Rubia M. & Peiteado, M. (2008) Control of Functional Microstructure in  $\text{WO}_3$ -doped  $\text{Bi}_4\text{Ti}_3\text{O}_{12}$  Ceramics. *J. Am. Ceram. Soc.*, 91, 1083.
- Jardiel, T.; Villegas, M.; Caballero, A.; et al. (2008) Solid-State Compatibility in the System  $\text{Bi}_2\text{O}_3$ - $\text{TiO}_2$ - $\text{Bi}_2\text{WO}_6$ . *J. Am. Ceram. Soc.*, 91, 278.
- Jardiel, T.; Caballero, A.; Frutos J. & Villegas, M. (2006) Sintering and Electrical Properties of  $\text{Bi}_6\text{Ti}_3\text{WO}_{18}$  Ceramics. *Ferroelectrics* 336, 145.
- Jonscher, A. (1977) The 'Universal' Dielectric Response. *Nature*, 267, 673.
- Jaffe, B. (1971) Piezoelectric Ceramics India. Chap. 7.
- Jones, J.; Slamovich, E.; Bowman, K.; et al. (2005) Domain Switching Anisotropy in Textured Bismuth Titanate Ceramics. *J. Appl. Phys.*, 98, 104102.
- Kohlrausch, R. (1954) Theorie Des Elektrischen Rückstandes in Der Leidner Flasche. *Prog. Ann. Phys.*, 91,

- Li, J. & Sun. Q. (2008) Effects of  $\text{Cr}_2\text{O}_3$  Doping on the Electrical Properties and the Temperature Stabilities of PZT Binary Piezoelectric Ceramics. *Rare Metals*, 27, 362.
- Kumar, M. & Ye. Z. (2001) Dielectric and electric properties of the donor- and acceptor-doped ferroelectric  $\text{SrBi}_2\text{Ta}_2\text{O}_9$ . *J. Appl. Phys.* 90, 934.
- Kan, Y.; Jin, X.; Zhang, G.; et al. (2004) Lanthanum Modified Bismuth Titanate Prepared by a Hydrolysis Method. *J. Mater. Chem.*, 14, 3566.
- Lopatin, S. (1989) Translated from *Izvestiya Akademii Nauk SSSR, Neorganicheskie Materialy* 24, 1551.
- Luo, S.; Noguchi, Y.; Miyayama M. & Kudo. T. (2001) Rietveld Analysis and Dielectric Properties of  $\text{Bi}_2\text{WO}_6\text{-Bi}_4\text{Ti}_3\text{O}_{12}$  Ferroelectric System. *Mater. Res. Bull.*, 36, 531.
- Luo, S.; Noguchi, Y.; Miyayama M. & Kudo. T. (2001) Rietveld Analysis and Dielectric Properties of  $\text{Bi}_2\text{WO}_6\text{-Bi}_4\text{Ti}_3\text{O}_{12}$  Ferroelectric System. *Mater. Res. Bull.*, 36, 531.
- Macedo, P.; Moynihan, C.; Bose. R. (1972) Role of Ionic Diffusion in Polarization in Vitreous Ionic Conductors. *Phys. Chem. Glasses*, 13, 171.
- Markovec, D.; Pribošić, I.; Samardžija, Z.; Drofenik. M. (2001) Incorporation of Aliovalent Dopants into the Bismuth-Layered Perovskite-Like Structure of  $\text{BaBi}_4\text{Ti}_4\text{O}_{15}$ . *J. Am. Ceram. Soc.* 84, 2702.
- Noguchi, Y.; Miwa, I.; Goshima, Y.; et al. (2000) Oxygen-vacancy-induced  $90^\circ$ -domain clamping in ferroelectric  $\text{Bi}_4\text{Ti}_3\text{O}_{12}$  single crystals. *Jpn. J. Appl. Phys.* 39, L1259.
- Nagata, H. (2004) Ceramic Transactions. Ceramic Materials and Multilayer Electronic Devices. *J. Am. Ceram. Soc.*, 150.
- Nagata, H.; Chikushi, N.; Takenaka T. (1999) Piezoelectric Properties of Bismuth Layer-Structured Ferroelectric Ceramics with Sr-Bi-Ti-Ta System. *Jpn. J. Appl. Phys.* 38, 5497.
- Ngai, K.; Rendell, R.; Jain. H. (1984) Anomalous Isotope-mass Effect in Lithium Borate Glasses: Comparison with a Unified Relaxation Model. *Phys. Rev. B*, 30, 2133.
- Peiteado, M.; Rubia, M.; Fernandez, J.; et al. (2006) Thermal Evolution of  $\text{ZnO-Bi}_2\text{O}_3\text{-Sb}_2\text{O}_3$  System in the Region of Interest for Varistor. *J. Mater. Sci.*, 41, 2319.
- Rojero, M.; Romero, J.; Marcos, F.; et al. (2010) Intermediate Phases Formation During the Synthesis of  $\text{Bi}_4\text{Ti}_3\text{O}_{12}$  by Solid State Reaction. *Ceram. Int.*, 36, 1319.
- Shulman, H.; Damjanovic, D.; Setter. N. (2000) Niobium Doping and Dielectric Anomalies in Bismuth Titanate. *J. Am. Ceram. Soc.* 83, 528.
- Shulman, H.; Testorf, M.; Damjanovic, D.; Setter. N. (1996) Microstructure, Electrical Conductivity, and Piezoelectric Properties of Bismuth Titanate. *J. Am. Ceram. Soc.* 79, 3124.
- Shimazu, M.; Tanaka, J.; Muramatsu, K.; et al. (1980) Phase transition in the family  $\text{La}_x\text{Bi}_{4-x}\text{Ti}_3\text{O}_{12}$ : In relation to lattice symmetry and distortion. *J. Solid State Chem.* 35, 402.
- Sugibuchi, K.; Kurogi, Y.; Endo. N. (1975) Ferroelectric field-effect memory device using  $\text{Bi}_4\text{Ti}_3\text{O}_{12}$  film. *J. Appl. Phys.* 47, 2877.
- Snyder, R.; Fiala, J. & Bunge. J. (1999) Defect and Microstructure Analysis by Diffraction. International Union of Crystallography, Oxford Science Publication, Oxford.
- Subbarao, E. (1961). Ferroelectricity in  $\text{Bi}_4\text{Ti}_3\text{O}_{12}$  and Its Solid Solutions. *Phys. Rev.* 122, 804.
- Saito, Y.; Takao, H.; Tani, T.; et al. (2004) Lead-free piezoceramics. *Nature*, 432, 84.

- Shimakawa, Y.; Kubo, Y.; Tauchi, Y.; et al. (2000) Structural distortion and ferroelectric properties of  $\text{SrBi}_2(\text{Ta}_{1-x}\text{Nb}_x)_2\text{O}_9$ . *Appl. Phys. Lett.* 77, 2749.
- Takahashi, M.; Noguchi, Y. & Miyayama. M. (2003) Effects of V-Doping on Mixed Conduction Properties of Bismuth Titanate Single Crystals. *Jpn. J. Appl. Phys.*, 42, 6222.
- Takahashi, M.; Noguchi, Y.; Miyayama. M. (2004) Estimation of Ionic and Hole Conductivity in Bismuth Titanate Polycrystals at High Temperatures. *Solid State Ionics*, 172, 325.
- Takahashi, M. (1970) Space Charge Effect in Lead Zirconate Titanate Ceramics Caused by the Addition of Impurities. *Japan J. Appl. Phys.*, 9, 1236.
- Tang, Q.; Kan, Y.; Li, Y.; et al. (2006) Effect of Vanadium Doping on Fabrication and Property of  $\text{Bi}_4\text{Ti}_3\text{O}_{12}$  Ceramics. *Scripta Materialia*, 54, 2075.
- Tang, Q.; Kan, Y.; Li, Y.; et al. (2007) Ferroelectric and Dielectric Properties of Nd/V Co-doped  $\text{Bi}_4\text{Ti}_3\text{O}_{12}$  Ceramics. *Solid State Commun.*, 142, 1.
- Takenaka, T. & Sakata. K. (1981) Electrical properties of grain-oriented ferroelectric ceramics in some lanthanum modified layer-structure oxides. *Ferroelectrics*. 38, 769.
- Uchino, K. (2000) *Ferroelectric Devices*, New York. Chap. 7.
- Villegas, M.; Caballero, A.; Moure, C.; et al. (1999) Factors Affecting the Electrical Conductivity of Donor-Doped  $\text{Bi}_4\text{Ti}_3\text{O}_{12}$  Piezoelectric Ceramics. *J. Am. Ceram. Soc.* 82, 2411.
- Villegas, M.; Caballero, A.; Moure, C.; et al. (1999) Low-temperature sintering and electrical properties of chemically W-doped  $\text{Bi}_4\text{Ti}_3\text{O}_{12}$  ceramics. *J. Eur. Ceram. Soc.* 19, 1183.
- Villegas, M.; Jardiel, T & Farias. G. (2004) Sintering and Electrical Properties of  $\text{Bi}_4\text{Ti}_{2.95}\text{W}_x\text{O}_{11.9+3x}$  piezoelectric ceramics. *J. Eur. Ceram. Soc.*, 24, 1025.
- Vaish, R.; Varma. K. (2009) Dielectric Properties of  $\text{Li}_2\text{O}-3\text{B}_2\text{O}_3$  Glasses. *J. Appl. Phys.*, 106, 064106.
- Vaish, R.; Varma. K. (2009) Low Loss and Frequency (1 kHz-1 MHz) Independent Dielectric Characteristics of  $3\text{BaO}-3\text{TiO}_2-\text{B}_2\text{O}_3$  Glasses. *J. Appl. Phys.*, 106, 114109.
- Williams G. & Watts. D. (1970) Non-Symmetrical Dielectric Relaxation Behaviour Arising from a Simple Empirical Decay Function. *Trans. Faraday Soc.*, 66, 80.
- Yang, Z.; Zhang, R.; Yang, L.; et al. (2007) Effects of  $\text{Cr}_2\text{O}_3$  Doping on the Electrical Properties and the Temperature Stabilities of PNW-PMN-PZT Ceramics. *Mater. Res. Bull.*, 42, 2156.
- Zhang, H.; Yan H. and Reece. M. (2009) The Effect of Nd Substitution on the Electrical Properties of  $\text{Bi}_3\text{NbTiO}_9$  Aurivillius Phase Ceramics. *J. Appl. Phys.*, 106, 044106.
- Zhao, P. & Zhang. B. (2008) High Piezoelectric  $d_{33}$  Coefficient in Li/Ta/Sb-Codoped Lead-Free (Na,K)NbO<sub>3</sub> Ceramics Sintered at Optimal Temperature. *J. Am. Ceram. Soc.*, 91, 3078.
- Zhang, L.; Zhao, S.; Yu, H.; et al. (2004) Microstructure and Electrical Properties of Tungsten-Doped Bismuth Titanate Ceramics. *Jap. J. Appl. Phys.*, 43, 7613.
- Zhang, L.; Chu, R.; Zhao, S.; et al. (2005) Microstructure and Electrical Properties of Niobium Doped  $\text{Bi}_4\text{Ti}_3\text{O}_{12}$  Layer-structured Piezoelectric Ceramics. *Mater. Sci. Eng. B*, 116, 99.
- Zhou, Z.; Dong, X.; Yan, H.; et al. (2006) Doping Effects on the Electrical Conductivity of Bismuth Layered  $\text{Bi}_3\text{TiNbO}_9$ -based Ceramics. *J. Appl. Phys.*, 100, 044112.
- Zhang, Q.; Zhang, B.; Li, H.; et al. (2010) Effects of Sb content on electrical properties of lead-free piezoelectric  $[(\text{Na}_{0.535}\text{K}_{0.480})_{0.942}\text{Li}_{0.058}](\text{Nb}_{1-x}\text{Sb}_x)\text{O}_3$  ceramics. *J. Ally. Compd.*, 490, 260.

## **Part 3**

# **Magnetoelectrics and Multiferroics**



# Magnetolectric Multiferroic Composites

M. I. Bichurin<sup>1</sup>, V. M. Petrov<sup>1</sup> and S.Priya<sup>2</sup>

<sup>1</sup>Novgorod State University

<sup>2</sup>Virginia Tech

<sup>1</sup>Russia

<sup>2</sup>USA

## 1. Introduction

Magnetolectric (ME) multiferroics are materials in which ferromagnetism and ferroelectricity occur simultaneously and coupling between the two is enabled. Applied magnetic field  $\mathbf{H}$  gives rise to an induced polarization  $\mathbf{P}$  which can be expressed in terms of magnetic field by the expression,  $\mathbf{P}=\mathbf{aH}$ , where  $\mathbf{a}$  is the ME-susceptibility tensor. Most of the known single-phase ME materials are known to show a weak ME coupling (Fiebig, 2005; Kita et al., 1988; Wang et al., 2003; Prellier et al., 2005; Cheong et al., 2007). A composite of piezomagnetic and piezoelectric phases is expected to have relatively strong ME coupling. ME interaction in a composite manifests itself as inducing the electrical voltage across the sample in an applied ac magnetic field and arises due to combination of magnetostriction in magnetic phase and piezoelectricity in piezoelectric phase through mechanical coupling between the components (Ryu et al., 2001; Nan et al., 2008; Dong et al., 2003; Cai et al., 2004; Srinivasan et al., 2002).

In last few years, strong magneto-elastic and elasto-electric coupling has been achieved through optimization of material properties and proper design of transducer structures. Lead zirconate titanate (PZT)-ferrite and PZT-Terfenol-D are the most studied composites to-date (Dong et al., 2005; Dong et al.,2006b; Zheng et al., 2004a; Zheng et al., 2004b). One of largest ME voltage coefficient of  $500 \text{ Vcm}^{-1}\text{Oe}^{-1}$  was reported recently for a high permeability magnetostrictive piezofiber laminate (Nan et al., 2005; Liu et al., 2005). These developments have led to magnetolectric structures that provide high sensitivity over a varying range of frequency and DC bias fields enabling the possibility of practical applications.

In this paper, we focus on four broad objectives. First, we discuss detailed mathematical modeling approaches that are used to describe the dynamic behavior of ME coupling in magnetostrictive-piezoelectric multiferroics at low-frequencies and in electromechanical resonance (EMR) region. Expressions for ME coefficients were obtained using the solution of elastostatic/elastodynamic and electrostatic/magnetostatic equations. The ME voltage coefficients were estimated from the known material parameters. The basic methods developed for decreasing the resonance frequencies were analyzed. The second type of resonance phenomena occurs in the magnetic phase of the magnetolectric composite at much higher frequencies, called as ferromagnetic resonance (FMR). The estimates for electric field induced shift of magnetic resonance line were derived and analyzed for

varying boundary conditions. Our theory predicts an enhancement of ME effect that arises from interaction between elastic modes and the uniform precession spin-wave mode. The peak ME voltage coefficient occurs at the merging point of acoustic resonance and FMR frequencies.

Second, we present the experimental results on lead – free magnetostrictive –piezoelectric composites. These newly developed composites address the important environmental concern of current times, i.e., elimination of the toxic “lead” from the consumer devices. A systematic study is presented towards selection and design of the individual phases for the composite. Third, experimental data from wide range of measurement and literature was used to validate the theoretical models over a wide frequency range.

Lastly, the feasibility for creating new class of functional devices based on ME interactions is addressed. Appropriate choice of individual phases with high magnetostriction and piezoelectricity will allow reaching the desired magnitude of ME coupling as deemed necessary for engineering applications over a wide bandwidth including the electromechanical, magnetoacoustic and ferromagnetic resonance regimes. Possibilities for application of ME composites in fabricating ac magnetic field sensors, current sensors, transformers, and gyrators are discussed. ME multiferroics are shown to be of interest for applications such as electrically-tunable microwave phase-shifters, devices based on FMR, magnetic-controlled electro-optical and piezoelectric devices, and electrically-readable magnetic memories.

## 2. Low-frequency magnetoelectric effect in magnetostrictive-piezoelectric bilayers

We consider only (symmetric) extensional deformation in this model and at first ignore any (asymmetric) flexural deformations of the layers that would lead to a position dependent elastic constants and the need for perturbation procedures. For the polarized piezoelectric phase with the symmetry  $\infty m$ , the following equations can be written for the strain and electric displacement:

$$\begin{aligned} {}^p S_i &= {}^p s_{ij} {}^p T_j + {}^p d_{ki} {}^p E_k; \\ {}^p D_k &= {}^p d_{ki} {}^p T_i + {}^p \epsilon_{kn} {}^p E_n; \end{aligned} \quad (1)$$

where  ${}^p S_i$  and  ${}^p T_j$  are strain and stress tensor components of the piezoelectric phase,  ${}^p E_k$  and  ${}^p D_k$  are the vector components of electric field and electric displacement,  ${}^p s_{ij}$  and  ${}^p d_{ki}$  are compliance and piezoelectric coefficients, and  ${}^p \epsilon_{kn}$  is the permittivity matrix. The magnetostrictive phase is assumed to have a cubic symmetry and is described by the equations:

$$\begin{aligned} {}^m S_i &= {}^m s_{ij} {}^m T_j + {}^m q_{ki} {}^m H_k; \\ {}^m B_k &= {}^m q_{ki} {}^m T_i + {}^m \mu_{kn} {}^m H_n; \end{aligned} \quad (2)$$

where  ${}^m S_i$  and  ${}^m T_j$  are strain and stress tensor components of the magnetostrictive phase,  ${}^m H_k$  and  ${}^m B_k$  are the vector components of magnetic field and magnetic induction,  ${}^m s_{ij}$  and  ${}^m q_{ki}$  are compliance and piezomagnetic coefficients, and  ${}^m \mu_{kn}$  is the permeability matrix. Equation (2) may be considered in particular as a linearized equation describing the effect of

magnetostriction. Assuming in-plane mechanical connectivity between the two phases with appropriate boundary conditions, ME voltage coefficients can be obtained by solving Eqs.(1) and (2).

**2.1 Longitudinal ME effect**

We assume (1,2) as the film plane and the direction-3 perpendicular to the sample plane. The bilayer is poled with an electric field  $E$  along direction-3. The bias field  $H_0$  and the ac field  $H$  are along the same direction as  $E$  and the resulting induced electric field  $E$  is estimated across the sample thickness. Then we find an expression for ME voltage coefficient  $\alpha_{E,L} = a_{E,33} = E_3/H_3$ . The following boundary conditions should be used for finding the ME coefficient:

$$\begin{aligned} {}^p S_i &= {}^m S_i; (i = 1,2) ; \\ {}^p T_i &= -{}^m T_i(1-v) / v; (i = 1,2); \end{aligned} \tag{3}$$

where  $v = {}^p v / ({}^p v + {}^m v)$  and  ${}^p v$  and  ${}^m v$  denote the volume of piezoelectric and magnetostrictive phase, respectively. Taking into account Eqs. (1) and (2) and the continuity conditions for magnetic and electric fields, Eqs. (3) and open circuit condition enables one to obtain the following expressions for longitudinal ME voltage coefficient.

$$\begin{aligned} \alpha_{E,33} &= \frac{E_3}{H_3} = 2 \frac{\mu_0 v(1-v)^p d_{31}^m q_{31}}{\{2^p d_{31}^2(1-v) + {}^p \epsilon_{33} [({}^p s_{11} + {}^p s_{12})(v-1) - v({}^m s_{11} + {}^m s_{12})]\}} \times \\ &\times \frac{[({}^p s_{11} + {}^p s_{12})(v-1) - v({}^m s_{11} + {}^m s_{12})]}{\{\mu_0(v-1) - {}^m \mu_{33} v\} [v({}^m s_{12} + {}^m s_{11}) - ({}^p s_{11} + {}^p s_{12})(v-1)] + 2^m q_{31}^2 v^2} \end{aligned} \tag{4}$$

In deriving the above expression, we assumed the electric field to be zero in magnetic phase since magnetostrictive materials that are used in the case under study have a small resistance compared to piezoelectric phase. Thus the voltage induced across the piezoelectric layer is the output voltage. Estimate of ME voltage coefficient for cobalt ferrite (CFO) gives  $\alpha_{E,33} = 325$  mV/(cm Oe). However, considering CFO as a dielectric results in  $\alpha_{E,33} = 140$  mV/(cm Oe) (Osaretin & Rojas, 2010) while the experimental value is 74 mV/(cm Oe) (Harshe et al., 1993). We believe CFO should be considered as a conducting medium compared to dielectric PZT in the low-frequency region in accordance with our model. The discrepancy between theoretical estimates and data can be accounted for by features of piezomagnetic coupling in CFO and interface coupling of bilayer (Bichurin et al., 2003a). Harshe et al. obtained an expression for longitudinal ME voltage coefficient of the form

$$\alpha'_{E,33} = \frac{-2v(v-1)^p d_{13}^m q_{31}}{\left({}^m s_{11} + {}^m s_{12}\right)^p \epsilon^T_{33} v + \left({}^p s_{11} + {}^p s_{12}\right)^p \epsilon^T_{33} (1-v) - 2 \left({}^p d_{13}\right)^2 (1-v)} \tag{5}$$

The above equation corresponds to a special case of our theory in which one assumes  ${}^m \mu_{33} / \mu_0 = 1$ . Thus the model considered here leads to an expression for the longitudinal ME coupling and allows its estimation as a function of volume of the two phases, composite permeability, and interface coupling.

## 2.2 Transverse ME effect

This case corresponds to the poling direction along direction-3 and  $H_0$  and  $H$  along direction-1 (in the sample plane). Here we estimate the ME coefficient  $a_{E,T} = a_{E,31} = E_3/H_1$ . Once again, Eqs.(1)-(3) lead to the following expression for transverse ME voltage coefficient.

$$\alpha_{E,31} = \frac{E_3}{H_1} = \frac{-v(1-v)({}^m q_{11} + {}^m q_{21}){}^p d_{31}}{{}^p \epsilon_{33}({}^m s_{12} + {}^m s_{11})v + {}^p \epsilon_{33}({}^p s_{11} + {}^p s_{12})(1-v) - 2{}^p d_{31}^2(1-v)} \quad (6)$$

## 2.3 In-plane longitudinal ME effect

Finally, we consider a bilayer poled with an electric field  $E$  in the plane of the sample. The in-plane fields  $H_0$  and  $H$  are parallel and the induced electric field  $E$  is measured in the same direction (axis-1). The ME coefficient is defined as  $a_{E,IL} = a_{E,11} = E_1/H_1$ . Expression for  $a_E$  is given below.

$$\begin{aligned} \alpha_{E,11} = & \left( ({}^m q_{11} ({}^p s_{33} {}^p d_{11} - {}^p s_{12} {}^p d_{12}) + {}^m q_{12} ({}^p s_{11} {}^p d_{12} - {}^p s_{12} {}^p d_{11})) (1-v) + \right. \\ & \left. + ({}^m q_{11} ({}^m s_{11} {}^p d_{11} - {}^m s_{12} {}^p d_{12}) + {}^m q_{12} ({}^m s_{11} {}^p d_{12} - {}^m s_{12} {}^p d_{11})) v \right) v(1-v) / \\ & / \left( ((1-p) {}^m \epsilon_{11} + v {}^p \epsilon_{11}) [(1-v)^2 ({}^p s_{11} {}^p s_{33} - {}^p s_{12}^2) + (1-v)v ({}^m s_{11} {}^p s_{11} + {}^p s_{33} {}^m s_{11} - \right. \\ & - 2{}^p s_{12} {}^m s_{12}] + v^2 ({}^m s_{11}^2 - {}^m s_{12}^2) \Big) - v(1-p)^2 [2{}^p s_{12} {}^p d_{11} {}^p d_{12} - {}^p s_{33} {}^p d_{11}^2 - \\ & \left. - {}^p s_{11} {}^p d_{12}^2] + v^2 (1-v) ({}^m s_{11} {}^p d_{12}^2 + {}^m s_{11} {}^p d_{11}^2 - 2{}^m s_{12} {}^p d_{12} {}^p d_{11}) \right) \end{aligned} \quad (7)$$

The in-plane ME coefficient is expected to be the strongest amongst the cases discussed so far due to high values of  $q$  and  $d$  and the absences of demagnetizing fields.

## 3. ME effect at longitudinal modes of EMR

Since the ME coupling in the composites is mediated by the mechanical stress, one would expect orders of magnitude stronger coupling when the frequency of the ac field is tuned to acoustic mode frequencies in the sample than at non-resonance frequencies. Two methods of theoretical modeling can be used for calculating the frequency dependence of ME coefficients by solving the medium motion equation. First approach rests on considering the structure as an effective homogeneous medium and implies the preliminary finding the effective low-frequency material parameters (Bichurin et al., 2003b). The second approach is based on using the initial material parameters of components. A recently reported attempt to estimate ME coefficients using this approach consists in supposing the magnetic layer to move freely, ignoring the bonding to piezoelectric layer while vibration of piezoelectric layer is supposed to be a combination of motions of free magnetic layer and free oscillations of piezoelectric layer (Filippov, 2004, 2005). In case of perfect bonding of layers, the motion of piezoelectric phase is described by magnetic medium motion equation. As a result, the expressions for ME coefficients appear inaccurate. Particularly, the expressions give a wrong piezoelectric volume fraction dependence of ME voltage coefficient.

This section is focused on modeling of the ME effect in ferrite-piezoelectric layered structures in EMR region. We have chosen cobalt ferrite (CFO) - barium titanate as the

model system for numerical estimations. The ME voltage coefficients  $a_E$  have been estimated for transverse field orientations corresponding to minimum demagnetizing fields and maximum  $a_E$ . (Bichurin et al., 2010) As a model, we consider a ferrite-piezoelectric layered structure in the form of a thin plate with the length  $L$ .

We solve the equation of medium motion taking into account the magnetostatic and elastostatic equations, constitutive equations, Hooke's law, and boundary conditions. The equation of medium motion has the form:

$$\frac{\partial^2 u_1}{\partial x^2} = -k^2 u_1; \tag{8}$$

where  $u_1$  is displacement in the traveling direction  $x$ . For the transverse fields' orientation (poling direction of piezoelectric phase, dc and ac magnetic fields are parallel to  $x$ -axis), the wave value  $k$  is defined by expression:

$$k = \omega \sqrt{\left[ {}^p \rho v + {}^m \rho (1-v) \right] \left[ \frac{v}{{}^p s_{11}} + \frac{1-v}{{}^m s_{11}} \right]^{-1}}; \tag{9}$$

where  $\omega$  is the circular frequency,  ${}^p \rho$  and  ${}^m \rho$  are the piezoelectric and piezomagnetic densities,  $v = {}^p v / ({}^p v + {}^m v)$ , and  ${}^p v$  and  ${}^m v$  denote the volume of piezoelectric and phases, respectively. For the solution of the Eq. (8), the following boundary conditions are used:  ${}^p S_1 = {}^m S_1$  and  ${}^p T_1 v + {}^m T_1 (1-v) = 0$  at  $x=0$  and  $x=L$ , where  $L$  is the sample length. The ME voltage coefficient  $a_{E,13} = E_3/H_1$  is calculated from Eqs. (8), (9) and using the open circuit condition  $D_3=0$ .

$$\alpha_{E,31} = \frac{2 {}^p d_{31} {}^m g_{11} \mu_{\text{eff}} {}^p s_{11} v (1-v) \tan(kL/2)}{s_2 ({}^p d_{31}^2 - {}^p s_{11} {}^p \epsilon_{33}) kL - 2 {}^p d_{31}^2 v {}^m s_{11}^B \tan(kL/2)}; \tag{10}$$

where  $s_2 = v {}^m s_{11}^B + (1-v) {}^p s_{11}$  and  $\mu_{\text{eff}}$  is effective permeability of piezomagnetic layer. To take into consideration the energy loss, we set  $\omega$  equal to  $\omega' - i\omega''$  with  $\omega''/\omega' = 10^{-3}$ . The resonance enhancement of ME voltage coefficient for the bilayer is obtained at antiresonance frequency. ME voltage coefficient,  $a_{E,13}$  increases with increasing barium titanate volume, attains a peak value for  $v = 0.5$  and then drops with increasing  $v$  as in Fig. 1.

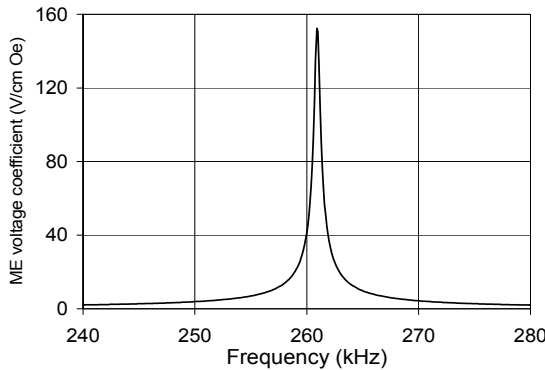


Fig. 1. Frequency dependence of  $a_{E,13}$  for the bilayer with  $v=0.5$

#### 4. ME effect at bending modes of EMR

A key drawback for ME effect at longitudinal modes is that the frequencies are quite high, on the order of hundreds of kHz, for nominal sample dimensions. The eddy current losses for the magnetostrictive phase can be quite high at such frequencies, in particular for transition metals and alloys and earth rare alloys such as Terfenol-D, resulting in an inefficient magnetoelectric energy conversion. In order to reduce the operating frequency, one must therefore increase the laminate size that is inconvenient for any applications. An alternative for getting a strong ME coupling is the resonance enhancement at bending modes of the composite. The frequency of applied ac field is expected to be much lower compared to longitudinal acoustic modes. Recent investigations have showed a giant ME effect at bending modes in several layered structures (Xing et al., 2006; Zhai et al., 2008; Chashin et al., 2008). In this section, we focus our attention on theoretical modeling of ME effects at bending modes. (Petrov et al., 2009)

An in-plane bias field is assumed to be applied to magnetostrictive component to avoid the demagnetizing field. The thickness of the plate is assumed to be small compared to remaining dimensions. Moreover, the plate width is assumed small compared to its length. In that case, we can consider only one component of strain and stress tensors in the EMR region. The equation of bending motion of bilayer has the form:

$$\nabla^2 \nabla^2 w + \frac{\rho b}{D} \frac{\partial^2 w}{\partial \tau^2} = 0; \quad (11)$$

where  $\nabla^2 \nabla^2$  is biharmonic operator,  $w$  is the deflection (displacement in  $z$ -direction),  $t$  and  $\rho$  are thickness and average density of sample,  $b = p t + m t$ ,  $\rho = (p \rho^p t + m \rho^m t) / b$ ,  $p \rho$ ,  $m \rho$ , and  $p t$ ,  $m t$ , are densities and thicknesses of piezoelectric and piezomagnetic, correspondingly, and  $D$  is cylindrical stiffness.

The boundary conditions for  $x=0$  and  $x=L$  have to be used for finding the solution of above equation. Here  $L$  is length of bilayer. As an example, we consider the plate with free ends. At free end, the turning moment  $M_1$  and transverse force  $V_1$  equal zero:  $M_1 = 0$  and  $V_1 = 0$  at

$x=0$  and  $x=L$ , where  $M_1 = \int_A z T_1 dz_1$ ,  $V_1 = \frac{\partial M_1}{\partial x}$ , and  $A$  is the cross-sectional area of the

sample normal to the  $x$ -axis. We are interested in the dynamic ME effect; for an ac magnetic field  $H$  applied to a biased sample, one measures the average induced electric field and calculates the ME voltage coefficient. Using the open circuit condition, the ME voltage coefficient can be found as

$$\alpha_{E31} = \frac{E_3}{H_1} = - \frac{\int_{z_0-p t}^{z_0} {}^p E_3 dz}{t H_1 {}^p \epsilon_{33}}; \quad (12)$$

where  $E_3$  and  $H_1$  are the average electric field induced across the sample and applied magnetic field. The energy losses are taken into account by substituting  $\omega$  for complex frequency  $\omega + i\omega''$  with  $\omega''/\omega = 10^{-3}$ .

As an example, we apply Eq. 12 to the bilayer of permendur and PZT. Fig. 2 shows the frequency dependence of ME voltage coefficient at bending mode for free-standing bilayer

with length 9.15 mm and thickness 3.22 mm for PZT volume fraction 0.67. Graph of  $a_{E,31}$  reveals a giant value  $a_{E,31}=6.6 \text{ V/cm Oe}$  and resonance peak lies in the infralow frequency range. Fig. 3 reveals the theoretical and measured frequency dependencies of transverse ME voltage coefficients for a permendur-PZT bilayer that is free to bend at both ends. According to our model, there is a strong dependence of resonance frequency on boundary conditions. The lowest resonance frequency is expected for the bilayer clamped at one end. One expects bending motion to occur at decreasing frequencies with increasing bilayer length or decreasing thickness.

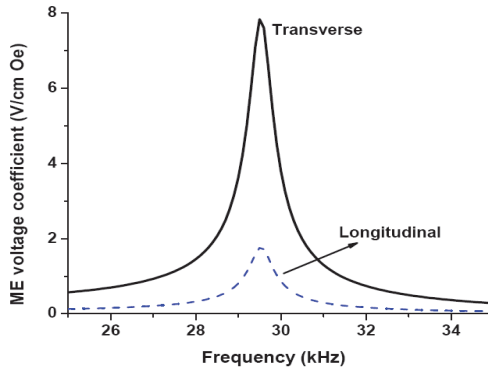


Fig. 2. Frequency dependence of longitudinal and transverse ME voltage coefficients for a bilayer of permendur and PZT showing the resonance enhancement of ME interactions at the bending mode frequency. The bilayer is free to bend at both ends. The sample dimensions are  $L = 9.2 \text{ mm}$  and total thickness  $t = 0.7 \text{ mm}$  and the PZT volume fraction  $v=0.6$ .

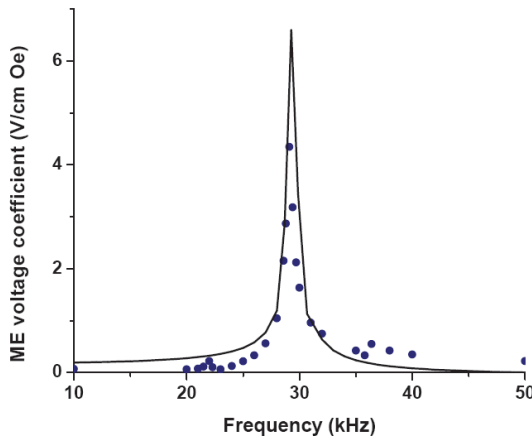


Fig. 3. Theoretical (line) and measured (circles) frequency dependence of transverse ME voltage coefficients for a permendur-PZT bilayer that is free to bend at both ends and with  $v=0.67$ .

## 5. Inverse magnetoelectric effect

In the case of inverse ME effect, external field  $E$  produces a deformation of piezoelectric layers due to piezoelectric coupling. The deformation is transmitted to magnetic layers. The inverse piezomagnetic effect results in a change of magnetic parameters of the structure. ME coefficient  $a_{H, ij} = H_i/E_j$  can be easily found similarly to ME voltage coefficient using the open magnetic circuit condition,  $B_i = 0$ . As an example, the expression for  $a_{H, 33}$  takes the form (Huang, 2006)

$$\alpha_{H,33} = \frac{-2d_{31}q_{31}{}^m v}{({}^m s_{11}^H + {}^m s_{12}^H)^p v + (p s_{11}^E + p s_{12}^E)^m v - 2(k_{31})^2 p s_{11}^E m v}, \quad (13)$$

where  $k_{31}$  is the coupling coefficient for the piezoelectric phase,  ${}^p v$  and  ${}^m v$  are the volume fractions of piezoelectric and magnetostrictive components.

### 5.1 Inverse magnetoelectric effect at electromechanical resonance

To obtain the inverse ME effect, a pick up coil wound around the sample is used to measure the ME voltage due to the change in the magnetic induction in magnetostrictive phase. The measured static magnetic field dependence of ME voltage has been attributed to the variation in the piezomagnetic coefficient for magnetic layer. The frequency dependence of the ME voltage shows a resonance character due to longitudinal acoustic modes in piezoelectric layer. Next we derive an expression for the ME susceptibility at EMR. (Fetisov et al., 2007) For the transverse field orientation, the equations for the strain tensor  $S_i$  in the ferrite and piezoelectric and the magnetic induction  $B$  have the form

$${}^p S_1 = {}^p s_{11} {}^p T_1 + {}^p d_{31} E_3, \quad (14)$$

$${}^m S_1 = {}^m s_{11} {}^m T_1 + {}^m g_{11} B_1,$$

$${}^m H_1 = B_1 / {}^m \mu_{33} - {}^m g_{11} {}^m T_1, \quad (15)$$

where  ${}^p s_{11}$  and  ${}^m s_{11}$  are the components of the compliance tensor at constant electric field for piezoelectric and at constant magnetic induction for ferrite, respectively;  ${}^m \mu_{33}$  is the component of the permeability tensor, and  ${}^p d_{31}$  and  ${}^m g_{11}$  are the piezoelectric and piezomagnetic coefficients, respectively. Here we take into account only stress components along  $x$  axis, because close to EMR we can assume  $T_1 \gg T_2$  and  $T_3$ . Expressing the stress components via the deformation components and substituting these expressions into the equation of the medium motion, we obtain a differential equation for the  $x$  projection of the displacement vector of the medium ( $u_x$ ). Taking into account the fact that the trilayer surfaces at  $x=0$  and  $x=L$  are free from external stresses, we find the solution to this equation. The magnetic induction arising due to the piezoelectric effect can be found from Eq. 15. The magnetic induction in the trilayer is expressed as:

$$B_1 = {}^m \mu_{33} \int_0^L ({}^m H_1 + {}^m g_{11} {}^m T_1) dx, \quad (16)$$

where  $W$  and  $L$  are the width and length of the sample. The ME susceptibility is defined by

$\alpha_{31} = \frac{\partial B_1}{\partial E_3}$ . Taking into account this definition, Eq. 16 yields:

$$\alpha_{31} = \frac{2v(1-v)^m q_{11}^p d_{31} \tan(kL/2)}{kL[v^m s_{11} + (1-v)^p s_{11}]} \tag{17}$$

where  $k = \omega \sqrt{\left[ \frac{p}{\rho} v + \frac{m}{\rho} (1-v) \right] \left[ \frac{v}{p s_{11}} + \frac{1-v}{m s_{11}} \right]^{-1}}$ ,  $v$  is the PZT volume fraction and  $\rho$  is average density. Eq. 17 does not take into account power waste therefore at resonant frequency the ME coefficient sharply increases. In real structures, there are losses that occur first of all in the contacts. These losses can be taken into account in Eq. 17 by substituting  $\omega$  for  $\omega' - i\omega''$  with  $\omega''/\omega' = 1/Q$  where  $Q$  is the measured quality factor of EMR. The estimated the ME susceptibility is shown in Fig. 5. The susceptibility determined from data on generated magnetic induction at opened magnetic circuit is also shown in Fig. 5. One observes a very good agreement between theory and data. The investigations carried out have enabled us to establish a relation between efficiencies of the direct and the inverse ME interactions and their frequency dependences.

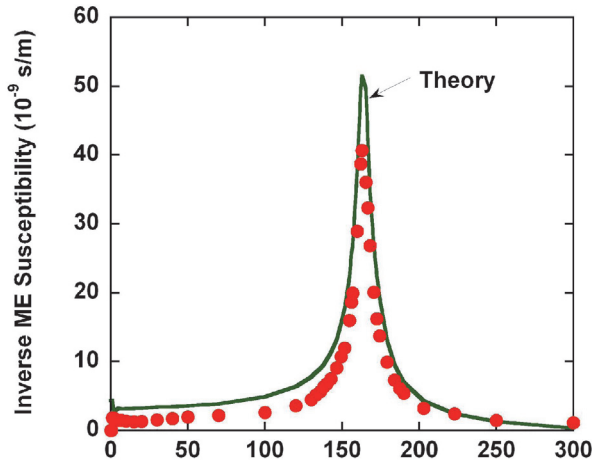


Fig. 4. Theoretical (line) and measured (filled circles) ME susceptibility for the PZT-Ni-PZT trilayer structure.

**5.2 Inverse magnetolectric effect at microwave range**

A thorough understanding of high frequency response of a ferrite - piezoelectric composite is critically important for a basic understanding of ME effects and for useful technologies. In a composite, the interaction between electric and magnetic subsystems can be expressed in terms of a ME susceptibility. In general, the susceptibility is defined by the following equations for the microwave region (Kornev et al., 2000; Bichurin, 1994; Bichurin et al., 1990).

$$\begin{aligned} \mathbf{p} &= \chi^E \mathbf{e} + \chi^{EM} \mathbf{h}, \\ \mathbf{m} &= \chi^{ME} \mathbf{e} + \chi^M \mathbf{h}. \end{aligned} \tag{18}$$

Here  $\mathbf{p}$  is the electrical polarization,  $\mathbf{m}$  is the magnetization,  $\mathbf{e}$  and  $\mathbf{h}$  are the external electrical and magnetic fields,  $\chi^E$  and  $\chi^M$  are the electrical and magnetic susceptibilities, and  $\chi^{EM}$  and  $\chi^{ME}$  are the ME susceptibilities, with  $\chi_{ik}^{ME} = \chi_{ki}^{EM}$ . In Eq. 18, the ac amplitudes are shown explicitly, but the susceptibilities also depend on constant fields.

We consider the magnetic susceptibility tensor of a composite which exhibits ME coupling. The sample is subjected to constant electric and magnetic fields and a ac magnetic field. The thermodynamic potential density can be written as:

$$W = W_0 + W_{ME}, \quad (19)$$

where  $W_0$  is the thermodynamic potential density at  $E = 0$ , and

$$W_{ME} = B_{ikn} E_i M_k M_n + b_{ijkn} E_i E_j M_k M_n. \quad (20)$$

Here  $B_{ikn}$  and  $b_{ijkn}$  are linear and bilinear ME constants, respectively. The number of independent components is determined by the material structure. The main contribution to  $W_{ME}$  arises from the linear ME constants  $B_{ikn}$  in polarized composites. If the composite is unpolarized, the bilinear ME constants is dominant. We used the effective demagnetization factor method to solve the linearized equation of motion of magnetization and obtained the following expression for the magnetic susceptibility:

$$\chi^M = \begin{bmatrix} \chi_1 & \chi_s + i\chi_a & 0 \\ \chi_s - i\chi_a & \chi_2 & 0 \\ 0 & 0 & 0 \end{bmatrix}, \quad (21)$$

where

$$\begin{aligned} \chi_1 &= D^{-1} \gamma^2 M_0 \left[ H_{03'} + M_0 \sum_i (N_{22'}^i - N_{33'}^i) \right]; \chi_2 = D^{-1} \gamma^2 M_0 \left[ H_{03'} + M_0 \sum_i (N_{11'}^i - N_{33'}^i) \right]; \\ \chi_s &= -D^{-1} \gamma^2 M_0^2 \sum_i N_{1'2'}^i; \chi_a = D^{-1} \gamma M_0 \omega; D = \omega_0^2 - \omega^2; \\ \omega_0^2 &= \gamma^2 \left[ H_{03'} + \sum_i (N_{11'}^i - N_{33'}^i) M_0 \right] \left[ H_{03'} + \sum_i (N_{22'}^i - N_{33'}^i) M_0 \right] - \left( \sum_i N_{1'2'}^i M_0 \right)^2 \end{aligned}$$

Here  $\gamma$  is the magneto-mechanical ratio,  $\omega$  is the angular frequency,  $N_{k'n'}^i$  are demagnetization factors describing the effective magnetic anisotropy fields, and  $1', 2', 3'$  is a coordinate system in which the axis  $3'$  is directed along the equilibrium magnetization. In Eq. 21 the summation is carried out over all types of magnetic anisotropy. The ME interaction results in an additional term ( $i = E$ )

$$N_{k'n'}^E = 2(B_{ikn} + b_{ijkn} E_{oj}) E_{oi} \beta_{k'k} \beta_{n'n'}, \quad (22)$$

where  $\beta$  is matrix of direction cosines of axes  $(1', 2', 3')$  relative to the crystallographic coordinate system  $(1, 2, 3)$ . It should be noted that  $\chi_{33}^M = 0$  in Eq. 21 since the sample is supposed to be magnetized by bias field that is high enough to drive the composite to a saturated (single-domain) state. Using Eq. 21 it can be easily shown that the resonance line shift under the influence of the electric field to the first order in  $N_{kl}^E$  has the form:

$$\delta H_E = -\frac{M_0}{Q_1} \left[ Q_2 (N_{11}^E - N_{33}^E) + Q_3 (N_{22}^E - N_{33}^E) - Q_4 N_{12}^E \right], \quad (23)$$

where

$$Q_1 = 2H_3 + M_0 \sum_{i \neq E} \left[ (N_{11}^E - N_{33}^E) + (N_{22}^E - N_{33}^E) \right]; \quad Q_2 = \left[ H_3 + M_0 \sum_{i \neq E} (N_{22}^E - N_{33}^E) \right];$$

$$Q_3 = \left[ H_3 + M_0 \sum_{i \neq E} (N_{11}^E - N_{33}^E) \right]; \quad Q_4 = 2M_0 \sum_{i \neq E} N_{12}^i.$$

Eq. 23 enables us to determine the ME constants of a composite and consequently to interpret the obtained data on the resonant ME effect. As an example, we consider the composite with  $3m$  or  $4mm$  symmetry. The general expression for the magnetic susceptibility tensor of a disk sample magnetized along the symmetry axis has the form

$$\chi_1 = \chi_2 = D^{-1} \gamma^2 M_0 H_{eff}; \quad \chi_s = 0; \quad \chi_a = D^{-1} \gamma M_0 \omega, \quad (24)$$

where

$$D = \omega_0^2 - \omega^2; \quad \omega_0 = \gamma H_{eff}; \quad H_a = K_1 / M_0;$$

$$H_{eff} = H_0 + 2H_a - 4\pi M_0 + 2M_0(B_{31} - B_{33})E_0 + 2M_0(b_{31} - b_{33})E_0^2$$

Assuming the dissipative term in the equation of motion of magnetization as  $i\omega\alpha(\mathbf{M}_0 \times \mathbf{m})/M_0$ , where  $\alpha$  is the dissipation parameter, the magnetic susceptibility tensor components are complex and take the form  $\chi_i = \chi' + i\chi''$ , where

$$\chi' = \chi_0 \frac{\omega_0^2 (\omega_0^2 - \omega^2 + 2\alpha^2 \omega^2)}{(\omega_0^2 - \omega^2)^2 + 4\alpha^2 \omega_0^2 \omega^2}, \quad \chi'' = \chi_0 \frac{\alpha \omega \omega_0 (\omega_0^2 + \omega^2)}{(\omega_0^2 - \omega^2)^2 + 4\alpha^2 \omega_0^2 \omega^2}, \quad \chi_0 = \gamma \frac{M_0}{\omega_0}. \quad (25)$$

It follows from Eqs. 21 and 24 that the dependence of the magnetic susceptibility on an external constant electric field is resonant. The nature of this dependence can be explained as follows. By means of ME interactions, the external electric field results in a change in the effective magnetic field  $H_{eff}$  in Eq. 24 with  $2H_{ME} = 2M_0(B_{31} - B_{33})E_0 + 2M_0(b_{31} - b_{33})E_0^2$ . The change originates from the piezoelectric phase mechanically coupled to the magnetostrictive phase, and is phenomenological described by ME constants  $B_{ikn}$  and  $b_{ijkn}$  in Eqs. 28 and 29. Thus the variation of the external constant electric field has the same effect as magnetic field variations and reveals a resonant behavior. Expressions for the susceptibility components could be obtained by using the demagnetization factors stipulated by ME interactions according to Eq. 26.

Next we consider specific composites and estimate the magnetic susceptibility and its electric field variation. (Bichurin et al., 2002) Three composites of importance for the estimation are lithium ferrite (LFO) - PZT, nickel ferrite (NFO) - PZT and yttrium iron garnet (YIG) - PZT because of desirable high frequency properties of LFO, NFO and YIG. We consider a simple structure, a bilayer consisting of single ferrite and PZT layers. In order to obtain the susceptibilities, one requires the knowledge of ME constants and the

loss parameter. Assuming that the poling axis of the piezoelectric phase coincides with [100] axis of the magnetostrictive phase and  $|\lambda_{100}| = 1.4 \cdot 10^{-6}$ ,  $23 \cdot 10^{-6}$  and  $46 \cdot 10^{-6}$  for YIG-PZT, LFO-PZT and NFO-PZT, respectively, we obtained  $2M_0(B_{31}-B_{33}) = 0.1$ ,  $0.6$  and  $1.4$  Oe-cm/kV for the three bilayer samples. For LFO the following parameters are used:  $m_{C11} = 24.47 \cdot 10^{10}$  N/m<sup>2</sup>;  $m_{C12} = 13.71 \cdot 10^{10}$  N/m<sup>2</sup>;  $m_{C44} = 9.36 \cdot 10^{10}$  N/m<sup>2</sup>;  $4\pi M_s = 3600$  G. Finally, the loss parameters are  $\alpha = 0.025$ ,  $0.05$  and  $0.075$  for YIG-PZT, LFO-PZT and NFO-PZT, respectively. Figure 5 shows the static magnetic field dependencies of real and imaginary parts of magnetic susceptibility for layered LFO-PZT, NFO-PZT and YIG-PZT. The results are for a bilayer disk sample with the H and E-fields perpendicular to the sample plane and for a frequency of 9.3 GHz. The static field range is chosen to include ferromagnetic resonance in the ferrite. For  $E = 0$ , one observes the expected resonance in the profiles. With the application of  $E = 300$  kV/cm, a down-shift in the resonance field is obvious. The magnitude of the shift is determined by ME constants which in turn is strongly influenced by the magnetostriction constant. The large magnetostriction for NFO leads to a relatively strong E-induced effect in NFO-PZT compared to YIG-PZT. The shift also correlates with resonance linewidth. It is possible to understand the correlation from the fact that the resonance linewidth is dependent on the effective anisotropy field, a parameter that is a function of the magnetostriction.

Figure 6 shows the estimated variation of the real and imaginary parts of the magnetic susceptibility as a function of E for a frequency of 9.3 GHz. The constant magnetic field is set equal to the field for ferromagnetic resonance (FMR). The width of resonance measured in terms of electric field is inversely proportional to the parameter  $2M_0(B_{31}-B_{33})$ . It follows from Eq. 29 that a narrow resonance is indicative of strong ME coupling in the composites. Thus NFO-PZT bilayer shows a sharp resonance in comparison to YIG-PZT.

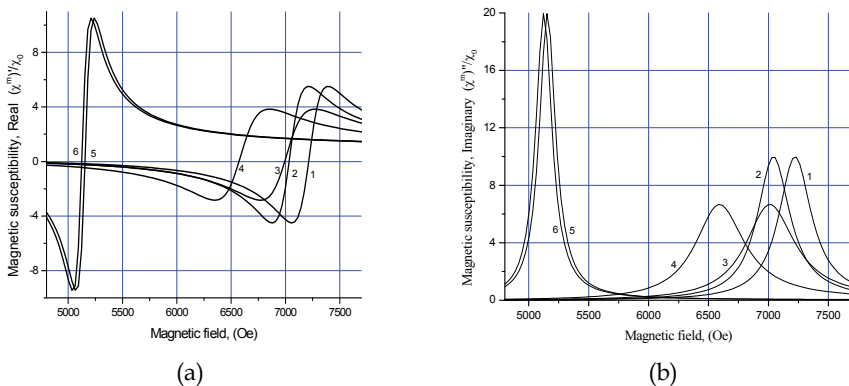


Fig. 5. Theoretical magnetic field dependence of the magnetic susceptibility for the multilayer composites of LFO-PZT (curves 1 and 2), NFO-PZT (curves 3 and 4) and YIG-PZT (curves 5 and 6) represents the real (a) and imaginary (b) parts of the susceptibility at 9.3 GHz. Curves 1, 3 are at  $E=0$  and curves 2, 4 at  $E=300$  kV/cm.

Figures 5 and 6 represent the magnetic spectra of the composites obtained by magnetic and electric sweep, respectively. Thus the presented model enables finding ME coefficients from data on the electric field induced shift of magnetic resonance line.

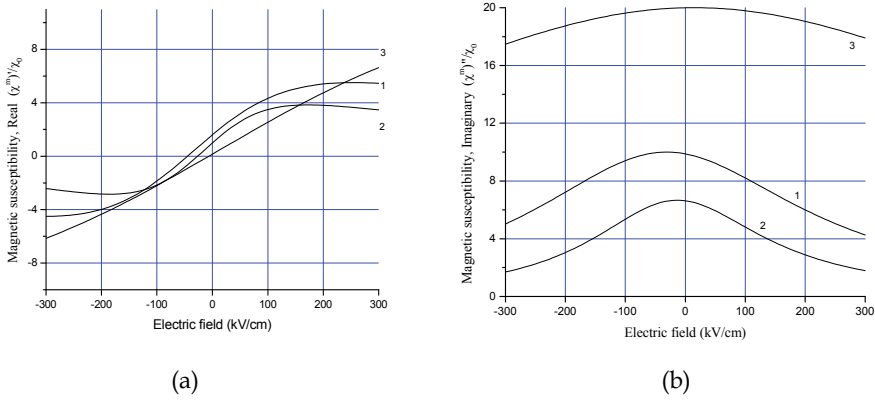


Fig. 6. Theoretical electric field dependence of the magnetic susceptibility for the multilayer composites of LFO-PZT (curves 1), NFO-PZT (curve 2) and YIG-PZT (curve 3) represents the real (a) and imaginary (b) parts of the susceptibility at 9.3 GHz.

**6. Magnetoelectric coupling in magnetoacoustic resonance region**

Here we provide a theory for ME interactions at the coincidence of FMR and EMR, at magnetoacoustic resonance (MAR). (Bichurin et al., 2005; Ryabkov et al., 2006) At FMR, spin-lattice coupling and spin waves that couple energy to phonons through relaxation processes are expected to enhance the piezoelectric and ME interactions. Further strengthening of ME coupling is expected at the overlap of FMR and EMR. We consider bilayers with low-loss ferrites such as nickel ferrite or YIG that would facilitate observation of the effects predicted in this work. For calculation we use equations of motion for the piezoelectric and magnetostrictive phases and equations of motion for the magnetization. Coincidence of FMR and EMR allows energy transfer between phonons, spin waves and electric and magnetic fields. This transformation is found to be very efficient in ferrite-PZT. The ME effect at MAR can be utilized for the realization of miniature/nanosensors and transducers operating at high frequencies since the coincidence is predicted to occur at microwave frequencies in the bilayers.

We consider a ferrite-PZT bilayer that is subjected to a bias field  $H_0$ . The piezoelectric phase is electrically polarized with a field  $E_0$  parallel to  $H_0$ . It is assumed that  $H_0$  is high enough to drive the ferrite to a saturated (single domain) state that has two advantages. When domains are absent, acoustic losses are minimum. The single-domain state under FMR provides the conditions necessary for achieving a large effective susceptibility. The free-energy density of a single crystal ferrite is given by  ${}^mW = W_H + W_{an} + W_{ma} + W_{ac}$ , where  $W_H = -\mathbf{M} \cdot \mathbf{H}_i$  is Zeeman energy,  $M$  is magnetization,  $H_i$  is internal magnetic field that includes demagnetizing fields. The term  $W_{an}$  given by  $W_{an} = K_1/M_0^4(M_1^2 M_2^2 + M_2^2 M_3^2 + M_3^2 M_1^2)$  with  $K_1$  the cubic anisotropy constant and  $M_0$  the saturation magnetization. The magnetoelastic energy is written as  $W_{ma} = B_1/M_0^2 (M_1^2 mS_1 + M_2^2 mS_2 + M_3^2 mS_3) + B_2/M_0^2 (M_1 M_2 mS_6 + M_2 M_3 mS_4 + M_1 M_3 mS_5)$  where  $B_1$  and  $B_2$  are magnetoelastic coefficients and  $S_i$  are the elastic coefficients. Finally, the elastic energy is  $W_{ac} = 1/2 mC_{11}(mS_1^2 + mS_2^2 + mS_3^2) + 1/2 mC_{44} (mS_4^2 + mS_5^2 + mC_{12} (mS_1 mS_2 + mS_2 mS_3 + mS_1 mS_3))$  and  $mC_{ij}$  is modulus of elasticity.

The generalized Hook's law for the piezoelectric phase can be presented as follows.

$$\begin{aligned} {}^pT_4 &= {}^p c_{44} {}^p S_4 - {}^p e_{15} {}^p E_2, \\ {}^pT_5 &= {}^p c_{44} {}^p S_5 - {}^p e_{15} {}^p E_1, \end{aligned} \quad (26)$$

where  $e_{p15}$  is piezoelectric coefficient and  ${}^pE$  is electric field. Equations of motion for ferrite and piezoelectric composite phases can be written in following form:

$$\begin{aligned} \partial^2({}^m u_1) / \partial t^2 &= \partial^2({}^m W) / (\partial x \partial {}^m S_1) + \partial^2({}^m W) / (\partial y \partial {}^m S_6) + \partial^2({}^m W) / (\partial z \partial {}^m S_5), \\ \partial^2({}^m u_2) / \partial t^2 &= \partial^2({}^m W) / (\partial x \partial {}^m S_6) + \partial^2({}^m W) / (\partial y \partial {}^m S_2) + \partial^2({}^m W) / (\partial z \partial {}^m S_4), \\ \partial^2({}^p u_1) / \partial t^2 &= \partial({}^p T_1) / \partial x + \partial({}^p T_6) / \partial y + \partial({}^p T_5) / \partial z, \\ \partial^2({}^p u_2) / \partial t^2 &= \partial({}^p T_6) / \partial x + \partial({}^p T_2) / \partial y + \partial({}^p T_4) / \partial z. \end{aligned} \quad (27)$$

The equation of motion of magnetization for ferrite phase has the form

$$\partial \mathbf{M} / \partial t = -\gamma [\mathbf{M}, \mathbf{H}_{\text{eff}}], \quad (28)$$

where  $\mathbf{H}_{\text{eff}} = -\partial({}^m W) / \partial \mathbf{M}$ . Solving Eqs. 31 and 32, taking into account Eq. 30 and open circuit condition, allows one to get the expression for ME voltage coefficient

$$\begin{aligned} |\alpha_E| &= |E^+ / H^+| = \gamma B_2 {}^p c_{44} {}^p k {}^p e_{15} (1 - \cos({}^p k {}^p L)) (1 - \cos({}^m k {}^m L) / \{(\omega - \gamma H_0 + 4\pi \gamma M_0) \\ &[{}^p k {}^p c_{44} \cos({}^m k {}^m L) (2 {}^p e_{15}^2 (1 - \cos({}^p k {}^p L)) + \sin({}^p k {}^p L) {}^p c_{44} {}^p \varepsilon_{11} {}^p k {}^p L) + \\ &+ {}^m k {}^m c_{44}^+ \sin({}^m k {}^m L) ({}^p e_{15}^2 \sin({}^p k {}^p L) + \cos({}^p k {}^p L) {}^p c_{44} {}^p \varepsilon_{11} {}^p k {}^p L)]\}, \end{aligned} \quad (29)$$

where  ${}^m k = \omega \sqrt{{}^m \rho ({}^m c_{44}^+)^{-1}}$ ,  ${}^p k = \omega \sqrt{{}^p \rho ({}^p c_{44})^{-1}}$ ,  $H^+ = H_1 + i H_2$ ,  $E^+ = E_1 + i E_2$ . Now we apply the theory to specific bilayer system of YIG-PZT. YIG has low-losses at FMR, a necessary condition for the observation of the enhancement in ME coupling at MAR that is predicted by the theory. The assumed thicknesses for YIG and PZT are such that the thickness modes occur at 5-10 GHz, a frequency range appropriate for FMR in a saturated state in YIG. The resonance field  $H_r$  is given by  $H_r = \omega / \gamma - 4\pi M_0$ . As  $H_0$  is increased to  $H_r$ ,  $\alpha_E$  is expected to increase and show a resonant character due to the resonance form for frequency dependence for mechanical displacement in the FMR region. Figure 7 shows estimated  $\alpha_E$  vs  $f$ . Signal attenuation is taken into account in these calculations by introducing a complex frequency and for an imaginary component of  $\omega = 10^7$  rad/s.

## 7. Lead-free ceramic for magnetoelectric composites

Owing to the prohibition on the use of Pb-based materials in some commercial applications the demand for lead-free ceramics has grown considerably in the last decade. Various systems for nonlead ceramics have been studied and some of these have been projected as the possible candidates for the replacement of PZT. However, the dielectric and piezoelectric properties of all the known nonlead materials is inferior as compared to that PZT and this has been the stimulant for growing research on this subject. For high piezoelectric properties perovskite is the preferred crystallographic family and large piezoelectric and electromechanical constants are obtained from alkali-based ceramics such

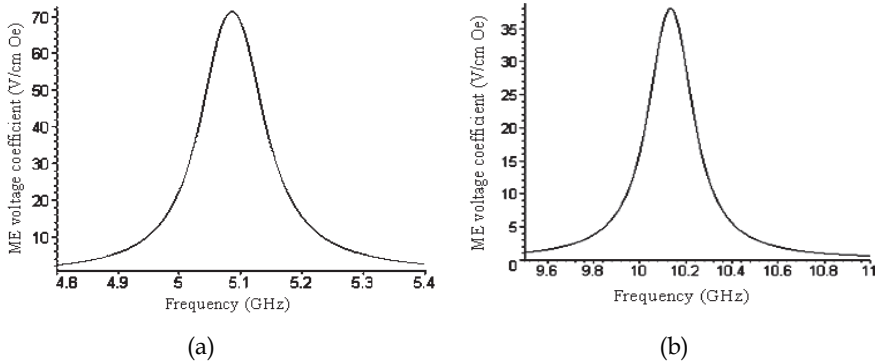


Fig. 7. The ME voltage coefficient  $a_E$  vs. frequency profile for a bilayer of PZT of thickness 100 nm and YIG of thickness 195 nm and for dc magnetic field of 3570 (a) and 5360 (b) Oe. The FMR frequency coincides with fundamental EMR mode (a) and second EMR mode (b) frequency.

as  $(Na_{1/2}Bi_{1/2})TiO_3$  (NBT),  $(K_{1/2}Bi_{1/2})TiO_3$  (KBT) and  $(Na_{0.5}K_{0.5})NbO_3$ . Table VII.1 compares the properties of the PZT and the prominent non-lead based systems. The data shown in this table has been collected from various publications (Nagata & Takenaka, 1991; Sasaki et al., 1999; Kimura et al., 2002; Priya et al., 2003a, 2003b). It can be easily deduced from the data shown in this table that none of the nonlead ceramics qualifies for the direct replacement of PZT. (Na, K)NbO<sub>3</sub> ceramics has good longitudinal mode and radial mode coupling factors along with high piezoelectric constants.

	Symbol	$\epsilon_{33}^T/\epsilon_0$	Qm	$d_{33}$ (pC/N)	$d_{31}$ (pC/N)	$k_{33}$ (%)	$k_p$ (%)	Tc (°C)
PZT (Mn, Fe doped)	PZT	1500	1000-2000	300	-100	60	50	300
$(Bi,Na)TiO_3$	BNT <sup>(1)</sup>	600	500	120	-40	45	25	260
Bi-layer	SBT <sup>(1)</sup>	150	>2000	20	-3	20	3	550
	NCBT <sup>(1)</sup>	150	-	15	-2	15	2	>500
	NCBT <sup>(1)</sup> (HF <sup>(2)</sup> , TGG <sup>(2)</sup> )	150	-	40	-2	40	2	>500
$(Na,K)NbO_3$	KNN <sup>(1)</sup>	400	500	120	-40	40	30	350
Tungsten Bronze	SBN <sup>(1)</sup>	500	-	120	-	30	-	250
Others	BT <sup>(1)</sup>	1100	700	130	-40	45	20	100

Table 1. Properties of lead-free piezoelectric ceramics. (1) BNT:  $(Bi_{1/2}Na_{1/2})TiO_3$ , SBT:  $SrBi_4Ti_4O_{15}$ , NCBT:  $(Na_{1/2}Bi_{1/2})_{0.95}Ca_{0.05}Bi_4Ti_4O_{15}$ , KNN:  $(K_{1/2}Na_{1/2})NbO_3$ , SBN:  $(Sr,Ba)Nb_2O_6$ , BT:  $BaTiO_3$ ; (2) HF: Hot Forging method, TGG: Templated grain growth method.

It is well known that the composition corresponding to 0.5/0.5 in the  $\text{NaNbO}_3 - \text{KNbO}_3$  (KNN) system has the maximum in the piezoelectric properties. Table VII.2 compares the properties of the annealed and un-annealed KNN samples. KNN has an intermediate phase transition from the ferroelectric orthorhombic phase ( $\text{FE}_o$ ) to the ferroelectric tetragonal phase ( $\text{FE}_t$ ) at around 200 °C. It is believed that annealing the sample in the tetragonal phase induces (100) oriented domains at room temperature. Since the spontaneous polarization is along  $\langle 110 \rangle$  in the orthorhombic phase, rapid cooling (100°C/min) from  $\text{FE}_t$  phase (spontaneous polarization along  $\langle 100 \rangle$ ) results in titling of the polarization which provides enhancement of piezoelectric properties.

Sintering Temperature (°C)	Density (gm/cm <sup>3</sup> )	Logp (Ω.cm)	tanδ (%)	ε
1150	4.23	9.4	10	720
1160 (Annealed)	4.44	9.97	4.05	616
1160 (Unannealed)	4.45	10.14	4.75	630

Table 2. Properties of unpoled KNN ceramics showing the affect of annealing.

Figure 8 (a) and (b) shows the dielectric constant and loss as a function of temperature for the poled KNN sample. The room temperature dielectric constant is of the order of 350. The dielectric constant curve shows a discontinuity at ~180 °C and 400 °C. These discontinuities are related to the transition from  $\text{FE}_o$  phase to  $\text{FE}_t$  phase and  $\text{FE}_t$  phase to  $\text{PE}_c$ . In the range of 0 – 180 °C, the dielectric loss magnitude remains in the range of 4.2 – 4.5%. No significant difference was observed in the dielectric behavior of the annealed and unannealed samples below 200 °C.

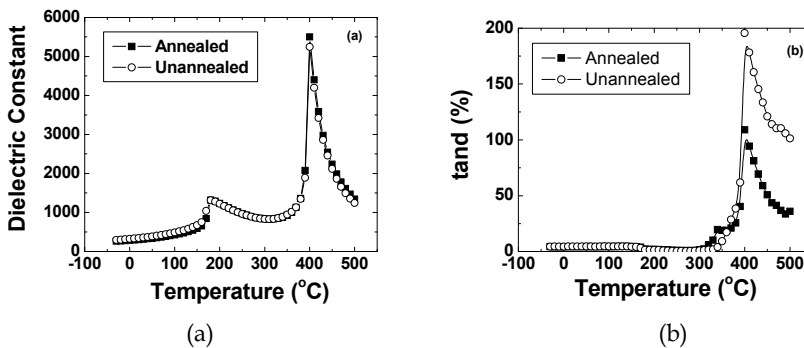


Fig. 8. Temperature dependence of dielectric constant and loss for KNN. (a) Dielectric constant and (b) Dielectric loss.

The magnitude of piezoelectric constants at room temperature for annealed samples was found to be:  $d_{33} = 148$  pC/N and  $d_{31} = 69$  pC/N. The magnitude of  $d_{33}$  for the unannealed sample was found to be 119 pC/N. Figure 9 (a) and (b) shows the radial mode electromechanical coupling factor ( $k_p$ ) and mechanical quality factor ( $Q_m$ ) as a function of

temperature. It can be clearly seen that piezoelectric properties remain almost constant until the  $FE_t$  phase appears at 180 °C. The magnitude of  $k_p$  at room temperature is of the order of 0.456 and  $Q_m$  is around 234. Since in this system the high temperature phase ( $FE_t$ ) is also ferroelectric there is no danger of depoling on exceeding the transition temperature. This provides a considerable advantage over the competing NBT-KBT and NBT-BT systems and for this reason KNN ceramics are the most promising high piezoelectric non-lead system.

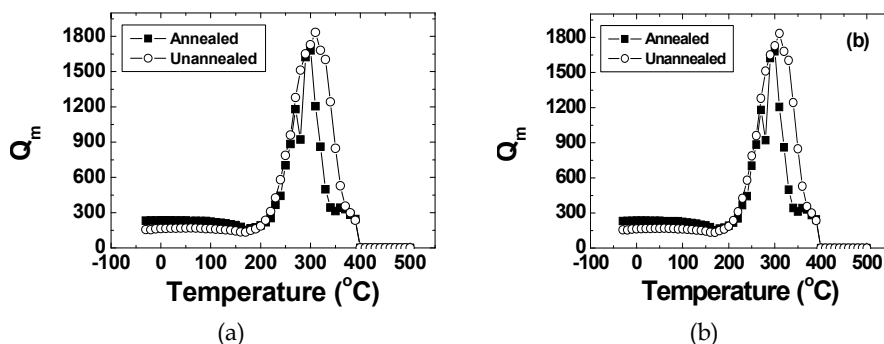


Fig. 9. Temperature dependence of piezoelectric properties for KNN. (a) Radial mode coupling factor and (b) Mechanical quality factor.

Further improvement in the properties of KNN can be obtained by synthesizing solid solution  $(1-x)(Na_{0.5}K_{0.5})NbO_3-xBaTiO_3$ . Three phase transition regions exist in  $(1-x)(Na_{0.5}K_{0.5})NbO_3-xBaTiO_3$  ceramics corresponding to orthorhombic, tetragonal, and cubic phases. The composition  $0.95(Na_{0.5}K_{0.5})NbO_3-0.05BaTiO_3$ , which lies on boundary of orthorhombic and tetragonal phase, was found to exhibit excellent piezoelectric properties. The piezoelectric coefficients of this composition were measured on a disk-shaped sample and were found to be as following:  $k_p=0.36$ ,  $d_{33}=225$  pC/N and  $\epsilon_{33}T/\epsilon_0=1058$  (Ahn et al., 2008). The properties of this composition were further improved by addition of various additives making it suitable for multilayer actuator application. The composition  $0.06(Na_{0.5}K_{0.5})NbO_3-0.94BaTiO_3$  was found to lie on the boundary of tetragonal and cubic phase. This composition exhibited the microstructure with small grain size and excellent dielectric properties suitable for multi-layer ceramic capacitor application. Table 3 shows the piezoelectric properties of modified  $0.95(Na_{0.5}K_{0.5})NbO_3-0.05BaTiO_3$  (KNN-BT) ceramics. It can be seen from this table that excellent piezoelectric properties with high transitions temperatures can be obtained in this system making it a suitable candidate for lead - free magnetoelectric composite.

The choice for the magnetostrictive phase in sintered or grown composites is spinel ferrites. In the spinel ferrites, the spontaneous magnetization corresponds to the difference between the sublattice magnetizations associated with the octahedral and tetrahedral sites. Results have shown enhanced magnitude of the ME coefficient for  $Ni_{0.8}Zn_{0.2}Fe_2O_4$  (NZF) and  $Co_{0.6}Zn_{0.4}Fe_2O_4$  (CZF). In the nickel zinc ferrite solid solution  $(Ni_{1-x}Zn_xFe_2O_4)$  as  $x$  is increased  $Zn^{2+}$  replaces  $Fe^{3+}$  in the tetrahedral sites and  $Fe^{3+}$  fills the octahedral sites emptied by  $Ni^{2+}$ . The net magnetization of nickel zinc ferrite is proportional to  $5(1+x) + 2(1-x) - 0(x) - 5(1-x) = 2 + 8x$ . Thus, the magnetic moment as a function of the Zn content increases until

there are so few  $\text{Fe}^{3+}$  ions remaining in tetrahedral sites that the superexchange coupling between tetrahedral and octahedral sites breaks down. Figure 10 shows our results on the PZT – NZF and PZT – CZF composites. It can be seen from this figure that CZF is a hard magnetic phase, requires higher DC bias, has lower remanent magnetization and results in larger reduction of the ferroelectric polarization as compared to NZF. On the other hand, a high increase in the resistivity of the Ni-ferrites is obtained by doping with Co. Thus, a combination of NZF and modified KNN-BT phase presents an opportunity to develop magnetoelectric composites with reasonable magnitude of coupling coefficient. Figure 11 (a) and (b) shows the ME response of  $(1-x) [0.948\text{K}_{0.5}\text{Na}_{0.5}\text{NbO}_3 - 0.052\text{LiSbO}_3] - x \text{Ni}_{0.8}\text{Zn}_{0.2}\text{Fe}_2\text{O}_4$  (KNNLS-NZF) composites. A reasonable magnitude of ME coefficient was obtained for the sintered composites (Yang et al., 2011). Compared to PZT based ceramics, this magnitude is about 50% smaller in magnitude.

Additives (in 0.95NKN-0.05BT)	$d_{33}$ (pC/N)	$k_p$	$\epsilon_3^T/\epsilon_0$	$Q_m$	$T_c$ ( $^{\circ}\text{C}$ )	Sin. T. ( $^{\circ}\text{C}$ )
None <sup>40,41</sup>	225	0.36	1,058	74	320	1,060
0.5 mol% $\text{MnO}_2$ <sup>53</sup>	237	0.42	1,252	92	294	1,050
1.0 mol% ZnO	220	0.36	1,138	71	-	1,040
2.0 mol% CuO <sup>47,54</sup>	220	0.34	1,282	186	286	950
2.0 mol% CuO + 0.5 mol% $\text{MnO}_2$ <sup>54</sup>	248	0.41	1,258	305	277	950

Table 3. Piezoelectric and dielectric properties of  $0.95(\text{Na}_{0.5}\text{K}_{0.5})-0.05\text{BaTiO}_3$  + additives.

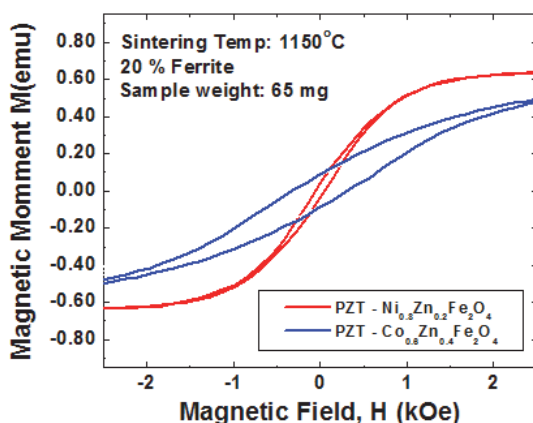


Fig. 10. Comparison of magnetic properties for PZT-NZF and PZT-CZF.

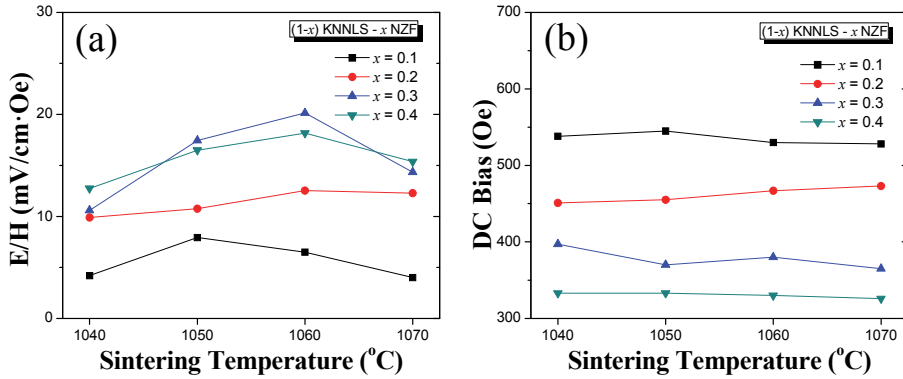


Fig. 11. ME coefficient and  $H_{bias}$  for (1-x) KNNLS - x NZF composites.

## 8. Devices based on magnetolectric interactions

### 8.1 Ac magnetic field sensors

The working principle of magnetic sensing in the ME composites is simple and direct. (Nan et al., 2008) When probing a magnetic field, the magnetic phase in the ME composites strains, producing a proportional charge in the piezoelectric phase.

Highly sensitive magnetic field sensors can be obtained using the ME composites with high ME coefficients. The ME composites can be used as a magnetic probe for detecting ac or dc fields.

Apart from a bimorph, a multilayer configuration of ME laminates has been reported that enables ultralow frequency detection of magnetic field variations. This configuration can greatly improve the low-frequency capability because of its high ME charge coupling and large capacitance. At an extremely low frequency of  $f=10$  mHz, the multilayer ME laminates can still detect a small magnetic field variation as low as  $10^{-7}$  T.

### 8.2 Magnetolectric gyrators

ME transformers or gyrators have important applications as voltage gain devices, current sensors, and other power conversion devices. An extremely high voltage gain effect under resonance drive has been reported in long-type ME laminates consisting of Terfenol-D and PZT layers. A solenoid with  $n$  turns around the laminate that carries a current of  $I_{in}$  was used to excite a  $H_{ac}$ . The input ac voltage applied to the coils was  $V_{in}$ . When the frequency of  $H_{ac}$  was equal to the resonance frequency of the laminate, the magnetolectric voltage coefficient was strongly increased, and correspondingly the output ME voltage ( $V_{out}$ ) induced in the piezoelectric layer was much higher than  $V_{in}$ . Thus, under resonant drive, ME laminates exhibit a strong voltage gain, offering potential for high-voltage miniature transformer applications. Figure 12 shows the measured voltage gain  $V_{out} / V_{in}$  as a function of the drive frequency for a ME transformer consisting of Terfenol-D layers of 40 mm in length and a piezoelectric layer of 80 mm in length. A maximum voltage gain of 260 was found at a resonance frequency of 21.3 kHz. In addition, at the resonance state, the maximum voltage gain of the ME transformer was strongly dependent on an applied  $H_{dc}$ ,

which was due to the fact that Terfenol-D has a large effective piezomagnetic coefficient only under a suitable  $H_{dc}$ . Other reports have shown that a ME laminate with a coil carrying current  $I_{in}$  has a unique current-to-voltage  $I$ - $V$  conversion capability. ME laminates actually act as a  $I$ - $V$  gyrator, with a high  $I$ - $V$  gyration coefficient (Dong et al., 2006a; Zhai et al., 2006). Fig. 13 shows ME gyration equivalent circuit. At electromechanical resonance, the ME gyrator shows a strong  $I$ - $V$  conversion of 2500 V/A, as shown in Fig. 10.

We also observed (i) reverse gyration: an input current to the piezoelectric section induced a voltage output across coils, and (ii) impedance inversion: a resistor  $R_i$  connected in parallel to the primary terminals of the gyrator resulted in an impedance  $G_2 / R_i$  in series with the secondary terminals.

### 8.3 Microwave devices

Ferrite-ferroelectric layered structures are of interest for studies on the fundamentals of high-frequency ME interaction and for device technologies. Such composites are promising candidates for a new class of dual electric and magnetic field tunable devices based on ME interactions (Bichurin et al., 2005; Tatarenko et al., 2006). An electric field  $E$  applied to the composite produces a mechanical deformation in the piezoelectric phase that in turn is coupled to the ferrite, resulting in a shift in the FMR field. The strength of the interactions is measured from the FMR shifts.

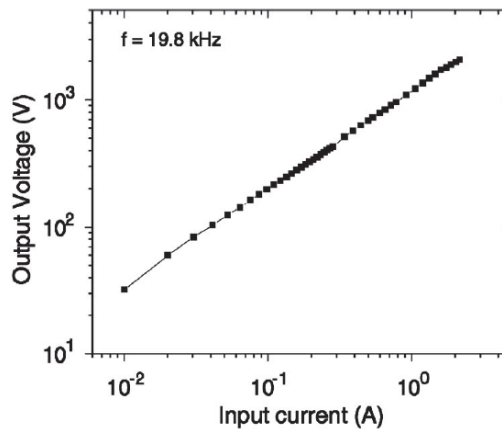


Fig. 12.  $I$ - $V$  gyration of the ME gyrator.

Ferrite-ferroelectric layered structures enable new paths for making new devices:

(1) Resonance ME effects in ferrite-piezoelectric bilayers, at FMR for the ferrite. The ME coupling was measured from data on FMR shifts in an applied electric field  $E$ . Low-loss YIG was used for the ferromagnetic phase. Single crystal PMN-PT and PZT were used for the ferroelectric phase; (2) Design, fabrication, and analysis of composite based devices, including resonators and phase shifters. The unique for such devices is the tunability with  $E$ . Our studies on YIG-PZT composites resulted in the design and characterization of a new class of microwave signal processing devices including resonators, filters, and phase shifters for use at 1-10 GHz. The unique and novel feature in ME microwave devices is the tunability with an electric field. The traditional "magnetic" tuning in ferrite devices is

relatively slow and is associated with large power consumption. The “electrical” tuning is possible for the composite and is much faster and has practically zero power consumption.

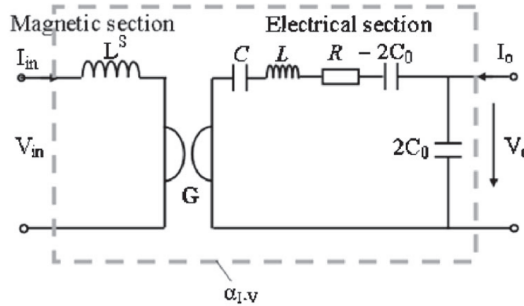


Fig. 13. ME gyration equivalent circuit.

The studies on microwave ME effects in YIG-PZT, YIG-PMNPT, and YIG-BST led to the design, fabrication, and characterization of a new family of novel signal processing devices that are tunable by both magnetic and electric fields. The device studied included YIG-PZT and YIG-BST resonators, filters, and phase shifters. As an example, a stripline ferrite-ferroelectric band-pass filters is considered. Design of our low-frequency ME filter is shown in Fig. 14 and representative data on electric field tuning are shown in Fig. 15. The single-cavity ME filter consists of a dielectric ground plane, input and output microstrips, and an YIG-PZT ME-element. Power is coupled from input to output under FMR in the ME element. A frequency shift of 120 MHz for  $E = 3$  kV/cm corresponds to 2% of the central frequency of the filter and is a factor of 40 higher than the line width for pure YIG. Theoretical FMR profiles based on our model are shown in Fig. 6 for bilayers with YIG, NFO, or LFO and PZT. For  $E = 300$  kV/cm, a shift in the resonance field  $\delta H_E$  that varies from a minimum of 22 Oe for YIG/PZT to a maximum of 330 Oe for NFO-PZT is predicted. The strength of ME interactions  $A = \delta H_E/E$  is determined by piezoelectric coupling and magnetostriction.

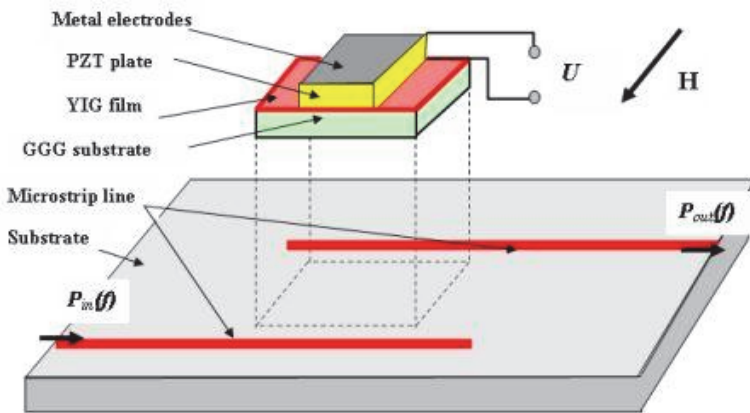


Fig. 14. ME band-pass filter. The ME resonator consisted of a 110  $\mu\text{m}$  thick (111) YIG on GGG bonded to PZT.

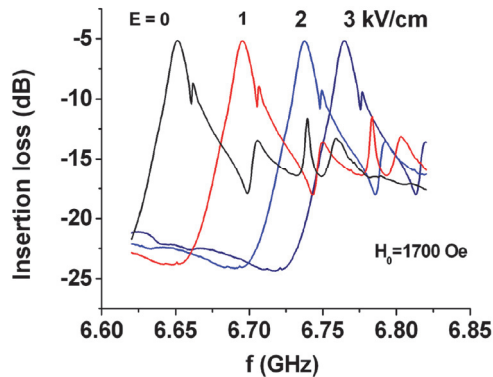


Fig. 15. Loss vs.  $f$  characteristics for a series of  $E$  for the YIG-PZT filter.

It is clear from the discussions here that ME interactions are very strong in the microwave region in bound and unbound ferrite-ferroelectric bilayers and that a family of dual electric and magnetic field tunable ferrite-ferroelectric resonators, filters, and phase shifters can be realized. The electric field tunability, in particular, is 0.1% or more of the operating frequency of filters and resonators. A substantial differential-phase shift can also be achieved for nominal electric fields.

## 9. Conclusions

We discussed detailed mathematical modeling approaches that are used to describe the dynamic behavior of ME coupling in magnetostrictive-piezoelectric multiferroics at low-frequencies and in electromechanical resonance (EMR) region. Our theory predicts an enhancement of ME effect that arises from interaction between elastic modes and the uniform precession spin-wave mode. The peak ME voltage coefficient occurs at the merging point of acoustic resonance and FMR frequencies. The experimental results on lead - free magnetostrictive -piezoelectric composites are presented. These newly developed composites address the important environmental concern of current times, i.e., elimination of the toxic “lead” from the consumer devices. A systematic study is presented towards selection and design of the individual phases for the composite.

There is a critical need for frequency tunable devices such as resonators, phase shifters, delay lines, and filters for next generation applications in the microwave and millimeter wave frequency regions. These needs include conventional radar and signal processing devices as well as pulse based devices for digital radar and other systems applications. For secure systems, in particular, one must be able to switch rapidly between frequencies and to do so with a limited power budget. Traditional tuning methods with a magnetic field are slow and power consumptive. Electric field tuning offers new possibilities to solve both problems.

Ferrite-piezoelectric composites represent a promising new approach to build a new class of fast electric field tunable low power devices based on ME interactions. Unlike the situation when magnetic fields are used for such tuning, the process is fast because there are no inductors, and the power budget is small because the biasing voltages involve minimal

currents. The critical goal for the future is in the development of a wide class of efficient wide band and low-loss electrically tunable magnetic film devices for battlefield radar, signal processing, and secure and experimental evaluation of characteristics. The anticipated advantages of ME devices are yet to be exploited.

## 10. References

- Ahn, C. W., Choi, C. H., Park, H. Y., Nahm, S., Priya, S. (2008) Dielectric and Piezoelectric Properties of  $(1-x)(\text{Na}_{0.5}\text{K}_{0.5})\text{NbO}_3\text{-xBaTiO}_3$  Ceramics, *J. Mat. Sci.* V. 43, (2008), p.p. 6784-6797.
- Bichurin, M. I., Petrov V.M., & Fomich, N.N. (1990) *Segnetomagnetic Substances*, Nauka, Moscow. (In Russian).
- Bichurin, M.I. (1997) Proceedings of the 3rd International Conference on Magnetoelectric Interaction Phenomena in Crystals (MEIPIC-3, Novgorod, Russia) *Ferroelectrics*, v. 204, (1997), P.p. 1-356.
- Bichurin, M.I., Kornev, I. A., Petrov, V. M., Tatarenko, A. S., Kiliba, Yu. V., & Srinivasan, G. (2001) Theory of magnetoelectric effects at microwave frequencies in a piezoelectric-magnetostrictive multilayer composite, *Phys. Rev. B* V. 64, (August 2001) p.p. 094409 (1-6). ISSN 1550-235X
- Bichurin, M. I., Petrov, V. M., Kiliba, Yu. V., & Srinivasan, G. (2002) Magnetic and magnetoelectric susceptibilities of a ferroelectric/ferromagnetic composite at microwave frequencies, *Phys. Rev. B* V. 66, (October 2002) p.p. 134404 (1-10).
- Bichurin, M. I., Petrov, V. M., & Srinivasan, G. (2003a) Theory of low-frequency magnetoelectric coupling in magnetostrictive-piezoelectric bilayers, *Physical Review B*, V. 68, Issue 5 (August 2003), p.p. 054402 (1-13), ISSN 1550-235X.
- Bichurin, M.I., Filippov, D.A., Petrov, V.M., Laletsin, V.M., Paddubnaya N., & Srinivasan, G. (2003b) Resonance magnetoelectric effects in layered magnetostrictive-piezoelectric composites, *Phys. Rev. B* 68, *Physical Review B*, V. 68, Issue 13 (October 2003), p.p. 132408 (1-4) , ISSN 1550-235X.
- Bichurin, M. I., Petrov, V. M., Ryabkov, O. V., Averkin, S. V., & Srinivasan, G. (2005) Theory of magnetoelectric effects at magnetoacoustic resonance in single-crystal ferromagnetic-ferroelectric heterostructures, *Phys. Rev. B*, V. 72, (August 2005), p.p. 060408 (1-4) (R).
- Bichurin, M. I., Petrov, V. M., Averkin, S. V., & Filippov, A. V. (2010) Electromechanical resonance in magnetoelectric layered structures, *Physics of the Solid State* V. 52, Number 10 (October 2010) p.p. 2116-2122. ISSN: 1090-6460
- Cai, N., Nan, C. W., Zhai, J. & Lin, Y. (2004) Large high-frequency magnetoelectric response in laminated composites of piezoelectric ceramics, rare-earth iron alloys, and polymers, *Applied Physics Letters*. V. 84, Number 18 (May 2004) p.p. 3516-3518, ISSN 1077-3118.
- Chashin, D.V., Fetisov, Y.K., Kamentsev, K.E., & Srinivasan, G. (2008) Resonance magnetoelectric interactions due to bending modes in a nickel-lead zirconate titanate bilayer, *Appl. Phys. Lett.* V. 92, Issue 10 (March 2008), p.p. 102511 (1-3), ISSN 1077-3118.
- Cheong, S. W. & Mostovoy, (2007) M. Multiferroics: a magnetic twist for ferroelectricity, *Nature Materials*, Vol. 6, (January 2007). p.p.13-20, ISSN 1476-4660.

- Dong, S., Li, J. F., & Viehland, D. (2003). Giant Magneto-Electric Effect in Laminate Composites, *Philosophical Magazine Letters* V. 83, Issue 12 (December 2003) p.p. 769-773, ISSN 1362-3036.
- Dong, S., Zhai, J., Bai, F., Li J. F., Viehland, D. (2005) Push-pull mode magnetostrictive/piezoelectric laminate composite with an enhanced magnetoelectric voltage coefficient, *Applied Physics Letters*. V. 87, Issue 6 (August 2005), p.p. 062502 (1-3), ISSN 1077-3118.
- Dong, S. X., Zhai, J. Y., Li, J. F., Viehland, D., & Bichurin, M. I. (2006a) Magnetolectric gyration effect in  $Tb_{1-x}Dy_xFe_{2-y}/Pb(Zr,Ti)O_3$  laminated composites at the electromechanical resonance, *Applied Physics Letters*. V. 89, Issue 24 (December 2006) p.p. 243512 (1-3) , ISSN 1077-3118.
- Dong, S., Zhai, J., Li, J., & Viehland D. (2006b) Near-ideal magnetoelectricity in high-permeability magnetostrictive/piezofiber laminates with a (2-1) connectivity *Applied Physics Letters*. V. 89, Issue 25 (December 2006), p.p. 252904 (1-3), ISSN 1077-3118.
- Fetisov, Y.K., Petrov, V.M., & Srinivasan, G. (2007) Inverse magnetoelectric effects in a ferromagnetic–piezoelectric layered structure, *Journal of Materials Research*. V. 22, Number 8 (August 2007) p.p. 2074-2080. ISSN: 0884-2914
- Fiebig, M. (2005). Revival of the magnetoelectric effect. *Journal of physics. D, Applied physics*, Vol. 38, Issue 8 (April 2005) p.p. R123–R152, ISSN 1361-6463.
- Filippov, D.A. (2004) Theory of Magnetoelectric Effect in Ferromagnetic–Piezoelectric Bilayer Structures, *Technical Physics Letters*, V. 30, Number 12 (December 2004), p.p. 983-986, ISSN 1090-6533.
- Filippov D.A., (2005) Theory of the Magnetoelectric Effect in Ferromagnetic–Piezoelectric Heterostructures, *Physics of the Solid State* V. 47, Number 6 (June 2005), p.p. 1118-1121. ISSN: 1090-6460
- Harshe, G., Dougherty, J. O., & Newnham, R. E. (1993) Theoretical Modelling of Multilayer Magnetolectric Composites. *Int. J.Appl. Electromagn. Mater.* V. 4, (1993), p.p. 145-159.
- Huanga, Z. (2006) Theoretical modeling on the magnetization by electric field through product property. *Journal of Applied Physics* V. 100, (2006)p.p. 114104(1-5)
- Kimura, M., Ogawa, T., Ando A., & Sakabe, Y. (2002) Piezoelectric properties of metastable (Li,Na)NbO<sub>3</sub> ceramics, *Proceedings of International Conference on Ferroelectrics*, Nara, Japan, 2002.
- Kita, E., Takano, S., Tasaki, A., Siratori, K., Kohn, K., & Kimura, S. (1988) Low-temperature phase of yttrium iron garnet (YIG) and its first-order magnetoelectric effect, *Journal of Applied Physics*, Vol. 64, Issue 10 (November 1988), p.p. 5659-5661, ISSN 1089-7550.
- Kornev, I., Bichurin, M., Rivera, J.-P., Gentil, S., Jansen, A. G. M., Schmid, H., & Wyder, P. (2000). Magnetoelectric properties of LiCoPO<sub>4</sub> and LiNiPO<sub>4</sub> *Phys. Rev. B* V. 62, Issue 18 (November 2000) p.p. 12247-12253, ISSN 1550-235X.
- Nagata, H. & Takenaka, T. (1991) (Na<sub>1/2</sub>Bi<sub>1/2</sub>)TiO<sub>3</sub> – BaTiO<sub>3</sub> System for Lead-Free Piezoelectric Ceramics, *Jpn. J. Appl. Phys.*, V. 30 [9B] (1991) p.p. 2236 – 2239 (1991).
- Nan, Ce-Wen, Liu, G., Lin Y., & Chen, H. (2005) Magnetic-Field-Induced Electric Polarization in Multiferroic Nanostructures, *Physical Review Letters*, V. 94, Issue 19 (May 2005), p.p. 197203 (1-4). ISSN 1079-7114.

- Nan, C.-W., Bichurin, M. I., Dong, S., Viehland, D., & Srinivasan, G. (2008), Multiferroic magnetoelectric composites: Historical perspective, status, and future directions, *Journal of Applied Physics*, Vol. 103, (February 2008), p.p. 031101 (1-35), ISSN 1089-7550.
- Osaretin, Idahosa A. & Rojas, Roberto G. (2010). Theoretical model for the magnetoelectric effect in magnetostrictive/piezoelectric composites, *Physical Review B*, V. 82, Issue 17 (November 2010), p.p. 174415 (1-8), ISSN 1550-235X.
- Petrov, V. M., Srinivasan, G., Bichurin, M. I., & Gupta, A. (2007), Theory of magnetoelectric effects in ferrite piezoelectric nanocomposites, *Phys. Rev. B* V. 75 (June 2007), p.p. 224407 (1-6). ISSN 1550-235X
- Petrov, V. M., Srinivasan, G., Bichurin, M. I. & Galkina, T. A. (2009) Theory of magnetoelectric effect for bending modes in magnetostrictive-piezoelectric bilayers, *Journal of Applied Physics* V. 105, Issue 6 (March 2009) p.p. 063911, ISSN 1089-7550.
- Prellier, W., Singh, M. P., & Murugavel, P. (2005) The single-phase multiferroic oxides: from bulk to thin film *Journal of Physics: Condensed Matter*. Vol. 17, No. 30, (August 2005), p.p. R803-R832.
- Priya, S., Ando A., & Sakabe, Y. (2003a) Nonlead Perovskite materials: Ba(Li<sub>1/4</sub>Nb<sub>3/4</sub>)O<sub>3</sub> and Ba(Cu<sub>1/3</sub>Nb<sub>2/3</sub>)O<sub>3</sub>, *J. Appl. Phys.*, V. 94 [2] (2003) p.p. 1171 - 1177.
- Priya, S., Kim H. W., & Uchino, K. (2003b) Design Consideration for Nonlead Piezoelectric Transformers *Proceedings of International Conference on Intelligent Materials*, State College, USA, 2003.
- Ryabkov, O. V., Petrov, V. M., Bichurin, M. I., & Srinivasan, (2006) *G. Tech. Phys. Lett.* V. 32, (2006) p.p. 1021.
- Ryu, J., Carazo, A. V., Uchino, K., & Kim, H. (2001). Magnetoelectric Properties in Piezoelectric and Magnetostrictive Laminate Composites, *Japanese Journal of Applied Physics*, V. 40 (May 2001), p.p. 4948-4951, ISSN 1347-4065
- Sasaki, A., Chiba, T., Mamiya, Y., & Otsuki, E. (1999) Dielectric and Piezoelectric Properties of (Na<sub>1/2</sub>Bi<sub>1/2</sub>)TiO<sub>3</sub> - (K<sub>1/2</sub>Bi<sub>1/2</sub>)TiO<sub>3</sub> Systems, V. 38 [9B] (1999) p.p. 5564 - 5567.
- Srinivasan, G., Rasmussen, E. T., Levin, B. J., & Hayes, R. (2002) Magnetoelectric effects in bilayers and multilayers of magnetostrictive and piezoelectric perovskite oxides. *Physical Review B*, V. 65, Issue 13 (March 2002), p.p. 134402 (1-7), ISSN 1550-235X.
- Tatarenko, A.S., Bichurin, M.I., & Srinivasan, G. (2005) Electrically tunable microwave filters based on ferromagnetic resonance in single crystal ferrite-ferroelectric bilayers, *Elec. Lett.*, V. 41, (2005), p. 596.
- Tatarenko, A.S., Srinivasan, G., & Bichurin, M.I. (2006) A magnetoelectric microwave phase shifter, *Appl. Phys. Lett.*, V. 88, (2006) p.p. 183507 (1-3).
- Wang, J., Neaton, J.B., Zheng, H., Nagarajan, V., Ogale, S.B., Liu, B., Viehland, D., Vaithyanathan, V., Schlom, D.G., Waghmare, U.V., Spaldin, N.A., Rabe, K.M., Wuttig, M., & Ramesh, R. (2003) Epitaxial BiFeO<sub>3</sub> Multiferroic Thin Film Heterostructures, *Science*, Vol. 299 (March 2003), p.p. 1719-1722, ISSN 1095-9203.
- Xing, Z., Dong, S., Zhai, Junyi, Yan, Li, Li, J. & Viehland, D. (2006) Resonant bending mode of Terfenol-D/steel/Pb(Zr,Ti)O<sub>3</sub> magnetoelectric laminate composites *Appl. Phys. Lett.* V. 89, Issue 11 (September 2006), pp. 112911 (1-3), ISSN 1077-3118.
- Yang, S.-C., Ahn, C.-W., Park, C.-S., & Priya, S. (2011) Synthesis and characterization of lead-free 0.8 [0.948K<sub>0.5</sub>Na<sub>0.5</sub>NbO<sub>3</sub> - 0.052LiSbO<sub>3</sub>] - 0.2 Ni<sub>0.8</sub>Zn<sub>0.2</sub>Fe<sub>2</sub>O<sub>4</sub> (KNNLS-NZF)

- island - matrix magnetoelectric composites and their application in nickel-based low frequency transducers, *J. Amer. Ceram. Soc.*, (2011) (accepted).
- Zhai, J. Y., Li, J. F., Dong, S. X., Viehland, D., & Bichurin, M. I. (2006) A quasi(unidirectional) Tellegen gyrator, *J. Appl. Phys.* V. 100, (2006) p.p. 124509 ISSN 1089-7550.
- Zhai, J., Xing, Z., Dong, S., Li, J., & Viehland, D. (2008) Thermal noise cancellation in symmetric magnetoelectric bimorph laminates *Appl. Phys. Lett.* V. 93, Issue 7 (August 2008) p.p. 072906 (1-3), ISSN 1077-3118.
- Zheng H., Wang J., Mohaddes-Ardabili, L., Wuttig, M., Salamanca-Riba, L., Schlom, D. G., & R. Ramesh, R. (2004) Three-dimensional heteroepitaxy in self-assembled BaTiO<sub>3</sub>-CoFe<sub>2</sub>O<sub>4</sub> nanostructures *Applied Physics Letters*. 85, Issue 11 (June 2004), p.p. 2035 (1-3), ISSN 1077-3118.

# Coupling Between Spins and Phonons Towards Ferroelectricity in Magnetoelectric Systems

J. Agostinho Moreira and A. Almeida

*IFIMUP-IN, Institute of Nanosciences and Nanotechnologies*

*Departamento de Física e Astronomia da Faculdade de Ciências da Universidade do Porto  
Portugal*

## 1. Introduction

Materials, which are either electrically or magnetically polarizable, have attracted the interest of the scientific community for long, due to both their potential technological applications and the emergent fundamental questions associated with the mechanisms tailoring their pertinent physical properties.<sup>1</sup>

Among them, a class of materials exists, exhibiting at least two ferroic ground states, which are known as multiferroic materials.<sup>2</sup> Another class is characterized by the emergence of a magneto-electric coupling, where multiferroicity is not even necessary to be present. This sort of materials yields the possibility to control the magnetic (polar) state through an applied electric (magnetic field). One of the most relevant examples is its use to processing of barriers and interfaces to spintronic devices, enabling to implement electrically controlled spin transport, but other interesting applications are currently under investigation.<sup>3-11</sup>

Unfortunately though, either magnetoelectric coupling coefficient is rather small, or the range of temperatures it occurs is far way from room temperature, precisely where devices are requested to have their working range. Based on theoretical and experimental results, an intensive research to designing new magnetoelectric materials has been undertaken aimed at overcoming the aforesaid drawbacks.<sup>12</sup> On designing new systems, their crystal structure has been addressed concerning both lattice and geometrical arrangements of their atomic or molecular constituents. This is particularly the case of the orthorhombic rare-earth manganites belonging to the  $\text{GdFeO}_3$  type structure.<sup>13</sup> In this sort of structure, rare-earth site alteration drives the magnitude of the orthorhombic distortion, so-called cooperative  $\text{GdFeO}_3$ -type distortion, wherein the increase of the Mn-O1-Mn bond angle of the  $\text{MnO}_6$  octahedra yields an increasing of the orthorhombic distortion, whenever a smaller-sized rare-earth ion is used.<sup>13</sup> Thus, by handling the Mn-O1-Mn bonds angle between consecutive  $\text{MnO}_6$  octahedra, drastic changes of their phase diagrams can be reached.<sup>13</sup> As it will be presented further below, this is highly predictable, since changing the Mn-O1-Mn bond angle directly modifies the balance between the competitive ferromagnetic and antiferromagnetic exchange interactions, existing in these materials. This is the background mechanism of magnetically induced ferroelectricity, in some rare-earth manganites.

Contrarily to well know ferroelectrics, like  $\text{BaTiO}_3$ , where hybridization between the titanium 3d states and the oxygen 2p states is at the very origin of ferroelectricity, in

magnetoelectric rare-earth materials it seems to stem from the emergence of spin-lattice interactions in modulated off-centre symmetric magnetic structures, which is in favour for the improper nature of the ferroelectric ground state. For some magnetoelectric materials, it has been proposed that ferroelectricity is originated from a variety of spiral magnetic structures, and can be explained in terms of the inverse Dzyaloshinski-Morya model.<sup>14-16</sup> On the grounds of this model, the interaction between spins, arranged in a modulated structure, deform the crystal lattice, yielding the loss of the spatial inversion centre and, thus, enabling the emergence of electric dipoles. As the electric polarization arises from lattice distortions, the study of the coupling between spins and phonons is of most relevant matter in systems, wherein magnetic and ferroelectric properties are coupled. Consequently, from both fundamental and application point of views, a deeper understanding of spin-phonon coupling remains a very important issue.

The most studied magnetoelectric materials are the orthorhombic rare-earth manganites, such as  $\text{EuMnO}_3$ ,  $\text{GdMnO}_3$ ,  $\text{TbMnO}_3$  and  $\text{DyMnO}_3$ .<sup>17-23</sup> These systems exhibit rather interesting phase diagrams, with magnetically driven ferroelectric phase transitions, for compounds with the lighter rare-earth ions, or magnetically switching of electric polarization, for those ones with the heavier rare-earth ions. These materials behave differently since, by changing rare-earth ion size, the Mn-O1-Mn bond angle changes accordingly and hence the balance between ferromagnetic and antiferromagnetic interactions. Unfortunately, the change of rare-earth ions also brings changes to the magnetic state through its own magnetic characteristics. If it is required to comprehend just the effect of ion radius size, the solid solution obtained by A-site substitution in europium manganite with a non-magnetic ion, with a radius smaller than europium will ensure the aforesaid requisites. Since neither yttrium nor europium ions possess magnetic moment, interchanging them does not change the total magnetic moment. It stems only from the  $\text{Mn}^{3+}$  ions. From the reasoning presented to above, it is apparent why Y-doped  $\text{EuMnO}_3$  system has been extensively studied to date.<sup>24-32</sup>

Several studies of the lattice dynamics by using Raman and infrared spectroscopies in Y-doped  $\text{EuMnO}_3$ , have revealed a coupling between magnetic excitations and phonons, through anomalous temperature behaviour of the phonon parameters or absorption across the magnetic phase transitions.<sup>33-38</sup> However, an overview of the experimental results in order to evidence the main mechanisms underlying the spin-phonon coupling is still missing.

In this book chapter, we will present a detailed review of the main theoretical and experimental results concerning the lattice dynamics and spin-phonon coupling in the case study:  $\text{Eu}_{1-x}\text{Y}_x\text{MnO}_3$  for  $0 \leq x \leq 0.5$ , where the structure is orthorhombic with the  $Pbnm$  space group. The main goal is to understand the mechanisms of coupling between magnetic excitations and phonons yielding the magnetically switching of ferroelectricity in spiral magnets and, in this way, the very origin of the ferroelectric ground state in these compounds.

## 2. Theoretical background

Important advances have been achieved towards a fundamental understanding of the stabilization of ferroelectric ground states in magnetoelectrics through experimental observation and investigation of the coupling mechanism between the ferroelectric and magnetic orders. Some examples involve the use of second harmonic light generation,

dielectric and magnetic measurements or structural investigation. In contrast, very little is known about the behaviour of phonons in magnetoelectrics, although studies of phonons have in the past played a crucial role in the understanding of classic ferroelectrics. Phonons are also known to be altered by spin correlations thus offering a complementary and maybe even unique powerful tool to investigate coupling mechanism in magnetoelectrics.<sup>39-41</sup>

Before going into details of phonon analysis and their coupling with spins, let us summarize some aspects associated with the origin and main characteristics of spin structure in orthorhombic rare-earth manganites. The main crystalline motif of their structure is the existence of  $\text{MnO}_6$  octahedra, which run over chains by sharing apical oxygen ions. The 3d electronic orbitals of the transition  $\text{Mn}^{3+}$  ions yield a rather multifaceted correlation between spin arrangements and crystalline structure, which is at the very origin of the broad range of physical properties observed in rare-earth manganites. In an ideal cubic crystal field environment, the 3d  $\text{Mn}^{3+}$  orbitals are splitted into two degenerate higher energy states, called  $d(x^2-y^2)$  and  $d(3z^2-z^2)$ , with  $e_g$  symmetry, and three degenerate lower energy states, ( $d_{xy}$ ,  $d_{xz}$ ,  $d_z$ ), with  $t_{2g}$  symmetry. Since  $e_g$  orbitals are much closer to the 2p oxygen electronic orbitals, Coulomb interaction yields a partial degeneracy lifting of the 3d orbitals. Moreover, if the magnitude of the crystal field is much larger than spin-orbit coupling, a quenching of the orbital angular momentum occurs, reflecting the actual spin structure in rare-earth manganites.<sup>42,43</sup>

Over Coulomb interaction, the 3d electrons of  $\text{Mn}^{3+}$  ions can assure different kinds of interactions. Whilst Hund and direct interactions favour ferromagnetic ordering of spins, Hubbard tends to align spins antiferromagnetically. Moreover, orbital degeneracy is at the origin of some types of superexchange interactions. From the substantial overlapping of these latter orbitals with 2p oxygen ones, a strong superexchange interaction is obtained. Contrarily, due to the orthogonal spatial orientation of the  $t_{2g}$  orbitals against the  $2p_o$  oxygen orbitals and just a reduced overlapping with the  $2p_\pi$  ones, weak superexchange interactions are thus expected.<sup>42,43</sup>

In orthorhombic rare-earth manganites a significant distortion occurs associated with  $\text{MnO}_6$  octahedra, which is known as the Jahn-Teller effect.<sup>44,45</sup> This distortion, which occurs along the molecular fourfold axes, has the effect of lifting both orbital and electronic degeneracies, leading to a decrease of the total energy.<sup>42,43</sup>

The coupling between spins and lattice has become one of the major mechanisms to understand the interplay between magnetism and ferroelectricity occurring in rare-earth manganites with intermediate-range magnitudes of the  $\text{GdFeO}_3$  distortion, as it is the case of  $\text{ReMnO}_3$ ,  $\text{Re}=\text{Eu, Gd, Tb, and Dy}$ . The so-called magnetoelectric effect has been understood in the scope of both phenomenological and microscopic theories. In the former case, contributions first from Landau and latter from Dzyaloshinskii and Moriya (DM) were presented, wherein symmetry conditions imposed by the magnetic point group are essential issues for understanding the emergence of the magnetoelectric effect.<sup>46-48</sup> In particular, both time and inversion symmetries are key issues for controlling the ME effect. Microscopic quantum theory of the ME effect has been developed by I. A. Sergienko *et al*<sup>16</sup> and Katsura *et al*.<sup>49</sup> These latter authors showed that ME effect and spin current are related to one another in non-linear spin structures, like spiral-like states. In fact, as both electric polarization and spin current belong to the same symmetry class, it is expected that are coupled together. The coupling was demonstrated by considering a cluster scheme with two transition metal ions intermediated by an oxygen atom shown in Figure 1.

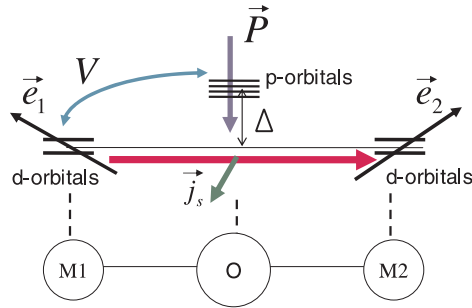


Fig. 1. The cluster model with two transition metal ions M1 and M2, and an oxygen atom between them. Reprinted figure from Ref. 49. Copyright (2005) by the American Physical Society.

By assuming the overlapping between the electronic wave functions of two adjacent sites  $i$  and  $i+1$  with mutually canted spins,  $\mathbf{S}_i$  and  $\mathbf{S}_{i+1}$ , the inverse Dzyaloshinskii-Moriya model yields a local polarization  $p_i$ , given by:<sup>50</sup>

$$\mathbf{p}_i = A \mathbf{e}_{i,i+1} \times (\mathbf{S}_i \times \mathbf{S}_{i+1}). \quad (1)$$

$\mathbf{e}_{i,i+1}$  stands for the unit vector linking both sites, being  $A$  a constant reflecting spin-orbit interactions and spin-exchange. Thus, the cycloidal spin arrangement in rare-earth manganites enables an electric polarization to emerge, obtained by summing all of the local polarization  $\mathbf{p}_i$ . It comes out from equation (1) that the polarization lays in the cycloidal plane. As a consequence, in rare-earth manganites, the ferroelectric polarizations expected along  $a$ - and  $c$ -direction lay in the  $ab$ - and  $cb$ -cycloidal planes, respectively (Figure 2).

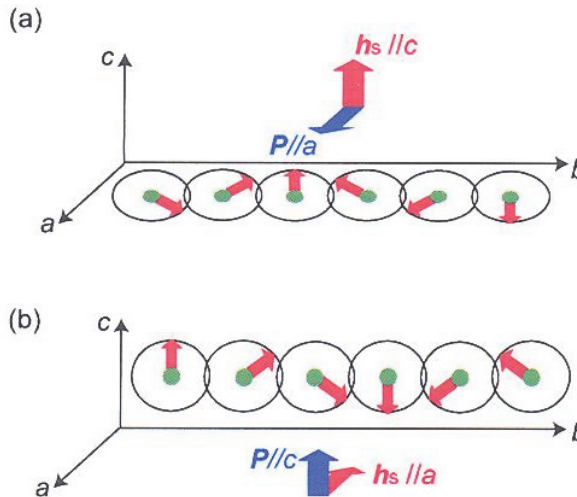


Fig. 2. Spatial scheme of the DM polarization against  $\mathbf{h}_i = \sum_j \mathbf{S}_j \times \mathbf{S}_{j+1}$  for (a)  $ab$ -cycloidal spin plane and (b)  $bc$ -cycloidal spin plane. Reprinted figure from Ref. 50. Copyright (2009) by the American Physical Society.

The inverse DM model has been successfully tested both theoretically and experimentally in a variety of magnetoelectric rare-earth manganite systems.<sup>15,16,51,52</sup> The emergence of inverse-DM induced polarization in rare-earth manganites depends on the magnitude of the GdFeO<sub>3</sub> distortion, characterized by the amplitude of the Mn-O1-Mn bond angle or the rare-earth ionic radius size. The following examples show that increasing (decreasing) the GdFeO<sub>3</sub> distortion (Mn-O1-Mn bond angle or the rare-earth radius size) enhances the inverse-DM magnetically induced polarization. The first example is the emergence of an electric polarization along the *c*-direction when changing from GdMnO<sub>3</sub> to TbMnO<sub>3</sub> and DyMnO<sub>3</sub>, which is associated with the increase of the GdFeO<sub>3</sub> distortion due to ionic radius size decrease.<sup>53,54</sup> Further examples can be found in Gd<sub>1-x</sub>Tb<sub>x</sub>MnO<sub>3</sub><sup>55,56</sup> and Eu<sub>1-x</sub>Y<sub>x</sub>MnO<sub>3</sub><sup>24,26,31,57,58</sup> solid solutions.

Changes of the polarization state are obtained by continuously control the GdFeO<sub>3</sub> distortion by increasing dopant content, decreasing in this way the ionic radius size. In fact, above a certain doping level a long-range ferroelectric ground state is stabilized at low temperatures associated with an *ab*-cycloidal spin state, where electric polarization emerges along the *a*-crystallographic direction. For larger dopant concentration the cycloidal *cb*-plane spontaneously flops at higher temperature to the *ab*-plane at lower temperatures, along with a rotation of the electric polarization from the *c*- to the *a*-direction.<sup>26</sup>

The examples referred to above undoubtedly evidence the role of the GdFeO<sub>3</sub> distortion to inducing electric polarization via inverse DM interaction. Moreover, it has been established that this distortion has a crucial effect on the balance between the ferromagnetic superexchange interaction, associated with the next-nearest (NN) spins, and the antiferromagnetic superexchange one of the next-next nearest (NNN) spins.<sup>13,50</sup> Increasing the GdFeO<sub>3</sub> distortion enhances the antiferromagnetic against the ferroelectric interactions. This mechanism apparently yields the reduction of the AFM(A) phase transition temperature with decreasing Mn-O1-Mn bond angle in orthorhombic rare-earth manganites, and the emergence of the AFM ordering or spiral spin ordering, where ferroelectric ground states can be stabilized.

Several attempts have been made in order to develop microscopic spin models to understand the phase diagrams of rare-earth manganites.<sup>13,16,59-62</sup> The essence of magnetoelectric properties can be described if they are mapped onto a frustrated classical S=2 Heisenberg model on a cubic lattice, with FM NN ( $J_{ab}$ ), and AFM NNN ( $J_2$ ) exchange interactions acting in the *ab*-plane, and AFM NN ( $J_c$ ) exchange interaction along the *c*-direction, as it is shown in figure 3. In the Hamiltonian the Mn S=2 spins are considered as classical vectors expressed as  $\mathbf{S}_i = (\sqrt{S^2 - S_c^2} \cos \theta_i, \sqrt{S^2 - S_c^2} \sin \theta_i, S_c)$ , with their components along *a*, *b*, and *c* axes of the *Pbnm* space group.

The Hamiltonian includes four terms involving superexchange and DM interactions, and contributions from both single ion and cubic anisotropies, expressed as follows:<sup>50</sup>

$$H = H_{ex} + H_{DM} + H_{sia} + H_{cub}, \quad (2)$$

wherein:

$$H_{ex} = -J_{ab} \sum_{\langle i,j \rangle}^{x,y} \mathbf{S}_i \cdot \mathbf{S}_j + J_2 \sum_{\langle i,j \rangle}^b \mathbf{S}_i \cdot \mathbf{S}_j + J_c \sum_{\langle i,j \rangle}^c \mathbf{S}_i \cdot \mathbf{S}_j, \quad (3)$$

$$H_{DM} = \sum_{\langle i,j \rangle} \mathbf{d}_{ij}^{\alpha} \cdot (\mathbf{S}_i \times \mathbf{S}_j), \quad (4)$$

$$H_{sia} = D \sum_i S_{\zeta i}^2 + E \sum_i (-1)^{i_x+i_y} (S_{\zeta i}^2 - S_{\eta i}^2), \quad (5)$$

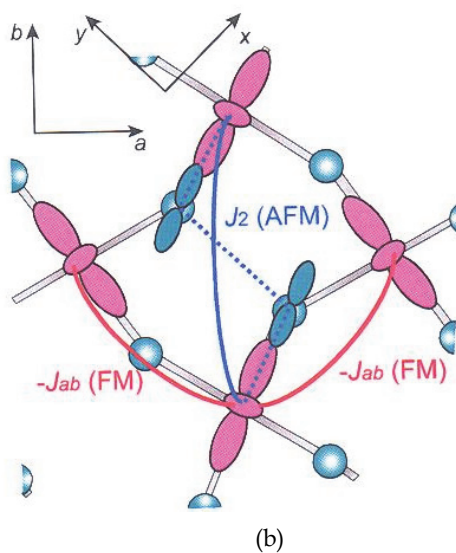
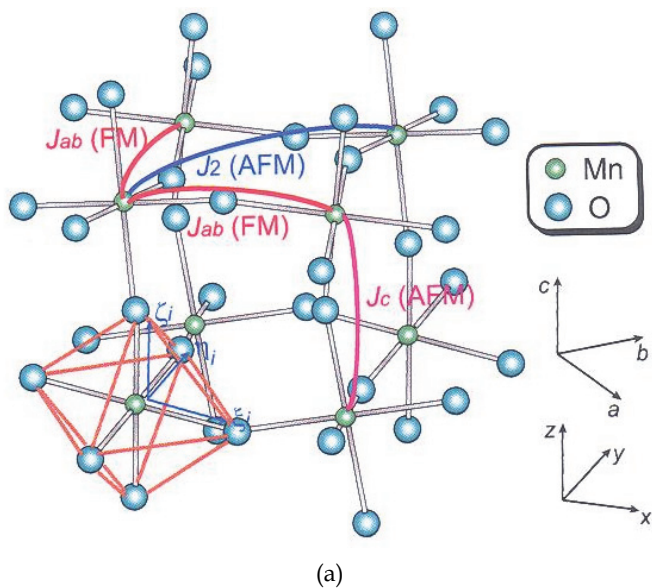


Fig. 3. (a) Exchange interactions in rare-earth manganites.  $J_{ab}$ -FM interactions on the Mn-Mn bonds along the cubic  $x$ - and  $y$ -axes,  $J_2$ -AFM interactions on the in-plane diagonal Mn-Mn bonds along the orthorhombic  $b$ -axis, and  $J_c$ -AFM interactions on the Mn-Mn bonds along the  $c$ -axis. (b)  $e_g$  occupied orbitals configuration and both  $J_{ab}$  and  $J_2$  interactions (solid lines) in the  $ab$ -plane. A dashed line marks  $J_2$  interaction path, via two oxygen  $2p$  orbitals. Reprinted figure from Ref. 50. Copyright (2009) by the American Physical Society.

and

$$H_{cub} = \frac{a}{s(s+1)} \sum_i (S_{xi}^4 + S_{yi}^4 + S_{zi}^4). \tag{6}$$

$i_x, i_y$  and  $i_z$  are the coordinates of the  $i$ -th manganese ion along the  $x, y$ , and  $z$  cubic axes. The superexchange term consists of NN FM  $J_{abr}$ , NNN AFM  $J_2$ , and AFM NN  $J_c$  interactions.  $J_{ab}$  is associated with the AFM arrangement of  $e_g$  orbitals in the  $ab$ -plane, while  $J_2$  stems from AFM exchange between the two Mn  $e_g$  orbitals in the  $b$ -direction, along the path defined by the two  $2p$  oxygen orbitals. AFM  $J_c$  comes from ferro-orbital stacking along the  $c$ -direction. As in manganites  $J_{ab}$  and  $J_c$  are comparable in magnitude, and  $J_2$  is strongly dependent on GdFeO<sub>3</sub> distortion, it is evident the important role played by changing the Mn-O1-Mn bond to alter the magnetic properties of rare-earth manganites. Thus, it is expected that by increasing  $J_2$  against  $J_{abr}$ , the GdFeO<sub>3</sub> distortion will tend to stabilize spiral spin ordering with ferroelectric properties. This is in perfect agreement with the experimental results obtained in the rare-earth manganite systems referred to above.

The second term of the Hamiltonian (Eq. 4) concerns the DM interactions.<sup>47,48,63</sup> The  $\mathbf{d}_{ij}^\alpha$  vector regards the Mn(i)-O-Mn(j) bond along the  $\alpha$  cubic axis ( $\alpha = x, y, z$ ). Figure 4 shows the DM in-plane and out-of-plane vectors in the vicinity of the Mn(i)-O-Mn(j).

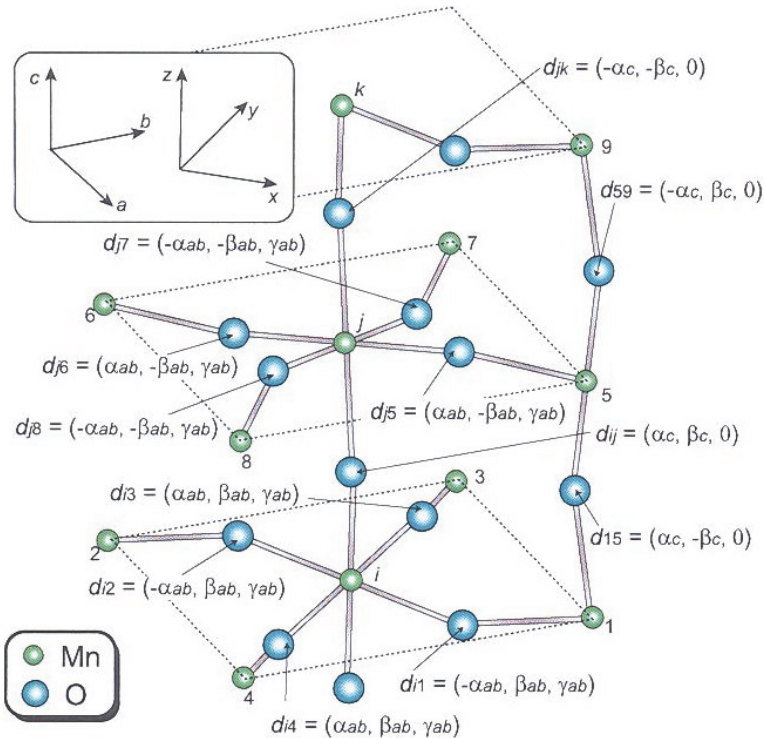


Fig. 4. DM vectors around the Mn(i)-O-Mn(j) bond, expressed as a function of the parameters  $\alpha_{ab}, \beta_{ab}, \gamma_{ab}, \alpha_c,$  and  $\beta_c$ . Reprinted figure from Ref. 50. Copyright (2009) by the American Physical Society.

From the spatial orientation of the  $e_g$  orbitals it can be reckoned that while the DM vectors regarding in-plane Mn-O-Mn bonds are almost perpendicular to the plane, those corresponding to out-of-plane bonds are not. Recent calculations yield a magnitude three times larger for the out-of-plane DM vector relative to the in-plane one. It is worthwhile to note that  $a_c$  has the same sign in each plane, though alternating along de  $c$  axis. Due to spin canting in the AFM(A) phase, a weak ferromagnetism is thus expected along  $c$  axis, in good agreement with earlier results.<sup>26,64</sup>

The single-ion anisotropy contribution is determined by the octahedron environment of the manganese ion. The first term of equation 5 implies that the  $c$ -axis becomes a hard magnetization axis, as  $\zeta_i$  is directed mainly along  $c$ . Contrarily, the second term evidences the existence of local magnetization axes along  $\xi_i$  and  $\eta_i$ , alternatively located in the  $ab$  plane. The cubic anisotropy term reflects the cubic anisotropy, which stems from the nearly cubic symmetry of the perovskite lattice. The contribution from orthorhombic distortion is not taken into account, since its magnitude is comparatively very small.

Earlier experimental results, which were aimed at studying the magnetic, electric and magnetoelectric properties of rare-earth manganites, reveal that the GdFeO<sub>3</sub> distortion plays a major role by enhancing the AFM exchange interactions  $J_2$  against the FM ones  $J_{ab}$ . Thus, it is challenging to trace the  $(T, J_2)$  phase diagrams in order to understand those obtained experimentally as a function of either the rare-earth radius size or the concentration of dopant ion. Figure 5 shows the  $(T, J_2)$  phase diagram obtained on the grounds of this model for  $a_c = 0.30$  meV, and tends to reproduce the main characteristics revealed by a variety of experimental  $(T, x)$  phase diagrams earlier presented for  $\text{Eu}_{1-x}\text{Y}_x\text{MnO}_3$ .<sup>24,26,31</sup>

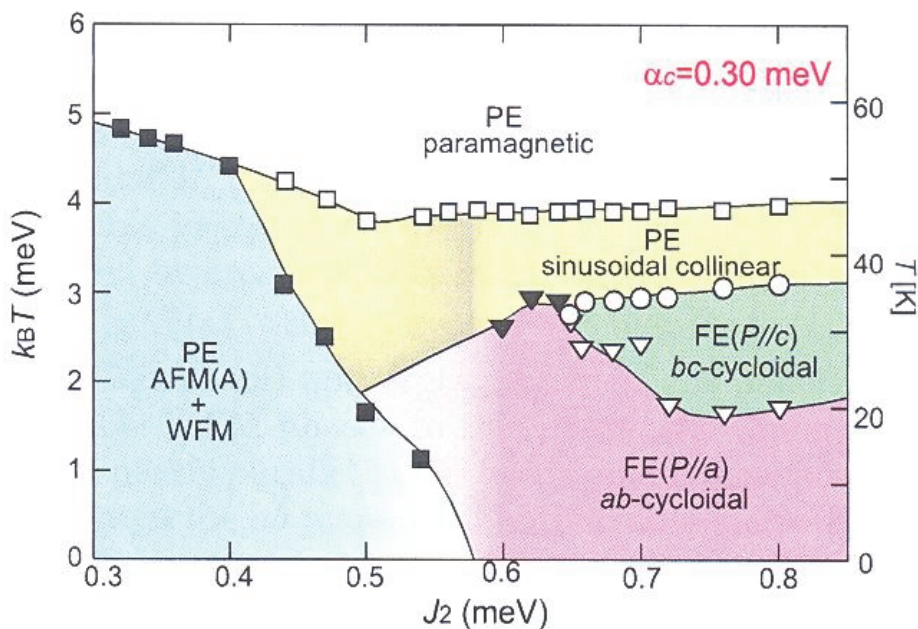


Fig. 5. Theoretical  $(T, J_2)$  phase diagram obtained for  $a_c = 0.30$  meV. Reprinted figure from Ref. 50. Copyright (2009) by the American Physical Society.

Except for some distinctive details regarding the trace of the phase boundaries, the diagram shown in Figure 5 reproduces quite well the phase arrangement obtained experimentally. WFM+AFM(A) phase emerges for lower values of  $J_2$ . For increasing  $J_2$  values, AFM modulated phases are stabilized, where modulation is a consequence of DM interaction, here determined by  $a_c = 0.30$  meV. The modulation of the AFM phases is needed for stabilizing the ferroelectric ground state.

It is also worth to note the flop of the polarization from  $P_c$  at high temperatures to  $P_a$  at low temperatures for higher values of  $J_2$ . This flop is though puzzling. Since the  $c$  axis in rare-earth manganites is always the magnetization hard axis due to the  $H_{sia} = D \sum_i S_{ci}^2$  single-ion anisotropy, it is expected a higher energy for the  $bc$ -cycloidal spin state than for the  $ab$  one. The reason for the stabilization of the  $bc$ -cycloidal spin state for high  $J_2$  values stems from considering the energy balance  $|\Delta E_{DM}^{bc} - \Delta E_{DM}^{ab}|$  due to DM term for both  $bc$ - and  $ab$ -spin states. In fact, this balance dominates for high  $J_2$  values the energetic disadvantage stemming from the hard  $c$ -magnetization axis. This means that the  $ab$ - and  $bc$ -cycloidal spin states are actually stabilized by single-ion anisotropy or DM interactions.

Moreover, as the spins in the  $bc$ -cycloidal state are mainly associated with  $a$  component of DM vectors on the out-of-plane Mn-O-Mn bonds, it is expected that  $a_c$  becomes an important parameter to determine the relative temperature range of both  $bc$ - and  $ab$ -spin states. It can be shown by increasing  $a_c$  up to 0.38 meV that the  $Gd_{1-x}Tb_xMnO_3$  phase diagram can be reproduced, where for high values of  $J_2$  just the  $bc$ -cycloidal spin state is stabilized in good agreement with earlier experimental results. Contrarily to earlier results, it is also evidenced that the flop of the cycloidal spin plane is quite independent of the  $f$ -electron moments, as it becomes clear from the  $(T, J_2)$  phase diagrams of  $Gd_{1-x}Tb_xMnO_3$  and  $Eu_{1-x}Y_xMnO_3$  systems.<sup>24,26,31</sup>

Additionally, by analysing the single-ion anisotropies, it can be reckoned that the  $GdFeO_3$  distortion energetically favours the orientation of the spins along the  $b$  axis in both the AFM(A) and sinusoidal collinear phases.

### 3. Case study: $Eu_{1-x}Y_xMnO_3$ ( $0 < x < 0.55$ )

The coupling between spin and phonons has been observed in a broad range of materials, exhibiting ferromagnetic, antiferromagnetic, magnetoresistive, or superconducting properties. Many of them do not present magnetoelectric effect, evidencing that the existence of that coupling does not necessary lead to the emergence of this effect.<sup>65-68</sup> Thus, if we aim at assessing the role of spin-phonon coupling to stabilize ferroelectric ground states, it will be undertaken in materials that exhibit magnetoelectric coupling. Orthorhombic rare-earth manganites are actually good candidates as magnetoelectricity can be gradually induced by simply changing the rare-earth ion.<sup>13,16,17,50</sup> This is the case of rare-earth ions passing from Nd, Sm, Eu, Gd, Tb, to Dy, which are quite suitable to study the way the magnetoelectric effect correlates with spin-phonon coupling. However, along with the change of the ionic radius size, an unavoidable change of the total magnetic moment will occur, due to the different magnitude of the magnetic moment of each rare-earth ion. The best way to have just the change of one variable is to preserve the magnetic moment by choosing a system that does not involve any other magnetic moments than those that stem from the manganese ions. There is at least one system that fulfils these requirements. The solid solution obtained by introducing yttrium ions at the A-site of  $EuMnO_3$ . Since both europium and yttrium ions do not possess any magnetic moment by interchanging them the

total magnetic moment remains constant. Most interesting is then what really changes? As yttrium has a smaller radius than europium by increasing yttrium content the effective A-site radius decreases accordingly. We have then a system worth to be studied, where by decreasing just the A-site effective site and consequently decreasing the Mn-O1-Mn bond angle, it will directly act on the balance of the ferromagnetic and antiferromagnetic interactions, tailoring in the way the phase diagram of the system. One of the consequences is the stabilization of spiral incommensurate antiferromagnetic spin structures, enabling the emergence of ferroelectric ground states on the basis of the DM model.

From the phase diagram presented to above it is reckoned that the different compositions for  $x$  less than 0.5 can be gathered in several sets with specific physical properties. Thus, the experimental data obtained will be shown by taking this division into sets in account. But before going into it, let us summarize the state-of-art of the yttrium doped  $\text{EuMnO}_3$  system.

### 3.1 General considerations about the phase diagram of $\text{Eu}_{1-x}\text{Y}_x\text{MnO}_3$ , $x < 0.55$

The possibility of systematic and fine tuning of the A-site size, without increasing the magnetic complexity arising from the rare-earth ion, is achieved by the isovalent substitution of the trivalent  $\text{Eu}^{3+}$  ion by  $\text{Y}^{3+}$ ,  $\text{Eu}_{1-x}\text{Y}_x\text{MnO}_3$ , with  $x < 0.55$ . This allows us for a continuous variation of the Mn-O1-Mn bond angle, which is associated with the development of the complex magnetic ground states and ferroelectric phases.

The main features of the phase diagram of  $\text{Eu}_{1-x}\text{Y}_x\text{MnO}_3$ , with  $0 \leq x < 0.55$ , has been described on the grounds of competitive NN ferromagnetic and NNN antiferromagnetic interactions, along with single-ion anisotropy and the Dzyaloshinsky-Morya interaction.<sup>50</sup> Therefore, this system exhibits a rich variety of phase transitions from incommensurate to commensurate antiferromagnetic phases, some of them with a ferroelectric character, depending on the magnitude of  $x$  substitution.

We should highlight the importance of this result as it definitely confirms assumptions forwarded in previously published works carried out in orthorhombically distorted rare-earth manganites.<sup>17-26</sup> What makes them a very interesting set of materials is the fact that they share a common  $\text{GdFeO}_3$ -distortion, where the tilt angle of the  $\text{MnO}_6$  octahedra becomes larger when the rare-earth radius decreases. This behaviour is illustrated in Figure 6 for several undoped rare-earth manganites and the  $\text{Eu}_{1-x}\text{Y}_x\text{MnO}_3$  doped system.<sup>31</sup> As it can be seen for undoped rare-earth manganites, by decreasing the ionic radius size, the Mn-O1-Mn bond angle decreases almost linearly. However, for the  $\text{Eu}_{1-x}\text{Y}_x\text{MnO}_3$  system, a significant deviation from the linear behaviour observed for undoped manganites, is detected. It is worthwhile to note that a much steeper slope is observed for the  $\text{Eu}_{1-x}\text{Y}_x\text{MnO}_3$  system. Since the slope of the Mn-O1-Mn bond angle as a function of  $x$  scales with the degree of competition between both the NN neighbour ferromagnetic and the NNN antiferromagnetic exchanges in the basal  $ab$ -plane, its phase diagram has then to exhibit very unique features, which distinguish the  $\text{Eu}_{1-x}\text{Y}_x\text{MnO}_3$  system from the others. Such features are apparent out from earlier phase-diagrams.<sup>24,26</sup>

Ivanov *et al*<sup>58</sup>, Hemberger *et al*<sup>24</sup>, and Yamasaki *et al*<sup>26</sup> have proposed ( $x$ ,T) phase diagrams, for  $\text{Eu}_{1-x}\text{Y}_x\text{MnO}_3$  single crystals, with  $0 \leq x < 0.55$ , obtained by using both identical and complementary experimental techniques. Although the proposed phase diagrams present discrepancies regarding the magnetic phase sequence and the ferroelectric properties for  $0.15 < x < 0.25$ , there is a good agreement concerning the phase sequence for  $0.25 < x < 0.55$ .

Recently, a re-drawn  $(x,T)$  phase diagram of  $\text{Eu}_{1-x}\text{Y}_x\text{MnO}_3$ , with  $0 \leq x < 0.55$ , based on X-ray diffraction, specific heat, dielectric constant and induced magnetization data, was published.<sup>31</sup> Figure 7 shows the more recent proposed  $(x,T)$ -phase diagram for this system.<sup>31</sup>

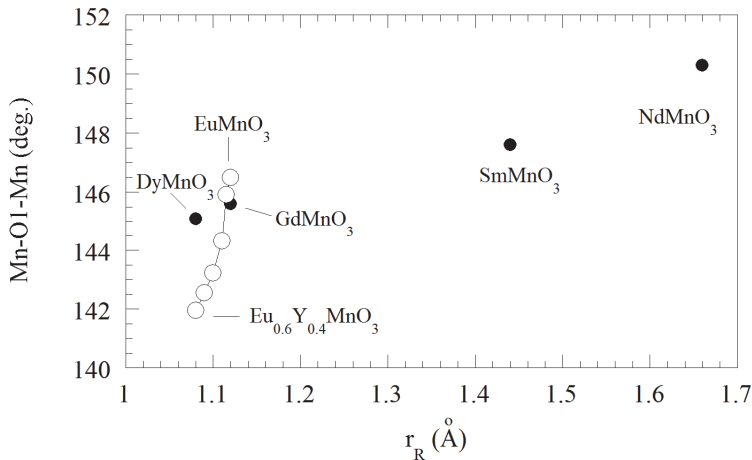


Fig. 6. Mn-O1-Mn bond angle as a function of the ionic radius of the A-site ion, for the  $\text{ReMnO}_3$ , with  $\text{Re} = \text{Nd}, \text{Sm}, \text{Eu}, \text{Gd}, \text{Dy}$  (closed circles), and for  $\text{Eu}_{1-x}\text{Y}_x\text{MnO}_3$  (open squares). Adapted figure from Ref. 31.

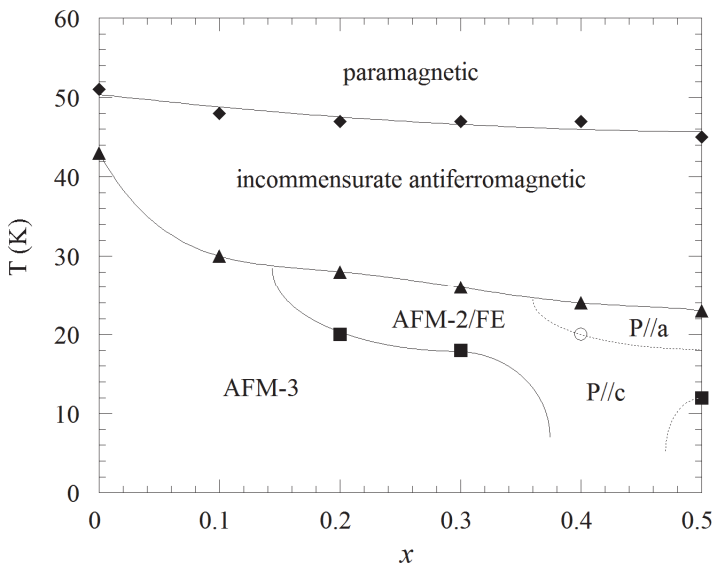


Fig. 7.  $(x,T)$  phase diagram of the  $\text{Eu}_{1-x}\text{Y}_x\text{MnO}_3$ . The dashed lines stand for guessed boundaries. Adapted from Ref. 31.

The phase boundaries were traced by considering the phase transition temperatures obtained from the set of data referred to above. Below the well-known sinusoidal incommensurate antiferromagnetic phase (hereafter designated by AFM-1), observed for all compounds, a re-entrant ferroelectric and antiferromagnetic phase (AFM-2) is stable for  $x = 0.2, 0.3,$  and  $0.5$ . The ferroelectric character of this phase was established by  $P(E)$  data analysis. Conversely, the AFM-3 phase is non-polar.<sup>31</sup> If the low temperature antiferromagnetic phase (AFM-3) were ferroelectric, as other authors reported previously, then, even though the coercive field had increased by decreasing temperatures, the remanent polarization would have increased accordingly. This is not confirmed by  $P(E)$  behaviour. In fact, the remanent polarization decreases to zero towards  $T_{AFM-3}$ , evidencing a low temperature non-polar phase. The decrease of the remanent polarization as the temperature decreases, observed for the compositions  $x = 0.2, 0.3,$  and  $0.5$ , can be associated with changes of both spin and lattice structures. As no ferroelectric behaviour was found for  $0 \leq x < 0.2$  down to 7 K, and taking into account magnetization data, we have considered a unique weakly ferromagnetic phase (AFM-3). Our current data do not provide any other reasoning to further split this phase. The phase boundary between AFM-2 and AFM-3 phases for  $0.3 < x < 0.5$  were not traced, since the experimental data do not indicate unambiguously whether a transition to a non ferroelectric phase occurs at temperatures below the lowest measured temperature. Moreover, it is not clear what are the phase boundaries associated with the polarization rotation from the  $c$  to the  $a$ -axis, in the neighbouring of the composition  $x = 0.5$ .

The aforementioned  $(x,T)$  phase diagram is significantly different from other earlier reported.<sup>24,26</sup> Evidence for a unique non-ferroelectric low temperature AFM-3 phase is actually achieved.<sup>31</sup>

The origin of the ferroelectricity in these compounds is understood in the framework of the spin-driven ferroelectricity model.<sup>16</sup> In these frustrated spin systems, the inverse Dzyaloshinsky-Morya interaction mechanism has been proposed. However, based on experimental results, the magnetic structure has been well established only for the compositions  $x = 0.4$  and  $0.5$ . For the other compositions, the magnetic structure is not yet determined. Moreover, the ferroelectric properties of the  $\text{Eu}_{1-x}\text{Y}_x\text{MnO}_3$  have been also studied by measurement of the electric current after cooling the sample under rather high-applied electric fields ( $E > 1$  kV/cm). As it was shown in Refs. 29, 30 and 32,  $\text{Eu}_{1-x}\text{Y}_x\text{MnO}_3$  exhibits a rather high polarizability, which can prevent the observation of the spontaneous polarization.

### 3.2 Experimental study and discussion

In order to ascertain the correlation between crystal structure and spin arrangements referred to above different approaches can be realized. One way is to use high-resolution X-ray diffraction using synchrotron radiation, to figure out the behaviour of structural parameters across the magnetic phase transitions. Very recently, a work on  $\text{Eu}_{1-x}\text{Y}_x\text{MnO}_3$  system was published showing the temperature behaviour of some structural parameters across the magnetic phase transitions.<sup>28</sup> Anomalies observed in the lattice parameters and both octahedra bond angle and bond distances clear evidence spin rearrangements occurring at phase transition temperatures, which are in favour of a significant spin-lattice coupling in these materials.<sup>28</sup>

Another alternative way to figure out magnetic-induced ferroelectric ground states is to study the phonon behaviour across the magnetic phase transition through Raman spectroscopy. As the electric polarization arises from lattice distortions, the study of the spin-phonon coupling is particularly interesting in systems that present strong spin-lattice coupling, as it is the case of rare-earth magnetoelectric manganites. Consequently, from both fundamental point of view and technological applications, to comprehend spin-phonon coupling is a central research objective.

A variety of Raman scattering studies of orthorhombic rare-earth manganites, involving Pr, Nd and Sm, has evidenced a significant coupling between spins and phonons close and below the Néel temperature.<sup>34</sup> We also note that the effect of the magnetic ordering is very weak in magnetoelectrics rare-earth manganites involving other rare-earth ions like Gd, Tb, Dy, Ho and Y.<sup>34</sup> Since the change of the GdFeO<sub>3</sub> distortion is accompanied with the change of the magnetic moment due to the rare-earth ions alteration, a comparative analysis of the coupling between spin degrees of freedom and phonons is a rather difficult task. This is not the case of the solid solution consisting of orthorhombic Eu<sub>1-x</sub>Y<sub>x</sub>MnO<sub>3</sub> system (0 ≤ x ≤ 0.5), since no magnetic contributions stem from europium and yttrium ions. In fact, the magnetic properties are entirely due to the manganese 3d spins. In the absence of other effects, a direct relation of spin-phonon coupling with the GdFeO<sub>3</sub> distortion can be achieved. We would like to emphasize that this distortion is a consequence of the Jahn-Teller cooperative effect and the tilting of the octahedra around the *a*-axis, which yield a lowering of the symmetry. As a consequence of this increasing lattice deformation, the orbital overlap becomes larger via the Mn-O1-Mn bond angle changing in turn the balance between ferromagnetic and antiferromagnetic exchange interaction.<sup>50</sup>

The main goal is to understand how phonons relate with both lattice distortions and spin arrangements, and to determine their significance to stabilizing ferroelectric ground states.

In the following, we will present and discuss the main experimental results obtained in the aforementioned system, in the form of polycrystalline samples. Details of the sample processing and experimental method could be found in Refs. 69 and 38.

The Raman spectra were analyzed in the framework of the sum of independent damped harmonic oscillators, according to the general formula:<sup>70</sup>

$$I(\omega, T) = (1 + n(\omega, T)) \sum_{j=1}^N A_{oj} \frac{\omega \Omega_{oj}^2 \Gamma_{oj}}{(\Omega_{oj}^2 - \omega^2)^2 + \omega^2 \Gamma_{oj}^2}, \quad (7)$$

by fitting this equation to the experimental data.  $n(\omega, T)$  stands for the Bose-Einstein factor, and  $A_{oj}$ ,  $\Omega_{oj}$  and  $\Gamma_{oj}$  are the strength, wave number and damping coefficient of the *j*-th oscillator, respectively.

In the orthorhombic rare-earth manganites, the activation of the Raman modes is due to deviations from the ideal cubic perovskite structure. Factor group analysis of the EuMnO<sub>3</sub> (with *Pbnm* orthorhombic structure) provides the following decomposition corresponding to the 60 normal vibrations at the  $\Gamma$ -point of the Brillouin zone:

$$\Gamma_{\text{acoustic}} = B_{1u} + B_{2u} + B_{3u}$$

$$\Gamma_{\text{optical}} = (7A_g + 7B_{1g} + 5B_{2g} + 5B_{3g})_{\text{Raman-active}} + (8A_u + 10B_{1u} + 8B_{2u} + 10B_{3u})_{\text{IR-active}}.$$

Since Raman-active modes should preserve the inversion centre of symmetry, the Mn<sup>3+</sup> ions do not yield any contribution to the Raman spectra. From the polycrystallinity of the

samples, the Raman spectra obtained involve all Raman-active modes. Earlier reports by Lavèrdiere *et al.*,<sup>34</sup> suggested that the more intense Raman bands are of  $A_g$  and  $B_{2g}$  symmetry. Therefore in our spectra, the  $A_g$  and  $B_{2g}$  modes are expected to be the more intense bands in  $\text{Eu}_{1-x}\text{Y}_x\text{MnO}_3$ . As these modes are the most essential ones for our study, we are persuaded that by using ceramics instead of single crystals, no significant data are in fact lost in regard to the temperature dependence of the mode parameters.

Figure 8 shows the unpolarized Raman spectra of  $\text{Eu}_{1-x}\text{Y}_x\text{MnO}_3$ , with  $x = 0, 0.1, 0.3, 0.4$  and  $0.5$ , taken at room temperature.

The spectral signature of all  $\text{Eu}_{1-x}\text{Y}_x\text{MnO}_3$  (with  $x \leq 0.5$ ) compounds is qualitatively similar in the  $300\text{--}800\text{ cm}^{-1}$  frequency range, either in terms of frequency, linewidth or intensity. Their similarity suggests that they all crystallize into the same space group, and that the internal modes of the  $\text{MnO}_6$  octahedra are not very sensitive to Y-doping. This results in excellent agreement with the quite similar structure, which is slightly dependent on Y-content.<sup>28,38</sup> Nevertheless, a fine quantitative analysis of the spectra evidenced some subtle changes as Y-concentration is altered. Some examples can be highlighted. The broad band emerging close to  $520\text{ cm}^{-1}$  becomes more noticeable by increasing the yttrium concentration. The frequency of the band located near  $364\text{ cm}^{-1}$  increases considerably with increasing  $x$ .

An earlier work by L. Martín-Carrón *et al.*,<sup>45</sup> regarding the frequency dependence of the Raman bands in some stoichiometric rare-earth manganites, has been used to assign the more intense Raman bands of each spectrum. The band at  $613\text{ cm}^{-1}$  is associated with a Jahn-Teller symmetric stretching mode involving the O2 atoms (symmetry  $B_{2g}$ ),<sup>33,45,71,72</sup> the band at  $506\text{ cm}^{-1}$  to a bending mode (symmetry  $B_{2g}$ ), the band at  $484\text{ cm}^{-1}$  to a Jahn-Teller type asymmetric stretching mode involving also the O2 atoms (symmetry  $A_g$ ), and the band at  $364\text{ cm}^{-1}$  to a bending mode of the tilt of the  $\text{MnO}_6$  octahedra (symmetry  $A_g$ ).<sup>45</sup>

From the mode assignment referred to above, it is now possible to correlate the  $x$ -dependence of the frequency of these Raman bands with the structural changes induced by the Y-doping. The more noticeable stretching modes in  $\text{ReMnO}_3$  are known to involve nearly pure Mn-O2 bond and they are found to be slightly dependent on the chemical pressure. In orthorhombic rare-earth manganites, the stretching modes change less than  $5\text{ cm}^{-1}$ , with the rare-earth ion substitution from La to Dy.<sup>33</sup> Figures 9 (a) and (c) show the frequency of the bands located close to  $613\text{ cm}^{-1}$  and  $484\text{ cm}^{-1}$ , respectively, as a function of  $x$ .<sup>38</sup>

The observed frequency changes of only  $2\text{ cm}^{-1}$  when  $x$  increases from 0 to 0.5, correlates well with a weak dependence of the Mn-O2 bond lengths with  $x$ .<sup>38</sup> The weak  $x$ -dependence of the frequency of these modes provides further evidence for a slight dependence of the  $\text{MnO}_6$  octahedron volume and Mn-O bonds lengths on the Y-doping, in agreement with literature work on other rare-earth manganites.<sup>28,45</sup> Contrarily, the modes  $B$  and  $T$  shown in Figures 9 (b) and (d) reveal a significant variation with  $x$ ,  $10$  to  $15\text{ cm}^{-1}$  when  $x$  increases from 0 to 0.5. This feature correlates well with the  $x$ -dependence of the tilt angle.<sup>38</sup> The largest variations with  $x$  is presented by the lower frequency  $T$  mode, which is an external mode  $A_g$  associated with the tilt mode of the  $\text{MnO}_6$  octahedra. A linear dependence of the frequency of  $T$  mode in the tilt angle was in fact observed (see Fig. 7 of Ref 38). The slope found,  $5\text{ cm}^{-1}/\text{deg}$ , is much less than the slope obtained for other orthorhombic manganites ( $23\text{ cm}^{-1}/\text{deg}$ ).<sup>33</sup> Mode  $B$  is assigned to the bending mode  $B_{2g}$  of the octahedra.<sup>33</sup> The two broad shoulders observed at round  $470\text{ cm}^{-1}$  and  $520\text{ cm}^{-1}$  are likely the  $B_{2g}$  in-phase O2 scissor-like and out-of-plane  $\text{MnO}_6$  bending modes.

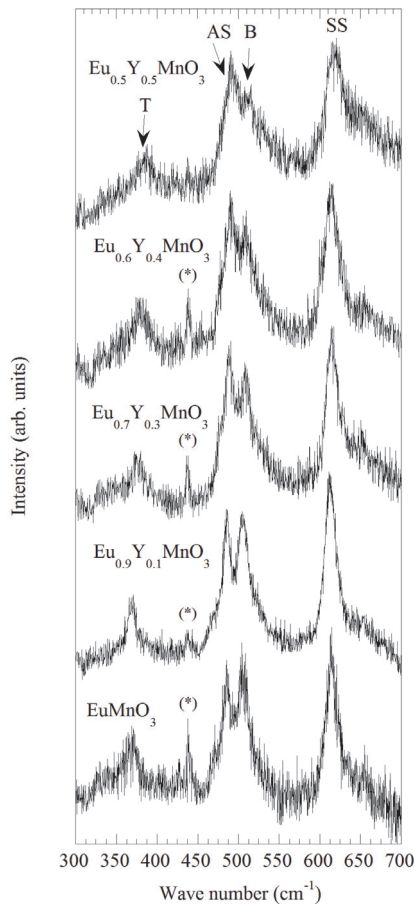


Fig. 8. Unpolarized Raman spectra of  $\text{Eu}_{1-x}\text{Y}_x\text{MnO}_3$ , for  $x = 0, 0.1, 0.3, 0.4$  and  $0.5$ , recorded at room temperature. The laser plasma line is indicated by (\*). Mode assignment: SS-symmetric stretching mode (symmetry  $B_{2g}$ ); AS – Jahn-Teller type asymmetric stretching mode (symmetry  $A_g$ ); B – bending mode (symmetry  $B_{2g}$ ); T – tilt mode of the  $\text{MnO}_6$  octahedra (symmetry  $A_g$ ). Reprinted figure from Ref. 38. Copyright (2010) by the American Physical Society.

Let us address to the temperature dependence of the frequency of Raman active modes. Figure 10 shows the unpolarized Raman spectra of  $\text{EuMnO}_3$  and  $\text{Eu}_{0.5}\text{Y}_{0.5}\text{MnO}_3$ , recorded at 200K and 9K.

As it can be seen in Figure 10, the spectra at 200K and 9K show only very small changes in their profiles. Especially, no new bands were detected at low temperatures. The lack of emergence of infrared Raman-active bands, even for those compositions where the stabilization of a spontaneous ferroelectric order is expected, may have origin in two different mechanisms: either the inverse centre is conserved or the ferroelectric phases for  $x \geq 0.2$  are of an improper nature.

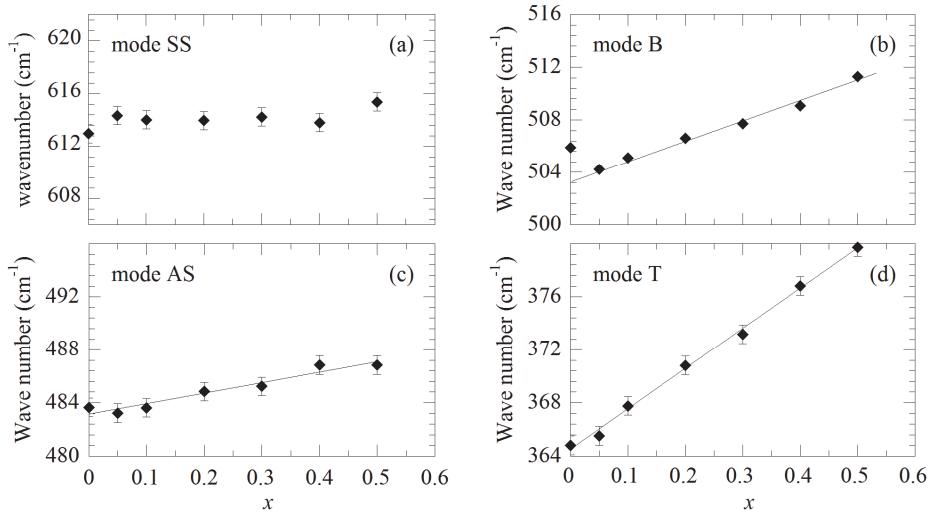


Fig. 9. Dependence of the frequency of the symmetric stretching mode (SS) (a), bending mode (B) (b), antisymmetric stretching mode (AS) (c) and tilt mode (T) (d), on the Y-content. The solid lines are guides for the eyes. Adapted from Ref. 38. Copyright (2010) by the American Physical Society.

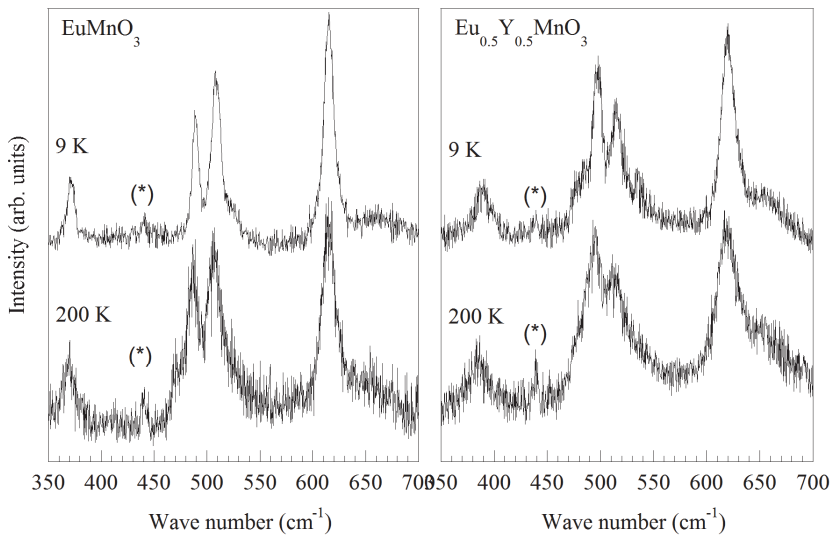


Fig. 10. The Raman spectra of  $\text{EuMnO}_3$  and  $\text{Eu}_{0.5}\text{Y}_{0.5}\text{MnO}_3$ , recorded at 200 and at 9 K. The laser plasma line is indicated by (\*). Adapted from Ref. 38.

Despite the absence of new Raman-active bands, an analysis of the spectra reveals striking anomalies in the temperature dependence of some phonon parameters throughout the magnetic phase transitions.

According to the spin-phonon coupling models, one should expect detectable changes in the phonon frequencies on entering the magnetic phases, reflecting the phonon renormalization, proportional to the spin-spin correlation function for the nearest  $\text{Mn}^{3+}$  spins. Aiming at searching for a spin-phonon coupling in  $\text{Eu}_{1-x}\text{Y}_x\text{MnO}_3$ , we have followed the temperature dependence of the parameters characterizing the  $\text{MnO}_6$  Raman-active modes. We have found that the symmetric stretching mode (SS) close to  $615 \text{ cm}^{-1}$  is the most sensitive to the magnetic ordering. In fact, this mode senses any change in the geometrical parameters associated with the spontaneous orthorhombic strain  $e$  and, so a strong coupling between the  $B_{2g}$  symmetric stretching mode and the electronic degrees of freedom is ascertained. In other rare-earth manganites, like Ca-doped  $\text{PrMnO}_3$ , this mode is so strongly coupled with the electronic system that it can be used to control a metal-insulator transition, by its coherent manipulation through selective mode excitation.<sup>73</sup> The temperature dependence of the  $B_{2g}$  symmetric stretching mode frequency for different yttrium concentrations is shown in Figure 11, together with the insets, which reflect the temperature dependence of the corresponding linewidths.

In order to evaluate the effect of magnetic exchange interactions on the phonon behaviour, we start by defining the purely anharmonic temperature dependence of the frequency and of the linewidth of the different modes by the model:<sup>74</sup>

$$\omega(T) = \omega(0) + C \left( 1 - \frac{2}{e^{y-1}} \right) \quad (8)$$

for the temperature dependence of the frequency of the transverse mode and:<sup>74</sup>

$$\Gamma(T) = \Gamma(0) \left( 1 - \frac{2}{e^{y-1}} \right) \quad (9)$$

for the temperature dependence of its linewidth. In equations (8) and (9),  $\omega(T)$  and  $\omega(0)$  are the frequencies of the optical mode at the temperature  $T$  and  $0 \text{ K}$ , respectively,  $y = \frac{\hbar\omega_0}{2k_B T}$

where  $\omega_0$  is the characteristic frequency of the mode,  $\Gamma(T)$  and  $\Gamma(0)$  are the linewidths of the mode at the temperature  $T$  and  $0 \text{ K}$ , respectively.<sup>74</sup> The solid lines in Figure 11 correspond to the best fit of these equations to the high-temperature range data ( $T > 100 \text{ K}$ ), with the adjustable parameters  $C$ ,  $\omega(0)$ ,  $\Gamma(0)$  and  $\omega_0$ .

The results displayed in Figure 11 clearly show that for  $\text{Eu}_{1-x}\text{Y}_x\text{MnO}_3$ , with  $x = 0, 0.3$  and  $0.4$ , only a faint frequency shift is observed at  $T_N$  in the temperature dependence of the phonon frequency, from the normal anharmonic behaviour. Contrarily, a significant negative frequency shift is found for  $x = 0.2$ , along with a negative and positive shifts observed for  $x = 0.1$  and  $x = 0.5$ , respectively.

For all these compounds the shifts appear well above the onset of the magnetic order and consequently it is very unlikely that these effects are driven by any sort of long range spin ordering. It may be that the shifts emerge when the temperature allows for some kind of local spin ordering.

The frequency shift of a given phonon as a function of temperature, due to the spin-phonon coupling, is determined by the spin-spin correlation function:<sup>68,75</sup>

$$\omega = \omega_0 + \gamma \langle \vec{S}_i \cdot \vec{S}_j \rangle, \quad (10)$$

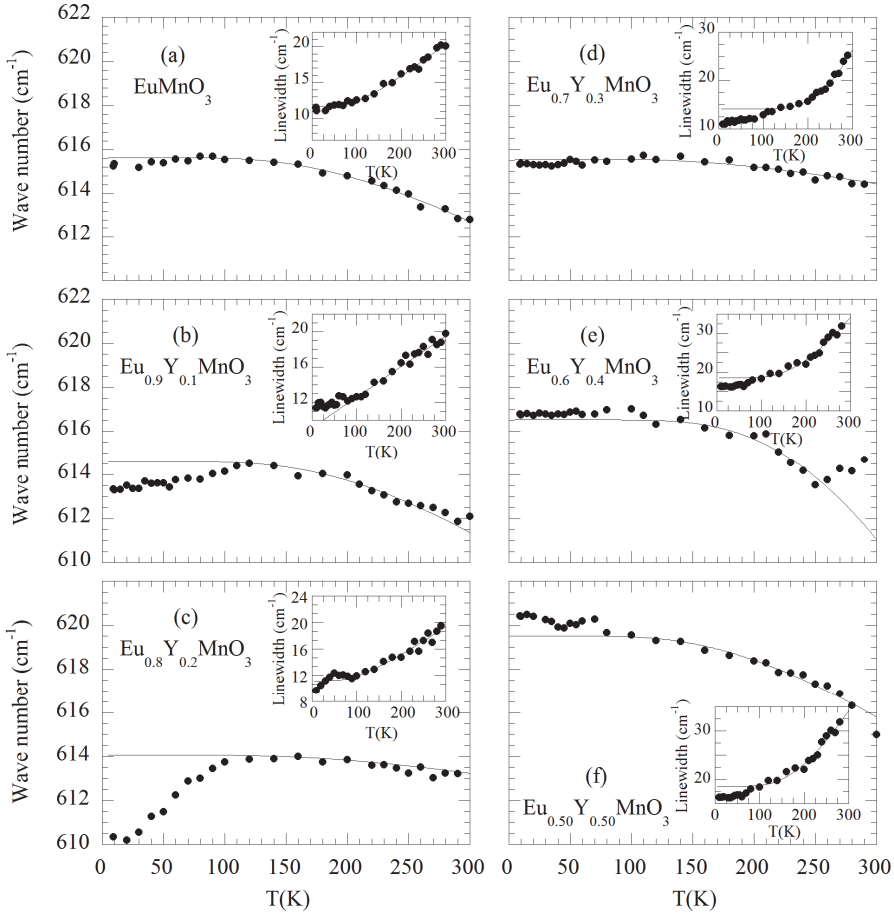


Fig. 11. Temperature dependence of the frequency of the  $B_{2g}$  symmetric stretching mode (SS) for  $\text{Eu}_{1-x}\text{Y}_x\text{MnO}_3$ , with  $x = 0, 0.1, 0.2, 0.3, 0.4$ , and  $0.5$ . The insets show the temperature dependence of the damping coefficient of the same mode as a function of the temperature. The solid lines were obtained from the best fit of Eq. 8 and 9, respectively. Reprinted figure from Ref. 38. Copyright (2010) by the American Physical Society.

where  $\omega$  is the renormalized phonon frequency at a fixed temperature,  $\omega_0$  denotes the frequency in the absence of spin-phonon coupling, and  $\gamma$  is the spin-phonon coupling constant.

When ferromagnetic and antiferromagnetic competitive interactions are present, it was proposed for the frequency shift:<sup>75,76</sup>

$$\omega - \omega_0 \propto -R_1 \langle \vec{S}_i | \vec{S}_j \rangle + R_2 \langle \vec{S}_i | \vec{S}_k \rangle \quad (11)$$

where  $R_1$  and  $R_2$  are spin dependent force constants of the lattice vibrations deduced as the squared derivatives of the exchange integrals with the respect to the phonon displacement.

$R_1$  is associated with the ferromagnetic nearest neighbour and  $R_2$  is associated with the antiferromagnetic next-nearest neighbour exchange.<sup>75</sup> The magnetic properties are determined mainly by the exchange integrals, which depend on the number of ferromagnetic and antiferromagnetic interactions in the system. This model predicts negative or positive frequency shifts depending on the relative strength between the ferromagnetic and antiferromagnetic exchange interactions, associated with the normal mode being considered. On the grounds of the model presented to above, the Raman frequency shifts displayed in Figure 11 can be understood by assuming the coexistence of ferromagnetic and antiferromagnetic competitive exchange interactions, and spin-phonon coupling in  $\text{Eu}_{1-x}\text{Y}_x\text{MnO}_3$ . As it has been assumed in current literature, we consider that the spin correlation functions of the nearest neighbours and the next-nearest neighbours have almost the same temperature dependence,<sup>37</sup> and thus, we take the same correlation functions for  $\langle \vec{S}_i | \vec{S}_j \rangle$ ,  $\langle \vec{S}_i | \vec{S}_k \rangle$  and  $\langle \vec{S}_i | \vec{S}_l \rangle$ . Moreover, as we are dealing with the same eigenmode, we also assume constant values for  $R_1$  and  $R_2$ . So, Equation (11) can be written as follows:

$$\omega - \omega_0 \propto (R_2 - R_1) \langle \vec{S}_i | \vec{S}_j \rangle. \quad (12)$$

For  $x = 0, 0.1$  and  $0.2$ , the Raman shift is negative, increasing as the  $x$  value increases up to  $0.2$ , where it takes its maximum value. This means that the difference  $R_2 - R_1$  becomes more negative with  $x$  up to  $0.2$ . For  $x = 0.3$ , the Raman frequency shift is also negative, but with a small value. On the other hand, for  $x = 0.4$  and  $0.5$  a clear positive Raman shift is observed. It is worthwhile to stress that the weak ferromagnetic character of the compounds with  $x$  between  $0$  and  $0.2$  cannot be explain by this model, as it is associated with the number of the exchange integrals and not with the second derivatives to the phonon displacements, represented by the  $R_1$  and  $R_2$  coefficients. This in good agreement with fact that the ferromagnetic features in these compounds arise below  $45 \text{ K} - 28 \text{ K}$ , depending on  $x$  (see phase diagram in Figure 5 of Ref. 50), which is far below  $100 \text{ K}$  where the spin-phonon coupling mechanism emerges.

Except for  $\text{EuMnO}_3$ , the linewidth deviates, around  $100 \text{ K}$ , from the purely anharmonic temperature dependence behaviour. For  $x = 0.20$ , the linewidth presents a further anomaly at  $T_N \approx 50 \text{ K}$  where the temperature derivative of the wave number is maximum.

In order to search for further corroboration of the spin-phonon coupling, we have also studied the temperature behaviour of the lattice mode associated with the rotational  $A_g$  mode of the  $\text{MnO}_6$  octahedra, which scales directly with the Mn-O1-Mn bond angle. Figure 12 shows the results obtained for  $x = 0.3$  and  $0.4$ . Both anomalies at  $T_N$ , for  $x = 0.3$  and  $0.4$ , and at  $T_{\text{AFM-2}}$  (only for  $x = 0.4$ ) and deviations from the normal anharmonic behaviour, for both  $x = 0.3$  and  $0.4$ , entirely corroborates the role of spin-phonon coupling mechanism in  $\text{Eu}_{1-x}\text{Y}_x\text{MnO}_3$ . It is still worth noting, that the sign of the shifts is fully consistent with the magnetic character of both compositions. The negative (positive) shift obtained for  $x=0.3$  ( $x=0.4$ ) confirms the relative predominance of the ferromagnetic (antiferromagnetic) exchanges against the antiferromagnetic (ferromagnetic) ones. This feature is in favour of an increasing range of stability of the ferroelectric ground state as the yttrium concentration increases. The different configuration of the low temperature part of the  $\text{Eu}_{1-x}\text{Y}_x\text{MnO}_3$  phase diagram is in good agreement with the very distinct behaviour of the Mn-O-Mn bond angle versus the average A-site size, when compared with the one of other magnetoelectric rare-earth manganites (see Fig. 6).

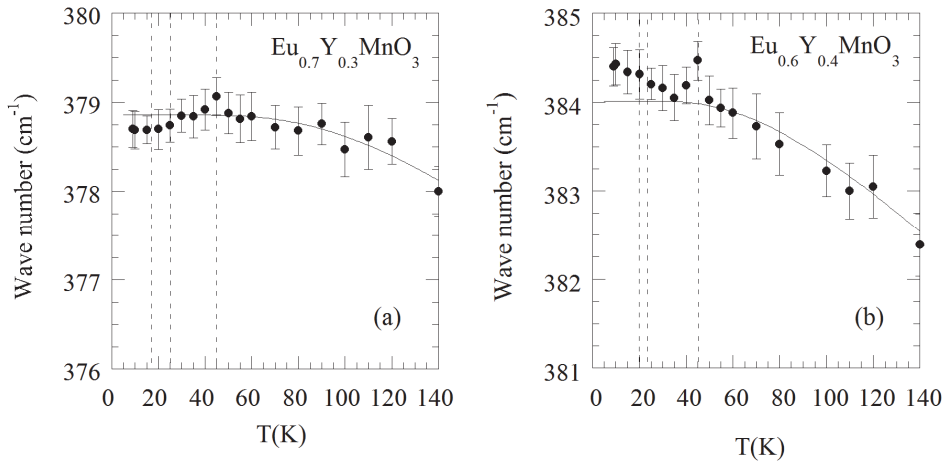


Fig. 12. Temperature dependence of the frequency of the  $A_g$  external mode ( $T$ ) for  $\text{Eu}_{1-x}\text{Y}_x\text{MnO}_3$ , with  $x = 0.3$  and  $0.4$ . The solid lines were obtained from the best fit of Eq. 8 and 9, respectively. Reprinted figure from Ref. 38. Copyright (2010) by the American Physical Society.

#### 4. Conclusions

The experimental results obtained in  $\text{Eu}_{1-x}\text{Y}_x\text{MnO}_3$ , with  $0 \leq x \leq 0.5$ , using Raman spectroscopy noticeably reveal the existence of spin-phonon coupling in this system: shifts of the frequency of the normal modes relative to anharmonic temperature dependence, energy transfer mechanisms between modes, anomalies in the mode parameters both above and below to  $T_N$ . This is most evidenced by the symmetric stretching and tilt modes associated with  $\text{MnO}_6$  octahedra.

Despite the existence of the spin-phonon coupling for all  $x$  values studied, spin-phonon coupling is not a sufficient condition to the emergence of ferroelectricity. As it can be observed in  $(x,T)$  phase diagram, ferroelectricity occurs only above  $x = 0.15$ , which means that other mechanisms are required. These mechanisms were theoretically established on the grounds of the model presented to above.<sup>50</sup> The relative magnitude of the Hamiltonian terms shape the  $(x,T)$  phase diagram, as  $J_2$  increases. In fact, the emergence of the re-entrant ferroelectric phase stems from the increasing magnitude of the AFM against the FM interactions and of DM interaction.<sup>30,38,50</sup>

An alternative way towards ferroelectricity is to apply an external magnetic field.<sup>77</sup> Experiments carried out in  $\text{Eu}_{1-x}\text{Y}_x\text{MnO}_3$  under magnetic field up to 55 T, can induce magnetic transitions to a multiferroic phase.<sup>77</sup> This same effect was also observed in  $\text{GdMnO}_3$ , but for much lower values of the external magnetic field.<sup>17</sup> Figure 13 shows the frequency of the  $A_g$  external mode as a function of the magnetic field, recorded at 10 K.

The anomalies mark the emergence of ferroelectricity for a magnetic field of 3 T, in good agreement with earlier published results.<sup>17</sup> This is in favour of the presence of a significant spin-phonon coupling in GdMnO<sub>3</sub>.

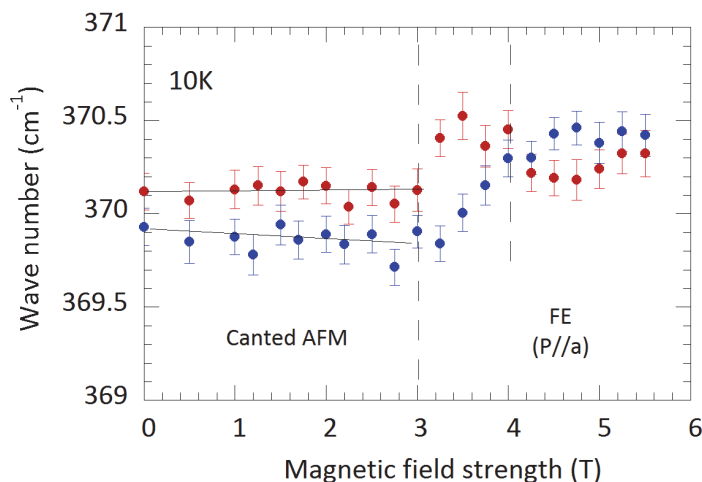


Fig. 13. Magnetic field dependence of the  $A_g$  external mode frequency of GdMnO<sub>3</sub>, at 10 K. Blue solid circles: increasing magnetic field strength; red solid circles: decreasing magnetic field strength. The vertical dashed lines mark the phase boundaries between the canted antiferromagnetic and the ferroelectric (P//a) phases, according to Ref. 17.

Our results also yield the existence of spin-phonon coupling even above  $T_N$ , which is in favour of a coupling between phonons and magnetic ordering in the paramagnetic phase. In fact, our experimental results correlate with terahertz transmittance data in  $\text{Eu}_{1-x}\text{Y}_x\text{MnO}_3$ .<sup>27,36</sup> They yield the existence of electromagnons for  $x = 0.20, 0.30$  and  $0.50$ , yielding information on the static dielectric constant below  $T_1$ , and evidencing a broad background absorption observed up to  $T_N + 50\text{K}$ .<sup>27,36</sup> We have also observed a frequency deviation from purely anharmonic behaviour, well above  $T_N$ , associated with spin-phonon coupling. Laverdière *et al*<sup>34</sup> have observed a softening for  $A_g$  and  $B_{2g}$  stretching modes in, e.g. NdMnO<sub>3</sub> and DyMnO<sub>3</sub>, starting well above  $T_N$ , which they relate to a small Mn-O expansion. Since manganites have peculiar local electronic and magnetic structures, it is also reasonable to associate this behaviour with local magnetic fluctuations, like in rare-earth nickelates.<sup>78-80</sup> Aguilar *et al*<sup>27</sup> have associated the existence of the terahertz background absorption in the paramagnetic phase with phonon-electromagnon coupling. We have reconsidered the correlation between the total spectral weight below  $140\text{ cm}^{-1}$ , depicted in Fig 2 of Ref. 27, and the frequency shift calculated from our results for  $x = 0.20$ . The results are shown in Figure 14.

This result evidences a mechanism that involves spin-spin interactions, since the shift of the measured frequency (proportional to  $\vec{S}_i \cdot \vec{S}_j$ ) for  $x = 0.2$  scales with the spectral weight displayed in Figure 2 of the Ref. 27, in the temperature range 50 K - 100 K. The spectral

weight, calculated from the sample with  $x = 0.25$ , is reported to be proportional to the phonon-electromagnon coupling in the paramagnetic phase, and it is also proportional to  $\vec{S}_i \cdot \vec{S}_j$ .

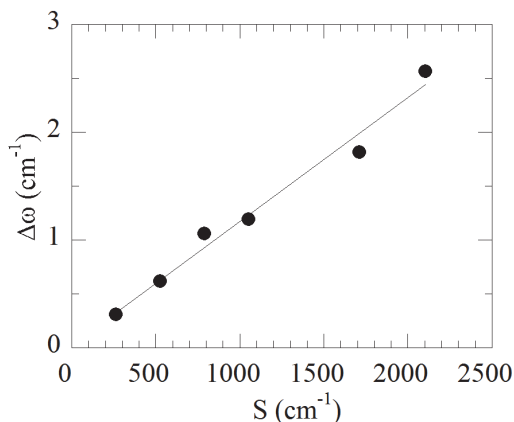


Fig. 14. Frequency deviation from the extrapolated temperature behaviour for  $T > 100\text{K}$ , of the symmetric stretching mode of  $\text{Eu}_{0.8}\text{Y}_{0.2}\text{MnO}_3$ , versus the spectral weight calculated from the terahertz data, below  $140\text{ cm}^{-1}$ , for the sample  $\text{Eu}_{0.75}\text{Y}_{0.25}\text{MnO}_3$  (Ref. 27). The straight line is a guide for the eyes. Copyright (2010) by the American Physical Society.

## 5. Acknowledgements

We would like to deeply thank Prof. Maria Renata Chaves and Dr. Jens Kreisel for very helpful discussions and distinct contributions. We thank Welberth Santos Ferreira for his technical assistance. We thank Fundação para a Ciência e Tecnologia through the Project No. PTDC/CTM/67575/2006.

## 6. References

- [1] For a review on this topic see the special issues: The European Physical Journal B 71 (2009); J.Phys.: Condens. Matter 20 (2008), and references therein presented.
- [2] W. Eerenstein, N. D. Mathur, J. F. Scott, Nature 442, 759 (2006)
- [3] M. Bibes and A. Barthelemy, IEEE Trans. Electron. Devices 54, p1003 (2007).
- [4] B. B. van Aken, T. T. Palstra, M. Filipetti, and N. A. Spaldin, Nat. Mater. 3, 164 (2004).
- [5] H. Béa, M. Bibes, and S. Cherifi, Appl. Phys. Lett. 89, 242114 (2006).
- [6] R. Ramesh and N. A. spaldin, Nat. Mater. 6, 21 (2007).
- [7] P. Rovillain, R. de Sousa, Y. Gallais, A. Sacuto, M. A. Méasson, D. Colson, A. Forget, M. Bibes, A. Barthélémy, M. Cazayous, Nat. Mater. 9, 975 (2010).
- [8] Marin Alexe, Dietrich Hesse, Nat. Communications 2, 256 (2011).

- [9] Q. He, Y. -H. Chu, J. T. Heron, S. Y. Yang, W. I. Liang, C.Y. Kuo, H. J. Lin, P. Yu, C. W. Liang, R. J. Zeches, W. C. Kuo, J. Y. Juang, C. T. Chen, E. Arenholz, A. Scholl, and R. Ramesh, *Nat. Communications* 2, 225 (2011).
- [10] N. Choudhury, L. Walizer, S. Lisenkov, L. Bellaiche, *Nature* 470, 513-517 (2011).
- [11] S. M. Wu, Shane A. Cybart, P. Yu, M. D. Rossell, J. X. Zhang, R. Ramesh, R. C. Dynes, *Nat. Mater.* 9, 756 (2010).
- [12] N. A. Hill, *J. Phys. Chem. B* 104, 6694 (2000).
- [13] T. Kimura, S. Ishihara, H. Shintani, T. Arima, K. T. Takahashi, K. Ishizaka, and Y. Tokura, *Phys. Rev. B* 68, 060403 (2003).
- [14] H. Katsura, N. Nagaosa, and A. V. Balatsky, *Phys. Rev. Lett.* 95, 057205 (2005).
- [15] M. Mostovoy, *Phys. Rev. Lett.* 96, 067601 (2006).
- [16] A. Sergienko and E. Dagotto, *Phys. Rev. B* 73, 094434 (2006).
- [17] T. Goto, T. Kimura, G. Lawes, A. P. Ramirez, and Y. Tokura, *Phys. Rev. Lett.* 92, 257201 (2004).
- [18] T. Kimura, G. Lawes, T. Goto, Y. Tokura, and A. P. Ramirez, *Phys. Rev. B* 71, 224425 (2005).
- [19] T. Kimura, T. Goto, H. Shintani, K. Ishizaka, T. Arima, and Y. Tokura, *Nature* 426, 55 (2033).
- [20] O. Prokhnenko, R. Feyerherm, M. Mostovoy, N. Aliouane, E. Dudzik, A. U. B. Wolter, A. Maljuk, and D. N. Argyriou, *Phys. Rev. Lett.* 99, 177206 (2007).
- [21] T. Arima, T. Goto, Y. Yamasaki, S. Miyasaka, K. Ishii, M. Tsubota, T. Inami, Y. Murakami, and Y. Tokura, *Pjys. Rev. B* 72, 100102 (2005).
- [22] K. Noda, S. Nakamura, J. Nagayama, and H. Kuwahara, *J. Appl. Phys* 97, 10C103 (2005).
- [23] J. Baier, D. Meier, K. Berggold, J. Hemberger, A. Balbashov, J. A. Mydosh, and T. Lorenz, *Pjys. Rev. B* 73, 100402 (2006).
- [24] J. Hemberger, F. Schrettle, A. Pimenov, P. Lunkenheimer, V. Yu. Ivanov, A. A. Mukhin, A. M. Balbashov, and A. Loidl, *Phys. Rev. B* 75, 035118 (2007).
- [25] Y. Takahashi, Y. Yamasaki, N. Kida, Y. Kaneko, T. Arima, R. Shimano, and Y. Tokura, *Phys. Rev. B* 79, 214431 (2009).
- [26] Y. Yamasaki, S. Miyasaka, T. Goto, H. Sagayama, T. Arima, and Y. Tokura, *Phys. Rev. B* 76, 184418 (2007).
- [27] R. Valdés Aguilar, A. B. Sushkov, C. L. Zhang, Y. J. Choi, S.-W. Cheong, and H. D. Drew, *Phys. Rev. B* 76, 060404 (2007).
- [28] J. Agostinho Moreira, A. Almeida, W. S. Ferreira, J. P. Araújo, A. M. Pereira, M. R. Chaves, M. M. R. Costa, V. A. Khomchenko, J. Kreisel, D. Chernyshov, S. M. F. Vilela, and P. B. Tavares, *Phys. Rev. B* 82, 094418 (2010).
- [29] J. Agostinho Moreira, A. Almeida, W. S. Ferreira, M. R. Chaves, B. Kundys, R. Ranjith, W. Prellier, S. F. M. Vilela, and P. B. Tavares, *J. Appl. Phys.* 107, 024108 (2010).
- [30] J. Agostinho Moreira, A. Almeida, W. S. Ferreira, M. R. Chaves, J. P. Araújo, A. M. Pereira, S. F. M. Vilela, and P. B. Tavares, *J. Phys.: Condens. Matter* 22, 125901 (2010).

- [31] J. Agostinho Moreira, A. Almeida, W. S. Ferreira, M. R. Chaves, J. B. Oliveira, J. M. M. da Silva, M. A. Sá, S. F. M. Vilela, and P. B. Tavares, *Solid. State Commun.* 151, 368 (2011).
- [32] J. Agostinho Moreira, A. Almeida, W. S. Ferreira, M. R. Chaves, B. Kundys, R. Ranjith, W. Prellier, S. F. M. Vilela, and P. B. Tavares, *J. Phys.: Condens. Matter* 21, 446002 (2009).
- [33] M. N. Iliev, M. V. Abrashev, J. Laverdière, S. Jandl, M. M. Gospodinov, Y.-Q. Wang, and Y.-Y. Sun, *Phys. Rev. B* 73, 064302 (2006).
- [34] J. Laverdière, S. Jandl, A. A. Mukhin, V. Yu. Ivanov, V. G. Ivanov, and M. N. Iliev, *Phys. Rev. B* 73, 214301 (2006).
- [35] S. Issing, A. Pimenov, V. Yu. Ivanov, A. A. Mukhin, and J. Geurts, *Phys. Rev. B* 81, 024304 (2010).
- [36] Pimenov, A. Loidl, A. A. Mukhin, V. D. Travkin, V. Yu. Ivanov, and A. M. Balbashov, *Phys. Rev. B* 77, 014438 (2008).
- [37] W. S. Ferreira, J. Agostinho Moreira, A. Almeida, M. R. Chaves, J. P. Araújo, J. B. Oliveira, J. M. Machado Da Silva, M. A. Sá, T. M. Mendonça, P. Simeão Carvalho, J. Kreisel, J. L. Ribeiro, L. G. Vieira, P. B. Tavares, and S. Mendonça, *Phys. Rev. B* 79, 054303 (2009).
- [38] J. Agostinho Moreira, A. Almeida, W. S. Ferreira, J. P. Araújo, A. M. Pereira, M. R. Chaves, J. Kreisel, S. M. F. Vilela, and P. B. Tavares, *Phys. Rev. B* 81, 054447 (2010).
- [39] S. Kamba, D. Nuzhnyy, M. Savinov, J. Sebek, J. Petzelt, J. Prokleska, R. Haumont, J. Kreisel, *Phys. Rev. B* 75, 024403 (2007).
- [40] R. Haumont, J. Kreisel, P. Bouvier, F. Hippert, *Phys. Rev. B* 73, 132101 (2006).
- [41] P. Hermet, M. Goffinet, J. Kreisel, P. Ghosez, *Phys. Rev. B* 75, 220102 (2007).
- [42] K. H. J. Buschow and F. R. de Boer, *Physics of Magnetism and Magnetic Materials*. Kluber Academic Press. (2003).
- [43] G. F. Dionne. *Magnetic Oxides*. Springer. (2009).
- [44] M. V. Abrashev, J. Bäckström, L. Börjesson, M. Pissas, N. Kolev, and M. N. Iliev, *Phys. Rev. B* 64, 144429 (2001).
- [45] L. Martín-Carrón, A. de Andrés, M. J. Martínez-Lope, M. T. Casais, and J. A. Alonso, *Phys. Ver. B* 66, 174303 (2002).
- [46] L. D. Landau and E. Lifshitz, *Electrodynamics of Continuous Media*. Butterworth-Heinemann. Oxford (2002).
- [47] Dzyaloshinskii, *J. Phys. Chem. Solids* 4, 241 (1958).
- [48] T. Moriya, *Phys. Rev.* 120, 91 (1960).
- [49] H. Katsura, N. Nagaosa, and A. V. Balatsky, *Phys. Rev. Lett.* 95, 057205 (2005).
- [50] M. Mochizuki and N. Furukawa, *Phys. Rev. B* 80, 134416 (2009).
- [51] Y. Yamasaki, H. Sagayama, T. Goto, M. Matsuura, K. Hirota, T. Arima, and Y. Tokura, *Phys. Rev. Lett.* 98, 147204 (2007).
- [52] H. J. Xiang, Su-Huai Wei, M.-H. Whangbo, and Juarez L. F. da Silva, *Phys. Rev. Lett.* 101, 037209 (2008).

- [53] M. Kenzelmann, A. B. Harris, S. Jonas, C. Broholm, J. Schefer, S. B. Kim, C. L. Zhang, S.-W. Cheong, O. P. Vajk, and J. W. Lynn, *Phys. Rev. Lett.* 95, 087206 (2005).
- [54] R. Feyerherm, E. Dudzik, N. Aliouane, and D. N. Argyriou, *Phys. Rev. B* 73, 180401 (2006).
- [55] T. Goto, Y. Yamasaki, H. Watanabe, T. Kimura, and Y. Tokura, *Phys. Rev. B* 72, 220403 (2005).
- [56] Y. Yamasaki, H. Sagayama, N. Abe, T. Arima, K. Sasai, M. Matsuura, K. Hirota, D. Okuyama, Y. Noda, and Y. Tokura, *Phys. Rev. Lett.* 101, 097204 (2008).
- [57] V. Yu. Ivanov, A. A. Mukin, V. D. Travkin, A. S. Prokhorov, A. M. Kadomtsev, Yu. F. Popov, G. P. Vorobev, K. I. Kamilov, and A. M. Balbashov, *J. Magn. Magn. Mater.* 300, e130 (2006).
- [58] V. Yu. Ivanov, A. A. Mukin, V. D. Travkin, A. S. Prokhorov, Yu. F. Popov, A. M. Kadomtsev, G. P. Vorob'ev, K. I. Kamilov, and A. M. Balbashov, *Phys. Status Solidi B* 243, 107 (2006).
- [59] Yoshimori, *J. Phys. Soc. Jpn.* 14, 807 (1959).
- [60] T. A. Kaplan, *Phys. Rev.* 116, 888 (1959).
- [61] J. Villain, *J. Phys. Chem. Solids* 11, 303 (1959).
- [62] S. Dong, R. Yu, S. Yunoki, J.-M. Liu, and E. Dagotto, *Phys. Rev. B* 78, 155121 (2008).
- [63] T. Moriya, *Phys. Rev. Lett.* 4, 228 (1960).
- [64] V. Skumryev, F. Ott, J. M. D. Coey, A. Anane, J. -P. Renard, L. Pinsard\_Gaudart, and A. Revcolevschi, *Euro. Phys. J. B* 11, 40 (1999).
- [65] J. Hemberger, T. Rudolf, H.-A. Krug von Nidda, F. Mayr, A. Pimenov, V. Tsurkan, and A. Loidl, *Phys. Rev. Lett.* 97, 087204 (2006).
- [66] Jiasi Xu, Jung H. Park, and Hyun M. Jang, *Phys. Rev. B* 75, 012409 (2007).
- [67] E. Granado, A. Garca, J. A. Sanjurjo, C. Rettori, I. Torriani, F. Prado, R. D. Sanchez, A. Caneiro, and S. B. Oseroff, *Phys. Rev. B* 60, 11879 (1999).
- [68] D. J. Lockood, and M. G. Cottam, *J. Appl. Phys.* 64, 5876 (1988).
- [69] J. Agostinho Moreira, A. Almeida, W. S. Ferreira, M. R. Chaves, J. B. Oliveira, J. M. M. da Silva, M. A. Sá, S. F. M. Vilela, and P. B. Tavares, *J. Electro. Ceram.* 25, 203 (2010).
- [70] W. Hayes and R. Loudon. *Scattering of light by crystals.* John Wiley and Sons (1978).
- [71] M. N. Iliev, M. V. Abrashev, H. G. Lee, V. N. Popov, Y. Y. Sun, C. Thomsen, R. L. Meng, and C. W. Chu, *Phys. Rev. B* 57, 2872(1998).
- [72] V. A. Amelichev, B. Güttler, O. Yu. Gorbenko, A. R. Kaul, A. A. Bosak, and A. Yu. Ganin, *Phys. Rev. B* 63, 104430 (2001).
- [73] M. Rini, R. Tobey, N. Dean, J. Itatani, Y. Tomioka, Y. Tokura, R. W. Schoenlein, and A. Cavalleri, *Nature* 449, 72 (2007).
- [74] M. Balkanski, R. F. Wallis, and E. Haro, *Phys. Rev. B* 28, 1928 (1983).
- [75] W. Baltensperger and J. S. Helman, *Helv. Phys. Acta* 41, 668 (1968).
- [76] K. Wakamura and T. Arai, *J. Appl. Phys.* 63, 5824 (1988).
- [77] M. Tokunaga, Y. Yamasaki, Y. Onose, M. Mochizuki, N. Furukawa, and Y. Tokura, *Phys. Rev. Lett.* 103, 187202 (2009).
- [78] J. M. Wesselinowa, and A. T. Apostolov, *J. Phys.: Condens. Matter* 8, 473 (1996).

- [79] C. Girardot, J. Kreisel, S. Pignard, N. Caillault, and F. Weiss, *Phys. Rev. B* 78, 104101 (2008).
- [80] G. Catalan, *Phase Transitions* 81, 729 (2008).

# Ferroelectric Field Effect Control of Magnetism in Multiferroic Heterostructures

Carlos A. F. Vaz<sup>1</sup> and Charles H. Ahn<sup>2</sup>

<sup>1</sup>SwissFEL, Paul Scherrer Institut, Villigen PSI

<sup>2</sup>Department of Applied Physics, Yale University, New Haven, Connecticut

<sup>1</sup>Switzerland

<sup>2</sup>U.S.A.

## 1. Introduction

Nanotechnology stands for a new paradigm in materials science that aims at exploring and controlling new physical phenomena and enhanced functionalities that emerge at the nanoscale. These opportunities are a direct consequence of reduced dimensionality and/or interfacial phenomena from proximity effects between dissimilar materials Zubko et al. (2011). Progress in growth techniques Chambers (2010); Eckstein & Bozovic (1995); Martin et al. (2010); McKee et al. (1998); Posadas et al. (2007); Reiner et al. (2009); Schlom et al. (1992); Vaz et al. (2009a); Vrejoiu et al. (2008), nanoscale characterization tools Zhu (2005), and first principles calculations Cohen (2000); Fennie (2008); Picozzi & Ederer (2009); Rabe & Ghosez (2007); Spaldin & Pickett (2003); Waghmare & Rabe (2005) have been instrumental to our present ability to control matter down to the atomic scale and to fabricate nanoscale device structures with the potential for technological applications. Examples of current research work that aims at addressing some of the current grand challenges include the search for ultrasensitive sensors and actuators for applications in areas such as medicine and energy harvesting, the development of smaller and more energy efficient electronic devices that could replace current CMOS switches, and the design of intelligent systems that incorporate complex operations at the core processing level. While the approach employed to date has relied on building up complexity from basic building blocks (e.g., complex microprocessor units formed of MOSFET devices), a new approach is being developed that directly explores the complex state of matter to achieve integrated functionalities and more complex operations at a fundamental level. Key to this effort has been the sustained research work aimed at understanding the properties of strongly correlated systems, and at controlling such properties down to the atomic scale, from a device physics perspective.

In this context, a particularly interesting class of materials are so-called *multiferroic* systems, which are characterized by the presence of simultaneous magnetic and ferroelectric order. As such, they offer the possibility of achieving control of the magnetic state via applied electric fields, or vice versa, which could find applications in ultrasensitive magnetic sensors and transducers, solid state transformers, magneto-electrooptic devices, energy harvesting and storage, and new spin-based logic devices in the context of *spintronics* Bibes & Barthélémy (2007); Cibert et al. (2005); Žutić et al. (2004). In most single phase multiferroic materials, the origin of magnetic and ferroelectric orders is largely independent, with the consequence that the coupling between magnetism and ferroelectricity (mediated by the spin-orbit coupling)

is weak; in those instances where the coupling is strong, the critical temperatures tend to be small Khomskii (2006; 2009); Picozzi & Ederer (2009). To overcome the weak magnetoelectric coupling of single-phase multiferroic materials, alternate approaches have been developed that explore proximity and interfacial effects between magnetic and ferroelectric materials to form composite structures with enhanced coupling between electric and magnetic properties. By judiciously engineering the interfacial properties at the nanoscale, a strong coupling between magnetic and ferroelectric order parameters can be achieved. This new class of artificially structured composite materials exhibits magnetoelectric couplings that are orders of magnitude larger than those typical of single-phase, intrinsic multiferroics Fiebig (2005); Ma et al. (2011); Vaz et al. (2010a).

An example of the promise afforded by this approach is provided by the particular case of the multiferroic perovskite  $\text{BiFeO}_3$ , characterized by magnetic and ferroelectric critical temperatures well above room temperature ( $T_c^m = 643 \text{ K}$  and  $T_c^e = 1100 \text{ K}$ , respectively) Catalan & Scott (2009).  $\text{BiFeO}_3$  has generated much interest recently, following the first report of the growth of epitaxial thin films Wang et al. (2003) and the demonstration of very large electric polarizations in high quality single crystalline films and in bulk crystals Lebeugle et al. (2007); Shvartsman et al. (2007); Wang et al. (2003). In this system, ferroelectricity originates from the lone-pair active Bi cations Neaton et al. (2005); Ravindran et al. (2006), while the magnetic order originates from the oxygen-mediated superexchange interaction between the Fe cations, which favors an antiferromagnetic coupling between nearest neighbor spins Kiselev et al. (1963). The magnetic state is modified further by a break in center of symmetry and the presence of a ferroelectric polarization, which gives rise to a local spin canting between the two spin sublattices (and to a weak magnetic moment) through the Dzyaloshinskii-Moriya interaction Dzialoshinskii (1957); Moriya (1960). In addition, the coupling of the polarization to gradients of the magnetization leads to an inhomogeneous spin configuration characterized by an incommensurate rotation of the total local spin along a  $\langle 10\bar{1} \rangle_{\text{pc}}$  direction (indexed to the pseudocubic perovskite structure) and lying in the  $\{1\bar{2}1\}_{\text{pc}}$  plane, defined by the cycloid propagation direction and the electric polarization (with easy axes along  $\langle 111 \rangle_{\text{pc}}$ ), with a period of about 62 nm (*spin cycloid*) Catalan & Scott (2009); Picozzi & Ederer (2009); Sosnowska et al. (1982). This spin cycloid averages out the magnetic moment and leads to a vanishing linear magnetoelectric coupling and to a small effective magnetoelectric response; however, at the nanoscale, there is a strong coupling between the electric polarization and the magnetic spins, since they are constrained to point perpendicular to each other, indicating that a change in the orientation of the electric polarization will result in a change in the spin direction Cazayous et al. (2008); Lebeugle et al. (2008). Such a phenomenon has been demonstrated experimentally Lee et al. (2008); Zheng et al. (2006) and has been explored in exchange-bias coupled multiferroic heterostructures to change the magnetization direction of a ferromagnetic layer exchange-coupled to the  $\text{BiFeO}_3$  Chu et al. (2008); Wu et al. (2010). This approach to magnetoelectric coupling illustrates the current trend towards engineering larger magnetoelectric couplings by relying on interfacial effects between different materials, an approach that can be traced back to the 1970s, when the first attempts to grow strain-mediated ferroelectric-ferromagnetic composites were made van Suchtelen (1972). In fact, the most common approach to date for achieving a magnetoelectric coupling in composites relies on strain to mediate the magnetic and electrical properties by inducing crystal deformations on either the magnetic phase through the converse piezoelectric effect, or in the ferroelectric phase through magnetostriction Fiebig (2005); Ma et al. (2011); Ramesh & Spaldin (2007); Thiele et al. (2007); Vaz et al. (2009b; 2010a). The effect is indirect, but can be optimized to yield large magnetoelectric responses by a suitable choice of the material components and device geometry Nan et al. (2008); Srinivasan (2010); Wang et al. (2009). Another promising route

involves a direct, charge-mediated magnetoelectric coupling in ferroelectric/ferromagnetic oxide composite multiferroic heterostructures, where the spin state of the magnetic oxide is controlled via charge doping induced by the electric polarization of a ferroelectric Molegraaf et al. (2009); Vaz et al. (2010b). For  $\text{Pb}(\text{Zr}_{0.2}\text{Ti}_{0.8})\text{O}_3/\text{La}_{0.8}\text{Sr}_{0.2}\text{MnO}_3$  (PZT/LSMO) heterostructures, the effect is electronic in origin and results from a change in the magnetic spin configuration as a function of the ferroelectric polarization direction, demonstrating electric field control of magnetism in this system (Section 3).

In this chapter, we consider the recent developments in the electric field control of magnetism in artificial heterostructures based on electrostatic doping. This approach has been explored in various systems, including dilute magnetic semiconductors, transition metals, and complex oxides; an overview of the work carried out in each of these systems is given in Section 2. The focus will be on complex oxide heterostructures, and in particular on our recent work demonstrating a strong magnetoelectric coupling in PZT/LSMO multiferroic heterostructures (Section 3). Due to strong electron correlations, complex oxides offer an inexhaustible range of possibilities for the study of novel phenomena that arise from the sensitivity of these materials to charge, strain, electric and magnetic fields, among other control parameters, with the attendant promise for device applications Imada et al. (1998); Tokura (2006); Tokura & Nagaosa (2000).

## 2. Electrostatic control of magnetism in artificial heterostructures

One approach to artificial multiferroic structures exploits the electric field effect to achieve an electrostatic modification of the charge carrier density and to induce changes in the magnetic state. The working concept is similar to that of a field effect transistor, where an induced or spontaneous electric polarization at the gate dielectric interface is screened by charge carriers from the channel layer, leading to charge accumulation or depletion over a thickness determined by the screening length of the material. In materials where the magnetic properties are intimately linked to charge, a change in carrier doping results in a change in the magnetic properties. The amount of charge carrier modulation required will depend on the particular system. For strongly correlated oxides, where typical carrier densities are of the order of  $10^{21} \text{ cm}^{-3}$ , the requisite modulation in the charge carrier doping can be achieved by using a ferroelectric for the gate dielectric, an approach termed the *ferroelectric field effect* Ahn et al. (2006); Venkatesan et al. (2007). In this approach to electrostatic doping, the charge carriers screen the large surface bound charge of the ferroelectric; for a ferroelectric such as  $\text{Pb}(\text{Zr,Ti})\text{O}_3$  (PZT), the charge carrier modulation is of the order of  $10^{14} \text{ cm}^{-2}$ , much larger than is possible to attain using silicon oxide as the gate dielectric Ahn et al. (2003). The field effect approach has been explored to control a variety of properties in complex systems, including superconductivity Ahn et al. (1999); Caviglia et al. (2008); Frey et al. (1995); Parendo et al. (2005); R. E. Glover & Sherrill (1960); Talyansky et al. (1996) and metal-insulator transitions Dhoot et al. (2009); Hong et al. (2005; 2003). Ferroelectric gates have also been proposed for non-volatile field effect transistors (FET), where the on/off states are maintained by the ferroelectric polarization Brown (1957); Looney (1957); Miller & McWhorter (1992); Park et al. (2003). Electrostatic control of magnetism has been reported in the last decade for a variety of systems, including dilute magnetic semiconductors (DMS), transition metal ferromagnets, and complex oxides, as discussed briefly below.

The phenomenology of the magnetoelectric coupling in materials has been discussed extensively, and we refer to a recent review for details and for the relevant literature Vaz et al. (2010a). The figure of merit that characterizes the coupling between the electric and magnetic order parameters is the magnetoelectric susceptibility, which measures the change in magnetic

moment for a given applied electric field. In the case where the magnetoelectric response is linear, the magnetoelectric susceptibility  $\alpha = \mu_0 dM/dE_0$  (in S.I., where  $\mu_0$  is the permeability of vacuum,  $M$  is the magnetization, and  $E_0$  is the external applied electric field) is well defined, but it is less so in the more general case where the magnetoelectric response is non-linear. In such instances, it is common to define an effective magnetoelectric constant corresponding to the change in magnetization for a given applied electric field (or conversely, the change in electric polarization for a given applied magnetic field). In composite systems relying on interfacial effects, it is useful to define a surface (interface) magnetoelectric coefficient  $\alpha_s$ , corresponding to the change in surface magnetization for a given applied electric field Duan et al. (2008); Fechner et al. (2008); Niranjana et al. (2009). With the definition given above, the linear magnetoelectric constant has units of  $\text{s m}^{-1}$  in S.I. units, while in cgs units it is dimensionless Rivera (1994); they are related one to the other by the speed of light in vacuum, such that a dimensionless relative magnetoelectric constant ( $\alpha_r$ ) independent of the system of units can be defined, in analogy with the magnetic and electric relative permittivities Hehl et al. (2008; 2009). Often, however,  $\alpha$  is given in mixed units, such as  $\text{Oe cm V}^{-1}$ . We list in Table 1 the magnetoelectric response of charge-mediated multiferroic heterostructures reported in the literature, both in terms of the interfacial and relative magnetoelectric coupling coefficients.

System	$10^3\alpha$	$10^{12}\alpha_s$	$\alpha_r$	$T$ (K)	Reference
bcc Fe(001)	0.002	0.024	0.0005	Theory	Duan et al. (2008)
hcp Co(0001)	0.0008	0.016	0.0002	Theory	Duan et al. (2008)
fcc Ni(001)	0.002	0.03	0.0005	Theory	Duan et al. (2008)
9 ML Fe/MgO	0.008	0.11	0.0023	Theory	Niranjana et al. (2010)
2 ML Fe/BaTiO <sub>3</sub>	10	200	3.0	Theory	Duan et al. (2006)
1 ML Fe/BaTiO <sub>3</sub>	16	230	4.8	Theory	Fechner et al. (2008)
Fe/BaTiO <sub>3</sub> /Pt	3	43	0.9	Theory	Cai et al. (2009)
1 ML Fe/PbTiO <sub>3</sub>	73	1000	22	Theory	Fechner et al. (2008)
Ni/BaTiO <sub>3</sub> /Pt	15	260	4.5	Theory	Cai et al. (2009)
hcp Co/BaTiO <sub>3</sub> /Pt	4	81	1.2	Theory	Cai et al. (2009)
CrO <sub>2</sub> /BaTiO <sub>3</sub> /Pt	10	150	3.0	Theory	Cai et al. (2009)
Fe <sub>3</sub> O <sub>4</sub> /BaTiO <sub>3</sub>	20	200	5.7	Theory	Niranjana et al. (2008)
SrRuO <sub>3</sub> /SrTiO <sub>3</sub>	0.05	2	0.015	Theory	Rondinelli et al. (2008)
SrRuO <sub>3</sub> /BaTiO <sub>3</sub>	1.1	42	0.32	Theory	Rondinelli et al. (2008)
SrRuO <sub>3</sub> /BaTiO <sub>3</sub>	5.9	230	1.8	Theory	Niranjana et al. (2009)
PZT/LSMO ( $x = 0.2$ )	0.8	310	2.4	100 K	Molegraaf et al. (2009)
PZT/LSMO ( $x = 0.2$ )	6.2	2900	22	100 K	Vaz et al. (2010b;c)
PZT/LSMO ( $x = 0.2$ )	-13.5	-6300	-49	180 K	Vaz et al. (2010c)

Table 1. Values of the magnetoelectric coupling coefficient reported in the literature for charge-driven multiferroic heterostructures.  $\alpha$  is given in units of  $\text{Oe cm V}^{-1}$ ,  $\alpha_s$  in units of  $\text{Oe cm}^2 \text{V}^{-1}$ ;  $T$  is the temperature. When not directly provided, the surface magnetoelectric coupling coefficient  $\alpha_s$  is estimated by multiplying  $\alpha$  by 1 ML of the corresponding magnetic material; for the case of the PZT/LSMO structures,  $\alpha_s$  and  $\alpha_r$  are estimated by multiplying the experimental value of  $\alpha$  by the LSMO film thickness.

The nature of the magnetoelectric effect due to charge screening can be distinguished between (i) enhanced spin imbalance at the Fermi level due to screening and the corresponding modification in the magnetic moment of the system as a function of the electric field Zhang (1999); (ii) changes in magnetic moment due to changes in electronic bonding at the polarized

dielectric interface Duan et al. (2006); (iii) changes in the magnetic order with the charge density Gerhard et al. (2010); Kudasov & Korshunov (2007); Ovchinnikov & Wang (2008); Sun et al. (2010); Vaz et al. (2010b), whereby the magnetic state of the system is modified due to changes in the charge carrier density, either between magnetic and non-magnetic states, or between states with different magnetic spin configurations; and (iv) changes in the magnetic anisotropy that lead to different global magnetic states for different applied electric fields Maruyama et al. (2009); Niranjana et al. (2010).

### 2.1 Electrostatic control of magnetism in dilute magnetic semiconductors

The field effect approach to controlling magnetism is well suited for dilute magnetic semiconductors (DMS), such as (In,Mn)As, (Ga,Mn)As, and  $\text{Mn}_x\text{Ge}_{1-x}$ , where integration with semiconductor substrates, such as GaAs, follows naturally from the film growth process. In the DMS systems, the ferromagnetic interaction between the Mn spins (mediated by hole carriers) competes with the antiferromagnetic superexchange, and becomes dominant at sufficiently high hole doping Dietl et al. (2000). The demonstration of electric field modulation of magnetism in a 5 nm epitaxial (In,Mn)As layer was reported by Ohno et al. (2000), using a thick polyimide layer as the gate dielectric. By varying the charge carrier doping through the application of a gate voltage, a change in the critical temperature by about 2 K ( $T_c = 25$  K at zero electric field) is achieved between the accumulation and depletion states. The size of the effect is found to agree with a Zener model used to describe the onset of magnetism in zinc-blend magnetic semiconductors Dietl et al. (2000). Besides (In,Mn)As Chiba et al. (2003); Ohno et al. (2000), electric field control of magnetism in magnetic semiconductors has been reported for  $\text{Mn}_x\text{Ge}_{1-x}$  Chen et al. (2007); Park et al. (2002); Xiu et al. (2010), (Zn,Mn)Se Kneip et al. (2006), and (Ga,Mn)As Chiba et al. (2008); Endo et al. (2010a); Nazmul et al. (2004); Owen et al. (2009); Riester et al. (2009); Stolichnov et al. (2008). In the report by Stolichnov et al. (2008), a ferroelectric polymer (polyvinylidene fluoride with trifluoroethylene, or P(VDF-TrFE)) is employed as the gate dielectric to achieve non-volatile control of ferromagnetism in a (Ga,Mn)As channel layer, as manifested by changes in the coercivity of the magnetic hysteresis loop and in the critical temperature as a function of the ferroelectric polarization direction.

### 2.2 Electrostatic control of magnetism in transition metals

The electrostatic control of magnetism in transition metals has been demonstrated by Weisheit et al. (2007), who report a modulation of the magnetic coercivity in ordered FePt and FePd intermetallic alloys subject to an applied field when immersed in an electrolyte. More recently, Maruyama et al. (2009) have shown that the perpendicular magnetic anisotropy of 2-4 monolayers (ML) Fe films can be modified by electric fields by using a polyimide layer as the gate dielectric (up to 40% for applied fields of the order of 1 MV/cm). The effect is particularly promising and could be explored to devise Fe/MgO/Fe magnetic tunnel junctions, where the tunnel magnetoresistance (TMR) is tuned electrostatically by controlling the magnetic anisotropy—and the relative magnetization alignment—of the Fe layers. Record high tunnel magnetoresistance ratios have been reported for Fe/MgO/Fe Bowen et al. (2001); Parkin et al. (2004); Yuasa et al. (2004), making this system a promising candidate for spintronic device applications. Indeed, control of the magnetic easy axis from in-plane to out of plane has been recently demonstrated for  $\text{Fe}_{80}\text{Co}_{20}$  Shiota et al. (2009), while modulation of the magnetic anisotropy has been shown in  $\text{Fe}_{80}\text{Co}_{20}/\text{MgO}/\text{Fe}$  tunnel junctions Nozaki et al. (2010) and in  $\text{MgO}/\text{Co}_{40}\text{Fe}_{40}\text{B}_{20}/\text{Ta}$  structures Endo et al. (2010b). Another demonstration of electric field modulation of magnetism relies on the magnetic and structural instabilities of elemental Fe, where the application of an electric field is found to induce changes in the crystal structure of

Fe/Cu(111) islands, from the ferromagnetic bcc to the antiferromagnetic fcc structure Gerhard et al. (2010); first principles calculations show that the effect originates from changes in the Fe interatomic distances with the applied electric field as a result of electronic charge screening that tilts the energy of the system to favor a ferromagnetic or antiferromagnetic state Gerhard et al. (2010).

The theoretical study of the magnetoelectric coupling in metal-based multiferroic heterostructures has been the subject of intensive investigation. One can distinguish two approaches, one that considers the effect of charge screening in free standing metal layers subject to an external electric field, and the other that considers charge screening at the interface with a dielectric. In the latter case, contributions from chemical bonding between metal and dielectric need to be considered. The nature of the magnetoelectric effect that appears in metals can also be distinguished between enhanced spin imbalance at the Fermi level due to screening Zhang (1999), changes in the chemical bonding at the interface with the polarized dielectric, changes in the magnetic order with the charge density Gerhard et al. (2010); Kudasov & Korshunov (2007); Ovchinnikov & Wang (2008); Sun et al. (2010), and changes in the magnetic anisotropy Haraguchi et al. (2011); Maruyama et al. (2009); Nakamura et al. (2009); Niranjana et al. (2010); Tsujikawa & Oda (2009). The magnetoelectric effect of free standing metal films has been investigated for bcc Fe(001), fcc Ni(001), and hcp Co(0001) subject to a uniform electric field, where the charge screening induced spin-imbalance gives rise to surface magnetoelectric coupling coefficients of the order of  $2 - 3 \times 10^{-14}$  Oe cm<sup>2</sup> V<sup>-1</sup> Duan et al. (2008), see Table 1. The magnetoelectric effect due to screening is enhanced in the presence of a dielectric due to the larger dielectric constant (compared to vacuum), in addition to effects induced by chemical bonding. For Fe/BaTiO<sub>3</sub>(001), the results of density functional theory (DFT) calculations predict a large surface magnetoelectric response whose origin is largely attributed to changes in the chemical bonding at the interface, in particular, to hybridization between the Ti 3d, Fe 3d and O 2p orbital states, which is found to change significantly upon reversal of the ferroelectric polarization direction due to the displacement of the Ti atoms. The magnetoelectric coupling coefficient for 2 ML Fe/BaTiO<sub>3</sub> is estimated to be  $\alpha = 0.01$  Oe cm V<sup>-1</sup> Duan et al. (2006) while for 1 ML Fe/PbTiO<sub>3</sub>,  $\alpha = 0.073$  Oe cm V<sup>-1</sup> Fechner et al. (2008); the effect of Fe oxidation has been predicted not to affect significantly the magnetoelectric coupling Fechner et al. (2009). In Fe/MgO(001), a surface magnetoelectric coupling  $\alpha_s = 1.1 \times 10^{-13}$  Oe cm<sup>2</sup> V<sup>-1</sup> is found, significantly larger by a factor of 3.8 than that of a free standing Fe layer Niranjana et al. (2010); also in this system a linear change in the magnetocrystalline anisotropy with the applied electric field is reported. A different type of electric field control of magnetism consists of turning the magnetic state on and off; this approach has been investigated in the NiCu alloy at the composition corresponding to the boundary between magnetic and paramagnetic states. By capacitively charging the system, magnetic order can be modulated by effectively controlling the balance between the kinetic and exchange energies that determine the onset of magnetism Ovchinnikov & Wang (2008). The voltage sensitivity of ferromagnetic metallic systems near the critical temperature has also been studied in detail by the same authors Ovchinnikov & Wang (2009a,b). A related effect has been predicted for Pd, which is known to be a paramagnetic system with a Stoner parameter slightly short of fulfilling the condition for ferromagnetism by about 5-10%. First principles calculations suggest that depleting the Pd interface of charge carriers by means of an applied electric field can bring the Fermi level down and increase the density of states to favor an exchange-split (magnetic) state Kudasov & Korshunov (2007); Sun et al. (2010). A scheme for making the interfacial magnetoelectric effect additive consists of breaking the symmetry of ferromagnetic/dielectric bilayer structures by adding a non-magnetic metal at the other interface of the dielectric; this has been proposed by Cai et al. (2009), who have carried out

ab initio calculations for Fe, Co, Ni, CrO<sub>2</sub>/BaTiO<sub>3</sub>/Pt systems to demonstrate this procedure (see Table 1). This approach ensures that spin accumulation at one interface is not canceled by depletion at the other interface and that the magnetoelectric response will increase linearly with the number of interfaces in a superlattice structure.

### 2.3 Electrostatic control of magnetism in complex oxides

The bulk of the experimental work aiming at controlling the magnetic state electrostatically in complex oxide materials has focused on the “colossal” magnetoresistive (CMR) manganites, which are characterized by rich magnetic and electronic phase diagrams as a function of chemical doping (see Section 3). In these compounds, the magnetic critical temperature is found to coincide approximately with a peak in the resistivity versus temperature curve, corresponding to a metal to insulator transition Urushibara et al. (1995). In turn, the temperature at which the resistivity peaks has been taken as a measure of the magnetic ordering temperature, providing a convenient, if indirect, method of probing the magnetic properties of thin films and device structures. Large changes in the resistivity peak temperature are observed in Pb(Zr<sub>0.2</sub>Ti<sub>0.8</sub>)O<sub>3</sub>/La<sub>0.8</sub>Sr<sub>0.2</sub>MnO<sub>3</sub> (PZT/LSMO) heterostructures, by 35 K for a 4.0 nm LSMO film Hong et al. (2003) and 50 K for a 3.8 nm LSMO film Hong et al. (2005); changes up to 43 K have also been reported for 7 u.c. La<sub>0.7</sub>Sr<sub>0.3</sub>MnO<sub>3</sub> side-gated channels Pallecchi et al. (2008); and for a 5 nm La<sub>0.8</sub>Ca<sub>0.2</sub>MnO<sub>3</sub>/electrolyte field effect device, where a change of 32 K in the resistivity peak is observed between depletion and accumulation states. However, although closely related to the onset of magnetic order, the resistivity peak need not coincide with the magnetic critical temperature Bertacco et al. (2005); Lofland et al. (1997); indeed, a direct comparison between the resistivity and magnetization data in PZT/LSMO structures shows that while the peak in resistivity changes by 35 K between depletion and accumulation states, the critical temperature changes only by 20 K Vaz et al. (2010b). Direct measurements of the magnetic order parameter as a function of the applied electric field have been reported for PZT/10 nm La<sub>0.85</sub>Ba<sub>0.15</sub>MnO<sub>3</sub> Kanki et al. (2006), in PZT/4 nm La<sub>0.8</sub>Sr<sub>0.2</sub>MnO<sub>3</sub> Molegraaf et al. (2009); Vaz et al. (2010b) structures, and in 4–6 nm La<sub>0.67</sub>Sr<sub>0.33</sub>MnO<sub>3</sub>/SrTiO<sub>3</sub> field effect device structures Brivio et al. (2010) using magneto-optic magnetometry. In the latter study, both top and bottom gated structures were investigated; the experimental results show that the critical temperature is modulated only for the top gated structure, i.e., for the structure where the screening occurs at the top LSMO interface Brivio et al. (2010). This result indicates that the properties of the bottom interface, characterized by the presence of an electric and magnetically “dead layer,” is less amenable to field modulation. For the PZT/LBMO device structures Kanki et al. (2006), a change in the magnetic hysteresis loops is observed as the PZT polarization is switched, with the magnetic signal decreasing when going from the accumulation to the depletion state, a trend opposite to that found in the PZT/LSMO system Molegraaf et al. (2009); Vaz et al. (2010b), whose discussion we defer to Section 3.

The study of the magnetoelectric coupling in complex oxide heterostructures has also been carried out from the vantage point of first principles calculations. For Fe<sub>3</sub>O<sub>4</sub>/BaTiO<sub>3</sub>(001), a magnetoelectric response of  $\alpha_s \sim 2 \times 10^{-10}$  Oe cm<sup>2</sup> V<sup>-1</sup> for TiO<sub>2</sub>-terminated BaTiO<sub>3</sub>(001) is found Niranjana et al. (2008), comparable to the value obtained for Fe/BaTiO<sub>3</sub> Duan et al. (2006); the magnetoelectric effect in both these systems is attributed to changes in the bonding length of the Fe cations as a function of the direction of the ferroelectric polarization, giving rise to large changes in the magnetic moment of Fe. A magnetoelectric coupling based on charge screening and in the enhancement of the spin imbalance at the Fermi level has been studied in a symmetric SrTiO<sub>3</sub>/SrRuO<sub>3</sub>/SrTiO<sub>3</sub> structure, where the spin imbalance is described in terms of a spin capacitor effect, with the spin asymmetry stored at the interfaces

in a fashion similar to that of charge in a normal capacitor Rondinelli et al. (2008). A measure of the spin response of the interface is given in terms of the ratio of the surface spin polarization to the surface charge density, which is found to attain the value  $\eta = 0.37$ ; this value remains the same when the SrTiO<sub>3</sub> is replaced by BaTiO<sub>3</sub>, although the change in magnetic moment in the SrRuO<sub>3</sub> is much larger with BaTiO<sub>3</sub>, a direct consequence of the larger amount of charge required to screen the ferroelectric polarization. The magnetoelectric response of SrRuO<sub>3</sub>/BaTiO<sub>3</sub>(001) has also been studied, showing that, when subject to an electric field, the magnetic moment and the exchange splitting of SrRuO<sub>3</sub> are modified due to screening, resulting in a magnetoelectric coefficient  $\alpha_s = 2.3 \times 10^{-10}$  Oe cm<sup>2</sup> V<sup>-1</sup> Niranjana et al. (2009). For half-metallic systems, the charge carrier density also determines the magnetic moment, and a simple argument shows that a universal magnetoelectric constant due to charge screening is expected,  $\alpha_s = \mu_B/ec^2 \approx 6.44 \times 10^{-14}$  Oe cm<sup>2</sup> V<sup>-1</sup> Cai et al. (2009); Duan et al. (2009). A different magnetoelectric coupling mechanism is predicted theoretically in La<sub>1-x</sub>A<sub>x</sub>MnO<sub>3</sub>/BaTiO<sub>3</sub>(001) ( $A = \text{Ca, Sr, or Ba}$ ) Burton & Tsymbal (2009), which relies on charge-induced modifications of the magnetic ground state of the CMR manganites Molegraaf et al. (2009). By choosing a doping level near the boundary between the ferromagnetic and antiferromagnetic state of La<sub>1-x</sub>A<sub>x</sub>MnO<sub>3</sub>, the electrostatic doping arising from the ferroelectric polarization acts to favor either the ferromagnetic state (depletion state) or antiferromagnetic state (accumulation state), giving rise to a large change in the total magnetic moment for the two states of the ferroelectric polarization. This mechanism to magnetoelectric coupling had been suggested to occur in PZT/LSMO heterostructures Molegraaf et al. (2009) and will be discussed in more detail from an experimental perspective in the next section.

### 3. Magnetoelectric coupling in PZT/LSMO multiferroic heterostructures

The doped lanthanum manganites are complex oxides characterized by a strong interplay between charge, spin, and crystal lattice distortions, which is at the origin of the multifunctional behavior that is a hallmark of this class of compounds Moreo et al. (1999); Tokura & Tomioka (1999). Examples of the rich electronic and magnetic behavior found in the doped lanthanum manganites include magnetic and charge-ordered states, colossal magnetoresistance (CMR), high spin polarizations, and various electron transport regimes. The doped manganites crystallize in the pseudo-cubic AMnO<sub>3</sub> perovskite structure, where the 12-fold coordinated *A*-site cations are occupied by a large ion (e.g., alkaline and rare earths), while the Mn cations occupy octahedrally coordinated sites Johnsson & Lemmens (2007). Starting with the parent compound lanthanum manganite, LaMnO<sub>3</sub>, where the Mn cations are in a trivalent state, the chemical substitution of La by a divalent alkaline earth removes the  $e_g$  electron from the Mn cation, effectively adding a hole carrier to the system. The addition of carriers leads to profound modifications in the electronic and magnetic properties, resulting in complex phase diagrams as a function of chemical doping that include several electronic ground states Dagotto et al. (2001); Tokura (2006). This sensitivity to charge suggests that large susceptibilities to external electric fields can be attained when the system lies at the boundary separating two different ground states; by driving the system across the phase boundary using electrostatic doping, a change in the magnetic ground state of the system may be achieved. This approach has been explored in PZT/La<sub>0.8</sub>Sr<sub>0.2</sub>MnO<sub>3</sub> heterostructures, where the LSMO system is near the boundary separating insulating and metallic ferromagnetic ground states; large changes in the magnetic properties are expected by using the ferroelectric field effect approach to modulate the charge carrier doping of the LSMO film. For optimal use of the ferroelectric field effect, the channel layer thickness should be comparable to the screening

length Ahn et al. (2003); for LSMO ( $x = 0.2$ ), with a charge carrier concentration of the order of  $10^{21} \text{ cm}^{-3}$ , the screening length has been estimated experimentally to be about 1 u.c. Hong et al. (2005). Hence, the growth of complex oxide field effect devices requires precise control of the thickness down to the unit cell level. Such fine control can be achieved with molecular beam epitaxy Vaz et al. (2010d) or pulsed laser deposition Huijben et al. (2008), where the film growth can be monitored layer-by-layer in real time by using the oscillations in the intensity of reflection high energy electron diffraction patterns. In the following, we provide an overview of the recent work demonstrating a large magnetoelectric coupling in PZT/LSMO heterostructures, as determined by probing directly the magnetic order parameter using local magneto-optic Kerr effect magnetometry Molegraaf et al. (2009). By using advanced spectroscopy techniques, we show that the observed effect is electronic in origin, and that it results from a change in the valence state of the Mn cations with the change in the hole carrier density Vaz et al. (2010b).

The sample structures consist of 250 nm  $\text{Pb}(\text{Zr}_{0.2}\text{Ti}_{0.8})\text{O}_3/\text{La}_{0.8}\text{Sr}_{0.2}\text{MnO}_3/\text{SrTiO}_3(001)$ , grown by a combination of molecular beam epitaxy for the LSMO film and off axis r.f. magnetron sputtering for the PZT layer. The LSMO film thickness is chosen to lie at the transition between the insulating and metallic states, typically 10-12 u.c. for  $x = 0.2$  doping. The structures are single crystalline, with atomically flat and sharp interfaces Vaz et al. (2010d); PZT/LSMO films are deposited on both unpatterned and prepatterned  $\text{SrTiO}_3(001)$  substrates; the latter consist of Hall bar device structures, defined prior to film deposition by optical lithography and with dimensions optimised for optical spectroscopy measurements Vaz et al. (2010d) (see Fig. 1(b), inset). A 10 nm Au gate electrode is then deposited onto the PZT layer, defining the active area of the device (i.e. the sample region where the PZT polarization is switched), using the LSMO layer as the bottom contact. The Au layer is chosen to be sufficiently thin to allow transmission of visible light for magneto-optic Kerr effect (MOKE) magnetometry measurements. MOKE relies on the fact that the polarization of light is modified upon reflection from a magnetic surface; it is a technique particularly well suited for this study, since it allows a direct and local measurement of the magnetic order parameter. In one implementation of this technique, a linearly polarized laser beam is reflected off the sample surface (with the plane of incidence parallel to the applied field direction, called the longitudinal MOKE geometry), and the Kerr rotation or ellipticity, which is proportional to the magnetization, is measured using a polarimeter unit Vaz et al. (2010e).

The individual electric and magnetic characteristics of the PZT/LSMO heterostructure are shown in Fig. 1(a) and (b), respectively. The electric polarization versus electric field ( $P$ - $E$ ) response shows abrupt electric switching and a saturation polarization of about  $85 \mu\text{C cm}^{-2}$ ; the magnetic hysteresis ( $M$ - $H$ ) curves, for both the accumulation and depletion states, show that the system is ferromagnetic at 100 K and that there is a marked difference in the magnetic properties for the two states of the ferroelectric polarization, namely, a larger coercivity and a smaller saturation magnetization for the accumulation state as compared to the depletion state. These individual ferroic curves are the classical hysteresis curves of ferroelectrics and ferromagnets; the magnetoelectric coupling is demonstrated by the magnetic response of the system as a function of the applied electric field ( $M$ - $E$  loop) shown in Fig. 1(c), where the saturation magnetization is found to switch hysteretically and reversibly between a low and high magnetic moment at the electric field values corresponding to the switching of the ferroelectric polarization. This result demonstrates the presence of a magnetoelectric coupling in these multiferroic heterostructures, showing in particular that the direction of the PZT ferroelectric polarization modifies the magnetic state of the LSMO layer. Note that the difference in magnetic moment persists at zero applied electric field, which excludes electrostrictive or piezoelectric effects (strain) as being the cause of the observed

magnetoelectric effect. The magnetoelectric effect in the PZT/LSMO system is robust and has been observed in structures where the LSMO film has been grown by off axis magnetron sputtering Molegraaf et al. (2009) and molecular beam epitaxy Vaz et al. (2010b).

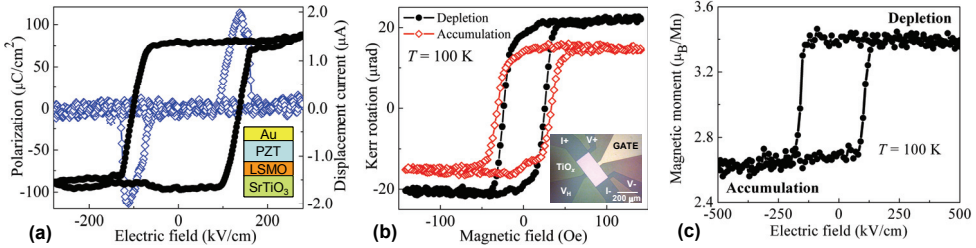


Fig. 1. Composite multiferroic heterostructure characterized by a coupling between the classical ferroelectric (a) and magnetic (b) ferro responses, as shown in (c). While the  $M$ - $H$  and  $P$ - $E$  loops are standard, the  $M$ - $E$  characteristic is new. The example shown is for a PZT/12 u.c.  $\text{La}_{0.8}\text{Sr}_{0.2}\text{MnO}_3$  composite multiferroic heterostructure, from Vaz et al. (2010b; 2011). Figures (a) and (b): Copyright 2010 by The American Physical Society. Figure (c) reprinted with permission from C.A.F. Vaz et al., J. Appl. Phys., 109, 07D905 (2011). Copyright 2011, American Institute of Physics.

The variation of the magnetization as a function of temperature for the two states of the PZT polarization is shown in Fig. 2(a) Molegraaf et al. (2009); Vaz et al. (2010c). The magnetization curves are characteristic of a ferromagnetic system, with a critical temperature separating the high temperature paramagnetic regime and a ferromagnetically ordered state at low temperatures. What is striking in these data is that the direction of the PZT polarization determines the magnetic properties of the system, including an increase in the critical temperature (by about 20 K) and a decrease in the ground state magnetization when switching from the depletion to the accumulation state (in agreement with the  $M$ - $H$  hysteresis curve of Fig. 1(b)). One sees that the state corresponding to the highest Curie temperature has the lowest saturation magnetization, which agrees qualitatively with what is expected from the behavior of bulk LSMO, since hole doping changes the ionic state of  $\text{Mn}^{3+}$ , with spin  $S = 2$ , to  $\text{Mn}^{4+}$ , with spin  $S = 3/2$ , so that we expect a decrease in magnetization with increasing doping Jonker & van Santen (1950).

As shown in Fig. 1(c), the magnetoelectric response of the PZT/LSMO multiferroic heterostructure is strongly non-linear, and the response of the system is best described in terms of an effective magneto-electric susceptibility  $\Delta M/\Delta E = \Delta M/2E_c$ , where  $E_c$  is the ferroelectric coercive field; at 100 K, we find  $\Delta M/\Delta E = 6.2 \times 10^{-3} \text{ Oe cm V}^{-1}$ . This value is significantly larger, by 2-3 orders of magnitude, than typical magneto-electric coupling coefficients of single-phase multiferroics and comparable to the value obtained for strain-mediated composites Fiebig (2005); Ma et al. (2011); Vaz et al. (2010a). Given the interfacial nature of the magneto-electric effect in this system, one alternate measure of the magneto-electric effect is given in terms of the surface (interface) magneto-electric coefficient  $\alpha_s$ , which is obtained by multiplying  $\Delta M/2E_c$  by the LSMO film thickness, yielding  $\alpha_s = 2.9 \times 10^{-9} \text{ Oe cm}^2 \text{ V}^{-1}$  at 100 K. In Vaz et al. (2010c), the variation of the magneto-electric response of PZT/LSMO as a function of the temperature is studied, as shown in Fig. 2(b).  $\Delta M/2E_c$  is found to have a strong, non-monotonic, temperature variation, including a change in signal at around 150 K; in particular, one finds that the magneto-electric response is largest at around 180 K, with  $\Delta M/\Delta E = -13.5 \times 10^{-3} \text{ Oe cm V}^{-1}$  ( $\alpha_s = -6.3 \times 10^{-9} \text{ Oe cm}^2 \text{ V}^{-1}$ ),

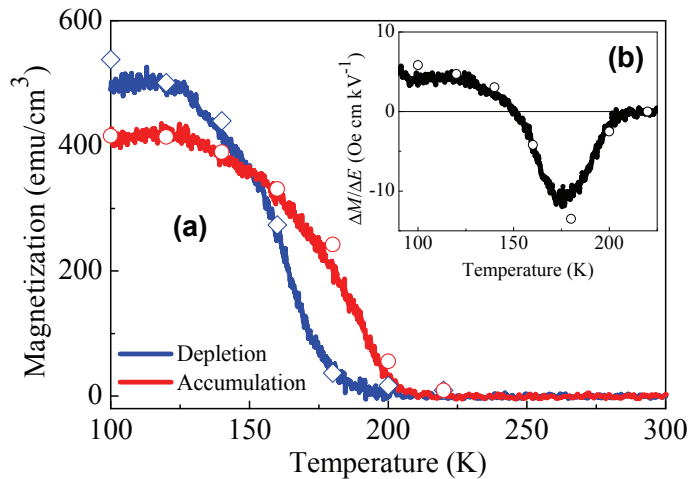


Fig. 2. (a) Magnetic response of the system as a function of temperature for the two states of the PZT polarization. (b) Variation in the magnetoelectric coupling coefficient  $\Delta M/2E_c$  as a function of temperature. After Vaz et al. (2010c).

near the magnetic critical point, where the difference between the magnetization for the depletion and accumulation states is largest, as shown in Fig. 2(a). The change in sign of the magnetoelectric response can be understood with reference to the magnetization data shown in Fig. 2(a). One finds that 150 K separates a low temperature regime, where the magnetization for the depletion state is larger than that of the accumulation state, from a high temperature regime (up to the paramagnetic state), where the opposite behavior occurs due to the faster decay of the magnetization of the system in the depletion state on approaching its magnetic critical temperature. What is particularly promising in this system is that  $\Delta M/\Delta E$  peaks at temperatures near the critical region, showing that the largest magnetoelectric response is achieved at the highest temperature where the system remains magnetic. A key aspect of composite multiferroics is that they need not obey reciprocity relations that limit the size of the magnetoelectric susceptibility in single phase compounds Brown et al. (1968).

The microscopic origin of the magnetoelectric effect is investigated by x-ray absorption near edge spectroscopy (XANES). XANES is a technique particularly well suited to study the changes in the electronic structure of Mn as a function of the applied electric field, due to its sensitivity to changes in the valence state. In XANES, one excites electrons from a core shell to empty states in the valence band (1s to 4p states for the case of the Mn *K* edge). This excitation energy depends on the formal valence state of the cation, with the more electronegative cations requiring higher energy photons to excite core electrons Kirichok et al. (1985). One key advantage of x-ray absorption spectroscopy is its ability to probe buried layers, which is not possible with some other spectroscopic techniques, such as photoelectron spectroscopy. Details of the experimental set-up and measurement conditions are given in Vaz et al. (2010b;e).

The room temperature variation of the x-ray light absorption as a function of the incident photon energy across the absorption *K* edge of Mn, for the depletion and accumulation states, is shown Fig. 3(a) Vaz et al. (2010b). The key result is the observation of an energy shift in the absorption edge of Mn between the depletion and accumulation states, by 0.3 eV, which corresponds to about 10% of the total shift expected for the full LSMO doping range Bindu

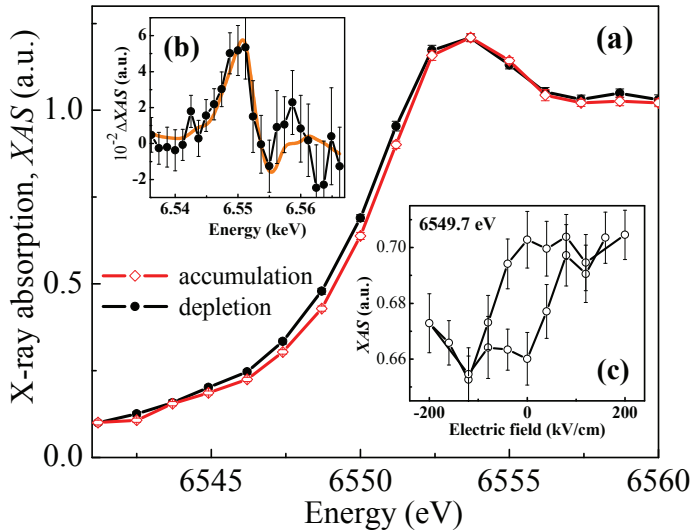


Fig. 3. (a) Room temperature XANES results for the two polarization states of the PZT. (b) Difference in x-ray absorption for the two PZT polarization states; the full line models this difference assuming a rigid shift in the Mn absorption edge. (c) Variation of the x-ray light absorption as a function of the applied gate voltage at a fixed energy,  $E = 6549.7$  eV. The error bars reflect counting statistics. After Vaz et al. (2010b).

et al. (2005); Shibata et al. (2003). The shift in the absorption edge can also be observed in the difference x-ray absorption spectrum, shown in Fig. 3(b). The observation of a shift in the absorption K edge of Mn shows that the valence state of Mn changes with charge doping induced by the ferroelectric polarization and demonstrates the electronic nature of the magnetoelectric coupling in these multiferroic heterostructures. The same result is observed at low temperature (20 K). From the observed energy shift we estimate the average change in valency across the LSMO film,  $\Delta x = 0.1$  per Mn, using the results by Shibata et al. (2003) showing a linear variation in the energy shift with the formal average valency of Mn,  $\Delta E = 3.0x$ , where  $x$  is the LSMO doping.

One can now compare the change in valency as determined by XANES with the values obtained from the electric and magnetic characterization of the same device structure. From the saturation electric polarization,  $P_s = 85 \mu\text{C cm}^{-2}$ , one can deduce the expected change in the carrier doping,  $\Delta n = 0.13$  e/Mn. This value is in good agreement with the change in valency determined from XANES,  $\Delta x = 0.1$  per Mn, showing that the electric polarization is screened effectively by hole carriers from the LSMO layer. Changing the valency of Mn from 3+ to 4+ leads to a change in spin state by 1/2 and to a change in magnetic moment of  $gS \approx 1 \mu_B$  (where  $g \approx 2$  is the  $g$ -factor), so one expects a change in the average magnetic moment of  $0.1 \mu_B/\text{Mn}$ . However, from MOKE (Fig. 1(b)) in combination with SQUID magnetometry, one obtains a change in magnetic moment of about  $0.76 \mu_B/\text{Mn}$ . This change is much larger than the expected change of  $0.1 \mu_B/\text{Mn}$  from the change in spin state. One sees therefore that the change in magnetic moment cannot be explained simply by the change in the Mn spin state. From these results, and from the amplitude of the change in the magnetic moment, one concludes that a change in both the spin state and spin configuration must occur, whereby

the depletion state remains in a ferromagnetic state, while the accumulation state exhibits an antiferromagnetic configuration confined to the PZT interface where charge screening occurs. A model depicting the magnetic reordering is shown in Fig. 4. In this picture, the interface layer in the accumulation state consists of strongly depopulated  $3d\ z^2$  states, weakening the double-exchange interaction at these orbitals and favoring superexchange, leading to an antiferromagnetic coupling of the interfacial layer. This picture is in qualitative agreement with first principles calculations in strained LSMO Fang et al. (2000), and in particular with recent ab initio calculations by Burton and Tsymbal on  $\text{La}_{1-x}\text{Ba}_x\text{MnO}_3/\text{BaTiO}_3$  Burton & Tsymbal (2009), where the low energy state of the system at  $x = 0.5$  in the accumulation state corresponds to an antiparallel spin configuration of the interfacial spins. In this simplified model, the change in the interfacial spin configuration leads to a change in magnetic moment of about  $0.6\ \mu_B/\text{Mn}$  between depletion and accumulation states, which agrees with the experimental results. This mechanism gives rise to a much more dramatic change in the average magnetic moment and explains the large magnetoelectric coupling observed in this system. One direct consequence of these results is that one can control electrostatically both the spin state and magnetic spin configuration of the interfacial LSMO layer. Given that this layer is also responsible for charge transport, and given the high spin polarization characteristic of LSMO Park et al. (1998), this system constitutes a potential platform for the design of spintronics devices, such as lateral spin-valve structures, where the magnetic and transport properties are controlled by applied electric fields.

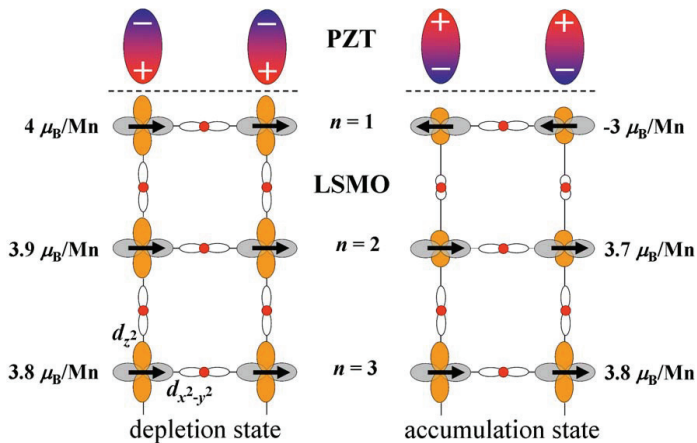


Fig. 4. Schematic model of the spin configurations in LSMO at the PZT interface for the depletion and accumulation states, showing the changes in the Mn and O orbital states and the expected changes in the magnetic moment per layer. The arrows indicate the spin orientation in the Mn cations and  $n$  denotes the unit cell number below the PZT. The Mn  $d$  orbitals are drawn in orange, and gray, and the lobes of the p orbitals are shown around the oxygen atoms (red). After Vaz et al. (2010b), Copyright 2010 by The American Physical Society.

#### 4. Conclusion and outlook

To summarize, we illustrate how novel functionalities can be engineered by exploring the new phenomena that arise at the interface between dissimilar materials and how such

an approach can be used to achieve electrostatic control of magnetism in multiferroic heterostructures. By exploiting the sensitivity of the ground state properties of the CMR manganites to charge, we showed that large, charge-driven, magnetoelectric coupling in PZT/LSMO multiferroic heterostructures can be achieved. The effect is electronic in origin, as demonstrated by advanced spectroscopic techniques, and is therefore compatible with current CMOS technology, in particular since the growth of crystalline oxides on Si(001) is now well established McKee et al. (1998; 2001); Reiner et al. (2008). Further, we show that both the spin state and the magnetic configuration can be controlled electrostatically. One research challenge remains the optimization of the materials properties to allow room temperature operation; possible solutions are the use of optimal doping or the use of other magnetic oxides, such as the double perovskites. Another area that needs to be addressed is the dynamic magnetoelectric response of these multiferroic heterostructures, both in terms of the electric field modulation of the spin wave spectra and in terms of the electrostatic switching time of the magnetic state. Given that in these multiferroics the processes are electronically driven, one may expect very fast switching times, limited by the ferroelectric switching process. As this chapter aims to show, demonstrating the electrostatic switching of magnetism in a range of materials has been achieved as a proof of concept, and much remains to be investigated in terms of materials optimization, development and characterization of new systems, and understanding of the interfacial processes mediating the magnetoelectric coupling. The work achieved thus far illustrates how novel device structures enabling electric field control of the magnetic spin state can be tailored to provide the requisite characteristics that will make them potential candidates for next generation electronic devices.

## 5. Acknowledgments

This work supported by FENA, NSF 1006256, ONR, and from EU's Seventh Framework Programme IFOX (NMP3-LA-2010-246102). CAFV acknowledges M. Kläui for his continuing support.

## 6. References

- Ahn, C. H., Bhattacharya, A., Ventra, M. D., Eckstein, J. N., Frisbie, C. D., Gershenson, M. E., Goldman, A. M., Inoue, I. H., Mannhart, J., Millis, A. J., Morpurgo, A. F., Natelson, D. & Triscone, J.-M. (2006). *Rev. Mod. Phys.* 78: 1185.
- Ahn, C. H., Gariglio, S., Paruch, P., Tybell, T., Antognazza, L. & Triscone, J.-M. (1999). *Science* 284: 1152.
- Ahn, C. H., Triscone, J.-M. & Mannhart, J. (2003). *Nature* 424: 1015.
- Bertacco, R., Riva, M., Cantoni, M., Signorini, L. & Ciccacci, F. (2005). *Appl. Phys. Lett.* 86: 252502.
- Bibes, M. & Barthélémy, A. (2007). *IEEE Trans. Electron Dev.* 54: 1003.
- Bindu, R., Pandey, S. K., Kumar, A., Khalid, S. & Pimpale, A. V. (2005). *J. Phys.: Condens. Matter* 17: 6393.
- Bowen, M., Cros, V., Petroff, F., Fert, A., Boubeta, C. M., Costa-Krämer, J. L., Anguita, J. V., Cebollada, A., Briones, F., de Teresa, J. M., Morellón, L., Ibarra, M. R., Güell, F., Peiró, F. & Cornet, A. (2001). *Appl. Phys. Lett.* 79: 1655.
- Brivio, S., Cantoni, M., Petti, D. & Bertacco, R. (2010). *J. Appl. Phys.* 108: 113906.
- Brown, Jr., W. F., Hornreich, R. M. & Shtrikman, S. (1968). *Phys. Rev.* 168: 574.
- Brown, W. L. (1957). U.S. Patent 2,791,759.
- Burton, J. D. & Tsymbal, E. Y. (2009). *Phys. Rev. B* 80: 174406.

- Cai, T., Ju, S., Lee, J., Sai, N., Demkov, A. A., Niu, Q., Li, Z., Shi, J. & Wang, E. (2009). *Phys. Rev. B* 80: 140415(R).
- Catalan, G. & Scott, J. F. (2009). *Adv. Mater.* 21: 2463.
- Caviglia, A. D., Gariglio, S., Reyren, N., Jaccard, D., Schneider, T., Gabay, M., Thiel, S., Hammerl, G., Mannhart, J. & Triscone, J.-M. (2008). *Nature* 456: 624.
- Cazayous, M., Gallais, Y., Sacuto, A., de Sousa, R., Lebeugle, D. & Colson, D. (2008). *Phys. Rev. Lett.* 101: 037601.
- Chambers, S. A. (2010). *Adv. Mater.* 22: 219.
- Chen, J., Wang, K. L. & Galatsis, K. (2007). *Appl. Phys. Lett.* 90: 012501.
- Chiba, D., Sawicki, M., Nishitani, Y., Nakatani, Y., Matsukura, F. & Ohno, H. (2008). *Nature* 455: 515.
- Chiba, D., Yamanouchi, M., Matsukura, F. & Ohno, H. (2003). *Science* 301: 943.
- Chu, Y.-H., Martin, L. W., Holcomb, M. B., Gajek, M., Han, S.-J., He, Q., Balke, N., Yang, C.-H., Lee, D., Hu, W., Zhan, Q., Yang, P.-L., Fraile-Rodríguez, A., Scholl, A., Wang, S. X. & Ramesh, R. (2008). *Nature Mater.* 7: 478.
- Cibert, J., Bobo, J.-F. & Lüders, U. (2005). *C. R. Physique* 6: 977.
- Cohen, R. E. (2000). *J. Phys. Chem. Solids* 61: 139.
- Dagotto, E., Hotta, T. & Moreo, A. (2001). *Phys. Rep.* 344: 1.
- Dhoot, A. S., Israel, C., Moya, X., Mathur, N. D. & Friend, R. H. (2009). *Phys. Rev. Lett.* 102: 136402.
- Dietl, T., Ohno, H., Matsukura, F., Cibert, J. & Ferrand, D. (2000). *Science* 287: 1019.
- Duan, C.-G., Jaswal, S. S. & Tsymbal, E. (2006). *Phys. Rev. Lett.* 97: 047201.
- Duan, C.-G., Nan, C.-W., Jaswal, S. S. & Tsymbal, E. Y. (2009). *Phys. Rev. B* 79: 140403(R).
- Duan, C.-G., Velev, J. P., Sabirianov, R. F., Zhu, Z., Chu, J., Jaswal, S. S. & Tsymbal, E. (2008). *Phys. Rev. Lett.* 101: 137201.
- Dzialoshinskii, I. E. (1957). *Sov. Phys. JETP* 5: 1259.
- Eckstein, J. N. & Bozovic, I. (1995). *Annu. Rev. Mater. Sci.* 25: 679.
- Endo, M., Chiba, D., Shimotani, H., Matsukura, F., Iwasa, Y. & Ohno, H. (2010a). *Appl. Phys. Lett.* 96: 022515.
- Endo, M., Kanai, S., Ikeda, S., Matsukura, F. & Ohno, H. (2010b). *Appl. Phys. Lett.* 96: 212503.
- Fang, Z., Solovyev, I. V. & Terakura, K. (2000). *Phys. Rev. Lett.* 84: 3169.
- Fechner, M., Maznichenko, I. V., Ostanin, S., Ernst, A., Henk, J., Bruno, P. & Mertig, I. (2008). *Phys. Rev. B* 78: 212406.
- Fechner, M., Ostani, S. & Mertig, I. (2009). *Phys. Rev. B* 80: 094405.
- Fennie, C. J. (2008). *Phys. Rev. Lett.* 100: 167203.
- Fiebig, M. (2005). *J. Phys. D: Appl. Phys.* 38: R123.
- Frey, T., Mannhart, J., Bednorz, J. G. & Williams, E. J. (1995). *Phys. Rev. B* 51: 3257.
- Gerhard, L., Yamada, T. K., Balashov, T., Takács, A. F., Wesselink, R. J. H., Däne, M., Fechner, M., Ostanin, S., Ernst, A., Mertig, I. & Wulffhkel, W. (2010). *Nature Nanotechnology* 5: 792.
- Haraguchi, S., Tsujikawa, M., Gotou, J. & Oda, T. (2011). *J. Phys. D: Appl. Phys.* 44: 064005.
- Hehl, F. W., Obukhov, Y. N., Rivera, J.-P. & Schmid, H. (2008). *Phys. Rev. A* 77: 022106.
- Hehl, F. W., Obukhov, Y. N., Rivera, J.-P. & Schmid, H. (2009). *Eur. Phys. J. B* 71: 321.
- Hong, X., Posadas, A. & Ahn, C. H. (2005). *Appl. Phys. Lett.* 86: 142501.
- Hong, X., Posadas, A., Lin, A. & Ahn, C. H. (2003). *Phys. Rev. B* 68: 134415.
- Huijben, M., Martin, L. W., Chu, Y.-H., Holcomb, M. B., Yu, P., Rijnders, G., Blank, D. H. A. & Ramesh, R. (2008). *Phys. Rev. B* 78: 094413.
- Imada, M., Fujimori, A. & Tokura, Y. (1998). *Rev. Mod. Phys.* 70: 1039.

- Johnsson, M. & Lemmens, P. (2007). Crystallography and chemistry of perovskites, in H. Kronmüller & S. Parkin (eds), *Handbook of Magnetism and Advanced Magnetic Materials*, Vol. 4, John Wiley & Sons, p. 1.
- Jonker, G. H. & van Santen, J. H. (1950). *Physica* 16: 337.
- Kanki, T., Tanaka, H. & Kawai, T. (2006). *Appl. Phys. Lett.* 89: 242506.
- Khomskii, D. I. (2006). *J. Magn. Magn. Mater.* 306: 1.
- Khomskii, D. I. (2009). *Physics* 2: 20.
- Kirichok, P. P., Kopaev, A. V. & Pashchenko, V. P. (1985). *Russian Physics Journal* 28: 849.
- Kiselev, S. V., Ozerov, R. P. & Zhdanov, G. S. (1963). *Sov. Phys. — Doklady* 7: 742.
- Kneip, M. K., Yakovlev, D. R., Bayer, M., Slobodskyy, T., Schmidt, G. & Molenkamp, L. W. (2006). *Appl. Phys. Lett.* 88: 212105.
- Kudasov, Y. B. & Korshunov, A. S. (2007). *Phys. Lett. A* 364: 348.
- Lebeugle, D., Colson, D., Forget, A. & Viret, M. (2007). *Appl. Phys. Lett.* 91: 022907.
- Lebeugle, D., Colson, D., Forget, A., Viret, M., Bataille, A. M. & Gusakov, A. (2008). *Phys. Rev. Lett.* 100: 227602.
- Lee, S., Ratcliff, W., Cheong, S.-W. & Kiryukhin, V. (2008). *Appl. Phys. Lett.* 92: 192906.
- Lofland, S. E., Bhagat, S. M., Ghosh, K., Greene, R. L., Karabashev, S. G., Shulyatev, D. A., Arsenov, A. A. & Mukovskii, Y. (1997). *Phys. Rev. B* 56: 13705.
- Looney, D. H. (1957). U.S. Patent 2,791,758.
- Ma, J., Hu, J., Li, Z. & Nan, C.-W. (2011). *Adv. Mater.* 23: 9.
- Martin, L. W., Chu, Y.-H. & Ramesh, R. (2010). *Materials Science and Engineering R* 68: 89.
- Maruyama, T., Shiota, Y., Nozaki, T., Ohta, K., Toda, N., Mizuguchi, M., Tulapurkar, A. A., Shinjo, T., Shiraishi, M., Mizukami, S., Ando, Y. & Suzuki, Y. (2009). *Nature Nanotechnology* 4: 158.
- McKee, R. A., Walker, F. J. & Chisholm, M. F. (1998). *Phys. Rev. Lett.* 81: 3014.
- McKee, R. A., Walker, F. J. & Chisholm, M. F. (2001). *Science* 293: 468.
- Miller, S. L. & McWhorter, P. J. (1992). *J. Appl. Phys.* 72: 5999.
- Molegraaf, H. J. A., Hoffman, J., Vaz, C. A. F., Gariglio, S., van der Marel, D., Ahn, C. H. & Triscone, J.-M. (2009). *Adv. Mater.* 21: 3470.
- Moreo, A., Yunoki, S. & Dagotto, E. (1999). *Science* 283: 2034.
- Moriya, T. (1960). *Phys. Rev.* 120: 91.
- Nakamura, K., Shimabukuro, R., Fujiwara, Y., Akiyama, T., Ito, T. & Freeman, A. J. (2009). *Phys. Rev. Lett.* 102: 187201.
- Nan, C.-W., Bichurin, M. I., Dong, S., Viehland, D. & Srinivasan, G. (2008). *J. Appl. Phys.* 103: 031101.
- Nazmul, A. M., Kobayashi, S., Sugahara, S. & Tanaka, M. (2004). *Physica E* 21: 937.
- Neaton, J. B., Ederer, C., Waghmare, U. V., Spaldin, N. A. & Rabe, K. M. (2005). *Phys. Rev. B* 71: 014113.
- Niranjan, M. K., Burton, J. D., Velev, J. P., Jaswal, S. S. & Tsymbal, E. Y. (2009). *Appl. Phys. Lett.* 95: 052501.
- Niranjan, M. K., Duan, C.-G., Jaswal, S. S. & Tsymbal, E. Y. (2010). *Appl. Phys. Lett.* 96: 222504.
- Niranjan, M. K., Velev, J. P., Duan, C.-G., Jaswal, S. S. & Tsymbal, E. Y. (2008). *Phys. Rev. B* 78: 104405.
- Nozaki, T., Shiota, Y., Shinjo, T. & Suzuki, Y. (2010). *Appl. Phys. Lett.* 96: 022506.
- Ohno, H., Chiba, D., Matsukura, F., Omiya, T., Abe, E., Dietl, T., Ohno, Y. & Ohtani, K. (2000). *Nature* 408: 944.
- Ovchinnikov, I. V. & Wang, K. L. (2008). *Phys. Rev. B* 78: 012405.
- Ovchinnikov, I. V. & Wang, K. L. (2009a). *Phys. Rev. B* 79: 020402(R).
- Ovchinnikov, I. V. & Wang, K. L. (2009b). *Phys. Rev. B* 80: 012405.

- Owen, M. H. S., Wunderlich, J., Novák, V., Olejník, K., Zemen, J., Výborný, K., Ogawa, S., Irvine, A. C., Ferguson, A. J., Sirringhaus, H. & Jungwirth, T. (2009). *New J. Phys.* 11: 023008.
- Pallecchi, I., Pellegrino, L., Bellingeri, E., Siri, A. S., Marré, D., Tebano, A. & Balestrino, G. (2008). *Phys. Rev. B* 78: 024411.
- Parendo, K. A., Tan, K. H. S. B., Bhattacharya, A., Eblen-Zayas, M., Staley, N. E. & Goldman, A. M. (2005). *Phys. Rev. Lett.* 94: 197004.
- Park, J.-H., Vescovo, E., Kim, H.-J., Kwon, C., Ramesh, R. & Venkatesan, T. (1998). *Nature* 392: 794.
- Park, Y. D., Hanbicki, A. T., Erwin, S. C., Hellberg, C. S., Sullivan, J. M., Mattson, J. E., Ambrose, T. F., Wilson, A., Spanos, G. & Jonker, B. T. (2002). *Science* 295: 651.
- Park, Y.-G., Kanki, T., Lee, H.-Y., Tanaka, H. & Kawai, T. (2003). *Solid-State Electronics* 47: 2221.
- Parkin, S. S. P., Kaiser, C., Panchula, A., Rice, P. M., Hughes, B., Samant, M. & Yang, S.-H. (2004). *Nature Mater.* 3: 862.
- Picozzi, S. & Ederer, C. (2009). *J. Phys.: Condens. Matter* 21: 303201.
- Posadas, A.-B., Lippmaa, M., Walker, F. J., Dawber, M., Ahn, C. H. & Triscone, J.-M. (2007). Growth and novel applications of epitaxial oxide thin films, in K. Rabe, C. H. Ahn & J.-M. Triscone (eds), *Physics of ferroelectrics*, Vol. 105 of *Topics in Applied Physics*, Springer-Verlag, p. 219.
- R. E. Glover, I. & Sherrill, M. D. (1960). *Phys. Rev. Lett.* 5: 248.
- Rabe, K. & Ghosez, P. (2007). First-principles studies of ferroelectric oxides, in K. Rabe, C. H. Ahn & J.-M. Triscone (eds), *Physics of ferroelectrics*, Vol. 105 of *Topics in Applied Physics*, Springer-Verlag.
- Ramesh, R. & Spaldin, N. A. (2007). *Nature Mater.* 6: 21.
- Ravindran, P., Vidya, R., Kjekshus, A., Fjellvåg, H. & Eriksson, O. (2006). *Phys. Rev. B* 74: 224412.
- Reiner, J. W., Posadas, A., Wang, M., Ma, T. P. & Ahn, C. H. (2008). *Microelectronic Engineering* 85: 36.
- Reiner, J. W., Walker, F. J. & Ahn, C. H. (2009). *Science* 323: 1018.
- Riester, S. W. E., Stolichnov, I., Trodahl, H. J., Setter, N., Rushforth, A. W., Edmonds, K. W., Campion, R. P., Foxon, C. T., Gallagher, B. L. & Jungwirth, T. (2009). *Appl. Phys. Lett.* 94: 063504.
- Rivera, J.-P. (1994). *Ferroelectrics* 161: 165.
- Rondinelli, J. M., Stengel, M. & Spaldin, N. A. (2008). *Nature Nanotechnology* 3: 46.
- Schlom, D. G., Haeni, J., Lettieri, J., Theis, C. D., Tian, W., Jiang, J. C. & Pan, X. Q. (1992). *Mater. Sci. Eng. B* 87: 282.
- Shibata, T., Bunker, B. A. & Mitchell, J. F. (2003). *Phys. Rev. B* 68: 024103.
- Shiota, Y., Maruyama, T., Nozaki, T., Shinjo, T., Shiraishi, M. & Suzuki, Y. (2009). *Appl. Phys. Express* 2: 063001.
- Shvartsman, V. V., Kleemann, W., Haumont, R. & Kreisel, J. (2007). *Appl. Phys. Lett.* 90: 172115.
- Sosnowska, I., Peterlin-Neumaier, T. & Steichele, E. (1982). *J. Phys. C: Sol. State Phys.* 15: 4835.
- Spaldin, N. A. & Pickett, W. E. (2003). *J. Solid State Chem.* 176: 615.
- Srinivasan, G. (2010). *Annu. Rev. Mater. Res.* 40: 153.
- Stolichnov, I., Riester, S. W. E., Trodahl, H. J., Setter, N., Rushforth, A. W., Edmonds, K. W., Campion, R. P., Foxon, C. T., Gallagher, B. L. & Jungwirth, T. (2008). *Nature Mater.* 7: 464.
- Sun, Y., Burton, J. D. & Tsymbal, E. Y. (2010). *Phys. Rev. B* 81: 064413.
- Talyansky, V., Ogale, S. B., Takeuchi, I., Doughty, C. & Venkatesan, T. (1996). *Phys. Rev. B* 53: 14575.

- Thiele, C., Dörr, K., Bilani, O., Rödel, J. & Schultz, L. (2007). *Phys. Rev. B* 75: 054408.
- Tokura, Y. (2006). *Rep. Prog. Phys.* 69: 797.
- Tokura, Y. & Nagaosa, N. (2000). *Science* 288: 462.
- Tokura, Y. & Tomioka, Y. (1999). *J. Magn. Magn. Mater.* 200: 1.
- Tsujikawa, M. & Oda, T. (2009). *Phys. Rev. Lett.* 102: 247203.
- Urushibara, A., Moritomo, Y., Arima, T., Asamitsu, A., Kido, G. & Tokura, Y. (1995). *Phys. Rev. B* 51: 14103.
- van Suchtelen, J. (1972). *Philips Res. Repts* 27: 28.
- Vaz, C. A. F., Wang, H.-Q., Ahn, C. H., Henrich, V. E., Baykara, M. Z., Schwendemann, T. C., Pilet, N., Albers, B. J., Schwarz, U., Zhang, L. H., Zhu, Y., Wang, J. & Altman, E. I. (2009a). *Surf. Sci.* 603: 291.
- Vaz, C. A. F., Hoffman, J., Posadas, A.-B. & Ahn, C. H. (2009b). *Appl. Phys. Lett.* 94: 022504.
- Vaz, C. A. F., Hoffman, J., Ahn, C. H. & Ramesh, R. (2010a). *Adv. Mater.* 22: 2900.
- Vaz, C. A. F., Hoffman, J., Segal, Y., Reiner, J. W., Grober, R. D., Zhang, Z., Ahn, C. H. & Walker, F. J. (2010b). *Phys. Rev. Lett.* 104: 127202.
- Vaz, C. A. F., Segal, Y., Hoffman, J., Grober, R. D., Walker, F. J. & Ahn, C. H. (2010c). *Appl. Phys. Lett.* 97: 042506.
- Vaz, C. A. F., Segal, Y., Hoffman, J., Walker, F. J. & Ahn, C. H. (2010d). *J. Vac. Sci. Technol. B* 28: C5A6.
- Vaz, C. A. F., Hoffman, J., Segal, Y., Walker, F. J. & Ahn, C. H. (2010e). *Proc. of SPIE* 7760: 776013.
- Vaz, C. A. F., Hoffman, J., Segal, Y., Marshall, M. S. J., Reiner, J. W., Grober, R. D., Zhang, Z., Walker, F. J. & Ahn, C. H. (2011). *J. Appl. Phys.* 109: 07D905.
- Venkatesan, T., Kundaliya, D. C., Wu, T. & Ogale, S. B. (2007). *Phil. Mag. Lett.* 87: 279.
- Vrejoiu, I., Alexe, M., Hesse, D. & Gösele, U. (2008). *Adv. Mater.* 18: 3892.
- Waghmare, U. V. & Rabe, K. M. (2005). Dielectric properties of simple and complex oxides from first principles, in A. A. Demkov & A. Navrotsky (eds), *Materials Fundamentals of Gate Dielectrics*, Springer, Dordrecht, p. 215.
- Wang, J., Neaton, J. B., Zheng, H., Nagarajan, V., Ogale, S. B., Liu, B., Viehland, D., Vaithyanathan, V., Schlom, D. G., Waghmare, U. V., Spaldin, N. A., Rabe, K. M., Wuttig, M. & Ramesh, R. (2003). *Science* 299: 1719.
- Wang, K. F., Liu, J. M. & Ren, Z. F. (2009). *Adv. Phys.* 58: 321.
- Weisheit, M., Fähler, S., Marty, A., Souche, Y., Poinson, C. & Givord, D. (2007). *Science* 315: 349.
- Wu, S. M., Cybart, S. A., Yu, P., Rossell, M. D., Zhang, J. X., Ramesh, R. & Dynes, R. C. (2010). *Nature Mater.* 9: 756.
- Xiu, F., Wang, Y., Kim, J., Hong, A., Tang, J., Jacob, A. P., Zou, J. & Wang, K. L. (2010). *Nature Materials* 9: 337.
- Yuasa, S., Nagahama, T., Fukushima, A., Suzuki, Y. & Ando, K. (2004). *Nature Mater.* 3: 868.
- Zhang, S. (1999). *Phys. Rev. Lett.* 83: 640.
- Zheng, H., Straub, F., Zhan, Q., Yang, P.-L., Hsieh, W.-K., Zavaliche, F., Chu, Y.-H., Dahmen, U. & Ramesh, R. (2006). *Adv. Mater.* 18: 2747.
- Zhu, Y. (ed.) (2005). *Modern techniques for characterizing magnetic materials*, Kluwer Academic Publishers, Boston.
- Zubko, P., Gariglio, S., Gabay, M., Ghosez, P. & Triscone, J.-M. (2011). *Ann. Rev. Condens. Matter Phys.* 2: 141.
- Žutić, I., Fabian, J. & Das Sarma, S. (2004). *Rev. Mod. Phys.* 76: 323.

# Effects of Doping and Oxygen Nonstoichiometry on the Thermodynamic Properties of Some Multiferroic Ceramics

Speranta Tanasescu<sup>1</sup>, Alina Botea<sup>1</sup>  
and Adelina Ianculescu<sup>2</sup>

<sup>1</sup>*Department of Chemical Thermodynamics, Institute of Physical Chemistry  
Romanian Academy, Bucharest*

<sup>2</sup>*Polytechnics University of Bucharest, Bucharest  
Romania*

## 1. Introduction

In order to find new ways to tune, enhance and optimize the properties of novel materials designed for different applications, the thorough knowledge of their thermodynamics is essential. The determination of the thermodynamic data and the thermochemical investigation of the formation reactions are essential for evaluating the long term stability and compatibility when the compounds are used in different applications. A careful search for experimental values is very important so much the more the literature is rather scarce as concerns the quantitative thermodynamic data for many multicomponent systems exhibiting balances of competing interactions. The focus of our present work is on multiferroic ceramics, which represents a "complex materials" class presenting a combination of magnetic and electrical properties which make the studies of novel multifunctional structures a very important issue of research.

BiFeO<sub>3</sub> (BFO) of perovskite structure it is well known for its magnetic and ferroelectric ordering temperatures ( $T_N \sim 640$  K,  $T_C \sim 1100$  K) being one of the most attractive single phase multiferroic materials. For this reason there have been extensive studies of the structure, magnetic and electrical properties in bulk and in thin films, as well. Nevertheless, the wide potential for magnetoelectric applications of BFO may be inhibited because some major problems. Besides the small remanent polarization, the high coercive field and the inhomogeneous magnetic spin structure, the large leakage current it is still one of the major problems limiting device applications of BFO. The high conductivity and leakage found especially at higher temperatures were firstly considered caused by the high difficulty to produce single phase of BiFeO<sub>3</sub> (Catalan, 2009; Carvalho, 2008; Mitoseriu, 2005; Yuan, 2006). Very small impurities or parasitic phases segregated at grains at boundaries could have a doping effect and transform the dielectric into a semiconductor. Besides, as in most ferrites, the leakage current in BiFeO<sub>3</sub> could be attributed to the spontaneous change of the oxidation state of Fe (the partially reduction of Fe<sup>3+</sup> ions to Fe<sup>2+</sup>) causing a high number of oxygen vacancies as a result of electrical neutrality requirement, giving rise to thermal activated hopping conductivity and resulting in low

electrical resistivity (Palkar, 2002; Wang, 2004). Impurities and oxygen vacancies are also important for thin films, because they are known to artificially enhance the remanent magnetization (Catalan, 2009).

Forming binary solutions with other perovskites with good dielectric properties (like  $\text{BaTiO}_3$ ,  $\text{PbTiO}_3$  or  $\text{LnFeO}_3$ ) was explored as a possible route for diminish the mentioned problems (Buscaglia, 2006; Ismailzade, 1981; Ianculescu, 2008; Kim, 2004, 2007; Kumar, 1999, 2000; Singh, 2008, 2009; Zhu 2004, Prihor Gheorghiu, 2010; Wang, 2005). The coexistence of ferroelectric and magnetic properties in  $\text{Bi}_{1-x}\text{Ba}_x\text{Fe}_{1-x}\text{Ti}_x\text{O}_3$  materials was noticed up to high temperatures (Kumar, 2000). However, in the  $\text{BiFeO}_3$ -rich region, these ceramics show weak magnetoelectric (ME) coupling effect, the problem of losses being only partially solved (Kumar, 1999).

The substitution of other elements for the Bi- and/or Fe-site was shown to enhance the ferroelectric and magnetic ordering in  $\text{BiFeO}_3$ . Doping with small amounts of rare earths proved to suppress the inhomogeneity of magnetic spin structure, stabilizing macroscopic magnetization of  $\text{BiFeO}_3$  (Ivanova, 2003; Jiang, 2006; Sahu, 2007). Even though there are still questions about the structural evolution with composition (Catalan, 2009), previous studies on La-substituted  $\text{BiFeO}_3$  indicate the decreasing of  $T_C$  and the increasing of  $T_N$  with La concentration (Chen, 2008; Sahu, 2007). On the other hand, substituting with Mn in  $\text{BiFeO}_3$ -based compounds was shown to improve the leakage current density and to induce changes in the magnetic order of the system, especially in the thin films (Azuma, 2007; Singh, 2007; Sahu, 2007; Habouti, 2007, Fukumura, 2009, Takahashi, 2007; Selbach, 2009, Wang, 2010). The simultaneous influence of La and Mn substitutions on the structural and functional properties of  $\text{BiFeO}_3$  was discussed in a few papers (Bogatko, 1998; Ianculescu, 2009, Gagulin, 1997; Habouti, 2007; Kothari, 2007; Palkar, 2003; Pradhan, 2008; Zheng, 2010). Very little work was reported on the thermodynamic behaviour in the co-doped  $(\text{Bi,L a})(\text{Fe,Mn})\text{O}_3$  solid solutions (Gagulin, 1997; Tanasescu, 2010).

Recent investigations using advanced techniques, motivated by the prospect of new applications, have uncovered rich complexities that had not previously been recognized, when the development of new multifunctional bismuth ferrite perovskites, that combine sensitive responses to electric, magnetic, and stress fields, is intended [Ederer, 2005; Ramesh, 2007; Stroppa, 2010]. These phenomena occur at the crossover from localized to itinerant electronic behaviour and from ferroelectric (FE) to antiferromagnetic (AFE) displacive transitions, and are associated with dynamic, cooperative local deformations that are invisible to conventional diffraction studies. Due to the progress in methods for experimental analyzing distribution of elements at interfaces, some information has been accumulated on the chemical stabilities and properties of micro and nanostructured multifunctional materials. However the fundamental understanding was limited to rather simple cases. Such analyses need the thermodynamic data, because the driving forces for chemical reactions and diffusion can be given properly in terms of thermodynamic properties. This constitutes a considerable field of investigation, which is starting to be explored for both basic and applicative purposes (Boyd, 2011; Selbach, 2009; Tanasescu, 2004, 2008).

The present studies are focused upon the investigation of the effect of different compositional variables on the thermochemical properties and thermodynamic stability of multiferroic ceramics. Some compounds from specific systems were selected for discussion: multiferroic lead-free ceramics based on the  $(1-x)\text{BiFeO}_3 - x\text{BaTiO}_3$  ( $0 \leq x \leq 0.30$ ) solid solutions and  $\text{Bi}_{1-x}\text{La}_x\text{Fe}_{1-y}\text{Mn}_y\text{O}_3$  with  $x = 0.1$ ;  $y = 0 - 0.5$  perovskite-type materials.

## 2. Experimental

### 2.1 Sample preparation

$(1-x)\text{BiFeO}_3 - x\text{BaTiO}_3$  ( $0 \leq x \leq 0.30$ ) ceramic samples were prepared by classical solid state reaction method from high purity oxides and carbonates:  $\text{Bi}_2\text{O}_3$  (Fluka),  $\text{Fe}_2\text{O}_3$  (Riedel de Haen),  $\text{TiO}_2$  (Merck) and  $\text{BaCO}_3$  (Fluka), by a wet homogenization technique in isopropyl alcohol. The place of the selected compositions on the  $\text{BiFeO}_3 - \text{BaTiO}_3$  tie line of the quaternary  $\text{Bi}_2\text{O}_3 - \text{BaO} - \text{Fe}_2\text{O}_3 - \text{TiO}_2$  system is also presented in Fig. 1(a).

The mixtures were granulated using a 4 % PVA (polyvinyl alcohol) solution as binder agent, shaped by uniaxial pressing at 160 MPa into pellets of 20 mm diameter and ~3 mm thickness. The presintering thermal treatment was carried out in air, at 923 K, with 2 hours plateau. The samples were slowly cooled, then ground, pressed again into pellets of 10 mm diameter and 1- 2 mm thickness and sintered in air, with a heating rate of 278 K/min, for 1 hour at 973 and 1073 K, respectively (Ianculescu, 2000; Prihor, 2009; Prihor Gheorghiu, 2010).

$\text{Bi}_{0.9}\text{La}_{0.1}\text{Fe}_{1-x}\text{Mn}_x\text{O}_3$  ( $0 \leq x \leq 0.5$ ) ceramics have been prepared by the same route, in the same conditions and starting from the same raw materials (Ianculescu, 2009). The place of the investigated compositions in the quaternary  $\text{Bi}_2\text{O}_3 - \text{La}_2\text{O}_3 - \text{Fe}_2\text{O}_3 - \text{Mn}_2\text{O}_3$  system is presented in Fig. 1(b).

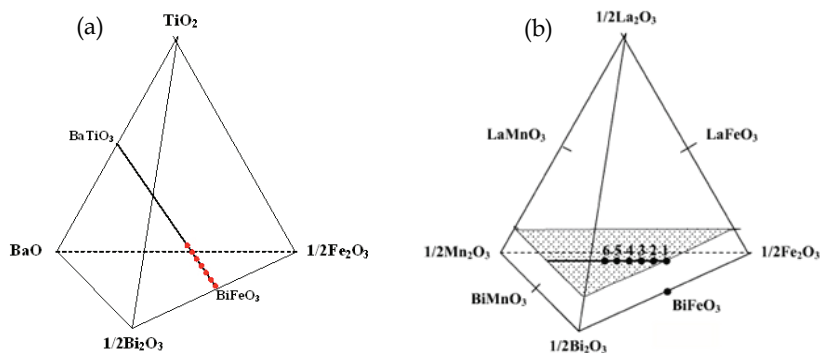


Fig. 1. Place of the investigated compositions: (a)  $\text{Bi}_{1-x}\text{Ba}_x\text{Fe}_{1-x}\text{Ti}_x\text{O}_3$  in the quaternary  $\text{Bi}_2\text{O}_3 - \text{BaO} - \text{Fe}_2\text{O}_3 - \text{TiO}_2$  system; (b)  $\text{Bi}_{0.9}\text{La}_{0.1}\text{Fe}_{1-x}\text{Mn}_x\text{O}_3$  in the quaternary  $\text{Bi}_2\text{O}_3 - \text{La}_2\text{O}_3 - \text{Fe}_2\text{O}_3 - \text{Mn}_2\text{O}_3$  system

### 2.2 Sample characterization

In both  $\text{Bi}_{1-x}\text{Ba}_x\text{Fe}_{1-x}\text{Ti}_x\text{O}_3$  and  $\text{Bi}_{0.9}\text{La}_{0.1}\text{Fe}_{1-x}\text{Mn}_x\text{O}_3$  systems, the phase composition and crystal structure of the ceramics resulted after sintering were checked with a SHIMADZU XRD 6000 diffractometer with Ni-filtered  $\text{CuK}\alpha$  radiation ( $\lambda = 1.5418 \text{ \AA}$ ), 273.02 K scan step and 1 s/step counting time. To estimate the structural characteristics (unit cell parameter and rhombohedral angle) the same step increment but with a counting time of 10 s/step, for  $2\theta$  ranged between 293–393 K was used. Parameters to define the position, magnitude and shape of the individual peaks are obtained using the pattern fitting and profile analysis of the original X-ray 5.0 program. The lattice constants calculation is based on the Least Squares Procedure (LSP) using the linear multiple regressions for several XRD lines, depending on the unit cell symmetry.

A HITACHI S2600N scanning electron microscope SEM coupled with EDX was used to analyze the ceramics microstructure.

The solid-oxide electrolyte galvanic cells method was employed to obtain the thermodynamic properties of the samples. As shown in previous papers (Tanasescu, 1998, 2003, 2009) the thermodynamic stability limits of the  $ABO_{3-\delta}$  perovskite-type oxides are conveniently situated within the range of oxygen chemical potentials that can be measured using galvanic cells containing 12.84 wt.% yttria stabilized zirconia solid electrolyte and an iron-wüstite reference electrode. The design of the apparatus, as well as the theoretical and experimental considerations related to the applied method, was previously described (Tanasescu, 1998, 2011).

The measurements were performed in two principal different ways:

- Under the open circuit conditions, keeping constant all the intensive parameters, when the electromotive force (EMF) measurements give information about the change in the Gibbs free energy for the virtual cell reaction. The EMF measurements were performed in vacuum at a residual gas pressure of  $10^{-7}$  atm. The free energy change of the cell is given by the expression:

$$\Delta G_{\text{cell}} = \mu_{\text{O}_2} - \mu_{\text{O}_{2(\text{ref})}} = 4FE \quad (1)$$

where  $E$  is the steady state EMF of the cell in volts;  $\mu_{\text{O}_2}$ ,  $\mu_{\text{O}_{2(\text{ref})}}$  are respectively, the oxygen chemical potentials of the sample and the reference electrode and  $F$  is the Faraday constant ( $F=96.508$  kJ/V equiv.).

By using the experimental values of the electromotive force of the cell and knowing the free energy change of the reference electrode (Charette, 1968; Kelley 1960, 1961), the values of the relative partial molar free energy of the solution of oxygen in the perovskite phase and hence the pressures of oxygen in equilibrium with the solid can be calculated:

$$\Delta \bar{G}_{\text{O}_2} = RT \ln p_{\text{O}_2} \quad (2)$$

The relative partial molar enthalpies and entropies were obtained according to the known relationships (Tanasescu, 1998, 2011):

$$\frac{\partial \frac{\Delta \bar{G}_{\text{O}_2}}{T}}{\partial T} = -\frac{\Delta \bar{H}_{\text{O}_2}}{T^2} \quad (3)$$

$$\Delta \bar{G}_{\text{O}_2} = \Delta \bar{H}_{\text{O}_2} - T \Delta \bar{S}_{\text{O}_2} \quad (4)$$

The overall uncertainty due to the temperature and potential measurement (taking into account the overall uncertainty of a single measurement and also the quoted accuracy of the voltmeter) was  $\pm 1.5$  mV. This was equivalent to  $\pm 0.579$  kJ mol<sup>-1</sup> for the free energy change of the cell. Considering the uncertainty of  $\pm 0.523$  kJ mol<sup>-1</sup> in the thermodynamic data for the iron-wüstite reference (Charette, 1968; Kelley 1960, 1961), the overall data accuracy was estimated to be  $\pm 1.6$  kJ mol<sup>-1</sup>. For the enthalpies the errors were  $\pm 0.45$  kJ mol<sup>-1</sup> and for the entropies  $\pm 1.1$  J mol<sup>-1</sup> K<sup>-1</sup>. Errors due to the data taken from the literature are not included in these values because of the unavailability of reliable standard deviations.

- By using a coulometric titration technique coupled with EMF measurements (Tanasescu, 2011), method which proved to be especially useful in the study of the compounds with properties highly sensitive to deviations from stoichiometry. The obtained results allow us to evidence the influence of the oxygen stoichiometry change on the thermodynamic properties. The titrations were performed *in situ* at 1073 K by using a Bi-PAD Tacussel Potentiostat. A constant current ( $I$ ) is passed through the cell for a predetermined time ( $t$ ). Because the transference number of the oxygen ions in the electrolyte is unity, the time integral of the current is a precise measure of the change in the oxygen content (Tanasescu, 1998; 2011). According to Faraday's law, the mass change  $|\Delta m|$  (g) of the sample is related to the transferred charge  $Q$  (A sec) by:

$$|\Delta m| = 8.291 \cdot 10^{-5} Q \quad (5)$$

As one can see, a charge of  $1 \cdot 10^{-5}$  A sec, which is easily measurable corresponds to a weight change of only  $8 \times 10^{-10}$  g. This makes it possible to achieve extremely high compositional resolution, and very small stoichiometric widths in both deficient and excess oxygen domains can be investigated. Thus, the effect of the oxygen stoichiometry can be correlated with the influence of the A- and B-site dopants.

After the desired amount of electricity was passed through the cell, the current circuit was opened, every time waiting till the equilibrium values were recorded (about three hours). Practically, we considered that EMF had reached its equilibrium value when three subsequent readings at 30 min intervals varied by less than 0.5 mV. After the sample reached equilibrium, for every newly obtained composition, the temperature was changed under open-circuit condition, and the equilibrium EMFs for different temperatures between 1073 and 1273 K were recorded.

Differential scanning calorimetric measurements were performed with a *SETSYS Evolution Setaram* differential scanning calorimeter (Marinescu, in press; Tanasescu, 2009). For data processing and analyses the Calisto-AKTS software was used. The DSC experiments were done on ceramic samples under the powder form, at a heating rate  $10^\circ\text{C}/\text{min}$ . and by using Ar with purity  $> 99.995\%$  as carrier gas. For measurements and corrections identical conditions were set (Marinescu, in press). The critical temperatures corresponding to the ferro-para phase transitions, the corresponding enthalpies of transformations as well as heat capacities were obtained according to the procedure previously described (Marinescu, in press; Tanasescu, 2009).

### 3. Results and discussion

#### 3.1 BiFeO<sub>3</sub>-BaTiO<sub>3</sub> system

##### 3.1.1 Phase composition and crystalline structure

The room temperature XRD patterns (Fig. 2(a)) show perovskite single-phase, in the limit of XRD accuracy for all the investigated compositions after pre-sintering at 923 K/2 h followed by sintering at 1073 K/1 h and slow cooling. For all investigated ceramics, perovskite structure of rhombohedral R3c symmetry was identified, with a gradual attenuation of the rhombohedral distortion with the increase of BaTiO<sub>3</sub> content. This tendency to a gradual change towards a cubic symmetry with the BaTiO<sub>3</sub> addition is proved by the cancellation of the splitting of the XRD (110), (111), (120), (121), (220), (030) maxima specific to pure BiFeO<sub>3</sub> ( $2\theta \approx 31.5^\circ, 39^\circ, 51^\circ, 57^\circ, 66^\circ, 70^\circ, 75^\circ$ ), as observed in the detailed representation from Fig.

2(b). The evolution of the structural parameters provides an additional evidence for the influence of  $\text{BaTiO}_3$  admixture in suppressing rhombohedral distortion (Fig. 3). Besides, the expansion of the lattice parameters induced by an increasing barium titanate content in  $(1-x)\text{BiFeO}_3 - x\text{BaTiO}_3$  system was also pointed out (Prihor, 2009).

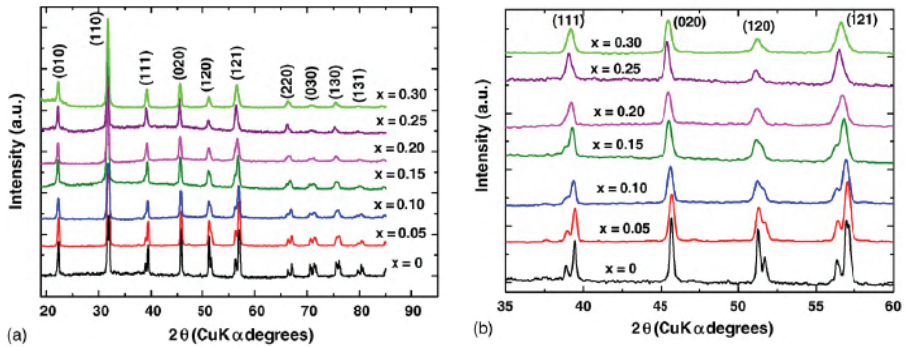


Fig. 2. (a) Room temperature X-ray diffraction patterns of the  $(1-x)\text{BiFeO}_3 - x\text{BaTiO}_3$  ceramics pre-sintered at 923 K/2 h, sintered at 1073 K/1 h and slow cooled; (b) detailed XRD pattern showing the cancellation of splitting for (1 1 1), (1 2 0) and (1 2 1) peaks, when increasing  $x$ .

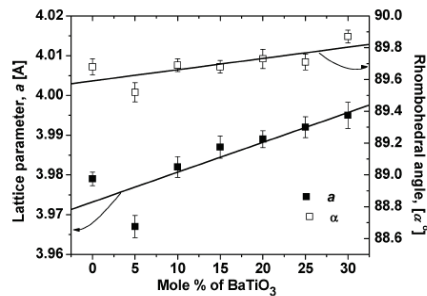


Fig. 3. Evolution of the structural parameters versus  $\text{BaTiO}_3$  content.

### 3.1.2 Microstructure

Surface SEM investigations were performed on both presintered and sintered samples. The SEM image of  $\text{BiFeO}_3$  ceramic obtained after presintering at 923 K shows that the microstructure consists of intergranular pores and of grains of various size (the average grain size was estimated to be  $\sim 20 \mu\text{m}$ ), with not well defined grain boundaries, indicating an incipient sintering stage (Fig. 4(a)). The SEM images of samples with  $x = 0.15$  and  $x = 0.30$  (Figs. 4(b) and 4(c)) indicate that barium titanate addition influences drastically the microstructure. Thus, one can observe that  $\text{BaTiO}_3$  used as additive has an inhibiting effect on the grain growth process and, consequently, a relative homogeneous microstructure, with a higher amount of intergranular porosity and grains of  $\sim$  one order of magnitude smaller than those ones of non-modified sample, were formed in both cases analyzed here.

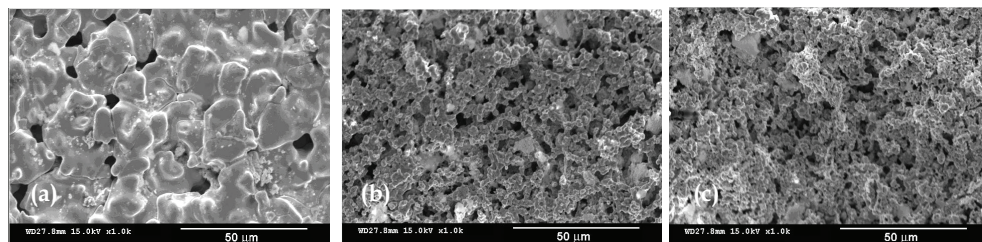


Fig. 4. Surface SEM images of  $(1-x)\text{BiFeO}_3 - x\text{BaTiO}_3$  ceramics obtained after presintering at 923 K/2 hours: (a)  $x = 0$ , (b)  $x = 0.15$  and (c)  $x = 0.30$

$\text{BiFeO}_3$  pellet sintered at 1073 K/1h exhibits a heterogeneous microstructure with bimodal grain size distribution, consisting from large grains with equivalent average size of  $\sim 25 \mu\text{m}$  and small grains of 3 - 4  $\mu\text{m}$  (Fig. 5(a)). The micrograph of the ceramic sample with  $x = 0.15$  (Fig. 5(b)) shows that the dramatic influence of the  $\text{BaTiO}_3$  on the microstructural features is maintained also after sintering. Thus, a significant grain size decrease was observed for sample with  $x = 0.15$ . Further increase of  $\text{BaTiO}_3$  content to  $x = 0.30$  (Fig. 5(c)) seems not to determine a further drop in the average grain size. Consequently, in both cases a rather monomodal grain size distribution and relative homogenous microstructures, consisting of finer (submicron) grains were observed (Ianculescu, 2008; Prihor, 2009). Irrespective of  $\text{BaTiO}_3$  content, the amount of intergranular porosity is significantly reduced in comparison with the samples resulted after only one-step thermal treatment. This indicates that sintering strongly contributes to densification of the  $\text{Bi}_{1-x}\text{Ba}_x\text{Fe}_{1-x}\text{Ti}_x\text{O}_3$  ceramics.

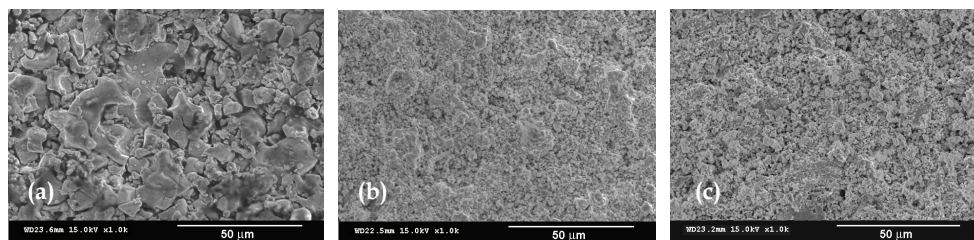


Fig. 5. Surface SEM images of  $(1-x)\text{BiFeO}_3 - x\text{BaTiO}_3$  ceramics obtained after presintering at 923 K/2 hours and sintering at 1073 K/1 hour: (a)  $x = 0$ , (b)  $x = 0.15$  and (c)  $x = 0.30$

### 3.1.3 Thermodynamic properties of $\text{Bi}_{1-x}\text{Ba}_x\text{Fe}_{1-x}\text{Ti}_x\text{O}_3$

Of particular interest for us is to evidence how the appropriate substitutions could influence the stability of the  $\text{Bi}_{1-x}\text{Ba}_x\text{Fe}_{1-x}\text{Ti}_x\text{O}_3$  perovskite phases and then to correlate this effect with the charge compensation mechanism and the change in the oxygen nonstoichiometry of the samples.

In a previous work (Tanasescu, 2009), differential scanning calorimetric experiments were performed in the temperature range of 773-1173 K in order to evidence the ferro-para phase transitions by a non-electrical method. Particular attention is devoted to the high temperature thermodynamic data of these compounds for which the literature is rather scarce. Both the temperature and composition dependences of the specific heat capacity of

the samples were determined and the variation of the Curie temperature with the composition was investigated. The effect of the BaTiO<sub>3</sub> addition to BiFeO<sub>3</sub> was seen as the decrease of the Curie transition temperature and of the corresponding enthalpy of transformation and heat capacity values (Tanasescu, 2009) (Fig. 6). A sharp decline in the  $T_C$  was pointed out for BiFeO<sub>3</sub> rich compositions (Fig. 6). In fact, the  $C_p$  of the rhombohedral phase ( $x = 0$ ) is obviously larger than that of the Bi<sub>1-x</sub>Ba<sub>x</sub>Fe<sub>1-x</sub>Ti<sub>x</sub>O<sub>3</sub> perovskite phases, whereas the  $C_p$  of each phase shows a weak composition dependence below the peak temperature. In particular, the value of  $C_p$  for  $x = 0.3$  was found to be fairly low, which we did not show in the figure. The decreasing of the ferroelectric – paraelectric transition temperature with the increase of the BaTiO<sub>3</sub> amount in the composition of the solid solutions with  $x = 0 \div 0.15$  indicated by the DSC measurements is in agreement with the dielectric data reported by Buscaglia et al (Buscaglia, 2006).

Some reasons for this behaviour could be taken into account. First of all, these results confirm our observations that the solid solution system BiFeO<sub>3</sub> – BaTiO<sub>3</sub> undergoes structural transformations with increasing content of BaTiO<sub>3</sub>. The decrease of the ferroelectric-paraelectric transition temperature  $T_c$  observed for the solid solution (1- $x$ )BiFeO<sub>3</sub> –  $x$ BaTiO<sub>3</sub> may be ascribed to the decrease in unit cell volume caused by the BaTiO<sub>3</sub> addition. Addition of Ba<sup>2+</sup> having empty p orbitals, reduces polarization of core electrons and also the structural distortion. The low value obtained for  $C_p$  at  $x = 0.3$  is in accordance with the previous result indicating that ferroelectricity disappears in samples above  $x \sim 0.3$  (Kumar, 2000).

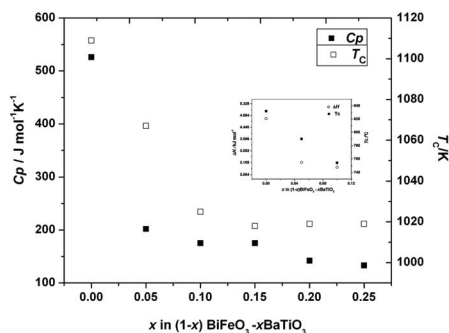


Fig. 6. Variation of the Curie transition temperature  $T_C$  and of the heat capacity  $C_p$  with composition. Inset: Variation of  $T_C$  and enthalpy of transformation for BiFeO<sub>3</sub> rich compositions ( $x=0; 0.05; 0.1$ ) (Tanasescu, 2009)

At the same time, the diffused phase transitions for compositions with  $x > 0.15$  could be explained in terms of a large number of A and B sites occupied by two different, randomly distributed cationic specimens in the perovskite ABO<sub>3</sub> lattice. Previous reports on the substituted lanthanum manganites indicate that the mismatch at the A site creates strain on grain boundaries which affect the physical properties of an ABO<sub>3</sub> perovskite (Maignan, 2000). Besides, the role of charge ordering in explaining the magnetotransport properties of the variable valence transition metals perovskite was emphasized (Jonker, 1953). Investigating the influence of the dopants and of the oxygen nonstoichiometry on spin dynamics and thermodynamic properties of the magnetoresistive perovskites, Tanasescu et

al (Tanasescu, 2008, 2009) pointed out that the remarkable behaviour of the substituted samples could be explained not only qualitatively by the structural changes upon doping, but also by the fact that the magneto-transport properties are extremely sensitive to the chemical defects in oxygen sites.

Though the effects of significant changes in the overall concentration of defects is not fully known in the present system of materials, extension of the results obtained on substituted manganites, may give some way for the correlation of the electrical, magnetic and thermodynamic properties with the defect structure. The partial replacement of  $\text{Bi}^{3+}$  with  $\text{Ba}^{2+}$  cations acting as acceptor centers could generate supplementary oxygen vacancies as compensating defects, whereas the  $\text{Ti}^{4+}$  solute on  $\text{Fe}^{3+}$  sites could induce cationic vacancies or polaronic defects by  $\text{Fe}^{3+} \rightarrow \text{Fe}^{2+}$  transitions. The presence of the defects and the change of the  $\text{Fe}^{2+}/\text{Fe}^{3+}$  ratio is in turn a function not only of the composition but equally importantly of the thermal history of the phase. Consequently, an understanding of the high temperature defect chemistry of phases is vital, if an understanding of the low temperature electronic and magnetic properties is to be achieved. To further evaluate these considerations, and in order to discriminate against the above contributions, experimental insight into the effects of defect types and concentrations on phase transitions and thermodynamic data could give a valuable help.

For discussion was chosen the compound  $\text{Bi}_{0.90}\text{Ba}_{0.10}\text{Fe}_{0.90}\text{Ti}_{0.10}\text{O}_3$  for which strong magnetoelectric coupling of intrinsic multiferroic origin was reported (Singh, 2008). The results obtained in the present study by using EMF and solid state coulometric titration techniques are shown in the following.

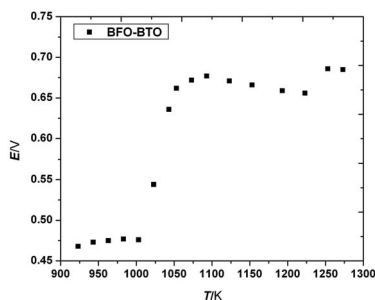


Fig. 7. Temperature dependence of EMF for  $\text{Bi}_{0.90}\text{Ba}_{0.10}\text{Fe}_{0.90}\text{Ti}_{0.10}\text{O}_3$

The recorded EMF values obtained under the open circuit condition in the temperature range 923-1273 K are presented in Fig. 7. The thermodynamic data represented by the relative partial molar free energies, enthalpies and entropies of the oxygen dissolution in the perovskite phase, as well as the equilibrium partial pressures of oxygen have been calculated and the results are depicted in Figs. 8-11. A complex behavior which is dependent on the temperature range it was noticed, suggesting a change of the predominant defects concentration for the substituted compound.

As one can see in Fig. 7, at low temperatures, between 923 and  $\sim 1000$  K, EMF has practically the same value  $E=0.475$  V. Then, Fig. 7 distinctly shows a break in the EMF vs. temperature relation at about 1003 K, indicating a sudden change in the thermodynamic parameters. A strong increase of the partial molar free energy and of the partial pressure of oxygen was

observed until 1050 K (Figs. 8 and 9) which can be due to structural transformation related to the charge compensation of the material system. Then, on a temperature interval of about 40 K the increasing of the energies values is smaller. After  $\sim 1090$  K a new change of the slope in the  $\Delta\overline{G}_{O_2}$  and  $\log p_{O_2}$  variation is registered on a temperature interval of about 130 degrees, followed again, after 1223 K, by a sudden change of the thermodynamic data, the higher  $\Delta\overline{G}_{O_2}$  value being obtained at about 1260 K.

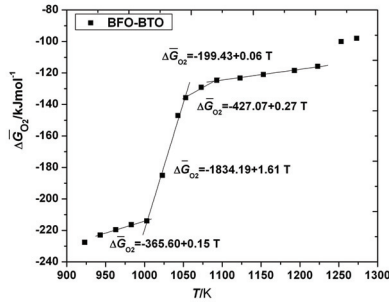


Fig. 8. Variation of  $\Delta\overline{G}_{O_2}$  with temperature - linear fit in the selected temperature ranges: 943-1003 K, 1003-1053 K, 1053-1093 K and 1093-1223 K

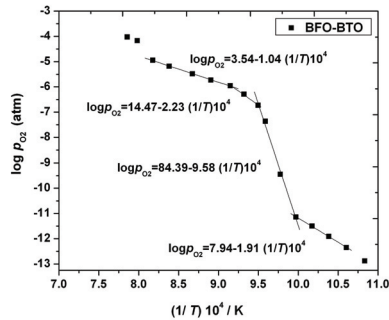


Fig. 9. The plot of  $\log p_{O_2}$  vs.  $1/T$  for the selected temperatures ranges

The break point at about 1003 K is mainly due to first order phase transition in  $\text{Bi}_{0.90}\text{Ba}_{0.10}\text{Fe}_{0.90}\text{Ti}_{0.10}\text{O}_3$  associated with the ferroelectric to the paraelectric transition  $T_C$ . The 10%  $\text{BaTiO}_3$  substitution reduces the ferroelectric transition temperature of  $\text{BiFeO}_3$  with about 100K. This transition is also evident from calorimetric measurements (Tanasescu, 2009). The less abrupt first order transition at 1050 K is qualitatively in concordance with the transition to the  $\gamma$  polymorph which was previously identified in the literature for  $\text{BiFeO}_3$  at 1198-1203K (Arnold, 2010; Palai, 2008; Selbach, 2009).

In Fig. 10 we represented the partial molar free energies of oxygen dissolution obtained in this study for both  $\text{Bi}_{0.90}\text{Ba}_{0.10}\text{Fe}_{0.90}\text{Ti}_{0.10}\text{O}_3$  and  $\text{BiFeO}_3$  at temperatures lower than their specific ferroelectric transition temperatures. We would like to specify that in the case of  $\text{BiFeO}_3$ , the EMF measurements were performed at temperatures not higher than 1073 K due

to the instability of  $\text{BiFeO}_3$  at higher temperatures. As one can see in Fig. 10, at 923 K, the partial molar free energies of oxygen dissolution in  $\text{BiFeO}_3$  and  $\text{Bi}_{0.90}\text{Ba}_{0.10}\text{Fe}_{0.90}\text{Ti}_{0.10}\text{O}_3$  samples are near each other. With increasing temperature, the highest  $\Delta\bar{G}_{\text{O}_2}$  values were obtained for  $\text{BiFeO}_3$ , suggesting an increased oxygen vacancies concentration in this compound. The result could be explained by the fact that at low temperatures the conduction is purely intrinsic and the anionic vacancies created are masked by impurity conduction. As the temperature increases, conduction becomes more extrinsic (Warren, 1996), and conduction due to the oxygen vacancies surface. This fact is also evident from the density measurements (Kumar, 2000), as well as electron paramagnetic resonance studies on perovskites (Warren, 2006). The increased concentration of oxygen vacancies in  $\text{BiFeO}_3$  is consistent with the large leakage current reported for  $\text{BiFeO}_3$  (Gu, 2010; Qi, 2005; Palkar, 2002; Wang, 2004). The electrical characteristics (Qi, 2005) indicated that the main conduction mechanism for pure BFO was space charge limited, and associated with free carriers trapped by oxygen vacancies. The coexistence of  $\text{Fe}^{3+}$  and  $\text{Fe}^{2+}$  causes electron hopping between  $\text{Fe}^{3+}$  and  $\text{Fe}^{2+}$  ions, oxygen vacancies acting as a bridge between them, which increases the leakage current. According to the defect chemistry theory, doping  $\text{BiFeO}_3$  with aliovalent ions should change the oxidation state of iron and the concentration of oxygen vacancies. Qi and coworkers (Qi, 2005) have suggested as possible mechanisms to achieve the charge compensation in the 4+ cation-doped material: filling of oxygen vacancies, decrease of cation valence by formation of  $\text{Fe}^{2+}$ , and creation of cation vacancies. Based on our results, the doping with  $\text{Ti}^{4+}$  is expected to eliminate oxygen vacancies causing the decreasing of  $\Delta\bar{G}_{\text{O}_2}$  and  $\log p_{\text{O}_2}$  values.

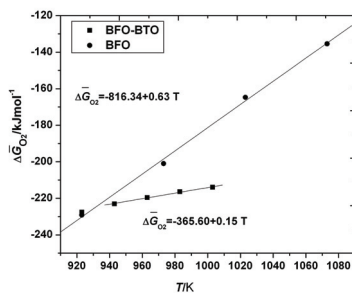


Fig. 10. Variation of  $\Delta\bar{G}_{\text{O}_2}$  with temperature - linear fit in the temperature range 943-1003 K for  $\text{Bi}_{0.90}\text{Ba}_{0.10}\text{Fe}_{0.90}\text{Ti}_{0.10}\text{O}_3$  (BFO-BTO) and 923-1073 K for  $\text{BiFeO}_3$  (BFO)

Further clarification could be achieved by determining  $\Delta\bar{H}_{\text{O}_2}$  and  $\Delta\bar{S}_{\text{O}_2}$  values in particular temperature ranges in which the partial molar free energies are linear functions of temperature. Comparing the values obtained for  $\text{Bi}_{0.90}\text{Ba}_{0.10}\text{Fe}_{0.90}\text{Ti}_{0.10}\text{O}_3$  in the temperature interval of 943-1003 K with the corresponding enthalpies and entropies values of  $\text{BiFeO}_3$  in the 923-1073 K range (Fig. 11) one can observe that for the substituted compound,  $\Delta\bar{H}_{\text{O}_2}$  and  $\Delta\bar{S}_{\text{O}_2}$  values strongly increase (with  $\sim 450 \text{ kJ mol}^{-1}$  and  $\sim 480 \text{ J mol}^{-1} \text{ K}^{-1}$  respectively). This finding can be explained by the relative redox stability of the B-site ions which seems to modify both the mobility and the concentration of the oxygen vacancies. It is interesting to note that increasing temperature, after the first transition point, the enthalpies and entropies values strongly decrease (with  $\sim 468 \text{ kJ mol}^{-1}$  and  $\sim 1.4 \text{ kJ mol}^{-1} \text{ K}^{-1}$  respectively) up to more

negative values. The negative values obtained for the relative partial entropies of oxygen dissolution at high temperature are indicative for a metal vacancy mechanism. Above 1053 K both the enthalpy and entropy increase again with increasing the temperature. The thermal reduction for transition metals tends to be easier with Ba doping. These may explain the reason for the different behaviors at higher temperature zone. Besides, oxygen vacancy order also show contribution to the observed phenomena, the increasing of the enthalpy and entropy values being an indication that the oxygen vacancies distribute randomly on the oxygen sublattice.

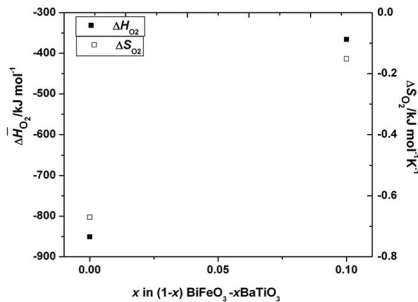


Fig. 11.  $\Delta\bar{H}_{O_2}$  and  $\Delta\bar{S}_{O_2}$  as a function of  $BaTiO_3$  content ( $x$ ) at temperatures lower than ferroelectric transition temperatures.

In order to further evaluate the previous results, the influence of the oxygen stoichiometry change on the thermodynamic properties has to be examined. The variation of the thermodynamic data of oxygen deficient  $Bi_{0.90}Ba_{0.10}Fe_{0.90}Ti_{0.10}O_{3-\delta}$  samples was analyzed at the relative stoichiometry change  $\Delta\delta = 0.01$ . In Figures 12 (a) and (b), two sets of data obtained before and after the isothermal titration experiments are plotted. Higher  $\Delta\bar{G}_{O_2}$  and  $\log p_{O_2}$  values are obtained after titration at all temperatures until 1223 K; above 1223 K, the values after titration are lower than the corresponding values before titration.

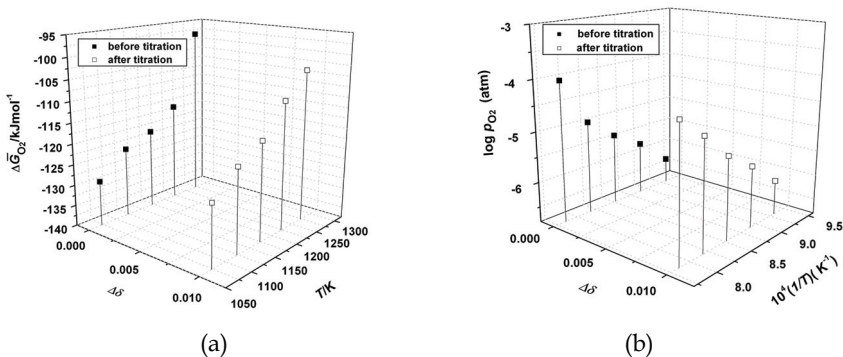


Fig. 12. Variation of (a)  $\Delta\bar{G}_{O_2}$  and (b)  $\log p_{O_2}$  with temperature and oxygen stoichiometry change for  $Bi_{0.90}Ba_{0.10}Fe_{0.90}Ti_{0.10}O_3$

Regarding the changes of  $\Delta\bar{H}_{O_2}$  and  $\Delta\bar{S}_{O_2}$  corresponding to the temperature range of 1093–1223 K (Fig. 13), one can observe that for  $\text{Bi}_{0.90}\text{Ba}_{0.10}\text{Fe}_{0.90}\text{Ti}_{0.10}\text{O}_3$ , both the variations of enthalpy and entropy decrease with the stoichiometry change suggesting the increase in the binding energy of oxygen and the change of order in the oxygen sublattice of the perovskite-type structure. The values of the relative partial entropies of oxygen dissolution are negative and this is indicative for a metal vacancy mechanism (Töfeld, 1974). Due to the large decrease in  $\Delta\bar{S}_{O_2}$ , it is considered that the oxygen vacancies would not randomly distribute on all of the oxygen sites but they would be distributed to some particular oxygen sites. It is also possible that the vacancy distribution is related to some crystallographic distortions or ordering of metal sites.

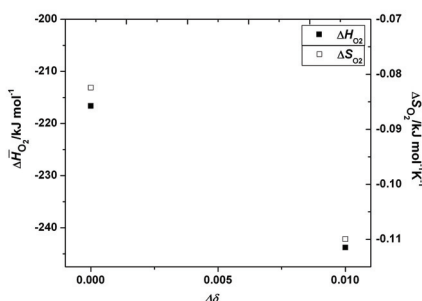


Fig. 13.  $\Delta\bar{H}_{O_2}$  and  $\Delta\bar{S}_{O_2}$  as a function of the oxygen stoichiometry change ( $\Delta\delta = 0.01$ )

Presently, however, further details and measurements of the energy and entropy of oxygen incorporation into  $\text{BiFeO}_3$ -based materials at different values of nonstoichiometry  $\delta$  are necessary in order to make clear the vacancy distribution with the stoichiometry change.

### 3.2 $\text{Bi}_{1-x}\text{La}_x\text{Fe}_{1-y}\text{Mn}_y\text{O}_3$ ( $x=0.1$ ; $y=0-0.5$ )

#### 3.2.1 Phase composition and crystalline structure

The room temperature X-ray diffraction pattern obtained for the presintered sample corresponding to the mixture 1 ( $\text{Bi}_{0.9}\text{La}_{0.1}\text{FeO}_3$ ) shows a single phase composition, consisting of the well-crystallized perovskite phase (Fig. 14(a)). A small Mn addition ( $x \leq 0.1$ ) does not change the phase composition. The increase of the manganese amount to  $x = 0.2$  determines the segregation of a small amount of  $\text{Bi}_{36}\text{Fe}_2\text{O}_{57}$  secondary phase identified at the detection limit. For  $x \geq 0.4$  also small quantities of  $\text{Bi}_2\text{Fe}_4\text{O}_9$  was detected as secondary phase, indicating the beginning of a decomposition process (Fig 14(a)).

From the structural point of view the XRD data pointed out that all the samples exhibit hexagonal  $R3c$  symmetry, similar to the structure of the paternal non-modified  $\text{BiFeO}_3$  compound. Similar to  $\text{Bi}_{1-x}\text{Ba}_x\text{Fe}_{1-x}\text{Ti}_x\text{O}_3$  solid solutions, the increase of the manganese content does not determine the change of spatial group. However, certain distortions clearly emphasized by the cancellation of the splitting of some characteristic XRD peaks take place. Thus, Fig. 14(b) shows the evolution of the profile and position of the neighbouring (006) and (202) peaks specific to the  $\text{Bi}_{0.9}\text{La}_{0.1}\text{O}_3$  composition when Mn is added in the system. One can observe that an amount of only 10% Mn replacing  $\text{Fe}^{3+}$  in the perovskite structure is enough to eliminate the (006) peak in the characteristic XRD pattern. A shift of the position

of the main diffraction peaks toward higher  $2\theta$  values was also pointed out (for example the (002) peak shifts from  $2\theta = 39.5^\circ$  for  $\text{Bi}_{0.9}\text{La}_{0.1}\text{FeO}_3$  to  $2\theta = 39.82^\circ$  for  $\text{Bi}_{0.9}\text{La}_{0.1}\text{Fe}_{0.5}\text{Mn}_{0.5}\text{O}_3$ ). The increase of the manganese concentration determines the decrease of both  $a$  and  $c$  lattice parameters (Fig. 15(a)) and therefore a gradual contraction of the unit cell volume (Fig. 15(b)). This evolution suggests that most of the manganese ions are more probably incorporated on the  $B$  site of the perovskite network as  $\text{Mn}^{4+}$ , causing the decrease of the network parameters because of the smaller ionic radius of  $\text{Mn}^{4+}$  (0.60 Å), comparing with that one corresponding to  $\text{Fe}^{3+}$  (0.64 Å). These results are in agreement with those ones reported by Palkar et al (Palkar, 2003).

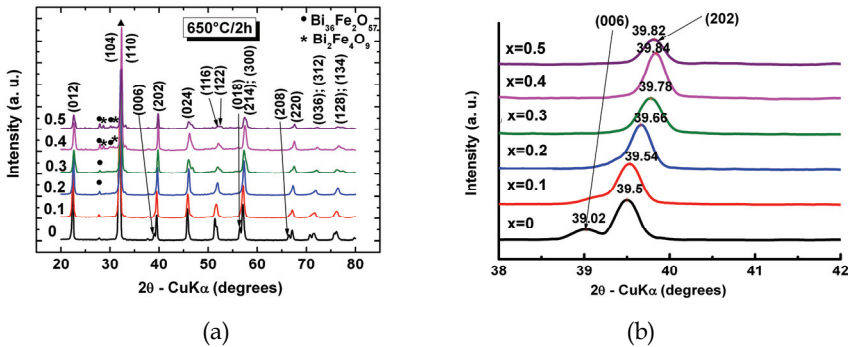


Fig. 14. (a) Room temperature X-ray diffraction patterns for  $\text{Bi}_{0.9}\text{La}_{0.1}\text{Fe}_{1-x}\text{Mn}_x\text{O}_3$  ceramics thermally treated at 923 K for 2 hours; (b) detailed XRD pattern showing the disappearance of (0 0 6) peak

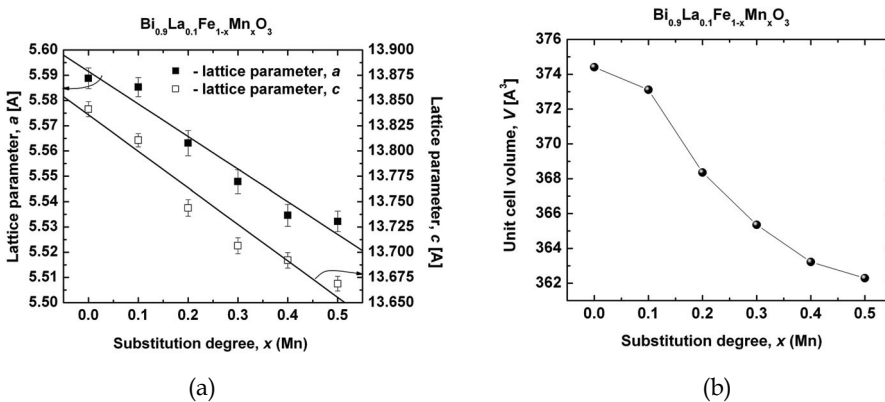


Fig. 15. Evolution of the structural parameters versus Mn content for the  $\text{Bi}_{0.9}\text{La}_{0.1}\text{Fe}_{1-x}\text{Mn}_x\text{O}_3$  ceramics sintered at 1073 K for 1 hour: (a) lattice parameters and (b) unit cell volume

### 3.2.2 Microstructure

As for  $\text{Bi}_{1-x}\text{Ba}_x\text{Fe}_{1-x}\text{Ti}_x\text{O}_3$  ceramics, SEM analyses were performed firstly on the pellets surface thermally treated at 923 K/2h. The surface SEM image of the  $\text{Bi}_{0.9}\text{La}_{0.1}\text{FeO}_3$  sample

indicates the obtaining of a non-uniform and porous microstructure, consisting from grains of variable sizes and a significant amount of intergranular porosity (fig. 16(a)). For the sample with  $x = 0.20$ , the presence of the manganese in the system induces the inhibition of the grain growth process and has a favourable effect on the densification (Fig. 16(b)).

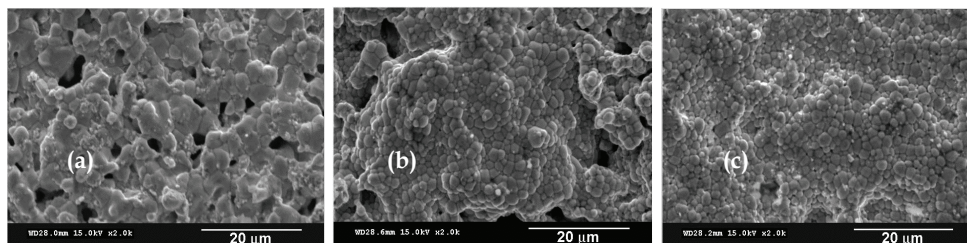


Fig. 16. Surface SEM images of: (a)  $\text{Bi}_{0.9}\text{La}_{0.1}\text{FeO}_3$ ; (b)  $\text{Bi}_{0.9}\text{La}_{0.1}\text{Fe}_{0.8}\text{Mn}_{0.2}\text{O}_3$  and (c)  $\text{Bi}_{0.9}\text{La}_{0.1}\text{Fe}_{0.5}\text{Mn}_{0.5}\text{O}_3$  presintered at 925 K for 2 hours

The further increase of the Mn content to  $x = 0.50$  enhances the densification, but seems to have not anymore a significant influence on the average grain size. Thus, the  $\text{Bi}_{0.9}\text{La}_{0.1}\text{Fe}_{0.5}\text{Mn}_{0.5}\text{O}_3$  ceramic shows a dense, fine-grained (average grain size of  $\sim 2 \mu\text{m}$ ) and homogeneous microstructure with a monomodal grain size distribution (Fig. 16(c)).

The same trend of the decrease of the average grain size with the addition of both La and Mn solutes was also observed in the case of the ceramics sintered at 1073 K for 1 hour. Thereby, unlike the non-homogeneous, rather coarse-grained  $\text{BiFeO}_3$  sample (Fig. 5(a)), the average grain size in the La-modified  $\text{Bi}_{0.9}\text{La}_{0.1}\text{FeO}_3$  ceramic is of only  $\sim 4 \mu\text{m}$  (Fig. 17(a)). The increase of Mn addition causes a further decrease of the average grain size to  $\sim 2 \mu\text{m}$  and a tendency to coalescence of the small grains in larger, well-sintered blocks (Fig. 17(b) and 17(c)).

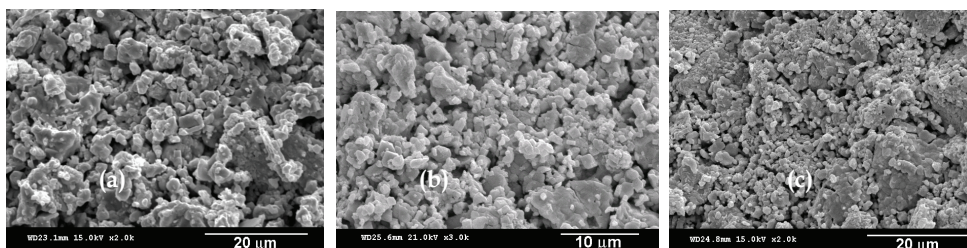


Fig. 17. Surface SEM images of: (a)  $\text{Bi}_{0.9}\text{La}_{0.1}\text{FeO}_3$ ; (b)  $\text{Bi}_{0.9}\text{La}_{0.1}\text{Fe}_{0.8}\text{Mn}_{0.2}\text{O}_3$  and (c)  $\text{Bi}_{0.9}\text{La}_{0.1}\text{Fe}_{0.5}\text{Mn}_{0.5}\text{O}_3$  ceramics sintered at 1073 K for 1 hour.

### 3.3.3 Thermodynamic properties of $\text{Bi}_{1-x}\text{La}_x\text{Fe}_{1-y}\text{Mn}_y\text{O}_3$ ( $x=0.1$ ; $y=0.2$ ; $0.3$ )

Emphasizing the role of charge ordering in explaining the magnetotransport properties of the manganites, Jonker and van Santen considered that the local charge in the doped manganites is balanced by the conversion of Mn valence between  $\text{Mn}^{3+}$  and  $\text{Mn}^{4+}$  and the creation of oxygen vacancies, as well (Jonker, 1953). Investigating the influence of the dopants and of the nonstoichiometry on spin dynamics and thermodynamic properties of

the magnetoresistive perovskites, Tanasescu et al (Tanasescu, 2008, 2009) demonstrated that the formation of oxygen vacancies and the change of the  $Mn^{3+}/Mn^{4+}$  ratio on the B-site play important roles to explain structural, magnetic and energetic properties of the substituted perovskite.

In  $BiFeO_3$ - $BiMnO_3$  system was already pointed out that, even though the Mn substitution does not alter the space group of  $BiFeO_3$  for  $x \leq 0.3$ , the possible variation of the valence state of Mn manganese together the oxygen hiperstoichiometry as a function of temperature and oxygen pressure could affect the crystallographic properties, electrical conductivity and phase stability of  $BiFe_{1-x}Mn_xO_{3+\delta}$  (Selbach, 2009, 2009). Excepting the communicated results on DSC investigation of  $Bi_{1-x}La_xFe_{1-y}Mn_yO_3$  ( $x=0.1$ ;  $y=0-0.5$ ) (Tanasescu, 2010), no other work related to the thermodynamic behaviour of  $Bi_{1-x}La_xFe_{1-y}Mn_yO_3$  were reported in the literature. In that study the evolution of heat of transformation and heat capacity in the temperature range of 573 – 1173 K was analyzed. The ferroelectric transition was shifted to a lower temperature for  $Bi_{0.9}La_{0.1}FeO_3$  comparative to  $BiFeO_3$ , in agreement with literature data (Chen, 2008). However, a non-monotonous change of  $T_C$ , as well as of the thermochemical parameters is registered for the La and Mn co-doped compositions, depending on the Mn concentration, comparatively with undoped  $BiFeO_3$ . A sharp decline in the  $T_c$  was pointed out for  $x=0.3$ . One reason to explain this behavior is sustained by the structural results which were already pointed out in the previous section. The increase of the manganese concentration determines the decrease of both  $a$  and  $c$  lattice parameters and therefore a gradual contraction of the unit cell volume. This evolution suggests that most of the manganese ions are more probably incorporated on the B-site as  $Mn^{4+}$ . Besides, as already was shown, in our samples the decreasing of the average grain size with the addition of both La and Mn solutes was observed in the case of presintered, as well as ceramics sintered at 1273 K (Ianculescu, 2009; Tanasescu, 2010). For finer particles where defect formation energies are likely to be reduced, the lattice defects, oxygen nonstoichiometry etc. appear to be sizable and significant changes in overall defect concentration are expected. So, an excess of  $Mn^{4+}$  ions and an increased oxygen nonstoichiometry are more likely. Due to the linear relationship between the Mn-O distortion and the  $Mn^{3+}$  content, one could expect to find in our samples a strong dependence of the energetic parameters on the  $Mn^{3+}/Mn^{4+}$  ratio and the oxygen nonstoichiometry.

In order to understand how the thermodynamic properties are related to the oxygen and manganese content in the substituted  $BiFeO_3$ , the thermodynamic properties represented by the relative partial molar free energies, enthalpies and entropies of oxygen dissolution in the perovskite phase, as well as the equilibrium partial pressures of oxygen have been obtained in a large temperature range (923-1123 K) by using solid electrolyte electrochemical cells method.

The obtained results are plotted in Figures 18 - 20. At low temperatures, between 923 and  $\sim 950$  K for  $x=0.3$  and between 923 and  $\sim 1000$  K for  $x=0.2$ , the  $\Delta\bar{G}_{O_2}$  values are increasing with temperature (Fig. 18(a)). The same trend is accounted for the  $\log p_{O_2}$  variation (Fig. 18(b)). The break points at  $\sim 963$  K and  $\sim 993$  K obtained for  $x=0.3$  and  $x=0.2$ , respectively (Fig. 18 (a)) are consistent with the  $T_c$  values of ferro-para transition in substituted samples. These values are near the ferroelectric Curie temperatures reported in the literature for  $BiFe_{0.7}Mn_{0.3}O_3$  (926-957 K) and  $BiFe_{0.8}Mn_{0.2}O_3$  ( $\sim 990$  K) with no La addition (Selbach, 2009; Sahu, 2007). However we have to notice that at the same Mn concentration  $x=0.3$ , the  $T_c$

value is slightly higher for the sample in which lanthanum is present, comparatively with the sample without La.

In Fig. 19 we represented the partial molar free energies of oxygen dissolution obtained in this study for  $\text{Bi}_{0.9}\text{La}_{0.1}\text{Fe}_{0.8}\text{Mn}_{0.2}\text{O}_3$  and  $\text{Bi}_{0.9}\text{La}_{0.1}\text{Fe}_{0.7}\text{Mn}_{0.3}\text{O}_3$  samples at temperatures lower than their specific ferroelectric transition temperatures, and for comparison, the  $\Delta\bar{G}_{\text{O}_2}$  values of  $\text{BiFeO}_3$ . As one can see in Fig. 19, the partial molar free energies of oxygen dissolution in the substituted samples are highest than the  $\Delta\bar{G}_{\text{O}_2}$  values obtained for  $\text{BiFeO}_3$ , suggesting the increasing oxygen vacancies concentration with doping. Determining the  $\Delta\bar{H}_{\text{O}_2}$  and  $\Delta\bar{S}_{\text{O}_2}$  values in particular temperature ranges until  $T_C$  in which the partial molar free energies are linear functions of temperature (Figs. 19 and 20) one can observe that for the substituted compounds, the  $\Delta\bar{H}_{\text{O}_2}$  and  $\Delta\bar{S}_{\text{O}_2}$  values strongly increase in the doped compounds. Due to the relative redox stability of the  $\text{B}^{3+}$  ions (at the same A-site composition), both the mobility and the concentration of the oxygen vacancies will be modified. However it was noticed that the increase in B-site substitution from  $x = 0.20$  to  $x = 0.30$  at temperatures below 1000 K is followed by the decrease of  $\Delta\bar{H}_{\text{O}_2}$  and  $\Delta\bar{S}_{\text{O}_2}$  values with  $\sim 117.6 \text{ kJ mol}^{-1}$  and  $\sim 126 \text{ J mol}^{-1} \text{ K}^{-1}$  respectively (Fig. 20), suggesting the increase of the binding energy of oxygen and an increase of order in the oxygen sublattice of the perovskite-type structure with the Mn concentration.

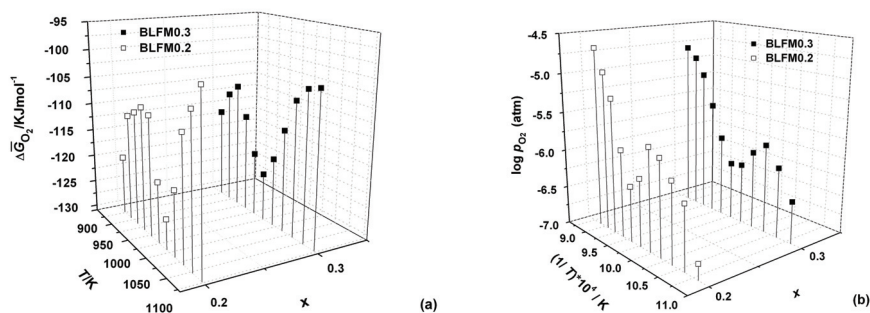


Fig. 18. Variation of  $\Delta\bar{G}_{\text{O}_2}$  (a) and  $\log p_{\text{O}_2}$  (b) with temperature and Mn content ( $x$ )

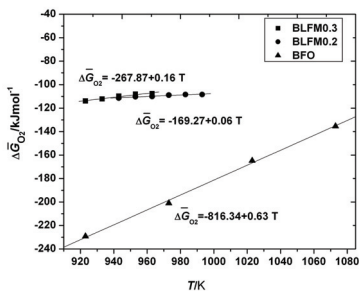


Fig. 19. Variation of  $\Delta\bar{G}_{\text{O}_2}$  with temperature - linear fit in the temperature ranges under the ferroelectric transition temperatures

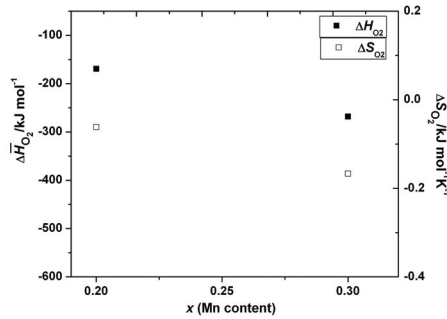


Fig. 20.  $\Delta \bar{H}_{O_2}$  and  $\Delta \bar{S}_{O_2}$  as a function of Mn content ( $x$ ) at temperatures lower than  $T_C$

After the ferroelectric transition temperatures and until 1043 K (for  $x=0.2$ ), respectively until 1023 K (for  $x=0.3$ ), a sharp decrease of the  $\Delta \bar{G}_{O_2}$  values (Fig. 18(a)), together positive values of the enthalpies and entropies are revealed for both samples, indicating the decreasing of the thermodynamic driving force for oxygen vacancies formation and low ionic mobility. Taking into account the working conditions and the existing information as concerns the phase correlations of systems (Selbach, 2009, 2009, Carvalho, 2008), the dissociation reaction of the perovskite could be assumed to proceed in this temperature interval,  $\text{Bi}_{0.9}\text{La}_{0.1}\text{Fe}_{1-x}\text{Mn}_x\text{O}_3$  being in equilibrium with other two solid phases, namely sillenite and mullite type-phases ( $\text{Bi}_{25}\text{Fe}_{1-y}\text{Mn}_y\text{O}_{39}$  and  $\text{Bi}_2\text{Fe}_{4-z}\text{Mn}_z\text{O}_9$ , respectively). Increasing the temperature until 1083 K (for  $x=0.2$ ) and 1073 K (for  $x=0.3$ ), the equilibrium will be driven back to the perovskite formation, the  $\Delta \bar{G}_{O_2}$  values of the sample with  $x=0.3$  keeping higher than those of the sample with  $x=0.2$  (Fig. 18(a)). At 1083 K (for  $x=0.2$ ) and 1073 K (for  $x=0.3$ ), the registered  $\Delta \bar{G}_{O_2}$  values have practically the same values as for the samples before decomposition. The next phase transition registered at 1093 K for  $\text{Bi}_{0.9}\text{La}_{0.1}\text{Fe}_{0.7}\text{Mn}_{0.3}\text{O}_3$  is qualitatively in concordance with the transition to the  $\gamma$  polymorph which was previously identified in the literature for  $\text{BiFeO}_3$  at 1198-1203K (Arnold, 2010; Palai, 2008; Selbach, 2009) and for  $\text{BiFe}_{0.7}\text{Mn}_{0.3}\text{O}_3$  at 1145-1169 (Selbach, 2009). The temperature of transition to the  $\gamma$  phase corresponding to  $\text{Bi}_{0.9}\text{La}_{0.1}\text{Fe}_{0.8}\text{Mn}_{0.2}\text{O}_3$  could be higher than 1123 K; it was not registered in our present experiment because the highest temperature of these measurements was 1123 K.

The obtained results evidenced the complex behavior of the partial molar thermodynamic data in substituted samples, suggesting a change of the predominant defects concentration as a function of temperature range and Mn concentration. Increasing the manganese content, the decreasing of the ferroelectric Curie temperature and of the transition temperature from paraelectric to  $\gamma$  phase it is noted.

To further evaluate the previous results, the influence of the oxygen stoichiometry change on the thermodynamic properties has been investigated. The variation of the partial molar thermodynamic data of  $\text{Bi}_{0.9}\text{La}_{0.1}\text{Fe}_{0.8}\text{Mn}_{0.2}\text{O}_3$  (noted as BLFM0.2) and  $\text{Bi}_{0.9}\text{La}_{0.1}\text{Fe}_{0.7}\text{Mn}_{0.3}\text{O}_3$  (noted as BLFM0.3) was examined before and after two successive titrations by the same relative oxygen stoichiometry change of  $\Delta\delta = 0.02$  in the oxygen excess region (Figures 21 and 22). Thus, the effect of the oxygen stoichiometry can be correlated with the influence of the substituent.

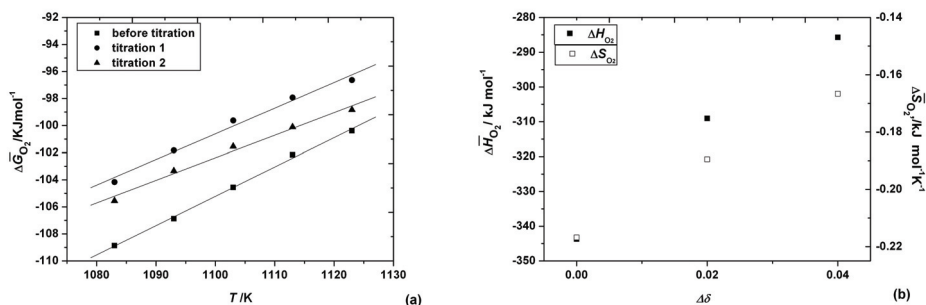


Fig. 21. (a) Variation of  $\Delta \bar{G}_{O_2}$  with temperature and oxygen stoichiometry change for  $\text{Bi}_{0.9}\text{La}_{0.1}\text{Fe}_{0.8}\text{Mn}_{0.2}\text{O}_{3+\delta}$  (b)  $\Delta \bar{H}_{O_2}$  and  $\Delta \bar{S}_{O_2}$  of  $\text{Bi}_{0.9}\text{La}_{0.1}\text{Fe}_{0.8}\text{Mn}_{0.2}\text{O}_{3+\delta}$  as a function of the oxygen stoichiometry change ( $\Delta \delta = 0; 0.02; 0.04$ )

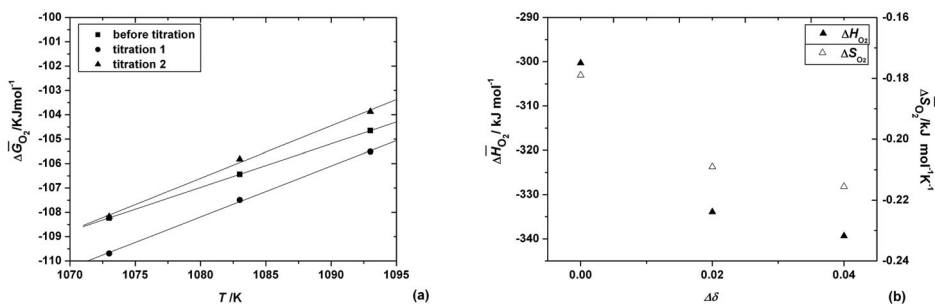


Fig. 22. (a) Variation of  $\Delta \bar{G}_{O_2}$  with temperature and oxygen stoichiometry change for  $\text{Bi}_{0.9}\text{La}_{0.1}\text{Fe}_{0.7}\text{Mn}_{0.3}\text{O}_{3+\delta}$  (b)  $\Delta \bar{H}_{O_2}$  and  $\Delta \bar{S}_{O_2}$  of  $\text{Bi}_{0.9}\text{La}_{0.1}\text{Fe}_{0.7}\text{Mn}_{0.3}\text{O}_{3+\delta}$  as a function of the oxygen stoichiometry change ( $\Delta \delta = 0; 0.02; 0.04$ )

For  $x=0.2$  higher values of the partial molar thermodynamic data are obtained after titration (Fig. 21). It is expected that the change in  $\Delta \bar{S}_{O_2}$  with  $\delta$  in this case to be essentially determined by the change in  $S_O$  (config) and, therefore, the oxygen randomly distribute on the oxygen sites. Instead for  $x=0.3$ , both the variations of enthalpy and entropy decrease with the stoichiometry change (Fig. 22(b)), suggesting the increase in the binding energy of oxygen and change of order in the oxygen sublattice of the perovskite-type structure comparatively with the undoped compound. However it is interesting to note that the enthalpies obtained for  $x=0.3$  after the first and the second titrations are near each other, suggesting a smaller dependence of the  $\Delta \bar{H}_{O_2}$  on the oxygen stoichiometry change at higher departure from stoichiometry. This result tends to agree with the assumption that metal vacancies prevail, since a value for enthalpy which is independent of nonstoichiometry is expected for randomly distributed and noninteracting metal vacancies (van Roosmalen, 1994; Tanasescu, 2005). The model based on excess oxygen compensated by cation vacancies and partial charge disproportionation of manganese ions was also proposed for other related systems, like  $\text{LaMnO}_{3+\delta}$  (van Rosmalen, 1995; Töpfer, 1997),

$\text{BiMnO}_{3+\delta}$  (Sundaresan, 2008),  $\text{BiFe}_{0.7}\text{Mn}_{0.3}\text{O}_{3+\delta}$  (Selbach, 2009),  $\text{La}_{0.5}\text{Bi}_{0.5}\text{Mn}_{0.5}\text{Fe}_{0.5}\text{O}_{3+\delta}$  (Kundu, 2008). However, the model could not explain the observed relationship in the entire oxygen-excess region. This statement was also discussed in the case of  $\text{LaMnO}_{3+\delta}$  (Mizusaki, 2000; Nowotny, 1999; Tanasescu 2005) and could be subject for further discussion.

Considering the partial pressure of oxygen as a key parameter for the thermodynamic characterization of the materials, we investigated the variation of  $\log p_{\text{O}_2}$  with the temperature, oxygen stoichiometry and the concentration of the B-site dopant (Fig. 23). Before titration, the  $\log p_{\text{O}_2}$  values of the  $\text{Bi}_{0.9}\text{La}_{0.1}\text{Fe}_{0.7}\text{Mn}_{0.3}\text{O}_3$  are higher than  $\log p_{\text{O}_2}$  for  $\text{Bi}_{0.9}\text{La}_{0.1}\text{Fe}_{0.8}\text{Mn}_{0.2}\text{O}_3$ , excepting the value at 1123 K which is smaller for  $x=0.3$  comparatively with the corresponding value for  $x=0.2$ , the result being correlated with the structural phase transformation noted for the composition with  $x=0.3$  under 1123 K.

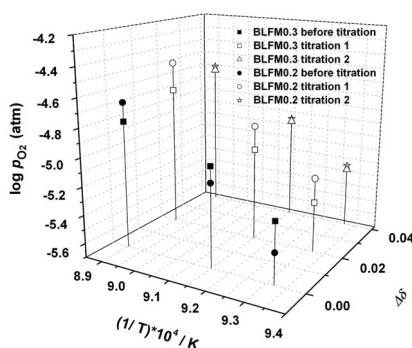


Fig. 23. Variation of  $\log p_{\text{O}_2}$  with temperature and oxygen stoichiometry change

It is obtained that for both compounds, after titration, at the same deviation of the oxygen stoichiometry,  $\log p_{\text{O}_2}$  shifted to higher values with increasing temperature. At the same temperature, the high deviation in the  $\log p_{\text{O}_2}$  values with the stoichiometry change is obtained for the sample with  $x=0.2$ . Besides, at  $x=0.2$ , higher values of  $\log p_{\text{O}_2}$  are obtained after the second titration, even though, increasing deviation from stoichiometry, a smaller increase of the partial pressure of oxygen was noted (Fig. 23). This could be explained by the fact that at high temperature, less excess oxygen is allowed. The sample with  $x=0.3$  presents a smaller dependence of the  $\log p_{\text{O}_2}$  on the oxygen nonstoichiometry. For small deviation from stoichiometry ( $\Delta\delta=0.02$ ), a small decrease in  $\log p_{\text{O}_2}$  values is obtained, but after the second titration, the partial pressure increase again. At 1073 K, after the second titration, the same value as before titration is obtained. Increasing temperature to 1123 K,  $\log p_{\text{O}_2}$  values increase again comparatively with the value before titration.

The obtained results could be correlated with some previously reported conductivity measurements. Singh et al (Singh, 2007) reported that small manganese doping in thin films of  $\text{BiFeO}_3$  improved leakage current characteristic in the high electric field region, reducing the conductivity; others authors noted the increasing of the conductivity with increasing manganese content (Chung, 2006; Selbach, 2009, 2010). If the polaron hopping mechanism is supposed for the electrical conductivity at elevated temperatures, the electronic conductivity will increase in the samples with hiperstoichiometry. According to the evolution of the

partial molar thermodynamic data of the oxygen dissolution, a decrease in the oxygen ionic conductivity (together the increasing of the electronic conductivity due to the electron-hole concentration increasing) will result in the sample with increased Mn content.

Even though there are disagreements between different works regarding the nature and the symmetry of the high temperature phases in the pure and substituted  $\text{BiFeO}_3$ , based on our data, we would like to point out that, in the condition of our experimental work, we may close to the stability limit of the Mn doped materials at temperatures around 1123 K. This is in accordance with theoretical consideration of the stability of  $\text{ABO}_3$  compounds based on Goldschmidt tolerance factor relationship (Goldschmidt, 1926). The evolution with temperature and oxygen stoichiometry of the thermodynamic data suggest that excess oxygen causing an increase of the tolerance factor of the system will lead to the stabilization of the cubic phase at lower temperature with increasing the departure from stoichiometry.

At this point further studies are in progress, so that correlations could be established with the observed properties at different departures of oxygen stoichiometry, in both deficit and excess region for  $\text{Bi}_{0.9}\text{La}_{0.1}\text{Fe}_{1-x}\text{Mn}_x\text{O}_3$  materials.

#### 4. Conclusions

$\text{Bi}_{1-x}\text{Ba}_x\text{Fe}_{1-x}\text{Ti}_x\text{O}_3$  ( $0 \leq x \leq 0.30$ ) and  $\text{Bi}_{0.9}\text{La}_{0.1}\text{Fe}_{1-x}\text{Mn}_x\text{O}_3$  ( $0 \leq x \leq 0.50$ ) ceramics were prepared by the conventional mixed oxides route, involving a two-step sintering process. Single phase perovskite compositions resulted for all the investigated ceramics, in the limit of XRD accuracy. For both cases, the presence of foreign cations replacing  $\text{Bi}^{3+}$  and/or  $\text{Fe}^{3+}$  in the perovskite lattice induces the diminishing of the rhombohedral distortion and causes significant microstructural changes, mainly revealed by the obvious decrease of the average grain size.

In order to evidence how the appropriate substitutions could influence the stability of the perovskite phases and then to correlate this effect with the charge compensation mechanism, the thermodynamic data represented by the relative partial molar free energies, enthalpies and entropies of the oxygen dissolution in the perovskite phase, as well as the equilibrium partial pressures of oxygen have been obtained by solid state electrochemical (EMF) method. The influence of the oxygen stoichiometry change on the thermodynamic properties was examined using the data obtained by a coulometric titration technique coupled with EMF measurements.

New features related to the thermodynamic stability of the multiferroic  $\text{Bi}_{1-x}\text{Ba}_x\text{Fe}_{1-x}\text{Ti}_x\text{O}_3$  and  $\text{Bi}_{0.9}\text{La}_{0.1}\text{Fe}_{1-x}\text{Mn}_x\text{O}_3$  ceramics were evidenced, the thermodynamic behavior being explained not only by the structural changes upon doping, but also by the fact that the energetic parameters are extremely sensitive to the chemical defects in oxygen sites.

The decreasing of the ferroelectric - paraelectric transition temperature in the substituted samples was evidenced by both EMF and DSC measurements. Besides, the phase transition qualitatively corresponding to the phase transformation from paraelectric to a new high temperature phase was evidenced and the partial molar thermodynamic data describing the different phase stability domains were presented for the first time.

Bearing in mind the role of charge ordering and of the defects chemistry in explaining the electrical, magnetic and thermodynamic behavior of the doped perovskite-type oxides, it should be possible to find new routes for modifying the properties of these materials by controlling the average valence in B-site and the oxygen nonstoichiometry. Preparation

method also strongly could influence the behavior of the powder in terms of non-stoichiometry, which ultimately will affect its electrical properties since they are dependent upon the presence of oxygen ion vacancies in the lattice. Besides the doping with various foreign cations, the decreasing of the grain sizes, as well as the thin film technology could be efficient methods for tuning the electrical, magnetic and thermodynamic properties of BiFeO<sub>3</sub>-based compounds to be used as multiferroic materials.

## 5. Acknowledgments

Support of the EU (ERDF) and Romanian Government that allowed for acquisition of the research infrastructure under POS-CCE O 2.2.1 project INFRANANOCHEM - Nr. 19/01.03.2009, is gratefully acknowledged. This work also benefits from the support of the PNII-IDEAS program (Project nr. 50 / 2007).

## 6. References

- Arnold, D. C.; Knight, K. S.; Catalan, G.; Redfern, S. A. T.; Scott, J. F.; Lightfoot, P. & Morrison, F. D. (2010). The  $\beta$ -to- $\gamma$  transition in BiFeO<sub>3</sub>: a powder neutron diffraction study. *Advanced Functional Materials*, Vol. 20, No. 13, pp. 2116-2123, ISSN 1616-301X
- Azuma, M.; Kanda, H.; Belik, A. A.; Shimakawa, Y. & Takano, M. (2007). Magnetic and structural properties of BiFe<sub>1-x</sub>Mn<sub>x</sub>O<sub>3</sub>, *Journal of Magnetism and Magnetic Materials*, Vol. 310, No. 2, Part. 2, pp. 1177 -1179, ISSN 0304-8853
- Bogatko, V. V.; Fadeeva, N. V.; Gagulin, V. V.; Korchagina, S. K. & Shevchuk, Y. A. (1998). Structure and properties of BiFeO<sub>3</sub>-LaMnO<sub>3</sub> seignettomagnetic solid-solutions, *Inorganic Materials*, Vol. 34, No. 11, pp. 1141-1143, ISSN 0020-1685
- Boyd, G. R.; Kumar, P. & Phillpot, S. R. (2011). Multiferroic thermodynamics, *Materials Science*, arXiv:1101.5403v1
- Buscaglia, M. T.; Mitoseriu, L.; Buscaglia, V.; Pallecchi, I.; Viviani, M.; Nanni, P. & Siri, A. S. (2006). Preparation and characterization of the magneto-electric xBiFeO<sub>3</sub>-(1-x)BaTiO<sub>3</sub> ceramics, *J. Eur. Ceram. Soc.*, Vol. 26, No. 14, pp. 3027-3030, ISSN 0955-2219
- Carvalho, T. T. & Tavares, P. B. (2008). Synthesis and thermodynamic stability of multiferroic BiFeO<sub>3</sub>, *Materials Letters*, Vol. 62, No. 24, pp. 3984-3986, ISSN. 0167-577X
- Catalan, G. & Scott, J. F. (2009). Physics and application of bismuth ferrite. *Advanced Materials*, Vol. 21, No. 14, pp. 2463-2485, ISSN: 09359648
- Charette, G. G. & Flengas, S. N. (1968). Thermodynamic Properties of the Oxides of Fe, Ni, Pb, Cu, and Mn, by EMF Measurements, *J. Electrochem. Soc.*, Vol. 115, No. 8, pp. 796-804
- Chen, J. R.; Wang, W. L.; Li, J.-B. & Rao, G. H. (2008). X-ray diffraction analysis and specific heat capacity of (Bi<sub>1-x</sub>La<sub>x</sub>)FeO<sub>3</sub> perovskites, *J. Alloys Compd.*, Vol. 459, No. 1-2, pp. 66-70, ISSN 0925-8388
- Chung, C. F.; Lin, J. P.; & Wu, J. M. (2006). Influence of Mn and Nb dopants on electric properties of chemical-solution-deposited BiFeO<sub>3</sub> films, *Appl. Phys. Lett.*, Vol. 88, No. 24, pp. 242909.1-242909.3, ISSN 0003-6951
- Ederer, C. & Spaldin, N. A. (2005). Weak ferromagnetism and magnetoelectric coupling in bismuth ferrite, *Phys. Rev.*, Vol. B 71, No. 6, pp. 060401.1 - 060401.4

- Ederer, C. & Spaldin, N. A. (2005). Influence of strain and oxygen vacancies on the magnetoelectric properties of multiferroic bismuth ferrite, *Physical Review*, Vol. 71, No. 22, pp. 224103.1-224103.9
- Fukumura, H.; Matsui, S.; Tonari, N.; Nakamura, T.; Hasuike, N.; Nishio, K.; Isshiki, T. & Harima, H. (2009). Synthesis and characterization of Mn-doped BiFeO<sub>3</sub> nanoparticles, *Acta Physica Polonica A*, Vol. 116, No.1, pp. 47-50
- Gagulin, V. V.; Korchagina, S. K. ; Shevchuk, Y. A. ; Fadeeva, N. V. & Bogatko, V. V. (1997). Synthesis and physical properties of new high temperature seignettomagnetics in the systems with perovskite type structure, *Ferroelectrics*, Vol. 204, No. 1, pp. 345-355
- Goldschmidt, V. M. (1926). The laws of crystal chemistry, *Naturwissenschaften*, Vol. 14, pp. 477-485
- Gu, Y. H.; Wang, Y.; Chen, F.; Chan, H. L. W. & Chen, W. P. (2010). Nonstoichiometric BiFe<sub>0.9</sub>Ti<sub>0.05</sub>O<sub>3</sub> multiferroic ceramics with ultrahigh electrical resistivity, *Journal of Applied Physics*, Vol. 108, No. 9, pp. 094112.1 -094112.5
- Habouti, S.; Solterbeck, C.H. & Es-Souni, M.; (2007). LaMnO<sub>3</sub> effects on the ferroelectric and magnetic properties of chemical solution deposited BiFeO<sub>3</sub> thin films, *Journal of Applied Physics*, Vol. 102, No. 7, pp. 074107.1-074107.4, ISSN 0021-8979
- Ianculescu, A.; Mitoseriu, L.; Chiriac, H.; Carnasciali, M. M.; Braileanu, A. & Trusca, R. (2008). Preparation and magnetic properties of the (1-x)BiFeO<sub>3</sub> - xBaTiO<sub>3</sub> solid solutions, *J. Optoelect. & Adv. Mater.*, Vol. 10, No. 7, pp. 1805-1809, ISSN 1454-4164
- Ianculescu, A.; Prihor, F.; Postolache, P.; Mitoseriu, L.; Dragan, N. & Crisan, D. (2009). Preparation and properties of Mn-doped La<sub>0.1</sub>Bi<sub>0.9</sub>FeO<sub>3</sub> ceramics, *Ferroelectrics*, Vol. 391, No. 1, pp. 67-75
- Ismailzade, I. H.; Ismailov, R. M.; Alekberov, A. I. & Salaev F. M. (1981). Investigation of the magnetoelectric effect in the system BiFeO<sub>3</sub>-LaFeO<sub>3</sub>, *Physica Status Solidi (a)*, Vol. 66, No. 1, pp. 119-123
- Ivanova, V. V.; Gagulin, V. V.; Korchagina, S. K.; Shevchuk, Y. A. & Bogatko V. V. (2003). Synthesis and properties of BiFeO<sub>3</sub>-DyMnO<sub>3</sub> solid solutions, *Inorganic Materials*, Vol. 39, No. 7, pp. 745-748, ISSN 0020-1685
- Jiang, Q. H.; Nan C. W. & Shen, Z. J. (2006). Synthesis and Properties of Multiferroic La-Modified BiFeO<sub>3</sub> Ceramics, *J. Am. Ceram. Soc.*, Vol. 89, No. 7, pp. 2123-2127
- Jonker, G. H. & van Santen, J. H. (1953). Magnetic compounds with perovskite structure, *Physica*, Vol. 19, No. 1-12, pp. 120-130
- Kelley, K. K. (1960). *U. S. Bur of Mines Bull*, Vol. 584
- Kelley, K. K. & King, E. G.; (1961) *U. S. Bur of Mines Bull.*, Vol. 592
- Kim, S. J. & Cheon, C. II. (2004). Weak ferromagnetism in the ferroelectric BiFeO<sub>3</sub>- ReFeO<sub>3</sub>-BaTiO<sub>3</sub> solid solution (Re=Dy, La). *Journal of Applied Physics*, Vol. 96, No.1, pp. 468-474
- Kim, S. J.; Cheon, C. I.; Kang, H. J. & Jang, P. W. (2007). High temperature properties of multiferroic BiFeO<sub>3</sub>-DyFeO<sub>3</sub>-BaTiO<sub>3</sub> solid solutions, *Journal of the European Ceramic Society*, Vol. 27, No. 13-15, pp. 3951-3954, ISSN 0955-2219
- Kothari, D.; Reddy, V. R.; Gupta, A.; Phase, D. M.; Lakshmi, N.; Deshpande, S. K. & Awasthi, A. M. (2007). Study of the effect of Mn doping on the BiFeO<sub>3</sub> system, *Journal of Physics: Condensed Matter*, Vol.19, No. 13, pp. 136202.1-136202.8

- Kumar, M. M.; Srinivas, A.; Kumar, G. S. & Suryanarayana, S. V. (1999). Investigation of the magnetoelectric effect in BiFeO<sub>3</sub>-BaTiO<sub>3</sub> solid solutions, *J. Phys.: Condens. Matter*, Vol. 11, No. 41, 8131
- Kumar, M. M.; Srinivas, A. & Suryanarayana, S. V. (2000). Structure property relations in BiFeO<sub>3</sub>/ BaTiO<sub>3</sub> solid solutions, *Journal of Applied Physics*, Vol. 87, No. 2, pp. 855-862
- Kumar, M. M.; Palkar, V. R.; Srinivas, K. & Suryanarayana, S. V. (2000). Ferroelectricity in a pure BiFeO<sub>3</sub> ceramic, *Appl. Phys. Lett.*, Vol. 76, No. 19, pp. 2764-2766
- Kundu, A. K.; Ranjith, R.; Kundys, B.; Nguyen, N.; Caignaert, V.; Pralong, V.; Prellier, W. & Raveau, B. (2008). A multiferroic ceramic with perovskite structure: (La<sub>0.5</sub>Bi<sub>0.5</sub>)(Mn<sub>0.5</sub>Fe<sub>0.5</sub>)O<sub>3.09</sub>, *Applied Physics Letters*, Vol. 93, No. 5, pp. 052906.1-052906.3, ISSN 0003-6951
- Maignan, A.; Martin, C. & Raveau, B. (2000). Magnetoresistance properties in manganese and cobalt oxides, *Journal of Superconductivity*, Vol. 13, No. 2, pp. 313-328
- Marinescu, C.; Sofronia, A. & Tanasescu, S. (in press). Differential scanning calorimetry: Part A: temperature calibration of differential scanning calorimeter (DSC) in the heating mode, *Revue Roumaine de Chimie*, RRC 251
- Mitoseriu, L. (2005). Magnetoelectric phenomena in single-phase and composite systems, *Boletín de la Sociedad Española de Cerámica y Vidrio*. Vol. 44, No. 3, pp. 177-184
- Mizusaki, J.; Mori, N.; Takai, H.; Yonemura, Y.; Minamiue, H.; Tagawa, H.; Dokiya, M.; Inaba, H.; Naraya, K.; Sasamoto T. & Hashimoto, T. (2000). Oxygen nonstoichiometry and defect equilibrium in the perovskite-type oxides La<sub>1-x</sub>Sr<sub>x</sub>MnO<sub>3+δ</sub>, *Solid State Ionics*, Vol. 129, No. 1-4, pp. 163-177, ISSN 0167-2738
- Nowotni, J. & Rekas, M. (1998). Defect chemistry of (La,Sr)MnO<sub>3</sub>, *Journal of the American Ceramic Society*, Vol. 81, No. 1, pp. 67-80
- Palai, R.; Katiyar, R. S.; Schmid, H.; Tissot, P.; Clark, S. J.; Robertson, J.; Redfern, S. A. T.; Catalan, G. & Scott, J. F. (2008). β phase and γ-β metal-insulator transition in multiferroic BiFeO<sub>3</sub>, *Physical Review*, Vol. B 77, No. 1, pp. 014110.1-014110.11
- Palkar, V. R. & Pinto, R. (2002). BiFeO<sub>3</sub> thin films: Novel effects, *Pramana Journal of Physics*, Vol. 58, No. 5-6, pp.1003-1008
- Palkar, V. R.; Darshan, C.; Kundaliya, C. & Malik, S. K. (2003). Effect of Mn substitution on magnetoelectric properties of bismuth ferrite system, *J. Appl. Phys.*, Vol. 93, No. 7, pp. 4337-4339, ISSN 0021-8979
- Pradhan, D. K.; Choudhary, R. N. P.; Tirado, C. M. & Katiyar, R. S. (2008). Effect of La/Mn substitution on electrical properties of BiFeO<sub>3</sub> multiferroics, *Indian Journal of Engineering & Materials Sciences*, Vol. 15, pp. 87-90, ISSN 0971-4588
- Prihor, F.; Postolache, P.; Curecheriu, L.; Ianculescu, A. & Mitoseriu, L. (2009). Functional properties of the (1- x) BiFeO<sub>3</sub> - xBaTiO<sub>3</sub> solid solutions, *Ferroelectrics*, Vol. 391, No.1, pp. 76-82, ISSN 0015-0193
- Prihor Gheorghiu, F.; Ianculescu, A.; Postolachea, P.; Lupu, N.; Dobromira, M.; Luca, D. & Mitoseriu, L. (2010). Preparation and properties of (1-x)BiFeO<sub>3</sub> - xBaTiO<sub>3</sub> multiferroic ceramics, *J. Alloy Compd.*, Vol. 506, No. 2, pp. 862-867
- Qi, X.; Dho, J. & Tomov, R. (2005). Greatly reduced leakage current and conduction mechanism in aliovalent-ion-doped BiFeO<sub>3</sub>, *Applied Physics Letters*, Vol. 86, No. 6, pp. 062903.1-062903.3
- Ramesh, R. & Spaldin, N. A. (2007). Multiferroics: progress and prospects in thin films, *Nature Publishing Group*, Vol. 6, No.1, pp. 21-29

- Sahu, J. R. & Rao, C. N. R. (2007). Beneficial modification of the properties of multiferroic BiFeO<sub>3</sub> by cation substitution, *Solid State Sci.*, Vol. 9, No. 10, pp. 950-954
- Selbach, S. M.; Tybell, T.; Einarsrud, M.-A. & Grande, T. (2009). Structure and properties of multiferroic oxygen hyperstoichiometric BiFe<sub>1-x</sub>Mn<sub>x</sub>O<sub>3+δ</sub>. *Chemistry of Materials*, Vol. 21, No. 21, pp. 5176-5186
- Selbach, S. M.; Tybell, T.; Einarsrud, M.-A. & Grande, T. (2009). High-temperature semiconducting cubic phase of BiFe<sub>0.7</sub>Mn<sub>0.3</sub>O<sub>3+δ</sub>, *Physical Review*, Vol. 79, No. 21, pp. 214113.1-214113.5
- Selbach, S. M.; Tybell, T.; Einarsrud, M.-A. & Grande, T. (2010). Phase transitions, electrical conductivity and chemical stability of BiFeO<sub>3</sub> at high temperatures. *Journal of Solid State Chemistry*, Vol. 183, No. 5, pp. 1205-1208
- Singh, S. K. & Ishiwara, H. (2007). Microstructure and frequency dependent electrical properties of Mn-substituted BiFeO<sub>3</sub> thin films. *Journal of Applied Physics*, Vol. 102, No. 9, pp. 094109.1-094109.5, ISSN 0021-8979
- Singh, A.; Pandey, V.; Kotnala, R. K. & Pandey, D. (2008). Direct evidence for multiferroic magnetoelectric coupling in 0.9 BiFeO<sub>3</sub>-0.1 BaTiO<sub>3</sub>, *Phys. Rev.Lett.*, Vol. 101, 247602
- Singh, A.; Patel, J. P. & Pandey, D. (2009). High temperature ferroic phase transition and evidence of paraelectric cubic phase in the multiferroic 0.8 BiFeO<sub>3</sub>-0.2 BaTiO<sub>3</sub>. *Applied Physics Letters*, Vol. 95, No. 14, pp. 142909.1-142909.3
- Stroppa, A. & Picozzi, S. (2010). Hybrid functional study of proper and improper multiferroics, *Physical Chemistry Chemical Physics*, Vol. 12, No. 20, pp. 5405-5416
- Sundaresan, A.; Mangalam, R. V. K.; Iyo, A.; Tanaka, Y. & Rao, C. N. R. (2008). Crucial role of oxygen stoichiometry in determining the structure and properties of BiMnO<sub>3</sub>, *J. Mater. Chem.*, Vol. 18, pp. 2191-2193
- Takahashi, K. & Tonouchi, M. (2007). Influence of manganese doping in multiferroic bismuth ferrite thin films, *Journal of Magnetism and Magnetic Materials*, Vol. 310, No. 2, pp. 1174-1176, ISSN 0304-8853
- Tanasescu, S.; Maxim, F.; Teodorescu, F. & Giurgiu, L. (2008). The influence of composition and particle size on spin dynamics and thermodynamic properties of some magnetoresistive perovskites, *Journal of Nanoscience and Nanotechnology*, Vol. 8, pp. 914-923
- Tanasescu, S.; Grecu, M. N.; Marinescu, C.; Giurgiu, L. M.; Chiriac, H. & Urse, M. (2009). Effects of dopants and oxygen nonstoichiometry on the thermodynamic, magnetic and electrical properties of micro- and nanostructured perovskite-type materials, *Advances in Applied Ceramics*, Vol. 108, No. 5, pp. 273-279
- Tanasescu, S.; Marinescu, C.; Sofronia, A.; Ianculescu, A. & Mitoseriu, L. (2010). Communication at *Electroceramics XII*, 13<sup>th</sup> - 16<sup>th</sup> of June 2010, Trondheim, Norway
- Tanasescu, S.; Marinescu, C.; Maxim, F.; Sofronia, A. & Totir, N. (2011). Evaluation of manganese and oxygen content in La<sub>0.7</sub>Sr<sub>0.3</sub>MnO<sub>3-δ</sub> and correlation with the thermodynamic data, *Journal Solid State Electrochemistry*, Vol. 15, No. 1, pp. 189-196
- Töfeld, B. C. & Scott, W. R. (1974). Oxidative nonstoichiometry in perovskites, an experimental survey; the defect structure of an oxidized lanthanum manganite by powder neutron diffraction, *J. Solid State Chem.*, Vol. 10, No. 3, pp. 183-194
- Töpfer, J. & Goodenough, J. B. (1997). Transport and magnetic properties of the perovskites La<sub>1-y</sub>MnO<sub>3</sub> and LaMn<sub>1-z</sub>O<sub>3</sub>, *Chem. Mater.*, Vol. 9, No. 6, pp. 1467-1474

- van Roosmalen, J. A. M. & Cordfunke, E. H. P. (1994). The defect chemistry of  $\text{LaMnO}_{3+\delta}$ : 5. Thermodynamics, *Journal of Solid State Chemistry*, Vol. 110, No. 1, pp. 113-117
- van Roosmalen, J. A. M.; van Vlaanderen, P.; Cordfunke, E. H. P.; Ijdo, W. L. & Ijdo, D. J. W. (1995). Phases in the perovskite-type  $\text{LaMnO}_{3\delta}$  solid solution and the  $\text{La}_2\text{O}_3$ - $\text{Mn}_2\text{O}_3$  phase diagram, *J. Solid State Chem.*, Vol. 114, pp. 516-23
- Wang, Y. P.; Zhou, L.; Zhang, M. F.; Chen, X. Y.; Liu, J. M. & Liu, Z. G. (2004). Room temperature saturated ferroelectric polarization in  $\text{BiFeO}_3$  ceramics synthesized by rapid liquid phase sintering, *Applied Physics Letters*, Vol. 84, No. 10, id. 1731
- Wang, N.; Cheng, J.; Pyatakov, A.; Zvezdin, A. K.; Li, J. F.; Cross, L. E. & Viehland, D. (2005). Multiferroic properties of modified  $\text{BiFeO}_3$ - $\text{PbTiO}_3$ -based ceramics: Random-field induced release of latent magnetization and polarization, *Phys. Rev.*, Vol. B 72, No. 10, pp. 390-392, ISSN 1099-4734
- Wang, H.; Huang, H. & Wang, B. (2010). Effect of Mn substitution for Fe in multiferroic  $\text{BiFeO}_3$ : a first-principles study, *Science of Advanced Materials*, Vol. 2, No. 2, pp. 184-189
- Warren, W. L.; Vanheusden, K.; Dimos, D.; Pike, G. E. & Tuttle, B. A. (1996), Oxygen vacancy motion in perovskite oxides, *Journal of the American Ceramic Society*, Vol. 79, No. 2, pp. 536-538
- Yuan, G. L.; Or, S. W.; Wang, Y. P.; Liu, Z. G. & Liu, J. M. (2006). Preparation and multi-properties of insulated single-phase  $\text{BiFeO}_3$  ceramics, *Solid State Communication*, Vol. 138, No. 2, pp. 76-81
- Zheng, X.; Xu, Q.; Wen, Z.; Lang, X.; Wu, D.; Qiu, T. & Xu, M. X. (2010). The magnetic properties of La doped and codoped  $\text{BiFeO}_3$ , *Journal of Alloys and Compounds*, Vol. 499, No.1, pp. 108-112
- Zhu, W. M. & Ye, Z. G. (2004). Effects of chemical modification on the electrical properties of  $0.67\text{BiFeO}_3$ - $0.33\text{PbTiO}_3$  ferroelectric ceramics, *Ceram. Int.*, Vol. 30, No. 7, pp. 1435-1442

# Multifunctional Characteristics of *B*-site Substituted BiFeO<sub>3</sub> Films

Hiroshi Naganuma

*Department of Applied Physics, Graduate school of Engineering, Tohoku University  
Japan*

## 1. Introduction

In recent times, BiFeO<sub>3</sub> has been considered as an important material for the development of multifunctional devices because of its distinctive ferroelectric, magnetic, piezoelectric, and optical properties. These include a high Currie temperature of ferroelectricity ( $T_C \sim 1100$  K), (Venevtsev *et al.*, 1960), high Néel temperature of antiferromagnetism ( $T_N \sim 650$  K), (Kiselev *et al.*, 1963) lead-free piezoelectricity, and large flexibility in the wavelength of visible light region. These features make BiFeO<sub>3</sub> particularly applicable in the fields of ferroelectrics, magnetics, piezoelectrics, and optics; in addition, the cross correlation of these properties can be expected above room temperature (RT). [Fig. 1] BiFeO<sub>3</sub> has a perovskite-type crystal structure that is rhombohedrally distorted in the [111] direction and crystallized in the space group  $R3c$  [Fig. 2]. (Kubel *et al.*, 1990) The ferroelectric performance of BiFeO<sub>3</sub> is comparable to that of conventional ferroelectric materials such as Pr(Zr,Ti)O<sub>3</sub> (PZT) because BiFeO<sub>3</sub> exhibits excellent spontaneous polarization at RT. Theoretically, spontaneous polarization corresponds to crystal symmetry, wherein the rhombohedral and tetragonal BiFeO<sub>3</sub> structures are expected to show spontaneous polarizations of  $\approx 100$   $\mu\text{C}/\text{cm}^2$  in the [111] direction and  $\approx 150$   $\mu\text{C}/\text{cm}^2$  in the [001] direction, respectively. [Fig. 3(a)] (Ederer *et al.*, 2005) In fact, these theoretically predicted large spontaneous polarizations in BiFeO<sub>3</sub> are almost consistent with the experimental results [Figs. 3(b) and 3(c)] (Li *et al.*, 2004, Yun *et al.*, 2004), stating that BiFeO<sub>3</sub> is favorable for use in ferroelectric random access memory (FeRAM) applications. However, the practical application of BiFeO<sub>3</sub> thin films has been limited by their large leakage current density and large coercive field at RT, (Naganuma *et al.*, 2007, Pabst *et al.*, 2007) as a result, BiFeO<sub>3</sub> thin films easily undergo electrical breakdown when a large leakage current passes through them before the polarization is switched. Therefore, in order for BiFeO<sub>3</sub> films to find practical future application, the leakage current and/or coercive field of these films must be reduced. In term of magnetic properties, BiFeO<sub>3</sub> is antiferromagnetic with a G-type spin configuration; (Kubel *et al.*, 1990, Ederer *et al.*, 2005) that is, nearest neighbor Fe moments are aligned antiparallel to each other, and there is a sixfold degeneracy, resulting in an effective "easy magnetization plane" for the orientation of the magnetic moments within the (111) plane. It should be noted that the antiferromagnetic (111) plane is orthogonal to the ferroelectric polarization direction [111] in the rhombohedral structure. [Fig. 4(a)] The orientation of the antiferromagnetic sublattice magnetization is coupled through ferroelastic strain due to crystal symmetry, and it should always be perpendicular to the ferroelectric polarization [111] direction. Therefore, a polarization switch to either 71° or 109° should

change the orientation of the antiferromagnetic plane. This change in orientation would, however, not occur in the case of  $180^\circ$  to  $180^\circ$  ferroelectric polarization switching. [Fig. 4(b)-4(d)] In fact, experimentally, (Zhao *et al.*, 2006) the ferroelectric domain and antiferromagnetic domain in  $\text{BiFeO}_3$  (100) epitaxial films are strongly coupled (magneto-electric (ME) coupling) in the orthogonal configuration, and the orientation of the antiferromagnetic plane is switched by a  $109^\circ$  switch in the ferroelectric domain. In effect, the magnetization configuration can be controlled by the application of an electric field through ferroelectric domain switching; by means of this mechanism, it is possible to realize voltage control of magnetic random access memory (V-MRAM). The use of V-MRAM can drastically reduce electrical consumption when compared with spin-MRAM which is operated by spin-polarized current. In terms of “how to detect the change of magnetization induced by ferroelectric domain switching”, it can be seen that owing to Dzyaloshinskii-Moriya (DM) interaction, (Dzyaloshinskii, 1957, Moriya, 1960) the symmetry permits a canting of the antiferromagnetic sublattices, resulting in a local weak spontaneous magnetization. This magnetization is macroscopically canceled by a spiral spin structure caused by the rotation of the antiferromagnetic axis through the crystal with an incommensurately long-wavelength period of 62 nm. (Sosnowska *et al.*, 1982) This spiral spin structure might be suppressed in the film form of  $\text{BiFeO}_3$  and the resulting magnetic moment is caused by a weak ferromagnetism of  $\sim 0.1 \mu_B/\text{Fe}$  atom. However, this small magnetic moment is not suitable for application in devices such as spintronics because of the difficulty associated with the direction of a weak magnetic moment using a magnetic sensor, as well as the spin-filter effect. Therefore, in order to detect the change of magnetic states driven by ferroelectric domain switching (i) introduction of ferrimagnetic spin order into  $\text{BiFeO}_3$  having a rhombohedral structure or (ii) detection of the ferromagnetization change through exchange coupling with  $\text{BiFeO}_3$  (Chu *et al.*, 2008) are the predominant candidates. In addition, the  $\text{BiFeO}_3$  films show distinctive optical properties, as previously mentioned.  $\text{BiFeO}_3$  has the highest flexibility among the oxide materials: a flexibility of 3.22 at a wavelength of 600 nm; this flexibility is expected to cross-correlate with the other physical properties. (Shima *et al.*, 2009) The details of the optical properties of  $\text{BiFeO}_3$  films have been relegated to a subsequent

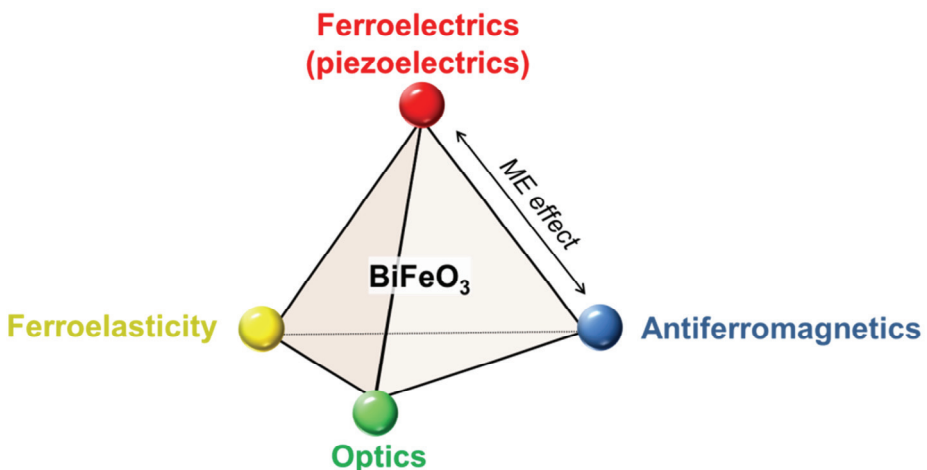


Fig. 1. Schematic illustration of cross correlation between ferroelectricity (piezoelectrics), ferroelasticity, optical properties and antiferromagnetism for  $\text{BiFeO}_3$ .

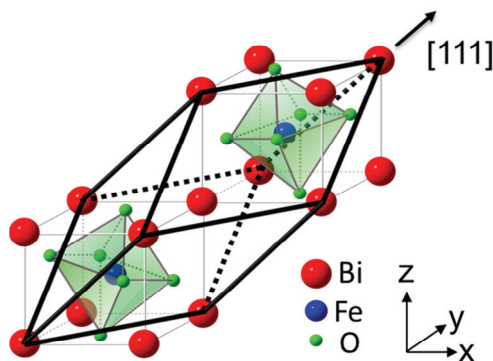


Fig. 2. Schematic drawing of the crystal structure of perovskite BiFeO<sub>3</sub> (space group: *R3c*). Two crystals along [111] direction are shown in the figure.

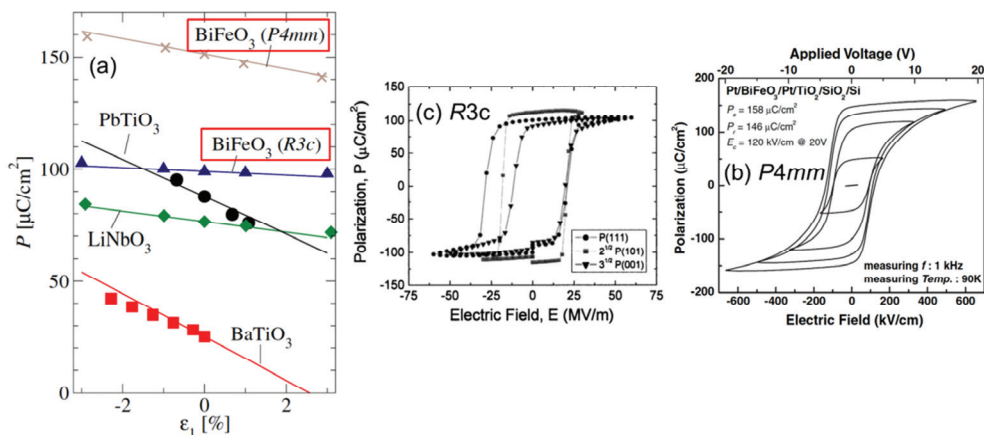


Fig. 3. (a) First-principle calculation of spontaneous polarization for BiFeO<sub>3</sub> with tetragonal (*P4mm*) and rhombohedral (*R3c*) symmetry.  $\epsilon_1$  indicates the epitaxial strain. Symbols represent directly calculated values. (Ederer *et al.*, 2005) (b) Experimental result of BiFeO<sub>3</sub> with tetragonal structure, and (c) with rhombohedral structure.

discussion. Based on these background considerations, the main focus of this chapter is the structure, ferroelectricity, and magnetism of BiFeO<sub>3</sub> films. In addition, we discuss the effect of the substitution of various 3*d* transition metals into the B-site of BiFeO<sub>3</sub> films on the films' structural, ferroelectric, and magnetic properties. We also propose a new multiferroic material having a ferrimagnetic spin order and large spontaneous polarization at RT. This chapter includes three sections. Section 1 presents the fundamental characteristics of pure BiFeO<sub>3</sub> films. Section 2 describes substitution of various 3*d* transition metals for Fe in BiFeO<sub>3</sub> films, in small amount (~5 at.%), in order to achieve ferrimagnetic spin ordering together with low leakage current density. Finally, in Section 3, we demonstrate the substitution of a large amount of Co (~58 at.%).

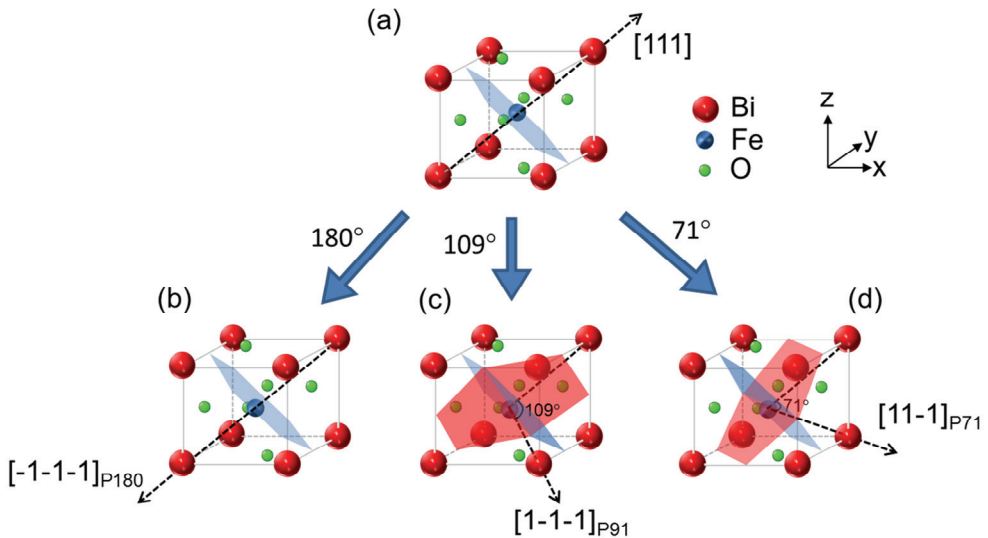


Fig. 4. Schematic illustration of cross correlation between ferroelectric polarization and antiferromagnetic plane. Antiferromagnetic plane was defined as the direction of magnetic moment of weak ferromagnetism due to DM interaction.

## 2. Structural, electronic, and magnetic properties of BiFeO<sub>3</sub> films

In order to elucidate the fundamental properties of BiFeO<sub>3</sub> films, here, we begin by systematically investigating the effect of annealing temperature on the structural, electrical, and magnetic properties of BiFeO<sub>3</sub> polycrystalline film. The results described in this section is based on our recent work as follows; Naganuma *et al.* TMRJ, 2007, Naganuma *et al.* MT, 2007, Naganuma *et al.* IF, 2007, Naganuma *et al.* TUFFC, 2008, Naganuma *et al.* JJAP, 2008, Naganuma *et al.* APEX, 2008, Naganuma *et al.* JCSJ, 2010, Naganuma *et al.* JAP, 2011.

Polycrystalline BiFeO<sub>3</sub> films were prepared by a chemical solution deposition (CSD) method. The preparation processes are shown in Fig. 5 and can be summarized as follows: an enhanced-metal-organic-decomposition (E-MOD) solution (with stoichiometric composition Bi:Fe=1:1, 0.2 mol/l) was used as the precursor solution. The precursor solution was spin-coated onto Pt (150 nm)/Ti (5 nm)/SiO<sub>2</sub>/Si (100) substrates at a rotation speed between 4000 and 6000 rpm for 50 s. Pt and Ti were deposited by r.f. magnetron sputtering using Ar gas at RT. The spin-coated films were dried at 150°C for 1 min and calcined at 350°C for 5 min. The spin coating and calcination processes were repeated 4-5 times, after which the films were sintered in air at 400 - 800°C for 10 min by rapid thermal annealing (RTA; ULVAC mila-5000). The films had a thickness of approximately 200 nm. The surface morphology of the films was observed by atomic force microscopy (AFM; SII SPI3800N) and scanning electron microscopy (SEM; JEOL JSM-6380). The crystal structure and orientation were confirmed by X-ray diffraction (XRD; PANalytical X'Pert MRD) with Cu-K $\alpha$  radiation and transmission electron microscopy (TEM; JEOL JEM-2100F, JEOL JEM-3000F, LEO-922) working at 200 and 300 kV. The leakage current density was measured using a pico-ampere

meter (HP 4140B). The ferroelectric hysteresis ( $P$ - $E$ ) loop of the films was measured using a ferroelectric tester (aixACCT TF-2000, TOYO FCE-1A) with a single triangular pulse. Positive-Up-Negative-Down (PUND) measurement was also used for evaluating electrical properties. The magnetic properties were measured with a vibrating sample magnetometer (VSM; Tamakawa) at RT, and a superconducting quantum interference device (SQUID; Quantum design MPMS) magnetometer was used for the in-plane direction.

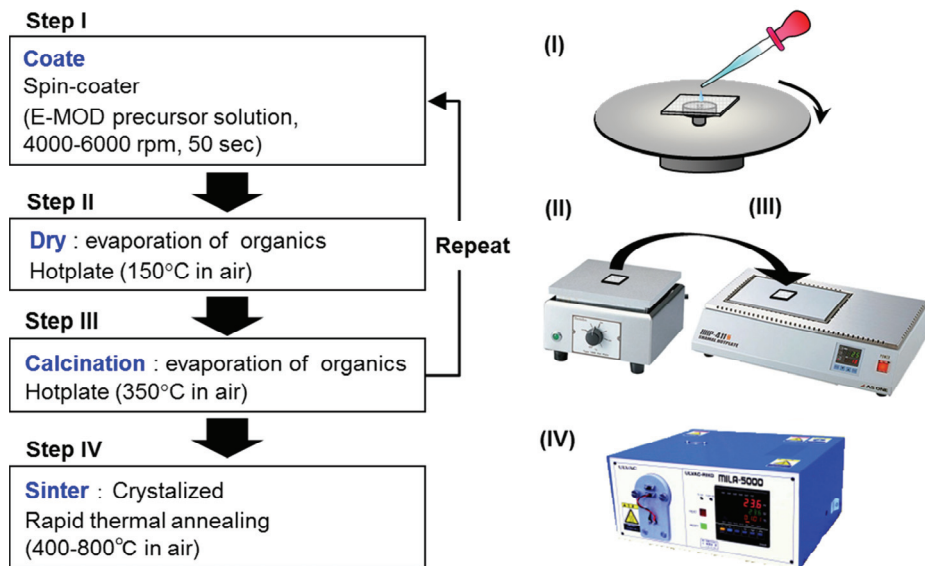


Fig. 5. Schematic illustration of preparation process using CSD.

Figure 6 shows the XRD profiles of BiFeO<sub>3</sub> films deposited on Pt/Ti/SiO<sub>2</sub>/Si(100) substrates annealed at various temperatures. For each annealing temperature, a strong diffraction peak at  $2\theta = 39.8^\circ$  was observed due to the Pt (111) plane. At an annealing temperature of 400°C, a weak diffraction peak was observed in the region of  $2\theta = 46^\circ$ ; however, it was not clear whether this diffraction peak originated from BiFeO<sub>3</sub> (024) at  $2\theta = 45.74^\circ$  or Pt (200) at  $2\theta = 46.24^\circ$ . Therefore, in order to clarify the origin of the diffraction peak in the region of  $2\theta = 46^\circ$ , XRD analyses were undertaken for the Pt/Ti/SiO<sub>2</sub>/Si(100) substrate only. On the basis of this experiment, the diffraction peak in the region of  $2\theta = 46^\circ$  was identified as Pt (200) for the sample annealed at 400°C. Therefore, the structure of the film annealed at 400°C was amorphous or nanocrystalline. The formation of the polycrystalline BiFeO<sub>3</sub> films for annealing temperature above 450°C was indicated by the appearance of numerous diffraction peaks attributed to the BiFeO<sub>3</sub> structure above the stated temperature. The strong [111] orientation of the bottom Pt layer did not affect BiFeO<sub>3</sub> crystal growth. At annealing temperature above 700°C, secondary phases such as  $\alpha$ -Fe<sub>2</sub>O<sub>3</sub> and BiPt were formed. The observation of these phases indicates that the excess Fe formed  $\alpha$ -Fe<sub>2</sub>O<sub>3</sub> due to diffusion of Bi into the Pt electrode at high annealing temperatures. The indication is that the single phase of randomly oriented polycrystalline BiFeO<sub>3</sub> film was formed at annealing temperatures between 450 and 650°C.

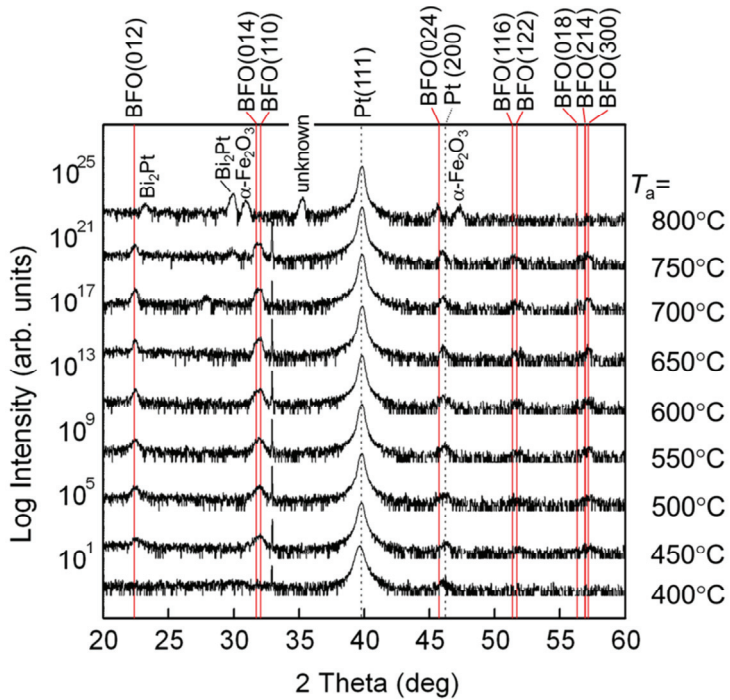


Fig. 6. XRD profiles of BiFeO<sub>3</sub> films deposited on Pt/Ti/SiO<sub>2</sub>/Si(100) substrates annealed at various temperatures

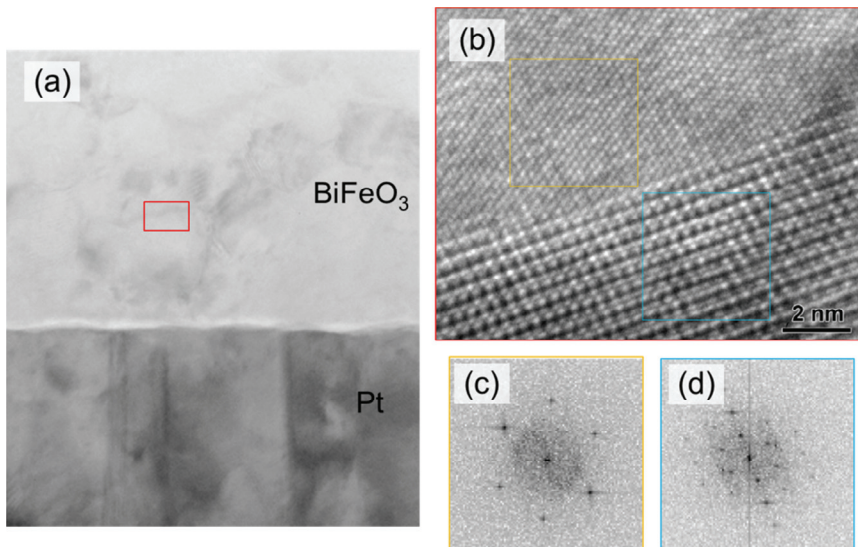


Fig. 7. Cross-sectional TEM images of polycrystalline BiFeO<sub>3</sub> films annealed at 550°C.

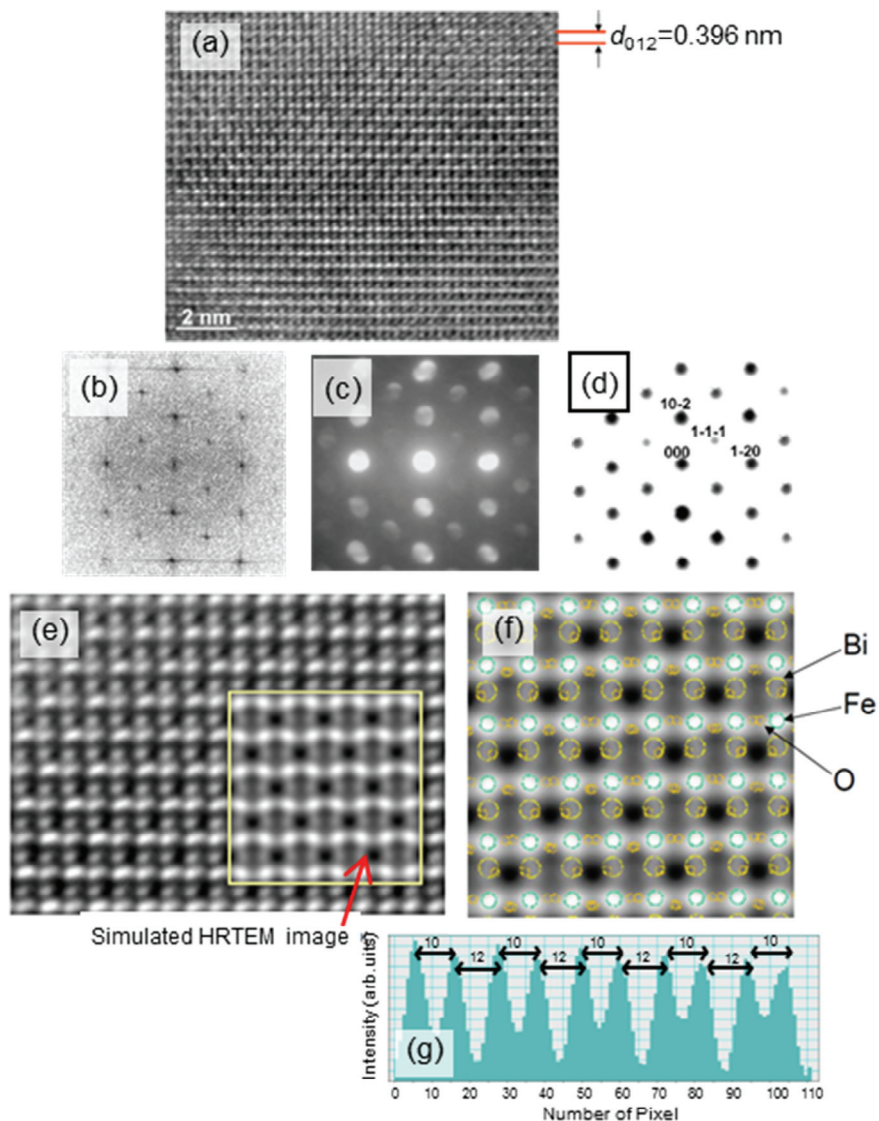


Fig. 8. (a) HRTEM image, (b) corresponding FFT pattern image, (c) NBD pattern, (d) simulated electron diffraction pattern, (e) simulated lattice fringe image embedded in observed HRTEM image, (f) atom position, and (g) distance between atoms.

Cross-sectional TEM observation was used to investigate the quality of the polycrystalline BiFeO<sub>3</sub> films annealed at 550°C. The observation, presented in Fig 7(a) indicates that the bottom Pt layer shows the (111) texture structure, which is consistent with the XRD profiles. High-resolution (HR) TEM was used to investigate the grain boundary phases in the polycrystalline structure within the square area outlined in Fig. 7(a). The HRTEM image of

the grain boundary [Fig. 7(b)] and fast Fourier transform (FFT) pattern from two grains [Fig. 7(c), 7(d)] are shown. These investigations show that high quality polycrystalline BiFeO<sub>3</sub> films were successfully fabricated by means of the CSD method

In the case of BiFeO<sub>3</sub>, crystal symmetry exerts a strong influence on the ferroelectric polarization; (Ederer *et al.*, 2005) therefore, the crystal symmetry of BiFeO<sub>3</sub> was determined by simulation of the HRTEM images and nanobeam diffraction (NBD) patterns. Figure 8(a) shows the HRTEM image (a), corresponding FFT pattern (b), NBD pattern (c), simulated electron diffraction pattern (d), simulated lattice fringe image embedded in the observed HRTEM image (e), atom position (f), and distance between atoms (g). The HRTEM image contains periodic lattice fringes along the [012] direction with spacings of approximately 0.396 nm which is in good agreement with Kubel's report. (Kubel *et al.*, 1990) The electron diffraction pattern was simulated using the MacTEMPAS computer program by applying the multislice method (Kirkland *et al.*, 1998) and using the lattice parameters of the rhombohedral *R3c* and the tetragonal *Pbmm* lattices. (Kubel *et al.*, 1990, Wang *et al.*, 2003, Yun *et al.*, 2004) A comparison of the simulated electron diffraction pattern with the NBD and FFT patterns shows that the BiFeO<sub>3</sub> layer has a rhombohedral *R3c* structure. The simulated lattice fringe image of *R3c* corresponded exactly to the HRTEM image. The position of the atoms in the HRTEM image and the periodicity of the atoms based on *R3c* symmetry are indicated in Fig. 8(d) and 8(e).

Figure 9 shows the AFM and SEM images of the BiFeO<sub>3</sub> films as a function of annealing temperature. At temperatures of 400 and 450°C [Fig. 9(a) and 9(b)], a homogeneous surface was formed and no obvious grains were detected for the sample annealed at 400°C. The appearance of grains was observed in samples annealed at temperatures above 450°C. In the wide area AFM images, very little variation in the grain size was seen with an increase in the annealing temperature between 450 and 750°C. In contrast, the expanded AFM images show grains with sizes of several tens of nanometers, indicating that the micron sized grains consisted of an agglomeration of small grains, several tens of nanometers in diameter. [Fig. 9(c)] The size of the smaller grains increased as the annealing temperature increased. In particular, there was a drastic increase in the size of the smaller grains above 700°C. The sample annealed at 800°C could not be analyzed using AFM because the specimen was easily stripped away from the substrate. Therefore, the surface morphology of this specimen was observed using SEM. [Fig. 9(i)] Square-shaped grains were observed after annealing at 800°C; this can be identified as the secondary phases of  $\alpha$ -Fe<sub>2</sub>O<sub>3</sub> and BiPt. These observations indicate that the microstructure of BiFeO<sub>3</sub> films is drastically influenced by the annealing temperature.

There are many reports that focus on leakage current density; however, only a few of these have discussed the mechanism underlying the leakage current. Hence, the topic of leakage current density is still open to discussion and can be considered an important issue from the viewpoint of memory applications. Herein, the leakage current mechanism operating in the BiFeO<sub>3</sub> film is discussed as a function of the annealing temperature. Figure 10 shows (a) the leakage current density ( $J$ ) v.s. electric field ( $E$ ), (b) Schottky emission plot ( $\log J$  v.s.  $E^{1/2}$ ), (c) Ohmic plot (double logarithm plots), (d) Fowler-Nordheim plot ( $\log(J/E^2)$  vs  $1/E$ ), (e) Poole-Frenkel plot ( $\log(J/E)$  v.s.  $E^{1/2}$ ) plots, and (f) space-charge-limited current ( $\log(J/E)$  v.s.  $\log V$ ) for the BiFeO<sub>3</sub> film annealed at various temperatures. (Naganuma & Okamura, JAP 2007, Naganuma *et al.*, IF 2007) The measurement was carried out at RT. As shown in Fig. 10(a), the leakage current density of BiFeO<sub>3</sub> films tended to increase with increasing annealing

temperature. Careful observation of the slopes of the curves shows three steps corresponding to three kinds of leakage current mechanisms. First, we discuss the interfacial limited leakage current mechanism, taking into consideration Schottky emission. Using Schottky emission, the relative permittivity and barrier height were estimated to be 0.4 and 0.6 eV, respectively [Fig. 10(b)]. On the other hand, the inclination at a low electric field in the double logarithm plots, as shown in Fig. 10(c) was around 1.1–1.2. Compared to the Schottky-emission conduction, Ohmic conduction seems to be adaptable at low electric field. The inclination at a high electric field in the double logarithm plots in Fig. 10(b) was around 2, indicating that the leakage current behavior at high electric field was dominated

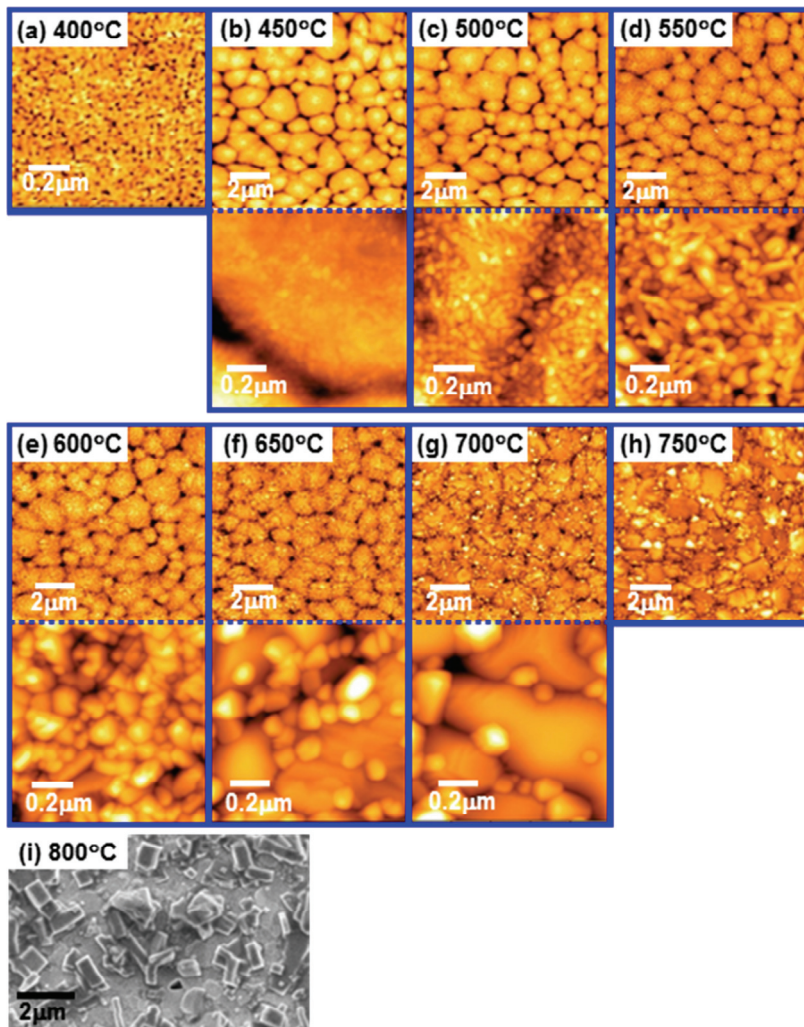


Fig. 9. AFM and SEM images of the BiFeO<sub>3</sub> films as a function of annealing temperature.

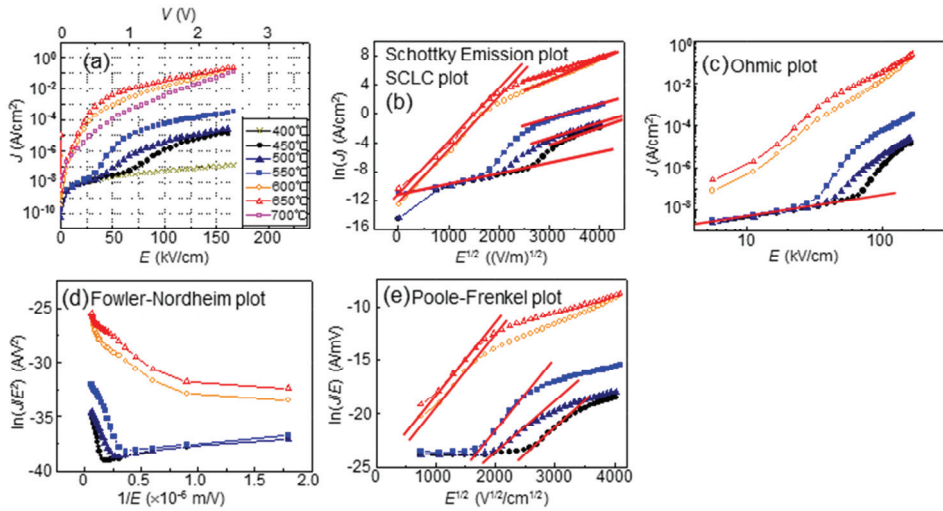


Fig. 10. Leakage current mechanism for BiFeO<sub>3</sub> at various annealing temperatures.

by space-charge-limited current (SCLC). Next, we discuss the leakage current mechanism before the start of the SCLC. The barrier height deduced from the Fowler-Nordheim equation was around 0.019 eV [Fig. 10(d)]. This barrier height is quite small for Fowler-Nordheim tunneling conduction. The relative permittivity calculated using the Poole-Frenkel equation was around 0.1–0.2 [Fig. 10(e)]. Here, it is thought that the leakage current mechanism changed as follows: Ohmic conduction occurred at a low electric field; Poole-Frenkel trap limited conduction appeared as the electric field increased; and SCLC was activated at a high electric field.

Figure 11 shows the  $P$ - $E$  hysteresis loops of the BiFeO<sub>3</sub> films annealed at various temperatures. The  $P$ - $E$  hysteresis loop was measured at RT using a frequency of 2 kHz

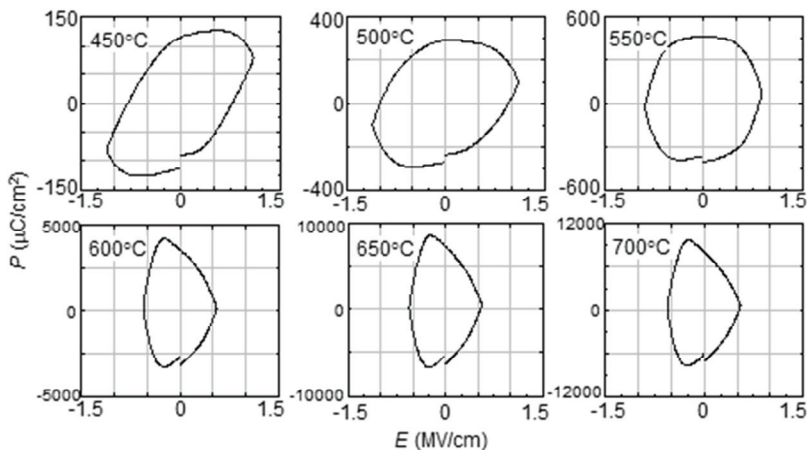


Fig. 11. Ferroelectric ( $P$ - $E$ ) hysteresis loops of the BiFeO<sub>3</sub> films annealed at various temperatures.

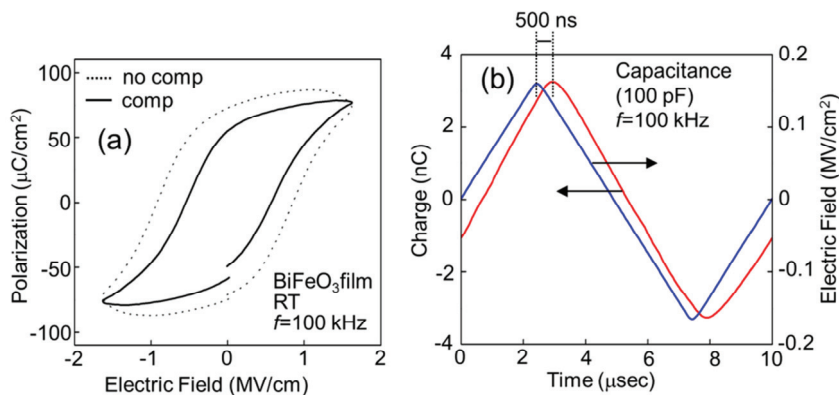


Fig. 12. (a) Compensation of phase delay using high frequency 100 kHz system. Solid line indicates the use of phase-delay compensation, and the dotted line indicates the case in which there was no compensation. (b) changes in the electric field and polarization against time for standard capacitor.

(aixACCT TF-2000). The  $P$ - $E$  hysteresis loop has an unsaturated, loose shape even in the case of the BiFeO<sub>3</sub> film annealed at 450°C, which is indicative of a low leakage current density.

Two methods were employed in order to reduce the influence of leakage current density on the  $P$ - $E$  hysteresis measurements: (i) a high frequency system was used and (ii) measurements were taken at low temperatures. Figure 12(a) shows the  $P$ - $E$  hysteresis loops for BiFeO<sub>3</sub> film annealed at 450°C; the loops were obtained using the 100 kHz high frequency system. The solid line indicates the use of phase-delay compensation, and the dotted line indicates the case in which there was no compensation.

The compensation of phase delay from the high voltage amplifier and circuit cable was estimated by using a standard capacitor of 100 pF. The changes in the electric field and polarization against time are shown in Fig. 12(b). Changes in polarization appear to be delayed with respect to the changes in the applied electric field by approximately 500 nsec. When a phase delay compensation of 500 nsec was applied, the shape of the  $P$ - $E$  hysteresis loop was improved to high squareness when compared with the low frequency measurement system, as shown in Fig. 11. The details of the compensation method are addressed elsewhere (Naganuma *et al.*, JCSJ 2010).

Figure 13 show the  $P$ - $E$  hysteresis loops for BiFeO<sub>3</sub> films annealed at various temperatures, measured at RT using a high frequency 100 kHz system. For the BiFeO<sub>3</sub> films annealed at 400°C, the paraelectrics due to amorphous structure was observed. The  $P$ - $E$  hysteresis begins to be observed from 450°C and a relatively high remanent polarization of 80-90 μC/cm<sup>2</sup> was obtained for the BiFeO<sub>3</sub> film annealed at 500°C. However, it seems that leakage current still influences the shape of the hysteresis loops for films annealed at high temperatures. Above 600°C, the  $P$ - $E$  loops assume an unsaturated, loose shape and spontaneous polarization cannot be estimated. Figure 13(h) shows the electric field ( $E$ ) dependence of remanent polarization ( $P_r$ ) estimated from the  $P$ - $E$  hysteresis loops. The  $P_r$  increased with increasing electric field and there was no clear tendency to saturate. It can thus be seen that the influence of leakage current on the  $P$ - $E$  hysteresis loops was clearly reduced by increasing the measurement frequency.

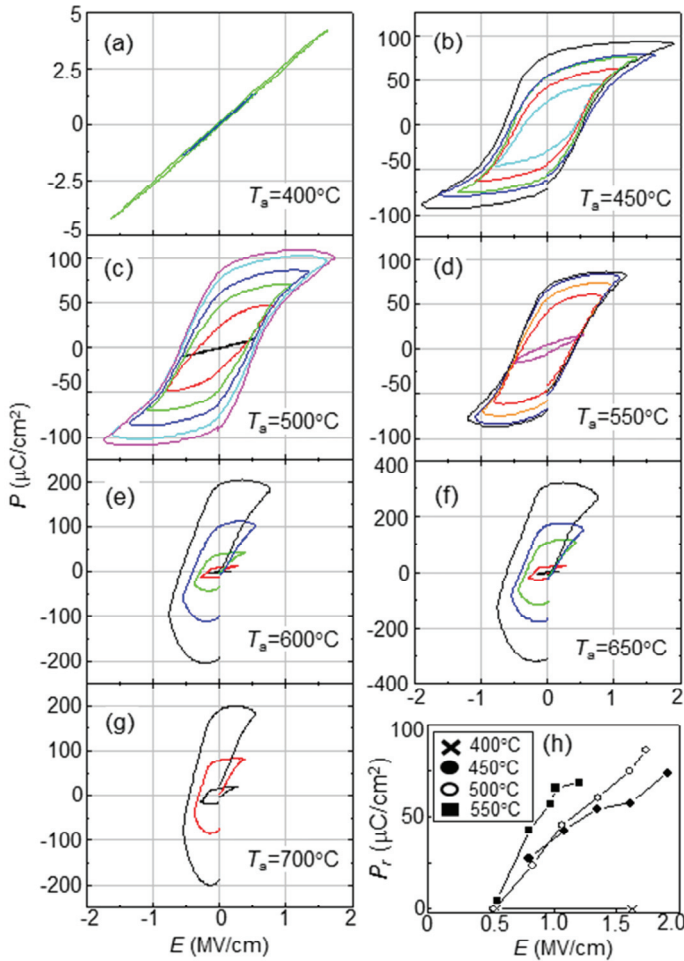


Fig. 13.  $P$ - $E$  hysteresis loops measured at RT using high frequency 100 kHz system for  $\text{BiFeO}_3$  films annealed at various temperatures.

Figure 14 shows the  $P$ - $E$  hysteresis loops for  $\text{BiFeO}_3$  films annealed at various temperatures, measured at  $-183^\circ\text{C}$  using a measurement frequency of 1 kHz. At  $-183^\circ\text{C}$ , the leakage current density was significantly decreased to below  $1.0 \times 10^{-8} \text{ A/cm}^2$  at 0.1 MV/cm; therefore, the influence of leakage current density on the ferroelectric measurement could be excluded. By decreasing the measurement temperature, the  $P$ - $E$  hysteresis loops could be observed for the samples annealed in the temperature range between  $450$  and  $750^\circ\text{C}$ . No ferroelectricity was observed at the annealing temperature of  $800^\circ\text{C}$  due to the disappearance of the  $\text{BiFeO}_3$  phase. The shape of the  $P$ - $E$  hysteresis loops varied for each annealing temperature. Double  $P$ - $E$  hysteresis loops were observed for the samples annealed at  $450^\circ\text{C}$ , whereas the shape of the  $P$ - $E$  hysteresis loop for the sample annealed at  $500^\circ\text{C}$  was insufficiently saturated. This is

because the electric coercive field was high for the sample annealed at the lower temperature, and it was not enough to saturate the polarization by the electric field at around 1.3 MV/cm. The remanent polarization and electric coercive field as a function of the annealing temperature are summarized in Fig. 14(g). The remanent polarization of the BiFeO<sub>3</sub> films increased linearly with increasing annealing temperature up to 650°C and decreased above the annealing temperature of 700°C. The electric coercivity field of the BiFeO<sub>3</sub> films decreased as the annealing temperature increased. The highest remanent

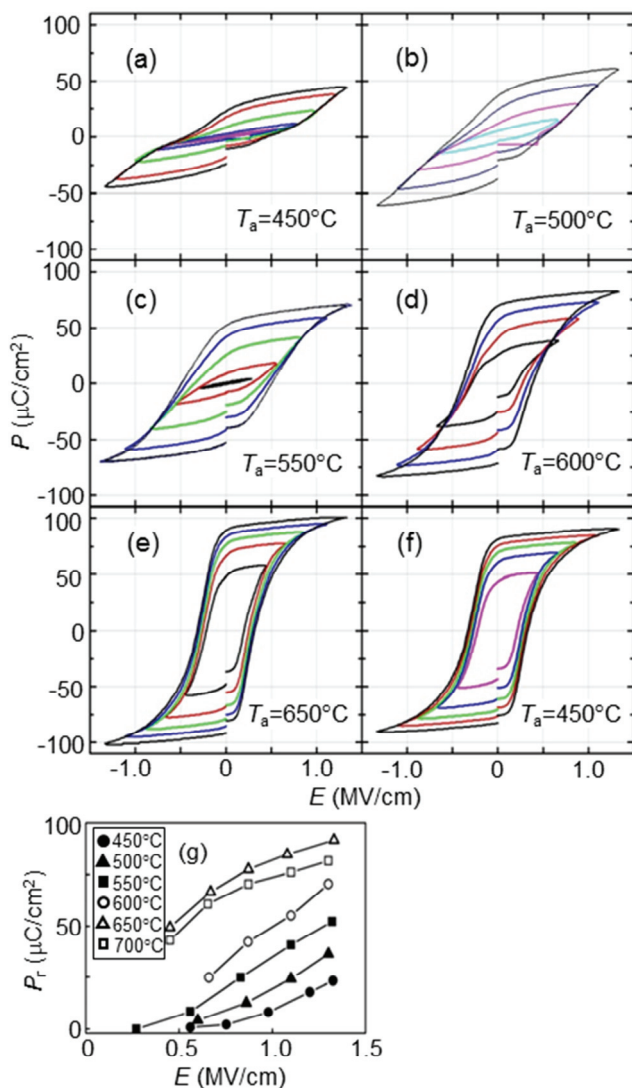


Fig. 14.  $P$ - $E$  hysteresis loops of BiFeO<sub>3</sub> films annealed at various temperatures, measured at -183°C.

polarization, as well as the lowest electric coercive field of the BiFeO<sub>3</sub> film appeared at the annealing temperature of 650°C. The remanent polarization and the electric coercive field were 89 μC/cm<sup>2</sup> and 0.31 MV/cm, respectively, which are comparable to the recent reports of high remanent polarization. These results reveal that the ferroelectric properties such as remanent polarization and the electric coercive field of the BiFeO<sub>3</sub> films are strongly affected by the annealing temperature of the CSD processes even though single phase, the polycrystalline BiFeO<sub>3</sub> films were formed.

Figure 15 shows the magnetization ( $M$ - $H$ ) curve at RT for the BiFeO<sub>3</sub> film annealed at 650°C. The magnetization increased linearly at high magnetic field due to the antiferromagnetic spin structure. In the zero fields region, nonlinear hysteresis with a very small remanent magnetization was observed, which might be considered to be the weak ferromagnetism due to DM interaction (Dzyaloshinskii, 1957, Moriya, 1960) or strain induced magnetization. Interestingly, non-linearity is often reported near the zero fields for the film form of BiFeO<sub>3</sub>; (Kiselev *et al.*, 1963, Naganuma *et al.*, TUFFC 2008, Yun *et al.*, 2004, Bai *et al.*, 2005) however, non-linearity has not been observed in the case of bulk BiFeO<sub>3</sub>. (Bai *et al.*, 2005, Lebeugle *et al.*, 2007) This means that the non-linearity of the  $M$ - $H$  curves is mainly affected by strain-induced changes of the spiral structure in the film. There are several reports which discuss the strain induced changes of the spiral structure in BiFeO<sub>3</sub> films. However, the details of the process are still debatable.

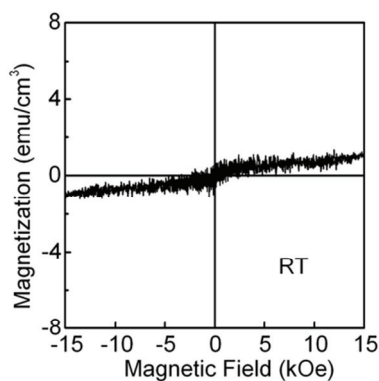


Fig. 15. Magnetization ( $M$ - $H$ ) curve at RT for BiFeO<sub>3</sub> film annealed at 650°C.

### 3. Effect of $B$ -site substitution of Cr, Mn, Co, Ni, and Cu for Fe in BiFeO<sub>3</sub> on structural, electrical and magnetic properties

In the second section, single phase of polycrystalline BiFeO<sub>3</sub> films were successfully fabricated on Pt/Ti/SiO<sub>2</sub>/Si(100) substrates, and a high polarization of 89 μC/cm<sup>2</sup> with a switching field of 0.31 MV/cm was obtained at -183°C for films annealed at 650°C. However, the large leakage current, relatively large switching field of polarization, and antiferromagnetic spin configuration of BiFeO<sub>3</sub> films make it difficult to use these films in novel electrical applications such as spintronics devices. In this section, engineering of these physical properties is investigated by substitution of Fe in BiFeO<sub>3</sub> with various 3d transition metals. (Naganuma *et al.*, APL 2008, Naganuma *et al.*, JAP 2008, Naganuma *et al.*, JE 2009, Naganuma *et al.*, JMSJ 2009)

Cr, Mn, Co, Ni, and Cu substituted BiFeO<sub>3</sub> films (200 nm in thickness) were fabricated by the CSD method onto Pt/Ti/SiO<sub>2</sub>/Si (100) substrates followed by post annealing in air at 650°C for 10 min. The composition of the E-MOD was adjusted as follows: Bi(Fe<sub>0.95</sub>M<sub>0.05</sub>)O<sub>3</sub> where M = Cr, Mn, Co, Ni, and Cu. The film structure was confirmed by the  $\theta/2\theta$  XRD pattern. The ferroelectric properties were measured using ferroelectric testers (TOYO Corporation: FCE-1A for RT and aixACCT: TF-2000 for -183°C). The leakage current was measured using a picoampere meter and the pulse response forms of the PUND measurement. The details of the estimation method are discussed elsewhere (Naganuma *et al.*, APEX 2008). The magnetic properties were measured using a VSM at RT for the in-plane direction.

Figure 16(a) shows the XRD profiles of Cr, Mn, Co, Ni, and Cu of 5 at. % substituted BiFeO<sub>3</sub> films: [Bi(M<sub>0.05</sub>Fe<sub>0.95</sub>)O<sub>3</sub>, M= Cr, Mn, Co, Ni, and Cu]. Diffraction peaks caused by the BiFeO<sub>3</sub> structure were observed, indicating the formation of a polycrystalline structure. The (012) diffraction peak of the Co-substituted BiFeO<sub>3</sub> film was stronger than those of the other substitutive metals; this implies the formation of a 012-textured structure. In the case of Cr-substituted BiFeO<sub>3</sub>, a secondary phase of Bi<sub>7</sub>CrO<sub>12.5</sub> was formed in addition to the BiFeO<sub>3</sub> phase.

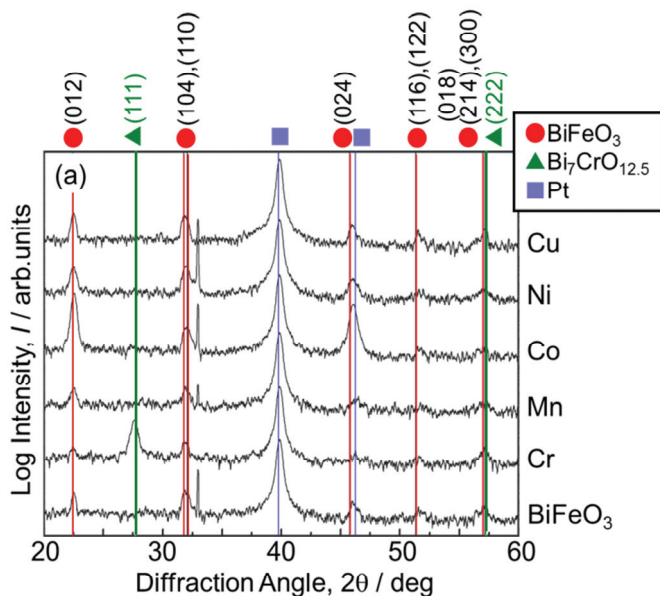


Fig. 16. XRD profiles of Cr, Mn, Co, Ni, and Cu of 5 at. % substituted BiFeO<sub>3</sub> films [Bi(M<sub>0.05</sub>Fe<sub>0.95</sub>)O<sub>3</sub>, M= Cr, Mn, Co, Ni, and Cu].

Figure 17 shows the leakage current density of Bi(M<sub>0.05</sub>Fe<sub>0.95</sub>)O<sub>3</sub> films measured with the picoampere meter at RT. The leakage current density of the Ni-substituted BiFeO<sub>3</sub> film could not be precisely evaluated because of a considerably high leakage current. The leakage current density of the pure BiFeO<sub>3</sub> film increased more rapidly than those of the films with substitutions in response to increases in the electric field. However, even for the

transmission metal (TM) substituted films, it was difficult to measure the leakage current density above 0.2 MV/cm using the picoampere meter because of dielectric breakdown. In order to evaluate the leakage current density at higher electric fields, the leakage current density was estimated from the pulse response forms of the PUND measurements. In this way, the leakage current at high electric field can be measured by the reduction in the Joule heat damage. (Naganuma *et al.*, APEX 2008) An electric field more than 0.36 MV/cm could be applied, which is higher than that measured by the picoampere meter. Figure 17(b) shows the leakage current density estimated from the response forms of the up pulse. The leakage current density of the Ni-substituted BiFeO<sub>3</sub> film could also be measured by this method, and it was found to be considerably higher than that of the pure BiFeO<sub>3</sub> film. This indicates that the PUND method can be used for materials with a high leakage current density. The substitutions of Mn, Co, and Cu to the BiFeO<sub>3</sub> films effectively reduced the leakage current density in the high electric field region.

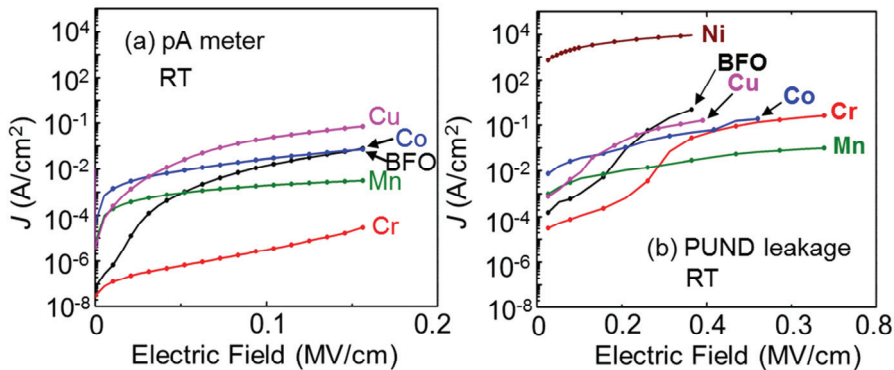


Fig. 17. (a) Leakage current density of Bi(M<sub>0.05</sub>Fe<sub>0.95</sub>)O<sub>3</sub> films measured with the picoampere meter, and (b) by PUND measurement.

Figure 18 shows the ferroelectric hysteresis loops of the Bi(M<sub>0.05</sub>Fe<sub>0.95</sub>)O<sub>3</sub> films measured with a 100 kHz driving system at RT using the ferroelectric tester, and those measured at -183°C using a 2 kHz driving system. Ferroelectric hysteresis loops could not be observed for the Ni-substituted BiFeO<sub>3</sub> film. The pure BiFeO<sub>3</sub> film showed an expanded hysteresis loop at RT [Fig. 18(a)], which could be attributed to the leakage current component. The squareness of the ferroelectric hysteresis loops was clearly improved by the substitution of Mn, Co, and Cu to the BiFeO<sub>3</sub> films. This squareness is attributed to the reduction in the leakage current density in the high electric field region. Although the leakage current density is reduced by the substitution of Mn, Co, and Cu, it is still difficult to apply a high electric field at RT. Therefore, the ferroelectric hysteresis loops were measured at -183°C using the 2 kHz driving system [Fig. 18(b)]. At -183°C, the leakage current density was considerably lower than the inversion current due to domain switching, as inferred from the current response of the PUND measurements. In fact, the ferroelectric hysteresis loops did not expand and showed high squareness at -183°C.  $E_c$  versus  $E$  plots [Fig. 18(c)] show that the  $E_c$  was reduced by the substitution of Co and Cu. In contrast, the substitution of Mn and Cr to the BiFeO<sub>3</sub> films produced a higher  $E_c$  compared to the pure BiFeO<sub>3</sub> film. In the Co- and Cu-substituted BiFeO<sub>3</sub> films, the  $P_r$  versus  $E$  plots [Fig. 18(d)] almost overlapped up to 1.3

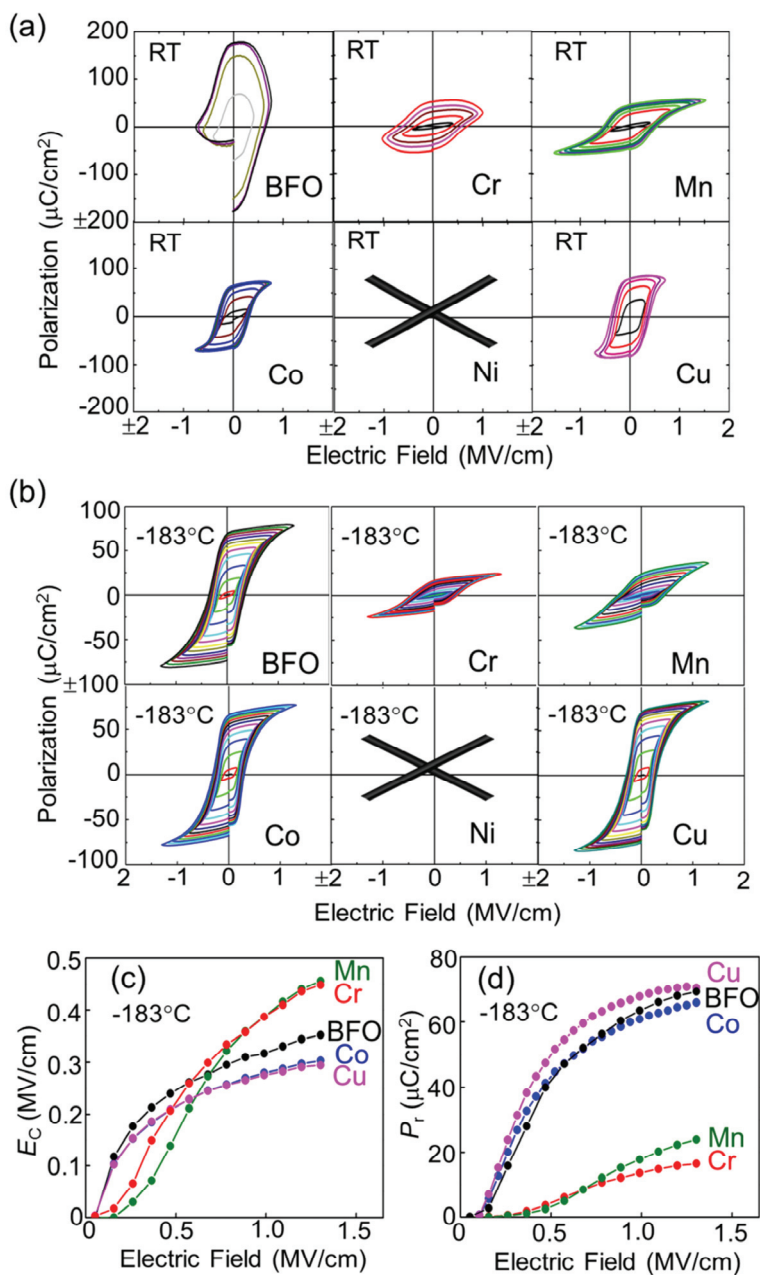


Fig. 18. Ferroelectric hysteresis loops of the Bi(M<sub>0.05</sub>Fe<sub>0.95</sub>)O<sub>3</sub> films measured at RT using the ferroelectric tester with a 100 kHz driving system and measured at -183°C using a 2 kHz driving system.

MV/cm. Thus, Co and Cu substitution reduced the  $E_c$  of polycrystalline  $\text{BiFeO}_3$  films without reducing  $P_r$ , which is suitable for memory and/or piezoelectric devices.

Figure 19 shows the magnetization curves of the  $\text{Bi}(M_{0.04}\text{Fe}_{0.96})\text{O}_3$  films measured at RT. As mentioned in the previous section, the pure  $\text{BiFeO}_3$  films showed small magnetization. However, the substitution of Co, Ni, and Cu caused an increase in the magnetization, indicating substitution of these TM into the B sites of Fe, although it was not clear whether all the TMs were substituted into the B-sites. In the case of Co-substituted  $\text{BiFeO}_3$ , there was an increase in magnetization accompanied by the appearance of spontaneous magnetization and the coercive field of 2 kOe was observed at RT. In addition, according to other report, (Zhang *et al.*, 2010) clear observation of the magnetic domain structure using magnetic force microscopy (MFM) at RT was observed in 4 at.% Co-substituted  $\text{BiFeO}_3$  has been reported. Based on these results, the increased magnetization in Co-substituted  $\text{BiFeO}_3$  was confirmed by both macroscopic and local measurement methods.

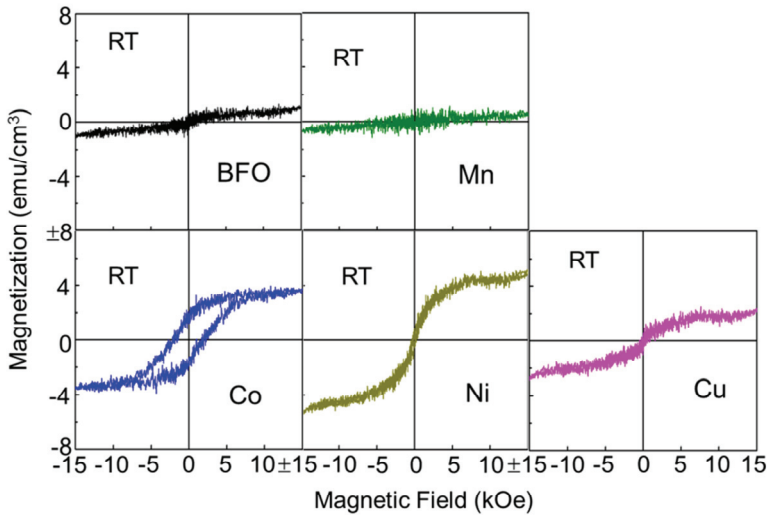


Fig. 19. Magnetization curves of the  $\text{Bi}(M_{0.05}\text{Fe}_{0.95})\text{O}_3$ ,  $M = \text{Cr, Mn, Co, Ni, and Cu}$  films measured at RT.

Cross-sectional TEM observation was carried out in order to clarify the influence of magnetic impurities on spontaneous magnetization in Co-substituted  $\text{BiFeO}_3$  films. (Naganuma *et al.*, JMSJ 2009) Co-substituted  $\text{BiFeO}_3$  film was deposited on a Pt/Ti/ $\text{SiO}_2$ /Si (100) substrate having a relatively flat surface. Grains of approximately hundreds of nm in size were formed. [Fig. 20(a)] Obvious secondary phases could not be observed in the wide area images. Figure 20(b) shows the NBD patterns for the  $[-1\ 3\ -2]$  direction of the Co-substituted  $\text{BiFeO}_3$  layer. Analysis of the NBD pattern shows that the crystal symmetry is rhombohedral with a  $R3c$  space group, and the lattice parameters are  $a = 0.55\text{ nm}$ ,  $c = 1.39\text{ nm}$ . The high-resolution TEM image around the grain boundary is shown in Fig. 20(c). Grain boundary formation is evident but the grain boundary phases could not be observed in this film. Therefore, it can be inferred that Co was substituted for Fe in  $\text{BiFeO}_3$ , and the magnetization enhancement might not be attributed to magnetic impurity phases. It was

concluded that the substitution of small of Co into the *B*-sites of BiFeO<sub>3</sub> could improve the leakage current property, reduce the electric coercive field without degrading the remanent polarization, and induce spontaneous magnetization at RT.

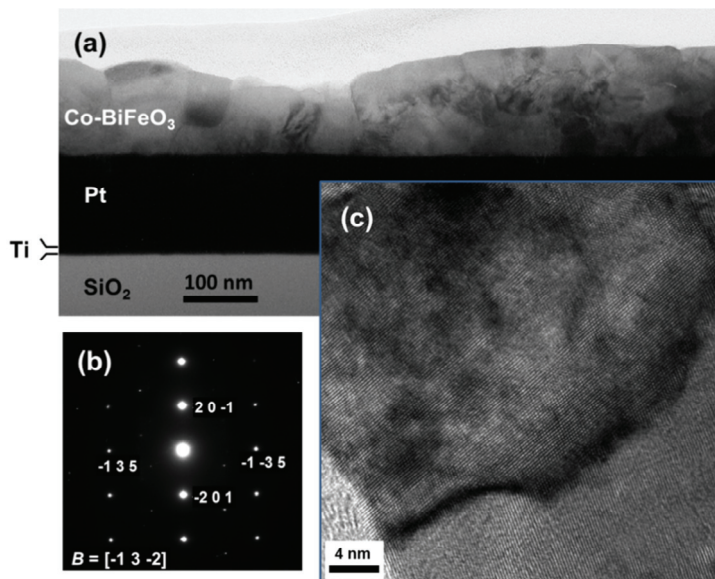


Fig. 20. Cross sectional TEM images of polycrystalline Co-BiFeO<sub>3</sub> film.

#### 4. Multifunctional characteristics of BiCoO<sub>3</sub>-BiFeO<sub>3</sub> solid solution epitaxial films

As clarified in the third section, the 4 or 5 at.-%-Co-substituted BiFeO<sub>3</sub> polycrystalline films exhibited excellent electrical and magnetic characteristics. Substitution with larger amounts of Co was expected to result in further enhancement of the electrical and magnetic properties. It should be noted that high-pressure behavior becomes dominant in the highly Co-substituted BiFeO<sub>3</sub> films due to the high-pressure phase of BiCoO<sub>3</sub>. In fact, a maximum of approximately 8 at.-% Co can be substituted for Fe in the case of polycrystalline films while maintaining a single phase, whereas secondary phases of BiO<sub>x</sub> are formed at Co concentrations above 8 at.-%. (Naganuma *et al.*, JAP 2008) Because the character of BiCoO<sub>3</sub> is strongly influenced at high Co-substitution, hereafter, we refer to highly Co-substituted BiFeO<sub>3</sub> films as BiCoO<sub>3</sub>-BiFeO<sub>3</sub>. In one of our studies, (Naganuma *et al.*, JAP 2009) the high-pressure phase of BiMnO<sub>3</sub> was successfully stabilized in a thin-film form by using epitaxial strain. In accordance with this study, solid solution films of BiCoO<sub>3</sub>-BiFeO<sub>3</sub> having a high BiCoO<sub>3</sub> content could also be stabilized on SrTiO<sub>3</sub> (100) single crystal substrates by epitaxial strain. In this section, the structural, (Yasui *et al.*, JJAP 2007) ferroelectric, (Yasui *et al.*, JJAP 2008, Yasui *et al.*, JAP 2009) and magnetic properties (Naganuma *et al.*, JAP 2011) of epitaxial BiCoO<sub>3</sub>-BiFeO<sub>3</sub> films grown on SrTiO<sub>3</sub> substrates up to a BiCoO<sub>3</sub> concentration of ~58 at.-% are systematically investigated. The BiFeO<sub>3</sub> - BiCoO<sub>3</sub> solid solution films were grown on SrTiO<sub>3</sub> (100) substrates at 700°C by metalorganic chemical vapor deposition (MOCVD) established in Funakubo laboratory, and

Bi $[(\text{CH}_3)_2(2 - (\text{CH}_3)_2\text{NCH}_2\text{C}_6\text{H}_4)]$ , Fe $(\text{C}_2\text{H}_5\text{C}_5\text{H}_4)_2$ , Co $(\text{CH}_3\text{C}_5\text{H}_4)_2$  and oxygen gas was used as the source materials. A vertical glass type reactor maintained at a pressure of 530 Pa was used for the film preparation. The films were deposited by MOCVD using pulse introduction of the mixture gases with Bi, Fe, and Co sources (pulse-MOCVD). The thickness of these films was approximately 200 nm. (Yasui *et al.*, JJAP 2007) The crystal structure of the deposited films was characterized by high-resolution XRD (HRXRD) analysis using a four-axis diffractometer (Philips X'pert MRD). HRXRD reciprocal space mapping (RSM) around SrTiO<sub>3</sub> 004 and 204 was employed for a detailed analysis of crystal symmetry. The cross-sectional TEM (Hitachi HF-2000) observation working at 200 kV was used for microstructural analysis. The crystal symmetry was also identified using Raman spectroscopy by K. Nishida. (Yasui *et al.*, JJAP 2007) Raman spectra were measured using a subtractive single spectrometer (Renishaw SYSTEM1000) with a backward scattering configuration. A laser beam was focused on the film surface, and the beam spot was approximately 1  $\mu\text{m}$ . The measurement time was fixed at 100 s. The leakage current v.s. electrical field and  $P$ - $E$  loops were measured with a semiconductor parameter analyzer (HP4155B, Hewlett-Packard) and ferroelectric tester (TOYO Corporation, FCE-1A). The magnetic properties were measured in the in-plane direction using SQUID.

Figure 21 shows the typical  $\theta/2\theta$  and pole-figure HRXRD profiles of BiFeO<sub>3</sub> - BiCoO<sub>3</sub> solid solution films (BiCoO<sub>3</sub> concentrations of 0, 16, 21, and 33 at.%) grown on SrTiO<sub>3</sub> (100) substrates. Although Bi<sub>2</sub>O<sub>3</sub> of secondary phase has a tendency to be formed at a high BiCoO<sub>3</sub> concentration, the single phase of BiFeO<sub>3</sub> - BiCoO<sub>3</sub> was successfully obtained by optimizing preparation conditions. The pole-figure HRXRD profiles indicate that all the films were epitaxially grown on SrTiO<sub>3</sub> (100) substrates. The magnified  $\theta/2\theta$  XRD profiles around BiFeO<sub>3</sub> - BiCoO<sub>3</sub> 002 indicate that the 002 peak shifted to high angle upon increasing the BiCoO<sub>3</sub> concentration, which indicates that the lattice constant for the out-of-plane direction approximated that of the SrTiO<sub>3</sub> substrates at high BiCoO<sub>3</sub> concentration.

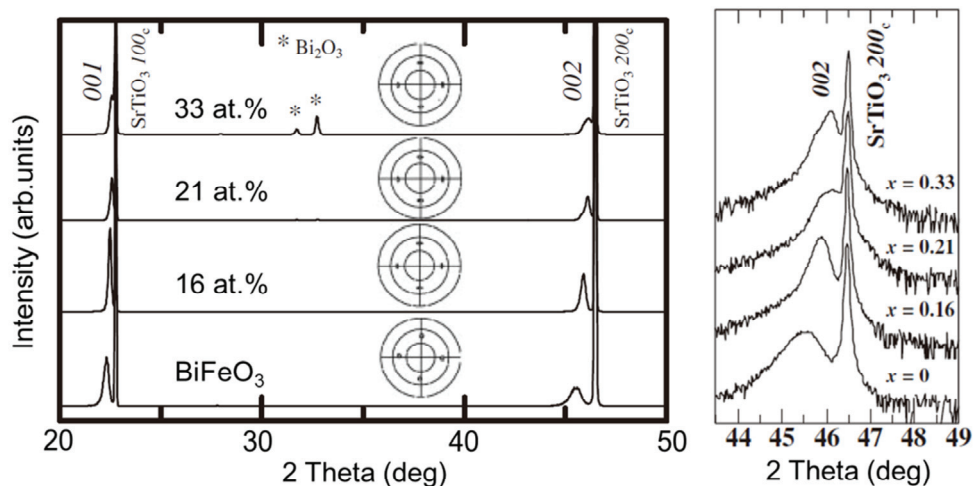


Fig. 21.  $\theta/2\theta$  and pole-figure HRXRD profiles of BiFeO<sub>3</sub> - BiCoO<sub>3</sub> solid solution films (BiCoO<sub>3</sub> concentration of 0, 16, 21, and 33 at.%) grown on SrTiO<sub>3</sub> (100) substrates.

The structures of the bulk forms of BiFeO<sub>3</sub> and BiCoO<sub>3</sub> are rhombohedral and tetragonal, respectively. Conventional  $\theta/2\theta$  XRD measurement cannot be used to identify whether the crystal symmetry is rhombohedral or tetragonal in the case of the BiFeO<sub>3</sub> – BiCoO<sub>3</sub> solid solution films. Therefore, HRXRD-RSM measurements around SrTiO<sub>3</sub> 004 and 204 were employed in the investigation of the crystal symmetry of the films. [Fig. 22] The pure BiFeO<sub>3</sub> film exhibited rhombohedral/monoclinic symmetry, as indicated by the existence of two asymmetric 204 spots in Fig. 22(b) and only one center spot of 004 in Fig. 22(a). This result is in agreement with that reported by Saito *et al.* for epitaxial BiFeO<sub>3</sub> films grown on SrRuO<sub>3</sub> (100)/SrTiO<sub>3</sub> (100) substrates. (Saito *et al.*, JJAP 2006) On the other hand, only single 204 and 004 spots were found for the film with a BiCoO<sub>3</sub> of 33 at.% [Figs. 22(g) and 22(h)], which indicates tetragonal crystal symmetry. Figures 22(c), 22(d), 22(e), and 22(f) show the HRXRD-RSM profiles for the films with 16 and 21 at.% BiCoO<sub>3</sub>, respectively. Three peaks including one parallel spot and two tilting spots with a SrTiO<sub>3</sub> [001] orientation for 204, in both films, represented the existence of a mixture of (rhombohedral/monoclinic) and tetragonal symmetries.

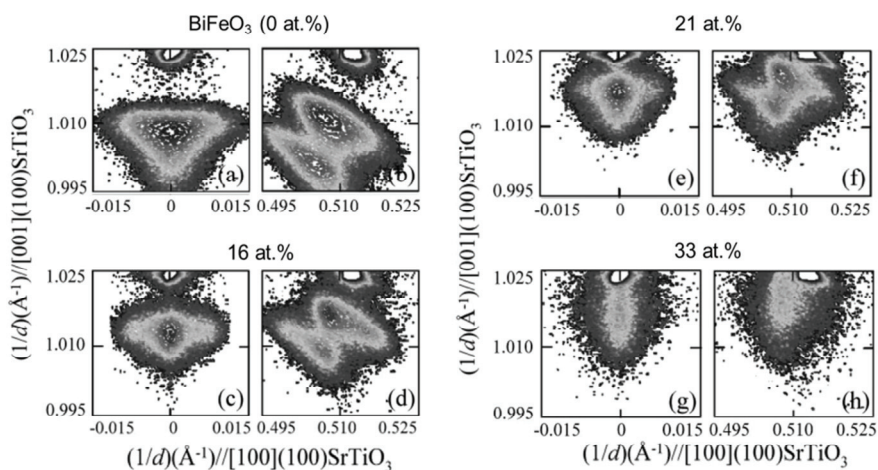


Fig. 22. HRXRD-RSM measurements around SrTiO<sub>3</sub> 004 and 204.

Raman spectroscopy was carried out in order to precisely check the change in crystal symmetry by K Nishida. (Yasui *et al.*, JJAP 2007) Raman spectra of the BiFeO<sub>3</sub>-BiCoO<sub>3</sub> films and that of the SrTiO<sub>3</sub> substrate are shown in Fig. 23. The SrTiO<sub>3</sub> substrate shows a peak at 81 cm<sup>-1</sup>, which is shifted to a value within 75-78 cm<sup>-1</sup> for the films with 0-33 at.% BiCoO<sub>3</sub>. It was confirmed that the peak observed for the films does not originate from the SrTiO<sub>3</sub> substrate. The decrease in the intensity of the SrTiO<sub>3</sub> peak with increasing film thickness for pure BiFeO<sub>3</sub> and the disappearance of the peak at ~600 cm<sup>-1</sup>, as shown in Fig. 23, are also in agreement with the above results. The typical rhombohedral symmetry observed for bulk BiFeO<sub>3</sub> was indicated for the pure BiFeO<sub>3</sub> film and 16 at.% BiCoO<sub>3</sub> film. Different patterns with rhombohedral symmetry were observed for the film with 33 at.% BiCoO<sub>3</sub>, which was shown to have tetragonal symmetry from the analysis of the HRXRD-RSM data. Furthermore, this peak of film was very similar to that of BiCoO<sub>3</sub> powder which has been confirmed to have tetragonal symmetry. For the films with 21 at.% BiCoO<sub>3</sub>, it was ascertained from Fig. 23 that

the tetragonal and rhombohedral symmetries coexisted, which is almost consistent with the findings of the HRXRD-RSM experiment. It was revealed that the phase transition in  $\text{BiFeO}_3$  -  $\text{BiCoO}_3$  from (rhombohedral/monoclinic) symmetry to tetragonal symmetry is similar to the morphotropic phase boundary (MPB) in  $\text{Pb}(\text{Zr}_x\text{Ti}_{1-x})\text{O}_3$ .

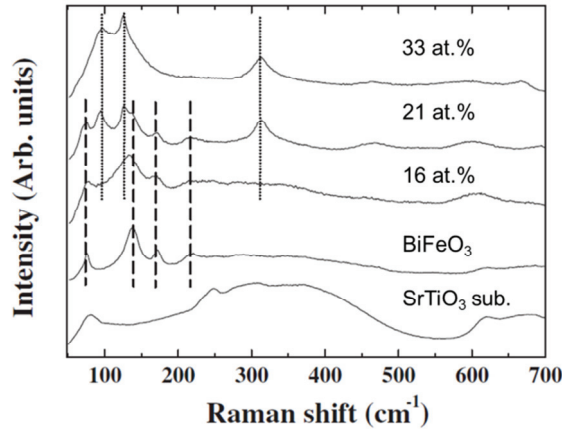


Fig. 23. Raman spectra of the  $\text{BiFeO}_3$ - $\text{BiCoO}_3$  films and the  $\text{SrTiO}_3$  substrate

Figure 24 shows the leakage current v.s. electrical field measurements taken at RT and  $P$ - $E$  hysteresis loops measured at  $-193^\circ\text{C}$  for the  $\text{BiFeO}_3$ - $\text{BiCoO}_3$  films. The leakage current

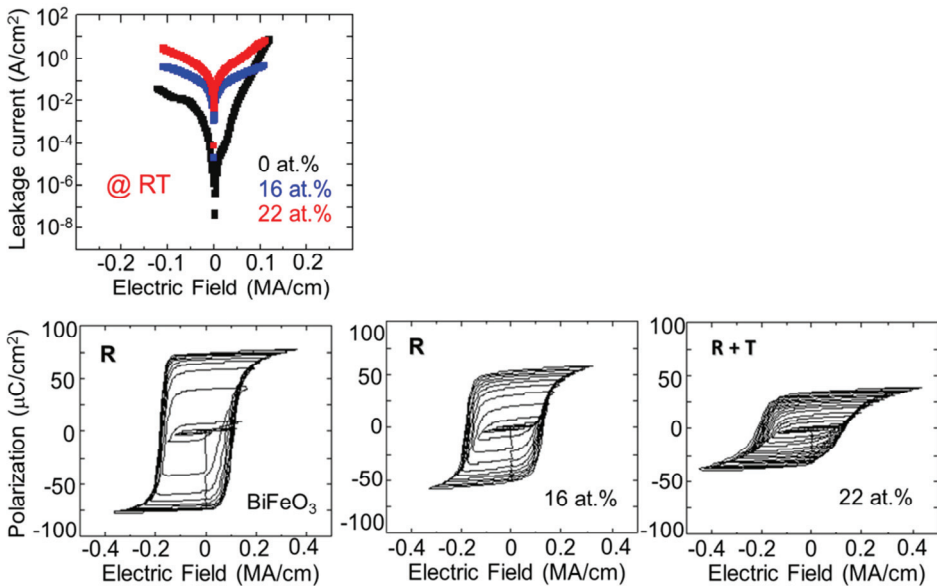


Fig. 24. Leakage current vs electric field measured at RT and  $P$ - $E$  hysteresis loops measured at  $-193^\circ\text{C}$  for the  $\text{BiFeO}_3$ - $\text{BiCoO}_3$  epitaxial films.

density at RT was very large for the BiFeO<sub>3</sub>-BiCoO<sub>3</sub> films with high BiCoO<sub>3</sub> concentration, and the leakage current density increased with increasing BiCoO<sub>3</sub> concentration. Because of the magnitude of the leakage current at a BiCoO<sub>3</sub> concentration of 33 at.%, a leakage current measurement could not be evaluated for this film at RT using the semiconductor parameter analyzer. Although the previous discussions indicated that a small amount of Co-substitution can effectively reduce the leakage current, it can be seen from these that a large amount of Co-substitution degraded the leakage current property. In order to reduce the influence of leakage current density on the *P-E* hysteresis measurement for samples having a high BiCoO<sub>3</sub> concentration, the *P-E* loops were measured at a low temperature of -193°C. The *P-E* loops observed at -193°C were of relatively high squareness and the influence of leakage current density on the *P-E* loops could be successfully excluded at this temperature, except for the BiCoO<sub>3</sub> concentration of 33 at.%. At -193°C, spontaneous polarization decreased, and the coercive field of BiFeO<sub>3</sub>-BiCoO<sub>3</sub> films increased with increasing BiCoO<sub>3</sub> concentration.

In the case of films with weak ferromagnetism such as BiFeO<sub>3</sub> films on substrates, eliminating the magnetization of the substrates from the films is important for accurate evaluation of the magnetic properties of the films. Therefore, here, the magnetic properties of SrTiO<sub>3</sub> substrates were carefully evaluated. Figure 25(a) shows the *M-H* curves for two different weights of SrTiO<sub>3</sub> substrates. The SrTiO<sub>3</sub> substrates show a negative slope due to diamagnetism. The magnetization at 50 kOe ( $M_{50\text{kOe}}$ ) for various weights of the SrTiO<sub>3</sub> substrates is plotted in Fig. 25(b). The absolute value of magnetization decreases with a decrease in the substrate weight, but some of the magnetization is retained even at zero weight. This retained magnetization is considered to be the background caused by the straw of the sample holder. In this study, standard straws produced by Quantum Design Inc. were used. Figure 25(c) shows the *M-H* curves of the SrTiO<sub>3</sub> substrate (weight = 0.0471 g) at 10 and 300 K. The hysteresis was not observed near the zero-field even at 10 K, indicating low magnetic impurity in the SrTiO<sub>3</sub> substrates and sample holder. The temperature dependence of  $M_{50\text{kOe}}$  is shown in Fig. 25(d). The diamagnetism slope decreased slightly with the temperature, however, it was not strongly influenced by the temperature. In this study, the magnetic properties of the films were carefully evaluated by eliminating SrTiO<sub>3</sub> substrate magnetization, and the same sample holder was used in all the magnetic measurements to exclude the effect of differences among straws.

Figure 26 shows the *M-H* curves measured at 300 K and the corresponding magnetic parameters that were estimated from the *M-H* curves. For pure BiFeO<sub>3</sub>, the magnetization increased linearly at a high magnetic field. [Fig. 26(a)] Small hysteresis was observed near the zero fields, which is relatively obvious compared with that of polycrystalline BiFeO<sub>3</sub> films. [Fig. 15] For BiCoO<sub>3</sub> concentrations of 18–25 at.%, magnetization was clearly enhanced, and  $H_c$  was observed. [Figs. 26(b) and 26(c)] For a BiCoO<sub>3</sub> concentration of 58 at.%, the *M-H* curve was almost identical to that of pure BiFeO<sub>3</sub> films. There is an apparent linear increase in the magnetization at high-magnetic field for all the specimens. It was reported that by substituting *A*-site Bi ions in bulk BiFeO<sub>3</sub> with Gd or Nd, spontaneous magnetization was observed, and the magnetization increased linearly in the high-magnetic field region, which is in agreement with our results. Although it is difficult to accurately evaluate the slope at a high field due to film form, it can be considered that the antiferromagnetic spin structure still remained after substitution at the *A*- or *B*-site. The magnetic parameters  $M_{50\text{kOe}}$ , remanent magnetization ( $M_r$ ), and coercive field ( $H_c$ ),

estimated from the  $M$ - $H$  curves are shown in Figs. 26(d) - 26(g).  $M_{10\text{kOe}}$  for polycrystalline  $\text{BiCoO}_3$ - $\text{BiFeO}_3$  films is also plotted in Fig. 26(e). The acronyms  $M_{50\text{kOe}}$  and  $M_{10\text{kOe}}$  indicate the magnetization at 50 kOe and 10 kOe, respectively. It was revealed that the  $M_{50\text{kOe}}$ ,  $M_r$ , and  $H_c$  values increased with the  $\text{BiCoO}_3$  concentration in the rhombohedral structure. This indicates the formation of ferro-like magnetic ordering.  $M_{50\text{kOe}}$ ,  $M_r$ , and  $H_c$  were maximally enhanced at MPB composition. For a  $\text{BiCoO}_3$  concentration above 30 at.%, corresponding to a tetragonal structure,  $M_{50\text{kOe}}$ ,  $M_r$ , and  $H_c$  showed a tendency to decrease. These results indicate that the enhancement of the magnetic ordering in the MPB cannot be explained simply by ferrimagnetism in a double-perovskite structure, because maximum magnetization does not take place at the half-composition. In addition, the clear relationship between the change in the magnetization and the phase transition shows that the enhancement of magnetization was not attributable to magnetic impurities.

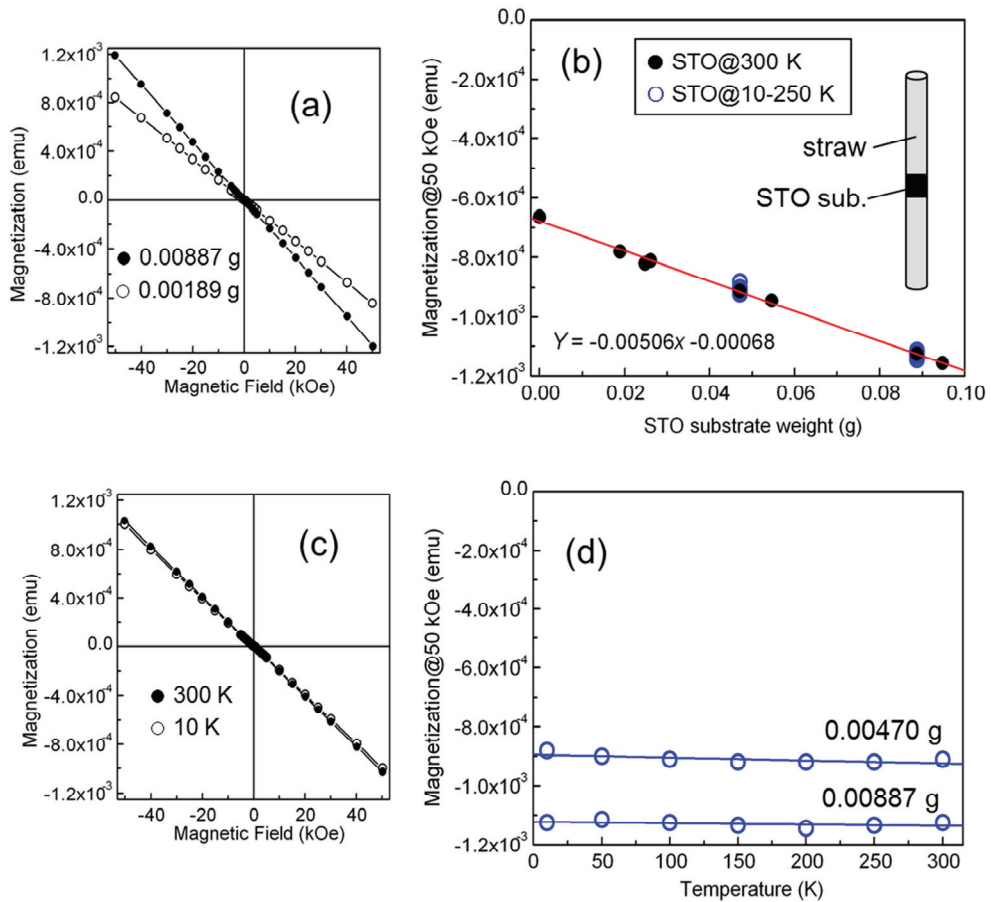


Fig. 25.  $\text{SrTiO}_3$  substrate weight dependence of magnetization at 300 K, (a, b), and temperature dependence of magnetization of  $\text{SrTiO}_3$  substrate with 0.00471 g (c, d).

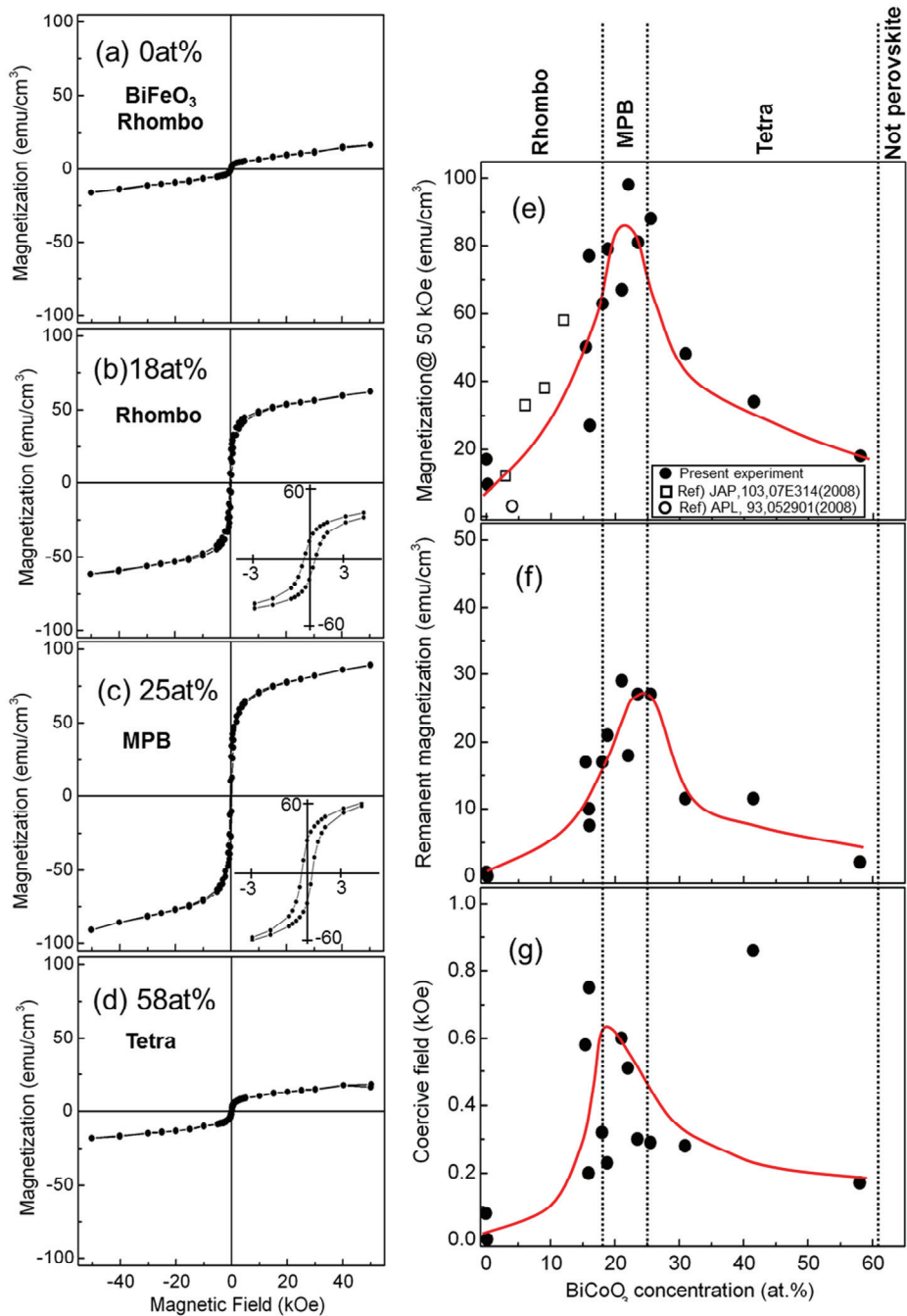


Fig. 26. *M-H* curves and corresponding magnetic parameters at 300 K.

Figure 27(a) and 27(b) show the  $M$ - $H$  curves for 300 and 10 K for the  $\text{BiFeO}_3$ - $\text{BiCoO}_3$  film with 15 at.% of  $\text{BiCoO}_3$  concentration. Interestingly, the slope at high magnetic field became larger when decreased the temperature to 10 K. Figure 27(c) shows the temperature dependence  $M_{50\text{kOe}}$ ,  $M_r$ , and  $H_c$ .  $M_{50\text{kOe}}$  and  $M_r$  increased with decreasing temperature; however, these were not show strong temperature dependence. In contrast,  $H_c$  clearly increased with decreasing temperature.

Because  $\text{BiFeO}_3$  and  $\text{BiCoO}_3$  are synthesized under atmospheric pressure and a very high pressure phase, respectively, it is possible that the formation of magnetic impurities such as Co,  $\text{CoFe}_2\text{O}_4$ , and  $\text{Fe}_3\text{O}_4$  etc., may adversely affect the magnetic properties at high concentrations of  $\text{BiCoO}_3$ . In our previous studies, apparent magnetic impurities were not observed in the XRD measurement; however, nanosized magnetic particles are difficult to detect by XRD measurements. The superparamagnetic limit is a few nanometers in diameter for Co,  $\text{CoFe}_2\text{O}_4$ , and  $\text{Fe}_3\text{O}_4$  etc. Particles with such small sizes can be detected by TEM. Therefore, the microstructure of the film was confirmed by a cross-sectional TEM observation for a  $\text{BiCoO}_3$  concentration of 17 at.%. [Fig. 28] No obvious magnetic impurities were observed in the TEM image, [Fig. 28(a)] and there was no diffraction spot attributed to magnetic impurities in the NBD pattern. [Fig. 28(b)] Our previous studies on nanoparticles suggest that particles that are a few nanometers in size can be confirmed by NBD, indicating that the influence of magnetic impurities might be ignored in our discussion. Although a further detailed investigation of the microstructure by high-resolution TEM observation is necessary, the enhancement of the magnetic properties might be attributable to ferro-like magnetic ordering.

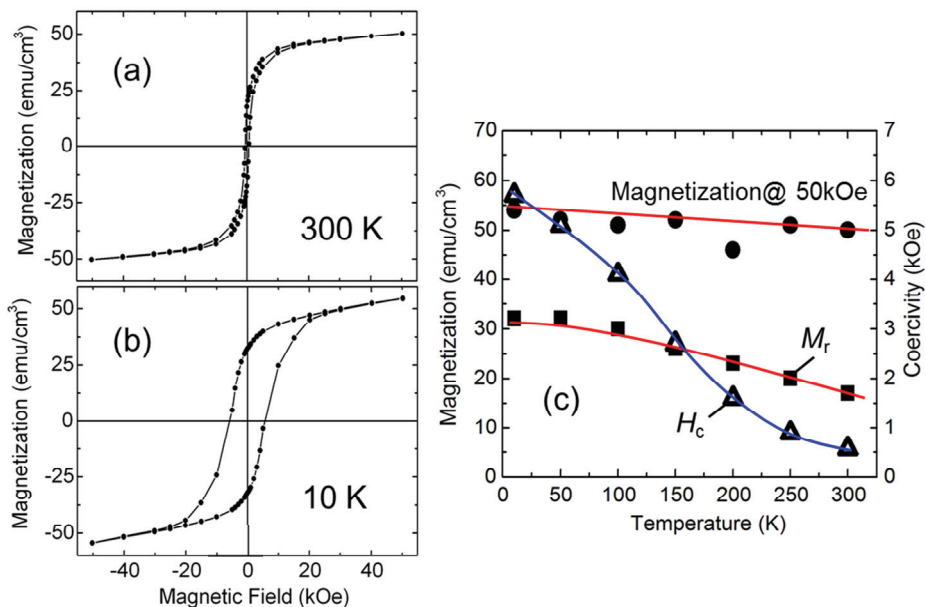


Fig. 27.  $M$ - $H$  curves for 300 (a) and 10 K (b) for the  $\text{BiFeO}_3$ - $\text{BiCoO}_3$  film with 15 at.% of  $\text{BiCoO}_3$  concentration, and temperature dependence of magnetization at 50 kOe ( $M_{50\text{kOe}}$ ), remanent magnetization ( $M_r$ ), and coercivity ( $H_c$ ) (c).

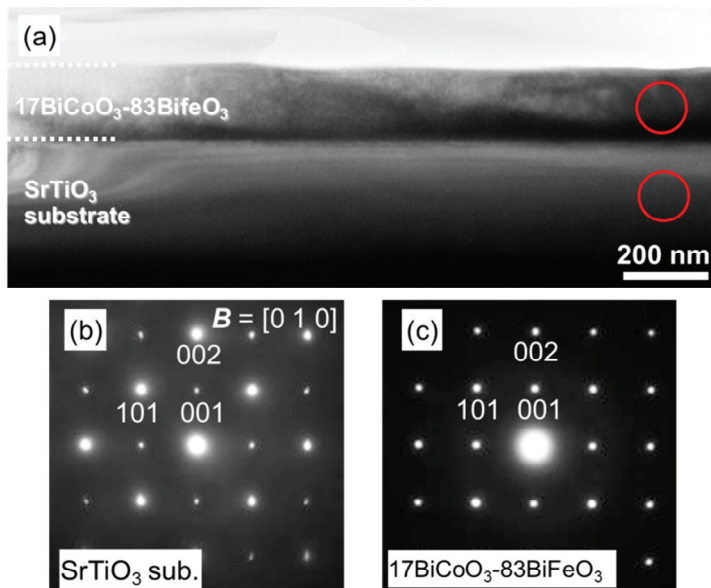


Fig. 26. Cross-sectional TEM observation for film with BiCoO<sub>3</sub> concentration of 17 at. %.

Here, we briefly discuss about possibility of the magneto-electric (ME) effect at RT in BiCoO<sub>3</sub>-BiFeO<sub>3</sub> solid solution. As mentioned above, the magnetization of BiCoO<sub>3</sub>-BiFeO<sub>3</sub> films was enhanced with rhombohedral structure at a BiCoO<sub>3</sub> concentration below 18 at. %. In previous report, (Chu *et al.*, 2008) for BiFeO<sub>3</sub> with rhombohedral structure, a strong coupling was reported between the ferroelectric domains of rhombohedral 71° and 109° and the antiferromagnetic domains, and the antiferromagnetic domains were reversed by ferroelectric switching at RT. In accordance with this BiFeO<sub>3</sub> regime, the BiCoO<sub>3</sub>-BiFeO<sub>3</sub> films below BiCoO<sub>3</sub> concentration 18 at. % can potentially exhibit the ME effect with a macroscopic magnetization change because the rhombohedral domains exist at BiCoO<sub>3</sub> concentration below 18 at. %. The macroscopic magnetization changes operated at RT are useful in spintronics applications such as multi-valued memory using a spin-filter device *etc.* To confirm the ME effect, we will clarify the role of the substitution of Fe atom for Co atom and the origin of the enhanced magnetization in BiCoO<sub>3</sub>-BiFeO<sub>3</sub> films. In addition, we expect to observe the magnetization changes driven by the electric field as well as external pressure in the MPB (BiCoO<sub>3</sub> concentration of 20 - 25 at. %) because the MPB phase shows a large displacement due to a large piezoelectric effect.

## 5. Conclusion

High quality single phase BiFeO<sub>3</sub> polycrystalline films with a space group of R3c were fabricated on Pt/Ti/SiO<sub>2</sub>/Si (100) substrates. The leakage current density of the films at RT was large and strongly affected the ferroelectric measurement. The ferroelectric measurement was carried out at low temperature to reduce the leakage current, and a large polarization of 89 μC/cm<sup>2</sup> and a coercive field of 0.31 MV/cm were observed. The magnetic properties at RT were primarily due to antiferromagnetism. The magnetic properties at RT

were drastically enhanced by substitution of Fe in BiFeO<sub>3</sub> with 4 at % Co, which implies the induction of ferro-like magnetic ordering. The large leakage current and coercive field were simultaneously successfully reduced by substitution of Fe with 5 at.% Co. Epitaxial strain was employed in the preparation of films with high levels of Co substitution for Fe in BiFeO<sub>3</sub> because, under these conditions, the high-pressure phase of BiCoO<sub>3</sub> dominates stability. (hereafter, we refer to these highly Co-substituted BiFeO<sub>3</sub> films as BiCoO<sub>3</sub>-BiFeO<sub>3</sub>). The magnetization of the BiCoO<sub>3</sub>-BiFeO<sub>3</sub> films increased drastically with an increase in the BiCoO<sub>3</sub> concentration, and the maximum magnetization was observed at 20-25 at.% substitution. Above a BiCoO<sub>3</sub> concentration of 25 at.%, there is a decrease in magnetization, which corresponds to the change from rhombohedral to tetragonal structural composition. Interestingly, the magnetization was maximally enhanced at the MPB of the rhombohedral structure of BiFeO<sub>3</sub> and the tetragonal structure of BiCoO<sub>3</sub>. It is well known that large piezoelectricity can be expected in the MPB; therefore, the cross-correlation between piezoelectricity and magnetism can be expected in the MPB. Furthermore, this material has the capacity possibility to show wide cross-correlation among magnetism, ferroelectricity, piezoelectricity, and optical properties. Epitaxial BiCoO<sub>3</sub>-BiFeO<sub>3</sub> solid solutions can open up an avenue for the development of new multifunctional materials, may have potential application in devices such as multivalued memories, spin-filter devices, V-MRAM, magnetic/electric field tunability or flexibility, and piezoelectric materials with MPB *etc.*

## 6. Acknowledgements

The author extends appreciation for the collaborative contribution of Prof. S. Okamura, Tokyo University of Science, to the entire study. Prof. H. Funakubo and Ph.D. student S. Yasui, Tokyo Institute of Technology, Prof. K. Nishida, National Defense Academy of Japan, Dr. T. Iijima, National Institute of Advanced Industrial Science and Technology collaborated strongly in the preparation and characterizations of BiFeO<sub>3</sub>-BiCoO<sub>3</sub> epitaxial films presented in Section 3. The TEM observations were carried out by Dr. Andras Kovacs of Oxford University and Dr. Bae In-Tae, Binghamton University, State University of New York. The author also expresses gratitude to Prof. Y. Ando for the opportunity to write this chapter. This study was partly supported by the Grant-in-Aid for Young Scientist Start-up program (Grant No. 18860070), Young Scientists B (No. 20760474), Young Scientists A (No. 22686001), Grand-in-Aid for Scientific Research and the Elements Science and Technology Project from the Ministry of Education, Culture, Sports, Science and Technology of Japan, by the Sasakawa Scientific Research Grant from The Japan Society (Grant No. 19-216), by Tohoku University Exploratory Research Program for Young Scientists (TU-ERYS), and by TANAKA Co, Ltd research found (No. J090809317).

## 7. References

- Venevtsev, Y. N.; Zhadanow, G. & Solov'ev, S. (1960), *Soviet Physics Crystallography* Vol. 4, 1960, pp. 538.
- Kiselev, S. V.; Ozerov, R. P. & Zhdanov, G. S. (1963) Detection of Magnetic Order in Ferroelectric BiFeO<sub>3</sub> by Neutron Diffraction, *Soviet Physics DOKLADY*. Vol 7, February 1963, pp. 742-743.

- Kubel, F.; & Schmid, H. (1990) Structure of Ferroelectric and Ferroelastic Monodomain Crystal of the Perovskite BiFeO<sub>3</sub>, *Acta Crystallography Sect. B: Structure*. Vol. 46, June 1990, pp. 698-702.
- Ederer, C.; and Spaldin N. A. (2005) Effect of Epitaxial Strain on the Spontaneous Polarization of Thin Film Ferroelectrics, *Physical Review Letters*, Vol. 95, December 2005, pp. 257601-1-4.
- Li, J.; Wang, J; Wuttig M., Ramesh, R.; Wang, N.; Ruetter, B.; Pyatakov, A. P.; Zvezdin, A. K.; & Viehland, D.; (2004) Dramatically enhanced polarization in (001), (101), and (111) BiFeO<sub>3</sub> thin films due to epitaxial-induced transitions, *Applied Physics Letters*, Vol. 84, June 2004, pp.5261-5263.
- Yun, K. Y.; Ricinchi D.; Kanashima, T.; Noda, M.; & Okuyama, M.; (2004) Giant Ferroelectric Polarization Beyond 150 C/cm<sup>2</sup> in BiFeO<sub>3</sub> Thin Film, *Japanese Journal of Applied Physics Letters*, Vol. 43, April 2004, L647-648.
- Naganuma, H.; & Okamura, S. (2007) Structural, magnetic, and ferroelectric properties of multiferroic BiFeO<sub>3</sub> film fabricated by chemical solution deposition, *Journal of Applied Physics*, Vol. 101, December 2007, pp. 09M103-1-3.
- Pabst, G. W.; Martin, L. W.; Chu, Y. H.; & Ramesh, R. (2007) Leakage mechanisms in BiFeO<sub>3</sub> thin films, *Applied Physics Letters*, Vol. 90, February 2007 pp. 072902-1-3.
- Ederer, C.; & Spaldin, N. A. (2005) Weak ferromagnetism and magnetoelectric coupling in bismuth ferrite, *Physical Review B*, Vol. 71, February 2005, pp. 060401(R)-1-4.
- Zhao, T.; Scholl A.; Zavaliche F.; Lee K.; Barry, M.; Doran A.; Cruz, M. P.; Chu, Y. H.; Ederer C.; Spaldin, N. A.; Das, R. R.; Kim, D. M.; Baek, S. H.; Eom, C. B.; & Ramesh, R. (2006) Electrical control of antiferromagnetic domains in multiferroic BiFeO<sub>3</sub> films at room temperature, *Nature Materials*, Vol. 5, September 2006, pp.823-829.
- Dzyaloshinskii, I. E. (1957) *Soviet Physics JEPT*, Vol. 5, No. 6, February 1957, pp. 1259-1272.
- Moriya, T. (1960) Anisotropic Superexchange Interaction and Weak Ferromagnetism, *Physical Review*, Vol. 120, May 1960, pp.91-98.
- Sosnowska, I.; Peterlin-Neumaier, T.; & Streichele, E. (1982) Spiral Magnetic ordering in Bismuth Ferrite, *Journal of Physics C*, Vol. 15, January 1982, pp. 4835-4846.
- Chu, Y.-H.; Martin, L. W.; Holcomb, M. B.; Gajek M.; Han, S.-J.; He, Q.; Balke, N.; Yang, C.-H.; Lee, D.; Hu, W.; Zhan, Q.; Yang, P.-L.; Fraile-Rodriguez, A.; Scholl, A.; Wang, S. X. & Ramesh, R. (2008), Electric-field control of local ferromagnetism using a magnetoelectric multiferroic, *Nature Materials*, Vol. 7, April 2008, pp. 478-482.
- Shima, H.; Kawae, T.; Morimoto, A.; Matsuda, M.; Suzuki, M.; Tadokoro, T.; Naganuma, H.; Iijima, T.; Nakajima, T. & Okamura, S. (2009) Optical Properties of BiFeO<sub>3</sub>-System Multiferroic Thin Films, *Japanese Journal of Applied Physics*, Vol. 48, September 2009, pp. 09KB01-1-4.
- Naganuma, H.; Kovacs, A.; Y. Hirotsu, Y. Inoue, and Okamura, S. (2007) Preparation and Characterization of Multiferroic BiFeO<sub>3</sub> Films, *Transactions of the Materials Research Society of Japan*, 2007, Vol. 32, pp. 39-42.

- Naganuma, H.; Kovacs, A.; Hirata, A.; Hirotsu, Y. & Okamura, S., (2007) Structural Analysis of Polycrystalline BiFeO<sub>3</sub> Films by Transmission Electron Microscopy, *Materials Transaction*, Vol. 48, August 2007, pp. 2370-2373.
- Naganuma, H.; Inoue, Y. & Okamura, S. (2007) Leakage Current Mechanism of Polycrystalline BiFeO<sub>3</sub> Films with Pt Electrode, *Integrated Ferroelectrics*, Vol. 46, 2007, pp.6948-6951. ISSN 1058-4587.
- Naganuma, H.; Inoue, Y. & Okamura, S. (2008) Dependence of Ferroelectric and Magnetic Properties on Measuring Temperatures for Polycrystalline BiFeO<sub>3</sub> Films, *IEEE Transactions on Ultrasonics, Ferroelectrics, and Frequency Control*, Vol. 55 No. 5, pp.1046-1050.
- Naganuma, H.; Inoue, Y. & Okamura, S. (2008) Estimation of Leakage Current Density and Remanent Polarization of BiFeO<sub>3</sub> Films with Low Resistivity by Positive, Up, Negative, and Down Measurements, *Japanese Journal of Applied Physics*, Vol. 47, July 2008, pp.5558-5560.
- Naganuma, H.; Inoue, Y. & Okamura, S. (2008) Evaluation of Electrical Properties of Leaky BiFeO<sub>3</sub> Films in High Electric Field Region by High-Speed Positive-Up-Negative-Down Measurement, *Applied Physics Express*, Vol. 1, pp.061601-1-3.
- Naganuma, H.; Miyazaki, T.; Ukachi, A.; Oogane, M.; Mizukami, S. & Ando, Y. Structural characterization of epitaxial multiferroic BiFeO<sub>3</sub> films grown on SrTiO<sub>3</sub> (100) substrates by crystallizing amorphous Bi-Fe-O<sub>x</sub>, *Journal of Ceramic Society of Japan*, Vol. 118, June 2010, pp. 648-651.
- Naganuma, H.; Oogane, M. & Ando, Y. (2011) Exchange biases of Co, Py, Co<sub>40</sub>Fe<sub>40</sub>B<sub>20</sub>, Co<sub>75</sub>Fe<sub>25</sub>, and Co<sub>50</sub>Fe<sub>50</sub> on epitaxial BiFeO<sub>3</sub> films prepared by chemical solution deposition, *Journal of Applied Physics*, 2011 in-press.
- Kirkland, E. J.; *Advanced Computing in Electron Microscopy* (Plenum, New York, 1998).
- Wang, J.; Neaton, J. B.; Zheng, H.; Nagarajan, V.; S. Ogale, B.; Liu, B.; Viehland, D.; Vaithyanathan, V.; Schlom, D. G.; Waghmare, U. V.; Spaldin, N. A.; Rabe, K. M.; Wuttig, M. & Ramesh, R. (2003) Epitaxial BiFeO<sub>3</sub> Multiferroic Thin Film Heterostructures, *Science* Vol. 299, February 2003, pp.1719-1722.
- Yun, K. Y.; Noda, M.; Okuyama, M.; Saeki, H.; Tabata, H. & Saito, K. (2004) Structural and multiferroic properties of BiFeO<sub>3</sub> thin films at room temperature, *Journal of Applied Physics*, Vol. 96, May 2004, pp.3399-3403.
- Naganuma, H.; Y. Inoue, & Okamura, S. (2010) Evaluation of ferroelectric hysteresis loops of leaky multiferroic BiFeO<sub>3</sub> films using a system with a high driving frequency of 100 kHz system, *Journal of Ceramics Society of Japan*, Vol. 118, June 2010, pp.656-658.
- Bai, F.; Wang, J.; Wuttig, M.; Li, J. F.; Zvezdin, A. K.; Cross, L. E.; & Viehland, D.; (2005) Destruction of spin cycloid in (111)<sub>c</sub>-oriented BiFeO<sub>3</sub> thin films by epitaxial constraint: Enhanced polarization and release of latent magnetization, *Applied Physics Letters*, Vol. 86, pp. 032511-1-3.
- Lebeugle, D.; Colson, D.; Forget, A.; Viret, M.; Bonville, P.; Marucco, J. F. & Fusil S. (2007) Room-temperature coexistence of large electric polarization and magnetic order in BiFeO<sub>3</sub> single crystals, *Physical Review B*, Vol. 76, July 2007, pp. 024116-1-8.

- Naganuma, H.; Miura, J. & Okamura, S. (2008) Ferroelectric, electrical and magnetic properties of Cr, Mn, Co, Ni, Cu added polycrystalline BiFeO<sub>3</sub> films, *Applied Physics Letters*, Vol. 93, August 2008, pp. 052901-1-3.
- Naganuma, H.; Miura, J. & Okamura, S. (2009) Annealing temperature effect on ferroelectric and magnetic properties in Mn-added polycrystalline BiFeO<sub>3</sub> films, *Journal of Electroceramics*, Vol. 22, January 2008, pp.203-208.
- Naganuma, H.; Shimura, N.; Miura, J.; Shima, H.; Yasui, S.; Nishida, K.; Katoda, T.; Iijima, T.; Funakubo, H.; & Okamura, S. (2008) Enhancement of ferroelectric and magnetic properties in BiFeO<sub>3</sub> films by small amount of cobalt addition, *Journal of Applied Physics*, Vol. 103, pp.07E314-1-3.
- Naganuma, H.; Miura, J.; Nakajima, M.; Shima, H.; Okamura, S. Yasui, S.; Funakubo, H.; Nishida, K.; Iijima, T., Azuma, M.; Ando, Y.; Kamishima, K.; Kakizaki K.; & Hiratsuka, N. (2008) Annealing Temperature Dependences of Ferroelectric and Magnetic Properties in Polycrystalline Co-Substituted BiFeO<sub>3</sub> Films, *Japanese Journal of Applied Physics*, Vol. 47, pp. 7574-7578.
- Naganuma, H.; Miura, J.; Kamishima, K.; Kakizaki, K.; Hiratsuka, N.; Ando, Y.; Okamura, S. (2009) Room Temperature Ferroelectric and Magnetic Properties of Multiferoic Cobalt Substituted Bi Ferrite Films, *Journal of Magnetic Society of Japan*, Vol. 33, pp. 237-241.
- Zhang, Q.; Kim, C. H.; Jang, Y. H.; Hwang, H. J.; & Cho, J. H. (2010) *Applied Physics Letters*, Vol. 96, April 2010, 99. 152901-1-3.
- Naganuma, H.; Kovacs, A.; Harima, T.; Shima, H.; Okamura, S.; & Hirotsu, Y. (2009) Structural analysis of interfacial strained epitaxial BiMnO<sub>3</sub> films fabricated by chemical solution deposition, *Journal of Applied Physics*, Vol. 105, March 2009, pp.07D915-1-3.
- Yasui, S.; Nishida, K.; Naganuma, H.; Okamura, S.; Iijima, T. & Funakubo, H. (2007) Crystal Structure Analysis of Epitaxial BiFeO<sub>3</sub> - BiCoO<sub>3</sub> Solid Solution Films Grown by Metalorganic Chemical Vapor Deposition, *Japanese Journal of Applied Physics*, Vol. 46, October 2007, pp.6948-6951.
- Yasui, S.; Naganuma, H.; Okamura, S.; Nishida, K.; Yamamoto, T.; Iijima, T.; Azuma, M.; Morioka, H.; Saito, K.; Ishikawa, M.; Yamada, T.; & Funakubo, H. (2008) Crystal Structure and Electrical Properties of {100}-Oriented Epitaxial BiCoO<sub>3</sub>-BiFeO<sub>3</sub> Films Grown by Metalorganic Chemical Vapor Deposition, *Japanese Journal of Applied Physics*, Vol. 47, September 2008, pp.7582-7585.
- Yasui, S.; Nakajima, M.; Naganuma, H.; Okamura, S.; Nishida, K.; Yamamoto, T.; Iijima, T.; Azuma, M.; Morioka, H.; Saito, K.; Ishikawa, M.; Yamada, T.; & Funakubo, H. (2009) Composition control and thickness dependence of {100}-oriented epitaxial BiCoO<sub>3</sub>-BiFeO<sub>3</sub> films grown by metalorganic chemical vapor deposition, *Journal of Applied Physics*, Vol. 105, March 2009, pp.061620-1-5.
- Naganuma, H.; Yasui, S.; Nishida, K.; Iijima, T.; Funakubo, H.; & Okamura, S. (2011) Enhancement of magnetization at morphotropic phase boundary in epitaxial BiCoO<sub>3</sub>-BiFeO<sub>3</sub> solid solution films grown on SrTiO<sub>3</sub> (100) substrates by metalorganic chemical-vapor deposition, *Journal of Applied Physics*, in-press.

---

Saito, K.; Ulyanenkov, A.; Grossmann, V.; Röss, H.; Brüggemann, L.; Ohta, H.; Kurosawa, T.; Ueki, S.; & Funakubo, H. (2006) Structural Characterization of BiFeO<sub>3</sub> Thin Films by Reciprocal Space Mapping, *Japanese Journal of Applied Physics*. Vol. 45, September 2006, pp.7311-7314.

## **Part 4**

### **Liquid Crystals and Optical Effects**



# Ferroelectric Liquid Crystals with High Spontaneous Polarization

Slavomír Pirkl and Mílada Glogarová  
*University of Pardubice, Faculty of Chemical Technology, Pardubice  
Institute of Physics, Academy of Sciences of the Czech Republic, Prague  
Czech Republic*

## 1. Introduction

Liquid crystalline (LC) materials are example of self-assembling media on a nanoscale level (de Gennes & Prost, 1993; Gray, 1987; Lagerwall, 1999). Composed of anisotropic molecules, LC compounds exhibit a great variability of structures, which are strongly susceptible to external fields as well as to interaction with the surfaces. For particular molecules assembled in specific architectures a permanent dipole moment can appear thus forming structures with dipolar order, namely ferroelectric (FE) or antiferroelectric (AF) phases. Their physical properties have been intensively investigated, as they promised large variety of applications, e.g. in displays, displays with a memory, TV screens, spatial light modulators, applications in optical processing, computing, *etc.* (Clark & Lagerwall, 1983; Goodby et al., 1991; Lueder, 2010; Yang & Wu, 2006). Recently, also a display based on AF SmC\* materials has been reported profiting from their higher threshold electric field for switching (Lagerwall, 1999). The application potentialities stimulated a great progress in the synthesis and research of these materials.

The outstanding physical properties of the FE (and possibly AF) smectic LCs (SmC\*) are attracting attention especially after the nematic liquid crystal materials have been developed to the limits of their performance.

The chapter is structured as follows. In the first part, we recall the main structural characteristics of LC molecules and their assembling in liquid crystalline phases, with stress to formation of FE phases. The origin of the spontaneous polarization from the molecular structure and supramolecular alignment is described.

The value of spontaneous polarization is a main characteristic of ferroelectric liquid crystals (FLC) and it is also an important parameter considered when selecting a material for specific applications. Therefore, designing the molecular structure with the aim to influence and particularly enhance the spontaneous polarization value of the resulting ferroelectric phase is the principal goal of the second part of this contribution. In particular, we discuss influence of molecular and intramolecular rotations, an asymmetry of the chiral centre, transversal molecular dipole moments, the presence of polar groups in the chiral centre, the lateral substitutions, the presence of heteroaromatic rings in the central skeleton of the molecule, etc.

One paragraph concerns ferroelectric mixtures, as in any application of FLC, as well as of any LCs, mixtures of several compounds are used with optimized properties.

Finally, a brief survey of a new type of liquid crystalline materials is devoted to polar liquid crystals composed of non-chiral bent-core molecules (so called banana liquid crystals), which may exhibit AF phases and quite exceptionally FE phases. In both cases their spontaneous polarization is high.

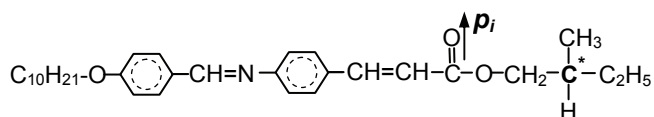
## 2. Liquid crystalline phases

Liquid crystals are partially ordered anisotropic fluids, thermodynamically located between the three-dimensionally ordered solid state (crystal) and the isotropic liquid. They may flow like a liquid, but their molecules may be oriented in a crystal-like way. Typical constituents of liquid crystals are elongated rod-like organic molecules (de Genes & Prost, 1999; Gray, 1987) the ratio between the length and the diameter of such molecules being about 5 or larger. Due to fast thermal rotation (of the order of  $10^{-9}$  s) around the long molecular axis they can be regarded as a cylinder. The molecules consist of rigid core with two or more aromatic rings with a flexible linear terminal substituent(s). Polar substituents are needed if electro-optic behavior is expected. With balanced rigid and flexible parts of molecules, the compound exhibits liquid crystalline phases (mesophases). Besides the positional order typical for the solid state, the molecules with strongly anisotropic form may also possess orientational order. There are many types of mesophases differing in the type and range of both orientational and positional order. These phases can be distinguished by their physical properties, which exhibit specific anisotropy reflecting the phase symmetry.

### 2.1 Ferroelectric liquid crystalline phases

An idea of the ferroelectric mesophase was presented by R.B. Meyer at the 5<sup>th</sup> International Liquid Crystal Conference in 1974. From symmetry considerations the author deduced that all tilted smectic phases composed of chiral molecules (without mirror symmetry) have to exhibit a (local) spontaneous polarization if the molecules contain a transverse permanent dipole moment.

The first synthesized compound fulfilling Meyer's specification is known by an acronym DOBAMBC, standing for (S)-(-)-p'-decyloxybenzylidene p'-amino 2-methylbutyl cinnamate (Meyer et al., 1975). The molecule of DOBAMBC



contains an asymmetric carbon atom  $C^*$  rendering molecular chirality, while a lateral  $-C=O$  group provides a transverse permanent dipole moment  $p_i$ . The aliphatic chain attached to the other end of the molecule by an oxygen atom is relatively long, favoring the SmC mesophase. In this phase molecules are arranged in fluid layers with no long-range translational order that can slide one over the other. On average, molecules are tilted from the layer normal by an angle  $\theta$ . The phase is optically biaxial. For review of basic properties of ferroelectric liquid crystals see (Goodby et al., 1991, Kitzerow & Bahr, 2001). The molecular structure of the chiral smectic C mesophase (SmC\*, star standing for chirality) is depicted in Fig. 1. Each layer is similar to that of the usual SmC phase, but because of

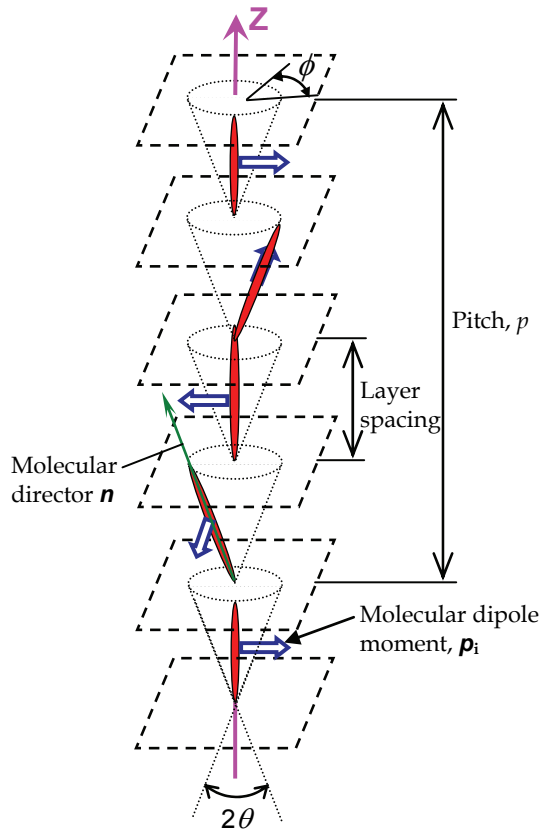


Fig. 1. The helicoidal structure of chiral smectic C ( $\text{SmC}^*$ ) liquid crystal. The molecular dipole moment  $p_i$  is always perpendicular to the director  $n$  and tangential to the circle of intersection of the cone with the boundary plane of the layer. Azimuthal angle  $\phi$  is a function of the coordinate  $z$  parallel to the layer normal,  $\theta$  is the tilt angle.

chirality there is a non-zero in-layer spontaneous dipole moment which is perpendicular to the average molecular direction (director  $n$ ) and to the tilt direction. To understand the origin of the layer dipole moment one has to consider that in contrast to the non-chiral molecules, the chiral ones do not rotate freely along their long axes. The chiral centre represents a steric hindrance for the molecular rotation, which results in a non-compensated part of the transversal molecular dipole moment  $p_i$ . Due to random head-tail alignment of molecules only an in-layer component of the dipole moment remains, and create the layer dipole moment  $P$ .

The other aspect of chirality is rotation of the director and thus also of the direction of dipole moment  $P$  about the smectic layer normal (see Fig. 1). The helix can be either right-handed or left-handed depending on the chirality of constituent molecules. Due to formation of the helical superstructure the spontaneous polarization is compensated to zero within one pitch of the helix,  $p$ , and the material appears to be non-polarized. Thus, strictly speaking, the  $\text{SmC}^*$  phase is not ferroelectric, but used to be regarded as helielectric.

Under an external electric field the local polarization  $P$  is aligned to the field direction thus unwinding the helical structure. In an alternating (a.c.) electric field a typical ferroelectric switching current, as well as electrooptical response is observed. This effect, being relatively fast ( $\sim 10 \mu\text{s}$ ), represents the main principle of technical applications.

From the switching current the value of the macroscopic spontaneous polarization,  $P_s$ , of the material can be evaluated.

To understand the origin of the layer dipole moment  $P$  several models have been suggested. In very simple one (Beresnev & Blinov, 1981), the molecules are considered as being tilted within layers and randomly distributed head to tail (Fig. 2). The chiral centre is depicted as an uneven tripod with unequally long arms. From steric reason the molecules prefer to tilt in the direction shown in Fig. 2a rather than in Fig. 2b and all the transverse molecular dipoles lie preferentially in one direction, orthogonal to the tilt direction. In reality, the molecules are spinning rapidly, and this preferred tilt direction then becomes a more energetically favored position due to steric hindrance if an mirror symmetry is absent in the layer.

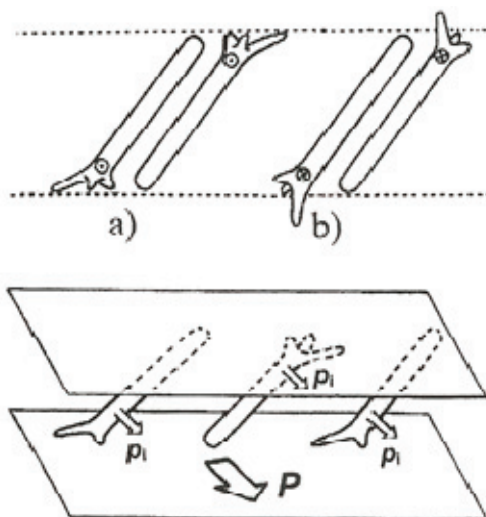


Fig. 2. Schematic arrangement of chiral molecules in the  $\text{SmC}^*$  phase,  $p_i$  being the molecular dipole moment. Due to chiral group, depicted by the tripod, the molecules prefer (a) rather than (b) and thus all the molecular dipole moments lie in the direction as shown in lower part of the figure as  $P$ .

For application of FLCs in electrooptical displays, the helicoidal structure must be suppressed otherwise an optically homogeneous field cannot be reached. It is achieved in so called Surface Stabilized Ferroelectric Liquid Crystal (SSFLC) being only about  $1 \mu\text{m}$  thick (Clark & Lagerwall, 1983).

It is necessary to accent that in many FLCs the value of  $P_s$  is considerably temperature dependent. With increasing temperature  $P_s$  decreases and disappears at the transition to the high temperature  $\text{SmA}$  phase, chiral nematic phase ( $\text{N}^*$ ) or isotropic liquid at specific temperature  $T_c$ . Typical behavior of such temperature dependence is seen in Fig. 3.

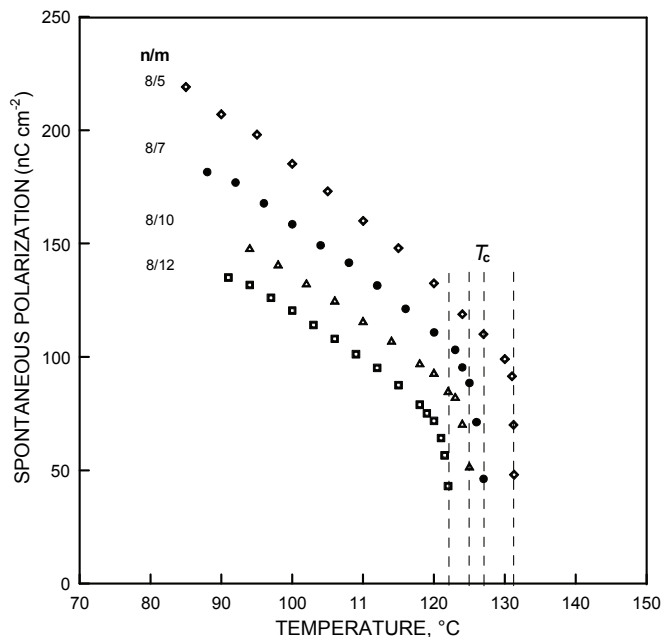


Fig. 3. Temperature dependence of the spontaneous polarization for series of compounds XV for  $X = F$ ;  $n, m$  are numbers of carbon atoms in aliphatic chains (see Tab. 8),  $T_c$  is a temperature at which the  $\text{SmC}^*$  phase transforms to a phase without spontaneous polarization.

In addition, temperature range of the  $\text{SmC}^*$  phase strongly differs for various substances. Therefore, for comparison of the spontaneous polarization of different compounds values of  $P_s$  at a definite temperature  $T$  below  $T_c$  use to be given (usually for  $T_c - T = 5, 10$  or  $20$  K). But still comparison of the spontaneous polarization for different substances at the same temperature is solitary.

Let us point out that both FE and AF dipolar order exists also in tilted chiral smectic phases, in which (in contrast to the  $\text{SmC}^*$  phase) the smectic layers exhibit a hexatic molecular arrangement due to a strong bond orientational order, or in so called low temperature chiral tilted smectics with a hexagonal or square molecular arrangement within the smectic layers and long range correlations in the direction of the smectic layer normal. These types of phases are not suitable for application as the polarization switching as well as the electrooptic response is significantly slower or are not switchable at all.

### 3. Relation of the molecular structure and the $\text{SmC}^*$ phase formation

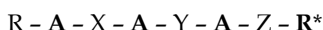
Basic requirements on molecules to be able to create the  $\text{SmC}^*$  mesophase can be described as follows:

1. Rod-like shape and ability to form a layered mesophase where the long axes of constituent molecules are tilted with respect to the layer planes. In more detail see e.g. (Goodby et al., 1991).

2. Chirality (either right- or left-handed), ensured by the presence of at least one asymmetric carbon, located usually on one or on both ends of molecules. Location of the asymmetric carbon in the central part of molecule is very rare (Barbera et al., 1989).
3. The existence of a transversal dipole moment borne by a functional group e.g.  $-C=O$ ,  $-CN$ ,  $-Cl$ , etc. This dipole moment is not averaged to zero by the molecular rotation because of hindering by the chiral centre. As for the intramolecular motion, rotation between the polar and chiral groups is not free.

In the following discussion we limit oneself to substances containing asymmetrical carbon only in one side of molecule, since possibilities of practical use of materials with asymmetrical carbon on both ends and/or in the central core of a molecule are scarce. Only a few such substances are known to establish generally valid relations.

For the following consideration, it is advantageous to divide a typical rod-like FLC molecule to several parts:



- a. Central linear rigid core is formed as a rule by two or three aromatic or heteroaromatic rings denoted as **A**, which are connected by linkage groups **X** and **Y**. As a rule **X** and **Y** represent a simple bond, e.g.  $-COO-$ ,  $-CH=N-$ ,  $-N=N-$  etc.
- b. Non-chiral terminal chain **R** (as a rule an unbranched alkyl- or alkyloxy group).
- c. Chiral terminal chain **R\*** with one or more asymmetric carbons **C\***, most frequently it is  $-C^*H(CH_3)-(CH_2)_mCH_3$ ,  $m = 1$  to  $5$ .
- d. Linkage group **Z** between the core and the terminal chains formed either by a single bond or combination of more groups, some of them bringing the molecule transverse dipole moment (e.g.  $-CH_2-$ ,  $-CH=CH-$ ,  $-COO-$ ,  $-CO-$ ).

Presently, number of substances composed of rod-like molecules and forming the ferroelectric mesophase amounts to thousands. Unfortunately, in many of them the values of  $P_s$  at temperatures relevant for comparison are not available. Therefore, evaluation of factors influencing  $P_s$  is rather difficult. The most promising ways for  $P_s$  increase are discussed below.

#### 4. Ways of spontaneous polarization enhancement

For the value of the spontaneous polarization  $P_s$  the existence of the lateral molecular dipole moments  $p_i$  is essential and increasing of  $p_i$  seems to be the first natural way for  $P_s$  increasing. One has to realize that the  $P_s$  value is not just a result of a simple addition of  $p_i$  values in the volume. Rotation of LC molecules around their long axes and various intramolecular rotations lower this value significantly. Therefore, restriction of these rotations is further and very important way to  $P_s$  enhancement. Both ways closely relate to configuration of the chiral centre in the molecule, to number of asymmetric carbons in the molecule and are connected with nature of the bond between the chiral part and central linear rigid core. Therefore, still new substituents have been examined (see Table 1), which finally resulted in preparation of compounds with very high spontaneous polarization up to the order of  $10^2$  nC cm<sup>-2</sup>.

In all Tables hereafter substituents  $C_mH_{2m+1}$  and  $C_nH_{2n+1}$  are linear. Aromatic rings are bonded in positions 1,4.

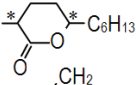
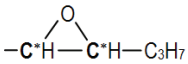
$-\text{C}^*\text{H}(\text{X})-\text{R}$	$\text{X}=\text{CH}_3, \text{F}, \text{Cl}, \text{Br}, \text{OH}$
	$\text{R} = \text{alkyl or alkyloxy group (m = 2-8)}$
$-\text{C}^*\text{F}(\text{CH}_3)-\text{COO}-\text{R}$	$\text{R} = \text{C}_m\text{H}_{2m+1}$
$-\text{C}^*\text{H}(\text{CF}_3)-\text{CH}_2-\text{COO}-\text{R}$	$\text{R} = \text{C}_m\text{H}_{2m+1}$
$-\text{C}^*\text{H}(\text{X})-\text{C}^*\text{H}(\text{CH}_3)-\text{R}$	$\text{X} = \text{F}, \text{Cl}, \text{Br} \quad \text{R} = \text{C}_2\text{H}_5$
$-\text{C}^*\text{H}(\text{CH}_3)-\text{Q}-\text{C}^*\text{H}(\text{CH}_3)-\text{R}$	$\text{Q} = -\text{O}-\text{CH}_2-, -\text{COO}- \quad \text{R} = \text{C}_2\text{H}_5, \text{COO}-\text{C}_2\text{H}_5$
$-\text{C}^*\text{H}(\text{CH}_3)-\text{Q}-\text{R}$	$\text{Q} = -\text{COO}-, -\text{CH}_2-\text{COO}- \quad \text{R} = \text{C}_m\text{H}_{2m+1} \quad (\text{m} = 1-8)$
	
$-\text{C}^*\text{H}-\text{C}-\text{(CH}_3)_2$	
	

Table 1. Examples of chiral substituents.

#### 4.1 Restriction of molecular rotations

Molecular dipole moment  $p_i$  rotates together with LC molecule as a whole around its long axis but this rotation is hindered because of various restrictions. It means that both molecular short (lateral) axis and molecular dipole moment are directed in preferred orientation for longer time. The uncompensated molecular dipole moment is an origin of the spontaneous polarization within the  $\text{SmC}^*$  layer.

Degree of molecular alignment with respect to the director can be described by an (orientational) order parameter  $S_k^1$ , which has very low value for orientation of the short axis. Measurable values of the spontaneous polarization are expected for  $S_k > 10^{-3}$ . The larger  $S_k$  the higher probability of lateral molecular axes to be directed in preferred direction and the larger contribution of  $p_i$  to  $P_s$ .

Steric hindrances participate in a restriction of molecular rotations very effectively. In this respect the chiral centre, depicted as an uneven tripod with unequally long arms (see Fig. 2), plays an important role. With increasing asymmetry of the tripod its restrictive effect as well as  $S_k$  increases. This effect has been observed for numerous compounds (Chin et al., 1988; Nakauchi et al., 1989; Sakurai et al., 1984; Yoshizawa et al., 1989), some examples of compounds with the chiral centre  $-\text{C}^*\text{H}(\text{CH}_3)-\text{C}_m\text{H}_{2m+1}$  are shown in Table 2. Of course, the increase of  $P_s$  in this way is limited. An optimal length of the aliphatic chain exists for which  $P_s$  has a maximal value and additional lengthening leads to the spontaneous polarization decrease (see Table 2).

On the other hand branching of a terminal substituent and lengthening of aliphatic chains suppresses in many cases thermal stability of the mesophase narrowing the temperature

<sup>1</sup>Orientalional order parameter,  $S_k$ , characterizes degree of molecular alignment with respect to the director. It takes the values between zero and one. For a completely random and isotropic sample,  $S=0$ , whereas for a perfectly aligned sample  $S=1$ .

range of the mesophase or fully prevents its formation. This negative effect can be compensated by elongation of the central linear rigid core of the molecule. Therefore, the most of ferroelectric liquid crystals with strongly asymmetric chiral center  $R^*$  ( $m=6$ ) has three aromatic or heteroaromatic rings in the central core.

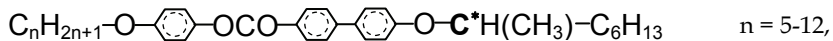
$$\text{II } C_8H_{17}-O-\text{C}_6\text{H}_4-\text{C}_6\text{H}_4-\text{COO}-\text{C}_6\text{H}_4-\text{CO}-\text{C}^*H(\text{CH}_3)-C_mH_{2m+1}$$

$$\text{III } C_{10}H_{21}-O-\text{C}_6\text{H}_4-\text{C}_6\text{H}_4-\text{COO}-\text{C}_6\text{H}_4-\text{COO}-\text{C}^*H(\text{CH}_3)-\text{CH}_2-\text{COO}-C_mH_{2m+1}$$

Compound	$m$	$P_s$ (nC cm <sup>-2</sup> )	SmC* range (°C)
II	2	130	68 - 130
II	6	403	60 - 132
II	8	210	70 - 125
III	1	26	103 - 120
III	3	70	52 - 110
III	5	29	49 - 96

Table 2. Temperature range of the SmC\* mesophase and maximum values of the spontaneous polarization  $P_s$  for compounds II (Yoshizawa et al., 1989) and III (Nakauchi et al., 1989). Influence of the chiral centre asymmetry.

Combination of mentioned chiral centre with tricyclic rigid molecular core of the ester type provided first chemically stable substances



with rather high spontaneous polarization ( $P_s \sim 50$  nC cm<sup>-2</sup>) (Inukai et al., 1986). First commercial ferroelectric mixtures (Japan CHISSO Corp.) designed for electro-optical applications working in a broad temperature range around room temperature were based on the mentioned compounds. Similarly, the first Czech experimental memory electro-optical cells with surface stabilized ferroelectric liquid crystal (SSFLC) were realized with this material already in the year 1987 (PirkI, 1990).

It is hardly possible to assess unambiguously the effect of others factors on molecule rotation either for lack of data, or because of combination of impacts (e.g. a side substituent on the central core in addition to the steric constraint brings also a significant transverse dipole moment).

## 4.2 Restriction of intramolecular rotations

Strength of the spontaneous polarization can be increased considerably by restricting the freedom of the chiral center rotation in relation to the molecule as a whole. Many single bonds in FLC molecules enable more or less independent rotation of particular parts of the molecule around its long axis. This is regarded as the second main reason of a low contribution of molecules to resulting dipole moment of the smectic layer. The lowering is particularly strong if the dominant transversal molecular dipole moment rotates independently of the chiral group.

Generally, shortening the distance and lowering the amount of longitudinal bonds between the position of the molecular transverse dipole moment and asymmetric carbon is regarded as a way for suppressing the negative influence of intramolecular rotations. The most radical way would be to introduce the dipole moment directly to the chiral group, as will be discussed below.

Definitely, the methyl group located at the linkage position Z lowers the  $P_s$  value significantly (see Table 3).

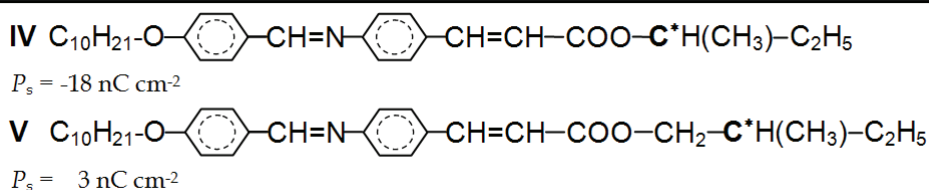


Table 3. Maximum values of the spontaneous polarization  $P_s$  for compounds IV (Sakurai et al., 1984) and V (Uemoto et al., 1981). Influence of a bridge group Z ( $-\text{CH}_2-$ ).

The effect of various molecular constituents should not be considered separately, as the complex molecular configuration plays a role. For example, the characteristic free rotation of both rings about the central linkage of biphenyl group can be restricted by suitable neighboring groups, which increases the order of the chemical bond due to mesomeric effect. The result of this conception is documented in Table 4. In compound VI one can suppose that mesomeric as well as induction effect increase the dipole moment of the central carbonyl group and together with strongly asymmetric chiral centre bring about the increase of the  $P_s$  value.

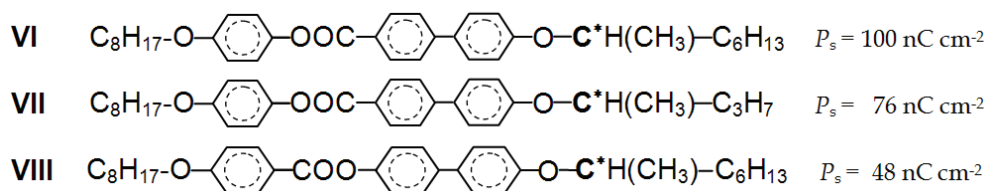


Table 4. Values of the spontaneous polarization  $P_s$  at temperatures  $T_c - 20^\circ\text{C}$  below the  $\text{SmC}^* - \text{SmA}$  transition (Inukai et al., 1986). Influence of the mesomeric effect.

### 4.3 Enhancement of transversal molecular dipole moment

Enhancement of the transversal molecular dipole moment represents one of the effective ways for the increase of the  $P_s$  value, the location of this dipole moment as well as the volume of the lateral substituent being important. In the absolute majority of FLC one of the functional group built in the central skeleton or in the linkage group Z is the source of the transversal dipole moment. Frequently it is the carbonyl group  $>\text{C}=\text{O}$ , the dipole moment of which can be increased due to mesomeric effect.

The additional increase of  $P_s$  can be achieved by lateral substitution of electronegative atoms or functional groups that behave as acceptors of electrons. The location of the substitution is very important for the increase of  $P_s$ . In the following, two main cases are considered separately.

#### 4.3.1 The effect of the lateral substitution on molecular core

This substitution is effective in the vicinity of the asymmetric carbon as well as on distant parts of the central skeleton. It brings additional transversal dipole moment and influences steric hindrance of both rotations of molecules about the longitudinal axis and intramolecular rotations. Besides, the lateral substituents may influence the temperature stability of the mesophase. Halogens (F, Cl, Br), nitril group ( $-\text{C}\equiv\text{N}$ ), or methyl group ( $-\text{CH}_3$ ) are the mostly used substituents. One of the possible effects of such substituents is shown in Table 5.

IX $\text{C}_n\text{H}_{2n+1}-\text{O}-\text{C}_6\text{H}_4-\text{OOC}-\text{C}_6\text{H}_4-\text{C}_6\text{H}_3(\text{X})-\text{O}-\text{C}^*\text{H}(\text{CH}_3)-\text{C}_6\text{H}_{13}$			
X	$P_s$	$\text{SmC}^*$ range ( $^\circ\text{C}$ )	
H	76	78 - 103	
F	85	52 - 104	
Cl	161	31 - 78	
Br	166	44 - 66	
CN	189	41 - 57	

Table 5. Values of the spontaneous polarization  $P_s$  ( $\text{nC cm}^{-2}$ ) at temperatures  $T_c - 10$   $^\circ\text{C}$  and a temperature range of the  $\text{SmC}^*$  mesophase. Influence of a substitution on the central core near an asymmetric carbon in an ortho position to the linkage group Z ( $-\text{O}-$ ), (Furukawa et al., 1988).

With increasing volume of the substituent thermal stability of the mesophase decreases and its temperature range becomes narrower. The substitution of chlorine appeared as the optimal one. The significant increase of  $P_s$  is a result of two effects: in preferential conformation specified by MM method (Furukawa et al., 1988) the dipole moments of C-X bond and ether group  $-\text{O}-$  are nearly parallel and thus are added up (see Fig. 4a) and simultaneously the steric hindrance in the chiral centre between the phenyl and methyl group restricts the rotation of the chiral group.

For another type of the central skeleton the expected increase of  $P_s$  occurs in the following sequence of substituents  $\text{H} < \text{F} < \text{Cl} < \text{Br} < \text{CN}$  (see Table 6). On the other hand the influence on the thermal stability of the mesophase is lower and not so unequivocal (Furukawa et al., 1988).



Fig. 4. Preferential conformation and mutual orientation of dipole moments  $p_i$  and polar groups near the chiral centre of compounds IX (a) and XVII (b).

X	$P_s$ (nC cm <sup>-2</sup> )	SmC* range (°C)
H	-45	78 - 99
F	-78	64 - 97
Cl	-123	72 - 95
Br	-131	42 - 87
CN	-160	67 - 90

Table 6. Values of the  $P_s$  at temperatures  $T_c - 10$  °C and a temperature range of the SmC\* mesophase. Influence of a substitution on the central core near an asymmetric carbon in an ortho position to the linkage group Z (–O–), (Furukawa et al., 1988).

Probably the best result has been found for the substitution by the nitrogroup (–NO<sub>2</sub>) as is shown for compound XIII in Table 7.

<b>XII</b>	
	$P_s$ (max) = -80 nC cm <sup>-2</sup>
<b>XIII</b>	
	$P_s$ (max) = -550 nC cm <sup>-2</sup>
<b>XIV</b>	
	$P_s$ (max) = -310 nC cm <sup>-2</sup>

Table 7. Maximum measured values of the spontaneous polarization  $P_s$  at compounds XII (Inukai et al., 1986), XIII and XIV (Walba et al., 1991). Influence of a substitution on the central core near the asymmetric carbon in an ortho position to the linkage group Z.

In Table 8 one can mention positive impact of the various lateral substitutions located on the molecular end opposite to the asymmetric carbon (Pachomov, 1997; Hamplová et al., 2007) on the increase of the spontaneous polarization  $P_s$ . The methoxy substitution was the only resulting in the decrease of  $P_s$ , which has not been reliably explained so far.

On the other hand increase of  $P_s$ , due to lateral substituent cannot be expected e.g. when connecting group Z is formed by carboxyl –COO–. Then at the preferential conformations the dipole moments of C–X and C=O bonds are antiparallel (see Fig. 2b) resulting in a decrease of  $P_s$ , which is shown in Table 9. Thus proximity of polar group and the chiral centre does not assure increase of  $P_s$  (Furukawa et al., 1988).

The value of the spontaneous polarization can be also significantly increased when the phenyl ring in the central core is exchanged for the heterocycle (mainly nitrogenous). An example with pyrimidine core is given in Table 10.

n/m	X = H	X = F	X = Cl	X = Br	X = CH <sub>3</sub>	X = OCH <sub>3</sub>
8/5	9	127	153		121	66
8/7	82	15	148			50
10/7				152		

X = H		X = Cl		X = CH <sub>3</sub>	
118		206		153	

Values of the  $P_s$  for X = H and X = Cl at  $T = T_c - 20^\circ \text{C}$ ; for X = CH<sub>3</sub> at  $T = T_c - 5^\circ \text{C}$ .

Table 8. Values of the  $P_s$  (nC cm<sup>-2</sup>), at a substitution of the central core far from asymmetric carbon in the meta position to the non-chiral substituent R (Pachomov, 1997). Values of the  $P_s$  at  $T = T_c - 10^\circ \text{C}$  (unless otherwise indicated).

X = H	$P_s = 70 \text{ nC.cm}^{-2}$	$T_c = 122^\circ \text{C}$	
X = F	$P_s = 60 \text{ nC.cm}^{-2}$	$T_c = 124^\circ \text{C}$	
X = Cl	$P_s = 78 \text{ nC.cm}^{-2}$	$T_c = 97^\circ \text{C}$	

Table 9. Values of the  $P_s$ , at a substitution of the central core near the asymmetric carbon in the ortho position to the linkage group Z (Furukawa et al., 1988). Values of the  $P_s$  at  $T = T_c - 10^\circ \text{C}$ .

<b>XVIII</b>		$P_s = 438 \text{ nC cm}^{-2}$
<b>XIX</b>		$P_s = 87 \text{ nC cm}^{-2}$

Table 10. Rise of the spontaneous polarization  $P_s$  owing to a heterocyclic ring in the central core of molecule (Hirai et al. 1992). Values of the  $P_s$  are maximal measured.

#### 4.3.2 The effect of the lateral substitution on the asymmetric carbon

Introduction of the transversal dipole moment directly to the chiral centre proved to be efficient, as it eliminates intramolecular rotations. The impact of this type of substitution on  $P_s$  values is shown in Table 11. The substitution of fluorine in various configurations

increased the  $P_s$  values up to the factor of 8. Introduction of chlorine gives still higher increase of  $P_s$  (cf. compounds XXIV and XXV in Table 12). The value of  $P_s$  has been still doubled in compound XXVI with additional asymmetric carbon introduced in the chiral group (Table 12).

$\text{C}_8\text{H}_{17}\text{-O}-\text{C}_6\text{H}_4-\text{C}_6\text{H}_4-\text{COO}-\text{C}_6\text{H}_4-\text{OOC}-\text{C}^*-\text{R}$		
Compound	R	$P_s$ (nC cm <sup>-2</sup> )
<b>XX</b>	$-\text{H}(\text{CH}_3)-\text{C}_4\text{H}_9$	15
<b>XXI</b>	$-\text{H}(\text{CF}_3)-\text{C}_4\text{H}_9$	98
<b>XXII</b>	$-\text{H}(\text{F})-\text{C}_4\text{H}_9$	86
<b>XXIII</b>	$-\text{F}(\text{CH}_3)-\text{C}_4\text{H}_9$	122

Table 11. Influence of fluorine atom in the chiral centre on the spontaneous polarization  $P_s$  at temperatures  $T = T_c - 20^\circ \text{C}$  (Hirai et al., 1992).

$\text{C}_8\text{H}_{17}\text{-O}-\text{C}_6\text{H}_4-\text{C}_6\text{H}_4-\text{OOC}-\text{C}^*\text{H}-\text{R}$		
Compound	R	$P_s$ (nC cm <sup>-2</sup> )
<b>XXIV</b>	$-(\text{CH}_3)-\text{C}_2\text{H}_5$	- 6
<b>XXV</b>	$-(\text{Cl})-\text{CH}(\text{CH}_3)_2$	140
<b>XXVI</b>	$-(\text{Cl})-\text{C}^*\text{H}(\text{CH}_3)-\text{C}_2\text{H}_5$	290

Table 12. Maximal values of the spontaneous polarization  $P_s$  at compounds XXIV (Terashima et al., 1986), XXV and XXVI (Bahr & Heppke, 1986).

The FLCs consisting of molecules with the heterocycle in the molecular core usually have rather high values of the  $P_s$ . Therefore, combination of the fluorine substitution with heterocyclic compounds yields very good results for the  $P_s$  values as it is demonstrated in Table 13.

$\text{C}_6\text{H}_{13}\text{-O}-\text{C}_6\text{H}_4-\text{N}(\text{C}_6\text{H}_4)-\text{N}(\text{C}_6\text{H}_4)-\text{OOC}-\text{C}^*-\text{R}$		
Compound	R	$P_s$ (nC cm <sup>-2</sup> )
<b>XXVII</b>	$-(\text{CH}_3)\text{F}-\text{C}_5\text{H}_{11}$	269
<b>XXVIII</b>	$-(\text{CH}_3)\text{H}-\text{C}_4\text{H}_9$	32
<b>XXIX</b>	$-(\text{F})\text{H}-\text{C}_4\text{H}_9$	192

Table 13. Combined influence of the fluorine substitution in the chiral centre with the heterocycle in the molecular core on the spontaneous polarization  $P_s$  at temperatures  $T = T_c - 10^\circ \text{C}$  (Hirai et al., 1992).

From Tables 11 and 13 one can infer the role of the exact position of the halogen substitution on the asymmetric carbon. It is seen that the substitution of the hydrogen atom results in the highest  $P_s$  value.

In contrast to the substitution on the molecular core the effect of the halogen on  $P_s$  increases according to sequence  $\text{Br} < \text{Cl} < \text{F}$  (see Table 14). As the differences in the dipole moment of the C-X bond are small, apparently the volume of the halogen atom plays a role. Extremely high  $P_s$  has been found for compounds based on 5-alkylpentano-5-lacton (Nakauchi et al., 1989; Sakashita et al., 1992). Such high values results from a synergic effect of two asymmetric carbons (see Table 15) and a polar group located directly in the chiral centre, which represents steric precondition for hindering of the molecular rotation.

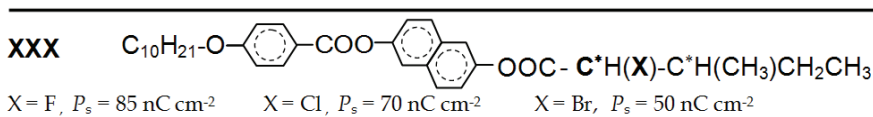


Table 14. Values of the spontaneous polarization  $P_s$  at temperature  $T = T_c - 10^\circ \text{C}$ . Influence a substitution with halogen atom on asymmetric carbon (Sierra et al., 1992).

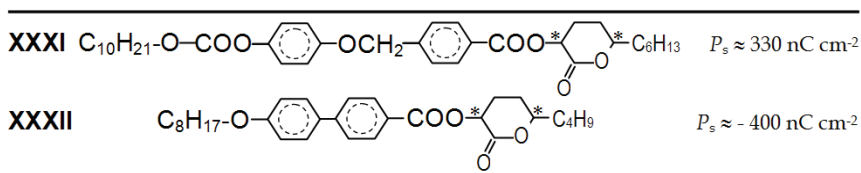


Table 15. Maximum measured values of the spontaneous polarization  $P_s$  at compounds with a valerolactone chiral centre at temperature  $T = T_c - 10^\circ \text{C}$ , XXXI (Nakauchi et al., 1989) and XXXII (Sakashita et al., 1992).

#### 4.4 Other effects

Properly chosen linkage  $Z$  can be significant for increase of the  $P_s$  value, as it is evident from Table 16.

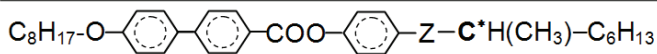
$\text{C}_8\text{H}_{17}\text{-O-}$		
Compound	Z	$P_s \text{ (nC cm}^{-2}\text{)}$
<b>II</b>	CO	403
<b>XVII</b>	COO	70
<b>XI</b>	O	-45

Table 16. Influence of the linkage group  $Z$  on the spontaneous polarization  $P_s$ .

Another factor, which favorably affects the spontaneous polarization, is presence of more polar groups with a suitable preferential conformation near the asymmetric carbon atom. For example see substances with the lactic acid moiety in which the chiral carbon atom is

flanked by two lateral dipoles  $p_i$  (Fig. 5). Because of the proximity of the methyl group on the central chiral atom to adjacent lateral carbonyl dipoles and consequent steric hindrance, such arrangement may produce materials with relatively high  $P_s$  (see Table 17).

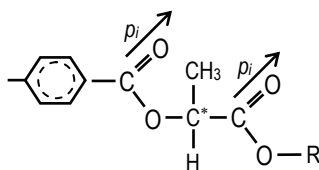


Fig. 5. A chiral centre with the asymmetric carbon atom which is flanked by two lateral carbonyl dipoles (R is non-chiral aliphatic chain)

<b>XXXIII</b>	
<b>XXXIV</b>	
	SmC* range (°C) $P_s$ ( $T_c - 20^\circ\text{C}$ ) $P_s$ (max)
XXXIII	96 - 145                  120                  210
XXXIV	79 - 101                  117                  117

Table 17. Temperature range of the SmC\* mesophase, maximum measured values of the spontaneous polarization  $P_s$  (nC cm<sup>-2</sup>) and values of the  $P_s$  at temperatures  $T = T_c - 20^\circ\text{C}$  at compounds XXXIII (Zu-Sheng Xu et al., 1999) and XXXIV (Kašpar et al., 2004).

The FLCs consisting of molecules with two or more asymmetric carbon atoms at one end usually have rather high  $P_s$ . Nevertheless, there is not a simple relation between the value of  $P_s$  and a number of C\* atoms. The chiral centre configuration namely relative orientation of dipole moments around the asymmetric carbon atoms, and degree of intramolecular rotation hindrance play an important role. The situation can be illustrated on a rather rare compound with three asymmetric carbon atoms (XXXVII, Table 18). In this compound, CH<sub>2</sub> linkage between the second and third asymmetric carbon atoms has non-convenient influence on  $P_s$ .

Compound	R	$\Delta T_{\text{SmC}^*}$ (°C) $P_s$ (max)
XXXV	C*(H)(CH <sub>3</sub> )-COO-C <sub>7</sub> H <sub>15</sub>	3 - 61                  55 nC cm <sup>-2</sup>
XXXVI	C*(H)(CH <sub>3</sub> )-COO-C*(H)(CH <sub>3</sub> )-COO-C <sub>6</sub> H <sub>13</sub>	59 - 88                  93 nC cm <sup>-2</sup>
XXXVII	C*(H)(CH <sub>3</sub> )-COO-C*(H)(CH <sub>3</sub> )-COO-CH <sub>2</sub> -C*(H)(CH <sub>3</sub> )-C <sub>2</sub> H <sub>5</sub>	98-104                  113 nC cm <sup>-2</sup>

Table 18. Temperature range  $\Delta T$  of the SmC\* mesophase and maximum measured values of the spontaneous polarization  $P_s$ . Influence of number of the asymmetric carbon atoms at compounds XXXV (Taniguchi et al., 1988) and XXXVI, XXXVII (Kašpar et al., 2001).

Very high spontaneous polarization was established for compounds with strongly fluorinated terminal alkyl chains (Table 19). Such compounds exhibit also antiferroelectric phases ( $\text{SmC}_A^*$ ). Other effects, e.g. number of carbon atoms in the linear aliphatic chain far-away from the chiral centre, are less important and often also ambiguous.

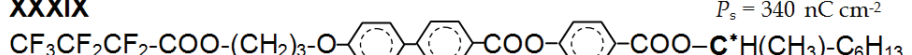
<b>XXXVIII</b>		$P_s = 155 \text{ nC cm}^{-2}$
<b>XXXIX</b>		$P_s = 340 \text{ nC cm}^{-2}$

Table 19. Values of the spontaneous polarization  $P_s$  at temperatures  $T = T_c - 30^\circ \text{C}$ . Influence of fluorination of the terminal alkyl chain R (Dabrowski, 2000).

## 5. Ferroelectric liquid crystalline materials for applications

The value of the spontaneous polarization  $P_s$  is a crucial parameter for behavior of FLCs in an electric field and thus must be carefully optimized for specific electro-optical cells. Other parameters as the helical pitch length, optical and dielectric anisotropy, viscosity and tilt angle value are important as well for satisfying operation of different FLC electro-optic equipments (e.g. displays). Furthermore, the type of the mesophase existing at temperatures above the FE  $\text{SmC}^*$  phase (either the cholesteric or the smectic  $A^*$  phase) is important for alignment of the liquid crystalline materials in the electro-optic cells. Unfortunately, it is quite impossible to find all suitable properties for practical use in one ferroelectric compound. The only solution how to create a suitable material with desirable properties is mixing of several liquid crystalline components, both chiral and non-chiral substances.

Typically, an eutectic non-chiral  $\text{SmC}$  mixture is prepared with desirable properties that are stable in a wide temperature range (including room temperature). Ferroelectricity is then induced by adding a suitable chiral dopant exhibiting the  $\text{SmC}^*$  phase. For this purpose the spontaneous polarization of this dopant must be extremely high in order to achieve a desirable  $P_s$  value of the mixture with the lowest concentration and thus with only a minimum affection of others parameters. The use of only low amount of chiral dopant in the resulting FE material intended for application also lower the costs, as the chiral component is by far its the most expensive ingredient.

Single compounds with extremely high  $P_s$  (or possibly mixtures of them) are applied only for realization of fast modulated electro-optical cells ( $10^6 \text{ Hz}$ ) on the basis of electroclinic effect in the  $\text{SmA}^*$  mesophase.

## 6. Banana liquid crystals

In 1996 new polar phases have been discovered in materials composed of molecules with a bent-core (Niori et al., 1996). Such molecules are bent-shaped (banana) and can create, so called banana liquid crystals. As an example two formulas of the molecules creating banana liquid crystals are shown for example in Table 20.

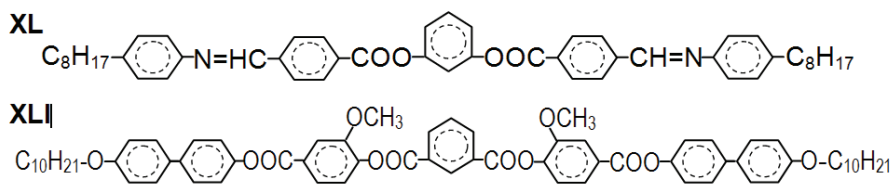


Table 20. Examples of the bent-core (banana) molecules XL (Matsunaga & Miyamoto (1993) and XLI (Kašpar et al. (2002))).

Molecular models of a typical rod-like molecule (VIII) and banana-like molecule (XL) are presented for comparison in Figure 6.

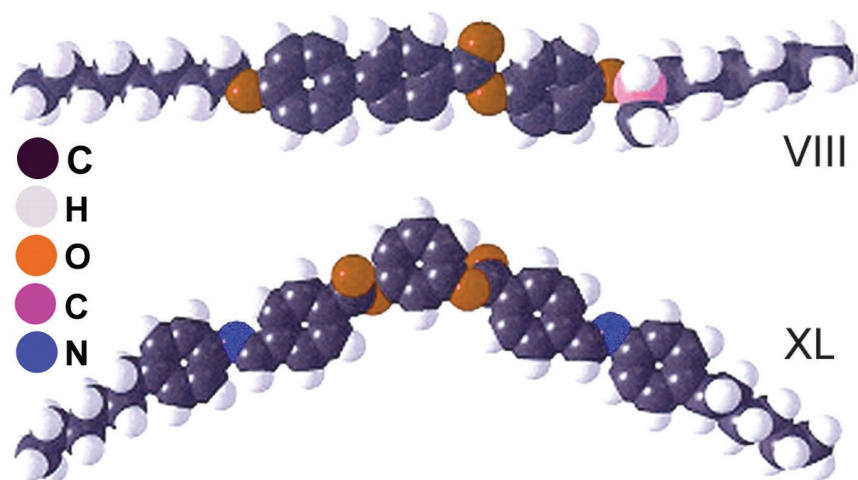


Fig. 6. Three dimensional molecular models of a rod-like molecule (VIII) with the asymmetric atom (pink colored) and banana-like molecule (XL).

Packing of these molecules in the smectic layers creates the structural layer chirality even though the molecules are non-chiral. Moreover, the mesomorphic properties of the bent-shaped compounds are richer than those of classical materials with rod-like molecules.

So far 8 types of so-called B-phases have been discovered and their structural properties investigated. These new mesophases are denoted by the letter B, which refers to the characteristic bent or banana molecular shape. Chronologically the terms B1, B2, B3, etc have been used in the literature to designate different phases as they were discovered (for review see e.g. Pelzl et al. 1999; Takezoe & Takanishi, 2006; Reddy et al. 2006). Among them, only B2 phase (sometimes denoted as SmCP) is fully and easily switchable. This phase exhibits mostly AF and quite exceptionally FE properties. The first FE banana B2 phase was reported in (Gorecka et al. 2000) for a compound with bent-shaped molecules, but with a chiral centers introduced in end chains. In non-chiral bananas the FE phase has been found mostly for non-symmetrical bent-shaped molecules (Novotná et al. 2006) or for molecules having a hockey-stick form (see Fig. 7).

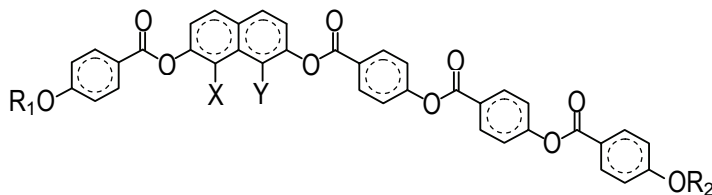


Fig. 7. Molecules of the hockey-stick shape (Novotná et al., 2008).  $R_{1,2}$  are alkyl chains, X, Y stand for H,  $\text{CH}_3$ , Cl, or CN.

It was found that B2 phase exhibits typically strong non-linear electro-optic effect and subsequently strong SHG signal exceeding by several orders the SHG signal of classical liquid crystals (Novotná et al., 2008). The spontaneous polarization is typically up to the order of several hundreds, usually more than  $700 \text{ nC cm}^{-2}$  (Pelzl et al., 1999; Reddy et al., 2006). These properties indicate potential of these materials in pyro- or piezo-electric applications. Of course, despite extensive work in this area, many questions remain to be answered. Among others, sample alignment is not only goal for applications but also for basic research.

Liquid crystals composed of molecules having hockey-stick form (see Fig. 7) represent an intermediate material in which phases typical for both rod-like and bent-shaped molecules can exist in different temperature ranges or in different homologues. Thus they exhibit nematic phases as well as smectic FE and AF phases, in some cases also banana type phases as B2 (Reddy et al., 2006; Novotná et al., 2008). Investigation of various forms of molecules that can form liquid crystalline state can help to explain some general structure-property relationships concerning the formation of polar order and structural chirality.

In any case, the investigation of bent shaped liquid crystals is a typical multidisciplinary field where many questions remain still open.

## 7. Conclusions

Hundreds of thousands of FE liquid crystals have been synthesized and characterized so far. Still full data on the spontaneous polarization are not available for overwhelming part of them, particularly in case the  $P_s$  is temperature dependent. This is one of the reasons why it is difficult to find definite molecular configuration for a compound with value of  $P_s$  desired for a specific application. The other reason is strongly complex influence of each molecular structural feature on the resulting material properties. This contribution formulates main general rules that lead to increase of  $P_s$ , namely increase of lateral molecular dipole moment and hindering of both molecular and intramolecular rotations. It is also shown that the problem solving is not straightforward as each step may cause non-intended negative effects on the stabilization of the FE phase in sufficiently broad and low temperature range, which is demanded for technical applications. Also the nature of the high temperature phase (above the FE one), which is also watched when considering specific applications, can be easily influenced by even slight change of the molecular structure.

In summary, the results discussed here can be useful for designing the molecular structure for applications. Besides, they contribute to general knowledge on the molecular structure – material property relation in liquid crystals. Some important problems yet remain to be solved. Nevertheless, ferroelectric liquid crystals gain a niche market, for example, in fast

high-resolution microdisplays for near-eye applications, such as view-finders for digital cameras or camcorders.

## 8. Acknowledgment

This work was financially supported by the Ministry of Education, Youth and Sports of Czech Republic under the research project VZ1 MSM0021627501 and the Czech Science Foundation project No. 204/11/0723.

## 9. References

- Bahr, Ch. & Heppke, G. (1986). Ferroelectric liquid crystals with high spontaneous polarization. *Mol. Cryst. Liq. Cryst. Lett.* Vol. 4, No.2, pp. 31-37
- Barberá, J.; Omenat, A. & Serrano, J. L. (1989). New chiral smectic liquid crystals with the asymmetrical carbon in the central part of the molecule. *Mol. Cryst. Liq. Cryst.* Vol. 166, pp.167-171
- Beresnev, L. A. & Blinov, L. M. (1981). Pyroelectric properties of liquid crystals. *Ferroelectrics* Vol. 33, pp. 129-138
- Bone, M.F.; Bradshaw, M. J.; Chan, L. K. M.; Coates, D.; Constant, J.; Gemmell, P. A.; Gray, G. W.; Lacey D.
- Chin, E.; Goodby, J.W. & Patel, J.S. (1988). The liquid-crystalline properties of some chiral derivatives of the 4-n-alkanoyloxibiphenyl-4'-carboxylic acid. *Mol. Cryst. Liq. Cryst. Inc. Nonlin. Opt.* Vol. 157, pp. 163-191
- Clark, N.A. & Lagerwall, S.T. (1983). Submicrosecond bistable electro-optic switching in liquid crystals. *Appl. Phys. Lett.* Vol. 36, pp. 899-901
- Dabrowski, R. (2000). Liquid crystals with fluorinated terminal chains and antiferroelectric properties. *Ferroelectrics*, Vol. 243, pp. 1-18
- de Gennes, P.G. & Prost, J. (1993). *The Physics of Liquid Crystals*, Clarendon Press, ISBN 0-19-852024-7, Oxford, England
- Finkenzeller, U.; Pausch, A. E.; Poetsch, E. & Suermann, J. (1993). Ferroelectric Smectic Displays and Materials. *Kontakte - Merck (Darmstadt)* (1993) No. 2, pp. 3-14
- Furukawa, K.; Terashima, K.; Ichihashi, M.; Saitoh, S.; Miyazawa, K. & Inukai, T. (1988). Chiral smectic C liquid crystals having an electronegative substituent ortho to the chiral tail group – a study of a factor determining the magnitude of spontaneous polarization. *Ferroelectrics* Vol. 85, 451-459
- Goodby, J.W. (Ed.). (1991). *Ferroelectric Liquid Crystals. Principles, Properties and Applications*. Gordon and Breach Science Publishers S.A., ISBN 2-88124-282-0, London, United Kingdom
- Gorecka, E., Pocięcha, D., Araoka, F., Link, D.R., Nakata, M., Thisayukta, J., Takanishi, Y., Ishikawa, K., Watanabe, J., & Takezoe, H. (2000). Ferroelectric Phase in a chiral bent-core smectic liquid crystal: Dielectric and optical second harmonic generation measurements. *Phys. Rev. E* Vol. 65, No.4, pp. R4524-R4527
- Gray, G.W. (Ed.). (1987). *Thermotropic Liquid Crystals*. John Wiley & Sons, Ltd., ISBN 0-471-91504-1, Chichester, United Kingdom
- Hirai, T.; Yoshizawa, A.; Shiratori, N.; Yokoyama, A.; Herman, C.; Pagano-Stauffler, L.; Vohra, R. & Wand, M. (1992). Ferroelectric liquid crystals possessing a novel

- fluorinated chiral moiety. *Proceedings Series of the SPIE - The International Society for Optical Engineering - Liquid Crystal Materials, Devices, and Applications*, Vol. 1665, pp. 134-145, San Jose, California, February 1992
- Inukai, T.; Saitoh, S.; Inoue, H.; Miyazawa, K.; Terashima, K. & Furukawa, K. (1986). Physical properties of some chiral smectic liquid crystals having 1-methyl-alkoxy – phenyl group. *Mol. Cryst. Liq. Cryst.* Vol. 141, pp. 251-266
- Kašpar, M.; Bubnov, A.; Hamplová, V.; Pirkl S. & Glogarová M. (2004). New ferroelectric liquid crystalline materials with an azo group in the molecular core. *Liquid Crystals* Vol. 31, No. 6, pp. 821-830
- Kašpar, M.; Hamplová, V.; Novotná, V.; Glogarová, M.; Pocięcha D. & Vaněk, P. (2001). New series of ferroelectric liquid crystals with two or three chiral centers exhibiting antiferroelectric and hexatic phases. *Liquid Crystals*. Vol. 28, No. 8, pp.1203-1209
- Kašpar, M.; Hamplová, V.; Novotná, V.; Glogarová, M. & Vaněk, P. (2002) . New banana-type liquid crystal with a methoxy group substituted near the central ring. *J. Mater. Chem.* Vol. 12, pp. 2221-24
- Kentischer, F., Macdonald, R., Warnick, P., & Heppke G. (1998). Second harmonic generation (SHG) investigations of different phases of banana shaped molecules. *Liquid Crystals* Vol. 25, No. 3, pp. 341-347
- Kašpar, M.; Bubnov, A.; Hamplová, V.; Málková, Z.; Pirkl, S. & Glogarová, M. (2007). Effect of lateral substitution by fluorine and bromine atoms in ferroelectric liquid crystalline materials containing a 2- alkoxypropanoate unit. *Liquid Crystals* Vol. 34, No.10, pp. 1185-92
- Kitzerow, H-S. & Bahr, C. (Eds.). (2001). *Chirality in Liquid Crystals*. Springer, ISBN 0-387-98679-0, New York, USA
- Lagerwall, S. T. (1999). *Ferroelectric and Antiferroelectric Liquid Crystals*. VCH, ISBN 3-527-29831-2, Weinheim
- Lueder, E. (2010). *Liquid Crystal Displays* (2nd edition), John Wiley & Sons, Ltd., ISBN 978-0-470-74519-9 (H/B), Chichester, United Kingdom
- Matsunaga, Y. & Miyamoto, S. (1993). Mesomorphic behavior of 2,4-bis-(4-alkoxybenzylidene) cyclopentanones and related compounds. *Mol. Cryst. Liq. Cryst.* Vol. 237, pp. 311-317
- Meyer R.B.; Libert L.; Strzelecki L. & Keller, P. (1975). Ferroelectric liquid crystals. *J. Physique (France)* Vol. 36, pp. L69-L71
- Nakauchi, J.; Kageyama, Y.; Hayashi, S. & Sakashita K. (1989) . Novel ferroelectric liquid crystals derived from n-alkyl esters of (R)-3-hydroxybutanoic acid (II). *Bull. Chem. Soc. Jpn.* Vol. 62, pp. 1685-91
- Nakauchi, J.; Uematsu, M.; Sakashita, K.; Kageyama, Y.; Hayashi, S.; Ikemoto, T. & Mori, K. (1989). Novel ferroelectric liquid crystals with very large spontaneous polarization. *Jap. J. Appl. Phys.* Vol. 28, No. 7, pp. L 1258-L 1260
- Niori, T., Sekine, J., Watanabe, J., Furukawa, T., & Takezoe, H. (1996). Distinct ferroelectric liquid crystals consisting of banana shaped achiral molecules. *J. Mater. Chem.* Vol. 6, pp. 1231.
- Novotná, V., Kašpar, M., Hamplová, V., Glogarová, M., Lejček, L., Kroupa, J., & Pocięcha, D. (2006). Ferroelectric-like behaviour of the SmCP phase in liquid crystalline compounds with asymmetrical bent-core molecules. *J. Mater. Chem.* Vol. 16, pp. 2031-2038

- Novotná, V., Žurek, J., Kozmík, V., Glogarová, M., Kroupa, J., Pocięcha, D. (2008). Novel hockey-stick mesogens with the nematic, synclinic and anticlinic smectic C phase sequence. *Liquid Crystals* Vol. 35, No. 8, pp. 1023-1036
- Oswald, P. & Pieranski, P. (2006). *Smectic and columnar Liquid Crystals*. Taylor & Francis, ISBN 0-8493-9840-1, New York, USA
- Pachomov, S. (1997). Syntheses and studies of ferroelectric liquid crystals. *PhD Thesis*. Institute of Chemical Technology, p 1-142, Prague, Czech Republic, April 1997
- Pelzl, G., Diele, S. & Weissflog, W. (1999). Banana-Shaped Compounds-A New Field of Liquid Crystals. *Advanced Materials* Vol. 11, No. 9, pp. 707-727
- Pirkl, S. (1986). Molekulární struktura feroelektrických kapalných krystalů. (Molecular structure of ferroelectric liquid crystals). *Chemické listy* Vol.80, pp. 449-478
- Pirkl, S.; Tuček, J. & Schiffmann, V. (1990). Ferroelectric liquid crystal electrooptic cell with high contrast bistability. *Mol. Cryst. Liq. Cryst.* Vol. 192, pp. 317-321
- Pirkl, S. (1997). Feroelektrické kapalné krystaly pro elektrooptiku I, II. (Ferroelectric liquid crystals for electrooptics). *Sdělovací technika* Vol. 60, No.10, pp. 8-10, Vol. 60, No.11, 6-9
- Reddy, R.A. & Tschierske, (2006). Bent-core liquid crystals: polar order, superstructural chirality and spontaneous desymmetrisation in soft matter systems. *J. Mater. Chem.* Vol. 16, pp. 907-961
- Sakashita K.; Ikemoto T.; Nakaoka Y.; Kamimura S.; Kageyama Y.; Terada F.; Yoshihiro S. & Mori, K. (1992). Stereochemical studies of optically active 2-hydroxy-5-alkyl- $\delta$ -valerolactone derivatives as chiral dopant for ferroelectric liquid crystals. *Liquid Crystals* Vol. 12, No. 5, pp. 769-777
- Sakurai, T.; Sakamoto, K.; Honma, M.; Toshiho, K. & Ozaki, M. (1984). Synthesis and ferroelectric properties of new series of ferroelectric liquid crystals. *Ferroelectrics* Vol. 58, pp. 21-32
- Sierra, T.; Serrano, J. L.; Ros, M. B.; Ezcurra, A. & Zubia, J. (1992). Synthesis and study of new  $\alpha$ -haloacid ferroelectric liquid crystal derivatives. *J. Am. Chem. Soc.* Vol. 114, No. 20, pp. 7645-51
- Takezoe, H. & Takanishi, Y. (2006). Bent-Core Liquid Crystals: their Mysterious and Attractive World. *Jpn. J. Appl. Phys.* Vol. 45, No. 2A, pp. 597-625
- Taniguchi, H.; Ozaki, M.; Yoshino, K.; Satoh, K. & Yamasaki, N. (1988). Dependence of spontaneous polarization on orientation and position of several bond moments near chiral parts in ferroelectric liquid crystals. *Ferroelectrics* Vol. 77, pp. 137-144
- Terashima, K.; Ichihashi, M.; Kikuchi, M.; Furukawa, K. & Inukai, T. (1986). Some observations on the sense and magnitude of spontaneous polarization and twisting power of a number of ferroelectric liquid crystal types. *Mol. Cryst. Liq. Cryst.* Vol. 141, pp. 237-249
- Uemoto, T.; Toshiho, K. & Inuishi, Y. (1981). Electrical and optical properties of ferroelectric liquid crystals and influence of applied pressure. *Mol. Cryst. Liq. Cryst.* Vol. 67, 137-152
- Walba, D. M.; Ros, M. B.; Clark, N. A.; Shao, R.; Johnson, K. M.; Robinson, M. G.; Liu, J. Y. & Doroski, D. (1991). An approach to the design of ferroelectric liquid crystals with large second order electronic nonlinear optical susceptibility. *Mol. Cryst. Liq. Cryst.* Vol. 198, 51-60

- Yang, D. & Wu S. (2006). *Fundamentals of Liquid Crystal Devices*. John Wiley & Sons, Ltd., ISBN 978-0-470-01542-1, Chichester, United Kingdom
- Yoshizawa, A.; Nishiyama, I.; Fukumasa, M.; Hirai, T. & Yamane, M. (1989). New ferroelectric liquid crystal with large spontaneous polarization. *Jpn. J. Appl. Phys.* Vol. 28, No. 7, pp. L 1269-L 1270
- Zu-Sheng, Xu; Lemieux, R. P.; Natansohn, A.; Rochon, P. & Shashidhar, R. (1999). Synthesis and characterization of novel ferroelectric liquid crystals and copolymers containing biphenyl azobenzene and/or phenyl biphenyl carboxylate mesogenic group. *Liquid Crystals* Vol. 26, No. 3, pp. 351-359

# Ferroelectric Liquid Crystals Composed of Banana-Shaped Thioesters

Stanisław Wróbel<sup>1</sup>, Janusz Chruściel<sup>2</sup>, Marta Wierzejska-Adamowicz<sup>1</sup>,  
Monika Marzec<sup>1</sup>, Danuta M. Ossowska-Chruściel<sup>2</sup>,  
Christian Legrand<sup>3</sup> and Redouane Douali<sup>3</sup>

<sup>1</sup>*Institute of Physics, Jagiellonian University, Kraków*

<sup>2</sup>*Institute of Chemistry, Siedlce University of Natural Sciences and Humanities, Siedlce*

<sup>3</sup>*Université du Littoral Côte d'Opale, LEMCEL, Calais*

<sup>1,2</sup>Poland

<sup>3</sup>France

## 1. Introduction

Thermotropic liquid crystals composed of rod like molecules are known as calamitic liquid crystals. Flatten molecules of some organic compounds form discotic liquid crystals. Both kinds of compounds may exhibit nematic phase. Calamitic mesogens may also form lamellar smectic structures being so important for living systems, whereas discotic molecules make columnar mesophases. Banana-shaped (bow-shaped or bent-core) ferroelectric liquid crystals have been discovered in the last decade of the 20-th century (Noiri et al., 1996). Since then there has been a great interest in their dielectric and electro-optic properties due to potential applications (Sekine et al., 1997; Link et al., 1997; Pelzl et al., 1999). At the beginning some of the bent-core compounds were not chemically stable enough as to study them experimentally during cooling and heating runs in long lasting experiments (Wróbel et al., 2000). It came out that bent-core achiral thioesters are very stable materials showing either B<sub>1</sub> or B<sub>2</sub> phase (Rouillon et al., 2001; Ossowska-Chruściel, 2007, 2009). In this article we present complementary studies on B<sub>1</sub> and B<sub>2</sub> phases of 1,3-phenylene bis{4-[(4-alkoxybenzoyl)-sulfanyl]benzoates} (in short: nOSOR) having achiral symmetric bent-core molecules shown in Fig. 1.

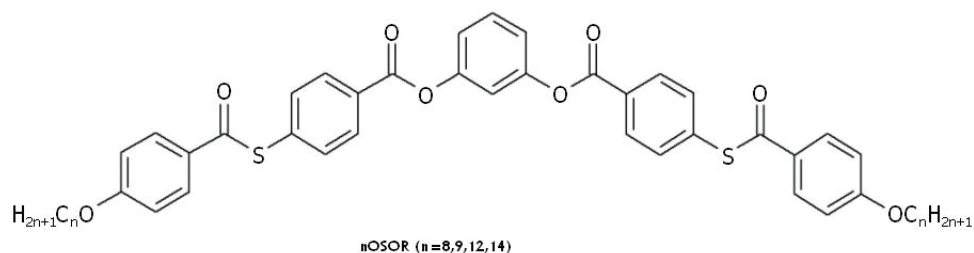


Fig. 1. Molecular structure of the symmetric thioester compounds studied

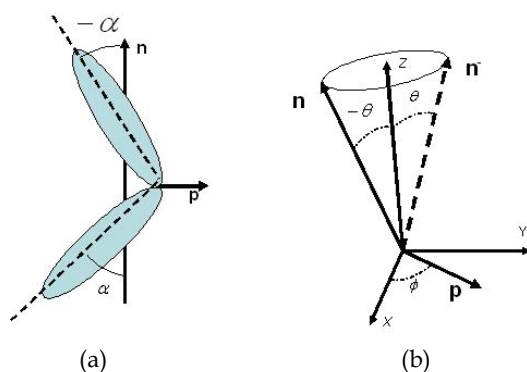


Fig. 2. (a) Simplified model of bent-core molecule and two directors  $n$  and  $p$ , (b) Primary  $n$  and secondary  $p$  directors in the  $(X, Y, Z)$  laboratory reference frame. In  $B_2$  phase the  $n$  director is tilted with respect to the smectic plane normal  $Z$  by the angle  $+\theta$  or  $-\theta$ . The  $n$  director is the average direction of the long molecular axis. The secondary director  $p$  is the average position for the short molecular in-plane axis. The other short axis is perpendicular to the  $(n, p)$  plane.

Because of the tilt sign (+ or -) of the  $n$  director (Fig. 2 (b)) and two directions of the  $p$  polar director ( $+p$  and  $-p$ ) there are four different structures of  $B_2$  phase: 1. Synclinc ferroelectric ( $SmC_S P_F$ ) - the tilt angle is positive or negative in all smectic layers and  $p$  vectors are parallel, 2. Synclinc antiferroelectric ( $SmC_S P_A$ ), 3. Anticlinic ferroelectric ( $SmC_A P_F$ ), and 4. Anticlinic antiferroelectric ( $SmC_A P_A$ ). The last one shows up for two symmetric compounds (12OSOR and 14OSOR) studied in this work. A general symbol of  $B_2$  phase can be written as follows:  $SmC_{SA}P_{FA}$ , where index "S" stands for synclinc, A - for anticlinic order of molecules in two neighboring layers, F - for ferroelectric and A - antiferroelectric order of polarization vectors.

Banana-shaped compounds may form both lamellar and/or columnar mesophases (Szydłowska, 2003) that have become a subject of intensive experimental (Reddy & Tschierske, 2006) and theoretical studies (Vaupotič, 2006) in the last decades. In the first place research on electro-optic switching in ferro- and anti-ferroelectric phases composed of bent-core molecules has been done because of possible practical applications (Walba et al., 2000; Reddy & Tschierske, 2006).

Since the discovery of ferroelectric order in smectic B phases composed of polar achiral banana-shaped molecules many experimental studies have been done that confirm ferro- or antiferroelectric order inside the layers and positive (ferroelectric) or negative (antiferroelectric) correlations between the layers. Theoretical studies were focused on intermolecular interactions within the layers as well as interlayer correlations (Vaupotič & Čopič, 2005; Vaupotič, 2006).

Liquid crystalline materials built of bent-core molecules are also attractive because they exhibit new physical properties. They possess two-dimensional smectic phases that display qualitatively different physical properties than the calamitic ferroelectric liquid crystals (Pelzl, 1999; Reddy & Tschierske, 2006). Bent-core non-chiral molecules show tendency to form a polar order within the smectic layers. Using a dielectric spectroscopy method it was found (Kresse et al., 2001, Kresse, 2003) that the reorientation of polar molecules is strongly

hindered in B<sub>2</sub> phase because of dense packing of bent-core molecules in smectic layers. Due to this the secondary order parameter (spontaneous polarization) is almost temperature independent.

Thin Langmuir-Blodgett films composed of bent-core molecules studied by reversal current method (Geivandov, 2006) reveal an interesting property that polarization of nano-layers is similar to bulk polarization. Both ferro- and anti-ferroelectric order have been observed. It was also found for nano-layers that the molecules are mobile in such restricted geometry what facilitates both ferro- and antiferroelectric switching.

Out of eight B phases: B<sub>1</sub>, B<sub>2</sub>, B<sub>3</sub>, ..., B<sub>7</sub>, and B<sub>8</sub> (Reddy & Tschierske, 2006) the most thoroughly investigated seems to be the B<sub>2</sub> phase which may show one of four types of order depending on the sign of tilt angle ( $+\theta$  or  $-\theta$ ) as well as on the sign of correlations (positive - ferroelectric order or negative - antiferroelectric order) between the polarization vectors of neighboring layers ( $\sim P_j \cdot P_{j+1}$ ). Complementary studies performed on a few homologous series show that compounds with shorter side chains (C<sub>5</sub> - C<sub>9</sub>) exhibit only a frustrated B<sub>1</sub> phase, whereas those having longer chains (C<sub>10</sub> - C<sub>14</sub>) generally display antiferroelectric B<sub>2</sub> phase (Bedel et al., 2000).

The main objective of this article is to present dielectric and electro-optic behavior of B<sub>1</sub> or B<sub>2</sub> phases of four selected members of nOSOR series (n=8, 9, 12 and 14). The first two show only B<sub>1</sub> phase, and the other two with even number of carbon atoms in the side alkoxy chains display only B<sub>2</sub> phase of SmC<sub>A</sub>P<sub>A</sub> type.

## 2. Experimental methods

To study phase transitions and physical properties of B<sub>1</sub> and B<sub>2</sub> phases the following complementary methods have been employed: DSC calorimetry, polarizing microscopy texture observation, linear dielectric spectroscopy, and reversal current method. Using the latter it was possible to record the reversal current spectra for the B<sub>2</sub> phase in form of two well separated current peaks what substantiates antiferroelectric order of this phase. As also found, the B<sub>1</sub> exhibits also some kind of ferroelectric order which is being gradually reduced upon temperature decreasing (Wierzejska-Adamowicz, 2010; Chruściel, 2011).

### 2.1 DSC calorimetric studies

Thermal properties of the substances investigated have been studied by differential scanning calorimetry using Pyris1 DSC made by Perkin Elmer Company. Transition temperatures and enthalpies of the transitions have been computed based on DSC heating and cooling thermograms. Fig. 3 presents DSC results for 8OSOR compound which possesses enantiotropic B<sub>1</sub> phase showing up during cooling in a wide temperature range of 40 degrees. As one can see the melting process of this material is complex - on heating there are two transitions (Cr-Cr<sub>2</sub>-Cr<sub>1</sub>) between solid modifications. Below the B<sub>1</sub> enantiotropic phase there seems to be an orientationally disordered crystal (ODIC).

As an example endothermic and exothermic curves are shown in Fig. 4 for 12OSOR. It is seen that the B<sub>2</sub> phase is also enantiotropic one. On heating two crystalline modifications (Cr<sub>1</sub> and Cr<sub>2</sub>) were found. One should point out that all compounds studied in this work are thermally very stable - their clearing points do not change after a few heating and cooling runs.

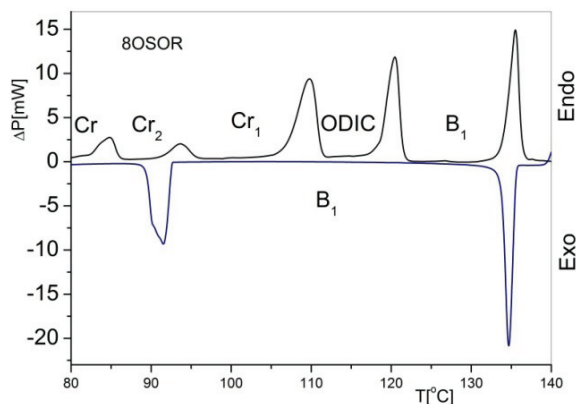


Fig. 3. Endothermic and exothermic runs obtained by Pyris 1 DSC for 8OSOR compound

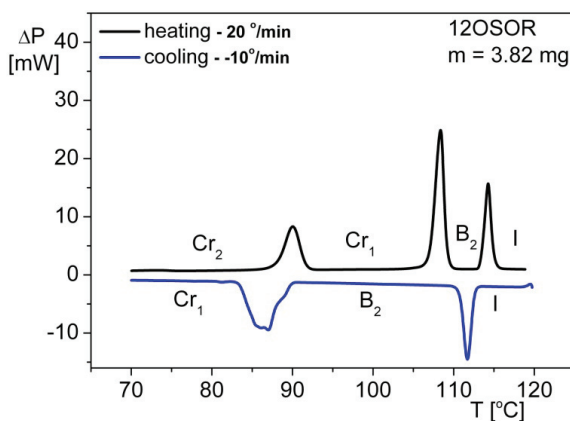


Fig. 4. DSC results obtained for 12OSOR compound on cooling and heating by using Pyris1 DSC

Studies of the physical properties of all compounds have been performed on cooling. The transition temperatures acquired by DSC method on cooling are as follows:

**8OSOR** - I 133.4 °C (16.9) → B<sub>1</sub> 92.7 °C (14.7) → Cr<sub>1</sub>

**9OSOR** - I 123.4 °C (16.0) → B<sub>1</sub> 82.6 °C (14.0) → Cr

**12OSOR** - I 112.6 °C (18.5) → B<sub>2</sub> 88.6 °C (38.7) → Cr<sub>1</sub>

**14OSOR** - I 114.6 °C (17.4) → B<sub>2</sub> 87.2 °C (57.6) → Cr

Transition enthalpies for the clearing and freezing points are given in round brackets in [kJ/mol]. As seen there are small differences between the clearing and freezing enthalpies for the first two homologs with B<sub>1</sub> phase.

## 2.2 Electro-optic methods

Texture observation and electro-optic switching between the planar and homeotropic textures for 12OSOR were done at LEMCEL using Olympus Polarizing Microscope BX60 and LINKAM temperature controller. Texture observations of 8OSOR, 9OSOR, 12OSOR, and 14OSOR were performed using Nikon Eclipse Polarizing Microscope LV100POL and INSTEC temperature controller in the Institute of Physics of the Jagiellonian University.

Polarizing microscopy measurements allowed us to identify phases and to observe a planar inhomogeneous (Fig. 5(a)) and homeotropic textures of  $B_2$  phase. The homeotropic texture (Fig. 6 (a)) was observed after applying bias field equal to  $26 V_{p-p} / \mu m$ . Figs. 5 (b) and 6 (b) present schematic molecular arrangements of the local planar and homeotropic alignments, respectively. Due to the splay deformation (Takanishi, 2003; Vaupotič, 2005) the texture is planar inhomogeneous (quasi-planar) with characteristic circular domains (Fig. 5 (a)). Under strong electric field ( $26 V_{p-p} / \mu m$ ) a fast transition to homeotropic texture is observed with secondary optical axis being perpendicular to the electrodes. Using triangular driving field at a certain voltage value a completely black homeotropic state was observed. Similar electro-optic behavior has been found for 14OSOR (Wierzejska-Adamowicz, 2010, Wierzejska-Adamowicz et al., 2010).

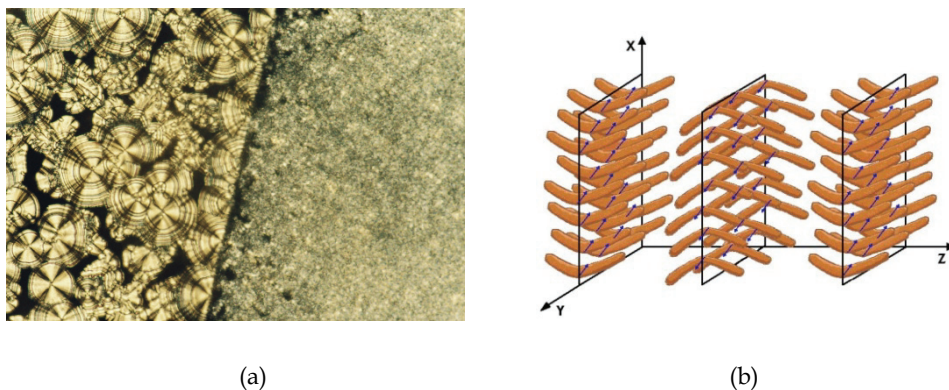


Fig. 5. (a) Planar texture of 12OSOR's  $B_2$  phase obtained at  $T=116.8^\circ C$ ,  $U=0 V_{p-p} / \mu m$ , AWAT HG cell -  $d=1.7 \mu m$  and (b) schematic local alignment of molecules in planar  $B_2$  phase.

This shows undoubtedly that there is an electro-optic switching between the two states  $SmC_A P_A \rightarrow SmC_S P_F$ . Upon applying triangular voltage wave the extinction directions of the characteristic circular domains (Fig. 5 (a)) reorient clockwise or counterclockwise depending on the field direction what was observed for symmetric (Walba et al., 2000; Sadashiva et al., 2000; Zhang et al., 2006) and asymmetric (Lee et al., 2010) banana-shaped systems. However, it was not possible to grow a mono-domain of uniform planar alignment even upon applying strong electric fields. Inhomogeneous planar texture (Fig. 5 (a)) was, consisting of Maltese crosses originated from concentric layer structures, was observed. Such structures were revealed by X-ray diffraction (Takanishi, 2003). Characteristic brushes forming Maltese crosses (Ortega et al., 2004) coincide with the polarizer-analyzer positions due to anticlinic order of molecules in two neighboring layers forming a pseudo-unit cell. The authors were able to grow  $B_2$  phase after applying a strong electric field to  $B_1$  phase.

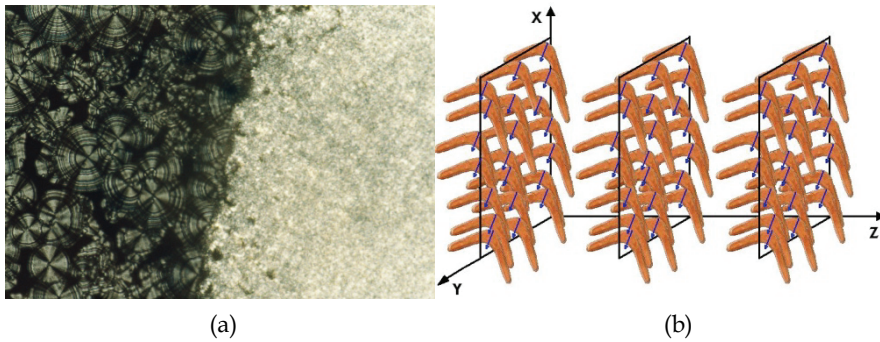


Fig. 6. (a). Quasi-homeotropic texture of 12OSOR's  $B_2$  phase observed at  $T=116.8^\circ\text{C}$ ,  $U=26$   $V_{p-p}/\mu\text{m}$ , AWAT HG cell -  $d=1.7 \mu\text{m}$  and (b) schematic local alignment of molecules in homeotropic  $B_2$  phase. Electric field is parallel to the X-axis. It is worth pointing out that upon applying triangular voltage wave a completely black state (homeotropic) was observed at a certain voltage value.

It is worth noting that the characteristic mosaic texture of  $B_1$  phase does not change at all under A.C. field and electro-optic switching is not observed (Ossowska-Chruściel, D.M. et al., 2007; Wierzejska-Adamowicz, 2010). Spontaneous polarization measurements were carried out - by means of reversal current method - using  $1.7 \mu\text{m}$  and  $3.2 \mu\text{m}$  AWAT HG ITO cells for 9OSOR and 12OSOR, respectively. The experimental set-up consists of

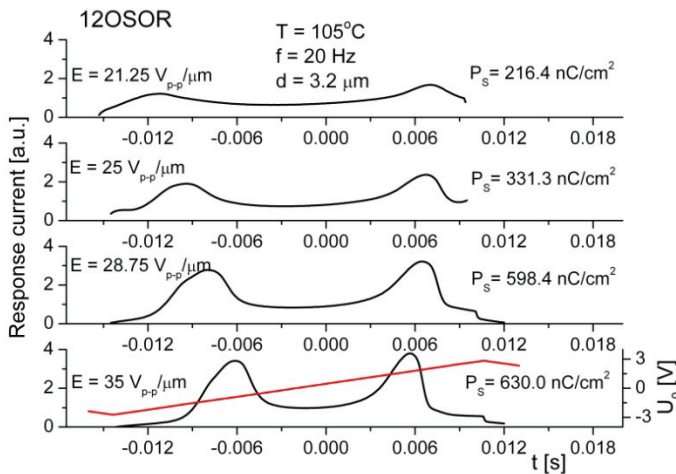


Fig. 7. Reversal current peaks obtained for antiferroelectric  $B_2$  phase of 12OSOR at different driving voltages - from threshold to saturation voltage (see also Fig. 9). The real value of the driving voltage was equal to  $U_0 \times 20 V_{p-p}$

Agilent 3310A wave form generator, FLC Electronics amplifier F20ADI and digital scope Agilent DSO6102A.

The  $B_2$  phases of 12OSOR and 14OSOR compounds are anticlinic and antiferroelectric ( $\text{SmCA}P_A$ ), so after applying to the electrodes a triangular wave two peaks are observed as

the current response of the sample in half a period of the driving voltage (Fig. 7). As seen in Fig. 8 spontaneous polarization of 12OSOR is very high - it reaches a value close to 600 nC/cm<sup>2</sup> and is weakly temperature dependent in the B<sub>2</sub> phase. The measurements were done applying driving electric field of 35 Vp-p/μm and frequency of 20 Hz. Spontaneous polarization of 14OSOR is slightly smaller and its temperature dependence is also weak (Chruściel, 2011)

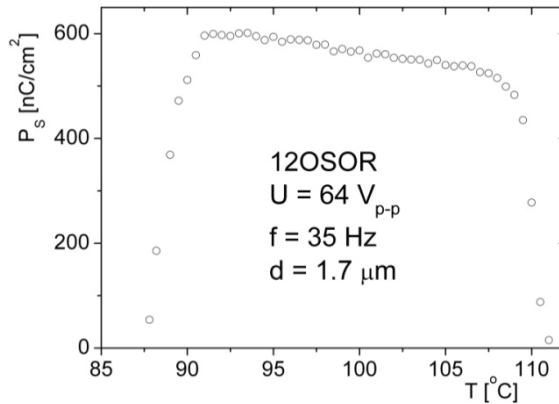


Fig. 8. Spontaneous polarization of B<sub>2</sub> phase vs. temperature for 12OSOR compound

As seen in Fig. 9 the polarization of B<sub>2</sub> phase depends non-linearly on electric field. Above 30V<sub>p-p</sub>/μm it becomes saturated reaching the value of spontaneous polarization. In addition this non-linear dependence begins above the threshold field (ca. 21 Vp-p/μm at 110 °C)

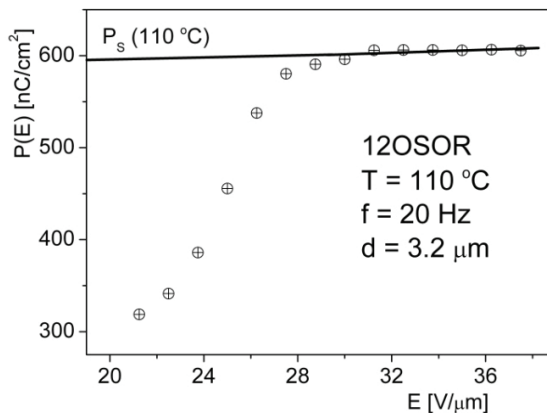


Fig. 9. Polarization vs. electric field of 12OSOR's B<sub>2</sub> phase at selected temperature of 110 °C

As seen in Figs. 8 and 9 the B<sub>2</sub> phase of 12OSOR exhibits large spontaneous polarization. As found before the B<sub>2</sub> phases composed of bent-core asymmetric molecules (Kohout et al., 2010) show distinctly smaller spontaneous polarization (from 200 to 380 nC/cm<sup>2</sup>) but upon cooling ferroelectric - antiferroelectric transition was observed.

As known, in  $B_1$  phase the side alkoxy chains of the molecules in one layer overlap on the cores of molecules in neighboring layers and there is a compensation of microscopic polarization (Reddy & Tschierske, 2006). However, using strong electric field one can induce polarization in this phase (Figs. 10 and 12) due to positive short range order of dipole moments inside the layers.

The  $B_1$  phase of 9OSOR shows a reasonable reversal current response (Fig. 10) which is typical for switching polarization vector from  $+P_s$  to  $-P_s$  in ferroelectrics. However, the temperature dependence of spontaneous polarization (Fig. 11) is not like that for a ferroelectric or antiferroelectric phase of classical ferroelectric liquid crystals (Wróbel et al., 2003). It can be treated as an induced polarization originating from molecular polar clusters created due to steric interactions inside the layers. It decreases with temperature decreasing due to inter- and/or intra-layer negative dipole-dipole correlation which are stronger at low temperatures.

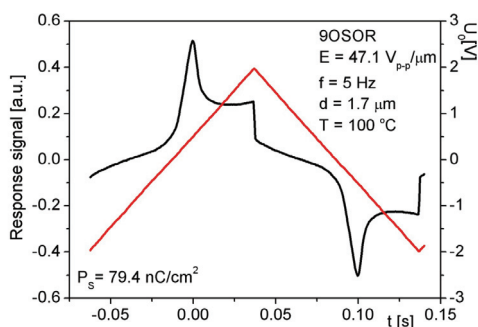


Fig. 10. Triangular driving voltage (right-hand side scale) applied vs. time and reversal current spectrum (left-hand side scale) of  $B_1$  phase of 9OSOR acquired for  $E = 47.1 \text{ V}_{p-p}/\mu\text{m}$ ,  $f = 5 \text{ Hz}$ ,  $d = 1.7 \mu\text{m}$  and at  $T = 100^\circ\text{C}$ . The real value of the driving voltage was equal to  $U_o \times 20 \text{ V}_{p-p}$

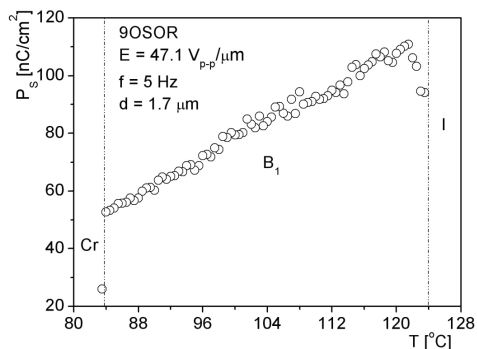


Fig. 11. Polarization of 9OSOR's ferroelectric  $B_1$  phase vs. temperature. Measurement conditions: triangular voltage wave -  $E = 47.1 \text{ V}_{p-p}/\mu\text{m}$ ,  $f = 5 \text{ Hz}$ ,  $d = 1.7 \mu\text{m}$

As found before by the dielectric relaxation spectroscopy, in the  $B_1$  phase there exists antiparallel dipole-dipole correlation of transverse dipole moments (Kresse et al., 2001; Kresse, 2003). There is also a strong retardation of molecular reorientational motions at the I- $B_1$  (or  $B_2$ )

phase transition which is being caused by high order of bent-core molecules in B phases. Large value of the transition enthalpies for the transition between the isotropic and liquid crystalline phase of these materials as well as weak temperature dependence of the spontaneous polarization of B<sub>2</sub> phase also substantiate high order of B phases. As one can additionally notice the enthalpy changes of melting and freezing points (Figs. 3 and 4) are distinctly smaller than those obtained for calamitic liquid crystals what reflects a distinctly smaller change of order between liquid crystalline and crystalline phase of bent-core systems.

It has been found in this study that the polarization of B<sub>1</sub> phase changes non-linearly with electric field applied (Fig. 12) yet it does not reach such large values as those obtained for the B<sub>2</sub> phase. Like for B<sub>2</sub> phase (Fig. 9) there is a threshold field of ca. 12 V/μm, above which a single reversal current peak shows up (Fig. 10), and above 25 V/μm the polarization of B<sub>1</sub> phase saturates but its value is smaller than 120 nC/cm<sup>2</sup>. This effect is most probably due to short range ferroelectric order and/or modulated structures (Szydłowska, 2003).

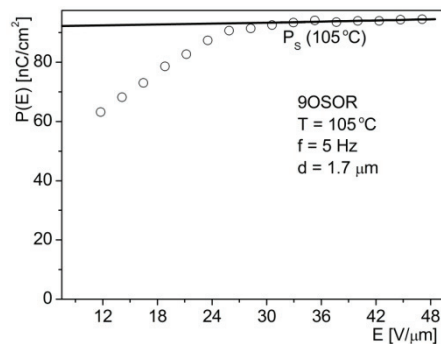


Fig. 12. Polarization vs. electric field applied to the sample of 9OSOR's ferroelectric B<sub>1</sub> phase. Parameters: frequency of the driving voltage -  $f = 5$  Hz, thickness of the sample  $d = 1.7$  μm.

### 2.3 Dielectric spectroscopy

Dielectric measurements were done using dielectric spectrometer based on Agilent 4294A precision impedance analyzer controlled by PC using a program written on VisualStudio.NET platform. Substances were put by means of capillary action into HG - 5μm AWAT cells with gold electrodes. The dielectric spectrometer allows one to measure dielectric spectra with high accuracy. The measurements have been done using the cells with gold electrodes covered with rubbed polymer layers what facilitates planar but for banana-shaped molecules inhomogeneous alignment. The dielectric spectra were acquired in the frequency range from 40 Hz to 25 MHz. More than 60 experimental points were acquired per one frequency decade. Bias field was used to align the biaxial B<sub>2</sub> phase so that the polar director  $\mathbf{p}$  is perpendicular to the electrodes. The B<sub>2</sub> is a biaxial phase having the dielectric permittivity tensor of the form:

$$\hat{\epsilon}^*(\omega) = \begin{pmatrix} \epsilon_{11}^*(\omega) & 0 & 0 \\ 0 & \epsilon_{12}^*(\omega) & 0 \\ 0 & 0 & \epsilon_{11}^*(\omega) \end{pmatrix} \quad (1)$$

In this study it was possible to measure two principal components of this tensor, namely  $\varepsilon_{\perp 1}^*(\omega)$  and  $\varepsilon_{\perp 2}^*(\omega)$ , where the latter was measured along the secondary optical axis. The difference:

$$\varepsilon_{\perp 2} - \varepsilon_{\perp 1} \equiv \delta\varepsilon \quad (2)$$

can be treated as a measure of biaxiality (Lagerwall, 1998) of the  $B_2$  phase. It has been shown by means of the dielectric spectroscopy (Ossowska-Chruściel et al., 2009; Wierzejska-Adamowicz et al., 2010; Chruściel, 2011) that with electric measuring fields being parallel to the polar director  $p$  one observes an enhanced dielectric absorption and electric permittivity as well. As found in scope of this work there is an asymmetry of the dielectric spectra between the positive and negative bias fields (Fig. 13 (a) and (b)). It means that the system studied has low point symmetry.  $B$  phases composed of bow-shaped molecules may exhibit one of the following low point symmetries:  $C_{2v}$ ,  $C_{2h}$ ,  $C_2$  and even  $C_1$  (Pelzl et al., 1999).

Exemplary dielectric spectra – obtained vs. bias field – are presented in Figs. 13 (a) and (b). As seen there is an asymmetry of the dielectric spectra – the intensity of dielectric absorption depends on the sign of bias voltage. The dielectric absorption of the high frequency dielectric relaxation process is distinctly larger for negative bias fields. On the other hand, the low frequency dielectric relaxation process is being stronger enhanced for positive than negative bias fields (Fig. 13 (a)).

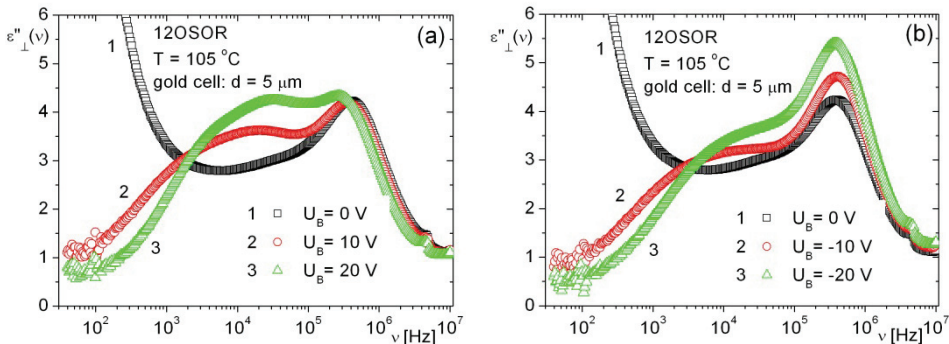


Fig. 13. Bias field dependences of dielectric spectrum measured for  $B_2$  phase of 12OSOR. (a) Dielectric spectra for positive and (b) negative bias voltages

The  $B_2$  phase is biaxial with the director  $n$  and polar director  $p$ . Using strong electric fields it was possible to observe in A.C. electric field transitions between a quasi-planar and homeotropic state with polar director  $p$  being normal to the electrodes. Using our HG gold cells and the experimental conditions it was not possible to study the dielectric spectrum of the  $B_2$  phase aligned homeotropically with primary director  $n$  being parallel to electric measuring field.

### 2.3.1 Bias field influence

The dielectric spectra were processed by using ORIGIN 7.0 software. The following complex function was fit to the experimental points measured without bias field:

$$\varepsilon_{\perp 1}^*(\omega) = \varepsilon_{\perp 1}(\infty) + \frac{\varepsilon_{\perp 1}(0) - \varepsilon_{\perp 1}(\infty)}{1 + (i\omega\tau)^{1-\alpha}} - \frac{i\sigma_{\perp 1}}{\varepsilon_0 v^M} + \frac{B}{v^N}, \quad (3a)$$

where  $\varepsilon_{\perp 1}(\infty)$  is a high frequency electric permittivity,  $\varepsilon_0$  - electric permittivity of the free space,  $\varepsilon_{\perp 1}(0)$  - static electric permittivity for planar alignment due to surface interaction,  $\tau$  - dielectric relaxation time,  $\alpha$  - distribution parameter of relaxation times ( $0 \leq \alpha \leq 1$ ),  $\sigma_{\perp 1}(\omega)$  - ionic conductivity,  $\omega = 2\pi\nu$  is a circular frequency and B, M, N - phenomenological fitting parameters. The last term in Eq. (3a) originates from electrode polarization effect. By fitting Eq. (3a) to the experimental points acquired without bias field (Fig. 14), the following dielectric parameters have been obtained:  $\varepsilon_{\perp 1}(\infty) = 3.78$ ,  $\varepsilon_{\perp 1}(0) = 13.51$ . The latter can be treated as the static dielectric constant for planar alignment. All fitting parameters are given in Fig. 14. In the low frequency range there are contributions to the dielectric relaxation spectrum coming from ionic conductivity and a sub-hertz relaxation process for the M parameter is distinctly smaller than 1.

Because the experimental dielectric spectra obtained under different bias fields for homeotropic alignment consist of two relaxation processes, the following complex fitting function was used for data analysis:

$$\varepsilon_{\perp 2}^*(\omega) = \varepsilon_{\perp 2}(\infty) + \frac{\varepsilon_{\perp 2}(01) - \varepsilon_{\perp 2}(\infty)}{1 + (i\omega\tau_2)^{1-\alpha_2}} + \frac{\varepsilon_{\perp 2}(0) - \varepsilon_{\perp 2}(01)}{1 + (i\omega\tau_1)^{1-\alpha_1}}, \quad (3b)$$

where  $\varepsilon_{\perp 2}(\infty)$  is a high frequency electric permittivity,  $\varepsilon_{\perp 2}(0)$  - static electric permittivity for homeotropic alignment,  $\varepsilon_{\perp 2}(01)$  - quasi-static electric permittivity,  $\tau_1$  and  $\tau_2$  - are relaxation times,  $\alpha_1$  and  $\alpha_2$  - distribution parameters of relaxation times, ( $0 \leq \alpha_i \leq 1, i = 1, 2$ ), and  $\omega = 2\pi\nu$  is a circular frequency. One should explain that in Eq. (3b) the conductivity and polarization electrode terms were omitted because bias fields suppress the ionic contribution to the dielectric spectra (see Figs. 15 and 22).

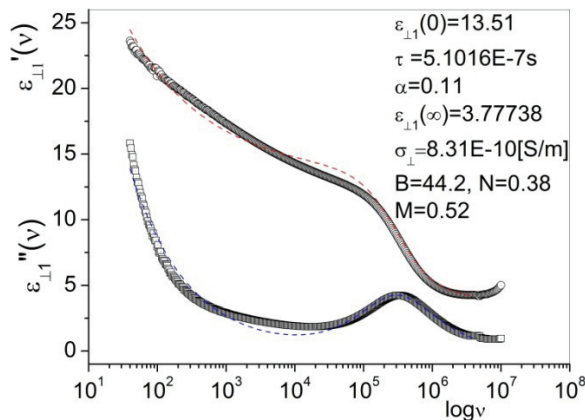


Fig. 14. Dielectric spectrum of antiferroelectric B<sub>2</sub> phase of 12OSOR obtained for planar alignment (without bias voltage) at T=95°C. Dispersion and absorption curves (dashed lines) were obtained by fitting Eq. (3a) to the experimental points.

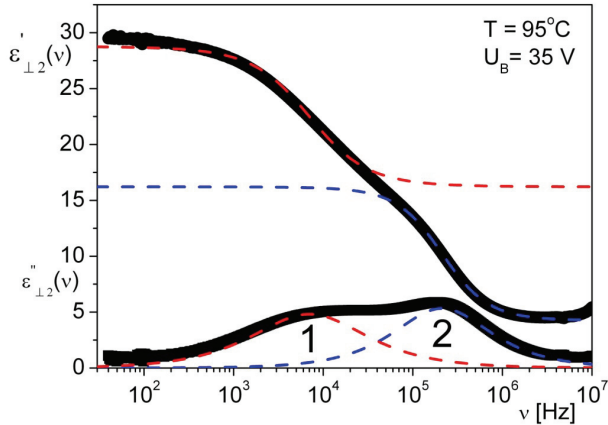


Fig. 15. Dielectric spectrum of antiferroelectric  $B_2$  phase of 12OSOR obtained with bias voltage (homeotropic alignment). Dispersion and absorption curves (dashed lines) were obtained by fitting Eq. (3b) to the experimental points.

T = 95 °C					
$U_B$ [V]	Process 1/2	$\epsilon_i(0)$	$\tau_i$ [s]	$\alpha_i$	$\epsilon_i(\infty)$
$U_B = 35$	1	29.84	1.6 E-5	0.36	12.67
	2	12.67	6.78 E-7	0.02	4.23
$U_B = 30$	1	30.45	1.88 E-5	0.35	12.55
	2	12.55	6.83 E-7	0.03	4.23
$U_B = 25$	1	31.77	1.84 E-5	0.38	11.32
	2	11.32	6.37 E-7	0.01	4.16
$U_B = 20$	1	32.68	1.8 E-5	0.42	9.96
	2	9.96	5.8 E-7	-0.04	4.07
$U_B = 15$	1	33.63	1.93 E-5	0.46	9.04
	2	9.04	5.39 E-7	-0.08	3.93
$U_B = 10$	1	34.40	2.23 E-5	0.49	8.86
	2	8.86	5.18 E-7	-0.10	3.77
$U_B = 5$	1	34.49	2.54 E-5	0.52	9.52
	2	9.52	5.07 E-7	-0.09	3.62

Table 1. Dielectric parameters vs. bias voltage obtained by fitting Eq. (3b) to the dielectric spectra measured at different positive bias voltages

T = 95 °C					
$U_B$ [V]	Process 1/2	$\epsilon_i(0)$	$\tau_i$ [s]	$\alpha_i$	$\epsilon_i(\infty)$
$U_B = -35$	1	30.73	1.56 E-5	0.35	13.62
	2	13.62	6.54 E-7	0.01	4.22
$U_B = -30$	1	30.97	1.5 E-5	0.36	13.47
	2	13.47	6 E-7	0.01	4.18
$U_B = -25$	1	31.08	1.7 E-5	0.37	13.43
	2	13.43	5.69 E-7	0.01	4.16
$U_B = -20$	1	31.32	1.9 E-5	0.39	12.99
	2	12.99	5.45 E-7	0.01	4.13
$U_B = -15$	1	31.96	2.13 E-5	0.42	11.96
	2	11.96	5.22 E-7	-0.02	4.06
$U_B = -10$	1	32.88	2.35 E-5	0.46	11.02
	2	11.02	5.07 E-7	-0.04	3.94
$U_B = -5$	1	34.13	2.66 E-5	0.51	10.35
	2	10.35	5.02 E-7	-0.07	3.74

Table 2. Dielectric parameters vs. bias voltage obtained by fitting Eq. (3b) to the dielectric spectra measured at different negative bias voltages

### 3. Results and discussion

Dielectric spectra of the aligned by electric field  $B_2$  phase consists of two relaxation processes (Fig. 16) which can be ascribed to the molecular reorientation (2) and the collective fluctuations (1) of ferroelectric domains, respectively.

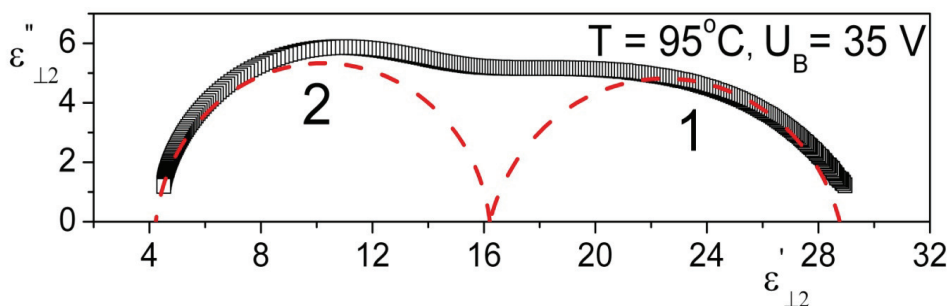


Fig. 16. Cole-Cole plot of the dielectric spectrum obtained at the highest bias field for 12OSOR's antiferroelectric  $B_2$  phase. Dashed lines were obtained by fitting Eq. (3b) to the experimental points.

The high frequency dielectric relaxation (2) is a Debye-type process originated from the reorientation of molecules around their long axes (see Fig. 2 (a)). Its Cole-Cole plot is a semicircle with the centre lying on the  $\epsilon_{1,2}$  axis. However, the numerical splitting of the complex spectrum is not fully unique as for high bias fields the  $\alpha_2$  distribution parameter has small but negative (unphysical) values (Tables 1 and 2). Figs. 17, 18 and 19 present, respectively, bias field dependences of the relaxation times, distribution parameters and boundary electric permittivities. All these Figs. as well as Fig. 13 show some asymmetry in bias field dependence of physical quantities measured for the B<sub>2</sub> phase. The low frequency dielectric relaxation process (1) exhibits a distribution of the relaxation times characterized by the  $\alpha_1$  parameter that decreases with bias field increasing (Fig. 18, Tables 1 and 2). The static electric permittivity ( $\epsilon_{1,2}(0)$ ) is being enhanced after application of small bias field but it decreases with D.C. bias field (Fig. 13) which may be due to partial suppression of the collective mode connected with modulated structure of the B<sub>2</sub> phase.

It is worth noting here that the low frequency dielectric dispersion ( $\epsilon'$ ) and absorption ( $\epsilon''$ ) are affected by ionic conductivity. In calamitic LCs the adequate contribution to the dielectric absorption is usually described by the well know term:  $\sigma/(\epsilon_0\omega)$ . As found for bow-shaped systems (Schmalfuss et al., 1999; Kresse et al., 2001, Chruściel et al., 2011) this term should be modified by introducing the  $M$  parameter (Eq. (3a)) to obtain better agreement between theory and experiment. The main reason for such a difference is merging of pure ionic contribution with the low frequency dielectric relaxation (or relaxations) originated from fluctuations of modulated (or undulated) polarization vectors.

One should notice that the Goldstone mode in classical ferroelectric liquid crystals is usually a Debye-type relaxation process characterized by a single relaxation time (Wróbel et al., 2003). Modulated structures in B phases cause a distribution of the relaxation times what is reflected in the large value of the  $\alpha_1$  parameter ( Fig. 18, Table 1 and 2)

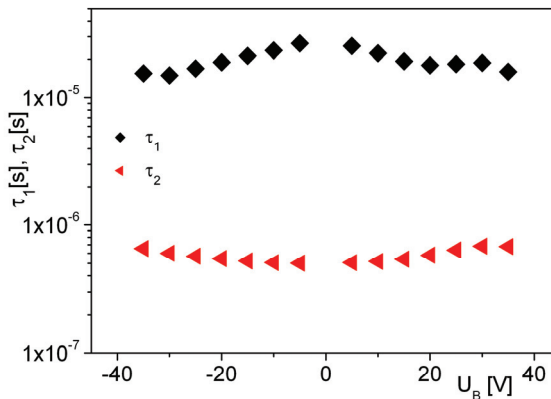


Fig. 17. Collective ( $\tau_1$ ) and molecular ( $\tau_2$ ) dielectric relaxation times obtained by fitting Eq. (3b) to the experimental dielectric spectra vs. bias field

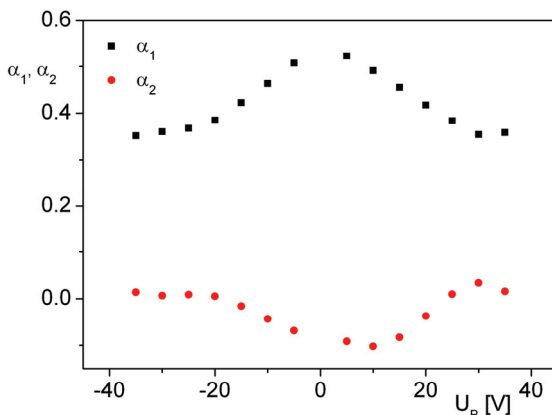


Fig. 18. Distribution parameters of molecular ( $\alpha_2$ ) and collective ( $\alpha_1$ ) relaxation processes obtained by fitting Eq. (3b) to the experimental dielectric spectra vs. bias field

### 3.2 Biaxiality of antiferroelectric B<sub>2</sub> phase

Fig.19 presents two static electric permittivities ( $\epsilon_{\perp 2}(0)$  and  $\epsilon_{\perp 2}(01)$ ) measured on the homeotropically aligned sample and vs. bias field. The values of  $\epsilon_{\perp 2}(0)$  and  $\epsilon_{\perp 2}(01)$  obtained at the highest bias voltages ( $U_B = \pm 35V$ ) seem to refer to homeotropic alignment.

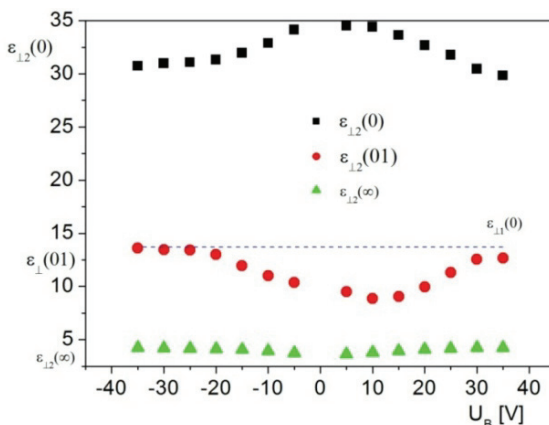


Fig. 19. Boundary electric permittivities vs. bias field computed for two principal directions by fitting Eqs. (3a) and (3b) to the experimental points

The value of  $\epsilon_{\perp 1}(0) = 13.51$ , represented in Fig. 19 by the dashed line, corresponds to the static electric permittivity obtained for planar alignment – without bias field. As seen in Fig. 19 the biaxiality of B<sub>2</sub> given by Eq. (2) is positive for positive bias at low frequencies ( $\delta\epsilon_1=16.33$ ) and negative ( $\delta\epsilon_2=-0.84$ ) above the frequencies higher than  $10^5$  Hz ( $1/\tau_1$ ). For negative bias field both these values are positive:  $\delta\epsilon_1=17.25$  and  $\delta\epsilon_2=0.11$ . It is due to asymmetry of the electric permittivity tensor (Eq. (1)).

### 3.3 Dielectric relaxation processes of B<sub>1</sub> phase

As found the dielectric spectra of molecular origin measured for B<sub>1</sub> phases of 8OSOR (Ossowska-Chruściel et al., 2007) and 9OSOR (Wierzejska-Adamowicz et al., 2010) do not depend on bias fields. Fig. 20 shows 3D graphs of the dielectric absorption measured without (a) and with (b) bias field for 9OSOR compound. As seen the adequate dielectric spectrum obtained with a D.C. bias is practically the same. In both cases only one relaxation process shows up and it is connected with molecule reorientation around the short axis which is perpendicular to the vectors  $\mathbf{n}$  and  $\mathbf{p}$  (Fig. 2 (a)). The activation energy obtained without bias field (Fig. 21) is equal to  $\Delta E=112$  kJ/mol which is typical value for reorientation around the short molecular axis. However, in the papers published before by other authors (Kresse et al., 2001) this process is interpreted as reorientation around the long molecular axis which is on the average parallel to the director  $\mathbf{n}$  (Fig. 2 (a)).

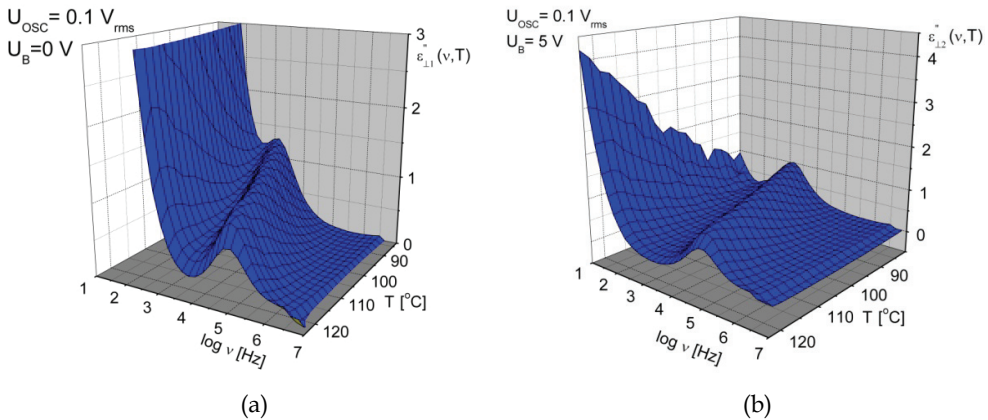


Fig. 20. Dielectric loss vs. frequency for B<sub>1</sub> phase in 9OSOR – (a) without bias field, (b) with bias field

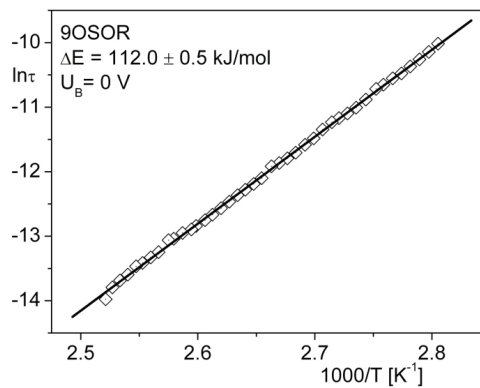


Fig. 21. Arrhenius plot for the dielectric relaxation process for B<sub>1</sub> phase observed without bias field

Similar dielectric relaxation spectrum was obtained before (Kresse, 2003; Ossowska-Chruściel, 2007). Our interpretation of the dielectric relaxation process observed in the  $B_1$  phase is based on the value of activation energy as well as on possible rectangular columnar structure of such phases (Sadashiva, 2000) what facilitates the reorientation around one of the short axes.

### 3.4 Dielectric relaxation processes of $B_2$ phase

Fig. 22 presents 3D graphs of the dielectric absorption spectra acquired without (a) and with (b) bias voltage equal to 15 V for 12OSOR compound. As seen the dielectric spectra measured with bias field show two well separated relaxation processes (see also Figs. 15 and 16) on the contrary to the  $B_1$  phase of 9OSOR which shows only one dielectric relaxation process. In the low frequency range the relaxation process is connected with fluctuations of ferroelectric domains showing up clearly in homeotropic structure of the  $B_2$  phase. The relaxation process observed in the high frequency range, appearing also without bias field, is connected with the molecule reorientation around the long axis. For 12OSOR the dielectric spectrum appears to be more complex: in the high temperature range of  $B_2$  phase it is connected with molecule reorientation around short molecular axis, whereas in the low temperature range – around the long axis (Wierzejska-Adamowicz, 2010). The activation barrier of the process connected with fluctuations of domains is equal to  $\Delta E=62$  kJ/mol (Fig. 23), whereas for the process connected with reorientation around long axis it is about 45 kJ/mol for measurements with and without bias field (Wierzejska-Adamowicz, 2010). The activation barrier found for reorientation around short molecular axis – observed in a narrow temperature range below the clearing point - is equal  $\Delta E=102$  kJ/mol (Wierzejska-Adamowicz, 2010).

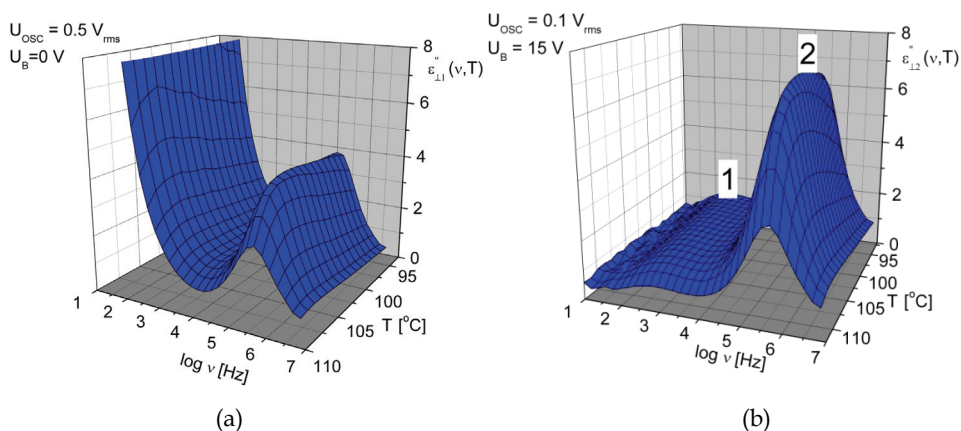


Fig. 22. 3D plot of dielectric loss vs. frequency for  $B_2$  phase of 12OSOR – (a) Without bias field, (b) With bias field

To sum up one should say the following: in  $B$  phases of bent-core systems the molecular rotational motions are slowed down due to strong steric interactions inside the layers. This effect is also substantiated by NMR studies (Domenici et al., 2006) where evidences of extremely slow rotational dynamics of bent-core molecules have been found.

As the  $\epsilon_{\perp 2}(\infty)$  is quite large and close to 4.0 (Fig. 19, Table 1 and 2), one should expect fast dielectric relaxation processes in the microwave frequency range. Intra-molecular reorientations of linear mesogenic units (Fig. 2 (a)) around their long axes and reorientations of the alkoxy chains contribute to electric permittivity at high frequencies.

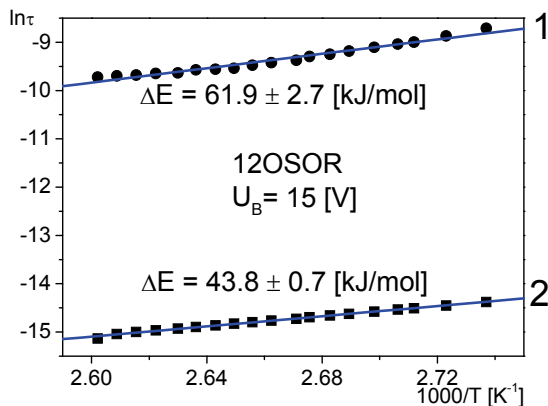


Fig. 23. Arrhenius plot for the two dielectric relaxation processes of the  $B_2$  phase studied under bias field

#### 4. Conclusions

Our studies show that  $B_1$  phase of 9OSOR does not exhibit any low frequencies dielectric relaxation of collective nature. Under strong electric fields  $B_1$  phase shows polarization which is due to short range ferroelectric order inside the smectic layers. This polarization linearly decreases with temperature decreasing. On the other hand, it displays non-linear dependence on electric field what is typical for ferroelectrics.

On the contrary 12OSOR and 14OSOR having even number of carbon atoms in alkoxy side chains exhibit anticlinic and antiferroelectric  $SmC_A P_A$  phase showing both collective and molecular dielectric relaxation processes. Two principal components ( $\epsilon_{\perp 1}^*(\omega)$  and  $\epsilon_{\perp 2}^*(\omega)$ ) of the dielectric permittivity tensor show qualitatively different dielectric relaxation spectra of this biaxial phase.

The  $B_2$  phase is biaxial with the primary director  $n$  and polar secondary order parameter  $p$ . Using strong electric fields, it was possible to observe a fast electro-optic switching between a quasi-planar and homeotropic state with polar director  $p$  being normal to the electrodes.

The dielectric spectroscopy studies on two principal alignments of the  $B_2$  phase shed some light upon the structure and dynamics of this phase.

#### 5. Acknowledgments

Financial support of the State Committee for Scientific Research (KBN) in scope of the grant No. N N202 076435 is gratefully acknowledged.

The research was carried out with the equipment purchased thanks to the financial support of the European Regional Development Fund in the framework of the Polish Innovation Economy Operational Program (contract no. POIG.02.01.00-12-023/08).

## 6. References

- Bedel, J. P., Rouillon, J. C., Marcerou, J. P., Laguerre, M., Achard, M. F. & Nguyen, H. T. (2000). Physical characterization of B<sub>1</sub> and B<sub>2</sub> phases in a newly synthesized series of banana shaped molecules. *Liq. Crystals*, Vol. 27, No. 1, pp. 103-113
- Chruściel, J., Wierzejska-Adamowicz, M., Ossowska-Chruściel, D. M., Marzec, M., Wawrzyniak, A., Douali, R., Legrand, Ch. & Wróbel, S. (2011). Dielectric Spectroscopy of Bent-core Thioesters' B Phases. *Mol. Cryst. & Liq. Cryst.* Vol. 541, pp. 490-499
- Domenici, V., Fodor-Csorba, K., Frezzato, D., Moro, G., & Veracini, C. A. (2006). Deuterium NMR Evidence of Slow Dynamics in the Nematic Phase of Banana-Shaped Liquid Crystals. *Ferroelectrics*, Vol. 344, pp. 19-28
- Geivandov, A. R., Palto, S.P. Yudin, S. G., Blinov, L. M., Pelzl, G. & Weissflog, W. (2006). Ferro- and Atiferroelectric Properties of Langmuir-Blogett Films Composed of Bent-Core Molecules. *Ferroelectrics*, Vol. 344, pp. 3-10
- Kohout, M., Chambers, M., Vajda, A., Galli, G., Domjan, A., Svoboda, J., Bubnov, A., Jakli, A. & Fodor-Csorba, K. (2010). Properties of non-symmetric bent-core liquid crystals with variable flexible chain length. *Liq. Crystals*, Vol. 37, pp. 537-545
- Kresse, H., Schmalfuss H., Weissflog, W., Tschierske, C. & Hauser, A. (2001). Dielectric Characterization of B<sub>n</sub> Phase. *Mol. Cryst. and Liq. Cryst.*, Vol. 366, pp. 505-517
- Kresse, H. (2003). Chap. 5.7, In: *Relaxation Phenomena*, Eds. W. Haase and S. Wróbel, pp. 400-422, ISBN 3-540-44269-3, Springer-Verlag, Berlin-Heidelberg-New York
- Lagerwall, S. (1998), Chap. 2, In: *Handbook of Liquid Crystals*. Vol. 2B: *Low molecular weight liquid crystals*. Eds. D. Demus, J.W. Goodby, G.W. Gray, H.W. Spiess & V. Vill, pp.513-664, ISBN 3-527-29502-X, WILEY-VCH Verlag, GmbH, D-60469 Weinheim (Federal Republic of Germany)
- Lee, S. K., Kang, S., Tokita, M. & Watanabe, J. (2010). Formation of homochiral antiferroelectric ground state in asymmetric bent-shaped achiral molecules. *Liq. Cryst.*, Vol. 37, No. 5, pp. 593-598
- Liang, H.-H. & Lee, J.-Y. (2011). Enhanced enantiotropic B<sub>2</sub> phase by mixing homologous chlorine-substituted molecules. *Liq. Crystals*, Vol. 38, No. 2, pp. 163-167
- Link, D.R., Natale, G., Shao, R., Maclennan, J.E., Clark, N.A., Körblova, E., Walba, D. M. (1997). Spontaneous Formation of Macroscopic Chiral Domains in a Fluid Smectic Phase of Achiral Molecules. *Science*. Vol. 278, pp. 1924-1927
- Noiri, T., Sekine, T., Watanabe, J., Furukawa, T. & Takezoe, H. (1996). Distinct ferroelectric smectic liquid crystals consisting of banana shaped achiral molecules. *J. Mater. Chem.* Vol. 6, No. 7, pp. 1231-1233
- Ortega, J., de la Fuente, M.R., Etxebarria, Folcia, C.L., Diez, S., Gallastegui, J.A., Gimeno, N., Ros, M.B. & Pérez-Jubindo, M.A. (2004). Electric-field-induced B<sub>1</sub>-B<sub>2</sub> transition in bent-core mesogens. *Phys. Rev. E*, Vol. 69, 011703-1(7)
- Ossowska-Chruściel, D.M., Kudłacz, K., Sikorska, A., Chruściel, J., Marzec, M., Mikułko, A., Wróbel, S., Douali, R. & Legrand, Ch. (2007). Ferroelectric properties of achiral banana-shaped and calamitic chiral thioesters. *Phase Transit.* Vol. 80, pp. 781-
- Ossowska-Chruściel, D. M., Wierzejska-Adamowicz, M., Marzec, M., Mikułko, A., Douali, R., Legrand, Ch., Chruściel, J., Sikorska, A. & Wróbel, S. (2009). Planar-Homeotropic Transition Observed for B<sub>2</sub> Phase of Banana-Shaped Thioester. *Phase Transit.* Vol. 82, No. 12, pp. 889-898

- Pelzl, G., Diele, S. & Weissflog, W. (1999). Banana-Shaped Compounds – A New Field of Liquid Crystals. *Adv. Mater.* Vol. 11, No. 9, pp.707-724
- Reddy, R. A. & Tschierske, C. (2006). Bent-core liquid crystals: polar order, superstructural chirality and spontaneous desymmetrisation in soft matter systems. *J. Mater. Chem.* Vol. 16, pp. 907-961
- Rouillon, J., Marcerou, J., Laguerre, M., Nguyen, H. & Achard, M. (2001). New banana-shaped thiobenzoate liquid crystals with B<sub>6</sub>, B<sub>1</sub> and B<sub>2</sub> phases. *J. Mater. Chem.* Vol. 11, 2946-2950
- Sadashiva, B.K., Raghunathan, V.A., Pratibha, R. (2000). Evidence of Columnar Structure ion Compounds Composed of Banana-Shaped Molecules, *Ferroelectrics*, Vol. 243, pp. 249-260
- Schmalzfuss, H., Shen, D., Tschierske, C. & Kresse, H. (1999). Dielectric investigations of the B<sub>2</sub> phase. *Liq. Crystals*, Vol. 26, 1767
- Sekine, T., Takanishi, Y., Noiri, T., Watanabe, J. & Takezoe, H. (1997). Ferroelectric Properties in Banana-Shaped Liquid Crystalline Systems. *Jpn. J. Appl. Phys.*, Vol. 36, L1201-L1203
- Szydłowska, J., Mieczkowski, J., Matraszek, J., Bruce, D.W., Górecka, E., Pociecha, D. & Guillon, D. (2003). Bent-core liquid crystals forming two- and three-dimensional modulated structures. *Phys. Rev. B*, Vol. 67, pp.031702-1(5)
- Takanishi, Y., Ogasawara, T., Ishikawa, K., & Takezoe, H., Watanabe, J., Takahashi, Y. & Iida, A. (2003), Local layer structures in circular domains of an achiral bent-core mesogen observed by X-ray microbeam diffraction. *Phys. Rev E*, Vol. 68, pp. 011706-1(5)
- Vaupotič, N. & Čopič, M. (2005). Polarization modulation instability in liquid crystals with spontaneous symmetry breaking, *Phys. Rev. E*, Vol. 72, 031701-1(4)
- Vaupotič, N. (2006). Landau-de Gennes Theory of the Polarization Modulated and Layer Undulated Structure in Liquid Crystals Made of Bent-Core Molecules. *Ferroelectrics*, Vol. 344, pp.151-159
- Walba, D. M., Körblova, E., Shao, Maclennan, J.E., R., Link, D.R., Glaser, M.A. & Clark, N.A. (2000). A Ferroelectric Liquid Crystal Conglomerate Composed of Racemic Molecules. *Science*. Vol. 288, pp. 2181-2184
- Wierzejska-Adamowicz, M., Ossowska-Chruściel, D. M., Marzec, M., Mikułko, A., Chruściel, J., Douali, R., Legrand, Ch. & Wróbel, S. (2010). Electrooptic and dielectric investigations of frustrated B<sub>1</sub> phase and antiferroelectric B<sub>2</sub> phases of banana-shaped thioesters. *Acta Phys. Polonica*, Vol. 117, pp. 557-561
- Wierzejska-Adamowicz, M., Ossowska-Chruściel, D. M., Czerwiec, J., Marzec, M., Mikułko, A., Chruściel, J., Douali, R., Legrand, Ch. & Wróbel, S. (2010). Bias field influence on dielectric spectra of B phases of bent-core thioesters. *Optical Review*, Vol. 17, pp.393-398
- Wierzejska-Adamowicz, M. (2010), *Ph D Thesis*, Jagiellonian University, Kraków 2010
- Wróbel, S., Haase, W., Kilian, D., Chien, L.-C. & Chong-Kwang, L. (2000). High Temperature Antiferroelectric Smectic Phase Composed of Banana-Shaped Achiral Molecules", *Ferroelectrics*, Vol. 243, pp. 277-289
- Wróbel, S., Haase, W., Fařara, A. & Marzec, M. (2003). Chap. 5.11, In: *Relaxation Phenomena*, Eds. W. Haase and S. Wróbel, pp. 485-510, ISBN 3-540-44269-3, Springer-Verlag, Berlin-Heidelberg-New York
- Zhang, Y., Wand, M., O'Callaghan, M.J., Walker, Ch. M. & Thurmes, W. (2006). Anticlinic Ferroelectric Bananas for Electro-optic Modulators. *Ferroelectrics*, Vol. 344, pp. 11-18

# Molecular Design of a Chiral Oligomer for Stabilizing a Ferrielectric Phase

Atsushi Yoshizawa and Anna Noji

*Department of Frontier Materials Chemistry, Hirosaki University  
Japan*

## 1. Introduction

Appearance of ferroelectricity and antiferroelectricity in chiral tilted smectic phases is an interesting phenomenon. It is not only attractive for use in applications to fast-response displays (Goodby et al., 1991; Walba, 1995); it also attracts fundamental interest related to synclinic or anticlinic ordering of the molecules (Lagerwall & Giesselmann, 2006; Lemieux, 2007; Nishiyama, 2010). The frustration between synclinic-ferroelectricity and anticlinic-antiferroelectricity in chiral smectic C phases causes temperature-induced successive phase transitions (Fukuda et al., 1994; Inui et al. 1996; Isozaki et al., 1993; Matsumoto et al., 1999; Osipov & Fukuda, 2000; Sandhya et al., 2009; Takezoe et al., 2010). When ferroelectric and antiferroelectric phases have equal free energy, intermediate ferrielectric sub-phases with a degenerated energy level can appear between ferroelectric and antiferroelectric phases.

At the outset of disclosing antiferroelectric  $\text{SmC}_A^*$  phase in MHPOBC, three other  $\text{SmC}^*$ -like phases were observed (Chandani et al., 1989a). These phases were designated as  $\text{SmC}_\omega^*$ ,  $\text{SmC}_\beta^*$ , and  $\text{SmC}_\gamma^*$  in order of decreasing temperature (Chandani et al., 1989b), the  $\text{SmC}_\beta^*$  phase was regarded as the ordinary ferroelectric  $\text{SmC}^*$  phase. Gorecka et al. soon proved that  $\text{SmC}_\gamma^*$  is a ferrielectric phase (Gorecka et al., 1990). Isozaki et al. confirmed that an antiferroelectric subphase might emerge between  $\text{SmC}_\beta^*$  and  $\text{SmC}_\gamma^*$  phases (Isozaki et al., 1992, 1993). Mach et al. reported the first direct structural observation of distinct multilayer periodicities of the subphases using resonant X-ray scattering (March et al., 1998, 1999). They confirmed three-layer and four-layer periodicities, respectively, in what they called Ferri 1 and Ferri 2 phases. Nguyen et al. identified the Ferri 1 as  $\text{SmC}\gamma^*$  (Nguyen et al., 1994). The Ferri 2 phase was found to have antiferroelectric characteristics (Aoki et al., 1999). Later, the  $\text{SmC}_\beta^*$  of MHPOBC was identified as Ferri 2 phase (Gorecka et al., 2002). At least two ferrielectric phases consisting of three-layer and four-layer unit cells exist. Other ferrielectric subphases induced by successive phase transition have been observed. Fukuda et al. proposed that the subphases are represented as  $\text{SmC}_A^*(qT)$ , where  $qT = F/(A+F)$  (Isozaki et al., 1993). In those equations,  $F$  denotes the number of synclinic layers in one periodicity;  $A$  represents the number of anticlinic layers in one periodicity. Figure 1 presents illustrations of antiferroelectric phase  $\text{SmC}_A^*(0)$ , ferrielectric subphase  $\text{SmC}_A^*(1/3)$ , antiferroelectric-like ferrielectric subphase  $\text{SmC}_A^*(1/2)$ , and ferroelectric phase  $\text{SmC}_A^*(1)$ .

Some theoretical and experimental studies have been undertaken to explain the appearance of ferrielectric phases (Cepic & Zeks, 2001; Cepic et al., 2002; Fukuda et al., 1994; Johnson et al., 2000; Matsumoto et al., 1999; Osipov & Fukuda, 2000; Yamashita & Miyajima, 1993).

Chirality is probably prerequisite for the appearance of the ferrielectric phases. Emelyanenko and Osipov proposed that effective coupling that is determined using a combination of spontaneous polarization, discrete flexoelectric effect, and an initial direct polarization coupling between adjacent layers stabilizes the ferrielectric phases (Emelyanenko & Osipov, 2003). The Emelyanenko-Osipov model predicts only mesophases with periodicity of 8, 5, 7, and 9 layers between  $\text{SmC}^*$  and  $\text{SmC}^*_A$  phases. However,  $\text{SmC}^*$  phase with six-layer periodicity has been discovered (Wang, et al, 2010). The physical origin of long-range interactions for ferrielectric phases remains unresolved.

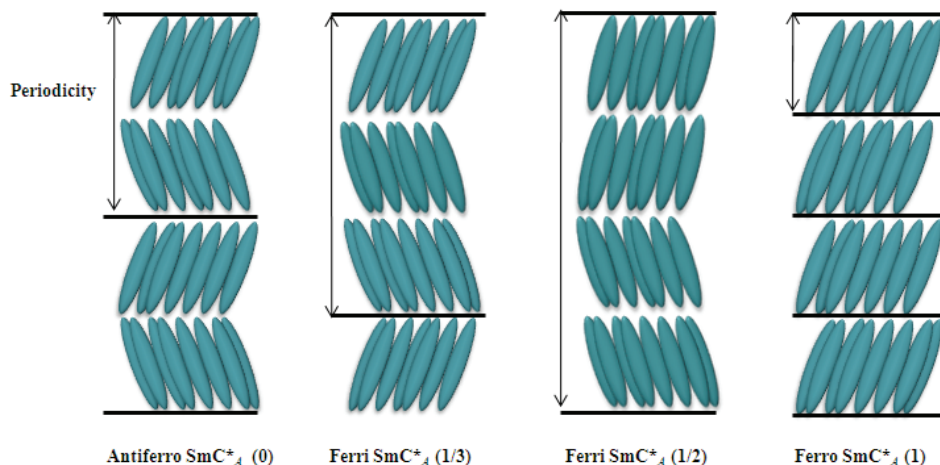
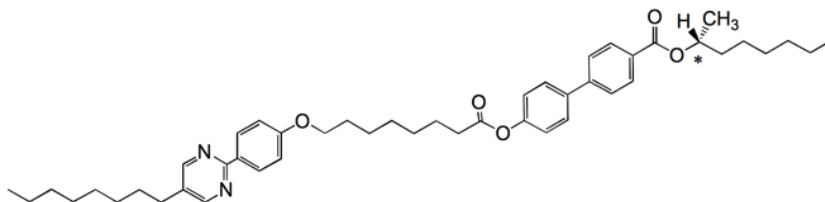


Fig. 1. Periodic structures of the frustrated smectic phases.

With respect to liquid-crystalline materials, ferrielectric phases have been observed for narrow temperature ranges of some highly chiral compounds. By decreasing the optical purity, a ferrielectric phase vanishes (Fukui et al., 1989; Gorecka et al., 2002). Nishiyama et al. reported a chiral twin molecule with wide temperatures of a ferrielectric phase (Nishiyama et al., 2001). In this case, the ferrielectric phase also disappears concomitantly with decreasing optical purity. Some mixtures of antiferroelectric chiral liquid crystals with highly chiral dopants of the same handedness were reported to exhibit ferrielectric phases with a range of 30 K (Jaradat et al., 2006). Asymmetric switching in a ferrielectric phase has been of interest in prospective devices (Jaradat et al., 2008, 2009). The molecular design for ferrielectric liquid crystals now constitutes an important issue not only because of their unusual phase structures but also because of their applications to optical devices.

Recently, we designed an asymmetric chiral dimer **(R)-I-(8,7)** and investigated its phase transition behaviour and electro-optical properties (Noji et al., 2009). The compound was found to exhibit ferrielectric phases with wide temperatures between antiferroelectric (Anti) and ferroelectric  $\text{SmC}^*$  (Ferro) phases. Ferrielectric-like ordering was observed in a racemic mixture of the enantiomers. The appearance of the ferrielectric-like ordering in the racemic system without spontaneous polarization cannot be explained by any present physical model. Furthermore, its derivative **(R)-II-(8,7)** possessing an octyloxy tail instead of an octyl tail of **(R)-I-(8,7)** exhibits a direct transition from isotropic liquid to the ferrielectric phase (Noji & Yoshizawa, 2011).

We prepared a homologous series of liquid crystal oligomers and observed their physical properties. This report describes structure-property relations of liquid crystals and presents an origin for stabilizing the ferrielectric phases of the present chiral oligomeric system.



(*R*)-**I**-(8,7): Cry 83.8 Anti 85.2 Ferri-L 98.5 Ferri-H 111.8 Ferro 114.2 Iso

Fig. 2. Molecular structure and phase transition temperatures (°C) of (*R*)-**I**-(8,7).

## 2. Experimental

### 2.1 Materials

For use in this study, 5-alkyl-2-(4-hydroxyphenyl)pyrimidine, 5-octyloxy-2-(4-hydroxyphenyl)pyridine, and 4-(4-hexyloxyphenyl)-1-(4-hydroxyphenyl)-2,3-difluorobenzene were purchased from Midori Kagaku Co. Ltd. The final compounds were prepared using a similar method to that used for (*R*)-**I**-(8,7), as reported in our previous paper (Noji et al., 2009). The synthetic scheme is depicted in Fig. 3. Purification of each final product was conducted using column chromatography over silica gel (63–210  $\mu\text{m}$ ; Kanto Chemical Co. Inc.) using dichloromethane-ethyl acetate mixture as the eluent with subsequent recrystallization from ethanol. The purities of all final compounds were checked using HPLC (JAIGEL-1H column, LC9101; Japan Analytical Industry Co. Ltd.). Chloroform was used as eluent. Detection of products was achieved using UV irradiation ( $\lambda = 254 \text{ nm}$ ). Purities of the final compounds were also checked using elemental analysis (EA 1110; CE Instruments Ltd.). Infrared (IR) spectroscopy (FTS-30; Bio-Rad Laboratories Inc.) and proton nuclear magnetic resonance ( $^1\text{H}$  NMR) spectroscopy (JNM-ECA500; JEOL) elucidated the structure of each final product. Analytical data for the compounds are listed below.

#### (*R*)-1-Methylheptyl 4'-[6-[4-(5-octylpyrimidin-2-yl)phenoxy]hexanoyloxy]biphenyl-4-carboxylate [(*R*)-**I**-(8,5)]

$^1\text{H}$  NMR (500 MHz, solvent  $\text{CDCl}_3$ , standard TMS)  $\delta\text{H}/\text{ppm}$ : 8.57 (s, 2H, Ar-H), 8.35 (d, 2H, Ar-H,  $J = 9.1 \text{ Hz}$ ), 8.10 (d, 2H, Ar-H,  $J = 8.3 \text{ Hz}$ ), 7.62 (d, 2H, Ar-H,  $J = 8.5 \text{ Hz}$ ), 7.60 (d, 2H, Ar-H,  $J = 8.6 \text{ Hz}$ ), 7.18 (d, 2H, Ar-H,  $J = 8.6 \text{ Hz}$ ), 6.99 (d, 2H, Ar-H,  $J = 8.8 \text{ Hz}$ ), 5.21–5.14 (m, 1H,  $-\text{OCH}(\text{CH}_3)-$ ), 4.08 (t, 2H,  $-\text{OCH}_2-$ ,  $J = 6.3 \text{ Hz}$ ), 2.65 (t, 2H, Ar- $\text{CH}_2-$ ,  $J = 7.4 \text{ Hz}$ ), 2.60 (t, 2H,  $-\text{OCOCH}_2-$ ,  $J = 7.6 \text{ Hz}$ ), 1.93–1.85 (m, 4H, Ar- $\text{CH}_2\text{CH}_2-$ ,  $-\text{OCH}_2\text{CH}_2-$ ), 1.79–1.58 (m, 6H, aliphatic-H), 1.43–1.28 (m, 18H, aliphatic-H), 1.35 (d, 3H,  $-\text{OCH}(\text{CH}_3)-$ ,  $J = 6.3 \text{ Hz}$ ), 0.88 (t, 6H,  $-\text{CH}_3$ ,  $J = 6.9 \text{ Hz}$ ); IR (KBr)  $\nu_{\text{max}}/\text{cm}^{-1}$ : 2928, 2855 (C-H str.), 1761, 1706 (C=O str.), 1609, 1584 (C=C str.). HPLC: 100%. Anal. Calcd. for  $\text{C}_{45}\text{H}_{58}\text{N}_2\text{O}_5$ : C, 76.45%; H, 8.27%; N, 3.96%. Found: C, 76.56%; H, 8.17%; N, 4.01%.

#### (*R*)-1-Methylheptyl 4'-[7-[4-(5-octylpyrimidin-2-yl)phenoxy]heptanoyloxy]biphenyl-4-carboxylate [(*R*)-**I**-(8,6)]

$^1\text{H}$  NMR (500 MHz, solvent  $\text{CDCl}_3$ , standard TMS)  $\delta\text{H}/\text{ppm}$ : 8.57 (s, 2H, Ar-H), 8.35 (d, 2H, Ar-H,  $J = 8.7 \text{ Hz}$ ), 8.10 (d, 2H, Ar-H,  $J = 8.5 \text{ Hz}$ ), 7.62 (d, 2H, Ar-H,  $J = 8.4 \text{ Hz}$ ), 7.60 (d, 2H,

Ar-H,  $J = 8.5$  Hz), 7.17 (d, 2H, Ar-H,  $J = 8.7$  Hz), 6.99 (d, 2H, Ar-H,  $J = 9.1$  Hz), 5.20-5.14 (m, 1H, -OCH(CH<sub>3</sub>)-), 4.06 (t, 2H, -OCH<sub>2</sub>-,  $J = 6.4$  Hz), 2.62 (t, 2H, Ar-CH<sub>2</sub>-,  $J = 7.5$  Hz), 2.60 (t, 2H, -OCOCH<sub>2</sub>-,  $J = 7.7$  Hz), 1.89-1.80 (m, 4H, Ar-CH<sub>2</sub>CH<sub>2</sub>-, -OCH<sub>2</sub>CH<sub>2</sub>-), 1.80-1.23 (m, 26H, aliphatic-H), 1.35 (d, 3H, -OCH(CH<sub>3</sub>)-,  $J = 6.3$  Hz), 0.88 (t, 6H, -CH<sub>3</sub>,  $J = 6.9$  Hz); IR (KBr)  $\nu_{\max}/\text{cm}^{-1}$ : 2948, 2852 (C-H str.), 1765, 1713 (C=O str.), 1607, 1582 (C=C str.). HPLC: 100%. Anal. Calcd. for C<sub>46</sub>H<sub>60</sub>N<sub>2</sub>O<sub>5</sub>: C, 76.63%; H, 8.39%; N, 3.89%. Found: C, 76.91%; H, 8.35%; N, 3.97%.

**(R)-1-Methylheptyl 4'-[9-[4-(5-octylpyrimidin-2-yl)phenyloxy]nonanoyloxy]biphenyl-4-carboxylate [(R)-I-(8,8)]**

<sup>1</sup>H NMR (500 MHz, solvent CDCl<sub>3</sub>, standard TMS)  $\delta\text{H}/\text{ppm}$ : 8.57 (s, 2H, Ar-H), 8.34 (d, 2H, Ar-H,  $J = 9.0$  Hz), 8.10 (d, 2H, Ar-H,  $J = 8.5$  Hz), 7.62 (d, 2H, Ar-H,  $J = 8.5$  Hz), 7.61 (d, 2H, Ar-H,  $J = 8.6$  Hz), 7.18 (d, 2H, Ar-H,  $J = 8.7$  Hz), 6.83 (d, 2H, Ar-H,  $J = 9.1$  Hz), 5.20-5.14 (m, 1H, -OCH(CH<sub>3</sub>)-), 4.04 (t, 2H, -OCH<sub>2</sub>-,  $J = 6.6$  Hz), 2.60 (t, 4H, Ar-CH<sub>2</sub>-, OCOCH<sub>2</sub>-,  $J = 7.5$  Hz), 1.86-1.72 (m, 5H, aliphatic-H), 1.67-1.59 (m, 3H, aliphatic-H), 1.52-1.28 (m, 26H, aliphatic-H), 1.35 (d, 3H, -OCH(CH<sub>3</sub>)-,  $J = 6.3$  Hz), 0.88 (t, 6H, -CH<sub>3</sub>,  $J = 7.0$  Hz); IR (KBr)  $\nu_{\max}/\text{cm}^{-1}$ : 2930, 2854 (C-H str.), 1767, 1710 (C=O str.), 1608, 1584 (C=C str.). HPLC: 100%. Anal. Calcd. for C<sub>48</sub>H<sub>64</sub>N<sub>2</sub>O<sub>5</sub>: C, 76.97%; H, 8.61%; N, 3.74%. Found: C, 77.01%; H, 8.59%; N, 3.75%.

**(R)-1-Methylheptyl 4'-[6-[4-(5-dodecypyrimidin-2-yl)phenyloxy]hexanoyloxy]biphenyl-4-carboxylate [(R)-I-(12,5)]**

<sup>1</sup>H NMR (500 MHz, solvent CDCl<sub>3</sub>, standard TMS)  $\delta\text{H}/\text{ppm}$ : 8.57 (s, 2H, Ar-H), 8.36 (d, 2H, Ar-H,  $J = 8.8$  Hz), 8.10 (d, 2H, Ar-H,  $J = 8.5$  Hz), 7.63 (d, 2H, Ar-H,  $J = 8.4$  Hz), 7.61 (d, 2H, Ar-H,  $J = 8.7$  Hz), 7.18 (d, 2H, Ar-H,  $J = 8.6$  Hz), 6.99 (d, 2H, Ar-H,  $J = 8.8$  Hz), 5.20-5.14 (m, 1H, -OCH(CH<sub>3</sub>)-), 4.08 (t, 2H, -OCH<sub>2</sub>-,  $J = 6.3$  Hz), 2.65 (t, 2H, Ar-CH<sub>2</sub>-,  $J = 7.4$  Hz), 2.60 (t, 2H, -OCOCH<sub>2</sub>-,  $J = 7.7$  Hz), 1.93-1.85 (m, 4H, Ar-CH<sub>2</sub>CH<sub>2</sub>-, -OCH<sub>2</sub>CH<sub>2</sub>-), 1.79-1.58 (m, 6H, aliphatic-H), 1.45-1.26 (m, 24H, aliphatic-H), 1.35 (d, 3H, -OCH(CH<sub>3</sub>)-,  $J = 6.3$  Hz), 0.88 (t, 6H, -CH<sub>3</sub>,  $J = 6.9$  Hz); IR (KBr)  $\nu_{\max}/\text{cm}^{-1}$ : 2921, 2850 (C-H str.), 1760, 1709 (C=O str.), 1608, 1585 (C=C str.). HPLC: 100%. Anal. Calcd. for C<sub>50</sub>H<sub>68</sub>N<sub>2</sub>O<sub>5</sub>: C, 77.13%; H, 8.72%; N, 3.67%. Found: C, 77.13%; H, 8.73%; N, 3.71%.

**(R)-1-Methylheptyl 4'-[8-[4-(5-octyloxy pyridin-2-yl)phenyloxy]octanoyloxy]biphenyl-4-carboxylate [(R)-III-(8,7)]**

<sup>1</sup>H NMR (500 MHz, solvent CDCl<sub>3</sub>, standard TMS)  $\delta\text{H}/\text{ppm}$ : 8.33 (d, 1H, Ar-H,  $J = 2.9$  Hz), 8.10 (d, 2H, Ar-H,  $J = 8.4$  Hz), 7.85 (d, 2H, Ar-H,  $J = 9.0$  Hz), 7.62 (d, 2H, Ar-H,  $J = 8.3$  Hz), 7.61 (d, 2H, Ar-H,  $J = 8.7$  Hz), 7.57 (d, 1H, Ar-H,  $J = 8.7$  Hz), 7.22 (dd, 1H, Ar-H,  $J = 8.9$  Hz,  $J = 3.0$  Hz), 6.97 (d, 2H, Ar-H,  $J = 9.0$  Hz), 5.20-5.14 (m, 1H, -OCH(CH<sub>3</sub>)-), 4.03 (t, 2H, -OCH<sub>2</sub>-,  $J = 5.7$  Hz), 2.60 (t, 2H, -OCOCH<sub>2</sub>-,  $J = 7.4$  Hz), 1.86-1.72 (m, 8H, aliphatic-H), 1.65-1.29 (m, 24H, aliphatic-H), 1.35 (d, 3H, -OCH(CH<sub>3</sub>)-,  $J = 6.2$  Hz), 0.89 (t, 3H, -CH<sub>3</sub>,  $J = 6.6$  Hz), 0.88 (t, 3H, -CH<sub>3</sub>,  $J = 6.9$  Hz); IR (KBr)  $\nu_{\max}/\text{cm}^{-1}$ : 2924, 2854 (C-H str.), 1754, 1714 (C=O str.), 1609, 1582 (C=C str.). HPLC: 100%. Anal. Calcd. for C<sub>48</sub>H<sub>63</sub>NO<sub>6</sub>: C, 76.87%; H, 8.47%; N, 1.87%. Found: C, 77.38%; H, 8.47%; N, 1.86%.

**(R)-1-Methylheptyl 4'-[8-[4-(4-(4-hexylphenyl)-2,3-difluorophenyl)]phenyloxy]octanoyloxy]biphenyl-4-carboxylate [(R)-IV-(6,7)]**

<sup>1</sup>H NMR (500 MHz, solvent CDCl<sub>3</sub>, standard TMS)  $\delta\text{H}/\text{ppm}$ : 8.09 (d, 2H, Ar-H,  $J = 8.1$  Hz), 7.62 (d, 2H, Ar-H,  $J = 8.6$  Hz), 7.61 (d, 2H, Ar-H,  $J = 8.6$  Hz), 7.53-7.49 (m, 4H, Ar-H), 7.28 (d,

2H, Ar-H,  $J = 8.1$  Hz), 7.23-7.21 (m, 2H, Ar-H), 7.18 (d, 2H, Ar-H,  $J = 8.6$  Hz), 6.99 (d, 2H, Ar-H,  $J = 8.6$  Hz), 5.20-5.14 (m, 1H, -OCH(CH<sub>3</sub>)-), 4.03 (t, 2H, -OCH<sub>2</sub>-,  $J = 5.6$  Hz), 2.66 (t, 2H, Ar-CH<sub>2</sub>-,  $J = 8.0$  Hz), 2.60 (t, 2H, -OCOCH<sub>2</sub>-,  $J = 7.5$  Hz), 1.87-1.28 (m, 28H, aliphatic-H), 1.35 (d, 3H, -OCH(CH<sub>3</sub>)-,  $J = 6.3$  Hz), 0.90 (t, 3H, -CH<sub>3</sub>,  $J = 7.2$  Hz), 0.88 (t, 3H, -CH<sub>3</sub>,  $J = 6.9$  Hz); IR (KBr)  $\nu_{\max}/\text{cm}^{-1}$ : 2931, 2855 (C-H str.), 1754, 1718 (C=O str.), 1613, 1527 (C=C str.). HPLC: 100%. Anal. Calcd. for C<sub>53</sub>H<sub>62</sub>F<sub>2</sub>O<sub>5</sub>: C, 77.91%; H, 7.65%. Found: C, 78.57%; H, 7.69%.

**(S)-4-[4-(2-Methyloctanoyl)phenyl]phenyl octanoate [(S)-V-(8,7)]**      **8-[4-(5-octylpyrimidin-2-yl)phenoxy]phenyl**

<sup>1</sup>H NMR (500 MHz, solvent CDCl<sub>3</sub>, standard TMS)  $\delta\text{H}/\text{ppm}$ : 8.57 (s, 2H, Ar-H), 8.35 (d, 2H, Ar-H,  $J = 8.7$  Hz), 8.02 (d, 2H, Ar-H,  $J = 8.5$  Hz), 7.66 (d, 2H, Ar-H,  $J = 8.5$  Hz), 7.62 (d, 2H, Ar-H,  $J = 8.6$  Hz), 7.19 (d, 2H, Ar-H,  $J = 8.6$  Hz), 6.98 (d, 2H, Ar-H,  $J = 8.9$  Hz), 4.04 (t, 2H, -OCH<sub>2</sub>-,  $J = 6.6$  Hz), 3.52-3.45 (m, 1H, -COCH(CH<sub>3</sub>)-), 2.60 (t, 2H, Ar-CH<sub>2</sub>-,  $J = 7.5$  Hz), 2.59 (t, 2H, -OCOCH<sub>2</sub>-,  $J = 7.6$  Hz), 1.87-1.77 (m, 6H, aliphatic-H), 1.68-1.24 (m, 26H, aliphatic-H), 1.21 (d, 3H, -OCH(CH<sub>3</sub>)-,  $J = 6.9$  Hz), 0.88 (t, 6H, -CH<sub>3</sub>,  $J = 6.9$  Hz); IR (KBr)  $\nu_{\max}/\text{cm}^{-1}$ : 2925, 22851 (C-H str.), 1748, 1674 (C=O str.), 1586, 1542 (C=C str.). HPLC: 100%. Anal. Calcd. for C<sub>47</sub>H<sub>62</sub>N<sub>2</sub>O<sub>4</sub>: C, 78.51%; H, 8.69%; N, 3.90%. Found: C, 78.80%; H, 8.65%; N, 3.93%.

## 2.2 Physical properties

The initial phase assignments and corresponding transition temperatures for the final products were determined using polarized optical microscopy (POM) with a polarizing microscope (Optiphot-pol; Nikon Corp.) equipped with a hot stage (FP82; Mettler Inst. Corp.) and a control processor (FP80; Mettler Inst. Corp.). The heating and cooling rates were 5 °C min<sup>-1</sup>. Temperatures and enthalpies of transition were investigated using differential scanning calorimetry (DSC, DSC6200; Seiko Instruments Inc.). The materials were studied at a scanning rate of 5 °C min<sup>-1</sup> after encapsulation in aluminium pans. The X-ray diffraction (XRD) patterns of the powder samples on cooling processes were obtained using a real-time X-ray diffractometer (D8 Discover; Bruker AXS GmbH). A sample was put on a convex lens, which was placed in a custom-made temperature stabilized holder (stability within  $\pm 0.1$  °C). The textural observations were conducted using polarized light microscopy with a CCD camera. The X-ray apparatus was equipped with a cross-coupled Göbel mirror on a platform system with a two-dimensional position-sensitive proportional counter (PSPC) detector (HI-Star; Bruker AXS GmbH). X-rays were generated at 40 kV and 40 mA; a parallel Cu K $\alpha$  X-ray beam was used to irradiate the sample.

Electro-optical studies were conducted using commercially available evaluation cells (E. H. C. Co., Ltd., Japan). The inner surfaces had been coated with a polyimide aligning agent and had been buffed unidirectionally. The cells were made with 5  $\mu\text{m}$  spacings. Switching current and optical tilt angle across the temperatures of tilted smectic phases were measured using standard electro-optic techniques (Goodby et al., 1991). The optical tilt angle was determined by finding the extinction direction when an electric field was applied to the specimen in increasing or decreasing steps. A Kikusui Electric Regulated DC Power Supply was used to supply the d.c. field.

## 3. Results and discussion

We prepared a homologous series of the chiral dimesogenic compound and investigated the effects of terminal chain, central spacer, core structure, and chiral moiety of the chiral dimesogenic compound on appearance of the ferrielectric phase.

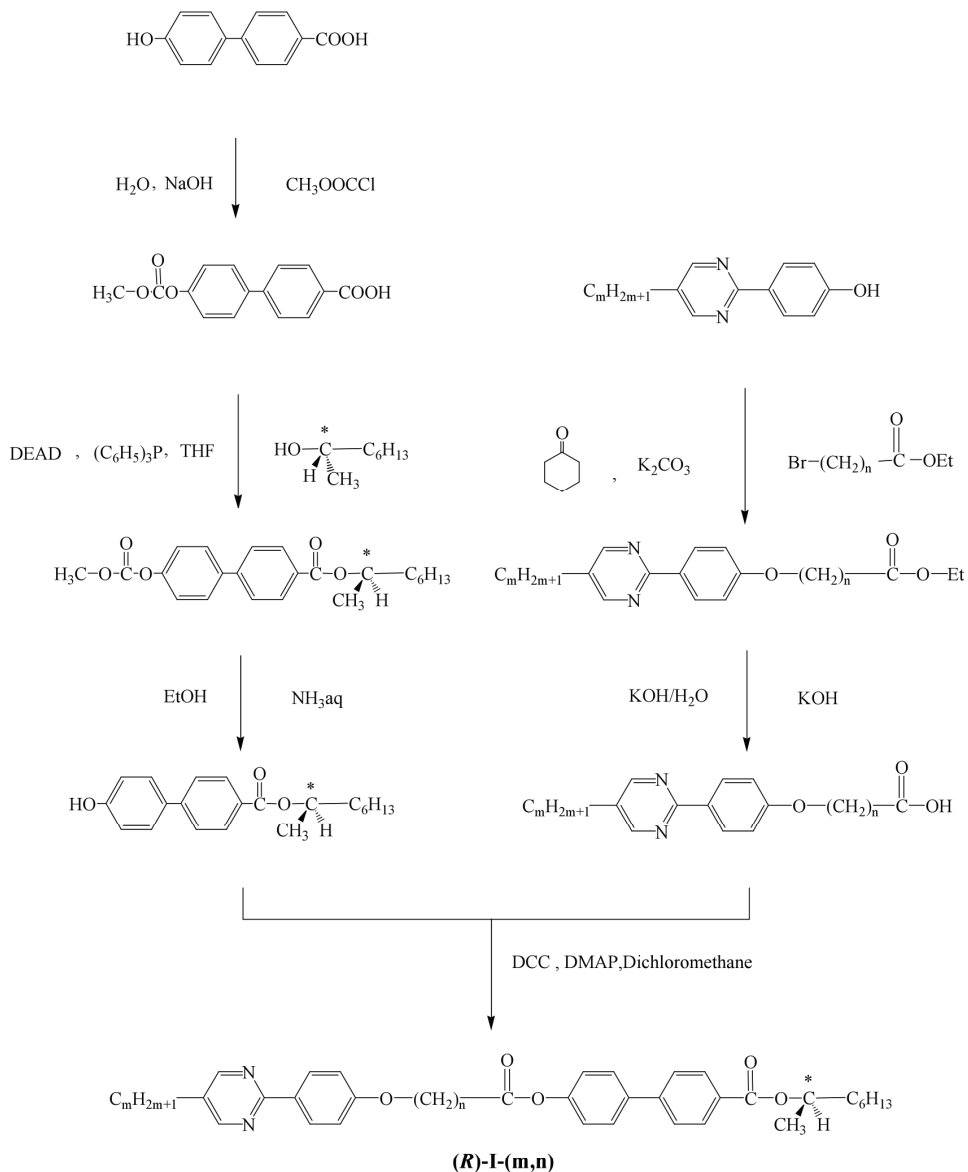
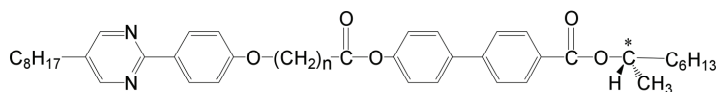


Fig. 3. Synthetic scheme of compound **(R)-I-(m,n)**.

### 3.1 Effects of the central spacer

We investigated effects of parity of the central spacer of the compounds on the phase transition behaviour. Transition temperatures and associated entropy changes,  $\Delta S/R$  for **(R)-I-(m,n)** are listed in Table 1. The parity of the space is calculated as  $n$  (methylene number) plus 3 (one carbon and two oxygens). Compounds **(R)-I-(8,5)** and **(R)-I-(8,7)** with the even-

numbered spacer exhibited Ferro, Ferri-H, Ferri-L, and Anti phases, whereas compounds **(R)-I-(8,6)** and **(R)-I-(8,8)** with the odd-numbered spacer showed Ferro, Ferri-L, Anti, chiral smectic I (SmI\*), and unidentified SmX phases. Furthermore, compound **(R)-I-(8,6)** showed a SmC\*<sub>α</sub> phase. The ferrielectric phases were distinguishable from the antiferroelectric or ferroelectric phase under a polarized microscope because the characteristic texture with constant motion as domains form, coalesce, and disappear was observed, as reported for monomeric (Goodby et al., 1992) and dimeric materials (Nishiyama et al., 2001).



**(R)-I-(8,n)**

n	Cr	SmX	SmI*	Anti	Ferri-L	Ferri-H	Ferro	SmC* <sub>α</sub>	Iso
5	• 82.5			[• 78.8] (0.55)	• 114.3 (-)	• 126.5 (-)	• 130.7 (5.37)		•
6	• 71.6	[• 50.8 (0.49)	• 65.6 (-)	• 69.6 (-)	• 73.6 (-)		• 83.0 (-)	• 85.0 (5.11)	•
7	• 83.8			• 85.2 (0.76)	• 98.5 (-)	• 111.8 (-)	• 114.2 (6.34)		•
8	• 78.5	[• 69.3 (0.36)	• 72.0 (0.24)	• 75.7 (-)	• 76.3 (-)		• 83.1 (6.71)		•

Table 1. Transition temperatures (°C) and  $\Delta S/R$  (in parentheses) for **(R)-I-(8,n)**. Square brackets represent a monotropic transition.

Figure 4 depicts optical textures of SmC\*<sub>α</sub>, Ferro, Ferri-L, Anti, SmI\*, and SmX phases of **(R)-I-(8,6)**. The typical fan texture in planar alignment regions and dark texture attributable to the short pitch helical structure in homeotropic regions were observed in the SmC\*<sub>α</sub> phase [Fig. 4(a)]. In the Ferri-L phase [Fig. 4(c)], a characteristic texture with vigorous constant movement was observed. The constant motion in the Ferri-L phase was weaker than that in Ferri-H phase. Upon cooling to the Anti phase, the homeotropic alignment exhibited a dark texture and the constant movement was no longer present [Fig. 4(d)].

Figure 5 portrays a cooling thermogram of **(R)-I-(8,6)**. Neither Ferro-to-Ferri-L nor the Ferri-L-to-Anti transition accompanied enthalpy change. In contrast, the Ferri-L-to-Anti transition of **(R)-I-(8,7)** showed clear enthalpy change.

Odd-even effects were observed not only for the phase sequence but also for the Iso-Ferro (or SmC\*<sub>α</sub>) phase transition temperature. The transition temperatures of the even-numbered series are higher than those of the odd-numbered series. However, it is noteworthy that such an odd-even effect was not observed for the associated entropy changes. Typical liquid crystal dimers show marked odd-even effects not only on the transition temperature but also on the associated entropy changes. The effects on the entropy changes are interpreted as follows (Imrie & Luckhurst, 1998). In the isotropic phase, approximately half the conformers of an even-membered dimer are essentially linear; for an odd-membered dimer, only 10% are linear. A synergy exists between conformation and orientational order. Therefore, many of the bent conformers are converted to a linear form at the transition to the nematic phase for even-membered dimers, which enhances the orientational order of the nematic phase, engendering a larger nematic-isotropic entropy than would be expected for a monomer. For odd-membered dimers, however, the difference in free energy between the bent and linear conformers is such that the orientational order of the nematic phase is insufficient to convert

bent into linear conformers. Consequently, the orientational order is not enhanced and a smaller nematic-isotropic entropy is expected. In the present system, compound **(R)-I-(8,8)** with an odd-numbered spacer has larger entropy change at the Iso-Ferro transition than compound **(R)-I-(8,7)** with an even-numbered spacer. The unusually larger entropy change for the odd-membered series reflects that not only the even-membered compounds but also the odd-membered compounds exhibit the conformational change from bent to linear at the Iso-to-Ferro (or  $\text{SmC}^*_\alpha$ ) transition. Therefore, both even-membered and odd-membered compounds exist as linear conformers in their respective Ferro and Ferri phases.

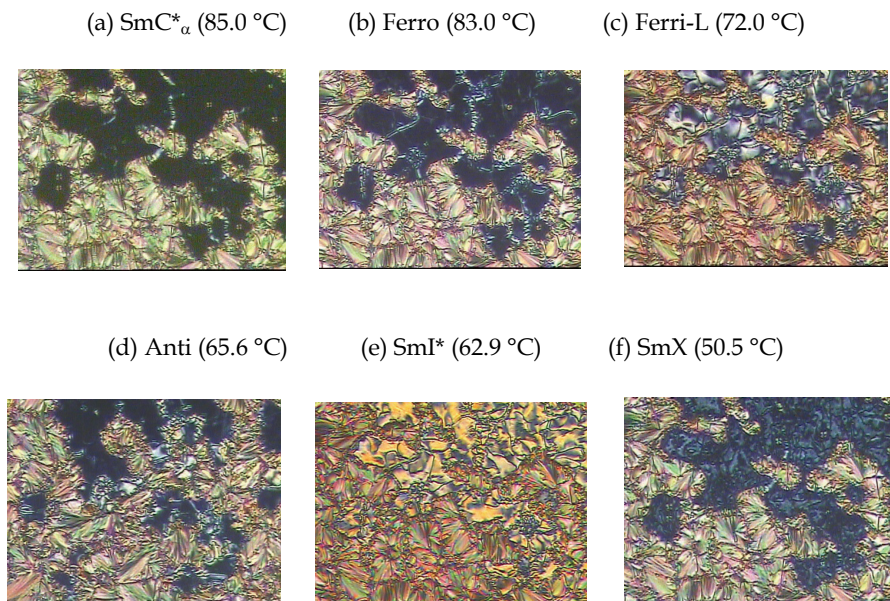


Fig. 4. Optical textures of **(R)-I-(8,6)** on a glass with a cover glass.

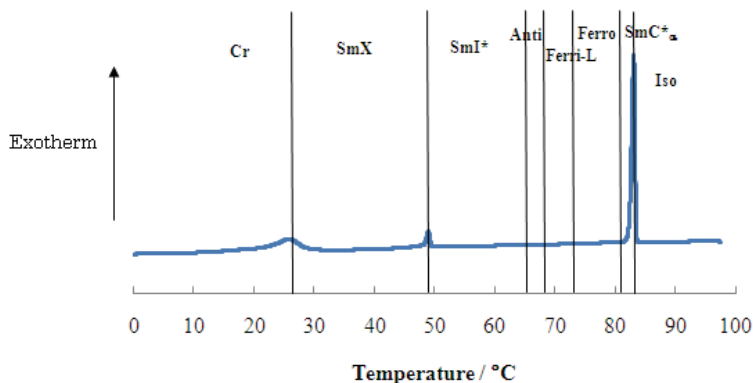


Fig. 5. Cooling DSC thermogram of **(R)-I-(8,6)** at a scanning rate of 5 °C min<sup>-1</sup>.

Ferrielectric properties in the Ferri-L phase of compound **(R)-I-(8,6)** were studied using measurements of the apparent tilt angle as a function of the applied voltage. Figure 6(a) presents the applied voltage dependence of the apparent tilt angle in the Ferri-L phase. When the applied voltage is increased, the apparent tilt angle increases and reaches a saturated value corresponding to the electrically induced ferroelectric ordering via characteristic multi-step change (Nishiyama et al., 2001). Figure 6(b) portrays the temperature dependence of a saturated tilt angle corresponding to the electrically induced ferroelectric state with an electric field of  $8 \text{ V } \mu\text{m}^{-1}$ . The tilt angle increases concomitantly with decreasing temperature in the Ferro and Ferri-L phases.

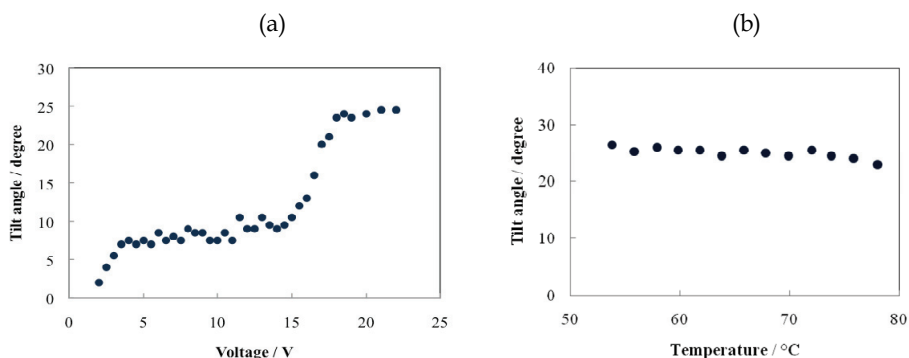


Fig. 6. (a) Applied voltage dependence of the apparent tilt angle in the Ferri-L phase of compound **(R)-I-(8,6)** at  $71 \text{ }^\circ\text{C}$ . The cell gap was  $5 \text{ } \mu\text{m}$ . (b) The saturated tilt angle as a function of temperature, corresponding to the electrically induced ferroelectric state of **(R)-I-(8,6)** with an electric field of  $8 \text{ V } \mu\text{m}^{-1}$ . The cell gap was  $5 \text{ } \mu\text{m}$ .

Layer spacings in the Ferro and Ferri-L phases of compound **(R)-I-(8,6)** were investigated using XRD measurements. A sharp peak was observed in the small angle region. Layer spacings corresponding to the peak are  $44.6 \text{ } \text{Å}$  in the Ferro phase and  $44.1 \text{ } \text{Å}$  in the Ferri-L phase. The molecular lengths were obtained from MOPAC as about  $46 \text{ } \text{Å}$  for a bent conformer and  $44 \text{ } \text{Å}$  for a linear conformer. According to the larger transition entropy at the Iso-to- $\text{SmC}^*_\alpha$  as discussed above, we assume that compound **(R)-I-(8,6)** forms a linear conformation in the Ferro and Ferri phases. The Ferri-L phase of compound **(R)-I-(8,6)** is thought to have a monolayer structure, as does that of **(R)-I-(8,7)**.

Figure 7 shows the binary phase diagram between compounds **(R)-I-(8,6)** and **(R)-I-(8,7)**. The  $\text{SmC}^*_\alpha$  phase disappears as increasing content of compound **(R)-I-(8,7)**. It is particularly interesting that the Ferro phase disappears between 50–75 mol% of compound **(R)-I-(8,7)**, and the direct transition from Iso to Ferri-H was observed. The Ferri-L phase of both compounds proved to be miscible across the full composition range. Therefore, the Ferri-L phase of compound **(R)-I-(8,6)** has the same structure as that of compound **(R)-I-(8,7)**.

To summarize the effects of the central spacer on the appearance of the ferrielectric phases of the chiral dimesogenic compound, the compounds possessing an even-numbered spacer show both Ferri-H and Ferri-L phases with a wide temperature range, although the compounds possessing an odd-numbered spacer show only a Ferri-L phase. Furthermore, no significant difference was found in the electro-optical properties in the Ferri-L phase

between even- and odd-membered series. Both even- and odd-membered compounds have a monolayer structure in the smectic phases. Unusual entropy change observed at the Iso-Ferro or Iso-SmC\*<sub>α</sub> of the odd-membered compounds indicates that they exist as a linear conformer in the Ferro and Ferri-L phases.

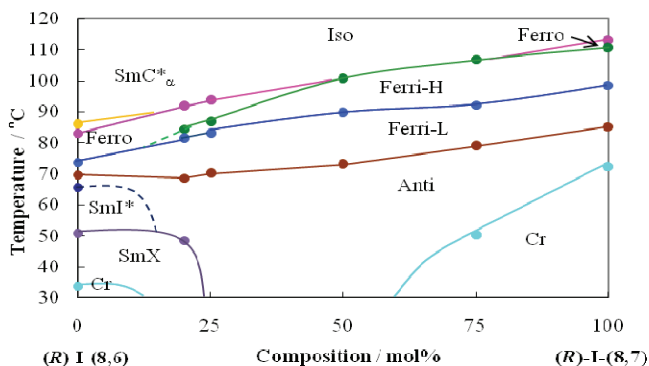
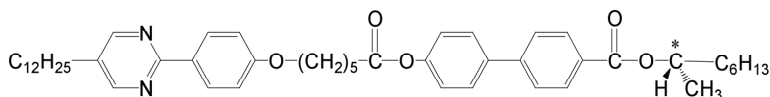


Fig. 7. Binary phase diagram between compounds (R)-I-(8,6) and (R)-I-(8,7).

### 3.2 Effects of the terminal chain

We prepared compound (R)-I-(12,5) possessing a decyl chain instead of an octyl chain of compound (R)-I-(8,5) and investigated its physical properties. Figure 8 depicts its molecular structure and transition properties. Compound (R)-I-(12,5) shows Ferro, Ferri-H, Ferri-L, and Anti phases, as does the corresponding compound (R)-I-(8,5). In addition to the phases, an unidentified SmX phase was observed for compound (R)-I-(12,5). The Iso-to-N and Ferri-L-to-Anti phase transition temperatures are almost identical among them. However, compound (R)-I-(12,5) shows lower transition temperatures for the Ferro-to-Ferri-H and Ferri-H-to-Ferri-L phase transition than compound (R)-I-(8,5) does. Increasing the terminal chain length destabilizes both Ferri-H and Ferri-L phases. The terminal alkyl chain is thought to play an important role in the interlayer interaction stabilizing the ferroelectric phases.



(R)-I-(12,5): Cry 76.6 [SmX 60.8(0.36)] Anti 79.6(-) Ferri-L 87.1(-) Ferri-H 105.3(-) Ferro 128.4(5.93) Iso

Fig. 8. Molecular structure, transition temperatures (°C) and  $\Delta S/R$  for (R)-I-(12,5).

Recent reports describe that the octyloxy derivative (R)-II-(8,7) exhibits a direct Iso-to-Ferri-H transition (Noji & Yoshizawa, 2011). Figure 9 shows the molecular structure and the transition properties. Compound (R)-II-(8,7) shows Ferro, Ferri-H, Ferri-L, Anti, and SmI\* phases. The temperature range of the enantiotropic ferroelectric phases was about 28 K. According to a binary phase diagram between compounds (R)-II-(8,7) and (R)-I-(8,7), both Ferri-H and Ferri-L phases of compound (R)-II-(8,7) present a similar structure to those of compound (R)-I-(8,7). Comparing compound (R)-II-(8,7) with (R)-I-(8,7), the alkoxy tail



With respect to the Ferri-L phase, its three asymmetric peaks suggest that switching between two ferroelectric states occurs via two intermediate states. Figure 12 shows a model for the switching behaviour assuming that the intermediate state has three-layer periodicity.

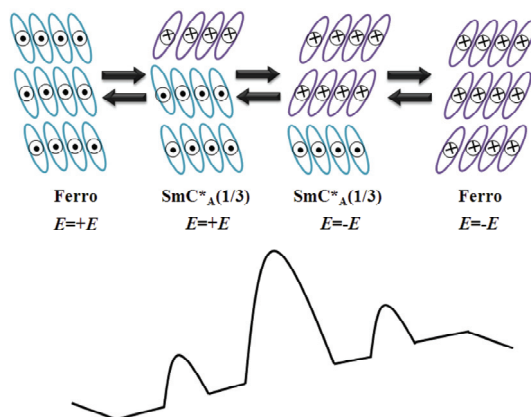


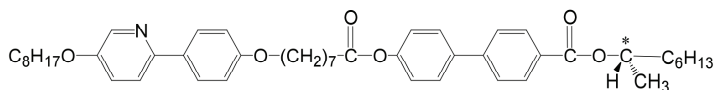
Fig. 12. Schematic model for electrical switching behaviour in the Ferri-L phase.

Asymmetric switching was observed in both the Ferri-H and Ferri-L phases. We have no explanation for the asymmetric switching. It is possible that the Ferri-H and Ferri-L phases have a more complex periodicity.

A ferrielectric phase normally arises at the lower temperature end of the ferroelectric smectic C phase. A direct transition is unusual. The introduction of the alkoxy tail to the chiral oligomeric system produces marked stability of the ferrielectric phases.

### 3.3 Effects of the mesogenic core structure

We introduced a phenylpyridine core or a 2,3-difluoro-1,4-diphenylbenzene core into the chiral oligomeric system instead of a phenylpyrimidine core and investigated the liquid-crystalline properties. Figure 13 shows the molecular structure and phase transition properties of compound **(R)-III-(8,7)** possessing a phenylpyridine core with greater tilt ability than that of a phenylpyridine core.



**(R)-III-(8,7)**: Cry 108.7 Anti 122.7(1.72) Ferri-L 125.0(-)Ferri-H 134.7 Ferro 139.3(7.24) Iso

Fig. 13. Molecular structure, transition temperatures ( $^{\circ}\text{C}$ ) and  $\Delta S/R$  for **(R)-III-(8,7)**.

Figure 14 depicts optical textures of Ferro, Ferri-H, Ferri-L, and Anti phases of **(R)-III-(8,7)**. Ferro-to-Ferri-H and Ferri-H-to-Ferri-L transition temperatures of compound **(R)-III-(8,7)** are almost identical as those of compound **(R)-II-(8,7)**, suggesting that no significant difference exists in stability of the ferrielectric phases between those compounds. However, the Ferro phase appears in compound **(R)-III-(8,7)**. Furthermore, the Ferri-L-to-Anti phase transition temperature of compound **(R)-III-(8,7)** is much higher than that of compound **(R)-**

**II-(8,7)**. Therefore, the temperature ranges of the ferrielectric phases of compound **(R)-III-(8,7)** are narrower than that of compound **(R)-II-(8,7)**.

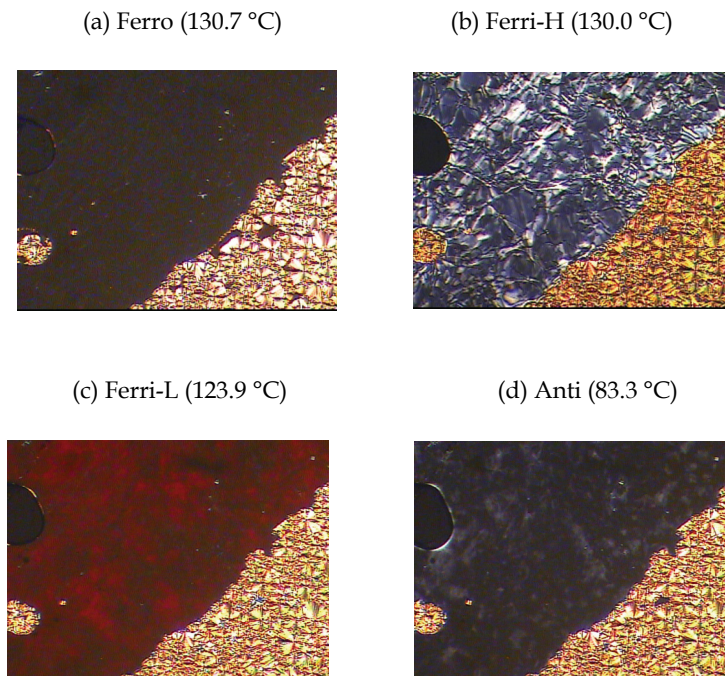
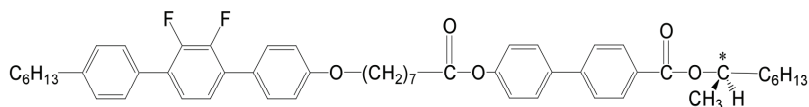


Fig. 14. Optical textures of **(R)-III-(8,7)** on a glass with a cover glass.

Figure 15 shows molecular structure and phase transition properties of compound **(R)-IV-(6,7)** possessing a 2,3-difluoro-1,4-diphenylbenzene core that stabilizes a nematic phase.



**(R)-IV-(6,7)**: Cry 108.2 [SmX 79.5 (1.36) Anti 95.3 (-)] Ferro 111.0 (-) SmA 156.9 (4.66) Iso

Fig. 15. Molecular structure, transition temperatures (°C) and  $\Delta S/R$  for **(R)-IV-(6,7)**.

Compound **(R)-IV-(6,7)** exhibited smectic A, Ferro, Anti, and unidentified SmX phases. No ferrielectric phase was observed.

A phenylpyridine core having larger tilting ability than a phenylpyrimidine core enhances the stability of the Ferro and Anti phases; however, it does not affect that of the ferrielectric phases. Intermolecular tilting interactions between adjacent mesogenic units make no large contribution to the stability of the ferrielectric phases. A 2,3-difluoro-1,4-diphenylbenzene core making the mesogenic units to align along the director induces a SmA phase but eliminates both of the Ferri-H and Ferri-L phases. A phase sequence of

SmA-Ferro-Ferri is often observed for some monomeric chiral compounds. However, the ferroelectric phases of the present chiral oligomeric system are thought unlikely to coexist with a SmA phase.

### 3.4 Effects of chirality

The appearance of ferroelectric phases is known to be highly dependent on the optical purity of the system. Actually, ferroelectric phases are seen only in high enantiomer excess areas. We reported that ferroelectric-like ordering was observed in a racemic mixture of (*R*)-**I-(8,7)** and its enantiomer (Noji et al., 2009). Figure 16 depicts a binary phase diagram for mixtures of (*S*)-**I-(8,7)** and (*R*)-**I-(8,7)**. Stabilities of both the ferroelectric and antiferroelectric phases were independent of the optical purity. The Ferro-to-Ferri-H transition temperature decreases concomitantly with decreasing optical purity, although the Ferri-H-to-Ferri-L transition temperature increases slightly and then decreases concomitantly with decreasing optical purity. Surprisingly, the Ferri-L phase does not disappear with decreasing optical purity close to 0% enantiomer excess. The results indicate that a ferroelectric phase appears in a system with a low degree of chirality, and ferroelectric-like ordering exists in the racemic mixture.

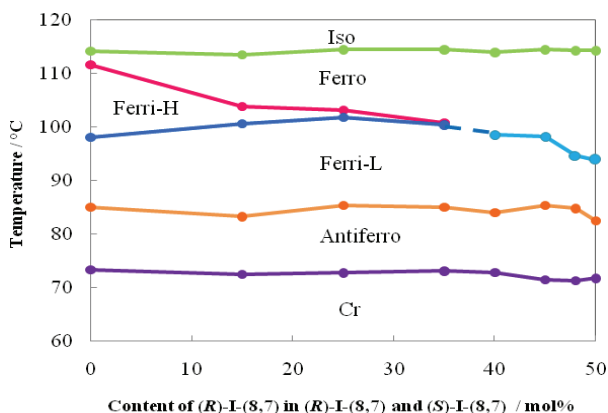
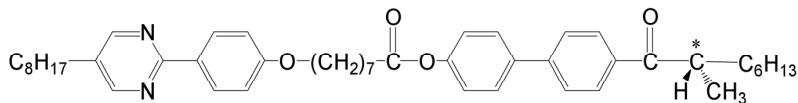


Fig. 16. Binary phase diagram for mixtures of (*S*)-**I-(8,7)** and (*R*)-**I-(8,7)** (Noji et al., 2009).

We prepared compound (*S*)-**V-(8,7)** possessing a (*S*)-2-methylalkanoyl group as the chiral structure. A ferroelectric liquid crystal possessing a 2-methylalkanoyl group gives usually larger spontaneous polarization in the ferroelectric SmC\* phase than that possessing a 1-methylheptyl carboxylate group (Yoshizawa et al. 1989). Therefore, compound (*S*)-**V-(8,7)** is thought to have a higher degree of chirality than (*R*)-**I-(8,7)** has. Figure 17 presents the molecular structure and phase transition properties of compound (*S*)-**V-(8,7)**.



(*S*)-**V-(8,7)**: Cry 95.1 [SmX 91.8 (1.09)] Anti 109.5 (-) Ferro 115.5 (6.10) Iso

Fig. 17. Molecular structure, transition temperatures (°C) and  $\Delta S/R$  for (*S*)-**V-(8,7)**.

Compound **(S)-V-(8,7)** exhibited Ferro and Anti phases without accompanying any ferrielectric phase. Comparing transition temperatures of compound **(S)-V-(8,7)** with those of compound **(R)-I-(8,7)**, the Iso-to-Ferro transition temperature of **(S)-V-(8,7)** is almost identical to that of **(R)-I-(8,7)**, whereas the Ferro-to-Anti transition temperature of **(S)-V-(8,7)** is much higher than the Ferri-L-to-Anti transition temperature of **(R)-I-(8,7)**. The disappearance of a ferrielectric phase for **(S)-V-(8,7)** is attributed to the higher stability of the Anti phase of **(S)-V-(8,7)**. Furthermore, significant difference exists in the molecular shape between compounds **(R)-I-(8,7)** and **(S)-V-(8,7)**. Figure 18 presents MOPAC models for those compounds. The 2-methyloctanoyl group has a bent structure because of the keto carbon, as presented in Fig. 18(b). The inclined structure between the core and the alkyl chain disturbs the interlayer interaction related to the appearance of the ferrielectric phase.

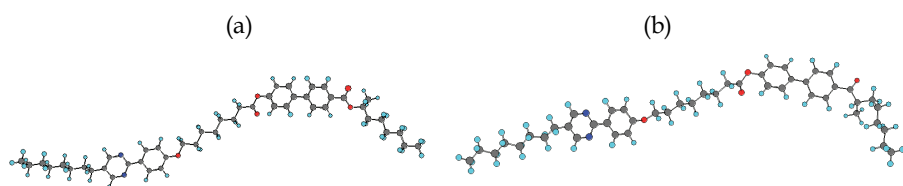


Fig. 18. MOPAC models for (a) **(R)-I-(8,7)** and (b) **(S)-V-(8,7)**.

### 3.5 Origin for stabilizing the ferrielectric phases

Electrical response studies of compound **(R)-II-(8,7)** reveal that the Ferri-H and Ferri-L phases respectively have a four-layer periodicity as  $\text{SmC}^*_A(1/2)$  and a three-layer periodicity as  $\text{SmC}^*_A(1/3)$ . We discuss the origin for stabilizing the ferrielectric phases in terms of preorganization and interlayer interaction, and show molecular organization models for the ferrielectric phases.

#### 3.5.1 Preorganized effects

According to the XRD measurements, both the Ferri-H and Ferri-L phases have a monolayer structure. Comparison of tilt angles determined by POM with those determined by XRD of **(R)-I-(8,7)** reveals that the tilt of the mesogenic units is greater than that of the long axis (Noji et al., 2009). The dimesogenic system has an inherent tilt within the molecule. The two mesogenic units are connected via a central spacer. Assuming that all *trans* conformation for the spacer, then compounds **(R)-I-(8,n)** possessing an even-numbered spacer can form a linear conformation with two coparallel mesogenic units, as presented in Fig. 19(a). Optical tilt angles in the Ferro, Ferri-H, Ferri-L, and Anti phases of these compounds are attributed to the tilt of the mesogenic units with respect to the layer normal. However, compounds **(R)-I-(8,n)** possessing an odd-numbered spacer are thought to form a bent conformation in which two mesogenic units are inclined with respect to each other. The unusual large entropy change at the Iso-Ferro (or  $\text{SmC}^*$ ) suggests that the conformational change from bent to linear occurs at the phase transition. In the Ferri-L phase of the odd-members, the molecules are thought to exist as a linear conformer in which two mesogenic units are coparallel, as presented in Fig. 19(b). Therefore, both even- and odd-membered compounds have two mesogenic units tilted

with respect to the long axis in their smectic phases. The inherent tilt within a single molecule can stabilize the ferroelectric phases. However, it might disturb the appearance of a smectic A phase for these ferroelectric compounds.

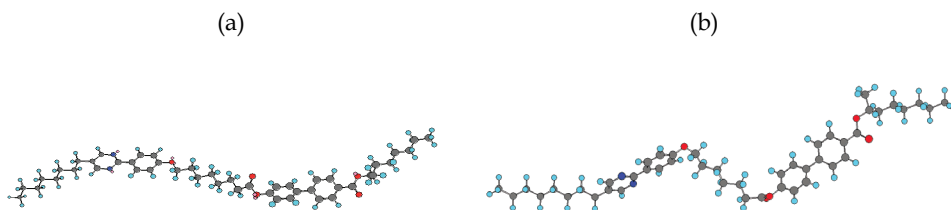


Fig. 19. Linear conformations for (a) the even-member **(R)-I-(8,7)** and (b) the odd-member **(R)-I-(8,6)**.

### 3.5.2 Interlayer interactions

It is generally accepted that the appearance of a ferroelectric phase is explained in terms of macroscopic chirality, i.e. helicity or spontaneous polarization. In this system, the Ferri-H phase is destabilized by decreasing optical purity. However, the macroscopic chirality does not affect the stability of the Ferri-L phase. Another model is necessary to explain the stabilization of the ferroelectric phase. We infer interlayer interactions among the preorganized molecules in adjacent layers via chiral recognition to discuss the stability of the Ferri-L phase. Interlayer interactions are known to govern tilt- and helical-correlation between molecules in adjacent layers (Yoshizawa et al., 1995; Yoshizawa & Nishiyama, 1995). Two molecular arrangements for the chiral interaction exist as presented in Fig. 20. One is a parallel twin ordering in which two oligomer units are coparallel, thereby inducing

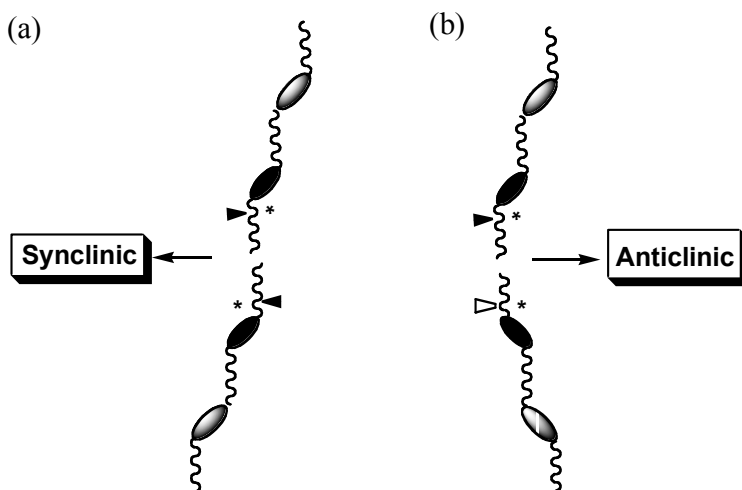


Fig. 20. Schematic sketches for (a) parallel twin ordering and (b) bent twin ordering via chiral interaction.

synclinc ordering. The other is a bent twin ordering in which they are inclined with respect to each other, inducing anticlinc ordering. The alkoxy tail substituted to the pyrimidine ring stabilizes the Ferri-L phase much more than the Ferri-H phase. Introduction of the alkoxy tail is thought to enhance the electrostatic dipole-quadrupole interaction and to stabilize the Ferri-L phase. The chiral dimeric system can induce favourable positional correlation among molecules in adjacent layers.

### 3.5.3 Molecular organization model

According to the theoretical study (Emelyanenko & Osipov 2003), ferrielectric phases are stabilized by two factors:

1. chirality-dependent direct polarization coupling between adjacent layers; and
2. electrostatic dipole-quadrupole interaction between positionally correlated molecules in adjacent layers.

Furthermore, our experimentally obtained results indicate that interlayer interaction via chiral recognition between preorganized molecules in adjacent layers is important for stabilization of the ferrielectric phases of the present dimesogenic system.

Figure 21 shows models for molecular organization in the Ferro, Ferri-H, Ferri-L, and Anti phases of the chiral system. A circle or cross is inserted at each interlayer region. Circles

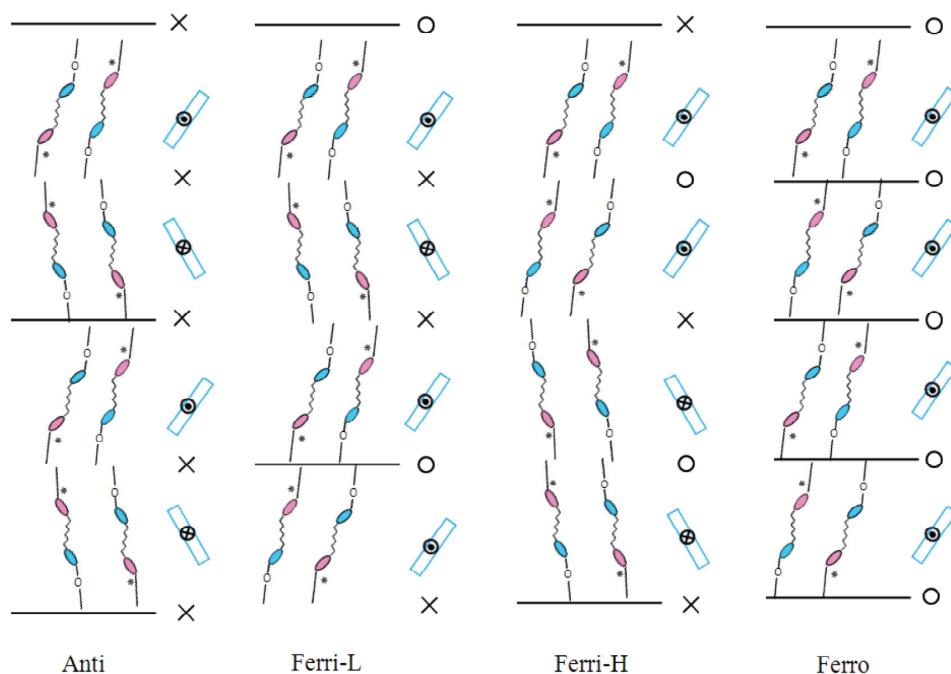


Fig. 21. Possible models for molecular organization in the Ferro, Ferri-H, Ferri-L, and Anti phases of the chiral system. The spontaneous polarization direction is indicated by arrows into or out of the page; the tilt direction is shown by solid lines. Open circles represent synclinc ordering in adjacent layers; crosses represent anticlinc ordering. The elliptical shapes represent mesogenic units within the molecules (Noji et al., 2009).

represent synclinc ordering in adjacent layers and crosses represent anticlinc ordering. In the Ferro phase, the tilt direction in each layer is the same between adjacent layers and polarization has the same direction. The Ferro phase consists of parallel twin orderings. In the Ferri-H phase, the two successive layers of the four periodic layers have the same tilt and polarization directions, whereas the other two layers have alternative ones. Such is the case for  $\text{SmC}^*_A(1/2)$ . The sequence of bent-parallel-bent-parallel-bent for the twin ordering is apparent at five nodes in the periodic four layers. The Ferri-H phase is destabilized by decreasing optical purity. Direct Iso-to-Ferri-H phase transition was observed for **(R)-II-(8,7)** possessing an alkoxy tail. These results suggest that chirality-dependent direct polarization coupling between adjacent layers is playing an important role in the stabilization of the Ferri-H phase. In the Ferr-L phase, two layers of the periodic three layers have the same tilt and polarization directions, although the other layer has alternative ones. Such is the case for  $\text{SmC}^*_A(1/3)$ . The sequence of parallel-bent-bent-parallel is apparent at four nodes in the periodic three layers. The stability of the Ferri-L phase was unaffected by macroscopic chirality. However, introduction of an alkoxy tail instead of an alkyl tail stabilizes the Ferri-L phase. Stabilization of the Ferri-L phase might therefore be governed by electrostatic dipole-quadrupole interaction in addition to microscopic chiral recognition. In the Anti phase, tilt and polarization directions are alternated between adjacent layers. The antiferroelectric phase consists of bent twin orderings.

With respect to the dimesogenic compounds with an odd-numbered spacer, many of bent conformers are converted to a linear form at the transition to the liquid-crystalline phase. This conversion accompanies a *trans* to *gauche* conformational change for some methylene units in the spacer. The orientational order organized by the interlayer interactions of the present frustrated phases is enhanced by the energetically unfavourable conversion.

#### 4. Conclusion

We prepared a homologous series of chiral dimesogenic compounds and investigated their structure-property relations. The dimesogenic compounds possessing an even-numbered spacer show the Ferri-H and Ferri-L phases, whereas those possessing an odd-numbered spacer show the Ferri-L phase. The Ferri-H and Ferri-L phases were found to have a four-layer periodicity as  $\text{SmC}^*_A(1/2)$  and a three-layer periodicity as  $\text{SmC}^*_A(1/3)$ , respectively. Large entropy changes at the Iso-to-Ferro phase transition were observed not only for the even-members but also for the odd-members, indicating that both members form a linear shape in which two mesogenic units are coparallel mutually in their ferrielectric phases. Therefore, they have a preorganized structure in which an inherent tilt exists. The Ferri-H phase is destabilized by decreasing optical purity. However, the stability of the Ferri-L phase is unaffected by optical purity. Significant differences were found in chiral effect on the stabilization of a ferrielectric phase between Ferri-H and Ferri-L phases. Chirality-dependent direct polarization between adjacent layers is playing an important role in the stabilization of the Ferri-H phase. The stability of the Ferri-L phase is governed by interlayer interaction via microscopic chiral recognition between the preorganized molecules in adjacent layers. Furthermore, the induced positional correlation between molecules in adjacent layers can enhance interlayer dipole-quadrupole interaction to stabilize the Ferri-L phase. Our findings yield fundamental insights into the nature of long-range interaction producing clinicity in ferroelectric liquid

crystals in addition to a new approach to molecular design for supermolecules exhibiting a hierarchical phase structure.

## 5. Acknowledgments

We thank Professors J. Yamamoto and Y. Takanishi for X-ray measurements. We also thank Dr. I. Nishiyama for fruitful discussion. This work was partially supported by a Grant-in-Aid for Scientific Research (B) from the Japan Society for the Promotion of Science (No. 22350078) and a Grant for Hirosaki University Institutional Research.

## 6. References

- Aoki, T.; Chao, Ke.; Fukuda, A.; Takanishi, Y.; Ishikawa, K.; Takezoe, H. & Nguyen, H. T. (1999). Antiferroelectricity of a Phase with the Four-Layered Periodicity that was Confirmed by Resonant X-ray Scattering, *Proceedings of 1999 Japanese Liquid Crystal Conference*, pp. 110-111, Toyama, Japan, September 29 - October 1, 1999.
- Cepic, M. & Zeks, B. (2001). Flexoelectricity and Piezoelectricity: The Reason for the Rich Variety of Phases in Antiferroelectric Smectic Liquid Crystals. *Phys. Rev. Lett.* Vol. 87, 085501/1-4, ISSN 1079-7114.
- Cepic, M.; Gorecka, E.; Pocięcha, D.; Zeks, B. & Nguyen, H.T. (2002). Theoretical and Experimental Study of the Intermediate Sm C\*FI2 and the Sm C\*FI1 Phases in Antiferroelectric Liquid Crystals. *J. Chem. Phys.*, Vol. 117, pp. 1817-1826, ISSN 1089-7690.
- Chandani, A. D. L.; Gorecka, E.; Ouchi, Y.; Takezoe, H. & Fukuda, A. (1989a). Antiferroelectric Chiral Smectic Phases Responsible for the Tristable Switching in MHPOBC. *Jpn. J. Appl. Phys.*, Vol. 28, pp. L1265-L1268, ISSN 1347-4065.
- Chandani, A. D. L.; Ouchi, Y.; Takezoe, H.; Fukuda, A.; Terashima, K.; Furukawa, K. & Kishi, K. (1989b). Novel Phases Exhibiting Tristable Switching. *Jpn. J. Appl. Phys.*, Vol. 28, pp. L1261-L1264, ISSN 1347-4065.
- Emelyanenko, A.V. & Osipov, M.A. (2003). Theoretical Model for the Discrete Flexoelectric Effect and a Description for the Sequence of Intermediate Smectic Phases with Increasing Periodicity. *Phys. Rev. E*, Vol. 68, 051703/1-16, ISSN 1550-2376.
- Fukuda, A.; Takanishi, Y.; Isozaki, K. & Takezoe, H. (1994). Antiferroelectric Chiral Smectic Liquid Crystals. *J. Mater. Chem.*, Vol. 4, pp. 997-1016, ISSN 1364-5501.
- Fukui, M.; Orihara, H.; Yamada, Y. & Ishibashi, Y. (1989). New Phases in the Ferroelectric Liquid Crystal MHPOBC Studied by Differential Scanning Calorimetry. *Jpn. J. Appl. Phys.*, Vol. 28, pp. 849-850, ISSN 1347-4065.
- Goodby, J.W.; Blinc, R.; Clark, N.A.; Largerwall, S.T.; Osipov, M.A.; Pikin, S.A.; Sakurai, T.; Yoshino, K. & Saks, B. (1991). Ferroelectric Liquid Crystals: Principles, Properties and Applications, pp. 166, 167, and 19-192, ISBN 2-88124-282-0, Philadelphia, Gordon & Breach.
- Goodby, J.W.; Patel, J.S. & Chin, E. (1992). Ferroelectric, Ferrielectric and Antiferroelectric Properties in the (R)- and (S)-1-Methylalkyl 4'-(4''-n-alkoxybenzoyloxy) biphenyl-4-carboxylate Liquid Crystals. *J. Mater. Chem.*, Vol. 2, pp. 197-207, ISSN 1364-5501.

- Gorecka, E.; Chandani, A.D.L.; Ouchi, Y.; Takezoe, H. & Fukuda, A. (1990). Molecular Orientational Structures in Ferroelectric, Ferrielectric and Antiferroelectric Smectic Liquid Crystal Phases as Studied by Conoscope Observation. *Jpn. J. Appl. Phys.*, Vol. 29, pp. 131-137, ISSN 1347-4065.
- Gorecka, E.; Pocięcha, D.; Cepić, M.; Zeks, B. & Dabrowski, R. (2002). Enantiomeric Excess Dependence of the Phase Diagram of Antiferroelectric Liquid Crystals. *Phys. Rev. E* Vol. 65, 061703/1-4, ISSN 1550-2376.
- Imrie, C. T. & Luckhurst, G. R. (1998). Liquid Crystal Dimers and Oligomers, *Handbook of Liquid Crystals* Vol. 1, Demus, D.; Goodby, J. W.; Gray, G. W.; Spiess, H. -W. & Vill, V. (Eds), pp. 801-833, ISBN 3-527-29296-9, Weinheim, Wiley-VCH.
- Inui, S.; Imura, N.; Suzuki, T.; Iwane, H.; Miyachi, K.; Takanishi, Y. & Fukuda, A. (1996). Thresholdless Antiferroelectricity in Liquid Crystals and Its Application to Displays. *J. Mater. Chem.*, Vol. 6, pp. 671-673, ISSN 1364-5501.
- Isozaki, T.; Fujisawa, T.; Takezoe, H.; Fukuda, A.; Hagiwara, T.; Suzuki, Y. & Kawamura, I. (1992). Competition between Ferroelectric and Antiferroelectric Interactions Stabilizing Varieties of Phases in Binary Mixtures of Smectic Liquid Crystals. *Jpn. J. Appl. Phys.*, Vol. 31, pp. L1435-L1438, ISSN 1347-4065.
- Isozaki, T.; Fujisawa, T.; Takezoe, H.; Fukuda, A.; Hagiwara, T.; Suzuki, Y. & Kawamura, I. (1993). Devil's Staircase Formed by Competing Interactions Stabilizing the Ferroelectric Smectic-C\* Phase and the Antiferroelectric Smectic-C<sub>A</sub>\* Phase in Liquid Crystalline Binary Mixtures. *Phys. Rev. B*, Vol. 48, pp. 13439-13450, ISSN 1550-235X.
- Jaradat, S.; Roberts, N. W.; Wang, Y.; Hirst, L.S. & Gleeson, H.F. (2006). Remarkably Wide Four-layer Smectic Phases in Mixtures of Liquid Crystals and Highly Chiral Dopants. *J. Mater. Chem.*, Vol. 16, pp. 3753-3761, ISSN 1364-5501.
- Jaradat, S.; Brimicombe, P. D.; Roberts, N. W.; Southern, C.; Gleeson, H. F. (2008). Asymmetric Switching in a Ferrielectric Liquid Crystal Device. *Appl. Phys. Lett.*, Vol. 93, 153506/1-3, ISSN 1079-7114.
- Jaradat, S.; Brimicombe, P. D.; Southern, C.; Siemianowski, S. D.; DiMasi, E.; Pindak, R. & Gleeson, H. F. (2009). Stable Field-induced Ferrielectric Liquid Crystal Phases in Devices. *Appl. Phys. Lett.*, Vol. 94, 153507/1-3, ISSN 1079-7114.
- Johnson, P. M.; Olson, D. A.; Pankratz, S.; Nguyen, T.; Goodby, J. W.; Hird, M. & Huang, C. C. (2000). Structure of the Liquid-Crystal Ferrielectric Phases as Determined by Ellipsometry. *Phys. Rev. Lett.*, Vol. 84, pp. 4870-4873, ISSN 1092-0145.
- Lemieux, R. (2007). Molecular Recognition in Chiral Smectic Liquid Crystals: The Effect of Core-Core Interactions and Chirality Transfer on Polar Order. *Chem. Soc. Rev.*, Vol. 36, 2033-2045, ISSN 1460-4744.
- Lagerwall, J. P. F. & Giesselmann, F. (2006). Current Topics in Smectic Liquid Crystals Research. *ChemPhysChem.*, Vol. 7, pp. 20-45, ISSN 1439-7641.
- Mach, P.; Pindak, R.; Levelut, A. -M.; Barois, P.; Nguyen, H. T.; Huang, C. C. & Furenlid, L. (1998). Structural Characterization of Various Chiral Smectic-C Phases by Resonant X-Ray Scattering. *Phys. Rev. Lett.*, Vol. 81, pp. 1015-1018, ISSN 1092-0145.
- Mach, P.; Pindak, R.; Levelut, A. -M.; Barois, P.; Nguyen, H. T.; Baltes, H.; Hird, M.; Seed, A. J.; Goodby, J. W.; Huang, C. C. & Furenlid, L. (1999). Structures of Chiral Smectic-C

- Mesophases Revealed by Polarization-Analyzed Resonant X-Ray Scattering. *Phys. Rev. E*, Vol. 60, pp. 6793-6802, ISSN 1550-2376.
- Matsumoto, T.; Fukuda, A.; Johno, M.; Motoyama, Y.; Yui, T.; Seomun, S.-S. & Yamashita, M. (1999). A Novel Property Caused by Frustration Between Ferroelectricity and Antiferroelectricity and Its Application to Liquid Crystal Displays—Frustoelectricity and V-Shaped Switching. *J. Mater. Chem.*, Vol. 9, pp. 2051-2080, ISSN 1364-5501.
- Nguyen, H. T.; Rouillon, J. C.; Cluzeau, P.; Sigaud, G.; Destrade, C. & Isaert, N. (1994). New Chiral Thiobenzoate Series with Antiferroelectric Mesophases, *Liq. Cryst.*, Vol. 17, pp. 571-583, ISSN 1366-5855.
- Nishiyama, I.; Yamamoto, J.; Goodby, J.W. & Yokoyama, H. (2001). A Symmetric Chiral Liquid-Crystalline Twin Exhibiting Stable Ferrielectric and Antiferroelectric Phases and a Chirality-Induced Isotropic-Isotropic Liquid Transition. *J. Mater. Chem.*, Vol. 11, pp. 2690-2693, ISSN 1364-5501.
- Nishiyama, I. (2010). Remarkable Effect of Pre-organization on the Self Assembly in Chiral Liquid Crystals, *The Chemical Record*, Vol. 9, pp. 340-355, ISSN 1528-0691.
- Noji, A.; Uehara, N.; Takanishi, Y.; Yamamoto, J. & Yoshizawa, A. (2009). Ferrielectric Smectic C Phases Stabilized Using a Chiral Liquid Crystal Oligomer. *J. Phys. Chem. B*, Vol. 113, pp. 16124-16130, ISSN 1520-5207.
- Noji, A. & Yoshizawa, A. (2011). Isotropic Liquid-Ferrielectric Smectic C Phase Transition Observed in a Chiral Nonsymmetric Dimer. *Liq. Cryst.*, Vol. 38, pp. 451-459., ISSN 1366-5855.
- Osipov, M. A. & Fukuda, A. (2000). Molecular Model for the Anticlinic Smectic- $C_A$  Phase *Phys. Rev. E*, Vol. 62, pp. 3724-3735, ISSN 1550-2376.
- Sandhya, K.L.; Vij, J.K.; Fukuda A. & Emelyanenko, A.V. (2009). Degeneracy Lifting Near the Frustration Points Due to Long- Range Interlayer Interaction Forces and the Resulting Varieties of Polar Chiral Tilted Smectic Phases. *Liq. Cryst.*, Vol. 36, pp. 1101-1118, ISSN 1366-5855.
- Takezoe, H.; Gorecka, E. & Cepic, M. (2010). Antiferroelectric Liquid Crystals: Interplay of Simplicity and Complexity. *Rev. Mod. Phys.*, Vol. 82, pp. 897-937, ISSN 1530-0756.
- Walba, D. M. (1995). Fast Ferroelectric Liquid-Crystal Electrooptics. *Science*, Vol. 270, pp. 250-251, ISSN 1095-9203.
- Wang, S.; Pan, L.; Pindak, R.; Liu, Z.Q.; Nguyen, H.T. & Huang, C.C. (2010). Discovery of a Novel Smectic- $C^*$  Liquid-Crystal Phase with Six-layer Periodicity. *Phys. Rev. Lett.*, Vol. 104, 027801/1-4, ISSN 1092-0145.
- Yamashita, M. & Miyajima, S. (1993). Successive Phase Transition - Ferro-, Ferri-and Antiferro-Electric Smectics. *Ferroelectrics*, Vol. 148, pp. 1-9, ISSN 1563-5112.
- Yoshizawa, A. Nishiyama, I.; Fukumasa, M.; Hirai, T. & Yamane, M. (1989). New Ferroelectric Liquid Crystal with Large Spontaneous Polarization. *Jpn. J. Appl. Phys.*, Vol. 28, pp. L1269-L1271, ISSN 1347-4065.
- Yoshizawa, A ; Kikuzaki, H. & Fukumasa, M. (1995). Microscopic Organization of Molecules in Smectic A and Chiral (Racemic) Smectic C Phases: Dynamic Molecular Deformation Effect on the  $S_A$  to  $S_C^*$  ( $S_C$ ) Transition. *Liq. Cryst.*, Vol. 18, pp. 351-366, ISSN 1366-5855.

Yoshizawa A. & Nishiyama I. (1995). Interlayer Correlation in Smectic Phases Induced by Chiral Twin Molecules. *Mol. Cryst. Liq. Cryst.*, Vol. 260, pp. 403-422, ISSN 1563-5287.

# Memory Effects in Mixtures of Liquid Crystals and Anisotropic Nanoparticles

Marjan Krašna<sup>1</sup>, Matej Cvetko<sup>1,2</sup>, Milan Ambrožič<sup>1</sup> and Samo Kralj<sup>1,3</sup>

<sup>1</sup>*University of Maribor, Faculty of Natural Science and Mathematics*

<sup>2</sup>*Regional Development Agency Mura Ltd*

<sup>3</sup>*Jožef Stefan Institute, Condensed Matter Physics Department  
Slovenia*

## 1. Introduction

For years there is a substantial interest on impact of disorder on condensed matter structural properties (Imry & Ma, 1975) (Bellini, Buscaglia, & Chiccoli, 2000) (Clever, Kralj, Sluckin, & Allen, 1996). Pioneering studies have been carried out in magnetic materials (Imry & Ma, 1975). In such system it has been shown that even relatively weak random perturbations could give rise to substantial degree of disorder. The main reason behind this extreme susceptibility is the existence of the Goldstone mode in the continuum field describing the orientational ordering of the system. This fluctuation mode appears unavoidably due to continuous symmetry breaking nature of the phase transition via which a lower symmetry magnetic phase was reached. For example, the Imry Ma theorem (Imry & Ma, 1975), one of the pillars of the statistical mechanics of disorder, claims, that even arbitrary weak random field type disorder could destroy long range ordering of the unperturbed phase and replace it with a short range order (SRO). Note that this theorem is still disputable because some studies claim that instead of SRO a quasi long order could be established (Clever, Kralj, Sluckin, & Allen, 1996).

During last decades several studies on disorder have been carried out in different liquid crystal phases (LC) (Oxford University, 1996), which are typical soft matter representatives. These phases owe their softness to continuous symmetry breaking phase transitions via which these phases are reached on lowering the symmetry. In these systems disorder has been typically introduced either by confining soft materials to various porous matrices (e.g., aerogels (Bellini, Clark, & Muzny, 1992), Russian glasses (Aliev & Breganov, 1989), Vycor glass (Jin & Finotello, 2001), Control Pore Glasses (Kralj, et al., 2007) or by mixing them with different particles (Bellini, Radzihovsky, Toner, & Clark, 2001) (Hourri, Bose, & Thoen, 2001) of nm (nanoparticles) or micrometer (colloids) dimensions. It has been shown that the impact of disorder could be dominant in some measured quantities. In particular the validity of Imry-Ma theorem in LC-aerosil mixtures was proven (Bellini, Buscaglia, & Chiccoli, 2000).

In our contribution we show that binary mixtures of LC and rod-like nanoparticles (NPs) could also exhibit random field-type behavior if concentration  $p$  of NPs is in adequate regime. Consequently, such systems could be potentially exploited as memory devices. The plan of the contribution is as follows. In Sec. II we present the semi-microscopic model used

to study structural properties of LCs perturbed by NPs. We express the interaction potential, simulation method and measured quantities. In Sec. III the results of our simulations are presented. We calculate percolation characteristics of systems of our interest. Then we first study examples where LC is perturbed by quenched random field-type interactions. We analyze behavior i) in the absence of an external ordering field  $B$ , ii) in presence of  $B$ , and iii)  $B$  induced memory effects. Afterwards we demonstrate conditions for which LC-NP mixtures effectively behave like a random field-type system.

## 2. Model

### 2.1 Interaction potential

We consider a bicomponent mixture of liquid crystals (LCs) and anisotropic nanoparticles (NPs). A lattice-spin type model (Lebwohl & Lasher, 1972) (Romano, 2002) (Bradač, Kralj, Svetec, & Zumer, 2003) is used where the lattice points form a three dimensional cubic lattice with the lattice constant  $a_0$ . The number of sites equals  $N^3$ , where we typically set  $N = 80$ . The NPs are randomly distributed within the lattice with probability  $p$  (For  $p = 1$  all the sites are occupied by NPs).

Local orientation of a LC molecule or a nanoparticle at a site  $\vec{r}_i$  is given by unit vectors  $\vec{s}_i$  and  $\vec{m}_i$ , respectively. We henceforth refer to these quantities as nematic and NP spins. We take into account the head-to-tail invariance of LC molecules (De Gennes & Prost, 1993), i.e., the states  $\pm \vec{s}_i$  are equivalent. It is tempting to identify the quantity  $\vec{s}_i$  with the local nematic director which appears in continuum theories. We allow NPs to be ferromagnetic or ferroelectric. In these cases  $\vec{m}_i$  points along the corresponding dipole orientation. Also other sources of NP anisotropy are encompassed within the model. For example,  $\vec{m}_i$  might simulate a local topological dipole consisting of pair defect-antidefect.

The interaction energy  $W$  of the system is given by (Lebwohl & Lasher, 1972) (Romano, 2002) (Bradač, Kralj, Svetec, & Zumer, 2003)

$$W = - \sum_{ij} J_{ij}^{(LC)} (\vec{s}_i \cdot \vec{s}_j)^2 - \sum_{ij} J_{ij}^{(NP)} \vec{m}_i \cdot \vec{m}_j - \sum_{ij} w_{ij} (\vec{s}_i \cdot \vec{m}_j)^2 - \sum_i \chi_B B^2 (\vec{s}_i \cdot \vec{e}_B)^2 - \sum_i B \vec{m}_i \cdot \vec{e}_B \quad (1)$$

The constants  $J_{ij}^{(LC)}$ ,  $J_{ij}^{(NP)}$ , and  $w_{ij}$  describe pairwise coupling strengths LC-LC, NP-NP, and LC-NP, respectively. The last two terms take into account a presence of *homogeneous* external electric or magnetic field  $\vec{B} = B \vec{e}_B$ , where  $\vec{e}_B$  is a unit vector; the  $B^2$  term acts on nematic spins while linear  $B$  term acts on magnetic spins.

Only first neighbor interactions are considered. Therefore  $J_{ij}^{(LC)}$ ,  $J_{ij}^{(NP)}$ , and  $w_{ij}$  are different from zero only if  $i$  and  $j$  denote neighbouring molecules. The Lebwohl Lasher-type term describes interaction among LC molecules, where  $J_{ij}^{(LC)} = J > 0$ . Therefore, a pair of LC molecules tend to orient either parallel or antiparallel. The coupling between neighboring NPs is determined with  $J_{ij}^{(NP)} = J_{NP} > 0$  which enforces parallel orientation. On the contrary, neighboring LC-NP pairs tend to be aligned perpendicularly by the interaction strength  $w_{ij} = w < 0$ .

We also consider the case when the anisotropic particles act as a *random* field. For this purpose we use the interaction potential (Bellini, Buscaglia, & Chiccoli, 2000) (Romano, 2002).

$$W^{(RAN)} = -\sum_{ij} J_{ij}^{(LC)} (\bar{s}_i \cdot \bar{s}_j)^2 - \sum_i w_i (\bar{s}_i \cdot \bar{e}_i)^2 - \sum_i B^2 (\bar{s}_i \cdot \bar{e}_B)^2 \quad (2)$$

The first LC-LC ordering term is already described above. In the second term the quantity  $w_i$  plays the role of a local quenched field. LC molecules are occupying all the lattice sites and only a fraction  $p$  of them experiences the quenched random field. These "occupied" sites are chosen randomly. In the cases  $w_i = w > 0$  or  $w < 0$  the random field tends to align LC molecules along  $\bar{e}_i$  or perpendicular to it, respectively. The direction of the unit vector  $\bar{e}_i$  is chosen randomly and is distributed uniformly on the surface of a sphere.

In all subsequent work, distances are scaled with respect to  $a_0$  and interaction energies are measured with respect to  $J$  (i.e.,  $J = 1$ ).

## 2.2 Simulation method

Each site is enumerated with three indices:  $p, q, r$ , where  $1 \leq p \leq N$ ,  $1 \leq q \leq N$ ,  $1 \leq r \leq N$ .

The equilibrium director configuration is obtained by minimizing the total interaction energy with respect to all the directors by taking into account the normalization condition

$|\bar{n}_{pqr}|^2 = 1$ . The resulting potential to be minimized reads  $W^* = \sum_{pqr} W_{pqr}^*$ , where

$$W_{pqr}^* = \lambda_{pqr} (|\bar{n}_{pqr}|^2 - 1) + W_{pqr}, \quad (3)$$

and  $\lambda_{pqr}$  are Lagrange multipliers. We minimize the potential  $W^*$  and obtain the following set of  $N^3$  equations which are solved numerically. We give here the corresponding equations just for the free energy given in Eq. (2).

$$\sum_{p'q'r'} \bar{g}(\bar{n}_{pqr}, \bar{n}_{p'q'r'}) + w_{pqr} \bar{g}(\bar{n}_{pqr}, \bar{e}_{pqr}) + B^2 \bar{g}(\bar{n}_{pqr}, \bar{e}_B) = 0, \quad (4)$$

where the vector function  $\bar{g}$  is defined as

$$\bar{g}(\bar{v}_1, \bar{v}_2) = (\bar{v}_1 \cdot \bar{v}_2) [\bar{v}_2 - (\bar{v}_1 \cdot \bar{v}_2) \bar{v}_1]. \quad (5)$$

The system of Eq. (4) is solved by relaxation method which has been proved fast and reliable. We used periodic boundary conditions for spins at the cell boundaries, for instance, the "right" neighbor of the spin with indices  $(N, q, r)$  is the spin with indices  $(1, q, r)$ , and similarly in other boundaries.

## 2.3 Calculated parameters

In simulations we either originate from randomly distributed orientations of directors, or from homogeneously aligned samples along a symmetry breaking direction. In the latter case the directors are initially homogeneously aligned along  $\bar{e}_x$ . We henceforth refer to these cases as the i) *random* and ii) *homogeneous* case, respectively. The i) *random* case can be experimentally realized by quenching the system from the isotropic phase to the ordered phase without an external field (i.e.,  $B = 0$ ). This can be achieved either via a sudden

decrease of temperature or sudden increase of pressure. ii) The *homogeneous* case can be realized by applying first a strong homogeneous external field  $\vec{B}$  along a symmetry breaking direction. After a complete alignment is achieved the field is switched off.

In order to diminish the influence of statistical variations we carry out several simulations (typically  $N_{\text{rep}} \sim 10$ ) for a given set of parameters (i.e.,  $w$ ,  $p$  and  $a$  chosen initial condition).

From obtained configurations of directors we calculate the orientational correlation function  $G(r)$ . It measures orientational correlation of directors as a function of their mutual separation  $r$ . We define it as (Cvetko, Ambrozic, & Kralj, 2009)

$$G(r) = \frac{1}{2} \left\langle 3 \left( \vec{s}_i \cdot \vec{s}_j \right)^2 - 1 \right\rangle \quad (6)$$

The brackets  $\langle \dots \rangle$  denote the average over all lattice sites that are separated for a distance  $r$ . If the directors are completely correlated (i.e. homogeneously aligned along a symmetry breaking direction) it follows  $G(r) = 1$ . On the other hand  $G(r) = 0$  reflects completely uncorrelated directors. Since each director is parallel with itself, it holds  $G(0) = 1$ . The correlation function is a decreasing function of the distance  $r$ . We performed several tests to verify the isotropic character of  $G(r)$ , i.e.  $G(\vec{r}) = G(r)$ .

In order to obtain structural details from a calculated  $G(r)$  dependence we fit it with the ansatz (Cvetko, Ambrozic, & Kralj, 2009)

$$G(r) = (1 - s) e^{-(r/\xi)^m} + s \quad (7)$$

where the  $\xi$ ,  $m$ , and  $s$  are adjustable parameters. In simulations distances are scaled with respect to  $a_0$  (the nearest neighbour distance). The quantity  $\xi$  estimates the average domain length (the coherence length) of the system. Over this length the nematic spins are relatively well correlated. The distribution width of  $\xi$  values is measured by  $m$ . Dominance of a single coherence length in the system is signalled by  $m = 1$ . A magnitude and system size dependence of  $s$  reveals the degree of ordering within the system. The case  $s = 0$  indicates the short range order (SRO). A finite value of  $s$  reveals either the long range order (LRO) or quasi long range order (QLRO). To distinguish between these two cases a finite size analysis  $s(N)$  must be carried out. If  $s(N)$  saturates at a finite value the system exhibits LRO. If  $s(N)$  dependence exhibits algebraic dependence on  $N$  the system possesses QLRO (Cvetko, Ambrozic, & Kralj, 2009).

Note that the external ordering field ( $B$ ) and NPs could introduce additional characteristic scales into the system. The relative strength of elastic and external ordering field contribution is measured by the external field extrapolation length (De Gennes & Prost, 1993)  $\xi_B \sim \sqrt{J}/B$ . In the case of ordered LC-substrate interfaces the relative importance of surface anchoring term is measured by the surface extrapolation length (De Gennes & Prost, 1993)  $d_e \sim J/w$ . The external ordering field is expected to override the surface anchoring tendency in the limit  $d_e/\xi_B \gg 1$ . However, if LC-substrate interfaces introduce a disorder into the system, then instead of  $d_e$  the so called Imry-Ma scale  $\xi_{IM}$  characterizes the ordering of the system. It expresses the relative importance of the elastic ordering and local surface term. It roughly holds (Imri & Ma, 1975):

$$\xi_{IM} \propto w_{dis}^{\frac{2}{d-4}} \quad (8)$$

where  $w_{dis} \propto w$  measures the disorder strength. Parameter  $d$  in the exponent of Eq. (8) denotes the dimensionality of physical system: in our case  $d = 3$ , thus  $\xi_{IM} \propto w_{dis}^{-2}$ .

### 3. Results

#### 3.1 Percolation

One expects that systems might show qualitatively different behaviour above and below the percolation threshold  $p = p_c$  of *impurities*. For this reason we first analyze the percolation behaviour of 3D systems for typical cell dimensions implemented in our simulations.

On increasing the concentration  $p$  of *impurities* a percolation threshold is reached at  $p = p_c$ . This is well manifested in the  $P(p)$  dependence shown in Fig. 1, where  $P$  stands for the probability that there exists a connected path of *impurity* sites between the bottom and upper (or left and right) side of the simulation cell. In the thermodynamic limit  $N \rightarrow \infty$  the  $P(p)$  dependence displays a phase transition type of behaviour, where  $P$  plays the role of order parameter, i.e.,  $P(p > p_c) = 1$  and  $P(p < p_c) = 0$ . For a finite simulation cell a pretransitional tail appears below  $p_c$ , and at  $p \sim 0.30$  the  $P(p)$  steepness decreases with decreasing  $N$ . In simulations we use large enough values of  $N$ , so that finite size effects are negligible.

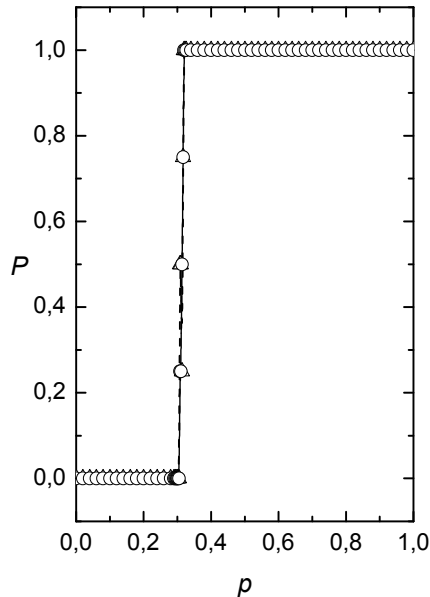


Fig. 1. The percolation probability  $P$  as a function of  $p$  and system size  $N^3$ . For a finite value of  $N$  the percolation threshold ( $p = p_c$ ) is defined as the point where  $P = 0.5$ . We obtain  $p_c \sim 0.3$  roughly irrespective of the system size. ( $\Delta$ )  $N = 60$ ; ( $\circ$ )  $N = 80$ .

### 3.2 Structural properties in absence of external fields

We first consider the case where LC is perturbed by random field. Therefore LC configurations are solved by minimizing potential given by Eq. (2).

In Fig. 2 we plot typical correlation functions for the *random* and *homogeneous* initial conditions. One sees that in the *random* case correlations vanish for  $r \gg \xi$  (i.e.,  $s = 0$ ) which is characteristic for SRO. On the contrary  $G(r)$  dependencies obtained from *homogeneous* initial condition yield  $s > 0$ .

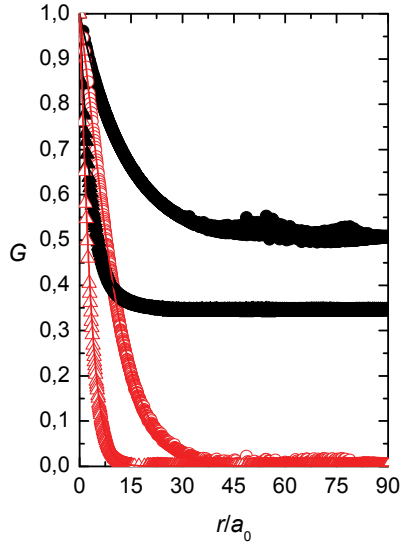


Fig. 2.  $G(r)$  for  $p > p_c$  and  $p < p_c$  for the *homogeneous* and *random* case,  $B = 0$ ,  $w = 3$ ,  $p_c \sim 0.3$ ,  $N = 80$ . ( $\bullet$ )  $p = 0.2$ , *homogeneous*; ( $\blacktriangle$ )  $p = 0.7$ , *homogeneous*; ( $\circ$ )  $p = 0.2$ , *random*; ( $\triangle$ )  $p = 0.7$ , *random*.

More structural details as  $p$  is varied for a relatively weak anchoring ( $w = 3$ ) are given in Fig. 3. By fitting simulation results with Eq. (7) we obtained  $\xi(p)$ ,  $m(p)$  and  $s(p)$  dependences that are shown in Fig. 3. One of the key results is that values of  $\xi$  strongly depend on the history of systems for a weak enough anchoring strength  $w$ . A typical domain size is larger if one originates from the *homogeneous* initial configuration. We obtained a scaling relation between  $\xi$  and  $p$ , which is again history dependent. We obtain  $\xi \propto p^{-0.92 \pm 0.03}$  for the *homogeneous* case and  $\xi \propto p^{-0.95 \pm 0.02}$  for the *random* case.

Information on distribution of domain coherence lengths about their mean value  $\xi$  is given in Fig. 3b where we plot  $m(p)$ . For the *homogeneous* case we obtain  $m \sim 0.95$ , and for the *random* case  $m \sim 1.17$ . A larger value of  $m$  for the *random* case signals broader distribution of domain coherence length values in comparison with the *homogeneous* case. Our simulations do not reveal any systematic changes in  $m$  as  $p$  is varied. Note that values of  $m$  are strongly scattered because structural details of  $G(r)$  are relatively weakly  $m$ -dependent.

In Fig. 3c we plot  $s(p)$ . In the *random* case we obtain  $s = 0$  for any  $p$ . Therefore, if one starts from isotropically distributed orientations of  $\vec{s}_i$ , then final configurations exhibit SRO. In

the *homogeneous* case  $s$  gradually decreases with  $p$ , but remains finite for the chosen anchoring strength ( $w = 3$ ).

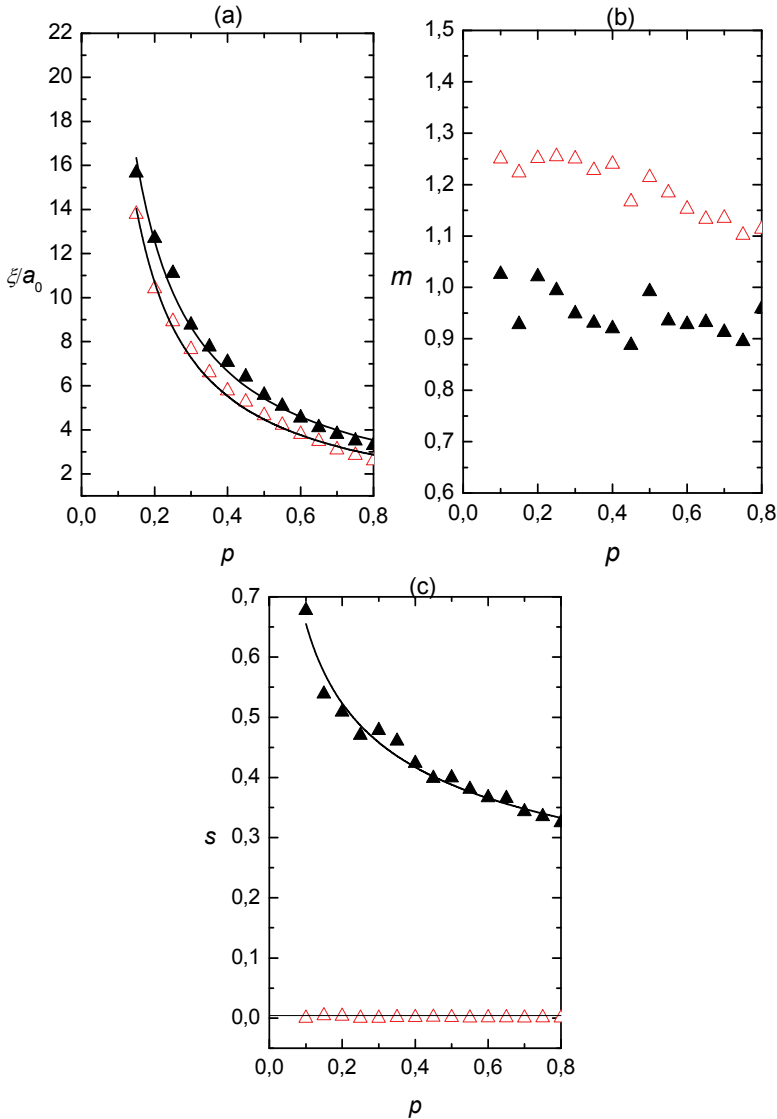


Fig. 3. Structural characteristics as  $p$  is varied for  $B = 0$  and  $w = 3$ . a)  $\xi(p)$ , b)  $m(p)$ , c)  $s(p)$ . ( $\blacktriangle$ ) *homogeneous*, ( $\triangle$ ) *random*. Lines denote the fits to power law.

For two concentrations we carried out finite size analysis, which is shown in Fig. 4. One sees that  $s(N)$  dependencies saturate at a finite value of  $s$ , which is a signature of long-range order. We carry out simulations up to values  $N = 140$ .

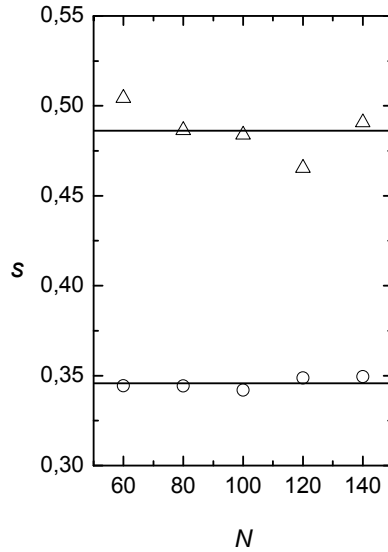


Fig. 4. Finite size analysis  $s(N)$  for  $p < p_c$  and  $p > p_c$  for the *homogeneous* case;  $B = 0$ ,  $w = 3$ , ( $\Delta$ )  $p = 0.2$ ; ( $\circ$ )  $p = 0.7$ . Lines denote average values of  $s$ .

We now examine the  $\xi(w)$  dependence. The Imry-Ma (Imry & Ma, 1975) theorem makes a specific prediction that this obeys the universal scaling law in Eq. (8):  $\xi \propto w^{-2}$  holds for  $d = 3$ . We have analyzed results for  $p = 0.3$ ,  $p = 0.5$ , and  $p = 0.7$ , using both random and homogeneous initial configurations and we fitted results with

$$\xi = \xi_0 w^{-\gamma} + \xi_\infty \quad (9)$$

We expect that even in the strong anchoring limit, the finite size of the simulation cells will induce a non-zero coherence length. The fit with Eq. (9) shows Imry-Ma behavior at low  $w$  only for cases where we originate from *random* initial configurations. The fitting parameters for some calculations are summarized in Table 1.

Initial condition	P	$\gamma$	$\xi_0$	$\xi_\infty$
r ( <i>random</i> )	0.3	2.11±0.33	62±17	1.38±0.57
r ( <i>random</i> )	0.5	1.97±0.19	37±4	0.35±0.32
r ( <i>random</i> )	0.7	2.20±0.32	36±7	0.00±0.36
h ( <i>homogeneous</i> )	0.3	3.29±0.23	297±60	0.90±0.28
h ( <i>homogeneous</i> )	0.5	3.29±0.13	159±14	0.80±0.15
h ( <i>homogeneous</i> )	0.7	3.15±0.26	99±18	0.50±0.22

Table 1. Values of fitting parameters defined by Eq. (9) for representative simulation runs.

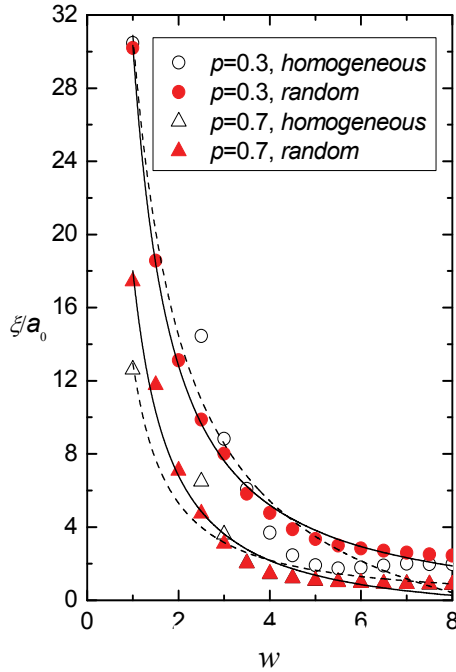


Fig. 5.  $\xi(w)$  variations for different initial configurations for  $N = 80$ . Imry-Ma theorem is obeyed only for the *random* initial configuration.

### 3.3 External field effect

We next include external field  $B$  and still consider system described by interactional potential given by Eq. (2). A typical  $G(r)$  dependence is shown in Fig. 6 where we see the impact of  $B$ . We plot  $G(r)$  for both *homogeneous* and *random* initial configuration in the presence of external field and without it. For  $B = 0$  it holds  $\xi^{(\text{hom})} > \xi^{(\text{ran})}$ , where superscripts (hom) and (ran) denote correlation lengths in samples with *homogeneous* and *random initial* configurations, respectively. The reasons behind this are stronger elastic frustrations in the latter case (denotation *random samples*). Furthermore,  $\xi^{(\text{ran})}$  roughly obeys the Imry-Ma scaling for low enough external fields (i.e.  $\xi^{(\text{ran})} < \xi_B$  where  $\xi_B \sim \sqrt{J}/B$ ), suggesting  $\xi^{(\text{ran})} \sim \xi_{IM}$ . The presence of  $B$  becomes apparent when  $\xi_B < \xi_{IM}$ , which is shown in Fig. 6.

In Fig. 6 we see that the presence of external field can enforce a finite value of  $s$  also in *random samples*.

In Fig. 7 we plot  $\xi$  as a function of  $1/B$  for both *homogeneous* and *random samples*. For strong enough magnetic fields one expects  $\xi \sim \xi_B \propto 1/B$ . On the other hand for a weak enough  $B$  the value of  $\xi$  is dominantly influenced by the disorder strength. Indeed, we observe a crossover behavior in  $\xi(B)$  dependence on varying  $B$ . The crossover between two qualitatively different regimes roughly takes place at the crossover field  $B_c$ . We define it as the field below which the difference between  $\xi^{(\text{ran})}$  and  $\xi^{(\text{hom})}$  is apparent. Below  $B_c$  the

*disordered regime* takes place, where  $\xi$  exhibits weak dependence on  $B$ , i.e.  $\xi \sim \xi_{IM}$ . Above  $B_c$  the *ordered regime* exists, where  $\xi \sim \xi_B \propto 1/B$ . Therefore, for  $B > B_c$  it holds  $\xi^{(ran)} \sim \xi^{(hom)} \sim \xi_B$  and in the *random regime* one observes  $\xi^{(hom)} > \xi^{(ran)} \sim \xi_{IM}$ .

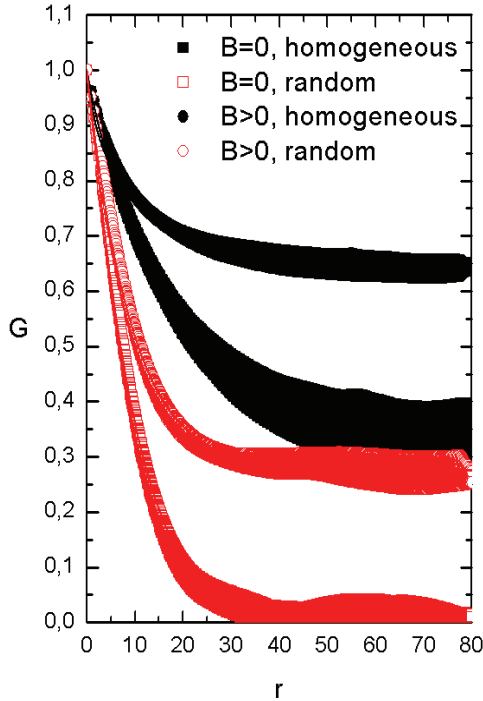


Fig. 6. The orientational correlation function as a function of separation  $r$  between LC molecules. In *random samples*  $G(r)$  vanishes for large enough values of  $r$  for  $B = 0$  while in *homogeneous samples* it could saturate at a finite plateau (if  $p$  or  $w$  are low enough). For  $B > 0$  a finite plateau can be observed also in *random samples*. Parameters:  $p = 0.3$ ,  $w = 2.5$ .

The corresponding  $s(B)$  dependence is shown in Fig. 8. As expected  $s$  monotonously increases on increasing  $B$ , because the external field tends to increase the degree of ordering. Note that in *random samples*  $s(B = 0) = 0$  and the presence of  $B$  gives rise to  $s > 0$ .

In Fig. 9 we show  $m(B)$  dependence. For weak enough fields ( $B < B_c$ ) one typically observes  $m^{(ran)} > m^{(hom)} \approx 1$ . Therefore, in *random samples* we have larger dispersion of  $\xi$  values than in *homogeneous samples*. With the increasing external field both  $m^{(ran)}$  and  $m^{(hom)}$  asymptotically approach the value  $m = 1$ . In the latter case the distribution of  $\xi$  values is sharply centered at  $\xi \sim \xi_B$ .

The crossover field  $B_c$  as a function of  $p$  is shown in Fig. 10. Indicated lines roughly separate ergodic ( $B > B_c$ ) and nonergodic regimes ( $B < B_c$ ). With increasing  $p$  one the degree of frustration within the system increases. Consequently larger values of  $B$  are needed to erase disorders induced memory effects.

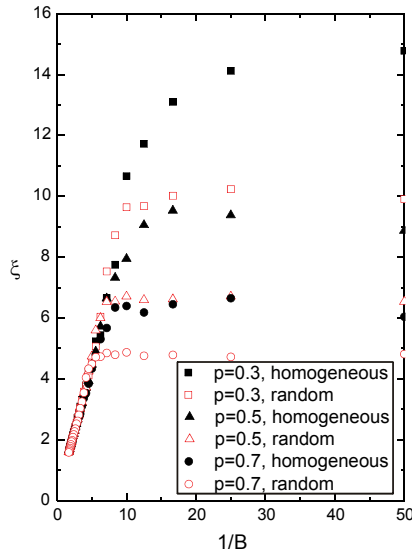


Fig. 7. Correlation length  $\xi$  as a function of  $1/B$  for *homogeneous* and *random* samples for three different concentrations of impurities. The  $\xi(B)$  dependence displays a crossover between the *disordered* and *ordered regime*. The *disordered regimes* extends at  $(B > B_c)$ , where  $\xi^{(hom)} > \xi^{(ran)}$ . In the *ordered regime*  $(B < B_c)$  one observes  $\xi^{(ran)} \sim \xi^{(hom)} \sim \xi_B$ . Parameters:  $w = 2.5, N = 100$ .

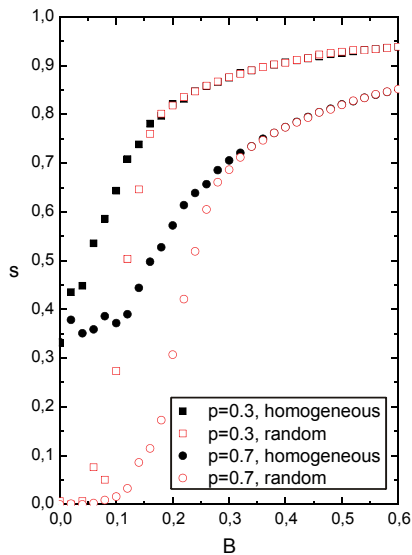


Fig. 8. The  $s(B)$  dependence for *homogeneous* and *random* samples for two different  $p$ . For  $s(B = 0)$  we obtain  $s^{(ran)} = 0$ . In the *disordered regime* it holds  $s^{(hom)} > s^{(ran)}$  and  $s^{(hom)} \sim s^{(ran)}$  in the *ordered regime*. Parameters:  $w = 2.5, N = 100$ .

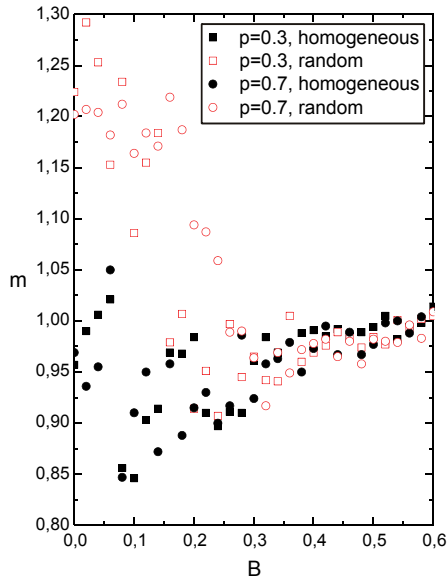


Fig. 9. The  $m(B)$  dependence for *homogeneous* and *random samples* for two different  $p$ . In the *disordered regime* it holds  $m^{(\text{ran})} > m^{(\text{hom})} \approx 1$ . In the *ordered regime* we obtain  $m^{(\text{ran})} \sim m^{(\text{hom})}$  which asymptotically approach one on increasing  $B$ . Parameters:  $w = 2.5$ ,  $N = 100$ .

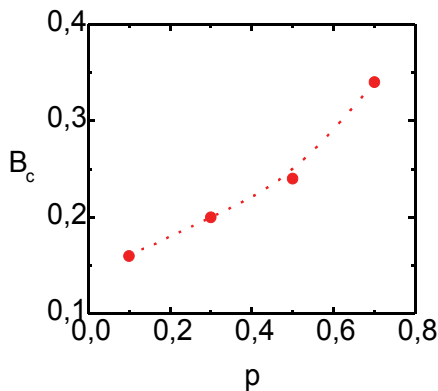


Fig. 10. The crossover field  $B_c$  on varying  $p$ . Indicated dotted curve roughly separates ergodic ( $B > B_c$ ) and nonergodic regimes ( $B < B_c$ ). With increasing  $p$  one the degree of frustration within the system increases. Consequently larger values of  $B$  are needed to erase disorders induced memory effects. The points are calculated and the dotted line serves as a guide for the eye. Parameters:  $w = 2.5$ ,  $N = 100$ .

### 3.4 Memory effects

We further analyze how one could manipulate the domain-type ordering with external magnetic or electric ordering field. For this purpose we originate from the *random* initial configuration. We then apply an external field of strength  $B$  and calculate configuration for different concentrations of *impurities*. Then we switch off the field and calculate again the configuration, to which we henceforth refer as the *switch-off configuration*. The corresponding calculated  $s$  and  $\xi$  behaviour is shown in Fig. 11 and Fig. 12. Dashed lines mark values of observables in the presence of field of strength  $B$ , while full lines mark values after the field was switched off. From Fig. 11 we see that the presence of external field develops QLRO or LRO (we have not carried time consuming finite size analysis to distinguish between the two cases). This range of ordering remained as the field was switched off, although the correlation strength is reduced. Note that above the threshold field strength the degree of ordering in the *switch-off configuration* is saturated, i.e., becomes independent of  $B$ .

The corresponding changes in  $\xi$  are shown in Fig. 12. With increasing  $B$  the  $\xi$  values for samples with different  $p$  decrease and converge to the same value, which is equal to the external field coherence length. In the *switched-off configuration* the average domain coherence length increases and again for a large enough value of  $B$  saturates at a fixed value.

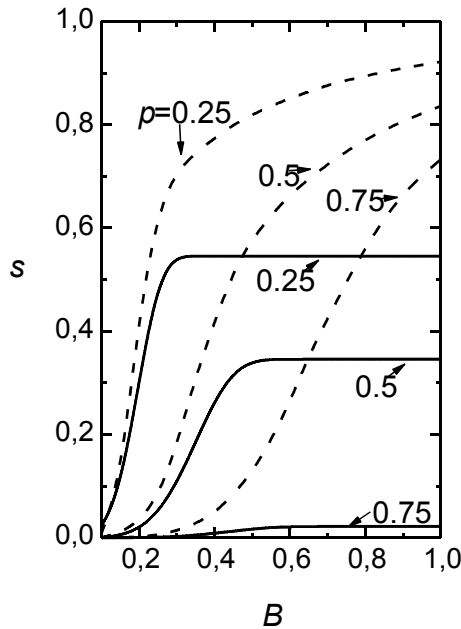


Fig. 11.  $s(B)$  for  $w = 4$ ,  $N = 60$ ; *random* case. Dashed curves: configurations are calculated in the presence of external field  $B$ . Full curves: configurations are calculated after the field was switched off.

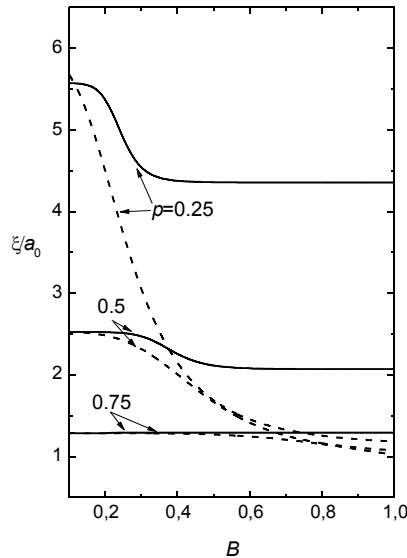


Fig. 12.  $\xi(B)$  for  $w = 4$ ,  $N = 60$ ; *random* case. Dashed curves: configurations are calculated in the presence of external field  $B$ . Full curves: configurations are calculated after the field was switched off.

#### 4. Mixtures

We next consider a mixture of LCs and NPs. The presence of NPs enforces to LC a certain amount of disorder. Our expectation is that if one quenches the system from the isotropic phase the established domain pattern could be stabilized by NPs. In the following we show that there indeed exists a regime where a binary mixture behaves like LC system perturbed by a random field-type perturbation.

We calculate the LC correlation by minimizing Eq. (1). In simulations mixtures are quenched from the isotropic phase. The LC correlation function is calculated from Eq. (6) from which we extract  $\xi$  and  $s$  by using Eq. (7). Typical results are shown in Fig. 13 where we plot  $\xi(p)$  and  $s(p)$ . A strong presence of disorder is observed for concentrations roughly between  $p = 0.1$  till percolation threshold. This is indicated by  $s(p) \sim 0$ , which signals presence of short range order. For  $p > p_c$  the  $s(p)$  becomes again apparently larger than zero.

#### 5. Conclusions

We study structural properties of nematic LC phase which is perturbed by presence of anisotropic NPs. Simulations are performed at the semi-microscopic level, where orientational ordering of LCs and NPs is described by vector fields taking into account head-to-tail invariance. Such modeling approximately describes entities exhibiting cylindrical symmetry. We focused on orientational ordering of LC molecules as a function of concentration  $p$  of NPs or random sites, interaction strength  $w$  between LC molecules and perturbing agents and external ordering field strength  $B$ .

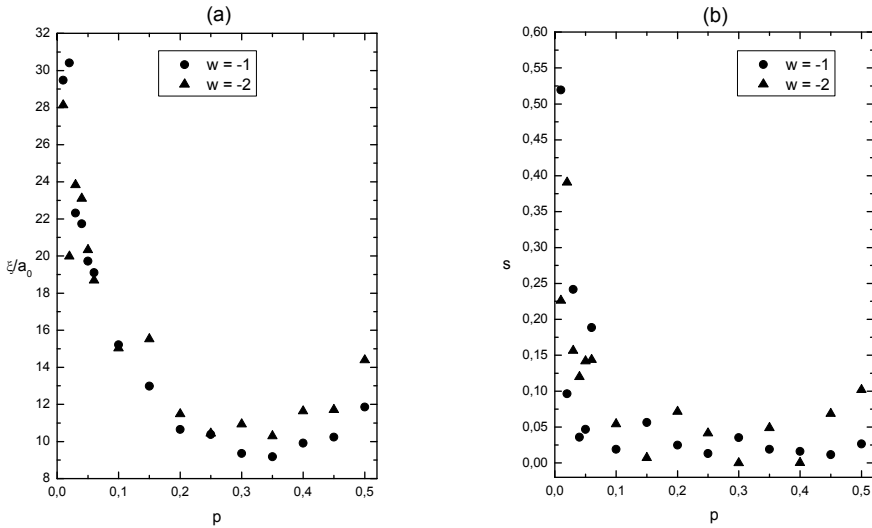


Fig. 13. Structural characteristics for the mixture. One sees that the *random* field regime extends roughly between  $p = p_{RF} \sim 0.1$  and  $p = p_c \sim 0.3$ . a)  $\xi(p)$  and b)  $s(p)$  dependence. The other interaction constants are set to 1.

We determined percolation properties of NPs, which exhibit the percolation threshold  $p_c \sim 0.3$  in three dimensions. Then we first studied cases, where impact of NPs could be mimicked by a random field type interaction. Studies for  $B = 0$  showed that the Imry-Ma type behavior is expected only in the case, where ensembles were quenched from the isotropic phase. In this case a short range ordering is realized. Studies in presence of an external ordering field  $B$  followed. We estimated boundaries separating ergodic and nonergodic regimes. We explored memory effects by exposing LCs to different strengths of  $B$  and then switching it off. We determined regimes where memory effects are apparent and are roughly proportional to values of  $B$ . Finally we demonstrated under which conditions structural behavior in mixtures of NPs and LCs could be mimicked by random-field type models. The findings of our investigations might be useful in order to design soft matter based memory devices in mixtures of LCs and appropriate NPs.

## 6. Acknowledgments

Matej Cvetko acknowledges support of the EU European Social Fund. Operation is performed within the Operative program for development of human resources for the period 2007-2013.

## 7. References

Aliev, F. M., & Breganov, M. N. (1989). Dielectric polarization and dynamics of molecular-motion of polar liquid-crystals in micropores and macropores. *Zhurnal Eksperimentalnoi i Teoreticheskoi Fiziki*, 95(1), 122-138.

- Bellini, T., Buscaglia, M., & Chiccoli, C. (2000). Nematics with quenched disorder: What is left when long range order is disrupted? *Physical Review Letters*, 85(5), 1008-1011.
- Bellini, T., Clark, N. A., & Muzny, C. D. (1992). Phase-behavior of the liquid-crystal 8cb in a silica aerogel. *Physical Review Letters*, 69(5), 788-791.
- Bellini, T., Radzihovsky, L., Toner, J., & Clark, N. A. (2001). Universality and scaling in the disordering of a smectic liquid crystal. *SCIENCE*, 294(5544), 1074-1079.
- Bradač, Z., Kralj, S., Svetec, M., & Zumer, S. (2003). Annihilation of nematic point defects: Postcollision scenarios. *Physical Review E*, 67(5), 050702.
- Cleaver, D. J., Kralj, S., Sluckin, T. J., & Allen, M. P. (1996). *Liquid Crystals in Complex Geometries: Formed by Polymer and Porous Networks*. London: Oxford University Press.
- Cvetko, M., Ambrozic, M., & Kralj, S. (2009). Memory effects in randomly perturbed systems exhibiting continuous symmetry breaking. *Liquid Crystals*, 36(1), 33-41.
- De Gennes, P. G., & Prost, J. (1993). *The Physics of Liquid Crystals*. Oxford: Oxford University Press.
- Hourri, A., Bose, T. K., & Thoen, J. (2001). Effect of silica aerosil dispersions on the dielectric properties of a nematic liquid crystal. *Physical Review E*, 63(5), 051702.
- Imry, Y., & Ma, S. (1975). Random-field instability of ordered state of continuous symmetry. *Physical Review Letters*, 35(21), 1399-1401.
- Jin, T., & Finotello, D. (2001). Aerosil dispersed in a liquid crystal: Magnetic order and random silica disorder. *Physical Review Letters*, 86(5), 818-821.
- Kralj, S., Cordoyiannis, G., Zidansek, A., Lahajnar, G., Amentsch, H., Zumer, S., et al. (2007). Presmectic wetting and supercritical-like phase behavior of octylcyanobiphenyl liquid crystal confined to controlled-pore glass matrices. *Journal of Chemical Physics*, 127(15), 154905.
- Lebwohl, P. A., & Lasher, G. (1972). Nematic-liquid-crystal order - monte-carlo calculation. *Physical Review A*, 6(1), 426.
- Oxford University. (1996). *Liquid Crystals in Complex Geometries Formed by Polymer and Porous Networks*. (S. Zumer, & G. Crawford, Eds.) London: Taylor & Francis.
- Romano, S. (2002). Computer simulation study of a nematogenic lattice-gas model with fourth-rank interactions. *International Journal of Modern Physics*, 16(19), 2901-2915.

# Photorefractive Ferroelectric Liquid Crystals

Takeo Sasaki

*Tokyo University of Science  
Japan*

## 1. Introduction

The photorefractive effect is one of the phenomena that can form hologram images in a material. Currently, 3D displays are expected to be widely used as next generation displays. However, current 3D displays are basically stereograms. Holographic displays that can realize natural 3D images that can be seen by the naked eye are anticipated. The photorefractive effect is a phenomenon wherein a change in the refractive index is induced by a combined mechanism of photovoltaic and electro-optic effects. A transparent material that exhibits both photovoltaic and electro-optic effects can potentially be used as a photorefractive material. The interference of two laser beams in a photorefractive material establishes a refractive index grating (**Figure 1**). When two laser beams interfere in an organic photorefractive material, charge generation occurs at the bright positions of the interference fringes. The generated charges diffuse or drift within the material. Since the mobilities of positive and negative charges are different in most organic materials, a charge separated state is formed. The charge with higher mobility diffuses over a longer distance than the charge with lower mobility, so that while the low mobility charge stays in the bright areas, the high mobility charge moves to the dark areas. The bright and dark positions of the interference fringes are thus charged with opposite polarities, and an internal electric field (space charge field) is generated in the area between the bright and dark positions. The refractive index of this area between the bright and dark positions is changed through the electro-optic effect. Thus, a refractive index grating (or hologram) is formed. One material class that exhibits high photorefractivity is glassy photoconductive polymers doped with high concentrations of D- $\pi$ -A chromophores (in which donor and acceptor groups are attached to a  $\pi$ -conjugate system). In order to obtain photorefractivity in polymer materials, a high electric field of 10–50 V/ $\mu\text{m}$  is usually applied to a polymer film. This electric field is necessary to increase the charge generation efficiency.

The photorefractive effect has been reported in surface-stabilized ferroelectric liquid crystals (SS-FLCs) doped with a photoconductive compound. Liquid crystals are classified into several groups. The most well known are nematic liquid crystals and smectic liquid crystals (**Figure 2**). Nematic liquid crystals are used in LC displays. On the other hand, smectic liquid crystals are very viscous and hence are not utilized in any practical applications. Ferroelectric liquid crystals (FLCs) belong to the class of smectic liquid crystals that have a layered structure. The molecular structure of a typical FLC contains a chiral unit, a carbonyl group, a central core, which is a rigid rod-like structure such as biphenyl, phenylpyrimidine, phenylbenzoate, and a flexible alkyl chain (**Figure 3**).

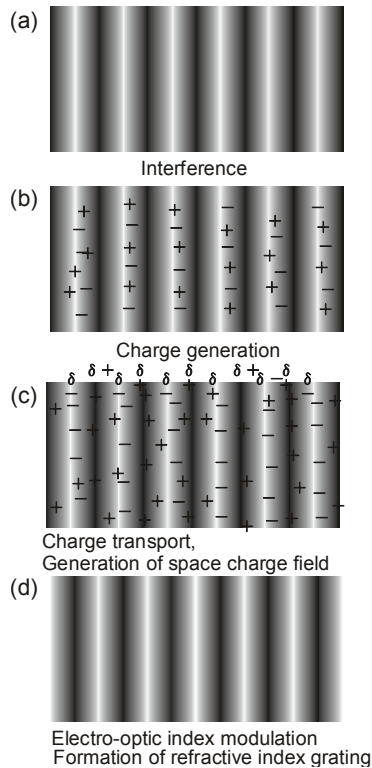


Fig. 1. Schematic illustration of the mechanism of the photorefractive effect. (a) Two laser beams interfere in the photorefractive material; (b) charge generation occurs at the light areas of the interference fringes; (c) electrons are trapped at the trap sites in the light areas, holes migrate by diffusion or drift in the presence of an external electric field and generate an internal electric field between the light and dark positions; (d) the refractive index of the corresponding area is altered by the internal electric field generated.

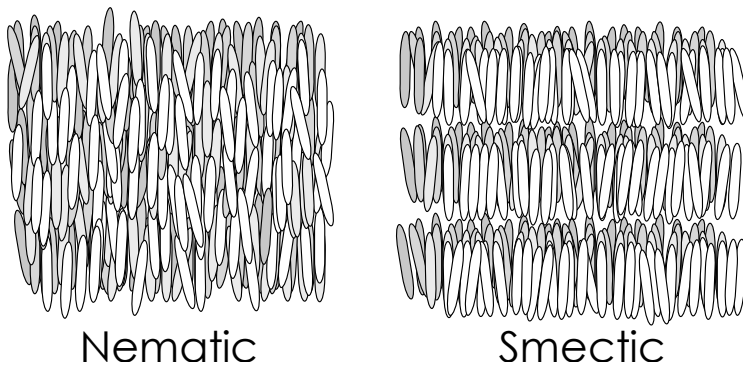


Fig. 2. Structures of the nematic and smectic phase.

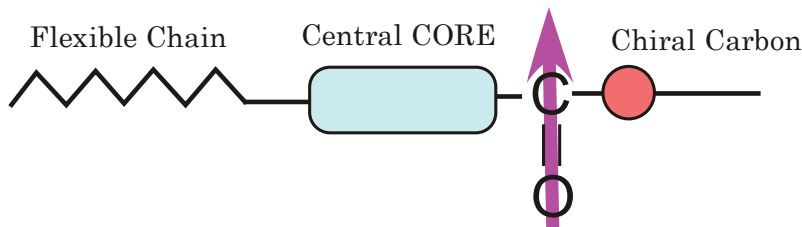
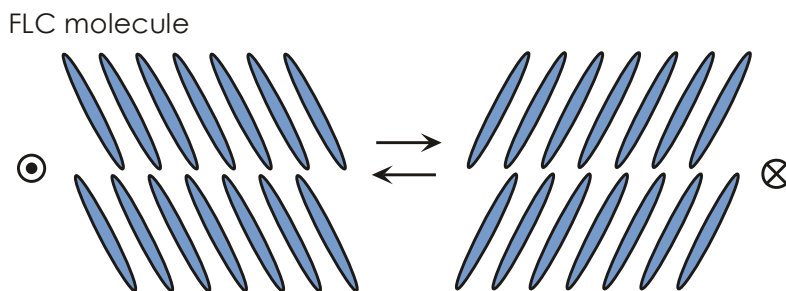


Fig. 3. Molecular structure of ferroelectric liquid crystals.

Thus, the dipole moment of a FLC molecule is perpendicular to the molecular long axis. FLCs exhibit a chiral smectic C phase ( $\text{SmC}^*$ ) that possesses a helical structure. It should be mentioned here that in order to observe ferroelectricity in these materials, the ferroelectric liquid crystals must be formed into thin films. The thickness of the film must be within a few micrometers. When an FLC is sandwiched between glass plates to form a film a few micrometers thick, the helical structure of the smectic C phase uncoils and a surface-stabilized state (SS-state) is formed in which spontaneous polarization ( $P_s$ ) appears (**Figure 4**).



## Electro-optic effect in FLCs

Fig. 4. Electro-optical switching in the surface-stabilized state of FLCs.

For display applications, the thickness of the film is usually  $2\ \mu\text{m}$ . In such thin films, FLC molecules can align only in two directions. This state is called a surface-stabilized state (SS-state). The alignment direction of the FLC molecules changes according to the direction of the spontaneous polarization. The direction of the spontaneous polarization is governed by the photoinduced internal electric field, giving rise to a refractive index grating with properties dependent on the direction of polarization. **Figure 5** shows a schematic illustration of the mechanism of the photorefractive effect in FLCs. When laser beams interfere in a mixture of an FLC and a photoconductive compound, charge separation occurs between bright and dark positions and an internal electric field is produced. The internal electric field alters the direction of spontaneous polarization in the area between the bright and dark positions of the interference fringes, which induces a periodic change in the orientation of the FLC molecules. This is different from the processes that occur in other photorefractive materials in that the molecular dipole rather than the bulk polarization responds to the internal electric field. Since the switching of FLC molecules is due to the response of bulk polarization, the switching is extremely fast.

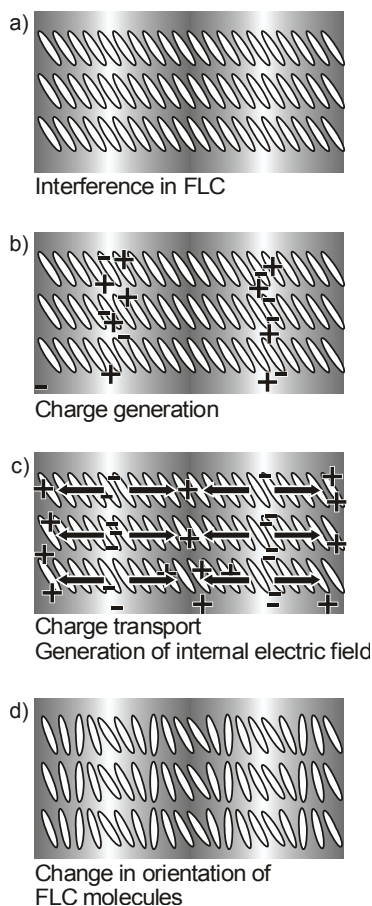


Fig. 5. Schematic illustration of the mechanism of the photorefractive effect in FLCs. (a) Two laser beams interfere in the surface-stabilized state of the FLC/photoconductive compound mixture; (b) charge generation occurs at the bright areas of the interference fringes; (c) electrons are trapped at the trap sites in the bright areas, holes migrate by diffusion or drift in the presence of an external electric field to generate an internal electric field between the bright and dark positions; (d) the orientation of the spontaneous polarization vector (i.e., orientation of mesogens in the FLCs) is altered by the internal electric field.

## 2. Characteristics of the photorefractive effect

Since a change in the refractive index via the photorefractive effect occurs in the areas between the bright and dark positions of the interference fringe, the phase of the resulting index grating is shifted from the interference fringe. This is characteristic of the photorefractive effect that the phase of the refractive index grating is  $\pi/2$ -shifted from the interference fringe. When the material is photochemically active and is not photorefractive, a photochemical reaction takes place at the bright areas, and a refractive index grating with the same phase as that of the interference fringe is formed (**Figure 6(a)**).

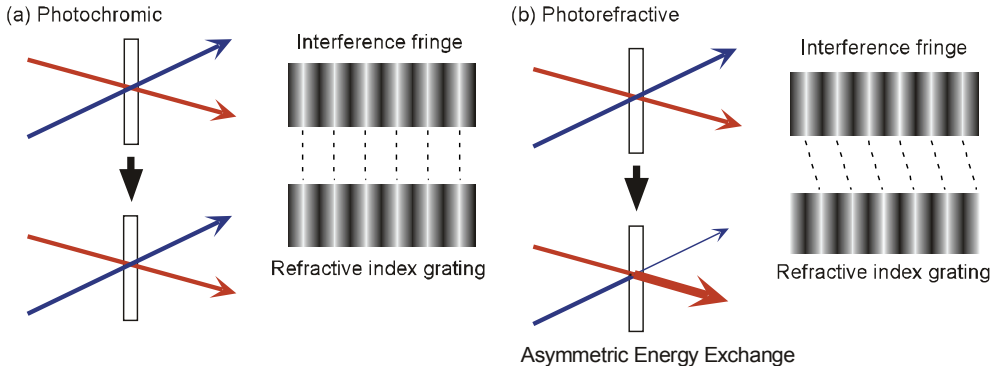


Fig. 6. (a) Photochromic grating, and (b) photorefractive grating.

The interfering laser beams are diffracted by this grating, however, the apparent transmitted intensities of the laser beams do not change because the diffraction is symmetric. Beam 1 is diffracted in the direction of beam 2 and beam 2 is diffracted in the direction of beam 1. However, if the material is photorefractive, the phase of the refractive index grating is shifted from that of the interference fringes, and this affects the propagation of the two beams. Beam 1 is energetically coupled with beam 2 for the two laser beams. Consequently, the apparent transmitted intensity of beam 1 increases and that of beam 2 decreases (Figure 6(b)). This phenomenon is termed asymmetric energy exchange in the two-beam coupling experiment. The photorefractivity of a material is confirmed by the occurrence of this asymmetric energy exchange.

### 3. Measurement of photorefractivity

The photorefractive effect is evaluated by a two-beam coupling method and also by a four-wave mixing experiment. Figure 7 (a) shows a schematic illustration of the experimental setup used for the two-beam coupling method. A p-polarized beam from a laser is divided into two beams by a beam splitter, and the beams are interfered within the sample film.

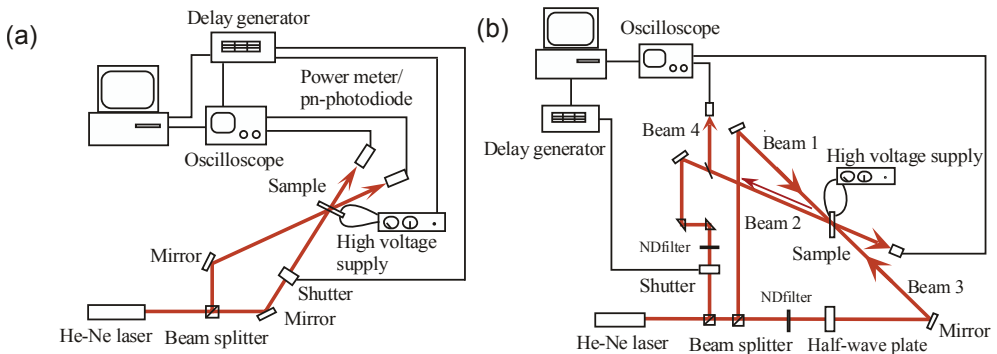


Fig. 7. Schematic illustrations of the experimental set-up for the (a) two-beam coupling, and (b) four-wave-mixing techniques.

An electric field is applied to the sample using a high voltage supply unit. This external electric field is applied in order to increase the efficiency of charge generation in the film. The change in the transmitted beam intensity is monitored. If a material is photorefractive, an asymmetric energy exchange is observed. The magnitude of photorefractivity is evaluated using a parameter called the gain coefficient, which is calculated from the change in the transmitted intensity of the laser beams induced through the two-beam coupling. In order to calculate the two-beam coupling gain coefficient, it must be determined whether the diffraction condition is in the Bragg regime or in the Raman-Nath regime. These diffraction conditions are distinguished by a dimensionless parameter  $Q$ .

$$Q = 2\pi\lambda L / n\Lambda^2 \quad (1)$$

$Q > 1$  is defined as the Bragg regime of optical diffraction. In this regime, multiple scattering is not permitted, and only one order of diffraction is produced. Conversely,  $Q < 1$  is defined as the Raman-Nath regime of optical diffraction. In this regime, many orders of diffraction can be observed. Usually,  $Q > 10$  is required to guarantee that the diffraction is entirely in the Bragg regime. When the diffraction is in the Bragg diffraction regime, the two-beam coupling gain coefficient  $\Gamma$  ( $\text{cm}^{-1}$ ) is calculated according to the following equation:

$$\Gamma = \frac{1}{D} \ln \left( \frac{gm}{1+m-g} \right) \quad (2)$$

where  $D = L / \cos(\theta)$  is the interaction path for the signal beam ( $L$  = sample thickness,  $\theta$  = propagation angle of the signal beam in the sample),  $g$  is the ratio of the intensities of the signal beam behind the sample with and without a pump beam, and  $m$  is the ratio of the beam intensities (pump/signal) in front of the sample.

A schematic illustration of the experimental setup used for the four-wave mixing experiment is shown in **Figure 7 (b)**. S-polarized writing beams are interfered in the sample film and the diffraction of a p-polarized probe beam, counter-propagating to one of the writing beams, is measured. The diffracted beam intensity is typically measured as a function of time, applied (external) electric field, writing beam intensities, etc. The diffraction efficiency is defined as the ratio of the intensity of the diffracted beam and the intensity of the probe beam that is transmitted when no grating is present in the sample due to the writing beams. In probing the grating, it is important that beam 3 does not affect the grating or interact with the writing beams. This can be ensured by making the probe beam much weaker than the writing beams, and by having the probe beam polarized orthogonal to the writing beams.

## 4. Photorefractive effect of FLCs

### 4.1 Two-beam coupling experiments on FLCs

The photorefractive effect in an FLC was first reported by Wasielewsky et al. in 2000. Since then, details of photorefractivity in FLC materials have been further investigated by Sasaki et al. and Golemme et al. The photorefractive effect in a mixture of an FLC and a photoconductive compound was measured in a two-beam coupling experiment using a 488 nm  $\text{Ar}^+$  laser. The structures of the photoconductive compounds used are shown in **Figure 8**. A commercially available FLC, SCE8 (Clariant), was used. CDH was used as a

photoconductive compound, and TNF was used as a sensitizer. The concentrations of CDH and TNF were 2 wt% and 0.1 wt% respectively. The samples were injected into a 10- $\mu\text{m}$ -gap glass cell equipped with 1  $\text{cm}^2$  ITO electrodes and a polyimide alignment layer (**Figure 9**).

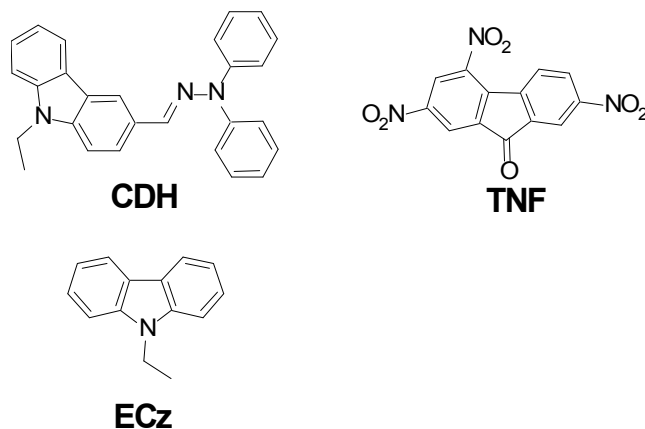


Fig. 8. Structures of the photoconductive compound CDH, ECz and the sensitizer TNF

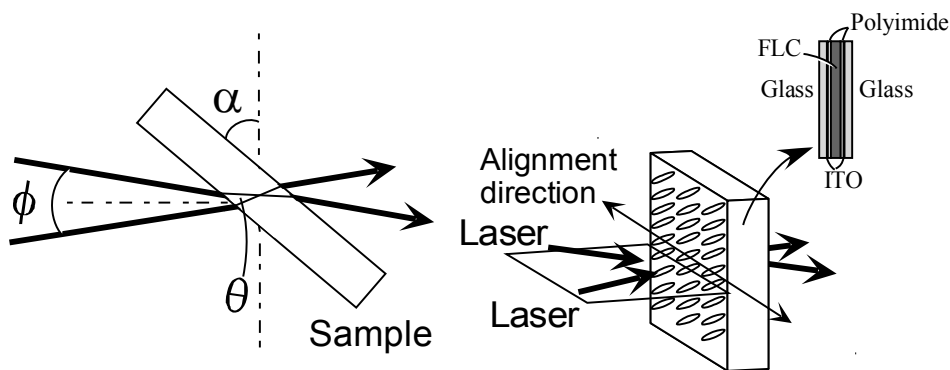


Fig. 9. Laser beam incidence condition and the structure of the LC cell.

**Figure 10** shows a typical example of asymmetric energy exchange observed in the FLC(SCE8)/CDH/TNF sample under an applied DC electric field of 0.1  $\text{V}/\mu\text{m}$ . Interference of the divided beams in the sample resulted in increased transmittance of one beam and decreased transmittance of the other. The change in the transmitted intensities of the two beams is completely symmetric, as can be seen in **Figure 10**. This indicates that the phase of the refractive index grating is shifted from that of the interference fringes. The grating formation was within the Bragg diffraction regime, and no higher order diffraction was observed under the conditions used.

The temperature dependence of the gain coefficient of SCE8 doped with 2 wt% CDH and 0.1 wt% TNF is shown in **Figure 11 (a)**. Asymmetric energy exchange was observed only at temperatures below 46°C. The spontaneous polarization of the identical sample is plotted as a function of temperature in **Figure 11 (b)**.

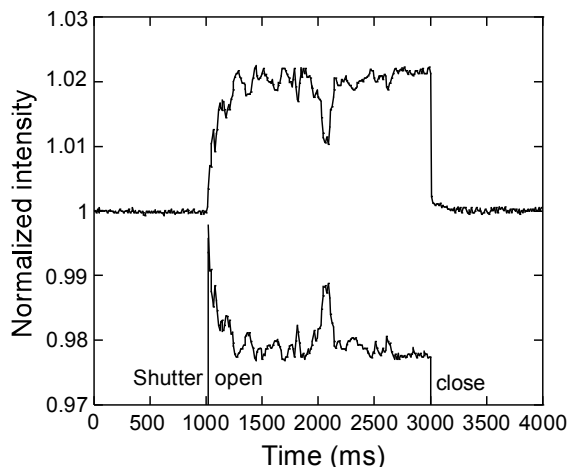


Fig. 10. Typical example of asymmetric energy exchange observed in an FLC (SCE8) mixed with 2 wt% CDH and 0.1 wt% TNF. An electric field of  $+0.3 \text{ V}/\mu\text{m}$  was applied to the sample.

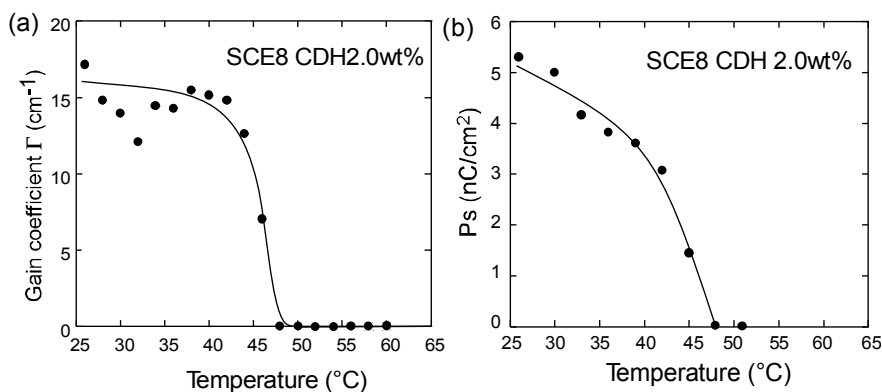


Fig. 11. Temperature dependence of (a) gain coefficient and (b) spontaneous polarization of an FLC (SCE8) mixed with 2 wt% CDH and 0.1 wt% TNF. For two-beam coupling experiments, an electric field of  $0.1 \text{ V}/\mu\text{m}$  was applied to the sample.

Similarly, the spontaneous polarization vanished when the temperature was raised above  $46^\circ\text{C}$ . Thus, asymmetric energy exchange was observed only in the temperature range in which the sample exhibits ferroelectric properties, in other words, the  $\text{SmC}^*$  phase. Since the molecular dipole moment of the FLCs is small and the dipole moment is aligned perpendicular to the molecular axis, large changes in the orientation of the molecular axis cannot be induced by an internal electric field in the  $\text{SmA}$  or  $\text{N}^*$  phase of the FLCs. However, in the  $\text{SmC}^*$  phase, reorientation associated with spontaneous polarization occurs due to the internal electric field. The spontaneous polarization also causes orientation of FLC molecules in the corresponding area to change accordingly. A maximum resolution of  $0.8 \mu\text{m}$  was obtained in this sample.

FLC	Ps at 25 °C (nC/cm <sup>2</sup> )	Phase transition temperature <sup>a</sup> (°C)	Response time $\tau^b$ ( $\mu$ s)	Rotational viscosity $\gamma_\phi$ (mPas)	Tilt angle (deg.)
015/000	9	- SmC* 71 SmA 83 N* 86 I	70	60	24
015/100	33	- SmC* 72 SmA 83 N* 86 I	21	80	23
016/000	-4.3	- SmC* 72 SmA 85 N* 93 I	70	61	25
016/030	-5.9	- SmC* 72 SmA 85 N* 93 I	47	82	25
016/100	-10.5	- SmC* 72 SmA 85 N* 94 I	20	60	27
017/000	9.5	- SmC* 70 SmA 76 N* 87 I	93	47	26
017/100	47	- SmC* 73 SmA 77 N* 87 I	23	116	27
018/000	23	- SmC* 65 SmA 82 N* 88 I	59	68	22
018/100	40	- SmC* 67 SmA 82 N* 89 I	30	97	23
019/000	8.3	- SmC* 60 SmA 76 N* 82 I	262	37	19
019/100	39	- SmC* 64 SmA 78 N* 87 I	53	75	20
SCE8	-4.5	- SmC* 60 SmA 80 N* 104 I	50	76	20
M4851/000	-4.0	- SmC* 64 SmA 69 N* 73 I	40	-	25
M4851/050	-14	- SmC* 65 SmA 70 N* 74 I	22	65	28

<sup>a</sup> C, crystal; SmC\*, chiral smectic C phase; SmA, smectic A phase; N\* chiral nematic phase; I, isotropic phase

<sup>b</sup> Response time to a 10 V/ $\mu$ m electric field at 25 °C in a 2- $\mu$ m cell.

Table 1. Physical properties of the FLCs investigated

## 4.2 Comparison of photorefractive properties of FLCs

The photorefractive properties of a series of FLCs with different properties were investigated. The properties of the FLCs are shown in **Table 1**. Unfortunately, the chemical structures of these FLCs are not exhibited. All the FLCs listed in **Table 1** exhibited finely aligned SS-states when they were not mixed with photoconductive compounds (CDH and TNF). **Figure 12** shows typical examples of the textures observed in the 017/000, M4851/050 and SCE8 FLCs.

As the CDH concentration increased, defects appeared in the texture. The M4851/050 and SCE8 FLCs retained the SS-state with few defects for CDH concentrations below 2 wt%. All the FLCs listed in **Table 1**, except for SCE8 and M4851/050, exhibited distorted SS-states, and light scattering was very strong when mixed with CDH at concentrations higher than 0.5 wt%. The SCE8 and M4851/050 FLCs displayed finely aligned SS-state domains in a 10  $\mu$ m-gap cell and exhibited asymmetric energy exchange. FLCs that formed an SS-state with many defects did not exhibit clear asymmetric energy exchange. In these distorted SS-states, the laser beams are strongly scattered, precluding the formation of a refractive index grating.

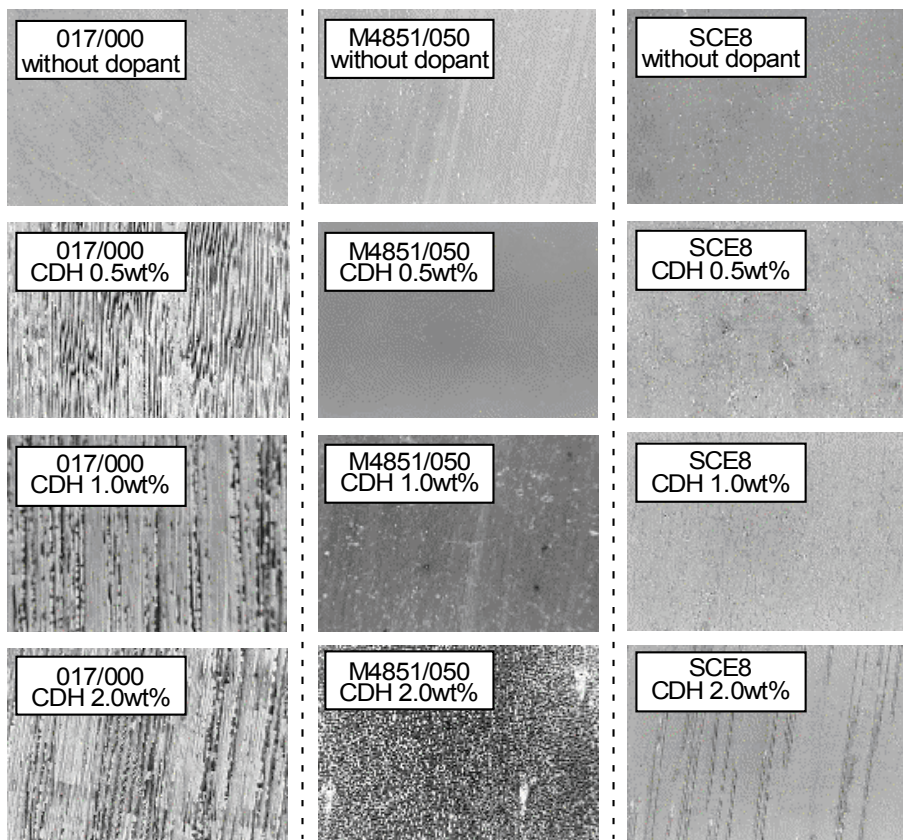


Fig. 12. Textures observed by POM observation of SS-states in FLCs.

#### 4.3 Effect of the magnitude of the applied electric field

In polymeric photorefractive materials, the strength of the externally applied electric field is a very important factor. The external electric field is necessary to increase the charge separation efficiency sufficiently to induce a photorefractive effect. In other words, photorefractivity of the polymer is obtained only with application of a few  $V/\mu m$  electric field.<sup>3-5</sup> The thickness of the polymeric photorefractive material commonly reported is about  $100 \mu m$ , so the voltage necessary to induce the photorefractive effect is a few kV. On the other hand, the photorefractive effect in FLCs can be induced by applying a very weak external electric field. The maximum gain coefficient for the FLC (SCE8) sample was obtained using an electric field strength of only  $0.2-0.4 V/\mu m$ . The thickness of the FLC sample is typically  $10 \mu m$ , so that the voltage necessary to induce the photorefractive effect is only a few V. The dependence of the gain coefficient of a mixture of FLC (SCE8)/CDH/TNF on the strength of the electric field is shown in **Figure 13**. The gain coefficient of SCE8 doped with  $0.5-1 \text{ wt\%}$  CDH increased with the strength of the external electric field. However, the gain coefficient of SCE8 doped with  $2 \text{ wt\%}$  CDH decreased when the external electric field exceeded  $0.4 V/\mu m$ . The same tendency was observed for

M4851/050 as well. The formation of an orientational grating is enhanced when the external electric field is increased from 0 to 0.2 V/ $\mu\text{m}$  as a result of induced charge separation under a higher external electric field. However, when the external electric field exceeded 0.2 V/ $\mu\text{m}$ , a number of zig-zag defects appeared in the surface-stabilized state. These defects cause light scattering and result in a decrease in the gain coefficient.

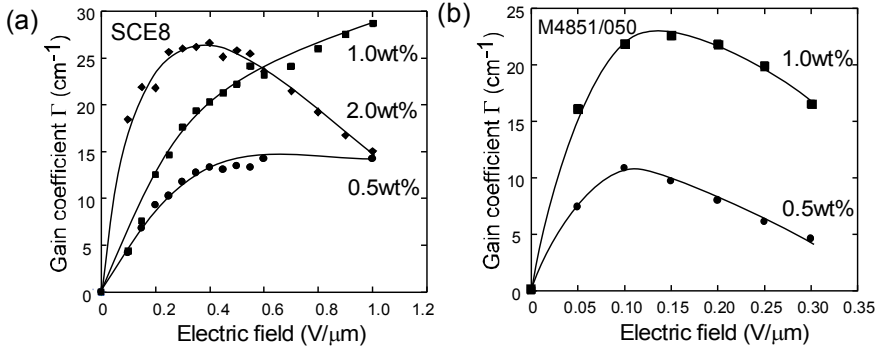


Fig. 13. Electric field dependence of the gain coefficient of SCE8 and M4851/050 mixed with several concentrations of CDH and 0.1 wt% TNF in a 10  $\mu\text{m}$ -gap cell measured at 30  $^{\circ}\text{C}$ .

#### 4.4 Refractive index grating formation time

The formation of a refractive index grating involves charge separation and reorientation. The index grating formation time is affected by these two processes, and both may be rate-determining steps. The refractive index grating formation times in SCE8 and M4851/050 were determined based on the simplest single-carrier model of photorefractivity, wherein the gain transient is exponential. The rising signal of the diffracted beam was fitted using a single exponential function, shown in equation (3).

$$\gamma(t) - 1 = (\gamma - 1)[1 - \exp(-t/\tau)]^2 \quad (3)$$

Here,  $\gamma(t)$  represents the transmitted beam intensity at time  $t$  divided by the initial intensity ( $\gamma(t) = I(t)/I_0$ ) and  $\tau$  is the formation time. The grating formation time in SCE8/CDH/TNF is plotted as a function of the strength of the external electric field in **Figure 14 (a)**. The grating formation time decreased with increasing electric field strength due to the increased efficiency of charge generation. The formation time was shorter at higher temperatures, corresponding to a decrease in the viscosity of the FLC with increasing temperature. The formation time for SCE8 was found to be 20 ms at 30 $^{\circ}\text{C}$ . As shown in **Figure 14 (b)**, the formation time for M4851/050 was found to be independent of the magnitude of the external electric field, with a time of 80-90 ms for M4851/050 doped with 1 wt% CDH and 0.1 wt% TNF. This is slower than for SCE8, although the spontaneous polarization of M4851/050 ( $-14 \text{ nC}/\text{cm}^2$ ) is larger than that of SCE8 ( $-4.5 \text{ nC}/\text{cm}^2$ ), and the response time of the electro-optical switching (the flipping of spontaneous polarization) to an electric field ( $\pm 10 \text{ V}$  in a 2  $\mu\text{m}$  cell) is shorter for M4851/050. The slower formation of the refractive index grating in M4851/050 is likely due to the poor homogeneity of the SS-state and charge mobility.

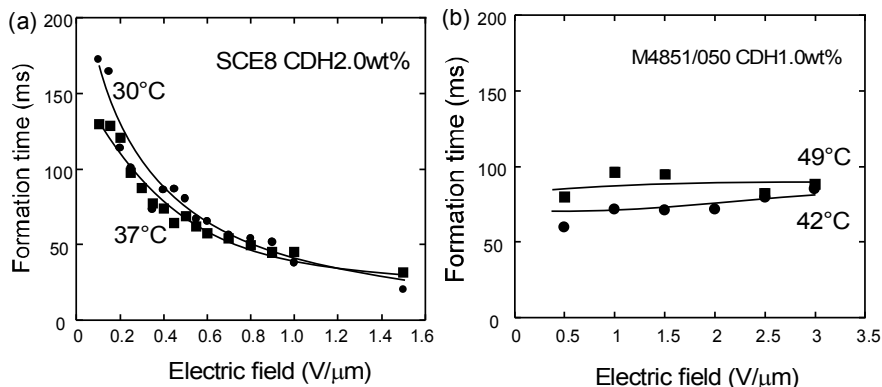


Fig. 14. Electric field dependence of the index grating formation time. (a) SCE8 mixed with 2 wt% CDH and 0.1 wt% TNF in the two-beam coupling experiment. ●, measured at 30 °C ( $T/T_{SmC^*-SmA}=0.95$ ); ■, measured at 36 °C ( $T/T_{SmC^*-SmA}=0.97$ ). (b) M4851/050 mixed with 1 wt% CDH and 0.1 wt% TNF in a two-beam coupling experiment. ●, measured at 42 °C ( $T/T_{SmC^*-SmA}=0.95$ ); ■, measured at 49 °C ( $T/T_{SmC^*-SmA}=0.97$ ).

#### 4.5 Formation mechanism of the internal electric field in FLCs

Since the photorefractive effect is induced by the photoinduced internal electric field, the mechanism of the formation of the space-charge field in the FLC medium is important. The two-beam coupling gain coefficients of mixtures of FLC (SCE8) and photoconductive compounds under a DC field were investigated as a function of the concentration of TNF (electron acceptor). The photoconductive compounds, CDH, ECz and TNF (Figure 8), were used in this examination. When an electron donor with a large molecular size (CDH) relative to the TNF was used as the photoconductive compound, the gain coefficient was strongly affected by the concentration of TNF (Figure 15(a)). However, when ethylcarbazole (ECz), whose molecular size is almost the same as that of TNF, was used, the gain coefficient was less affected by the TNF concentration (Figure 15(b)).

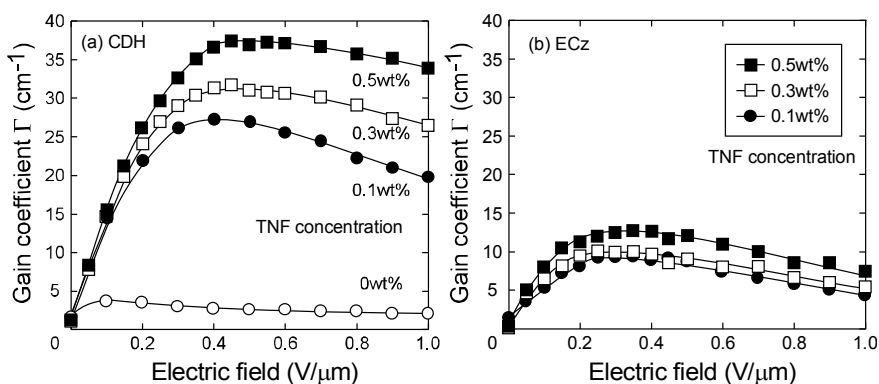


Fig. 15. Dependence of the TNF concentration on the gain coefficients of an FLC doped with photoconductive dopants. (a) SCE8 doped with 2 wt% CDH, (b) SCE8 doped with 2 wt% ECz. An electric field of  $\pm 0.5$  V/μm, 100 Hz was applied.

As shown in **Figure 16**, the difference in the change in absorbance at 488 nm upon addition of TNF was not significant when comparing CDH and ECz. Therefore, the results shown in **Figure 15** cannot be explained based on this difference.

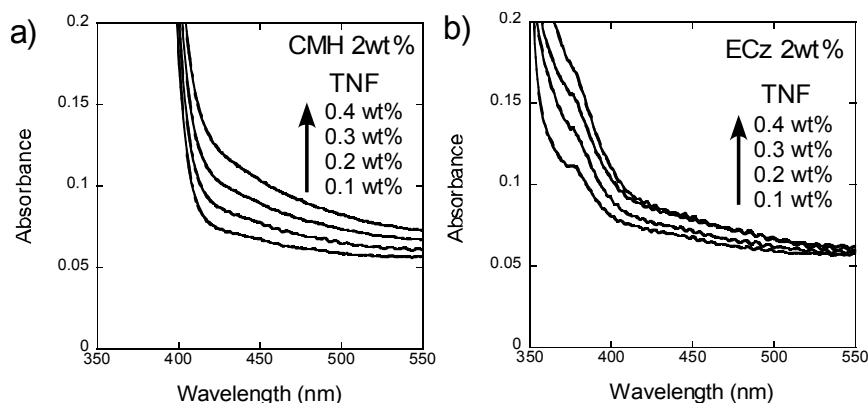


Fig. 16. Absorption spectra of mixtures of FLC (SCE8) and CDH in a 10  $\mu\text{m}$ -gap cell. The concentrations of the photoconductive compounds were fixed at 2 wt% and the TNF concentration was varied from 0 to 0.5 wt%. The reflection at the cell surface and light scattering in the LC are not subtracted.

These findings suggest that ionic conduction plays a major role in the formation of the space-charge field. The mobility of the CDH cation is smaller than that of the TNF anion, and this difference in mobility is thought to be the origin of the charge separation. In this case, the magnitude of the internal electric field is dominated by the concentration of the ionic species. On the other hand, the difference in the mobilities of ECz and TNF is small, and thus, less effective charge separation is induced, indicating that the internal electric field is independent of the concentration of ionic species.

## 4.6 Photorefractive effect in FLC mixtures containing photoconductive chiral compounds

### 4.6.1 Photoconductive chiral dopants

The photorefractive effect in FLCs was investigated using commercially available FLC mixtures until 2010 (the compositions of these FLC materials are not shown here). Compared to nematic LCs, the FLCs are more crystal than liquid, and the preparation of fine FLC films requires sophisticated techniques. Obtaining a uniformly aligned, defect-free, surface-stabilized FLC (SS-FLC) using a single FLC compound is very difficult, and mixtures of several LC compounds are usually used to obtain fine SS-FLC films. The FLC mixtures are composed of the base LC (SmC phase of the forming LC), which is also a mixture of several LC compounds and a chiral compound. The chiral compound introduces a helical structure into the LC phase through supramolecular interactions. In order to utilize an FLC as a photorefractive material, photoconductive compounds must be added to the FLC. However, the introduction of such non-LC compounds into the FLC deteriorates the formation of a uniformly aligned SS-state. Thus, adequate design of the photoconductive compounds is crucial. Sasaki et al. have synthesized chiral compounds that also show photoconductivity (photoconductive chiral dopants); these chiral compounds were

synthesized and mixed with the base LC compounds. The structures of the photoconductive chiral dopants and base LCs are shown in **Figure 17**. A photorefractive FLC material is obtained by just mixing a photoconductive chiral dopant with the base LC.

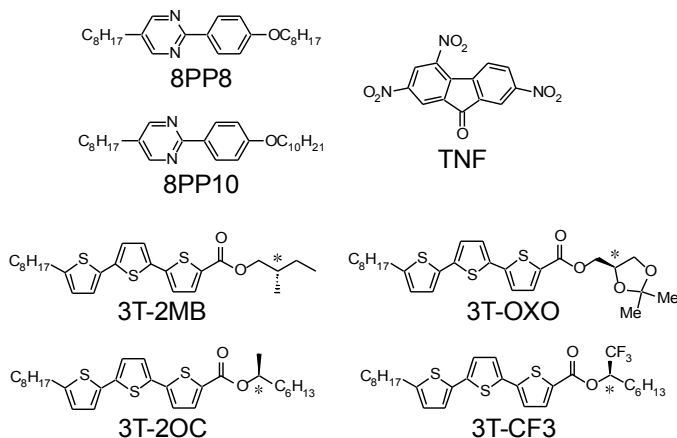


Fig. 17. Structures of the smectic LCs (8PP8 and 8PP10), photoconductive chiral dopants (3T-2MB, 3T-2OC, 3T-OXO and 3T-CF3) and the sensitizer TNF used in this work.

#### 4.6.2 Ferroelectricity and photoconductivity of the FLC mixture

The base LC, which is a 1:1 mixture of 8PP8 and 8PP10, was mixed with the photoconductive chiral dopant and the electron acceptor, which is TNF in this case. The concentration of TNF was set to 0.1 wt%. The phase diagrams of the base LC, TNF, and chiral dopants are shown in **Figure 18**.

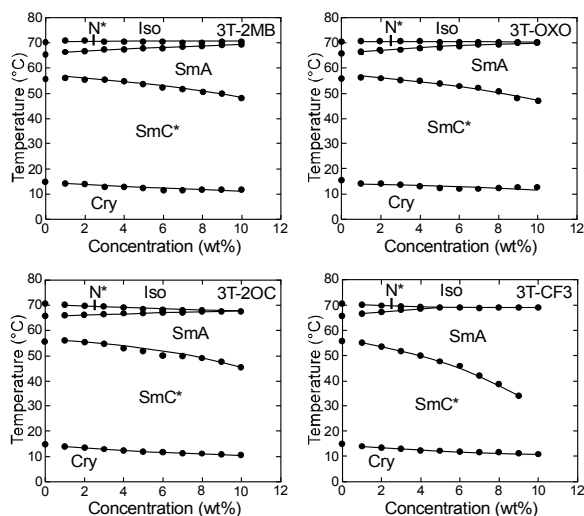


Fig. 18. Phase diagrams of mixtures of the base LC and chiral compounds. The concentration of TNF was set to 0.1 wt%.

The terthiophene chiral dopant used in this study had high miscibility with the phenyl pyrimidine-type smectic LC. The chiral smectic C ( $\text{SmC}^*$ ) phase appeared in all mixtures of the base LC and chiral dopants used in this study. With increasing concentration of the chiral dopants, the temperature range of the  $\text{SmC}^*$  phase and the chiral nematic ( $\text{N}^*$ ) phase was reduced, whereas that of the smectic A ( $\text{SmA}$ ) phase was enhanced. The miscibility of the 3T-CF3 with the base LC was the lowest among the four chiral dopants used in this study. The dipole moment of the trifluoromethyl-substituted group is large, so that the 3T-CF3 molecules tended to aggregate. The magnitude of spontaneous polarization ( $P_s$ ) of the FLC mixtures (mixtures of the base LC with photoconductive dopants and TNF) was measured by the triangular waveform voltage method. A  $P_s$  flip signal observed in the triangular wave method measurement and the magnitude of the  $P_s$  as a function of the concentration of a chiral dopant are shown in **Figure 19**.

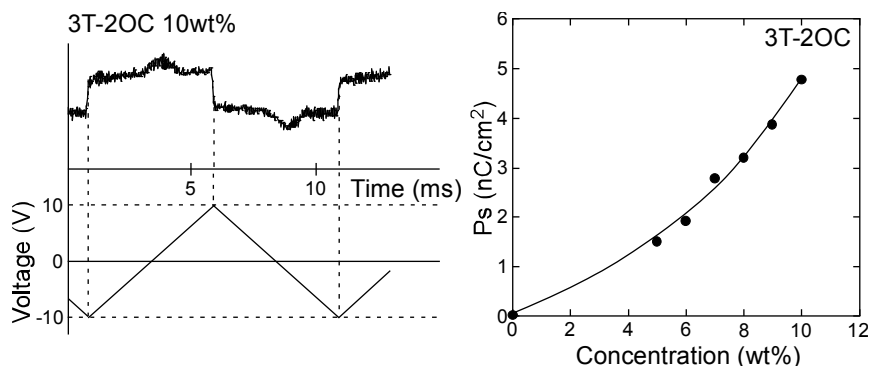


Fig. 19. Spontaneous polarization observed in mixtures of the base LC and 3T-2OC. (a) A typical example of the observed signal in the triangular waveform method. (b) Magnitude of the spontaneous polarization plotted as a function of the concentration of 3T-2OC.

The magnitude of the  $P_s$  of the mixtures of the base LC with chiral dopants was in the range of a few  $\text{nC}/\text{cm}^2$ . The mixtures of the base LC with 3T-2MB and 3T-OXO exhibited  $P_s$  values smaller than  $1 \text{ nC}/\text{cm}^2$ , which is the measurement limit of our equipment. The spontaneous polarization increased with the 3T-2OC concentration, and a  $P_s$  value of  $4.8 \text{ nC}/\text{cm}^2$  was obtained at a 10 wt% concentration. The UV-vis absorption spectra of the photoconductive chiral dopants in chloroform solutions are shown in **Figure 20**. All the samples exhibited absorption maxima at 394 nm. Absorption at 488 nm (wavelength of the laser used in this study) was small.

The small absorption at the laser wavelength is advantageous for minimizing optical loss. The photocurrents in mixtures of the base LC, photoconductive chiral dopant and TNF were measured. As shown in **Figure 21**, the samples were good insulators in the dark. When the samples were irradiated with 488 nm laser light, photocurrents were clearly observed. The magnitudes of the photocurrents were slightly different in the four samples. The only difference in the molecular structures of these compounds is the chiral substituent. Thus, this variation in the photocurrent cannot be attributed to the difference in the molecular structure. It is possible that the miscibility of the photoconductive chiral compounds in the LC and the homogeneity of the LC phase affected the magnitude of the photocurrent.

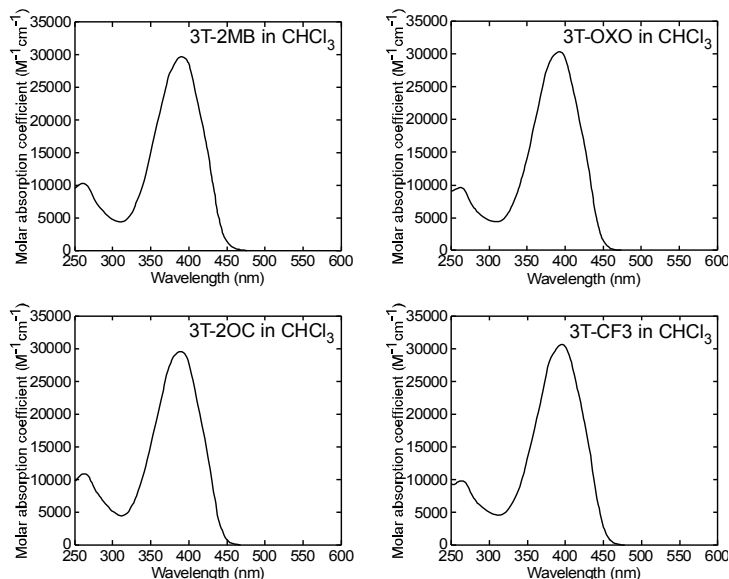


Fig. 20. Absorption spectra of chloroform solutions of the chiral compounds. (a) 3T-2MB; (b) 3T-2OC; (c) 3T-OXO; (d) 3T-CF<sub>3</sub>. The concentration of the chiral compounds was  $6.3 \times 10^{-4}$  mol/L.

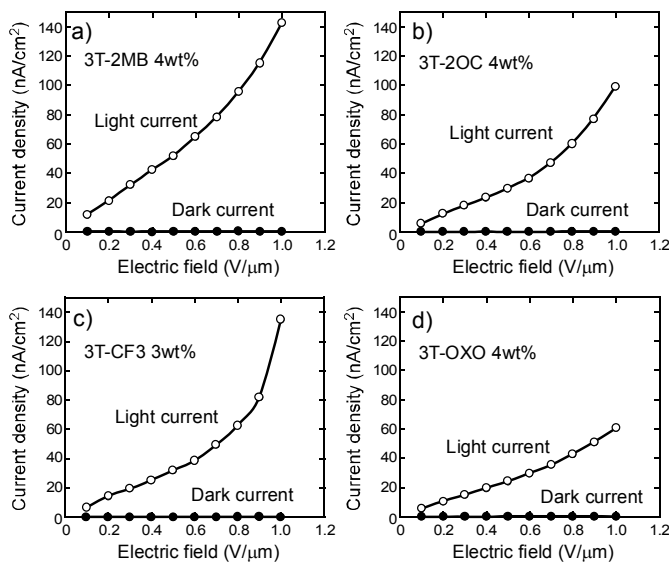


Fig. 21. Magnitudes of light-current and dark-current of mixtures of the base LC, photoconductive chiral compound and TNF measured in a 10- $\mu$ m-gap LC cell as a function of the external electric field. An electric field of 0.1 V/ $\mu$ m was applied. A 488 nm Ar<sup>+</sup> laser (10 mW/cm<sup>2</sup>, 1 mm diameter) was used as the irradiation source.

### 4.6.3 Two-beam coupling experiment on photoconductive FLC mixtures

The difference in the gain coefficients in mixtures of the base LC, photoconductive chiral dopant (3T-2MB, 3T-2OC, 3T-OXO, or 3T-CF3), and TNF was investigated. All the samples formed a finely aligned SS-state in 10- $\mu\text{m}$ -gap cells with a LX-1400 polyimide alignment layer and clearly exhibited photorefractivity in the ferroelectric phase. Asymmetric energy exchange was observed only in the temperature range in which the sample exhibited ferroelectric properties ( $\text{SmC}^*$  phase). The gain coefficients of the samples are plotted as a function of the magnitude of the external electric field in **Figure 22**. As the concentration of the photoconductive chiral dopant increased, so did the gain coefficient. This may be due to increased charge mobility in the FLC medium and an increase in the magnitude of Ps. All the samples exhibited relatively large photorefractivity. A gain coefficient higher than  $100\text{ cm}^{-1}$  was obtained in the 3T-2OC (6 wt%) sample with the application of an electric field of only  $0.2\text{ V}/\mu\text{m}$ . A gain coefficient higher than  $100\text{ cm}^{-1}$  was also obtained in the 3T-2MB sample at an applied electric field of  $0.5\text{ V}/\mu\text{m}$ . In order to obtain photorefractivity in polymer materials, the application of a high electric field in the range of  $10\text{--}50\text{ V}/\mu\text{m}$  to the polymer film is typically required. The small electric field necessary for activating the photorefractive effect in FLCs is thus a great advantage for photorefractive devices. The grating formation time in the mixtures of the base LC, photoconductive chiral dopant and TNF is plotted as a function of the strength of the external electric field in **Figure 23**.

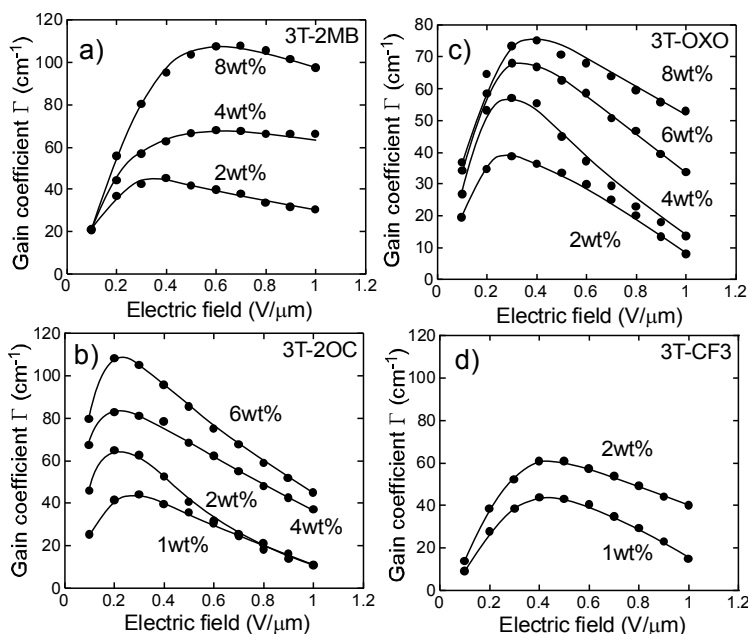


Fig. 22. Electric field dependence of the gain coefficients of the mixtures of the base LC, photoconductive chiral compounds, and TNF. (a) 3T-2MB; (b) 3T-2OC; (c) 3T-OXO; (d) 3T-CF3.

The grating formation time decreased with increasing electric field strength due to the increased efficiency of charge generation. The shortest formation time was obtained to be 5–

8 ms at 1 V/ $\mu\text{m}$  external electric field for all the chiral compounds. The 3T-CF3 sample exhibited the fastest response, because of the larger polarity of 3T-CF3.

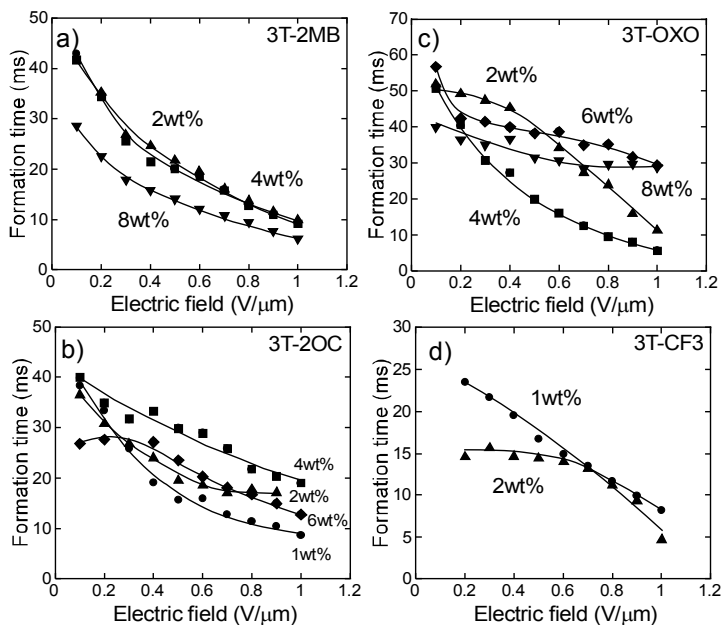


Fig. 23. Electric field dependence of the index grating formation times of mixtures of the base LC, photoconductive chiral compounds, and TNF measured at 30 °C. (a) 3T-2MB; (b) 3T-2OC; (c) 3T-OXO; (d) 3T-CF3.

#### 4.6.4 Mechanism of the photoconductivity in FLC mixtures

The effect of the electron acceptor (TNF) on the gain coefficient was investigated. As shown in **Figure 24**, when the concentration of the 3T-2OC was 1 wt%, the magnitude of the gain coefficient increased with the concentration of the TNF.

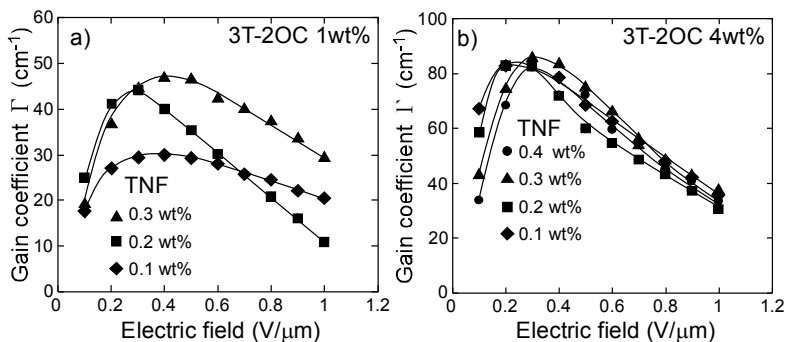


Fig. 24. Dependence of the gain coefficients of the mixture of the base LC, photoconductive chiral compound and TNF on the magnitude of the external electric field. (a) Base LC doped with 1 wt% 3T-2OC; (b) base LC doped with 4 wt% 3T-2OC.

It was considered that the mechanism of the formation of the space-charge field in this case is based on ionic conduction. As discussed in our previous paper, the formation of the space-charge field is based on the difference in the mobilities of the cation and anion generated at the light positions of the interference fringes. A cation of 3T-2OC and an anion of TNF were generated at the interference fringes through photoinduced electron transfer. Both ions drift under the application of an external electric field. The molecular length of 3T-2OC is larger than that of TNF, and thus, the mobility of the 3T-2OC cation is smaller than that of the TNF anion. This difference in mobility is the origin of the charge separation. In this case, the magnitude of the internal electric field is dominated by the concentration of the ionic species. On the other hand, when the concentration of 3T-2OC was 4 wt%, the magnitude of the gain coefficient was independent of the concentration of TNF. Thus, the mechanisms of the formation of the space-charge field are different in the 1 wt% samples and the 4 wt% samples. It was considered that when the concentration of 3T-2OC is high, conduction based on a hopping mechanism occurs. In this case, TNF acts as just the electron acceptor that introduces electron holes into the 3T-2OC molecules.

## 5. Conclusion

The reorientational photorefractive effect based on the response of bulk polarization was observed in dye-doped FLC samples. Photorefractivity was observed only in the ferroelectric phase of these samples, and the refractive index formation time was found to be shorter than that of nematic LCs. The response time was in the order of ms and is dominated by the formation of the internal electric field. These results indicate that the mechanism responsible for refractive index grating formation in FLCs is different from that for non-ferroelectric materials, and is clearly related to the ferroelectric properties of the material. The photorefractivity of FLCs was strongly affected by the properties of the FLCs themselves. Besides properties such as spontaneous polarization, viscosity, and phase transition temperature, the homogeneity of the SS-state was also found to be a major factor. The gain coefficient, refractive index grating formation time (response time) and stability of the two-beam coupling signal were all affected strongly by the homogeneity of the SS-state. Therefore, a highly homogeneous SS-state is necessary to create a photorefractive device. The techniques employed recently in the development of fine LC display panels will be utilized in the future in the fabrication of the photorefractive devices.

## 6. Acknowledgment

The authors would like to thank the Japan Science and Technology Agency (JST) S-innovation and the Canon Foundation for support.

## 7. References

- Solymar, L.; Webb, J.D.; Grunnet-Jepsen, A. *The Physics and Applications of Photorefractive Materials*; Oxford: New York, 1996.
- Yeh, P. *Introduction to Photorefractive Nonlinear Optics*; John Wiley: New York, 1993.
- Moerner, W. E.; Silence, S. M. *Chem. Rev.* 1994, 94, 127-155.
- Kippelen, B.; Peyghambarian, N. *Advances in Polymer Science, Polymers for Photonics Applications II*, Springer, 2002, 87-156.

- Ostroverkhova, O.; Moerner, W. E. *Chem. Rev.*, 2004, 104, 3267-3314.
- Tay, S.; Blanche, P.A.; Voorakaranam, R.; Tunc, A.V.; Lin, W.; Rokutanda, S.; Gu, T.; Flores, D.; Wang, P.; Li, G.; Hilarie, P.; Thomas, J.; Norwood, R.A.; Yamamoto, M.; Peyghambarian, N. *Nature*, 2008, 451, 694-698.
- Blanche, P.A.; Bablumian, A.; Voorakaranam, R.; Christenson, C.; Lin, W.; Gu, T.; Flores, D.; Wang, P.; Hsieh, W.Y.; Kathaperumal, M.; Rachwal, B.; Siddiqui, O.; Thomas, J.; Norwood, R.A.; Yamamoto, M.; Peyghambarian, N. *Nature*, 2010, 468, 80-83.
- Sasaki, T. *Polymer Journal*, 2005, 37, 797-812.
- Meerholz, K.; Volodin, B.L.; Kippelen, B.; Peyghambarian, N. *Nature* 1994, 371, 497-500.
- Kippelen, B.; Marder, S.R.; Hendrickx, E.; Maldonado, J.L.; Guillemet, G.; Volodin, B.L.; Steele, D.D.; Enami, Y.; Sandalphon; Yao, Y.J.; Wang, J.F.; Röckel, H.; Erskine, L.; Peyghambarian, N. *Science* 1998, 279, 54-56.
- Wiederrecht, G.P.; Yoon, B.A.; Wasielewski, M.R. *Adv. Materials* 2000, 12, 1533-1536.
- Sasaki, T.; Katsuragi, A.; Mochizuki, O.; Nakazawa, Y. *J. Phys. Chem. B*, 2003, 107, 7659-7665.
- Sasaki, T.; Mochizuki, O.; Nakazawa, Y.; Noborio, K. *J. Phys. Chem. B*, 2004, 108, 17083-17088.
- Talarico, M.; Termine, R.; Prus, P.; Barberio, G.; Pucci, D.; Ghedini, M.; Goelemme, A. *Mol. Cryst. Liq. Cryst.*, 2005, 429, 65-76
- Talarico, M.; Goelemme, A. *Nature Mater.*, 2006, 5, 185-188.
- Sasaki, T.; Mochizuki, O.; Nakazawa, N.; Fukunaga, G.; Nakamura, T.; Noborio, K. *Appl. Phys. Lett.*, 2004, 85, 1329-1331.
- Sasaki, T.; Moriya, N.; Iwasaki, Y. *J. Phys. Chem. C*, 2007, 111, 17646-17652.
- Skarp, K.; Handschy, M.A. *Mol. Cryst. Liq. Cryst.* 1988, 165, 439-569.

# Linear and Nonlinear Optical Properties of Ferroelectric Thin Films

Bing Gu and Hui-Tian Wang  
*School of Physics, Nankai University  
China*

## 1. Introduction

Nowadays, nonlinear optical materials play a crucial role in the technology of photonics, nano-photonics, and bio-photonics. Among a wide variety of materials, thin films have the additional design advantage of small volume and good compatibility with fabrication of waveguide and integrated nonlinear photonics devices over solutions and single crystals.

Interestingly, most ferroelectric thin films exhibit notable physical characteristics of large spontaneous polarization, high dielectric constant, high optical transparency, and large nonlinear response with respect to the electromagnetic radiation in the optical range. During the past decade, ferroelectric thin films such as  $\text{Bi}_2\text{Nd}_2\text{Ti}_3\text{O}_{12}$ ,  $\text{Ba}_{0.6}\text{Sr}_{0.4}\text{TiO}_3$ , and  $\text{Bi}_{3.25}\text{La}_{0.75}\text{Ti}_3\text{O}_{12}$  have been received intense interest due to their high optical transparency and remarkable optical nonlinearity for potential applications on nonlinear photonic devices (Gu et al., 2004, Liu et al., 2006, Shi et al., 2006, Shin et al., 2007). Moreover, most of these investigations have been performed under the excitation of nanosecond and picosecond laser pulses. Owing to today's fast advance of laser sources with ultrashort pulse duration, the femtosecond nonlinear optical response has been detected in several ferroelectric thin films. Enlightened by a recent report on the third-order nonlinear optical response presented in  $\text{CaCu}_3\text{Ti}_4\text{O}_{12}$  at a wavelength of 532 nm (Ning et al., 2009), observations indicate that the optical nonlinearities depend strongly on the pulse duration of the excitation laser, although many reports declared that the observed nonlinear effect is an instantaneous optical nonlinearity in the nanosecond and picosecond regimes. Apparently, it is imperative to gain an insight on the underlying physical mechanisms for the observed optical nonlinearities at different time scales.

In this chapter, the linear transmittance spectrum and Z-scan technique are used to characterize the linear and nonlinear optical properties of ferroelectric thin films, respectively. Two methodologies are based on measurements of the sample's transmittance under weak or intense light excitation. The nonlinear optical properties of representative ferroelectric films in nanosecond, picosecond, and femtosecond regimes are presented. In particular, the underlying mechanisms for the observed optical nonlinearities are also discussed in details.

## 2. Concept of linear and nonlinear optics

The interaction of light with matter will modify either the direction of propagation, spatial profile, or transmission of an applied optical field through a material system. The

fundamental parameter in this light-matter interaction theory is the electric polarization of the material induced by light. In the case of conventional (i.e., linear) optics, the polarization depends linearly upon the electric field strength in a manner that can often be written as

$$\vec{P} = \varepsilon_0 \chi^{(1)} \cdot \vec{E}, \quad (1)$$

where the constant of proportionality  $\chi^{(1)}$  is the linear susceptibility and  $\varepsilon_0$  is the permittivity of free space. In an isotropic medium, the real and imaginary parts of  $\chi^{(1)}$  in SI units, respectively, are related to the linear index of refraction and absorption coefficient by

$$n_0 = \sqrt{1 + \text{Re}[\chi^{(1)}]}, \quad (2)$$

$$\alpha_0 = \frac{\omega}{n_0 c} \text{Im}[\chi^{(1)}]. \quad (3)$$

Here  $c$  is the speed of light in vacuum and  $\omega$  is the optical frequency. The refractive index of ferroelectric films is attributed to the following factors which are related to the crystallinity of the film density, electronic structure, and defects. Owing to high dielectric constant, generally, the index of refraction in the ferroelectric film is over 2 in the visible region. The linear absorption coefficient of materials usually contains the contributions of two parts: one is the elastic scattering caused by the defects and optical inhomogeneity and another is the inherent linear absorption. In general, the linear absorption coefficient of ferroelectric thin films is close to  $10^4 \text{ cm}^{-1}$ . The main reason is that the elastic scattering is the dominant factor to the linear absorption (Gu et al., 2004, Leng et al., 2007). Typical values of  $n_0$  and  $\alpha_0$  of representative ferroelectric thin films are listed in Tables 1 and 2.

In nonlinear optics, nonlinear processes are responsible for the nonlinearity of materials. Accordingly, the polarization induced by the applied optical field in the material system can be expressed as a power series in the electric field amplitude (Boyd, 2009):

$$\vec{P} = \varepsilon_0 \chi^{(1)} \cdot \vec{E} + \varepsilon_0 \chi^{(2)} : \vec{E}\vec{E} + \varepsilon_0 \chi^{(3)} : \vec{E}\vec{E}\vec{E} + \dots \quad (4)$$

The quantities  $\chi^{(2)}$  and  $\chi^{(3)}$  are called the second- and third-order nonlinear optical susceptibilities of the sample, respectively. The theoretical formalism has been presented for the calculation of nonlinear susceptibilities components in ferroelectrics (Murgan et al., 2002). Generally, the nonlinear susceptibilities depend on the frequencies of the applied light fields, but under the assumption of instantaneous response, one takes them to be constants. The  $\chi^{(2)}$  related nonlinear processes include second-harmonic generation, optical rectification, and sum- and difference-frequency generation. Such processes are out of the scope of this book chapter. More details with respect to second-order optical nonlinearities in ferroelectrics can be found elsewhere (Murgan et al., 2002, Tsai et al., 2004, Kumar et al., 2008, Kityk et al., 2010). The coefficient  $\chi^{(3)}$  describes the intensity-dependent third-order nonlinear effect, such as self-focusing or defocusing, two-photon absorption, and three-harmonic generation. The intensity-dependent refractive index  $n_2$  and absorption coefficient  $\alpha_2$  are most two important of all third-order processes in ferroelectrics, which are related to the real and imaginary components of  $\chi^{(3)}$  in SI units, respectively, by (Chen et al., 2006)

$$n_2 = \frac{3 \operatorname{Re}[\chi^{(3)}]}{4 \varepsilon_0 c n_0^2}, \quad (5)$$

$$\alpha_2 = \frac{3\pi \operatorname{Im}[\chi^{(3)}]}{2 \varepsilon_0 c n_0^2 \lambda}, \quad (6)$$

where  $n_2$  and  $\alpha_2$  take the units of  $\text{m}^2/\text{W}$  and  $\text{m}/\text{W}$ , respectively. And  $\lambda$  is the wavelength of laser in vacuum.

### 3. Physical mechanisms of optical nonlinearities in ferroelectric thin films

Optical nonlinear response of the ferroelectric thin film partly depends on the laser characteristics, in particular, on the laser pulse duration and on the excitation wavelength, and partly on the material itself. The optical nonlinearities usually fall in two main categories: the instantaneous and accumulative nonlinear effects. If the nonlinear response time is much less than the pulse duration, the nonlinearity can be regarded justifiably as responding instantaneously to optical pulses. On the contrary, the accumulative nonlinearities may occur in a time scale longer than the pulse duration. Besides, the instantaneous nonlinearity (for instance, two-photon absorption and optical Kerr effect) is independent of the laser pulse duration, whereas the accumulative nonlinearity depends strongly on the pulse duration. Examples of such accumulative nonlinearities include excited-state nonlinearity, thermal effect, and free-carrier nonlinearity. The simultaneous accumulative nonlinearities and inherent nonlinear effects lead to the huge difference of the measured nonlinear response on a wide range of time scales.

#### 3.1 Nonlinear absorption

In general, nonlinear absorption in ferroelectric thin films can be caused by two-photon absorption, three-photon absorption, or saturable absorption. When the excitation photon energy and the bandgap of the film fulfil the multiphoton absorption requirement  $[(n-1)h\nu < E_g < nh\nu]$  (here  $n$  is an integer.  $n=2$  and  $3$  for two- and three-photon absorption, respectively), the material simultaneously absorbs  $n$  identical photons and promotes an electron from the ground state of a system to a higher-lying state by virtual intermediate states. This process is referred to a one-step  $n$ -photon absorption and mainly contributes to the absorptive nonlinearity of most ferroelectric films. When the excitation wavelength is close to the resonance absorption band, the transmittance of materials increases with increasing optical intensity. This is the well-known saturable absorption. Accordingly, the material has a negative nonlinear absorption coefficient.

#### 3.2 Nonlinear refraction

The physical mechanisms of nonlinear refraction in the ferroelectric thin films mainly involve thermal contribution, optical electrostriction, population redistribution, and electronic Kerr effect. The thermal heat leads to refractive index changes via the thermal-optic effect. The nonlinearity originating from thermal effect will give rise to the negative nonlinear refraction. In general, the thermal contribution has a very slow response time (nanosecond or longer). On the picosecond and femtosecond time scales, the thermal contribution to the change of the refractive index can be ignored for it is much smaller than the electronic contribution. Optical

electrostriction is a phenomenon that the inhomogeneous optical field produces a force on the molecules or atoms comprising a system resulting in an increase of the refractive index locally. This effect has the characteristic response time of nanosecond order. When the electron occurs the real transition from the ground state of a system to an excited state by absorbing the single photon or two identical photons, electrons will occupy real excited states for a finite period of time. This process is called a population redistribution and mainly contributes the whole refractive nonlinearity of ferroelectric films in the picosecond regime. The electronic Kerr effect arises from a distortion of the electron cloud about atom or molecule by the optical field. This process is very fast, with typical response time of tens of femtoseconds. The electronic Kerr effect is the main mechanism of the refractive nonlinearity in the femtosecond time scale.

### 3.3 Accumulative nonlinearity caused by the defect

For many cases, the observed absorptive nonlinearity of ferroelectric thin films is the two-photon absorption type process. Moreover, the measured two-photon absorption coefficient strongly depends on the laser pulse duration (see Table 1). This two-photon type nonlinearity originates from two-photon as well as two-step absorptions. The two-step absorption is attributed to the introduction of electronic levels within the energy bandgap due to the defects (Liu et al., 2006, Ambika et al., 2009, Yang et al., 2009).

The photodynamic process in ferroelectrics with impurities is illustrated in Fig. 1. Electrons in the ground state could be promoted to the excited state and impurity states based on two- and one-photon absorption, respectively. The electrons in impurity states may be promoted to the excited state by absorbing another identical photon, resulting in two-step two-photon absorption. At the same time, one-photon absorption by impurity levels populates new electronic states. This significant population redistribution produces an additional change in the refractive index, leading to the accumulative nonlinear refraction effect. This accumulative nonlinearity is a cubic effect in nature and strongly depends on the pulse duration of laser. Similar to the procedure for analyzing the excited-state nonlinearity induced by one- and two-photon absorption (Gu et al., 2008b and 2010), the effective third-order nonlinear absorption and refraction coefficients arising from the two-step two-photon absorption can be expressed as

$$\alpha_2^{\text{imp}} = \frac{\sigma_{\text{imp}} \alpha_0}{h\nu} \frac{\sqrt{2}}{\sqrt{\pi}\tau} \int_{-\infty}^{+\infty} \exp\left(-\frac{t^2}{\tau^2}\right) \left\{ \int_{-\infty}^t \exp\left(-\frac{t'^2}{\tau^2}\right) \exp\left(\frac{t'-t}{\tau_{\text{imp}}}\right) dt' \right\} dt, \quad (7)$$

$$n_2^{\text{imp}} = \frac{\eta_{\text{imp}} \alpha_0}{h\nu} \frac{\sqrt{2}}{\sqrt{\pi}\tau} \int_{-\infty}^{+\infty} \exp\left(-\frac{t^2}{\tau^2}\right) \left\{ \int_{-\infty}^t \exp\left(-\frac{t'^2}{\tau^2}\right) \exp\left(\frac{t'-t}{\tau_{\text{imp}}}\right) dt' \right\} dt. \quad (8)$$

Here  $\sigma_{\text{imp}}$  and  $\eta_{\text{imp}}$  are the effective absorptive and refractive cross-sections of the impurity state, respectively.  $\tau$  is the half-width at  $e^{-1}$  of the maximum for the pulse duration of the Gaussian laser. And  $\tau_{\text{imp}}$  is the lifetime of the impurity state.

## 4. Characterizing techniques to determine the films' linear and nonlinear optical properties

In general, the ferroelectric thin film is deposited on the transparent substrate. The fundamental optical constants (the linear absorption coefficient, linear refraction index, and bandgap energy) of the thin film could be determined by various methods, such as the

prism-film coupler technique, spectroscopic ellipsometry, and reflectivity spectrum measurement. Among these methods, the transmittance spectrum using the envelope technique is a simple straightforward approach. To characterize the absorptive and refractive nonlinearities of ferroelectric films, the single-beam Z-scan technique is extensively adopted.

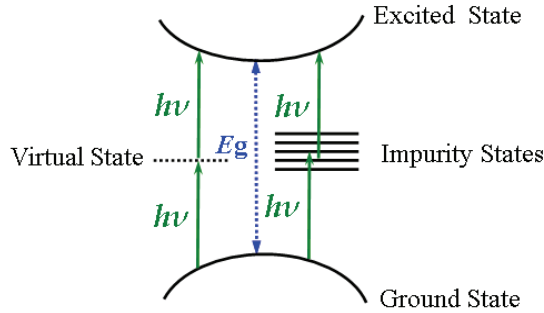


Fig. 1. Schematic diagram of one- and two-step two-photon absorption in ferroelectrics with the defects.

**4.1 Linear optical parameters obtained from the transmittance spectrum using the envelope technique**

The practical situation for a thin film on a thick finite transparent substrate is illustrated in Fig. 2. The film has a thickness of  $d$ , a linear refractive index  $n_0$ , and a linear absorption coefficient  $\alpha_0$ . The transparent substrate has a thickness several orders of magnitude larger than  $d$  and has an index of refraction  $n_0^{sub}$  and an absorption coefficient  $\alpha_0^{sub} \approx 0$ . The index of the surrounding air is equal to 1.

Taking into account all the multiple reflections at the three interfaces, the rigorous transmission could be devised (Swanepoel, 1983). Subsequently, it is easy to simulate the transmittance spectrum from the given parameters ( $d$ ,  $n_0$ ,  $\alpha_0$ ,  $d^{sub}$ , and  $n_0^{sub}$ ). The oscillations in the transmittance are a result of the interference between the air-film and film-substrate interface (for example, see Fig. 4). In contrast, in practical applications for determining the optical constants of films, one must employ the transmittance spectrum to evaluate the optical constants. The treatment of such an inverse problem is relatively difficult. From the measured transmittance spectrum, the extremes of the interference fringes are obtained (see dotted lines in Fig. 4). Based on the envelope technique of the transmittance spectrum, the optical constants ( $d$ ,  $n_0$ , and  $\alpha_0$ ) could be estimated (Swanepoel, 1983).

The refractive index as a function of wavelength in the interband-transition region can be modelled based on dipole oscillators. This theory assumes that the material is composed of a series of independent oscillators which are set to forced vibrations by incident irradiances. Hereby, the dispersion of the refraction index is described by the well-known Sellmeier dispersion relation (DiDomenico & Wemple, 1969):

$$n_0^2(\lambda) = 1 + \sum_{j=0}^M \frac{b_j \lambda^2}{\lambda^2 - \lambda_j^2} \tag{9}$$

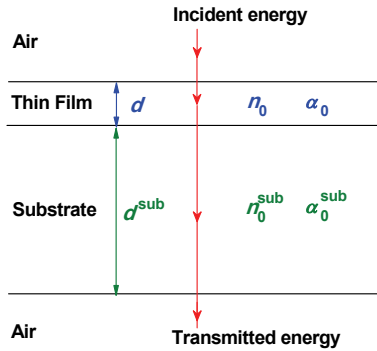


Fig. 2. Thin film on a thick finite transparent substrate.

where  $\lambda_j$  is the resonant wavelength of the  $j$ th oscillator of the medium, and  $b_j$  is the oscillator strength of the  $j$ th oscillator. In general, one assumes that only one oscillator dominates and then takes the one term of Eq. (9). This single-term Sellmeier relation fits the refractive index quite well for most materials. In some cases, however, to accurately describe the refractive index dispersion in the visible and infrared range, the improved Sellmeier equation which takes two or more terms in Eq. (9) is needed (Barboza & Cudney, 2009). Analogously, replacing  $n_0$  by  $\alpha_0$  in Eq. (9), this equation describes the dispersion of linear absorption coefficient (Wang et al., 2004, Leng et al., 2007). In this instance, the parameters of  $\lambda_j$  and  $b_j$  have no special physical significance.

The optical bandgap ( $E_g$ ) of the thin film can be estimated using Tauc's formula  $(\alpha_0 h\nu)^{2/m} = \text{Const.}(h\nu - E_g)$ , where  $h\nu$  is the photon energy of the incident light,  $m$  is determined by the characteristics of electron transitions in a material (Tauc et al., 1966). Here  $m=1$  and 4 correspond to the direct and indirect bandgap materials, respectively.

#### 4.2 Z-scan technique for the nonlinear optical characterization

To characterize the optical nonlinearities of ferroelectric thin films, a time-averaging technique has been extensively exploited in Z-scan measurements due to its experimental simplicity and high sensitivity (Sheik-Bahae et al., 1990). This technique gives not only the signs but also the magnitudes of the nonlinear refraction and absorption coefficients.

##### 4.2.1 Basic principle and experimental setup

On the basis of the principle of spatial beam distortion, the Z-scan technique exploits the fact that a spatial variation in intensity distribution in transverse space can induce a lenslike effect due to the presence of space-dependent refractive-index change via the nonlinear effect, which affects the propagation behaviour of the beam itself, and generates a self-focusing or defocusing effect. The resulting phenomenon reflects on the change in the far-field diffraction pattern.

To carry out Z-scan measurements, the sample is scanned across the focus along the z-axis, while the transmitted pulse energies in the presence or absence of the far-field aperture are probed, producing the closed- and open-aperture Z-scans, respectively. The characteristics of the closed- and open-aperture Z-scans can afford both the signs and the magnitudes of the nonlinear refractive and absorptive coefficients. Figures 3(a) and 3(b) schematically show the closed- and open-aperture Z-scan experimental setup, respectively.

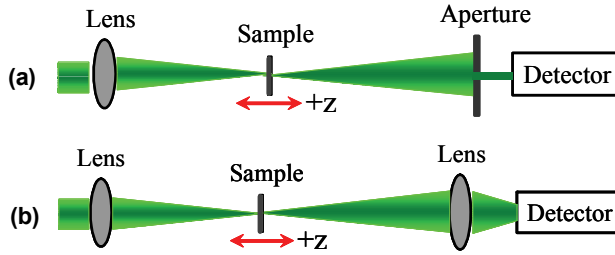


Fig. 3. Experimental setup of the (a) closed-aperture and (b) open-aperture Z-scan measurements.

In this book chapter, the nonlinear-optical measurements were conducted by using conventional Z-scan technique as shown in Fig. 3. The laser source was a Ti: sapphire regenerative amplifier (Quantronix, Tian), operating at a wavelength of 780 nm with a pulse duration of  $\tau_p=350$  fs (the full width at half maximum for a Gaussian pulse) and a repetition rate of 1 kHz. The spatial distribution of the pulses was nearly Gaussian, after passing through a spatial filter. Moreover, the laser pulses had near-Gaussian temporal profile, confirming by the autocorrelation signals in the transient transmission measurements. In the Z-scan experiments, the laser beam was focused by a lens with a 200 mm focal length, producing the beam waist at the focus  $\omega_0 \approx 31 \mu\text{m}$  (the Rayleigh range  $z_0=3.8$  mm). To perform Z-scans, the sample was scanned across the focus along the z-axis using a computer-controlled translation stage, while the transmitted pulse energies in the present or absence of the far-field aperture were probed by a detector (Laser Probe, PkP-465 HD), producing the closed- and open-aperture Z-scans, respectively. For the closed-aperture Z-scans, the linear transmittance of the far-field aperture was fixed at 15% by adjusting the aperture radius. The measurement system was calibrated with carbon disulfide. In addition, neither laser-induced damage nor significant scattering signal was observed from our Z-scan measurements.

#### 4.2.2 Z-scan theory for characterizing instantaneous optical nonlinearity

Assuming that the nonlinear response of the sample has a characteristic time much shorter than the duration of the laser pulse, i.e., the optical nonlinearity responds instantaneously to laser pulses. As a result, one can regard that the nonlinear effect depends on the instantaneous intensity of light inside the samples and each laser pulse is treated independently. For the sake of simplicity, we consider an optically thin sample with a third-order optical nonlinearity and the incoming pulses with a Gaussian spatiotemporal profile. The open-aperture Z-scan normalized transmittance can be expressed as

$$T(x, s = 1) = \sum_{m=0}^{\infty} \frac{(-q_0)^m}{(x^2 + 1)^m (m + 1)^{3/2}} \quad \text{for } |q_0| < 1. \quad (10)$$

where  $x=z/z_0$  is the relative sample position,  $q_0=\alpha_2 I_0(1-R)L_{\text{eff}}$  is the on-axis peak phase shift due to the absorptive nonlinearity,  $L_{\text{eff}}=[1-\exp(-\alpha_0 L)]/\alpha_0$  is the effective sample length. Here  $z_0$  is the Rayleigh length of the Gaussian beam;  $I_0$  is the on-axis peak intensity in the air;  $R$  is the Fresnel reflectivity coefficient at the interface of the material with air;  $s$  is the linear transmittance of the far-field aperture; and  $L$  is the sample physical length.

The Z-scan transmittance for the pinhole-aperture is deduced as (Gu et al., 2008a)

$$T(x, s \approx 0) = 1 + \frac{1}{\sqrt{2}} \frac{4x\phi_0 - (x^2 + 3)q_0}{(x^2 + 1)(x^2 + 9)} + \frac{1}{\sqrt{3}} \frac{4\phi_0^2(3x^2 - 5) + q_0^2(x^4 + 17x^2 + 40) - 8\phi_0q_0x(x^2 + 9)}{(x^2 + 1)^2(x^2 + 9)(x^2 + 25)}, \quad (11)$$

where  $\phi_0 = 2\pi n_2 I_0 (1-R) L_{\text{eff}} / \lambda$  is the on-axis peak nonlinear refraction phase shift. It should be noted that Eq. (11) is applicable to Z-scans induced by laser pulses with weak nonlinear absorption and refraction phase shifts. For arbitrary nonlinear refraction phase shift  $\phi_0$  and arbitrary aperture  $s$ , the Z-scan analytical expression is available in literature (Gu et al., 2008a).

### 4.2.3 Z-scan theory for a cascaded nonlinear medium

Ferroelectric thin film with good surface morphology was usually deposited on the quartz substrate by pulsed laser deposition, chemical-solution deposition, or radio-frequency magnetron sputtering. Generally, the thicknesses of the thin film and substrate are about sub-micron and millimetre, respectively. As shown in Fig. 2, the transparent substrate has a thickness three orders of magnitude large than that of the film. The quartz substrate has the nonlinear absorption coefficient of  $\alpha_2^{\text{sub}} \sim 0$  and the third-order refractive index of  $n_2^{\text{sub}} = 3.26 \times 10^{-7} \text{ cm}^2/\text{GW}$  in the near infrared region (Gu et al., 2009a). The nonlinear refractive index of ferroelectric thin films in the femtosecond regime is usually three orders of magnitude larger than that of quartz substrate. Thus, the nonlinear optical path of the film ( $n_2 L_{\text{eff}} I_0$ ) is comparable with that of the substrate. In this instance, Z-scan signals arise from the resultant nonlinear response contributed by both the thin film and the substrate.

To separate each contribution, rigorous analysis should be adopted by the Z-scan theory for a cascaded nonlinear medium (Zang et al., 2003). Accordingly, the total nonlinear phase shifts due to the absorptive and refractive nonlinearities,  $q_0$  and  $\phi_0$ , could be extracted from the measured Z-scan experimental data for film/substrate. We can simplify  $q_0$  and  $\phi_0$  as follows:

$$q_0 = I_0 (1-R) [\alpha_2 L_{\text{eff}} + (1-R') \alpha_2^{\text{sub}} L_{\text{eff}}^{\text{sub}}], \quad (12)$$

$$\phi_0 = 2\pi I_0 (1-R) [n_2 L_{\text{eff}} + (1-R') n_2^{\text{sub}} L_{\text{eff}}^{\text{sub}}] / \lambda. \quad (13)$$

Here  $R = (n_0 - 1)^2 / (n_0 + 1)^2$  and  $R' = (n_0^{\text{sub}} - n_0)^2 / (n_0^{\text{sub}} + n_0)^2$  are the Fresnel reflection coefficients at the air-sample and sample-substrate interfaces, respectively. Note that  $I_0$  is the peak intensity just before the sample surface, whereas  $I_0' = (1-R)I_0$  and  $I_0'' = (1-R')I_0'$  are the peak intensities within the sample and the substrate, respectively.

To unambiguously determine the optical nonlinearity of the thin film from the detected Z-scan signal, the strict approach is presented as follows (Gu et al., 2009a). Firstly, under the assumption that both the thin film and the substrate only exhibit third-order nonlinearities, the total nonlinear response of absorptive nonlinearity,  $q_0$ , and refractive nonlinearity,  $\phi_0$ , are evaluated from the best fittings to the measured Z-scan traces for the composite system of thin film and substrate by using the Z-scan theory described subsection 4.2.2. Such evaluations are carried out for the Z-scans measured at different levels of  $I_0$ . Secondly, the nonlinear absorption  $\alpha_2$  and the nonlinear refraction index  $n_2$  of the thin film can then be extracted from Eqs. (12) and (13). As such, the nonlinear coefficients of  $\alpha_2$  and  $n_2$  for the thin

film at different values of  $I_0$  are determined unambiguously and rigorously. Such the values of  $\alpha_2$  and  $n_2$  as a function of  $I_0$  provide a clue to the optical nonlinear origin of ferroelectrics.

#### 4.2.4 Z-scan theory for the material with third- and fifth-order optical nonlinearities

Owing to intense irradiances of laser pulses, the higher-order optical nonlinearity has been observed in several materials, such as semiconductors, organic molecules, and ferroelectric thin films as we discussed in subsection 6.3.

For materials exhibiting the simultaneous third- and fifth-order optical nonlinearities, there is a quick procedure to evaluate the nonlinear parameters as follows (Gu et al., 2008b): (i) measuring the Z-scan traces at different levels of laser intensities  $I_0$ ; (ii) determining the effective nonlinear absorption coefficient  $\alpha_{\text{eff}}$  and refraction index  $n_{\text{eff}}$  of the film at different  $I_0$  by using of the procedures described in subsections of 4.2.2 and 4.2.3; and (iii) fitting linearly the obtained  $\alpha_{\text{eff}} \sim I_0$  and  $n_{\text{eff}} \sim I_0$  curves by the following equations

$$\alpha_{\text{eff}} = \alpha_2 + 0.544\alpha_3 I_0, \quad (14)$$

$$n_{\text{eff}} = n_2 + 0.422n_4 I_0. \quad (15)$$

Here  $\alpha_3$  and  $n_4$  are the fifth-order nonlinear absorption and refraction coefficients, respectively. If there is no fifth-order absorption effect, plotting  $\alpha_{\text{eff}}$  as a function of  $I_0$  should result in a horizon with  $\alpha_2$  being the intercept with the vertical axis. As the fifth-order absorption process presents, one obtains a straight line with an intercept of  $\alpha_2$  on the vertical axis and a slope of  $\alpha_3$ . Analogously, by plotting  $n_{\text{eff}} \sim I_0$ , the non-zero intercept on the vertical axis and the slope of the straight line are determined the third- and fifth-order nonlinear refraction indexes, respectively. It should be emphasized that Eqs. (14) and (15) are applicable for the material exhibiting weak nonlinear signal.

## 5. Linear optical properties of polycrystalline BiFeO<sub>3</sub> thin films

The BiFeO<sub>3</sub> ferroelectric thin film was deposited on the quartz substrate at 650°C by radio-frequency magnetron sputtering. The relevant ceramic target was prepared using conventional solid state reaction method starting with high-purity (>99%) oxide powders of Bi<sub>2</sub>O<sub>3</sub> and Fe<sub>2</sub>O<sub>3</sub>. It is noted that 10 wt % excess bismuth was utilized to compensate for bismuth loss during the preparation. During magnetron sputtering, the Ar/O<sub>2</sub> ratio was controlled at 7:1. The X-ray diffraction analysis demonstrated that the sample was a polycrystalline structure of perovskite phase. The observation from the scanning electron microscopy showed that the BiFeO<sub>3</sub> thin film and the substrate were distinctive and no evident inter-diffusion occurred between them.

The linear optical properties of the BiFeO<sub>3</sub> thin film were studied by optical transmittance measurements. The optical transmittance spectra of both the BiFeO<sub>3</sub> film on the quartz substrate and the substrate were recorded at room temperature with a spectrophotometer (Shimadzu UV-3600). The optical constants of the quartz substrate are  $d_{\text{sub}}=1$  mm,  $n_0^{\text{sub}}=1.51$ , and  $\alpha_0^{\text{sub}} \approx 0$ . Accordingly, the transmission of the quartz is 0.92, in agreement with the experimental measurement (dashed line in Fig. 4). As displayed in Fig. 4, it is clear that the BiFeO<sub>3</sub> thin film is highly transparent with transmittance between 58% and 91% in the visible and near-infrared wavelength regions. The oscillations in the transmittance are a result of the interference between the air-film and film-substrate interface. The well-

oscillating transmittance indicates that the BiFeO<sub>3</sub> film has a flat surface and a uniform thickness. The transparency of the film drops sharply at 500 nm and the absorption edge is located at 450 nm. With these desired qualities, the BiFeO<sub>3</sub> thin film should be a promising candidate for applications in waveguide and photonic devices.

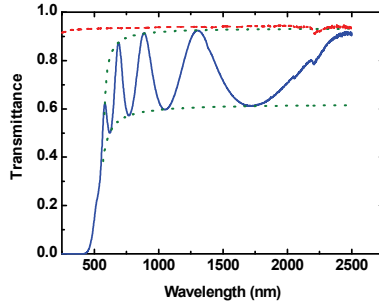


Fig. 4. Optical transmittance spectrum of BiFeO<sub>3</sub> thin film on a quartz substrate (solid line) and its envelope (dotted lines). For comparison, the result of quartz substrate is also presented (dashed line).

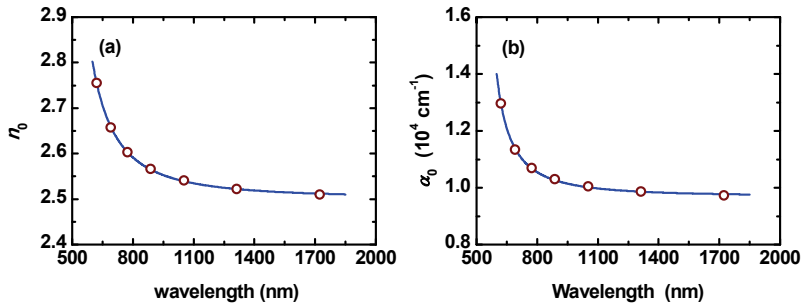


Fig. 5. Wavelength dispersion curve dependence of (a) the linear refractive index and (b) the absorption coefficient of the BiFeO<sub>3</sub> thin film. The circles are the calculated data and the solid lines are the theoretical fittings by improved Sellmeier-type formulae.

Figure 5 presents both the linear refractive index  $n_0$  and absorption coefficient  $\alpha_0$  of the BiFeO<sub>3</sub> thin film obtained from the transmittance curve using the envelope technique described in subsection 4.1. The circles represent the data obtained by transmittance measurements, which is well fitted to an improved Sellmeier-type dispersion relation (solid lines). As illustrated in Fig. 5(a), the refractive index decreases sharply with increasing wavelength (normal dispersion), suggesting a typical shape of a dispersion curve near an electronic interband transition. At 780 nm, the linear refractive index  $n_0$  and the absorption coefficient  $\alpha_0$  are calculated to be 2.60 and  $1.07 \times 10^4 \text{ cm}^{-1}$  though the improved Sellmeier-type dispersion fitting (Barboza & Cudney, 2009), respectively. The film thickness calculated in this way is determined to be  $510 \pm 23 \text{ nm}$ .

The optical bandgap of the BiFeO<sub>3</sub> film can be estimated using Tauc's formulae  $(\alpha_0/h\nu)^{2/m} = \text{Const.}(h\nu - E_g)$ . Although plotting  $(\alpha_0/h\nu)^{1/2}$  versus  $h\nu$  is illustrated in the insert of Fig. 6, the film is not the indirect bandgap material. From the data shown in Fig. 6, one

obtains  $m=1$  and extrapolates  $E_g=2.80$  eV, indicating that the BiFeO<sub>3</sub> ferroelectric has a direct bandgap at 443-nm wavelength. The observation is very close to the reported one prepared by pulse-laser deposition (Kumar et al., 2008). Of course, line and planar defects in the crystalline film and the crystalline size effect could result in a variation of the bandgap. Besides, the bandgap energy also depends on the film processing conditions.

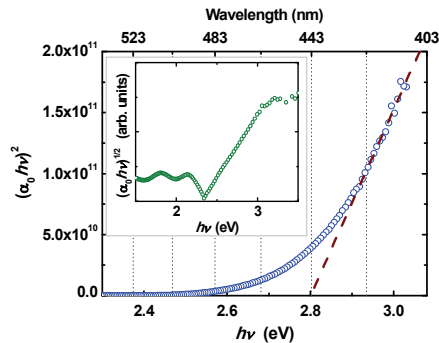


Fig. 6. Plot of  $(\alpha_0/h\nu)^2$  versus the photon energy  $h\nu$  for the BiFeO<sub>3</sub> film. The inset is  $(\alpha_0/h\nu)^{1/2}$  versus  $h\nu$ .

## 6. Optical nonlinearities of ferroelectric thin films

For the ferroelectric thin films, the large optical nonlinearity is attributed to the small grain size and good homogeneity of the films. During the past two decades, the optical nonlinear response of ferroelectric films has been extensively investigated. In this section, the nonlinear optical properties of some representative ferroelectrics in the nanosecond, picosecond, and femtosecond regimes are presented. Correspondingly, the physical mechanisms are revealed.

### 6.1 Third-order optical nonlinear properties of ferroelectric films in nanosecond and picosecond regimes

It has been demonstrated that ferroelectric thin films exhibit remarkable optical nonlinearities under the excitation of nanosecond and picosecond laser pulses. Most of these investigations have been mainly performed at  $\lambda=532$  and 1064 nm (or corresponding the excitation photon energy  $E_p=2.34$  and 1.17 eV). Table 1 summarizes the third-order optical nonlinear coefficients (both  $n_2$  and  $\alpha_2$ ) of some representative thin films in the nanosecond and picosecond regimes.

The magnitudes of the nonlinear refraction and absorption coefficients in most ferroelectrics at 532 nm are about  $10^{-1}$  cm<sup>2</sup>/GW and  $10^4$  cm/GW, respectively. However, the nonlinear responses of thin films at 1064 nm are much smaller than that at 532 nm. This is due to the nonlinear dispersion and could be interpreted by Kramers-Kronig relations (Boyd, 2009). Interestingly, although the excitation wavelength ( $\lambda=1064$  nm) for the measurements fulfills the three-photon absorption requirement ( $2h\nu < E_g < 3h\nu$ ), the nonlinear absorption processes in undoped and cerium-doped BaTiO<sub>3</sub> thin films are the two-photon absorption, which arises from the interaction of the strong laser pulses with intermediate levels in the forbidden gap induced by impurities (Zhang et al., 2000).

As is well known, the optical nonlinearity depends partly on the laser characteristics, in particular, on the laser pulse duration and on the wavelength, and partly on the material itself. As shown in Table 1, the huge difference of both  $n_2$  and  $\alpha_2$  in  $\text{CaCu}_3\text{Ti}_4\text{O}_{12}$  thin films with a pulse duration of 25 ps is two orders of magnitude smaller than that with 7 ns (Ning et al., 2009). In what follows, the origin of the observed optical nonlinearity in  $\text{CaCu}_3\text{Ti}_4\text{O}_{12}$  films is discussed briefly. As Ning et al. pointed out, the nonlinear absorption mainly originates from the two-photon absorption process because (i) both excitation energy ( $E_p=2.34$  eV) and bandgap ( $E_g=2.88$  eV) of  $\text{CaCu}_3\text{Ti}_4\text{O}_{12}$  films fulfil the two-photon absorption requirement ( $h\nu < E_g < 2h\nu$ ); and (ii) the free-carrier absorption effect can be negligible because the concentration of free carriers is very low in  $\text{CaCu}_3\text{Ti}_4\text{O}_{12}$  films as a high-constant-dielectric material. If the observed nonlinear absorption mainly arises from instantaneous two-photon absorption, the obtained  $\alpha_2$  should be independent of the laser pulse duration, which is quite different from the experimental observations. In fact, the

Films	$\lambda$ (nm)	$n_0$	$\alpha_0$ (cm <sup>-1</sup> )	$E_g$ (eV)	Pulse width	$n_2$ (cm <sup>2</sup> /GW)	$\alpha_2$ (cm/GW)	References
$\text{CaCu}_3\text{Ti}_4\text{O}_{12}$	532	2.85	$4.50 \times 10^4$	2.88	7 ns	15.6	$4.74 \times 10^5$	Ning et al. 2009
$(\text{Ba}_{0.7}\text{Sr}_{0.3})\text{TiO}_3$	532	2.00	$1.18 \times 10^4$	--	7 ns	0.65	$1.20 \times 10^5$	Shi et al. 2005
$\text{PbTiO}_3$	532	2.34	--	3.50	5 ns	--	$4.20 \times 10^4$	Ambika et al. 2009
$\text{Pb}_{0.5}\text{Sr}_{0.5}\text{TiO}_3$	532	2.27	--	3.55	5 ns	--	$3.50 \times 10^4$	Ambika et al. 2009
$\text{PbZr}_{0.53}\text{Ti}_{0.47}\text{O}_3$	532	--	--	3.39	5 ns	--	$7.0 \times 10^4$	Ambika et al. 2011
$(\text{Pb},\text{La})(\text{Zr},\text{Ti})\text{O}_3$	532	2.24	$2.80 \times 10^3$	3.54	38 ps	-2.26	--	Leng et al. 2007
$\text{SrBi}_2\text{Ta}_2\text{O}_9$	1064	2.25	$5.11 \times 10^3$	--	38 ps	0.19	--	Zhang et al. 1999
$\text{BaTiO}_3$	1064	2.22	$3.90 \times 10^3$	3.46	38 ps	--	51.7	Zhang et al. 2000
$\text{BaTiO}_3:\text{Ce}$	1064	2.08	$2.44 \times 10^3$	3.48	38 ps	--	59.3	Zhang et al. 2000
$\text{Bi}_{3.25}\text{La}_{0.75}\text{Ti}_3\text{O}_{12}$	532	2.49	$2.46 \times 10^3$	3.79	35 ps	0.31	$3.0 \times 10^4$	Shin et al. 2007
$\text{Bi}_{3.75}\text{Nd}_{0.25}\text{Ti}_3\text{O}_{12}$	532	2.01	$1.02 \times 10^3$	3.56	35 ps	0.94	$5.24 \times 10^4$	Wang et al. 2004
$\text{Bi}_2\text{Nd}_2\text{Ti}_3\text{O}_{12}$	532	2.28	$1.95 \times 10^3$	4.13	35 ps	0.70	$3.10 \times 10^4$	Gu et al. 2004
$\text{CaCu}_3\text{Ti}_4\text{O}_{12}$	532	2.85	$4.50 \times 10^4$	2.88	25 ps	0.13	$2.69 \times 10^3$	Ning et al. 2009

Table 1. Linear optical parameters and nonlinear optical coefficients of some representative ferroelectric thin films in nanosecond and picosecond regimes.

observed nonlinear absorption mainly originates from the instantaneous two-photon absorption and the accumulative process. As discussed in subsection 3.3, the physical mechanisms of  $\text{CaCu}_3\text{Ti}_4\text{O}_{12}$  films can be understood as follows. Under the pulsed excitation of 25 ps, two-photon absorption and population distribution are the main mechanisms of the nonlinear absorption and refraction, respectively. In a few nanosecond time scales, the accumulative absorption (two-step two-photon absorption) and refraction processes by impurities mainly contribute to the nonlinear absorption and refraction effects, respectively.

**6.2 Femtosecond third-order optical nonlinearity of polycrystalline  $\text{BiFeO}_3$**

As a new multifunctional material, ferroelectric thin films of  $\text{BiFeO}_3$  have many notable physical characteristics, such as prominent ferroelectricity, magnetic and electrical properties, and ferroelectric and dielectric characteristics. Besides high optical transparency and excellent optical homogeneity, the  $\text{BiFeO}_3$  thin films also exhibit remarkable optical nonlinearity (Gu et al., 2009a).

To give an insight into the detailed optical nonlinearities and to identify the corresponding physical mechanisms, the Z-scan measurements at different levels of laser intensities  $I_0$  were carried out. To exclude the optical nonlinearity from the substrate, Z-scan measurements on a 1.0-mm-thick quartz substrate were also performed. The nonlinear absorption coefficient of  $\alpha_2^{\text{sub}} \sim 0$  and the third-order refractive index of  $n_2^{\text{sub}} = 3.26 \times 10^{-7} \text{ cm}^2/\text{GW}$  are extracted from the best fittings between the Z-scan theory for characterizing the instantaneous optical nonlinearity (see subsection 4.2.2) and the experimental data illustrated in Fig. 7(a) at  $I_0 = 156 \text{ GW}/\text{cm}^2$ . The measured  $n_2^{\text{sub}}$  value is independent of  $I_0$  under our experimental conditions. Figure 7(b) displays typical open- and closed-aperture Z-scan traces for the 510-nm-thick  $\text{BiFeO}_3$  thin film on the 1.0-mm-thick quartz substrate at  $I_0 = 156 \text{ GW}/\text{cm}^2$ , showing positive signs for both absorptive and refractive nonlinearities, respectively.

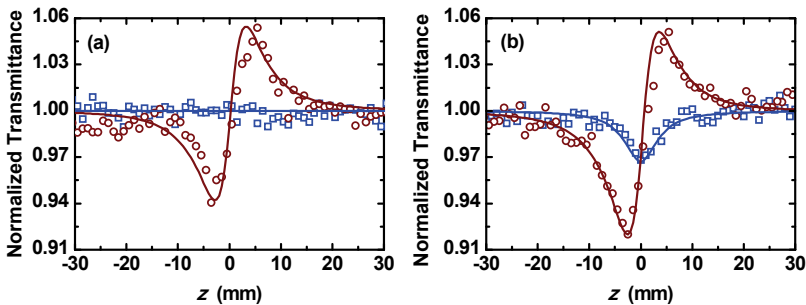


Fig. 7. Examples of Z-scans at  $I_0 = 156 \text{ GW}/\text{cm}^2$  for (a) the quartz substrate and (b) the  $\text{BiFeO}_3$  thin film deposited on the quartz substrate. Squares and circles are the open- and closed-aperture Z-scans, respectively; the solid lines are the best-fit curves calculated by the Z-scan theory.

Rigorous analysis is adopted Z-scan theory for a cascaded nonlinear medium (see subsection 4.2.3). The obtained nonlinear coefficients of  $\alpha_2$  and  $n_2$  for the  $\text{BiFeO}_3$  thin film at different levels of  $I_0$  display in Fig. 8. Clearly, the values of  $\alpha_2$  and  $n_2$  are independent of the optical intensity, indicating that the observed optical nonlinearities are of cubic nature; and  $\alpha_2 = 16.0 \pm 0.6 \text{ cm}/\text{GW}$  and  $n_2 = (1.46 \pm 0.06) \times 10^{-4} \text{ cm}^2/\text{GW}$  at 780 nm. It should be emphasized

that the above-said nonlinear coefficients are average values due to the polycrystalline, multi-domain nature of the BiFeO<sub>3</sub> film.

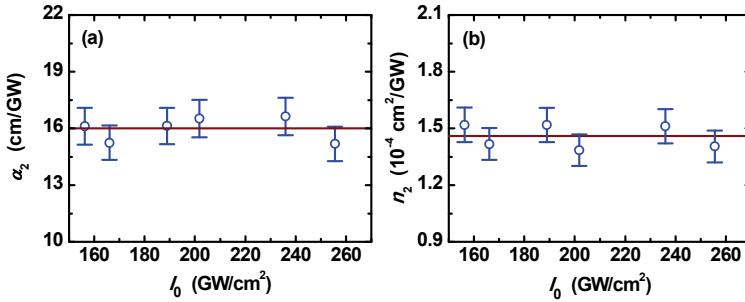


Fig. 8. Intensity independence of (a) nonlinear absorption coefficient  $\alpha_2$  and (b) nonlinear refraction index  $n_2$  for the BiFeO<sub>3</sub> thin film, respectively.

The physical mechanisms of the femtosecond optical nonlinearities in the BiFeO<sub>3</sub> film can be understood as follows. The positive nonlinear absorption mainly originates from the two-photon absorption process because (i) the Z-scan theory on two-photon absorbers fits open-aperture Z-scan experimental data well; and (ii) both excitation photon energy ( $h\nu=1.60$  eV) and bandgap ( $E_g=2.80$  eV) of the BiFeO<sub>3</sub> film fulfill the two-photon absorption requirement ( $h\nu < E_g < 2h\nu$ ). It is also known that the ultrafast femtosecond pulses can eliminate the contributions to the refractive nonlinearity from optical electrostriction and population redistribution since those effects have a response time much longer than 350 fs. Moreover, accumulative thermal effects are negligible because the experiments were conducted at a low repetition rate of 1 kHz. Consequently, the measured  $n_2$  should directly result from the electronic origin of the refractive nonlinearity in the BiFeO<sub>3</sub> thin film.

Films	$\lambda$ (nm)	$n_0$	$\alpha_0$ (cm <sup>-1</sup> )	$E_g$ (eV)	Pulse width	$n_2$ (cm <sup>2</sup> /GW)	$\alpha_2$ (cm/GW)	References
Ba <sub>0.6</sub> Sr <sub>0.4</sub> TiO <sub>3</sub>	790	2.20	--	3.64	60 fs	$6.1 \times 10^{-5}$	$8.7 \times 10^{-2}$	Liu et al. 2006
Bi <sub>5</sub> TiNbO <sub>9</sub>	800	2.28	$1.37 \times 10^2$	3.40	80 fs	--	$1.44 \times 10^4$	Yang et al. 2009
Bi <sub>1.95</sub> La <sub>1.05</sub> TiNbO <sub>9</sub>	800	2.02	$3.04 \times 10^4$	3.53	100 fs	--	$5.95 \times 10^3$	Chen et al. 2010
Ba <sub>0.6</sub> Sr <sub>0.4</sub> TiO <sub>3</sub>	800	2.25	$8.50 \times 10^3$	3.48	120 fs	$3.0 \times 10^{-4}$	1.70	Ning et al. 2011
Bi <sub>3.25</sub> La <sub>0.75</sub> Ti <sub>3</sub> O <sub>12</sub>	800	2.39	$1.73 \times 10^3$	--	140 fs	$1.9 \times 10^{-3}$	$-6.76 \times 10^{-3}$	Shi et al. 2006
BiFeO <sub>3</sub>	780	2.60	$1.07 \times 10^4$	2.80	350 fs	$1.5 \times 10^{-4}$	16	Gu et al. 2009a
BLFM	780	2.52	$5.77 \times 10^3$	2.90	350 fs	$2.0 \times 10^{-4}$	7.4	Gu et al. 2009b

Table 2. Linear optical parameters and femtosecond nonlinear optical coefficients of some representative ferroelectric thin films in the near infrared region.

With the proliferation of femtosecond laser systems, the understanding of the ultrafast nonlinear responses of ferroelectric thin films is of direct relevance to both academic interest and technological applications. As such, more and more efforts are concentrated on investigating the femtosecond nonlinear optical properties of ferroelectric films, since the complete understanding of these phenomena is still incomplete. Table 2 summarizes the femtosecond nonlinear optical response of some representative ferroelectric thin films in the near infrared region. The typical value of nonlinear refractive index  $n_2$  is about  $10^{-4}$  cm<sup>2</sup>/GW; whereas the nonlinear absorption coefficient  $\alpha_2$  is on a wide range of magnitudes from  $10^{-2}$  to  $10^4$  cm/GW, depending on both the laser characteristics and on the material itself. In the femtosecond regime, the accumulative effect could be minimized from the contribution of the optical nonlinearity. Thus, the nonlinear absorptive coefficient and refractive index measured with femtosecond laser pulses are closer to the intrinsic value. The electronic Kerr effect and two-photon absorption are the main mechanisms of the third-order nonlinear refraction and absorption, respectively.

### 6.3 Fifth-order optical nonlinearity in Bi<sub>0.9</sub>La<sub>0.1</sub>Fe<sub>0.98</sub>Mg<sub>0.02</sub>O<sub>3</sub> thin films

The ferroelectric Bi<sub>0.9</sub>La<sub>0.1</sub>Fe<sub>0.98</sub>Mg<sub>0.02</sub>O<sub>3</sub> (BLFM) thin films were deposited on quartz substrates at 650°C by radio frequency magnetron sputtering. The optical transmittance spectrum measurements indicate that the BLFM film has a flat surface, a uniform thickness, and good transparency (Gu et al., 2009b).

The nonlinear optical properties of BLFM films were characterized by the femtosecond Z-scan experiments at different levels of optical intensities  $I_0$ . To exclude the optical nonlinear contribution from the substrate, Z-scan measurements on a 1.0-mm-thick quartz substrate were performed. The measured  $\alpha_{2\text{sub}} \sim 0$  and  $n_{2\text{sub}} = 3.26 \times 10^{-7}$  cm<sup>2</sup>/GW are independent of  $I_0$  within the limit of  $I_0 \leq 270$  GW/cm<sup>2</sup>. As examples, for the BLFM thin film deposited on 1.0-mm-thick quartz substrate, typical open- and closed-aperture Z-scans at  $I_0 = 156$  and 225 GW/cm<sup>2</sup> are shown in Figs. 9(b) and 10(b), respectively. All the open-aperture Z-scans exhibit a symmetric valley with respect to the focus, typical of an induced positive nonlinear absorption effect. Apparently, the observed nonlinear absorption originates from the BLFM thin film only. In the closed-aperture Z-scans, the resultant nonlinear refraction arises from both the BLFM film and the substrate. At a relatively low intensity [see Fig. 9(b)], the closed-aperture Z-scan resembles to the substrate's signal [circles in Fig. 9(a)], suggesting that the nonlinear refraction signal from the BLFM is very weak. Under the excitation of high intensity [see Fig. 10(b)], however, it is noteworthy that the closed-aperture Z-scan displays a much lower peak-to-valley value in contrast with circles in Fig. 10(a), indicating that the BLFM film exhibits a negative nonlinear refraction effect. These facts may imply that both third- and higher-order nonlinearities, rather than a pure third-order process, simultaneously make contributions to the observed signal.

Adopting Z-scan theory for a cascaded nonlinear medium as described in subsection 4.2.3, the effective nonlinear coefficients (both  $\alpha_{\text{eff}}$  and  $n_{\text{eff}}$ ) of the BLFM film as a function of  $I_0$  are illustrated in Fig. 11. If the film only possesses a cubic nonlinearity in nature, the values of  $\alpha_{\text{eff}}$  and  $n_{\text{eff}}$  should be independent on the excitation intensity. As shown in Fig. 11, the values of  $\alpha_{\text{eff}}$  (or  $n_{\text{eff}}$ ) increases (or decreases) with increasing intensity, suggesting the occurrence of higher-order nonlinear processes. Applying the theory presented in subsection 4.2.4, the measured  $\alpha_{\text{eff}}$  and  $n_{\text{eff}}$  values are analyzed. The best fit shown in Fig. 11(a) indicates that  $\alpha_2 = 7.4 \pm 0.8$  cm/GW and  $\alpha_3 = (8.6 \pm 0.6) \times 10^{-2}$  cm<sup>3</sup>/GW<sup>2</sup>. From Fig. 11(b), we obtain  $n_2 = (2.0 \pm 1.2) \times 10^{-4}$  cm<sup>2</sup>/GW and  $n_4 = -(2.4 \pm 1.5) \times 10^{-6}$  cm<sup>4</sup>/GW<sup>2</sup> for the BLFM thin film

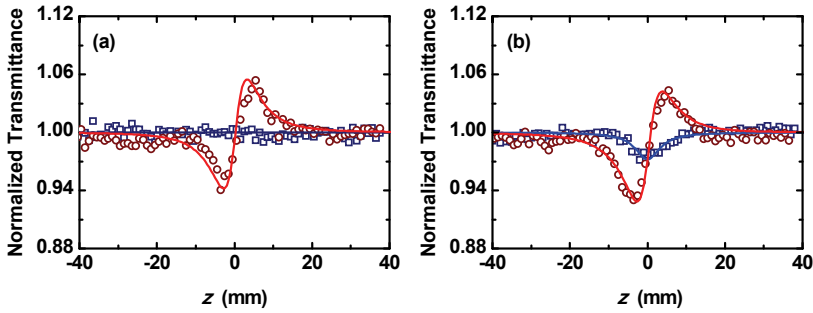


Fig. 9. Examples of Z-scans at  $I_0=156$  GW/cm<sup>2</sup> for both (a) the quartz substrate and (b) the BLFM thin film deposited on the quartz substrate. Squares and circles are the open- and closed-aperture Z-scans, respectively; while the solid lines are the best-fit curves calculated by the Z-scan theory.

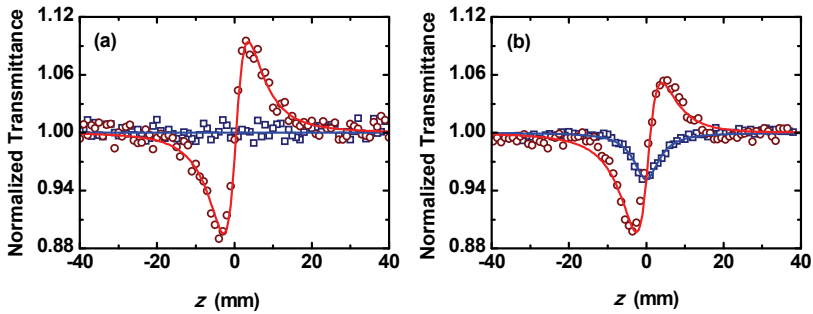


Fig. 10. Examples of Z-scans at  $I_0=225$  GW/cm<sup>2</sup> for both (a) the quartz substrate and (b) the BLFM thin film deposited on the quartz substrate. Squares and circles are the open- and closed-aperture Z-scans, respectively; while the solid lines are the best-fit curves calculated by the Z-scan theory.

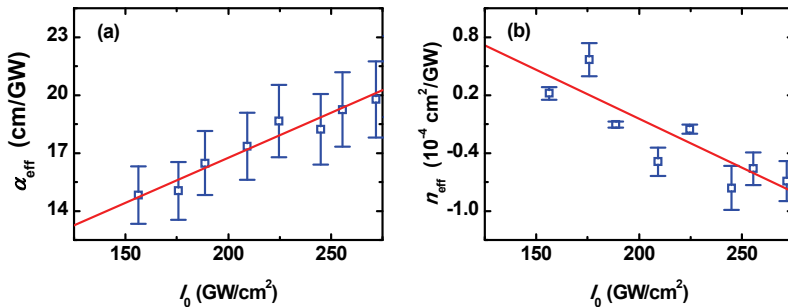


Fig. 11. Intensity dependence of (a) nonlinear absorption coefficient  $\alpha_{\text{eff}}$  and (b) nonlinear refraction index  $n_{\text{eff}}$  for the pure BLFM thin film, respectively. The solid lines are for guidance to the eyes.

within the limit of  $I_0 \leq 270 \text{ GW/cm}^2$ . Note that in our Z-scan analysis, the intensity change in the film transmission due to the light-induced nonlinear phase in the interference was ignored. This is because that the nonlinear path ( $n_{\text{eff}} L_{\text{eff}} I_0$ ) is estimated to be less than 3% of the wavelength with the parameters mentioned above, and too small to be detectable. For comparison, the obtained  $n_2$  value is three orders of magnitude larger than that of the substrate and is close to that of representative ferroelectric thin films in femtosecond regime as presented in Table 2.

The underlying mechanisms of the optical nonlinearities in the BLFM film are described in the following. As is well known, the nonlinear optical response strongly depends on the laser pulse duration. For instance, the population redistribution is the dominant mechanism of the third-order nonlinear refraction in the ferroelectric thin films in the picosecond regime (Shin et al, 2007). Under the excitation of the femtosecond pulses, the third-order refractive nonlinearity mainly arises from the distortion of the electron cloud. Besides, the accumulative thermal effect is negligible in our experiments because effort was taken to eliminate its contribution by employing ultrashort laser pulses at a low repetition rate (1 kHz in our laser system). Consequently, the measured  $n_2$  gives evidence of the electronic origin of the optical nonlinearity. In addition, the third-order nonlinear absorption is attributed to two-photon absorption because the excitation photon energy ( $h\nu=1.60 \text{ eV}$ ) and the bandgap ( $E_g=2.90 \text{ eV}$ ) of the BLFM films are satisfied with the two-photon absorption requirement ( $h\nu < E_g < 2h\nu$ ).

In general, there are at least two possible mechanisms contributing to the fifth-order nonlinearities: the intrinsic  $\chi^{(5)}$  susceptibility and a sequential  $\chi^{(3)}$ :  $\chi^{(1)}$  effect. We believe that the observed fifth-order nonlinearity mainly originates from an equivalent stepwise  $\chi^{(3)}$ :  $\chi^{(1)}$  process because the tendency of the measured coefficients (see Fig. 11) are analogous to those of two-photon-induced excited-state nonlinearities in organic molecules (Gu et al., 2008b) and two-photon-generated free-carrier nonlinearities in semiconductors (Said et al., 1992). The observation can be understood as follows. In the BLFM thin film, the population redistribution assisted by two-photon absorption produces an additional change in both the absorptive coefficient and refractive index, leading to an equivalent stepwise  $\chi^{(3)}$ :  $\chi^{(1)}$  process. Using the theory of two-photon-induced excited-state nonlinearities (Gu et al, 2008b), the absorptive and refractive cross-sections of populated states are estimated to be  $\sigma_a=(2.6\pm 0.3)\times 10^{-17} \text{ cm}^2$  and  $\sigma_r=(0.72\pm 0.46)\times 10^{-21} \text{ cm}^3$ , respectively, from the formulae  $\alpha_3=(3\pi)^{1/2}\sigma_a\alpha_2\tau_F/[8(2\ln 2)^{1/2}h\nu]$  and  $n_4=(3\pi)^{1/2}\sigma_r\alpha_2\tau_F/[8(2\ln 2)^{1/2}h\nu]$ . These values are on the same order of magnitude as the findings for organic molecules (Gu et al., 2008b) and semiconductors (Said et al., 1992), confirming that our inference of the origin of fifth-order effect is reasonable.

## 7. Summary and prospects

This book chapter describes the linear and femtosecond nonlinear optical properties of ferroelectric thin films. The fundamental optical constants (the linear absorption coefficient, linear refraction index, and bandgap energy) of the thin film are determined by optical transmittance measurements. The nonlinear optical response of the film is characterized by single-beam femtosecond Z-scan technique. The femtosecond third-order optical nonlinearity of polycrystalline BiFeO<sub>3</sub> thin film is presented. Moreover, the simultaneous third- and fifth-order nonlinearities in ferroelectric Bi<sub>0.9</sub>La<sub>0.1</sub>Fe<sub>0.98</sub>Mg<sub>0.02</sub>O<sub>3</sub> films are observed. Most importantly, the nonlinear optical properties of representative ferroelectric thin films in nanosecond, picosecond, and femtosecond regimes are summarized. The underlying mechanisms for the optical nonlinearities of ferroelectric thin films are discussed in details.

In literature, the optical nonlinearity will be enhanced by the dielectric and local field effect as well as the homogeneity in diameter, distribution and orientation in the ferroelectric films (Ruan et al., 2008). Researchers found that the nonlinear optical properties of ferroelectric films are also dependent on both fabrication techniques and deposited temperature (Saravanan et al., 2010). The ions (Pb, Mn, or K) dopant as the acceptor in ferroelectric films could reduce the dielectric loss and enhance the third-order optical nonlinearity (Zhang et al., 2008, Ning et al., 2011). By altering the lattice defect and subsequent the density of intermediate energy states, it is possible to tune the optical nonlinear response of ferroelectric thin films (Ambika et al., 2011). Metal nanoparticles doped ferroelectrics will introduce additional absorption peak arising from the surface plasmon resonance of nanoparticles. Accordingly, one could detect the huge enhancement of the near resonance nonlinearity in ferroelectric composite films (Chen et al., 2009). Besides, novel ferroelectric hybrid compounds, such as ferroelectric inorganic-organic hybrids, show the high thermal stability, insolubility in common solvents and water, and wide transparency range, which make them potential candidates for nonlinear photon devices (Zhao et al., 2009).

## 8. Acknowledgments

We acknowledge financial support from the National Science Foundation of China (Grant Number: 10704042) and the program for New Century Excellent Talents in University.

## 9. References

- Ambika, D.; Kumar, V.; Sandeep, C. S. S. & Philip, R. (2009). Non-linear optical properties of  $(\text{Pb}_{1-x}\text{Sr}_x)\text{TiO}_3$  thin films. *Applied Physics B – Lasers and Optics*, 97, 3 (Nov): 661-664.
- Ambika, D.; Kumar, V.; Sandeep, C. S. S. & Philip, R. (2011). Tunability of third order nonlinear absorption in  $(\text{Pb},\text{La})(\text{Zr},\text{Ti})\text{O}_3$  thin films. *Applied Physics Letters*, 98, 1 (Jan): 011903.
- Barboza, N. A. & Cudney, R. S. (2009). Improved Sellmeier equation for congruently grown lithium tantalate. *Applied Physics B – Lasers and Optics*, 95, 3 (Jun): 453-458.
- Boyd, R. W. (2009). *Nonlinear Optics*, Elsevier Inc., 978-981-272480-9 Singapore.
- Chen, K. S.; Gu, H. S.; Cai, Y. X.; Xiong, J. & Wang, A. M. (2009). Fe/SrBi<sub>2</sub>Nb<sub>2</sub>O<sub>9</sub> composite thin films with large third-order optical nonlinearities. *Journal of Alloys and Compounds*, 476, 1-2 (May): 635-638.
- Chen, H. Z.; Yang, B.; Zhang, M. F.; Wang, F. Y.; Cheah, K. & Cao, W. W. (2010). Third-order optical nonlinear absorption in Bi<sub>1.95</sub>La<sub>1.05</sub>TiNbO<sub>9</sub> thin films. *Thin Solid Films*, 518, 19 (Jul): 5585-5587.
- Chen, Y. F.; Beckwitt, K.; Wise, F. W.; Aitken, B. G.; Sanghera, J. S. & Aggarwal, I. D. (2006). Measurement of fifth- and seventh-order nonlinearities of glasses. *Journal of the Optical Society of American B – Optical Physics*, 23, 2 (Feb): 347-352.
- DiDomenico, M. & Wemple, S. H. (1969). Oxygen-octahedra ferroelectrics. I. Theory of electro-optical and nonlinear optical effects. *Journal of Applied Physics*, 40, 2 (Feb): 720-734.
- Gu, B.; Wang, Y. H.; Peng, X. C.; Ding, J. P.; He, J. L. & Wang, H. T. (2004). Giant optical nonlinearity of a Bi<sub>2</sub>Nd<sub>2</sub>Ti<sub>3</sub>O<sub>12</sub> ferroelectric thin film. *Applied Physics Letters*, 85, 17(Oct): 3687-3689.

- Gu, B.; Ji, W. & Huang, X. Q. (2008a). Analytical expression for femtosecond-pulsed z scans on instantaneous nonlinearity. *Applied Optics*, 47, 9 (Mar): 1187-1192.
- Gu, B.; Sun, Y. & Ji, W. (2008b). Two-photon-induced excited-state nonlinearities. *Optics Express*, 16, 22 (Oct): 17745-17751.
- Gu, B.; Wang, Y.; Wang, J. & Ji, W. (2009a). Femtosecond third-order optical nonlinearity of polycrystalline BiFeO<sub>3</sub>. *Optics Express*, 17, 13(June): 10970-10975.
- Gu, B.; Wang, Y.; Ji, W. & Wang, J. (2009b). Observation of a fifth-order optical nonlinearity in Bi<sub>0.9</sub>La<sub>0.1</sub>Fe<sub>0.98</sub>Mg<sub>0.02</sub>O<sub>3</sub> ferroelectric thin films. *Applied Physics Letters*, 95, 4(Aug): 041114.
- Gu, B.; Lou, K.; Chen, J.; Li, Y. N.; Wang, H. T. & Ji, W. (2010). Excited-state enhancement of third-order optical nonlinearities: photodynamics and characterization. *Optics Express*, 18, 26 (Dec): 26843-26853.
- Kityk, A. V.; Czaplicki, R.; Klöpperpieper, A.; Andrushchak, A. S. & Sahraoui, B. (2010). Spontaneous and electric field induced quadratic optical nonlinearity in ferroelectric crystals AgNa(NO<sub>2</sub>)<sub>2</sub>. *Applied Physics Letters*, 96, 6 (Feb): 061911.
- Kumar, A.; Rai, R. C.; Podraza, N. J.; Denev, S.; Ramirez, M.; Chu, Y. H.; Martin, L. W.; Ihlefeld, J.; Heeg, T.; Schubert, J.; Schlom, D. G.; Orenstein, J.; Ramesh, R.; Collins, R. W.; Musfeldt, J. L. & Gopalan, V. (2008). Linear and nonlinear optical properties of BiFeO<sub>3</sub>. *Applied Physics Letters*, 92, 12 (Mar): 121915.
- Leng, W. J.; Yang, C. R.; Ji, H.; Zhang, J. H.; Tang, J. L.; Chen, H. W. & Gao, L. F. (2007). Linear and nonlinear optical properties of (Pb, La)(Zr, Ti)O<sub>3</sub> ferroelectric thin films grown by radio-frequency magnetron sputtering. *Journal of Physics D – Applied Physics*, 40, 4 (Feb): 1206-1210.
- Liu, S. W.; Xu, J.; Guzun, D.; Salamo, G. J.; Chen, C. L.; Lin, Y. & Xiao, M. (2006). Nonlinear optical absorption and refraction of epitaxial Ba<sub>0.6</sub>Sr<sub>0.4</sub>TiO<sub>3</sub> thin films on (001) MgO substrates. *Applied Physics B-Lasers and Optics*, 82, 3(Mar): 443-447.
- Murgan, R.; Tilley, D. R.; Ishibashi, Y.; Webb, J. F. & Osman, J. (2002). Calculation of nonlinear-susceptibility tensor components in ferroelectrics: cubic, tetragonal, and rhombohedral symmetries. *Journal of the Optical Society of American B – Optical Physics*, 19, 9 (Sep): 2007-2021.
- Ning, T. Y.; Chen, C.; Zhou, Y. L.; Lu, H.; Zhang, D. X.; Ming, H. & Yang, G. Z. (2009). Larger optical nonlinearity in CaCu<sub>3</sub>Ti<sub>4</sub>O<sub>12</sub> thin films. *Applied Physics A – Materials Science & Processing*, 94, 3 (Mar): 567-570.
- Ning, T. Y.; Chen, C.; Wang, C.; Zhou, Y. L.; Zhang, D. X.; Ming, H. & Yang, G. Z. (2011). Enhanced femtosecond optical nonlinearity of Mn doped Ba<sub>0.6</sub>Sr<sub>0.4</sub>TiO<sub>3</sub> films. *Journal of Applied Physics*, 109, 1 (Jan): 013101.
- Ruan, K. B.; Gao, A. M.; Deng, W. L.; Chen, X. M. & Bao, D. (2008). Orientation dependent photoluminescent properties of chemical solution derived Bi<sub>4-x</sub>Eu<sub>x</sub>Ti<sub>3</sub>O<sub>12</sub> ferroelectric thin films. *Journal of Applied Physics*, 104, 3 (Aug): 036101.
- Said, A. A.; Sheik-Bahae, M.; Hagan, D. J.; Wei, T. H.; Wang, J. & Van Stryland, E. W. (1992). Determination of bound-electronic and free-carrier nonlinearities in ZnSe, GaAs, CdTe, and ZnTe. *Journal of the Optical Society of American B – Optical Physics*, 9, 3 (Mar): 405-414.
- Saravanan, K. V.; Raju, K. C. J.; Krishna, M. G.; Tewari, S. P. & Rao, S. V. (2010). Large three-photon absorption in Ba<sub>0.5</sub>Sr<sub>0.5</sub>TiO<sub>3</sub> films studied using Z-scan technique. *Applied Physics Letters*, 96, 23(Jun): 232905.

- Sheik-Bahae, M.; Said, A. A.; Wei, T. H.; Hagan, D. J. & Van Stryland, E. W. (1990). Sensitive measurement of optical nonlinearities using a single beam. *IEEE Journal of Quantum Electronics*, 26, 4(Apr): 760-769.
- Shi, F. W.; Meng, X. J.; Wang, G. S.; Sun, J. L.; Lin, T.; Ma, J. H.; Li, Y. W. & Chu, J. H. (2006). The third-order optical nonlinearity of  $\text{Bi}_{3.25}\text{La}_{0.75}\text{Ti}_3\text{O}_{12}$  ferroelectric thin film on quartz. *Thin Solid Films*, 496, 2 (Feb): 333-335.
- Shi, P.; Yao, X.; Zhang, L. Y.; Wu, X. Q.; Wang, M. Q. & Wan, X. (2005). Third-order optical nonlinearity of  $(\text{Ba}_{0.7}\text{Sr}_{0.3})\text{TiO}_3$  ferroelectric thin films fabricated by soft solution processing. *Soild State Communications*, 134, 9 (Jun): 589-593.
- Shin, H.; Chang, H. C.; Boyd, R. W.; Choi, M. R. & Jo, W. (2007). Large nonlinear optical response of polycrystalline  $\text{Bi}_{3.25}\text{La}_{0.75}\text{Ti}_3\text{O}_{12}$  ferroelectric thin films on quartz substrates. *Optics Letters*, 32, 16 (Aug): 2453-2455.
- Swanepoel, R. (1983). Determination of the thickness and optical constants of amorphous silicon. *Journal of Physics E: Scientific Instruments*, 16, 12 (Dec): 1214-1222.
- Tauc, J.; Gigorovici, R. & Vancu, A. (1966). Optical properties and electronic structure of amorphous germanium. *Physica Status Solidi B*, 15, 2 (Mar): 627-637.
- Tsai, C. A.; Wu, A. Y.; Liou, W. R. & Lin, W. C. (2004). Second harmonic generation in Barium Titanate thin films on silica glass by corona poling. *Japanese Journal of Applied Physics*, 43, 4A (Apr): 1348-1356.
- Wang, Y. H.; Gu, B.; Xu, G. D. & Zhu, Y. Y. (2004). Nonlinear optical properties of neodymium-doped bismuth titanate thin films using Z-scan technique. *Applied Physics Letters*, 84, 10 (Mar): 1686-1688.
- Yang, B.; Chen, H. Z.; Zhang, M. F.; Wang, F. Y.; Cheah, K. & Cao, W. W. (2009). Nonlinear optical absorption in  $\text{Bi}_3\text{TiNbO}_9$  thin films using Z-scan technique. *Applied Physics A – Materials Science & Processing*, 96, 4 (Sep): 1017-1021.
- Zang, W. P.; Tian, J. G.; Liu, Z. B.; Zhou, W. Y.; Zhang, C. P. & Zhang, G. Y. (2003). Study on Z-scan characteristics of cascaded nonlinear media. *Applied Physics B-Lasers and Optics*, 77, 5(Oct): 529-533.
- Zhang, T.; Zhang, W. F.; Chen, Y. H. & Yin, J. (2008). Third-order optical nonlinearities of lead-free  $(\text{Na}_{1-x}\text{K}_x)_{0.5}\text{Bi}_{0.5}\text{TiO}_3$  thin films. *Optics Communications*, 281, 3(Feb): 439-443.
- Zhang, W. F.; Zhang, M. S.; Yin, Z.; Gu, Y. Z.; Du, Z. L. & Yu, B. L. (1999). Large third-order optical nonlinearity in  $\text{SrBi}_2\text{Ta}_2\text{O}_9$  thin films. *Applied Physics Letters*, 95, 7(Aug): 902-904.
- Zhang, W. F.; Huang, Y. B.; Zhang, M. S. & Liu, Z. G. (2000). Nonlinear optical absorption in undoped and cerium-doped  $\text{BaTiO}_3$  thin films using Z-scan technique. *Applied Physics Letters*, 76, 8(Feb): 1003-1005.
- Zhao, H. R.; Li, D. P.; Ren, X. M.; Song, Y. & Jin, W. Q. (2009). Larger spontaneous polarization ferroelectric inorganic-organic hybrids:  $[\text{PbI}_3]_\infty$  chains directed organic cations aggregation to Kagomé-shaped tubular architecture. *Journal of the American Chemical Society*, 132, 1 (Jan): 18-†.

# Localized States in Narrow-Gap Ferroelectric-Semiconductor PbSnTe: Injection Currents, IR and THz Photosensitivity, Magnetic Field Effects

Alexander Klimov and Vladimir Shumsky  
*Rzhanov Institute of Semiconductor Physics, Siberian Branch of RAS  
 Russia*

## 1. Introduction

For the first time, unusual properties of solid solutions  $\text{Pb}_{1-x}\text{Sn}_x\text{Te}:\text{In}$  with  $x \approx 0.24-0.29$  (below,  $\text{PbSnTe}:\text{In}$ ) were reported in the literature in 1979 (Vul et al., 1979; Akimov et al., 1979). Today, ample experimental data on the properties of  $\text{PbSnTe}:\text{In}$  and theoretical models to explain those properties, and also many reviews of known data for this material (Kaidanov & Ravich, 1985; Volkov et al., 2002), are available. Primary attention was focused on explanation of the following revealed features:

- Fermi-level pinning at the middle of the forbidden band in samples with certain compositions and indium contents, and a low conductivity of the material at temperatures  $T \leq 20$  K;
- a high photosensitivity of the material:  $\text{PbSnTe}:\text{In}$  readily responds to extremely low radiation fluxes, including those emitted by heated bodies whose temperature only slightly exceeds the sample temperature;
- long-term photosignal decay and residual conduction observed in  $\text{PbSnTe}:\text{In}$  samples after the illumination is switched off.

From the literature (Herrmann & Mollmann, 1983; Vinogradov & Kucherenko, 1991) it was known that in  $\text{PbSnTe}:\text{In}$  samples cooled to temperatures below 20 K spontaneous polarization arises. In the same temperature interval the samples exhibit a pronounced (up to two orders of magnitude) decrease of static dielectric permittivity, whose dependence on temperature yields for the ferroelectric phase transition point a value  $T_C = 17 \pm 20$  K. Like for the well-known isotopic ferroelectric solid solution  $(\text{SrTiO}_3^{18})_{1-x}(\text{SrTiO}_3^{16})_x$  (Mitsuru & Ruiping, 2000), for  $\text{Pb}_{1-x}\text{Sn}_x\text{Te}:\text{In}$  there exists a certain critical value of  $x$  such that with less Sn the solid solution behaves as a virtual ferroelectric with a negative temperature  $T_C$  while at greater values of  $x$  it behaves as an ordinary ferroelectric with temperature  $T_C$  dependent on the composition  $x$ . Although the occurrence of a “metal-dielectric transition” in  $\text{PbSnTe}:\text{In}$  at temperatures  $T \leq 20$  K presents a widely recognized fact, manifested as Fermi-level pinning at the middle of the energy gap of  $\text{PbSnTe}:\text{In}$  and resulting in a low (almost intrinsic) concentration of charge carriers in the material, available literature tacitly assumes that in dielectric state no contact injection occurs in  $\text{PbSnTe}$  samples, and only equilibrium charge carriers define the charge transport in the material. Yet, it was firmly established in

(Akimov et al., 2005) that at helium temperatures in electric fields stronger than about 100 V/cm PbSnTe:In samples become dominated by space-charge-limited injection currents in the presence of electron traps, with the temperature dependence of the current showing a good agreement with calculations performed by the theory of space-charge-limited currents on the assumption of temperature-dependent static dielectric permittivity of the material. It was found that the behavior of static dielectric permittivity as a function of temperature depends on the strength of an electric field superimposed onto the sample, this fact complicating the description of the current versus voltage and temperature (Klimov & Shumsky, 2003). It is clear that with just equilibrium charge carriers taking part in the charge transport the static dielectric permittivity itself and its variation with temperature would not be factors affecting the transport and current-voltage characteristics of the samples.

As stated above, the photoelectric properties of PbSnTe:In at helium temperatures from the very beginning griped fixed attention of researchers; those properties have also triggered many subsequent studies in this field. In steady state, a pronounced sensitivity even to radiation emitted by moderately heated objects with temperatures  $T = 30\text{--}35$  K was observed. In the latter situation, at a working temperature  $T=4.2$  K the photosignal could display decay times ranging from several fractions of millisecond to many hours and even days.

There are several possible explanations to the high photosensitivity and long-term photocurrent relaxation. Until recently, the most frequent explanation rested on an assumption of Yang-Teller (YT) instability that could occur in the crystal surrounding of some point defects in PbSnTe:In; more specifically, it was assumed that an electron capture into some trap could result in lowering of the electronic level of the trap (Volkov & Pankratov, 1980). The electron transition from the conduction band of PbSnTe to the YT center and the reverse transition, electron emission from the center, are thermally activated processes with an activation energy of 0.01 eV, and this leads to a photoconduction decay time increased at  $T=4$  K by a factor of  $10^{12}$  in comparison with the case of no-barrier trapping.

Other alternative explanations were also reported (Vinogradov et al., 1980; Drabkin & Moizhes, 1983) resting on the possibility of emergence, on electron excitation, of a potential barrier that acts to hamper the electron recombination at the level from which the electron was excited by absorbed radiation. The quenching of photoconduction with increasing temperature or following an application of a strong electric-field pulse was normally attributed to increased probability of electron penetration through the potential barrier.

The spectral dependence of photoconduction corresponds to the fundamental absorption band of PbSnTe (band-to-band transitions) (Zasavitskii et al., 1986); nonetheless, photoconduction around wavelengths 115  $\mu\text{m}$  and 220  $\mu\text{m}$  (Romcevic et al, 1991), and also in extended wavelength regions 100 to 200 and around 336  $\mu\text{m}$ , was also reported (Khokhlov et al., 2000; Akimov et al., 2006; Klimov et al., 2007).

In a certain range of applied electric field and illumination intensities, current self-oscillations were observed in PbSnTe (Akimov et al., 1993; Borodin et al., 1997a), which until recently were given no exhaustive explanation.

Recently, the idea about the existence of negative-U centers was revisited by some workers. Possible emergence of the latter situation is described within the frame of two models. In the first, «deformation» model, the energy of a center is defined by the distortion of its nearest crystal surrounding (Volkov & Pankratov, 1980). The second model draws attention to the variable valence of group 3 impurities that may appear in single-charged acceptor state ( $s^2p^1$ ), in neutral state ( $s^1p^2$ ), or in single-charged donor state ( $s^0p^3$ ) (Drabkin & Moizhes,

1981). Those levels are deep; nonetheless, there may also exist shallow levels split from the conduction-band bottom by the Coulomb potential of the center or a system of centers in the state ( $s^0p^3$ ) (Volkov & Ruchaiski, 1995). As it was noted in (Volkov et al., 2002), both models are capable of providing a reasonable explanation to the effects observed in PbSnTe:In.

Available models, however, disregard the influence the ferroelectric properties of PbSnTe have on the photoelectric phenomena in the material, and the dark conduction and photoconduction in it is not treated in those models with due allowance for the contribution due to contact-injected charge carriers. The change of the slope of the temperature dependence of current at low temperatures was most often attributed to the variation of the energy position of the level due to indium impurities in the band gap without any explanation given to possible reasons for this phenomenon.

The purpose of the present publication is a data analysis and a development of the concept resting on the following basic ideas:

- transport of charge carriers in PbSnTe:In with  $x \approx 0.24-0.29$  is defined by contact injection;
- the energy gap of PbSnTe:In contains localized states acting as electron traps;
- the ferroelectric phase transition has a substantial influence on the observed electrical, magnetic, and photoelectric properties of PbSnTe:In and, above all, on the current-voltage characteristics of samples and on the relaxation of conduction-band electrons injected into the material by an electric field or radiation;
- the dielectric state of PbSnTe:In at helium temperatures is related with the compositional disorder of the material as a solid solution.

We believe that the discussion of the listed, still poorly studied points will enable a better understanding of transport phenomena in PbSnTe:In, including the situation in magnetic fields, and will elucidate the role of the ferroelectric phase transition in PbSnTe transport properties.

## **2. Temperature dependence of conductivity and capacitance, photodielectric effect**

### **2.1 Experimental samples and measurement procedure**

We examined PbSnTe:In films MBE-grown on BaF<sub>2</sub> substrates (Klimov & Shumsky, 2001a, 2003). The thickness of the films was about 1  $\mu\text{m}$ , their tin content was  $x \approx 0.26$ , and the indium content,  $\cong 3\%$ . For measuring the current-voltage and capacitance-voltage characteristics, special comb structures formed by two metal contacts were prepared. The length of the gap between the contacts was 15 000  $\mu\text{m}$ , and the gap width was 16 to 64  $\mu\text{m}$ . In calculating the capacitance of the structure, the parallel-plate capacitor approximation was used; the applicability of this approximation was justified by the high value of dielectric permittivity,  $\epsilon \geq 400$ . For Hall measurements, a standard Hall bar with four potentiometric contacts was employed. The measured sample was contained in a metal chamber that screened it from background radiation.

As the source of radiation, two sources were used. The first source, in what follows to be referred to as the source IR<sub>1</sub>, was a small-size incandescent lamp in glass bulb installed directly in the chamber with the sample; this lamp emitted radiation with  $\lambda \leq 2 \mu\text{m}$  that, following absorption, caused band-to-band transitions in PbSnTe:In. The second source, to be referred to as the source IR<sub>2</sub>, was a tungsten incandescent-lamp spiral mounted in an evacuated volume with a polyethylene exit window; behind the window, a combined filter

was installed that allowed only radiation with quantum energies lower than the band-gap energy of PbSnTe:In to come from the volume.

## 2.2 Experimental data

At low temperatures,  $T < 20$  K, at zero voltage in the measurement circuit an electric current was registered; this current could be due to the spontaneous voltage induced in PbSnTe:In by the ferroelectric phase transition (Herrmann & Mollmann, 1983; Nasybbulin et al., 1983; Vinogradov & Kucherenko, 1991; Klimov & Shumsky, 2001b). The strength of the observed current decreased in time below  $10^{-14}$  A, going beyond the measurement accuracy.

At bias voltages below 0.01 V and  $T = 4.2$  K without illumination, no direct measurement of sample resistance was possible because the current was too weak ( $< 10^{-14}$  A). The dark resistance of the sample was therefore evaluated from the proportion between the dark current and the current under illumination, also easily measurable at low voltages, which could be approximated into the interval of low bias voltages. The estimate gave a value greater than  $10^{14}$  Ohm, translating into a specific-resistance value  $\rho > 5 \cdot 10^{12}$  Ohm·cm (Klimov & Shumsky, 2001a).

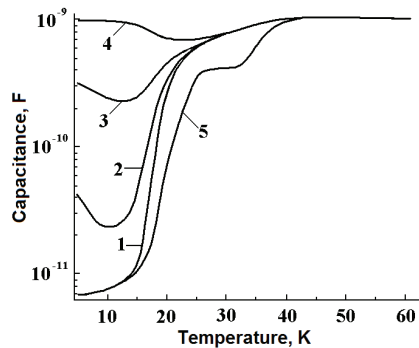


Fig. 1. The curves of sample capacitance versus temperature measured in the dark (1, 5) and under illumination with source  $IR_1$  (2-4). The dc bias voltages are 0 V for curves 1-4 and 1.55 V for curve 5. The voltage supplied to the source, or illumination intensity, increases on going from curve 2 (0.14 V) to curve 4 (1.52 V), the nominal operating voltage of the source being 6 V.

Figure 1 shows the curves of capacitance versus temperature in a sample under zero bias voltage measured in the dark and under illumination, and also a similar curve measured in the dark under dc bias voltage  $U = 1.55$  V at frequency  $f = 3.3$  kHz (Klimov & Shumsky, 2001a, 2003). A specific feature displayed by the curves is a decrease of capacitance reaching approximately one hundred times on decreasing the temperature from  $T = 25$  K to  $T = 15$  K without illumination, and also a weak variation of the capacitance in the same temperature interval under illumination. In other words, illumination of the sample at temperatures below 20 - 30 K resulted in increased capacitance of the structure. Another important feature here is the shift towards higher temperatures of the temperature range in which the dark capacitance exhibited strong variations on superimposing a sufficiently strong electric field across the sample. In the latter situation, in the curve of capacitance versus temperature there arises a characteristic shelf in the temperature interval  $T = 25 \div 30$  K.

In (Vinogradov & Kucherenko, 1991) a similar temperature dependence of capacitance was interpreted as an indication for a ferroelectric phase transition. In our samples, the dependence of inverse dielectric permittivity on temperature has yielded for the Curie point a value  $T_C=17.5$  K under zero bias voltage and a value 19.5 K under bias voltage 1.55 V. The active and capacitive components of sample conductivity show an increase over the temperature interval from 4.2 to 30 K both during increase of temperature under no-illumination conditions (a) and at fixed temperature during increase of illumination intensity (b). The relation between the concentration of free charge carriers and the sample capacitance in both indicated situations, a and b, for the sources IR<sub>1</sub> and IR<sub>2</sub> proved to be rather intricate.

Figure 2 shows the experimental dependences of the capacitance of structure on its conductance,  $C=f(\sigma)$ . It could be expected that, providing that the capacitance variations were defined by the variation of the concentration of free charge carriers in the samples, then, no matter how the latter variation was achieved, the dependence of capacitance versus conductivity would follow one and the same curve in the coordinates  $\sigma$ -C.

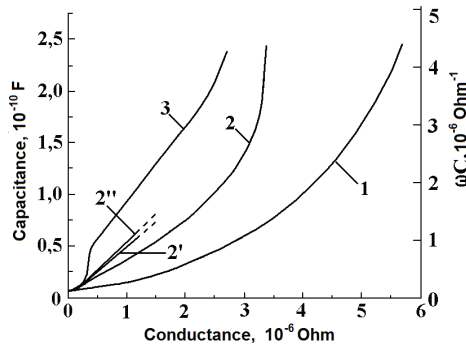


Fig. 2. The proportion between the active conductance of the sample  $R^{-1}$  and its capacitance (left axis) or the capacitive conductance (right axis). Frequency  $f=3.3$  kHz. Curve 1 – growth of conductivity and resistance due to increase of temperature from  $T=4.2$  K to approximately  $T=25$  K. Curves 2, 2', and 2'' – growth of conductivity under turned-on illumination from source IR<sub>1</sub>, 3 – the same with source IR<sub>2</sub>. The rise time of conductivity to its maximum value: 2, 3 – 600 s, 2' – 6 s, 2'' – 0.4 s. The curve under illumination were measured at  $T=4.2$  K.

However, the relation between the conductivity and capacitance under temperature variations (curve 1) proved to be fundamentally different from that in illuminated sample at liquid-helium temperature (see Figure 2). Moreover, the curve of capacitance versus conductance in the sample illuminated with far-IR source IR<sub>2</sub> (curve 3) was found to show qualitative differences from the curve displayed under illumination with source IR<sub>1</sub> (curves 2, 2', 2''). Here, although an increase in illumination intensity from source IR<sub>1</sub> provides for a sharper initial growth of the curve  $C=f(\sigma)$ , the slope of this curve tends to saturation, always remaining several times lower than the slope of the similar curve registered with source IR<sub>2</sub>. Measurements of sample capacitance versus the strength of constant electric field superimposed onto sample performed at various temperatures under no-illumination conditions showed that on decreasing the temperature the above dependence became less

pronounced (Klimov & Shumsky, 2001b). Here, in the temperature interval  $T < 20$  K the capacitance behaves non-monotonically as a function of electric-field strength, with an emerging characteristic maximum whose position moves towards higher fields with decreasing temperature.

The shape of the dependences dramatically depends on the rate of change of the electric field (Klimov & Shumsky, 2001b). Under slowly increased field, «quenching of photocapacitance» to the dark level is observed already under electric-field intensities of 400 V/cm. At a rapid sweep of the electric field, the dependences show an intricate behavior with a characteristic peak displayed at  $E = 400$  V/cm. The curves  $C(V)$  measured with decreasing electric field differ in shape from the curves registered during an increase of the electric field. Thus, the observed dependences with a capacitance maximum observed at a certain electric-field strength exhibit a non-stationary dynamic pattern.

### 2.3 Summary

1. The current-voltage characteristics measured under illumination were linear only at low bias voltages ( $< 0.015$  V); the current-voltage curves measured in the dark proved to be linear at even lower voltages.
2. At helium temperatures the films showed a spontaneous voltage typical of ferroelectrics.
3. A photodielectric effect in PbSnTe:In films was observed. This effect consisted in a strong (by two orders of magnitude) increase of low-frequency dielectric permittivity at temperatures below 20 K in samples exposed to electromagnetic radiation. The effect can be attributed to charging processes of impurity centers and to an increase of the effective radii of those centers.
4. A more pronounced increase of capacitance (and dielectric permittivity) was observed in samples exposed to radiation in the fundamental absorption band of PbSnTe:In.
5. The shape of measured curves of capacitance versus field strength was found to be dependent on the rate of change of the field  $\partial E/\partial t$ .

## 3. Space-charge-limited currents

### 3.1 Current-voltage characteristics at $T=4.2$ K

In «dielectric state», discussed in Introduction, at low concentrations of charge carriers in the allowed bands transport of charge carriers should obey the theory of space-charge-limited currents (Akimov et al., 2005). With traps for charge carriers present in PbSnTe:In, the filling of such traps should have an influence both on the current-voltage characteristics and on the photoconduction relaxation. Experimental structures used for measuring current-voltage characteristics were similar to the structures described in Section 2.1. They were formed by two metal contacts prepared on the surface of PbSnTe:In films. The length of the gap between the contacts was 2 000 to 15 000  $\mu\text{m}$ , and the gap width was 16 to 64  $\mu\text{m}$ . Current-voltage characteristics were measured in the interval of voltages up to 7-8 V using dc sources. In measuring current-voltage characteristics at voltages in excess of 8 V, a generator of rectangular pulses was used to avoid heating of the sample. The pulses followed at time intervals  $3 \cdot 10^{-4}$  s, and the width of the pulses was 1, 4, or 8  $\mu\text{s}$ , depending on the voltage range.

Figure 3 shows the current-voltage curve of an PbSnTe:In structure measured at  $T=4.2$  K. In the curve, the following features are distinctly seen: a) a weak growth of the current at a

level of  $(2-3) \cdot 10^{-13}$  A; b) voltage intervals over which the current shows first a linear and, then, a quadratic growth; c) a transition region; and d) a quadratic dependence of the current on voltage in the range of voltages 20 – 60 V.

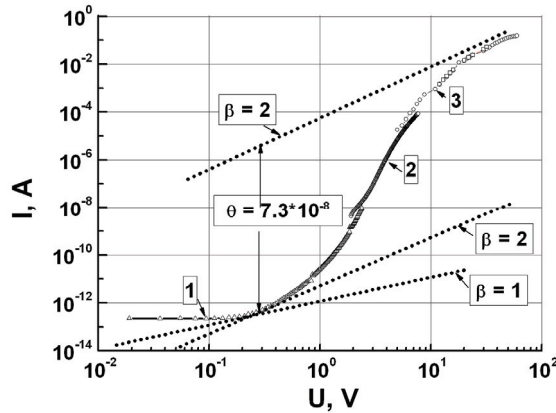


Fig. 3. Current-voltage characteristics of a PbSnTe:In sample at  $T = 4.2$  K. The curves were measured: (1) and (2) - under dc conditions; (3) - in pulsed mode (3).

In the region above  $U \approx 0.2$  V, the current-voltage characteristics can be understood within the theory of space-charge-limited currents (Lampert & Mark, 1970). The extended transition region with a sharp growth of current over the voltage interval 1 to 10 V points to the presence of various traps in the structure that at  $U > 20$  V become filled with charge carriers. Measurements of current-voltage characteristics at three different widths of the inter-contact gap, 16, 32, and 64  $\mu\text{m}$ , showed that, with decrease of the effective inter-contact separation owing to metal diffusion taken into account, the experimentally measured current values within  $\pm 10\%$  obey the proportion  $I_1 : I_2 : I_3 = L_1^{-3} : L_2^{-3} : L_3^{-3}$ , in line with the theory of space-charge-limited currents.

### 3.2 Temperature dependence of the current

In the experimental dependences of the current on reciprocal temperature at different voltages (see Figure 4), the following fact is engaging attention: the activation energies  $\Delta E$  calculated from the relation  $i = i_0 \exp(-\Delta E/kT)$  at low temperatures have different values at different voltages: the lower the bias voltages, the lower is the activation energy.

Yet, in the temperature region  $T > 20$  K the activation energies become roughly identical for all curves. From the standpoint of the theory of space-charge-limited currents, here we have an increase in the concentration of equilibrium electrons, with the ohmic current dominating the conduction. At low temperatures and not too high voltages, when the injection is still weak, deep traps get occupied with electrons, and the activation energy determined from the slope of  $i = f(10^3/T)$  gives the trap energy. On increasing the bias voltage in excess of the values at which complete filling of traps occurs ( $U > 3 \div 3.5$  V) the electric current becomes weakly dependent on temperature in the temperature region  $T < 10 \div 20$  K. A slight growth of electric current with increasing temperature in this temperature region can be attributed to variation of static dielectric permittivity in the material; this matter will be discussed in

more detail in the next section. Note that, if the dielectric permittivity increases with temperature, at fixed temperature it decreases with increasing the bias voltage. This circumstance affects the observed behavior the electric current shows as a function of temperature at the three bias voltages in Figure 4.

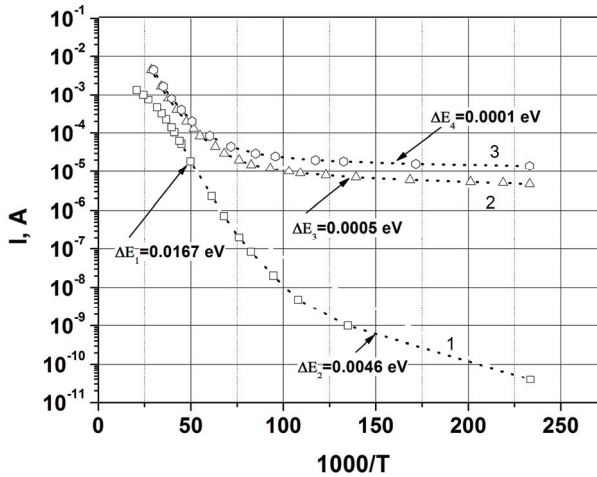


Fig. 4. Temperature dependence of the current through an PbSnTe:In film with  $x=0.25$  under bias voltages 1.55 V (1), 4.65 V (2), and 5.6 V (3). The calculated activation energies are indicated with arrows.

### 3.3 The energy distribution of traps in the forbidden band of PbSnTe:In

In (Klimov & Shumsky, 2009), current-voltage characteristics were used to extract from them the energy distribution of traps in the forbidden band of PbSnTe:In. The current-voltage characteristics were measured at  $T = 4.2$  K on samples directly immersed into liquid helium and screened from background radiation. A typical characteristic measured on one of the samples is exemplified by Fig. 5.

Following an increase of the bias voltage from 0.7 to 20 V, the electric current increases by more than 13 orders. In a narrow range of bias voltages from 1.82 to 1.92 V the electric current grows in value approximately by four orders. Within the theory of space-charge-limited injection currents, this narrow range of bias voltages can be identified as a range inside which deep traps with a discrete energy level capture electrons to finally become completely filled with them. With further increase of bias voltage, the current grows in value more slowly yet much faster than the quadratic dependence  $I \sim U^2$  does. Such a behavior displayed by the current-voltage curves can be attributed to a filling process in which trap levels lying higher in energy than the above-mentioned discrete level become filled with electrons. In the range  $U \geq 15$  V, the current tends to follow the dependence  $I \sim U^2$ , which behavior corresponds to complete filling of all mentioned traps with subsequent limitation of the electric current with the space charge induced in the material by free rather than trapped electrons.

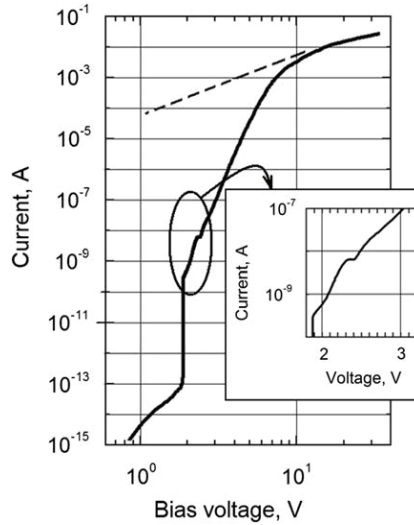


Fig. 5. A current-voltage characteristic measured at  $T = 4.2$  K. Solid line – experiment, dashed line – quadratic dependence for the current.

The energy distribution of electron traps in our samples was calculated under an assumption that the spatial distribution of electrons in between the contacts was uniform, this assumption being a standard one in the theory of space-charge-limited currents. In a biased sample, for the electric current we have:

$$I = q\mu n(U)wd \frac{U}{L}.$$

Here,  $\mu$  is the electron mobility, and  $n(U)$  is the density of free electrons in the material. From here, we readily obtain:

$$n(U) = \frac{IL}{q\mu wdU}.$$

For our sample, the effective density of conduction-band states  $N_c$  was calculated as described in (Anderson, 1980); at  $T = 4.2$  K this density was found to equal  $N_c \approx 4 \cdot 10^{14} \text{ cm}^{-3}$ . The calculations showed that in the interval of bias voltages  $U \leq 10$  V the density of free electrons  $n(U)$  was smaller than  $N_c$  and, hence, the energy position of the Fermi quasi-level for electrons could be estimated using the simple relation

$$E_{fn} - E_c = kT \ln \frac{n(U)}{N_c}.$$

Under conditions with space-charge-controlled limitation of the electric current, the total charge due to free and trapped electrons is

$$Q = CU = q[n(U) + n_t(U)]wdL,$$

where  $C$  is the experimentally measured capacitance of the structure, and  $n_t(U)$  is the density of electrons trapped in the material. Using the values of  $n(U)$  and  $E_{fn}(U)$ , we can determine, from the current–voltage curve, the dependence  $n_t = f(E_{fn})$ . In an energy interval between  $E_0$  and  $E$ , the density of trapped electrons is

$$n_t(E) = \int_{E_0}^E g_t(E) f(E) dE,$$

where  $g_t(E)$  is the energy distribution of traps in the material, and  $f(E)$  is the Fermi–Dirac distribution function. Treating the Fermi–Dirac distribution function as a step function with  $f(E) = 0$  at energies  $E > E_{fn}$  and  $f(E) = 1$  at energies  $E < E_{fn}$ , we can put the upper integration limit equal to  $E_{fn}$ . After integration over  $E_{fn}$ , we then obtain:

$$g_t(E) = \frac{\partial [n_t(E_{fn})]}{\partial E_{fn}}.$$

The energy distribution of traps calculated by this formula from the experimental current–voltage characteristic is shown in Figure 6. It should be emphasized here that the maxima and minima distinctly observed in the trap spectrum have emerged as a result of an analysis of an accurately measured experimental current–voltage curve. With the adopted algorithm, trap levels below the energy level 0.01 eV from the conduction-band edge could not be reliably identified since this could only be done by accurately measuring the current–voltage curve in the range of currents  $I < 10^{-16}$  A.

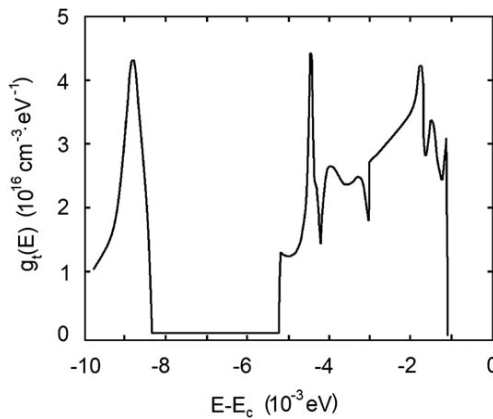


Fig. 6. The energy distribution of traps extracted from measured current–voltage characteristic.

### 3.4 Summary

The experimental data indicate that in PbSnTe:In samples, in which a «transition to dielectric state» is observed, at helium temperatures the electric current remains ohmic only in weak electric fields. On increasing the field intensity the current becomes limited by the

space charge due to electrons injected from contacts, including trapped electrons. In structures with different separations between the contacts the current varies in inverse proportion to the inter-electrode separation raised to the third power  $I \sim L^{-3}$ ; this finding confirms the applicability of the theory of space-charge-limited currents to PbSnTe:In. An analysis of the temperature dependence of the current at different bias voltages showed that in the coordinates  $\lg I = f(10^3/T)$  the slope of the curves in the temperature range from 4.2 to 35 K strongly depends on the bias voltage. This observation can be attributed to the fact that, on raising temperature, we have different proportions between the injected and ohmic current. The exact value of this proportion is defined by the behavior of dielectric permittivity as a function of temperature (the dielectric permittivity increases with increasing temperature) and electric-field strength (the permittivity decreases with field intensity). Thus, under conditions with space-charge-controlled limitation of the electric current the slope of the curves  $\lg I = f(10^3/T)$  depends on the field intensity; this slope can therefore be used for determination of trap activation energies only in weak fields. The aforesaid also applies to interpretation of Hall data.

#### 4. Transport of charge carriers in PbSnTe:In in a magnetic field

##### 4.1 Samples

Experimental type-1 structures (S1) with metal electrodes formed on the surface of PbSnTe:In films of thickness 1  $\mu\text{m}$  were similar to the structures described in Section 2.1; these structures are shown in Figure 7 a. Three orientations of magnetic field with respect to the electric-field direction and the substrate-normal direction were used (Klimov et al., 2009).

The influence of gap orientation in the film plane on the current value was examined on type-2 structures (S2), each structure comprising eighteen 0.2-cm long gaps with 30- $\mu\text{m}$  inter-electrode spacing (see Figure 7 b). In structure S2, each inter-electrode gap was turned through angle  $10^\circ$  in the film plane with respect to the previous gap.

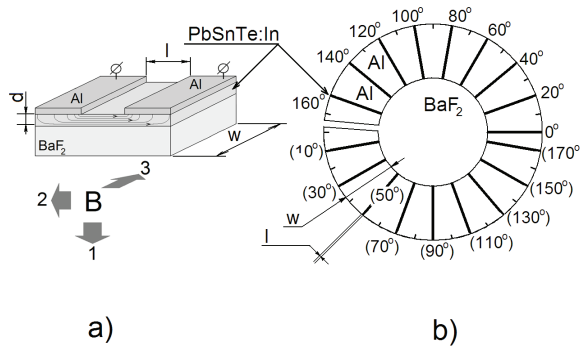


Fig. 7. Experimental structures for examining anisotropic effects in magnetic field. a) inter-electrode gap ( $d=1 \mu\text{m}$ ,  $w=0.2 \text{ cm}$ ,  $l=30 \mu\text{m}$ ). b) arrangement of eighteen gaps on a single crystal and their angular orientation (the «zero angle» is chosen arbitrarily).

##### 4.2 Current anisotropy in magnetic field

Curves of relative current in magnetic field  $I_B/I_{B=0}$  versus bias voltage in an S1 structure are shown in Figure 8 a. The current strength could be increasing or decreasing with bias

voltage depending on mutual orientation of the magnetic and electric fields and the normal to the substrate. Moreover, for orientation 3 the current showed both positive and negative

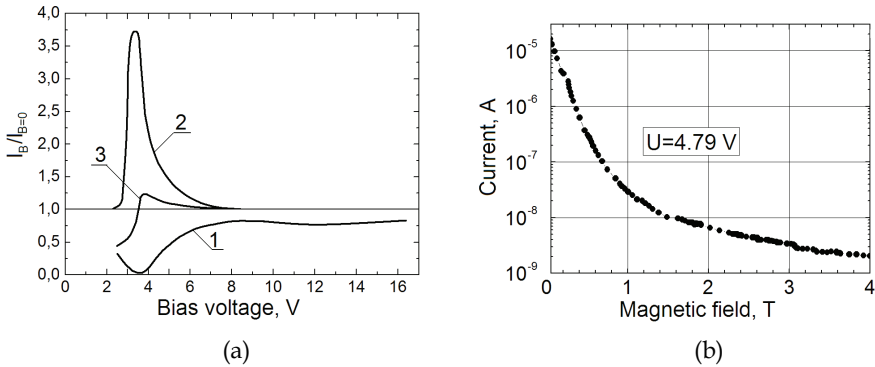


Fig. 8. a - Curves of relative current versus bias voltage measured at  $B=0.22$  T. Curves 1, 2, and 3 refer to magnetic-field vector orientations indicated in Fig. 4.1 a with the same numerals. b - Curve of electric current versus magnetic-field strength measured at  $U=4.79$  V. Here, the magnetic-field vector was normal to the  $BaF_2$  substrate.

changes with increasing bias voltage. The largest change of current was observed for orientation 1 (Figure 7a). The relative change of current versus magnetic field for this orientation is shown in Figure 8 b. It is seen that at  $B=4$  T the current increases by a factor of  $10^4$ .

Figure 9 shows the angular dependences of the effect at fixed bias-voltage values in magnetic field  $B=0.22$  T at  $T=4.2$  K. On tuning-on and turning-off the field  $\vec{B}$ , current relaxation over a time 10-30 sec was observed; the relaxation pattern depended on the orientation of the field  $\vec{B}$  and on the sample temperature.

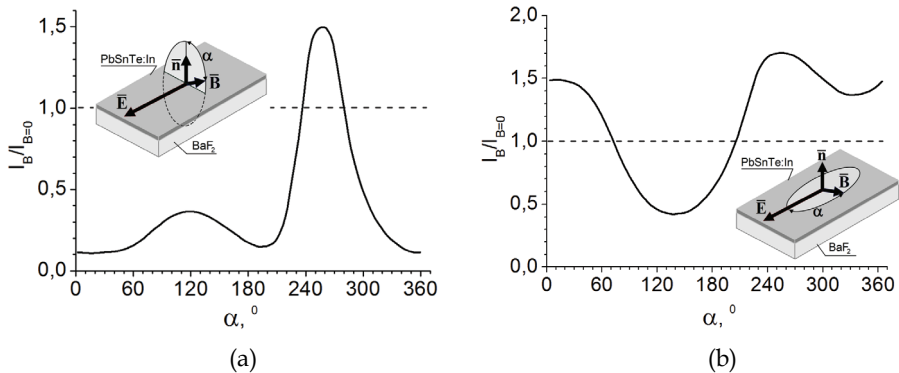


Fig. 9. a - The electric current versus the angle  $\alpha$  between the magnetic-field vector  $\vec{B}$  and the normal  $\vec{n}$  to the  $BaF_2$  substrate in the plane normal to the electric-field vector  $\vec{E}$ . b - The electric current versus the angle  $\alpha$  between the fields  $\vec{B}$  and  $\vec{E}$  in the substrate plane. The bias voltages are  $U=4$  V (a) and  $U=5$  V (b).

In the experiment (see Figure 9), the magnetic field was rotated through the angle  $360^\circ$  during 8 minutes so that at each angle a quasi-equilibrium magnitude of the current could establish. Both dependences in Figure 9 show no pronounced angular symmetry. Nonetheless, it is seen from Figure 9 a that two minima of the current lie in the vicinity of the angles  $0^\circ$  and  $180^\circ$ , for which the vector  $\vec{B}$  was normal to the substrate. The position of the most pronounced maximum is near the angle  $270^\circ$ , at which the field  $\vec{B}$  was normal to the substrate. Yet, the other «local» maximum, located at  $120^\circ$ , is observed rather far from the angle  $90^\circ$ , at which the vector  $\vec{B}$  is also parallel to the substrate.

In Figure 9 b the angle between the two maxima is close to  $240^\circ$ , with the «main» minimum being located at the middle point of the maxima with angular spacing of approximately  $120^\circ$  from either maximum. In principle, this position of the three extrema correlates with the orientation of the BaF<sub>2</sub> (111) substrate. Yet, the position of the second «local» minimum shows no such regularity.

The behavior demonstrated by the current in a strong magnetic field also substantially depends on the orientation of this field with respect to the electric-field vector and the normal to the substrate, and it can appear nonmonotonic with variation of  $\vec{B}$ . Figure 10 shows the curves of relative current for mutual orientation 2 of the two fields (Fig. 7 a) at various bias voltages. The maximum increase in current (over 200 times) was reached approximately at  $B=1.3$  T and at bias-voltage value  $U \approx 3$  V, i.e. in the vicinity of the voltage at which the effect in weak magnetic fields was also most pronounced (Fig. 8 a)).

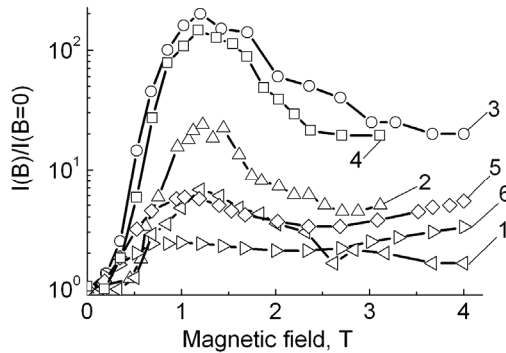


Fig. 10. The ratio  $I(B)/I(B=0)$  versus magnetic-field strength. Here, the magnetic field and the electric field are parallel to each other. Bias voltage  $U$ , V = 2.66 (1); 2.77 (2); 2.93 (3); 3.1 (4); 4.05 (5); 5.2 (6).

### 4.3 Discussion

Consider possible factors causing the variation of the electric current under the action of a constant magnetic field. In Section 3 it was shown that at helium temperatures the behavior of current-voltage characteristics of PbSnTe:In films obeys the theory of space-charge-limited current in the presence of electron traps. In the case under discussion, the change of current-voltage characteristics in a magnetic field should be attributed to a change of dielectric permittivity (polarizability) of the medium providing that such a change does take place.

Consider possible change of the effective value of  $\epsilon$  as a factor causing variation of the current-voltage curves. Assuming variation of dielectric permittivity by  $\pm 30\%$ , we performed numerical calculations of the current-voltage characteristics; the calculated data are shown in Figure 11, curves 1, 2, and 3, together with experimental data. As it is seen from the figure, a good agreement between the calculated and experimental data is observed.

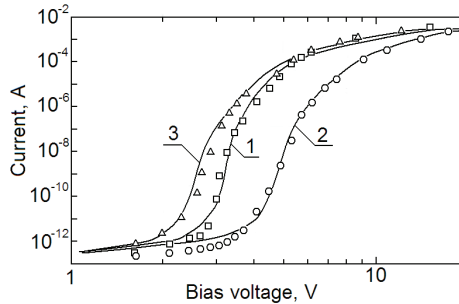


Fig. 11. Current-voltage characteristics of a PbSnTe:In sample at  $T=4.2$  K. Symbols – experimental data; solid lines – calculated data. 1 and squares –  $B=0$ , 2 and circles –  $B=4$  T, orientation 2 in Figure 7 a, 3 and triangles –  $B=1.33$  T, orientation 2 in Figure 7 a.

Of course, here we do not mean the variation of  $\epsilon$  under the action of magnetic field. The magnetic field can alter the current direction by the Hall angle, which in PbSnTe:In can be rather large because of a high value of charge-carrier mobility. In turn, it is the polarizability of the medium in the direction of current that will affect the space-charge magnitude and the current strength, thus making the latter quantities dependent on the direction and strength of magnetic field. If we assume that precisely this factor defines the anisotropic effects in magnetic field, then the dependence of  $\epsilon$  on field orientation can also be expected to take place without the magnetic field. To clarify this point, at  $B=0$  we examined the angular dependence of  $\epsilon$  and the shape of current-voltage characteristics of structures S2 under conditions with space-charge-controlled limitation of injection current at various orientations of the external electric field.

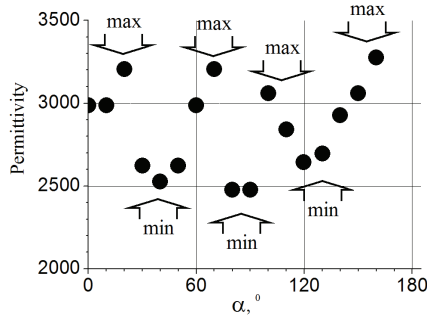


Fig. 12. Dependence of  $\epsilon$  on gap orientation in structure S2. The wide arrows indicate the approximate angular position of the maximal and minimal values of  $\epsilon$ .

The angular dependence of  $\epsilon$  was measured on an experimental structure shown in Figure 7 b. The experimental data measured at frequency  $f=10^4$  Hz are shown in Fig. 12. The dependence shows distinct minima and maxima whose presence in the dependence can be identified by 2 to 4 experimental points within each feature.

The experimentally revealed dependence of  $\epsilon$  on electrical-field orientation explains the observed transformation of current-voltage characteristics in a magnetic field. Yet, factors causing the variation of  $\epsilon$  need further discussion. At room temperature PbSnTe has a face-centered cubic lattice with the NaCl structure (space group  $O_h^5 Fm\bar{3}m$ ). As a result of the ferroelectric phase transition, the lattice becomes rhombohedral, involving equivalent [111] spontaneous-polarization axes of «free» crystal. As far as our knowledge goes, so far no data on the dependence of static dielectric permittivity on crystallographic direction in PbSnTe:In have been reported; on the other hand, for thoroughly studied ferroelectrics, such as, for instance, barium titanate, the dielectric-permittivity values measured along directions [010] and [001] form a tensor, whose components in some temperature range can differ by ten to hundred times (Vinogradov & Kucherenko, 1991). The axis along which spontaneous polarization in PbSnTe:In occurs seems to be not parallel to the surface normal, being instead one of the three equivalent type [111] axes directed at an angle to the substrate. The projections of those axes onto the substrate plane are separated with  $60^\circ$  angles. One factor making the indicated three axes nonequivalent on large scale and leading to spontaneous polarization along one of those axes can be some deviation from singularity that inevitably occurs in preparation of BaF<sub>2</sub>(111) substrates.

In principle, if spontaneous polarization along one of the three equivalent type-[111] axes does occur, a 60- or 120-deg angular symmetry of the effect in the substrate plane can be expected; such a symmetry is probably manifested in Fig. 9 b. Simultaneously, geometric factors, such as, for instance, a large length of the inter-electrode gap, a small film thickness, and also a multi-domain structure of the film, could also induce distortions into this type of symmetry.

Of course, the model discussed above is a simplified model. In particular, the experimental current-voltage characteristic in substrate-normal magnetic field in Figure 11 and the calculated current-voltage curve can be brought in agreement assuming 30% variation of  $\epsilon$ , while measured angular variations of  $\epsilon$  are restricted to within 20%. Finally, the model ignores the influence of possible multi-domain structure of PbSnTe:In films on the shape of current-voltage curves, which may appear rather substantial.

#### 4.4 Summary

The giant (up to  $10^4$ ) change in the electric current in Pb<sub>1-x</sub>Sn<sub>x</sub>Te:In films placed in a magnetic field can be explained within the frame of the following model. The polarizability of PbSnTe:In films in ferroelectric phase at  $T=4.2$  K is anisotropic and, in such films, there exists a preferential direction of spontaneous polarization in which the static dielectric permittivity  $\epsilon$  is maximal. The latter assumption is qualitatively corroborated by experimental data on anisotropic properties of the films in zero magnetic field. Since the measured currents are space-charge-limited injection currents, the magnitude of these currents depends on the value of  $\epsilon$  in the direction in which the current flows. It can therefore be expected that a magnetic-field-induced change of current direction will alter the magnitude of the current. The observed effect can be explained on the assumption that, on

the change of current direction, the voltage  $U_t$  at which the traps in the film become filled with electrons also undergoes a change in the magnetic field, because this voltage is inversely proportional to  $\epsilon$ . In a narrow interval of voltages around  $U_t$  the electric current increases by several orders. As a result, at a fixed bias voltage even a small change in  $\epsilon$  in the above interval will lead to a drastic change of the electric current, this change amounting in the experiments to several orders. Within this model, the complex anisotropy displayed by the effect also receives qualitative explanation. Namely, the magnetic-field-induced increase or decrease of the electric current is defined by the mutual orientation of electric field, magnetic field, spontaneous polarization, and the normal to substrate plane.

## 5. Photosensitivity of PbSnTe in the fundamental absorption band and in THz spectral region

### 5.1 Photocurrent in the fundamental absorption band

It is known from literature (Emtage, 1976; Lishka et al., 1984) that the predominant recombination mechanism in undoped PbSnTe samples is Auger recombination. Low concentrations of electrons and holes in PbSnTe:In make the Auger recombination a less probable process. In (Borodin et al., 1997b), it was found that in PbSnTe:In films a satisfactory agreement between experimental and calculated data could be achieved on the assumption that a predominant contribution was due to radiative recombination.

In calculating the photocurrent (Klimov & Shumsky, 2008), it was assumed that the Fermi level under equilibrium conditions lay at the middle of the forbidden band, the concentrations of electrons and holes were negligible, and the concentration of free electrons was defined by the injection current. It was also assumed that there was just one trap level in the material, available in a concentration  $5 \cdot 10^{13} \text{ cm}^{-3}$  and located at energy 0.0065 eV below the conduction-band bottom.

In the dark, in the PbSnTe:In bulk there is an uncompensated negative charge due to electrons, and an injection current flows through the sample. In an illuminated material, optically excited electrons recombine with holes, the role of equilibrium electron concentration here being played by the sum of equilibrium and injected electrons. In performing numerical calculations, the concentration of field-injected electrons in the conduction band and the rate of optical generation of charge carriers were set separately. The total concentration of free electrons defined the energy position of Fermi level and trap occupation values under steady-state conditions. In calculating the Auger lifetime, for the Auger recombination coefficient a value  $\eta_n = \eta_p = 5 \cdot 10^{-26} \text{ cm}^6 \cdot \text{s}^{-1}$  was adopted (Emtage, 1976). The radiative lifetime was calculated based on the detailed balance principle (Roesbroeck & Shockley, 1954).

The temperature dependence of both, Auger and radiative, lifetimes at various contact injection levels is shown in Figure 13 a. At helium temperatures, the chosen minimal total concentration of equilibrium and field-injected electrons refers to the case of almost empty traps, while the maximal total concentration of electrons, to almost completely filled traps (Akimov et al., 2005).

Measurements showed that our PbSnTe:In films were dominated by radiative recombination. Under monopolar electron injection, the hole concentration decreases with increasing injected concentration of free electrons. Illumination produces additional amounts of localized electrons and free holes. Capture of electrons at traps decreases the rate of band-to-band recombination and increases the steady-state hole concentration, thus

increasing the photocurrent value. The calculated electron and hole components of the photocurrent as functions of bias voltage are shown in Fig. 13 b.

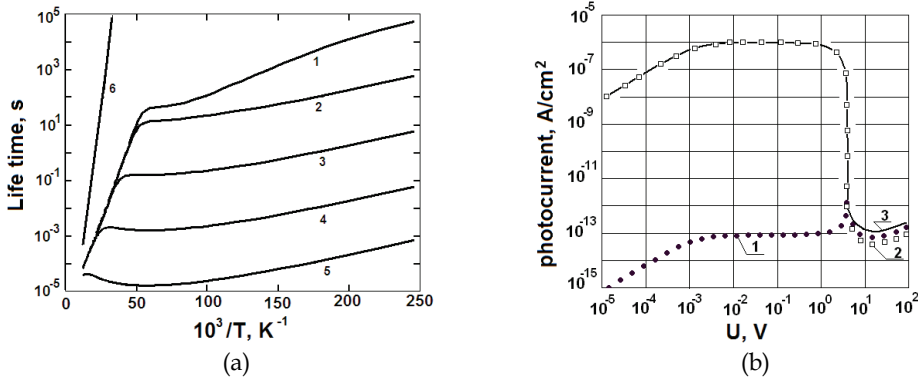


Fig. 13. Temperature-dependent radiative lifetime (a) and calculated dependences of the photocurrent on bias voltage (b).

a - radiative (1-5) and Auger (6) lifetimes of holes at  $\Delta n_{ph}=10^6 \text{ cm}^{-3}$  and  $n_0+n_{inj} = 10^6, 10^8, 10^{10}, 10^{12}, 10^{14}$  (curves 1 – 6, respectively).

b - photocurrent component due to electrons (1), due to holes (2) , and the total current (solid line 3) versus bias voltage at  $g_0=10 \text{ cm}^{-3}\cdot\text{s}^{-1}$ .

The prevalence of the hole photocurrent component over an interval of bias voltages up to the voltage at which the traps become filled with electrons is due to the fact that, because of the electron capture at traps, the concentration of free holes here far exceeds the concentration of free electrons. Under such conditions, the hole lifetime is defined by the net concentration of electrons in the conduction band. With further increase of bias voltage, the concentration of conduction-band electrons increases while the lifetime and concentration of optically generated holes start decreasing. In the end, after all traps become filled with electrons, the concentration of excess electrons becomes roughly equal to the concentration of excess holes, and the lifetime of those holes, defined by the concentration of injected electrons. Since the latter concentration is high, the lifetime is short, and the photocurrent is weak.

An important outcome of the calculations is a prediction that until the onset of the regime with completely filled traps the photocurrent should be due to holes.

It was shown experimentally (Klimov & Shumsky, 2008) that in weak fields a hole-type conductivity was observed, with the Hall coefficient being almost independent of bias voltage. In strong fields a current due to electrons is observed, with the Hall effect exhibiting a strong dependence on bias voltage.

## 5.2 Photocurrent in the THz region

With the previously determined energy distribution of localized centers, the sensitivity of PbSnTn to radiation in submillimeter spectral region due to electron excitation from a center into the conduction band can be calculated (Klimov & Shumsky, 2009). A specific feature of the photocurrent under conditions with space-charge-controlled limitation of current is a strong dependence of photocurrent on the occupation of the local level, this occupation

being in turn dependent on the electron injection level, or bias voltage. This dependence is expected to be manifested most sharply when the trap level lies far from the equilibrium Fermi level. The steady-state concentration of optically generated electrons can be calculated, in principle, similarly to calculations of impurity photoconductivity.

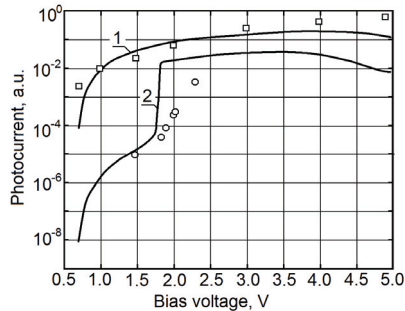


Fig. 14. Current-voltage characteristics of PbSnTe samples illuminated at laser-radiation wavelengths 130  $\mu\text{m}$  (curve 1 – calculated data; squares – experimental data) and 198  $\mu\text{m}$  (curve 2 – calculated data; triangles – experimental data).

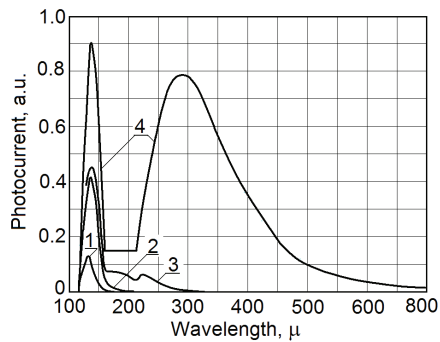


Fig. 15. Spectral dependences of the photocurrent in a structure with an energy distribution of states over the PbSnTe forbidden band shown in Fig. 4, Section 2.  $U=1.16$  (1), 1.79 (2), 1.83 (3), 2.95 V.

The calculated photocurrent values in a sample illuminated with radiation at wavelengths 130  $\mu\text{m}$  ( $h\nu=9.54$  meV) and 198  $\mu\text{m}$  ( $h\nu=6.26$  meV) versus bias voltage are shown in Figure 14. The same figure shows the photocurrent values measured in our experiments at the indicated wavelengths.

Figure demonstrates the difference between the curves of photocurrent versus bias voltage for quantum energies  $h\nu=9.54$  meV and 6.26 meV. In the former case, on increasing the bias voltage from 0.7 V to 5 V the photocurrent varies over an interval of current values slightly in excess of two orders. In the latter case, the photocurrent exhibits variation within the same range of current values on increasing the bias voltage from 1.5 to 2.3 V, the photocurrent growth here being much sharper. Qualitatively, such a behavior complies with the one expected from the energy distribution of states in the forbidden band of PbSnTe.

Calculated values of spectral photosensitivity in a PbSnTe structure under various bias voltages are shown in Fig. 15. It is seen that an increase in the injection level results in a growth of the photocurrent throughout the whole spectral region, this growth being most pronounced at wavelengths  $\lambda > 200 \mu\text{m}$ .

### 5.3 Discussion

The experimental data obtained in our study of photoelectric properties of PbSnTe:In films, and also performed calculations, allow the following conclusions to be drawn:

1. On the passage to «dielectric state», the rate of recombination of optically excited charge carriers becomes predominantly defined by the radiative lifetime, whose magnitude depends on the field-injection level of electrons, on the values of trap parameters, and on the optical injection level.
2. Trapping of optically generated electrons at low field-injection levels leads to prevalence of the photocurrent component due to holes, which on increasing the field-injection level decreases due to recombination of optically excited holes. At high field-injection levels, the photocurrent component due to electrons becomes prevailing. The latter explains the photocurrent quenching by a voltage pulse.
3. The calculated data have found confirmation in measurement of Hall effect in weakly illuminated samples, whose conductivity varies from p-type conductivity at low field-injection levels to n-type conductivity at high field-injection levels.
4. The presence of localized electron traps distributed in energy over the PbSnTe forbidden band may lead to non-exponential photocurrent decay, and also to some other effects such as self-oscillations that were observed, among other things, in Hall effect measurements of weakly illuminated samples.
5. Our calculations of the photocurrent in THz region showed a good agreement with experimental data. Excitation of electrons trapped at energy-distributed localized states in the forbidden band of PbSnTe seems to be capable of providing a reasonable explanation to the high sensitivity of PbSnTe:In films to radiation emitted by weakly heated bodies.
6. Dependence of photosensitivity spectrum in this spectral region on the occupation of traps can be employed in the development of a THz radiation detector controlled by bias voltage applied to the PbSnTe:In structure.

## 6. Oscillating transient currents in samples screened from background radiation

### 6.1 Experimental results

Under conditions with screened background radiation at  $T=4.2 \text{ K}$ , we examined the dynamics of injection currents in “dielectric” PbSnTe:In films of thickness  $1\div 1.5 \mu\text{m}$  grown by molecular-beam epitaxy on (111) BaF<sub>2</sub> substrates. The specific resistance of the films at  $T=4.2 \text{ K}$  was  $\rho=10^{10}\div 10^{12} \text{ Ohm cm}$ . A sample was cooled to  $T=4.2 \text{ K}$  at zero bias voltage, and then a new voltage in the range  $U=2.5 \text{ to } 6.0 \text{ V}$  was applied to it to register the curve of transient current. At each set value of bias voltage, measurements were repeated thrice. After registration of the first curve (during 40-200 s), the applied voltage was removed from the sample and, after the same time elapsed, the voltage was again applied to the sample to register a second transient-current curve. Then, the sample was “warmed” to a temperature

of 30 K to be again cooled to 4.2 K. Afterwards, the same bias voltage was applied to the sample to register a third transient-current curve.

Figure 16 a, b shows the curves of transient current for bias-voltage values  $U=2.5$  V and  $U=4.0$  V. It is seen that the current in the second measurement was roughly the same as the current at the end of the first measurement; this observation proves that the transition process was over. In the third measurement, the curve of transient current closely followed the curve obtained in the first measurement; the former curve is therefore not shown in the figure. A characteristic feature of the relaxation process was involvement of self-oscillations in the relaxation. The current decay is not monotonic, displaying instead an oscillating behavior. The frequency and amplitude of the oscillations depended on the applied voltage value.

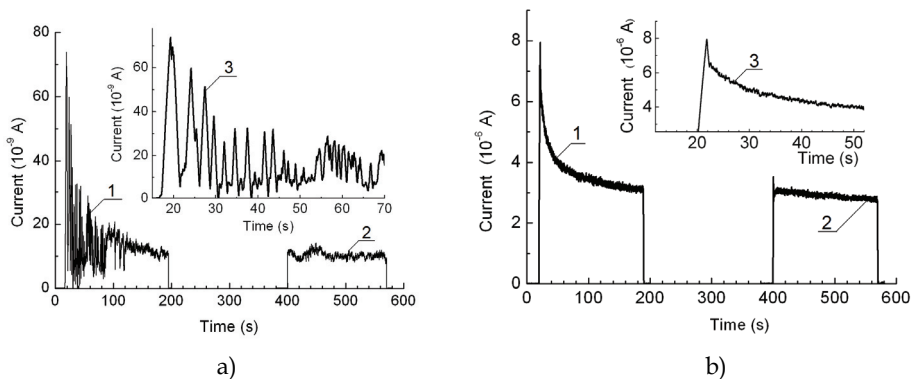


Fig. 16. The curves of transient current registered on application of a voltage step to the sample. The bias voltages are  $U=2.5$  V (a) and  $U=4.0$  V (b). The inserts show the curves of transient current on an enlarged scale.

## 6.2 Discussion

It is a well-known fact that under certain conditions undamped oscillations can arise in semiconductor structures whose current-voltage characteristics display curve portions with negative differential resistance (NDR). Simultaneously, under certain combinations of external parameters such as temperature, field strength, and illumination intensity, similar self-oscillations were also observed in materials without NDR, for instance, in compensated Si and Ge, and in PbSnTe:In (Akimov et al., 1993).

In applicable theories, the emergence of self-oscillations was related to the occurrence of either trap recharging waves (Suris & Fuks, 1975) or recombination waves in the samples (Bonch-Bruevich & Kalashnikov, 1965); however, in all cases a positive feedback, leading to current growth, was necessary. Such a positive feedback can be ensured by an illumination causing transitions of trapped electrons to the conduction band, collisional ionization of excited electron traps, etc. For instance, according to (Bonch-Bruevich & Kalashnikov, 1965), for emergence of self-oscillations in a unipolar semiconductor the concentration of free charge carriers has to be controlled not only by trapping at one of the centers with a capture cross-section dependent on field intensity, but also by optical generation of free carriers from an impurity level of another type. In our experiments, measurements were carried out

under conditions with background radiation screening, so that the feedback was ensured by some other mechanism.

Previously, we showed (Akimov et al., 2005) that electron transport in semi-insulating PbSnTe:In at helium temperatures cannot be treated without regard for monopolar injection of electrons out of contacts and space-charge-controlled limitation of the current with capture of electrons into localized centers in the forbidden band of PbSnTe. Such an approach has allowed us to explain the shape of current-voltage curves, the high photosensitivity of PbSnTe in the fundamental absorption band, and the emergence of photosignal during excitation of the material in submillimeter band; additionally, an analysis of current-voltage characteristics has allowed us to determine the energy spectrum of localized electron traps (Klimov & Shumsky, 2009). The presence of electron traps and possible recharging of these traps may have an influence on the transition processes. It should be noted that the experimentally observed undamped current oscillations bear no relation to the self-oscillations considered in (Suris & Fuks, 1975; Bonch-Bruevich & Kalashnikov, 1965); the former self-oscillations were observed as an oscillating decay to a steady state after application of a voltage step to the sample. This means that, here, the feedback mechanism, or the mechanism causing an increase of electric current, gradually ceases its operation.

In (Klimov & Shumsky, 2001) we discussed the so-called “photodielectric effect”, experimentally observed in PbSnTe:In, that consisted in a considerable (up to two orders) increase of static dielectric permittivity in samples under illumination. This increase can be related to a growth of electronic dielectric susceptibility observed in disordered semiconductors with localization of electrons at discrete levels (Bonch-Bruevich, 1974).

The observed undamped current oscillations can be explained as follows. In the forbidden band of a PbSnTe:In film, there is a quasi-continuous distribution of electron traps; in subsequent discussion, we will treat this distribution by replacing it with a discrete-level set, the levels within the set having different concentrations, energy positions, and electron capture cross-sections. We assume that the steady-state Fermi level is located below the  $i$ -th center, and the temperature is sufficiently low for those centers at equilibrium to be empty, for the concentration of conduction-band electrons to be negligible, and for the current through sample to be limited by the space charge and by the trapping of injected electrons at those centers.

On application of a voltage step, injection of an electron concentration  $n_{inj} = \varepsilon_0 \varepsilon_s U / (qL^2)$  into the sample takes place, where  $\varepsilon_0$  is the dielectric constant,  $\varepsilon_s$  is the static dielectric permittivity of the sample,  $U$  is the bias voltage,  $q$  is the electron charge, and  $L$  is the spacing between the contacts. Consider the variation of the electron concentration in the conduction band and at localized centers starting from a moment  $t_0 > \tau_M$ , where the latter time is the Maxwell relaxation time. We use an approximation that disregards the diffusion currents and the spatial distribution of electrons over the sample length. Under this assumption, a system of continuity equations with given concentrations and energies of centers can be solved numerically.

Here, a situation may emerge in which a predominant fraction of conduction-band electrons will be first captured by a center with a large capture cross-section, and then the electrons from this center will be emitted into the conduction band to subsequently become trapped at a next center, and so on. Since at an arbitrary time we have  $n(t) = n_{inj} - \sum_i m_i(t)$ , then the

time dependence of the current can be written as

$$j(t) = q\mu m(t)E = \frac{\varepsilon_s \varepsilon_0 \mu U^2}{L^3} - q\mu \frac{U}{L} \sum_i m_i(t).$$

The above equation shows that the current will decrease in time exhibiting features dependent on the effective time of electron capture into traps up to the establishment of a steady state. Yet, as it follows from (Klimov & Shumsky, 2001), in PbSnTe:In there exist one or several centers which, as they capture electrons, enhance the static dielectric permittivity due to increased electronic dielectric susceptibility. In the latter case, the current is given by

$$j(t) = \frac{\varepsilon_s \varepsilon_0 \mu U^2}{L^3} + q\mu \frac{U}{L} \left[ \frac{\varepsilon_0 U}{qL^2} \sum_i \beta_i m_i(t) - \sum_i m_i(t) \right], \quad (1)$$

where  $\beta_i$  is the contribution to polarizability due to one electron captured at the  $i$ -th center. An analysis of expression (1) shows that at the initial time ( $t=t_0$ ) the current is defined by the first term; at subsequent times, an increase or a decrease of the current is defined by the sign of the bracketed expression. Thus, after application of the voltage step the system can come into a steady state experiencing damped current oscillations. For damped current oscillations to emerge, it is required that the expression in squared brackets would be changing its sign as the centers with a longer time  $\tau_{CM_i}$  get filled with electrons.

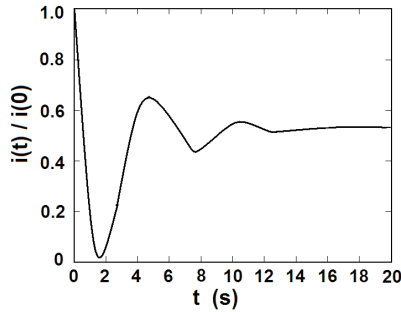


Fig. 17. Calculated current self-oscillations on application of a voltage step  $U=0.02$  V to the sample. The parameter values of the centers are indicated in the text.

The data obtained in numerical calculations of the ratio  $j(t)/j(0)$  for the model with four discrete levels belonging to centers making different contributions to dielectric susceptibility on electron captures at those levels are shown in Figure 17. The values of trap parameters were chosen rather arbitrarily; they were as follows:  $M_1=1.8 \cdot 10^{12}$  cm<sup>-3</sup>,  $\Delta E_{M1}=4$  meV,  $\gamma_1=1.8 \cdot 10^{-13}$  cm<sup>3</sup>/s,  $\beta_1=0.5 \cdot 10^{-9}$ ;  $M_2=1.9 \cdot 10^{12}$  cm<sup>-3</sup>,  $\Delta E_{M2}=5$  meV,  $\gamma_2=6.6 \cdot 10^{-14}$  cm<sup>3</sup>/s,  $\beta_2=0.8 \cdot 10^{-9}$ ;  $M_3=3.0 \cdot 10^{12}$  cm<sup>-3</sup>,  $\Delta E_{M3}=6$  meV,  $\gamma_3=6.3 \cdot 10^{-15}$  cm<sup>3</sup>/s,  $\beta_3=1.65 \cdot 10^{-9}$ ;  $M_4=5.8 \cdot 10^{12}$  cm<sup>-3</sup>,  $\Delta E_{M4}=8$  meV,  $\gamma_4=2.0 \cdot 10^{-16}$  cm<sup>3</sup>/s, and  $\beta_4=1.1 \cdot 10^{-9}$ . The numerical values of  $\beta_i$  were chosen such that an increase of current due to increased dielectric permittivity would occur when electrons were getting trapped into the third center in terms of energy.

It is seen from Figure 17 that even involvement of a single such level can lead to damped current oscillations in the trap charging and recharging process. Qualitatively, it is clear that, with the injected electron concentration being much greater than the total concentration of

traps, the charging processes of the various traps will proceed simultaneously without emergence of notable current oscillations. The latter situation refers to the case of high voltages at which a reduction of the current oscillation amplitude and, then, complete vanishing of oscillations were observed in the experiment.

Thus, involvement of the mechanism of current decrease due to trapping-induced reduction of free-electron concentration, on the one hand, and involvement of the mechanism of current increase owing to recharging-induced change of trap polarizability, on the other hand, can result in an oscillating dynamics of the current decay to a steady-state value of the current.

## 7. Conclusions

The object under study being solid solution Pb-Sn-Te with a substantial (up to a few atomic per cents) In content, this object has to be considered as a disordered system presenting a solid without long-range ordering, with the potential energy of charge carriers no longer being a periodic function of coordinates. The violation of long-range ordering is related to the fact that any chosen site of the metal sublattice may contain, with certain probability, any of the three components. Electronic processes in such systems, namely, in amorphous germanium and silicon, and also in chalcogenide glasses, were considered in (Mott & Davis, 1979). Such properties of PbSnTe:In as the Fermi-level pinning, the absence of an EPR signal, and deviations from linearity in the temperature dependence  $\log \sigma = f(1/T)$  are similar to chalcogenide properties. J. Marshall and A.E. Owen (Marshall & Owen, 1976) considered a state density model assuming that the forbidden band of PbSnTe contains deep donors with energy levels below the acceptor energy (see Figure 18).

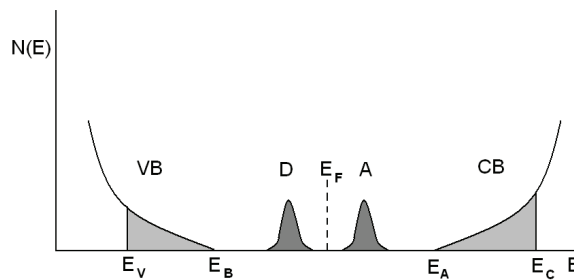


Fig. 18. Density of states in a non-crystalline semiconductor. VB – valence band; CB – conduction band;  $E_F$  - Fermi level; D – donors; A – acceptors;  $E_V$ ,  $E_C$  – mobility edges;  $E_B$  – valence-band ceiling;  $E_A$  – conduction-band bottom. Shaded are localized states.

The states in the forbidden band of PbSnTe pin the Fermi level at the middle of the energy gap, thus leading to decreased conductivity. If the deep acceptor and donor states do not overlap, then unpaired electrons, normally causing an EPR signal, are lacking, except for those due to magnetic impurities. Without going into details, we can state that the model by I.A. Drabkin and B.Ya. Moizhes (Drabkin & Moizhes, 1981) mentioned in Section 1 closely follows the theory by P.W. Anderson (Anderson, 1975).

The unique possibility of creating injecting contacts to PbSnTe:In has allowed researchers to examine charge transport processes related to the recharging phenomena of localized states

in PbSnTe:In both under conditions with screened background radiation and under sample illumination in a broad spectral range, from IR to THz radiation.

The fact that PbSnTe:In is a ferroelectric has widened available possibilities in studying the effect of magnetic field on the charge transport due to electrons.

Of course, the data described in the present publication present no final results; yet, we believe that space-charge-controlled limitation of the electric current, and also capture of electrons into localized traps and their emission from those traps, which affect sample polarizability, are factors that need to be taken into account in developing theoretical models.

## 8. Acknowledgments

This work was supported by the Programs of Russian Academy of Sciences No. 5.4, 21.20 and, 21.34.

## 9. References

- Akimov A.N., Erkov V.G., Klimov A.E., Molodtsova E.L., Suprun S.P. & Shumsky V.N. (2005). Injection currents in narrow-gap (Pb<sub>1-x</sub>Sn<sub>x</sub>Te):In insulators, *Semiconductors*, Vol. 39, No. 5, pp. 533-538, ISSN 1063-7826
- Akimov A. N., Erkov V. G., Kubarev V. V., Molodtsova E. L., Klimov A. E. & Shumski V. N. (2006). Photosensitivity of Pb<sub>1-x</sub>Sn<sub>x</sub>Te:In films in the terahertz region of the spectrum, *Semiconductors*, Vol. 40, No. 2, pp. 164-168, ISSN 1063-7826
- Akimov B.A., Brandt N.B., Bogoslovskii S.A., Riabova L.I. & Choudnev S.M. (1979). Non-equilibrium metal state in Pb<sub>1-x</sub>Sn<sub>x</sub>Te(In) alloys. *JETP Letters*, Vol. 29, No. 1, pp. 9-12, ISSN 0021-3640
- Akimov B.A., Ryabova L.I., Shumsky V.N. & Petikov N.I. (1993). An operating regime based on switching effect for photodetectors of PbSnTe<In> MBE films, *Infrared Phys.*, Vol. 34, No. 4, pp. 375-378, ISSN 1350-4495
- Anderson W. W. (1975). Model for the electronic structure of amorphous semiconductors, *Phys Rev Lett.*, Vol. 34, pp. 953-955, ISSN 0031-9007
- Anderson W.W. (1980). Tunnel contribution to Hg<sub>1-x</sub>Cd<sub>x</sub>Te and Pb<sub>1-x</sub>Sn<sub>x</sub>Te p-n junction diode characteristics, *Infrared Phys.*, Vol. 20, pp. 353-361, ISSN 1350-4495
- Bonch-Bruevich V.L. (1974). Electronic dielectric susceptibility of a disordered semiconductor, *JETP Letters*, Vol. 19, No. 4, p. 122, ISSN: 0370-274X
- Bonch-Bruevich V.L. & Kalashnikov G. (1965). On possible recombination instability in semiconductors, *Fizika Tverdogo Tela (in Russian)*, Vol. 7, No. 3, pp. 750-758, ISSN 0367-3294
- Borodin V.V., Klimov A.E. & Shumsky V.N. (1997). Photocurrent oscillations in PbSnTe<In> films, In: *Narrow Gap Semiconductors*, Shen S.C., Tang D.V., Zheng G.V., Bauer G., pp. 365-368, World Scientific
- Borodin V.V., Klimov A.E., Shumsky V.N. (1997). Recombination in PbSnTe <In> at low temperatures, In: *Narrow Gap Semiconductors*, Shen S.C., Tang D.V., Zheng G.V., Bauer G., pp. 361-364, World Scientific
- Drabkin I. A. & Moizhes B. Ya. (1981). Spontaneous dissociation of neutral impurity states to positive and negative charge states, *Fizika i Tekhnika Poluprovodnikov (in Russian)*, Vol. 15, No. 4, pp. 625-647, ISSN 0015-3222

- Drabkin I.A. & Moizhes B.Ya. (1983). On the photoconductivity of  $Pb_{1-x}Sn_xTe$  doped with In. *Fizika i Tekhnika Poluprovodnikov (in Russian)*, Vol. 17, No. 6, pp. 969-972, ISSN 0015-3222
- Emtage P.R. (1976). Auger recombination and junction resistance in lead-tin-telluride, *J. Appl. Phys.*, Vol. 47, No. 6, p. 2565-2576, ISSN 0021-8979
- Herrmann K.H. & Mollmann K.-P. (1983). Curie temperature as a critical temperature for dielectric, galvanomagnetic and photoelectrical phenomena in strongly doped  $Pb_{1-x}Sn_xTe$ . *Phys. Stat. Sol. (a)*, Vol. 80, pp. K101-K104, ISSN 0031-8965
- Kaidanov V.P. & Ravich Yu.I. (1985). Deep and resonant states in  $A^{IV}B^{VI}$ -type semiconductors. *Usp. Fiz. Nauk (in Russian)*, Vol. 145, No. 1, pp. 51-86, ISSN: 0042-1294
- Khokhlov D.R., Ivanchik I. I., Rains S. N., Watson D. M. & Pipher J. L. (2000). Performance and spectral response of  $Pb_{1-x}Sn_xTe(In)$  far-infrared photodetectors, *Appl. Phys. Lett.*, Vol. 76, pp. 2835-2837, ISSN 0003-6951
- Klimov A.E. & Shumsky V.N. (2001). Photodielectric effect in epitaxial  $Pb_{1-x}Sn_xTe<In>$  films produced by molecular beam epitaxy, *Optoelectronics, Instrumentation and Data Processing*, No. 3, pp. 53-62, ISSN 8756-6990
- Klimov A.E. & Shumsky V.N. (2001). Giant light-modulated permittivity of  $Pb_{0.74}Sn_{0.26}Te<In>$  narrow band-gap isolator: new approach to relaxation processes and potential applications, *Proceedings of International Semiconductor Device Research Symposium (ISDRS 2001)*, Washington, USA, December 2001
- Klimov A. E. & Shumsky V.N. (2003). Photocapacitance effect in narrow band gap  $PbSnTe<In>$ , *Proceedings SPIE*, Vol. 5126, pp. 341-346, ISSN 0277-786X
- Klimov A., Shumsky V. & Kubarev V. (2007). Terahertz sensitivity of  $Pb_{1-x}Sn_xTe:In$ , *Ferroelectrics*, Vol. 347, pp. 111-119, ISSN 0015-0193
- Klimov A.E. & Shumsky V.N. (2008). Photosensitivity of  $Pb_{1-x}Sn_xTe:In$  films in the region of intrinsic absorption, *Semiconductors*, Vol. 42, No. 2, pp. 149-15, ISSN 1063-7826
- Klimov A., Sherstyakova V. & Shumsky V. (2009). Giant magnetoresistance in narrow-gap ferroelectric-semiconductor  $PbSnTe:In$ , *Ferroelectrics*, Vol. 378, pp. 101-110, ISSN 0015-0193
- Klimov A.E. & Shumsky V.N. (2009). Shallow traps and the space-charged-induced limitation of the injection current in  $PbSnTe:In$  narrow-gap ferroelectric, *Physica B*, Vol. 404, No. 23-24, pp. 5028-5031, ISSN 0921-4526
- Lampert M.A. & Mark P. (1970). *Current injection in solids*, Academic Press, N.Y.-London.
- Lishka K., Durstberger R., Lindermann G., Staudinger H. (1984). Defect states in  $Pb_{1-x}Sn_xTe$ , *Phys. Stat. Sol. (a)*, Vol. 123, pp. 319-324, ISSN 0031-8965
- Marshall J. & Owen A.E., (1976). Field-effect measurements in disordered  $As_{30}Te_{48}Si_{12}Ge_{10}$  and  $As_2Te_3$ , *Philosophical Magazine*, Vol. 33, p. 457, ISSN 1478-6435
- Mitsuru I. & Ruiping W. (2000). Quantum ferroelectricity in  $SrTiO_3$  induced by oxygen isotope exchange, *Appl. Phys. Lett.*, Vol. 76, pp. 221-223, ISSN 0003-6951
- Mott N.F. & Davis E.A. (1979). *Electron processes in non-crystalline materials*, Clarendon Press. Oxford
- Nasybbulin R. A., Girshberg Ya. N., Trunov N. N., Kalimullin R. H., Kukharskii A. A., Kharionovskii Yu. S., Shapkin V. V. & Bursian E. V. (1983). Non-monotone dependence on composition of the ferroelectric phase transition temperature in

- $Pb_{1-x}Sn_xTe$ , *Fizika Tverdogo Tela (in Russian)*, Vol. 25, No. 4, pp. 784–788, ISSN 0367-3294
- Romcevic N., Popovic Z.V., Khokhlov D., Nikorich A.V. & Konig W. (1991). Far-infrared study of In doped  $Pb_{0.75}Sn_{0.25}Te$  single crystals, *Infrared Phys.*, Vol. 31, No. 3, pp. 225-230, ISSN 1350-4495
- Suris R.A. & Fuks B.I. (1975). Sample impedance of compensated material under the conditions of the space-charge wave excitation, *Fizika i Tekhnika Poluprovodnikov (in Russian)*, Vol. 9, No. 1717-1727, ISSN 0367-3294
- Van Roesbroeck W. & Shockley W. (1954). Photon-radiative recombination of electrons and holes in germanium, *Phys. Rev.*, Vol. 94, No. 6, pp. 1558-1560, ISSN 0031-899X
- Vinogradov V. S. , Voronova I. D., Kalyuzhnaya G. A. , Ragimova T. Sh. & Shotov A. P. (1980). Hall effect and photoconductivity of  $Pb_{1-x}Sn_xTe$  with indium, *JETP Letters*, Vol. 32, No. 1, pp. 20-24, ISSN 0021-3640
- Vinogradov V.S. & Kucherenko I.V. (1991). Ferroelectric properties of  $Pb_{1-x}Sn_xTe$  ( $x=0.25$ ) crystals doped with indium. *Fizika Tverdogo Tela (in Russian)*, Vol. 33, No. 9, pp. 2572-2578, ISSN 0367-3294
- Volkov B. A. & Pankratov O. A. (1980). Yan-Teller instability of crystal environment of point defects in  $A^4B^6$  semiconductors, *Doklady Akademii Nauk (in Russian)*, Vol. 255, No. 1, pp. 93-97, ISSN 0869-5652
- Volkov B. A. & Ruchaiski O. M. (1995). Intracenter Coulomb correlations, charge states, and spectrum of group-III impurities in IV-VI narrow-gap semiconductors, *JETP Lett.*, Vol. 62, No. 3, pp. 217-222, ISSN 0021-3640
- Volkov B.A., Ryabova L.I. & Khokhlov D.R. (2002). Mixed-valence impurities in lead telluride-based solid solutions. *Physics Uspekhi*, Vol. 45, No. 8, p. 819-846, ISSN 1063-7869
- Vul B.M., Voronova I.D., Kaliuzhnaya G.A., Mamedov T.S. & Rakhimova T.Sh. (1979). Peculiarities of transport phenomena in  $Pb_{0.78}Sn_{0.22}Te$  with large content of indium. *JETP Letters*, Vol. 29, No. 1, pp. 18-22, ISSN 0021-3640
- Zasavitskii I.I., Matvienko A.V., Matsonoshvili B.N. & Trofimov V.T. (1986). Photoconductivity spectrum of  $Pb_{1-x}Sn_xTe:In$  epitaxial layers, *Fizika i Tekhnika Poluprovodnikov (in Russian)*, Vol. 20, No. 2, pp. 214-220, ISSN 0015-3222

# Piezo-optic and Dielectric Behavior of the Ferroelectric Lithium Heptagermanate Crystals

A. K. Bain<sup>1</sup>, Prem Chand<sup>1</sup> and K. Veerabhadr Rao<sup>2</sup>

<sup>1</sup>*Department of Physics, Indian Institute of Technology Kanpur*

<sup>2</sup>*Advanced Center for Materials Science, Indian Institute of Technology Kanpur  
India*

## 1. Introduction

It is well known that piezo-optic and electro-optic effects in crystals find wide ranging applications in laser devices. The photoelastic behavior of crystals forms a necessary prelude to study the electro-optical effect of ferroelectric crystals. Lithium heptagermanate  $\text{Li}_2\text{Ge}_7\text{O}_{15}$  (LGO) is regarded as a weak ferroelectric and its curie point  $T_c$  is 283.5K (Wada et al., 1981, 1983). Due to its intermediate behaviour between order-disorder and displacive types in a conventional grouping of ferroelectric materials LGO remains a subject of interest from both the theoretical and the application point of view. The paraelectric phase above  $T_c$  is orthorhombic  $D_{2h}^{14} \sim \text{pbcn}$  and below  $T_c$  the ferroelectric phase is  $C_{2v}^5 \sim \text{pbc}2_1$  with four formula units in a unit cell in both the phases. Below  $T_c$  LGO shows dielectric hysteresis loop and the permittivity shows a sharp peak at  $T_c$  (Preu, 1982; Wada et al., 1981, 1983). The Raman scattering spectrum shows a soft mode whose frequency tends to zero as  $T_c$  is approached from below (Wada & Ishibashi, 1983). Below  $T_c$  the spontaneous polarization appears along the c-axis. The nature of the second order phase transition is not simple because according to Raman spectra the transition is suggested to be a displacive phase transition. But the temperature dependence of the permittivity  $\epsilon$  is indicative of the order disorder character of the phase transition (Preu, 1982; Wada et al., 1981, 1983) and does not agree with the behaviour expected of a displacive phase transition.

Many interesting physical properties of LGO such as birefringence (Kaminsky & Haussühl, 1990), elastic (Haussühl et al., 1980), thermal expansion (Wada & Ishibashi, 1983), dielectric susceptibility (Preu, 1982; Kudzin, 1994a, 1995b), electron paramagnetic resonance (EPR) of doped ions  $\text{Mn}^{2+}$  and  $\text{Cr}^{3+}$  (Trubitsyn et al., 1992; Bain, 1994) and photoluminescence (Bain, 1994) exhibit strong anomalies around  $T_c$ . However, the optical properties vary only to such a small degree that the transition could not be detected with the aid of a standard polarization microscope (Kaminsky & Haussühl, 1990). Interestingly with the help of a high resolution polarization device, Kaminsky and Haussühl (Kaminsky & Haussühl, 1990) studied the birefringence in LGO near  $T_c$  and observed anomalies at the phase transition.

The study of piezo-optic dispersion of LGO (un-irradiated and irradiated) in the visible region of the spectrum of light at room temperature ( $RT=298$  K) shows an optical zone/window in between  $5400\text{\AA}$  and  $6200\text{\AA}$  with an enhanced piezo-optical behavior (Bain et al., 2008). The temperature dependence of the photoelastic coefficients of the ferroelectric

crystals  $\text{Li}_2\text{Ge}_7\text{O}_{15}$  (both un-irradiated and x-irradiated) in a cooling and a heating cycle between room temperature and 273K shows an interesting observation including the lowering of the  $T_c$  under uniaxial stress contrary to the increase of  $T_c$  under hydrostatic pressure and observation of thermal photoelastic hysteresis similar to dielectric behavior (Bain et al., 2009). The study of a.c. electrical impedance ( $Z$ ) along the c-axis of the crystals LGO in the temperature range 283.5 K to 573 K at the frequency range 10kHz – 10,000 kHz shows a sharply decrease of the magnitude of  $|Z|$  with increasing frequency and tends to zero value at about the frequency 10,000kHz.

This chapter will include basic properties of the ferroelectric Lithium heptagermanate ( $\text{Li}_2\text{Ge}_7\text{O}_{15}$ ) crystals, related experimental studies on this crystal including growth of single crystals, agreement and disagreement between the results of different experimental investigations. The brief description on the theory of photoelasticity, fabrication process of the ferroelectric  $\text{Li}_2\text{Ge}_7\text{O}_{15}$  crystals, experimental methods of the photoelastic coefficients of LGO (un-irradiated and irradiated) at different wave length and temperatures around the phase transition temperature  $T_c$  and also the practical applications of the LGO crystals in the opto-electronic devices will be discussed.

### 1.1 Growth and structure of $\text{Li}_2\text{Ge}_7\text{O}_{15}$ crystals

Single crystals of  $\text{Li}_2\text{Ge}_7\text{O}_{15}$  are grown in an ambient atmosphere by Czochralski method from stoichiometric melt, employing a resistance heated furnace. Stoichiometric mixture of powdered  $\text{Li}_2\text{CO}_3$  and  $\text{GeO}_2$  in the ratio of 1.03 and 7.0 respectively was heated at 1100 K for 24 hours to complete the solid state reaction for the raw material for the crystal growth. The crystals were grown by rotating the seed at the rate of 50 rpm with a pulling rate of 1.2 mm/hour. The cooling rate of temperature in the process of growth was 0.8-1.2 K/hour. The crystals grown were colorless, fully transparent and of optical quality. The crystal axes were determined by x-ray and optical methods.

The desired impurities such as  $\text{Cr}^{+3}$ ,  $\text{Mn}^{+2}$ ,  $\text{Bi}^{+2}$  and  $\text{Eu}^{+2}$  etc are also introduced in desired concentration by mixing the appropriate amount of the desired anion salt in the growth mixture. The crystal structure of LGO above  $T_c$  is orthorhombic (psedohexagonal) with the space group  $D_{2h}^{14}$  (Pbcn). The cell parameters are a: 7.406 Å, b: 16.696 Å, c: 9.610 Å,  $Z = 4$  and  $b \sim \sqrt{3}c$ . Below  $T_c$  a small value of spontaneous polarization occurs along c-axis and the ferro-phase belongs to  $C_{2v}^5$  (Pbc2<sub>1</sub>) space group. The crystal structure contains strongly packed layers of  $\text{GeO}_4$  tetrahedra linked by  $\text{GeO}_8$ -octahedra to form a three dimensionally bridged frame work in which Li atoms occupy the positions in the vacant channels extending three dimensionally (Haussühl et al., 1980; Wada et al., 1984, 1988; Iwata et al., 1987). The size of the unit cell ( $Z = 4$ ) does not change at the phase transition and ferroelectric phase transition is associated with a relaxational mode as well as the soft phonon (Wada, 1988).

### 1.2 Theory of photoelasticity

If a rectangular parallelepiped with edges parallel to  $x[100]$ ,  $y[010]$  and  $z[001]$  axes is stressed along z-axis and observation is made along y-axis, as shown in Fig.1, then the path retardation  $\delta_{zy}$  introduced per unit length due the stress introduced birefringence is given by

$$\delta_{zy} = (\Delta n_z - \Delta n_x) = C_{zy} P_{zz} \quad (1)$$

where  $\Delta n_z$  and  $\Delta n_x$  are the changes in the corresponding refractive indices,  $(\Delta n_z - \Delta n_x)$  is the corresponding stress induced birefringence,  $P_{zz}$  is the stress along z-axis and  $C_{zy}$  is a constant called the Brewster constant or the relative photoelastic coefficient. In general the Brewster constant is related to the stress optical and strain optical tensors of fourth rank (Narasimhamurty, 1981) and is a measure of the stress induced (piezo-optic) birefringence. It is conveniently expressed in the unit of  $10^{-13}$  cm<sup>2</sup>/dyne per cm thickness along the direction of observation is called a Brewster (Narasimhamurty, 1981).

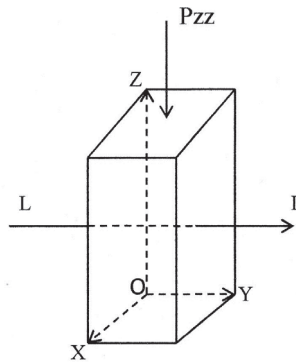


Fig. 1. A solid under a linear stress of stress-optical measurements ( $P_{zz}$  is the applied stress and LL is the direction of light propagation and observation).

### 1.3 Experimental method of determining the photoelastic constants

To study the piezo-optical birefringence the experimental set up consists of a source of light (S), a lens (L) to render the rays parallel, a polarizer (P), an analyzer Polaroid (A), a Babinet compensator (B) and a detector (D), as shown in Fig.2. The P and A combination are adjusted for optimal rejection of light. The sample with stressing arrangement and a Babinet compensator are placed between P and A. A monochromator and a gas flow temperature controlling device are used to obtain the piezo-optic coefficients ( $C_\lambda$ ) at different wavelengths and temperature. The subscript  $\lambda$  in the symbol  $C_\lambda$  denotes that the piezo-optic coefficient depends on the wavelength of light used to measure it. The experiments are carried out for different wavelengths using white light and a monochromator and the monochromatic sodium yellow light. An appropriate stress along a desired direction of the sample is applied with the help of a stressing apparatus comprising a mechanical lever and load.

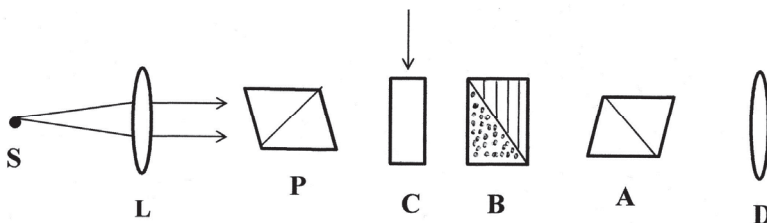


Fig. 2. A schematic diagram of the experimental setup for the measurement of photoelastic constants of the crystals at room temperature. Source of light (S), Lense (L), Polarizer (P), Crystals (C) under stress, Babinet Compensator (B), Analyzer (A) and Detector (D).

To start with, the Babinet compensator is calibrated and the fringe width is determined for different wavelengths of light in the visible region. The crystal specimen is placed on the stressing system so that the stress could be applied along vertical axis and observation made along horizontal axis. A load on the crystal shifts the fringe in the Babinet compensator and this shift is a measure of the piezo-optic behavior. The piezo-optic coefficients ( $C_\lambda$ ) are now calculated using the calibration of the Babinet compensator. The experiment is repeated for other orientations of the crystals and the results are obtained.

#### 1.4 Piezo-optic dispersion of $\text{Li}_2\text{Ge}_7\text{O}_{15}$ crystals

The experimental procedure for the piezo-optic measurements is described in section 1.3. The polished optical quality samples worked out to dimensions i) 5.9 mm, 9.4 mm and 5.0 mm; ii) 3.17 mm, 5.88 mm and 6.7 mm, along the crystallographic a, b and c axes respectively. The stress was applied with an effective load of ~23 kg in each case (Bain et al., 2008).

The values of  $C_\lambda$  thus obtained at different wavelengths are given in Table 1 and the results are plotted in Fig. 3. Here  $C_{pq}$  is the piezo-optic coefficient with the stress direction being p and observation direction being q. The results show an interesting piezo-optic behavior. A survey of literature indicates that the piezo-optic behavior of materials studied till now shows a reduction of  $C_\lambda$  with increasing wavelength in the visible region (Narasimhamurty, 1981). In the present case,  $C_\lambda$  decreases with wavelength up to a certain wavelength as in other normal materials and then suddenly shows a peak and later on the usual behavior of reduction in the values of piezo-optic coefficients is observed.

Obs.	$C_{pq}$	Wavelengths				
		4358Å	4880Å	5390Å	5890Å	6140Å
1	$C_{xy}$	4.024	3.819	3.722	4.328	3.677
2	$C_{xz}$	5.243	4.895	4.770	5.552	4.451
3	$C_{yx}$	4.084	3.525	3.092	3.562	2.913
4	$C_{yz}$	4.353	4.118	3.946	4.261	3.866
5	$C_{zy}$	4.179	2.814	3.177	3.713	3.172
6	$C_{zx}$	3.312	2.991	2.650	4.190	2.618

Table 1. Stress optical coefficients  $c_{pq}$  (in Brewster) for  $\text{Li}_2\text{Ge}_7\text{O}_{15}$  at different wave lengths.

To the best knowledge of the authors this behavior is unique to the LGO crystals. For the sake of convenience we denote  $C_\lambda$  measured at  $\lambda = 5890 \text{ \AA}$  as  $C_{5890}$  and so on. The results show that sometimes the value of  $C_{5890}$  is even higher than that at  $C_{4400}$ , the value of piezo-optic coefficient obtained at the lowest wavelength studied here. This is the case with  $C_{xy}$ ,  $C_{zx}$  and  $C_{xz}$ . For other orientations the value is lower than that at  $4400 \text{ \AA}$ . Further,  $C_\lambda$  is found to have increased to more than 50% in the case of stress along  $[001]$  and observation along  $[100]$ . Also, it is interesting to note that the value of  $C_{6140}$ , is less than that of  $C_{5390}$ , in tune with usual observation of piezo-optic dispersion. Thus one can see an "optical window" in between  $5400 \text{ \AA}$  and  $6200 \text{ \AA}$ . The height of this optical window is different for various orientations, though the width seems approximately the same. The maximum height of about 1.5 Brewster was found for  $C_{zx}$  followed by  $C_{xz}$  with about 0.9 Brewster. It should be noted here that Z-axis is the ferroelectric axis for LGO. It is also interesting to note that the change in height is more in the former while the actual value of  $C_\lambda$ , is less compared to that of the latter. The percentage dispersion also is different for various orientations. It is very high, as high as 25% for  $C_{zy}$ , while it is just 10% for  $C_{xy}$ .

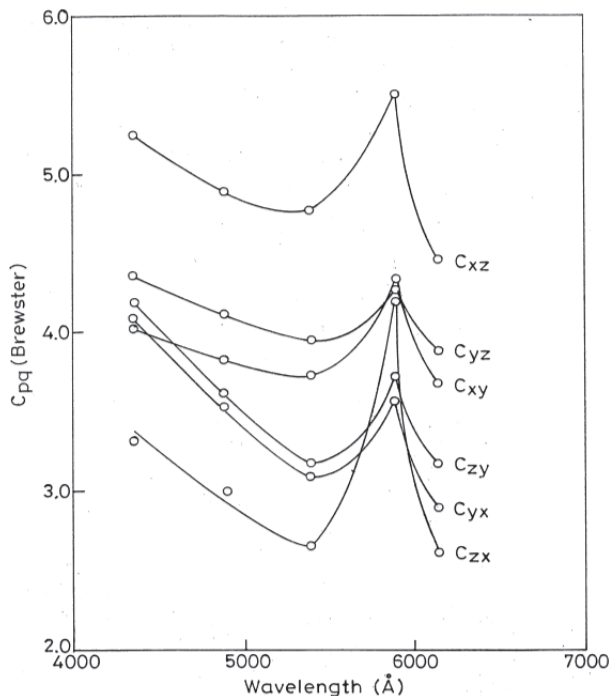


Fig. 3. Stress optical dispersion of  $\text{Li}_2\text{Ge}_7\text{O}_{15}$  crystals with wavelength at room temperature (298 K).

Figure 4 shows the variation of  $C_{zx}(\lambda)$  at the temperatures ranging from 298K to 283K on cooling process of the sample LGO. It is clear from the figure that the distinct peak of  $C_{zx}(\lambda)$  appears only at the sodium yellow wavelength of  $5890 \text{ \AA}$  for the whole range of temperatures (298 K-283 K) investigated. It is also interesting to note that a temperature anomaly is also observed around 283 K. LGO undergoes a second order phase transition at 283.5 K from the high temperature paraelectric phase to the low temperature ferroelectric phase. So this anomaly is related to this phase transition of the LGO crystal.

The observed peculiarity of piezo-optic behavior could be due to many factors, viz., i) anomalous behavior of refractive index or birefringence ii) anomalous ferroelastic transformation at some stage of loading iii) shift of absorption edge due to loading. The following have been done to identify the reasons for this peculiar behaviour.

Birefringence dispersion has been investigated in the visible region and no anomalies in its behavior has been observed. This rules out the first of the reasons mentioned. The reason due to ferroelastic behavior also is ruled out since the effect would be uniform over all the wavelengths investigated. It was not possible to investigate the effect of load on the absorption edge. Hence an indirect experiment has been performed. If there is a shift in the absorption edge due to loading the sample, the peak observed now at sodium yellow light would shift with load. No clear shift of the peak could be observed within the experimental limits. Another interesting experiment was done to identify the source of the anomaly. It is well known that  $T_c$  of LGO changes under uniaxial stress. The measurements were made near  $T_c$  under different stress (loads). Although  $T_c$  was found to shift a little with load the

dispersion peak did not show any discernible shift. No particular reason could be established as to why a dispersion peak appears around sodium yellow region. Another interesting work in this direction is on  $Gd_2(MoO_4)_3$  – where an anomalous peak was recorded in spontaneous birefringence at 334.7 nm (Saito et al., 1994), an observation made for the first time.

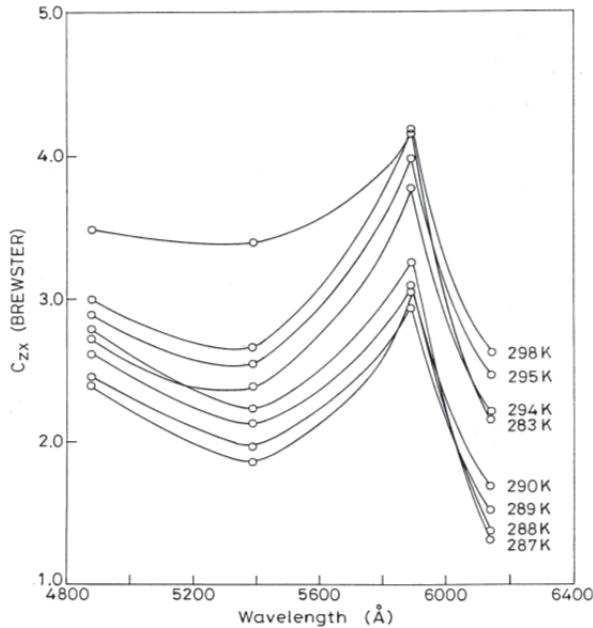


Fig. 4. The variation of  $C_{zx}(\lambda)$  at the temperatures ranging from 298 K to 283 K on cooling process of the sample  $Li_2Ge_7O_{15}$ .

It is well known that the photoelasticity in crystals arises due to change in number of oscillators, effective electric field due to strain and the polarisability of the ions. In the present case, as the wavelength approaches around 5400 Å, the ionic polarisability seems to be changing enormously. There is no optical dispersion data available on LGO. We have conducted an experiment on transmission spectra of LGO along x, y and z-axes, which shows a strong absorption around 5400 Å. The observed anomaly in the piezo-optic dispersion may be attributed to the absorption edge falling in this region. This explanation needs further investigation in this direction. It is also known that the strain optical dispersion arises due to the shift in absorption frequencies and a change in the oscillator strength caused by the physical strain in the crystal.

### 1.5 Irradiation effect on Piezo-optic dispersion of $Li_2Ge_7O_{15}$ crystals

The ferroelectric single crystals  $Li_2Ge_7O_{15}$  was irradiated by x-ray for one hour and the experimental processes described in section 1.4 were repeated for the crystal (irradiated) LGO in order to understand the radiation effect on piezo-optical birefringence dispersion (Bain et al., 2008). The values of  $C_\lambda$  of the crystal (irradiated) LGO thus obtained at different wavelengths are given in Table 2 and the results are plotted in Fig. 5.

Obs.	$C/p_q$	Wavelengths				
		4358Å	4880Å	5390Å	5890Å	6140Å
1	$C/_{xy}$	4.08	3.87	3.72	4.33	3.73
2	$C/_{xz}$	5.35	5.00	4.88	5.59	4.55
3	$C/_{yx}$	4.02	3.47	3.01	3.50	2.83
4	$C/_{yz}$	4.39	4.19	4.01	4.26	3.90
5	$C/_{zx}$	4.63	4.46	4.41	4.66	4.29
6	$C/_{zy}$	3.71	3.26	2.97	3.43	2.72

Table 2. Stress Optical Coefficients  $C_{pq}$  (in Brewsters) for  $\text{Li}_2\text{Ge}_7\text{O}_{15}$  (irradiated) at different wavelengths.

Some interesting results are obtained in the case of irradiated crystal LGO. The peak value of  $C/_{zx}$  has decreased about 18% and that of  $C/_{zy}$  has increased about 25% at the wave length  $\lambda = 5890 \text{ \AA}$ . Also, it is interesting to note that the value of  $C_{6140}$ , is less than that of  $C_{5390}$  for the un-irradiated and irradiated sample of LGO crystal, in tune with usual observation of piezo-optic dispersion.

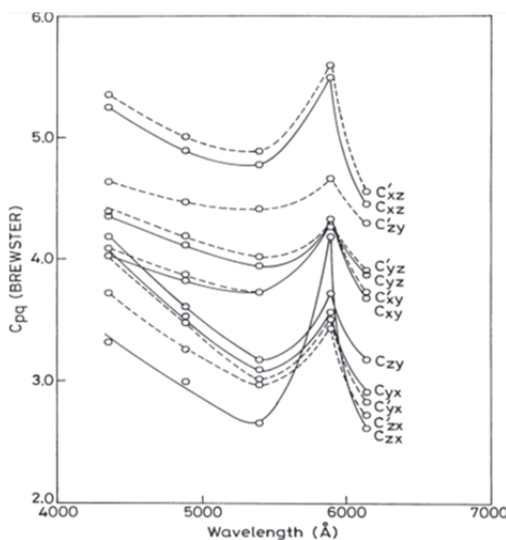


Fig. 5. Stress optical dispersion of  $\text{Li}_2\text{Ge}_7\text{O}_{15}$  crystals (un-irradiated and irradiated) with Wavelength at room temperature (298 K).

Irradiation of crystals can change physical properties of the crystals. Irradiation brings about many effects in the crystal such as creating defects, internal stress and electric fields etc. These irradiation effects in turn are supposed to affect the physical properties of the irradiated crystal as compared to un-irradiated crystal. While there was no appreciable change in the lattice parameters, a significant drop in the value of dielectric constant and  $\tan \delta$  was observed upon x-irradiation of ferroelectric glycine phosphate. An appreciable shift in the phase transition temperature towards the lower temperature was observed. These changes are attributed to the defects produced in it by irradiation (Vanishi & Bhat, 2005). The studies of triglycine sulphate (TGS) showed that very small doses of x-irradiation

can give large changes of the ferroelectric properties. The direct evidence of domain clamping by defects was obtained from optical studies. With increasing dosage the dielectric constant peak and polarization curve broaden and move to lower temperatures. In our present studies, the x-irradiation is believed to produce internal stress and electric fields inside the crystals LGO due to defects that can change the values of piezo-optic constants (Lines & Glass, 2004).

## 2. Dielectric property of lithium heptagermanate crystals

Lithium heptagermanate  $\text{Li}_2\text{Ge}_7\text{O}_{15}$  (LGO) belongs to weak ferroelectric crystals and it has a high nonlinearity of dielectric constant  $\epsilon$  near  $T_c$ . The curie-Weiss law holds only within a narrow temperature interval close to  $T_c$  with a small value of the Curie constant. This high nonlinearity may be influenced by the external and internal electric field. The dielectric permittivity has been shown (Wada & Ishibashi, 1983) to be sensitive to sample history, so that reproducible results could be obtained only after a prolonged sample anneal at a temperature substantially above  $T_c$ . The nature of such behavior of  $\epsilon$  is not clear.

### 2.1 Space charge effect in $\text{Li}_2\text{Ge}_7\text{O}_{15}$ crystals

An attempt is made to study the dielectric permittivity  $\epsilon$  during the phase transition. The plate-like specimens for the electrical measurements were polished and then silver electrodes were deposited. The dielectric constants were measured along the c-axis at the frequency of 1 MHz by means of a LCR meter (E7-12) in the temperature range from 298 K to 273 K (Bain, 1994; Kudzin et. al., 1994, 1995).

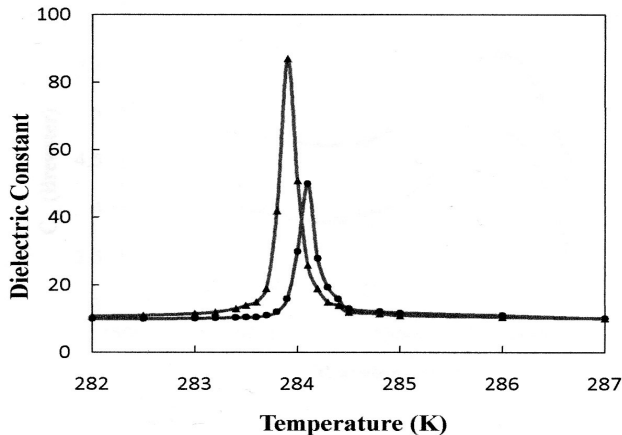


Fig. 6. The temperature dependence of dielectric constant  $\epsilon$  of  $\text{Li}_2\text{Ge}_7\text{O}_{15}:0.7\% \text{Bi}$  crystal at 1 MHz on cooling ( $\blacktriangle$ ) and heating ( $\bullet$ ) process.

Figure 6 shows the dielectric constant  $\epsilon$  of  $\text{Li}_2\text{Ge}_7\text{O}_{15}:0.7\% \text{Bi}$  measured on cooling and heating at 1 MHz as a function of temperature. It is found that the dielectric constant shows a sharp peak around  $T_c$ . The values at the peak are about 87 at cooling and about 50 at heating. The function  $\epsilon(T)$  is represented after the sample heating up to 290 K during about an hour.

Sample	$\epsilon_{\max}$	$\Delta\epsilon_{\max}$	$\Delta\epsilon_{\max}/\epsilon_{\max}, \%$
LGO	74.9	19.9	26
LGO: 0.2%Bi	114.1	44.1	38
LGO: 0.3%Bi	120.18	49.73	41
LGO: 0.5%Bi	39.41	9.03	23
LGO: 0.7%Bi	87.19	37.42	42.9
LGO: 0.6%Eu	79.51	27.25	34
LGO: 0.3%Cr	9.86	1.62	16

Table 3. The relative change of  $\Delta\epsilon_{\max}/\epsilon_{\max}$  for  $\text{Li}_2\text{Ge}_7\text{O}_{15}$  crystals and with different percentage of impurity ions Bi, Eu and Cr.

The Curie-Wess plot of  $\epsilon$  of  $\text{Li}_2\text{Ge}_7\text{O}_{15}:0.7\%\text{Bi}$  is shown in Figure 7, taking  $\epsilon_0$  as 7.1. It is found that the Curie-Wess law holds only within a narrow temperature region around  $T_c$ . The Curie constant is about 2.6 K above the phase transition temperature and 1.3 K below  $T_c$ . The characteristic behavior of  $\epsilon$  appeared substantially different from the value  $\epsilon_{\max}$  which is obtained under the sample heating and cooling. The relative change of  $\Delta\epsilon_{\max}/\epsilon_{\max}$  for different percentage of impurity ions are shown in table. 3.

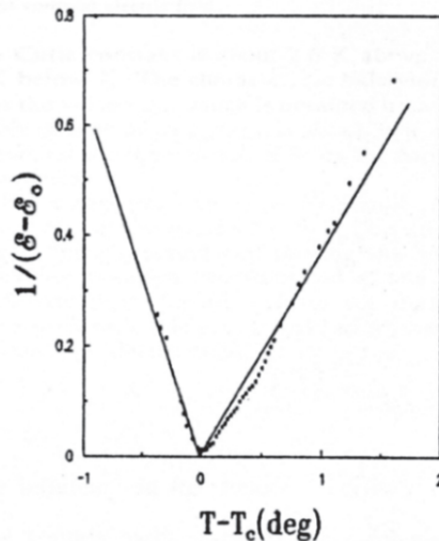


Fig. 7. The temperature dependence of reciprocal dielectric constant along the c-axis of  $\text{Li}_2\text{Ge}_7\text{O}_{15}:0.7\%\text{Bi}$  on cooling. Solid line shows  $\epsilon - \epsilon_0 = C(T - T_c)^{-1}$ , where  $\epsilon_0 = 7.1$ ,  $T_c = 283.9$  K and  $C = 2.6$  K above  $T_c$ , while  $C = 1.3$  K below  $T_c$ .

The dielectric constant  $\epsilon$  is also measured at the frequency of 1 MHz at a constant electric field. It is observed that the value of  $\epsilon$  at  $T_c$  decreases with the increase of constant electric field during cooling and heating the sample and it is also observed that the difference between two values of  $\epsilon$  decreases at  $T_c$  with the increase of constant electric field. Fig.8 shows the dielectric constant  $\epsilon$  of  $\text{Li}_2\text{Ge}_7\text{O}_{15}:0.7\%\text{Bi}$  measured on cooling at 1 MHz as a function of temperature for different values of constant electric field.

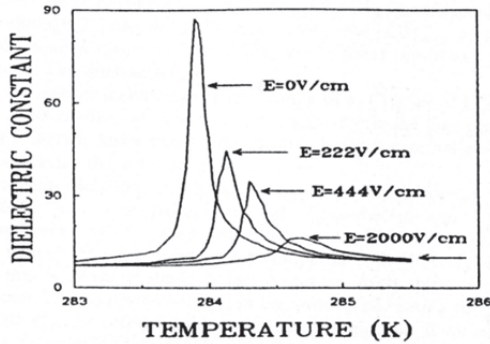


Fig. 8. The temperature dependence of dielectric constant  $\epsilon$  of  $\text{Li}_2\text{Ge}_7\text{O}_{15}:0.7\%\text{Bi}$  at 1 MHz on cooling for different values of constant electric field.

The spontaneous polarization  $P_s$  and the coercive field  $E_c$  were studied at 50 Hz by the well known Sawyer-Tower technique. Both  $P_s$  and  $E_c$  were found to be independent of the Bismuth ion concentration in  $\text{Li}_2\text{Ge}_7\text{O}_{15}$  (within the concentration range investigated). The temperature dependence of  $P_s$  for  $\text{Li}_2\text{Ge}_7\text{O}_{15}:0.7\%\text{Bi}$  crystals is shown in Fig.9.

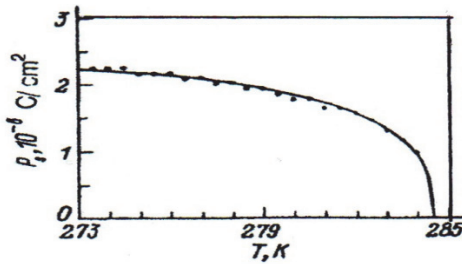


Fig. 9. Temperature dependence of the spontaneous polarization  $P_s$  in  $\text{Li}_2\text{Ge}_7\text{O}_{15}:0.7\%\text{Bi}$  crystals.

Under heating, spontaneous polarization first falls off slowly until  $\sim 280$  K, then faster, and vanishes at  $T_c$ , without revealing a noticeable discontinuity. Fig.10 displays the temperature dependence of the coercive field for  $\text{Li}_2\text{Ge}_7\text{O}_{15}:0.7\%\text{Bi}$  crystals. It is seen to fall off linearly under heating up to  $\sim 280$  K, then faster, to vanish at  $T_c$ .

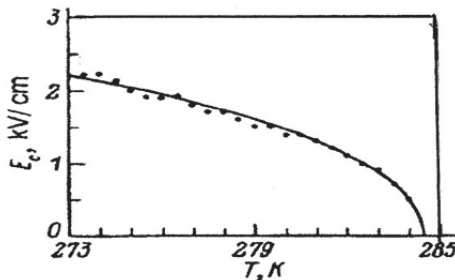


Fig. 10. Temperature dependence of the coercive field  $E_c$  in  $\text{Li}_2\text{Ge}_7\text{O}_{15}:0.7\%\text{Bi}$  crystals.

Domain structure may influence on the dielectric permittivity by means of two mechanisms. 1) The crystals that contain many domains are mechanically (piezoelectric) stressed. The relation between dielectric permittivity at the mechanically stressed and at the mechanically free state is given by (Nye, 1957)

$$\varepsilon^{\varepsilon_3} - \varepsilon^{\varepsilon_0} = d_{33}^2 c E_{33}^2 \quad (\Gamma = \text{Constant}) \quad (2)$$

Here  $\varepsilon^{\varepsilon_3}$  is the dielectric permittivity at the mechanically stressed state and  $\varepsilon^{\varepsilon_0}$  is the dielectric permittivity at the mechanically free state,  $d_{33}$  is the piezoelectric modulus, and  $c E_{33}^2$  is the modulus of elasticity at the constant electric field. This must cause the decrease of  $\varepsilon$  in multi domain crystals. But the estimation shows that this mechanism does not allow to explain the strong difference in  $\varepsilon_{\max}$  at  $T_c$ . 2) The contribution to the dielectric permittivity may give displacements of  $180^\circ$  domain boundary (Nakamura et al., 1984). Crystals of LGO become multi domain near  $T_c$  during heating the sample. After heating the sample only at 1-2 K above  $T_c$  and by subsequent cooling through  $T_c$ , one obtains a very small value of  $\Delta\varepsilon_{\max}$ , as crystals of LGO are multi domain. So, basically it does not connect the hysteresis of dielectric permittivity with domain structure.

There is another mechanism of the change of  $\varepsilon$ . Crystals of LGO have a small spontaneous polarization, which becomes apparent in the high dielectric nonlinearity. It is already known that a comparatively weak external electric field leads to the substantial decrease of  $\varepsilon_{\max}$  (Kholodenko, 1971). Experiments show (Volnyanskii et al., 1992) that the crystals of LGO are monodomain at the temperature  $T_c - 10$  K. The compensation of the field  $E_p$  connected with  $P_s$  may take place by the redistribution of charges inside the crystals. These space charges create an electric field inside the crystals, which compensates the field  $E_p$ . It is possible to assume that this field of space charges is comparatively stable (electret state). In such a case, the decrement of  $\varepsilon_{\max}$  in the process of heating the sample may be connected with the influence of internal field of electret. If we suppose that the effects of external and internal electric field are the same, then the field of electret is  $\sim 160$  V/cm.

Consecutive heating and cooling of a sample from the temperatures 293, 289.25, 285.5 and 284.5 K shows the value of  $\varepsilon_{\max}$  to decrease successively in the cooling runs while remaining constant during heating. This supports the existence of an internal electric field in the sample during the heating process.

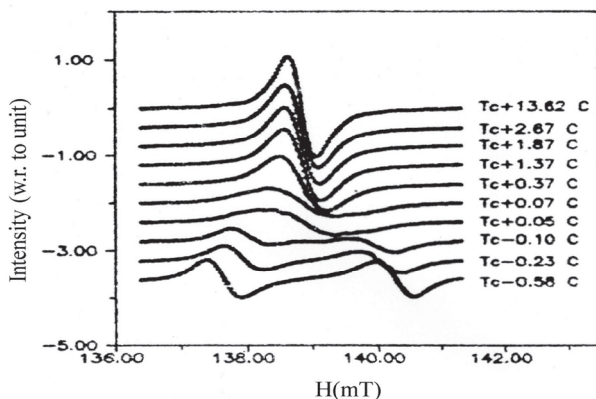


Fig. 11. Temperature dependence of EPR lines of  $\text{Li}_2\text{Ge}_7\text{O}_{15}:\text{Cr}^{3+}$  crystals for  $|M| = \frac{1}{2} \leftrightarrow 3/2$ ,  $H \parallel a$ ,  $H \perp c$  near  $T_c$  during cooling process.

The EPR (Electron Paramagnetic Resonance) spectroscopy of the transition metal ion doped crystals of LGO ( $Mn^{2+}$ ,  $Cr^{3+}$ ) has also been studied both in Paraelectric (PE) and ferroelectric (FE) phases in the temperature interval from 298 K to 279 K during cooling and heating cycles (Trubitsyn et. al., 1992; Bain, 1994). It is observed that on approaching  $T_c$  in a cooling cycle, the EPR lines are slightly shifted to the high field direction and undergo substantial broadening. At the temperature  $T_c$  ( $\approx 283.4$  K), the EPR lines are splitted into two components which are shifted to the higher and lower field directions progressively as a result of cooling the sample below  $T_c$  as shown in Fig.11.

During heating cycle (i.e. approaching  $T_c$  from below), the phenomena occurred were just opposite to the above processes observed in the cooling cycle. However, the EPR line width (peak to peak  $\Delta H_{pp}$ ) for  $H_{\parallel c}$ ,  $H_{\perp a}$  was found to decrease to about one third of its value at  $T_c$  in a heating cycle as compared to its value in the cooling cycle. The shape of the EPR resonance lines far from  $T_c$  has a dominant Lorentzian character (a Lorentzian line shape) but very near to  $T_c$ , the line shape has been described mainly by Gaussian form of distribution (a Gaussian line shape). All the peculiarities observed are attributed to the PE  $\leftrightarrow$  FE phase transition of the LGO crystals. The line width reduction near  $T_c$  is attributed to the internal space charge (electret state) effects which produce an internal electric field inside the crystals on heating process from the ferroelectric phase. This observation is similar to the dielectric hysteresis behavior of the crystals LGO near  $T_c$ .

## 2.2 Study of impedance in $Li_2Ge_7O_{15}$ crystals

The temperature dependence of a.c. electrical impedance ( $Z$ ) was studied along the  $c$ -axis in ferroelectric  $Li_2Ge_7O_{15}$  (LGO) single crystals in 10 kHz - 10,000 kHz frequency range by means of impedance analyzer (Agilent HP4294A) in the temperature interval from 298 K to 273 K during cooling and heating process including  $T_c = 283.5$  K is shown in Fig 12 (Bain et. al., "in print"). A rather temperature hysteresis of impedance is observed in a cooling and heating cycle at  $T_c = 283.5$  K. The relative change of  $\Delta |Z|_{(min)} / |Z|_{(min)}$  at the frequencies 100 kHz - 10,000 kHz is shown in Table 4. The relative change of  $\Delta |Z|_{(min)} / |Z|_{(min)}$  is about 26% and it remains almost constant at the frequencies 100 kHz - 10,000 kHz. Here the value of  $|Z|_{(min)} = |Z|_{room} - [|Z|_{T_c} \text{ (on cooling)}]$  and  $\Delta |Z|_{(min)} = [|Z|_{T_c} \text{ (on heating)}] - [|Z|_{T_c} \text{ (on cooling)}]$ .

Frequency (kHz)	$ Z _{(min)}$ (K- $\Omega$ )	$\Delta  Z _{(min)}$ (K- $\Omega$ )	$\Delta  Z _{(min)} /  Z _{(min)}$ , %
100	3.895	0.97	25.0
200	2.275	0.6	26.4
500	0.374	0.1	26.5
1,000	0.229	0.06	26.2
10,000	0.0224	0.0056	25.0

Table 4. The relative change of  $\Delta |Z|_{(min)} / |Z|_{(min)}$  for  $Li_2Ge_7O_{15}$  crystal at different frequencies.

Like Fig.12, a similar kind of hysteresis was observed in the dielectric behavior of LGO, as described in section 2.1 and the appearance of the dielectric hysteresis is attributed to the internal space charge (electret state) effects which produce an internal electric field in LGO on heating from the ferroelectric phase. It was possible to compensate the internal electric field effects in dielectric measurements by an external electric field (Kudzin et al., 1994, 1995; Bain, 1994). It is suspected that the impedance ( $Z$ ) hysteresis also occurs due to similar effects.

The frequency dependence of  $|Z|$  of the crystal LGO was studied in the temperature range 283.5 K to 573 K, which covers the phase transition temperature ( $T_c$ ) of 283.5 K as shown in Fig.13. It is observed that the magnitude of  $|Z|$  decreases sharply with increasing of frequency and tends to zero value at about the frequency of 10,000 kHz. This may be due to the release of space charges. The curves also display single relaxation process and indicate an increase in a.c. conductivity with frequency. So, in the application point of view, LGO is suitable for conductivity even at the room temperature and frequency controlled switch.

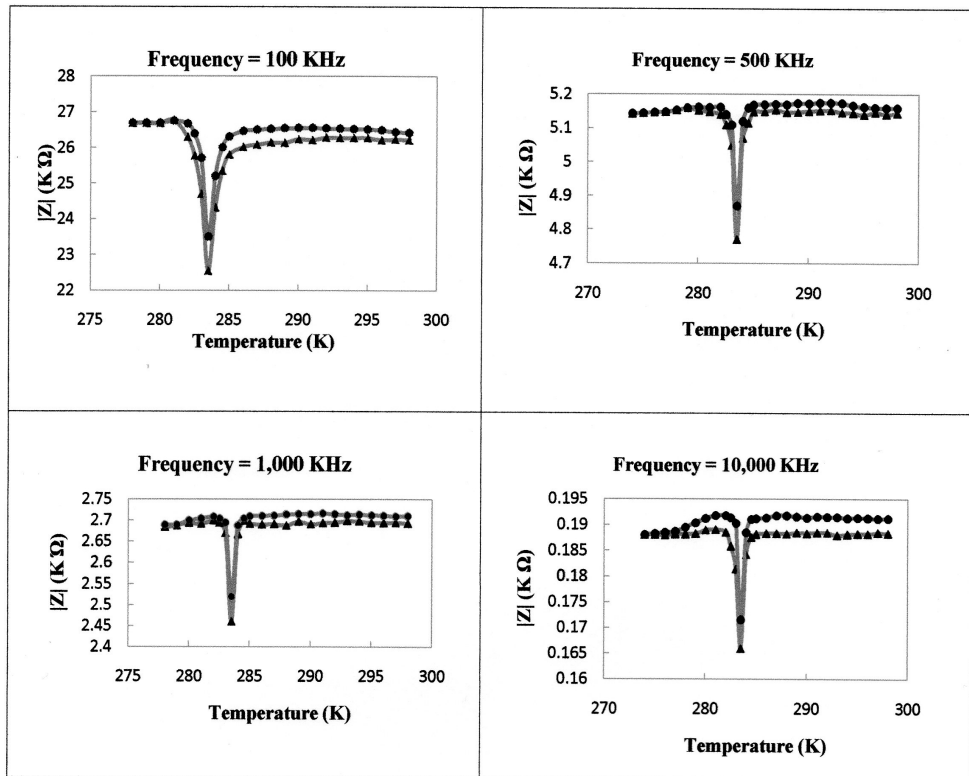


Fig. 12. The temperature dependence of a.c. impedance ( $|Z|$ ) of  $\text{Li}_2\text{Ge}_7\text{O}_{15}$  at 100 kHz, 500 kHz, 1,000 kHz and 10,000 kHz on cooling (▲) and heating (●) processes.

Fig.14 shows the temperature dependence of impedance  $|Z|$  of the crystal LGO at frequency range 100 kHz - 10,000 kHz. It is observed that the value of impedance  $|Z|$  decreases gradually with increasing temperature. This may be related with the space charge relaxation at low frequencies.

At low temperatures the conductivity is dominated by short range hopping of charge carriers. Whereas at high temperatures, more space charges are accumulated at the electrode interfaces and grain boundaries, thus resulting in a strong space charge relaxation (Kim et al., 2002; James et al., 1999).

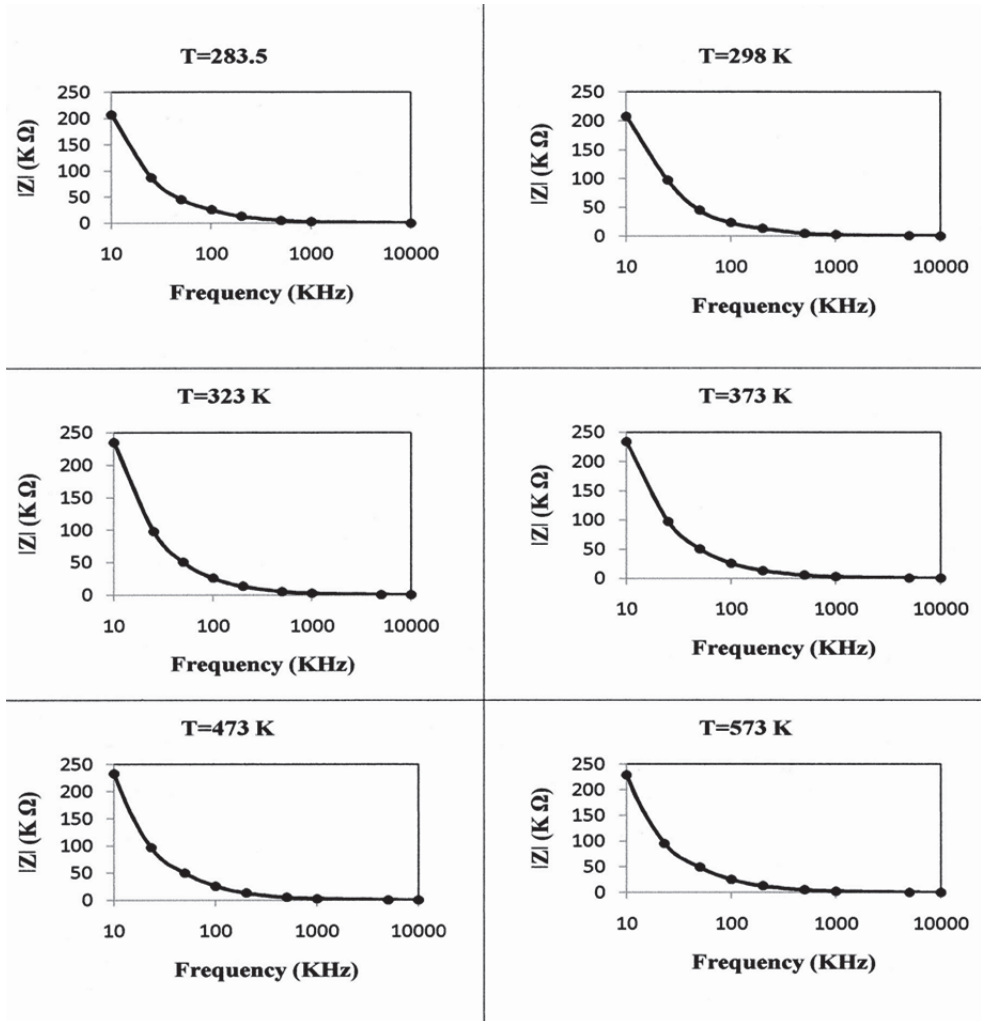


Fig. 13. The frequency dependence of impedance ( $|Z|$ ) of  $Li_2Ge_7O_{15}$  crystal at the temperature range 283.5 K to 573 K.

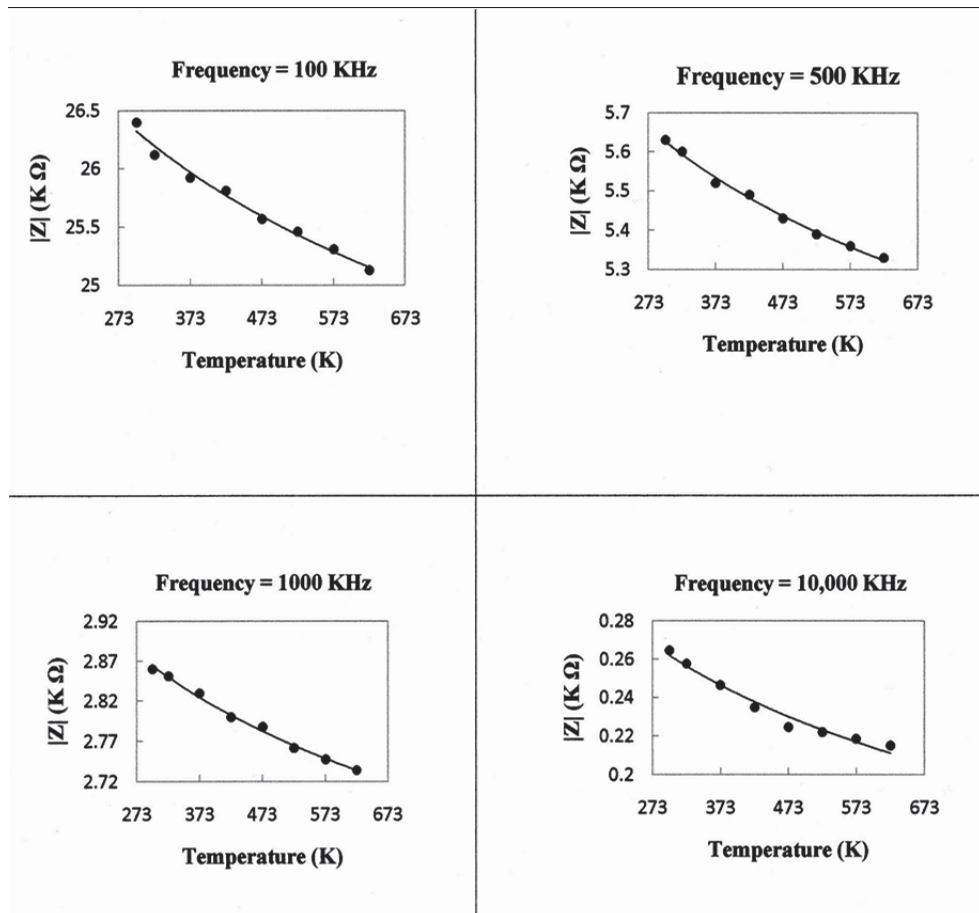


Fig. 14. Temperature dependence of impedance ( $|Z|$ ) of  $\text{Li}_2\text{Ge}_7\text{O}_{15}$  crystal at Frequency range 100 kHz - 10,000 kHz.

### 3. Piezo-optic birefringence in $\text{Li}_2\text{Ge}_7\text{O}_{15}$ crystals

The temperature dependence of the photoelastic coefficients of the ferroelectric crystals  $\text{Li}_2\text{Ge}_7\text{O}_{15}$  in a cooling and heating cycle between 298 K and 273 K was carried out with the experimental procedure described in section 1.4 (Bain et. al., 2009). A special arrangement was made to vary the temperature of the sample. The temperature was recorded with a digital temperature indicator and a thermocouple sensor in contact with the sample.

The temperature dependence of piezo-optic coefficients  $C_{pq}$  of the crystals  $\text{Li}_2\text{Ge}_7\text{O}_{15}$  between 298 K and 273 K were determined and are shown in Fig. 15 and Fig. 16. The values of  $C_{pq}$  at 291 K and 278 K were reported in paper (Bain et.al., 1998) and it was observed that there were large changes in the values of  $C_{zy}$  and  $C_{yz}$  at 278 K and 291 K as compared to other components and  $C_{zy}$  did not show a peak in its temperature dependence between 291K and 278 K.

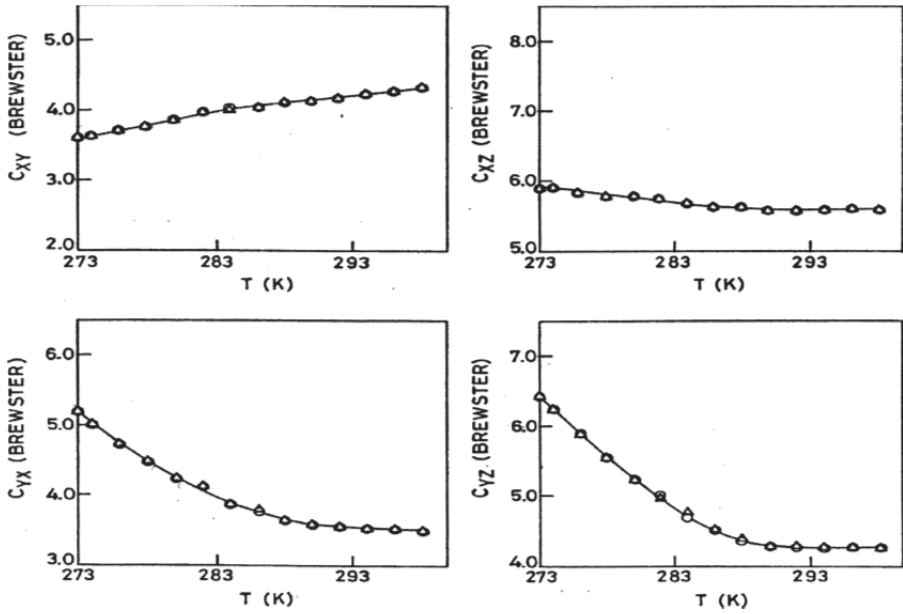


Fig. 15. Temperature dependence of the piezo-optic coefficients  $C_{xy}$ ,  $C_{xz}$ ,  $C_{yz}$  and  $C_{yx}$  of the crystals LGO in a cooling (○) and heating (△) cycle.

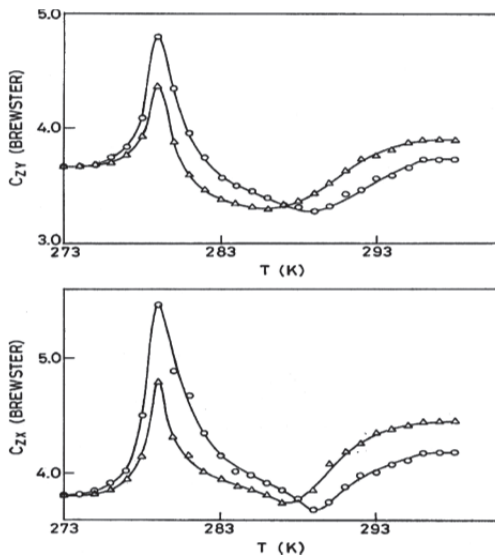


Fig. 16. Anomalous temperature dependence of the piezo-optic coefficients  $C_{zx}$  and  $C_{zy}$  of the crystals LGO in a cooling (○) and heating (△) cycle.

Here in contrast we observed a peak in the temperature dependence of both  $C_{zy}$  and  $C_{zx}$  at 279 K. The temperature dependence of  $C_{pq}$  are quite interesting, for example the piezo-optic coefficients  $C_{yz}$ ,  $C_{yx}$  and  $C_{zx}$  have negative temperature derivatives but  $C_{xy}$  has a positive temperature derivative. In complete contrast both  $C_{zy}$  and  $C_{zx}$  have both positive and negative temperature derivatives at different temperature intervals between 298 K and 273 K (Table: 5). Besides a clear thermal hysteresis is observed in  $C_{zy}$  and  $C_{zx}$  in a complete cooling and heating cycle (Fig. 16) whereas no discernible hysteresis is observed in rest of the piezo-optic coefficients (Fig. 15). The two distinct anomalies in the temperature dependence of  $C_{zy}$  and  $C_{zx}$  are characterized by a valley at  $T_m$  (~289 K) and a peak at  $T_c$  (~279 K). Anomalous temperature dependence of  $C_{zx}$  at different wave lengths is also shown in Fig. 17. The temperature dependence of the dielectric permittivity along the c-axis of LGO shows a sharp peak at  $T_c$  (283.5 K) and the Curie-Weiss law holds only for a narrow range of temperature ( $T_c \pm 4$  K) (Wada & Ishibashi, 1983; Kudzin et al., 1994, 1995) as shown in Fig. 6 and Fig. 7. The peak for piezo-optic coefficient is attributed to the paraelectric to ferroelectric phase transition of LGO at  $T_c$ . To check the curie-Weiss law like dependence near  $T_c$  the following relation is used.

$$C_{pq}^T - C_{pq}^0 = K_{pq}/(T - T_c) \quad (3)$$

Where  $C_{pq}^T$  and  $C_{pq}^0$  denote the value of the corresponding piezo-optic coefficients at temperature  $T$  and 273 K respectively and  $K_{pq}$  is a constant. Figure 18 shows the  $(C_{pq}^T - C_{pq}^0)^{-1}$  vs  $(T - T_c)$  curve for  $C_{zx}$  and  $C_{zy}$ . It is clear from these curves that like dielectric constant the relation fits well only within a narrow range of temperature near  $T_c$  ( $T_c \pm 4$  K). The solid lines denote the theoretical curves with the following values.

$$\begin{aligned} K_{zx} &= 1.05; & K_{zy} &= 0.92 & \text{for } T > T_c \\ K_{zx} &= -0.40; & K_{zy} &= -0.34 & \text{for } T < T_c \\ T_c &= 279 \text{ K} \end{aligned}$$

Further more the magnitudes of the ratio of the temperature derivatives below and above  $T_m$  and  $T_c$  are given in Table 5 and we can see that the ratio near  $T_c$  comes out to be about 2. Therefore it satisfies the law of two for the ratio of such derivatives of quantities which are coupled with the spontaneous polarization in second order ferroelectric phase transition such as in the case of triglycine sulphate (Haussühl & Albers, 1977) and LGO. Therefore the peak around  $T_c$  is (Kaminsky & Haussühl, 1990; Kudzin et al., 1994, 1995) attributed to the paraelectric to ferroelectric phase transition of LGO. The smallness of  $K_{pq}$  and the applicability of relation (3) above only in a narrow range of temperature suggest that LGO may be an improper ferroelectric. The law of two does not hold for the ratio at  $T_m$  (Table 5). Therefore this anomaly is not related to the spontaneous polarization.

From the behaviour that only  $C_{zx}$  and  $C_{zy}$  show anomalous it is obvious that birefringence  $(\Delta n_z - \Delta n_y)$  and  $(\Delta n_z - \Delta n_x)$  show steep increase around  $T_c$  and below  $T_c$  show a  $(T - T_c)^{1/2}$  behaviour correlated to the spontaneous polarization which is parallel to the z-axis (crystallographic c-axis). From the behaviour of  $C_{xy}$  and  $C_{yx}$  which do not show any temperature anomaly we may say that only  $n_z$  is responsible for the anomaly in accordance with the behaviour of the dielectric properties where only  $\epsilon_{33}$  is strongly affected by the phase transition. These observations are in accordance with the results of Faraday effect and birefringence in LGO (Kaminsky & Haussühl, 1990).

$C_{pq}$	Value of Derivative (Brewster/K)	Temperature Range	Ratio
$C_{zx}$	0.013	296K-289K	-1.69
	-0.022	289K-283K	
	-0.090	282K-279K	-2.0
0.181	279K-276K		
$C_{xz}$	~0	276K-273K	-0.75
	-0.003	293K-273K	
	0.020	296K-289K	
-0.015	289K-283K		
$C_{zy}$	-0.095	282K-279K	-1.9
	0.179	279K-276K	
	~0	276K-273K	-0.75
$C_{yz}$	-0.026	293K-273K	
$C_{xy}$	0.007	293K-273K	
$C_{yz}$	-0.023	293K-273K	

Table 5. The temperature derivative  $[dl_n C_{pq}/dT]$  of the piezo-optic coefficients of  $\text{Li}_2\text{Ge}_7\text{O}_{15}$ .

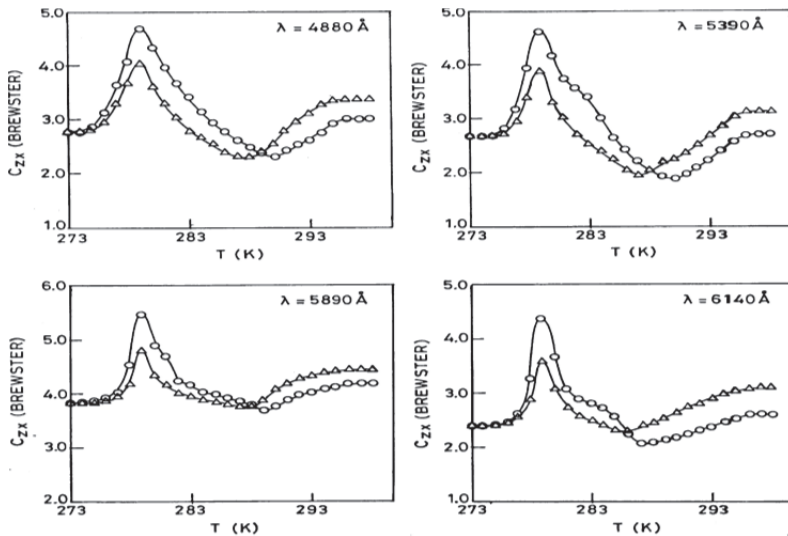


Fig. 17. Anomalous temperature dependence of piezo-optic coefficient  $C_{zx}$  of the crystals LGO at different wave lengths in a cooling (○) and heating (△) cycle.

As mentioned by Lines and Glass (Lines & Glass, 2004), under an external pressure  $T_c$  of a ferroelectric phase transition may be shifted. This shift may be to the higher or the lower side of normal  $T_c$ . Wada et al. (Wada et al., 1981) studied the pressure effect on the

ferroelectric phase transition in LGO through the dielectric and Raman scattering measurements and found a positive pressure coefficient  $dT_c/dp = 14.6$  K/kbar. Preu and Haussühl (Preu and Haussühl, 1982) studied the dependences of dielectric constants on hydrostatic and uniaxial pressure as well as temperature. They observed a shift of  $T_c$  at a rate of 14.02 K/kbar for the hydrostatic pressure and  $\sim 7$  K/kbar for the uniaxial pressure. In the present case the position of the peak of  $C_{zy}$  is found to depend on the stress applied. If the peak position is believed to represent the  $T_c$ , it appears to shift to the lower side under the uniaxial stress. To see whether  $T_c$  shifts linearly with uniaxial stress similar to the earlier observations (Preu and Haussühl, 1982; Wada et al., 1981), we used different stresses within the elastic limits of LGO for  $C_{zx}$  and found a linear relationship (Fig. 19). However, a negative stress coefficient  $dT_c/dp \sim -22$  K/kbar is obtained in this case which agrees only in magnitude with the hydrostatic pressure coefficient. The linear curve (Fig. 19) extrapolates to a  $T_c = 281.5$  K in the unstressed state instead of 283.5K as determined by dielectric measurements (Wada & Ishibashi, 1983; Kudzin et al., 1994, 1995). This may be due to a non linear dependence of shift of  $T_c$  under stress near 283.5 K.

Now we turn to the anomaly around  $T_m$ . Morioka et al. (Morioka et al., 1988) proposed that there is an interaction between the soft phonon mode and a relaxational mode in the paraelectric phase in the temperature interval 300 K to  $T_c$ . The critical slowing down of the relaxational mode near  $T_c$  is expected to cause the increase of the fluctuation of the spatially homogeneous polarization and thereby the increase of the fluctuation of the hyperpolarizability with  $k_c = 0$ . Wada et al. (Wada et al., 1991) measured the soft phonon mode with the help of their newly designed FR-IR spectrometer and proposed that as  $T_c$  is approached from above soft phonon mode becomes over damped and transforms to a relaxational mode.

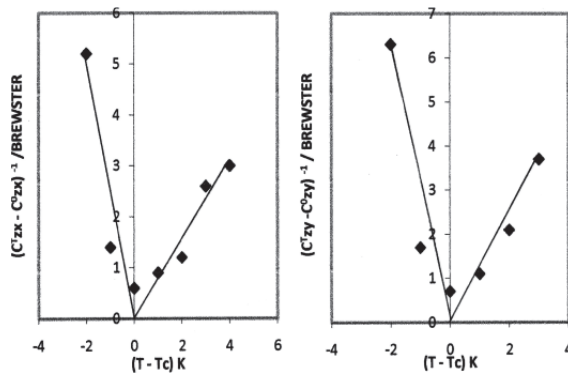


Fig. 18. Plots of  $(C^T_{pq} - C^0_{pq})^{-1}$  vs  $(T - T_c)$  curve for  $C_{zx}$  and  $C_{zy}$ .

On the other hand there may exist a relaxational mode with an independent degree of freedom as well as the soft phonon mode and the character of the softening transfers from the phonon to the relaxational mode. This is an important problem in determining the dynamics of the peculiar ferroelectric phase transition of LGO, where both the dielectric critical slowing down characteristic of the order-disorder phase transition and the soft phonon mode characteristic of the displacive phase transition are observed (Wada & Ishibashi, 1983; Haussühl et al., 1980). In the light of the above discussion we may say that the change up to  $T_m$  is caused by the softening of mode and the softening character

transforms to the relaxations mode near  $T_m$  causing a change in the trend below  $T_m$  and near  $T_c$  the relaxational mode becomes dominant. The valley around  $T_m$  is perhaps caused by the interplay between the competitive relaxational mode and the soft phonon mode. It has been observed that softening of the velocity and rise of the damping of acoustic phonon occur in the paraelectric phase of LGO even quite far from  $T_c$ , i.e.  $(T-T_c) \sim 30$  K and the effect is attributed to the fluctuation induced contributions (Sinii et al., 1990).

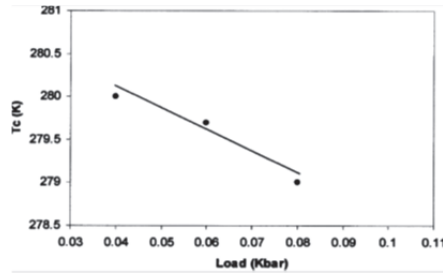


Fig. 19. The stress dependence of the shift of  $T_c$  for  $C_{zx}$ .

Another interesting aspect is the observation of a significant thermal photoelastic hysteresis (Fig. 16). Although the peak position does not shift in the heating cycle the values of the photoelastic constants get reduced significantly in the heating cycle as compared to the corresponding values in a cooling cycle. A similar kind of hysteresis was observed in the dielectric behaviour of LGO (Kudzin et al., 1994, 1995; Bain, 1994) and the appearance of the dielectric hysteresis is attributed to the internal space charge (electrets state) effects which produce an internal electric field in LGO on heating from the ferroelectric phase as described in section 2.1. It was possible to compensate the internal electric field effects in dielectric measurements by an external electric field (Kudzin et al., 1994, 1995; Bain, 1994). It is suspected that the photoelastic hysteresis also occurs due to similar effects. Although it was not possible to try to compensate the electric field effects in the present investigation, it is possible to attempt experiment under the simultaneous application of a suitable electric field and stress along z-direction.

Obs.	$C_{pq}$	Paraelectric (PE)	At $T_c = 279$ K phase (RT)
1	$C_{xy}$	4.38	3.85
2	$C_{xz}$	5.55	5.85
3	$C_{yx}$	3.60	4.46
4	$C_{yz}$	4.26	5.50
5	$C_{zy}$	3.71	4.83
6	$C_{zx}$	4.19	5.45

Table 6. Stress optical coefficients  $c_{pq}$  (in brewsters) of  $Li_2Ge_7O_{15}$  at  $RT=298$  K and at  $T_c = 279$  K.

The Stress optical coefficients  $C_{pq}$  of the crystals  $Li_2Ge_7O_{15}$  at paraelectric phase ( $RT = 298$  K) and at  $T_c = 279$  K are presented in Table 6. It is important to compare the values of  $C_{pq}$  for  $Li_2Ge_7O_{15}$  with other ferroelectric crystals given in Table 7 particularly with Rochelle-salt (RS) which belongs to the orthorhombic class like LGO (Bain et al., 1998).

Obs	$C_{pq}$	Rochelle Salt (RS)	KDP	ADP	Remarks
1	$C_{xz}$	3.74	0.28	1.25	Ref. [9] for RS
2	$C_{yz}$	4.29	0.28	1.25	a- polar axis
3	$C_{yx}$	3.56	1.04	4.30	Ref. [26] for KDP
4	$C_{zx}$	0.85	1.54	3.50	Ref. [27] for ADP
5	$C_{zy}$	2.61	1.54	3.50	
6	$C_{xy}$	3.04	1.04	4.30	

Table 7. Piezo-optic coefficients  $c_{pq}$  (in Brewsters) for some ferroelectric crystals in their paraelectric (PE) phases.

The values of  $C_{pq}$  are significantly higher for LGO as compared to these ferroelectric systems. So, the large photoelastic coefficients and the other properties like good mechanical strength, a transition temperature close to room temperature and stability in ambient environment favour LGO as a potential candidate for photoelastic applications.

#### 4. Irradiation effect on photoelastic coefficients in $\text{Li}_2\text{Ge}_7\text{O}_{15}$ crystals

The photoelastic coefficients  $C_{pq}$  of the ferroelectric crystals  $\text{Li}_2\text{Ge}_7\text{O}_{15}$  (x-irradiated) in a cooling and heating cycle between 298 K and 273 K was carried out with the experimental procedure described in section 1.4 and are shown in Fig. 20 (Bain et.al., "in print"). The results show an interesting photoelastic behaviour.

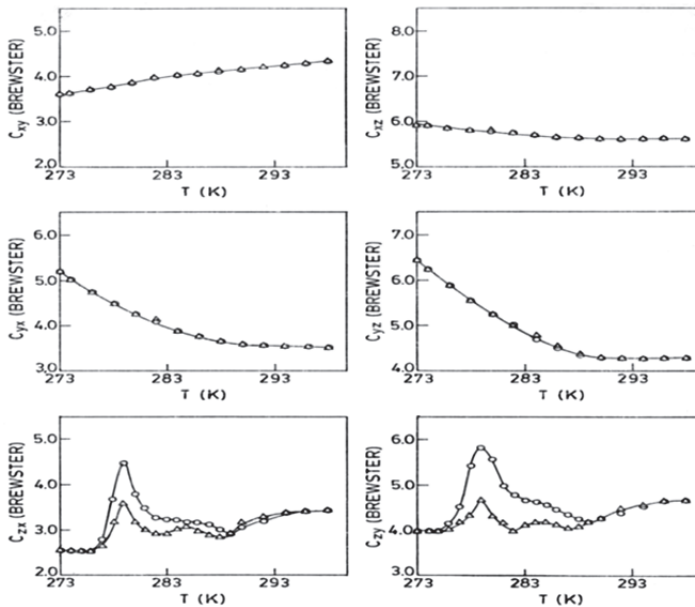


Fig. 20. Temperature dependence of photoelastic coefficients  $C_{xy}, C_{xz}, C_{yz}, C_{yx}, C_{zx}$  and  $C_{zy}$  of the crystal (x-irradiated) LGO in a cooling (○) and heating (△) cycle.

Peaks are observed in the temperature dependence of the photoelastic coefficients  $C_{zy}$  and  $C_{zx}$  at temperature  $\sim 279$  K in a complete cooling and heating cycle whereas no discernible hysteresis is observed in rest of the photoelastic coefficients. Anomalous temperature dependence of  $C_{zx}$  of the crystal (x-irradiated) LGO at different wave lengths are shown in Fig.21.

It is observed that the peak value of  $C_{zy}$  has increased about 25% and that of  $C_{zx}$  has decreased about 18% at the wave length  $\lambda=5890 \text{ \AA}$  during cooling process of the crystal (Fig.16 and Fig.20). The peak value of  $C_{zx}$  of the crystal (un-irradiated and x-irradiated) LGO thus obtained at different wave lengths (Fig.17 and Fig.21) are given in Table 8 and the results are plotted in Fig.22.

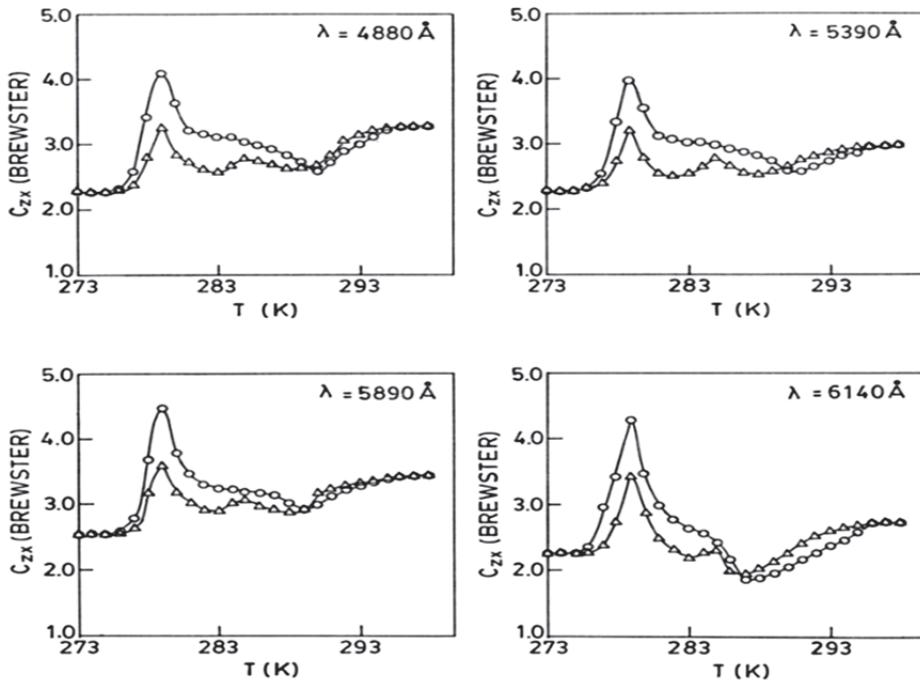


Fig. 21. Temperature dependence of photoelastic coefficient  $C_{zx}$  of the crystal (x-irradiated) LGO at different wave lengths in a cooling (O) and heating ( $\Delta$ ) cycle.

It has been observed that the changes in the value of photoelastic coefficients  $C_{zy}$  and  $C_{zx}$  of the crystal (x-irradiated) LGO in a cooling and heating cycle occur only if the crystal is stressed along the polar axis (c-axis). It is known that the irradiation of crystals can change physical properties of the crystals.

Irradiation brings about many effects in the crystal such as creating defects, internal stress and electric fields etc (Lines & Glass, 2004). In our present studies, the x-irradiation is believed to produce internal stress and electric fields inside the crystals  $\text{Li}_2\text{Ge}_7\text{O}_{15}$  due to defects that can change the values of photoelastic coefficients.

Wave lengths (Å)	$C_{zx}$ (un-irradiated)		$C_{zx}$ (x-irradiated)	
	Cooling	Heating	Cooling	Heating
4880	4.8	4.0	4.05	3.3
5390	4.7	3.9	3.95	3.2
5890	5.6	4.8	4.6	3.7
6140	4.5	3.6	4.3	3.4

Table 8. The peak value of  $C_{zx}$  (in Brewster) for the Crystal (un-irradiated and x-irradiated) LGO at different wave lengths in the cooling and heating cycles.

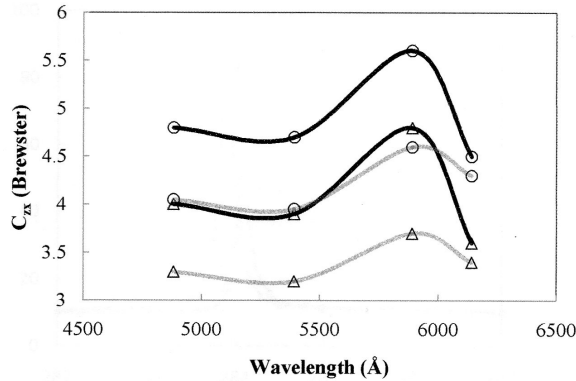


Fig. 22. The peak value of  $C_{zx}$  for the un-irradiated (black colour) and x-irradiated (ash colour) crystal LGO at different wave lengths in a cooling (○) and heating (△) cycle.

## 5. Summary

It is known that the high optical quality, good mechanical strength and stability in ambient environment, large photoelastic coefficients in comparison with other ferroelectric crystals like Rochelle-salt, KDP and ADP favors the crystals LGO as a potential candidate for photoelastic applications.

The piezo-optic dispersion of the crystals (un-irradiated and x-irradiated) LGO in the visible region of the spectrum of light at room temperature (298 K) have been described in section 1.4 and 1.5. It shows an "optical zone or optical window" in between 5400 Å and 6200 Å with an enhanced piezo-optical behavior. This peculiar optical window can have a technical importance. This window region can act as an optical switch for acousto-optical devices. From the studies undertaken it may be concluded that LGO is an attractive acousto-optic material which deserves further probe. It may be possible to understand the observed behavior if extensive piezo-optic and refractive index data become available over an extended range of wavelengths.

It has been observed in section 2.2 that the value of impedance of the crystals LGO decreases sharply with increasing frequency and tends to zero value at about the frequency 10,000 kHz. So, in the application point of view, LGO is also suitable for conductivity even at room temperature and frequency controlled switch.

The temperature dependence of the photoelastic coefficients of the crystals (un-irradiated and x-irradiated) LGO in a cooling and heating cycle between room temperature (298 K) and

273 K have been studied in section 3 and 4. It shows an interesting observation including the lowering of the  $T_c$  under uniaxial stress contrary to the increase of  $T_c$  under hydrostatic pressure and observation of thermal photoelastic hysteresis similar to dielectric hysteresis behavior. In our studies, the x-irradiation is believed to produce internal stress and electric fields inside the crystals LGO due to defects that can change the values of photoelastic coefficients, as described in section 1.5 and 4.

## 6. References

- Bain, A.K. (1994). Study of Peculiarities of Ferroelectric Phase Transition of the Crystals  $\text{Li}_2\text{Ge}_7\text{O}_{15}$  (Ph.D. Thesis), Dniepropetrovsk State University, Ukraine.
- Bain, A.K.; Chand, P. ; Rao, K.V.; Yamaguchi, T. & Wada, M. (1998). Determination of the Photoelastic Coefficients in Lithium heptagermanate Crystals, *Ferroelectrics*, Vol. 209, No. 1, (April 1998), pp. 553-559, ISSN 0015-0193.
- Bain, A.K.; Chand, P. ; Rao, K.V.; Yamaguchi, T. & Wada, M. (2008). Piezo-optic Dispersion of  $\text{Li}_2\text{Ge}_7\text{O}_{15}$  Crystals, *Ferroelectrics*, Vol. 366, No.1, (October 2008), pp. 16-21, ISSN: 0015-0193.
- Bain, A.K.; Chand, P. ; Rao, K.V.; Yamaguchi, T. & Wada, M. (2008). Irradiation Effect on Piezo-optic Dispersion of  $\text{Li}_2\text{Ge}_7\text{O}_{15}$  Crystals. , *Ferroelectrics*, Vol. 377, No. 1, (December 2008), pp. 86-91, ISSN: 0015-0193.
- Bain, A.K.; Chand, P. ; Rao, K.V.; Yamaguchi, T. & Wada, M. (2009). Anomalous Temperature Dependence of Piezo-optic Birefringence in  $\text{Li}_2\text{Ge}_7\text{O}_{15}$  Crystals. *Ferroelectrics*, Vol. 386, No. 1, pp. 152-160, ISSN: 0015-0193.
- Bain, A.K. & Chand, P. (in print). Study of Impedance in Ferroelectric  $\text{Li}_2\text{Ge}_7\text{O}_{15}$  Crystals, *Integrated Ferroelectrics*.
- Bain, A.K. & Chand, P. (in print). Irradiation Effect on Photoelastic Coefficients in Ferroelectric  $\text{Li}_2\text{Ge}_7\text{O}_{15}$  Crystals, *Integrated Ferroelectrics*.
- Haussühl, S. & Albers, J.(1977). Elastic and thermoelastic constants of triglycine sulphate (TGS) in the paraelectric phase. *Ferroelectrics*, Vol. 15, No. 1, pp. 73-75, ISSN 0015-0193.
- Haussühl, S.; Wallrafen, F.; Recker, K. & Eckstein, J. (1980). Growth, Elastic Properties and Phase Transition of Orthorhombic  $\text{Li}_2\text{Ge}_7\text{O}_{15}$ . *Z.krist.*, Vol. 153, pp. 329-337, ISSN 0044 2968.
- Iwata, Y.; Shibuya, I.; Wada, M.; Sawada, A. & Ishibashi, Y. (1987). Neutron Diffraction study of structural Phase Transition in Ferroelectric  $\text{Li}_2\text{Ge}_7\text{O}_{15}$ . *J. Phys. Soc. Jpn.* Vol. 56, No. 7, (February 13, 1987), pp. 2420-2427, ISSN 0031 9015.
- James, A.R.; Balaji, S. & Krupanidhi, S.B. (1999). Impedance-fatigue correlated studies on  $\text{SrBi}_2\text{Ta}_2\text{O}_9$ , *Mater. Sci. Eng., B* 64, No. 3, pp. 149-156, ISSN 0921-5107.
- Kholodenko, L. P. (1971). *Thermodynamic Theory of Ferroelectrics of Barium Titanate Family* (in Russian), Riga.
- Kaminsky, W. & Haussühl, S. (1990). Faraday effect aid birefringence in orthorhombic  $\text{Li}_2\text{Ge}_7\text{O}_{15}$  near the ferroelectric phase transition. *Ferroelectrics Lett.*, Vol. 11, No. 3, pp. 63-67, ISSN 0731-5171.
- Kudzin, A.Yu.; Volnyanskii, M.D. & Bain, A.K. (1994). Temperature Hysteresis of the Permittivity of  $\text{Li}_2\text{Ge}_7\text{O}_{15}$ . *Phys.Solid State*. Vol. 36, No. 2, pp. 228- 230.

- Kudzin, A.Yu.; Volnyanskii, M.D. & Bain, A.K. (1995). Influence of Space Charges on Ferroelectric Property of Weak Ferroelectric  $\text{Li}_2\text{Ge}_7\text{O}_{15}$ . *Ferroelectrics*, Vol. 164, No. 1, (February 1995), pp. 319-322, ISSN 0015-0193.
- Kim, I.W.; Ahn, C.W.; Kim, J.S.; Song, T.K. & Lee, J.S. (2002). Low-frequency dielectric relaxation and ac conduction of  $\text{SrBi}_2\text{Ta}_2\text{O}_9$  thin film grown by pulsed laser deposition, *Appl. Phys. Lett.* Vol. 80, No. 21, pp. 4006, ISSN 0003-6951.
- Lines, M. E. & Glass, A. M. (2004). *Principles and Applications of Ferroelectrics and Related Materials*, Clarendon press, ISBN 0-19-850778-X, Oxford.
- Morioka, Y.; Wada, M. & Swada, A. (1988). Hyper-Raman Study of Ferroelectric Phase Transition of  $\text{Li}_2\text{Ge}_7\text{O}_{15}$ . *J.Phys. Soc. Jpn.*, Vol. 57, No. 9, (February 15, 1988), pp. 3198-3203, ISSN 0031 9015.
- Nye, J. F. (1957). *Physical Properties of Crystals*, Clarendon Press, ISBN 0-19-851165-5, Oxford.
- Narasimhamurty, T. S.; Rao, K. V. & Petterson, H.E. (1973). Photoelastic Constants of ADP, *J. Mat. Sci.*, Vo.8, No. 4, pp. 577-580, ISSN 0022-2461 .
- Narsimhamurty, T.S. (1981). "Photoelastic and Electro-optic properties of Crystals", Plenum Press, ISBN 0-306-31101-1, New York.
- Nakamura, E.; Ushio, S. & Abe, K. (1984). Ferroelectric Domain Formation in Short Circuited  $\text{KH}_2\text{PO}_4$ , *J. Phys. Soc. Jpn.*, Vol. 53, No. 1(August 2, 1983), pp. 403-407, ISSN: 0031 9015.
- Preu, P. & Haussühl, S. (1982). Dielectric Properties and Phase Transition in  $\text{Li}_2\text{Ge}_7\text{O}_{15}$ . *Solid State Commun.*, Vol. 41, No. 8, pp. 627-630.
- Rao, K. V. & Narasimhamurty, T. S. (1975). Photoelastic behavior of KDP, *J. Mat. Sci.*, Vol.10, No.6, pp. 1019-1021, ISSN 0022-2461.
- Sinii, I.G.; Fedoseev, A.I. & Volnyanskii, M.D. (1990). *Sov. Phys. Solid State*, Vol.32, pp. 1817.
- Saito, K.; Ashahi, T.; Takahashi, N.; Hignao, M.; Kamiya, I.; Sato, Y.; Okubo, K. & Kobayashi, J. (1994). Optical activity of  $\text{Gd}_2(\text{MoO}_4)_3$ , *Ferroelectrics*, Vol. 152, No. 1, (February 1994), pp. 231-236, ISSN 0015-0193.
- Trubitsyn, M.P.; Kudzin, A.Yu.; Volnyanski, M.D. & Bain, A.K. (1992). Critical Broadening of EPR lines near the Ferroelectric Phase Transition in  $\text{Li}_2\text{Ge}_7\text{O}_{15}:\text{Mn}^{2+}$ , *Sov. Phys. Solid State*, Vol.34, No.6, p. 929-32.
- Volnyanskii, M.D.; Kudzin, A.Yu. & Shevets, T.V. (1992). Abstracts of ISFD-2, Nantes.
- Vanishri, S. & Bhat, H. L. (2005). Irradiation Effects on Ferroelectric Glycine Phosphite Single Crystal, *Ferroelectrics*, Vol. 323, No. 1, (August 2005), pp. 151-156, ISSN 0015-0193.
- Wada, M.; Swada, A. & Ishibashi, Y. (1981). Ferroelectricity and Soft Mode in  $\text{Li}_2\text{Ge}_7\text{O}_{15}$ . *J.Phys. Soc.Jpn.*, Vol. 50, No.6, (March 20, 1981), pp. 1811-1812, ISSN 0031 9015.
- Wada, M.; Orihara, H. ; Midorikawa, M.; Swada A. & Ishibashi, Y. (1981). Pressure Effect on the Ferroelectric Phase Transition in  $\text{Li}_2\text{Ge}_7\text{O}_{15}$ . *J. Phys. Soc. Jpn.*, Vol. 50, No. 9, (July 10, 1981), pp. 2785-2786, ISSN 0031 9015.
- Wada, M. & Ishibashi, Y. (1983). Ferroelectric Phase Transition in  $\text{Li}_2\text{Ge}_7\text{O}_{15}$ . *J.Phys. Soc. Jpn.*, Vol. 52, No. 1, (July 29, 1982), pp. 193-199, ISSN 0031 9015.

- Wada, M.; Swada, A. & Ishibashi, Y. (1984). The Oscillator Strength of the Soft Mode in  $\text{Li}_2\text{Ge}_7\text{O}_{15}$ . *J. Phys. Soc. Jpn.*, Vol. 53, No. 10, (July 24, 1984), pp. 3319-3320, ISSN 0031 9015.
- Wada, M. (1988). Soft Mode Spectroscopy Study of Ferroelectric Phase Transition in  $\text{Li}_2\text{Ge}_7\text{O}_{15}$ . *Ind. J. Pure and Appl. Phys.*, Vol. 26, pp. 68-71, ISSN 0019-5596.
- Wada, M.; Shirawachi, K. & Nishizawa, S. (1991). A Fourier Transform Infrared Spectrometer with a Composite Interferometer for Soft Mode Studies. *Jpn. J. Appl. Phys.*, Vol. 30, No. 5, (March 16, 1991), pp. 1122-1126, ISSN 0021 4922.

# Compositional and Optical Gradient in Films of $\text{PbZr}_x\text{Ti}_{1-x}\text{O}_3$ (PZT) Family

Ilze Aulika\*

*Center for Space Human Robotics, Italian Institute of Technology - IIT@PoliTO, Italy*

## 1. Introduction

$\text{Pb}(\text{Zr}_x\text{Ti}_{1-x})\text{O}_3$  (PZT) ( $x = 0-1$ ) films have attracted the attention of researchers for the past 30 years due to their excellent ferroelectric (FE) and electromechanical properties, which have led to the commercialization of thin PZT films for ferroelectric random access memory (FeRAM), forming a market of several millions USD annually. Ferroelectricity of perovskite oxide thin films, especially PZT thin films, can be exploited in semiconductor devices to achieve non-volatile random access memory (NVRAM) with high-speed access and long endurance, which can overcome the barriers, encountered in current semiconductor memory technologies. The ferroelectricity can be also exploited to voltage dependent and thermally sensitive resistors, gas and humidity sensors. Besides, due to large pyroelectric coefficient of PZT, it has drawn interest for use in pyroelectric devices (Izyumskaya et al., 2007; Muralt, 2000; Whatmore et al., 2003).

PZT thin films have remarkable advantages over bulk materials:

- Can be directly deposited on platinized silicon to allow direct integration with electronics;
- Have superior electromechanical properties compared to other ferroelectric ceramics.

Thanks to that, PZT films have formed an integral part of the microelectromechanical systems (MEMS) in various applications such as sensors, actuated micromirrors for fine-tracking high-density optical data storage mechanisms (Yee et al., 2001), and tunable capacitors for high-frequency microwave applications, microelectromechanical systems, infrared detectors, applications in optical devices, for instance, rugate filters (Bovard, 1990), anti-reflection coatings (Oulette et al., 1991), and electro-optic modulators, to name a few.

Low density embedded FE memories are being considered for implementation not only in commercial devices, such as smart cards and cellular phones, but also for adaptive FE

---

\*Alexandr Dejnek<sup>2</sup>, Silvana Mergan<sup>3</sup>, Marco Crepaldi<sup>1</sup>, Lubomir Jastrabik<sup>2</sup>, Qi Zhang<sup>4</sup>, Andreja Benčan<sup>5</sup>, Maria Kosec<sup>5</sup> and Vismants Zauls<sup>6</sup>

<sup>1</sup>Center for Space Human Robotics, Italian Institute of Technology - IIT@PoliTO, Italy

<sup>2</sup>Institute of Physics, Academy of Science, Czech Republic

<sup>3</sup>HEARing CRC, University of Melbourne, Australia

<sup>4</sup>Cranfield University, School of Applied Sciences, United Kingdom

<sup>5</sup>"Jožef Stefan" Institute, Slovenia

<sup>6</sup>Institute of Solid State Physics, University of Latvia, Latvia

memories in space applications. FE oxides have demonstrated high resistance to radioactivity (Philpy et al., 2003; Sternberg et al., 2003), what is important characteristic for space applications. Radiation test results on a prototype 1 kbit FE memory demonstrated that FE memory core using FE storage capacitors (Philpy et al., 2003), combined with hardened-by-design (HBD) CMOS circuitry, can attain high levels of tolerance to total ionizing dose and single event effects. Preliminary tests indicate that the hardness of the prototype memory exceeds 2 Mrads total ionizing dose and 163 MeV·cm<sup>2</sup>/mg linear energy transfer (LET) latch-up without the need for shielding (Kamp et al., 2004). FE memory can be designed to compete with any number of traditional semiconductor memory architectures, including SRAM, SDRAM, EEPROM and Flash memory (Kamp et al., 2004). This is accomplished by trading off internal write voltage with retention and endurance and taking advantage of the very fast read/write times of FE memory. FE memory can be designed to be exactly pin and function compatible with the other memory types. It follows that the memory types, which much softer to radiation exposure, can be replaced with FE memory without redesign of the circuit board (Kamp et al., 2004).

Every application of MEMS requires a different thickness and high quality of the functional film, leading to the challenge of manufacturing the film of the required thickness, epitaxy and purity. Among many methods for the fabrication of PZT thin films, chemical solution deposition (CSD), pulsed laser deposition (PLD), metal organic chemical vapor deposition (MOCVD), and physical vapor deposition such as RF sputtering have been widely employed. Among these techniques, chemical solution deposition methods like sol-gel processing offer low-capital costs, large-scale coating capabilities and easy control of chemical composition and homogeneity (Izyumskaya et al., 2007). However, the minimum thickness limitation of around 100 nm per layer for a crack-free and dense film deposited via CSD requires multiple coatings to reach the final thickness.

The broad applications of PZT films, and inter alia the growing interest in graded refractive index films for applications in optical devices (Xi et al., 2007; Wang et al., 2001), and applications in space environment, make it imperative to study the depth profile of composition and optical properties of thin films throughout a single layer and an entire coating. Moreover graded PZT thin films, e.g., with amplitude of  $\pm 20\%$  at the 53/47 morphotropic phase boundary (MPB), have showed improved electrical performances (Ledermann et al., 2003), raising importance of depth profile analyses and control. Wherewith, information on the homogeneity of the films and the physical properties resulting from different processing methods represents crucial knowledge.

Gradients in optical properties (refractive index  $n$ , extinction coefficient  $k$ , absorption coefficient  $\alpha$ , band gap etc) and chemical composition gradients have been reported, e.g., for sputtered PZT films (Deineka et al., 1999 and 2001; Vidyarthi et al., 2007; Chang et al., 2005) and for CSD-fabricated PZT films (Aulika et al., 2009; Calamea and Muralt, 2007; Etin et al., 2006; Impey et al., 1998; Ledermann et al., 2003; Marcus and Schwartz, 2000; Watts et al., 2005). Variation of chemical composition throughout the film thickness due to inhomogeneity results in variation of physical properties such as optical properties of the films, resistance to irradiation, and lowers or improves the performance of electromechanical systems. The understanding of the compositional gradient and physical properties resulting from different processing methods is crucial. Thus, the knowledge of the optical gradient within a film allows identification and further optimization of the thin film performance and applications in piezo- and ferro-devices.

## 2. Depth profile detection methods

A challenging aspect of homogeneity studies lies in the development of an appropriate characterization method, since the compositional variation must be determined on a small scale, within 100 nm. Depth profile detection methods can be divided into two categories:

- Destructive,
- Non-destructive methods.

The 1<sup>st</sup> category typically allows local visualization of thin films and element concentration analyses, what requires etching or cross section of the sample accompanied with spectroscopy methods. For visualization of the films well established microscopy techniques such as scanning electron microscopy (SEM), transmission electron microscopy (TEM), and atomic force microscopy (AFM) are widely used in the practice. For compositional analyses (qualitative and quantitative) energy-dispersive x-ray spectroscopy (EDXS, known also as EDX or EDS), photoelectron spectroscopy (XPS), secondary ion mass spectrometry (SIMS), Rutherford back scattering (RBS), electron energy loss spectroscopy (EELS) and other spectroscopies are applied. For example, the approach can be thought of simply as the analytical implementation of rf-sputter etching, where the atomized material is analyzed by its characteristic optical emission. This method is known as radiofrequency glow discharge atomic emission spectroscopy (rf-GD-AES) (Marcus and Schwartz, 2000): permits the depth-resolved elemental analysis of metallic, semiconducting, and insulating materials over depths of 20 nm–150  $\mu\text{m}$  in a rapid fashion < 0.1–5  $\mu\text{m}/\text{min}$ . The analytical data are reported as elemental emission intensities as a function of sputtering time, termed a qualitative depth profile. Qualitative depth profile can be also analyzed by the detection of concentration gradients of the chemical elements of PZT thin films using Z contrast TEM with EDX (Ledermann et al., 2003). In the work of Watts et al., 2005, the EDX was performed on  $\text{PbZr}_{0.52}\text{Ti}_{0.48}\text{O}_3$  (PZT 52/48) thin films. Compositional profiles were determined along with analysis of the state of oxidation of the lead. The data were compared with bulk polycrystalline material as standard giving quantitative depth profile of the films.

Similar method to rf-GD-AES was presented in the work of Vidyarthi et al., 2007, where chemical composition and depth profiling of PZT films was investigated by glow discharge optical emission spectroscopy (GDOES). They used two samples, which chemical composition was measured by RBS, to calibrate GDOES for PZT quantitative compositional analysis.

SIMS was used to monitor the Pb, Zr, Ti, and C secondary ions in addition with the EDX to determine the oxidation state of the elements (Etin et al., 2006).  $\text{Pb}4f$ ,  $\text{Zr}3d$ , and  $\text{Ti}2p$  and  $\text{O}1s$  spectra were used for calculation of film composition as a function of depth using calibration equations (Sugiyama et al., 2003 and 2004) presenting quantitative depth profile analyses.

Fascinating work have been done by Parish et al., 2008, where the use of multivariate statistical analysis (MSA) of EDS spectrum images (SIs) in scanning TEM (STEM) was extended to allow the two-dimensional (2D) quantitative analysis of cation segregation and depletion in PLZT thin films. STEM-EDS SIs method allows high-resolution ( $\leq 10$  nm) quantification of cation distributions. Zr/Ti and La segregation are found to develop in a decidedly nonplanar fashion during crystallization, highlighting the need for 2D analysis.

The drawback for TEM and STEM-EDS SIs investigations is tedious and time-consuming sample preparation. Investigation using other methods such as RBS results in sample modification or even destruction after analysis. Also all other methods mentioned before

goes hand to hand with either sample distraction, compositional modification (e.g., impregnation of ions during milling with ion beam) or specific sample preparation needs. To conclude, examples given above for depth profile detection suffer from being “local”, intrusive, destructive and unsuitable for real-time, inline monitoring of processes and surface/interface modifications of thin films.

What about the 2<sup>nd</sup> category: non-destructive methods of depth profile detection? In this category only sensitive, accurate, contactless optical techniques are giving this opportunity to analyze thin films in non-destructive way. Well know optical methods are, for example, reflectometry, interferometry and spectroscopic ellipsometry (SE). SE have several advantages regarding other optical methods eliminating such disadvantages as dependence on the intensity of the light source (reflectometry), vibrations and atmospheric disturbances (interferometry). SE is nondestructive, nonintrusive, and noninvasive, contactless optical technique, applied not only for the optical characterization of bulk materials and thin films, but also for in situ real-time measurement of multilayered film structures, interfaces, surfaces, and composites, during fabrication and processing.

SE has long been recognized as a powerful method for the characterization of thin films and their inhomogeneity. It has already been applied to refractive index depth profile studies of oxynitride  $\text{SiO}_2\text{N}_x$  films (Callard et al., 1998; Nguyen et al., 1996; Snyder et al., 1992; Rivory, 1998;) (additionally confirmed by chemical etching (Callard et al., 1998)), lead silicate glass (Trolier-McKinstry and Koh, 1998), oxidized copper layers (Nishizawa et al., 2004), polymers (Guenther et al., 2002), semiconductor indium tin oxide (ITO) films (Losurdo, 2004; Morton et al., 2002), sol-gel PZT thin films (Aulika et al, 2009) confirmed by TEM and EDX, and RF-sputtered self-polarized PZT thin films (Deineka et al., 2001), and was confirmed by discharge optical emission spectroscopy (GD-OES) and pyroelectric profile measurements by the laser intensity-modulation method (LIMM) (Deineka et al, January, 2001; Suchanek et al., 2002). SE has also been applied to the study of ion implantation depth profiles in silicon wafers and confirmed by RBS (Boher et al., 1996; Fried et al, 2004). The sensitivity of SE was demonstrated on graded oxygen compositions in  $\text{YBa}_2\text{Cu}_3\text{O}_{7-\delta}$  (YBCO) thin films, in which it was able to detect changes in the oxygen concentration to within one unit cell (Gibbons, and Trolier-McKinstry, 1999).

SE cannot quantitatively examine cation distribution at a length scale comparable with the feature sizes like in a case of STEM-EDS SIs method (Parish et al., 2008) since the measured area depends on the diameter of the incident light spot of SE (typically  $\sim 3$  mm, by using focusing nuzzles it can be reduced till  $\sim 0.1$  mm). As the result it is easy to perform relatively large area scans of the sample using SE, and evaluate information (for example, depth profile) in average across many features simultaneously. And thus SE studies gives an opportunity in non-destructive, rather fast and easy way to analyze the inhomogeneity of material and helps to understand how processing affects structure and thus properties in this system. Now more in details about this method.

## 2.1 Spectroscopic ellipsometry

Not very long time ago the development of spectroscopic ellipsometry made it possible to investigate the complex refractive index of thin films and bulks in a wide spectral range (gives access to fundamental physical parameters; morphology, crystal quality, chemical composition, or electrical conductivity), and detecting inhomogeneities of thin films, eliminating such disadvantages of other non-destructive and contactless optical technique as

dependence on the intensity of the light source (reflectometry), vibrations and atmospheric disturbances (interferometry) (Tompkins and Irene, NY 2005).

Typical ellipsometers can accurately measure  $\psi$  and  $\Delta$  better than  $0.01^\circ$ . Due to such a high accuracy a change of the refractive index of  $10^{-3}$  –  $10^{-4}$ , and film thickness changes down to the sub-Å scale can easily be resolved with this technique (Tompkins and Irene, NY 2005). A reflectometer system can not accurately measure intensity values better than 0.1%, and therefore a reflectivity measurement is not sensitive enough for small changes of the material's optical properties and for thin film thicknesses.

With spectral ellipsometry one can measure the dispersion of the complex dielectric constant of bulk materials and thin films with very high accuracy. This technique does not require a large size of the sample; it is enough to have a size of  $\sim 5 \times 5$  mm. In situ spectral ellipsometry studies allow detecting phase transition in thin films and surfaces (Dejneka et al., 2009), as well as of the interface what is very important for thin film and crystal studies.

For advanced optoelectronics and bandgap engineering applications is important to investigate the relationship between the microstructure, sample preparation conditions & optical properties. SE gives opportunity to detect technologically and scientifically important properties of thin films such as optical band gap (Dejneka et al., 2010), thermo-optical properties (Aulika et al., 2007 and 2009; Dejneka et al., 2009), and optical gradient (Aulika et al., 2008 and 2009; Dejneka et al., January, 2001).

## 2.2 What ellipsometry measures?

Ellipsometry measures the change of the polarization state of light upon reflection. It overcomes two major problems of conventional spectroscopy or reflectivity: the phase problem (in ellipsometry the phase is measured and does not have to be calculated by Kramers-Kronig relation) and the reference problem (ellipsometry requires relative, not absolute, intensities). Paul Drude was the first to study optical properties using the ellipsometry technique. He published the equation of ellipsometry in 1887, and his experimental results in 1888. Generally, after reflection on a sample the polarization state of the light is elliptical (Fig. 1). The electrical field components parallel and perpendicular,  $E_{ip}$  and  $E_{is}$ , with respect to the plane of incidence change their amplitude and phases due to reflection upon the sample. These total reflective coefficients are connected with the main ellipsometric angles  $\psi$  and  $\Delta$  (Tompkins and Irene, NY 2005)

$$\tan \psi = \frac{|r_p|}{|r_s|} \quad \text{and} \quad \text{tg} \psi e^{i\Delta} = \frac{r_p}{r_s} = \frac{E_{ip}}{E_{is}} = \gamma,$$

where  $\gamma$  is the quantity of ellipticity, and  $\Delta = \delta_p - \delta_s$  is the phase shift of the  $p$  and  $s$ -polarized light (Fig. 1). Reflection and transmittance coefficients can be found from Fresnel formulas, which on the other hand are containing information about the optical constants, thickness of the thin film (or thin films in the case of multilayer) incident angle of the light, and phase suspension of the light.

$\psi = \psi(\epsilon, \sigma, \omega)$ , and  $\Delta = \Delta(\epsilon, \sigma, \omega)$ , where  $\epsilon$  is the real part of dielectric function,  $\sigma$  is the real part of conductivity, and  $\omega$  is the frequency. There are two equivalent descriptions: the first one operates with real and imaginary parts of the dielectric function  $\epsilon_1, \epsilon_2$ , the second one operates with the real part of the dielectric function and the real part of the conductivity. The ratio between conductivity and dielectric function  $\sigma \propto i\omega\epsilon$  makes these descriptions equivalent.

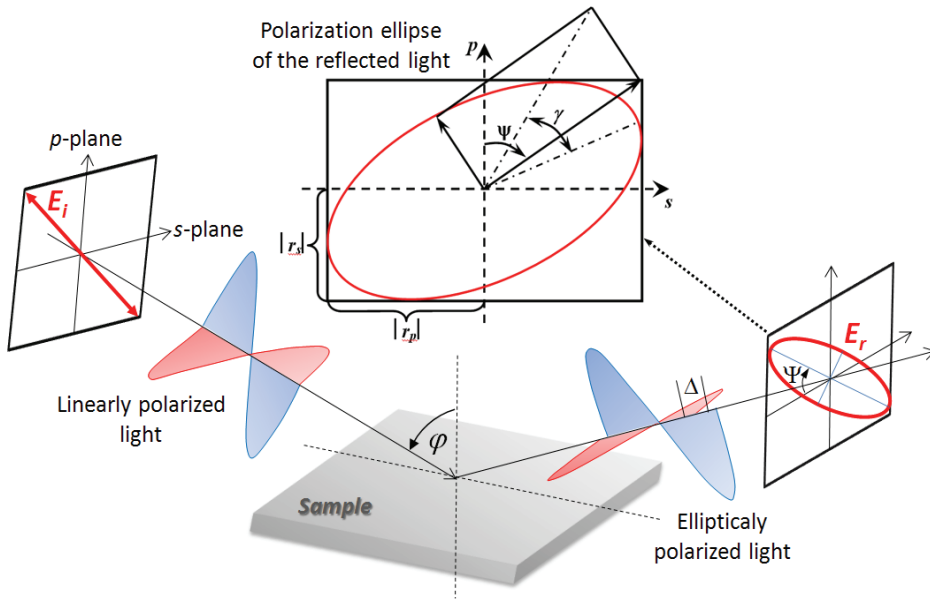


Fig. 1. Light reflecting from a sample at angle  $\varphi$ . The linearly polarized incident light has two electric field components  $E_{ip}$  and  $E_{is}$  in the directions parallel and perpendicular to the propagation plane, respectively. The reflected light has elliptical polarization.

The main ellipsometric angles  $\psi$  and  $\Delta$  are the functions of dielectric constants of the sample: Consider the complex refractive index as  $\tilde{n} = n - ik$ , where  $n$  - refractive index,  $k$  - extinction coefficient, it can be written in a form of dielectric permittivity  $\tilde{n} = n(1 - i\alpha) = \sqrt{\epsilon}$  (Born, and Wolf, Cambridge University, 1999), where  $\epsilon = \epsilon_1 - i\epsilon_2$  - complex dielectric permittivity, and  $\alpha = 4\pi k/\lambda$  - absorption coefficient. First, the dielectric permittivity is a response function, therefore  $\epsilon(-\omega) = \epsilon^*(\omega)$ . Second, from the causality principle we have the Kramers-Kronig (KK) relations (Tompkins and Irene, NY 2005)

$$\epsilon_1(\omega) - 1 = \frac{2}{\pi} P \int_0^{+\infty} \frac{x\epsilon_2(x)}{x^2 - \omega^2} dx \quad \text{and} \quad \epsilon_2(\omega) = -\frac{2\omega}{\pi} P \int_0^{+\infty} \frac{\epsilon_1(x) - 1}{x^2 - \omega^2} dx,$$

where  $P$  - is the symbol of the main quantity of the integral. For isotropic media  $\tilde{n}^2 = \epsilon(\omega)$ ,  $n^2 - k^2 = \epsilon_1(\omega)$ ,  $2nk = \epsilon_2(\omega)$ , then KK can be written in

$$n^2(\omega) - k^2(\omega) - 1 = \frac{4}{\pi} P \int_0^{+\infty} \frac{xn(x)k(x)}{x^2 - \omega^2} dx \quad \text{and} \quad n(\omega)k(\omega) = \frac{\omega}{\pi} P \int_0^{+\infty} \frac{n^2(x) - k^2(x) - 1}{x^2 - \omega^2} dx.$$

The combination of KK relations with physical arguments about the behavior of optical conducts us to the sum-rule expression.

Optical properties of materials can be modeled also by considering the field re-radiated by the induced dipoles of the classical oscillators. Such classical oscillators are Lorentz oscillator, for example. In this model the dipole radiation field interferes with the incident

field in such a way as to produce absorption or refraction. The Lorentz model assumed that an electron bound with the nucleus as a harmonic oscillator. By solving the equation of motions, distribution of the complex dielectric function can be found as  $\tilde{\epsilon}$  (Tompkins and Irene, NY 2005)

$$\tilde{\epsilon} = \epsilon_{\infty} \left( 1 + \frac{A^2}{(E_c)^2 - E(E - iB)} \right).$$

The model fitting parameters  $\epsilon_{\infty}$ ,  $E_c$ ,  $E$ ,  $B$  and  $A$  are in units of energy, and they are respectively: the high-frequency lattice dielectric constant, the centre energy of the oscillator, the photon energy, the vibration frequency (broadening) of the oscillator, and the amplitude (strength) of the oscillator.

Unfortunately the Lorentz oscillator (LO) does not fit well the characteristics of the complex dielectric function at the near ultraviolet and ultraviolet (UV) regions for ferroelectrics and some semiconductors (Bungay and Tiwald, 2004; Jellison et al., 1997; Synowicki and Tiwald, 2004). LO functions were used to model molecular or lattice vibrations in the infrared (Bungay and Tiwald, 2004), complex refractive index of conductive oxides (Synowicki, 1998), metals (Brevnov and Bungay, 2005), and ferroelectrics till the absorption edge (Lappalainen et al., 2005). LO is symmetric in shape, and the high and low energy sides of the function decrease at the same rate. It is because the low energy portions of the  $\epsilon'$  curves are most strongly affected by the area under of the curve (area is proportional to  $A \cdot B$ ), and the peak shifts to lower energies as broadening increases. As a result LO have long asymptotic tails away from the absorption peaks and can cause unacceptable absorption artifacts in transparent regions.

Tauc-Lorentz (Jellison and Modine, 1996) and Cody-Lorentz oscillator (TLO and CLO) are more flexible functions at the fundamental band gap  $E_g$  and higher energies in the UV, since these functions rapidly decrease to zero away from their center energy and do not have long asymptotic tails as LO which can result in unwanted absorption through the band gap and below. As the result the typical absorption of dielectrics due to the electrons transition from the valence band to the conductive band at high photon energies can be very well described. Depending on the material under the studies the most suitable oscillator has to be chosen for modeling its complex dielectric function.

### 2.3 Modeling of depth profile

For thin films the most interesting anomalies of the properties are related to their spatial nonuniformity. The details of this nonuniformity depend on the conditions on the film surfaces (substrates, electrodes). The most important characteristic of ferroelectric thin film is their **nonuniform polarization**. Its calculation can be performed on the base of phenomenological theory with polarization gradient in free energy density (Deineka et al., 2001; Glinchuk et al., 2000; Tilley, Gordon and Breach, Amsterdam, 1996; Wang et al., 1995; 2002). It was found (Glinchuk et al., 2000) that dielectric susceptibility is also inhomogeneous and it can be calculated, for example, on the base of Lamé equation. As a matter of the fact obtained polarization  $P(z)$  profile is related to that of optical refraction index:  $1/n^2 \sim (1/n_0^2) (1 + P(z)^2)$ . Due to the proportionality of the refractive index to the square of the spontaneous polarization, the inhomogeneity of the film can be detected as a refractive index depth profile.

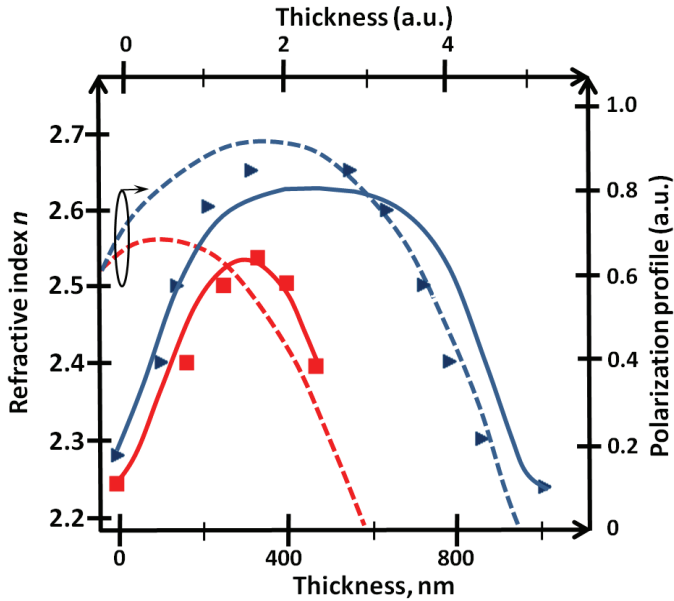


Fig. 2. Comparison the theoretically calculated (solid lines) and experimentally determined (symbols) refractive index depth profiles for PZT films of different thickness, and polarization profiles (discontinuous line) for the films with different thickness (Deineka et al., 2001).

Theoretically calculated and experimentally obtained optical profile for perovskite/pyrochlore double layer stacks of PZT (deposited using sputtering on platinized silicon wafers by Siemens AG, Munich (Germany) are presented in Fig. 2. According to theoretical prediction (Glinchuk et al., 2000), the behavior of polarization profile changes considerable for very thin PZT films. This is illustrated in Fig. 2b: the film polarization decreases monotonous with the thickness.

Polarization profile in ferroelectric thin films can be caused, e.g., during deposition, by chemical element distribution, by strains etc, and “reflected” in other physical properties of the film, for example, the refractive index profile. It should be noticed that any change in the sample structure will affect the polarization and optical properties of the material, irrespective of whether it is a result of the stoichiometry, compositional gradient, internal stresses, etc. Using spectroscopic ellipsometry it can be detected and modeled.

The depth profile of the optical properties is modeled by dividing the single layer by slices, and the shape of the grading profile is characterized using:

- Simple graded model, e.g., exponential variation of the refractive index  $n$  versus film thickness ( $n \sim ab^d$ );
- Function based graded model, e.g., polynomial ( $n \sim A_0 + A_1d + A_2d^2 + \dots$ ).

Some examples of the depth profile of  $n$  are represented in Fig.3.

If the film has no gradient of the refractive index, there is no change of  $n$ , and in case of the simple graded model, exponent is equal to 1. Variation of the refractive index from the substrate to the film surface is adjusted by exponent greater or smaller then 1. In this graded model the fitting parameters are value of exponent and variation of  $n$ . Optical gradient

typically is calculated in the wavelength region of 500 – 1000 nm, where ferroelectrics and dielectrics are not absorbing the light, to minimize fitting parameters correlation caused artifacts.

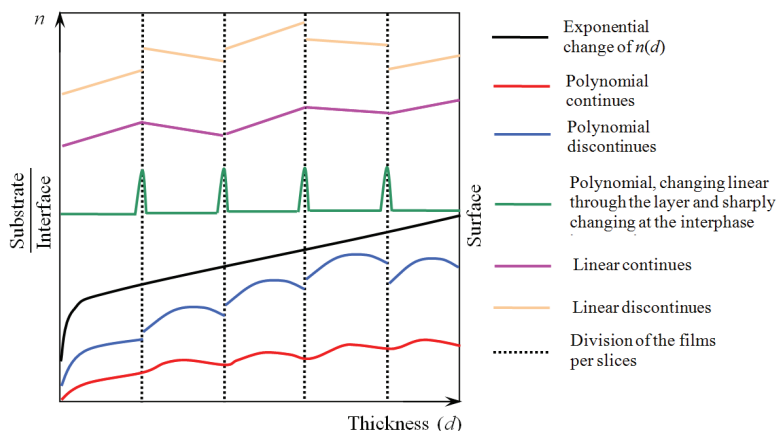


Fig. 3. The optical depth model examples applied to fit experimental SE data: exponential variation of  $n$  through the film, considering it as a one complete layer; discontinuities - exponential variation of  $n$  at the each layer of the film. The different shapes of exponent were accomplished by changing the value of exponent and variation of the refractive index.

### 3. Optical gradient in PZT

#### 3.1 Optical properties of PZT films

In the Fig. 4 refractive index  $n$  and extinction coefficient  $k$  as a function of photon energy for PZT thin films with different composition are presented. These are typical dispersions of optical constant for PZT thin films with no compositional gradient. With increase of Zr/Ti ratio refractive index decreases, while optical band gap is practically not changing, suggesting that the substitution of Ti by Zr does not change much the electronic band structure of PZT.

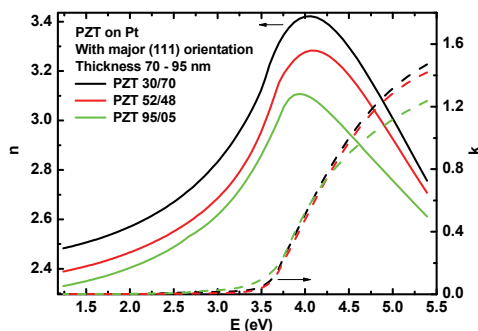


Fig. 4. Refractive index  $n$  and extinction coefficient  $k$  of sol-gel PZT thin films of 3 different compositions. Complex dielectric function of the PZT was evaluated by fitting experimental data of spectroscopic ellipsometry.  $n$  and  $k$  was modeled using Tauc-Lorentz oscillator.

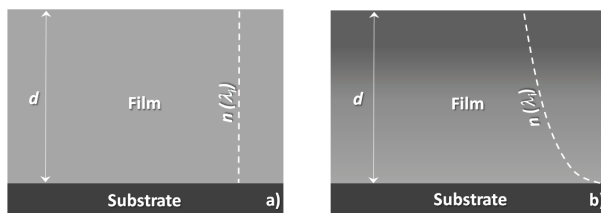


Fig. 5. Schematic illustration of the film with thickness  $d$  with a) no change of refractive index  $n$  and b) with change of  $n$  at wavelength  $\lambda_i$  from the bottom to the top of the film presenting optical gradient in the film. Change of  $n$  with  $d$  can have different nature (see Fig. 2), depending on the chemical/physical processes involved.

The most sensitive parameter to the composition change in PZT is refractive index, and compositional gradient can be detected as an optical gradient (e.g., refractive index change in the depth of the film). Film with no compositional gradient has no change of  $n$  and  $k$  within the film with the thickness  $d$ , while films with compositional gradient will have depth profile of optical constants as schematically presented in Fig. 5.

### 3.2 Factors inducing the gradient

Structural and ferroelectric properties, growth rate, phase composition, and stoichiometry of PZT films depend on a number of film deposition parameters, among which are:

- **Chemical solution deposition (CSD) or sol-gel technique:** precursor solution (lead content of the starting solution; thermal decomposition of raw components), a low-temperature heat treatment at 300-400°C (pyrolysis) to remove organic components, high-temperature annealing (600-700°C) to form a dense crystalline layer, substrate (difference in thermal expansion coefficient between the film and the bottom electrode), annealing atmosphere; how annealing was accomplished (furnace, hot plate, rapid thermal annealing etc)
- **Hydrothermal method:** Gas pressures, synthesis temperature;
- **Sputtering:** substrate temperature, gas pressure and composition, sputter power, target-to-substrate distance, and target composition;
- **Pulsed Laser Deposition (PLD):** laser parameters (laser spot size, fluence, wavelength, repetition rate, power), properties of the target material, ambient gas pressure and composition, substrate type and temperature, substrate-to-target distance and target-substrate geometry;
- **Metal-Organic Chemical Vapor Deposition (MOCVD):** substrate temperature, chamber pressure, and oxygen partial pressure.

The gradient (either compositional and/or optical) can be induced by following factors (see Fig. 6):

- Thermodynamically driven diffusion and/or kinetic demixing (Cabrera, and Mott, 1948; Impey et al., 1998; Ohba et al., 1994; Okamura et al., 1999; Wagner, 1971; Watts et al., 2001 and 2005);
- Stress (e.g., lattice mismatch and misfit stress with the substrate; stress dependence of film thickness), (Corkovic et al., 2008; Izyumskaya et al., 2007; Gkotsis et al., 2007);
- Nucleation processes (Izyumskaya et al., 2007; Ohba et al., 1994; Okamura et al., 1999).

Depending on deposition processes involved, some or even all of these factors can be incorporated and accountable for gradient formation in the films. For the same film

deposition technique different kind of chemical gradient can be obtained depending on deposition conditions.

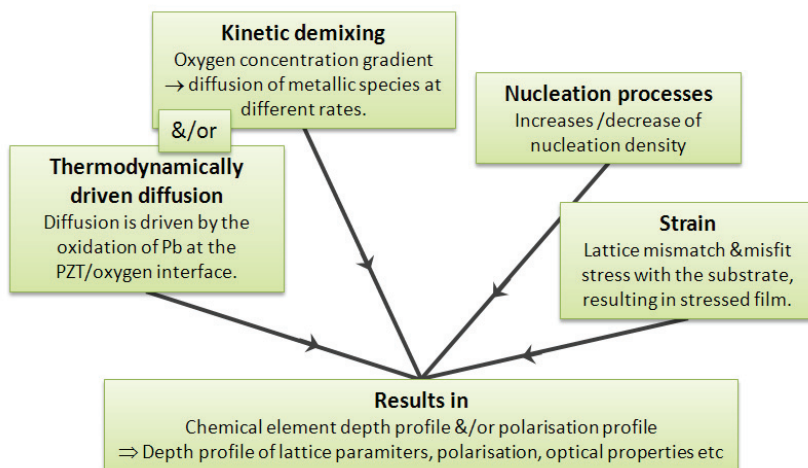


Fig. 6. Optical gradient formation reasons in thin films.

### 3.3 Gradient in PZT thin films prepared by sputtering and hydrothermal techniques

Some examples of compositional gradient for sputtering and hydrothermal techniques are summarized in Fig. 7. For sputtering methods it is quite common to obtain PZT films with enriched Pb and/or Pb/(Zr+Ti) towards the surface of the film resulting in increase of refractive index near the surface (Fig. 7, Case 1 and 2). It is due to the fact that sputtering techniques have difficulty in composition control due to high volatility of Pb or PbO.

Special profile of refractive index in the perovskite PZT films is induced by a selfpolarization formed during film deposition and cooling down (Deineka et al, 2001, Suchanek et al., 2002). For example, PZT thin films of about  $1\ \mu\text{m}$  thickness deposited by dc and RF-sputtering on Si/SiO<sub>2</sub>/adhesion layer/(1 1 1)Pt substrates had the Ti/Ti+Zr ratio nearly constant throughout the PZT film, while the surface was strongly lead enriched (Pb/Ti+Zr  $\approx$  1.6) and the bottom electrode interface was lead depleted (34). Obtained optical profile by SE was similar to that presented in Fig. 2.

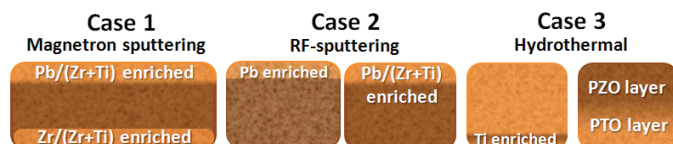


Fig. 7. Common compositional profiles for PZT thin film fabricated by sputtering and hydrothermal techniques. Case 1: based on the work of Vidyarthi et al., 2007; Case 2: Chang and He, 2005; Suchanek et al., 2002; Case 3: Morita et al., 1997; Ohba et al., 1994.

The situation is different with hydrothermal methods where, due to the low process temperature and relatively high pressure, Pb and PbO evaporation does not take place and

interdiffusion and chemical reaction between the film and the substrate is suppressed. For example, Ohba et al., 1994, observed a steep gradient of chemical composition between a substrate and a PZT layer: an interfacial Ti-rich PZT layer with low piezoelectric constant near the substrate. Contrary to this result, Morita et al., 1997, reported that separated PTO and PZO layers were deposited during the nucleation process; the PTO layer grew during the first 2 h of the nucleation process, followed by the PZO film growth (Fig. 7, Case 3).

### 3.4 Gradient in sol-gel PZT thin films

A great number of sol-gel processing parameters as temperature pyrolysis and final heat-treatment, heat treatment atmosphere and duration, solution composition, and seeding layer are strongly influencing the structural and, therefore, physical properties of PZT films. Broad studies have been done on chemical depth profile of sol-gel PZT films depending on the process conditions mentioned above. Some examples of chemical depth profile for sol-gel PZT films on platinized Si (regarding solvents, pyrolysis and annealing) are given in Fig.8. As can be seen it is not evident whether initial sol or annealing is responsible for the gradient appearance. One of the major limitations of the sol-gel technique is that it does not yield the desired perovskite phase directly. Thermodynamically driven diffusion and/or kinetic demixing for sol-gel films are strongly determined by how the annealing is accomplished (furnace, hot plate, rapid thermal annealing, temperature, duration etc), lead content of the starting solution, and also thermal decomposition of raw components. Quite often some of these factors are not mentioned in the publications and it makes difficult or even impossible to do comparisons and reasonable conclusions of these studies.

The formation of perovskite phase upon final annealing is preceded by an undesirable nonferroelectric pyrochlore phase. Pyrochlore inclusions are often observed in sol-gel derived perovskite films. An intermediate annealing step (pyrolysis) plays a pivotal role in determining the crystal orientation as well as ferroelectric and piezoelectric properties of the resultant PZT films (Izyumskaya et al., 2007). There are some studies done for this intermediate stage.

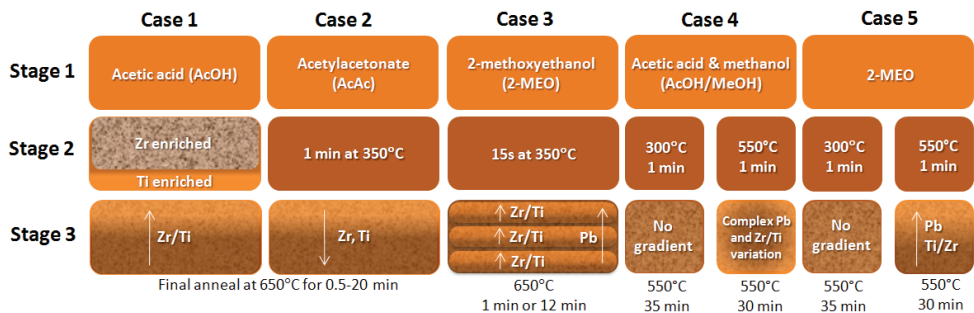


Fig. 8. Common compositional profiles for PZT thin film fabricated by sol-gel. Stage 1: Initial gel; Stage 2: Initial crystallization; Stage 3: Full crystallization. Case 1 and 2: based on work of Etin et al., 2006; Case 3: Ledermann et al., 2004; Case 4 and 5: Aulika et al., 2009.

The paper of Etin et al., 2006, proved that variation in Zr/Ti ratio in PZT films originates early in the crystallization process. These variations are caused by a mismatch in the thermal decomposition of the individual Zr/Ti components in the PZT precursor. Once created, the

compositional gradients cannot be eradicated by prolonged heat treatments. In the Cases 1 and 2, presented in Fig. 8, PZT films were prepared by two sol-gel precursor formulations. The difference between the two formulations is the stabilization of the zirconium precursor: a) Zr precursor is chemically stabilized with AcOH, or b) Zr is stabilized with acetylacetonate (AcAc). Formulation (a) led to opposite concentration gradients of Zr (increasing) and Ti (decreasing) towards surface, while formulation (b) gave rise to constant Zr and Ti concentrations towards the substrate throughout the films. The elemental depth distributions are governed by the thermal decomposition pattern of the individual metal compounds in the sol-gel precursor (Etin et al., 2006). In formulation (a) Zr precursor stabilized with AcOH showed faster pyrolysis and lower decomposition temperature than the Ti precursor. Thus, in formulation (a) Zr-rich phase can form in the bulk before the Ti precursor enters the reaction. After the Ti precursor decomposes, growth of Ti-rich PZT film proceeds from the interface with the Pt electrode leading to opposing concentration gradients of Zr and Ti in the film. In formulation (b) the decomposition of Ti and Zr precursors occurs simultaneously and therefore a uniform depth profile is obtained.

Distribution of the nearest neighbor and next nearest neighbor ions in the pyrochlore phase was demonstrated to be similar to those in the amorphous phase (Reaney et al., 1998). Therefore, although perovskite is the thermodynamically stable phase in the temperature range used in sol-gel fabrication, the transformation from amorphous to pyrochlore phase is kinetically more favorable than a straight transformation to the perovskite phase. The kinetics of transformation from the amorphous to perovskite phase as well as film orientation was shown to depend strongly on the pyrolysis conditions (Brooks et al., 1994; Reaney et al., 1998).

In the work of Ledermann et al., 2003, it is shown that sol-gel PZT thin films are Ti-rich closer to the substrate and Zr-rich closer to the surface for each layer of the film, as well as that the concentration of Pb increases directionally from the substrate to the surface (Fig. 8, Case 3). This is special case of controlled compositional gradient of sol-gel PZT thin films: the gradient has amplitude of  $\pm 20\%$  at the 53/47 morphotropic phase boundary (MPB), showing improved electrical performances. Thanks to the high development of film deposition techniques, in our days it is possible to fabricate controlled compositions, textures and structures of the films with dedicated properties.

These gradient studies show that selection of precursors (chemical solvents) and processing parameters (drying temperatures and time, crystallization temperature and time, etc.) for the deposition of sol-gel films is influential in controlling the homogeneity of the films.

Recently detailed studies of sol-gel PZT 52/48 thin and thick films were presented (Aulika et al., 2009), which were made by using two different solvent systems: a mixture of acetic acid and methanol (AcOH/MeOH) or 2-Methoxyethanol (2-MEO) (Fig. 8, Case 4 and 5). To crystallize the films, two different thermal profiles were applied: all layers crystallized together (LCT) at the same time, and each layer crystallized individually (LCI). The first profile employed the deposition of one layer followed by drying at  $300^\circ\text{C}$  for 1 min. When the final layer was deposited, the sample was placed on a hotplate at  $550^\circ\text{C}$  for 35 min to crystallize. The second thermal profile involved individual crystallization of each layer by holding the sample at  $300^\circ\text{C}$  for 1 min followed by  $550^\circ\text{C}$  for 5 min before the next layer was coated. The annealing time was sufficient for all films to crystallize.

Among all analyzed samples, the refractive index gradient was found only for two groups of films, which were made by crystallizing each layer before another layer was deposited (LCI) (Aulika et al., 2009): 1) One group of films was made using the AcOH/MeOH sol

(Fig. 9a) and 2) the other group was made with the 2-MEO sol (Fig. 9b). The gradient is different for all films of different thickness (Fig. 9). This is most likely due to recurrent annealing of already crystallized layers. The trend of  $n$  with depth presented in Fig. 9b can be caused by several reasons such as 1) residual stress in the film, 2) concentration gradients of Ti or Zr with the layer, 3) an increase in excess Pb (Aulika et al., 2009; Deineka et al., 2001; Ledermann et al., 2003; Watts et al., 2005), 4) polarization profile that is strongly dependent on film thickness (polarization is homogeneous in the greater part of the thick film except in small regions at the film boundaries, while it is completely inhomogeneous in thin films).

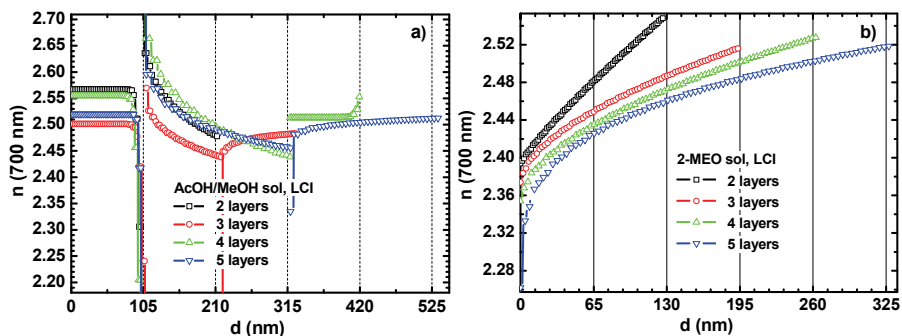


Fig. 9. Depth profile of refractive index  $n$  at the 700 nm of wavelength for the samples with different number of layers made using a) AcOH/MeOH, and b) 2-MEO sol. All figures taken from (Aulika et al., 2009). © The Electrochemical Society, Inc. [2009]. All rights reserved.

No optical gradient is found for films with different numbers of layers when all layers are crystallized at the same time, regardless of the sol used. This was also confirmed for the thick films (Aulika et al., 2009). The groups of films made with AcOH/MeOH sol and by the LCI routine show strong (111) orientation with some low intensity peaks of other orientations, such as (110), (112) or (001)/(100) (Fig. 10 cd). While films with optical gradient revealed (001)/(100) and (002)/(200) orientations (Fig. 10 ab).

Based on the XRD results (Aulika et al., 2009) of LCI films, a picture of how the orientation of the film changes when more layers are added was obtained. Thus, when processing the films using the LCI method, only the first layer crystallizes directly on the Pt substrate and all subsequently deposited layers crystallize on top of PZT 52/48. Since the thermal profile used assures (100) orientation of the film, we would expect the first layer to be (100) oriented, as well as all subsequently deposited layers, since the last layer also is crystallize on (100) PZT. Nevertheless, both groups of PZT 52/48 films processed with the LCI method in fact exhibit some (111) orientation for films having more than three layers. The appearance of (111) orientation can only be explained if some excess of PbO after crystallization is assumed, located close to the surface, as recently reported by Brennecka et al., 2008. Indeed, some pyrochlore was found for all LCI films made with AcOH/MeOH sol. It is thus possible that after the deposition of the next layer, the residual pyrochlore induced nucleation and growth in the (111) direction, consuming the uncrystallized matrix and accounting for the appearance of the (111) orientation at later stages within the first layer. Considering the work of Brennecka et al., 2008 and results of Aulika et al., 2009, the uncrystallized pyrochlore phase was most likely the lead deficient fluorite phase, which was also accompanied by a compositional gradient of Pb/Zr through the layer thickness.

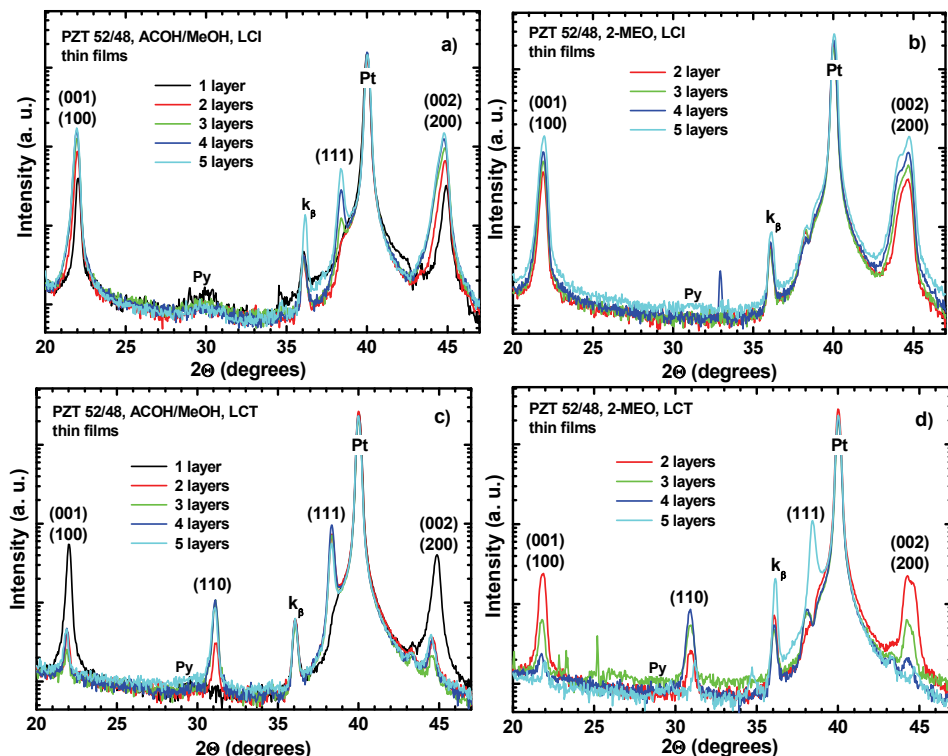


Fig. 10. The XRD of the LCI samples for a) AcOH/MeOH films, b) 2-MEO films, and LCT samples for c) AcOH/MeOH films, and d) 2-MEO films. All figures taken from (Aulika et al., 2009). © The Electrochemical Society, Inc. [2009]. All rights reserved.

In pinpointing the cause of the detected optical gradient, any change in orientation with number of layers can be eliminated based on the consideration that the films made with the LCT method showed more mixed orientation among the samples, and yet no optical gradient was found for these films. Moreover, the optical gradient was found in films made with the LCI route, where a strong variation in lattice parameter with increasing thickness was found, even though the type of gradient was dependent on the sol used.

On the other hand, it was reported that the  $n$  increases with increasing Ti/Zr concentration (Tang et al., 2007; Yang et al., 2006). It is likely that the appearance of the depth profile for the LCI films is connected with the fact that  $\text{PbTiO}_3$  (PTO) crystallizes before  $\text{PbZrO}_3$  (PZO) (Impey et al., 1998), while crystallizing layers together may avoid preferential PTO and PZO crystallization. Better quality PZT 52/48 composition thin films can be made by annealing the films at higher temperatures using rapid thermal annealing (RTA) or oven, or to have a different Zr/Ti concentration ratio in each layer with the goal to anticipate the selection and diffusion processes (Calamea and Murali, 2007). RTA usually needs fully crystallizing at  $> 650^\circ\text{C}$ , but in the study of Aulika et al., 2009, annealing temperature at  $550^\circ\text{C}$  on a hotplate was chosen so that the crystallization of the films started at the interface of Pt/ PZT and grew up to the top rather than crystallizing the films in a oven/RTA which would lead to the crystallization from everywhere and smeared the possible formation of gradient in

composition. This use of low annealing temperature led to the formation of pyrochlore (Fig. 10a, c).

To summarize, there are three possible origins of the refractive index gradient  $n(d)$ : 1) the above-mentioned polarization inhomogeneity close to the film surface, and 2) the varying Zr/Ti ratio and 3) varying Pb throughout the layer. The latter two can be attributed to the separate crystallization of each layer, causing the diffusion of Pb, Ti and Zr ions in the film. If we extrapolate this to the optical properties according to the fact that  $n$  increases with decreasing Zr/Ti ratio (Fig.3), then we can say from Fig. 8b that the Zr/Ti ratio decreases directionally from the substrate to the surface, which is opposite to the observations, e.g., of Ledermann by TEM. However, it is known that sol-gel thin films may have higher concentrations of Pb at the surface (Impey et al., 1998; Ledermann et al., 2003; Watts et al., 2005).

### 3.4.1 Surface enrichment in ferroelectric thin films

Surface enrichment of some elements has been reported by many authors (Impey et al., 1998, Watts et al., 2001, 2003 and 2005; Gusmano et al., 2002), and there are just few explanations for this phenomenon. An analogy may be drawn with the oxidation of metals such as Cu and Sn where the metals dif-fuse towards the reacting surface (Wagner, 1971; Cabrera and Mott, 1948).

The data presented by Watts et al indicates that the pyrolysis and crystallization steps for sol-gel films result in incomplete oxidation (Watts et al., 2005). The diffusion is driven by the oxidation of Pb at the PZT/oxygen interface. The second mechanism is kinetic demixing (Martin, 2003): diffusion of metallic species at different rates, usually in the direction of higher oxygen potential (even though the phase is thermodynamically stable under all these oxygen pressures). This mechanism is often applied for kinetics of solid solutions, but it was shown that a single phase can decompose under a chemical potential gradient (Wang and Akbar, 1992). Most likely that both processes (thermodynamically driven diffusion or kinetic demixing, (Fig. 6) are taking place since it is difficult to separate them due to the fact that the low oxygen content in the film promotes both processes.

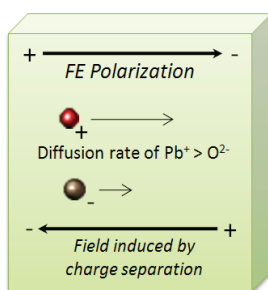


Fig. 11. Self-poling mechanism in ferroelectric thin films.

An electrical potential that polarizes the ferroelectric at high temperatures as it cools through the Curie temperature is created by the migration of cations in the film (Fig. 11). The spontaneous polarization allows the cations to diffuse faster and is the reason why surface enrichment is so significant in ferroelectric films (Watts et al., 2005). The ferroelectric (FE) polarization induced electrochemically by this mechanism is in the direction observed experimentally by Impey et al., 1998, and by Okamura et al., 1999.  $\text{Pb}^{2+}$  diffusion may also lead to self-polarization, which causes the polarization inhomogeneity discussed above.

### 3.4.2 Confirmation of optically detected gradient by TEM and EDX

Fine grains of pyrochlore phase between perovskite crystallites throughout the film thickness were observed for films made by LCI (Fig. 12a). A pyrochlore layer about 50 nm thick was found at the surface of the film. These results are in accordance with the XRD analysis (Fig. 10). The EDX results showed a strong variation in Pb and Zr concentrations throughout the thickness of the film (Fig. 12b), and this film had a strong optical gradient. Close to the surface where the pyrochlore layer was observed, a strong reduction in lead concentration and an increase in zirconium concentration were detected. The titanium concentration was not much affected by the phase separation. It can be concluded that these samples show the same two-phase structure reported by Brennecke et al within each layer, whereby the lead-deficient upper layer causes a compositional gradient.

For PZT 52/48 (LCT) film the columnar grains and additional  $\sim 10$  nm thin pyrochlore layer on the surface was found (Fig. 12c). This film had no optical gradient. No Py was detected by XRD analysis due to its low amount (see Fig. 10). As shown in Fig. 12d, a more uniform EDX concentration profile was obtained in comparison to Fig. 12b.

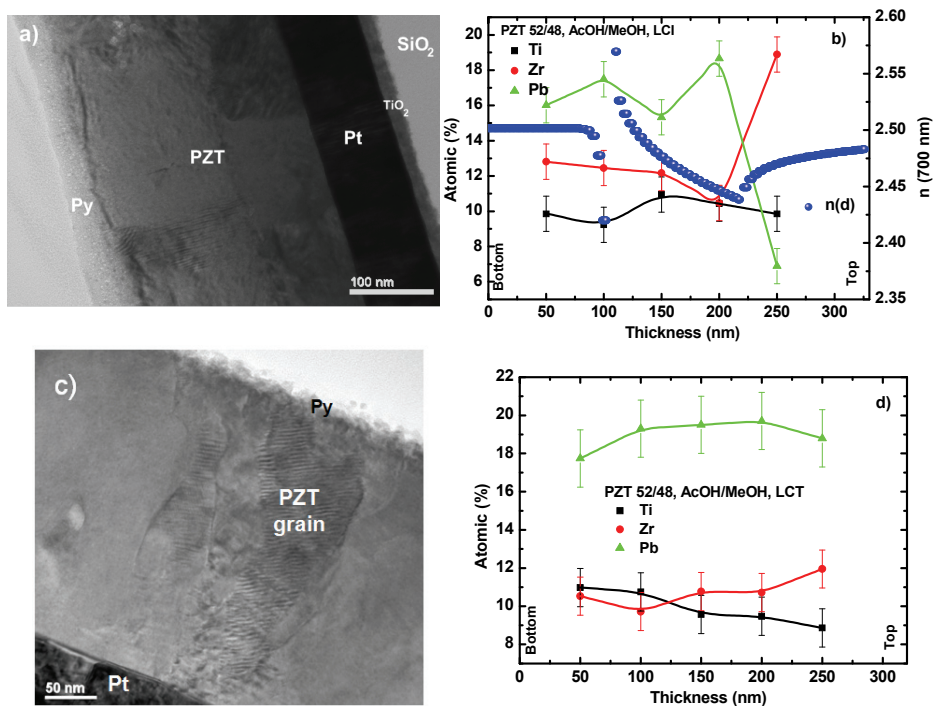


Fig. 12. TEM micrograph (dark field (a) and bright field (c)) of a cross-section of LCI film (a) and LCT film (c) showing pyrochlore phase (Py) between and on the surface of the PZT grains; EDX profile from substrate to the film surface (b, d) in comparison with the optical depth profile  $n(d)$  established by SE (b). All figures taken from (Aulika et al., 2009). © The Electrochemical Society, Inc. [2009]. All rights reserved.

The results obtained by EDX are in good agreement with the optical data evaluated by SE (Fig. 12b). There are almost no changes in variation of Pb, Zr, and Ti near the substrate of the film, which is “reflected” in optical analyses as no optical gradient  $n(d)$ . A significant decrease in Pb and increase in Zr can be seen in the optical data as a decrease in  $n(d)$ . Near the surface  $n(d)$  starts to increase, which is in good agreement with other results (Deineka et al., 1999, 2001, and January 2001; Suchanek et al., 2002).

#### 4. Conclusion

The brief introduction into the composition problems and composition control of  $\text{Pb}(\text{Zr}_x\text{Ti}_{1-x})\text{O}_3$  (PZT) films were laid out in this chapter. Structural and ferroelectric properties, growth rate, phase composition, and stoichiometry of PZT films depend on a number of film deposition parameters. Understanding the chemistry and physics behind the formation of PZT films are of basic and technological importance. The gradient (either compositional and/or optical) can be induced by such factors as thermodynamically driven diffusion and/or kinetic demixing, stress, and nucleation processes. Depending on deposition processes involved, some or even all of these factors can be incorporated and accountable for compositional and/or optical gradient formation in the films. For the same film deposition technique different kind of chemical gradient can be obtained depending on deposition parameters. Any change in the sample structure will affect the polarization and optical properties of the material, irrespective of whether it is a result of the stoichiometry, compositional gradient, internal stresses, etc.

Examples on the characterization methods both intrusive and nondestructive were given, underlining the advantages of optical methods, especially spectroscopic ellipsometry, for gradient detection in films.

The depth profile of the refractive index and composition was presented in details for sol-gel PZT 52/48 thin films made using different chemical solvents and annealing procedures. Thanks to the high development of film deposition techniques, in our days it is possible to fabricate controlled compositions, textures and structures of the films with dedicated and improved electrical properties.

It was also demonstrated that separate crystallization of the layers determines the gradient appearance, irrespective of the chemical solvents as AcOH/MeOH and 2-MEO. The analysis of the XRD results of PZT 52/48 films made with LCI has shown that these films have a preferred orientation of (001)/(100) in contrast to the films made with LCT, which have shown a predominant (111) orientation and no gradient in optical properties. A more refined analysis has shown that a refractive index gradient was apparent in the samples in which lattice parameters strongly change with thickness. For these films, EDX analysis showed significant variation in Pb and Zr. In addition, these qualitative spectroscopic ellipsometry analyses are in accordance with results obtained with other methods, like EDX and ERD. Thus, the spectroscopic ellipsometry method offers the opportunity to accomplish quality analysis of thin films in a relatively simple, fast, and non-destructive way.

To improve spectroscopic ellipsometry calculation for PZT films with complex optical gradients, the films should be considered as a media of two materials – PZT 52/48 and Py, where the  $\text{PbTiO}_3$  and  $\text{PbZrO}_3$  concentrations change within a PZT film. Such complex calculations can be obtained from SE experimental data if additional SE measurements are made on samples of pure Py,  $\text{PbTiO}_3$  and  $\text{PbZrO}_3$  films to extract their optical properties. Nevertheless, by applying a simple exponential gradient model to experimental SE data

analysis, reasonable qualitative data can be obtained which gives an idea of the quality of the sample, its optical properties, optical gradient and homogeneity. Moreover, these qualitative SE analyses are in accordance with results obtained with other methods, e.g., SIMS, EDX and XRD. Thus, the SE method offers the opportunity to accomplish optical analyses of thin films in a simple, fast, precise and non-destructive way, as well as acquire reasonable results and obtain justified information about the quality of thin films. SE is perfect also for real time monitoring of film growth, thickness, optical constants, interface, roughness, optical gradient detection.

Advantages of SE like speed and accuracy, nondestructiveness, no specific sample preparation requirements, compatible with liquid & solid samples, characterization on both absorbing & transparent substrates, thermo-optics (e.g., phase transition analyses), and inhomogeneities detection (porosity, surface roughness, interfaces, optical gradient etc) is of great significance not only from a fundamental, but also from a technological point of view due to intense developments in micro & nano-electronics for nanostructures engineering, where changes in interfaces, within the films and surfaces, and a requirement to detect it, plays very important role. And in this spectroscopic ellipsometry is unique as metrology instrumentation.

## 5. Acknowledgements

Some results published in this chapter were made within the 6th Framework Program of the Multifunctional & Integrated Piezoelectric Devices (MIND). This work was supported by the European Social Fund and UNESCO LÓREAL Latvian National Fellowship for Woman in Science, and grants KAN301370701 of the ASCR, 1M06002 of the MSMT CR, 2 202/09/J017 of GACR and AV0Z10100522. We would like to express our gratitude to Sebastjan Glinsek for TEM sample preparation.

## 6. References

- Aulika, I.; Corkovic, S.; Bencan, A.; D'Astorg, S.; Dejneka, A.; Zhang, Q.; Kosec M.; Zauls, V. (2009), The influence of processing parameters on the formation of optical gradients in chemical solution-derived  $\text{PbZr}_{0.52}\text{Ti}_{0.48}\text{O}_3$  thin films. *Journal of Electrochemical Society*, 156, G217
- Aulika, I.; Dejneka, A.; Lynnyk, A.; Zauls, V.; Kundzins, M. (2009), Thermo-optical investigations of  $\text{NaNbO}_3$  thin films by spectral ellipsometry. *Physica Status Solidi (c)*, 6, 2765
- Aulika, I.; Dejneka, A.; Zauls, V.; Kundzins, K. (2008), Optical gradient of the trapezium-shaped  $\text{NaNbO}_3$  thin films studied by spectroscopic ellipsometry, *Journal of Electrochemical Society*, 155, G209
- Aulika, I.; Deyneka, A.; Zauls V.; Kundzins, K. (2007), Thermo-optical studies of  $\text{NaNbO}_3$  thin films. *Journal of Physics, Conference Edition*, V93, 012016
- Boher, P.; Stehle, J. L.; Piel, J. P.; Fried, M.; Lohner, T.; Polgar, O.; Khanh, N. Q.; Barsony, I. (1996), Spectroscopic ellipsometry applied to the determination of an ion implantation depth profile. *Nuclear Instruments and Methods in Physics Research Section B*, 112, 160
- Born, M.; Wolf, E. (Cambrige University, 1999), *Principles of optics*, 7<sup>th</sup> (expended) edition

- Bovard, B.G. (1990), Rugate filter design: the modified Fourier transform technique, *Applied Optics*, 29, 24-30
- Brennecka, G.L.; Parish, C. M.; Tuttle, B. A.; Brewer, L. N.; Rodriguez, M.A. (2008), Reversibility of the Perovskite-to-Fluorite Phase Transformation in Lead-Based Thin and Ultrathin Films. *Advanced Materials*, 20, 1407
- Brevnov, D. A.; Bungay, C. (2005), Diameter-Dependent Optical Constants of Gold Mesoparticles Electrodeposited on Aluminum Films Containing Copper. *The Journal of Physical Chemistry B*, 109, 14529
- Brooks, K. G.; Reaney, I. M.; Klissurska, R.; Huang, Y.; Buzsill, L.; Setter, N. (1994), Orientation of rapid thermally annealed lead zirconate titanate thin films on (111) Pt substrates. *Journal of Material Research*, 9, 2540
- Bungay, C.; Tiwald, T. E.; (2004), Infrared spectroscopic ellipsometry study of molecular orientation induced anisotropy in polymer substrates. *Thin Solid Film*, 455 – 456 272;
- Cabrera, N.; Mott, N. F. (1948), Theory of the Oxidation of Metals. *Reports on Progress in Physics*, 12, 163-184
- Calamea, F.; Murali, P. (2007), Growth and properties of gradient free sol-gel lead zirconate titanate thin films. *Applied Physics Letters*, 90, 062907
- Callard, S.; Gagnaire, A.; Joseph, J. (1998), Characterization of graded refractive index silicon oxynitride thin films by spectroscopic ellipsometry. *Thin Solid Films*, 313-314, 384
- Chang, W.L.; He, J.L. (2005), Comparison of the microstructures and ferroelectric characteristics of sputter deposited PZT films with and without lead or lead oxide for compensation. *Ceramics International*, 31, 461-468
- Corkovic, S.; Whatmore, R. W.; Zhang, Q. (2008), Development of residual stress in sol-gel derived Pb(Zr,Ti)O<sub>3</sub> films: An experimental study. *Journal Applied Physics*, 103, 084101
- Deineka, A. M.; Glinchuk, D.; Jastrabik, L.; Suchaneck, G.; Gerlach, G. (January, 2001), Nondestructive investigations of the depth profile of PZT ferroelectric films. *Ferroelectrics* 264, 151
- Deineka, A.; Glinchuk, M. D.; Jastrabik, L.; Suchaneck, G.; Gerlach, G. (2001), Ellipsometry investigation of perovskite/pyrochlore PZT thin film stacks. *Ferroelectrics* 258, 271
- Deineka, A.; Glinchuk, M.; Jastrabik, L.; Suchaneck, G.; Gerlach, G. (2001), Ellipsometric Investigations of the Refractive Index Depth Profile in PZT Thin Films. *Physica Status Solidi A*, 188, 1549
- Deineka, A.; Jastrabik, L.; Suchaneck, G.; Gerlach, G. (1999), Optical Properties of Self-Polarized PZT Ferroelectric Films. *Ferroelectrics*, 273, 155-160
- Dejneka, A.; Aulika, I.; Makarova, M. V.; Hubicka, Z.; Churpita, A.; Chvostova, D.; Jastrabik, L.; Trepakov, V. A. (2010), Optical Spectra and Direct Optical Transitions in Amorphous and Crystalline ZnO Thin Films and Powders. *Journal of Electrochemical Society*, 157, G67
- Dejneka, A.; Aulika, I.; Trepakov, V.; Krepelka, J.; Jastrabik, L.; Hubicka, Z.; Lynnyk, A.; (2009), Spectroscopic ellipsometry applied to phase transitions in solids: possibilities and limitations. *Optics Express*, 3 14322
- Etin, A.; Shter, G. E.; Baltianski, S.; Grader, G. S.; Reisner, G. M. (2006), Controlled Elemental Depth Profile in Sol-Gel-Derived PZT Films, *Journal of American Ceramic Society*, 89, 2387-2393

- Fried, M.; Petrik, P.; Lohner, T.; Khánh, N. Q.; Polgár O.; Gyulai, J. (2004), Dose-dependence of ion implantation-caused damage in silicon measured by ellipsometry and backscattering spectrometry. *Thin Solid Films* 455-456, 404
- Gibbons, B.J.; Trolrier-McKinstry, S. (1999), The sensitivity limits of spectroscopic ellipsometry to oxygen content in  $\text{YBa}_2\text{Cu}_3\text{O}_{7-d}$  thin films. *Thin Solid Films* 352, 205
- Gkotsis, P.; Kirby, P.B.; Saharil, F.; Oberhammer, J.; Stemme, G. (2007), Thin film crystal growth template removal: Application to stress reduction in lead zirconate titanate microstructures. *Applied Physics Letters*, 91, 163504
- Glinchuk, M. D.; Eliseev, E. A.; Deineka, A.; Jastrabik, L. (2000), Optical refraction index and electric polarization profile of ferroelectric thin film. *Fine mechanics and optics*, 45, 338-342
- Glinchuk, M. D.; Eliseeva, E.A.; Stephanovich, V.A. (2002), The depolarization field effect on the thin ferroelectric films properties. *Physica B*, 322, 356-370
- Guenther, M.; Gerlach, G.; Suchanek, G.; Sahre, K.; Eichhorn, K.-J.; Wolf, B.; Deineka, A.; Jastrabik, L. (2002), Ion-beam induced chemical and structural modification in polymers. *Surface and Coatings Technology*, 158-159, 108
- Gusmano, G.; Bianco, A.; Viticoli, M.; Kaciulis, S.; Mattogno, G.; Pandolfi, L., (2002), Study of  $\text{Zr}_{1-x}\text{Sn}_x\text{TiO}_4$  thin films prepared by a polymeric precursor route. *Surface and Interface Analysis*, 34, 690-693
- Impey, S. A.; Huang, Z.; Patel, A.; Beanland, R.; Shorrocks, N. M.; Watton, R.; Whatmore, R. W. (1998), Microstructural characterization of sol-gel lead-zirconate-titanate thin films. *Journal of Applied Physics*, 83, 2202
- Izyumskaya, N.; Alivov, Y.-I.; Cho, S.-J.; Morkoc, H.; Lee, H.; Kang, Y.-S. (2007), Processing, Structure, Properties, and Applications of PZT Thin Films. *Critical Reviews in Solid State and Materials Sciences*, 32, 111-202
- Jellison, G. E.; Modine, F. A. (1996), Parameterization of the optical functions of amorphous materials in the interband region. *Applied Physics Letters*, 69, 371
- Jellison, G. E.; Modine, F. A.; Boatner, L. A. (1997), Measurement of the optical functions of uniaxial materials by two-modulator generalized ellipsometry: rutile ( $\text{TiO}_2$ ), *Optics Letters*, 22, 1808
- Kamp, D. A.; DeVilbiss, A. D.; Philpy, S. C.; Derbenwick, G. F. (2004), Adaptable ferroelectric memories for space applications. IEEE, Non-Volatile Memory Technology Symposium 2004, 10.1109/NVMT.2004.1380832
- Lappalainen, J.; Hiltunen, J.; Lantto, V. (2005), Characterization of optical properties of nanocrystalline doped PZT thin films. *Journal of European Ceramic Society*, 25, 2273
- Ledermann, N. ; Muralt, P. ; Baborowski, J.; Gentil, S.; Mukati, K.; Cantoni, M.; Seifert, A.; Setter, N. (2003), {1 0 0}-Textured, piezoelectric  $\text{Pb}(\text{Zr}_x, \text{Ti}_{1-x})\text{O}_3$  thin films for MEMS: integration, deposition and properties. *Sensors and Actuators A*, 105, 162-170
- Losurdo, M. (2004), Relationships among surface processing at the nanometer scale, nanostructure and optical properties of thin oxide films. *Thin Solid Films*, 455-456, 301
- Marcus, R. K.; Schwartz, R. W. (2000), Compositional profiling of solution-deposited lead zirconate-titanate thin films by radio-frequency glow discharge atomic emission spectroscopy (rf-GD-AES), *Chemical Physics Letters*, 318, 481-487
- Martin, M. (2003), Materials in thermodynamic potential gradients. *Journal of Chemical Thermodynamics*, 8, 1291-1308.

- Morita, T.; Kanda, T.; Yamagata, Y.; Kurosawa, M.; Higuchi, T. (1997), Single process to deposit lead zirconate titanate (PZT) thin film by a hydrothermal method. *Japanese Journal of Applied Physics*, 36, 2998
- Morozovskaa, A. N.; Eliseevb, E. A.; Glinchuk, M. D. (2007), Size effects and depolarization field influence on the phase diagrams of cylindrical ferroelectric nanoparticles. *Physica B*, 387, 358–366
- Morton, D. E.; Johs B.; Hale, J. (2002), Soc. of Vac. Coat. 505/856-7188, 45th Ann. Techn. Conf. Proc. ISSN 0737-5921, 1
- Muralt, P. (2000), Ferroelectric thin films for micro-sensors and actuators: A review. IOPscience:... *Journal of Micromechanics and Microengineering*, 10, 136-146
- Nguyen Van, V.; Brunet-Bruneau, A.; Fisson, S.; Frigerio, J. M.; Vuye, G.; Wang, Y.; Abelvs, F.; Rivory, J.; Berger, M.; Chaton, P. (1996), Determination of refractive-index profiles by a combination of visible and infrared ellipsometry measurements. *Applied Optics*, 35, 5540
- Nishizawa, H.; Tateyama, Y.; Saitoh, T. (2004), Ellipsometry characterization of oxidized copper layers for chemical mechanical polishing process. *Thin Solid Films*, 455-456, 491
- Ohba, Y.; Arita, K.; Tsurumi, T.; Daimon, M. (1994), Analysis of interfacial phase between substrates and lead zirconate titanate thin films synthesized by hydrothermal method. *Japanese Journal of Applied Physics*, 33, 5305
- Okamura, S.; Miyata, S.; Mizutani, Y.; Nishida, T.; Shiosaki, T. (1999), Conspicuous voltage shift of D-E hysteresis loop and asymmetric depolarization in Pb-based ferroelectric thin films. *Japanese Journal of Applied Physics*, 38, 5364–5367
- Okamura, S.; Miyata, S.; Mizutani, Y.; Nishida, T.; Shiosaki, T. (1999), Conspicuous voltage shift of D-E hysteresis loop and asymmetric depolarization in Pb-based ferroelectric thin films. *Japanese Journal of Applied Physics*, 38, 5364–5367
- Oulette, M. F.; Lang, R. V.; Yan, K. L.; Bertram, R. W.; Owle, R. S.; Vincent, D. (1991), Experimental studies of inhomogeneous coatings for optical applications. *Journal of Vacuum Science and Technology A*, 9, 1188- 1192
- Parish, C. M.; Brennecka, G. L.; Tuttle, B. A.; Brewer, L. N. (2008), Quantitative X-Ray Spectrum Imaging of Lead Lanthanum Zirconate Titanate PLZT Thin-Films. *Journal of American Ceramic Society*, 91, 3690
- Philpy, S. C.; Kamp D. A.; Derbenwick G. F. (2003), Hardened By Design Ferroelectric Memories for Space Applications," Non-Volatile Memory Technology Symposium 2003, San Diego, California
- Reaney, I. M.; Taylor, D. V.; Brooks, K. G. (1998), Ferroelectric PZT thin films by sol-gel deposition. *Journal of Sol-Gel Science and Technology*, 13, 813
- Rivory, J. (1998), Characterization of inhomogeneous dielectric films by spectroscopic ellipsometry. *Thin Solid Films*, 313-314, 333
- Snyder, P.G.; Xiong, Y.-M.; Woollam, J.A.; Al-Jumaily G.A.; Gagliardi, F.J. (1992), Graded refractive index silicon oxynitride thin film characterized by spectroscopic ellipsometry. *Journal of Vacuum Science and Technology A*, 10, 1462
- Sternberg, A.; Krumins, A.; Kundzins, K.; Zauls, V.; Aulika, I.; Cakare, L.; Bittner, R.; Weber, H.; Humer, K.; Lesnyh, D.; Kulikov D.; Trushin, Y. (2003), Irradiation effects in lead zirconate thin films. *Proceedings of SPIE*, 5122, 341

- Suchaneck, G.; Lin, W. -M.; Koehler, R.; Sandner, T.; Gerlach, G.; Krawietz, R.; Pompe, W.; Deineka, A.; Jastrabik, L. (2002), Characterization of RF-sputtered self-polarized PZT thin films for IR sensor arrays. *Vacuum* 66, 473
- Sugiyama, O.; Kondo, Y.; Suzuki, H.; Kaneko, S. (2003), XPS Analysis of Lead Zirconate Titanate Thin Films Prepared Via Sol-Gel Process. *Journal of Sol-Gel Science and Technology*, 26, 749-52
- Sugiyama, O.; Murakami, K.; Kaneko, S. (2004), XPS Analysis of Surface Layer of Sol-Gel-Derived PZT Thin Films, *Journal of European Ceramic Society*, 24, 1157-1160
- Synowicki, A. (1998), Spectroscopic ellipsometry characterization of indium tin oxide film microstructure and optical constants. *Thin Solid Film*, 313 - 314, 394
- Synowicki, R.A.; Tiwald, T. E. (2004), Optical properties of bulk c-ZrO<sub>2</sub>, c-MgO and a-As<sub>2</sub>S<sub>3</sub> determined by variable angle spectroscopic ellipsometry. *Thin Solid Film*, 455 - 456, 248
- Tang, X. G.; Liu, Q. X.; Jiang L. L.; Ding, A.L. (2007), Optical properties of  $\text{Pb}(\text{Zr}_x\text{Ti}_{1-x})\text{O}_3$  ( $x=0.4, 0.6$ ) thin films on Pt-coated Si substrates studied by spectroscopic ellipsometry. *Materials Chemistry and Physics*, 103, 329
- Tilley, D.R. (Gordon and Breach, Amsterdam, 1996), *Ferroelectric Thin Films*
- Tompkins, H. G. Irene, E. A. (NY 2005), *Handbook of ellipsometry*
- Trolier-McKinstry, S.; Koh, J. (1998), Composition profiling of graded dielectric function materials by spectroscopic ellipsometry. *Thin Solid Films*, 313-314, 389
- Vidyarathi, V.S.; Lin, W.-M.; Suchaneck, G.; Gerlach, G.; Thiele, C.; Hoffmann, V. (2007), Plasma emission controlled multi-target reactive sputtering for in-situ crystallized  $\text{Pb}(\text{Zr,Ti})\text{O}_3$  thin films on 6" Si-wafers, *Thin Solid Films*, 515, 3547-3553
- Wagner, C. (1971), Contribution to the thermodynamics of interstitial solid solutions. *Acta Metallurgica*, 19, 843-849
- Wang, C. C.; Akbar, S. A. (1992), Decomposition of  $\text{YBa}_2\text{Cu}_3\text{O}_x$  under an oxygen potential gradient using a YSZ-based galvanic cell. *Material Letters*, 13, 254-260
- Wang, X.; Masumoto, H.; Someno, Y.; Chen, L.; Hirai., T. (2001), Stepwise graded refractive-index profiles for design of a narrow-bandpass filter. *Applied Optics*, 40, 3746
- Wang, Y.G.; Zhong, W.L.; Zhang, P.L. (1995), Surface and size effects on ferroelectric films with domain structures. *Physical Review B*, 51, 5311
- Watts, B. E.; Leccabue, F.; Fanciulli, M.; Ferrari, S.; Tallarida, G.; Parisoli, D. (2001), The influence of low temperature baking on the properties of  $\text{SrBi}_2\text{Ta}_2\text{O}_9$  films from metallorganic solutions. *Integrated Ferroelectrics*, 37, 565-574.
- Watts, B. E.; Leccabue, F.; Fanciulli, M.; Tallarida, G.; Ferrari, S. (2003), Surface segregation mechanisms in ferroelectric thin films. *Journal of Electroceramics*, 11, 139-147
- Watts, B.E.; Leccabue, F.; Bocelli, G.; Padeletti, G.; Kaciulis, S.; Pandolfi, L. (2005), Lead enrichment at the surface of lead zirconate titanate thin films, *Journal of the European Ceramic Society*, 25, 2495-2498
- Whatmore, R.W.; Zhang, Q.; Huang, Z.; Dorey, R.A. (2003), Ferroelectric thin and thick films for microsystems. *Materials Science in Semiconductor Processing*, 5, 65-76
- Xi, J.-Q.; Schubert, M. F.; Kim, J. K.; Schubert, E. F.; Chen, M.; Lin, S.-Y.; Liu, W. ; Smart, J. A. (2007), Optical thin-film materials with low refractive index for broadband elimination of Fresnel reflection. *Nature Photonics*, 1, 176

- Yang, S.; Zhang Y.; Mo, D. (2006), A comparison of the optical properties of amorphous and polycrystalline PZT thin films deposited by the sol-gel method. *Materials Science and Engineering B*, 127, 117
- Yee, Y.; Nam, H.-J.; Lee, S.-H.; Uk Bu, J.; Lee, J.-W. (2001), PZT actuated micromirror for fine-tracking mechanism of high-density optical data storage. *Sensors and Actuators A*, 89, 166-173

# Photo-induced Effect in Quantum Paraelectric Materials Studied by Transient Birefringence Measurement

Toshiro Kohmoto and Yuka Koyama  
*Graduate School of Science, Kobe University,  
Japan*

## 1. Introduction

Strontium titanate  $\text{SrTiO}_3$  is known as a quantum paraelectric material, and its lattice dynamics and unusual dielectric character have been studied extensively. The cubic ( $O_h$ ) structure above the structural phase transition temperature ( $T_C = 105$  K) changes into the tetragonal ( $D_{4h}$ ) structure below  $T_C$ . At low temperatures, dielectric constant increases up to about  $3 \times 10^4$ , where the paraelectric phase is stabilized by quantum fluctuations even below the classical Curie temperature 37 K (Muller & Burkard, 1979).

Photo-induced effect in dielectric materials is an attractive topic. Some kind of ferroelectric materials such as SbSI (Ueda et al., 1967) and  $\text{BaTiO}_3$  (Volk et al., 1973; Godefroy et al., 1976) are known to show photo-induced effects. In this decade, much interest has been paid on the giant enhancement in dielectric constants under ultraviolet (UV) illumination and DC electric field in quantum paraelectrics, strontium titanate  $\text{SrTiO}_3$  and potassium tantalate  $\text{KTaO}_3$  (Takesada et al., 2003; Hasegawa et al., 2003; Katayama et al., 2003), because weak light illumination gives rise to an intense response in dielectricity.

The two models shown Fig. 1, the ferroelectric cluster model (Takesada et al., 2003; Hasegawa et al., 2003; Katayama et al., 2003) and the conductive-region model (Homes et al., 2001; Katayama et al., 2003), have been proposed to explain the origin of the giant dielectric constants. At present, however, it is still not clear which model is better. In the ferroelectric cluster model, the photo-induced ferroelectric region has a huge dipole moment, where it is expected that a photo-induced polar domain generates spatial lattice distortion. In the conductive-region model, on the other hand, the superposition of insulative and photo-induced conductive regions, which is characterized by the boundaries between the two regions, makes the apparent dielectric constants to be enormous.

Giant dielectric response has been observed in some types of nonferroelectric materials (Homes et al., 2001; Wu et al., 2002; Dwivedi et al., 2010). The enormous increase in dielectric constants is attributed to the formation of barrier layer capacitors and the resultant Maxwell-Wagner polarization or interfacial polarization. This giant dielectric response often occurs in materials with grains surrounded by the insulating grain boundary and is explained by the conductive-region model.

According to the measurement of dielectric constants, a doped crystal  $\text{Sr}_{1-x}\text{Ca}_x\text{TiO}_3$  undergoes a ferroelectric transition above the critical Ca concentration  $x_c = 0.0018$  (Bednorz

& Muller, 1984; Bianchi et al., 1994). Doped Ca ions are substituted for the Sr ions. The cubic structure above the structural phase transition temperature ( $T_{C1}$ ) changes into the tetragonal structure below  $T_{C1}$  and into the rhombohedral structure below the ferroelectric transition temperature  $T_{C2}$ . Off-centered impurity ions, which are assumed in the case of impurity systems such as Li-doped  $\text{KTiO}_3$  and Nb-doped  $\text{KTiO}_3$  (Vugmeister & Glinchuk, 1990), are supposed also in the case of Ca-doped  $\text{SrTiO}_3$ . Their polarized dipole moments show a ferroelectric instability below the ferroelectric transition temperature. In the case of Ca-doped  $\text{SrTiO}_3$ , a spontaneous polarization occurs along  $[110]$  directions within the  $c$  plane, where the tetragonal ( $D_{4h}$ ) symmetry is lowered to  $C_{2v}$ .

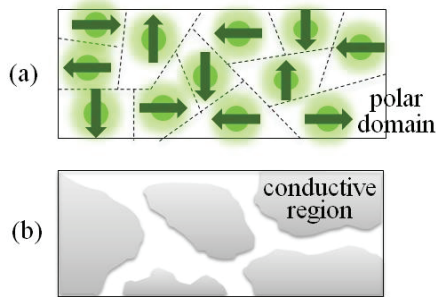


Fig. 1. Schematic pictures of (a) ferroelectric cluster model and (b) conductive-region model.

In Ca-doped  $\text{SrTiO}_3$ , a UV illumination causes a shift of the ferroelectric phase transition temperature toward the lower side (Yamada & Tanaka, 2008). The  $T_{C2}$  reduction under the UV illumination is considered to be caused by disequilibrium carriers which are captured by traps and screen the polarization field.

In the present study, we performed three types of experiment in pure and Ca-doped  $\text{SrTiO}_3$ ; (i) stationary birefringence measurement in UV light and DC electric fields, (ii) transient birefringence measurement in UV light and pulsed electric fields, and (iii) transient absorption and birefringence measurements after the optical pulse excitation using the pump-probe technique. The photo-induced dynamics of the lattice distortion, the dielectric polarization, and the relaxed excited state in  $\text{SrTiO}_3$  is studied in comparison with the lattice distortion in the doping-induced ferroelectric phase of Ca-doped  $\text{SrTiO}_3$ . We discuss which model explains the experimental results better.

The experiments are performed on single crystals of pure and Ca-doped  $\text{SrTiO}_3$  with the Ca concentration of  $x = 0.011$ .  $\text{SrTiO}_3$  was obtained commercially and Ca-doped  $\text{SrTiO}_3$  was grown by the floating zone method. The thickness of the samples is 0.2 mm. The structural phase-transition temperature,  $T_{C1}=180\text{K}$ , of the Ca-doped  $\text{SrTiO}_3$  was obtained from the temperature dependence of the birefringence (Koyama et al., 2010), and the ferroelectric phase-transition temperature,  $T_{C2} = 28\text{K}$ , was determined by the measurement of dielectric constants (Yamada & Tanaka, 2008).

## 2. Lattice distortion in the UV and DC fields in Ca-doped $\text{SrTiO}_3$

The stationary birefringence is studied to investigate the static properties of the lattice distortion generated by the UV illumination in comparison with that generated by the ferroelectric deformation.

### 2.1 Birefringence measurement in the UV light and DC electric fields

The schematic diagram of the birefringence measurement in the UV light and DC electric fields is shown in Fig. 2. The change in birefringence is detected as the change in the polarization of a linearly polarized probe light provided by a Nd:YAG laser (532 nm). The source of UV illumination is provided by the second harmonics (380 nm, 3.3 eV) of the output from a mode-locked Ti-sapphire laser, whose energy is larger than the optical band gap of SrTiO<sub>3</sub> (3.2 eV). The intensity of UV illumination is 1.6 mW/mm<sup>2</sup>. Since the repetition rate of the UV pulses is 80 MHz, this UV illumination can be considered to be continuous in the present experiment. The UV beam is illuminated on the gap between two Au electrodes. The electrodes with a gap of 0.8 mm are deposited on a (100) surface of the samples by sputtering. A DC electric field, whose amplitude is 375 V/mm, is applied between the two electrodes. The DC electric field is applied parallel to [100] direction of the crystal.

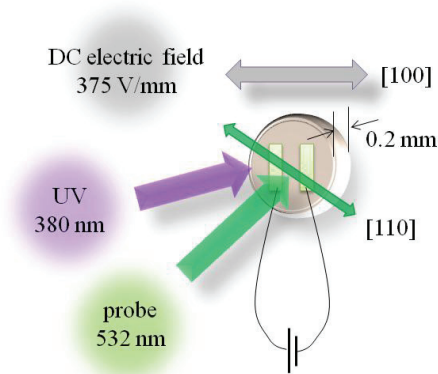


Fig. 2. Schematic diagram of the birefringence measurement in the UV light and DC electric fields.

The change in the polarization of the probe light is detected by a polarimeter. The construction of the polarimeter is shown in Fig. 3. The polarimeter (Kohmoto et al., 2000; Jones, 1976) detects the rotation of polarization plane of a light beam. A linearly-polarized beam is split by a polarized beam splitter (PBS) and incident on the two photodiodes (PD) whose photocurrents are subtracted at a resistor (R). When the polarized beam splitter is mounted at an angle of 45° to the plane of polarization of the light beam, the two photocurrents cancel. If the plane of polarization rotates, the two currents do not cancel and the voltage appears at the resistor.

In the present experiment, the birefringence generated by the lattice deformation is detected as the change in polarization of the probe beam using a quarterwave plate and a polarimeter. The birefringence generated in the sample changes the linear polarization before transmission to an elliptical polarization after transmission. The linearly-polarized probe beam is considered to be a superposition of two circularly-polarized components which have the opposite polarizations and the same intensities. The generated birefringence destroys the intensity balance between the two components. The two circularly-polarized beams are transformed by the quarterwave plate to two linearly-polarized beams whose polarizations are crossed each other, and the unbalance of circular polarization is

transformed to the unbalance of linear polarization or the rotation of polarization plane. This rotation is detected by the polarimeter as the signal of the lattice deformation.

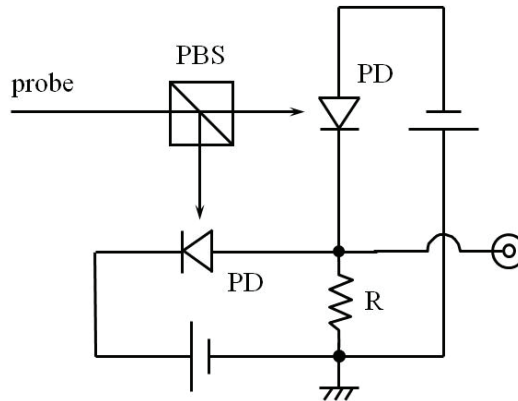


Fig. 3. Construction of the polarimeter.

## 2.2 UV intensity dependence of the birefringence

The ultraviolet intensity dependence of the change in birefringence in Ca-doped SrTiO<sub>3</sub> is shown in Fig. 4, where the temperature is 6 K and the polarization plane of the probe light is along the [110] and [100] axes, with which the lattice distortion along the [100] and [110] axes are detected, respectively. The birefringence increases nonlinearly as the UV intensity is increased. As is shown in Fig. 4(a), the change in birefringence appears at very weak UV intensity in the polarization plane only along the [110] axis, rises rapidly, and holds almost a constant value above 0.5 mW/mm<sup>2</sup>. Figure 4(b), where the horizontal axis is in a logarithmic scale, indicates that the structural deformation begins at the UV intensity of 10<sup>-3</sup> mW/mm<sup>2</sup>. The change in birefringence for the probe polarization along the [110] axis is much larger than that along the [100] axis. These facts imply that the UV illumination causes Ca-doped SrTiO<sub>3</sub> to undergo a first-order-like structural deformation and generates a lattice distortion along the [100] axis as a result of the competition between the UV-induced and ferroelectric deformations, and its threshold value is very small.

Figure 5 schematically shows the direction of the local lattice distortion in pure and Ca-doped SrTiO<sub>3</sub>. The observed direction of the lattice distortion in Ca-doped SrTiO<sub>3</sub> generated by the UV illumination is the same as that in the case of pure SrTiO<sub>3</sub> (Nasu, 2003).

## 2.3 Temperature dependence of the birefringence in the UV and DC fields

We investigated the temperature dependence of the change in birefringence for Ca-doped SrTiO<sub>3</sub> in the combination of two external fields, UV light (UV) and DC electric (DC) fields. The experimental result is shown in Fig. 6 where the polarization plane of the probe light is along the [110] and [100] axes. The sample is in the four types of fields; neither UV nor DC (no field), only DC (DC), only UV (UV), and both UV and DC (UV+DC). The changes in birefringence for the probe polarization along the [110] axis are much larger than those along the [100] axis. This means that the optical anisotropy is generated along the [100] axis. For the probe polarization along the [110] axis without the DC electric field, the change in birefringence for no field is similar to that for UV, as is seen in Fig. 6, while under the DC

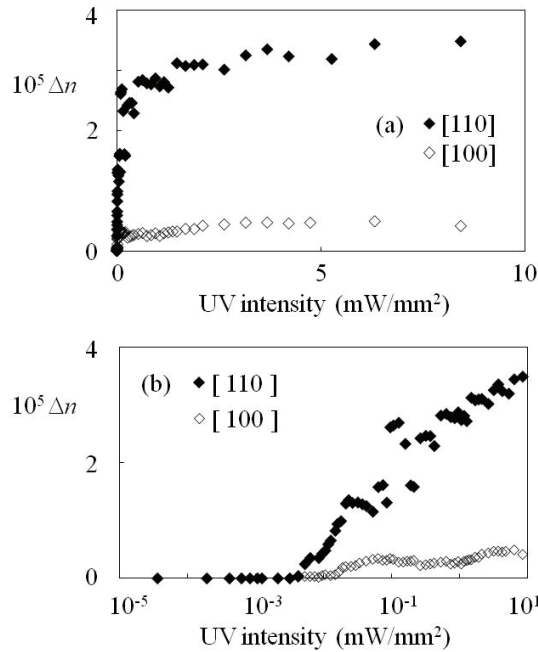


Fig. 4. UV intensity dependence of the change  $\Delta n$  in birefringence in Ca-doped SrTiO<sub>3</sub> at 6 K, where the probe-light polarization is along the [110] and [100] axes. The horizontal axis is (a) in a linear scale and (b) in a logarithmic scale.

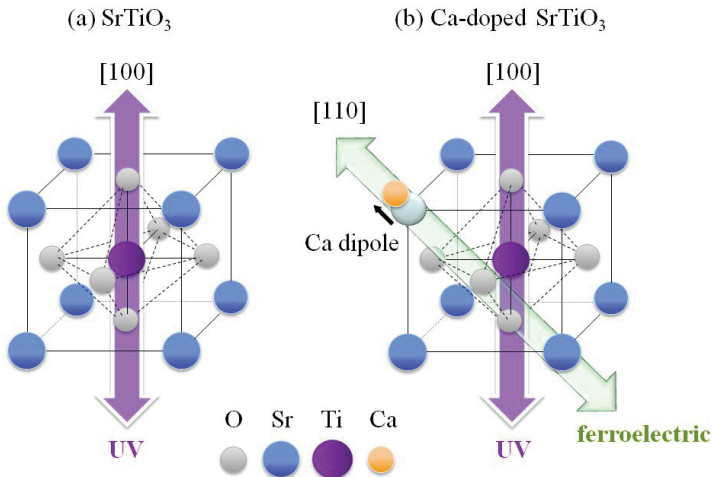


Fig. 5. Direction of the local lattice distortion (a) in SrTiO<sub>3</sub> and (b) in Ca-doped SrTiO<sub>3</sub>. The direction of local lattice distortion generated by the UV illumination is axial along the [100] axis both for pure and Ca-doped SrTiO<sub>3</sub>. The direction of the local lattice distortion in the ferroelectric phase of Ca-doped SrTiO<sub>3</sub> is diagonal along the [110] axis.

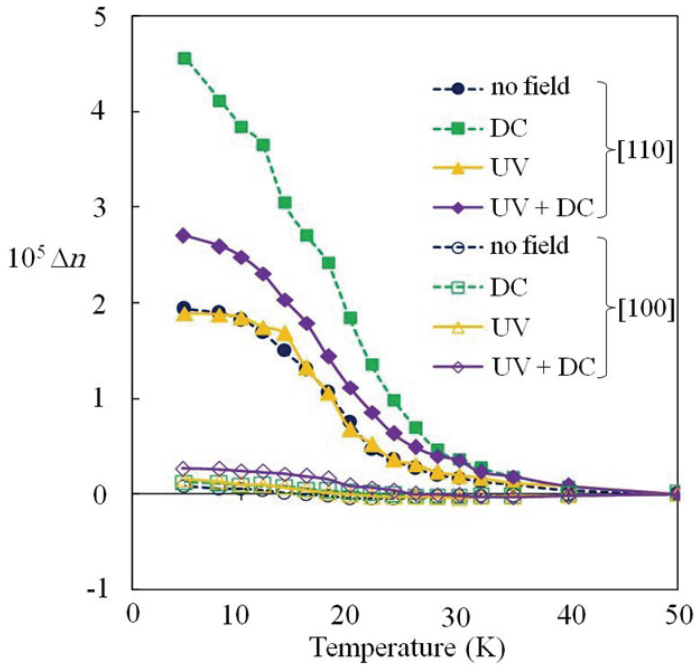


Fig. 6. Temperature dependence of the change in birefringence for Ca-doped SrTiO<sub>3</sub> in the combination of two external fields, UV light (UV) and DC electric (DC) fields, where the polarization plane of the probe light is along the [110] and [100] axes. The sample is in the four types of fields; neither UV nor DC (no field), only DC (DC), only UV (UV), and both UV and DC (UV+DC).

electric field the change for DC is different from that for UV+DC. The difference arises from that of the macroscopic optical anisotropy generated along the [100] axis by the UV illumination.

In the ferroelectric phase of Ca-doped SrTiO<sub>3</sub>, the direction of the local lattice distortion is diagonal along the [110] axis (Bednorz & Muller, 1984) as shown in Fig. 5(b). There are six equivalent diagonal sites where the distortion directions are [110], [1-10], [011], [01-1], [101], and [10-1]. In no field, it is expected that the six local sites distribute randomly as shown in Fig. 7(a), and no optical anisotropy is generated. The observed birefringence change  $\Delta n_{NO}$  for no field, however, shows that the optical anisotropy grows along the [100] axis at low temperatures. This may be because that the domain structure due to the structural phase transition violates the equivalency among the six sites.

In the DC electric field along the [100] axis, on the other hand, the six local diagonal sites in the ferroelectric phase are not equivalent as shown in Fig. 7(b). The two diagonal sites, [011] and [01-1] which are perpendicular to the [100] axis, are more unstable in the DC electric field along the [100] axis than the other four diagonal sites, [110], [1-10], [101], and [10-1]. The random distribution of the four diagonal sites generate a macroscopic optical anisotropy along the [100] axis. This explains the observed large increase of the birefringence change  $\Delta n_{DC}$  for the [110] probe and small change for the [100] probe.

As discussed in section 2.2, the lattice distortion generated by the UV illumination is axial along the [100] axis. In no DC electric field, its direction distributes randomly among the three equivalent directions, [100], [010], and [001] as shown in Fig. 7(c), where no macroscopic optical anisotropy is expected. The observed similar behavior between the birefringence changes  $\Delta n_{NO}$  for no field and  $\Delta n_{UV}$  for UV can be explained by the fact that the UV illumination changes the local distortion but does not add any macroscopic optical anisotropy.

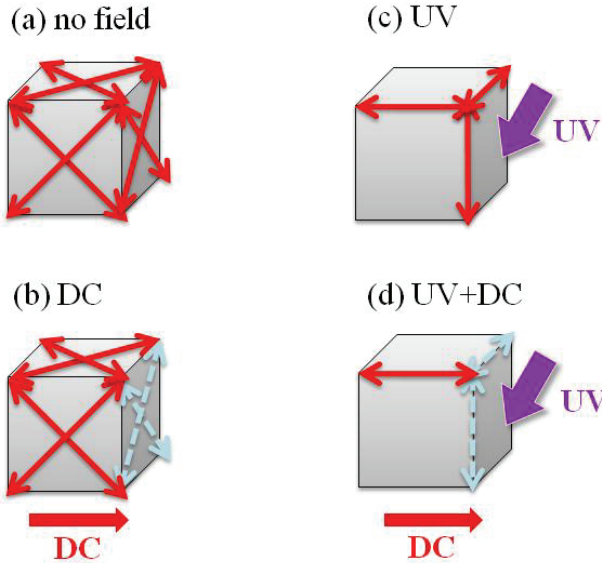


Fig. 7. Directions of the local lattice distortion in the ferroelectric phase of Ca-doped SrTiO<sub>3</sub>. (a) In no field, the six equivalent diagonal sites distribute randomly. (b) In the DC electric field along the [100] axis, the two diagonal sites perpendicular to the [100] axis are more unstable than the other four diagonal sites. (c) The three equivalent axial sites generated by the UV illumination distribute randomly in no DC electric field. (d) In the DC electric field, the two UV-generated axial sites perpendicular to the DC field direction are more unstable than the parallel UV-generated axial site. Macroscopic optical anisotropies are expected to be generated in the DC electric field (b) for DC and (d) for UV+DC, but are not expected (a) for no field and (c) for UV.

In the DC electric field along the [100] axis, the three axial sites generated by the UV illumination are not equivalent as shown in Fig. 7(d). The two axial sites [010] and [001], which are perpendicular to the [100] axis, are more unstable than the other axial site [100]. This axial site can also contribute to generate a macroscopic optical anisotropy along the [100] axis. The UV illumination changes some part of the local distortion from the diagonal site along the [110] axis to the axial site along the [100] axis. The UV illumination decreases the birefringence change in the DC electric field;  $\Delta n_{UV+DC} < \Delta n_{DC}$ , as is seen in Fig. 6. This result suggests that the sign of the optical anisotropy generated by the UV illumination is opposite to that by the diagonal distortion in the ferroelectric phase. It should be noted that the optical anisotropy due to the structural deformation generated by the UV illumination is of the same order of magnitude as that generated by the ferroelectric deformation.

### 3. Lattice distortion in the UV and pulsed electric fields in pure and Ca-doped SrTiO<sub>3</sub>

#### 3.1 Transient birefringence measurement in the UV light and pulsed electric fields

The transient birefringence in a pulsed electric field is studied to probe whether or not the lattice distortion generated by the UV illumination is affected by the electric field. In the experiment of transient birefringence, the change in birefringence is monitored by the probe light of 532 nm from the Nd:YAG laser, and its time evolution is obtained from the waveform digitized on an oscilloscope. A pulsed electric field, whose amplitude is 150 V/mm and pulse width is 1.2 ms, is applied between the two Au electrodes.

#### 3.2 Transient birefringence in SrTiO<sub>3</sub>

Figure 8(a) shows the change  $\Delta n(t)$  in birefringence in pure SrTiO<sub>3</sub> after the application of the electric-field pulse at  $t = 0$  between 4.5 K and 50 K, where the UV illumination is off and the polarization plane of the probe light is along the [110] axis. The signal of the birefringence change rises rapidly at the start of the electric-field pulse and holds a constant value during the pulse. As the temperature is decreased, the birefringence change induced by the electric-field pulse is increased. This means that the polarization, which is related to the dielectric constants, is increased at lower temperatures.

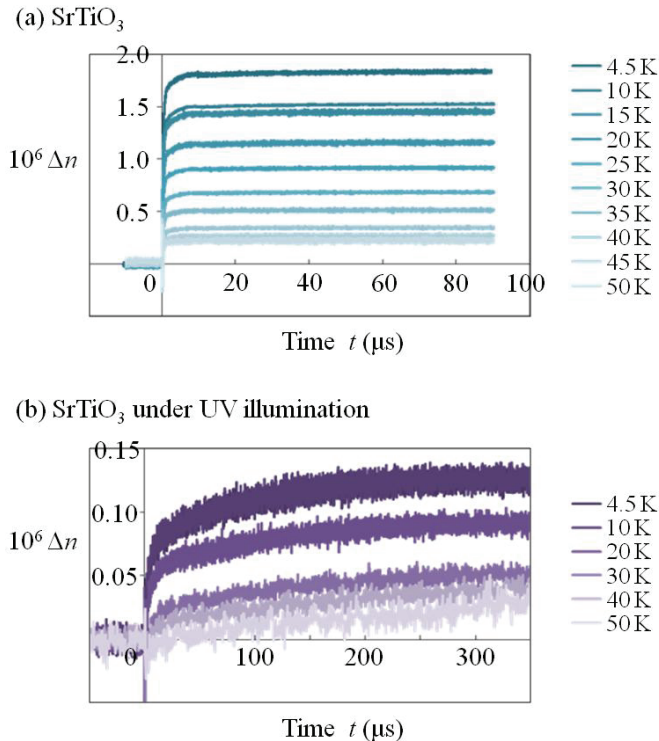


Fig. 8. Temperature dependence of the transient birefringence signal  $\Delta n(t)$  in SrTiO<sub>3</sub> in a pulsed electric field under the (a) dark and (b) UV illumination. The polarization plane of the probe light is along the [110] axis. The electric field of 150 V/mm is turned on at  $t = 0$ .

Figure 8(b) shows the change in birefringence in SrTiO<sub>3</sub> under the UV illumination. The dielectric response of relaxation type is observed at all temperatures. As the temperature is decreased, the relaxation rate becomes increased.

### 3.3 Transient birefringence in Ca-doped SrTiO<sub>3</sub>

The change  $\Delta n(t)$  in birefringence in Ca-doped SrTiO<sub>3</sub> is shown in Fig. 9(a), where some oscillating components appear. As the temperature is decreased, the amplitudes of these oscillating components are increased. These oscillations are considered to be caused by the doped Ca ions because they are not observed in pure SrTiO<sub>3</sub> but only in Ca-doped SrTiO<sub>3</sub>. The change in birefringence induced by the electric-field pulse is increased as the temperature is decreased, as well as in SrTiO<sub>3</sub>, which means that the dielectric polarization is increased at low temperatures. Figure 9(b) shows the change in birefringence in Ca-doped SrTiO<sub>3</sub> under the UV illumination. In Ca-doped SrTiO<sub>3</sub>, the dielectric response of relaxation type appears only above the ferroelectric phase transition temperature  $T_{c2}$ , and the oscillating components also disappear above  $T_{c2}$ .

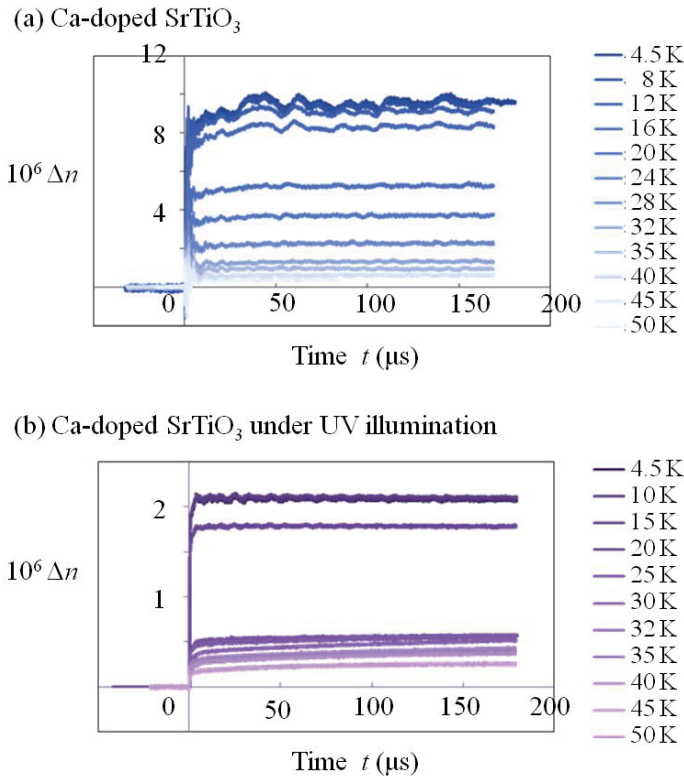


Fig. 9. Temperature dependence of the transient birefringence signal  $\Delta n(t)$  in Ca-SrTiO<sub>3</sub> in a pulsed electric field under the (a) dark and (b) UV illumination. The polarization plane of the probe light is along the [110] axis. The electric field of 150 V/mm is turned on at  $t = 0$ .

### 3.4 Temperature dependence of the transient birefringence amplitude

The temperature dependences of the transient birefringence amplitude  $\Delta n_S$  for pure and Ca-doped SrTiO<sub>3</sub> are shown in Fig. 10, where  $\Delta n_S$  is obtained from the value of  $\Delta n(t)$  at large enough time  $t$  in Figs. 8 and 9.

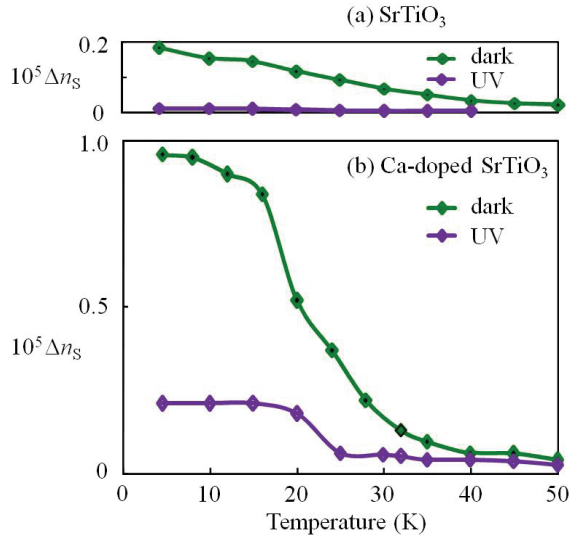


Fig. 10. Temperature dependence of the transient birefringence amplitude  $\Delta n_S$  induced by the electric-field pulse under the dark and UV illumination (a) in SrTiO<sub>3</sub> and (b) in Ca-doped SrTiO<sub>3</sub>.

For both samples, it is clear that the transient birefringence amplitude for the probe polarization along the [110] axis is reduced by the UV illumination, which indicates that the lattice deformation is reduced by the UV illumination and that the lattice distortion generated by the UV illumination is not affected by the electric field. This result is not consistent with the ferroelectric cluster model, where a large change in birefringence is expected in the pulsed electric field.

In Ca-doped SrTiO<sub>3</sub>, judging from the rising temperature of the transient birefringence amplitude, the ferroelectric phase transition temperature is shifted toward the lower temperature side under the UV illumination. This is consistent with the dielectric measurement (Yamada & Tanaka, 2008) and the coherent phonon experiment (Koyama et al., 2010). The doped Ca ions behave as permanent dipoles, and ferroelectric clusters are formed around the Ca dipoles with the high polarizability of the host crystal. The ferroelectric transition is caused by the ordering of the randomly distributed Ca dipoles. The ordering is prevented by the photo-excited carriers generated by the UV illumination.

## 4. Dynamics of the relaxed excited state after the optical pulse excitation in SrTiO<sub>3</sub>

Figure 11 illustrates the electronic states in SrTiO<sub>3</sub>. The UV illumination, whose photon energy is larger than the band-gap energy of SrTiO<sub>3</sub> (3.2 eV), excites the electrons from the ground

state to the excited state. The excited electrons are self-trapped in the relaxed excited state where the optically induced lattice distortion is created (Nasu, 2003). In the relaxed excited state, a broad absorption band appears (Hasegawa & Tanaka, 2001; Okamura et al., 2006).

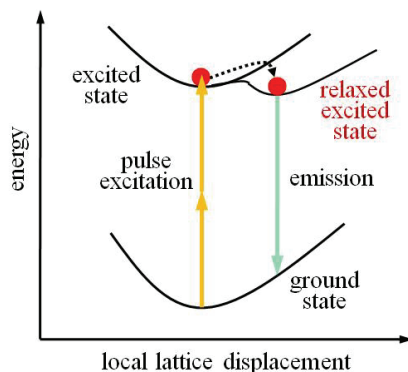


Fig. 11. Schematic diagram of the electronic states in SrTiO<sub>3</sub>.

Figure 12 shows the emission spectra observed under two types of optical excitation; the pulse excitation of 790 nm and the UV illumination of 380 nm. As is seen, the two spectra are almost the same as each other. This result indicates that the same relaxed excited state is generated by the pulse excitation through a multi-photon absorption process. We observed the dynamics of the optically induced lattice distortion in the relaxed excited state generated by ultrashort pump pulses. The transient absorption and birefringence after the optical pulse excitation, which is originated in the generation of the relaxed excited state, is studied by the pump-probe technique to investigate the dynamical properties of the optically induced lattice distortion.

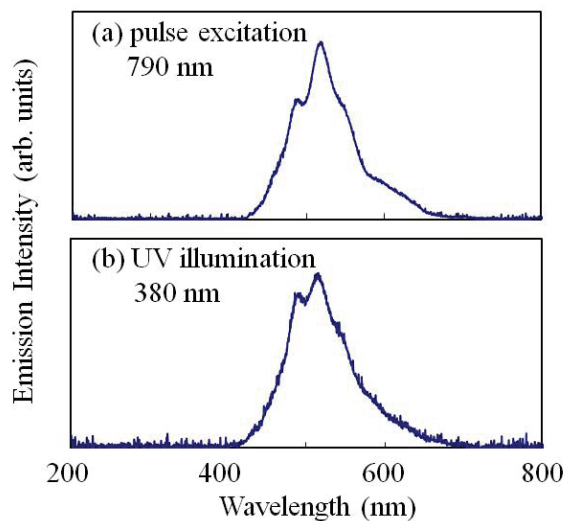


Fig. 12. Emission spectra observed (a) for the pulse excitation of 790 nm and (b) for the UV illumination of 380 nm.

#### 4.1 Pump-probe measurement after the optical pulse excitation

The dynamics of the optically induced lattice distortion was observed by transient absorption and birefringence with the pump-probe technique. The lattice distortion is generated in the relaxed excited state by a linearly polarized pump pulse through a multiphoton absorption process. Induced time-dependent absorption or anisotropy of refractive index after the pulse excitation is detected as the change of the transmission or polarization of a linearly polarized probe pulse. The time evolution of the signal was observed by changing the optical delay between the pump and probe pulse.

The pump pulse is provided by a Ti:sapphire regenerative amplifier whose wavelength, pulse energy, and pulse width at the sample are 790 nm, 2  $\mu\text{J}$ , and 0.2 ps, respectively. In the experiment in the picosecond region, the probe pulse is provided by an optical parametric amplifier whose wavelength, pulse energy, and pulse width are 700 nm, 0.1  $\mu\text{J}$ , and 0.2 ps, respectively. The repetition rate of the pulses is 1 kHz. The time evolution of the signal is observed by changing the optical delay between the pump and probe pulses. The pump pulse is switched on and off shot by shot by using a photoelastic modulator, a quarter-wave plate, and a polarizer, and the output from the polarimeter is lock-in detected to improve the signal-to-noise ratio. In the experiment in the millisecond region, a continuous-wave probe light provided by a laserdiode, whose wavelength is 660 nm, is used. The linearly polarized pump and probe beams are nearly collinear and perpendicular to the (001) surface of the sample, and are focused on the sample in a temperature-controlled refrigerator.

The transmission intensity is detected by a photodiode. The induced anisotropy of refractive index is detected by the polarimeter with a quarter-wave plate as the polarization change of the probe pulse. The plane of polarization of the probe pulse is tilted by  $45^\circ$  from that of the pump pulse. The two different wavelengths for the pump and probe lights and pump-cut filters are used to eliminate the leak of the pump light from the input of the photodiode or polarimeter.

#### 4.2 Transient absorption in the picosecond region

It is found that the transmission is decreased after the optical pulse excitation. The transient absorption signal in SrTiO<sub>3</sub> have the component rising in the picosecond region as shown in Fig. 13. This rise time, which is of the order of 100 ps, corresponds to the generation time of the relaxed excited state.

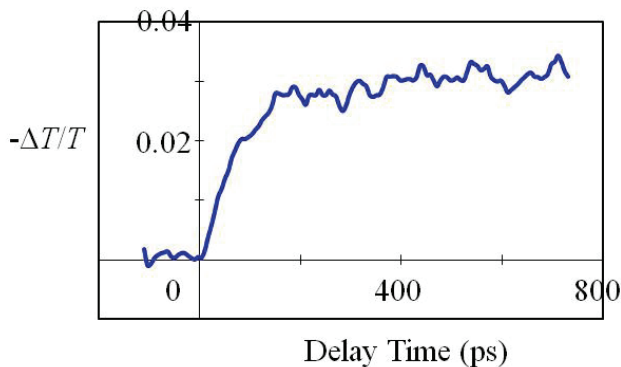


Fig. 13. Transient absorption signal in the picosecond region in SrTiO<sub>3</sub> at 6 K.

### 4.3 Transient absorption in the millisecond region

The temperature dependence of the transient absorption in the millisecond region in SrTiO<sub>3</sub> is shown in Fig. 14. The transient absorption signals have the decay time in the millisecond region. As the temperature is decreased, the signal amplitude is increased. The averaged occupation probability in the relaxed excited state strongly depends on the temperature and is large at low temperatures, where the photo-induced giant dielectricity is observed.

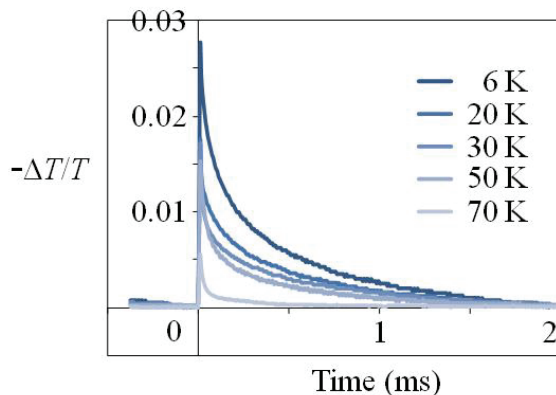


Fig. 14. Temperature dependence of the transient absorption in the millisecond region in SrTiO<sub>3</sub>.

### 4.4 Transient birefringence in the millisecond region

The time evolution of the lattice distortion is observed by transient birefringence measurement with the pump-probe technique. The temperature dependence of the transient birefringence in the millisecond region in SrTiO<sub>3</sub> is shown in Fig. 15. The observed signal curves of the transient birefringence and their temperature dependence show similar behavior to those of the transient absorption.

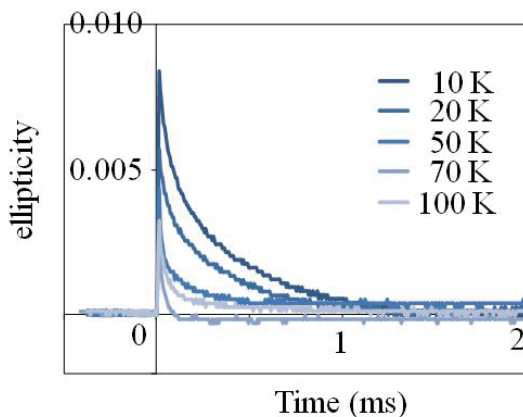


Fig. 15. Temperature dependence of the transient birefringence in the millisecond region in SrTiO<sub>3</sub>.

The photo-induced conductivity in SrTiO<sub>3</sub>, where the resistivity drops rapidly at low temperatures, has also been reported (Katsu et al., 2000). The photo-induced lattice distortion, absorption, and conductivity can be interpreted to have the same origin in the relaxed excited state. The experimental results suggest that the photo-induced effect in SrTiO<sub>3</sub> is consistent with the conductive-region model.

Giant dielectric response in nonferroelectric materials has been reported for grains surrounded by the insulating grain boundary and is explained by the Maxwell-Wagner model, namely the conductive-region model (Homes et al., 2001; Wu et al., 2002; Dwivedi et al., 2010). SrTiO<sub>3</sub> crystal is a stoichiometric material and has no grain structure. It may have a superposition of insulative and conductive regions under the UV illumination at low temperatures, whose structure may be related to the quantum paraelectricity under the dark illumination. However, the detail of the microscopic structure is unknown at present.

## 5. Conclusion

We observed the temperature dependences of the stationary birefringence, the transient birefringence in the pulsed electric field, and the transient absorption and birefringence after the optical pulse excitation to investigate the photo-induced effect in pure and Ca-doped SrTiO<sub>3</sub>.

The first-order-like structural deformation is found in the UV intensity dependence in Ca-doped SrTiO<sub>3</sub>, which begins at a very weak UV intensity of 10<sup>-3</sup> mW/mm<sup>2</sup>. The generated lattice distortion is along the [100] axis as in the case of pure SrTiO<sub>3</sub>. The shift of the ferroelectric phase transition temperature toward the lower temperature side is observed under the UV illumination.

From the temperature dependence of the change in birefringence in Ca-doped SrTiO<sub>3</sub> in the four types of fields, where a UV light field is on or off and a DC electric field is on or off, it is found that a structural deformation is generated along the [100] axis under the UV illumination and its magnitude is of the same order as that of the ferroelectric deformation along the [110] axis.

It is found that the photo-induced lattice distortion is not affected by the electric field. The photo-induced lattice distortion, absorption, and conductivity are generated in the relaxed excited state, whose lifetime is in the millisecond region. These facts suggest that the photo-induced giant electric field in SrTiO<sub>3</sub> is consistent with the conductive-region model rather than the ferroelectric cluster model.

SrTiO<sub>3</sub> is a very peculiar material in which the dielectricity of the Maxwell-Wagner type appears in a stoichiometric material only under UV illumination at low temperatures. The origin of the enormous dielectric constants under UV illumination is considered to be different from that under dark illumination, although the latter is still not made clear.

## 6. Acknowledgement

We would like to thank Dr. Y. Yamada and Prof. K. Tanaka for providing us the samples of Ca-doped SrTiO<sub>3</sub>.

## 7. References

Bednorz, J. G. & Muller, K. A. (1984). Sr<sub>1-x</sub>Ca<sub>x</sub>TiO<sub>3</sub>: An XY quantum ferroelectric with transition to randomness, *Phys. Rev. Lett.* Vol. 52, No. 25, (1984), pp. 2289-2292.

- Bianchi, U.; Kleeman, W. & Bednorz, J. G. (1994). Raman scattering of ferroelectric  $\text{Sr}_{1-x}\text{Ca}_x\text{TiO}_3$ ,  $x=0.007$ , *J. Phys. Condens. Matter*, Vol. 6, No. 6, (1994), pp. 1229-1238.
- Dwivedi, G. D.; Tseng, K. F.; Chan, C. L.; Shahi, P.; Lourembam, J.; Chatterjee, B.; Ghosh, A. K.; Yang, H. D. & Chatterjee, S. (2010). Signature of ferroelectricity in magnetically ordered Mo-doped  $\text{CoFe}_2\text{O}_4$ , *Phys. Rev. B*, Vol. 82, No. 13, (2010), 134428 (5 pages).
- Godefroy, G.; Jullien, P. & Cai, L. (1976). Photoconduction in doped  $\text{BaTiO}_3$  single crystals, *Ferroelectrics*, Vol. 13, No. 1, (1976), pp. 309-312.
- Hasegawa, T.; Mouri, S.; Yamada, Y. & Tanaka, K. (2003). Giant photo-induced dielectricity in  $\text{SrTiO}_3$ , *J. Phys. Soc. Jpn.*, Vol. 72, No. 1, (2003), pp. 41-44.
- Hasegawa, T. & Tanaka, K. (2001). Photo-induced polaron states in strontium titanate, *J. Lumin.*, Vol. 94-95, (2001), pp. 15-18.
- Homes, C. C.; Vogt, T.; Shapiro, S. M.; Wakimoto, S. & Ramirez, A. P. (2001). Optical response of high-dielectric-constant perovskite-related oxide, *Science*, Vol. 293, (2001), pp. 673-676.
- Jones, R. V. (1976). Rotary 'aether drag', *Proc. R. Soc. London, Ser. A*, Vol. 349, (1976), pp. 423-439.
- Katayama, I.; Ichikawa, Y. & Tanaka, K. (2003). Critical behaviors of photoinduced giant permittivity in potassium tantalate, *Phys. Rev. B*, Vol. 67, No. 10, (2003), 100102(R) (4 pages).
- Katsu, H.; Tanaka, H. & Kawai, T. (2000). Anomalous Photoconductivity in  $\text{SrTiO}_3$ , *Jpn. J. Appl. Phys.* Vol. 39, (2000), pp. 2657-2658.
- Kohmoto, T.; Fukuda, Y.; Kunitomo, M. & Isoda, K. (2000). Observation of ultrafast spin-lattice relaxation in  $\text{Tm}^{2+}$ -doped  $\text{CaF}_2$  and  $\text{SrF}_2$  crystals by optical means, *Phys. Rev. B*, Vol. 62, No. 1, (2000), pp. 579-583.
- Koyama, Y.; Moriyasu, T.; Okamura, H.; Yamada, Y.; Tanaka, K. & Kohmoto, T. (2010). Doping-induced ferroelectric phase transition in strontium titanate: Observation of the birefringence and the coherent phonons under the ultraviolet illumination, *Phys. Rev. B*, Vol. 81, No. 2, (2010), 024104 (6 pages).
- Muller, K. A. & Burkard, H. (1979).  $\text{SrTiO}_3$ : An intrinsic quantum paraelectric below 4 K, *Phys. Rev. B*, Vol. 19, No. 7, (1979), pp. 3593-3602.
- Nasu, K. (2003). Photogeneration of superparaelectric large polarons in dielectrics with soft anharmonic  $T_{1u}$  phonons, *Phys. Rev. B*, Vol. 67, No. 17 (2003), 174111 (8 pages).
- Okamura, H.; Matsubara, M.; Tanaka, K.; Fukui, K.; Terakami, M.; Nakagawa, H.; Ikemoto, Y. Moriwaki, T.; Kimura, H. & Nanba, T. (2006). Photogenerated carriers in  $\text{SrTiO}_3$  probed by mid-infrared absorption, *J. Phys. Soc. Jpn.*, Vol. 75, No. 2, (2006), 023703 (5 pages).
- Takesada, M.; Yagi, T.; Itoh, M. & Koshihara, S. (2003). A gigantic photoinduced dielectric constant of quantum paraelectric perovskite oxides observed under a weak DC electric field, *J. Phys. Soc. Jpn.*, Vol. 72, No. 1, (2003), pp. 37-40.
- Ueda, S.; Tatsuzaki, I.; & Shindo, Y. (1967). Change in the dielectric constant of  $\text{SbSI}$  caused by illumination, *Phys. Rev. Lett.*, Vol. 18, No. 12, (1967), pp. 453-454.
- Volk, T. R.; Grekov, A. A.; Kosonogov, N. A. & Fridkin, V. M. (1973). Influence of illumination on the domain structure and the Curie temperature of  $\text{BaTiO}_3$ , *Sov. Phys. Solid State*, Vol. 14, No. 11, (1973), pp. 2740-2743.
- Vugmeister, B. E. & Glinchuk, M. P. (1990). Dipole glass and ferroelectricity in random-site electric dipole systems, *Rev. Mod. Phys.*, Vol. 62, (1990), pp. 993-1026.

- Wu, J.; Nan, C. W.; Lin, Y. & Deng, Y. (2002). Giant dielectric permittivity observed in Li and Ti doped NiO, *Phys. Rev. Lett.*, Vol. 89, No. 21, (2002), 217601 (4 pages).
- Yamada, Y. & Tanaka, K. (2008). Mechanism of photoinduced dielectric response in ferroelectric  $\text{Sr}_{1-x}\text{Ca}_x\text{TiO}_3$ , *J. Phys. Soc. Jpn.* Vol. 77, No. 5, (2008), 54704 (10 pages).

# Photoluminescence in Doped PZT Ferroelectric Ceramic System

M. D. Durruthy-Rodríguez<sup>1</sup> and J. M. Yáñez-Limón<sup>2</sup>

<sup>1</sup>*Cybernetic, Mathematics and Physics Institute*

<sup>2</sup>*Centro de Investigación y de Estudios Avanzados del Instituto Politécnico Nacional*

<sup>1</sup>*Cuba*

<sup>2</sup>*Mexico*

## 1. Introduction

The photoluminescence (PL) it is a non thermal origin process, in that a chemical compound absorbs the photons (of the electromagnetic radiation), jumping to an electronic state of more energy, the inverse process happens and so call recombination (when passing to inferior energy level) and the materials radiating photons. The period between absorption and emission occur is in order to 10 nanoseconds. But under special circumstances, this period can extend in minutes or hours. The transition energy is determined by quantum mechanics rules. Different imperfection presents in the materials study will alter the recombination time or frequency.

Simpler PL processes are resonant radiations, in that a photon of a particular longitude wave is absorbed and an equivalent photon is emitted immediately. This process doesn't involve any transition in forbidden energy band and it is extremely quick (10 ns). The most interesting processes happen when the desexcitation energy transition is not direct at the basic level. The most common effect is the fluorescence that is also typically a quick process, but in that the original energy it is dissipated so that the slight photons emitted are of the lower energy that those absorbed. This phenomenon can happen for the isolated atoms, molecules or atoms and molecules in interaction excitement.

### 1.1 Atomic, molecular and atoms and molecules in interaction luminescence

The isolated atom excitement (making notice that a very rarefied gas can be considered as a group of isolated atoms) it drives to a spectrum of lines. The atom only absorb the frequency of the incident ray that corresponds to the allowed transitions (Figure 1). So all the isolated atoms can be luminescent.

That happens for the isolated atoms is also valid for the isolated molecules, but the laws are more complicated due to the vibrations and rotations molecular than they introduce supplementary energy levels as the sample the following diagram of figure 2.

The pressure of a gas it increases and a new transitions of excitement energy appear by collision, for the appearance of kinetic energy and metastable states. The return to the basic state is with a reduction of the yield of the luminescence and an expansion of the spectrum of the transmission. Then appears spectrum of band. The return to the fundamental state it doesn't always happen with light emission (transitions without radiation).

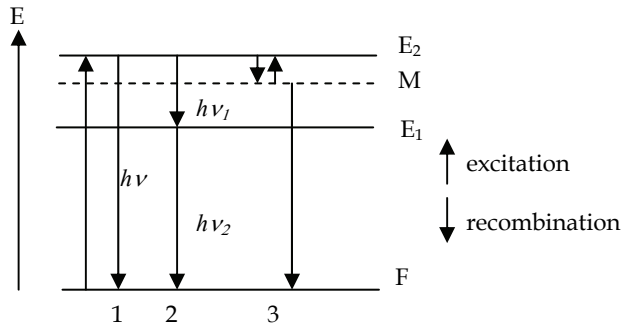


Fig. 1. Three possible luminescence types of an isolated atom:

- 1) direct transition, this is a resonance phenomenon;
- 2) indirect transition, distributing the energy in several photons  $h\nu_1$  and  $h\nu_2$ ,
- 3) indirect transition by a metastable state (M) following by interatomic collision (not very probable).

### 1.2 Crystalline luminescence

The luminescence of the crystalline bodies is due to the transmission centers (the activators). These centers are:

- physical imperfections in crystalline structure (vacancies, interstitial atoms, dislocations), this is intrinsic luminescence.

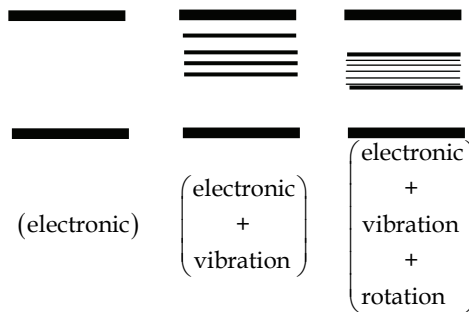


Fig. 2. Energy levels that appear in a molecule.

- chemical imperfections (impurity atoms) in interstitial or substitution position, this is extrinsic luminescence.

The mechanism of crystalline luminescence it is explained with the help of energy bands diagram (Figure 3).

Considering that in the perfect crystal any level doesn't exist in forbidden band, the presence of imperfection in the crystal introduces some levels allowed in the forbidden or in the allowed bands. These energy levels they can be:

- recombinations levels ( $h/e^-$ )
- metastable levels: the traps of  $e^-$  (Pe) or  $h^+$  (Pt)
- fundamental (F) and excited levels (E) of isolated centers

The spectra of crystalline luminescence differ notably of the atomic spectra for two fundamental aspects. 1): bands are observed and 2) the emitted radiation appears toward the longitude of big waves, this can made a mistake with the absorbed radiation. These two aspects are due to the interaction between the emission center and the crystalline lattice.

According to the type of imperfections there are the transitions way and therefore the energy of the transition.

A first transition consists on an electron that leaves a donor level and go toward the valency band. The energy of this transition is given for:  $E = E_{gap} - E_D$

Also, can be observed where an electron leaves to the conduction band to pass at acceptor level. In this case, the energy of the transition is given for:  $E = E_{gap} - E_A$

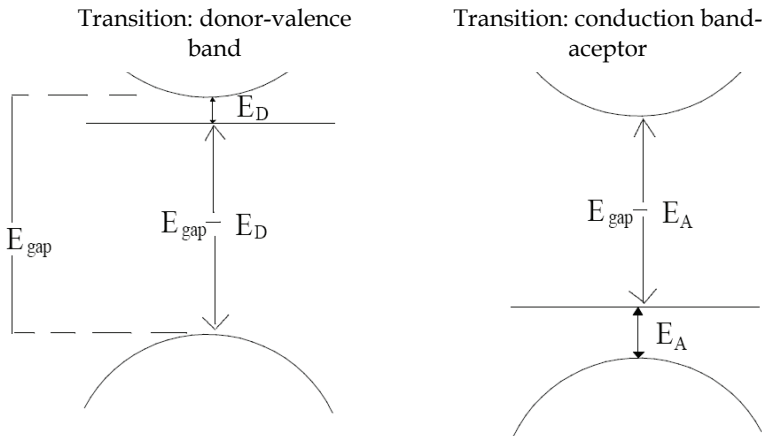


Fig. 3. Types of transitions among bands.

It is known that the energy  $E_D$  and  $E_A$  differ according to the chemical nature of the impurity. For this reason is allows to use the photoluminescence experiments to confirm the presence of a specific type of impurity in a material.

In many cases, the theory of the effective mass is a first valid approach, it predicts the value of the energy  $E_D$  and  $E_A$  for a given semiconductor.

$$E_D = \frac{13.6eV}{\epsilon^2} \frac{m_e^*}{m_0} \quad \text{and} \quad E_A = \frac{13.6eV}{\epsilon^2} \frac{m_h^*}{m_0} \quad (1)$$

In general  $m_h^* \gg m_e^*$ , it is explained, why the bond energy of acceptor levels is bigger than that donors levels.

Broad bands are observed for many optical transitions in the partly filled d-shell of transition metal ions (d - d transitions), but also for transitions between the 5d shell and the 4f shell of rare-earth ions (d - f transitions) and for emission on  $s^2$  ions (these ions possess a "lone pair" of s electrons), like  $Tl^+$ ,  $Pb^{2+}$ , or  $Sb^{3+}$ . Sharp emission bands are characteristic of optical transitions between electronic states with chemical bonding character (almost) the same for ground and excited state, and for the same reason also of optical transitions between electronic states that hardly participate in the chemical bonding (e.g., f - f transitions on rare-earth ions).

In the case of optical processes involving electronic states which participate in the chemical bonding, the nature of the bonding (covalent, ionic) and the symmetry of the site at which the emitting ion is incorporated play a very important role. This is generally described by the ligand field theory, which we do not treat here.

The emission generated reflects how the optical properties of the ion depend on its chemical environment. This luminescent material can be applied as green phosphor in very high-quality fluorescent lamps and also in plasma display (Ronda, 2008).

## 2. Luminescence in PZT

The width of luminescent band usually observed at room temperatures in crystals of perovskite type it is associated with the presence of imperfections or defects (Haertling, 1999; Anicete-Santosaet al., 2007), be already oxygen or lead vacancies. But other author explain apparition of PL to order-disorder presence in the structure (Chen et al., 1989; Suárez-Gómez et al., 2009; Shannigrahi, 2007) distortion of oxygen octahedral fundamentally.

Undoped PZT ceramics are seldom used. They are usually substituted in the A or B-sites of the perovskite structure  $ABO_3$  in order to improve dielectric, piezoelectric and mechanical properties. For example  $La^{3+}$  and  $Nb^{5+}$  are used satisfactorily (Durruthy et al., 1999, 2002; Bharadwaja et al., 2002). The excess of positive charge in (La/Nb) doped PZT is compensated by lead vacancies and the typical Kröger-Vink notation to describe the electroneutrality, have been reported in many papers previously (Eyraud et al, 2006; Jaffe et al., 1954).

The defects caused by the small dopant concentrations in A or B places of the structure could generate a combination of blue, green and red emission of light which is of great importance for optical devices applied in optoelectronics includes flat-screen, full-colour displays and compact laser devices operating in the blue region (Nakajima et al., 2004; Yang et al., 2008).

Recently M.S. Silva et. al., 2005, reported a theoretical and experimental result, and presents an alternative method to process PL in PZT and aim to explain why this phenomenon depends on the crystalline structure of the material. The wide bands at 2.1 and 2.67 eV respectively in PL emission in perovskite ceramics are associated to the oxygen vacancies provoked during the sintering process (Lines & Glass, 2001) or related to ensure electroneutrality process.

What happens with luminescence effect with A, B or A+B doped PZT?

We will try to respond this question with several examples.

All samples that show were prepared by a conventional processing method using mixed oxide powders. The photoluminescence (PL) spectra were obtained using a Jobin Yvon Horiba Fluoromax-3 spectrometer using the excitation band at 373 nm. The absorption spectra were acquired with an UV-vis Ocean Optics Spectrometer QE650000 using diffuse reflectance measurements the data was processed by using the Kubelka-Munk function:

$$F(R'_\infty) = \frac{(1 - R'_\infty)^2}{2R'_\infty} = \frac{a}{S} \quad (2)$$

$$R'_\infty = \frac{R_\infty(\text{sample})}{R_\infty(\text{standard})} \quad (3)$$

$R_{\infty} = (I/I_0)$  is diffuse reflectance at one wavelength from an opaque sample with infinite thickness ( $> 2 \mu\text{m}$ ),  $0 < R_{\infty} < 1$ ,  $\alpha$  is the absorbance in  $\text{cm}^{-1}$  and  $S$  is the scattering factor which is assumed to be independent of the wavelength for grain sizes greater than the wavelength of the light (Wendlandt & Hecht, 1966; Kottim, 1969).

Crystalline structure (Figure 4), like we will see later, influences in the shift energy of PL in the samples. For this reason it is advisable to carry out this study previously to PL analysis. All samples first were identify by X-ray diffraction (XRD). The XRD patterns of the polycrystalline samples show the tetragonal ( $\text{Zr}/\text{Ti} = 20/80, 40/60$ ) and rhombohedral ( $\text{Zr}/\text{Ti} = 60/40, 80/20$ ) PZT phases, and both phase together for  $\text{Zr}/\text{Ti} = 53/47$ . This is a classical behavior for this material and has been reported by some authors (Jaffe et al., 1971; Noheda, 2000, 2001).

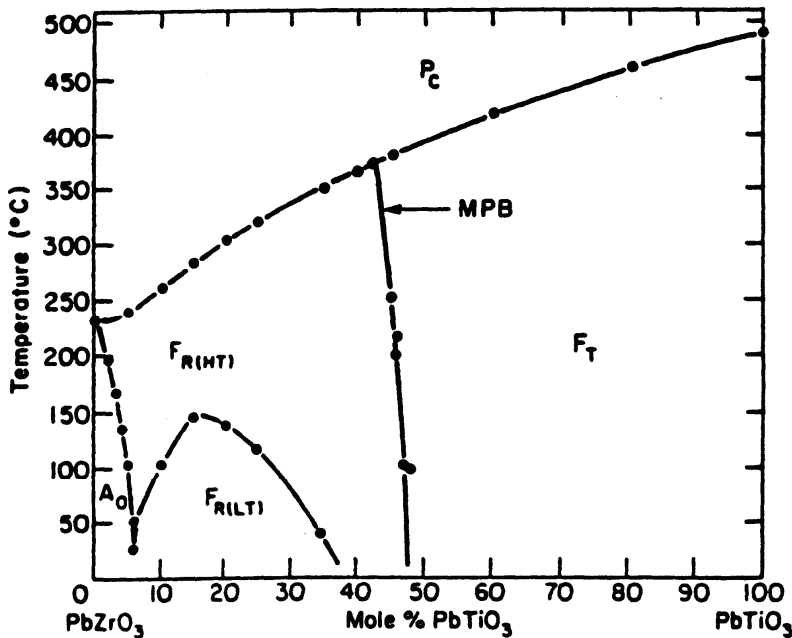


Fig. 4. Phases diagram of PZT, appear the existence range of each phase (tetragonal and rhombohedral), the morfotrópica phase boundary (MPB) according to Jaffe et al. (1971).

In our samples doped the compensation of charge provokes in all cases oxygen vacancies that should increase with the dopant concentration or saturates in a composition that denotes a limit of solubility. However, oxygen vacancies are easily induced during the sintering process because the PbO has low volatile temperature of about  $880^\circ\text{C}$ . This phenomenon takes place in all samples and also promotes lead and oxygen vacancies, which are quenched defects at low temperatures. Lead vacancies can only become mobile at high temperatures with high activation energy greater than oxygen mechanism values.

According to Eyraud *et al.* (2006) singly and doubly ionized lead and oxygen vacancies coexist in the PZT ceramic, then they may constitute donor and acceptor sites which are able to exchange electrons according to the following reactions:

$$\begin{aligned}
 V_{Pb} &\rightarrow V'_{Pb} + e \\
 V'_{Pb} &\rightarrow V''_{Pb} + e \\
 V_O &\rightarrow V^*_O + e \\
 V^*_O &\rightarrow V^{**}_O + e
 \end{aligned}
 \tag{4}$$

in our case at least three types of defects coexist  $V'_{Pb}$ ,  $V''_{Pb}$  and  $V^*_O$ , whose contribution to PL depends on the levels in the band gap.

The results of first-principle calculation reported by Ghasemifard et al., (2009) show that the PZT polycrystalline has a direct band gap between the X and  $\Gamma$  points of 3.03 eV (Baedi et al., 2008), then by assuming a direct band gap we can calculate the values of the energy gap (Eg) for all the samples. In general calculating the absorption coefficients of the synthesized powder in the strong absorption region needs both, the transmission and reflection spectra. In our case, we obtained the absorption spectra by diffuse reflectance measurements, and by using the Kubelka-Munk equation for all samples the band gap energy Eg was determined.

### 2.1 Substitution in A site

The substitution for  $La^{3+}$  in the A site of perovskite structure it's traditional. It is one of the classic sustituyentes in this system.

The emission spectra (PL) at 273, 325, 373, 413 and 457 nm were characterized to present different bands for PLZT 1-x/x/y (Figure 5), prevailing blue-violet band presence (2.4-2.75 eV), it's appears at bigger intensity for 413 nm. This evidences that PL effect has the same origin in all cases.

As it has been expressed previously, the energy of the spectra of PL demonstrates the presence of levels in the forbidden band. The calculations of first principles (Longo et al., 2005) have been demonstrated that disorder in provskite structure and the defects in the same one, they cause states in the forbidden band. On the other hand the experimental evidence of the presence of defects exists (oxygen vacancies) (Mansimenko et al., 1998) starting from mensurations of resonance electronic paramagnética (RPE) in the system PLZT.

If we consider to our materials as semiconductors of big gap, the presence of states in the forbidden band, what causes a contraction of the gap, is the causing of a well-known Burstein-Moss shift of emission spectrum (Yu & Cardona, 1996). It can associate to presence of picks around 2.65 eV to the presence of bands inside of forbidden band in the material, being more intensity when it's excited with  $\lambda = 413$  nm.

Analyzing the results associating them with the colors corresponding of the wave longitudes, we see that emissions exist (although of different intensity) in almost the whole visible spectrum, from the red one until the ultra violet, but the bands of very high intensity correspond to the bands of the blue-violet and ultraviolet.

The motive that causes this effect are similar when you doped these materials in B site, this will be explained in the next section.

### 2.2 Substitution in B site

In perovskita structure ( $ABO_3$ )  $N^{5+}$  substitute B site, occupied by  $Zr^{4+}$  and  $Ti^{4+}$  ion. The high volatility of lead oxide at elevated temperatures during the powder calcinations and the

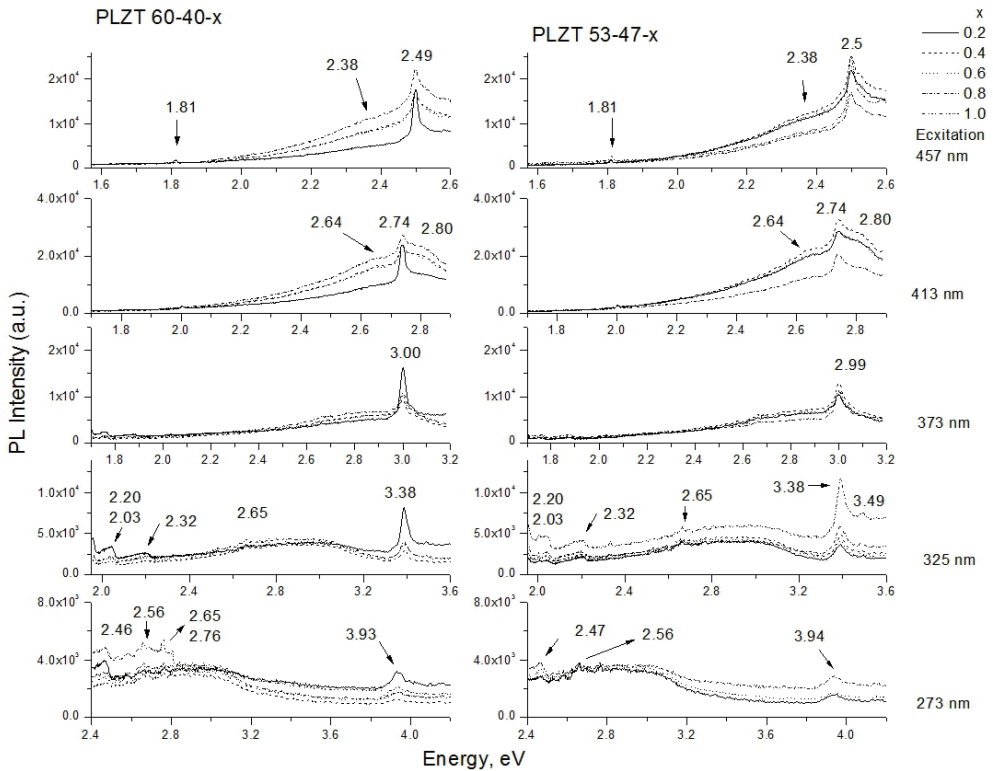


Fig. 5. PL spectra at room temperature, fixing the excitation band at 273, 325, 373, 413 and 457 nm in PLZT ferroelectric ceramics. Appear result for two point of PZT phase diagram doped at different  $La^{3+}$  concentration.

sintering stages in the PZT system is known, which provides both fully-ionized cationic lead  $V_{Pb}^{''}$  vacancies and anionic oxygen vacancies  $V_O^{''}$ . On the other hand, following Eyraud’s model (Sivasubramanian et al., 2007; Chang et al., 2001) the valence of the Niobium is assumed as donor doping in the PZT has a strong influence in the ionization state of extrinsic lead and oxygen vacancies.

Figure 6 shows the PL spectra of PZTN samples for compositions 80/20, 60/40, 53/47, 40/60 and 20/80 which have diverse dopant concentrations. The emission bands (PL response) when fixing the excitation bands (EB) at 373, 457 and 325 nm were observed in three regions: one is at around 1.72 eV (lowest energy region); the second is at around 2.56 – 2.61 eV which shows a higher intensity, and the third is at around 3.35 – 3.45 eV (highest energy region) respectively. The band at 2.56 eV is the most intense and narrow, and the band at 3.35 eV shows greater broadening. The band at 1.72 eV did not show any notable shift in the maximum position peaks for different compositions or dopant concentrations. Nevertheless, the bands at 2.56 and 3.35 eV show a shift in the maximum peak position which depending if the phase is rhombohedral or tetragonal will shift to 2.61 and 3.45 eV, respectively.

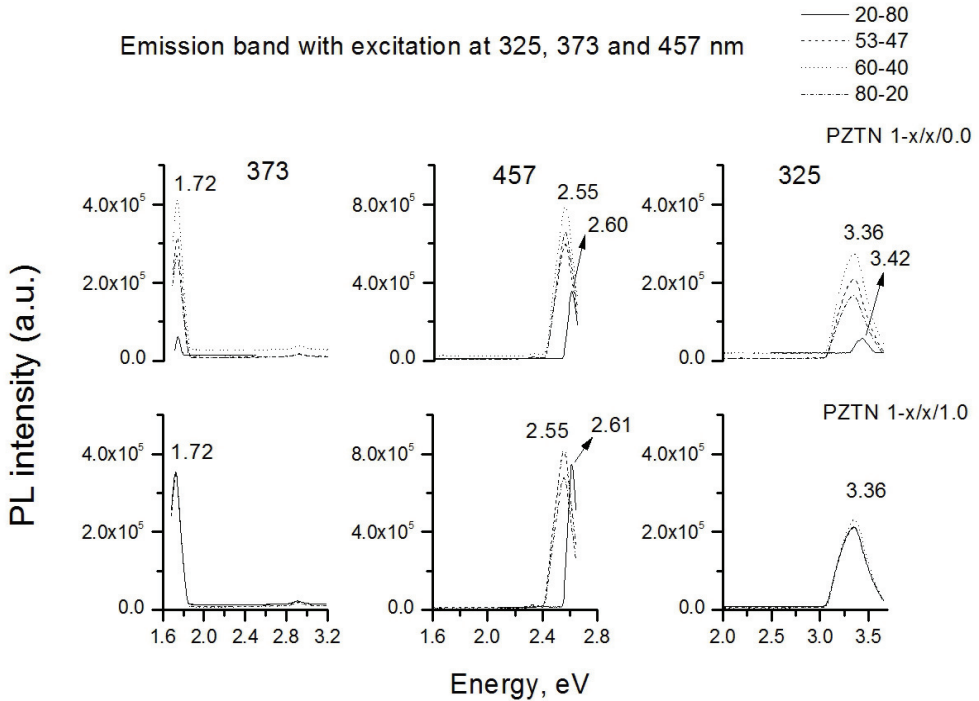


Fig. 6. Room temperature PL for PZTN note the dispersion for non doped materials. For PLZT  $1-x/x/1.0$  practically all the curves coincide for the same energy 1.72 and 3.36 for  $\lambda=373$  and 325 respectively.

Note that in the PZT polycrystalline samples without Nb, the three well resolved emission bands were also shown, in contrast with other reports (Longo et al., 2008; Chang et al., 2001) where the emission for polycrystalline PZT is very low and broad or absent. For these materials (PZTN) the emission is bigger in 1 or 2 order than PLZT. The PLE spectra for samples doped and without doped they present same character, appearing the same line, for what they have the same origin in both cases (Figure 7).

The  $E_g$  (in PZTN) values for tetragonal samples 20/80 and 40/60 are between 2.80 to 2.98 eV, the composition 53/47 are near the morphotropic phase boundary which shows a higher variation in  $E_g$  values as a function of the dopant concentration from 2.70 to 3.19 eV. For this composition and rhombohedral phases 60/40 and 80/20 the behavior of  $E_g$  values as a function of Nb concentration shows a minimum at 0.8% with values of approximately 2.67 to 2.70 eV. In our case, experimentally it is observed a transition ( $E_{PL}$ ) at 2.56 eV for samples PZTN 80/20/0.0.

Sintering stages in the PZT system is known, which provides both fully-ionized cationic lead  $V_{Pb}^+$  vacancies and anionic oxygen vacancies  $V_O^{\bullet\bullet}$ . On the other hand, following Eyraud's model (Sivasubramanian et al., 2007; Chang et al., 2001) the valence of the Niobium is assumed as donor doping in the PZT has a strong influence in the ionization state of extrinsic lead and oxygen vacancies.

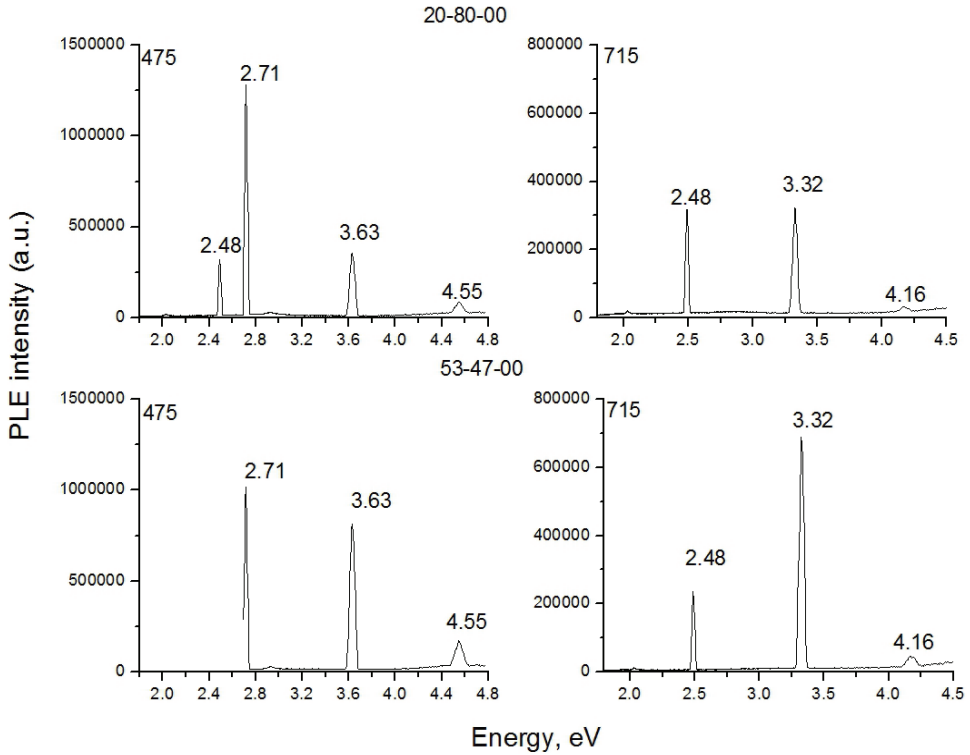


Fig. 7. Room temperature excitation spectra PLE for PZTN for an emission at 475 and 715 nm respectively.

The  $E_D$  values reported in Table 2 were calculated using  $E_g$  and  $E_{PL}$  obtained by excitation at  $E_B=457$  nm. Even the origins of these luminescence bands are not clearly understood. Figure 8 shows a schematic diagram to represent the recombination process for the three emission bands. The PL at a high energy region of approximately 3.35-3.45 eV, that overcomes the  $E_g$ , which is obtained when the excitation is at 3.81 eV.

% Nb	$E_{gap} (Zr/Ti)$									
	20/80		40/60		53/47		60/40		80/20	
	$E_g$	$E_D$	$E_g$	$E_D$	$E_g$	$E_D$	$E_g$	$E_D$	$E_g$	$E_D$
0.0	2.80	0.19	2.92	0.31	3.19	0.63	3.04	0.48	3.09	0.53
0.2	2.84	0.23	2.86	0.25	2.93	0.37	3.04	0.48	3.04	0.48
0.4	2.84	0.23	2.84	0.23	2.90	0.34	2.92	0.36	2.96	0.40
0.6	2.82	0.21	2.86	0.25	2.85	0.29	2.85	0.29	2.85	0.29
0.8	2.87	0.26	2.80	0.19	2.70	0.14	2.67	0.11	2.67	0.11
1.0	2.90	0.29	2.98	0.37	3.00	0.44	2.95	0.39	2.94	0.38

Table 1. Band gap energy ( $E_g$ ) for PZTN, determined using the diffuse reflectance principle (Kubelka-Munk expression). Error  $E_g = \pm 0.003$  eV.  $E_D$  values obtained with the  $E_g$  and more intense emission band at around 2.56 eV.

This corresponds to transitions between higher energy states in the conduction band to the valence band (hot luminescence), and the emission intensity shows a strong dependence on the Nb concentration.

The PL at 1.73 eV, the lowest energy region which is obtained with excitation energy of 3.32 eV, it could be follows a recombination mechanism:

1. from the localized states due to oxygen vacancies below the conduction band ( $V_O^{\bullet}$ ) to the localized states above the valence band due to lead vacancies ( $V_{Pb}'$ ) and/or
2. by recombination from band conduction to the localized states above the valence band due to lead vacancies ( $V_{Pb}''$ ).

The intensity emission of this band also shows a strong dependence on Nb concentration, and is present in all compositions indicating common defect types related to a deep level inside the band gap. In general, the incorporation of  $Nb^{5+}$  increases the PL intensity in this region due to the compensation of charge and induced defects ( $V_{Pb}'$  and  $V_{Pb}''$ ), as it was already seen previously.

In this case the simultaneous disorder of lead and oxygen vacancies should be created during the sintering process. The PL at 2.56 eV, which shows the highest intensity in all PZTN compositions and is associated to a transition between a shallow defect in the band gap and the valence band, see Figure 8. These levels are associated to oxygen vacancies, with simple or double ionization which is in accordance with the classification of Longo et al., (2008), vacancies bonded to clusters of  $TiO_5$  in disordered regions. In principle, the incorporation of  $Nb^{5+}$  in PZT samples would be producing more lead vacancies than oxygen vacancies. However, the higher intensities observed for peaks at 2.56 eV rather than peaks at around 1.73 eV is an indication that the oxygen vacancy concentration is higher than lead vacancies.

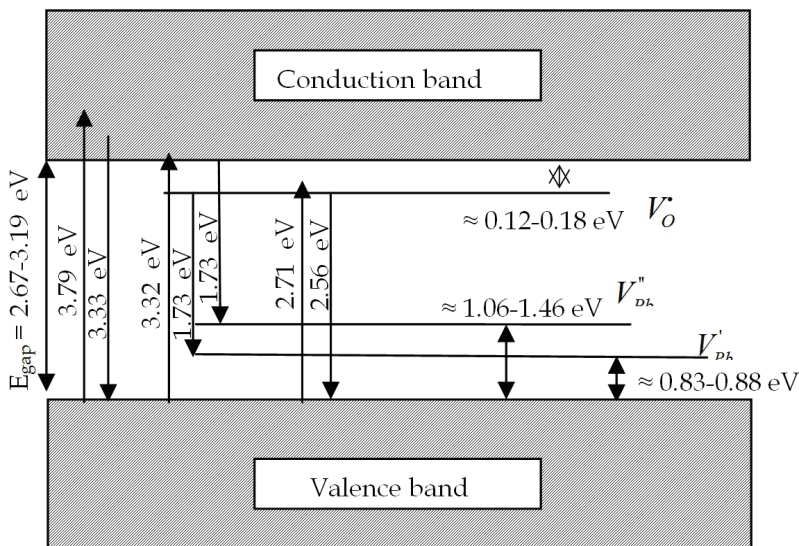


Fig. 8. Schematic diagram of recombination process associated with the emission bands in PZTN ceramics, for excitation energy 3.79, 3.31 and 2.71 eV.

### 2.3 Substitution in A + B site

We will present results of double substitution in place A and B for "hard" and "soft" well-known ceramic. For "hard" ceramics present  $\text{Sr}^{2+} + \text{Cr}^{3+}$  doped PZT ceramics and for "soft" ceramics present  $\text{La}^{3+} + \text{Nb}^{5+}$  doped PZT ceramic.

We will only present the behavior in the PZT morphotropic phase boundary region of phase diagram ( $\text{Zr}/\text{Ti}=53/47$ ).

In both type of samples (hard and soft) only appear two regions of emission bands, one at around 1.86 eV and other with higher intensity at around 3.00 eV when fixing the excitation band at 373 nm (3.4 eV) (Figure 9). Also, it is possible to observe emission band around 2.5-2.7, to a lot of smaller intensity. When fixing the excitation band at 412 nm (3.01 eV) only appear one signal wide at 3.28-3.31 eV (Figure 10).

PL show in the high energy region, the maximum position is around 3.00 eV for all composition, but the emission band is a broad band composed by two bands, at 2.98eV (414nm) and 3.03eV (408 nm) (Figure 9). PL lower energy region for PSZTC and PLZTN samples show the band at 1.87 eV (659 nm), additionally is observed that band at 1.74 eV is not present in all compositions and its intensity is reduced appreciably with the incorporation of Cr (Durruthy et al, 2010a, , 2011).

The general effect of the Cr doping is a decrement the PL intensity in both region bands with the increase of dopant. It is noted that the PL of doped  $\text{La}^{3+}$  and  $\text{Nb}^{5+}$  is larger than of undoped samples and increased with the composition of both ions at least one order of magnitude for PSZTC, but is two and three order to PZTN and PLZT respectively.

It was of waiting that doped  $\text{La}^{3+}$  and  $\text{Nb}^{5+}$  increase PL intensity in 1.87 eV (659 nm) in PL, it is well known that is associated with lead vacancies, due to the compensation of charge, in this case the disorder or lead vacancy should be associated to the substitution of  $\text{La}^{3+}$  by  $\text{Pb}^{2+}$  in the host structure and the typical presence of lead vacancy due to the sintering route (Calderón-Piñar et al, 2007; Silva et al., 2005). The presence of the peak at 1.87 eV, in PSZTC 0.2-0.5 mol % and PLZTN 1 mol% indicates a common defect related with a deep level inside the band gap. As we saw in the region of high energy (3.00 eV) results are similar to showed above previously.

The peaks that appear in zone (2.65) was associated with oxygen vacancies, simple or double ionized. In the sample PLZTN evidently that  $E_D$  will be  $\geq 0.54$  eV, and  $E_{PL}$  is lower 2.43-2.74. This is because  $E_D$  is not exactly one unique value because there are a distribution defects in the structure.

The analysis of the peak at 1.86 eV could be associated to the simultaneous presence of oxygen and lead vacancies (Guiffard et al, 2005; Durruthy et al, 2010a, b, 2011). The PL response in the donor-acceptor mechanism in this case between the levels associated to the oxygen near and below conduction band and the level of lead vacancies above the valence band. Analogously the theoretical quantum mechanical calculation reported by de Lazaro et al. (2007) justify that the presence of disorder associated to the substitution of Zr/Ti or displacement of the ions in the B sites produce an amorphous zone in the ceramic with a direct band gap with a separation near to 1.87eV. Beside this, we are detecting some small peaks whose energy is around of 2.00-2.80 eV which belong to the visible energy spectra too (Figure 9).

The calculated results of the band gap values for the PSZTC samples sintered at 1250 °C are summarized in Table 2. The figure 11 allows us to affirm that the dependence with Zr/Ti ratio is very strong, and has a maximum in the morphotropic phase boundary and the lowest values are for the composition 80/20, this behavior coincides with the calculations

carried out by J. Baedi et al. (2008). Figure 12 shows the way that would be materialize recombination in the PSZTC and PLZTN samples. We supposed that the main way was 1, 5 and 6 for the experimental results obtained, in this work.

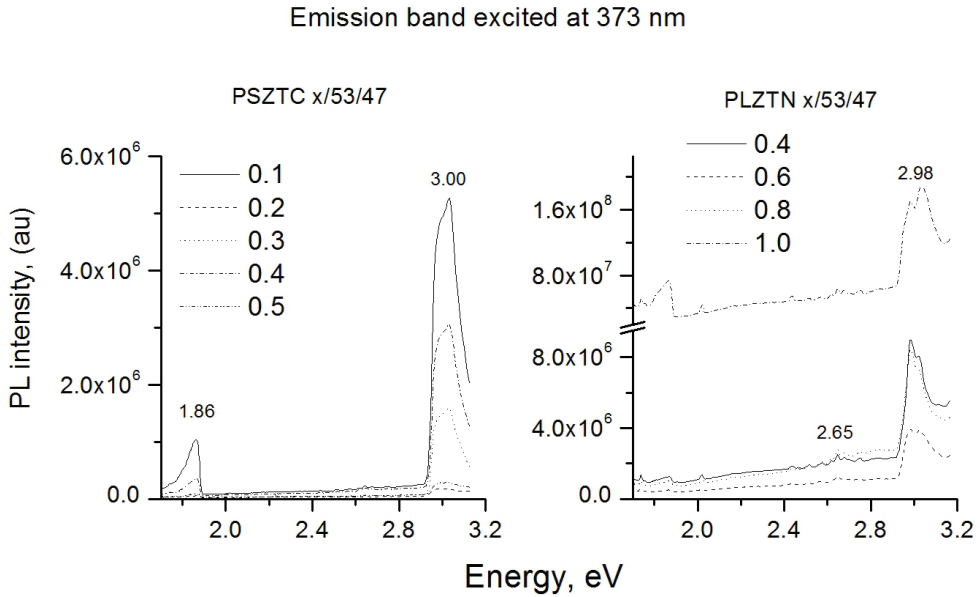


Fig. 9. Room temperature PL emission spectra for PSZTC and PLZTN ceramics at different dopant concentration, fixing excited band at 373 nm.

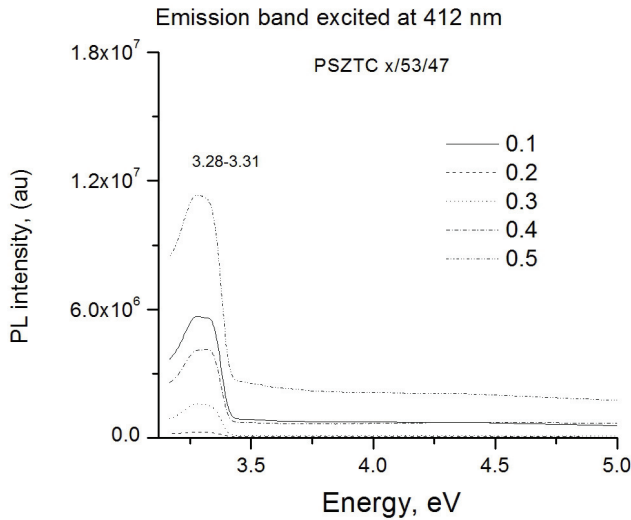


Fig. 10. PL emission spectra at room temperature for PSZTC fixing exciting at 412 nm.

PSZTC		PLZTN	
mole %	$E_{gap}$	mole %	$E_{gap}$
0.0	3.25	0.0	3.15
0.1	3.33	0.2	-
0.2	3.35	0.4	2.88
0.3	3.36	0.6	2.91
0.4	3.36	0.8	3.07
0.5	3.32	1.0	2.50

Table 2. Band gap energy ( $E_g$ ) for PZT soft and hard, determined using the diffuse reflectance principle (Kubelka-Munk expression). Error  $E_g = \pm 0.003$  eV. For  $E_{PL}$  supposed  $E_D = 0.54$ .

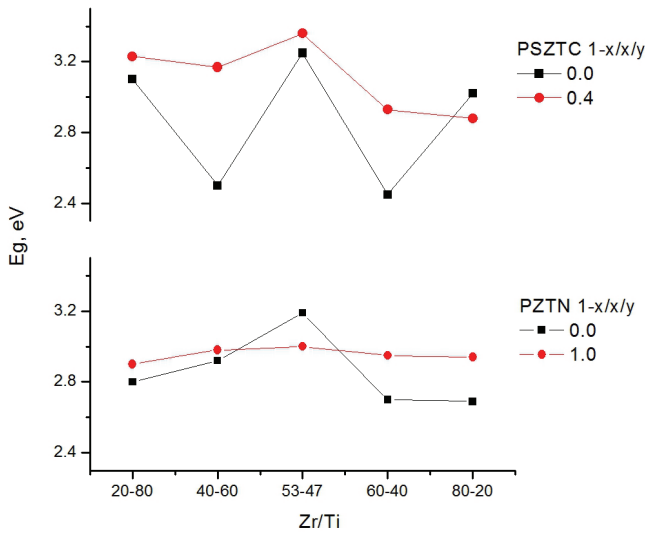


Fig. 11. Behavior of the forbidden band energy for PSZTC and PLZTN ceramics, which agrees with the results obtained for J. Baedi et al. (2008)

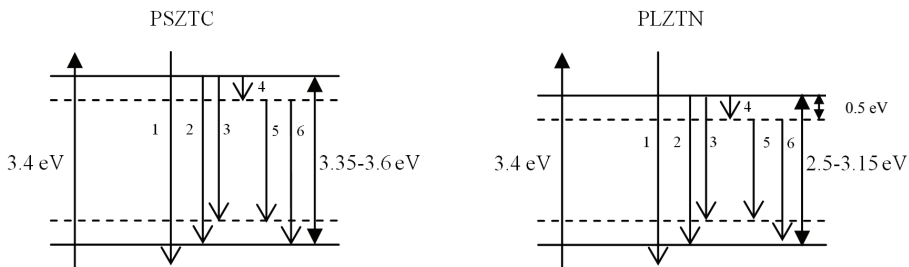


Fig. 12. Possible energetic process that will be happen in PZT ceramics. 3.4 eV is excitation energy (373 nm), 1-6 there are the possible recombination way (PL). We consider that occurred the way 1, 5 and 6 mainly.

### 3. Dielectric characteristic

Another characteristics of these materials that they are very affected by the presence of oxygen vacancies there are dielectric ( $\epsilon$ ) and loss ( $\tan \delta$ ), for this we present some results in different substitution type in  $ABO_3$  perovskite structure.

The dielectric curves reveal anomalies in the neighbor at transition temperatures corresponding to  $F_{R(HT)} - P_C (T_C)$  and  $F_T - P_C (T_{F-P})$  phase transitions. Strong influence of dopant La, Nb and La+Nb on the phase transition temperature ( $T_C$ ) is confirmed. The comparison of  $\epsilon(T)$  curves, obtained for the ceramic samples is shown in Figure 13, dielectric measurement shows a decreasing  $T_C$  and  $T_{F-P}$  when increasing the dopant concentration. The dielectric permittivity decreases for dopant concentration larger than 0.8 mol% (Figure 13), in particularity in Nb-doped ceramics permittivity decreases for concentrations up to about 0.8 mol %, and then it increases slightly, as the grain size behaves. The same as in PL, the permittivity is more intense for substitutions in B and A+B, in this case it is 4 times.

There is good agreement between the transition temperatures obtained from  $\epsilon$  and  $\text{tg}\delta$ , respectively, considering the range of measurement error ( $\delta t \sim 5^\circ\text{C}$ ), for almost every sample. Those compositions with 0.6 and 1.0 % La have  $T_{\text{tg}\delta_{\text{max}}}$  at 50 kHz differing 7.3-8.2  $^\circ\text{C}$  from the value obtained at 1 kHz. A possible cause of such differs is the presence of inhomogeneities as a result of compositional fluctuations (Gupta & Viehland, 1998; Garcia et al., 2001).

In those samples doped with La+Nb, there is not a sum of the separate effects of La and Nb. Note that temperatures are not as low as those for Nb, but compared to those for La they are 50  $^\circ\text{C}$  below.

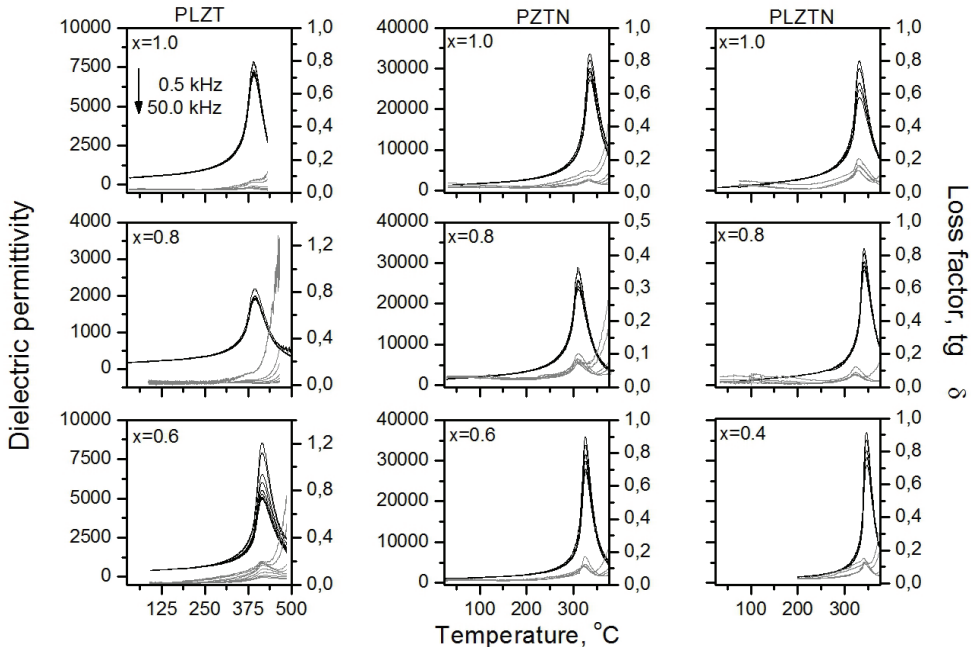


Fig. 13. Permittivity as a function of temperature, measured at various frequencies, for PZT 53/47 ceramics showing  $\text{La}_2\text{O}_3$ ,  $\text{Nb}_2\text{O}_5$ , and  $\text{Nb}_2\text{O}_5+\text{La}_2\text{O}_3$  content.

Grain size decrement implies domain size decrement (Figure 14). Thus, the domain walls become more movable, so the mechanical friction is small, and then the samples doped with Nb and La+Nb are more compositionally homogenous (the evidence is given by narrow plots of dielectric permittivity vs. temperature, that is, increasing permittivity). On the other hand, grain size increment contributes to higher values of the dielectric constant, as a measurement of the number of polarized unitary cells. The amount of polarization of such cells is related to the presence of  $\text{Nb}^{5+}$  and  $\text{La}^{3+}$  inside the crystalline structure and contributes to the orientation of the domain walls. An increasing dopant concentration produces the increment of the number of lead vacancies and so the dielectric permittivity grows. The values of  $\epsilon$  for PZTN samples are higher and attributed to the higher compositional homogeneity and the existence of only one phase in this composition. But is not the same for PLZTN and PLZT, XRD patterns of samples show the tetragonal and rhombohedral PZT phases together. (Figure 15) in all doped samples, with concentration near to MPB (53/47).

Decrements of  $T_c$  might be attributed to the integration of dopants into the crystalline structure.

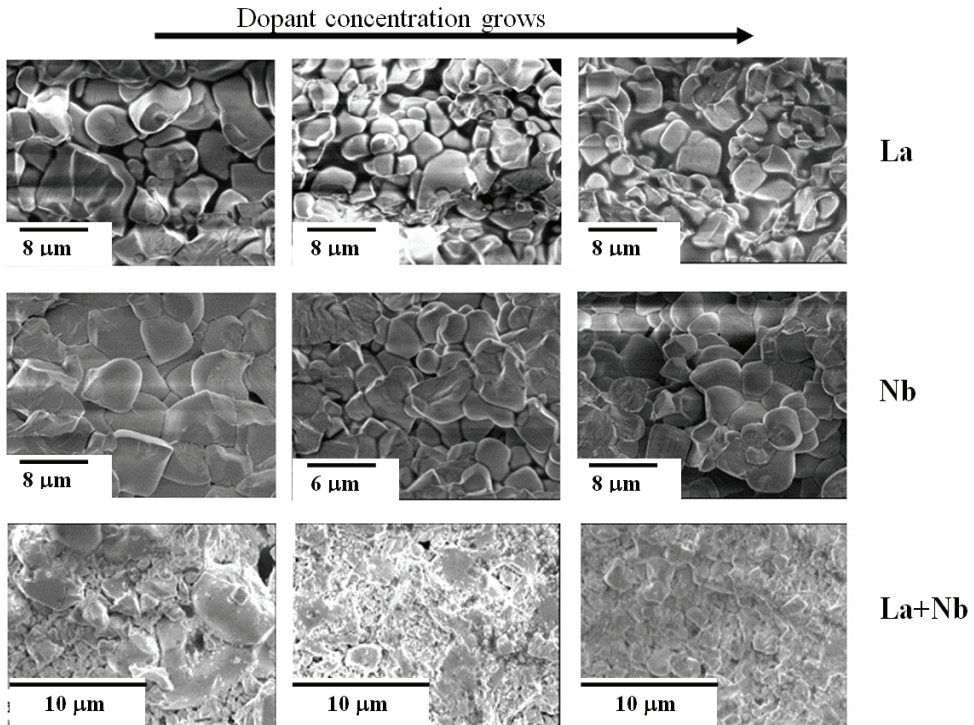


Fig. 14. SEM results for 0.6, 0.8 and 1.0 mol % dopant in study for samples near to MPB. In every case, the decrement of grain size as the dopant concentration increases is observed.

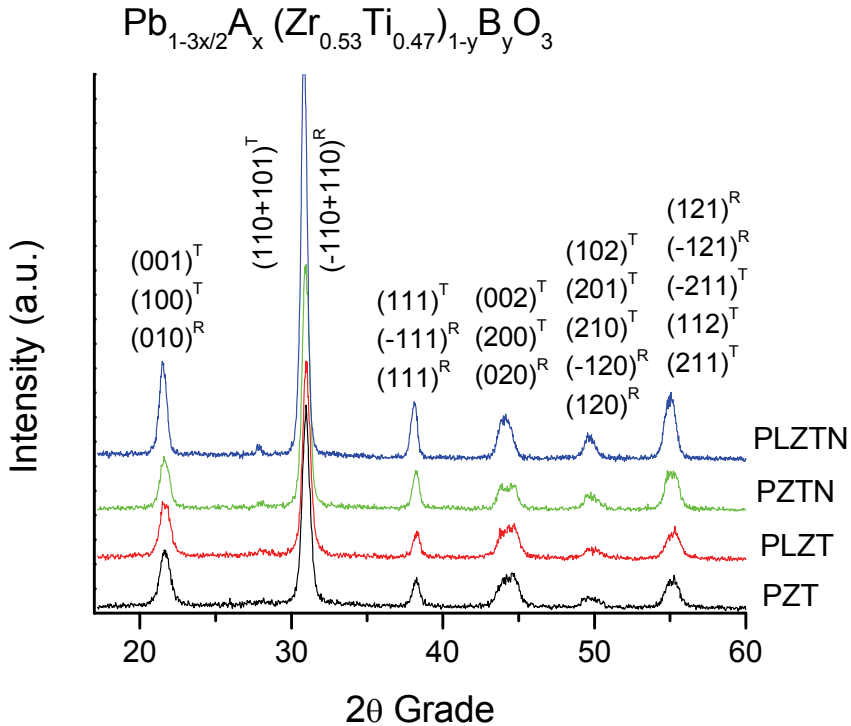


Fig. 15. Room temperature DRX patterns for PZT, PLZT, PZTN and PLZTN 53/47/1.0 sinter ceramics. Note for PZTN there are more tetragonal phase, observe better resolution of 002/200 plane.

To determine the factor most influential in dielectric permittivity behaviour with the dopant concentration, the influence of porosity was analyzed. As it was seen in Table 3 it varies in an appreciable way ( $\sim 14\%$ ) in the studied composition interval.

Among the models proposed to evaluate the properties of porous materials, applicable to systems with inferior porosity values at 0.6, it (the model) stands out the Bruggeman model. This model offers a satisfactory description of the properties of piezoelectric porous ceramic, in particular those based on PZT. A detailed explanation can it turns in works from Wersing et al (1986).

The model establishes a peculiar relationship between experimental permittivity  $[\varepsilon(p_0)]$  and the theoretical  $[\varepsilon_{p_0=0}]$ , through of porosity fraction ( $p_0$ ) given by the equation (5), considering connectivity (3-0).

$$\varepsilon(p_0) = \varepsilon_{p_0=0} * (1 - p_0^{2/3}) \quad (5)$$

Table 3 shows the results for the dielectric permittivity theoretical and experimental at room temperature. A marked difference exists among both, being bigger for the Nb and the La+Nb, what indicates the influence of this impurity in the evolution of the porosity, also  $\Delta\varepsilon$  to diminish with the frequency

Niobio						
Frecuencia kHz	0,2			1,0		
	$\epsilon(P_0)$	$\epsilon_{P_0=0}$	$\Delta\epsilon$	$\epsilon(P_0)$	$\epsilon_{P_0=0}$	$\Delta\epsilon$
0,5	830	1249	419	1373	1669	296
1	635	955	320	1335	1646	292
5	587	883	296	1307	1589	282
10	482	725	243	1297	1577	280
25	251	378	127	1269	1543	274
Lantano						
	0,6			1,0		
	$\epsilon(P_0)$	$\epsilon_{P_0=0}$	$\Delta\epsilon$	$\epsilon(P_0)$	$\epsilon_{P_0=0}$	$\Delta\epsilon$
0,5	343	395	52	566	658	92
1	286	329	43	549	638	89
5	155	180	25	425	494	69
10	128	148	20	304	354	50
25	109	126	17	160	186	26
Lantano+Niobio						
	0,4			1,0		
	$\epsilon(P_0)$	$\epsilon_{P_0=0}$	$\Delta\epsilon$	$\epsilon(P_0)$	$\epsilon_{P_0=0}$	$\Delta\epsilon$
0,5	343	588	245	784	1035	251
1	286	491	205	768	1015	247
5	155	204	49	734	970	236
10	128	220	92	710	934	224
25	109	187	78	654	864	210

Table 3. Theoretical and experimental permittivity and their difference at room temperature for 5 frequencies, for PZTN, PLZT and PLZTN 53/47/y ceramic, based on the Bruggeman model.

It is important to make notice that this model considers a materials as a not homogeneous médium and it start with two components: material and pores. In the material component there are all that is not pore, that doesn't have to be necessarily homogeneous, due to the procedure method.

The porosity is not the only factor that determines the permittivity variation with dopant concentration. The analysis for dopant type shows that to smaller concentration bigger porosity, but also bigger grain size, therefore is this last one the most influential in the variations of the dielectric parameter. For example, 0.6% of Nb, the smallest difference exists among the theoretical and experimental results, and the porosity has the fundamental rol, for this concentration "po" it is minimized; in the other concentrations exists a cooperative effect of the porosity and the grain size (Sundar et al. 1996), noted how for 1.0% "po" slightly increases the grain size and  $\Delta\epsilon$  (Table 3). In La3+ case,  $\Delta\epsilon$  diminishes with the frequency and increases with dopant concentration (Table 3), but  $\epsilon$  is increasing with grain size decrement, therefore both factors will contribute in a cooperative way in the relative permittivity (Figure 16). The samples doped with La+Nb have a grain size between 1 and 2 microns, in

addition the contribution of the porosity is strong in the behavior of dielectric permittivity, being greater even for the composition 0.8. The factors that determined the variation of the permittivity with increasing dopant concentration are the grain size (Cancarevic et al., 2006) and porosity, fundamentally.

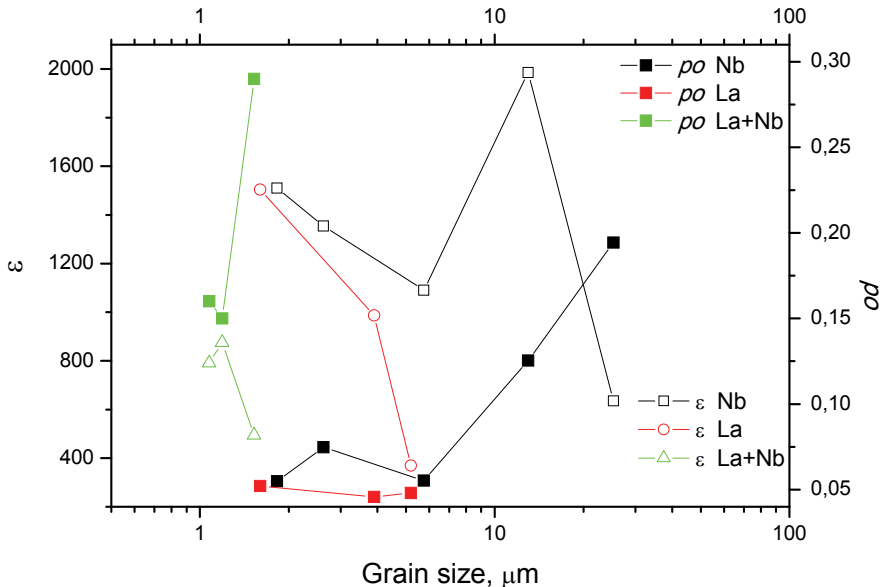


Fig. 16. Behavior at room temperature of dielectric constant ( $\epsilon$ ) and porosity ( $po$ ) as function of the grain size.

#### 4. Conclusion

The used of PL and diffuse reflectance measurement in polycrystalline ceramics to determine the band gap and the mechanism of the recombination in samples is possible. The experimental results agree with those calculated.

All system present show mainly two region of emission bands around 1.8 and 3 eV, the presence of broad band (1.8 eV) at the band gap can be associated to the vacancy defect common in all (containing lead) ceramics sintered at high temperatures, the emission at around 3eV correspond to direct recombination from CB to VB .

The emission at 2.56 eV, this present but it is not very intense in all the analyzed materials. Shows the highest intensity and a shift to higher energies in the tetragonal phases. The Nb concentration produces appreciably intensity changes and is associated to a transition from oxygen vacancy levels to valence band. PZTN presents the biggest intensity in this band, what indicates that the oxygen vacancy concentration is higher than lead vacancies.

But not all the dopant has same behavior, in all zone of PL spectra Cr diminish PL intensity with increase concentration, while  $La^{3+}$ ,  $Nb^{5+}$  and  $La^{3+}+Nb^{5+}$  increase PL intensity with the increase dopant concentration.

Another interesting aspect is that A+B doped produces an increment to 2-3 order in PL intensity, principally for "soft" doped.

On the other hand, a strong influence of dopants on the decrement of grain size as concentration grows is observed. The substitution in the A place and the simultaneous substitutions in the A and B places provokes mixture of (tetragonal and rhombohedral) phases, while substitution in the B place the structure is tetragonal at least in 95 %. A texture effect is also noticed, as it grows with the dopant concentration.

XRD results are confirmed by the obtained dielectric characteristics. In the PLZT, PLZTN and PSZTC samples which present phase mixture, two peaks in the  $1/\epsilon$  curves are observed and associated to Ferro-Ferro (rhombohedral-tetragonal) and Ferro-Para (tetragonal-cubic) phase transitions. Substitutions in the B place contribute more significantly to the Curie temperature drop, with a minimum for PZTN 0.8 %.

## 5. Acknowledgements

This work was supported by project PNCB 10/04, Cuba, Sabbatical program CONACYT, Mexico. The author appreciates work of Ing. M. Hernandez, Ing. F. Melgarejo, Ing. M. Landaverde and Ing. E. Urbina. And to Cybernetic, Mathematical and Physics Instituted.

## 6. Reference

- Anicete-Santosa, M., Silva, M.S., Orhan, E., Gomes, M. S., Zaghete, M. A., Paiva-Santos, C. O., Pizani, P. S., Cilense, M., Varela, J. A., Longo, E., (2007) Contribution of structural order-disorder to the room-temperature photoluminescence of lead zirconate titanate powders. *Journal of Luminescence*, Vol. 127, Issue 2, 689-695
- Baedi, J., Hosseini, S.M., Kompany, A., (2008) The effect of excess titanium and crystal symmetry on electronic properties of  $Pb(Zr_{1-x}Ti_x)O_3$  compounds. *Computational Materials Science*, Vol: 43, Issue: 4, 909-916, ISSN: 09270256.
- Bharadwaja, S.S.N., Saha, S., Bhattacharyya, S., Krupanidhi, S.B., (2002) Dielectric properties of La-modified antiferroelectric  $PbZrO_3$  thin films. *Materials Science and Engineering B* vol 88, issue 1, 22-25, ISSN 0921-5107
- Calderón-Piñar, F., Aguilar, J., García, O., Fuentes, J., Contreras, G., Durruthy-Rodríguez, M. D., Peláiz-Barranco, A., (2007) Mediciones de fotoluminiscencia en sistema PLZT para determinar su relación con los mecanismos de conducción. *Mediciones térmicas de materiales sinterizados tipo BSZT*. Instituto de Cibernética, Matemática y Física (I CIMAFA) Research Report 2007-412, ISSN 0138-8916
- Cancarevic, M., Zinkevich, M., Aldinger, F., (2006) Thermodynamic Assessment Of The Pzt System *Journal Of The Ceramic Society Of Japan*, Vol. 114, Issue:1335, 937-949, ISSN 0914-5400
- Chang, Q., Sun, Jin, D., Zhou, J., Li, S., Tay, B.K., Lau, S.P., Sun, X.W., Huang, H.T., Hing, P., (2001) *Intense and stable blue-light emission of  $Pb(Zr_xTi_{1-x})O_3$* . *Applied Physics Letters* Vol 79, No. 6, 1082-1084, ISSN 1077-3118
- Chen, J., Chan, H.M., Harmer, M., (1989) Ordering Structure and Dielectric Properties of Undoped and La/Na-doped  $Pb(Mg_{1/3}Nb_{2/3})O_3$ . *J. Am. Ceram. Soc.* Vol. 72, No. 4, 593-598, ISSN 0002-7820
- de Lazaro, S., Milanez, J., de Figueiredo, A.T., Longo, V.M., Mastelaro, V.R., de Vicente, F.S., Hernandez, A.C., Varela, J.A., Longo, E., (2007) Relation between

- photoluminescence emission and local order-disorder in the CaTiO<sub>3</sub> lattice modifier. *Applied Physics Letters* 90, 111904-1 - 111904-3, ISSN 0003-6951
- Dixit, A., Majumder, S. B., Katiyar, R. S., Bhalla, A. S., (2006) Studies on the Relaxor Behavior of Sol-Gel Derived Ba(Zr<sub>x</sub>Ti<sub>1-x</sub>)O<sub>3</sub> (0.30 ≤ x ≤ 0.70) Thin Films. *Journal of Materials Science* 41, 87, ISSN 0022-2461
- Durruthy, M. D., Fuentes, L., Hernandez, M., Camacho, H. (1999) Influence of the niobium dopant concentration on the Pb(Zr<sub>0.54</sub>Ti<sub>0.46</sub>)O<sub>3</sub> ceramics sintering and final properties. *Journal of Materials Science* 34 2311 - 2317
- Durruthy-Rodríguez, M.D., Hernández-García, M., Suárez- Gómez A. (2002) Lanthanum and niobium doping on PZT ceramic synthesis. *Revista CENIC Ciencias Químicas*, Vol. 33, No. 1, 29-33, ISSN 0254-0525
- Durruthy-Rodríguez, M.D., Costa-Marrero, J., Hernández-García, M., Calderón-Piñar, F., Yañez-Limón, J.M. (2010a) Photoluminescence in “hard” and “soft” ferroelectric ceramics. *Applied Physics A*, 98, 543–550, DOI 10.1007/s00339-009-5501-y
- Durruthy-Rodríguez, M. D., Costa-Marrero, J., Hernández-García, M., Calderón-Piñar, F., Malfatti, C., Yañez-Limón, J. M., Guerra, J. D. S. (2010b) Optical characterization in *Pb(Zr<sub>1-x</sub>Ti<sub>x</sub>)<sub>1-y</sub>Nb<sub>y</sub>O<sub>3</sub>* ferroelectric ceramic system. *Applied Physics A*, DOI 10.1007/s00339-010-6017-1, ISSN 1432-0630
- Durruthy-Rodríguez, M.D., Costa-Marrero, Calderón-Piñar, F., Yañez-Limón, J.M., Guerra, J. D. S., (2011) Photoluminescence in Pb<sub>0.95</sub>Sr<sub>0.05</sub>(Zr<sub>1-x</sub>Ti<sub>x</sub>)<sub>1-y</sub>CryO<sub>3</sub> ferroelectric ceramic system. *Journal of Luminiscence* (accepted), ISSN 0022-2313
- Eyraud, L., Guiffard, B., Lebrun, L., Guyomar, D., (2006) Interpretation of the Softening Effect in PZT Ceramics Near the Morphotropic Phase Boundary. *Ferroelectrics* Vol. 330, issue 1, 51-60, ISSN 0015-0193
- Garcia, S., Font, R., Portelles, J., Quiñones, R.J., Heiras, J., Siqueiros, J.M. (2001) Effect of Nb doping on (Sr,Ba) TiO<sub>3</sub> (BST) ceramic samples. *Journal of Electroceramics*, Vol. 6, No. 2, 101-108, ISSN 1385-3449
- Ghasemifard M., Hosseini S.M., Khorsand Zak A., Khorrami Gh. H. (2009) Microstructural and optical characterization of PZT nanopowder prepared at low temperature. *Physica E: Low-dimensional Systems and Nanostructures*, Volume 41, Issue 3, 418-422, ISSN 13869477
- Guiffard, B., Boucher, E., Eyraud, L., Lebrun, L., Guyomar, D., (2005) Influence of donor co-doping by niobium or fluorine on the conductivity of Mn doped and Mg doped PZT ceramics. *Journal of the European Ceramic Society*, Volume 25, Issue 12, 2487-2490, ISSN 0955-2219
- Gupta, S.M., Viehland, D., (1998) Tetragonal to rhombohedral transformation in the lead zirconium titanate lead magnesium niobate-lead titanate crystalline solution. *J. Appl. Phys.*, 83, 1407-414. ISSN 1089-7550
- Haertling, G. H. *Ferroelectric (1999) Ceramics: History and Technology*. *Journal of the American Ceramic Society*, Vol. 82, 4, 797-818, DOI:10.1111/j.1151-2916.1999.tb01840.x
- Jaffe, B., Roth, R.S., Marzullo, S. (1954) Piezoelectric Properties of Lead Zirconate-Lead Titanate Solid-Solution Ceramics. *Journal of Applied Physics*, Volume 25, Issue 6, 809-810, ISSN 0021-8979

- Jaffe, B.; Cook, W.R.; Jaffe, H., (1971) *Piezoelectric Ceramics*, Academic Press, London and New York, ISBN 0- 12-379550-8
- Kottim G. (1969) *Reflectance Spectroscopy*, Springer Verlag, New York. ISBN 0 19 850778x
- Lines, M. E., Glass, A. M., (2001) *Principles and applications of ferroelectrics and related materials*, Oxford University Press Inc., New York.
- Longo V. M., Cavalcante L. S., de Figueiredo A. T., Santos L. P. S., Longo E., Varela J. A., Sambrano J. R., Paskocimas C. A., De Vicente F. S. and Hernandez A. C. (2007) Highly intense violet-blue light emission at room temperature in structurally disordered SrZrO<sub>3</sub> powders. *Applied Physics Letters* 90, 091906-1 - 091906-3. ISSN: 0003-6951
- Longo, E., de Figueiredo, A.T., Silva, M.S., Longo, V.M., Mastelaro, V.R., Vieira, N.D., Cilense, M., Franco, R.W.A., Varela, J.A., (2008) Influence of Structural Disorder on the Photoluminescence Emission of PZT Powders. *J. Phys Chem A.* 112, 8953-8957, ISSN 1089-5639
- Mansimenko Y.L., Glinchuk M.D., Bykov I.P. (1998) Photoinduced Centers in the Optically Transparent PLZT(8/65/35) Ceramics. *Journal of the Korean Physical Society* 32, S1039-S1041, ISSN 0038-1098
- Nakajima H., Mori, T., Itoh, S., Watanabe, M., (2004) Photoluminescence properties of trace amounts of Pr and Tb in yttria-stabilized zirconia. *Solid State Communications* vol. 129, issue 7, 421-424
- Noheda, B., Cox, D.E., Shirane, G., Guo, R., Jones, B., Cross, L.E., (2001) Stability of the monoclinic phase in the ferroelectric perovskite  $Pb(Zr_{1-x}Ti_x)O_3$ . *Physical Review B (Condensed Matter)* 63, 014103-1, 1550-235X
- Noheda, B., Gonzalo, J.A., Cross, L.E., Guo, R., Park, S.E., Cox, D.E., Shirane, G., (2000) Tetragonal-to-monoclinic phase transition in a ferroelectric perovskite: The structure of  $Pb(Zr_{0.52}Ti_{0.48})O_3$ . *Physical Review B* 61, 8687-8695, DOI:10.1103/PhysRevB.61.8687
- Ronda C. (2008) *Luminescence: From Theory to Applications*. Edited by WILEY-VCH Verlag GmbH & Co. KGaA, ISBN: 978-3-527-31402-7, Weinheim.
- Shannigrahi, S.R., Tripathy, S. (2007) Micro-Raman spectroscopic investigation of rare earth-modified lead zirconate titanate ceramics. *Ceramics International* vol. 33, n 4, 595-600, ISSN 0272-8842
- Silva, M.S., Cilense, M., Orhan, E., Gomes, M.S., Machado, M.A.C., Santos, L.P.S., Paiva-Santos, C.O., Longo, E., Varela, J.A., Zaghete, M.A., Pizani, P.S., (2005) The nature of the photoluminescence in amorphized PZT. *Journal of Luminescence* 111, 205-213, DOI:10.1016/j.jlumin.2004.08.045
- Sivasubramanian V., Kesavamoorthy R., Subramanian V. (2007) Photoluminescence investigations on the nanoscale phase transition in  $Pb(Mg_{1/3}Nb_{2/3})O_3$ . *Solid State Communications* Vol. 142, Issue 11, 651-654, ISSN 0038-1098
- Suárez-Gómez, A., Durruthy, M. D., Costa-Marrero, J., Peláiz-Barranco, A., Calderón-Piñar, F., Saniger-Blesa, J. M., de Frutos, J. (2009) Properties of the PLZTN  $x/54/46$  ( $0.4 \leq x \leq 1.4$ ) ceramic system. *Materials Research Bulletin* vol. 44, 1116-1121, ISSN 0025-5408

- Sundar, V., Kim, N., Randall, C.A., Yimnirun, R., Newnham, R.E. (1996) The effect of Doping and grain size on Electrostriction in  $\text{PbZr}_{0.52}\text{Ti}_{0.48}\text{O}_3$ . IEEE, 1, 935-938, ISBN 0-7803-3355-1
- Tai, C.W. & Baba-Kishi, K.Z. (2002) *Microtexture studies of PST and PZT ceramics and PZT thin film by electron backscatter diffraction patterns*. Textures and Microstructures, Vol. 35, No. 2, 71-86, ISSN 1029-4961.
- Wendlandt, W.W., Hecht, H.G (1966) *Reflectance Spectroscopy*, Wiley Interscience, New York, BCIN Number 62796
- Wersing W., Lubitz K., Mohaupt J. (1986) Dielectric, elastic and piezoelectric properties of porous PZT ceramics. *Ferroelectrics*, 68, 77-79. ISSN 0015-0193
- Yang, Z., Liu, Q.-H., (2008) The structural and optical properties of ZnO nanorods via citric acid-assisted annealing route. *Journal of Materials Science*, Volume 43, Number 19, 6527-6530, ISSN 0022-2461
- Yu, P.Y., Cardona, M., (1996) *Fundamentals of semiconductors. Physics and Materials Properties*. Ed. Springer-Verlag, Berlin, ISBN 978-3-642-00710-1

# Photovoltaic Effect in Ferroelectric LiNbO<sub>3</sub> Single Crystal

Zhiqing Lu, Kun Zhao and Xiaoming Li  
*Laboratory of Optic Sensing and Detecting Technology, College of Science  
People's Republic of China*

## 1. Introduction

Lithium niobate (LiNbO<sub>3</sub>) is a human-made dielectric material and was first discovered to be ferroelectric in 1949. Properties and applications of LiNbO<sub>3</sub> have been widely studied, resulted in several thousands of papers on this material, since the crystal was successfully grown using the Czochralski method by Ballman in 1965 (Kong et al., 2005). It has been extensively researched for its excellent ferroelectric, piezoelectric, dielectric, pyroelectric, electric-optical and nonlinear optical properties (Wang et al., 2008; Chen et al., 2007; Sarkisov et al., 2000). Now LiNbO<sub>3</sub> is a very significant material for optical applications, such as acoustic wave transducers, acoustic delay lines, acoustic filters, optical amplitude modulators, optical phase modulators, second-harmonic generators, Q-switches, beam deflectors, dielectric waveguides, memory elements, holographic data processing devices, and others (Kim et al., 2001; Zhen et al., 2003; Pham et al., 2005; Liu et al., 2002; Zhou et al., 2006).

LiNbO<sub>3</sub> is a ferroelectric material which has the highest Curie temperature of about 1210 °C up to now and the largest spontaneous polarization of about 0.70 C/m<sup>2</sup> at room temperature. LiNbO<sub>3</sub> single crystals exhibit paraelectric phases above the Curie temperature and ferroelectric phases below the Curie temperature (Karapetyan et al., 2006; Bermúdez et al., 1996). Ferroelectric LiNbO<sub>3</sub> crystal is a member of the trigonal crystal system, exhibiting three-fold rotation symmetry about its c axis. Its structure consists of planar sheets of oxygen atoms in a distorted hexagonal close-packed configuration. The octahedral interstices in this structure are one-third filled by lithium atoms, one-third by niobium atoms, and one-third vacant. In the paraelectric phase the Li atoms and the Nb atoms are centered in an oxygen layer and an oxygen octahedral, making the paraelectric phase non-polar. But in ferroelectric phase the Li atoms and the Nb atoms shifted into new positions along the c axis by the elastic forces of the crystal, making the LiNbO<sub>3</sub> crystal exhibiting spontaneous polarization (Bergman et al., 1968).

Many methods were reported to determine the +c axis of ferroelectric LiNbO<sub>3</sub> single crystal. A standard method is to compress the crystal in the c axis direction. The +c axis is defined as being directed out of the c face that becomes negative upon compression. This can be understood that the Li and Nb ions move closer to their centered positions upon compression, leaving excess negative compensation charges on the +c face, causing the +c face to become negative. Another method to identify the +c face and -c face of the crystal is an etching technique with HF solution. The etching speed on the -c face is faster than on the +c face (Beghouel et al., 2008; Bourim et al., 2006). Other methods to determine the +c axis

were also reported such as to cool the crystal, observation of the terraces on a cleavage plane, x-ray diffraction techniques (Boyd et al., 1964; Kaminow et al., 1980).

In the past few years, various types of photodetectors were proposed, such as photoconductor, Schottky barrier detector, p-i-n junction photodiode, and heterogeneity junction (Wang et al., 2007; Jin et al., 2007). Photovoltaic effect plays an important role in the investigation of these photodetectors. Photovoltaic effects in  $\text{LiNbO}_3$  crystals were observed by Chen in 1969 (Chen, 1969). Then  $\text{LiNbO}_3$  was found to be in response to ultraviolet, visible, and infrared radiation of laser (Dai et al., 2005).  $\text{LiNbO}_3$  is a promising material for photodetector because of its high responsibility, good dielectric properties, and low cost. For example, ultraviolet photodetectors have attracted a strong interest owing to their broad potential applications in the fields of automatization, short-range communications security, biological researches, and military services. The band gap of  $\text{LiNbO}_3$  single crystal is  $\sim 4$  eV, which can be suggested as a promising material for UV photodetector since the present ultraviolet photodetectors based on various wide band gap semiconductors, such as III-V nitrides, silicon carbide, zincoxide, and diamond, require a complicated fabrication process and high-cost manufacturing (Razeghi & Rogalski, 1996; Topic et al., 2001; Tomm et al., 2000; Spaziani et al., 2003). In this chapter, photovoltaic effect in pure congruent  $\text{LiNbO}_3$  single crystals will be introduced, including vertical photovoltaic effect, lateral photovoltaic effect and photovoltaic effects in miscut  $\text{LiNbO}_3$  single crystals (Lu et al., 2009; Li et al., 2010).

## 2. Photovoltaic effects in $\text{LiNbO}_3$ single crystal

### 2.1 Vertical photovoltaic effects

Commercial optical grade z-cut  $\text{LiNbO}_3$  single crystal was used in the experiment, which was double polished with a dimension of  $5 \times 5 \times 0.5$  (mm) in the a, b, and c directions, respectively. The two silver paste electrodes were placed on the opposite two surfaces of the crystal respectively. An actively/passively mode locked Nd:yttrium-aluminum-garnet (Nd:YAG) laser (with pulse duration of 25 ps, repetition rate of 10 Hz) was used to irradiate the sample at the wavelengths of 1064, 532, and 355 nm at room temperature. The laser beam was directed onto the sample near to the electrode and passed through the crystal along the c axis, as shown in the inset in Fig.1. The diameter of the spot was 2 mm. The open circuit photovoltage were measured and recorded by a digital storage oscilloscope. Figure 1 presents the typical ultrafast photovoltaic signals observed under the pulsed laser of three different wavelengths. The laser pulse energy of 355, 532 and 1064 nm is 0.56, 0.60 and 0.58 mJ respectively. We can see that the response time is about 2 ns and the full width at half maximum (FWHM) is about 1.8 ns.

All the photovoltages measured by the oscilloscope were negative whether the laser pulse irradiated on the top surface or on the bottom surface of the crystal, shown in Fig.1. It has been known that the ferroelectric  $\text{LiNbO}_3$  exhibits spontaneous polarization below its Curie temperatures, which direction is from  $-c$  face to  $+c$  face of the crystal (Wemple et al., 1968). So there is a built-in electric field in  $\text{LiNbO}_3$  crystal in the direction from the positive end of spontaneous polarization to the negative end, antiparallel to the spontaneous polarization. Here we identified the  $-c$  face and  $+c$  face using an etching technique with HF solution of 40%. When the laser spot directed on the crystal, photo-excited electrons drifted toward the positive end of spontaneous polarization under the influence of the internal electric field, undergoing the course of excited-captured-reexcited-recaptured before they eventually

drifted to the +c face. So we always get a negative signal on the oscilloscope whether the laser irradiated on the +c face or on the -c face.

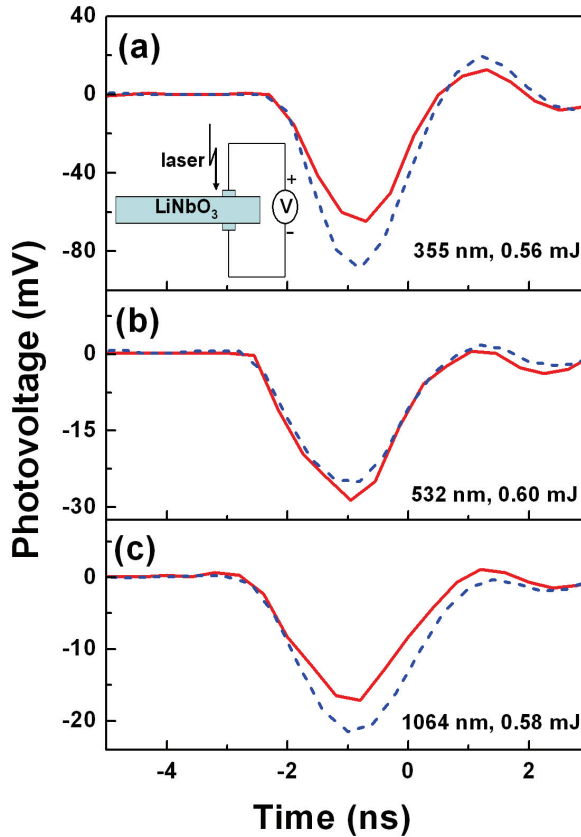


Fig. 1. Typical ultrafast photovoltage with time when the sample irradiated by pulsed laser of three different wavelengths. The solid line is the signal when irradiated on the +c face of the crystal and the short dash line is on the -c face. All the signals measured are negative.

The peak voltage values of open circuit verse the pulse energy has been also measured under the irradiation of the three different wavelengths. The results are summarized in Fig.2. We can see that the photovoltages under the three wavelengths increased linearly with the incident energy of each laser pulse.

The photovoltage  $V$  that appears in the crystal is (Feng et al., 1990)

$$V = \frac{J}{\sigma_d + \sigma_{ph}} l \quad (1)$$

where  $J$  is the photovoltaic current,  $\sigma_d$  and  $\sigma_{ph}$  are dark conductivity and photoconductivity of the crystal, respectively, and  $l$  is the distance between the electrodes. Since  $\sigma_d$  ( $<10^{-15}\Omega^{-1}cm^{-1}$ ) is much smaller than  $\sigma_{ph}$ , we can neglect it.

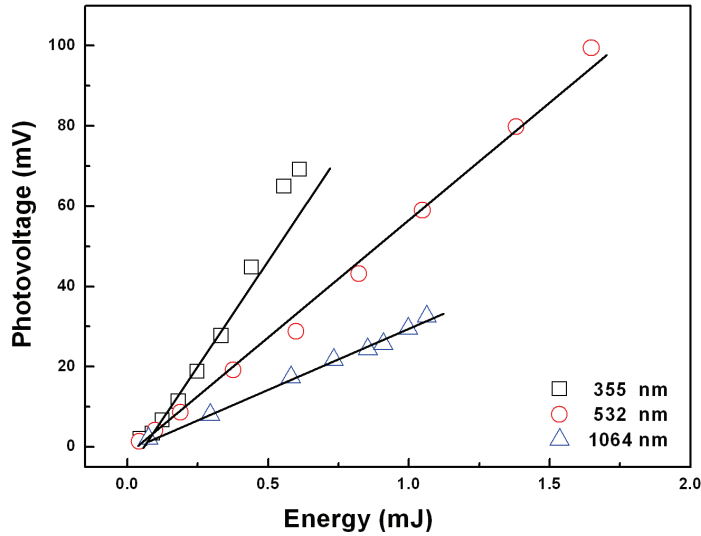


Fig. 2. The peak open-circuit photovoltage as a function of the energy of pulsed laser. The photovoltage is proportional to the intensity of incident laser of 355, 532 and 1064 nm, respectively.

The photovoltaic current of  $\text{LiNbO}_3$  crystal is given by (Glass et al., 1974)

$$J = \kappa\alpha I + \sigma_{ph}E + eD \frac{dn}{dz} \quad (2)$$

where  $\kappa$  is the glass coefficient,  $\alpha$  is the absorption coefficient,  $I$  is the intensity of the irradiated laser beam,  $E$  is the total electric field in the crystal,  $D$  is the diffusion coefficient, and  $n$  is the carrier concentration. The first term represents the photovoltaic current, the second term represents the drift current, and the third term represents the non-uniform laser irradiation in the sample.

The photoconductivity is given by (Nakamura et al., 2008)

$$\sigma_{ph} = \frac{\alpha I}{h\nu} \tau e \mu \quad (3)$$

where  $\tau$  is the lifetime of an excited carrier in the conduction band,  $\mu$  is the mobility, and  $h\nu$  is the photon energy.

The carrier concentration  $n$  should be proportional to the intensity of the laser due to the photoelectric effect. So the photovoltage  $V$  is proportional to the intensity of incident laser  $I$ , as shown in Fig.2.

Continuous-wave (CW) laser of 532 and 1064 nm were also used to irradiate on the sample. Negative photovoltage signal was also observed in the experiment, as shown in Fig.3. This is in agreement with the results of the experiments above using pulsed lasers in Fig.1. The reason is the existence of the spontaneous polarization and the internal electric field in the crystal. When the power of the incident laser was changed from 0.6 to 60.4 mW, we found that the peak photovoltages also increased linearly, as shown in Fig.4.

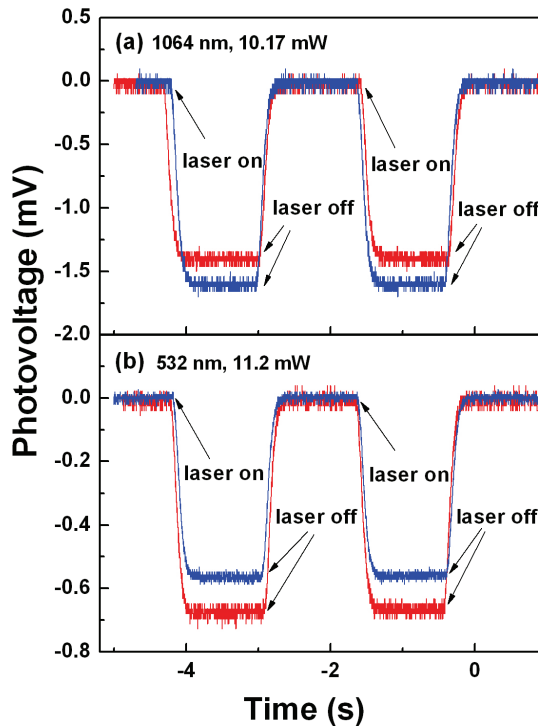


Fig. 3. The negative photovoltages under the irradiation of continuous-wave laser of 532 and 1064 nm.

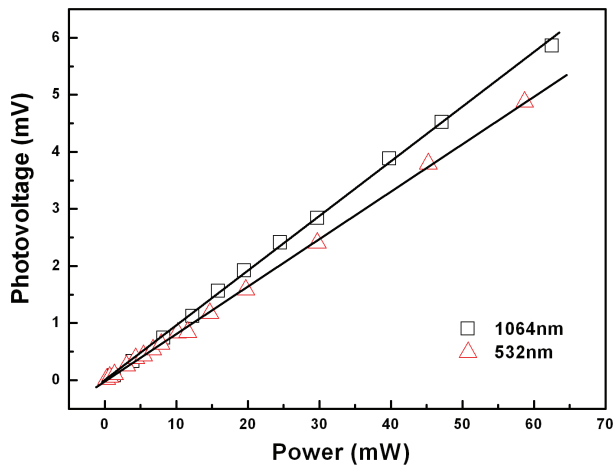


Fig. 4. The open-circuit photovoltages increased linearly with the intensity of the CW laser.

Defects in LiNbO<sub>3</sub> crystal are the main reason of the photovoltaic effect and the charge transport. There is at least about 1 mol % of intrinsic defects such as bipolarons and small

polarens in pure congruent  $\text{LiNbO}_3$  crystal (Schirmer et al., 2005). The absorption spectra of  $\text{LiNbO}_3$  (Fig.5) shows that the absorption peak of the sample is about at 310 nm, and there is a common absorption peak of bipolarons and small polarons at 628 nm. So the transition and migration of the electrons in  $\text{LiNbO}_3$  crystal is mainly between the defects and the conduction band.

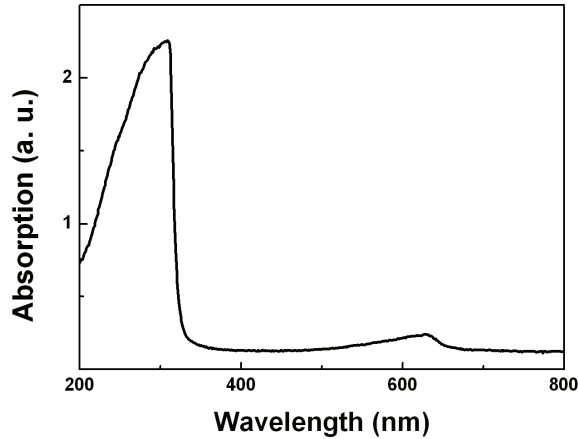


Fig. 5. The absorption spectra of  $\text{LiNbO}_3$  which shows two absorption peaks of the sample that one is for band to band absorption and another is the common absorption peak of bipolarons and small polarons.

On the basis of two-center model, for pure  $\text{LiNbO}_3$ , the deep center is dominated by bipolarons and the shallow center is governed by the small polarons. By laser pulses these bipolarons can be dissociated at room temperature and released photo-excited electrons to the conduction band. But the amount of the shallow center is very small in pure  $\text{LiNbO}_3$ . The energy between the deep center and the conduction band is about 2.0~2.5 eV. The photon energy of 355 nm is 3.5 eV. So when the sample was irradiated by the laser of 355 nm, a large amount of electrons in deep center can be excited into the conduction band. The photon energy of 532 nm is 2.3 eV, which is near to the energy between the deep center and the conduction band, so it can excited part of electrons in deep center. Therefore, the peak value of photovoltage of 355 nm is larger than that of 532 nm, as shown in Fig.2. The photon energy of 1064 nm is 1.2 eV, which can not excite the electrons in deep center. But the deep center can be dissociated not only by illumination but also heating. The temperature of the crystal increased during the irradiation of 1064 nm laser in the experiment, and the deep center is dissociated and released electrons. With the increase of the intensity of the incident laser, the transition between the deep center and the shallow center should be taken into account, for the dissociated energy of bipolarons is about 0.27 eV (Kong et al., 2005) .

## 2.2 Lateral photovoltaic effects

To investigate the lateral photovoltage in  $\text{LiNbO}_3$  single crystal, two silver paste electrodes were separated about 1.5 mm on the surface perpendicular to the c axis. The laser beam passed through the crystal along the c axis and irradiated normally at the back of one electrode, as shown in Fig. 6.

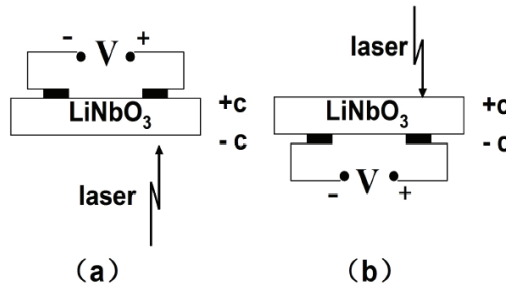


Fig. 6. Schematic of measurement for sample irradiated by laser through (a)  $-c$  face (mode 1) and (b)  $+c$  face (mode 2).

Typical ultrafast signals can be observed as shown in Fig. 7, with the rise time of about 1.5 ns and the FWHM of 1–2 ns. For mode 1, the signals were negative and positive when the laser pulse irradiated the positive and negative electrodes, respectively (Fig. 6(a)). While the reverse signals were recorded for mode 2 (Fig. 6(b)).

Due to inhomogeneous illumination in LiNbO<sub>3</sub> crystal, the concentration of photoelectrons is larger in the illumination region than in the dark region. And the photoelectrons will drift toward the  $+c$  face of the crystal because of the existence of a permanent electric field in the direction from  $-c$  to  $+c$  faces, then diffuse toward another electrode. Thus we can get the negative (positive) signals when the sample is irradiated at the back of positive electrode for mode 1 (mode 2). The same results can be also obtained when the CW laser is used to irradiate the crystal, as shown in Fig. 8. The dependence of the peak open-circuit photovoltages on the incident light intensity is studied experimentally. The results are summarized in Fig. 9. We can see that the photovoltages increase linearly with the laser intensity, which can be well explained by the photovoltaic effects in LiNbO<sub>3</sub> crystal.

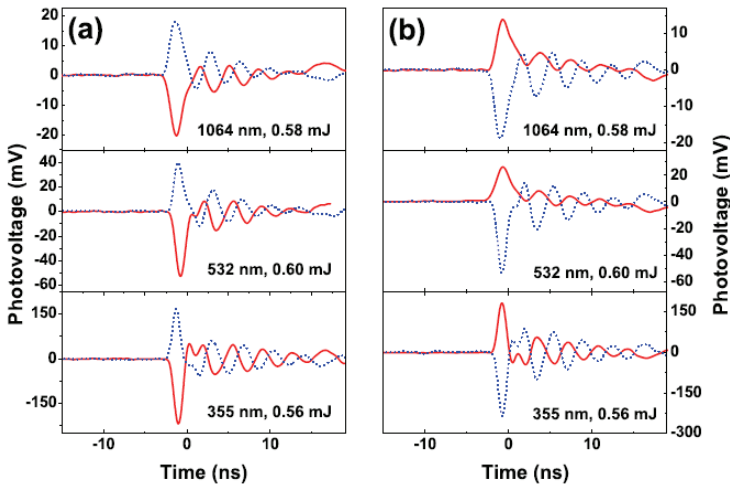


Fig. 7. Typical ultrafast photovoltages recorded for (a) mode 1 and (b) mode 2. Solid and short dot lines are for the signals when the laser pulse irradiates the positive and negative electrodes, respectively.

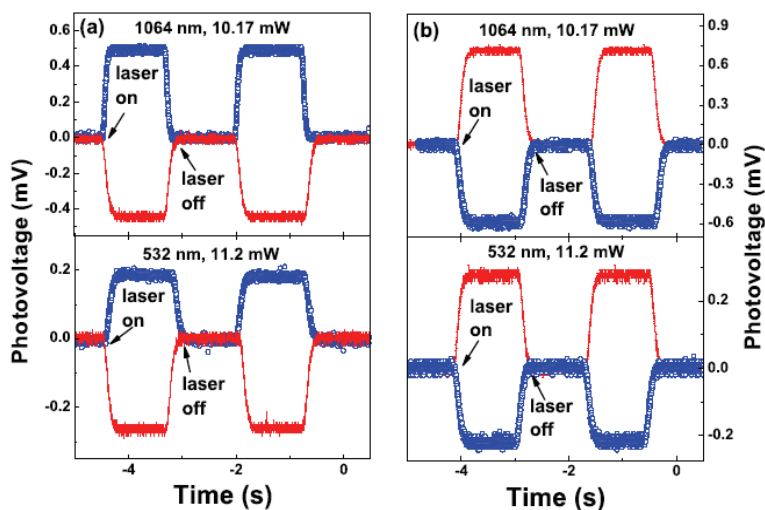


Fig. 8. Photovoltages for (a) mode 1 and (b) mode 2 under the irradiation of CW laser of 532 and 1064 nm. Solid line and open circle point are for the signals when the laser pulse irradiates the positive and negative electrodes, respectively.

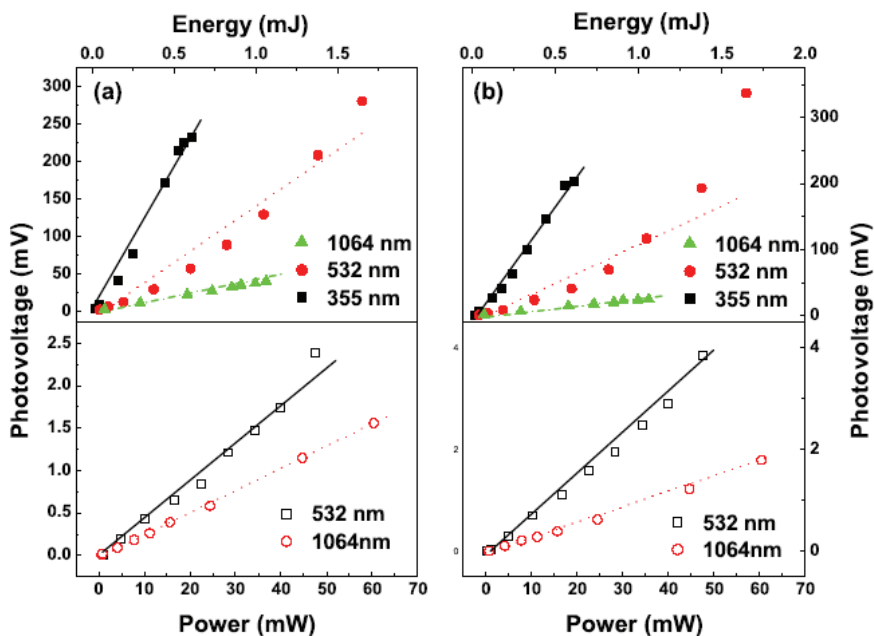


Fig. 9. Peak open-circuit photovoltages as functions of pulsed laser energy (solid point) and CW laser power densities (open point) for (a) mode 1 and (b) mode 2.

### 2.3 Photovoltaic effects in miscut LiNbO<sub>3</sub> single crystals

A single polished commercial LiNbO<sub>3</sub> single crystal with *c*-axis oriented is used for the photovoltaic studies. The sample geometry is 5×5 mm<sup>2</sup> with the thickness of 0.5 mm. The crystalline orientation is 10° miscut from the exact (001) orientation, which is characterized by x-ray diffraction with the usual  $\theta$ - $2\theta$  scan using Cu K $\alpha_1$  and K $\alpha_2$  radiations. As shown in Fig. 10, the offset point is set as  $\omega=a$  or  $45^\circ-a$  to satisfy Bragg's diffraction, where  $\alpha$  is the miscut angle. The two peaks arise from the (006) and (0012) plane of LiNbO<sub>3</sub> and are clearly apart for K $\alpha_1$  and K $\alpha_2$  radiations. The inset of Fig. 10 shows the UV-visible absorption spectrum of LiNbO<sub>3</sub> crystals as a function of the wavelength. The sharp absorption edge is about 310 nm, corresponding to the optical band gap of LiNbO<sub>3</sub> and indicating that UV light, e.g. 248 nm laser, can generate electron-hole carriers in LiNbO<sub>3</sub> crystals.

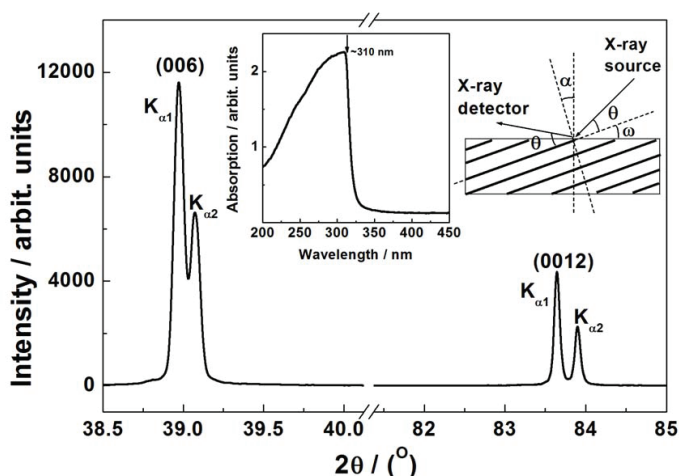


Fig. 10. The x-ray diffraction pattern of a miscut LiNbO<sub>3</sub> single crystal. The left inset shows the absorption spectrum of LiNbO<sub>3</sub> single crystal. The right inset shows the configuration of  $\theta$ - $2\theta$  scan, where  $\alpha$  is the miscut angle and  $\omega$  the offset point.

The photovoltaic properties are investigated under the illuminations of a KrF pulsed laser with the wavelength of 248 nm with 20 ns duration at a 10 Hz repetition. In order to study the influence of the thickness on the photovoltaic effect, the samples are polished mechanically into seven different thicknesses, which are 0.49, 0.45, 0.38, 0.28, 0.22, 0.17 and 0.09 mm, respectively. Before the photovoltaic measurements, the sample is cleaned by using an ultrasonic cleaner in alcohol and acetone under routine cleaning process. Two colloidal silver electrodes of about 1×5 mm<sup>2</sup> area, separated by 3 mm, are prepared on the mirror polished surface of the LiNbO<sub>3</sub> single crystal and the opposite surface is exposed wholly to the laser irradiation, as shown in the inset of Fig. 11. The photovoltaic signals are recorded by using a sampling oscilloscope terminating into 50  $\Omega$  at room temperature. All the measurements are carried out in the room temperature without any applied bias.

Typical voltage transients of the LiNbO<sub>3</sub> single crystal of different thicknesses to a pulsed laser illumination are presented in Fig. 11. The peak photovoltage as a function of the sample thicknesses is shown in Fig. 12, and the energies on the sample are 15.2 and 19.4 mJ,

respectively. With the decrease of the crystal thickness from 0.49 to 0.09 mm, the peak photovoltage increases rapidly at first and then descends. The maximum peak photovoltage occurs at the thickness of 0.38 mm and reaches 35.6 and 31.1 mV for 19.4 and 15.2 mJ, with the corresponding photovoltaic sensitivities of 1.83 and 2.04 mV/mJ, which is several times larger than that at 0.49 and 0.09 mm. In addition, the peak photovoltage is found to depend linearly on the on-sample energy from 13.5 to 20.9 mJ for selected crystal thicknesses of 0.22 and 0.09 mm, respectively, as shown in Fig. 13.

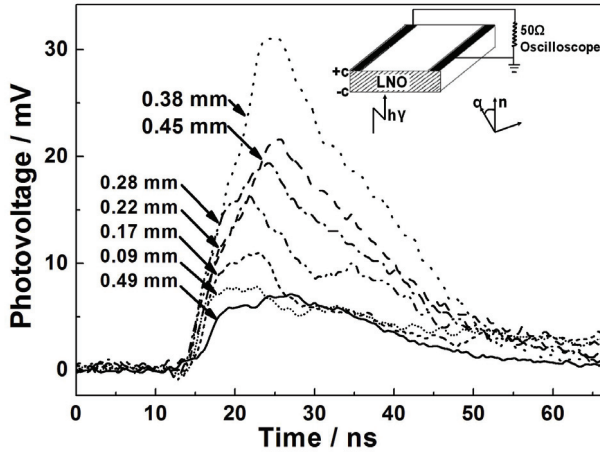


Fig. 11. The photovoltaic pulses for miscut  $\text{LiNbO}_3$  single crystal under the illumination of a 248 nm laser for seven different thicknesses recorded by an oscilloscope with an input impedance of  $50 \Omega$  at room temperature without any applied bias. The on-sample energy was 15.2 mJ. The inset displays the schematic circuit of the measurement.

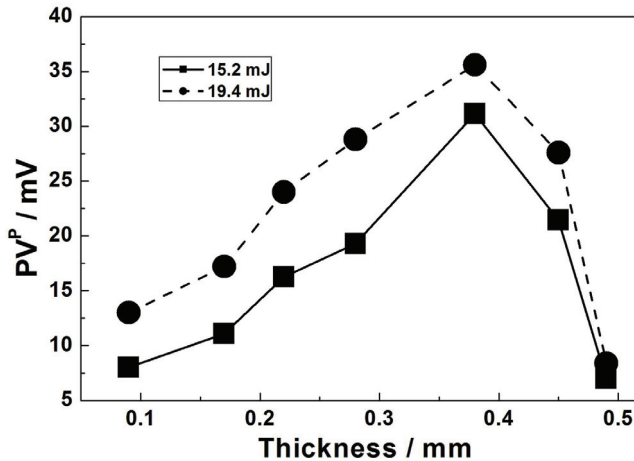


Fig. 12. The peak photovoltage dependence of the miscut  $\text{LiNbO}_3$  single crystal thickness.

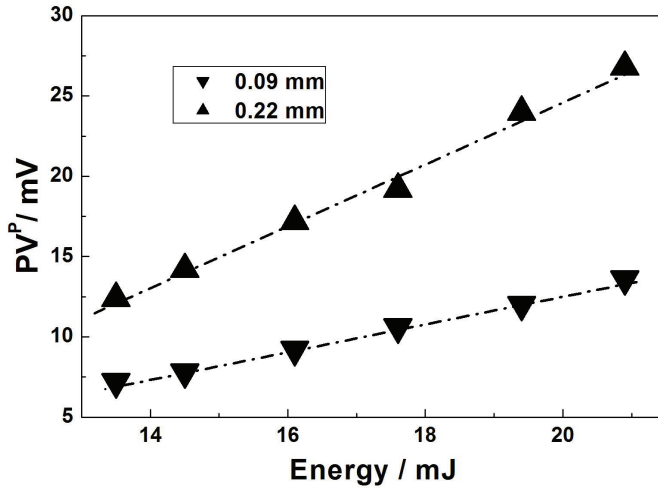


Fig. 13. The peak photovoltage of the miscut LiNbO<sub>3</sub> single crystal as a function of on-sample energy.

Figure 14 shows the 10%–90% rise time and FWHM as functions of the sample thickness for the on sample-energy of 15.2 and 19.4 mJ, respectively. With the decrease of sample thickness, the carriers reaches the two colloidal electrodes faster for thinner sample so that faster photovoltaic response can be observed. The rise time descends obviously from 11.83 ns at 0.49 mm to 3.946 ns at 0.09 mm, suggesting that decreasing the sample thickness is a useful way to obtain faster response detection. Since the miscut LiNbO<sub>3</sub> single crystal

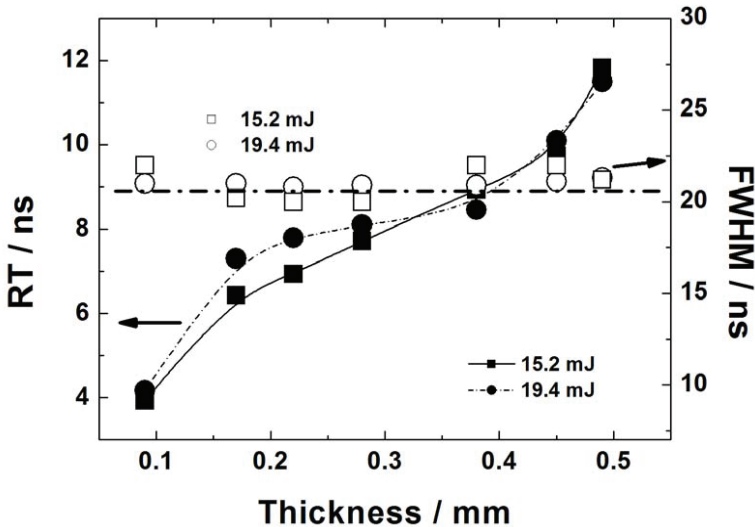


Fig. 14. The rise time and FWHM as functions of the sample thickness.

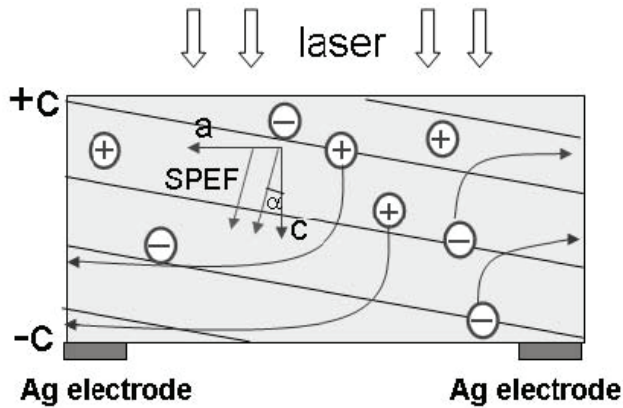


Fig. 15. The schematic diagram of the transporting photogenerated carriers, indicating that the carriers were separated and assembled at the two Ag electrodes by the SPEF.

exhibits an optical response time of  $\sim$ ns, it can be applied to detect the present laser pulse, which is further confirmed in Fig. 14, where the FWHM is independent of crystal thickness and almost keeps a constant of  $\sim$ 20 ns in accord with the 248 nm laser duration.

It is well known that pure congruent  $\text{LiNbO}_3$  is a spontaneous polarisation crystal and there exists a spontaneous polarisation electric field (SPEF) along the  $c$  axis. In the experiment, the crystalline orientation is  $10^\circ$  miscut from the exact (001) orientation, so is SPEF as shown in Fig. 15. Under the 248 nm laser irradiation, photo-induced carriers are separated and assembled at the two electrodes by the SPEF. Only those carriers reaching to the electrodes in the back can be collected and give rise to photovoltaic signals. With decrease of crystal thickness the amount of carriers collected by electrodes in the back increases due to lower loss, which is resulted from the shorter transport distances as well as less traps and recombination in thinner samples. Thus the signals for thinner samples are much larger than that for thicker samples. On the other hand, the decrease of thickness also leads to decrease of autologous carriers in  $\text{LiNbO}_3$  single crystals, which limits the amount of carriers collected by electrodes. The competition between the two above factors results into a maximum photovoltaic signal at an optimum thickness at 0.38 mm.

### 3. Conclusion

The characteristics of the photovoltaic effect in  $\text{LiNbO}_3$  single crystals were presented in detail in this chapter. Vertical and lateral photovoltaic effects in pure congruent  $\text{LiNbO}_3$  crystals were observed by using pulsed and continuous wave lasers with inhomogeneous irradiation, respectively. The typical ultrafast response time and FWHM were about 2ns for the open-circuit photovoltaic pulse, indicating the potential applications of  $\text{LiNbO}_3$  single crystal as photoelectronic detector. The thickness dependence of the photovoltaic effect in miscut  $\text{LiNbO}_3$  single crystal was also investigated. With the decrease of the crystal thickness, the photovoltaic response time decreased monotonically, the photovoltaic sensitivity is improved rapidly at first, and then decreases. The experimental results show that decreasing the crystal thickness is an effective method for obtaining faster response time and improving the photovoltaic sensitivity in single crystals.

#### 4. Acknowledge

This work was supported by the Program for NCET, NSFC, RFDP, Beijing Natural Science Foundation, Foresight Fund Program from China University of Petroleum (Beijing).

#### 5. References

- Kong Y. F.; Xu J. J.; Zhang G. Y.; Liu S. M. & Lu Y. (2005), *Multifunctional photoelectric material: LiNbO<sub>3</sub> crystals*. Science Press, ISBN 7-03-013660-8, Beijing
- Wang, K.; Li, J. F. & Liu, N. (2008). Piezoelectric properties of low-temperature sintered Li-modified (Na, K)NbO<sub>3</sub> lead-free ceramics. *Appl. Phys. Lett.*, 93, 092904
- Chen, J.; Li, Y. D.; Lu, W. Q.; Qi, J. W.; Cui, G. X.; Liu, H. B.; Xu, J. J. & Sun, Q. (2007). Observation of surface-plasmon-polariton transmission through a silver film sputtered on a photorefractive substrate. *J. Appl. Phys.*, 102, 113109
- Sarkisov, S. S.; Curley, M. J.; Williams, E. K.; Ila, D.; Svetchnikov, V. L.; Zandbergen, H. W.; Zykov, G. A.; Banks, C.; Wang, J. C.; Poker, D. B. & Hensley, D. K. (2000). Nonlinear optical waveguides produced by MeV ion implantation in LiNbO<sub>3</sub>. *Nuclear Instruments and Methods in Physics Research Section B: Beam Interactions with Materials and Atoms*, 166-167, 750-757
- Kim, R. H.; Park, H. H. & Joo, G. T. (2001). The growth of LiNbO<sub>3</sub> (006) on MgO (001) and LiTaO<sub>3</sub> (012) substrates by sol-gel procedure. *Appl. Surf. Sci.*, 169-170, 564-569
- Zhen, X. H.; Zhang, X. J.; Zhao, L. C. & Xu, Y. H. (2003). Growth and optical properties of In:Nd:LiNbO<sub>3</sub> crystals. *Solid State Commun.*, 126, 203-206
- Pham, V. T.; Lee, S. K.; Trinh, M. T.; Lim, K. S.; Hamilton, D.S. & Polgár, K. (2005). Nonvolatile two-color holographic recording in Tm-doped near-stoichiometric LiNbO<sub>3</sub>. *Opt. Commun.*, 248, 89-96
- Liu, Y.; Kitamura, K.; Takekawa, S.; Ravi, G. & Nakamura, M. (2002). Nonvolatile two-color holography in Mn-doped near-stoichiometric lithium niobate. *Appl. Phys. Lett.*, 81, 2686-2688
- Zhou, Q. F.; Cannata, J. & Shung, K. K. (2006). Design and modeling of inversion layer ultrasonic transducers using LiNbO<sub>3</sub> single crystal. *Ultrasonics*, 44, e607-e611
- Karapetyan, K. G.; Kteyan, A. A. & Vardanyan, R. A. (2006) Thermal reduction effect on Curie temperature of LiNbO<sub>3</sub> ferroelectrics. *Solid State Commun.*, 140, 474-476
- Bermúdez, V.; Dutta, P. S.; Serrano, M. D. & Diéguez, E. (1996). In situ poling of LiNbO<sub>3</sub> bulk crystal below the Curie temperature by application of electric field after growth. *J. Crystal Growth*, 169, 409-412
- Bergman, J. G.; Askin, A.; Ballman, A. A.; Dziedzic, J. M.; Levinstein, H. J. & Smith, R. G. (1968). Curie temperature, birefringence, and refringence, and phase-matching temperature variations in LiNbO<sub>3</sub> as a function of melt stoichiometry. *Appl. Phys. Lett.*, 12, 92-95
- Beghou, M. R.; Boudrioua, A.; Kremer, R.; Fontana, M. D.; Fougere, B.; Darraud, C.; Vareille, J. C. & Moretti, P. (2008). Micro-Raman spectroscopy investigation of the electron beam irradiation of LiNbO<sub>3</sub> surface for 2D photonic band gap grating inscription. *Opt. Mater.*, 31, 136-142
- Bourim, E. M.; Moon, C. W.; Lee, S. W. & Yoo, I. K. (2006). Investigation of pyroelectric electron emission from monodomain lithium niobate single crystals. *Physica B*, 383, 171-182

- Boyd, G. D.; Miller, R. C.; Nassau, K.; Bond, W. L. & Savage, A. (1964). LiNbO<sub>3</sub>: an efficient phase matchable nonlinear optical material. *Appl. Phys. Lett.*, 5, 234-236
- Kaminow, I. P.; Turner, E. H.; Barns, R. L. & Bernstein, J. L. (1980). Crystallographic and electro-optic properties of cleaved LiNbO<sub>3</sub>. *J. Appl. Phys.*, 51, 4379-4384
- Wang, Q.; Lu, J. H.; Xiong, D. P.; Zhou, J.; Huang, H.; Miao, A.; Cai, S. W.; Huang, Y. Q. & Ren, X. M. (2007). Metamorphic In<sub>0.53</sub>Ga<sub>0.47</sub>As p-i-n photodetector grown on GaAs substrates by low-pressure MOCVD. *Chin. Opt. Lett.* 5, 358-360
- Jin, K. J.; Zhao, K.; Lu, H. B.; Liao, L. & Yang, G. Z. (2007). Dember effect induced photovoltage in perovskite p-n heterojunctions. *Appl. Phys. Lett.* 91, 081906
- Chen, F. S. (1969). Optically Induced Change of Refractive Indices in LiNbO<sub>3</sub> and LiTaO<sub>3</sub>. *J. Appl. Phys.*, 40, 3389-3397
- Dai, C.; Liu, L. R.; Liu, D. A. & Zhou, Y. (2005). Refractive-index change and sensitivity improvement in holographic recording in LiNbO<sub>3</sub>:Ce:Cu crystals with green light. *Chin. Opt. Lett.* 3, 507-510
- Razeghi, M. & Rogalski, A. (1996). Semiconductor ultraviolet detectors. *J. Appl. Phys.*, 79, 7433-7474
- Topic, M.; Stiebig, H.; Krause, M. & Wagner, H. (2001). Adjustable ultraviolet-sensitive detectors based on amorphous silicon. *Appl. Phys. Lett.*, 78, 2387-2390
- Tomm, J. W.; Ullrich, B.; Qiu X. G.; Segawa, Y.; Ohtomo, A.; Kawasaki, M. & Koinuma, H. (2000). Optical and photoelectrical properties of oriented ZnO films. *J. Appl. Phys.*, 87, 1844-1849
- Spaziani, F.; Rossi, M. C.; Salvatori, S.; Conte, G. & Ascarelli, P. (2003). Optimized spectral collection efficiency obtained in diamond-based ultraviolet detectors using a three-electrode structure. *Appl. Phys. Lett.*, 82, 3785-3788
- Lu, Z. Q.; Zhao, K.; Liu, H.; Zhou, N.; Gao, L.; Zhao, S. Q. & Wang, A. J. (2009). Fast lateral photovoltaic effect in ferroelectric LiNbO<sub>3</sub> single crystals. *Chin. Opt. Lett.*, 7, 718-719
- Li, X. M.; Wang, F.; Zhao, K. & Zhao, S. Q. (2010). Ultraviolet laser-induced photovoltaic effects in miscut ferroelectric LiNbO<sub>3</sub> single crystals. *Chin. Phys. B*, 19, 077801
- Wemple, S. H.; DiDomenico, M. & Camlibel, I. (1968). Relationship between linear and quadratic electro-optic coefficients in LiNbO<sub>3</sub>, LiTaO<sub>3</sub>, and other oxygen-octahedra ferroelectrics based on direct measurement of spontaneous polarization. *Appl. Phys. Lett.*, 12, 209-212
- Feng, H. X.; Wen, J. K.; Wang, H. & Wang, H. F. (1990). Studies of absorption spectra and the photovoltaic effect in LiNbO<sub>3</sub>:Mg:Fe crystals. *Appl. Phys. A*, 51, 394-397
- Glass, A. M.; D.von der Linde & Negran, T. J. (1974). High-voltage bulk photovoltaic effect and the photorefractive process in LiNbO<sub>3</sub>. *Appl. Phys. Lett.*, 25, 233-236
- Nakamura, M.; Takekawa, S.; Liu, Y.; Kumaragurubaran, S.; Babu, S. M.; Hatano, H. & Kitamura, K. (2008). Photovoltaic effect and photoconductivity in Sc-doped near-stoichiometric LiNbO<sub>3</sub> crystals. *Opt. Mater.*, 31, 280-283
- Schirmer, O. F. & Linde, D. von der (1978). Two-photon and x-ray-induced Nb<sup>4+</sup> and O-small polarons in LiNbO<sub>3</sub>. *Appl. Phys. Lett.*, 33, 35-39